



## TAGUCHI EXPERIMENTAL DESIGN AND ARTIFICIAL NEURAL NETWORK SOLUTION OF STUD ARC WELDING PROCESS

Prof.Dr. Nabeel K. Abid Al-sahib

M.s.C Riyadh M.A Hamza

Ass.prof.Dr. Ismail I.Al-kazaz

Baghdad University

Baghdad university

Baghdad university

Alkhwarzmi college of engineering

College of engineering

College of Engineering

Mechatronic Eng. Dept

Mechanical Eng. Dept

Mechanical Eng. Dept

### ABSTRACT

Stud arc welding has become one of the most important unit operations in the mechanical industries. The need to reduce the time from product discovery to market introduction is inevitable. Reducing of standard deviation of tensile strength with desirable tensile strength joint as a performance character was use to illustrate the design procedure. The effects of (welding time, welding current, stud material, stud design, sheet material, sheet thickness, sheet cleaning and preheating) were studied. Design of Experiment (DOE) is a structured and organized method to determine relationships between factors affecting a process and output of the process itself. In order to design the best formulation it is of course possible to use a trial and error approach but this is not an effective way. Systematic optimization techniques are always preferable. Tensile strength quality is one of the key factors in achieving good stud welding process performance. 225 samples of stud welding was tested. Computer aided design of experiment for the stud welding process based on the neural network artificial intelligence by Matlab V6.5 software was also explain. The ANN was designed to create precise relation between process parameters and response. The proposed ANN was a supervised multi-layer feed forward one hidden layer with 8 input (control process parameters), 16 hidden and 2 output (response variables) neurons. The learning rule was based on the Levenberg-Marquardt learning algorithm.

The work of stud welding was performed at the engineering college laboratory, Baghdad University by using the DABOTEKSTUD welding machine, for 6 mm diameter stud. The

sheet materials are (K14358 and K52355) according to (USN standards, and stud materials are (54NiCrMoS6 and 40CrMnMoS8-6) according to (DIN standards).

The eight control parameters (welding time, sheet thickness, sheet coating, welding current, stud design, stud material, preheat sheet and surface condition) were studied in the mixed L16 experiments Taguchi experimental orthogonal array, to determine the optimum solution conditions.

The optimum condition was reached for the stud welding process tensile strength, where the researcher develops a special fixture for this purpose. The analysis of results contains testing sample under optimum condition, chemical composition of usage materials and micro structure of optimal condition sample.

According to that:

- Practicality: the influence parameters that affect the stud welding process are welding time, which have a major effect on stud welding process, followed by sheet material and stud material.
- The reduction in standard deviation was approximately (30.06 per cent) and for the range was as approximately (29.39 per cent). In the other side the increase in the tensile strength mean was as approximately (30.84 per cent). The influence parameters that affect the tensile strength stud welding process are: the factor welding time has a major effect on stud welding process, followed by factor C (sheet coating) and factor F (stud material).

### الخلاصة

تصميم التجارب هو طريقة هيكلية وتنظيم لحساب العلاقات بين عوامل تؤثر في إجراء معين ومخرجات هذا الإجراء، لإجراء تصميم معين بأفضل صياغة من الممكن استخدام طريقة التجربة والخطأ ولكنه ليست بالطريقة الفعالة. طرق الأفضلية المنظمة هي أمثل دائماً، وقد تم اختيار 225 نموذج من هذا اللحام فيها.

مع التصميم بمعاونة الحاسوب للجانب العملي لتجارب إجراء لحام البرغي اعتماداً على الشبكات العقدية للذكاء الصناعي باستعمال البرنامج الجاهز (Matlab V6.5)، صممت الشبكات العقدية لخلق دقة أكثر بين العوامل ومخرجات الإجراء لتصميم تجارب تاكوجي. الشبكات العقدية المقترحة هي متعددة الطبقات أمامية موجهة وظفت في ثماني عقد مدخلات (عوامل السيطرة للإجراء)، 16 عقدة مخيفة وعقدتين خارجيتين (متغيرات الاستجابة). قاعدة التعلم اعتماداً على آلية (Levenberg – Marquardt) للتعلم.

باستعمال ماكينة لحام البراغي (DABOTEK) في هذه الدراسة للحام القوس البرغي قياس قطر 6 ملم. معادن الصفائح K14358 و K52355 نسبة إلى (USN) ومعادن البرغي هي 54NiCrMoS6 و 40CrMnMoS8-6 نسبة إلى (DIN). عوامل سيطرة ثمانية هي (زمن اللحام، سمك الصفائح، طلاء الصفائح، تيار اللحام، تصميم البرغي، معدن البرغي، التسخين المسبق وحالة السطح) درست في مصفوفة تصميم تجارب تاكوجي L16 المختلطة عولمت لحساب حالة الحل الأفضل، خطوات التطوير لتحسين طريقة تاكوجي هي خطوة تحليل بيانات التجربة. كان الانخفاض في الانحراف المعياري (30.06%) تقريباً وكان الانخفاض في المدى كان (29.39%) تقريباً. من ناحية أخرى كانت الزيادة في متوسط مقاومة الشد (30.84%) تقريباً. العوامل الأكثر تأثيراً على الإجراء هي زمن اللحام ويليه نوعية معدن الصفائح ثم نوعية معدن البرغي.

**KEY WORDS:** Taguchi experimental Design, Stud Welding Optimization, Artificial Neural Network, Stud Welding.

## INTRODUCTION

Stud arc welding is a widely used operation in mechanical structure, where high tensile strength with minimum variation required. The variation of tensile strength affects the cost of stud welding unit operations such as rework and time consume. These are often limiting steps in mechanical manufacturing processes; therefore, significant cost reduction can be realized by producing the stud welding joint having reliable tensile strength.( Jibson J 1979).

Usually, to find the influence of controlling parameter on welding process a large number of experiments are needed. In order to avoid this, two statistical methods can be used to design the optimum number of experiments. Classical design of experiments (DOE) emphasizes prediction of future behavior of experiments from empirical model while running a fraction of full factorial design .However; the classical DOE suffers the following limitations: two designs for the same experiment may yield different results and the designs normally do not permit determination of the contribution of each parameter. Taguchi DOE method, based on the classical one, is standardized design methodology that can easily be applied by investigators. Furthermore, designs for the same experiment by two different investigators will yield similar data and lead to similar conclusions. (Montgomery D.C 1985)

Allen T.T. and et at 2002, present optimizing process settings method which was developed and demonstrated for the application in robotic GMAW of sheet metal. The study it include an objective formulation that addressed variation of noise factors. The method and the formulation allow direct maximization of the travel speed of the welding robot. As the formulation was implemented with standard spreadsheet software packages since it was based on ordinary least-square regression so the method required no special software and minimal training. Kackar R.N. 1985, introduces the concepts of off-line quality control and parameter design and discusses the Tguchi method for conducting parameter design experiments. At the product design stage, the objective of parameter design is to identify settings of product characteristics, which make the product's performance less sensitive to the effects of environmental variables, deterioration, and manufacturing variations. Because parameter design reduces performance variation by reducing the influence of the sources of variation rather than by controlling them, off-line quality control reduces cost-effective for impro ing product quality. Ottoy K. N. and Antonsson E. K. 1991, Taguchi's method was extended to involve a more design variables together with more ranges for these variables. The method is also extended to solve design problems with constraints, invoking the methods of constrained optimization. Finally, the Taguchi method uses a factorial method to search the design space,

with a confined definition of an optimal solution. The method is compared with others for finding optimal solution. Accordingly, Taguchi method can be used instead of other different searching techniques. Galdmez E.V.C. and Carpinetti L.C.R. 2004, describe the application of the experimental of designs and analysis of variance in the process of manufacture of products for plastic injection modeling. The led experiments brought significant results, the adjustment considered, only two factors, injection pressure and temperature of the machine, the researchers presented a significant effect on the quality characteristic considered. Coit D. W. Jackson B. T. and Smith A. E. 1998, consider practical aspects of building and validating neural network models of manufacturing processes, and illustrate the recommended approaches with two diverse case studies. When using a neural network to control and optimize a manufacturing process, the integrity and balance of the training and validation data sets dictate the quality of the resultant model. The experimental data was combined with the production data. and neural networks were trained and validated on the combined data set. Su c. and Miao C. 1998, apply neural networks to analyze an experiment with singly censored data (incomplete data). Iwo procedures are developed; the first procedure is quite straightforward and can be easily used to rapidly determine the optimal condition. Hsu C.M.2001 ,proposes a four-phased procedure based on neural networks and principal component analysis to resolve the parameter design problems with multiple responses. The quality characteristics of a product are first evaluated through Taguchis quality loss function a neural model is then trained to map out the functional relationship between control factors and responses' quality loss. The functional relationship is then fed into the principal component analysis procedure to transfer a set of responses into a set of uncorrelated principal components. A feasible combination of control factors can be obtained through the recalling function of a neural model.

Once the variation of tensile strength was chosen as the main performance characteristic (the measure of quality) then the design factors, which will have an influence on it, have to be selected. Since most welding experiments usually involve a significant number of factors, according to the Taguchi method, the number of experiments can be reduced. Using a special orthogonal array only a small set from all the possible ones is selected. The sense of the orthogonal arrays method lies in choosing the level combinations of the design factors for each experiment. A practical definition of experimental design that can be applied to stud of 6 mm diameter arc welding process is presented in this study.

The survey shows this method has some weakness in the required number of experiments where it equals the number of inner array multiplied by the number of outer array that may cause higher number of experiments than that which is needed, The survey also shows that it



can make a good relationship between the input parameters and the output with minimum error by using neural network.

### **Taguchi Approach to Parameter Design**

Taguchi method provides a systematic and efficient approach for conducting experimentation to determine near optimum settings of design parameters for performance and cost. The method pushes quality back to the design stage, seeking to design a product/process, which is insensitive to quality problems. The Taguchi method utilizes orthogonal arrays to study a large number of variables with a small number of experiments. It can reduce research and development cost by simultaneously studying a large number of parameters. Using orthogonal arrays the method can significantly reduce the number of experimental configurations. In order to analyze the results, the Taguchi method uses a statistical measure of performance called 'signal-to-noise' ratio, (S/N) After performing the statistical analysis of S/N ratio, an analysis of variance (ANOVA) needs to be employed for estimating error variance and determining the relative importance of various factors. From their relative importance and from the S/N ratio, the optimum condition of factors is chosen. The result at this point is estimated using equation:

$$R=T+\Sigma(A_i-T)$$

Where:

R= predicate mean response at the optimal condition

T= overall mean of all observation in the data

A<sub>i</sub>= average value of significant factors at level i

### **Cause and Effect Diagram**

The total variation in the stud arc process may be due to any or a combination of the six sources (machine, measurement, method, material, manpower and environment). For this study of stud arc welding the effect of manpower on variation is limited because the machine is operating in a semiautomatic process, also the experiments have been executed in the laboratory environment, so it includes consider the first four, the other are ignored. Problem identification is very important for any industrial experiment. One of the most used methods for identifying the problem is brainstorming. Brainstorming is an activity that promotes team participation, encourages creative thinking and generates many ideas in a short period of time. For an investigation into the possible causes of the undesirable variability in stud welding process, a cause-and-effect diagram that lists several suspected causes of this variability, is shown in figure (1). Brainstorming in conjunction with cause and effect analysis (CEA) is used to identify the control factors which are to be considered for the experiment.

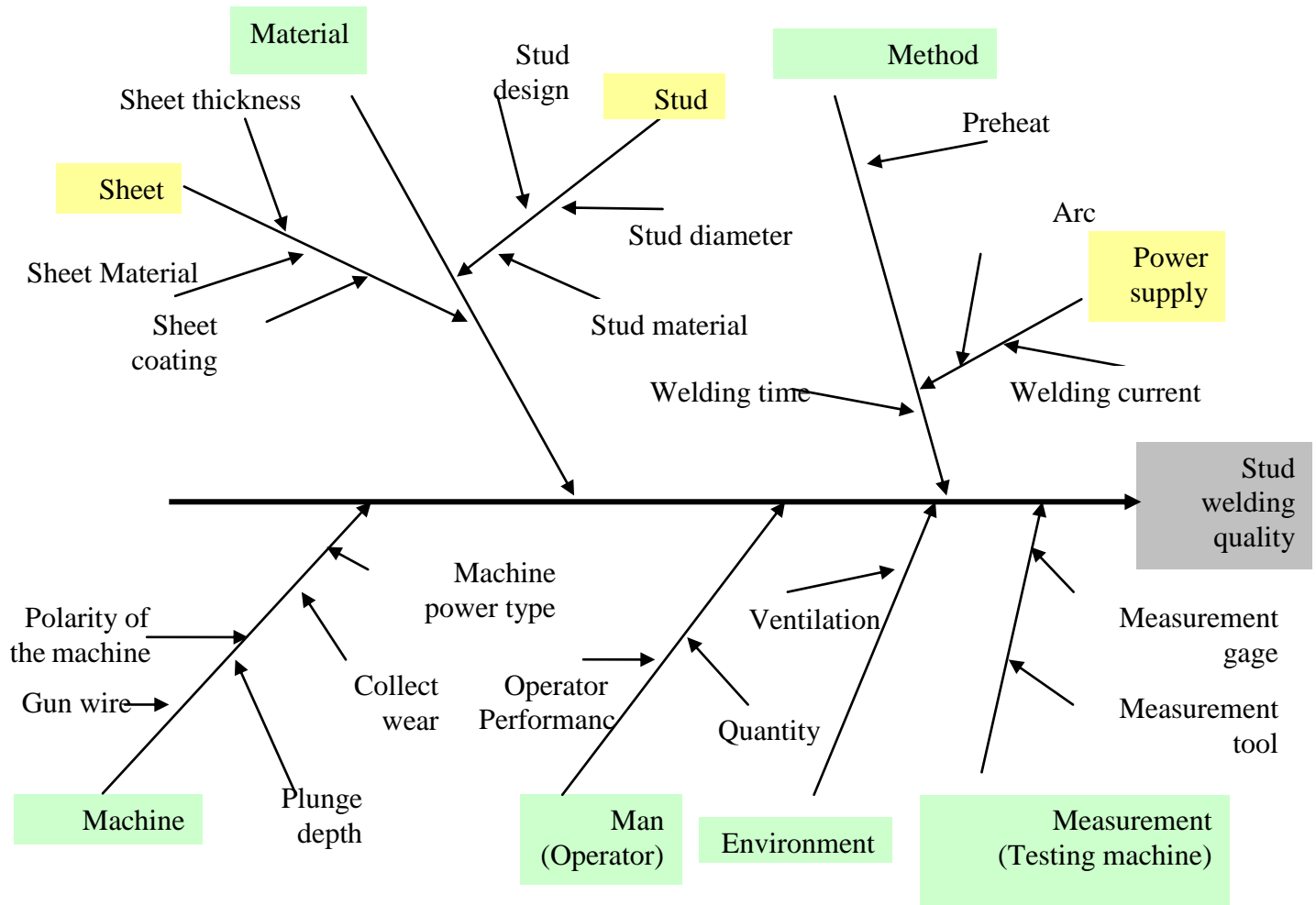


Figure (1) the suggested stud welding cause-and-effect diagram

## MATERIALS

The diameter of stud to be studied was (6 mm) that is widely used in the mechanical structure and also require low energy for welding from other stud diameter. For sheet, the first was galvanized (K52355 steel) and the second was non- galvanized (K14358steel), with two dimensions thickness gage 16 (1.6002 mm) and gage 12 (3.175 mm). For stud, the first was (54N1CrMoS6 steel) and the second was (40CrMnMoS8-6 steel).

### Method (Identification of Process Parameters)

There are (20) factors identified in this study. Eight independent control factors are considered to improve the stud welding process. These factors are (welding time, sheet thickness, sheet material, welding current, stud design, stud material, preheat sheet and surface cleaning). There other factors were classified as noise factors.

### Selection of Factor Levels and Range of Factor Setting

Once independent factors are decided, then the number level for each factor is selected. Selection of levels depends on how the outcome (tensile strength) is affected by different level settings.

Determining the number levels of selected factors from brainstorming is another major concern to many researchers in industries. Brainstorming session it was suggested that suitable to use eight factors on of them in multi-level. Seven of the eight control factors have two levels, and one has eight levels that is welding time.

After determining the number of levels required for each factor, it is needed to specify the range of operation for each control factor. It is usually best to experiment with the largest range feasible, so that the variation inherent in the process does not mask the factor effects on the response. The levels for welding time is shown in table (1), and the list of seven control factors and their level are shown in table (2).

Table (1) Levels of Welding Time Control Factor and for the Experiments

Factor	Factor label	Unit	Level 1	Level 2	Level 3	Level 4	Level 5	Level 6	Level 7	Level 8
Welding time (second)	A	second	0.15	0.2	0.25	0.3	0.35	0.4	0.45	0.5

Table (2) Control Factors and Levels for the Experiments

Factors	Factor labels	Unit	Level1	Level 2
Sheet thickness	B	mm	1.6	3.175
Sheet material	C	None	K52355	K14358
Welding current	D	Ampere	350	540
Stud design	E	None	Small stud	Flange stud
Stud material	F	None	54NiCrMoS6	40CrMnMoS8-6
Preheating	G	None	Preheating	No preheating
Surface cleaning	H	None	Oil sheet	Clean sheet

### Measurement (Tensile Testing Technique)

The response measurement should be well defined. This includes choosing the measurement and processing equipment to be used, how to measure, where to measure and where to document the data. The stud welding specimen is not the standard specimen tensile test dimension because one side is screw and the other is sheet, so the tensile testing was made by developing a special fixture for testing operation, special fixture is shown in figure (2):



Figure (2) the special fixture for the stud welding

### Design of Experiments

Normally, in the case of eight factors one of them in eight levels and other in two levels are  $8 \times 2^7 = 128$  experiments should be conducted. In accordance with the Taguchi's method the standard orthogonal array L16, with only 16 experiments (Table 3) could be used.

Table (3) code design matrix orthogonal array  $L_{16} 2^7 8^1$ .

run	welding time	sheet thickness	sheet material	welding current	stud design	stud material	preheat	surface cleaning
1	1	1	1	1	1	1	1	1
2	1	2	2	2	2	2	2	2
3	2	1	1	1	1	2	2	2
4	2	2	2	2	2	1	1	1
5	3	1	1	2	2	1	1	2
6	3	2	2	1	1	2	2	1
7	4	1	1	2	2	2	2	1
8	4	2	2	1	1	1	1	2
9	5	1	2	1	2	1	2	1
10	5	2	1	2	1	2	1	2
11	6	1	2	1	2	2	1	2
12	6	2	1	2	1	1	2	1
13	7	1	2	2	1	1	2	2
14	7	2	1	1	2	2	1	1
15	8	1	2	2	1	2	1	1
16	8	2	1	1	2	1	2	2

### Experimental Preparation and Process Run

The experimental preparation involves those activates that occur prior to actual running of the experiment. Poor preparation is the most frequent cause of inconclusive results. Errors in the experimental procedure this step can affect the experimental validity. The experiment of the study was conducted in a laboratory at which air conditioning is similar to outdoor environment. Also all the important material, machine was prepared in similar of an experimental area. In this step, the main task was to construct the uncoded design matrix for the experiment. The uncoded design matrix is shown table (4).

Table (4) uncoded design matrix array  $L_{16}2^78^1$

Run	welding time (second)	sheet thickness (mm)	sheet material	welding current (Ampere)	stud design	stud material	preheat	surface cleaning
1	0.15	1.6	K14358	350	Small	54NiCrMoS6	Preheat	Clean sheet
2	0.15	3.175	K52355	540	Large	40CrMnMoS8-6	No preh.	Oil sheet
3	0.2	1.6	K14358	350	Small	40CrMnMoS8-6	No preh.	Oil sheet
4	0.2	3.175	K52355	540	Large	54NiCrMoS6	Preheat	Clean sheet
5	0.25	1.6	K14358	540	Large	54NiCrMoS6	Preheat	Oil sheet
6	0.25	3.175	K52355	350	Small	40CrMnMoS8-6	No preh.	Clean sheet
7	0.3	1.6	K14358	540	Large	40CrMnMoS8-6	No preh.	Clean sheet
8	0.3	3.175	K52355	350	Small	54NiCrMoS6	Preheat	Oil sheet
9	0.35	1.6	K52355	350	Large	54NiCrMoS6	No preh.	Clean sheet
10	0.35	3.175	K14358	540	Small	40CrMnMoS8-6	Preheat	Oil sheet
11	0.4	1.6	K52355	350	Large	40CrMnMoS8-6	Preheat	Oil sheet
12	0.4	3.175	K14358	540	Small	54NiCrMoS6	No preh.	Clean sheet
13	0.45	1.6	K52355	540	Small	54NiCrMoS6	No preh.	Oil sheet
14	0.45	3.175	K14358	350	Large	40CrMnMoS8-6	Preheat	Clean sheet
15	0.5	1.6	K52355	540	Small	40CrMnMoS8-6	Preheat	Clean sheet
16	0.5	3.175	K14358	350	Large	54NiCrMoS6	No preh.	Oil sheet

The outer array of (12) noise factors with three combinations will be  $L_{16}$ , so the total number of runs to be conducted in this case would be  $16 \times 12 \times 2 = 384$  experiments as minimum. Performing of many unimportant experiments is costly and time consuming; the operating characteristic (OC) curve was used to develop the sample size. The experiment tensile outputs are shown in table (5)



Table (5) tensile strength runs

Run	actual run order	Tensile strength (N/mm <sup>2</sup> )						Mean N/mm <sup>2</sup>	Standard deviation N/mm <sup>2</sup>
1	5	175.73	213.23	143.66	195.09	210.50	155.60	182.302	28.860
2	9	288.70	251.20	330.40	284.99	225.90	300.70	280.315	36.946
3	13	284.39	198.56	225.89	245.87	276.24	263.54	249.082	32.539
4	3	359.99	420.50	428.42	300.03	387.38	367.54	377.310	46.790
5	12	190.70	245.87	235.90	298.46	164.33	289.46	237.453	52.977
6	11	370.45	392.68	191.74	360.38	288.70	383.26	331.202	77.637
7	8	321.60	139.00	349.05	310.00	362.93	457.50	323.375	104.318
8	1	331.96	326.32	331.15	401.60	387.26	314.78	348.828	36.095
9	4	388.10	233.60	372.20	287.95	225.43	278.00	297.547	68.611
10	2	530.00	460.72	549.85	375.12	410.53	375.89	450.352	76.343
11	15	305.40	383.20	456.00	378.00	478.00	375.00	395.933	62.388
12	7	152.09	160.74	170.76	166.80	250.88	132.45	172.287	40.835
13	16	219.19	152.97	250.85	257.16	266.78	198.75	224.283	43.258
14	10	155.65	180.45	289.40	220.68	225.35	248.78	220.052	47.705
15	14	289.36	215.62	318.43	256.84	288.23	145.63	252.352	62.900
16	6	185.32	178.45	223.21	155.82	298.33	188.43	204.927	50.651

### Analysis of variance

Equations for conducting the variance are presented in this section. Sum of squares ( $S_i$ ) of factor  $i$  at level  $k$  was calculated according to the equation:

$$S_i = \sum_k \frac{\left( \sum_j Y_{kj} \right)^2}{N_k} - \frac{\left( \sum_j Y_j \right)^2}{N}$$

Where,  $N$  is the total number of experiments.  $N_k$  the number experiments of each level and  $Y_j$  the mean response.

The total sum of squares ( $S_T$ ) was calculated using equation:

$$S_T = \sum_j Y_j^2 - \frac{\left( \sum_j Y_j \right)^2}{N}$$

Experimental error ( $S_e$ ) was calculated:

$$S_e = S_T - \sum S_i$$

Mean square of factor i ( $V_i$ ) was computed using the following equation:

$$V_i = \frac{S_i}{f_i}$$

Where,  $f_i$  is degree of freedom, which is one less than the number of levels. The total degree of freedom of the result ( $f_T$ ) is one less than the total number of experiments. The degree of freedom for error variance ( $f_e$ ) is the total degree of freedom minus sum of degree of freedom of factors. The next step was the calculation of the variance ratio ( $F_i$ ), which is the quotient of mean square of factor and error. The fraction of importance of each factor (in percents) was calculated according to the equation:

$$F_a = \frac{v_a}{v_e}$$

The variance ratio, commonly called F statistic (named after Sir Ronald A. Fisher), is the ratio of variance due to the effect of a factor and variance due to the error term. This ratio is used to measure the significance of the factors included in the error term. The F value obtained in the analysis of variance is compared with a value from standard F tables for a given statistical level of significance. Confidence interval, C.I., of the factor effect and estimated value of the result at the optimum condition was computed using the following equation:

$$\text{C.I. of } m = \hat{m} \pm \sqrt{\frac{F(\alpha, 1, f_2) \times v_e}{N_e}}$$

$F(\alpha, 1, f_2)$  = table value of F,  $\alpha$  significant level with 1 degree of freedom for the numerator and  $f_2$  degrees of freedom for the error term.

$v_e$  = error variance = MSE ,  $N_e$  = is effective number of replications ,Where each factor can be calculate from:

$$a = \left( \frac{s_a}{s_t} \right) \times 100, e = \left( \frac{s_e}{s_t} \right) \times 100$$

## Results and Discussion

After creating a Taguchi orthogonal array, the selected experiments were performed. A statistic analysis summary of the tensile strength, called S/N ratio, is employed to find the optimum level of the selected factors. The average s/n ratio of each run is shown in (Table 6).

$$S/N_{LTB} = -10 \log \left( \frac{\sum \frac{1}{y_i^2}}{n} \right)$$





Table (6) The SNR values for experimental trials

Trial no.	1	2	3	4	5	6	7	8	9	10	11	12	13	14	15	16
S/N (dB)	44.9	48.7	47.7	51.3	46.9	49.4	48.1	50.7	48.9	52.7	51.6	44.2	46.5	46.3	47.0	45.7

After obtaining the SNR values, the next step was to obtain the average response values of SNR at low and high levels of each factor and hence the effect of each factor on the SNR. The results are shown in table (7) and table (8).

Table ( 7) Average SNR Table for factor A

Factor A	Average SNR at level 1	Average SNR at level 2	Average SNR at level 3	Average SNR at level 4	Average SNR at level 5	Average SNR at level 6	Average SNR at level 7	Average SNR at level 8	Effect of the factor	rank
Factor Effect dB	46.83	49.53	48.19	49.43	50.84	47.96	46.41	46.38	4.52	1

Table (8) Average SNR Table for other factor

Factors	Average SNR at level 1 dB	Average SNR at level 2 dB	Effect of the factor dB	rank
B	47.73	48.69	0.96	6
C	47.10	49.31	2.21	2
D	48.18	48.23	0.05	8
E	48.23	48.46	0.23	7
F	47.41	49.00	1.69	3
G	48.98	47.43	-1.65	4
H	47.55	48.86	1.31	5

Tables (7) and (8) show that factors A and C have a dominant effect on the SNR, followed by factors F, G, H, B, F, and D. The main effects plot for the SNR is shown in figure (3).

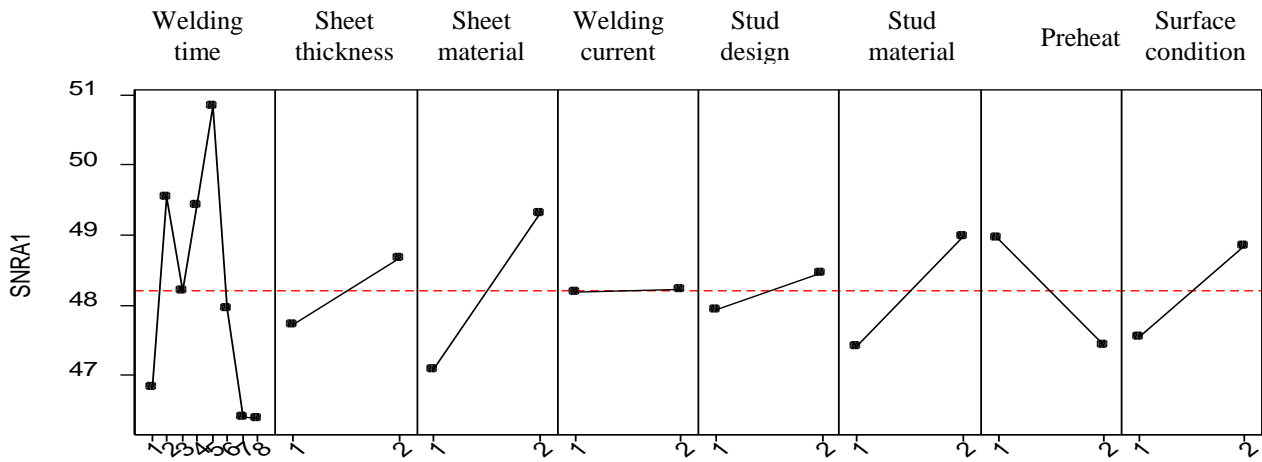


Figure (3) the main effects plot for S/N ratio

The relative magnitude of the effect of different factors can be obtained by decomposition of variance, called ANOVA (Table 9). The Sum of Squares column in Table (9) was calculated using equations (2), (3) and (4), the Mean Square column with equation (5) and the F-ratio column as calculated with equation (6). The ANOVA table has shown that the most dominant factor effects are D (welding current), E (stud design) and A (welding time). The optimal conditions setting of factors, which will maximize the SNR is (i.e. the best control factor settings) depend on the SNR are AS, 132. C2, D2, E2, F2, G1 and H2. The calculations of Analysis of Variance for the factors by using Matlab software are:

Table (9) ANOVA for the SNR

Source of variation	Sum of Squares	df	Mean Square	F-ratio
A	37.384	7	5.341	0.88
B	3.529	1	3.529	0.58
C	19.769	1	19.769	3.26
D	0.004	1	0.004	0.00
E	1.129	1	1.129	0.19
F	9.899	1	9.899	1.63
G	9.402	1	9.402	1.55
H	6.679	1	6.679	1.10
error	6.070	1	6.070	1
Total	93.865	15	6.257	



**Stage (2):** Performing the SNR analysis and (*S.D.*) analysis, then the next step was to identify the factor effects that have significant impact on the mean response. The average response values at each level of the factor A and the effects are present in table (10), and the average response values at low and high level for the other factors and their effects are present in table (11).

Table (10) the average response of welding time control factor

Factor A	Average mean at level 1	Average mean at level 2	Average mean at level 3	Average mean at level 4	Average mean at level 5	Average mean at level 6	Average mean at level 7	Average mean at level 8	Effect of the factor	rank
Factor Effect N/mm <sup>2</sup>	231.3	313.1	284.3	336.1	382.3	284.1	222.1	228.6	160.6	1

Table (11) the average response values at each level of the factors and their effects

Factors	Mean response at level 1 N/mm <sup>2</sup>	Mean response at level 2 N/mm <sup>2</sup>	Effect N/mm <sup>2</sup>	rank
B	270.29	298.16	29.96	6
C	257.07	313.47	56.4	3
D	278.73	291.81	13.08	8
E	278.43	292.11	13.68	7
F	255.61	314.93	59.32	2
G	310.17	260.37	-49.8	4
H	269.55	300.99	31.44	5

The main effects plot factor effects are illustrate in Figure (4).

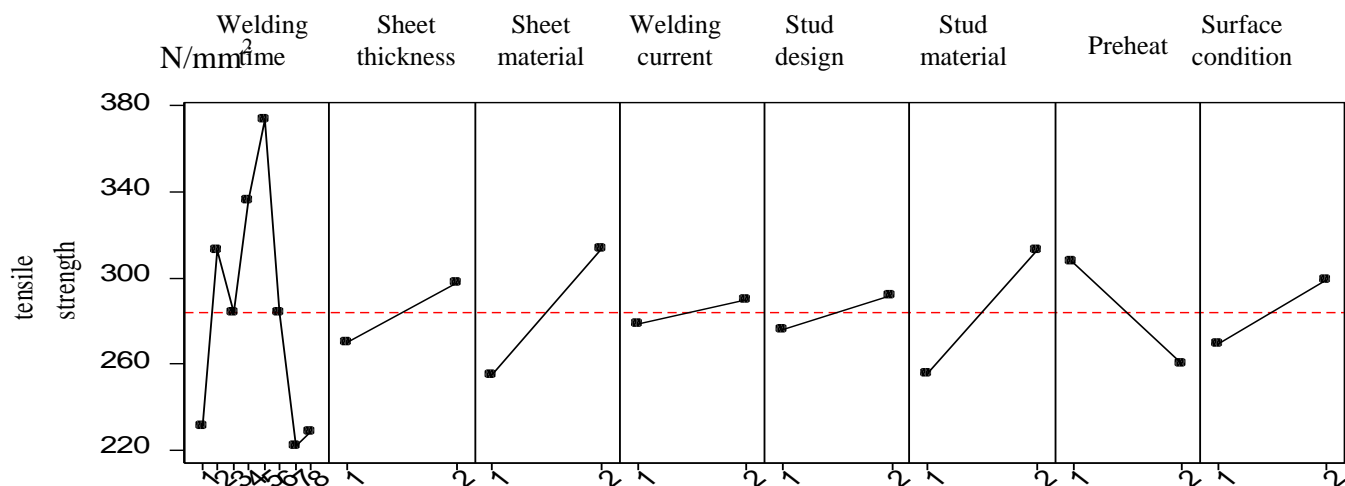


Figure (4) main effects plot for the mean response

Figure (4) shows factors A, C, E and F have a significant impact on the mean response (i.e. mean tensile strength). This will be followed by factors B, H, D and E.

The variance ratio (F-value statistic) represents the ratio of variance due to the effect of a factor and variance due to the error term. This ratio is used to measure the significance of factors included in the error term [17, 18]. The F value obtained in the analysis of variance is compared with a value from standard F tables, to decide significance of statistical level. It can be seen from table (12) that factor A (welding time) has a large affect on the mean of stud welding tensile strength (43.37° of fraction of importance). Value of factor C (sheet material) and F (stud material) are (13.84%). (13.53%) respectively.

Table (12) ANOVA for the response

Source of variation	Sum of Squares	df	Mean Square	F-ratio	Percent contribution (ρ)
A	42304.33	7	6043.48	42.35	43.37
B	3089.23	1	3089.23	21.6	3.17
C	13493.92	1	13493.92	95.14	13.84
D	519.19	1	519.19	3.35	0.53
E	1005.63	1	1005.63	63.25	1.04
F	13203.33	1	13203.33	91.04	13.53
G	8817.68	1	8817.68	63.25	9.05
H	3271.65	1	3271.65	23.94	3.35
error	11829.65	81	143.84	1	12.12
total	97534.58	95	1119.02	-	100

Added the factors B,D,E,G and H can be pooled. A new table without the above factors was constructed (table13)

Table (13) the pooled ANOVA for response

Source of variation	Sum of Squares	df	Mean Square	Variance ratio (F-ratio)	Percent contribution (ρ)
A	42644	7	6092	14.2	40.36
C	13686	1	13686	31.91	13.5
F	13095	1	13095	30.53	12.89
error	28779	86	428.86	1	33.25
total	98204	95	1033.72		100

The sum of squares of pooled factors was added to the error term, and then new mean square of the error term was calculated using equation:

$$V_e = \frac{\sum_i s_i^p + s_e}{\sum_i f_i^p + f_e}, \quad \text{Where superscript } p \text{ indicates the pooled factors.}$$

Since the degree of freedom of the factor A is 7 and for error term is 86, so,  $F_7 = 2.11$  at level of significance (95% confidence), see (F-table) (Fisher-table).

As the computed value of variance ratio (14.2), (table 13), is bigger than the value from (F table), so there is in 95% of confidence this factor A (welding time) has an effect on stud welding process. For (C and F) factors, the degree of freedom is 1 so the  $F_{1, 3.97}$ , since computed F-ratio are 31.91 and 30.53 respectively for each (table 13) which is higher than from F-table, then the above two factors also have an effect in the stud welding process, as well as for A.

After identifying the significant factor effects, the next step was to determine the optimal setting for these factors which will bring the mean response as close as possible to the target. The optimum condition (i.e. the best control factor settings) based on the mean response figure (4) was:

$$A_5, B_2, C_2, D_2, E_2, F_2, G_1 \text{ and } H_2.$$

Here the factors B, C, F and H are the same with the last setting (see stage one). While for factor A this is difference, when we choose A5 or A6, if choose A5 (the welding time is 0.35 second), then the tensile strength and standard deviation will be (382.341 N/mm<sup>2</sup> and 72.47 N/mm<sup>2</sup>) respectively, while when choose A6 (the welding time is 0.4 second), the tensile strength and standard deviation will be (284.110 N/mm<sup>2</sup> and 51.61 N/mm<sup>2</sup>). So, in this study an estimated of factor A (A6=0.38 second) is considered. For factor D, the mean and standard deviation of this factor, in level D1, is (278.73 N/mm<sup>2</sup>, 50.56 N/mm<sup>2</sup>) respectively, while them, in level D2, are (292.11 N/mm<sup>2</sup>, 58.04 N/mm<sup>2</sup>) respectively, so D1 would be considered. The same thing for factor E1. For factor G, the mean and standard deviation of this factor, in level G. are (310.17 N/mm<sup>2</sup>, 51.75 N/mm<sup>2</sup>) respectively, while them, in level C, are (260.37 N/mm<sup>2</sup>, 56.84 N/mm<sup>2</sup>) respectively, so C I would be considered. The factors levels are:

$$\hat{A}_6, B_2, C_2, D_1, E_1, F_2, G_1 \text{ and } H_2.$$

In order to reach the optimal factor settings, the factor setting that yields minimum quality loss can be study. The quality loss function for larger the better is:

$$L(y) = A_o \Delta_o^2 \frac{1}{y^2}$$

The summarized calculation is shown in table (14).

Table (14) loss function calculation

Run	(y <sup>^</sup> ) <sup>2</sup>	L(y)/K (money unit/piece)
<b>1</b>	<b>299094.4</b>	<b>3.3×10<sup>-6</sup></b>
2	202216.8	4.9×10 <sup>-6</sup>
3	230924.9	4.33×10 <sup>-6</sup>
4	125509.6	7.97×10 <sup>-6</sup>
5	243914.1	4.1×10 <sup>-6</sup>
6	163858.9	6.1×10 <sup>-6</sup>
7	174992.3	5.71×10 <sup>-6</sup>
8	145438.5	6.89×10 <sup>-6</sup>
9	190410.7	5.25×10 <sup>-6</sup>
10	83183.4	1.2×10 <sup>-5</sup>
11	160655.2	6.22×10 <sup>-6</sup>
12	290938.1	3.43×10 <sup>-6</sup>
13	256371.3	3.9×10 <sup>-6</sup>
14	260776.3	3.83×10 <sup>-6</sup>
15	230653.3	4.33×10 <sup>-6</sup>
16	276680.6	3.61×10 <sup>-6</sup>

From table (14), run (1) which represented in bold yield the minimum loss. Settings based on the loss-function analysis was therefore obtained as:

$$A_1, F_1, C_1, G_1 \text{ and } H_1$$

For factor A, level 1 will yield a very low tensile strength (182.302N/mm<sup>2</sup>), so this level is not taken. For the three factors F, C and G the level is the same, for factor H in level 1 the tensile strength is (269.55N/mm<sup>2</sup>), while in level 2 it is (300.99N/mm<sup>2</sup>) the reduction is also high, so the final optimum setting is:

$$\hat{A}_6, B_2, C_2, D_1, E_1, F_2, G_1 \text{ and } H_2.$$

**Predicted Mean Response at the Optimal Condition**

The predicted mean response at the optimal condition is estimated only from the significant main effects. The main factor effects, which has a significant impact on the mean response were A, F, C, C and H. The predicted mean response based on the optimal factor levels of A, F, C, C and H is given by:

$$R = T + (\bar{A} - T) + (C_2 - T) + (F_2 - T) + (G_1 - T) + (H_1 - T)$$

Where

R = predicted mean response at the optimal condition

T = overall mean of all observation in the data

$$R = 284.225 + (310.5 - 284.225) + (313.47 - 284.225) + (314.93 - 284.225) + (310.17 - 284.225) + (300.99 - 284.225)$$

$$R = 413.185 \text{ N/mm}^2$$

**Interpretation, Experimental Conclusions and Confidence Interval for the Predicted Mean Response**

After interpreted the results of the analysis, it is advisable to ensure that the experimental conclusions are supported by the data. The confidence interval is the variation of the estimated result at the optimum condition.

$$MSE = \text{error variance} = 143.84 \text{ N/mm}^2$$

$$F_{1,96} = 3.96$$

$$N_e = \frac{96}{7 + 1 + 1 + 1 + 1 + 1} = 8$$

Therefore, the 99 per cent confidence interval for the mean tensile strength is given by:

$$99 \text{ percent CI} = 413.185 \pm \sqrt{\frac{3.96 \times 143.84}{8}}$$
$$= 413.185 \pm 8.43 \text{ N/mm}^2$$

The result at the optimal condition is  $413.185 \pm 8.43 \text{ N/mm}^2$  at the 99 percent confidence level. After determination the confidence level for the predicate mean response, makes a confirmation experiment or run. The confirmation experiment/run is used to verify whether the predicated mean response based on the optimal combination of factor levels give process response within the confidence limits or not. If conclusive results are obtained from the confirmation run, a specific action on the process may be taken for improvement.

**Confirmation Run**

A confirmatory run/experiment (or follow-up experiment) is necessary in order to verify the results from the statistical analysis. This is to demonstrate that the factors and levels chosen for the influential factors do provide the desired results. The insignificant factors

should be set at their economic level during the confirmation run/experiment. If conclusive results have been obtained, improvement action on the product or process under investigation is recommended. On the other hand, if the result does not turn out as expected, further investigation may be required.

In industrial experiments, once the solution has been implemented, it is recommended to monitor the process by constructing control charts on the experiment's response variable (s) and critical factors that influence the response. Control charting will ensure that the problem does not reoccur [133]. For the study, the sample taken contains ten pieces were produced under the optimal condition that is in table (15):

Table (15): the optimum stud welding condition based on Taguchi methodology optimization

factor	level
$\hat{A}_6$ : welding time	0.38 second
$B_2$ : sheet thickness	3.175 mm
$C_2$ : sheet material	non- galvanized (K14358steel)
$D_1$ : welding current	350 Ampere
$E_1$ : stud design	Small stud
$F_2$ : stud material	40CrMnMoS8-6 steel
$G_1$	Preheating
$H_2$ : Surface cleaning	Clean sheet

The results are shown in table (16):

Table (16) the sample tensile strength based on Taguchi methodology optimization

Sample	Tensile strength N/mm <sup>2</sup>
1	443.52
2	421.32
3	410.63
4	390.48
5	472.40
6	422.67
7	398.93
8	431.88
9	408.33
10	524.55



The mean tensile strength from the confirmation run was 432.47 N/mm<sup>2</sup> the standard deviation is 39.950 N/mm<sup>2</sup> and the range is 134.07 N/mm<sup>2</sup>.

The effect of every factor of the study can be summarized as:

### **Welding Time**

This factor strongly effects on tensile strength measure. the mean value of tensile strength in levels (0.15 ,0.2 ,0.25 ,0.3 ,0.35 ,0.4 ,0.45 ,0.5) second is (231.3 ,313.196 ,284.32 ,336.1 ,373.95, 284.11 , 222.16 . 228.64) N/mm<sup>2</sup> respectively. The effect of factor on the mean is (42.3 9percent) which shows 110W much the variation of stud welding tensile strength from one level of welding time to another, The welding time has a relationship with the input energy rate; there is when the welding time increases the average input energy increases that lead to increase in tensile strength until value it decrease due to over energy.

### **Sheet Material**

Macrograph pictures show that the sheet material had two effects. First, galvanizing appeared to result in greater porosity in the joints. The mean of tensile strength in level 1(K52355) is 157.07 Nmm<sup>2</sup> and in level 2 (K14358) is 313.47 N/mm<sup>2</sup>. Also, there appeared to be considerably less heat and retained liquid metal in the joints on coated sheet. Second, the non-galvanized sheet (K14358stec1) indicates higher tensile strength, this may be due to the percentage of carbon contain (0.144%) is higher than for galvanized (K52355) sheet (0.0689%). The effect of factor on the mean tensile strength is (13.78percent).

### **Stud Material**

This factor also effects in the stud welding process, the different value of tensile strength call he shown from one level to another. The mean tensile strength in level 1(54NiCrMoS6) is 255.61 N/mm<sup>2</sup> and in level 2 (40CrMnMoS8-6) is 314.93 N/mm<sup>2</sup>.The effect of factor on the mean is (13.18percent). The higher value of strength for (40CrMnM0S8-6) from the strength for (54NiCrM0S6) may be due to the containing of carbon where for the first (0.229%) while for the second (0.139%) , as described previously for sheet material, and also due to other alloy elements for example tile percentage of Mg is (1.07%) ill 40CrMnMoS8-6 and (0.405%) in 54NiCrMoS6.

### **Preheating**

This factor gives a positive effect on both the increase of the tensile strength and a decrease in the variation of process. The mean tensile strength in level 1(preheating) is 310.17 N/mm<sup>2</sup> and in level 2 (no- preheating) is 260.37 N/mm<sup>2</sup> .The factor effect on the mean is (9.1 percent).

The base metal must be preheated to prevent the formation of cracks. This is similar to the effect on arc welding process for reducing heat effect (heat tear) that reducing the cooling rate for tile welding area and HAL which reducing the hardness of these areas especially when the carbon percentage more than 0,25 that yield hardness phases (without preheating). All oxyfuel gas heating torch is used for heating because only a localized preheated zone is needed; the preheating temperature is between (315-370) °C.

### **Stud Design**

The design of tile stud influenced the working area of the stud surface. This factor was found to completely dominate the tensile results. Despite of the fact that flange studs are going to have a greater area for welding and subsequently greater strengths, flange stud joints susceptible to porosity compared to smaller studs as micrographic pictures show, this appears to be due to a geometry effect. Tile mean of tensile strength in level 1 (small stud) is 278.43 N/mm<sup>2</sup> and in level 2 (flange stud) is 292.1 N/mm<sup>2</sup> Flange stud actually appeared to increase tensile strength performance and this is showing in many specimens but the variety is more may be due to preparing of flange stud is not at accuracy enough that causes porosity. The effect of this factor on the mean is (9.11 percent).

### **Surface Cleaning**

This factor has little effect on the measured tensile strength compared with tile previous factors; the effect of this factor on the mean is (3.36 percent). The mean of tensile strength in level 1 (oil sheet) is 269.55 N/mm<sup>2</sup> and in level 2 (clean sheet) is 300.99 N/mm<sup>2</sup> .The clean sheet already shows the greatest tensile strength and this is logic, but limited and which may be due to the welding area is small that lead to little effect.

### **Sheet Thickness**

Increasing sheet thickness has two effects; the first; a thicker sheet is stiffer during mechanical testing and this minimizes the peel characteristic of the tests and increases strength. The second thicker sheet present increase in the area of heat diffusion that lead to high cooling rate which creating inherently stronger welds. The mean of tensile strength in level 1 (1.6 mm) is 270.29 N/mm<sup>2</sup> and in level 2 (3.175 mm) is 298.16 N/mm<sup>2</sup> The effect of this factor on the mean is (3.0 percent).

### **Welding Current**

This factor has the smallest effect factor where the effect is (0.34 percent). The mean of tensile strength in level 1 (350 ampere) is 278.73 N/mm<sup>2</sup> and in level 2 (540 ampere) is 291.81 N/mm<sup>2</sup>. This result is far from the expected result where the welding current play important

role in arc welding process. But this happen here may be due to the two levels of welding current that choosing represent the boundaries of welding current, and there no intermediate grade between this two levels in the welding current selector of stud arc machine.

## CONCLUSIONS

The study has showed a significant improvement (approximately 30.84 percent) increase in stud joint tensile strength and (approximately 30.06 percent) decrease in stud joint tensile strength variation.

Measures of weld quality in this study included tensile strength testing and some macrograph photos. Statistical techniques used to produce a series of main effect plots for factors and results are analyzed. These robustness plots allowed direct observation of how weld quality measure was affected by each factor of interest. Specific conclusions from this study are as follows:

- Dominant factors in the Performance of Stud Welds - the dominated effective factors of stud welds performance are (welding time), (plate material) and (stud material) study.
- Effect of preheating plate - preheating has positive effects on the increasing of the tensile strength with reducing variability.
- Effect of Stud design - increasing stud area appeared to decrease of measures of tensile strength. This was true where the levels of internal porosity also increased with the larger studs.
- Effect of Plate Thickness - increasing thickness led to increases in mechanical measure (tensile strength) of weld quality. The benefits appeared to come from increased stiffness of the joint as well as increased peel strengths associated with the thicker material.
- Effect of Plate Material - Welding onto galvanized plates appears substantial porosity in the joint, so the non-galvanized plates obtain better tensile strength.
- Effect of Other Factors - weld quality measurements (tensile strength) as well as macrograph sections show the other factors in the study, welding current and the presence of surface cleaning, all had little effect.

## REFERENCES

- Jibson J.”Advance Welding”, John Wiley & Sons, 1997.
- Montgomery D.C” Design and Analysis of Experiments” Second Edition John Wiley & Sons, Inc., 2001.
- Montgomery D.C. "The Use of Statistical Process Control and Design of Experiments in Product and Process Improvement" JIB Transactions, Vol.24 No. 5. PP. 4-17, 1992.
- Montgomery D.C “Introduction to Statistical Quality Control” John Wiley & Sons, Inc.1985.
- Allen IT. and et al” Statistical Process Design for Robotic GMA We dipg of Sheet Metal” Welding Journal, PP.69-s\_77-s, May 2002.
- Kackar R.N.” Qft4Jng Quality Control, Parameter Decigppnd the Tagnehi ‘Vle/hod”. .1. Qual. Techn. , Vol. 17, No. 4, PP 176-188, 1985.
- Ottoy K. N. and Antonsson E. K.” Extensions to the Taguchi Method of Product ASME Journal of Mechanical Design. January 6, 1991.
- Galdmez E.V.C. and Carpinetti L.C.R. “Application as Design oLpgrimentu7 the Process of Manufcturing of Plastic Products”, ASME Journal of Manufacturing Science and Engineering, Vol. 122, PP. 360-369, 2004.
- Coit D. W. Jackson B. T. and Smith A. E.” Static Neural IVetwork Process Models: Considerations and Case Studies”. mt j. Prod. Res., Vol. 36. No. 11, 2953- 2967, 1998.
- Su C. and Miao C. “Neural Network\_Procedures fbr ExperpgjtilAigil.sisJ/h Censored Data”, International Journal of Quality Science, Vol.3, No.3, PP.239-253. 1998.
- Hsu C.M.” Solving Multi-Response Problems through Neural Networks aJgLj’il7cipp7 J22gnepd’ApqIJis”. Journal of the Chinese Institute of Industrial Engineers, Vol. 18. No. 5, pp. 47-54, 2001.
- Roy R., "Design of Experimental Using the Tagpchi Approach’ Wiley, New York, 2001.
- Montgomery D. C. “Design andAnalsis QjExperiments”. New York. Wiley. 1991.
- Buyske S. and Trout R.” Robust Design and Taguchi Methods” .Journal of Quality Technology, vol. 22, No. 1, PP. 15 22, Jan. 2003.
- Steiner 5.1-1. and MacKay R. J.” Statistical Engineering: an Algorithm far Reducing Variation in Majfpcturing Processes” American Society for Quality ASQ, 2005.
- Taguchi G. and Yokoyama Y.” Taguchi Method’s: Design of Experiments “Quad ity Engineering, Vol.4, Dearbon, MI, 1993.
- Mukhopadhyay S. K. and Chakraborty D. “Optimal Process Variance under Tqggjj Loss” International Journal of Quality & Reliability Management. Vol. 12 No. 9, PP. 14-29, 1995.
- Antony J. and et al “Process Optimization using Taguchi Me1fpfExperimeJ7/ul çin” Work Study, Volume 50, Number 2, PP. 51-57, 2001.
- Lofthouse T. “The Taguchi Loss Function” Work Study, Volume 48, Number 6. PP. 218-222, 1999.



## BENDING MOMENT INFLUENCE SURFACES FOR RECTANGULAR CONCRETE PLATES SIMPLY SUPPORTED AT THREE EDGES AND BUILT-IN AT THE FOURTH EDGE

Sabah S. Razouki

Prof. of Civil Engineering College of Engineering, Nahrain University, Baghdad-Iraq.

Zena R. Al-Ani

Assistant Lecturer in Civil Engineering, College of Engineering, Nahrain University, Baghdad-Iraq.

### ABSTRACT

Presented in this paper is a series of bending moment influence surfaces for concrete rectangular plates simply supported at three edges and built-in at the fourth edge. The solutions are obtained analytically on the basis of thin plate's theory with small deflection using double Fourier series. The influence surfaces are presented for two observation points namely the center of the plate as well as the midpoint of the built-in edge. A computer program was written in FORTRAN language to generate the influence surfaces making use of the developed analytical solutions of this work. The validity of the computer solution was confirmed by comparing its results with published results for zero Poisson's ratio and excellent agreement was obtained. An application of the influence surfaces for the case of a line load as well as a strip load is also presented.

The paper reveals that the bending moment influence surfaces depend on the actual value of Poisson's ratio, aspect ratio of the plate, and position of the observation point.

### الخلاصة

يقدم هذا البحث حلولاً تحليلية لسطوح التأثير لعزوم الانحناء لألواح كونكريتية مستطيلة بسيطة الاسناد في ثلاثة حافات ومثبتة في حافتها الرابعة اعتماداً على نظرية الألواح النحيفة ذات الأود القليل. أن سطوح التأثير التي تم تطويرها في هذا البحث، قد خصصت لإيجاد عزوم الانحناء في نقطتين من نقاط الملاحظة: الأولى في مركز اللوح والثانية في نقطة الوسط للحافة المبنية.

لقد تم كتابة برنامج على الحاسبة بلغة الفورتران لغرض إيجاد سطوح الانحناء وذلك بالاعتماد على الحلول التحليلية التي تم تطويرها في هذا البحث.

أظهرت مقارنة النتائج للحلول التحليلية التي طورت في هذا العمل توافقاً ممتازاً مع نتائج حلول متوفرة لنسبة بوسون تساوي صفر.

ان البحث يبين بأن سطوح التأثير لعزوم الانحناء تعتمد على نسبة بوسون والنسبة بين أبعاد اللوح (الطول/العرض) و موقع نقاط الملاحظة.

**KEYWORDS:** aspect ratio, bending moment, influence surfaces, plates, Poisson's ratio.

## INTRODUCTION

For bridge decks, the types of construction are divided into beam, grid, slab, beam and slab, and cellular. A slab deck behaves like a flat plate which is structurally continuous for the transfer of moments and torsions in all directions within the plane of the plate (**Hambly, 1976**).

In bridge design, the most important and most difficult task faced by the structural designer is the accurate estimation of the loads, which may be applied to a structure during its life. After loads are estimated the next problem is to decide the worst possible combinations of these loads which might occur at one time (**McCormac, 1989**). The concept of considering an actual bridge deck as an equivalent plate for the purpose of determining the distribution of stresses is well established (**Cusens and Pama, 1975**).

Influence lines can be used for two very important purposes (**Merritt, 1999**); the first purpose is, to determine what position of live loads will lead to a maximum value of the particular function for which an influence line has been constructed. The second purpose is the value of that function with the load so placed or, in fact, for any loading condition.

The influence surface represents a two-dimensional analogue of the one-dimensional influence lines. They are independent of the mode of loading and can be evaluated easily for each load case, for plane structures which are indispensable for the analysis of bridge structures (**Pucher, 1973**).

**Pucher (1973)** obtained influence surfaces for the internal forces of various plates but they are restricted to Poisson's ratio equal to zero with length to width ratio equal to 0.8, 1.0, and 1.2.

**Timoshenko and Woinowsky –Krieger (1989)** presented analytical results for the bending moments of rectangular plates with various edge conditions and a Poisson's ratio of 0.3.

**Razouki and Al-Lami (2005)** studied the effect of Poisson's ratio on the bending moment influence surfaces for simply supported rectangular plates. Also **Razouki and AL-Ani (2006)** studied the effect of Poisson's ratio on the bending moment influence surfaces for rectangular plates simply supported at two parallel edges and fixity at the other opposite edges.

It is worth mentioning that the software **LARSA** can deal with influence surfaces of plate-deck models using standard and new two-dimensional vehicle definitions that model both the length and width of the vehicle and tire contact area.



Finally, it is useful to note that **Boyd et.al (1999)** and **Wang et.al (2000)** made use of the influence surface theory of thin plate for representing mathematically the human knee joint surfaces.

### **POISSON'S RATIO:**

The Poisson's ratio of concrete is a basic function in analyzing and designing prestressed and ordinary reinforced concrete plates and shells (**Klink, 1985**).

**Francis et.al. (1991)** stated that Poisson's ratio was found to be insensitive to the age and the richness of concrete mix and may be taken as approximately 0.19 for concrete. According to **ACI Committee 363 (1984)**, the value for Poisson's ratio of light weight aggregate high strength concrete is equal to 0.2 and for normal weight high strength concretes, Poisson's ratio varies between 0.2 and 0.28.

According to **Kupfer and Gerstle (1973)**, Poisson's ratio for concrete shows some dependency on the stress ratios. They obtained a value of 0.2 for biaxial compression, 0.18 for biaxial tension and a range of 0.18 to 0.2 for tension compression state of stress. **Neville and Brooks (1987)** pointed out that Poisson's ratio for concrete has been observed to remain approximately constant up to a stress level of 80% of the concrete strength. Beyond this level, Poisson's ratio increases rapidly and values in excess of 1.0 have been measured by **Darwing and Pecknold (1977)**. **Mirza et.al (1979)** reported that Poisson's ratio under uniaxial tension is somewhat lower than in uniaxial compression. For the purpose of analysis in this work, the value of Poisson's ratio to be considered for concrete is 0.2. However, the analysis remains valid for any other material having a Poisson's ratio close to that for concrete.

### **KIRCHHOFF-LOVE THEORY OF THIN PLATES :**

**Timoshenko and Woinowsky –Krieger (1989)** differentiate between thin plate theory with small deflection and that for large deflection.

However, **Zehender et.al (1998)** reported that the crack tip stress field in a plate described in terms of the small deflection Kirchhoff plate theory is still valid for large deflections.

Thus , the use of thin plate with small deflection is quite justified.

According to **Szilard (1974)**, the small deflection plate theory which is attributed to Kirchhoff and Love, is governed by the following differential equation describing the behavior of isotropic plate which was obtained by Lagrange in 1811 (**Timoshenko and Woinowsky –Krieger , 1989**)

$$\frac{\partial^4 w}{\partial x^4} + 2 \frac{\partial^4 w}{\partial x^2 \partial y^2} + \frac{\partial^4 w}{\partial y^4} = \frac{q(x, y)}{D} \quad (1)$$

where

w=lateral displacement of the plate.

q(x, y)= intensity of lateral load.

D= flexural rigidity of the plate.

$$D = \frac{Eh^3}{12(1-\nu^2)} \quad (2)$$

E=modulus of elasticity of the plate material.

h=plate thickness.

$\nu$ =Poisson's ratio of the plate material.

The bending and twisting moments can be obtained in terms of deflection surface as follows  
(Timoshenko and Woinowsky –Krieger,1989):

$$\left. \begin{aligned} M_x &= -D \left( \frac{\partial^2 w}{\partial x^2} + \nu \frac{\partial^2 w}{\partial y^2} \right) \\ M_y &= -D \left( \frac{\partial^2 w}{\partial y^2} + \nu \frac{\partial^2 w}{\partial x^2} \right) \\ M_{xy} &= -M_{yx} = D(1-\nu) \frac{\partial^2 w}{\partial x \partial y} \end{aligned} \right\} \quad (3)$$

where

$M_x$ =bending moment per unit length acting on the sections parallel to the y- axis.

$M_y$ =bending moment per unit length acting on the sections parallel to the x- axis.

$M_{xy}, M_{yx}$ = Twisting moment per unit length of sections perpendicular to the x and y axes respectively.

According to **Timoshenko and Woinowsky-Krieger (1989)**, the analytical solution for rectangular plates simply supported at three edges and built-in at the fourth edge as shown in Fig.1 can be determined by superposition approach .This approach makes use of Navier solution and Levy solution for simply supported plate at all four edges as discussed below.

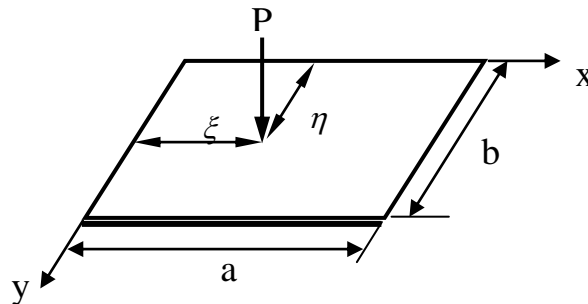


**Fig.1 point load on the plate.**



## BENDING MOMENTS FOR RECTANGULAR LOADED AREA ON THE PLATES:

Various methods of solution of the plate equation are available (**Girkmann 1963; Szilard 1974 and Taylor and Govindgee 2002**). However, the double Fourier series is adopted in this work as it ensures convergence.

For a simply supported rectangular plate at four edges subjected to rectangular loaded area as shown in Fig.2, **Timoshenko and Woinowsky-Krieger (1989)** stated that the deflected surface  $w_1(x, y)$  is

$$w_1(x, y) = \frac{16q_0}{\pi^6 D} \sum_{m=1}^{\infty} \sum_{n=1}^{\infty} \frac{\sin \frac{m\pi\xi}{a} \sin \frac{n\pi\eta}{b} \sin \frac{m\pi u}{2a} \sin \frac{n\pi v}{2b} \sin \frac{m\pi x}{a} \sin \frac{n\pi y}{b}}{mn \left[ \frac{m^2}{a^2} + \frac{n^2}{b^2} \right]^2} \quad (4)$$

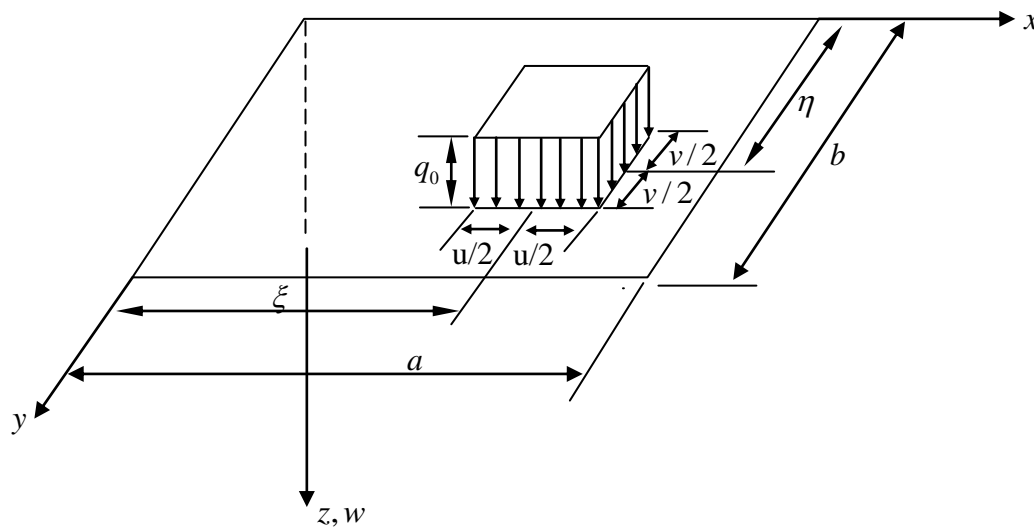


**Fig.2 simply supported rectangular plate with uniform loading on a rectangular area**

$a$ = the length of built-in edge.

$b$ = the dimension of the plate perpendicular to built-in edge.

The deflected surface for a simply supported rectangular plate subjected to distributed moment at the edge  $y_2=b/2$  as shown in Fig.3 becomes (**Timoshenko and Woinowsky-Krieger, 1989**):

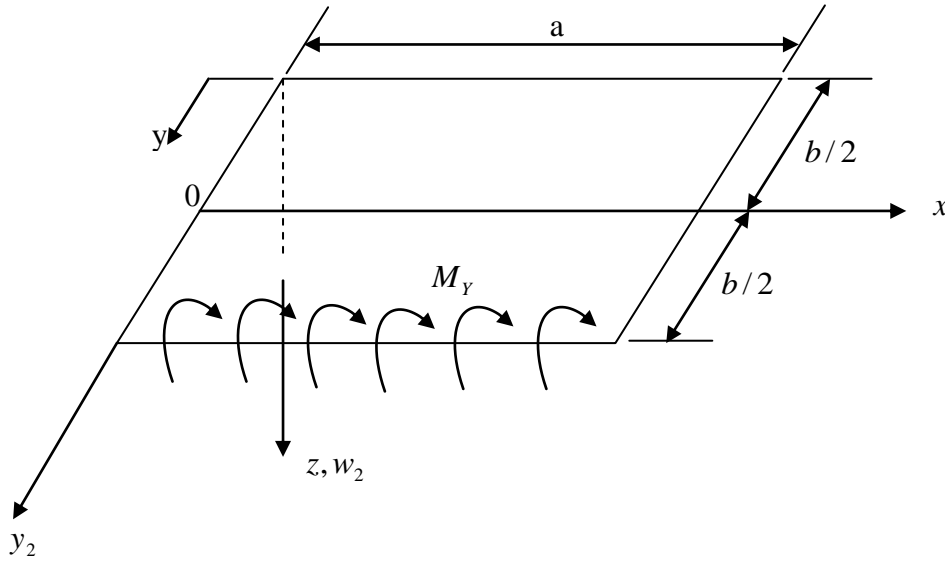


**Fig.3 distributed moment at the built-in edge  $y_2 = b/2$  after Szilard (1974)**

$$w_2(x, y) = \frac{a^2}{4\pi^2 D} \sum_{m=1}^{\infty} \frac{E_m \sin \frac{m\pi x}{a}}{m^2} \left[ \frac{1}{\cosh \alpha_m} \left( \alpha_m \tanh \alpha_m \cosh \frac{m\pi y_2}{a} - \frac{m\pi y_2}{a} \sinh \frac{m\pi y_2}{a} \right) + \frac{1}{\sinh \alpha_m} \left( \alpha_m \coth \alpha_m \sinh \frac{m\pi y_2}{a} - \frac{m\pi y_2}{a} \cosh \frac{m\pi y_2}{a} \right) \right] \quad (5)$$

where

$$y_2 = y - b/2$$

$$\alpha_m = \frac{m\pi b}{2a} \quad (6)$$

$E_m$  = coefficients of a single sine series of distributed moment at the edge  $y_2 = b/2$

The parameter  $E_m$  can be determined by using the condition at built-in edge which indicates that the two slopes are equal in magnitude and of opposite signs.

This means

$$\left( \frac{\partial w_1}{\partial y} \right)_{(x, y=b)} = - \left( \frac{\partial w_2}{\partial y_2} \right)_{(x, y_2=b/2)} \quad (7)$$

The slope  $\frac{\partial w_1}{\partial y}$  produced by rectangular loaded area can be determined from Eq.(4) as follows :

$$\left( \frac{\partial w_1}{\partial y} \right)_{y=b} = \frac{16q_0}{\pi^5 b D} \sum_{m=1}^{\infty} \sum_{n=1}^{\infty} \frac{\sin \frac{m\pi \xi}{a} \sin \frac{n\pi \eta}{b} \sin \frac{m\pi u}{2a} \sin \frac{n\pi v}{2b} \sin \frac{m\pi x}{a} \cos n\pi}{m \left[ \frac{m^2}{a^2} + \frac{n^2}{b^2} \right]^2}$$

The distributed moment  $M_y$  at the side  $y_2=b/2$  shown in Fig.2 produces the following slope from Eq.(5):

$$\left(\frac{\partial w_2}{\partial y_2}\right)_{y_2=b/2} = \frac{a}{4\pi D} \sum_{m=1}^{\infty} \frac{E_m \sin \frac{m\pi x}{a}}{m} \left[ \frac{1}{\cosh \alpha_m} \left( \alpha_m \tanh \alpha_m \sinh \frac{m\pi b}{2a} - \sinh \frac{m\pi b}{2a} - \frac{m\pi b}{2a} \cosh \frac{m\pi b}{2a} \right) + \right. \\ \left. \frac{1}{\sinh \alpha_m} \left( \alpha_m \coth \alpha_m \cosh \frac{m\pi b}{2a} - \cosh \frac{m\pi b}{2a} - \frac{m\pi b}{2a} \sinh \frac{m\pi b}{2a} \right) \right]$$

where {see Eq.(6)}

$$\alpha_m = \frac{m\pi b}{2a}$$

The substitution into above equation yields

$$\left(\frac{\partial w_2}{\partial y_2}\right)_{y_2=b/2} = \frac{a}{4\pi D} \sum_{m=1}^{\infty} \frac{E_m \sin \frac{m\pi x}{a}}{m} (\alpha_m \tanh^2 \alpha_m - \tanh \alpha_m + \alpha_m \coth^2 \alpha_m - \coth \alpha_m - 2\alpha_m) \quad (8)$$

Then,  $E_m$  can be obtained from the condition of Eq.(7) as follows:

$$E_m = \frac{-64 q_0 a^3}{\pi^4 b} \sum_{n=1}^{\infty} \frac{\sin \frac{m\pi \xi}{a} \sin \frac{n\pi \eta}{b} \sin \frac{m\pi u}{2a} \sin \frac{n\pi v}{2b} \cos n\pi}{\left[ m^2 + \frac{n^2 a^2}{b^2} \right]^2 (\alpha_m \tanh^2 \alpha_m - \tanh \alpha_m + \alpha_m \coth^2 \alpha_m - \coth \alpha_m - 2\alpha_m)} \quad (9)$$

or

$$E_m = \frac{-64 Pa^3}{\pi^4 buv} \sum_{n=1}^{\infty} \frac{\sin \frac{m\pi \xi}{a} \sin \frac{n\pi \eta}{b} \sin \frac{m\pi u}{2a} \sin \frac{n\pi v}{2b} \cos n\pi}{\left[ m^2 + \frac{n^2 a^2}{b^2} \right]^2 (\alpha_m \tanh^2 \alpha_m - \tanh \alpha_m + \alpha_m \coth^2 \alpha_m - \coth \alpha_m - 2\alpha_m)} \quad (10)$$

Thus, the bending moments can be obtained as follows:{ see Eq.(3)}

$$M_x = \frac{16 q_0 a^2}{\pi^4} \sum_{m=1}^{\infty} \sum_{n=1}^{\infty} \frac{\left[ m^2 + \nu \frac{n^2 a^2}{b^2} \right] \sin \frac{m\pi \xi}{a} \sin \frac{n\pi \eta}{b} \sin \frac{m\pi u}{2a} \sin \frac{n\pi v}{2b} \sin \frac{m\pi x}{a} \sin \frac{n\pi y}{b}}{mn \left[ m^2 + \frac{n^2 a^2}{b^2} \right]^2} + \\ \frac{1}{4} \sum_{m=1}^{\infty} E_m \sin \frac{m\pi x}{a} \left[ \frac{1}{\cosh \alpha_m} \left\{ (1-\nu) \left( \alpha_m \tanh \alpha_m \cosh \frac{m\pi y_2}{a} - \frac{m\pi y_2}{a} \sinh \frac{m\pi y_2}{a} \right) + 2\nu \cosh \frac{m\pi y_2}{a} \right\} + \right. \\ \left. \frac{1}{\sinh \alpha_m} \left\{ (1-\nu) \left( \alpha_m \coth \alpha_m \sinh \frac{m\pi y_2}{a} - \frac{m\pi y_2}{a} \cosh \frac{m\pi y_2}{a} \right) + 2\nu \sinh \frac{m\pi y_2}{a} \right\} \right] \quad (11)$$

$$M_y = \frac{16q_0a^2}{\pi^4} \sum_{m=1}^{\infty} \sum_{n=1}^{\infty} \left[ \frac{\left[ \nu m^2 + \frac{n^2 a^2}{b^2} \right] \sin \frac{m\pi\xi}{a} \sin \frac{n\pi\eta}{b} \sin \frac{m\pi u}{2a} \sin \frac{n\pi v}{2b} \sin \frac{m\pi x}{a} \sin \frac{n\pi y}{b}}{mn \left[ m^2 + \frac{n^2 a^2}{b^2} \right]^2} + \right. \\ \left. \frac{1}{4} \sum_{m=1}^{\infty} E_m \sin \frac{m\pi x}{a} \left[ \frac{1}{\cosh \alpha_m} \left\{ (\nu - 1) \left( \alpha_m \tanh \alpha_m \cosh \frac{m\pi y_2}{a} - \frac{m\pi y_2}{a} \sinh \frac{m\pi y_2}{a} \right) + 2 \cosh \frac{m\pi y_2}{a} \right\} + \right. \right. \\ \left. \left. \frac{1}{\sinh \alpha_m} \left\{ (\nu - 1) \left( \alpha_m \coth \alpha_m \sinh \frac{m\pi y_2}{a} - \frac{m\pi y_2}{a} \cosh \frac{m\pi y_2}{a} \right) + 2 \sinh \frac{m\pi y_2}{a} \right\} \right] \right] \quad (12)$$

To have a good check on the results obtained, use can be made of the case of full uniform loading over the whole plate treated by **Timoshenko and Woinowsky –Krieger (1989)** for which they presented the bending moments at the midpoint of the built-in edge and at the middle of the plate. For the case of full load  $u=a$ ,  $v=b$  and equations (11) and (12) give the dimensionless bending moments

$$m_x = \frac{M_x}{q_0 a^2} = \frac{16}{\pi^4} \sum_{m=1}^{\infty} \sum_{n=1}^{\infty} \left[ \frac{\left[ m^2 + \nu \frac{n^2 a^2}{b^2} \right] \sin \frac{m\pi\xi}{a} \sin \frac{n\pi\eta}{b} \sin \frac{m\pi}{2} \sin \frac{n\pi}{2} \sin \frac{m\pi x}{a} \sin \frac{n\pi y}{b}}{mn \left[ m^2 + \frac{n^2 a^2}{b^2} \right]^2} + \right. \\ \left. \frac{1}{4} \sum_{m=1}^{\infty} E_m^* \sin \frac{m\pi x}{a} \left[ \frac{1}{\cosh \alpha_m} \left\{ (1 - \nu) \left( \alpha_m \tanh \alpha_m \cosh \frac{m\pi y_2}{a} - \frac{m\pi y_2}{a} \sinh \frac{m\pi y_2}{a} \right) + 2 \nu \cosh \frac{m\pi y_2}{a} \right\} + \right. \right. \\ \left. \left. \frac{1}{\sinh \alpha_m} \left\{ (1 - \nu) \left( \alpha_m \coth \alpha_m \sinh \frac{m\pi y_2}{a} - \frac{m\pi y_2}{a} \cosh \frac{m\pi y_2}{a} \right) + 2 \nu \sinh \frac{m\pi y_2}{a} \right\} \right] \right] \quad (13)$$

$$m_y = \frac{M_y}{q_0 a^2} = \frac{16}{\pi^4} \sum_{m=1}^{\infty} \sum_{n=1}^{\infty} \left[ \frac{\left[ \nu m^2 + \frac{n^2 a^2}{b^2} \right] \sin \frac{m\pi\xi}{a} \sin \frac{n\pi\eta}{b} \sin \frac{m\pi}{2} \sin \frac{n\pi}{2} \sin \frac{m\pi x}{a} \sin \frac{n\pi y}{b}}{mn \left[ m^2 + \frac{n^2 a^2}{b^2} \right]^2} + \right. \\ \left. \frac{1}{4} \sum_{m=1}^{\infty} E_m^* \sin \frac{m\pi x}{a} \left[ \frac{1}{\cosh \alpha_m} \left\{ (\nu - 1) \left( \alpha_m \tanh \alpha_m \cosh \frac{m\pi y_2}{a} - \frac{m\pi y_2}{a} \sinh \frac{m\pi y_2}{a} \right) + 2 \cosh \frac{m\pi y_2}{a} \right\} + \right. \right. \\ \left. \left. \frac{1}{\sinh \alpha_m} \left\{ (\nu - 1) \left( \alpha_m \coth \alpha_m \sinh \frac{m\pi y_2}{a} - \frac{m\pi y_2}{a} \cosh \frac{m\pi y_2}{a} \right) + 2 \sinh \frac{m\pi y_2}{a} \right\} \right] \right] \quad (14)$$

Arly Eq.(10) becomes

$$E_m^* = \frac{E_m}{q_0 a^2} = \frac{-64a}{\pi^4 b} \sum_{n=1}^{\infty} \frac{\sin \frac{m\pi\xi}{a} \sin \frac{n\pi\eta}{b} \sin \frac{m\pi}{2} \sin \frac{n\pi}{2} \cos n\pi}{\left[ m^2 + \frac{n^2 a^2}{b^2} \right]^2 \left( \alpha_m \tanh^2 \alpha_m - \tanh \alpha_m + \alpha_m \coth^2 \alpha_m - \coth \alpha_m - 2\alpha_m \right)} \quad (15)$$

### BENDING MOMENTS FOR POINT LOAD ON THE PLATE:

For the case of a point load as shown in Fig.1 which is of interest for the generation of the influence surfaces, the coordinates  $\xi$  and  $\eta$  refer to the position of the point load, while those  $x$  and  $y$  refer to the position of the observation point and the value of  $E_m$  from Eq.(10) becomes :

$$E_m = \frac{-64Pa^3}{\pi^4 b} \lim_{\substack{u \rightarrow 0 \\ v \rightarrow 0}} \sum_{n=1}^{\infty} \frac{\sin \frac{m\pi\xi}{a} \sin \frac{n\pi\eta}{b} \sin \frac{m\pi u}{2a} \sin \frac{n\pi v}{2b} \cos n\pi}{uv \left[ m^2 + \frac{n^2 a^2}{b^2} \right]^2 \left( \alpha_m \tanh^2 \alpha_m - \tanh \alpha_m + \alpha_m \coth^2 \alpha_m - \coth \alpha_m - 2\alpha_m \right)}$$

Noting that  $\lim_{\substack{u \rightarrow 0 \\ v \rightarrow 0}} \sin \frac{m\pi u}{2a} \sin \frac{n\pi v}{2b} = \frac{mn\pi^2}{4ab}$  and by letting  $P=1$ , the above equation gives the dimensionless value of  $E_m$

$$E_m^* = \frac{E_m b}{Pa} = \frac{-16a}{\pi^2 b} \sum_{n=1}^{\infty} \frac{mn \sin \frac{m\pi\xi}{a} \sin \frac{n\pi\eta}{b} \cos n\pi}{\left[ m^2 + \frac{n^2 a^2}{b^2} \right]^2 \left( \alpha_m \tanh^2 \alpha_m - \tanh \alpha_m + \alpha_m \coth^2 \alpha_m - \coth \alpha_m - 2\alpha_m \right)} \quad (16)$$

Thus , the dimensionless bending moments  $m_x$  and  $m_y$  become:

$$m_x = \frac{M_x b}{a} = \frac{4}{\pi^2} \sum_{m=1}^{\infty} \sum_{n=1}^{\infty} \frac{\left[ m^2 + \frac{n^2 a^2}{b^2} \right] \sin \frac{m\pi\xi}{a} \sin \frac{n\pi\eta}{b} \sin \frac{m\pi x}{a} \sin \frac{n\pi y}{b}}{\left[ m^2 + \frac{n^2 a^2}{b^2} \right]^2} + \frac{1}{4} \sum_{m=1}^{\infty} E_m^* \sin \frac{m\pi x}{a} \left[ \frac{1}{\cosh \alpha_m} \left\{ (1-\nu) \left( \alpha_m \tanh \alpha_m \cosh \frac{m\pi y_2}{a} - \frac{m\pi y_2}{a} \sinh \frac{m\pi y_2}{a} \right) + 2\nu \cosh \frac{m\pi y_2}{a} \right\} + \frac{1}{\sinh \alpha_m} \left\{ (1-\nu) \left( \alpha_m \coth \alpha_m \sinh \frac{m\pi y_2}{a} - \frac{m\pi y_2}{a} \cosh \frac{m\pi y_2}{a} \right) + 2\nu \sinh \frac{m\pi y_2}{a} \right\} \right] \quad (17)$$

$$m_y = \frac{M_y b}{a} = \frac{4}{\pi^2} \sum_{m=1}^{\infty} \sum_{n=1}^{\infty} \frac{\left[ \nu m^2 + \frac{n^2 a^2}{b^2} \right] \sin \frac{m\pi\xi}{a} \sin \frac{n\pi\eta}{b} \sin \frac{m\pi x}{a} \sin \frac{n\pi y}{b}}{\left[ m^2 + \frac{n^2 a^2}{b^2} \right]^2} + \frac{1}{4} \sum_{m=1}^{\infty} E_m^* \sin \frac{m\pi x}{a} \left[ \frac{1}{\cosh \alpha_m} \left\{ (\nu-1) \left( \alpha_m \tanh \alpha_m \cosh \frac{m\pi y_2}{a} - \frac{m\pi y_2}{a} \sinh \frac{m\pi y_2}{a} \right) + 2 \cosh \frac{m\pi y_2}{a} \right\} + \frac{1}{\sinh \alpha_m} \left\{ (\nu-1) \left( \alpha_m \coth \alpha_m \sinh \frac{m\pi y_2}{a} - \frac{m\pi y_2}{a} \cosh \frac{m\pi y_2}{a} \right) + 2 \sinh \frac{m\pi y_2}{a} \right\} \right] \quad (18)$$

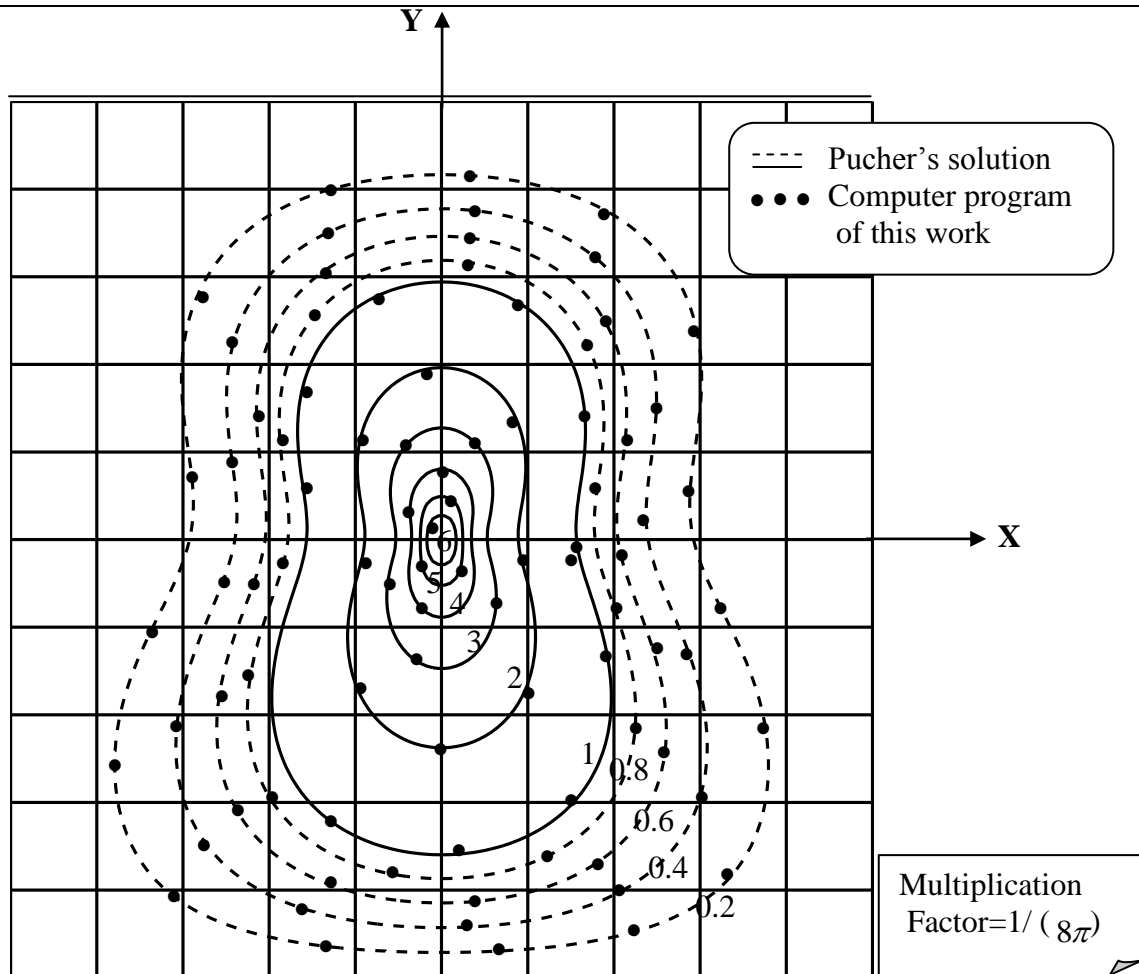
## GENERATION OF INFLUENCE SURFACES:

All influence surfaces were generated by applying the unit load to numerous points of the plate and evaluating the particular effect of moment produced at the observation point. The development of the influence surfaces is achieved by using a computer program written in this work in FORTRAN language and a program (**Surfer**) for plotting the contour-lines.

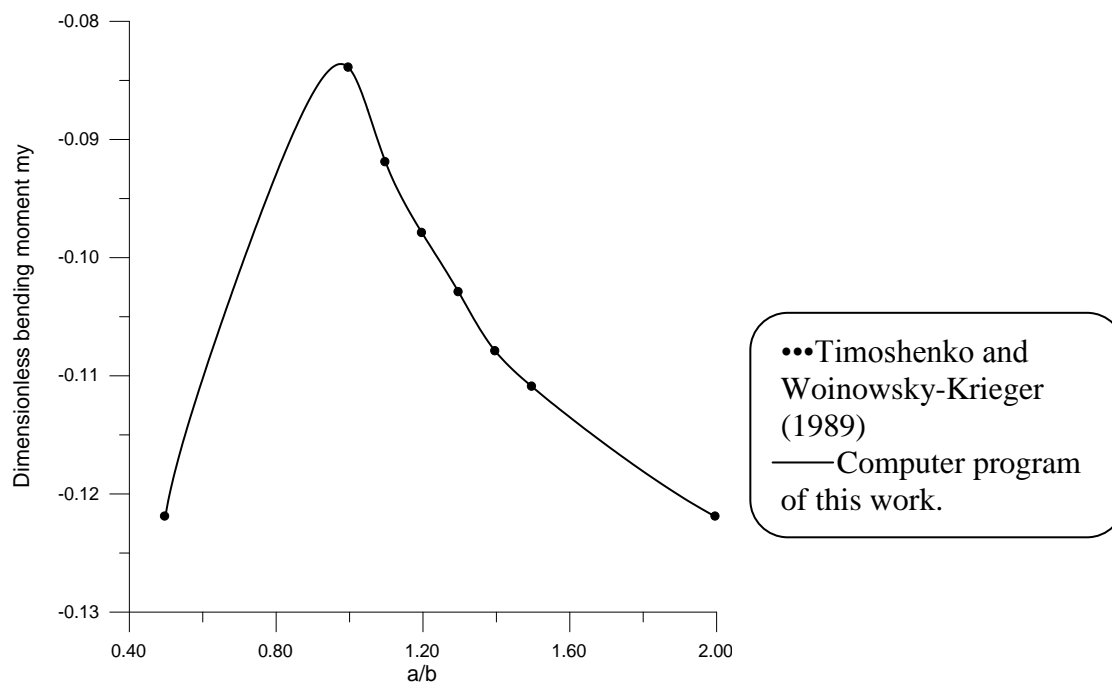
To show the validity of the developed solution and the written computer program, a comparison with available solutions is made. The case of a square plate ( $a/b=1.0$ ) having a Poisson's ratio equal to zero with the observation point at the center of the plate, has been chosen as the corresponding influence surface is available by **Pucher (1973)**.

Figure 4 shows that the contour lines obtained from the computer program are in excellent agreement with **Pucher's** solution.

To check the validity of the computer program dealing with the bending moment evaluation, the cases of rectangular plates with  $a/b= 0.5, 1.0, 1.1, 1.2, 1.3, 1.4, 1.5$  and  $2.0$  subjected to uniform load over the whole plate and having a Poisson's ratio of  $0.3$  have been chosen. This is due to the fact that data for the bending moment at the center of built-in edge are available by **Timoshenko and Woinowsky-Krieger (1989)**. Figure 5 shows that the results of the bending moment  $m_y$  at the center of the built-in edge are in excellent agreement with those obtained by **Timoshenko and Woinowsky-Krieger (1989)**.



**Fig.4 Comparison between the influence surface for  $m_x$  obtained from computer program with Pucher's (1973) solution for the center of a square plate having zero Poisson's ratio.**



**Fig.5 Comparison between Timoshenko and Woinowsky-Krieger(1989) and computer program for evaluation of bending moment  $m_y$  at the center of built-in edge of a rectangular plate with different values of aspect ratio  $a/b$  and having Poisson's ratio of 0.3**

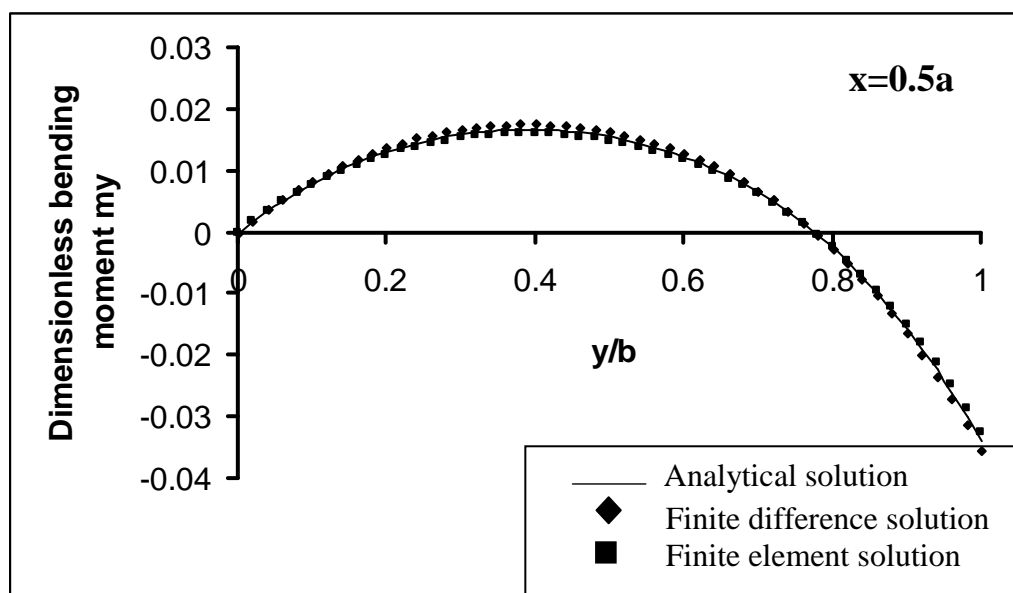
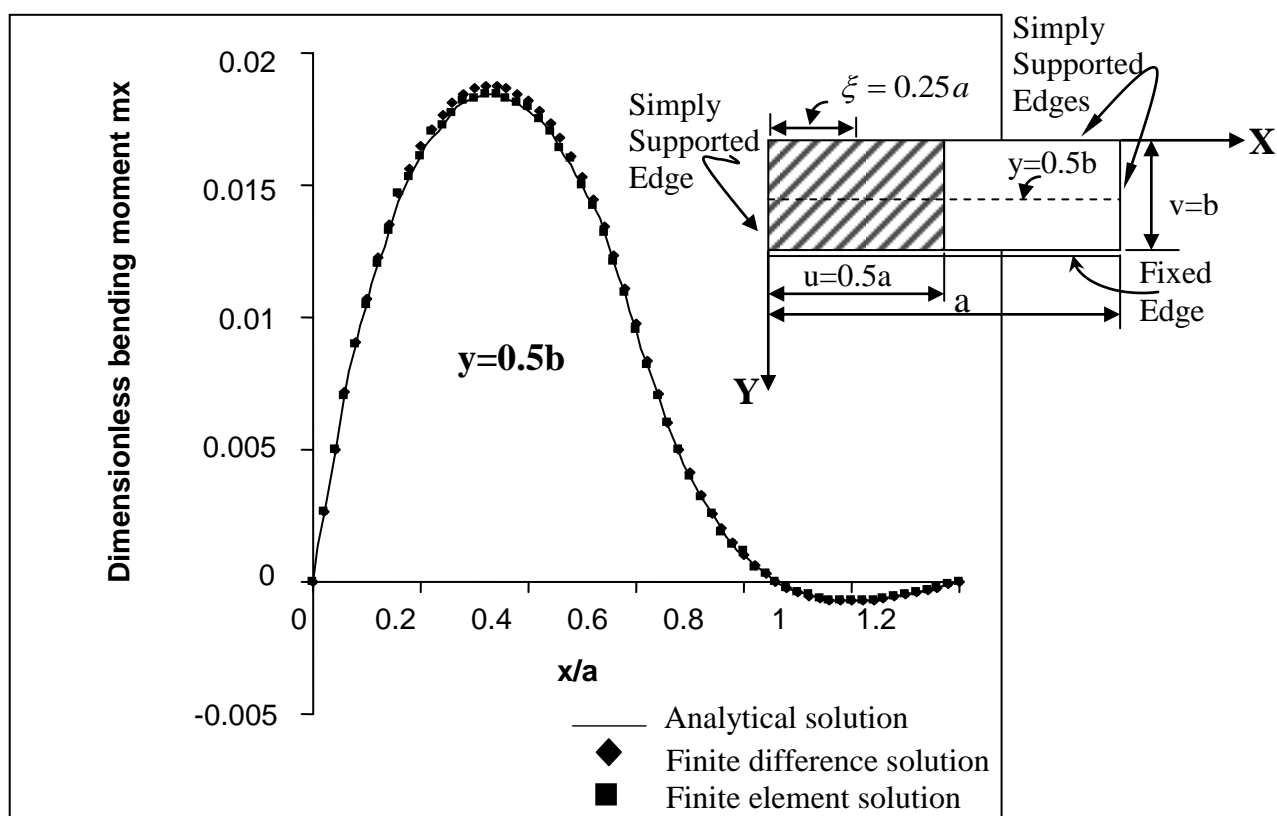


**Fig.6 Comparison between analytical, finite difference and finite element solutions for bending moments  $m_x$  at  $y=0.5b$  and  $m_y$  at  $x=0.5a$  for a rectangular plate ( $a/b=1.2$ ) with partial loading having Poisson's ratio of 0.2**

Figures 7 to 13 present influence surfaces for rectangular plates simply supported at three edges and built-in at the four edge with aspect ratio  $a/b$  equal to 0.6, 1.0, 1.4 and 2.0 respectively.



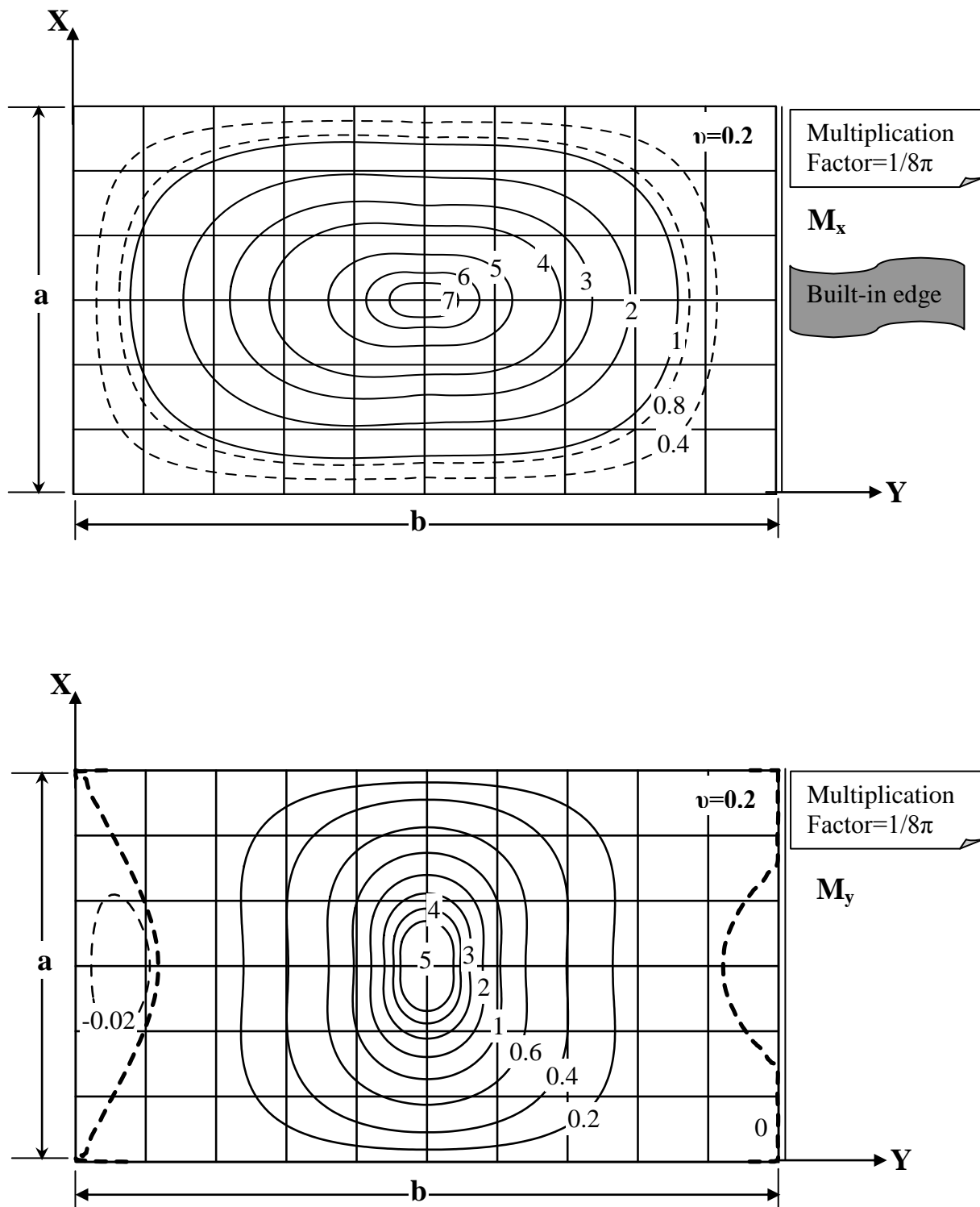


**Fig.7 influence surface for  $m_x$  and  $m_y$  at the center of a rectangular plate ( $a/b=0.6$ ) for Poisson's ratio of 0.2.**

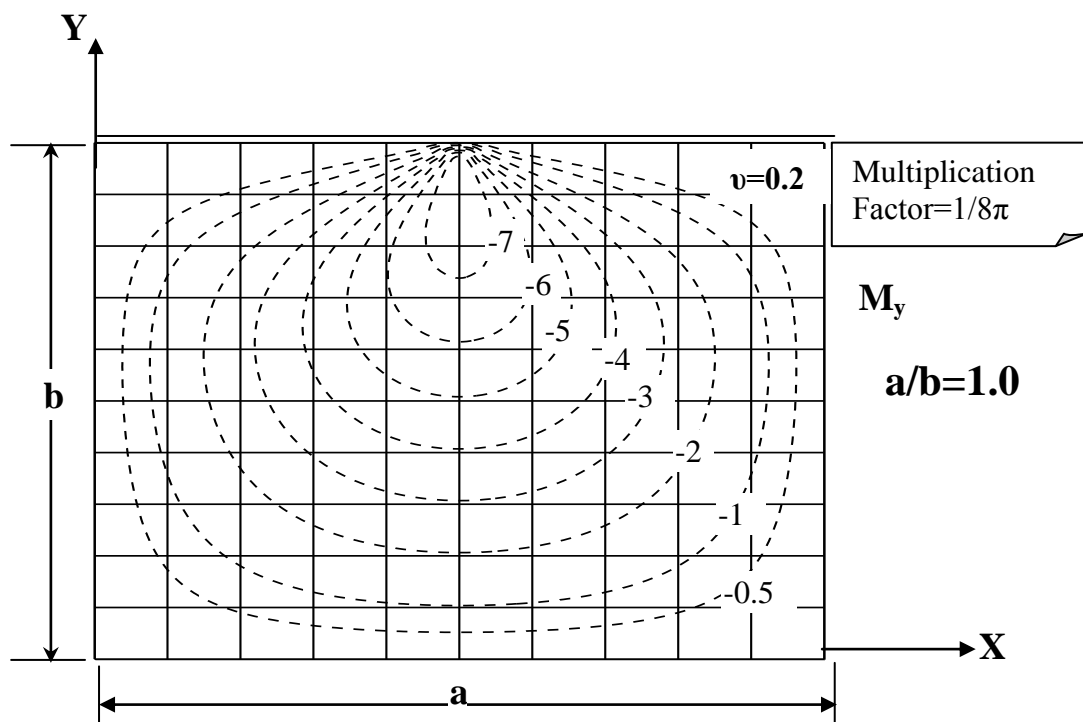
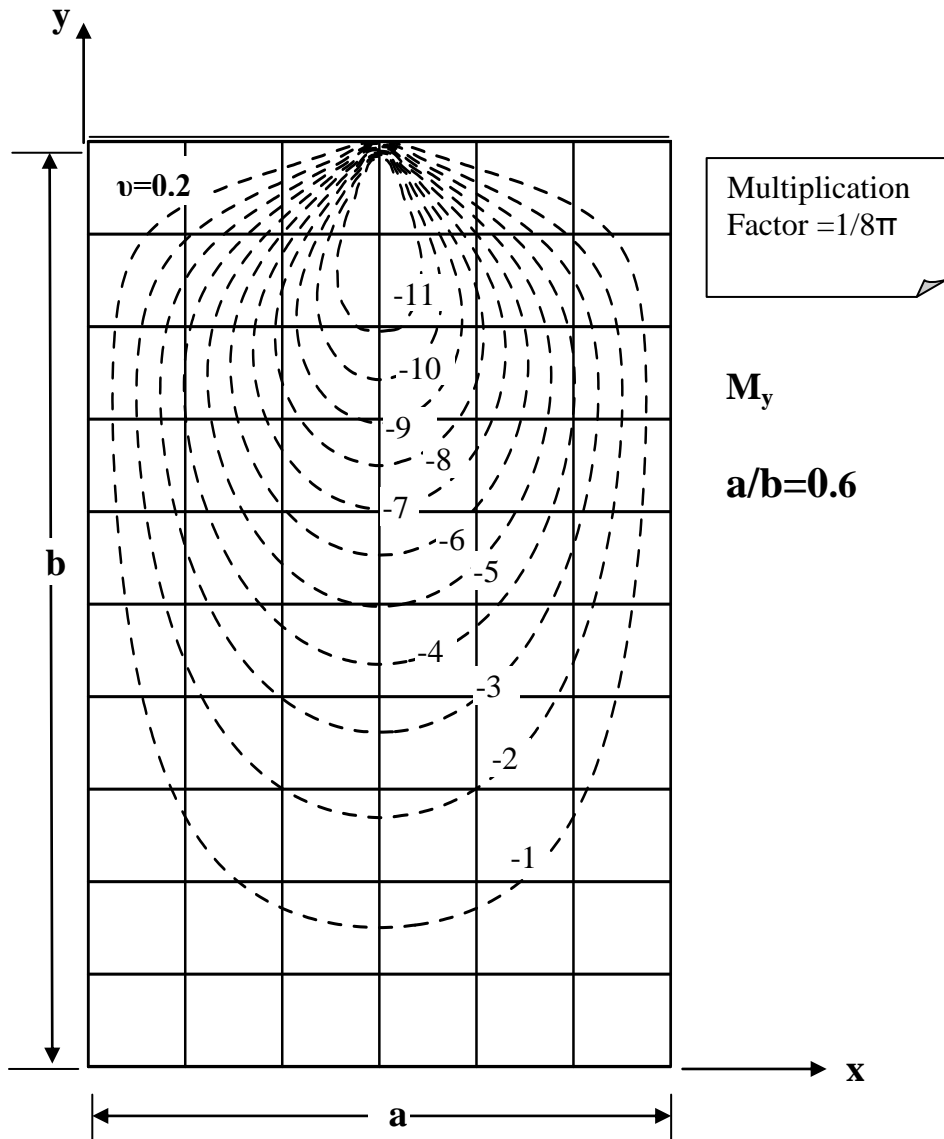


Fig.8 influence surface for  $m_y$  at the center of built-in edge of a rectangular plate ( $a/b=0.6$  and  $a/b=1.0$ ) for Poisson's ratio of 0.2.4808

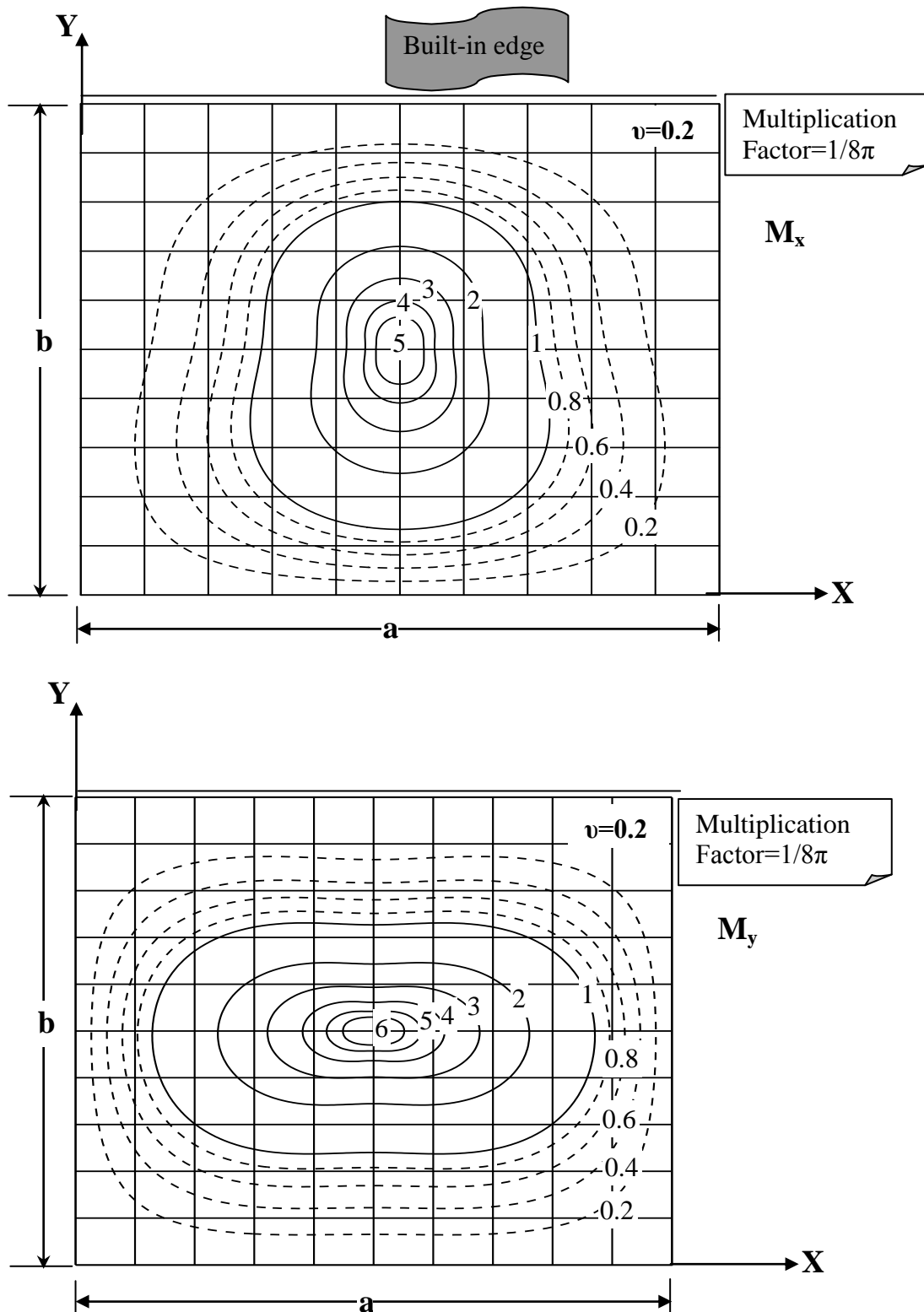


Fig.9 influence surface for  $m_x$  and  $m_y$  at the center of a rectangular plate ( $a/b=1.0$ ) for Poisson's ratio of 0.2.

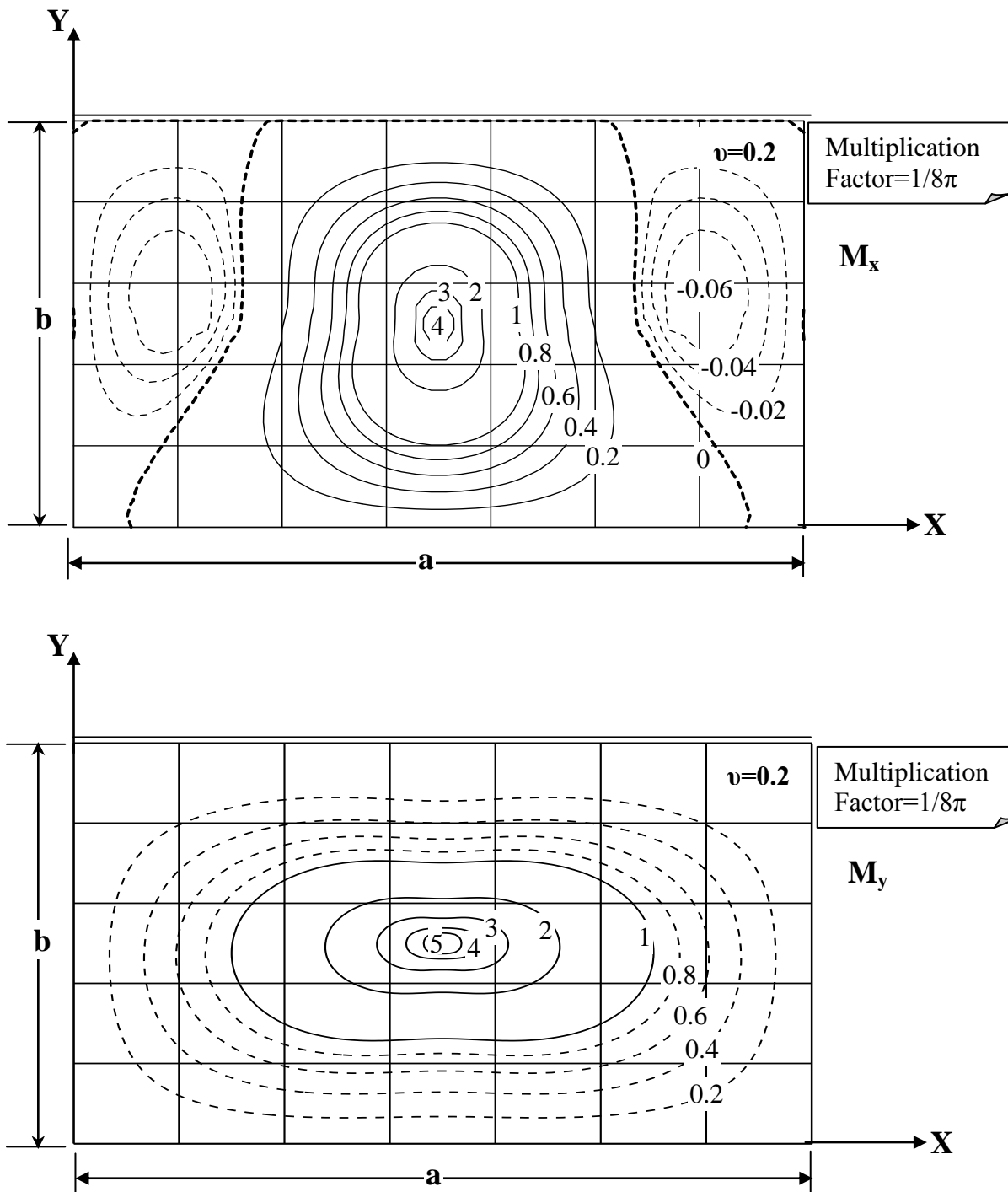


Fig.10 influence surface for  $m_x$  and  $m_y$  at the center of a rectangular plate ( $a/b=1.4$ ) for Poisson's ratio of 0.2.

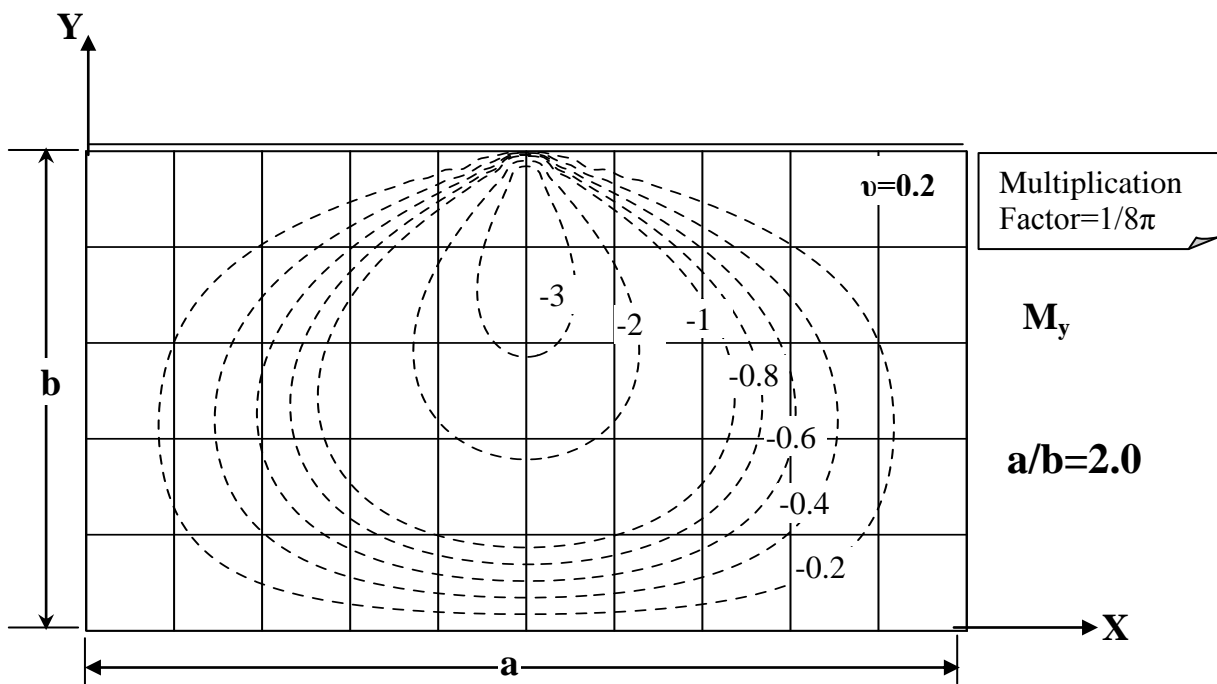
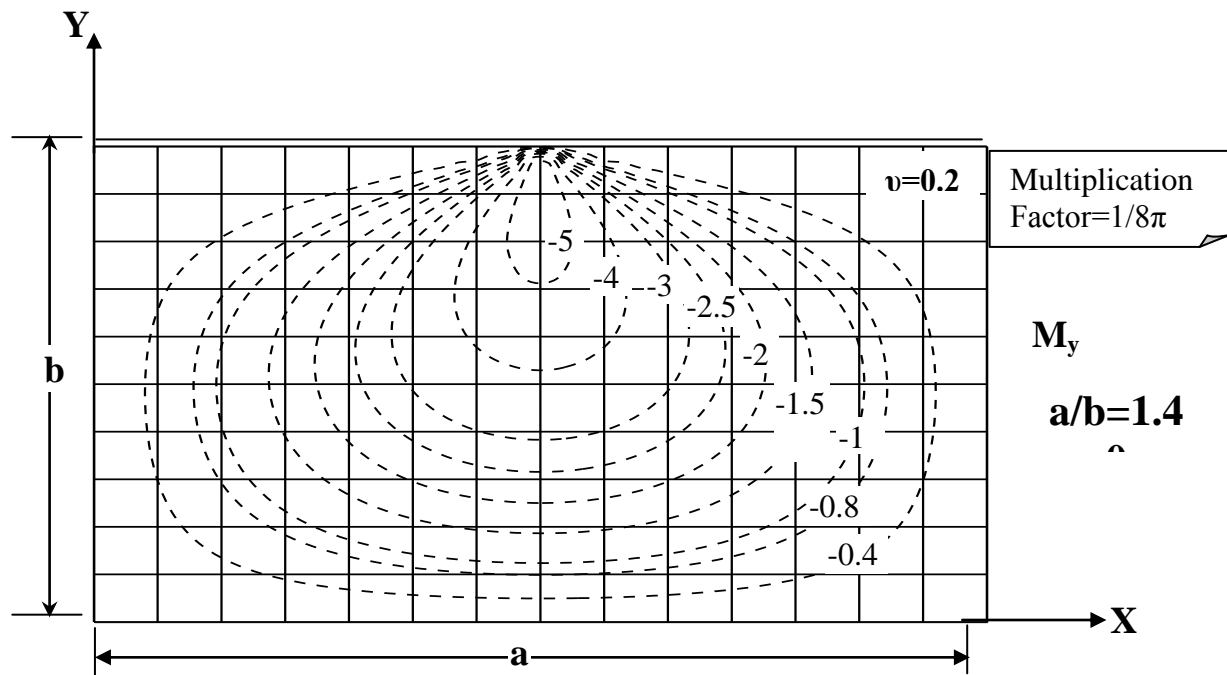


Fig.12 influence surface for  $m_y$  at the center of built-in edge of a rectangular plate ( $a/b=1.4$  and  $2.0$ ) for Poisson's ratio of  $0.2$ .

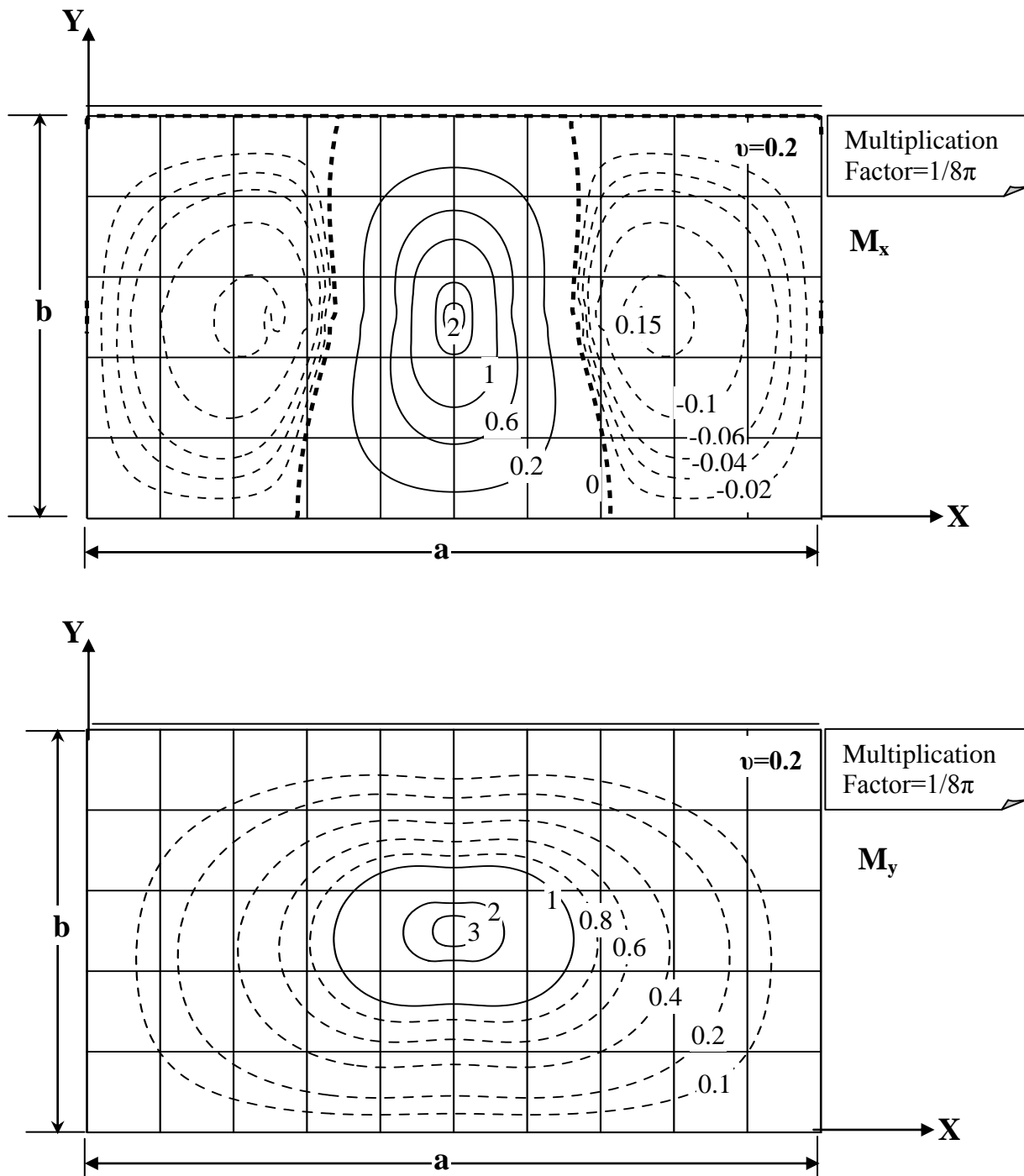


Fig.13 influence surface for  $m_x$  and  $m_y$  at the center of a rectangular plate ( $a/b=2.0$ ) for Poisson's ratio of 0.2.

It is observed from figure 9 that for the case of square plates the influence surfaces for both  $m_x$  and  $m_y$  are represented by positive contour lines only. The influence surfaces for  $m_x$  at the center of the rectangular plates for aspect ratio of 1.4 and 2.0, are represented by negative and Positive contour lines while those for  $m_y$  are represented by positive contour lines as shown in figures 11 to 12. For rectangular plates with aspect ratio smaller than 1.0, such as 0.6, the influence surfaces for both the  $m_x$  and  $m_y$  at the center of the plate are represented by positive contour lines as shown in figure 7. All influence surfaces for bending moment  $m_y$  at the center of built-in edge for rectangular plates having aspect ratio ranging from 0.6 to 2.0, are represented by negative contour lines as shown in figures 7-10-13. For partial loading, there is a possibility for negative bending moment  $m_x$  at the center of the plate which increases as the aspect ratio increases.

### APPLICATIONS:

To show how the influence surfaces can be used not only for concentrated loads but also for line and strip loads, the following applications are presented.

### EVALUATION OF THE BENDING MOMENT $M_x$ DUE TO A LINE LOAD:

For the case of a rectangular plate simply supported at three edges and built-in at the fourth edge with aspect ratio  $a/b=1.4$  and a Poisson's ratio of 0.2 subjected to a line load extending in the  $x$ -direction as shown in Figure 14, the evaluation of the bending moment  $M_x$  at the center of the plate can be achieved by using the corresponding influence surface as follows:

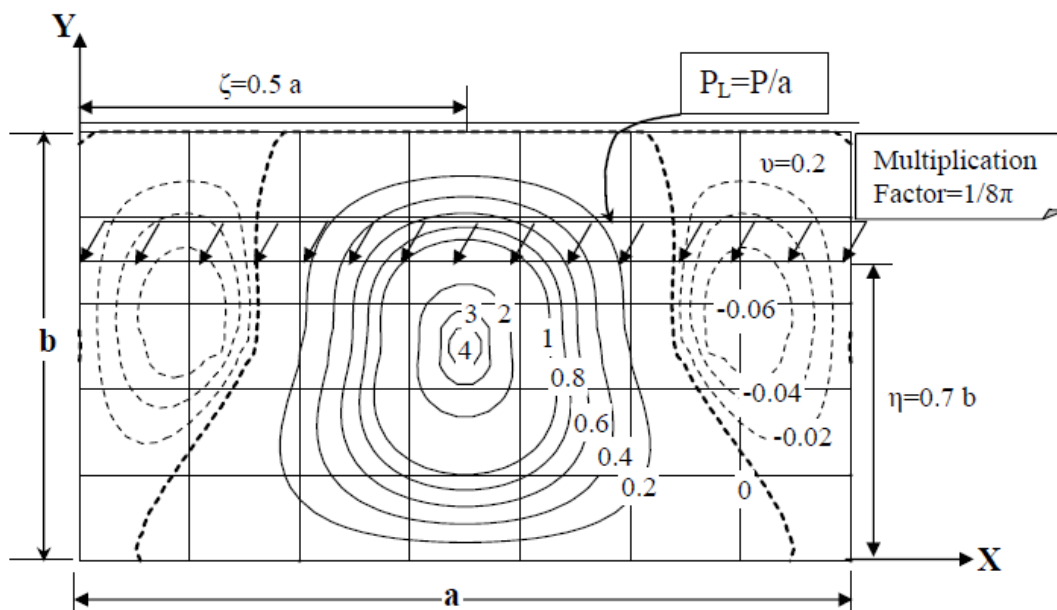


**Fig.14 influence surface for  $m_x$  of a rectangular plate having an aspect ratio of 1.4 and a Poisson's ratio of 0.2 subjected to a line load extending in the  $x$ -direction at  $\eta=0.7b$ .**

According to **Pucher(1973)**, the bending moment **M<sub>x</sub>** produced at the observation point (x, y) due to a line load can be calculated from this formula

$$(M_x)_{(x,y)} = \int_s p(s) \cdot \bar{X}(x, y) \cdot ds \quad (19)$$

where

x and y= coordinates of the observation point.

p(s) is the line load intensity.

$\bar{X}(x, y)$  are the influence values of the bending moment corresponding to applied line load.

The integration in Eq.(19) represents the area integral of the influence values over the loaded line which can be computed by using the Simpson's rule (**Saffand Snider, 2000**) as follows

$$\int_a^b f(x) \cdot dx = \frac{h}{3} \sum_{k=1}^n \{f(x_{2k-2}) + 4f(x_{2k-1}) + f(x_{2k})\} \quad (20)$$

where

$h=b-a/2n$  is the distance between any two points of the partition.

$f(x_0), f(x_1), f(x_2), \dots, f(x_{2n})$  are the functions of defined integral at the points  $x_0, x_1, x_2, \dots, x_{2n}$  respectively.

$2n$ =the number of equal parts of divided interval (a, b).

Because the influence surface for **m<sub>x</sub>** is symmetric about the y-direction through the center of the plate as shown in Figure (14), only one half of the corresponding influence values for **m<sub>x</sub>** are represented in Figure.(15).

The ordinates of the influence surface for **m<sub>x</sub>** in Figure (14) are dimensionless, therefore the area in Figure.(15) is obtained as a dimensionless quantity by applying the Simpson's rule on the influence values of **m<sub>x</sub>**.

Note that in Figure.(15), the influence values corresponding to line load are obtained from the influence surface at the interval of  $\Delta(x/a)=0.05$ .

This area becomes  $F=0.152$  and the dimensionless bending moment **m<sub>x</sub>** can be computed as follows:

$$\mathbf{m_x} = 2 \cdot F \cdot \text{multiplication factor} = 2 \cdot 0.152 \cdot (1/8\pi) = 0.012$$

According to Eq.(11) the bending moment **M<sub>x</sub>** at the plate center evaluated by using the influence surface becomes

$$M_x = \frac{m_x P_L a^2}{b} = 0.012 \frac{P_L a^2}{b} \quad (21)$$



The bending moment  $M_x$  at the plate center was calculated also using the computer program (EBM) which gave

$$M_x = \frac{m_x P_L a^2}{b} = 0.0125 \frac{P_L a^2}{b} \quad (22)$$

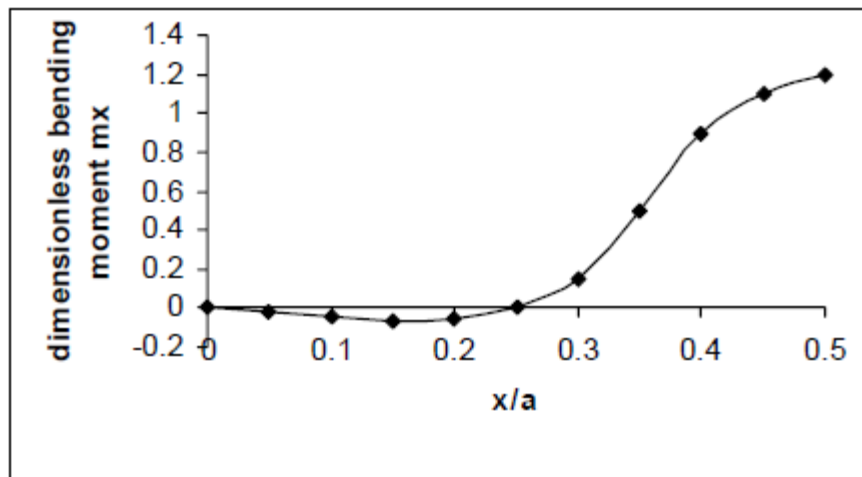


**Fig.(15) variation of the bending moment  $m_x$  at the center of a rectangular plate with  $a/b=1.4$  and a Poisson's ratio of 0.2 corresponding to a line load extending in the  $x$ -direction at a distance  $\eta=0.7b$  in the  $y$ -direction.**

The small difference in the results is due to the interpolation of  $m_x$  resulting from the influence surface at the chosen interval.

#### EVALUATION OF THE BENDING MOMENT $M_y$ DUE TO A STRIP LOAD:

For the case of a rectangular plate simply supported at three edges and built-in at the fourth edge with aspect ratio  $a/b=1.4$  and a Poisson's ratio of 0.2 subjected to a strip load extending in the  $y$ -direction at a distance of  $\zeta=0.8a$  in the  $x$ -direction as shown in Fig.(16) , the evaluation of the bending moment  $M_y$  at the center of the plate can be achieved by using the corresponding influence surface shown in Fig.(17)

According to **Pucher(1973)**, the bending moment  $M_y$  produced at the observation point  $(x, y)$  due to a distributed load can be calculated from this formula

$$(M_y)_{(x,y)} = \iint_A p(\xi, \eta) \bar{X}(x, y; \xi, \eta) . dx dy \quad (23)$$

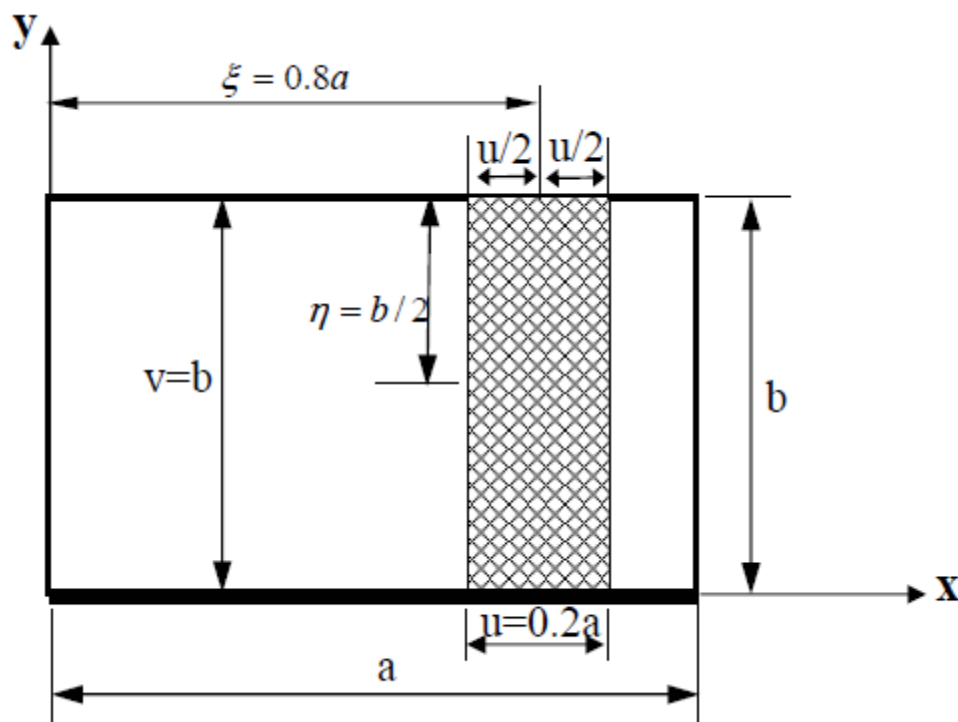


**Fig.(16) rectangular plate with aspect ratio of 1.4 and having a Poisson's ratio of 0.2 subjected to a strip load in the y-direction.**

Where

$\bar{X}(x, y; \xi, \eta)$  are the influence values of the bending moment corresponding to the applied distributed load.

$p(\xi, \eta)$  is the distributed load.

To evaluate the double integral of this formula, a strip load is plotted into the influence surface for  $\mathbf{m}_y$  and the area under this load is divided into five sections perpendicular to the  $x$ -direction of the plate as shown in Figure (17).

The evaluation of the individual areas is made by plotting the shape of the different sections separately as shown in Figure (18). Note that a uniform interval  $\Delta(y/b) = 0.05$  was used and the corresponding  $\mathbf{m}_y$  - values were interpolated from the corresponding influence surface.

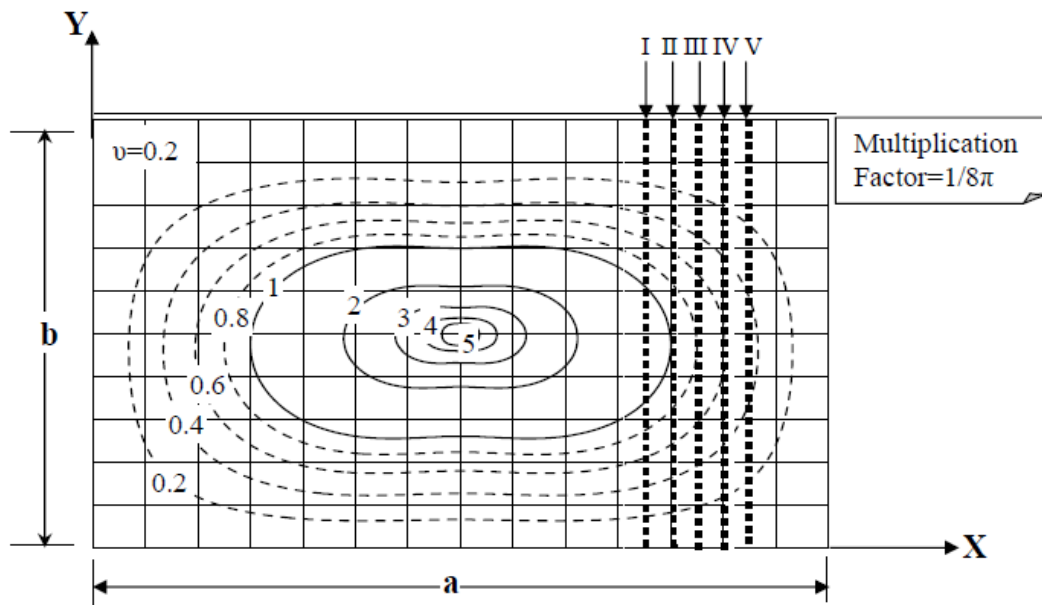


**Fig.(17) influence surface for  $m_y$  at the center of a rectangular plate ( $a/b=1.4$ ) for Poisson's ratio of 0.2 subjected to a strip load in the y-direction.**

Thus, the individual areas are computed by using Simpson's rule as discussed before and the following results are obtained

$$F_I=0.541, F_{II}=0.431, F_{III}=0.348, F_{IV}=0.301, F_V=0.22$$

The spacing between the individual sections  $\Delta(u/a)=0.05$  and the multiplication factor is  $1/8\pi$ . Thus, using Simpson's one third rule again, the dimensionless bending moment  $m_y$  becomes

$$m_y = 1/3 \cdot 0.05 \cdot (1/8\pi) \cdot F_I + 4F_{II} + 2F_{III} + 4F_{IV} + F_V = 0.003$$

According to Eq.(12) the bending moment  $M_y$  at the plate center becomes

$$M_y = m_y q_0 a^2 = 0.003 q_0 a^2 \quad (24)$$

The bending moment  $M_x$  at the plate center was evaluated also using the computer program (EBM) which gave

$$M_y = 0.0031 q_0 a^2 \quad (25)$$

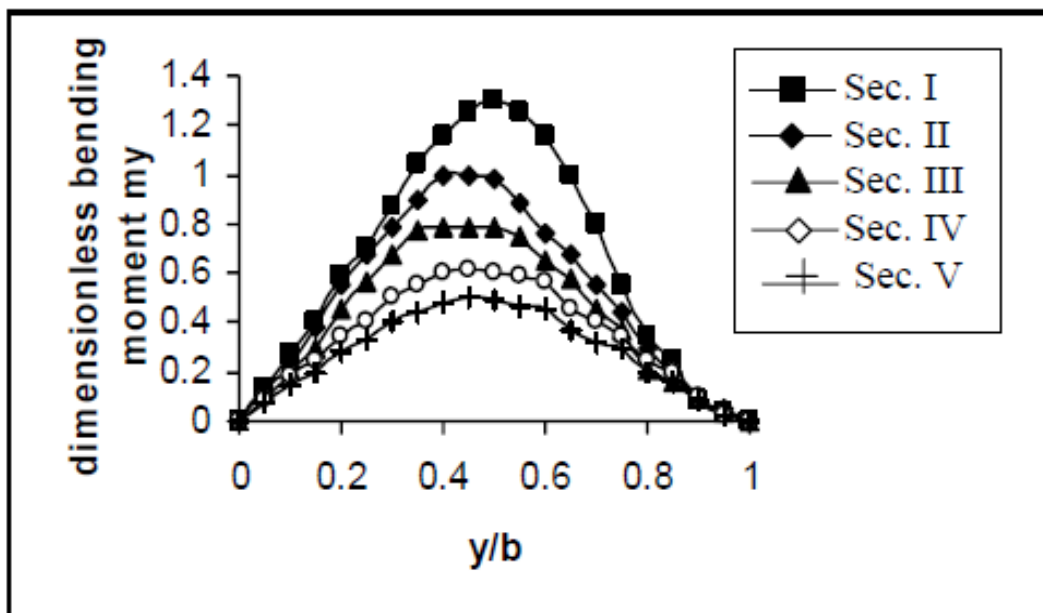


Fig.(18) the distribution of the bending moment  $m_y$  at the center of a rectangular plate with aspect ratio  $a/b=1.4$  and a Poisson's ratio of 0.2 corresponding to a strip load extending in the  $y$ -direction and having  $\zeta=0.8a$

This result is in excellent agreement with that obtained using the influence chart. It can be concluded from these applications that for practical purposes, the use of influence surfaces to evaluate the bending moments due to various cases of loading provides very satisfactory results which are in excellent agreement with those obtained using the computer program (EBM). To achieve higher accuracy with saving in time, the computer program (EBM) written in this work is strongly recommended.

## CONCLUSIONS:

- There is good agreement between the developed analytical solution with that presented by **Timoshenko and Woinowsky-Krieger (1989)** for the case of a rectangular plate with aspect ratio  $a/b=1.2$  and Poisson's ratio equal to 0.2 under the effect of uniform strip load.
- There is good agreement between the developed influence surface in this work with those presented by **Pucher (1973)** for the case of a square plate ( $a/b=1.0$ ) having a Poisson's ratio equal to zero with the observation point at the center of the plate.



- The negative regions of influence surfaces for bending moment  $m_x$  at the center of the plate increase as the aspect ratio increases while those for  $m_y$  decrease with increasing aspect ratio.

## REFERENCES

- ACI Committee 363, (1984), "**State of the Art Report on High-Strength Concrete** ", Journal of ACI, Vol.81, No.4-6, pp 383-384.
- Boyd, SK., Ronsky, JL., Lichti, DD., Salkauskas, D. and Chapman, MA. , (1999), "**Joint Surface Modeling With Thin- Plate Splines** " ASME, 121,pp 525-532.
- Cusens, A.R. and Pama, R.P., (1975), "**Bridge Deck Analysis** ", John Wiley and Sons.Inc., London-New York, Sydney, Toronto.
- Darwing , D and Pecknold, D. A., (1977), "**Nonlinear biaxial stress for concrete**" , ASCE, Engineering Mechanics Journal , Vol.103, EM.4, pp 229-241.
- Francis, A.; Bordette, E.G. and Deatherage, J.H., (1991), "**Elastic Modulus, Poisson's ratio, and Compressive Strength Relationships at Early ages** ", Journal of ACI, Vol.88, No.1, Jan, pp 3-10.
- Hambly, E.C,(1976), " **Bridge Deck Behaviour** ", Chapman and Hall, London- New York.
- Girkmann, K., (1963), "**Flaechentragwerke**" Sechste Auflage Springer-Verlag Wien
- Klink, S., (1985), "**Actual Poisson's Ratio of Concrete** ", Journal of ACI, Vol.82, No.5-6, pp813- 817.
- McCormac, J.C., (1989), "**Structural Steel Design** ", Harper and Row Publishers, New York,London, Sydney, Tokyo.
- Merritt, F.S., (1999), "**Structural Steel Designer's Handbook** ", Third Edition, McGraw-Hill , Inc.
- Mirza , S.A. , Hatzinivdas, M. and Mcgreger , J.C., (1979), "**Statistical description of strength of oncrete**" ASCE, Engineering Mechanics Journal, Vol.105, ST.6, pp 1021-1037.
- Razouki, S.S and Karim, B.H., (2005), "**Effect of Poisson's ratio on the Bending Moment Influence Surfaces for Simply Supported Rectangular Plates** ", Engineering Journal of the University of Qatar, Vol.18, pp. 67-92.
- Razouki, S.S and AL-Ani, S.H. (2009), "Bending moment influence surfaces for rectangular concrete slabs simply supported at two parallel edges and built-in at the others", paper accepted for publication in Engineering and Development Journal Al- Mustansiriya University, Baghdad.

- Kupfer, H.B. and Gerstle, H. (1973), "**Behavior of concrete under biaxial stress**" ASCE, Engineering Mechanics Journal, Vol.99, EM.4, pp 853-866.
- LARSA, (2006), "**Influence Line and Surface Analysis** " Email: info@Larsa4D.com
- Pucher, E.,(1973), " **Influence Surfaces of Elastic Plates** ", Fourth Edition, Springer-Verlag Wien, New York.
- Selvadurai, A.P.S, (1979), "**Elastic analysis of soil Foundation interaction** ", Elsevier Scientific
- Publishing Company,Amsterdam, Oxford, New York .
- Szilard, R., (1974), " **Theory and Analysis of Plates: Classical and Numerical Methods** ", Prentice-Hall Inc, Englewood, Cliffs, New Jersey.
- Taylor, R. L. and Govindjee S., (2004) "**Solution of Clamped Rectangular Plate Problems**" Structural Engineering Mechanics and Materials, Communi. Numer. Meth. Eng. 20, pp 757-765.
- Timoshenko, S.P and Woinowsky-Krieger, S., (1989), "**Theory of Plates and Shells** ", Second Edition, McGraw-Hill Book Company, New York, pp 79-198.
- Wang,HC., Ryu ,J. and Han, JS.,(2000), "**A New Method for the Representation of Articular Surfaces Using the Influence Surface Theory of Plates** " J Biomech, 33, pp 629-633.
- Zehnder, A. T., Hui, C. Y. and Potdar, Y., (1998), "**Fracture Mechanics of Thin, Cracked Plates Under Tension, Bending and Out-Of-Plane Shear Loading**" Proceedings of the Second joint NASA/FAA/DoD Conference on Aging Aircraft, (C. Harris, ed.), 33,pp. 627-634.



## NOTATIONS

Symbol	Definition
$a$	Length of the built-in edge
$a_{mn}$	Coefficients of a double Fourier sine expansion of any kind of loading $q(x, y)$
$b$	The dimension of the plate perpendicular to built-in edge
$D$	Flexural rigidity of the plate
$E$	Modulus of elasticity
$E_m$	Coefficient of a single sine Fourier series of distributed moment $M_y$ at the built-in edge
$h$	Plate thickness
$m$ and $n$	Integers 1,2,3,..... of the double Fourier series
$M_x$	Bending moment per unit length acting on the edges parallel to the $y$ -axis
$M_y$	Bending moment per unit length acting on the edges parallel to the $x$ -axis
$M_{xy}, M_{yx}$	Twisting moment per unit length of sections perpendicular to the $x$ and $y$ axes respectively
$m_x$ and $m_y$	Dimensionless bending moments
$p$	Concentrated load
$q$	Lateral load (load per unit area)
$q_0$	Intensity of the uniformly distributed load
$u$ and $v$	The sides of the rectangular loaded area parallel to the $x$ and $y$ - axes respectively
$w(x, y)$	Deflection surface
$x$ and $y$	Cartesian coordinates of the observation point
$\eta$	$y$ -coordinate of the centroid of the load
$\upsilon$	Poisson's ratio
$\zeta$	$x$ -coordinate of the centroid of the load

## IMPLEMENTATION OF R-TECHNIQUE IN PRODUCTION PLANNING AND CONTROL

Dr. Zuhair Issa Ahmed

Department of Mechanical Engineering  
College of Engineering  
University of Baghdad / Iraq

Eng. Fadhil Nassrallah Mahan

Department of Mechanical Engineering  
College of Engineering  
University of Baghdad / Iraq

### ABSTRACT

The planning engineering is considered a vital part in the industrial operations series that leads to achieve the proposed production plan. Because of scientific advancement and technical development in the industrial field, the managements of the companies and job shops start to automate the engineering and management activities for the aim of quickness and accuracy in making proper decisions for the production process in order to get final product in a better quality and minimum cost. This is achieved by the future estimation of production plan. The research concern with evaluating the size of work arrival to the manufacturing shops and determining the amount of capacity that is required to perform these evaluated job volume in a manner that warrant decreasing the cost of orders and machines waiting. To achieve this aim, a construction of simulation system by using Visual Basic computer program that helps the user in future estimation of job volume and determination of the best process capacity of the job shop which through it the job can be accomplished. Actual and realistic data that are collected from the documents of Electrical Industrial Company (EICO) factories is in random orders arriving to factories in one man-day and also the actual time to perform number of these orders. Through the designed software which is used as a tool for simulating of the target production system in this research, the best simulation daily process capacity was obtained for the job shop to be 130 hr per day where as, it achieved the minimum value of the total cost. There is a great effect for this increment of job shop daily process capacity in decrement of waiting of orders and this lead to optimal exploitation for these presented capacities. To verify simulation results and obtain the optimum selection for these results, the researcher used a modern technique called R-Technique or Response Surface Methodology (RSM), which the desirability function which is used as a dual-purpose standard to obtain the optimum value of job shop process capacity.

### الخلاصة

إن هندسة التخطيط تعتبر الجزء الحيوي في سلسلة العمليات الصناعية، التي تؤدي إلى تحقيق الخطة الإنتاجية المؤملة وبسبب التقدم العلمي والتطور التكنولوجي في المجال الصناعي أخذت إدارات الشركات والمعامل والورش بأتمتة سلسلة الفعاليات الهندسية والإدارية لغرض السرعة والدقة في اتخاذ القرارات الصحيحة للعملية الإنتاجية من أجل الوصول إلى منتج نهائي بأقل كلفة ويأتي هذا من خلال التخمين المستقبلي للخطة الإنتاجية. يهتم البحث بتقدير حجم العمل الواصل إلى الورشة وتحديد مقدار الطاقة الإنتاجية المطلوبة لإنجاز حجم العمل الواصل إلى الورشة بشكل يقلل كلف كلا من كلفة انتظار الطلبات والمكانن ولتحقيق هذا الهدف قام الباحث ببناء نظام محاكاة باستخدام الحاسوب (لغة الفيجوال بيسك) يساعد المستخدم في التنبؤ المستقبلي لحجم العمل وتحديد أفضل طاقته إنتاجية للورشة يمكن من خلالها إنجاز العمل. تم جمع بيانات واقعية وفعالية من سجلات معامل الشركة العامة للصناعات الكهربائية وهذه البيانات تخص عدد الطلبات العشوائية الواصلة لهذه المعامل في اليوم الواحد وكذلك



الزمن الفعلي لإنجاز عدد من هذه الطلبات. ومن خلال النظام الحاسوبي المصمم والذي استخدم كوسيلة لمحاكاة النظام الإنتاجي المستهدف بالبحث فقد تم الحصول على أفضل طاقه إنتاجيه يومية للورشة وهي 130 ساعة في اليوم والتي حققت أقل قيمه للكلفة الكلية. إن لهذه الزيادة في الطاقة الإنتاجية اليومية للورشة الأثر المهم في تقليل وقت الانتظار للطلبات بحيث أدى ذلك إلى الاستغلال الأمثل لهذه الطاقات المتزايدة وللتأكد من النتائج أعلاه والحصول على الانتخاب الأمثل لهذه النتائج، استخدم الباحث تقنيته حديثه تعرف بمنهجية الاستجابة السطحية والتي استخدمت فيها داله المرغوبية كمعيار ثنائي الهدف للحصول على القيمة المثلى للطاقة الإنتاجية المتاحة للورشة.

**KEYWORDS: Production Planning, Scheduling, Simulation, Optimization, Response Surface Methodology (RSM), R- Technique**

## CONTEXT AND MOTIVATIONS

Production planning is fundamental to the operation of a manufacturing enterprise. The basic problem is to determine the type and quantity of the products to produce, to meet uncertain demand in the future time periods (Venkateswaran et al., 2004). Operations planning and control systems cover three stages: planning, scheduling and execution (Volkman et al., 1997). The planning stage is concerned with balancing supply with demand. It includes demand management, resource planning and master scheduling. The scheduling stage produces more detailed plans for material and capacity requirements. Finally, in the execution stage orders are dispatched and fulfilled using the materials and resources that were allocated in earlier stages. In the classification of (Sheer 1994), scheduling is concerned with sequencing orders that have already been released for production and with deciding exactly when and on which machines jobs should be processed. The primary goals of scheduling are to avoid late job completion, minimize flow times and to maximize resource utilization (Vollmann et al., 1997). The job shop scheduling problem is the problem of finding a way to schedule a number of operations, such that the last operation is completed as soon as possible. Here an *operation* is a task that must be executed on a resource, called the machine (Lennartz, 1999). In job shop scheduling, any job can be processed on any machine in an order that is predetermined but can be different for each job (Lehtonen et al., 2003).

## SIMULATION IN PRODUCTION SCHEDULING

Simulation is emerging as a part of decision support systems for production scheduling. It provides an alternative when optimization approaches are too heavy and simple approaches such as priority rules are insufficient. Classical optimization techniques use an appropriate mathematical description of the scheduling problem that is minimized through the application of an algorithm (Sellers, 1996). The simulation approach provides a great level of detail without being computationally too heavy. A schedule is created by simply simulating the execution of the factory and taking the recorded execution history as the schedule (Smith, 1992). The result will be a feasible schedule if all the relevant constraints are included, which is easy as a simulation model can include a large number of details. However, the simulation model does not necessarily come up with the best schedule, although it will be a feasible one. (Roy and Meikle 1995) recommend discrete event simulation for estimating the operative performance of proposed schedules that are generated using other methods. As a part of a decision support system, simulation provides a way to get detailed information about the consequences of scheduling decisions, regardless of whether they are based on manual or optimization-based schedule generation. (Lehtonen et al., 2003).

## OPTIMIZATION

Optimization means finding the specific certain set of inputs to a function, such that any change to any of the inputs will result in a less desirable function output. Optimization approaches are generally thought of as either analytical/mathematical or direct/empirical. Regardless of the specifics, in an optimization routine in the most general sense is a procedure that, when applied to a model, will result in the determination of the best model as defined by the fitness of an objective

function. Most problems are solved by matching a modeling approach with an optimization, or solving approach. Simulation is a specific computer based modeling approach which uses a chain of cause and effect relationships to help the user build complex models from the ground up, one link at a time. On the other hand, optimization often requires a simplistic modeling approach in order to have a model that can be completely optimized (Hicks, 1999). In this paper we present an optimization approach to a real-world production planning problem. Response Surfaces Methodology was derived by evaluating the system at several points using computer simulation. The results were then used to depict them graphically.

### CHARACTERISTICS OF PRODUCTION SYSTEM

One of the Electrical Industrial Company (EICO) factories, is the Tools and Molds Factory. It is one of the major factories in the company. This factory produces several kinds of dies, tools, and fixtures which are used by the company; also making the required maintenance for these dies and tools, which may be damaged during the production operations. This factory contains the machines, as stated in Table (1).

Table (1): Machines of tools and molds factory.

No.	Type of machine	Quantity	Serial number
1	Milling	8	M (1 – 8)
2	Turning	8	T (9 –16)
3	Grinding	8	G (17-24)
4	Drilling	4	D (25-28)
5	Shapers	2	S(29-30)
6	Cutting	3	C (31-33)
7	Furnaces	4	F(34-37)
8	pressing	2	P(38-39)
9	Assembly bench	3	A(40-42)

### Assessment of Factory Capacity

The capacity of work for factory is represent by the number of machine in the tools & molds factory and the Spare parts factory. They are (57) machines, but they do not works completely daily, because of failures that occurs from the work and maintenance, and also because of broken machines which can not be repaired. Therefore the about number of working machines are (40) with (5) hours running per day are calculated using:

$$C_a = M \times h_r \dots \dots \dots \text{hr/day (1)}$$

Where:

$C_a$  : Process Capacity,  $M$  : Number of machine,  $h_r$  : Number of activity hours.

### Type of Order Arrivals

Orders arrive to the shop randomly between increasing or decreasing in the number and type and depend on customer needs and as shown in the Fig. (1).

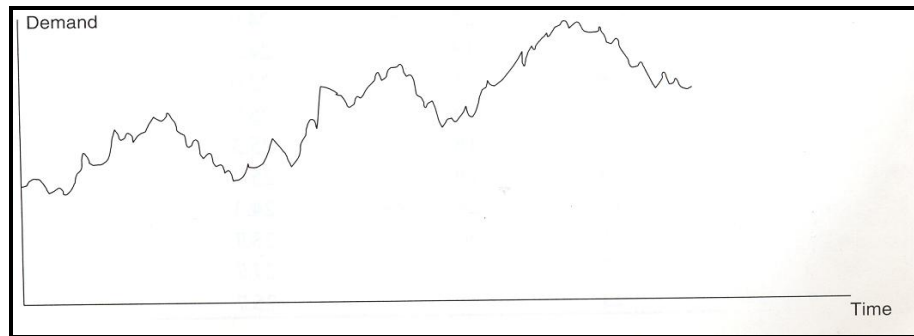


**Fig. (1): A random Order Pattern.**

### EXPERIMENTAL STUDY

Refereeing to the production planning in EICO, the establishment depends in programming of there random requirements and forecasting upon the experience of the technicians without making use of computers and updated software, a computer program is designed to be used in future calculation of the orders which arrive to the factories and at any period. In this section a description for the procedure for random orders arrivals approach is developed depending on a data base system, absolute records and other simulations method technique. Each order entails a certain number of machine hours, analysis of past records which are summarized in **Table (2)**.

**Table (2): Orders Data.**

Number of order	Days frequency	Sum. of orders
1	9	9
2	14	28
3	18	54
4	25	100
5	20	100
6	13	78
7	8	56
8	2	16
Total	109	441

### Collection of Data

The collected data shown in **Table (2)** from past records of the plant are random orders arrived to the job shop and were performed to determine the kind of the distribution which presents the shown in the above table. The histogram must be drawn as shown in the following steps:

$$R = xl - x_s \quad (2)$$

Where:

**R**: The range of orders

**xl**: Upper of limit

**x<sub>s</sub>** : Lower of limit

In our case study  $x_S = 0$ ,  $x_1 = 8$ .

$$H = R / K \quad (3)$$

Where:  $H$ : Ranking of period ,  $K$ : Number of ranking , in the case study  $K=7$ .

For calculation the relative frequency use the equation below:

$$F_R = (F_A / N_O) \times 100 \quad (4)$$

Where:

$F_R$  = Relative Frequency.

$F_A$  = Absolute Frequency.

$N_O$  = Number of Data.

### Data Analysis

From the continuation of the method for random orders arrival and the nature of the work in the associated factories, it was established that the arrival of random orders follows normal distribution as shown in the steps of the sketch of the histogram , that is the facts of manufacturing world show that a lot of changes take the curve trend of normal distribution. Therefore the normal distribution curve describes the changes of manufacturing which can be calculated from the following relation:

$$f(z) = [(1 / (2\pi))^{1/2}] \times e^{-0.5z^2} \quad (5)$$

Where:

$f(z)$ : Function of normal distribution curve where:

$e$ : 2.7182 ,  $\pi$  : 3.1415

$z$ :: random variable.

The form of normal distribution curve is depending upon the values of the arithmetic mean ( $\mu$ ) and standard deviation ( $\sigma$ ).

$$\mu = \frac{\sum x}{N} \quad (6)$$

where

$x$ = Orders number

$N$  = Number of data points

$$\sigma = \sqrt{\frac{\sum (x - \mu)^2}{N - 1}} \quad (7)$$

The value of  $\mu$  &  $\sigma$  in this research are 4&2 from **Table (2)** respectively. To calculate (the arithmetic mean)  $\mu$  and (standard deviation)  $\sigma$ , it must draw a normal distribution curve taking into consideration the limit of  $x$ , i.e.  $-\infty < x < +\infty$ . The assumption of normality is standard in the assumption of a shifted distribution does to some extent mitigate the effects of that assumption. **Fig. (2)** shows geometrically the relationship of the shifts to the long term fraction of conforming units

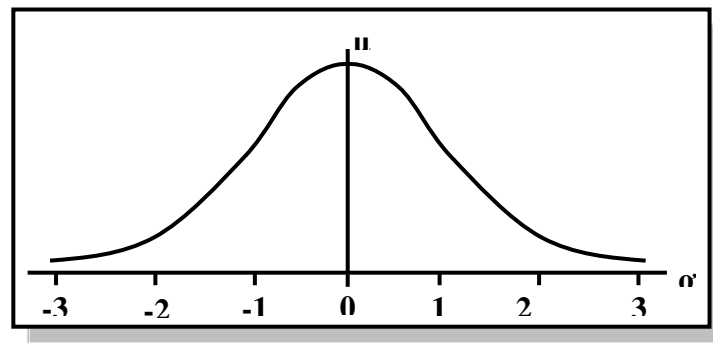


**Fig. (2): Quantities Used to Calculate the Proposed Distribution Function.**

From the **Table (2)** the maximum number of orders is (8) and the minimum number of orders is (1) / day. To represent the limits of order on the normal distribution curve, the ranges  $(-2\sigma, 2\sigma)$  is selected as shown in the following equation:

$$n = (x - \mu) / \sigma \quad (8)$$

Where:

$n$  =Limit of Range

$$1= \text{At } x=0, n = \frac{0-4}{2} \Rightarrow n = -2$$

$$2- \text{At } x=8, n = \frac{8-4}{2} \Rightarrow n = 2$$

### The Simulation Model

After collecting the required data which are concerned with flows, processes and the times of each single operation, the mathematical models are constructed so as to achieve results by using simulation technique as follow:

1- A mathematical model is used to the estimate the number of daily random orders arriving to the job shop as follow:

$$z = (x - \mu) / \sigma \quad (9)$$

Substituting the value of  $z$  with limits  $(-2\sigma, 2\sigma)$  using the represented mathematical model equation:

$$x = \mu + \text{random number } (\sigma) \quad (10)$$

Then the value of  $(x)$  is calculated by using one digit from a generated random numbers from the designed system. Where:

$x$ : number of estimated daily random orders arrivals.

2- Other mathematical model is used to estimate lead time to finish the orders which arrived to the job shop in the previous mathematical model. This model depends upon on available data recorded in the establishment for the same job shop. For that task a number of orders is tabulated and using the data of this table(table 2) in  $(x- y)$  chart. A curve which represents the 2<sup>nd</sup> mathematical model was established. By using two digits from a generated random numbers from the designed system which represent percentage accumulative frequency and by intersection of these numbers on the curve. The estimated time for each estimated random order arrived to the job shop can be calculated. All these data is arranged and interred to the computer system Automated Scheduling System (ASS) in order to get accurate results.

### The Industrial Case Study

The proposed case study was elaborated at the workshop of the tools and molds factory and spare parts factory that produces mechanical products by using machining and welding resources, assembly and inspection stations and some highly specialized machines. The goals of the implemented simulation model are: maxim utilization of one type of available resources (Available Daily Machine Capacity) and minimizing the inherent cost matched within the context. Execution within the discrete, event-driven simulation module beside the component that allows an interactive simulation, the simulator provides another interface to the optimization module. The second part of the research is the functional relationship between various factors which have been investigated in order to improve production capacity as well as to investigate a better planning process. Such part was implemented via Response Surface Methodology (R- Technique) by using a quadratic model for a Central Composite Design (CCD).

### Experimental Assumptions

The following assumptions are depended in order to facilitate the calculation of the actual time of work requirements in the job shop as mentioned below:

- 1- The daily actual time work for the job shop is (5) hours.
- 2- Processing times are modeled by independent random variables.
- 3- Setup times and removal times are included in processing times.
- 3- Transportation times are negligible.
- 4- Worker rest time not consider.
- 5- Machines break down un suppose.
- 6- Availability of skilled employee.
- 7- Availability of tools and production requirements operations.
- 8- A suitable workshop environments.
- 9- Friday is considered as a working day.

### Independent Variables

The main effective factors of the production operation are the availability of production capacity ( $C_a$ ) which depend upon the number of working machines. Shop capacity can be calculated as follow:

$$C_a = M \times hr \quad (11)$$

Where: :  $C_a$  Daily capacity,  $M$ : Number of machine,  $hr$ : Number of activity hours

### Dependent Variable

There are some dependent variables that appear when the system is working such as:

- 1- Average daily machine running time:

$$R_a = \frac{\sum_{i=1}^n Mh}{W_d} \quad (12)$$

Where:  $R_a$  : Average daily machine running time,  $Mh$  : machine hours,  $W_d$  : Working days.

- 2- Idle time: or machine waiting time, it appears in the production operation and is affected on the production capacity and can be calculated:

$$I_d = C_a - R_a \quad (13)$$

Where  $I_d$  : Idle time

3- Average daily order waiting time:

$$O_{dw} = \frac{\sum_{i=1}^n (Mh - C_a)}{w_d} \quad (14)$$

4-Cost of idle time:

$$C_{it} = I_d \times C_{hi} \quad (15)$$

Where  $C_{hi}$  : cost per hour of idle time.

5- Cost of waiting orders:

$$C_{ow} = O_{dw} \times C_{hw} \quad (16)$$

$C_{hw}$  : cost per hour for order waiting.

6-Total cost:

$$C_t = C_{ow} + C_{it} \quad (17)$$

$C_t$ , the total cost represented as a sum of  $C_{ow}$  and  $C_{it}$  must be small value and it's useful to identify the best capacity  $C_a$ .

## ARCHITECTURE OF THE SHOP-LEVEL PRODUCTION SCHEDULER

The deterministic job shop scheduling problem consists in finding a production capacity which minimizes a criterion. In order to solve this performance evaluation problem, two techniques are proposed: discrete event simulation and optimization technique based on Response Surface Methodology (R-Technique). While discrete event simulation is an extremely accurate modeling approach, capable of predicting system performance, model optimization improved output analysis of the simulation technique. Due to the complex requirements of the production simulation, in-house software in Visual Basic with a Microsoft Excel front-end is developed. The simulation model of the case-study implements dual frame architecture (Simulation & Optimization frames). Simulation is responsible for the data preparation, model creation, initialization and evaluation. The components of the system are created into the model frame in **Fig. (3)**. The object-oriented hierarchical simulation module of the proposed planning system is based on the functional decomposition approach. The simulation includes the modeled elements of the case study and is created following the simulation modeling process as described in book record data for the workshop. Automated Scheduling System (ASS) using visual basic 6 in designing the system main windows in addition to computation of arithmetic operations. The system ability to define the best process capacity for the workshop via determining the lowest cost through a real and continuo interactions between system components which are mainly constructed from the following:

A- User interface.

B- Data base.

C- Estimation number of orders arrival model.

D- Estimation machine hour's model.

E- Scheduling evaluation.

F- Capacity simulation.

G- Applying R-Technique (Response Surface Methodology) (RSM).

Simplified details for the main system components can be shown in Fig. (3).

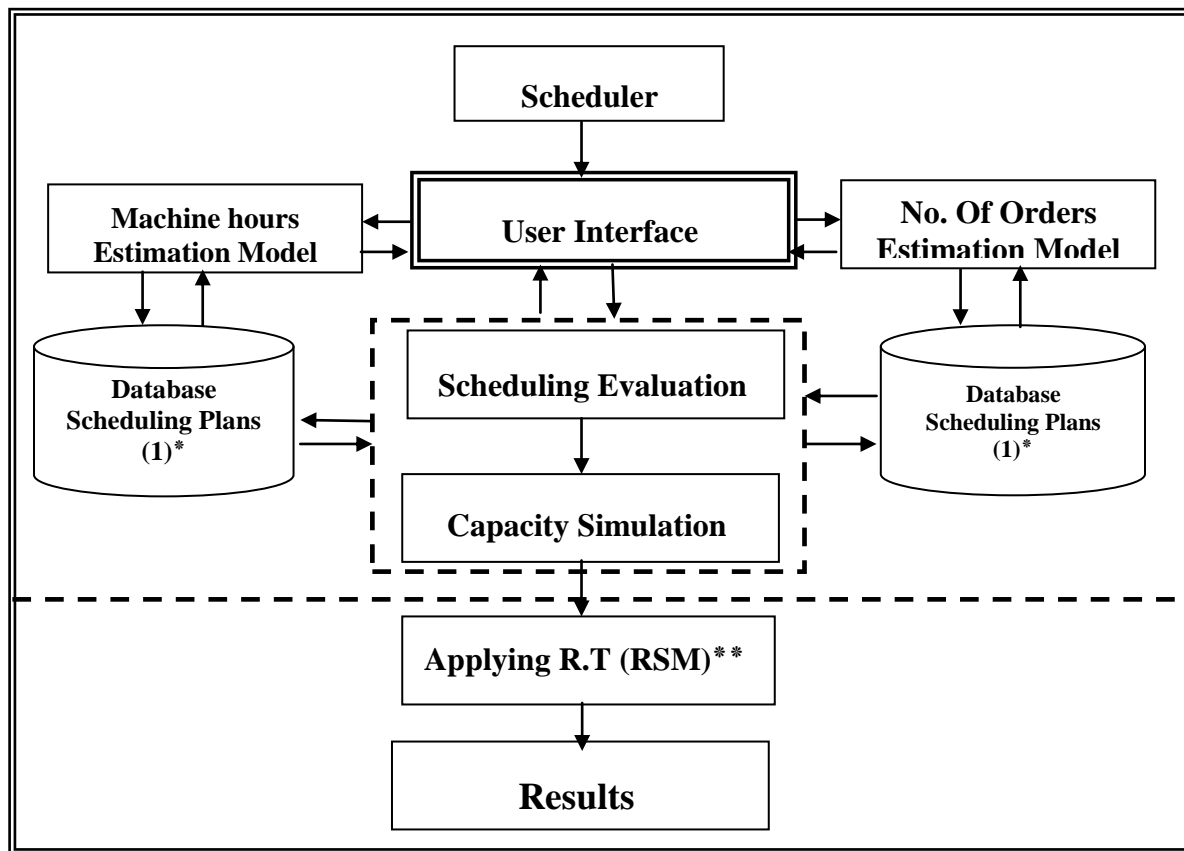


**Fig. (3): Architecture and the main process flow in the Shop-level Production Scheduler.\*: the same data, \*\*: software package.**

### Automated Scheduling System

At the program start to apply the designed system a preliminary window will appear to illustrate the system name Automated Scheduling System(ASS). ASS is an organized system to estimate the number of orders, machine hours, and selection of optimal capacity to assist decision makers at workshop level. it consist of:

- Number of orders estimating module.
- Machine hour's estimation module.
- Scheduling evaluation module.
- Capacity simulation module.

### ASS Context

The main characteristics of ASS approach, with respect to the other software, are respectively:

- Accurate and rapid computation of the arithmetic operations.
- The ability of the system to estimate any time period that is defined by the planner to the production operations
- The capability of the system estimate the data distribution types.
- The main logical steps that are performed is illustrated in figure (3).



## SOLUTION REPRESENTATION

### Preliminary Industrial Application

Using the result simulation system (ASS) for the current production capacity in the workshop, indicate that trade-offs between expected production cost and maximize available resource utilization under demand uncertainty is un justice. A review for current state of the daily capacity process in workshop through investigation by (ASS) system forecast the results shown in **Table (3)**.

According to that data, distinction needs to be made between the available daily capacity process and total cost associated with maximum utilization for that resource. The fitness is generated by increasing the level which allows to confirm to the objective.

**Table(3): Simulation results for current daily process level in workshop.**

Daily Capacity ( M/c.hr)	Average Daily Machine Running ( M/c.hr)	Average Daily Idle Machine Time ( M/c.hr)	Average Daily Waiting Orders Time ( M/c.hr)	Cost Idle Time (ID)	Waiting Orders Cost (ID)	Total Cost (ID)
100	91.53	8.47	141.79	42.35	283.58	325.43

### Improvement by Job Shop Production Scheduler (ASS)

For 75 work days in workshop, the proposed system evaluated that the optimum capacity lies at 130 machine hours. This value of daily process capacity ensure the performance criteria , maximize utilizing accomplished with minimum cost. The **Table (4)** and **Fig. (5)** and **(6)** indicated that result. This level of process capacity considered as aggregate solution and will be refining in next step by the technique optimization Response Surface Methodology (R-technique).

**Table (4): The Results (based on a period of 75 days).**

No.	Capacity(hr.)	Running(hr.)	IdealTime(hr.)	WaitingTime(hr.)	IdealTime	OrdersWaiting	Total
74	123	110.82	12.18	161.10	60.90	322.20	383.10
75	124	111.58	12.42	160.10	62.10	320.20	382.30
76	125	112.35	12.65	159.10	63.25	318.20	381.45
77	126	113.12	12.88	158.10	64.40	316.20	380.60
78	127	113.88	13.12	157.10	65.60	314.20	379.80
79	128	114.65	13.35	156.10	66.75	312.20	378.95
80	129	115.42	13.58	155.10	67.90	310.20	378.10
81	130	116.18	13.82	154.10	69.10	308.20	377.30
82	131	116.95	14.05	157.68	70.25	315.36	385.61
83	132	117.68	14.32	161.51	71.60	323.02	394.62
84	133	118.40	14.60	160.51	73.00	321.02	394.02
85	134	119.13	14.87	159.51	74.35	319.02	393.37
86	135	119.85	15.15	158.51	75.75	317.02	392.77

It can be noted from these results that when as assumption of values of daily process capacity, values of average daily machine running appear to be in continuous increment with every increment of the assumption of daily process capacity; i.e. the relation between them is proportional. After that the system calculate the values of machine waiting time (Idle time) which also appear to be in

continuous increment with any increment of the daily process capacity. Then the values of average daily order waiting time appears in **Table (4)** and it is in continuous decrement with every increment in the assumption of the values of daily process capacity, then the columns of the cost as shown in the same table. These columns illustrate the cost of idle time which appears to be in continuous increment because the idle time is already in continuous increment. The cost of order waiting time is always in decrement situation according to the decrement of the values of average daily order waiting time. After that the system sketches these results as a curves as shown in **Fig.(4)**. The same figures and tables show that the optimum capacity lies at 130 machine hours. This level of process capacity is considered as aggregate solution and will be refining in next step by technique optimization Response Surface Methodology (R-technique).

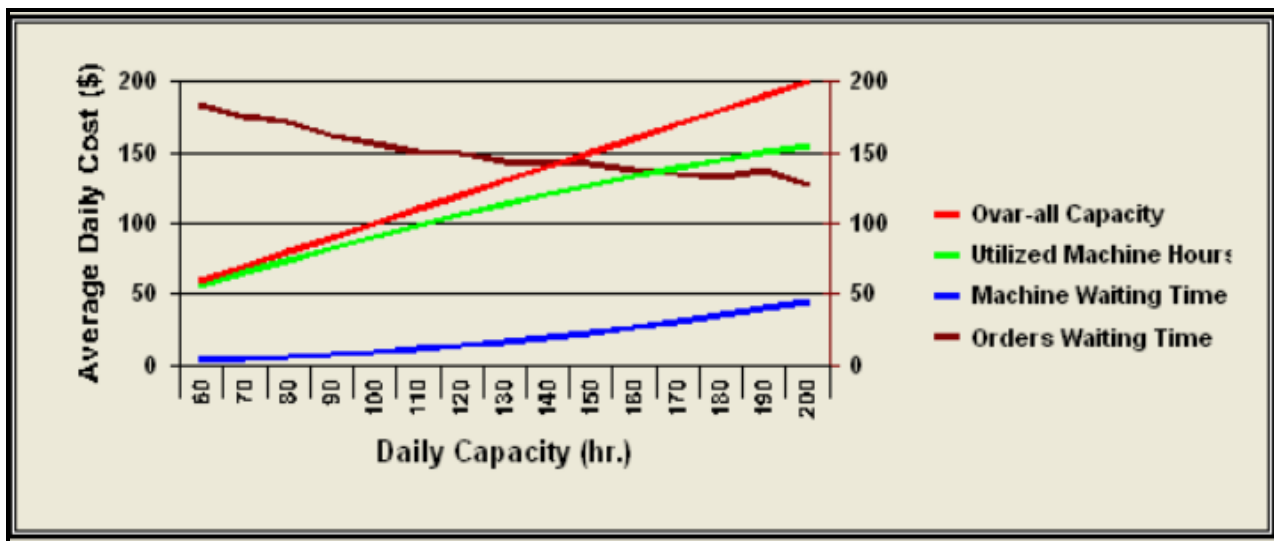


Fig. (4): Effect OF Altering the Plant Capacity.

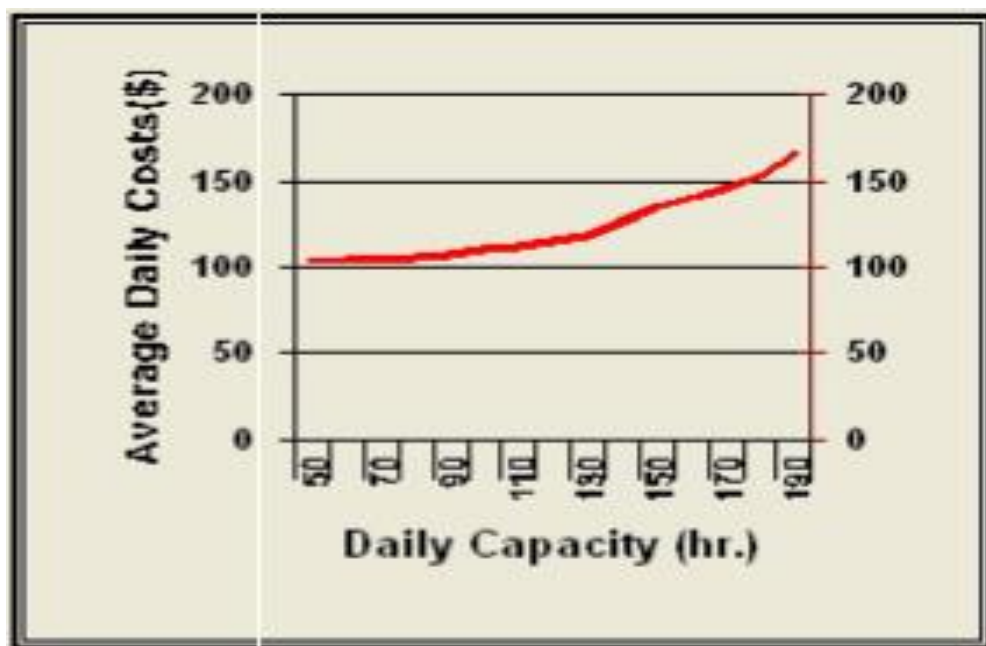


Fig. (5): Effect of Plant Capacity on Average Penalty Costs per Day.

After applying the daily process capacity which determined by ASS system in workshop, the queue of waiting order decreases as shown **Fig. (6)**.



**Fig. (6): Queue of Waiting Orders (measured in Machine Hours) when Capacity is 130hours).**

### Applying Optimization RSM Techniques to Refine the Design Solution

The objective of the proposed simulation-based optimization is to arrive at the closest to optimal solution alternative (in terms of a set of Daily Capacity value as a design parameters and a set of Total cost as a system performance metrics) at which the overall machine capacity utility score is maximized with minimum cost.

### Model Fitting

Once the simulation results are acquitted, model fitting technique can be implemented to portray analytically the relations between input factor (Daily Capacity) and the output measures (Average Daily Machine Running, Average Daily Machine idle time, Average Daily Order Waiting time, Idle Time Cost, Order Waiting Cost, Total Cost). Due to the effect of one factor, Linear Fitting is performed with respect to all performance measures. **Table (5)** is obtained from the Statistical Discovery Software™ (JMP) version 5.0 which was used in this research for regression and graphical analyses of the data obtained for the Idle Time Cost model. This table contain model-fitting measures, including coefficients of determination and the contribution of term to the model sum-of squares and the linear equations fitted by the method of least-squares for all output measures. This linear regression equation is obtained through the analysis of variance for the simulation results. Fitted values are as close as possible to observed values, namely, minimization of residuals or error of prediction. The required assumptions of uncorrelated error with mean zero and constant variance has to be carefully verified through residual analysis. Linear fit plot for the Idle Time Cost model presented in **Fig (7)**.

**Table (5): Summary of linear fit analysis with respect to the Idle Time Cost.**

<i>Analyses of Variance (ANOVA)</i>						
<i>Source</i>	<i>Sum-of-squares</i>	<i>DF</i>	<i>Mean square</i>	<i>R<sup>2</sup></i>	<i>F Ratio</i>	<i>p-value Prob &gt; F</i>
<i>Model</i>	2253.6562	2	448.461	0.99995	125.7436	< 0.0001
<i>Residual</i>	0.1131	38	3.566	0.054561	-	-

<i>Cor Total</i>	2253.7693	40	-	-	-	-
<i>Parameter Estimates</i>						
<i>Term</i>	<i>Estimate</i>	<i>Std Error</i>	<i>t Ratio</i>	<i>Prob &gt;  t </i>		
<i>Intercept</i>	-46.65721	3.216401	65.05	<.0001		
<i>Daily Capacity</i>	0.6254077	0.02464	-16.04	<.0001		
<i>Expected Idle Time Cost = -46.65721 + 0.6254077 Daily Capacity</i>						

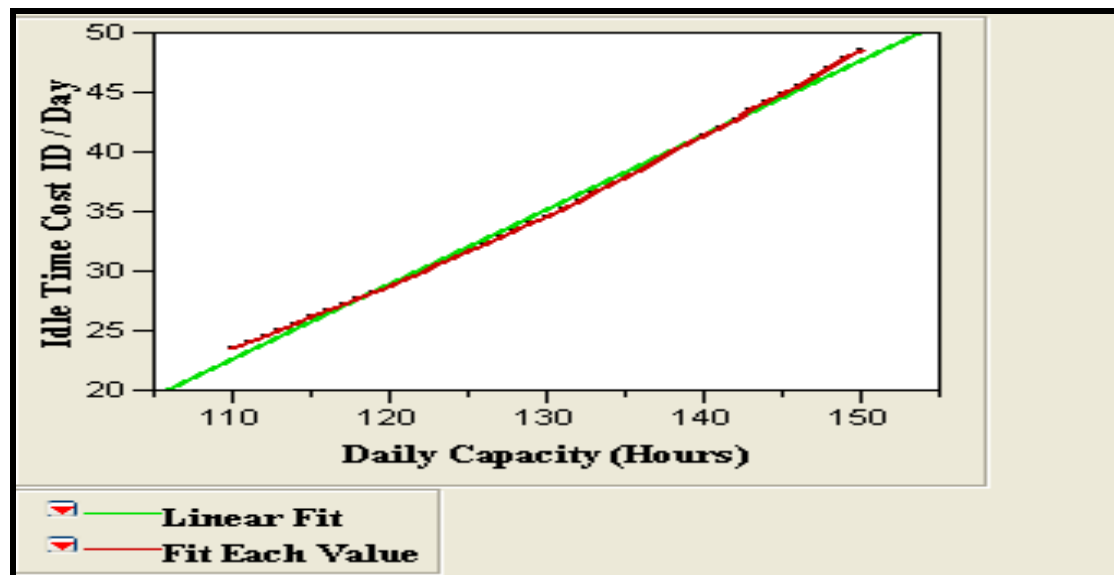


**Fig. (7): A Model Fitting plot for the Idle Time Cost.**

The statistical significance of the regression equations was checked by an F-test (ANOVA). The ANOVA results showed that the model of performance measures is appropriate. The models was lowly significant ( $p < .0001$ ) with a satisfactory value of determination coefficient  $R^2 = 0.999$  for idle time cost,  $R^2 = 0.868$  for Order waiting cost,  $R^2 = 0.969$  for total cost, indicating that 99 %, 86 %, and 96 % of the variability in the response could be explained by the expected model equations given above in **Table (6)**. This indicated a good agreement between the experimental and predicted values for out put measures.

**Table (6): Regression equations for all performance measures.**

<i>Performance Measure</i>	<i>Expected Model Equation</i>
<b>Idle Time Cost</b>	<b>-46.65721 + 0.6254077 Daily Capacity</b>
<b>Order Waiting Cost</b>	<b>104.59392 - 0.1973885 Daily Capacity</b>
<b>Total Cost</b>	<b>58.289843 + 0.4293258 Daily Capacity</b>

### Optimizing By RSM

The factor in the design was studied at 41 values starting by 110 hours and the increment by one hour for each run end at 150 hours. The minimum and maximum conditions for the performance measures is set with respect to their requirements centrifuged at the best resources utility, and low cost.

## Numerical Optimizing

### A- Performance Measures Settings

**Table (7): Input settings of both the Input Factor (Daily Capacity) and Performance Measures**

<i>Name</i>	<i>Goal</i>	<i>Lower Limit</i>	<i>Upper Limit</i>	<i>Lower Weight</i>	<i>Upper Weight</i>	<i>Importance</i>
<i>Daily Capacity</i>	<b>Is in Range</b>	110	150	1	1	3
<i>Idle Time Cost</i>	<b>Is in Range</b>	23.58	48.58	1	1	3
<i>Orders Waiting Cost</i>	<b>Is target <math>\leq 74.76</math></b>	74.76	83.6	1	1	3
<i>Total Cost</i>	<b>Minimize</b>	107.18	125.13	1	3	3

### B- Solutions for 41 Combinations of Categorical Factor Levels

**Table (8): 30 Solutions found for 41 Combinations of Categorical Factor Levels.**

<i>Number</i>	<i>Daily Capacity</i>	<i>Idle Time Cost</i>	<i>Orders Waiting Cost</i>	<i>Total Cost</i>	<i>Desirability</i>	
1	130	34.55	77.05	111.6	0.563	<b>Selected</b>
2	129	33.95	77.55	111.5	0.547	
3	128	33.38	78.05	111.43	0.528	
4	118	27.68	80.75	108.43	0.510	
5	127	32.8	78.55	111.35	0.508	
6	126	32.2	79.05	111.25	0.488	
7	121	29.33	80.4	109.73	0.478	
8	114	25.58	81.6	107.18	0.476	
9	117	27.15	81.25	108.4	0.464	
10	125	31.63	79.55	111.18	0.464	
11	120	28.75	80.9	109.65	0.443	
12	124	31.05	80.05	111.1	0.438	
13	116	26.63	81.75	108.38	0.412	
14	123	30.45	80.55	111	0.410	
15	119	28.2	81.4	109.6	0.401	
16	122	29.88	81.05	110.93	0.378	
17	131	35.13	78.84	113.97	0.360	
18	115	26.1	82.25	108.35	0.353	
19	111	24.58	82.6	107.18	0.336	
20	112	24.58	82.6	107.18	0.336	
21	139	40.65	77.26	117.91	0.216	
22	140	41.35	76.76	118.11	0.215	
23	138	39.98	77.76	117.74	0.215	
24	137	39.28	78.26	117.54	0.214	
25	141	42.05	76.26	118.31	0.213	
26	136	38.58	78.76	117.34	0.212	
27	142	42.75	75.76	118.51	0.211	
28	143	43.43	75.26	118.69	0.209	
29	135	37.88	79.26	117.14	0.208	
30	144	44.13	74.76	118.89	0.205	

Because the most important objective in the case study - workshop daily capacity machine level setting –closely related with total cost (Idle Time Cost & Orders Waiting Cost) , this fact take into consideration, the trade-offs between expected production cost and robust capacity planning.

**Table (7)** shows the input settings of both the input factor (daily process capacity) and performance measures that are used by optimization procedure.

### C- Optimum Solution

The results of performance measures for 41 combinations of categoric factor levels to yield a desirable answer of input factor as shown in **Table (8)** which indicated that similar results were obtained for the optimum value founded in search region for performance measures satisfied. The value found to be 130 hours with a predicted a desirability grade of 0.563. However, these are based on restrictive assumptions about the Input settings of both the Input Factor (Daily process Capacity) and Performance measures. **Table (9)** summarizes the values of performance measures associated with prediction optimum value of input factor listed in table. Therefore, it can be concluded that optimum daily process capacity level 130 hours as presented in **Fig. (8) & Fig. (9)**.

**Table (9): The values of Output Measures with respect to prediction optimum value of Input Factor.**

<i>Input Factor</i>			
<i>Name</i>	<i>Low Level</i>	<i>High Level</i>	<i>Predicted Value</i>
<i>Daily Capacity</i>	110 Hours	150 Hours	130 Hours
<i>Out Put Measures</i>			
<i>Name</i>		<i>Predicted Value</i>	
<i>Idle Time Cost</i>		34.55 ID / Day	
<i>Orders Waiting Cost</i>		77.05 ID / Day	
<i>Total Cost</i>		111.6 ID / Day	

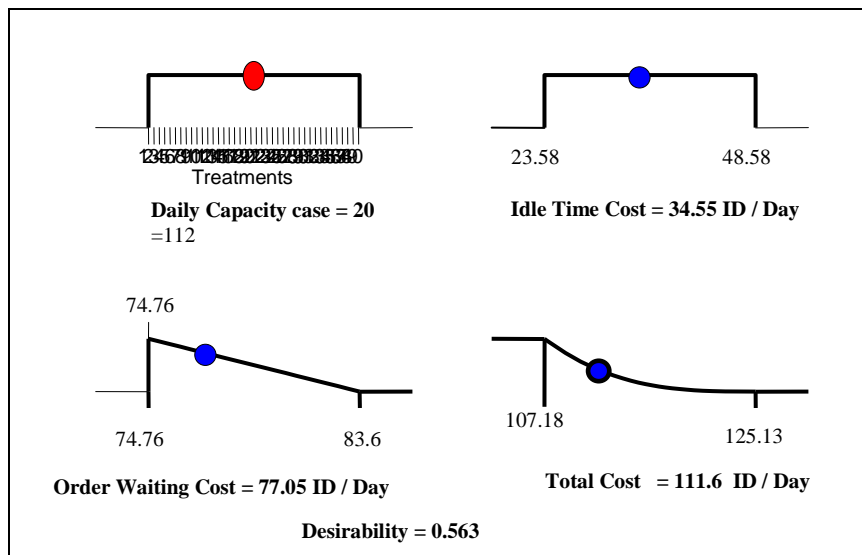


**Fig. (8): Input Factor and Output Measures Values of the Best Solution calculated by RSM technique.**



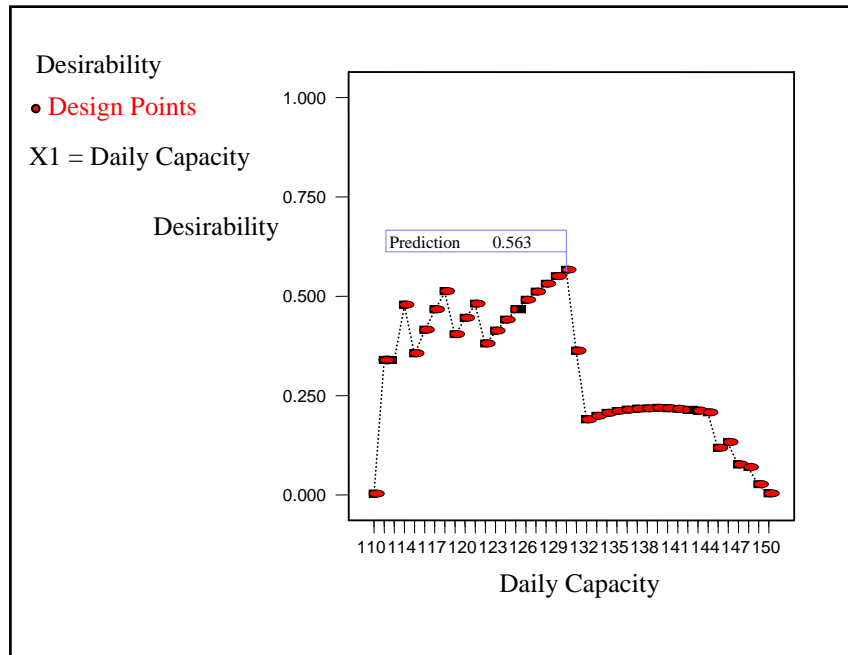


**Fig. (9): Desirability grade for prediction point of optimum daily capacity.**

These **Fig. (8) & Fig. (9)** reflects the role of input factor (Daily Process Capacity) on the controlled responses and then the out put measures (the costs) and this defined medium optimizing by one variable for determine the performance criteria , maximize utilizing accomplished with minimum cost. Further optimization for that variable to drawn at the desired value. Design Expert (Ver.7.0) was used in this investigation.

#### Graphical Optimizing

As mentioned, desirable feature for response surface design of input factor (daily process capacity) demonstrated at center point (130 hours), this factor was selected as key parameter to maximize the utility resources. **Fig. (10) and Fig (11)** present two-dimensional contour plots for the daily process capacity with respect to responses and output measures. The shapes of the contour plots, indicate that the interactions between the corresponding responses are significant and also indicates that the effects of input factor on responses & output measures on are significant. The optimum conditions inside the design boundary for daily process capacity were 130 hours.

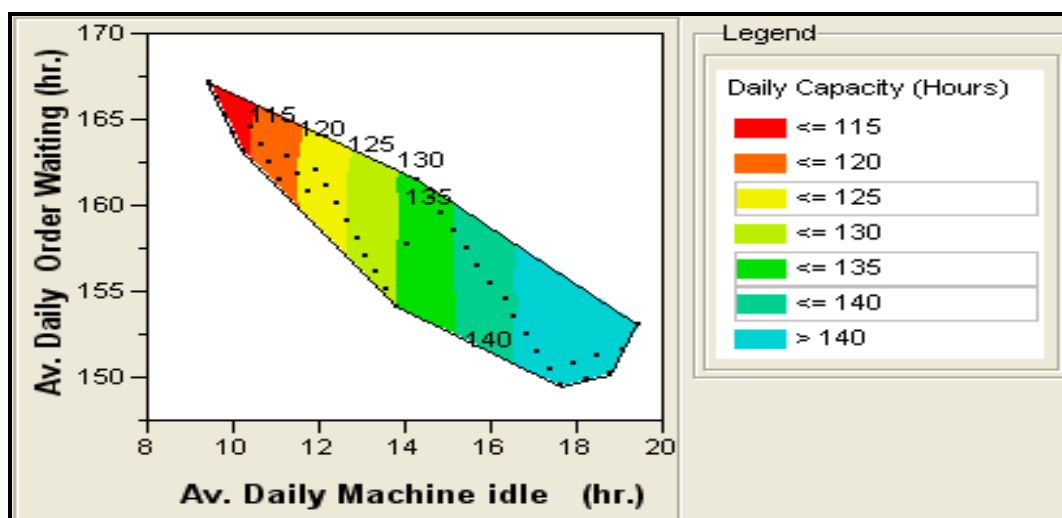


**Fig. (10): A counter plot of the daily process capacity with responses average daily orders waiting time & average daily machine idle time in figure.**

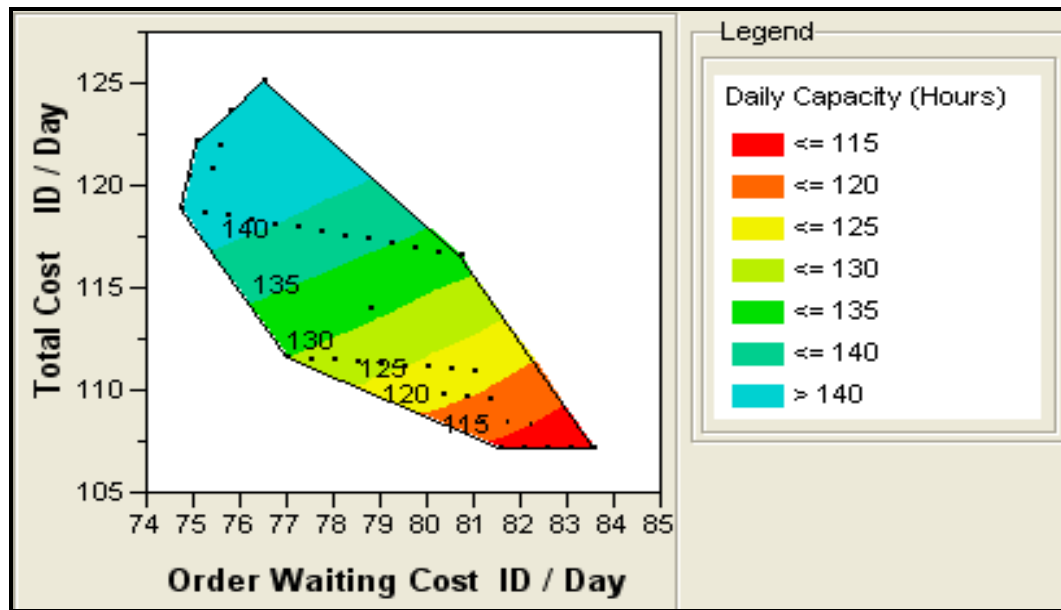


**Fig. (11): A counter plot of the daily process capacity with output measures Orders Waiting Cost, and Total Cost .**

In an optimization routine in the most general sense is a procedure that, when applied to a model, will result in the determination of the best model as defined by the fitness of an objective function. The optimization objectives can be formulated as follows: (a) maxim utilization of one type of available recourses (Available Daily Machine Capacity) (b) Minimizing the inherent cost matched within the context. From **Tables (8), and (9), Fig. (8),Fig. (9),Fig (10) and Fig. (11)**, it is evident that the input data for available daily machine capacity satisfies the optimization objectives in the case study is 130 hours.

## CONCLUSIONS

The practical investigation indicates that performance of a scheduling system is not evaluated to satisfy a single objective but to obtain a trade-off schedule regarding multiple objectives, this study provide a quick and favorable schedule for the addressed scheduling problem with minimization of one performance measure an economic criterion, namely minimum total cost and maximization of technological criterion utilization of overall capacity processes. Important entity is modeled using state variable that change only is available daily capacity. The simulation model advances by executing specific procedures at these values of variable and terminates when all values have passed. It can be concluded that:

1-In most cases, computerized tools enable an individual to simulate and evaluate a large number of design solutions with respect to multiple performance measures they overlook the effect of interactions among design factors that play significant role in the creating of best solution. RSM bridge these gaps by generating a set of alternative design solutions in systematic manner, and apply educated changes to configuration parameters. Such an approach enables to reach a satisfactory solution, with respect to both economical and technological measures, within limited number of examined solutions.

2- The proposed methodology emphasized the advantages of combining computerized tools such as simulation model system, and statistical design approaches such as RSM. Capacity planning is often characterized by continuous metric factors, such as daily capacity available, labor number, workdays,....., and cost that are well suited to be input factors to RSM.



## REFERENCES

- Hicks, D.A. 1999. *A four step methodology for using simulation and optimization technologies in strategic supply chain planning*. *Proceedings of the 1999 Winter Simulation Conference* P. A. Farrington, H. B. Nembhard, D. T. Sturrock, and G. W. Evans, eds. pp1215-1220.
- Lehtonen, J.M, Ilkka, M., Ruohola, T. and Patrik Appelqvist.2003. *Simulation-based finite scheduling at albany international*. *Proceedings of the 2003 Winter Simulation Conference* S. Chick, P. J. Sánchez, D. Ferrin, and D. J. Morrice, eds. pp 1449-1455.
- Lennartz, P.1999. *ALCOM-FT Deliverable D19 Production Planning Software Prototype ?*. Institute of Information and Computing Sciences. University Utrecht. The Netherlands.
- Roy, R. and S. E. Meikle. 1995. *The role of discrete event simulation techniques in finite capacity scheduling*. *Journal of the Operational Research Society* 46 (11):1310-1321.
- Scheer, A. W. 1994. *Business Process Engineering: Reference Models for Industrial Enterprises*, Springer Verlag.
- Sellers, D. W. 1996. *A survey of approaches to the job shop scheduling problem*. *28th Southeastern Symposium on System Theory*, Baton Rouge, LA.
- Smith, S. F. 1992. *Knowledge-based production management: Approaches, results and prospects*. *Production Planning & Control* 3 (4): 350-380.
- Venkateswaran, j., Son, Young-Jun and A. Jones.2004. *Hierarchical production planning using a hybrid system dynamic-discrete event simulation architecture*. *Proceedings of the 2004 Winter Simulation Conference* R .G. Ingalls, M. D. Rossetti, J. S. Smith, and B. A. Peters, eds. pp1094-1102.
- Vollmann, T. E., W. L. Berry and D. C. Whybark.1997. *Manufacturing planning and control systems*. USA, McGraw-Hill.

**LIST OF ABBREVIATIONS**

ASS	Automated Scheduling System
CR	Critical ratio
EICO	Electrical industrial company
ANOVA	Analysis of variance
ITC	Idle time cost
RSM	Response surface methodology

**LIST OF SYMBOLS**

$DF$	Degrees of Freedom
$d_i$	Individual Desirability Function
$D_k$	Multiple Objective Function
$F$ Value	The Mean Square for the term divided by the Mean Square for the Residual
$PRESS$	The Predicted Residual Sum of Squares for the model
$P$ -value	The Probability value that is associated with the F Value for the model
SD	Standard Error
$\lambda$	Mean arrival time (number of arrivals per unit of time)
$\mu$	Mean service rate per busy server (number of customers served per unit of time)
$L_q$	Average (expected) number of customers in the queue
$L_n$	Expected number of customers waiting in line excluding the time when the line is empty.
$\rho$	Utility factor
$C_a$	Process Capacity..... hr/day
$M$	Number of machine
$h_r$	Number of activity hours.
$R$	The range of orders

$x_l$	Upper of limit
$x_s$	Lower of limit
$H$	Ranking of period
$F_R$	Relative frequency
$K$	Number of ranking
$F_A$	Absolute frequency
$N_{O.}$	Number of data
$x$	Orders number
$\mu$	Arithmetic mean
$\sigma$	Standard deviation
$f(z)$	Function of normal distribution curve
$z$	Random variable
$n$	Limit of range
$I_d$	Idle time .....hr.
$R_a$	Average daily machine running time .....hr.
$W_d$	Working days
$Mh$	Machine hours.....hr.
$O_{dw}$	Average daily order waiting time..... hr.
$C_{it}$	Cost of idle time.....ID/day
$C_{hi}$	Cost per hour of idle time .....ID
$C_{ow}$	Cost of orders waiting .....ID/day
$C_{hw}$	Cost per hour for orders waiting.....ID
$C_t$	Total cost .....ID/day
M/C.H.	Machine hours.....hr.
C.F	Cumulative frequency



## NUMERICAL STUDY OF TWO-DIMENSIONAL TRANSIENT NATURAL CONVECTION IN AN INCLINED SHALLOW POROUS CAVITY EXPOSED TO A CONSTANT HEAT FLUX

Jasim M. A. Al-lateef  
University of Technology  
Diyala -Iraq

Ayad K. Hassan  
University of Diyala  
Baghdad-Iraq

### ABSTRACT

Numerical models are used to solve the two-dimensional transient natural convection heat transfer problem in an inclined shallow porous cavity. A constant heat flux is applied for heating and cooling all opposing walls. Solutions for laminar case are obtained within Rayleigh number varied from 20 to 500 and aspect ratio for porous cavity varied from 2 to 4. A finite difference method is used to obtain numerical solutions of full governing equations. Both vorticity and energy equation are solved using alternating direct implicit (ADI) method and stream function equation by successive over relaxation (SOR) method. The results are presented for the flow field, temperature distributions, and average Nusselt number in terms of the Rayleigh number, aspect ratio, and the inclination angle of cavity. the convection becomes more and more vigorous as the orientation angle of the cavity is increased and for high Rayleigh number no steady unicellular flow could be maintained in side the cavity. The effect of inclination angle on Nusselt number is more pronounced as the Rayleigh number is increased. When the inclination angle increased the Nusselt number increased and sudden transition appears and flow becomes unicellular and Nusselt number increased clearly. The value of mean Nusselt number strong function with the value of Rayleigh number, aspect ratio and the orientation of porous cavity.

### الخلاصة

الطرق العددية استخدمت لحل مسألة انتقال الحرارة ثنائي الابعاد بالحمل الحر للحالة غير المستقرة من خلال تجويف مسامي سطحي مائل. تم تسليط فيض حراري ثابت لتسخين وتبريد الجدران المتقابلة. الحل العددي كان ضمن حالة الجريان الطبقي ضمن رقم رالي يتراوح من 20 الى 50 ونسبة باعية تتراوح من 2 الى 4. تم استخدام طريقة الفروقات المحددة للحصول على الحل العددي للمعادلات الحاكمة. كل من معادلة الدوامية والطاقة تم حلها باستخدام طريقة الاتجاه الضمني المتناوب و معادلة دالة الانسياب تم حلها باستخدام طريقة التراخي فوق التعاقب. تم تمثيل نتائج الجريان وتوزيع درجات الحرارة ومعدلات رقم نسلت بدلالة رقم رالي ونسبة الباعة وزاوية ميلان التجويف. ان انتقال الحرارة بالحمل يصبح كبير واكثر فعالية عند زيادة زاوية الميلان للتجويف. عند قيم رقم رالي العالية لا يمكن الحفاظ على جريان مستقر واحادي الخلية داخل التجويف. ان تاثير زاوية الميلان على رقم نسلت يتضح اكثر عند زيادة رقم رالي. ان زيادة زاوية الميلان يؤدي الى زيادة رقم نسلت ويظهر تحول مفاجا والجريان يصبح احادي الخلية ورقم نسلت يزداد بوضوح. ان قيم رقم معدل رقم نسلت تعتمد بشكل كبير على رقم رالي ونسبة الباعة وزاوية ميلان التجويف المسامي.

**KEYWORD: Numerical Study, Transient , Natural Convection , Inclined ,Shallow Porous Cavity ,Constant Heat Flux**

## INTRODUCTION

Over the past years, natural convection heat transfer in cavities filled with a fluid-saturated, porous medium has several important geophysical and engineering applications. These include regenerative heat exchangers containing porous materials, high performance insulation for building and cold storage, solar power collection, underground spread of pollutants, and convection in the earth's crust Buchberg et al. (1976), Seki et al. (1978). Another important area of application is heat transfer from the storage of agriculture products which generate heat transfer as a result of metabolism. Natural convection effects on heat transfer in a differentially heated rectangular porous cavity, with top and bottom walls insulated, is of fundamental interest in each of these areas. Several investigators [Seki et al.(1978), Chan et al. (1970) , Burns et al. (1976), Walker and Homsy (1978) , Bejan (1979) , Simpkins and Blythe (1980) and Prasad and Kulacki, (1984) have presented analytical and experimental results for the case when both the vertical walls are at constant temperature. Analytical work includes numerical solutions, boundary layer solutions, integral analyses, and series solutions. Based on the past studies, various correlations, covering a wide range of Rayleigh number and cavity height- to-width (aspect) ratios, have been presented for heat transfer coefficients Seki et al. (1978), Chan et al. (1970), Walker and. Homsy (1978), Weber(1975) and Bories and Combarnous (1973).

The most previous theoretical publications deal with vertical Burns et al.(1976) and Weber (1975) or horizontal Eldr (1974) case. For situations involving inclined layers, available studies are relatively limited. The problem of a sloped porous layer, heated isothermal from below has been considered theoretically and experimentally by Bories and Combarnous (1973). Depending on the value of slope of the layer and Rayleigh number, different shapes of free convection movements have been observed.

Holst and Aziz (1972) considered temperature-dependent physical properties, investigated the heated transfer of a tilted square of porous material. More recently, the existence of multiple solutions, in a slightly inclined porous cavity heated from the below, has been studied numerically by Moya et al. (1981) and analytically by Caltagirone and Bories (1985) who determined their stability. It was demonstrated that for small angles of inclinations, three different real solutions may exist for a given Rayleigh number and aspect ratio. Vasseur et al. (1986), studied the effect of natural convection in an inclined, rectangular, porous layer when a constant heat flux is applied on two opposing walls, while the other two walls are maintained adiabatic.

Double-diffusion occurs in a wide range of scientific fields, such as oceanography, astrophysics, geology, biology and chemical processes; so, the author's interest more and more for the heat and mass transfer developed in enclosures or cavities. About these case of fluid flows generated by combined temperature and concentration gradients, the studies of double-diffusive natural convection have centered chiefly their analyses on the limit cases of dominating thermal buoyancy force or concentration buoyancy force. The considered spaces are enclosures comprising a fluid completely occupied by porous medium Alavyoon (1993), Chamkha and Al-Naser (2001) and Bennacer et al (2001).

The problem of double-diffusive flow inside an inclined square cavity which is divided by a porous medium was studied numerically by Rahli and Bouhadef(2004).The numerical finite volume method was employed to resolve the governing equations which describe the problem. Graphical results for various parametric conditions were presented and discussed. It was found that the heat and mass transfer mechanisms and the flow evolution inside the enclosure depend strongly on the dimensionless characteristic parameters (Lewis number  $Le$ , Darcy number  $Da$ , enclosure inclination angle  $\phi$  and



buoyancy ration).

Thus, the most above studies have considered cavities with isothermal walls, natural convection in porous enclosures, focused on the case of rectangular cavities heated and cooled only through two opposing sides while the other two sides are kept adiabatic, however in practice, all the faces of the enclosure may be thermally active. Despite the fact that in many engineering applications the temperature of a wall is not uniform but, rather, is a result of imposition of a constant heat flux Vasseur et al. (1986). Results available for situations where a constant heat flux is applied on one Prasad et al. (1984) or two Bejan (1983) walls have been reported only for the case of a vertical cavity.

The objectives of the present work is to analyze the behavior of natural convection flows in a shallow inclined porous layer, when all four faces of the rectangle enclosure are exposed to constant heat fluxes, opposite boundaries being heated and cooled, respectively, which are new to the author's knowledge.

When the porous layer is slightly inclined with respect to the horizontal line, several types of flow configurations appear Caltagirone and Bories (1985). During the last years, several authors have been studied the criterion for transition between the different configurations of such flows. Weber (1975) demonstrated that a three-dimensional perturbation is steadier than a two-dimensional one if the inclination angle is close to zero. The existence of different flow configurations and the transition between them was also investigated by means of two- and three-dimensional numerical simulations by Chan et al. (1970).

On the basis of the parallel flow approximation, a closed-form solution is obtained for the temperature and velocity distribution in the limit of a shallow enclosure ( $A \gg 1$ ). In the following section, the differential equations, which described the physical model considered here, are formulated in a standard manner assuming the validity of Darcy's law and the Boussinesq approximation. The full governing equations are solved numerically, using finite difference procedure. Effects of various parameter such as Ra, the Rayleigh number,  $\phi$ , angle of inclination, and A, aspect ratio, are analyzed.

## STATEMENT OF THE PROBLEM

Consider the natural convection motion of a fluid filling a homogenous, isotropic, porous medium on all sides by an impermeable rectangular box. The enclosure, shown in **Fig.1**, is of height H, width L and is tilted at an angle  $\phi$ , with respect to horizontal plane. A constant heat flux ( $q$ ) is applied along the top and bottom the y-axis boundaries which heat and cool respectively at the same rate. A constant heat flux ( $aq$ ), where ( $a$ ) is a constant, is also applied in the x-axis on the two boundaries, where ( $a$ ) assume equal unity in the present study to ensure uniform heat flux for all sides of porous layer.

Assuming the validity of Darcy's law and Boussinesq approximation, the equations describing conservation of mass, momentum and energy in the medium are as follows Vasseur et al. (1986) and Torrance (1985).

$$\frac{\partial u}{\partial x} + \frac{\partial v}{\partial y} = 0 \quad (1)$$

$$u = -\frac{K}{\mu} \left( \frac{\partial p}{\partial x} + \rho g \cos \phi \right) \quad (2a)$$

$$v = -\frac{K}{\mu} \left( \frac{\partial p}{\partial y} - \rho g \sin \phi \right) \quad (2b)$$

$$\frac{\partial T}{\partial t} + u \frac{\partial T}{\partial x} + v \frac{\partial T}{\partial y} = \alpha \left( \frac{\partial^2 T}{\partial x^2} + \frac{\partial^2 T}{\partial y^2} \right) \quad (3)$$

where  $u$ ,  $v$ ,  $p$ ,  $g$ ,  $K$ ,  $\mu$  and  $\alpha$  stand for the velocity components in  $x$  and  $y$  directions, pressure, gravitational acceleration, medium permeability, viscosity and thermal diffusivity, respectively. Here, it has been assumed that the fluid properties are constant, except for the density variation in producing the buoyancy force. Viscous drag and inertia terms are neglected because their magnitudes are small order compared to other terms. Also, heat transfer by radiation is assumed to be small compared to conduction and convection and hence is neglected in the formulation of the problem Vasseur et al. (1986) and Prasad and Kulacki (1984).

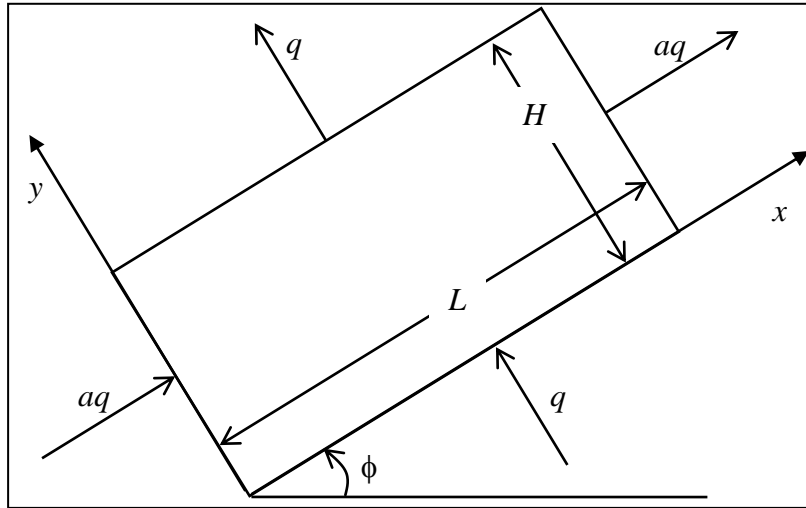


**Fig.1** The physical model and coordinate system

As usual, the governing equations are simplified if  $u$  and  $v$  is replaced by approaching define a stream function  $\Psi'$  which satisfies the continuity eq.(1) identically

$$u = \frac{\partial \Psi'}{\partial y}, \quad v = -\frac{\partial \Psi'}{\partial x} \quad (4)$$

Further, the pressure terms appearing in eq.(2) are eliminated through cross-differential. The momentum and energy equations become:

$$\nabla^2 \Psi' = \frac{-Kg\beta}{\nu} \left( \frac{\partial T}{\partial x} \cos \phi - \frac{\partial T}{\partial y} \sin \phi \right) \quad (5)$$



$$\nabla^2 T = \frac{1}{\alpha} \left( \frac{\partial \Psi}{\partial y} \frac{\partial T}{\partial x} - \frac{\partial \Psi}{\partial x} \frac{\partial T}{\partial y} \right) + \frac{1}{\alpha} \frac{\partial T}{\partial t} \quad (6)$$

where  $\nu$ - is the kinematics viscosity  $\mu/\rho$ .

Finally, eqs.(5,6) are put in non-dimensional form by defining a new set of variables

$$\tau = \frac{t\alpha}{L^2}, \quad X = \frac{x}{L}, \quad Y = \frac{y}{L}, \quad \Psi = \frac{\Psi'}{\alpha}, \quad \Theta = \frac{(T - T_o)}{\Delta T} \quad (7)$$

where

$T_o$ , is the temperature at the geometric center of the cavity and  $\Delta T = (qL)/k$ , a characteristic temperature difference.

The resulting equation for the stream function  $\Psi$  and temperature  $\Theta$  are :

$$\nabla^2 \Psi = -Ra \left( \frac{\partial \Theta}{\partial X} \cos \phi - \frac{\partial \Theta}{\partial Y} \sin \phi \right) \quad (8)$$

$$\nabla^2 \Theta = \left( \frac{\partial \Psi}{\partial Y} \frac{\partial \Theta}{\partial X} - \frac{\partial \Psi}{\partial X} \frac{\partial \Theta}{\partial Y} \right) + \frac{\partial \Theta}{\partial \tau} \quad (9)$$

where

$Ra$ , is a Rayleigh number based on the constant heat flux ( $q$ ) and the permeability  $K$  of the medium

$$Ra = \frac{g\beta KL^2 q}{\alpha \nu k} \quad (10)$$

The boundary conditions on  $\Psi$  and  $\Theta$  are:

$$\Psi = 0, \quad \frac{\partial \Theta}{\partial X} = \mp a \quad \text{on} \quad X = 0, A \quad (11a)$$

$$\Psi = 0, \quad \frac{\partial \Theta}{\partial Y} = \mp 1 \quad \text{on} \quad Y = 0, 1 \quad (11b)$$

where

$A = H/L$ , is the cavity aspect ratio.

$a$ , is a constant controlling the fraction of the heat flux imposed on the y-axis walls with respect to that imposed on the x-axis walls, assume equal unity in the present study.

The overall heat transfer cross the enclosure is expressed by average Nusselt number, defined by Vasseur et al. (1986).

$$\overline{Nu} = \left( \frac{q}{\Delta T} \right) \frac{L}{k} = \frac{1}{\Delta \Theta} \quad (12)$$

where



$\Delta\Theta = \Theta_{(A/2,1)} - \Theta_{(A/2,0)}$ , is the side to side temperature difference at the center of the cavity.

$\Delta\bar{T}$ , is the actual wall-to-wall temperature difference.

The parameters governing the present problem are the thermal Rayleigh number, Ra, the cavity aspect ratio, A, and the angle of inclination  $\phi$ .

The problem is to find the functions  $\Psi$  and  $\Theta$  which satisfy the governing eqs. (8) and (9) and boundary conditions (11a) and (11b) for the case of long shallow cavity, i.e. for the condition  $A \gg 1$  with fixed values of Ra.

### NUMERICAL SOLUTION

To obtain the numerical solutions of the complete governing eqs. (8) and (9), finite difference were used. The solution consists of stream function and temperature fields as well as the velocity distribution in x and y directions.

The energy equation was solved using the alternating direction implicit (ADI) method AZIZ and Hallums (1967). The stream function field was obtained from eq.(8) using successive over-relaxation method (SOR) and a known temperature distribution. Forward time and central space differences were used and the advective term in the energy equation was written in conservative form to preserve the transportive property.

To test the present method of formulation and the finite difference scheme, various combinations of mesh sizes were used to select one which give better accuracy and requires less computational time. The number of grid points in the x and y directions were varied, depending upon the aspect ratio, A, of the cavity. As expected it was found that the necessary number of grid lines depends on the Rayleigh number, Ra, and the aspect ratio, A, of the cavity. The following are the grid fields used for the several aspect ratios considered in the present work;

Grid field	A
41x31	2
41x31	3
51x41	4

In order to gain confidence in our results, we tried to compare ours with available previous published results. Thus, we compare our numerical solution but exposed to the same conditions by Vasseur et al. (1986). After obtaining confidence in our results, see **Table.1**, we processed to compute the transient mean Nusselt number.

**Table 1.** Mean Nusselt Number for Ra=250,  $\phi = 90^\circ$ , and A=4

Grid field	$\bar{Nu}$ [Present Study]	Grid field	$\bar{Nu}$ [Vasseur et al. (1986)]
51x41	4.327	51x51	4.587
81x81	4.411	81x81	4.546

The iterative procedure for the stream function was reported until the following condition was satisfied :

$$\frac{\sum_i \sum_j |\Psi_{i,j}^{n+1} - \Psi_{i,j}^n|}{\sum_i \sum_j |\Psi_{i,j}^{n+1}|} \leq 10^{-4} \quad (13)$$

where the superscripts (n) and (n+1) indicate the value of the (n)th and (n+1)th iterations respectively and i and j indices denote grid location in the (x,y) plane. Further decrease of the convergence criteria ( $10^{-4}$ ) did not cause any significant change in the final results.

The steady state was defined based on the following criteria:

$$\left| \frac{\overline{Nu}^{n+1} - \overline{Nu}^n}{\overline{Nu}^n} \right| \leq 10^{-4} \quad (14)$$

where  $\overline{Nu}$  is the average Nusselt number. The iterative procedure was carried out until above criteria was satisfied.

## RESULTS AND DISCUSSION

Computations were conducted for a range of Rayleigh number Ra, 20,100, and 500 with aspect ratio varied from 2, 3, and 4. The inclination angle of enclosure from horizontal plane also varied from  $0^\circ$  to  $180^\circ$ . Flow patterns and temperature fields for some typical values of Rayleigh number and aspect ratio are presented in **Figs 2-5**. Compared to the case of the constant temperature at both vertical walls Prasad and Kulacki (1984) and constant heat flux from two side and other is insulated Vasseur et al. (1986), constant heat flux on one vertical wall Prasad and Kulacki (1984), temperature fields in the present case are some different.

When an inclined porous layer saturated by a fluid satisfying the Boussinesq approximation is differentially heated, a wide range of two-three dimensional, stationary or non-stationary flow configuration appear Caltagirone and Bories (1985). These configuration depends on the geometric dimensions of the porous media (aspect ratio), angle of inclination  $\phi$ , and the Rayleigh number Ra.

The basic flow which develops in differentially heated inclined porous layer is of an unicellular two-dimensional type. Thus, when the porous layer slightly inclined with respect to the horizontal line, the flow which takes place spontaneously is of unicellular type. At lower value of Rayleigh number, the flow is setting up of longitudinal rolls and remains steady for wide range of inclination angle Caltagirone and Bories (1985).

Here isotherms for any size of cavity start either from the heated wall. Similar isotherms patterns have been reported for free convection in non porous vertical cavity by Said and Trupp (1982) and Balvanz and Kuehn (1983), though no adverse temperature gradients or “S” –shaped isotherms Said and Trupp (1982) are observed for the present case.

The thermal boundary thickness increases on the heated wall, for the velocity boundary layer thickness, the growth is different and is largely due to the change in bouncy effect. We can note that the convection becomes more and more vigorous as the orientation angle of the cavity is increased.

In the numerical results, the flow inside the cavity was steady and unicellular flow in the case of

tilted porous rectangular cavity. When the angle of inclination angle approaching to the horizontal position, the flow might be multicellular pattern, see **Figs. 5** and **6**. In fact, when the angle of inclination angle is approaching  $180^\circ$ , the flow might not be two-dimensional as assumed in the theoretical and numerical solutions Vasseur et al. (1986). Experimental observations and three-dimensional numerical simulations have show that, in the case of tilted, porous, rectangular cavity, the flow remains two-dimensional for  $0^\circ < \phi < 173^\circ$  but for  $\phi > 173^\circ$ , oblique rolls were obtained Bories and Combarnous (1973). Also, its should be denoted that for very high values of the Rayleigh number, no steady unicellular flow could be maintained inside the cavity.

Streamlines close to the heated surfaces are observed to run parallel to the wall over significantly large portion of its extent. This behavior becomes more prominent as the aspect ratio is increased and increasing in the inclination angle  $\phi$ . As excepted, the temperature field are strong function of Rayleigh number and aspect ratio. As Ra is increased (**Figs.2 - 4**), isotherms shifts toward the constant flux wall and corners. This result in an asymmetric core region flow. As increase in aspect ratio further pushes the isotherms towards the corner of heated surface indicating high velocity.

The value of Nusselt number is important for design proposed because its directly gives the value of a range temperature  $\Delta\Theta$ , for any applied heat flux which , in turn gives the order of the temperatures to be encountered any particular values of Rayleigh number and aspect ratio. The orientation angle  $\phi$  is seen to have a dominate effect on the Nusselt number for a given Rayleigh number. As the angle of inclination  $\phi$  approach to the horizontal position, the Nusselt number at low Rayleigh number tends towards unity, indicating that the heat transfer is mainly due to conduction. Most of the change in heat transfer occurs in the range  $0^\circ < \phi < 90^\circ$  and  $90^\circ < \phi < 180^\circ$ . Also, it's noticed that the Nusselt number is strong function of Rayleigh number.

For  $Ra > 500$ , there is no numerical results are presented since they did not provide sufficient additional insight into the problem and also the computing time necessary to obtained an accurate steady-state solution become rapidly prohibitive.

Generally, the average Nusselt number show fairly large dependence on inclination angle  $\phi$ . Also, we can note that, the effect of heating the cavity from  $0^\circ < \phi < 90^\circ$  on the Nusselt number is seen to be large in comparison with that heating from  $90^\circ < \phi < 180^\circ$ . It's also noticed that the effect of inclination angle on Nusselt number is some more pronounced as the Rayleigh number is increased. A similar tends, rather fore, has been reported in the case of inclined fluid cavities contain two opposite of thermal surfaces maintained at different temperature Ozoe et al. (1977) and for case Vasseur et al. (1986).

The results of numerical calculations for mean transition Nusselt number vs. dimensionless time  $\tau$ , are plotted in **Fig.7**. Generally, we can note that the dimensionless time increases with increasing aspect ratio and Rayleigh number.

**Fig.8**, presents the results of mean Nusselt number as a function of inclination angle  $\phi$ , at Rayleigh number Ra of 20, 100, 500 respectively and an aspect ratio  $A=3$ . For small inclination angles from horizontal position, the calculations lead to a stationary state consisting of rotating cells. When the angle  $\phi$  increases, the Nusselt number increases and sudden transition appears and flow becomes unicellular and the Nusselt numbers increase clearly. If the angle  $\phi$  continuous increase, the flow remains unicellular and the Nusselt number decrease when close to the vertical position. So, the value of mean Nusselt number strong function with the value of Rayleigh number, aspect ratio, and the orientation of the porous cavity.



## CONCLUSIONS

The numerical results of shallow porous cavity show that when the porous layer slightly inclined with respect to the horizontal line, the flow which takes place spontaneously is of unicellular type.

The thermal boundary thickness increases on the heated wall, for the velocity boundary layer thickness, the growth is different and is largely due to the change in bouncy effect.

The convection becomes more and more vigorous as the orientation angle of the cavity is increased. For very high values of the Rayleigh number, no steady unicellular flow could be maintained inside the cavity.

Streamlines close to the heated surfaces are observed to run parallel to the wall over significantly large portion of its extent. This behavior becomes more prominent as the aspect ratio is increased and increasing in the inclination angle.

As increase in aspect ratio further pushes the isotherms towards the corner of heated surface indicating high velocity.

The Nusselt number at low Rayleigh number tends towards unity, indicating that the heat transfer is mainly due to conduction.

When the angle  $\phi$  increases, the Nusselt number increases and sudden transition appears and flow becomes unicellular and the Nusselt numbers increase clearly. If the angle  $\phi$  continuous increase, the flow remains unicellular and the Nusselt number decrease when close to the vertical position. So, the value of mean Nusselt number strong function with the value of Rayleigh number, aspect ratio, and the orientation of the porous cavity.

## REFERENCES

- Alavyoon, F., (1993).” On natural convection in vertical porous enclosure due to prescribed fluxes of heat and mass at vertical boundaries”, *Int. J. Heat Mass Transfer* 36, 2479-2498.
- AZIZ,K., and J. D. Hallums,(1967).” Numerical solutions of the three dimensional equations of motion for laminar natural convection”, *the physics of fluids* 10,2,314-325.
- Balvanz, J. L. and Kuehn, T. H. (1983).” Effect of wall conduction and radiation on natural convection in a vertical slot with uniform heat generation on the heated wall”, cited in [Caltagirone and Bories (1985)].
- Bejan, A., (1979). “On the boundary layer regime in a vertical enclosure filled with a porous medium”, *Letters in Heat and Mass Transfer* 6, 93-102.
- Bejan, A., (1983). “The boundary layer regime in a porous layer with uniform heat flux from the side”, *Int. J. Heat Mass Transfer* 26, 1339-1346 .
- Bennacer, R., Tobbal, A., Beji, H., and Vasseur, P. (2001).” Double diffusive convection in a vertical enclosure filled with an isotropic porous media”, cited in [Rahli and Bouhadeb (2004)].
- Bories, S. A., and Combarnous, M. A., (1973). “Natural convection in a sloping porous layer”, *J. Fluid Mech.* 57, 63-79.
- Buchberg, H., Catton, I., and Edwards, D. K. (1976). “Natural convection in enclosed spaces-a review of application to solar energy collection”, *ASME J. Heat Transfer* 98,182-188.

- Burns, P. J., Chow L.C. and Tien, C. L. , (1976) “Convection in a vertical slot filled with porous insulation”, *Int. J. Heat Mass Transfer* 20, 919-926.
- Caltagirone, J. P., and Bories, S., (1985). “Solutions and stability criteria of natural convective flow in an inclined porous layer”, *J. Fluid Mech.* 155, 267-287.
- Chamkha, J., and Al-Naser, H. (2001). “Double-diffusive convection in an inclined porous enclosure with opposing temperature and concentration gradients”, , cited in [Rahli and Bouhadef (2004)].
- Chan, B. K. C., Ivey, C. M., and Barry, J. M. (1970). “ Natural convection in enclosed porous media with rectangular boundaries”, *ASME J. Heat Transfer* 2, 21-27.
- Chen, C.J. , and Taie, V., (1982).” Finite analytic numerical solution of laminar natural convection in two-dimensional inclined rectangular enclosure”, cited in [Vasseur et al. (1986)].
- Eldr, J. W., (1974). ”Convection in a porous media with horizontal and vertical temperature gradients”, *Int. J. Heat, Mass* 17, 241-248.
- Holst, P. H. and Aziz, K., (1972). “Transient natural convection in confined porous media”, *Int. J. Heat Mass* 15, 73-90.
- Inaba, H. , and Kanayama, K., (1983). “Natural convection heat transfer in an inclined rectangular cavity”, cited in [Vasseur et al. (1986)].
- Moya S. L., Ramos, E., and Sen, M (1980). “Numerical study of natural convection in a tilted rectangular porous material”, cited in [Bejan (1983)].
- Ozoe, H., Sayama, H., and Churchill, S. W., (1977) ” Natural convection in a long inclined rectangular box heated from below”, *Int. J. Heat Mass Transfer* 20, 123-129.
- Prasad, V. and Kulacki, F. A., (1984). “Natural convection in a rectangular porous cavity with constant heat flux on one vertical wall”, *J. Heat Transfer* 106, 152-157.
- Prasad V. and F. A. Kulacki, (1984). “Convection heat transfer in a rectangular porous cavity –effect of aspect ratio on flow structure and heat transfer”, *J. Heat Transfer* 106, 158-165.
- Rahli, O., and Bouhadef, K., (2004). “Double-diffusive natural convection in a partially porous square enclosure; effect of the inclination“, e-mail: khedbouh@yahoo .fr.
- Said, M. N. A., and Trupp (1982).” Laminar free convection in vertical air-filled cavities with mixed boundary conditions”, cited in [Caltagirone and Bories (1985)].
- Seki, N., Fukusako, S., and Inaba, H., (1978). “ Heat transfer in a confined rectangular cavity



packed with porous media”, Int. J. Heat Mass Transfer 21,985- 989.

- Simpkins, P. G. and Blythe, P. A. (1980). “Convection in a porous layer”, Int. J. Heat Mass Transfer 23, 881-887.
- Torrance K. E, (1985). “Numerical method in heat transfer “Hand Book of Heat transfer Fundamentals, McGraw-Hill, 2<sup>nd</sup> edition.
- Vasseur, M. G. Satish and L. Robillard, (1986). ” Natural convection in a thin
  - inclined porous layer exposed to a constant heat flux”, Int. J. Heat Mass Transfer 30, 537-549.
- Walker, K. L., and Homsy, G. M., (1978). “Convection in a porous cavity”, J. Fluid Mech. 97,449-474.
- Weber, J. E., (1975) ” The boundary layer regime for convection in a vertical porous layer”, Int. J. Heat Mass Transfer 18, 569-573.
- Weber, J. E., (1975) ” Thermal convection in a tilted porous layer”, Int. J. Heat Mass Transfer 18, 474-475.

## NOMENCLATURE

$A$	aspect ratio of the cavity, $H/L$
$c$	specific heat of fluid, $J/kg.K$
$g$	gravitational acceleration, $m/s^2$
$H$	thickness of the porous cavity, $m$
$k$	thermal conductivity of fluid saturated porous medium, $W/m.K$
$K$	permeability of porous medium, $m^2$
$L$	length of the porous cavity, $m$
$Nu$	Nusselt number
$P$	pressure, $kPa$
$q$	constant heat flux, $W/m^2$
$Ra$	Rayleigh number, $g\beta KL^2 q/k\alpha v$
$T$	temperature, $K$
$T_o$	reference temperature at $x=y=0$ , $K$
$\Delta T$	characteristic temperature difference, $qL/k$
$\Delta\theta$	wall-to-wall temperature difference at $x=0$ , eq. (12)
$u$	fluid velocity in x-direction
$v$	fluid velocity in y-direction
$U$	dimensionless velocity in x-direction, $uL/\alpha$
$V$	dimensionless velocity in y-direction, $vL/\alpha$

$x, y$     *cartesian coordinate, m*  
 $X$        *dimensionless distance on x-axis,  $x/L$*   
 $Y$        *dimensionless distance on y-axis,  $y/L$*

#### Greek symbols

$\alpha$     thermal diffusivity of porous medium,  $k/\rho c$   
 $\beta$     coefficient of thermal expansion,  $K^{-1}$   
 $\Theta$     dimensionless temperature  
 $\tau$     dimensionless time  
 $\mu$     dynamic viscosity of fluid,  $kg/m.s$   
 $\nu$     kinematic viscosity of fluid,  $m^2/s$   
 $\rho$     density of fluid,  $kg/m^3$   
 $\Psi$     stream function  
 $\phi$     angle of inclination of the enclosure

#### Superscript

-       average  
n       iteration

#### Subscript

i, j    indices denote grid location  
o       reference temperature



## HYDRODYNAMIC AND THERMAL TWO DIMENSIONAL BOUNDARY LAYERS DEVELOPMENT BETWEEN ROTATING TURBINE BLADES

Asst. Prof. Dr. Ihsan Y. Hussain  
Mech. Engr. Dept.  
College of Engineering  
University of Baghdad  
Baghdad – Iraq

Taif H. Salih  
Mech. Engr. Dept.  
College of Engineering  
University of Baghdad  
Baghdad – Iraq

### ABSTRACT

The hydrodynamic and thermal boundary layers have great effect on the fluid flow and heat transfer between rotating turbine blade. In the present work, the flow and heat transfer is analyzed numerically by solving two dimensional incompressible boundary layer equations. A  $(k - \epsilon)$  turbulence modeling is used to obtain the eddy viscosity. The finite volume method is introduced to carryout all computational solution with staggered grid arrangement. Due to complex physical domain the original coordinate system is transferred to non orthogonal coordinate system. The calculation of present work done for rotating two dimensional turbine cascade with different rotating speeds (1500 rad/s, 1800 rad/s, 1900 rad/s), and for different Reynolds number (5000, 10000, 100000), in subsonic flow ( $M < 1$ ). The two dimension fluid flow is described by presenting plots of vector and contour mapping for the velocity; pressure and heat transfer fields as well as Nusselt number variation. The results were verified through a comparison with published duct results, good agreement was obtained. The final results were then compared with published results for turbine blades and good agreement was also obtained, the overall comparison show good agreement.

### الخلاصة

الطبقة المتاخمة الهيدرو ديناميكية والحرارية لها تأثير كبير على الجريان وانتقال الحرارة بين ريش التوربين الدوارة. في البحث الحالي تم تحليل الجريان وانتقال الحرارة عددياً بحل معادلات الطبقة المتاخمة ثنائية البعد اللانظاظية. تم استخدام نموذج  $(k - \epsilon)$  للاضطراب للحصول على اللزوجة الدوامية. تم استخدام المركبات الكارتيزية للسرع والضغوط كمتغيرات معتمدة في معادلة الزخم. طريقة الحجوم المحددة تم استخدامها مع الشبكة المرحلة (staggered grid). بسبب التعقيد في المجال الفيزيائي للمسئلة، تم تحويل نظام الاحداثيات غير المتعامدة. تم حل معادلة الطبقة المتاخمة الهيدرو ديناميكية مع معادلة الطاقة في المجال العددي للمسئلة. تم استخدام طريقة SIMPLE للجريان اللانظاظي للحصول على الحل وتفصيله خلال ريشتي توربين دوارة تم ايجاد الحل لثلاث سرع دورانية (1500 rad/s , 1800 rad/s, 1900 rad/s) ولثلاث قيم من رقم رينولدز (5000 , 10000 , 100000). تم اعداد برنامج باستخدام (power station) لتنفيذ الحسابات المطلوبة. تم تمثيل الجريان الثنائي البعد برسم المتجهات وخطوط التساوي (contours) للسرع والضغوط ودرجات الحرارة، وكذلك تقييم رقم نسلت. تم تدقيق النتائج بمقارنتها مع نتائج منشورة للجريان داخل مجرى وتم الحصول على توافق جيد. بعد ذلك تمت مقارنة النتائج النهائية مع نتائج منشورة للجريان خلال ريش توربين، وتم الحصول على توافق جيد.



**Keywords: Turbine Blades, Rotating, Flow, Heat transfer**

## INTRODUCTION

The axial flow turbine has two main elements; the stationary vane called nozzle and a turbine rotor. One of the most important aspects of the turbine property is to choose the suitable blade profile. In the three dimensional flow inlets boundary layer separates and forms a horseshoe (or leading edge) vortex, with one leg of the vortex in one aerofoil passage and the other leg in the adjacent passage. Thus in a cascade flow, the part of the secondary flow that is called the passage vortex.

The main objective of present work is to investigate the fluid flow and heat transfer between two rotating turbine blades. This will be done by solving the governing continuity, momentum, and energy equations together with the  $(k - \epsilon)$  turbulence model, numerically by the finite volume method. An orthogonal curvilinear coordinate system that is rotating with the blade will be used. The development of both hydrodynamic and thermal boundary layers over the blade surface will also be considered. Many investigations have provide data for the flow between turbine blades. However, rather literature is available for flow analysis. Koya and Kotake studied numerically fully developed flow through aturbine stage. Dorfman applied Naveier Stocke equation for gas turbine, to gather with heat conduction. Gogzeh developed finite volume method and code for solving elliptic three dimensional fluid flows. Thomkens study the quazi three dimensional finite difference boundary layer analysis for rotating blade row

## MODELING

The blade profile is analyzed in frame work of an orthogonal curvilinear coordinate system rotating with blade.

The geometry under consideration is an impulse turbine blade as represented in figure (1), although it represents a three dimensional flow problem, a suitable simplification by assuming the flow throw a cascade construction will reduce it to a two dimensional problem. The blade dimensions are:-

Axial chord,  $b_x = 11.08$  in (0.2813m)

Chord / axial chord = 1.2242

Pitch / axial chord = 0.9555

Aspect ratio (span / axial chord) = 0.9888

$\beta_1 = 43.99^\circ$

$\beta_2 = 22.98^\circ$

In this problem the mean flow is considered to be steady, and the following assumptions were used

1. The corioles acceleration creates a pressure gradient normal to the blade surface  $\partial u / \partial y$  even though it's larger than in usual boundary layer calculation.
2. Assumption of zero pressure gradients across the boundary layer is adopted.
3. It will know assumed that the gradients of all flow property in the  $x_2$  direction are zero  $\frac{\partial}{\partial x_2} = 0$

This reduce the  $x_2$  momentum equation with the other equations.

4. Incompressible subsonic fluid flow.
5. Pure impulse turbine blade is adopted with zero degree of reaction.
6. The boundary layer assume to be turbulent from the leading edge of the blade



According to the above assumptions and the flow forces the governing equations will be; (Tompkins, 1982);

**Continuity:**

$$\frac{\partial}{\partial x_1}(\rho u_1 h_2) + \frac{\partial}{\partial x_2}(\rho u_2 h_1) + \frac{\partial}{\partial x_3}(\rho u_3 h_1 h_2) = 0 \quad (1)$$

**X<sub>1</sub> Momentum Eq. :**

$$\begin{aligned} \frac{\rho u_1}{h_1} \frac{\partial u_1}{\partial x_1} + \frac{\rho u_2}{h_2} \frac{\partial u_1}{\partial x_2} + \rho u_3 \frac{\partial u_1}{\partial x_3} + \rho u_2 \left[ \frac{u_1}{h_1 h_2} \frac{\partial h_1}{\partial x_2} - \frac{u_2}{h_2 h_1} \frac{\partial h_2}{\partial x_1} \right] \\ - 2 \rho \omega_3 u_2 - \frac{\rho \omega^2}{h_1} R \frac{\partial R}{\partial x_1} = - \frac{1}{h_1} \frac{\partial \rho}{\partial x_1} + \frac{\partial}{\partial x_3} \left[ \mu \frac{\partial u_1}{\partial x_3} - \rho u'_1 u'_3 \right] \end{aligned} \quad (2)$$

**X<sub>2</sub> Momentum Eq. :**

$$\begin{aligned} \frac{\rho u_1}{h_1} \frac{\partial u_2}{\partial x_1} + \frac{\rho u_2}{h_2} \frac{\partial u_2}{\partial x_2} + \rho u_3 \frac{\partial u_2}{\partial x_3} + \rho u_1 \left[ \frac{u_2}{h_1 h_2} \frac{\partial h_2}{\partial x_1} - \frac{u_1}{h_1 h_2} \frac{\partial h_1}{\partial x_2} \right] \\ + 2 \rho \omega_3 u_1 - \frac{\rho \omega^2}{h_2} R \frac{\partial R}{\partial x_2} = - \frac{1}{h_2} \frac{\partial P}{\partial x_2} + \frac{\partial}{\partial x_3} \left[ \mu \frac{\partial u_2}{\partial x_3} - \rho u'_2 u'_3 \right] \end{aligned} \quad (3)$$

**X<sub>3</sub> Momentum Eq.:**

$$\frac{\partial P}{\partial x_3} = 0 \quad (4)$$

**Energy Eq.**

$$\begin{aligned} \frac{\rho u_1}{h_1} \frac{\partial I}{\partial x_1} + \frac{\rho u_2}{h_2} \frac{\partial I}{\partial x_2} + \rho u_3 \frac{\partial I}{\partial x_3} = \frac{\partial}{\partial x_3} \left[ \frac{\mu}{p_r} \frac{\partial H}{\partial x_3} + \mu \left( 1 - \frac{1}{p_r} \right) \times \right. \\ \left. \left( u_1 \frac{\partial u_1}{\partial x_3} + u_2 \frac{\partial u_2}{\partial x_3} \right) \right] - \rho H' U'_3 \end{aligned} \quad (5)$$

Where

$I = H - 1/2 (\omega^2 R^2)$  is the rothalpy

$H$  = stagnation enthalpy

$\omega$  = blade row rotation speed

$R$  = perpendicular distance from the axis of rotation

$\pm 2\rho\omega(u,v)$  = Represent the corioles force component.

$\rho\omega^2 R$  = Represent the centrifugal force component

With the velocity component normal to the surface neglected. It is convenient at this point to express the Reynolds stress and turbulent energy transport.

For the steady state there are four types of boundaries in the physical flow domain, inlet, outlet, solid surfaces and periodic boundary. At the inlet of the blade duct the velocity components and turbulent kinetic energy are specified. Turbulence quantities, such as  $(k)$  and  $(\varepsilon)$  are normally not known, but they must be estimated. Usually  $(k)$  is set to :-

$$k=(2/3)(T_u.Ux)^2, \quad (6)$$

Where  $(T_u)$  is the turbulence intensity and its value  $(0.01 < T_u < 0.1)$ , **Davidson (2003)**.

$$\text{The dissipation is set to: - } \varepsilon_{in} = C_{\mu}^{\frac{2}{3}} \frac{k^{\frac{3}{2}}}{I_c} \quad (7)$$

Where  $I_c$  is a characteristic length and is taken as  $(0.015S)$ , where  $S$  is the cascade Pitch. Pressure is assumed to be unchanging in the flow direction at the inlet At the exit plane the values of the dependent variables are unknown. Therefore the outlet boundary should be placed far down from the region of interest

## NUMERICAL SOLUTION

In the present study we will work on the sequence of two– dimension grids in successive cross – section planes. The equations are formulated in two – dimension rectangular compensation domain  $(\xi, \eta)$  and are solved numerically over uniform, rectangular grid in that domain. The method of Thompson Thames and Mastin (TTM) is utilized. The method employs the following in- homogeneous Laplace eq. as the generation system and its solving results represented in figures (2), (3) and (4)

$$\begin{aligned} \xi_{xx} + \xi_{yy} &= pc(\xi, \eta) \\ \xi_{xx} + \xi_{yy} &= Q(\xi, \eta) \end{aligned} \quad (8)$$

### General conservative form

$$(\rho G1 \phi)_{\xi} + (\rho G2 \phi)_{\eta} = (\Gamma Ja1 \phi)_{\xi} + (\Gamma Ja2 \phi)_{\eta} + S_{total} \quad (9)$$

The table (1) clarifies equation (9) in general curvilinear coordinate

Equations	$\Phi$	$\Gamma$	$S_{total}$
Continuity	1	0	0
x-momentum	u	$\mu_e = \mu + \mu_t$	$\rho u_1 u_2 k_1 - 2\rho w_3 u_2 - \rho w^2 R \frac{\partial R}{\partial x_1}$ $\rho_e u_{1e} \frac{\partial u_{1e}}{\partial x_1} + \rho_e w^2 R \frac{\partial R}{\partial x_1} - \frac{\partial}{\partial x_3} \left[ \mu \left( 1 + \frac{\rho \epsilon_m}{\mu} \right) \frac{\partial u_1}{\partial x_3} \right] +$
y-momentum	v	$\mu_e = \mu + \mu_t$	$\rho u_1 k_1 + 2w_3 u_1 - \rho w^2 R \frac{\partial R}{\partial x_2}$ $+ \rho_e u_{1e} K_1 - 2\rho_e w_3 u_{1e} + \rho_e w^2 R \frac{\partial R}{\partial x_2} - \frac{\partial}{\partial x_3} \left[ \mu \left( 1 + \frac{\rho \epsilon_m}{\mu} \right) \frac{\partial u_2}{\partial x_3} \right] + S_{\xi, \eta}$



Energy	T	$\frac{\mu}{P_l} + \frac{\mu_t}{P_t}$	$\rho w^2 R \left[ u_1 \frac{\partial R}{\partial x_1} + u_2 \frac{\partial R}{\partial x_2} + u_3 \frac{\partial R}{\partial x_3} \right] - \frac{\partial}{\partial x_3} \left[ \frac{\mu}{P_r} \left( 1 + \frac{P_r}{P_{rt}} \frac{\rho \epsilon_m}{\mu} \right) \frac{\partial H}{\partial x_3} + \mu \left( 1 - \frac{1}{P_r} \right) \left( u_1 \frac{\partial u_1}{\partial x_3} \right) \right] + S_{\xi, \eta}$
k-equation	k	$\mu + \frac{\mu_t}{\sigma_k}$	$[G_k - \rho \epsilon] + S_{\zeta, \eta}$
$\epsilon$ – equation	$\epsilon$	$\mu + \frac{\mu_t}{\sigma_\epsilon}$	$\left[ \frac{\epsilon}{k} (C_{\epsilon 1} G_k - C_{\epsilon 2} \rho \epsilon) \right] + S_{\zeta, \eta}$

### The Nusselt Number

For forced convection of a single-phase fluid

$$q''_w = h(T_w - T^*) \quad \dots\dots\dots (12)$$

where  $h$  is called the heat transfer coefficient, with units of  $W/m^2$ , heat flux would be entirely due to fluid conduction through the layer:

$$q''_w = k(T_w - T^*)/L \quad \dots\dots\dots (13)$$

We define the Nusselt number as the ratio of these two:

$$NuL = \frac{q''_w(\text{convection})}{q''_w(\text{conduction})} = hL/k. \quad \dots\dots\dots (14)$$

### Sequence of solution steps

The overall solution procedures can be listed as follows:

- 1) An initial guess is given for all variables in the field of interest.
- 2) The proper boundary conditions are specified for all dependent variables.
- 3) The discretised momentum equation is solved to obtain the covariant velocity components.
- 4) Then the pressure correction equation is solved to obtain pressure correction field.
- 5) The pressure correction is then used to correct pressure fields using equation
- 6) Then the velocity and density fields are corrected using equation
- 7) The other dependent variables such as turbulence and energy equations are solved.
- 8) The density is calculated using the new temperature and pressure fields.

The whole procedure is repeated from step three until a convergent solution is obtained

### RESULTS and Discussion

In the beginning of running the computer program we solve the governing equation for simple rectangular duct as represented in figure (5) and (6), the turbulent modeling was also adopted for the duct flow and we can see the turbulent kinetic energy in duct flow in Fig (7) and (8) The velocity contours of the present work were made for three different values of Reynolds number.

The first Reynold's number was 5000 and its (U) velocity contours are presented in fig (9), in this figure we can see the uniform velocity at the entrance of the domain, this uniform flow is because the flow coming from a uniform source. This source is the stationary blade which works as a nozzle to increase the velocity and give the flow more stability. The flow velocity increases uniformly inside the domain and reaches a value over the entrance velocity in the region at the mid chord of the blade and also we see the same in Figures (10) and (11).

The V – velocity contour for the three Reynolds numbers are plotted in figures (12) to (14), which indicates a uniform velocity at the entrance and it decreases towards the exit.

The second important variable in the present work is the pressure distribution in the space between the rotating blades. Figures (18), to (20) show the predicted static pressure distribution at different planes for Reynolds numbers equal (5000, 10000, 100000) respectively, we can see higher pressure distribution near the pressure surface than that close to suction surface. This is due to the positive inclination (angle of attack) of the blades.

The figures (21) to (23) show the dimensionless turbulent kinetic energy for Reynolds numbers (5000, 10000, 100000) respectively. We observe the minimum value of turbulent kinetic energy near the wall and increases toward the center. The turbulent kinetic energy is minimum near the wall where the flow velocity is minimum.

Depending on the velocity value appearing during solving the governing equation we can get the velocity profile. These profiles are shown in Figures (25) to (28) and for Reynolds Number (100000 and 10000) for different locations in the core line for the blades. We fix the points where the velocity reaches the maximum flow velocity. We get the boundary layer form as shown in Fig (29).

After predicting the boundary layer profile we fix the point of velocity equal to 0.99 maximum velocity at the suction surface. These points provide us with the boundary layer, this process is done for 1500 rad/s rotating speed. This procedure is repeated for another rotating speed (1800 rad/s, 1900 rad/s) to see how the rotating speed affects the boundary layer behavior, the new boundary layer form is presented in fig(30). We see in this figure that increases in rotating speed have a bad effect on the boundary layer form specially at ( $x/c > 0.9$ ).

The figures (31 to 34) show the temperature distribution developing. For the case of constant upper blade temperature and thermally insulated lower blade for Reynolds ( $Re = 50,000$ ), we observe that the temperature increases in the direction of the flow and the temperature decreases in the vertical direction. In the middle of the geometry we observe the decrease is greater than decreases slightly toward the lower wall.

## CONCLUSION REMARKS

The present work solves the fluid flow and heat transfer between rotating impulse turbine blades. The following conclusions are drawn from the obtained results; the flow velocity increases uniformly inside the calculation domain and reaches a value over the uniform entrance velocity in the region at the mid chord of blade. The velocity vectors are more uniform at the middle section than at the entrance and they become unstable at the trailing edge section. The boundary layers are more uniform at the pressure side than at the suction side.

High pressure is observed near the pressure side than thus close to suction side, and denser pressure contours near the leading edge of the pressure side is also observed. A minimum value of turbulent kinetic energy is observed near the wall and it increases towards the center. Increase in rotational speed causes a deformation and increase in boundary layer thickness. A normal temperature distribution is obtained, and the large velocities on the suction side cause streamwise vortex that



continuously heat transfer. The Nusselt number is maximum at the entrance section and decreases with the flow direction until it reach approximately constant value. An acceptable agreement was obtained with previous published numerical and experimental results,

## REFERENCES

Davidson, L., 2003, "An Introduction to Turbulence Models", Chalmers University of Technology, Department of Fluid Dynamics

Dorfman A.S. (1996)" Advanced Calculation Method for the Surface Temperature of Turbine Blade" Journal of heat Transfer 48(1): pp.18 – 22.

Gogzeh, M.M. (2000)" Three Dimensional Turbulent flow Prediction between Two Axial Compressor Stator Blades Using Body Fitted Coordinate System "PhD. – theses. Mechanical Dep. University of Baghdad

Hoffmann, K. A., 1989, "Computational Fluid Dynamics for Engineers", Engineering Education System

K. M. Bernhared (2000)" Experimental Study of Effusion Cooling" Department of Thermo and fluid Dynamic Chalmers University of Technology. Sweden.

Koya M., and S. Kotake (1985) " Numerical Analysis of Fully Three – dimensional peridic flow Though a Turbine Stage" ASME Journal of Engineering for Gas Turbine and Power, Vol.107, No.4, pp. 945 - 952

Patankar, S. V., 1980, "Numerical Heat Transfer and Fluid Flow" Hemisphere, McGraw-Hill, New York.

Versteeg, H. K. and Malalasekera, W. (1995). An Introduction to Computational Fluid Dynamics, the finite volume method. Longman Scientific and technical

W. T. Thompkins (1982)" A – Quasi Three Dimensional Blade Surface Boundary Layer Analysis for Rotating Blade Rows" journeal of Engineering and Power. Vol. 104. pp.439 – 448.

**Table 2** definition of symbols used in present work

Symbol	Description	Units
$C$	Chord of the blade	m
$C_\mu$	Constant in turbulence model	
$C_{\varepsilon 1}$	Constant in turbulence model	
$C_{\varepsilon 2}$	Constant in turbulence model	
$C_x$	Axial chord of the blade	m
$G_1$	Contravariant velocity in $\zeta$ direction	m/s
$G_2$	Contravariant velocity in $\eta$ direction	m/s
$G_3$	Contravariant velocity in Z direction	m/s
$J$	Jacobian transformation	
$k$	Kinetic energy of turbulence	
$MUE$	Turbulent Viscosity	

$P$	Pressure	N/m <sup>2</sup>
$R$	Perpendicular distance	m
$Re$	Reynolds number ( $Re = \rho_{\infty} U_{\infty} C_x / \mu$ )	
$S$	Cascade pith	m
$S_{\phi}$	Source term of $\phi$	
$S_{\zeta\eta}$	Source term due to nonorthogonalit y	
$S_{total}$	Total source terms	
$t$	Time	s
$T$	Temperature	°C
$T_u$	Turbulence intensity	
$u$	Velocity component in x direction	m/s
$v$	Velocity component in y direction	m/s
$w$	Velocity component in z direction	m/s
$x$	Axial coordinate in the physical domain	
$Z$	Spanwise coordinate in the computational domain	
$\omega$	Rotating speed	Rad/sec

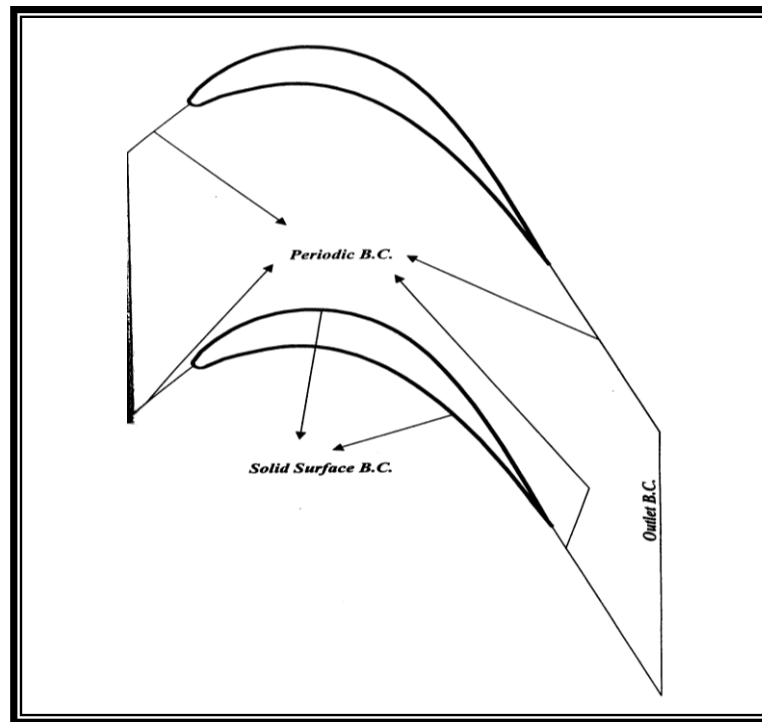


Fig (1) Two Dimension Blade

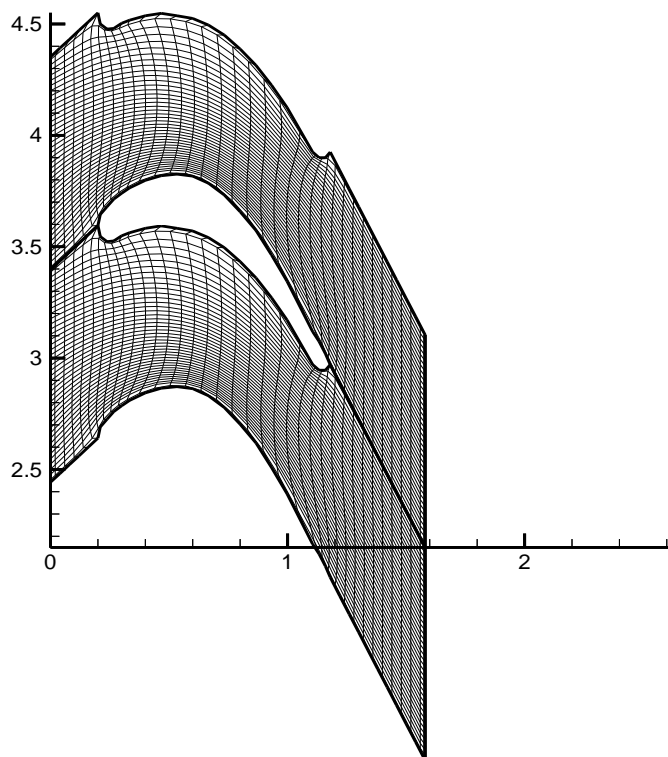


Fig (2) elliptical grid system for ( $M \times N = 33 \times 21$ )

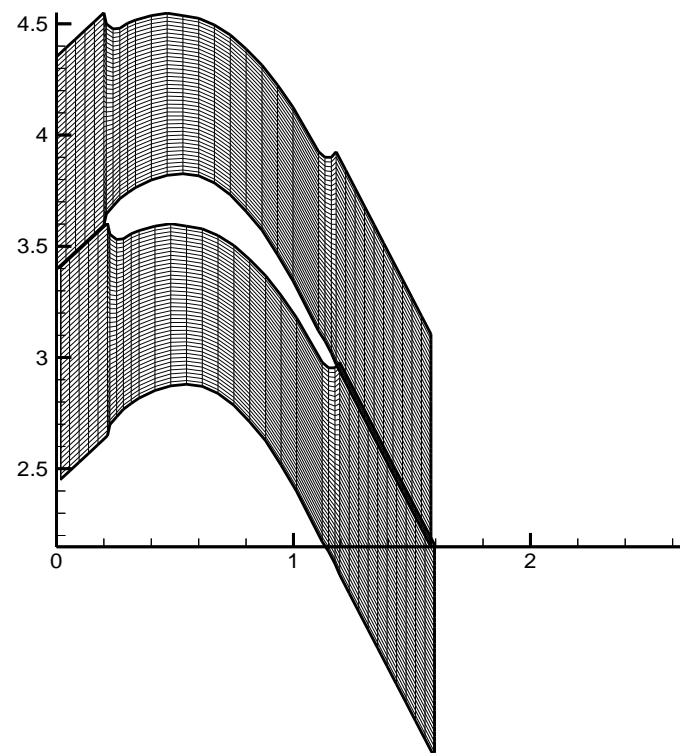


Fig (3) Algebraic Grid system for ( $M \times N = 33 \times 21$ )



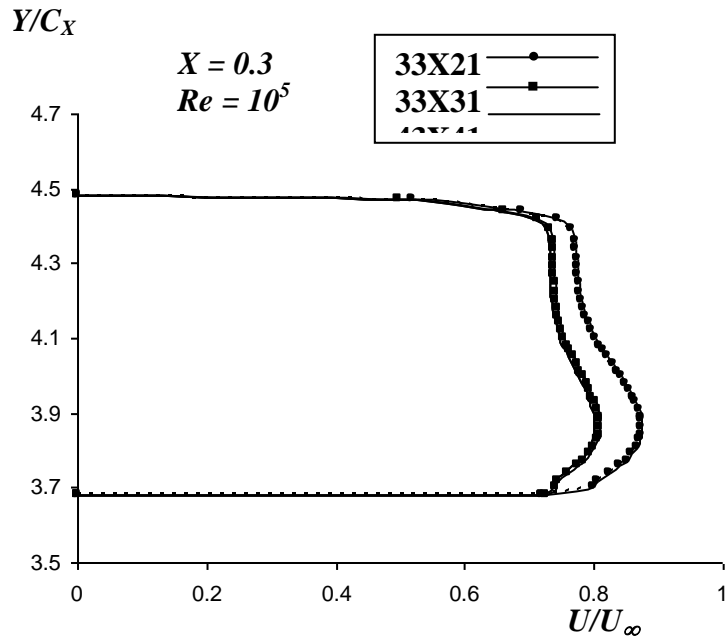


Fig.4: Ensemble – Averaged Velocity Profile at  $X = 0.3$  and  $Re = 10^5$  for Three Grids

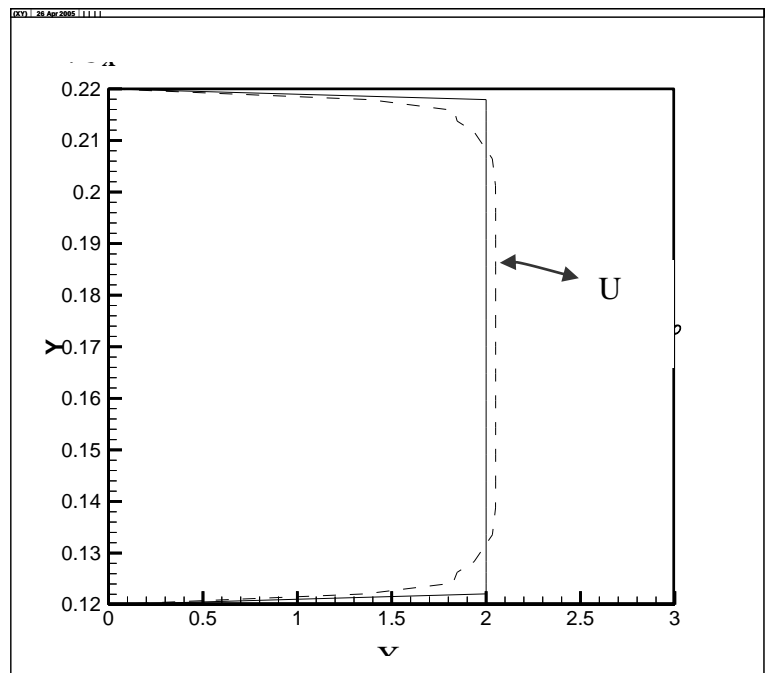


Fig. 5: Velocity profile for duct flow

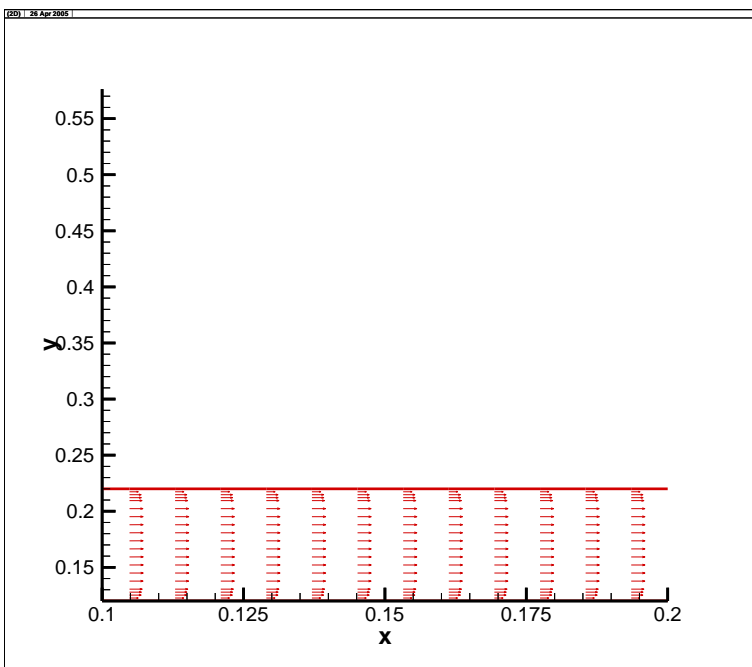


Fig.6: Velocity Vector for duct flow

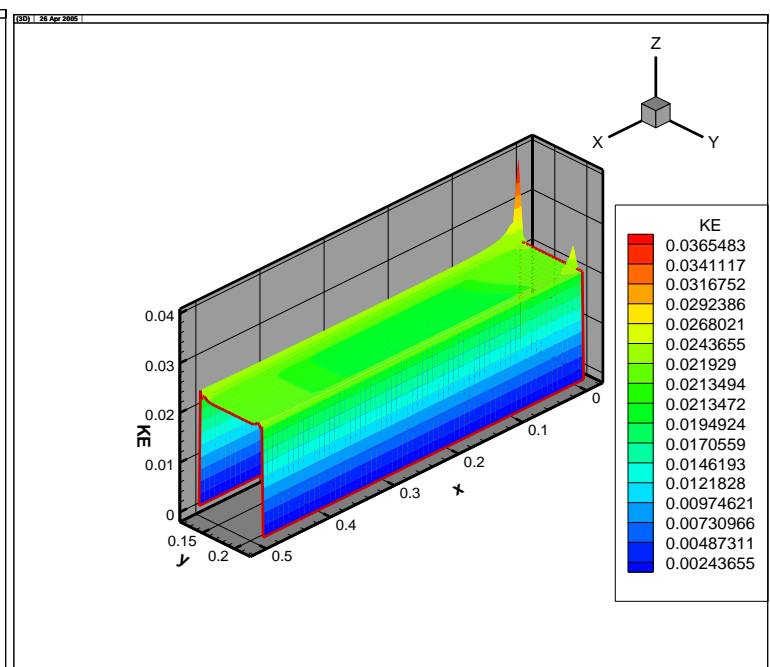


Fig. 7: KE for duct flow

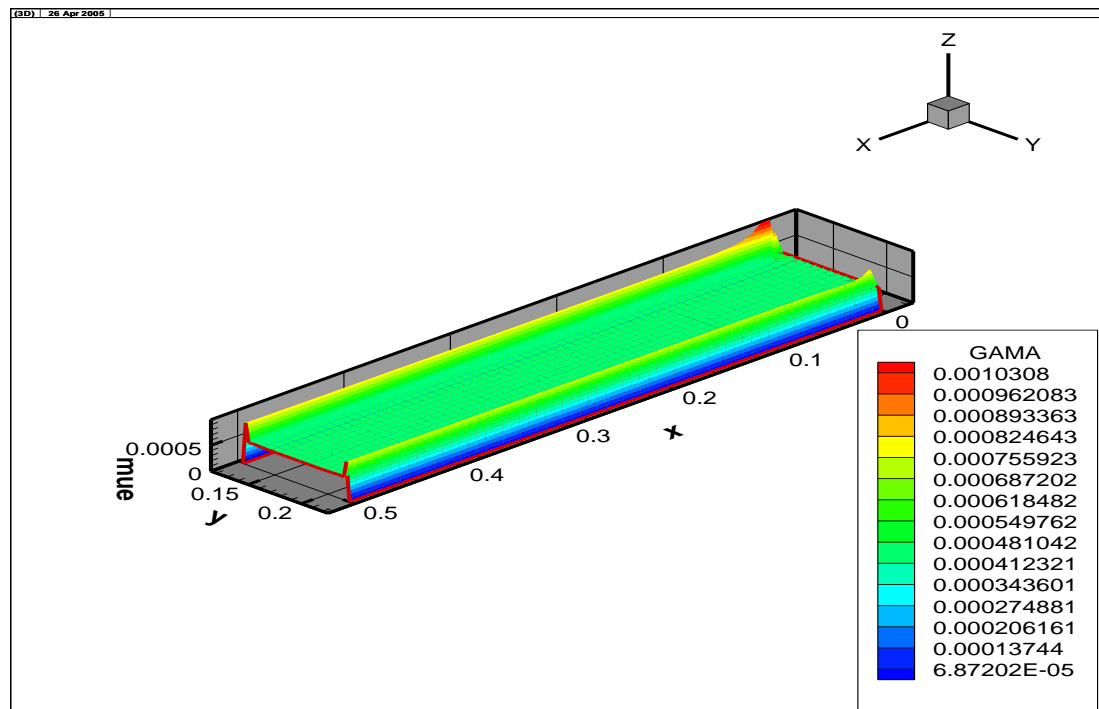
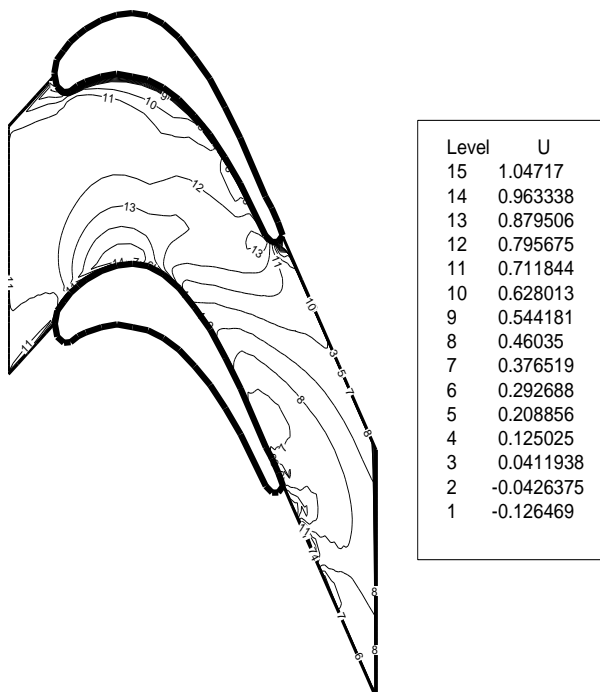
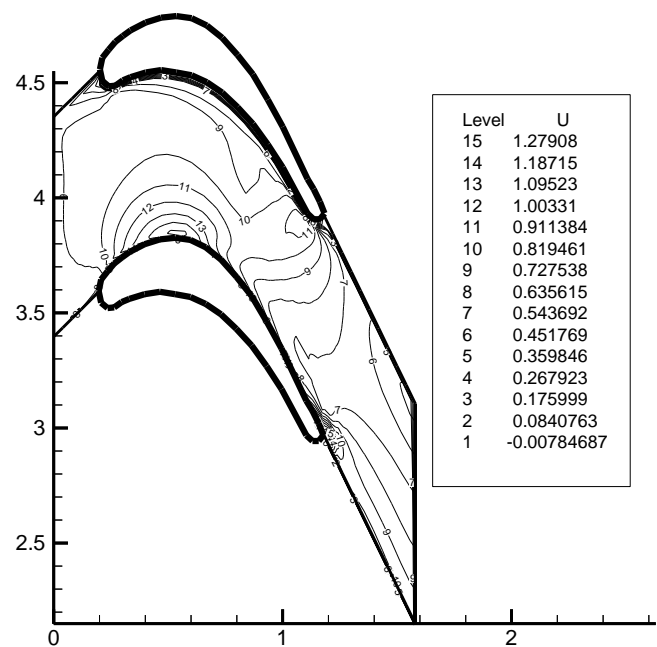


Fig. 8: MUE for duct flow

Fig. 9: U Velocity Contour at  $Re = 5000$ Fig. 10: U - Velocity Contour at  $Re = 10000$

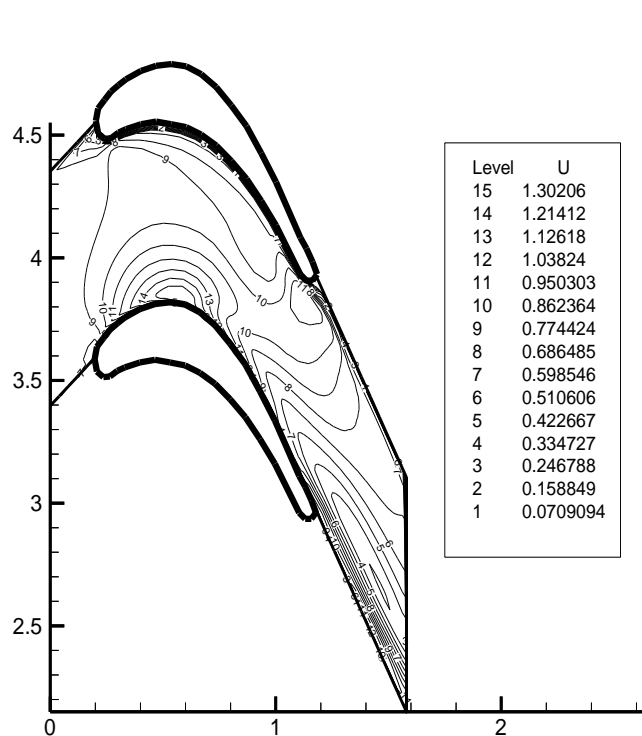


Fig. 11: U - Velocity Contour at Re = 100000

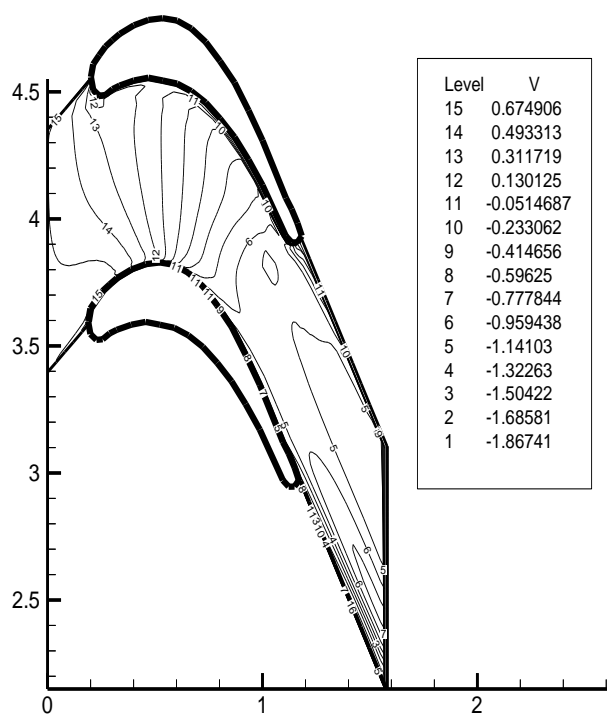


Fig. 12: V - Velocity Contour at Re= 5000

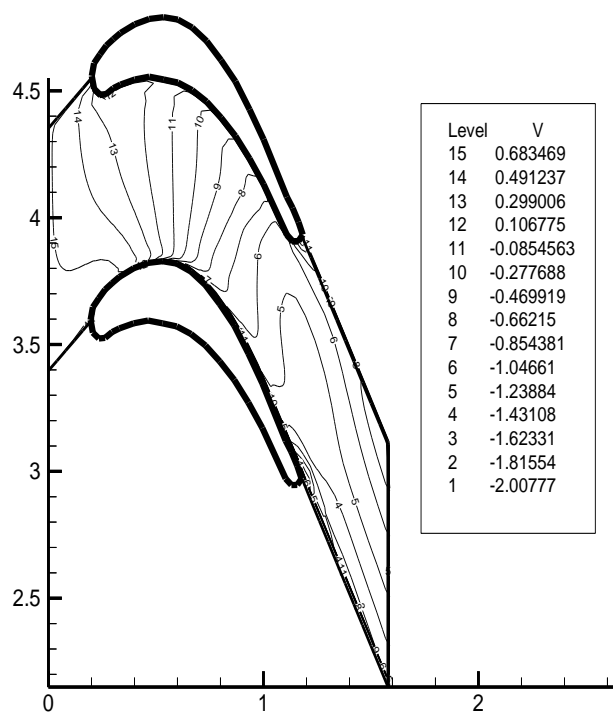


Fig. 13: V - Velocity Contour at Re= 10000

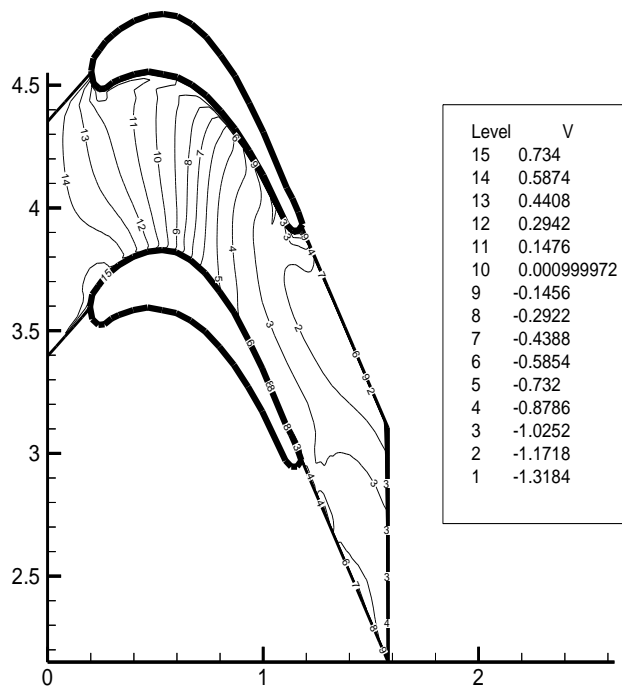
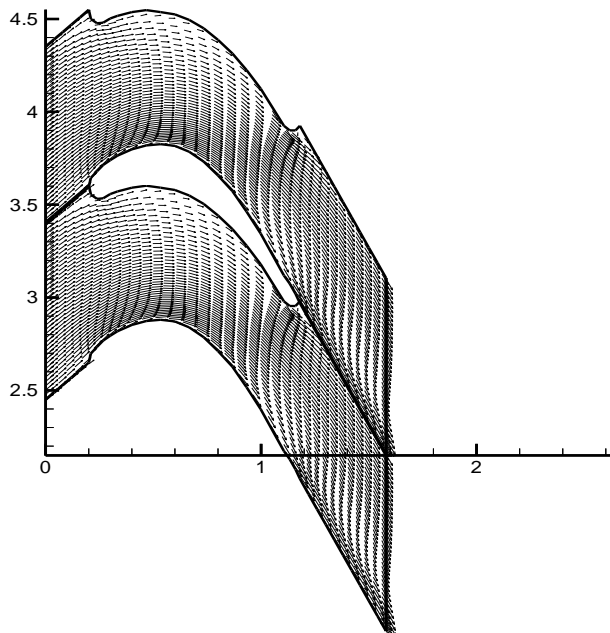
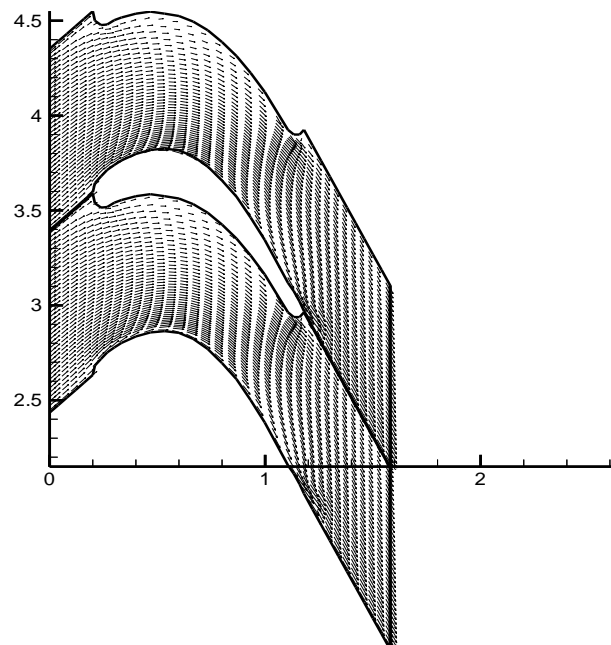
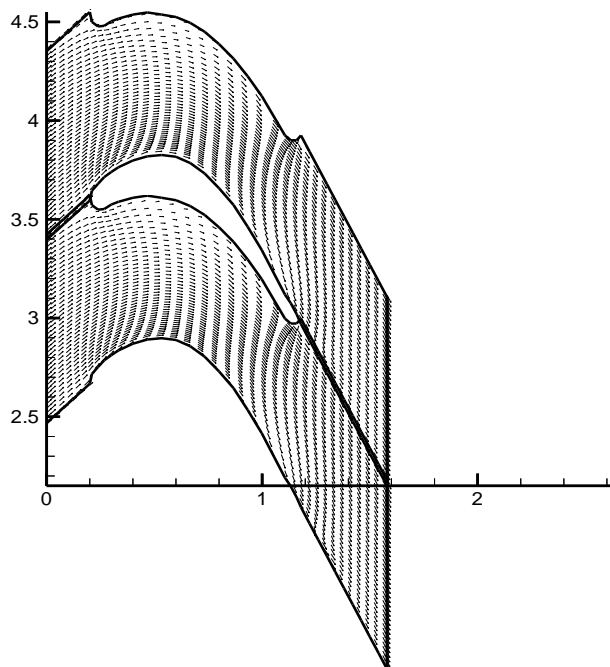
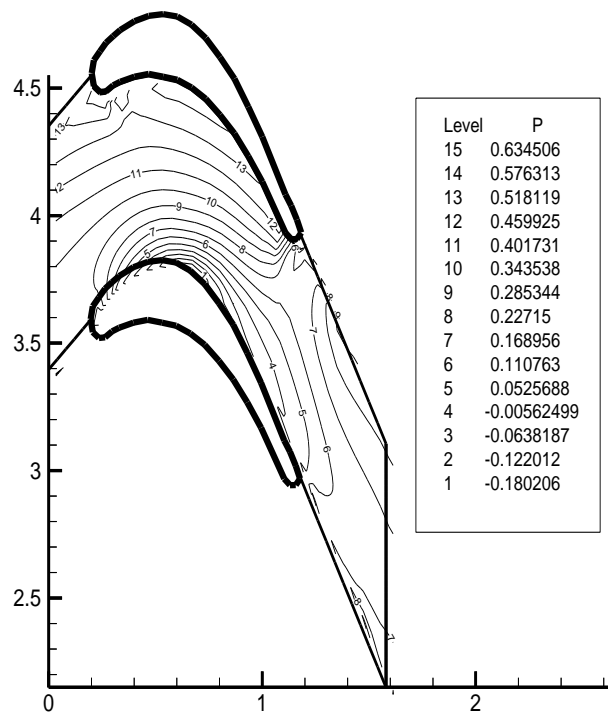


Fig. 14 V - Velocity Contour at Re= 100000

Fig. 15: U Velocity Vector at  $Re = 5000$ Fig. 16: U Velocity Vector at  $Re = 10000$ Fig. 17: U Velocity Vector at  $Re = 100000$ Fig. 18: Pressure Contour at  $Re = 5000$

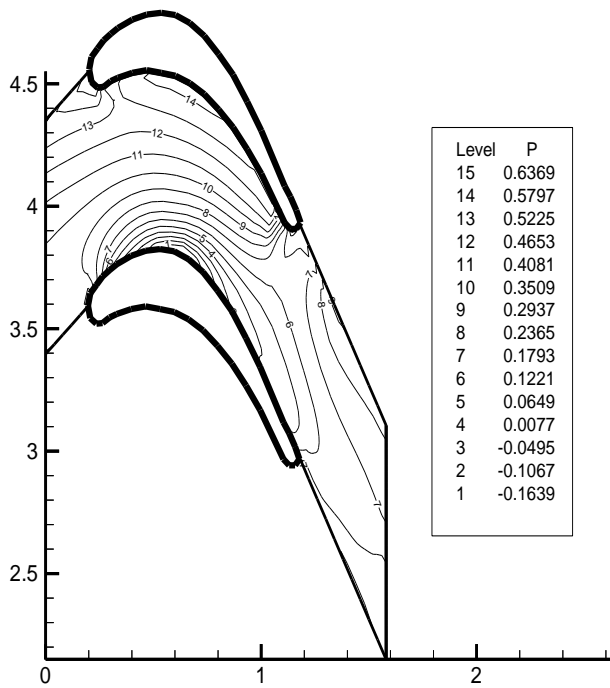


Fig. 19: Pressure Contour for  $Re = 10000$

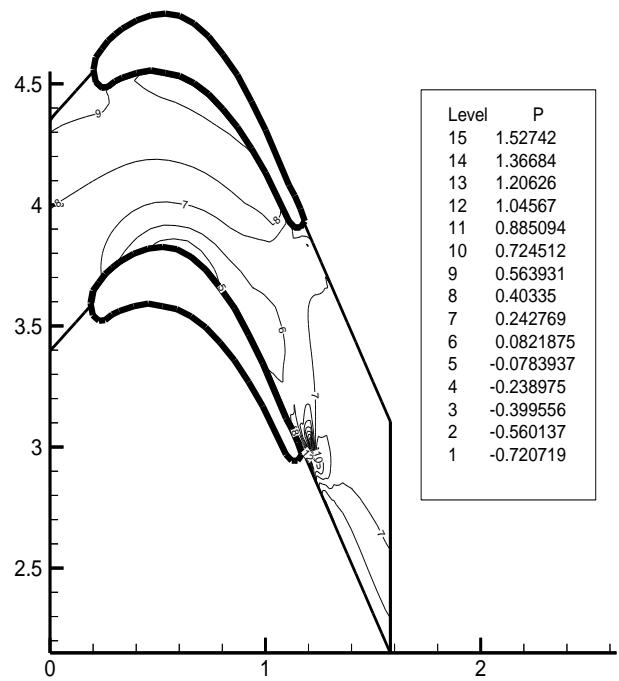


Fig. 20: Pressure Contour for  $Re = 100000$

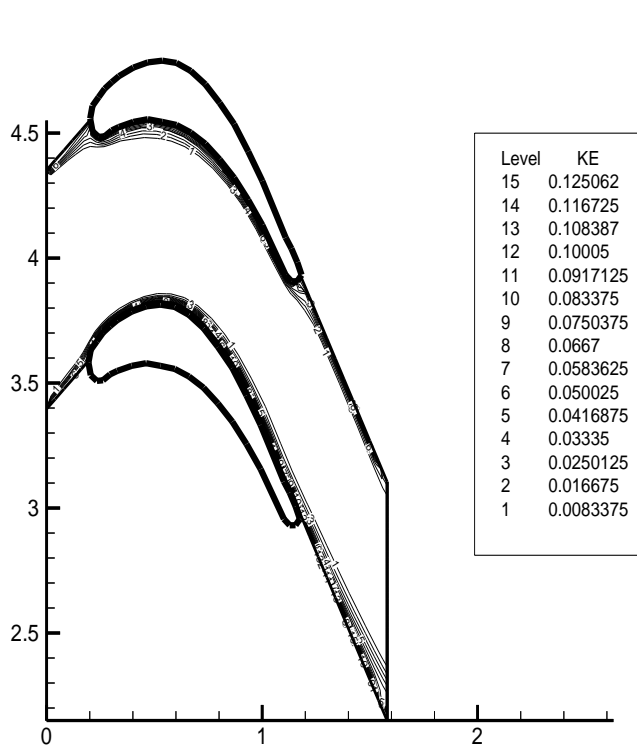


Fig. 21: KE Contour at  $Re = 5000$

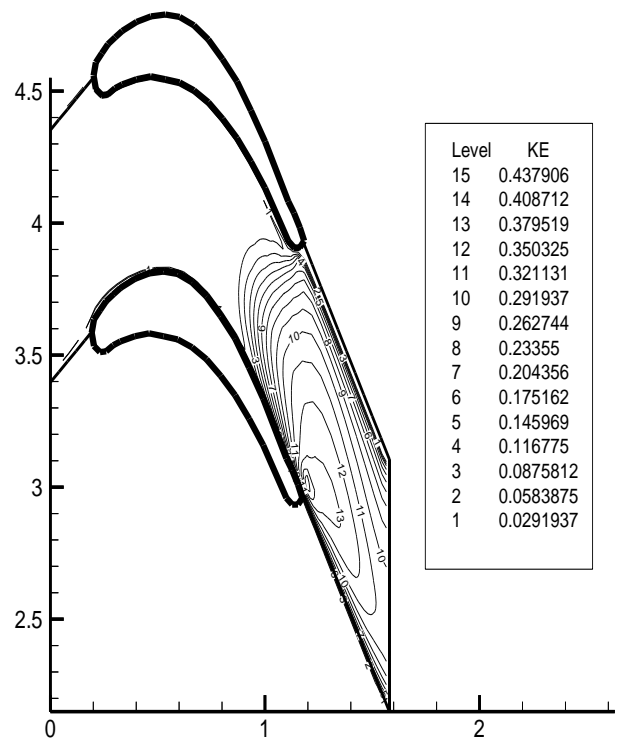
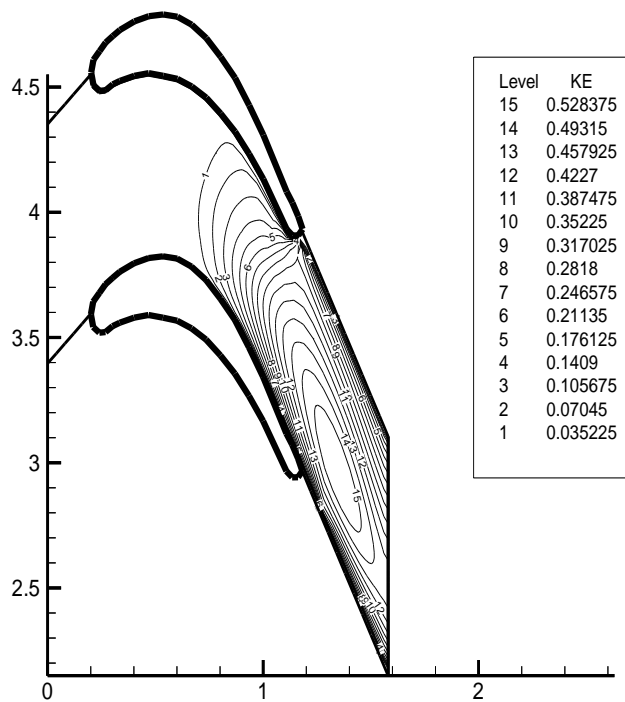
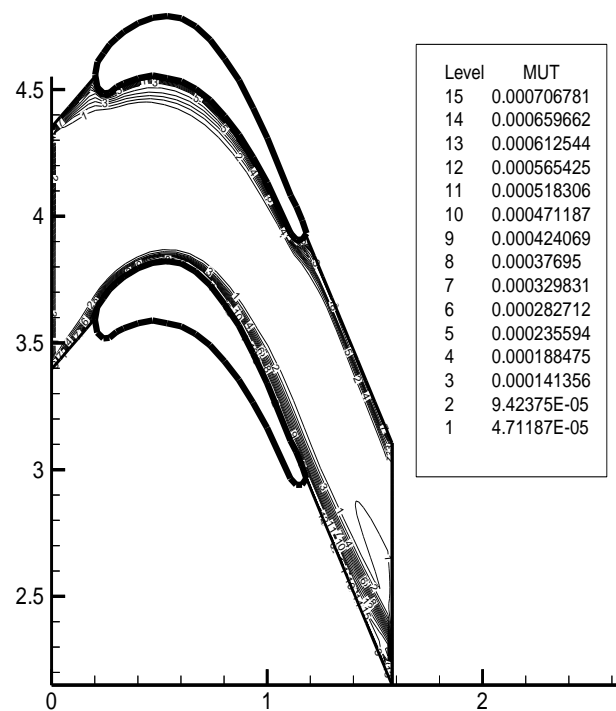
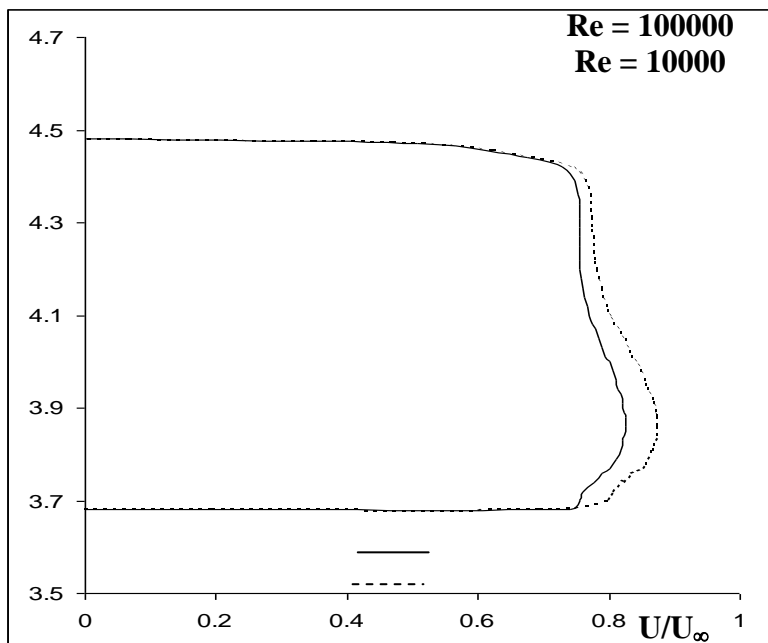
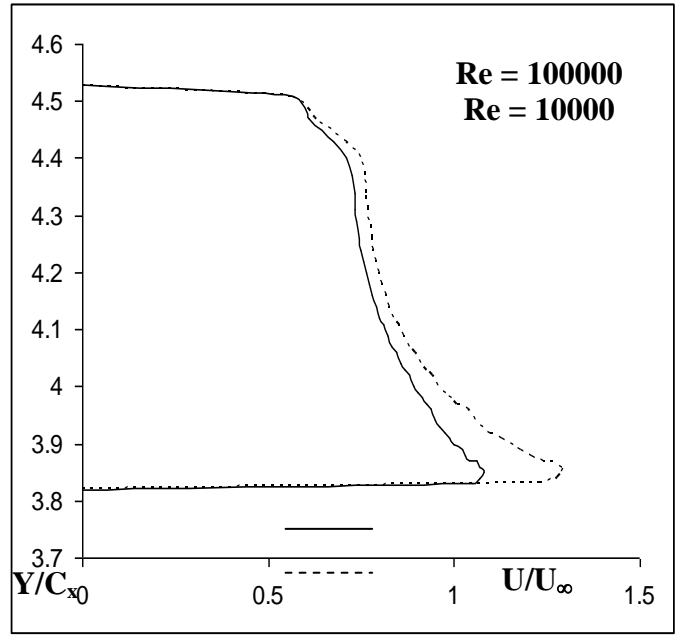


Fig. 22: KE Contour at  $Re = 10000$

Fig. 23: KE Contour at  $Re = 100000$ Fig. 24: MUT Contour at  $Re = 100000$ Fig. 25: Velocity profile at  $(X/C) = 0.33$ Fig. 26: Velocity profile at  $(X/C) = 0.6$

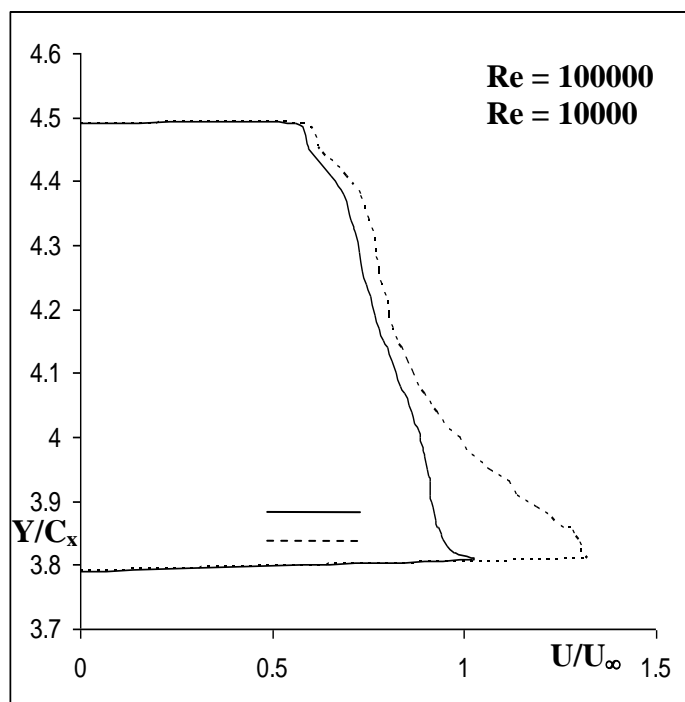


Fig. 27: Velocity profile at( X/C)= 0.8

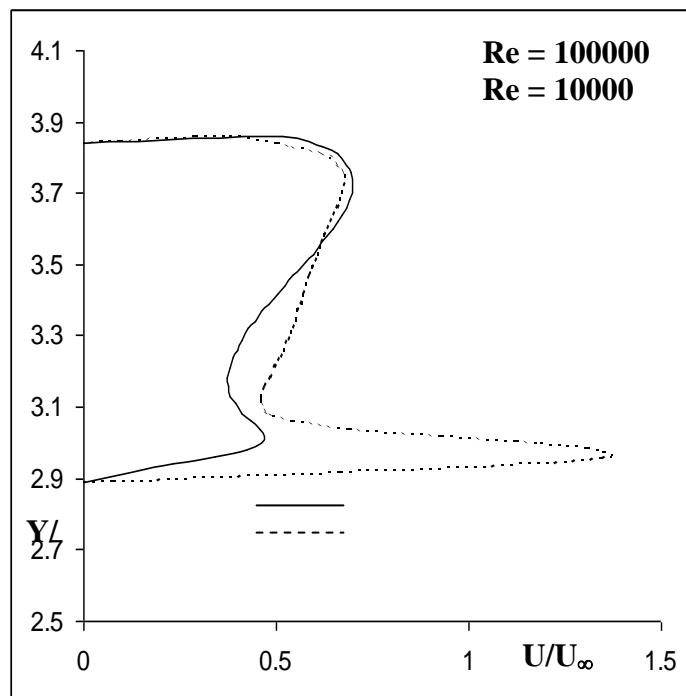


Fig. 28: Velocity profile at( X/C)= 1.22

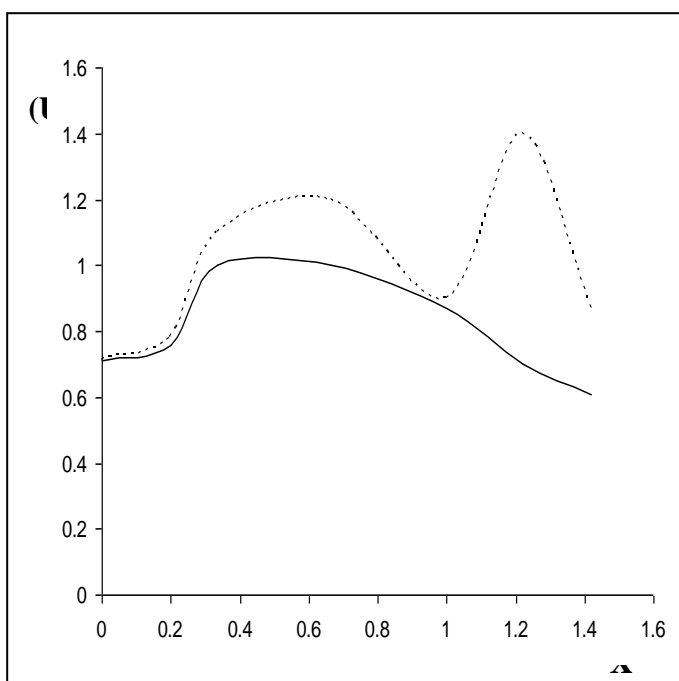


Fig. 29: Boundary Layer Form

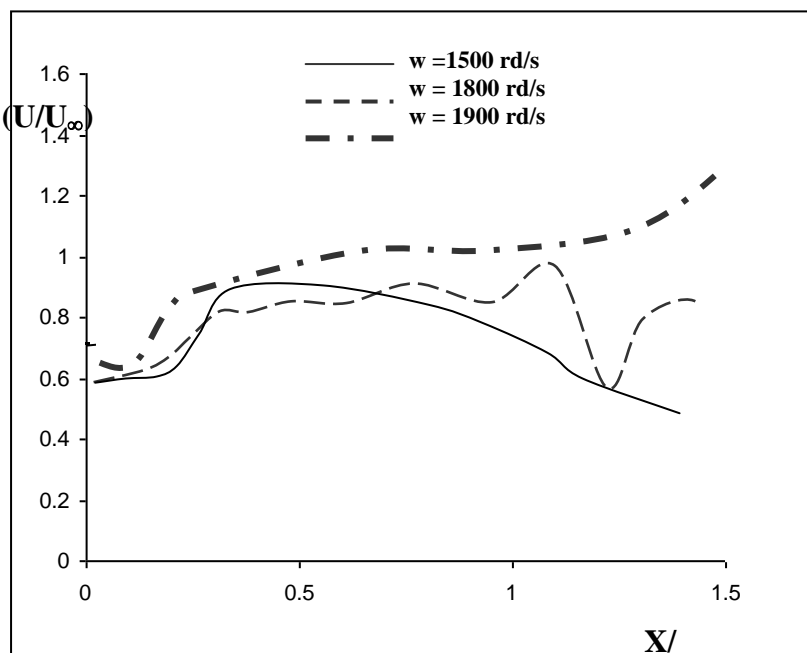
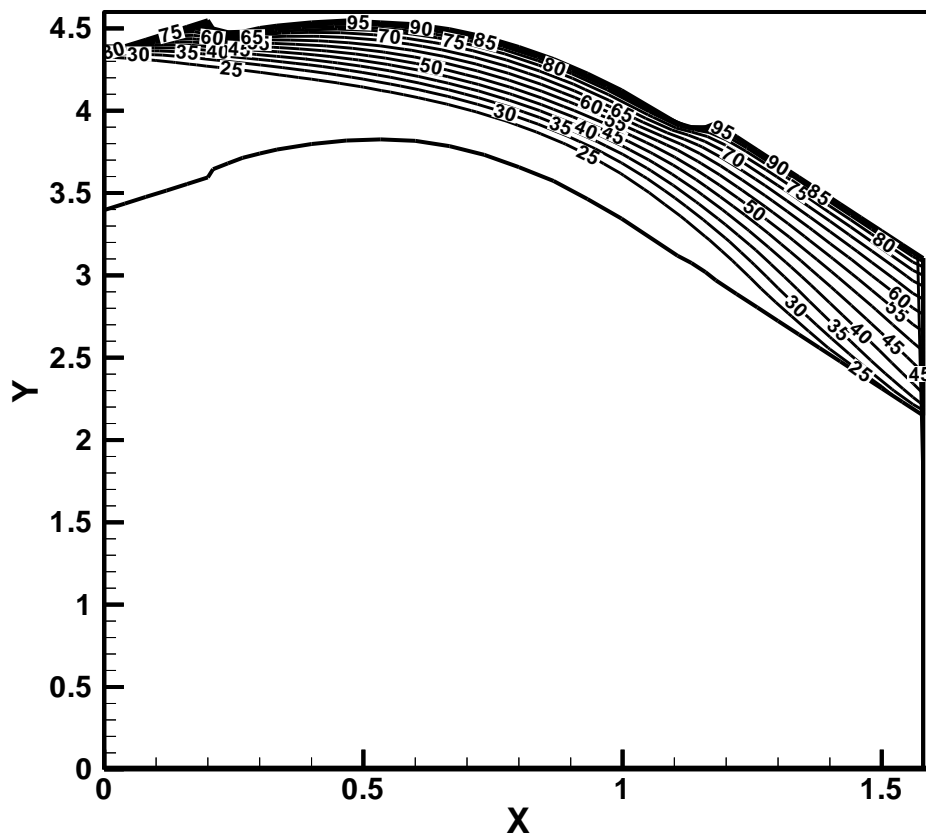
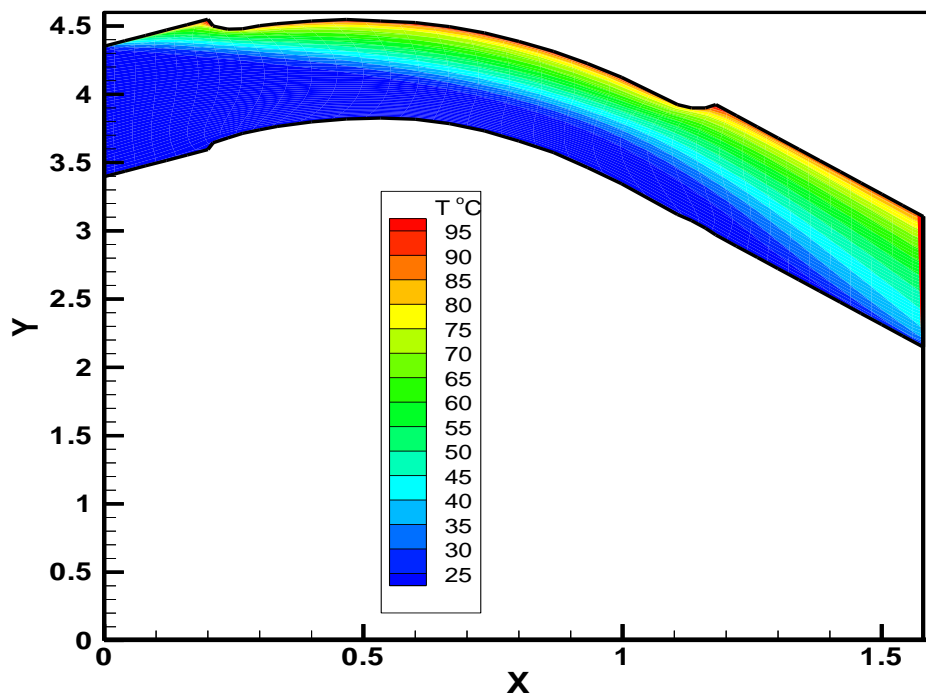


Fig. 30: Boundary Layer Form for Different Rotating Speed

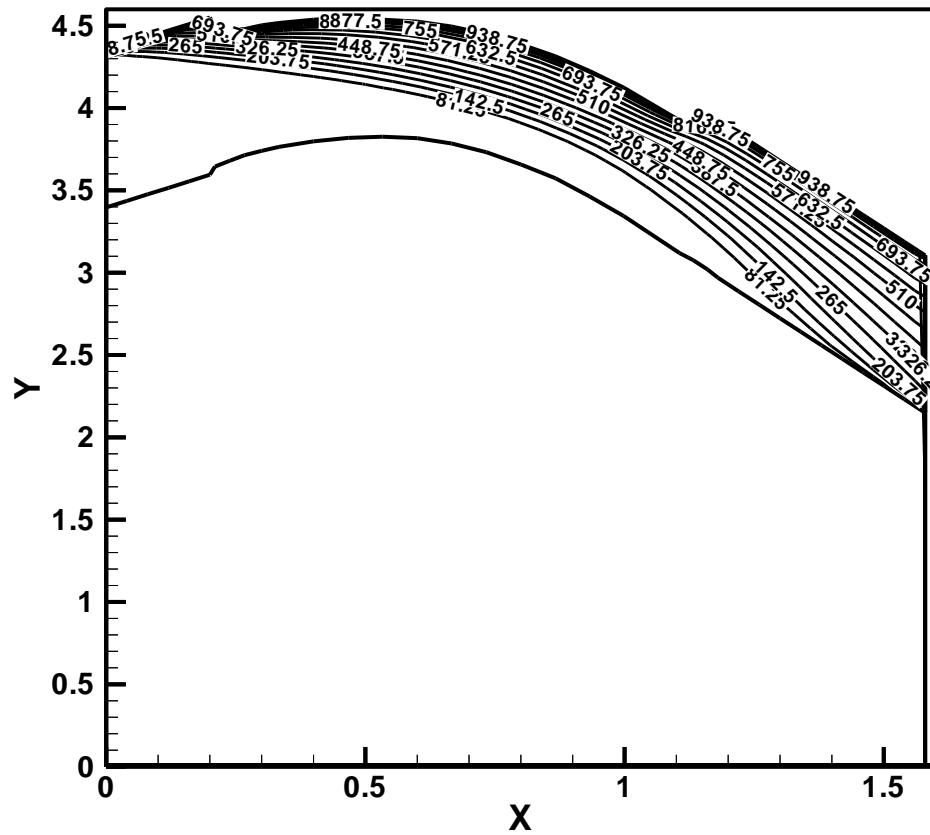


Figure(31): Contour (Lines) of temperature distribution for  $Re=50,000$  and constant wall temperature  $T_w=100\text{ }^{\circ}\text{C}$

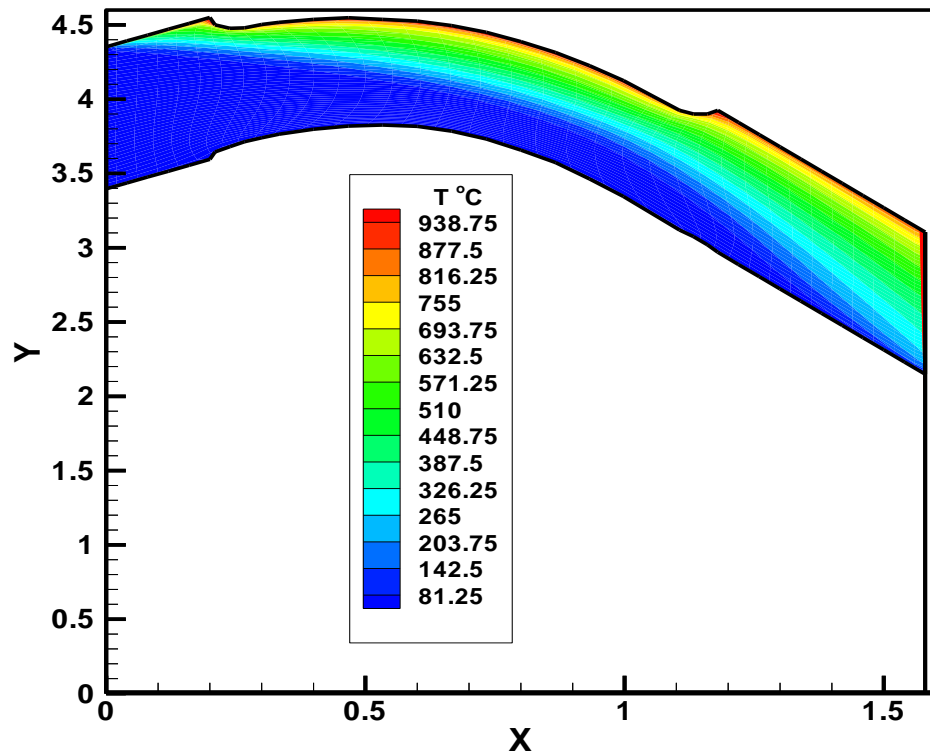


Figure(32): Contour (flood) of temperature distribution for  $Re=50,000$  and constant wall temperature  $T_w=100\text{ }^{\circ}\text{C}$

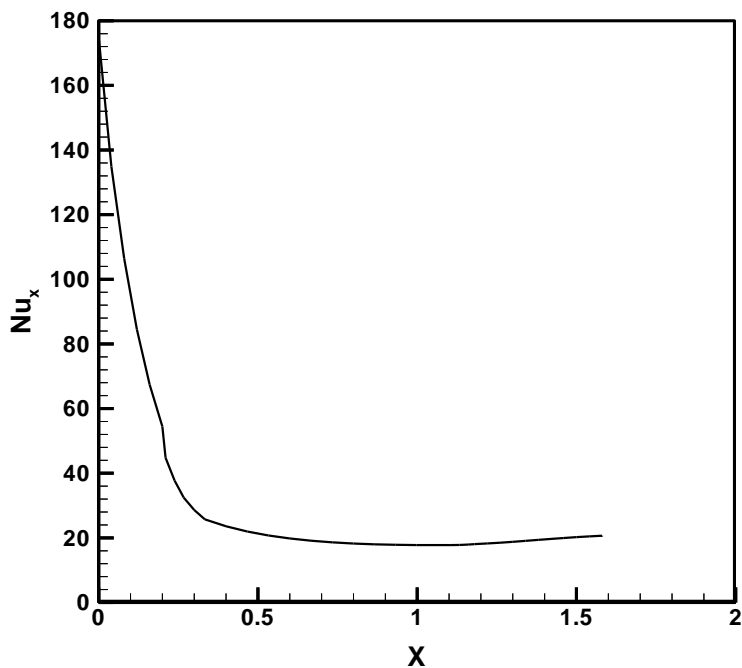




Figure(33): Contour (Lines) of temperature distribution for  $Re=50,000$  and constant wall temperature  $T_w=1000\text{ }^{\circ}\text{C}$



Figure(34): Contour (flood) of temperature distribution for  $Re=50,000$  and constant wall temperature  $T_w=1000\text{ }^{\circ}\text{C}$



Figure(35): Distribution of Local Nuselt Number for  $Re=50,000$  and  $T_w=1000\text{ }^{\circ}\text{C}$

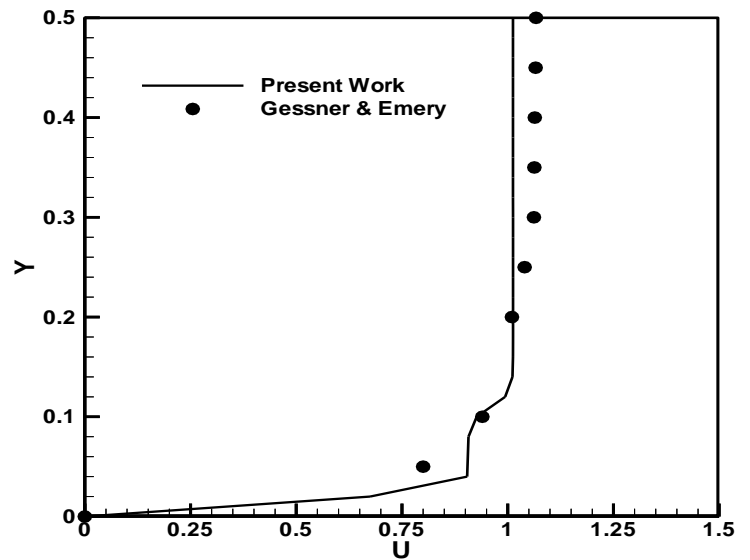


Fig.36: Boundary Layer Form comparison for duct flow

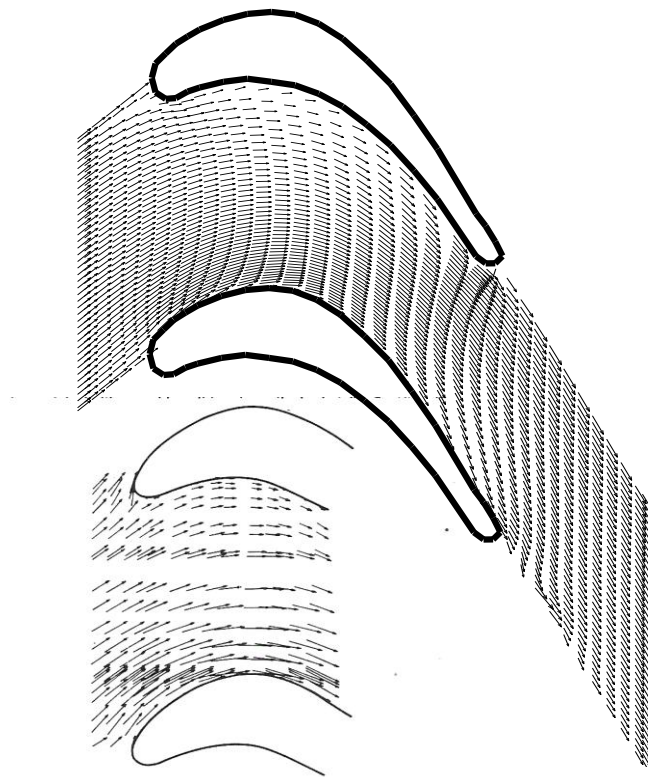


Fig. 37: Comparison Velocity Vector  $Re=5.9 \times 100000$  with Hah 1984

## FLOW SEPARATION OF AXIAL COMPRESSOR CASCADE BLADES

Dr. Arkan Kh. Al-Taie  
(Assist. Prof.) Mech. Eng. Dept., UOT  
Baghdad - Iraq

Sabah Faleh Habeeb  
(M.Sc. Student), Mech. Eng. Dept., UOT  
Baghdad - Iraq

### ABSTRACT

An experimental and theoretical investigation of the effect of flow separation on the performance of a cascade NACA 65\_(12)10 axial compressor blade has been carried out. The experimental work includes the fabrication of three blades from wood, each having a chord (100mm) but one of these blades having a span of (90mm) for smoke tunnel testing and the other two blades having a span of (380mm) for wind tunnel testing. The two blades were connected by suitable mechanism in order to be fixed in the wind tunnel protractor and rotated in the required stagger angle. The cascade was tested in an open type low-speed subsonic (Mach number=0.117) wind tunnel, for Reynolds number ( $Re=239605$ ) based on maximum velocity (35 m/s) and airfoil chord length. The total and static pressures were measured in selected points between the two blades for stagger angles of ( $4^\circ$ ,  $0^\circ$ ,  $-4^\circ$ ,  $-8^\circ$  and  $-12^\circ$ ) by using a multi-tube manometer and a pitot static tube. The small blade (90mm span) is tested in the smoke tunnel to visualize the real behavior of flow separation. The theoretical work includes using the software FLUENT (V6.2) to simulate the flow between the two blades. The study shows that the flow separation begins when the cascade are inclined at a stagger angle of ( $-4^\circ$ ) on the suction side of the lower blade at a position (96%chord experimentally and 98%chord theoretically). Then, the separation zone increases with increased stagger angle (in clockwise direction) and reach to the position (61%chord experimentally and 63%chord theoretically) at a stagger angle ( $-12^\circ$ ). These results are validated by a smoke tunnel tests. This separation affects the performance of the compressor, where the static pressure ratio ( $p_{s_e} / p_{s_i}$ ) decreases as the separation zone gets bigger. The range of working stagger angle is then calculated. It was found in the range ( $-18^\circ$  to  $36^\circ$ ). The flow behavior between the two blades shows that the blade-to-blade configuration works as nozzle-diffuser. The theoretical results were compared with the experimental results and good agreement was obtained.

### الخلاصة:

تم في هذا البحث اجراء دراسة عملية ونظرية لتاثير انفصال الجريان على اداء الريشتين المتعاقبتين للضاغطة المحورية من نوع [NACA 65\_(12)10]. الجزء العملي يتضمن تصنيع ثلاث ريش من مادة الخشب, وتر كل ريشة (100ملم) لكن احدى الريش ذات عرض (90 ملم) لاختبارات النفق الدخاني والريشتين المتبقتين ذواتا عرض (380ملم) لاختبارات النفق الهوائي. تربط الريشتين المستخدمتين لاختبارات النفق الهوائي بأليه مناسبة لكي تثبت بمنقلة النفق وبالتالي يمكن تدويرها بالزاوية المطلوبة. تم اختبار متعاقبة الريشتين في نفق هوائي تحت صوتي واطى السرعة لعدد رينولد ( $Re=239605$ ) المحسوب على اساس السرعة القصوى (35م/ثا) وطول وتر الريشة. لقد تم قياس الضغط الكلي والضغط الاستاتيكي للنقاط المختاره بين ريشتي الضاغطة لخمس زوايا انحراف هي (4,0,-8,-12) باستخدام مانوميتر متعدد الانابيب وأنبوب بيتوت-أستاتي. تم اختبار الريشة الصغيرة (ذات عرض 90 ملم) باستخدام النفق الدخاني لرؤية السلوك الحقيقي لأنفصال الجريان. الدراسة النظرية تتضمن استخدام

البرنامج الجاهز (FLUENT V6.2) لمحاكات الجريان بين الريشتين. أظهرت الدراسة بأن الانفصال يبدأ عندما تكون زاوية الانحراف (4-) حيث يحدث على السطح العلوي للريشة السفلى وبمسافة (96% من الوتر عمليا" و 98% من الوتر نظريا") من الدخول الى الخروج للمتعاقة. وبعد ذلك تزداد منطقة الانفصال بأزيد زاوية الانحراف (stagger angle) (بأتجاه عقرب الساعة) حتى تصل الى (61% من الوتر عمليا" و 63% من الوتر نظريا") من الدخول الى الخروج عند زاوية انحراف (12-) وهذا ما يوضحه اختبار النفق الدخاني. يؤثر الانفصال على أداء الريشتين المتعاقبتين حيث تقل نسبة الضغط (الضغط الستاتيكي الخارج الى الضغط الستاتيكي الداخل) بأزيد منطقة الانفصال. وبعد ذلك تم حساب المدى الشغال لزوايا الانحراف الذي وجد ضمن المدى (من-18 الى 36). أن سلوك الجريان بين الريشتين يبين بأن الريشتين المتعاقبتين تعملان كبوق متقارب- متباعد. تمت مقارنة النتائج النظرية مع النتائج العملية وجد تقارب جيد بين تلك النتائج.

**KEYWORDS:** Axial Compressor Cascade, Viscous Flow, Separation, FLUENT, Visualization

## INTRODUCTION:

The compressor, which is the important part of gas turbine engines, has to be given special attention during operation. The main task of the axial-flow compressor is to increase the pressure of air by converting air kinetic energy through a series of rotating and stationary blades. One of the most important problems that affect performance is the flow separation. Separation starts by deviation of fluid particles away from blade surface in the boundary layer. This causes a drop in kinetic energy, and cause the flow to re circulate [You D. AND Moin, P., 2006]. After stall region the fluid particles velocity reaches to zero in boundary layer near to blade surface and this deceleration causes increasing in boundary layer thickness and at a small distance after stall region the particles stop and reverse in direction due to positive pressure gradient. The low Reynolds number in conjunction with the local adverse pressure gradient makes it susceptible to flow separation [Meinhard T. Schobeiri et al, 2003]. This study consists of two major parts: the experimental part a cascade tested in an open jet low speed wind tunnel. The total and static pressure between two axial compressor blades were measured using a Pitot - static tube and a manometer. To visualize the flow a smoke tunnel was used. The stagger angle was taken equals ( $4^0$ ,  $0^0$ ,  $-4^0$ ,  $-8^0$ , and  $-12^0$ ). Secondary, in the theoretical part that depends on simulation the flow between the two blades by using a software **FLUENT**. The objectives of this paper are:

1. Study the effect of viscous flow separation (through the cascade of an axial compressor) on the flow variables (velocity, static pressure, total pressure...etc) by utilizing FLUENT (V6.2) software.
2. Investigate the effect of stagger angle on flow separation.
3. Comparison of the experimental results with the theoretical results.

## THEORITICAL PART:

### \* Assumptions:

The flow is steady, two-dimensional, incompressible , turbulent, Newtonian, isotropic and isothermal.

### \* Governing Equations:

The domain for which the model is build is shown in fig.(1) since the flow through a compressor is three-dimensional and quite complex, a simplified approach is adopted to analyze the fluid flow through cascade passage in two dimensions. Figs.(1) and (2) show the cascade and the physical domain. The equations of continuity, momentum and turbulence model are [Hill, P. G., 1965]:

- Continuity Equation:

$$\frac{\partial u}{\partial x} + \frac{\partial v}{\partial y} = 0 \quad (a).$$



- X-Momentum Equation:

$$\rho \frac{\partial u^2}{\partial x} + \rho \frac{\partial uv}{\partial y} - \frac{\partial}{\partial x} \left[ \mu_e \frac{\partial u}{\partial x} \right] - \frac{\partial}{\partial y} \left[ \mu_e \frac{\partial u}{\partial y} \right] = -\frac{\partial p}{\partial x} + \frac{\partial}{\partial x} \left[ \mu_e \frac{\partial u}{\partial x} \right] + \frac{\partial}{\partial y} \left[ \mu_e \frac{\partial v}{\partial x} \right] \quad (b).$$

- Y-Momentum Equation:

$$\rho \frac{\partial uv}{\partial x} + \rho \frac{\partial v^2}{\partial y} - \frac{\partial}{\partial x} \left[ \mu_e \frac{\partial v}{\partial x} \right] - \frac{\partial}{\partial y} \left[ \mu_e \frac{\partial v}{\partial y} \right] = -\frac{\partial p}{\partial y} + \frac{\partial}{\partial x} \left[ \mu_e \frac{\partial u}{\partial y} \right] + \frac{\partial}{\partial y} \left[ \mu_e \frac{\partial v}{\partial y} \right] \quad (c).$$

- The turbulence kinetic energy – dissipation model at high Reynolds number is used [Moult, A. et al, 1977].

A-Turbulence kinetic energy:  $K = 0.5(u'^2 + v'^2 + w'^2)$

$$\rho \left[ \frac{\partial Ku}{\partial x} + \frac{\partial Kv}{\partial y} \right] = \frac{\partial}{\partial x} \left[ \frac{\mu_e}{\sigma_k} \frac{\partial K}{\partial x} \right] + \frac{\partial}{\partial y} \left[ \frac{\mu_e}{\sigma_k} \frac{\partial K}{\partial y} \right] + G_k - \rho \varepsilon \quad (d).$$

The quantity  $G_k$  is the generation term for the kinetic energy of turbulence given by:

$$G_k = \mu_t \left\{ 2 \left[ \left( \frac{\partial u}{\partial x} \right)^2 + \left( \frac{\partial v}{\partial y} \right)^2 + \left( \frac{\partial u}{\partial y} + \frac{\partial v}{\partial x} \right)^2 \right] \right\} \quad (e).$$

$$\text{B-Dissipation: } \left[ \varepsilon = \nu \left( \frac{\partial u'}{\partial y} + \frac{\partial v'}{\partial x} \right)^2 \right]$$

$$\rho \left[ \frac{\partial \varepsilon u}{\partial x} + \frac{\partial \varepsilon v}{\partial y} \right] = \frac{\partial}{\partial x} \left[ \frac{\mu_e}{\sigma_\varepsilon} \frac{\partial \varepsilon}{\partial x} \right] + \frac{\partial}{\partial y} \left[ \frac{\mu_e}{\sigma_\varepsilon} \frac{\partial \varepsilon}{\partial y} \right] + (C_1 G_k - C_2 \rho \varepsilon) \varepsilon / K \quad (f).$$

The  $K - \varepsilon$  turbulence model was extended by ref. [Jones, W. P. and Launder, B. E., 1972] to low-Reynolds number flow as follows:

$$\rho \left[ \frac{\partial Ku}{\partial x} + \frac{\partial Kv}{\partial y} \right] = \frac{\partial}{\partial x} \left[ \left( \frac{\mu_t}{\sigma_k} + \mu \right) \frac{\partial K}{\partial x} \right] + \frac{\partial}{\partial y} \left[ \left( \frac{\mu_t}{\sigma_k} + \mu \right) \frac{\partial K}{\partial y} \right] + \mu_t \left[ 2 \left( \frac{\partial u}{\partial x} \right)^2 + 2 \left( \frac{\partial v}{\partial y} \right)^2 + \left( \frac{\partial u}{\partial y} + \frac{\partial v}{\partial x} \right)^2 \right] - 2\mu \left[ \frac{\partial K^{0.5}}{\partial x} + \frac{\partial K^{0.5}}{\partial y} \right]^2 - \rho \varepsilon \quad (g).$$

$$\rho \left[ \frac{\partial \varepsilon u}{\partial x} + \frac{\partial \varepsilon v}{\partial y} \right] = \frac{\partial}{\partial x} \left[ \left( \frac{\mu_t}{\sigma_\varepsilon} + \mu \right) \frac{\partial \varepsilon}{\partial x} \right] + \frac{\partial}{\partial y} \left[ \left( \frac{\mu_t}{\sigma_\varepsilon} + \mu \right) \frac{\partial \varepsilon}{\partial y} \right] + \frac{C_1 \mu_t}{K} \varepsilon \left[ 2 \left( \frac{\partial u}{\partial x} \right)^2 + 2 \left( \frac{\partial v}{\partial y} \right)^2 + \left( \frac{\partial u}{\partial y} + \frac{\partial v}{\partial x} \right)^2 \right] - \frac{\rho C_2 \varepsilon^2}{K} - 2\nu \mu_t \left[ \frac{\partial^2 u}{\partial x^2} + \frac{\partial^2 u}{\partial x \partial y} + \frac{\partial^2 v}{\partial x \partial y} + \frac{\partial^2 v}{\partial y^2} \right] \quad (h).$$

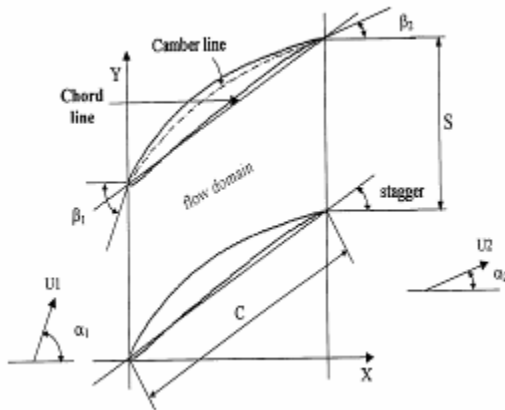


**Fig.(1): Compressor Cascade Geometry.**

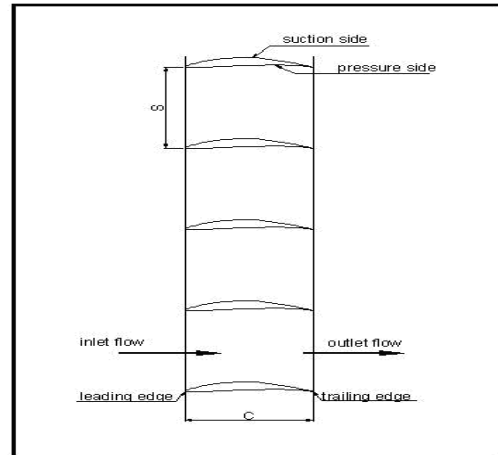


**Fig.(2): General View of the Cascade.**

**\* FLUENT Code:**

**- Analysis Steps:**

There are two processors used to solve the flow equations:

- A. preprocessor is a program that structure creates the geometry and grid by using GAMBIT as follows:
  - Modeling of geometry, fig.(3) and fig.(4).
  - Mesh generation (Discretization), fig.(5).
  - Boundary conditions. There are three type of boundary conditions:
    - a. Inlet boundary conditions(velocity and pressure inlet).
    - b. Outlet flow boundary conditions.
    - c. Solid surface(wall) boundary conditions.
    - d. Periodic boundary condition(flow regions before and after two blades).
- B. Postprocessor: is:
  - Solving Navier-Stokes equations (which includes continuity and momentum equations) as wall as turbulent flow model by using FLUENT software with ( ).
  - Plotting the results.

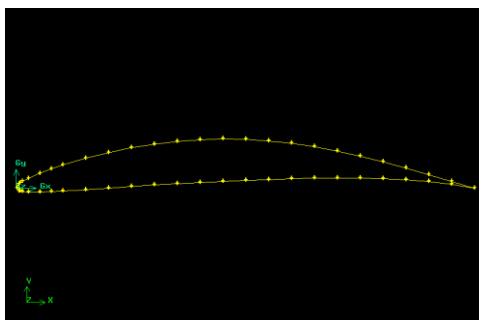


**Fig.(3):Axial compressor Blade by Points and Edges.**

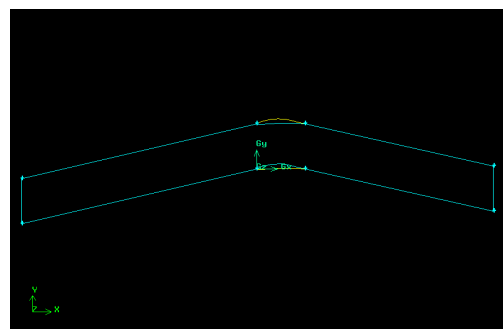


**Fig.(4):Axial Compressor Blade as a face.**

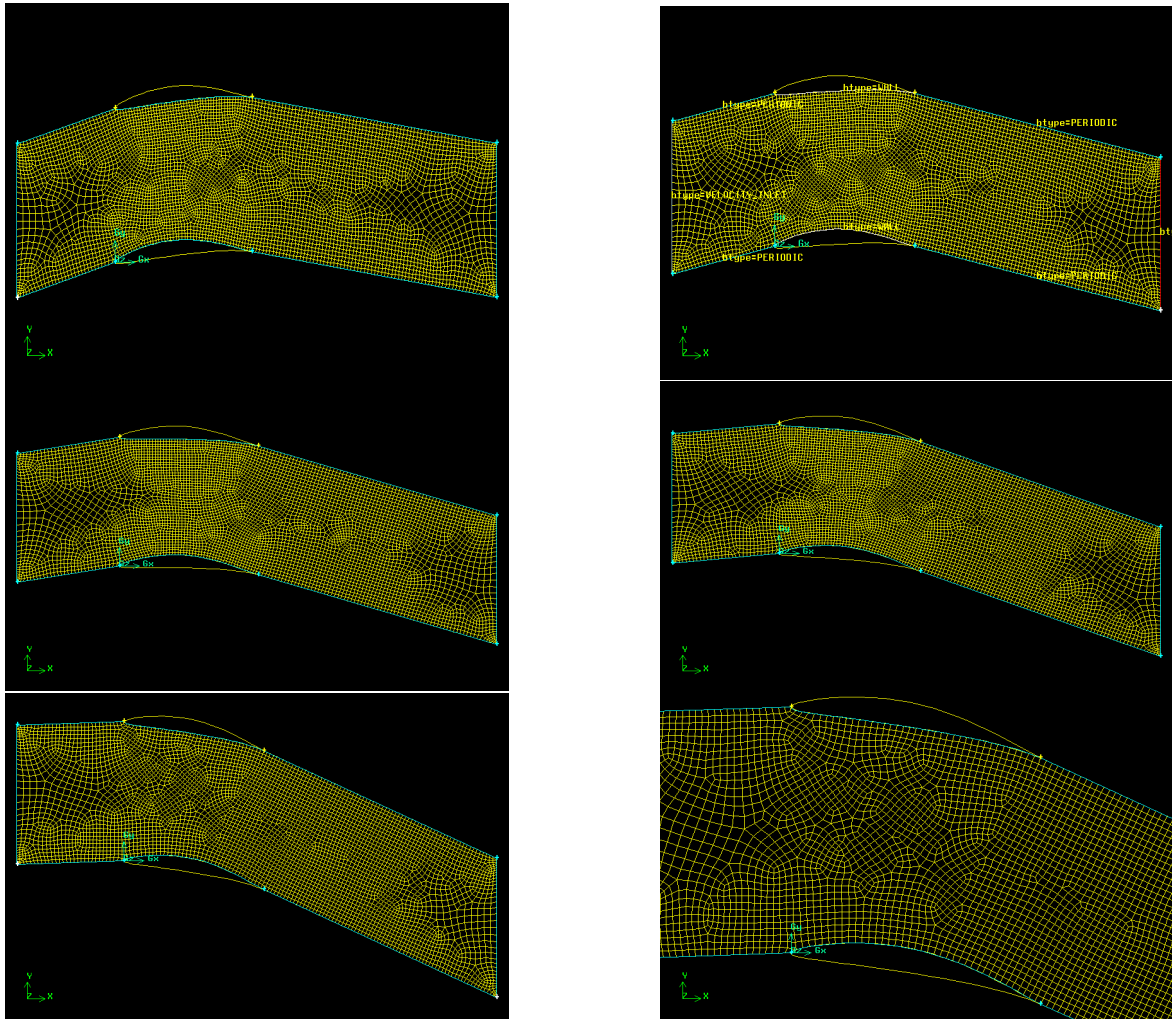


Fig. (5): Grid (Mesh) generation of axial compressor vanes passage for (stagger angle = $4^{\circ}$ ,  $0^{\circ}$ ,  $-4^{\circ}$ ,  $-8^{\circ}$  and  $-12^{\circ}$ ).

## EXPERIMENTAL WORK:

### \* Blade to Blade Configuration:

In the present work a cascade consists of two blades, each having a chord of (100mm) but one of these blades has a span of (90mm) and the other two blades have a span of (380mm) were made from wood fig.(6). The two blades of (380mm in span) are connected by suitable mechanism, as shown in fig.(7) in order to be fixed in wind tunnel protractor and achieved on required stagger angle. The two blades are fixed by aluminum plates, fig.(7).



Fig.(6): Axial Compressor Blades NACA 65\_ (12)10. Fig.(7): Blade to Blade Configuration.



**\* Apparatus:**

**- Subsonic Wind Tunnel:**

Low- speed subsonic (Mach number=0.117) open type wind tunnel is used in this work of cross section of (305mm\* 305mm). Wind speed of (35m/s) is achievable allowing experiments on many aspects of incompressible air flow and subsonic aerodynamics to be performed at satisfactory Reynolds number. Reynolds number is (Re=239605) based on inlet velocity and blade chord. The tunnel has a smooth contraction fitted with the protective screen. The test section is constructed of clear Perspex, to see the blade to blade configuration clearly with a square cross section of (305mm×305mm) and a length of (610mm). The blade to blade configuration was put inside the test section parallel to flow direction and connect by protractor to limit stagger angle. The control of the stagger angle of the blade to blade configuration was made by a suitable mechanism, fig.(9). The upper surface of the test section has a slot used to fix the pitot-static tube to measure the static pressure and total pressure. Fig.(8) is a photo of the wind tunnel and the working section. Downstream of the test section is a diffuser which leads to an axial flow fan driven by a (5.6kW three phase A.C motor). The flow is controlled by a butterfly valve before exhaust to atmosphere through exhaust section. The air enters the tunnel through a carefully shaped diffuser. The test section gives a full visibility of flow field.



**Fig.(8): Wind Tunnel Device (Open Circuit) and Multi-Tube Manometer.**



**Fig.(9): Protractor of Subsonic Low Speed Wind Tunnel.**

**- Multi Tube Manometer:**

A water multi tube manometer was used to measure total and static pressure between the two axial flow compressor blades, fig.(10). The manometer holes are connected to the Pitot - static tube by suitable connection pipes.

**- Pitot – Static Tube:**

The purpose of using pitot – static tube is to measure air static pressure, total pressure and then velocity inside test section. The external dimensions are (5mm) diameter, (200mm) arm length. Tube reading were corrected according to reference [Omran, K. J.,2003] as following:

$$\Delta p = p_d = p_t - p_s = \rho_{water} * g * \Delta H_{water} \quad (i).$$

$$p_d = \frac{1}{2} * E * \rho_{air} * U^2_{\infty} \quad (j).$$

$$\Delta p = \rho_{water} * g * \Delta H_{water} = \frac{1}{2} * E * \rho_{air} * U^2 \quad (k).$$

$$E = E_0 + \omega + \Omega \quad (l).$$



Where:  $E$ =Correction coefficient,  $\omega$ =Viscosity coefficients, its value(0),  $\Omega$ =Effect of distance from tube to wall which is found from fig.(11),  $E_0$ =Effect of static pressure holes distance of (0.9976) value.



**Fig.(10): Multi Tube Manometer.**

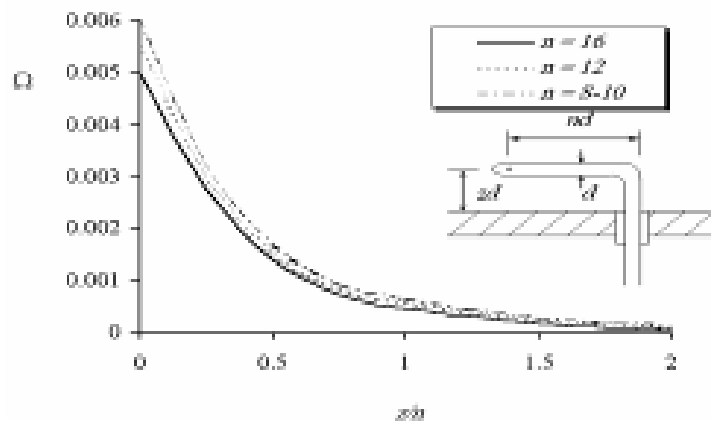


**Fig.(11): Correction of Pitot - static tube Distance. [Omran, K. J., 2003].**

### **Smoke Tunnel:**

To illustrate a real view of flow development and separation, a smoke tunnel was used as shown in fig.(12). The air is drawn by a fan which is rotated by an electrical motor of variable velocity at the top of the tunnel. The air enters to the tunnel at the base. The test section has dimensions of (180mm) width, (240mm) height and (100mm) deep. The models installed in the back wall of the test section, the front wall of the test section are easy to remove. It is made of clear Perspex. Smoke generation is controlled at the bottom of the tunnel. The section has (23) holes from it smoke enter. The space between any two adjacent holes is (7mm). A high light source is put in the sides of the test section to see smoke clearly. The smoke generated by a smoke generator which evaporates kerosene in class evaporator carried on the front wall of the smoke generator. The smoke generated is dragged by the fan at the top of the tunnel through the test section. Flow Photo is taken using a digital Camera.



**Fig.(12): Smoke Tunnel.**

### **\* Procedure of Experiments:**

The flow between two axial flow compressor blades was tested by wind tunnel as described in the following steps:

- Measure the atmospheric pressure and temperature before carrying out the experiments to calculate the air density accurately.
- Fix the blade to blade configuration in the test section with the required stagger angle.
- Prepare the multi tube manometer, controlling speed valve, and pitot static tube.

- Operating the wind tunnel for (15min) to reach steady state conditions.
- Reading the dynamic head by using pitot static-tube which is connected to multi tube manometer by suitable connection tubes.
- Repeating the previous procedure for other stagger angles ranges from ( $4^0$  to  $-12^0$ ).
- The experiments carried out in smoke tunnel were as following:
- Fill the bottle with Kerosene to the required limit.
- Put the model inside smoke tunnel test section and fixed at a certain angle indicated by protractor.
- 3. Turn on the smoke generator.
- 4. After about (3minutes) the smoke begins to formulate.
- 5. After smoke formulation the fan is turned on and controlled by the speed controller.
- 6. A high resolution digital camera was then used to photograph the models and flow.

## RESULTS AND DISCUSION:

### \* Experimental Results:

The experimental results are presented for three different curve lines located at (0.125, 0.5 and 0.875) of (S) as shown in fig.(13). The operating and boundary conditions of the blades and flow passage are listed in table(1).

**Table (1): Operating and Boundary Conditions.**

Case	Stagger Angle in (degree)	Inlet Velocity (m/s)	Number of grid points	Static Pressure Ratio
1	4	35	63	1.08
2	0	35	63	1.12
3	-4	35	63	1.1
4	-8	35	63	1.07
5	-12	35	63	1.04

The velocity and static pressure distribution (for the three sections) of flow between the two blades for stagger angle ( $4^0$ ,  $0^0$ ,  $-4^0$ ,  $-8^0$  and  $-12^0$ ) are presented in fig.(14) and (15). These figures show that the flow is accelerated along section 1 (0.125S) up to a certain position, (refer to third column of table(2)). Then the flow decelerates to the exit for stagger angles ( $4^0$  and  $0^0$ ) up to a certain position, see the fourth column of table (2) for stagger angles ( $-4^0$ ,  $-8^0$  and  $-12^0$ ) where the flow is separated. The flow decelerates along section 3 (0.875S) from the inlet to the exit for all taken stagger angles. The velocity and static pressure remains constant along the section 2 (0.5S) from the inlet to the exit for stagger angles ( $-8^0$  and  $-12^0$ ) and to a certain position for stagger angles ( $4^0$ ,  $0^0$  and  $-4^0$ ), the fifth column of table (2). Then the flow decelerates to the exit. The pressure ratio is the exit static pressure from blade to blade passage divided by inlet static pressure. The pressure ratio for all cases is shown in table (2).

The reason behind such behavior is the effect of stagger angle. Within a certain range of stagger angles (from  $4^0$  to  $-4^0$ ) the flow remains in contact with the blade surface. As the stagger angle is increased, the blade profile forces the flow away from its surface, hence, the flow starts to separate. Separation starts close to the trailing edge and progresses upwards as the stagger angle is changed (from  $-4^0$  to  $-12^0$ ). This effect is not clear in the middle section of the passage as the profile effects on flow behavior diminishes. The behavior of static pressure distribution is complimentary to the behavior of velocity. The flow separates from the suction side of the lower blade of cascade for stagger angle (from  $-4^0$  to  $-12^0$ ) because of adverse pressure gradient.

**Table (2): Experimental properties and behavior of flow between two blades in wind tunnel.**

Case	Stagger angles in (degrees)	Location of maximum velocity and minimum static pressure along section 1 (%chord)	Location of separation point along section 1 (%chord)	Location of flow deceleration along section 2 (%chord)	Pressure ratio
1	4	43	-	87.3	1.08
2	0	37.5	-	75	1.12
3	-4	36	96	73	1.1
4	-8	25	64	-	1.07
5	-12	12	61	-	1.04

The total pressure distribution of flow between two axial compressor blades for different stagger angle is presented in figure (16) .This figure show that the fluid total pressure decreases as it passage from the inlet to the exit due to friction losses. The total pressure losses increases when the stagger angle increases (in clockwise direction) and the maximum total pressure losses occurs for stagger angle (-12<sup>0</sup>) in separation region.

Figure (17) presents the pressure ratio distribution for stagger angles (4<sup>0</sup>, 0<sup>0</sup>, -4<sup>0</sup>, - 8<sup>0</sup> and - 12<sup>0</sup>). The pressure ratio decreases when the stagger angle increases and separation zone increases, see table (2). By using curve fitting method for this polynomial distribution, the concluded mathematical relationship between this pressure ratio and stagger angle for NACA 65\_(12)10 axial compressor cascade is:

$$\frac{P_{s_e}}{P_{s_i}} = 1.1057 - 0.0021\theta - 0.0007\theta^2 \quad (m).$$

Where:  $\theta$ : Stagger angle in (degrees).  $\frac{P_{s_e}}{P_{s_i}}$ : Pressure ratio.

By equating equation (m) to one, the range of stagger angle for NACA 65\_(12) 10 axial compressor blade aerofoil is (from -18<sup>0</sup> to 36<sup>0</sup>).

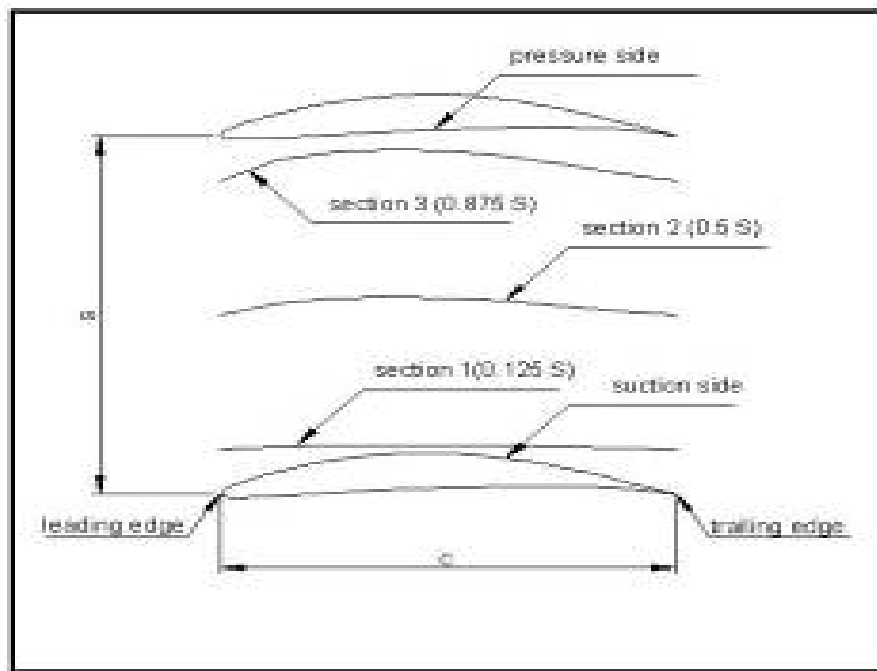
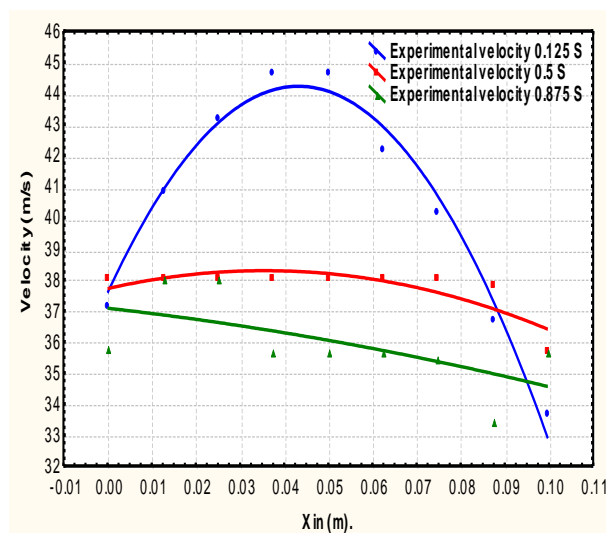
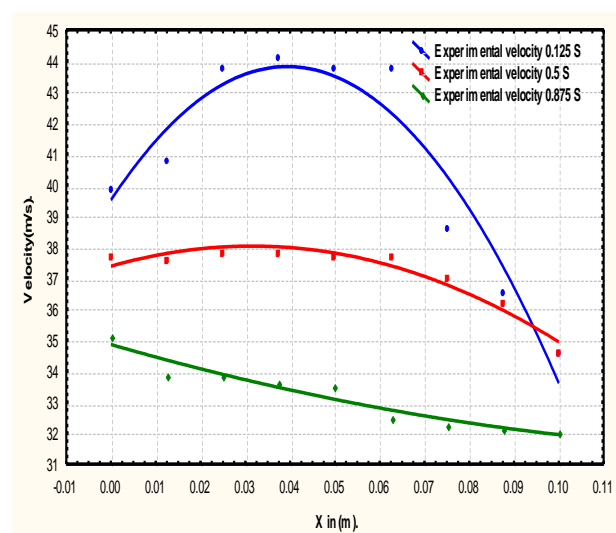


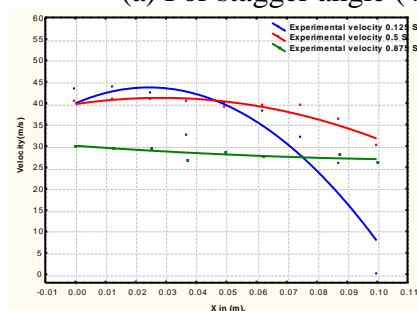
Fig.(13): Blade to blade configuration with taken three sections in flow passage.



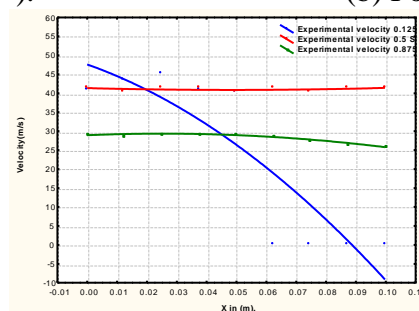
(a) For stagger angle ( $4^\circ$ ).



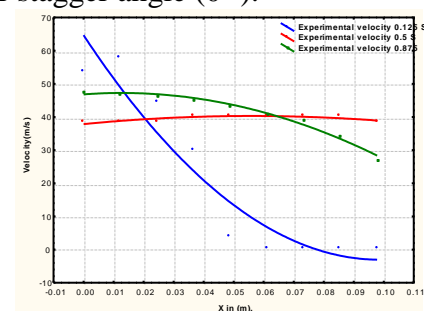
(b) For stagger angle ( $0^\circ$ ).



(c) For stagger angle=-4.

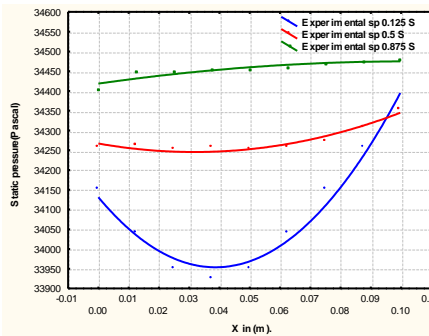


(d) For stagger angle=-8.

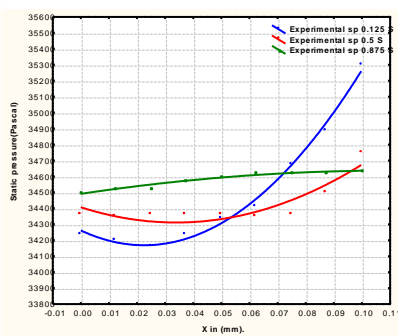


(e) For stagger angle=-12.

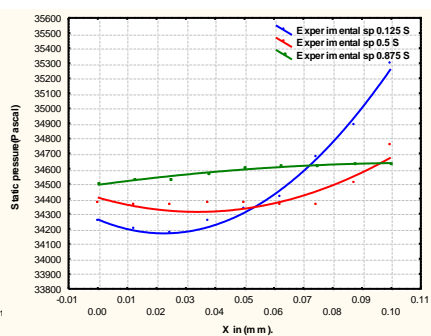
Fig.(14): Velocity distribution for (0.125S, 0.5S and 0.875S).



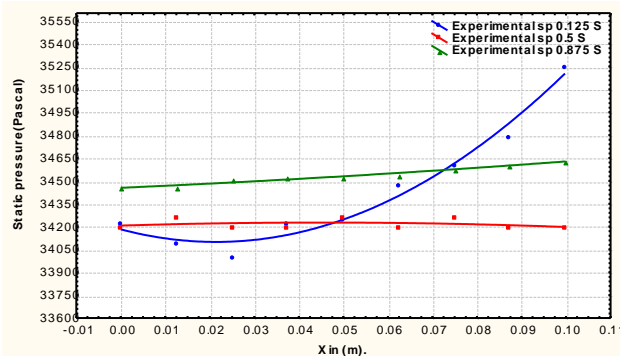
(a) For stagger angle=4.



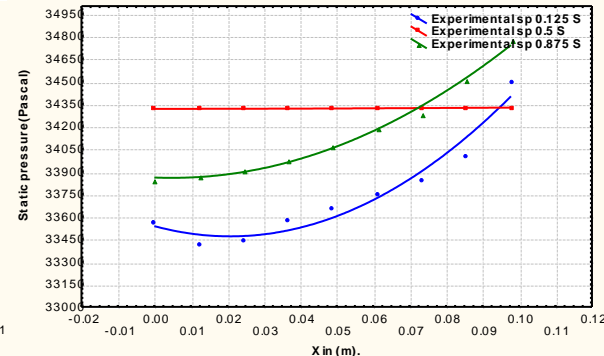
(b) For stagger angle=0.



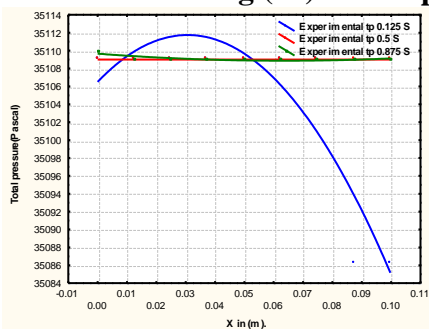
(c) For stagger angle=-4



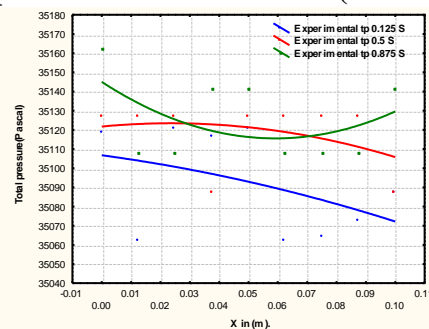
(d) For stagger angle=-8.



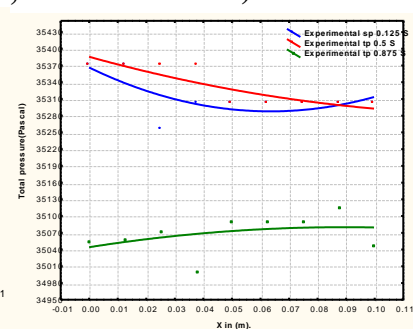
(e) For stagger angle=-12.

**Fig.(15): Static pressure distribution for (0.125S, 0.5S and 0.875S).**

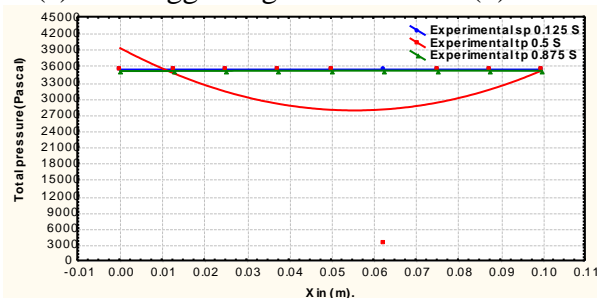
(a) For stagger angle=4.



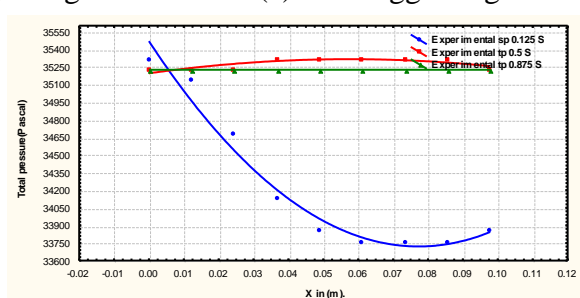
(b) For stagger angle=0.



(c) For stagger angle=-4.



(d) For stagger angle=-8.



(e) For stagger angle=-12.

**Fig.(16): Total pressure distribution for (0.125S, 0.5S and 0.875S).**

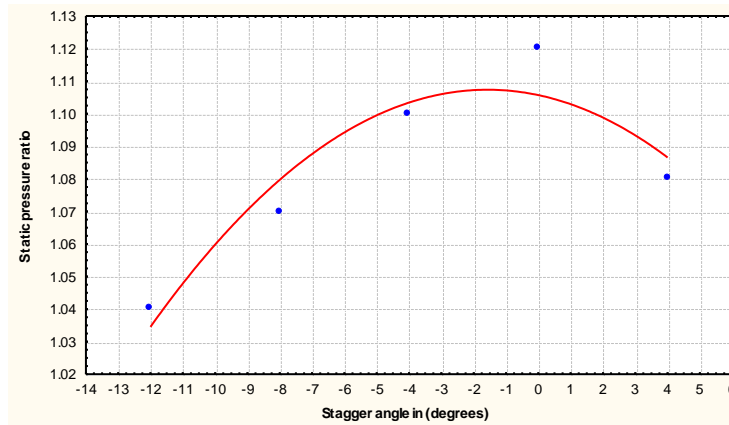


**Fig.(17): Correlation of pressure ratio with stagger angles.**

**\* Smoke Tunnel Results:**

To see the real view and stream lines of flow separation on blade surface, the blade tests in smoke tunnel for stagger angle ( $4^\circ$ ,  $0^\circ$ ,  $-4^\circ$ ,  $-8^\circ$  and  $-12^\circ$ ) are shown in fig.(18). The flow separation begins from the upper surface in stagger angle ( $-4^\circ$ ). As the stagger angle increases, separation propagates towards the leading edge.

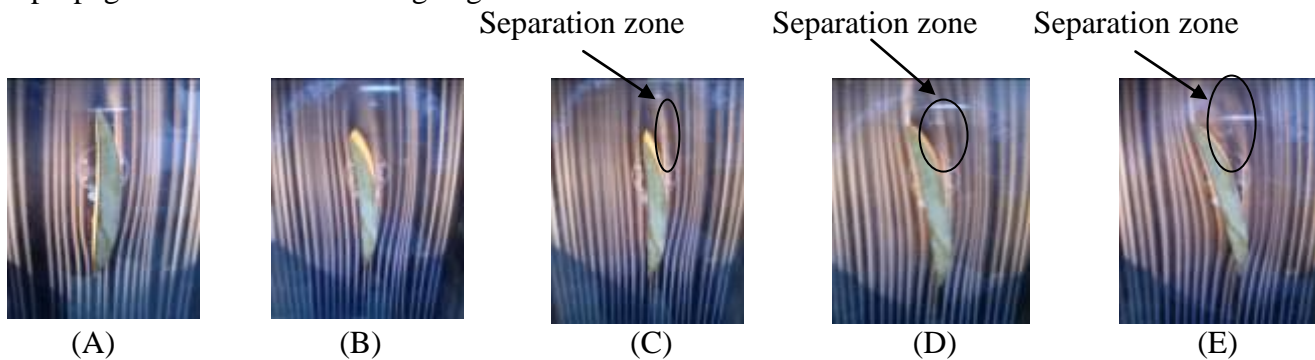


**Fig.(18): Stream line distribution on surface of axial compressor blade section NACA 65\_ (12)10: (A) Stagger angle =4. (B) Stagger angle =0. (C) Stagger angle =-4. (D) Stagger angle =-8. (E) Stagger angle =-12.**

**COMPUTATIONAL RESULTS:**

The operating and boundary conditions for the flow passage between two axial compressor blades are listed in Table (3).

**Table (3): Operating and Boundary Conditions.**

Case	Stagger Angle in (degree)	Inlet Velocity (m/s)	Number of grid points	Number of iterations to convergence	CPU time in (min).
1	4	35	5473	8398	73
2	0	35	5573	7492	62
3	-4	35	5528	8403	74
4	-8	35	5440	8881	86
5	-12	35	4888	1019	93

The velocity and static pressure contours of flow between two axial compressor blades for stagger angles ( $4^\circ$ ,  $0^\circ$ ,  $-4^\circ$ ,  $-8^\circ$  and  $-12^\circ$ ) are presented in fig.(19) and (20). These figures show that the fluid flow being accelerated near and along suction side (upper surface of lower blade) up to a certain position, see the third column of tables (4). Then the flow decelerates to the exit for stagger angles ( $4^\circ$  and  $0^\circ$ ) and to a certain position for stagger angles ( $-4^\circ$ ,  $-8^\circ$  and  $-12^\circ$ ), see the

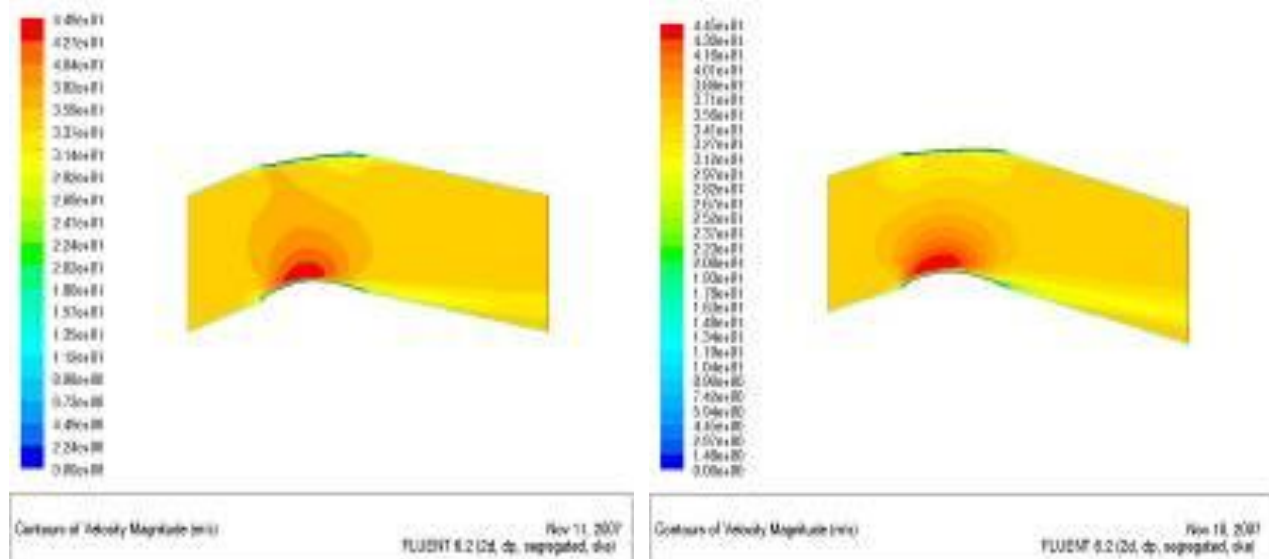
fourth column of table (4), where the flow separates from the blade surface. The flow decelerates near and along the pressure side (lower surface of upper blade) from the leading edge to the trailing edge along the chord line for all cases. The velocity and static pressure remains constant in the mid-space between the two blades from the inlet to the exit for stagger angles ( $-8^{\circ}$  and  $-12^{\circ}$ ) and to the certain position for stagger angles ( $4^{\circ}$ ,  $0^{\circ}$  and  $-4^{\circ}$ ), see the fifth column of tables (4). Then the flow decelerates to the exit. The fluid flow being accelerated as it passes through the contracting flow area after that the flow being decelerated to the trailing edge. These phenomena prove that the suction side works as a nozzle-diffuser, the pressure side works as a diffuser and the blade to blade configuration works as a nozzle-diffuser.

**Table (4): Theoretical properties and behavior of flow between two blades in FLUENT.**

No.	Stagger angles in (degrees)	Location of maximum velocity and minimum static pressure near and along the suction side (%chord)	Location of separation point near and along suction side (%chord)	Location of flow deceleration along mid-space between blades (0.5S)(%chord)
1	4	45	-	84
2	0	36	-	81
3	-4	35	98	74
4	-8	22	65	-
5	-12	12	63	-

The total pressure contours of flow between the two blades for stagger angle ( $4^{\circ}$ ,  $0^{\circ}$ ,  $-4^{\circ}$ ,  $-8^{\circ}$  and  $-12^{\circ}$ ) are presented in fig.(21). This figure shows that the total pressure decreases as it passes from the inlet to the exit due to friction losses. The total pressure losses increases when the stagger angle increases (in clockwise direction) and the maximum total pressure losses occurs when stagger angle ( $-12^{\circ}$ ) in separation region due to increased friction losses and adverse pressure gradient.

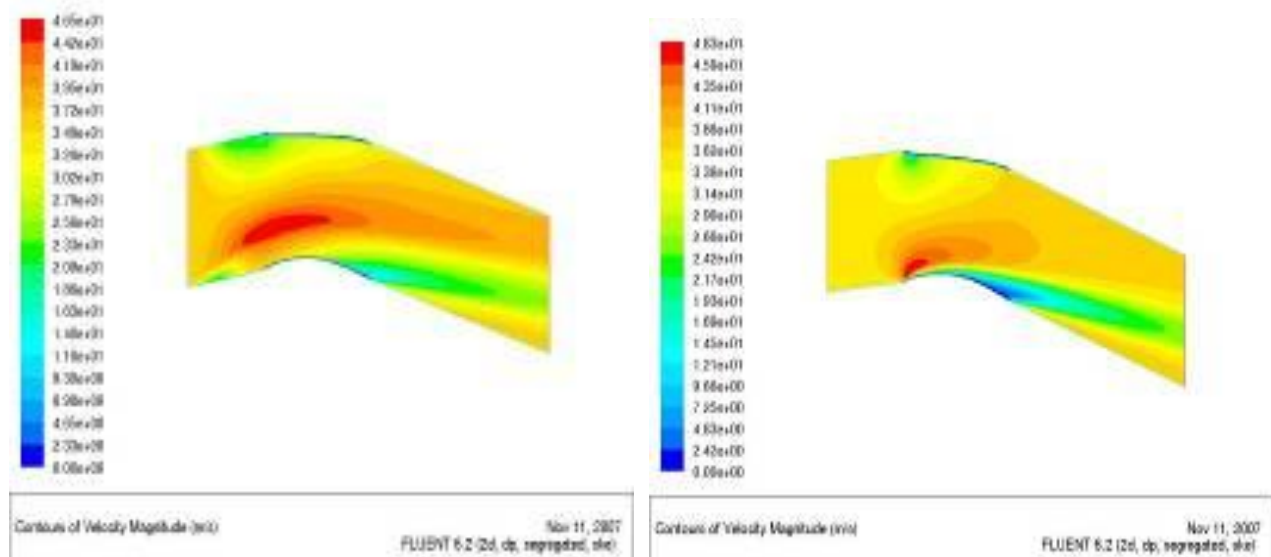
The flow separation affects the performance of a cascade and hence, affects the compressor performance where the pressure ratio decreases when the separation zone increases.



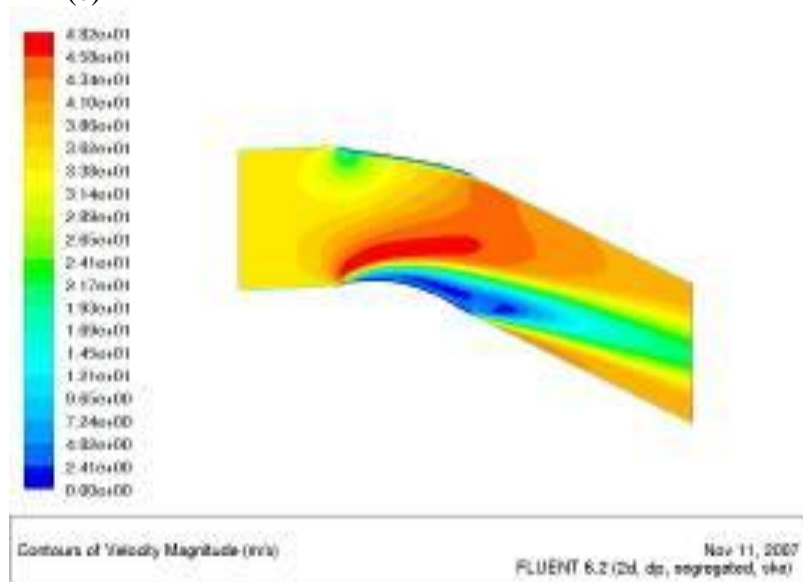
(a)

(b)



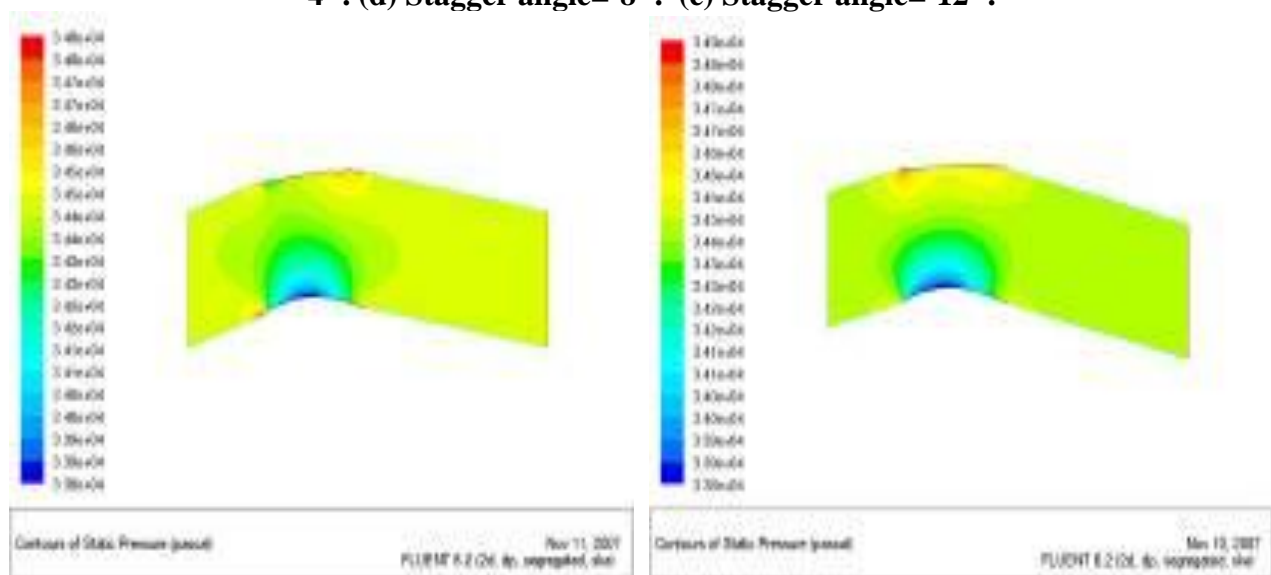


(c)



(e)

Fig.(19):Contours of velocity:(a) Stagger angle= $4^{\circ}$ . (b) Stagger angle= $0^{\circ}$ . (c) Stagger angle= $-4^{\circ}$ . (d) Stagger angle= $-8^{\circ}$ . (e) Stagger angle= $-12^{\circ}$ .



(a)

(b)



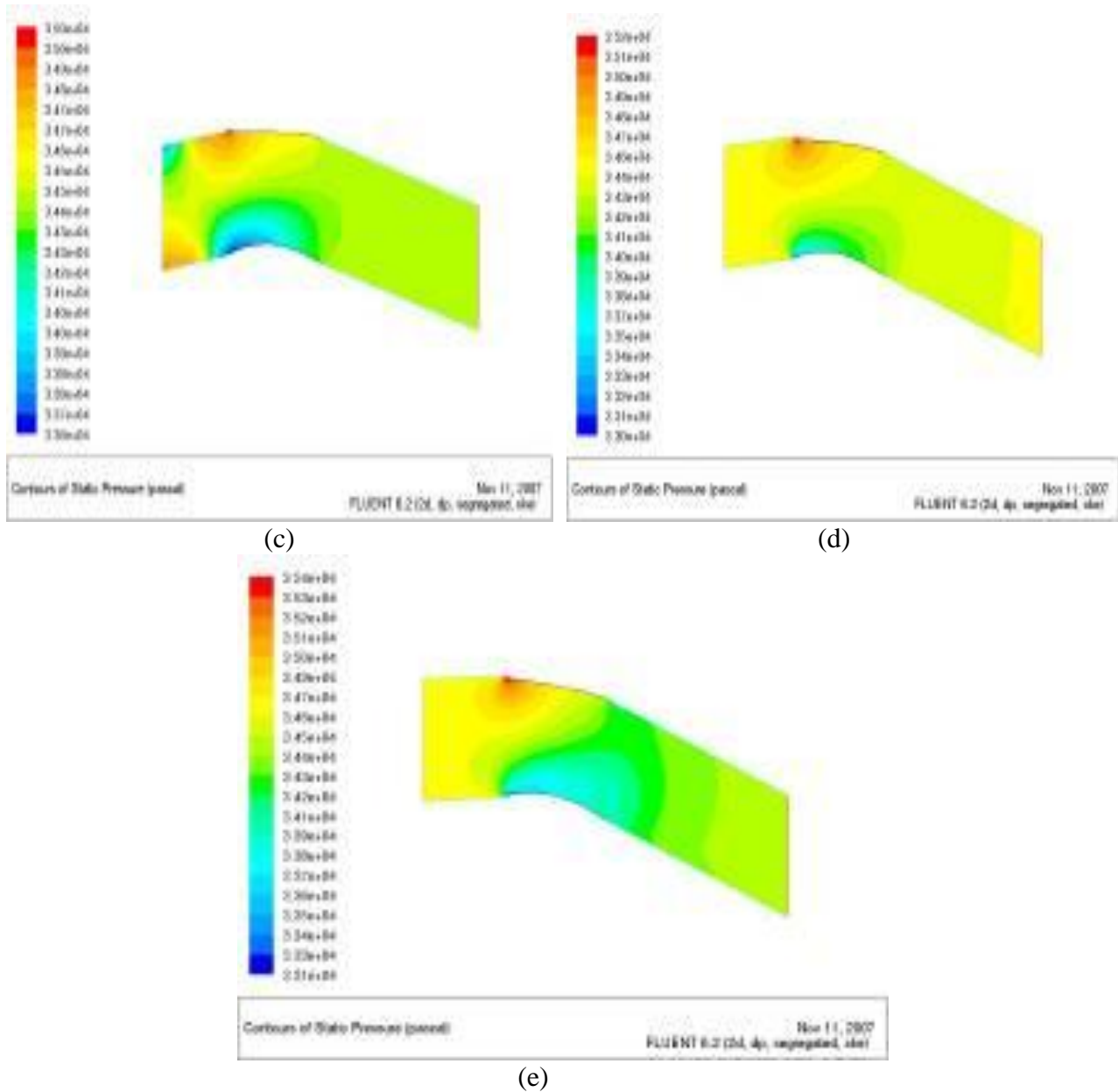


**Fig.(20):** Contours of static pressure: (a) Stagger angle= $4^\circ$ . (b) Stagger angle= $0^\circ$ . (c) Stagger angle= $-4^\circ$ . (d) Stagger angle= $-8^\circ$ . (e) Stagger angle= $-12^\circ$ .

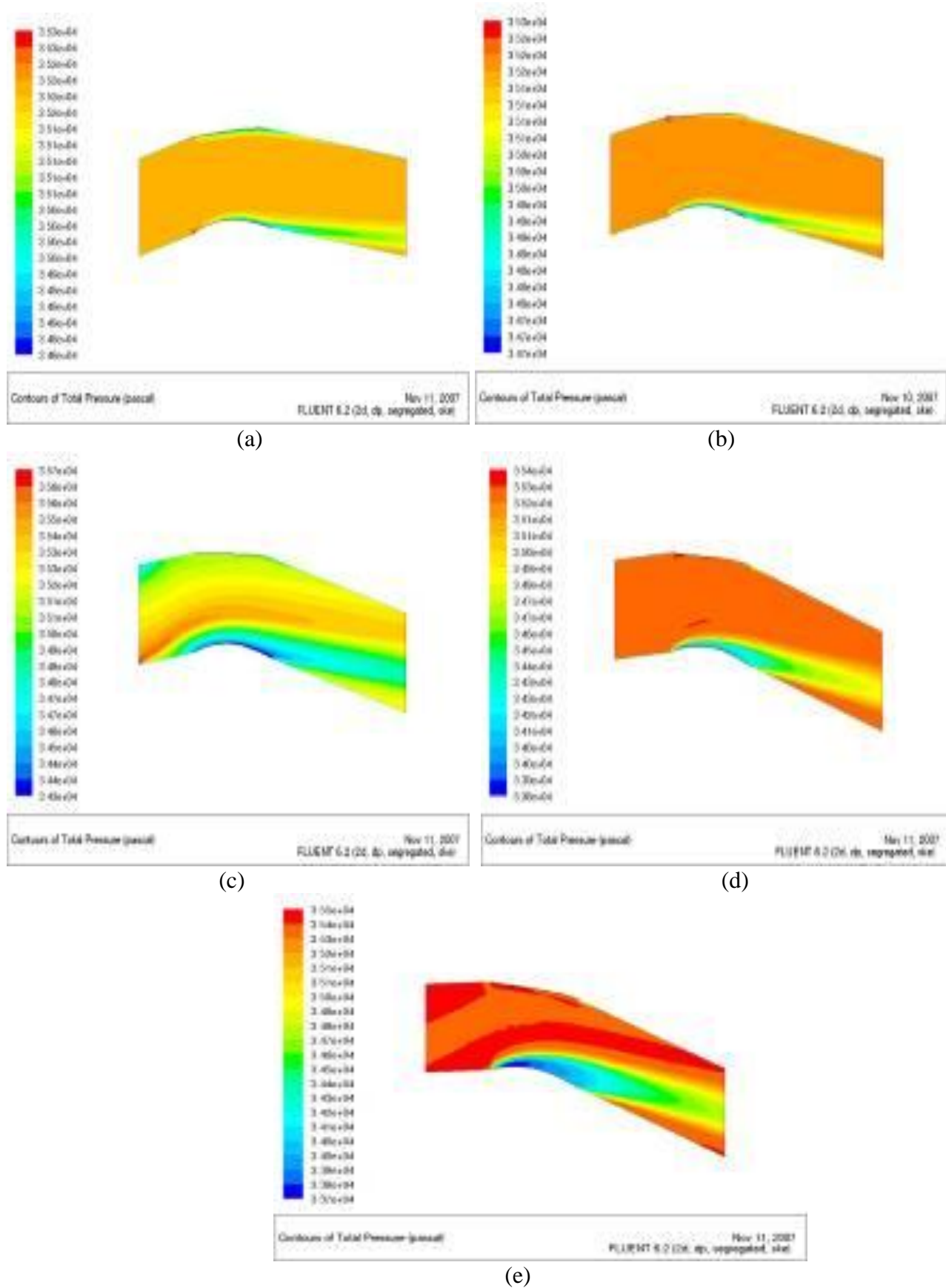


**Fig.(21): Contours of total pressure: (a) For stagger angle= $4^\circ$ . (b) For stagger angle= $0^\circ$ . (c) For stagger angle= $-4^\circ$ . (d) For stagger angle= $-8^\circ$ . (e) For stagger angle= $-12^\circ$ .**

### \* Accuracy of Solution:

The FLUENT (V6.2) code is considered as a high accuracy computational fluid dynamics software package. Fig.(22) presents the distribution of residual and number of iterations for continuity, momentum and k- $\epsilon$  model equations and for stagger angle ( $0^\circ$  and  $-8^\circ$ ). As the stagger angle increases, the number of iterations to convergence increases because the problem gets complicated when the flow separation occurs, see table (3).

### THE COMPARISON BETWEEN THE EXPERIMENTAL AND THEORETICAL RESULTS:

The theoretical results obtained in this study by using FLUENT (V6.2) were compared with those obtained experimentally using the wind tunnel. Fig.(23) shows this comparison for the velocity in the three locations of interest for stagger angle ( $0^\circ$ ). This figure shows good agreement between the theoretical and experimental results, where the flow behavior similar between these results and the range of different velocity between these results is (1-3)m/s.

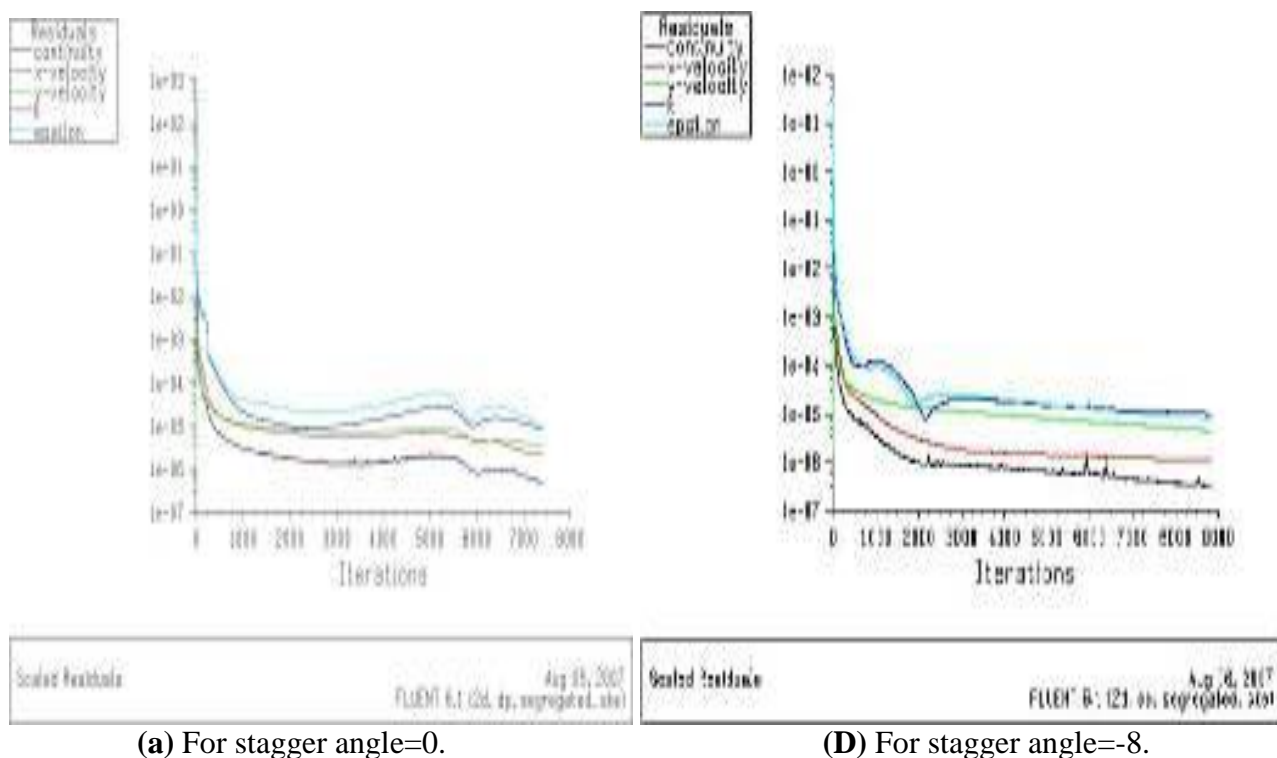


Fig.(22): Distribution of number of Iterations to convergence and Residuals for stagger angle ( $0^\circ$  and  $-8^\circ$ )

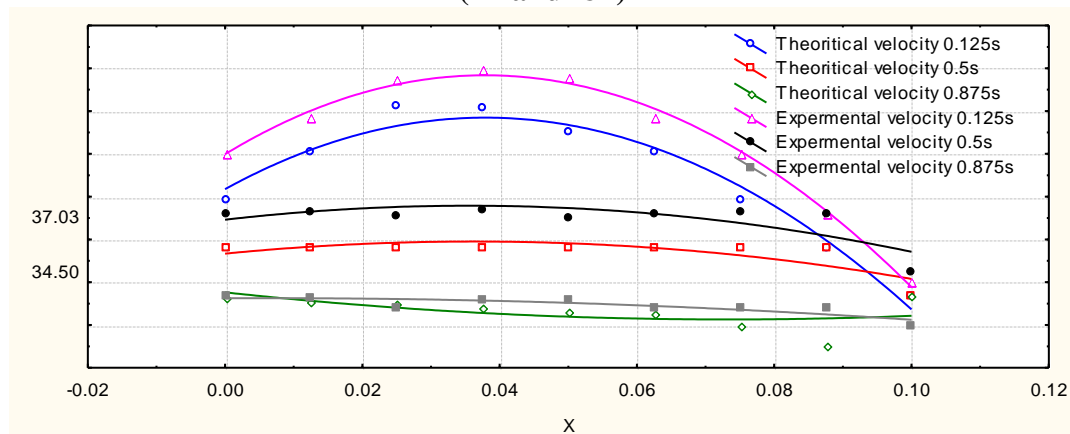


Fig.(23): The comparison of velocity distribution between the experimental results and the theoretical results.

**CONCLUSIONS:**

- 1-The area between two axial compressor blades for NACA 65\_ (12)10 works as a nozzle-diffuser.
- 2-Smoke tunnel was successfully used to show separation of flow from upper blade surface.
- 3-The flow separation was seen to start at a stagger angle of  $(-4^{\circ})$  experimentally and theoretically.
- 4- The mathematical relationship between the static pressure ratio and stagger angle for NACA 65\_ (12)10 axial compressor cascade is concluded by using curve fitting method for polynomial distribution.

$$\frac{P_{s_e}}{P_{s_i}} = 1.1057 - 0.0021 \theta - 0.0007 \theta^2 \quad (n).$$

The range of stagger angle for NACA 65\_ (12) 10 axial compressor blade aerofoil is calculated from this relationship. It was found in the range  $(-18^{\circ}$  to  $36^{\circ})$ .

- 5- Total pressure was seen to reduce through the blade passage. It drops sharply for the separation zone.
- 6- FLUENT (V6.2) was used successfully to predict separation as compared to the experimental measurements in the wind tunnel and as compared with other works.

**NOMENCLATURE****English Symbols**

Symbol	Description	Units
C	Blade chord line.	m
$C_1, C_2$	Constants in turbulence model.	m
d, nd, zd	Dimension of pitot static tube.	m
E	Correction coefficient.	
$E_0$	Effect of static pressure holes distance.	-
$G_k$	Production term of kinetic energy.	kJ
g	Acceleration of gravity.	m/s <sup>2</sup>
K	Kinetic energy of turbulence.	m <sup>2</sup> /s <sup>2</sup>
P	Pressure.	Pascal
n	Local coordinate normal to the wall.	m
Re	Reynolds number.	-
S	Space between two blades.	mm
x, y	Coordinates in X and Y- directions.	m
U	Velocity of air.	m/s
u, v, w	Velocity components in x, y and z directions	m/s

**Greek Symbol**

Symbol	Description	Units
$\alpha$	Flow angle.	degree
$\beta$	Blade angle.	degree
$\varepsilon$	Dissipation rate of turbulent kinetic energy.	m <sup>2</sup> /s <sup>2</sup>
$\mu$	Laminar viscosity.	kg/m.s
$\mu_e$	Effective viscosity.	kg/m.s
$\mu_t$	Turbulence viscosity.	kg/m.s



$\nu$	Kinematic viscosity.	$\text{m}^2/\text{s}$
$\omega$	Viscosity coefficients value.	-
$\theta$	Stagger angle.	degree
$\rho$	Density.	$\text{kg}/\text{m}^3$
$\sigma_k, \sigma_\varepsilon$	Effective prandtl numbers.	-
$\Omega$	Distance action from tube to wall.	-
$H\Delta$	Tube head in manometer.	$\text{cmH}_2\text{O}$
$P\Delta$	Change in pressure.	Pascal

### Superscripts

Symbol	Description
'	Fluctuating quantity.

### Subscripts

Symbol	Description
air	Air.
d	Dynamic.
s	Static.
$s_e$	Static exit.
$s_i$	Static inlet.
t	Total.
water	Water.
1	Inlet conditions.
2	Outlet conditions.

### Abbreviations

Symbol	Description
A.C motor	Alternating Current Motor.
CFD	Computational Fluid Dynamics.
Fig.	Figure.
NACA	National Advisory Committee for Aeronautics.
NASA	National Aeronautics and Space Administration.
SIMPLE	Simi – implicit method for pressure linked equations.
SIMPLEST	SIMPLE – Specially Treated (Newly developed).

## REFERENCES

- Chittiappa Muthanna, "Flow field Downstream of a Compressor Cascade with Tip Leakage", Ph.D. thesis, Virginia Polytechnic Institute and State University, Aerospace Engineering Department, November, 1998.
- Hill, P. G., and Peterson, C. R., "Mechanics and thermodynamics of propulsion", Addison-Wesley publishing Company, Inc. 1965.
- Jones, W. P. and Launder, B. E., "The Predication of Laminariztion With a Two-Equation Model of Turbulence", Journal of Heat and Mass Transfer, Vol.15, pp.301-314, 1972.
- Meinhard T. Schobeiri, Burak Öztürk and David E. Ashpis, "On the Physics of Flow Separation A long a Low Pressure Turbine Blade Under Unsteady Flow Conditions", Texas A&M University, Turbomachinery Performance and Flow Research Laboratory, College Station, Texas 77843, Available from: NASA Center for Aerospace Information 7121 Standard Drive Hanover, MD 21076, <http://gltrs.grc.nasa.gov> and National Technical Information Service 5285 Port Royal Road Springfield, VA 22100, June, 2003.
- Moul, A., and Srivatsa, S. K., "CORA-2 A computer program Code for Axi-Symmetrical Combustion chambers", CHAM Computer Code 201, 1977.
- Omran, K. J., "An Experimental Study of Backward Facing Step's Effect on The Aerodynamic Characteristics of Airfoil at Low Flight Speeds", M.Sc. Thesis, Aeronautical Specialization, Department of Machines and equipments, University of Technology, 2003
- You D. AND Moin, P., "Large-eddy simulation of flow separation over an airfoil with synthetic jet control", Center for Turbulence Research, Annual Research Briefs, 2006.

## ANALYSIS OF FUEL LONGTERM EFFECTS USING SUBCHANNEL CODES

E.A. AMIN  
M.Y. ABDUL — AHAD  
University of Baghdad  
College of engineering  
Nuclear Engineering Department

### ABSTRACT

Thermohydraulic computer codes such as COBRA3C are now becoming in practical use as part of power plant licensing process.

One of the areas of interest to reactor designer is the effect due to longterm operations and the changes that might occur either due to irradiation (burnup) effects or thermal stresses in the reactor.

The present study is an attempt to predict coolant channel temperature profiles at the core End Of Life. In addition deeper insight is given to the individual single partial contribution to the changes in Begin Of Life and End Of Life profiles. The effects due to fuel swelling, rod bowing, and changes in physical properties are studied in details using COBRA3C code.

The codes COBRA3C and the kinetic code AIREKMOD together a structure routine are joined in a modular system. As a result coupling between the different transient parameters in normal and abnormal operation conditions could be performed.

Results of such coupling are shown to improve the prediction of DNBR.

### الخلاصة :

لقد أصبحت المنظومات الحاسوبية المستخدمة للحسابات الترموهيدروليكية مثل المنظومة COBRA3C معتمدة علمياً كجزء من عملية ترخيص المحطة النووية.

إحدى الحقول المهمة لمصممي المفاعلات هو التأثير الناتج من التشغيل الطويل الأمد والتغيرات التي ربما تحدث نتيجة تأثير التشعيع (الاحتراق) أو نتيجة للاجهادات الحرارية داخل المفاعل .

الدراسة الحالية هي محاولة لاستنباط توزيع درجات الحرارة في قنوات التبريد عند نهاية عمر القلب . بالإضافة إلى ذلك أعطت هذه الدراسة ضوء عميق على التأثير المنفرد لكل عامل على حدة في بداية وفي نهاية عمر القلب .

التأثيرات الناتجة عن تضخم الوقود ، انحناء اقلام الوقود ، التغيرات في الخواص الفيزيائية تمت دراستها تفصيلياً بواسطة المنظومة COBRA3C . لقد تم ربط كل من البرنامج AIREKMOD و COBRA3C بالإضافة إلى روتين يتم فيه الحسابات التركيبية للوقود في نظام موحد . نتيجة لهذا الربط أمكن دراسة تأثير العوامل المتغيرة في الحالات الغير مستقرة.

نتائج الدراسة بالمنظومة الجديدة حسنت من حسابات (DNBR) .

## INTRODUCTION:

Thermal hydraulic margins are key determinants of plant operation flexibility and maximum attainable power rating and can therefore impact on plant availability and capacity factor.

Operating limits are established to ensure acceptable fuel conditions under normal as well as during abnormal operational transients or accident events. Examples of parameters that have to be limited to achieve these ends are linear generation rate, departure from nucleate boiling ratio (DNBR). Calculation of these parameters requires a detailed core subchannel thermal hydraulic analysis to provide the flow and fluid enthalpy in various regions of the fuel assembly. The important subchannel analysis computer codes that are in use for licensing calculations are : COBRA-IV, FLICA ,HAMBO, and COBRA3C ( C.L.WHEELER. *et.al*, 1976) , ( FAJEAU, M. , 1969) , ( BOURING,R.W, HAMBO , 1967), ( ROWE.D.S. , 1973) . These computer codes have been checked against experimental data and proved to predict accurately the critical parameters required to react or design.

A nuclear reactor operates for a long cycle (almost two years).During this time interval the reactor fuel is subject to drastic changes due to burnup and the presence of severe conditions of mechanical and thermal stresses beside the irradiation effects.

All these longterm effects influence the reactor performance to a large extent.

The longterm reactor behavior gains increasing importance with time. As a result, both experimental and computational efforts are spent to investigate the End Of Life (EOL) behavior because of its connection to reactor safety (PAUL.R, BETTEN, 1986), (HOFMAN *et.al*, 1980).

In recent study, (PAUL.R, BETTEN 1986), some experiments with instrumented fuel assembly were irradiated for 22 months and removed after it reached 8.8% burnup, (30568MWd). A comparison between calculations at the Begin Of Life and End of Life power reduction shows discrepancies between measured and calculated assembly temperature profiles by COBRA-IV. The differences were attributed to bowing in fuel elements.

In the present study the subchannel code COBRA3C is used to simulate a pressurized water reactor PWR fuel assembly. The LOFT reactor is considered as our model reactor. Some of the longterm parameters affecting performance are introduced. The parameters are introduced separately; this way the effect on temperature profile at EOL could be easily identified the parameters studied are: fuel swelling, rod bowing, changes of power distribution due to heterogeneous burnup.

Swelling, (MA .B.M. 1983), results from fission gas release during the fission process as well as fuel densification resulting from solid fission products. The direct effect of swelling is the change in the gap conductance. In case of severe conditions the fuel rod dimensions will increase at the expense of coolant channel dimensions.

Bowing results from temperature gradients which affect the mechanical properties of fuel rods. Bowing affects flow and therefore has great effect on heat transfer between fuel rods and coolant. We are going to investigate the effects of the above factors on the reactor assembly temperature profiles.



In the course of the present work it was found necessary to intercouple thermohydraulic, kinetic and structure calculations. The efficient method of performing such coupling is through a modular system. Brief description of the method and the results obtained are presented in section VI.

### **- PROBLEM MODELING IN COBRA3C:**

The model reactor used in the present study is the LOFT reactor. The LOFT reactor is designed to be representative of a large pressurized water reactor with reduction in power and size.

The reactor operates with a power level 50 MW at 2330 psi pressure, and core temperature of 595°F. The fuel rods are 36 inches in length.

The fuel enrichment is 2.27 and 4.95% of U235, The hottest assembly distribution layout with the section modeled in COBRA3C code are given in Fig. (1a). The assembly is 8×8 rods. In Fig.(1.b) the large number refer to the rod numbering in the code input ,and the small ones refer to subchannel numbers. Details about the LOFT COBRA3C calculation are given in (AL AHMADY, 1988).

The EOL power distribution of the hottest assembly is taken from neutronic calculation (AMIN .E.A. et. al, 1990). In this neutronic calculation a modified version of the diffusion burnup code FEVER-7 has been used. The modifications allowed for longterm behavior effects on fuel elements to be (AMIN .E.A. et. al, 1990) included during the burnup treatment. Fig. (2) gives the EOL power distribution as calculated by compared to that at the begin of life BOL. The rod region with higher power suffers higher burnup and the reduction in power is higher .This leads to a more uniform power distribution than at the begin of life, as is clear in Fig (2) .As a result to the previous effect the average power is closer to the regions of less power and the ratio pin power to average power increases for lower power regions.

### **- FUEL TEMPERATURE CHANGES DUE TO BURNUP:**

The fuel burnup leads to changes in the axial and radial power profiles .Beside the reduction of the overall power, the power peaking tends to reduce with irradiation. The axial power profile after 2000 hours operation is shown in Fig (2) (with control rod out) together with the initial power distribution.

The COBRA3C calculation with power distribution for the Begin Of Life and End Of Life are shown in Figs. (3) and (4). Fig. (4) gives the axial temperature profiles for the hottest pin. It is clear from this figure that the temperature tends to flatten with burnup.

The temperature profiles presented above the heat flux variation with burnup. The different burnup consequences are not considered in the COBRA3C calculation

### **BOWING:**

The results of reactor physics calculation reported by (C.L.WHEELER. et. al, 1976) showed that the maximum pin power is in the low enriched zone with power peaking factor of 1.6 and the highest pin power in the high enriched zone peaking factor of 1.51.

The neutronic calculation in the same reference showed also that the largest rod power gradient occurs in the high enriched rod.

The calculation for bowing prediction was performed as a result for this high enriched rod.

The calculation for bowing assumed that the fuel rod is a simply supported beam acted upon by bending moment. The resulted deflection could then be calculated. The assumption that temperature drop across the fuel pin is linear was also made.

The bending moment due to linear temperature across a plane of the cladding was taken from the formula given in the LOFT design report to be:

$$M_t = \frac{\Delta T E \alpha}{8 R_o} (R_o^4 - R_i^4)$$

Where:

- $M_t$  = thermal bending moment
- $\alpha$  = coefficient of thermal expansion
- $R_o$  = outside radius
- $R_i$  = inside radius
- $E$  = Young's modulus.

The midpoint deflection of the fuel pin simply supported at both ends of the active fuel length was calculated to be 0.0155 inch.  $\Delta T$  was calculated for the different axial nodes from the COBRA3C calculation.

For the bowing contribution to the HOT-spot, HOT channel-analysis, four rods are assumed to bow toward each other to give center to center dimensions of 0.530 inch.

This value for the effect of bowing was introduced in the COBRA3C input, the resulting radial temperature profiles are is given in Fig. (5).

It can be seen from the Fig. (5) that the effect of bowing is to increase the temperature. Since bowing is a longterm effect, it is most probable near the End of Life, its effect would be flattening of the temperature profile. It could be partially responsible for the power variation from BOL and EOL that is calculated from burnup alone.

### **Swelling; Effect of Fission Gas Release:**

Irradiation swelling induced by inert gases of fission products in the oxide fuel is less severe than that in metallic fuel, yet in both cases it limits the fuel performances, in particular the burnup.

Since the thermal properties of the fission gases are different from helium, the presence of the fission gases affects the-Heat transfer between the fuel and the clad. The COBRA3C calculations were performed once when the gap is filled with helium, in the second the gap was filled with fission gases. Published correlations (HOFMAN *et.al*, 1980), give the amount of fission gas produced as  $1.35 \times 10^3$  gram-mole/megawatt-day.

The results are shown in Fig. (6). The increase in temperature with the presence of fission gases in gap tends to saturation for high rod power. The maximum temperature increase in the rod central temperature amounts to 230° F. It was not possible in the present calculation to treat partial filled gaps, i.e. all the rods have the same fission gases.

The axial temperature profile for the hottest rod is shown in Fig. (6). The fission gas release and fuel temperature are interconnected, and therefore the hotter rod parts increase in temperature more than colder parts. The rod surface temperature increases by 13°F.

### **Coupling between thermohydraulic, kinetic and structure calculations:**

The most efficient and convenient method to couple thermohydraulic & kinetic and structure calculation can be achieved through a modular system. In the present system the codes

COBRA3C and AIREKMOD together with a structure routine are coupled in a modular system.

The communications between different modules occur either through a main database or through the common area. The overlay programming structure is adopted to minimize storage. Detail description of the system is given by (E. AMIN, 1990). The coupling between the different modules is governed by the module sequence and the input control parameters.

The following variations have been implemented in COBRA3C:

- Restart option.
- Heat flux profile varies with time.
- Channel flow rate variation with time.
- Gap thickness varies with time.

The heat flux profile variation with time is obtained from AIREKMOD calculation, whereas the gap thickness, flow rate and pressure variation are obtained from the structure calculations.

The restart option was found necessary in order to save the information from the previous time step. In this option all informations required are buffered out to the database and then read in the subsequent time step, together with the current information calculated by the other modules.

The AIREKMOD kinetic code calculates the axial power profile variation during the transient event according to the local thermal hydraulic conditions given by COBRA3C and the reactivity coefficients.

The variations in the AIREKMOD code to be implemented in the system are the restart option and the communication procedure with the system through the database and the common area.

Results of calculations using the above coupling procedure are discussed in the following:

Transients including partial loss of flow, anticipated transient without scram ATUS for the LOFT reactor is presented. The transient results in the reduction of the coolant mass flow rate from 100% to 90% with no scram occurring was run with and without AIREKMOD coupling.

The normalized total reactor core power and the coolant mass flow rate histories are shown in Fig. (6). The transient was first run using the kinetic coupling; the output is then used in the thermohydraulic module. A second run was made without kinetic coupling; the results are shown in Fig. (7). The DNBR was calculated using the Westinghouse w-3 correlation implemented in COBRA3C. The minimum axial values for both runs are given in Fig. (7).

It is shown in this figure that using coupled calculation improves the prediction of MDNBR i.e. it tends to the conservative side. Fig. (8) gives the relative axial heat flux profile for different transient times. It is clear that the axial heat flux profile is suppressed as the transient progresses in the upper region of the core due to the negative void coefficient which is larger in this part of the core.

The above results show, that using a fixed heat flux profile during the transient in the subchannel analysis codes introduces an inherent conservatism. The application of variable heat flux profile via kinetic codes removes this conservatism.

Another important effect is the gap conductance effect on the fuel and clad surface temperatures.

Results of calculation showing the effect of gap conductance variation on fuel and clad temperatures is shown in Figs. (9) and (10).

Both curves show that using dynamic gap conductance model i.e. allowing for gap thickness and conductance to vary with time gives higher values for both the clad and the fuel temperatures as the course of the transient progresses.

### **Summary and Conclusions:**

In the present work the COBRA3C thermohydraulic subchannel analysis code is used to show the effects of longterm parameters on fuel performance. Although the parameters studied are interconnected, yet for the purpose of identifying the single effects, they were considered to be independent. It has been shown that not only the burnup but the swelling and bowing could have relevant effects on the temperature distribution. In the present treatment each variation in the parameter studied needed new run for the code.

Coupling between thermohydraulic, kinetic and structure codes have been achieved through a modular system. Changes in both the codes COBRA3C and AIREKMOD have been made and a structure routine is written. It was therefore possible to study both steady state and transients. The present study gave quantitatively the effects of bowing and swelling in both cases.

The system developed in the present study is a good tool to obtain the influence of coupling calculation during transients.

### **References:**

1. AL AHMADY, (1988), 'Transient thermal hydraulic Calculation for PWP Reactor A Diss. Nucl Eng Dept Baghdad Uni.
2. AMIN .E.A. *et al*, (1990) 'Irradiation Induced Changes in Fuel Elements and Their effects on Nucl. Reactor Power Performance' Submitted to the present proceeding.
3. BOURING, R.W, HAMBO, (1967), "A Computer Program for the subchannel Analysis of Hydraulic and Burnout Characteristics of Rod Clusters ' AEEW-R 524 .
4. C.L.WHEELER. *et.al*, (1976), 'COBRA-IV: An Interim Version of COBRA for Transient Thermal Hydraulic Analysis of Rod Bundle Nuclear Fuel Elements and Cores' BNWL-1962 MARS.
5. E. AMIN, (1990) 'A Modular System for Thermohydraulic, Kinetic and Structure coupling 'to be published.
6. FAJEAU, M., (1969), " Programme FLICA Etude Thermodynamique d'un Reacteur ou d'une Boic; d'Essai' CEA-R-3716, Centre d'Etudes Nucleaires,. Saclay France.
7. HOFMAN *et.al* (1980). 'Irradiation Behavior of the Experimental Mark-II EBR II Drive Fuel' Nucl. Technol. 47, 7.
8. MA .B.M (1983), 'Nuclear Reactor Materials and Applications' Van Nostrand Reinhold.
9. MILLER C.S. 'LOFT Core Design Report' TID -4500.
10. PAUL.R, BETTEN (1986), 'Bowing OF Elements and changes in Radial Coolant Temperature Profile Over Subassembly' Trans .Am .Nucl, SOC. 52,532.
11. ROWE.D.S. (1973), " COBRA-3C: A Digital Computer Program for Steady State and Transient Thermal Hydraulic Analysis of Rod Bundle Nuclear Fuel Element .BNWL-1695 MARCH.

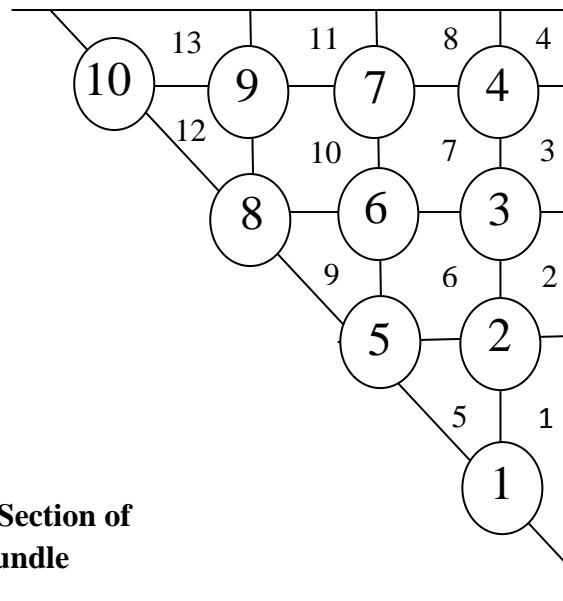


**Fig.(1.b) Sub-channel Layout For A 1/8 Section of Symmetry From A 6A – RDO Bundle**

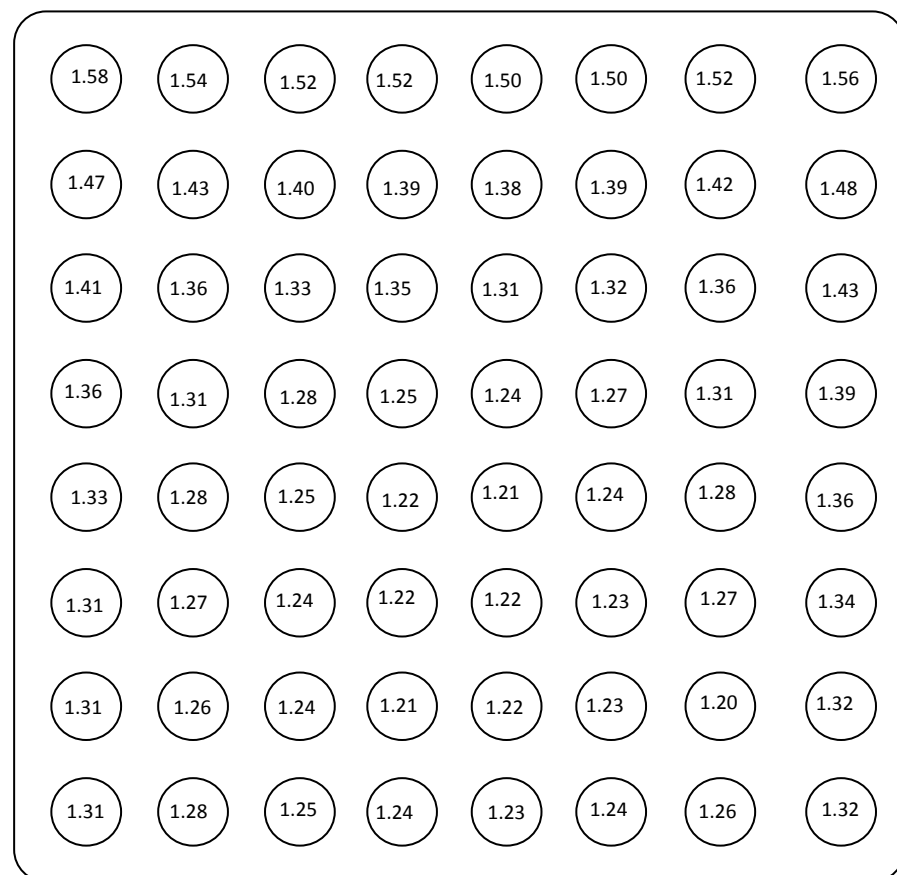


**Fig.(1.a) Relative Power Factor For Hottest Assembly**

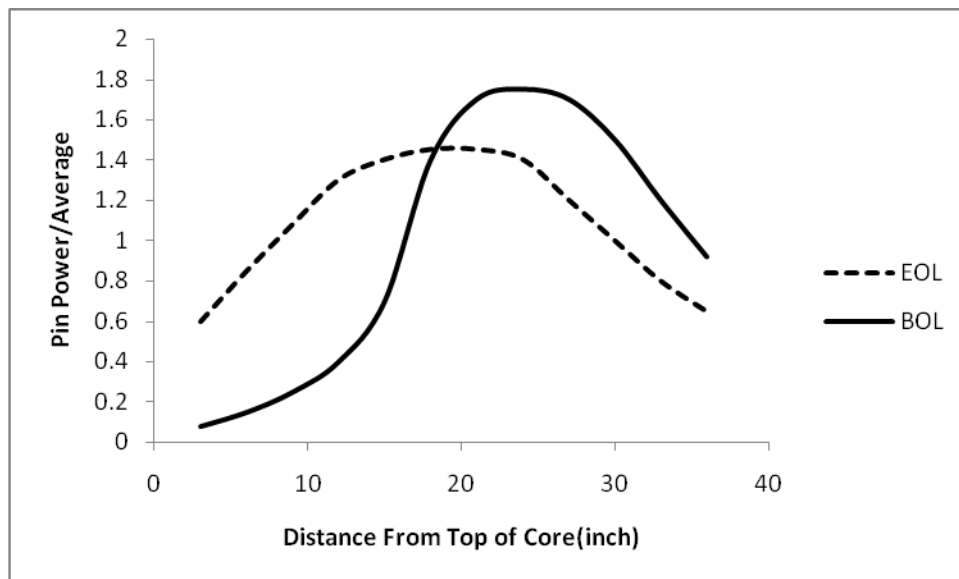
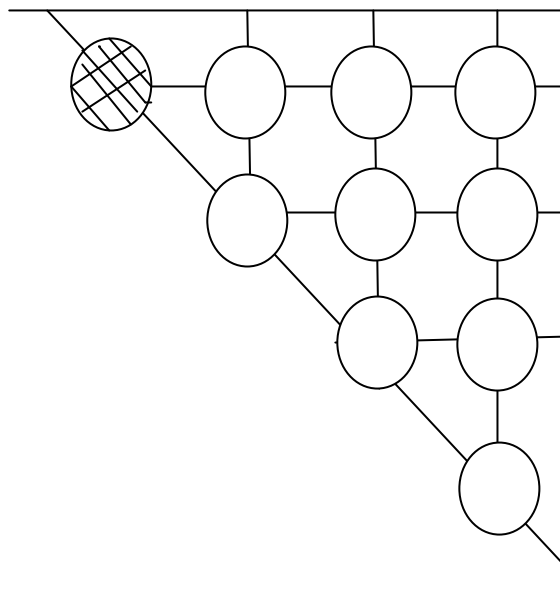


Fig.(2): Axial Power Profile For Begin Of Life and End Of Life (2000EFPH).



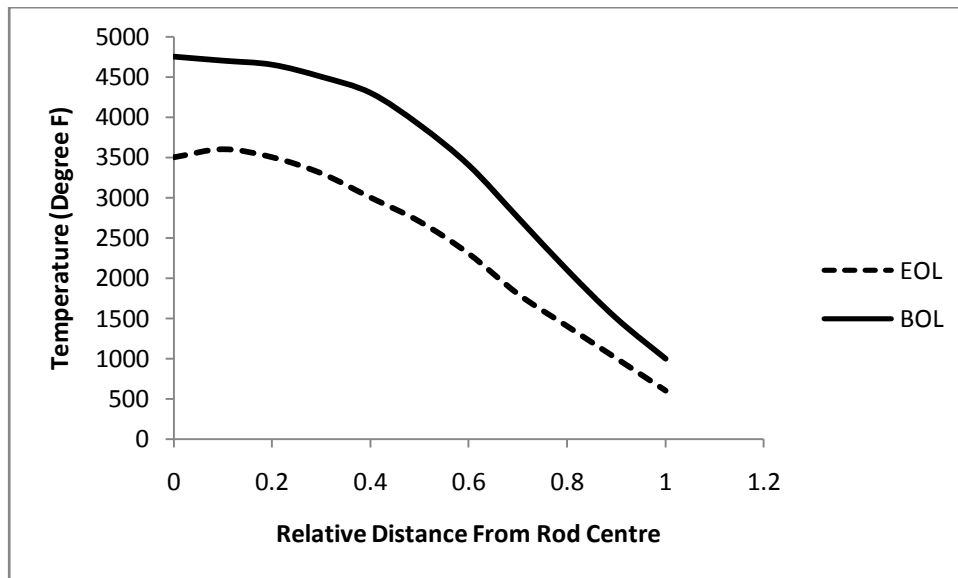
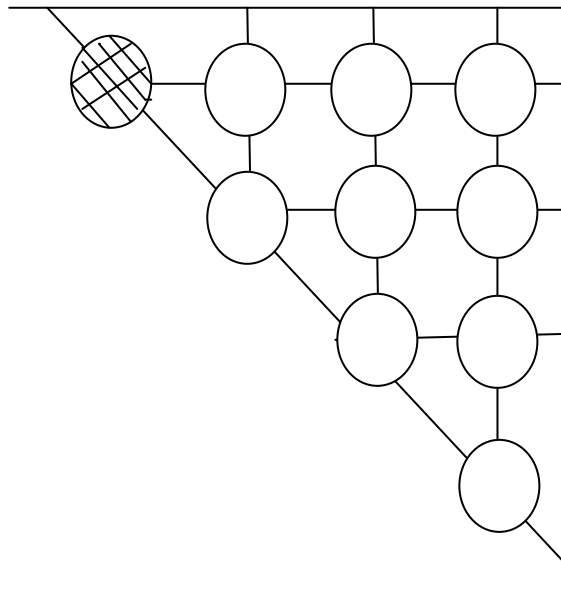


Fig.(3): Radial Temperature Profile and Effect of Burnup for the Hottest Rod.



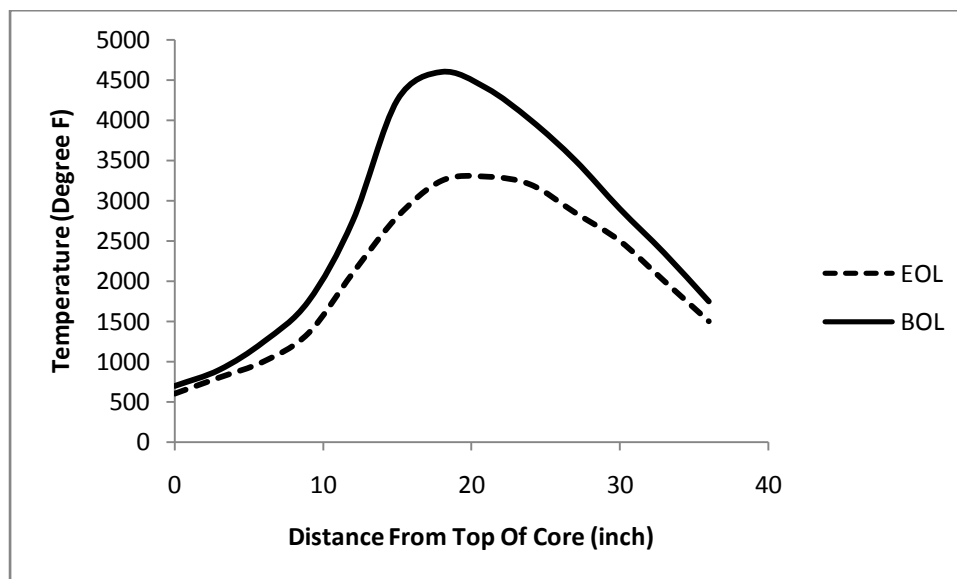


Fig. (4): Effect of Burnup on Axial Temperature Distribution For the Hottest Rod.

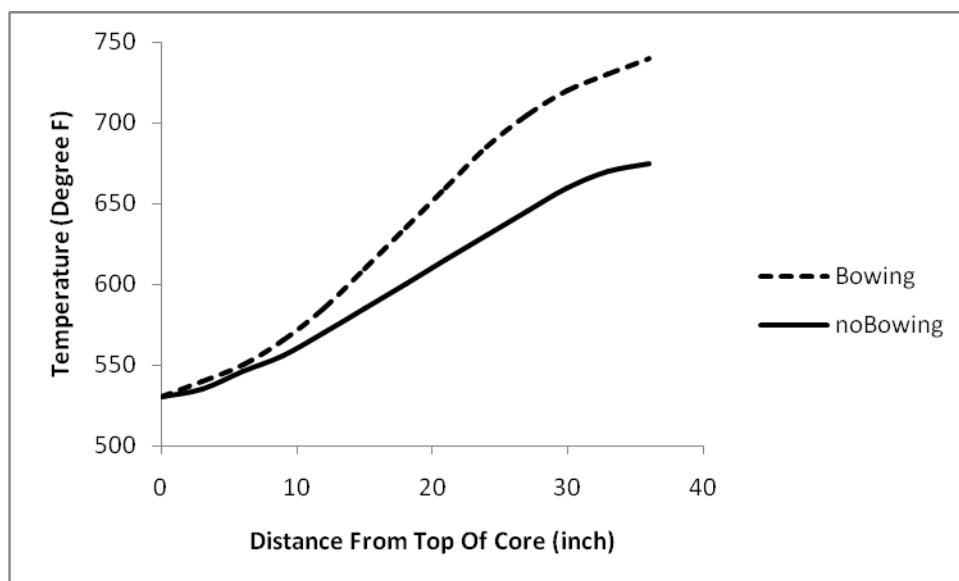


Fig.(5): Hottest Channel Axial Temperature Distribution and The Effect of Bowing.



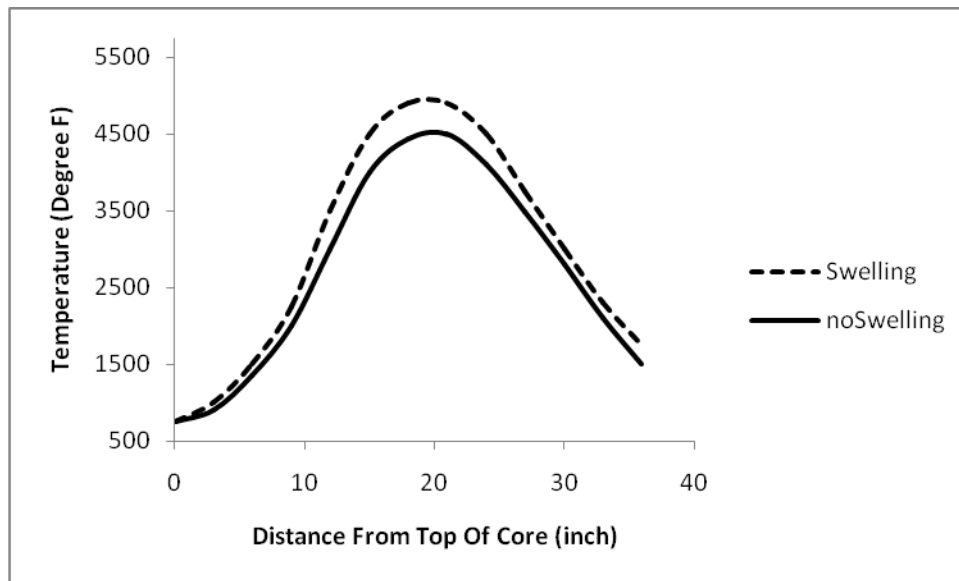


Fig.(6): Axial Temperature Distribution and The Effect of Swelling.

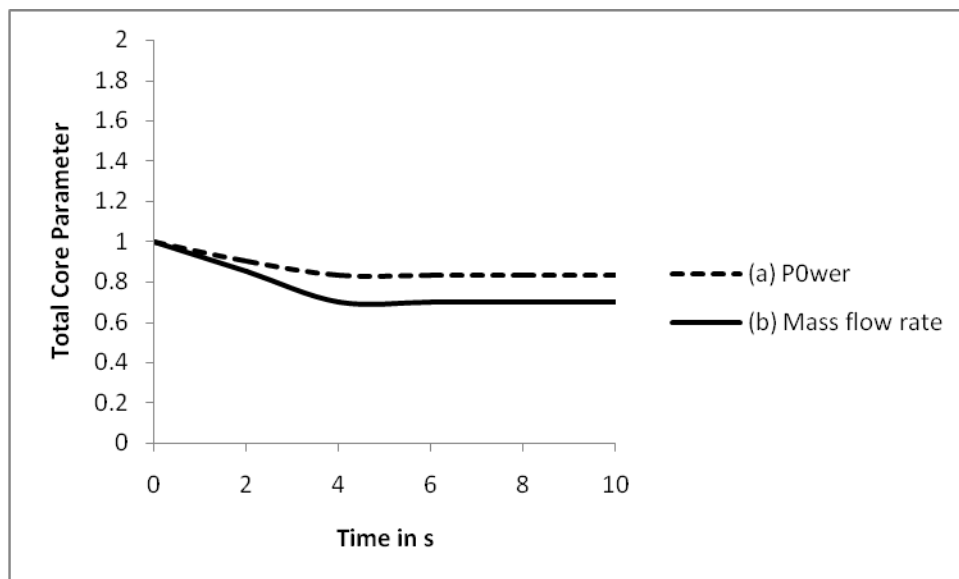


Fig.(7): Partial Loss of Flow ATWS Transient :

(a) Total Core Power

(b) Total Core Mass Flow Rate

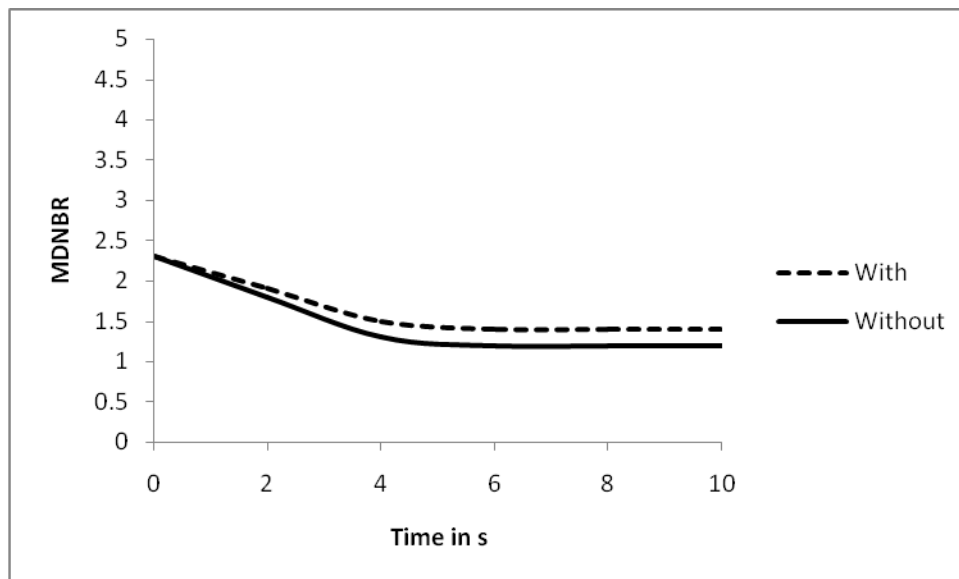


Fig.(8): Partial Loss of Flow ATWS Transient MDNBR for Transient With and Without Kinetic Coupling.

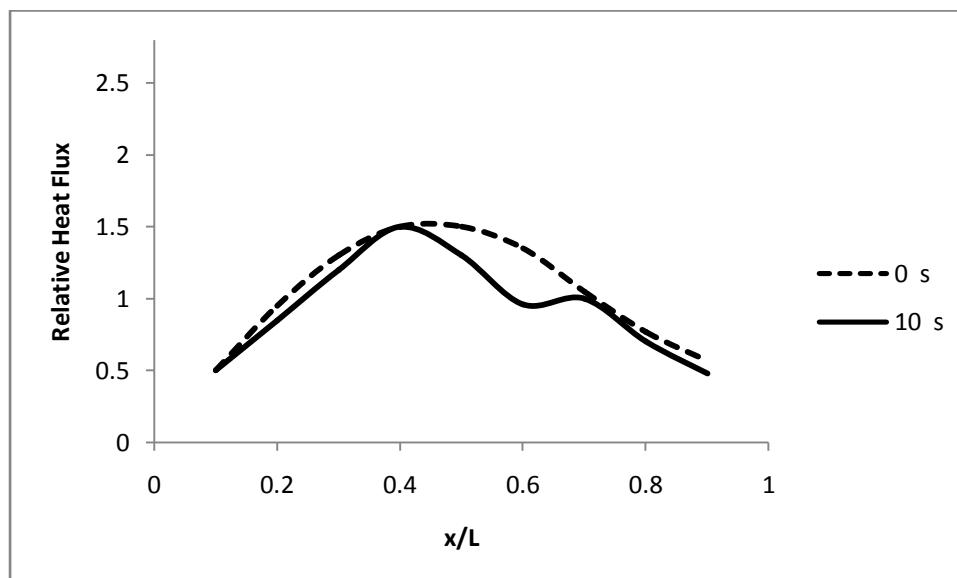


Fig.(9): Normalized Axial Heat Flux Profile at Time Steps 0 and 10 Seconds.

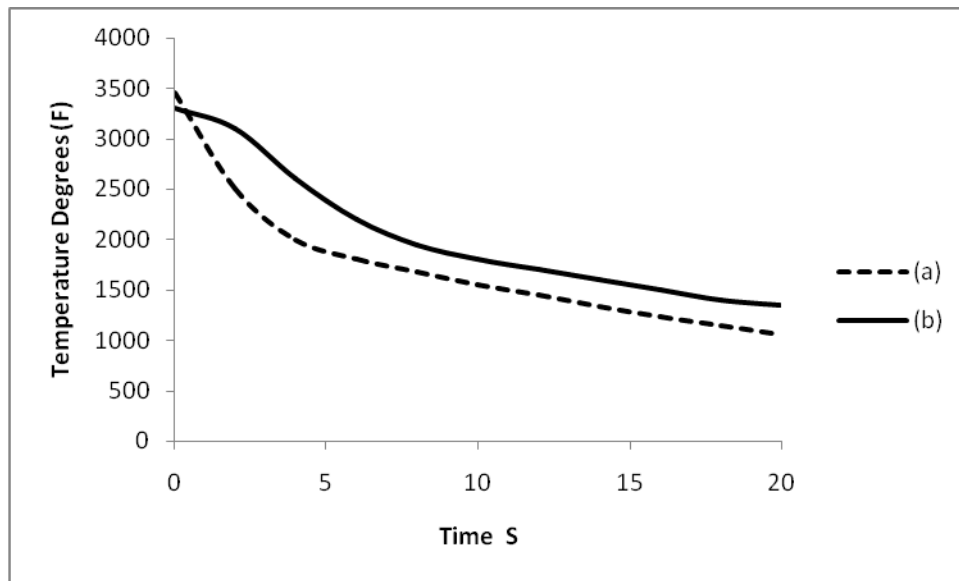


Fig.(10): Transient Peak Fuel Center Node Temperature:

(a) Fixed Gap Conductance.

(b) Dynamic Gap Conductance.

## SIMULATION OF TWO DIMENSIONAL FLOW AND CONJUGATE HEAT TRANSFER PROBLEM IN COOLED GAS TURBINE NOZZLE GUIDE VANE

Assist. Prof. Dr. AbdulKarim Ahmad Hassan  
Energy & fuel research center  
University of Technology  
Baghdad - Iraq

Mohammed Abdul-Nabi Aurybi  
Mech. Eng. Dep.  
University of Baghdad  
Baghdad - Iraq

### ABSTRACT

The coupled treatment (conjugate numerical methodology) allows the simultaneous solution of the external flow (steady, two dimensional, compressible and turbulent flow) and conduction within the metal (steady, two dimensional) of gas turbine nozzle guide vane (with and without internal convection cooling). Validation of the developed conjugate capability is investigated in the present work.

The numerical results were compared with experimental results for steady, two dimensional, compressible and turbulent flow through the gas turbine nozzle cooling guide vane type (NASA-C3X), and the results were found to be in good agreement with experiments by (Hylton 1983).

The study shows that the (conjugate numerical methodology) gives good and more accurate results than the un-coupled treatment. It also shows that the cooling of the vane reduced the thermal stresses which are focused in the trailing edge of the vane for being thin. Moreover, the cooling flow inside the passages of the vane reduced the temperature of vane body and that gives longer life to the vane for the same Turbine Inlet Temperature (TIT) and efficiency. Otherwise, it gives higher Turbine Inlet Temperature and high efficiency if one chose to keep same life of the vane.

Finally, the present study shows that the conjugate heat transfer simulation is a good tool in gas turbine design, and it serves as base future work with more complex geometries and cooling schemes for turbine blade.

### الخلاصة:

تم في هذا البحث استخدام ( الطريقة العددية المزدوجة) لتحقيق الازدواجية بين حقل الجريان الخارجي (لحالة المستقرة الثنائية الابعاد والانضغاطية وللجريان المضطرب) و الجزء الصلب (لحالة المستقرة الثنائية الابعاد) لريشة التوربين الموجهة للجريان المبردة داخليا بالحمل وغير المبردة. ان النتائج العددية لهذه الدراسة قد قورنت مع نتائج عملية للحالة المستقرة الثنائية الابعاد والانضغاطية وللجريان المضطرب خلال ريشة التوربين الموجهة للجريان والمبردة ومن نوع (NASA-C3X) ، وقد وجدت النتائج بانها ذات توافق جيد مع الحالة العملية بواسطة (Hylton 1983).

لقد بينت الدراسة بان ( الطريقة العددية المزدوجة) تعطي نتائج اكثر دقة من المعالجة غير المزدوجة وكذلك بينت الدراسة بان التبريد للريشة يقلل من الاجهادات الحرارية المتمركزة في نهاية الريشة لكون ريشة التوربين في هذه المنطقة تكون نحيفة، الى جانب ذلك فأن الجريان الداخلي المبرد للريشة يسبب نقصان في درجة حرارة جسم الريشة وهذا ما يؤدي الى زيادة عمر الريشة

ولنفس درجة حرارة الدخول الكلية للريشة و كفاءة المحرك التوربيني، وكذلك من الممكن زيادة درجة حرارة الدخول الكلية للريشة وبالتالي زيادة كفاءة المحرك التوربيني و لنفس عمر الريشة.

وأخيراً، بينت الدراسة الحالية بان ( الطريقة العددية المزدوجة) هي اداة جيدة في تصميم المحرك التوربيني، وهي تخدم العمل المستقبلي مع الاشكال المعقدة وطرق التبريد الاخرى لريش التوربين.

## INTRODUCTION

Advanced gas turbine engines operate at high temperatures (1200-1400°C) to improve thermal efficiency and power output. As the Turbine Inlet Temperature (TIT) increases, the heat transferred to the turbine blades also increase. The level and variation in the temperature within the blade material (which causes thermal stresses) must be limited to achieve reasonable durability goals. The operating temperatures are far above the permissible metal temperatures. Therefore, there is a need to cool the blades for safe operation. The blades are cooled by extracted air from the compressor of the engine. Since this extraction incurs a penalty to the thermal efficiency, it is necessary to understand and optimize the cooling technique, operating conditions, and turbine blade configuration.

The continuous increase in turbine inlet pressure and temperature definitely require reliable and accurate predictions of the main stream aerothermal characteristics and of the heat loads imposed to the blades so that a good design from a thermal point of view might allow a higher inlet temperature, less cooling air or a lighter design, thus increasing the performance or efficiency of the turbine and resulting in a longer engine life (**Qingluan Xue 2005**).

In several industrial applications it is becoming necessary to accompany the computation of flow and associated heat transfer in the fluid with the heat conduction within the adjacent solid. The coupling of these two models of heat transfer has been identified by the name “conjugate heat transfer” in the relevant literature. Typical applications where conjugate heat transfer effects can become important are, among others, the cooling of turbine blade, and cooling of electronics.

A conjugate numerical methodology used to predict the metal temperature of two or three-dimensional gas turbine stator blade (vane) or rotor blade. The conjugate heat transfer approach allows the simultaneous solution of the external flow, internal convection, and conduction within the metal vane or blade, eliminating the need for multiple, decoupled solutions, which are time-consuming and inherently less accurate when combined (**Canelli et al 2003**).

## AIM OF WORK

Predict the flow and the metal temperature through gas turbine nozzle guide vane (with and without cooling) of an axial flow turbine stator by using the fully-coupled approach (conjugate numerical methodology) by FLUENT code.

## MATHEMATICAL MODEL

### Assumptions

In order to adopt an applicable computational method, some assumptions are made:

- The entering fluid flow is a perfect gas, Newtonian, uniform, turbulent, and compressible.
- The fluid field is steady, adiabatic, ir-rotational, single-phase, and shock free.
- Cartesian coordinate system is used.

### Domain Description

The computational domain and the boundary conditions (B.C) that considered in the present work are shown in figure (1):

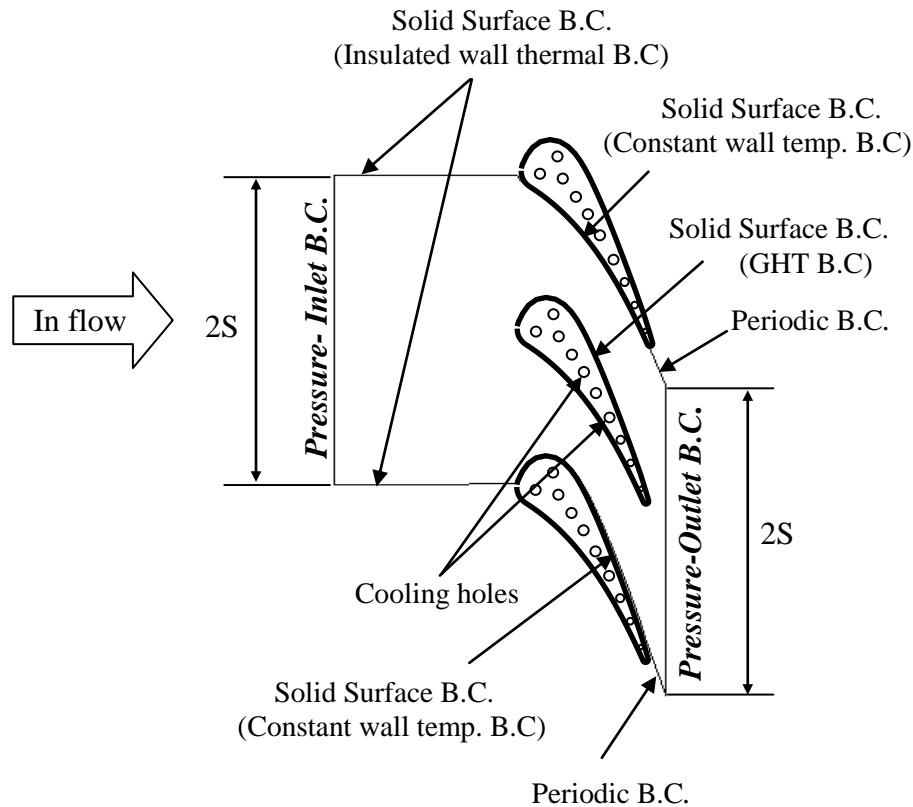


**Fig. (1): Computational domain and the boundary conditions of the flow through gas turbine nozzle guide vane with cooling.**

The compressible turbulent flow through gas turbine nozzle guide vane with and without cooling was predicted by solving numerically the two dimensional continuity and Navier-Stokes equations. Unstructured (triangle element) grid generation is adopted by using (GAMBIT code). Finite volume method with differencing scheme for diffusion term and up-wind scheme for convection term is employed to discretize the flow domain in the relevant transport equations. A SIMPLE algorithm pressure based method with collocated grid arrangement and (Rhie and Chow 1983) interpolation are employed to find the coupling of the pressure-velocity field. The Cartesian velocity components are used as the main dependent variables for the momentum equations. The ( $k-\epsilon$ ) turbulence model is used to close up the system of the momentum differential equations. In order to account for the compressibility effects, an equation of state and up-winding scheme is used to interpolate the density at control volume faces. Discretizing the governing equations (continuity, momentum, and energy) of fluid flow results in a system of linear algebraic equations, which are solved by Algebraic Multi-Grid Solver (AMGS). The fully-coupled approach between the flow and the solid vane was used. Conjugate heat transfer B.C for the external wall surface (for the solid vane) and constant wall temperature for internal convection cooling holes was used, and another type of B.C for the computational domain is shown in fig. (1). The Fourier equation for heat diffusion was solved in the solid zone (solid vane). The present simulations were run using the FLUENT<sup>TM</sup> 6.1.18 code from FLUENT INC., Inc.

## **Governing Equations**

The general form of three-dimensional instantaneous governing equations of mass and momentum for unsteady, viscous, and compressible flows written in tensor conservation form expressed in Cartesian coordinates system (**Wang and Komori 1998**).

Continuity Equation:

$$\frac{\partial \rho}{\partial t} + \frac{\partial}{\partial x_j} (\rho u_j) = 0 \text{-----(1)}$$

Momentum Equation:

$$\frac{\partial}{\partial t} (\rho u_i) + \frac{\partial}{\partial x_j} (\rho u_i u_j) = -\frac{\partial p}{\partial x_i} + \frac{\partial t_{ij}}{\partial x_j} \text{-----(2)}$$

Where  $t_{ij}$  is the viscous stress tensor, defined by: -

$$t_{ij} = \mu \left[ \left( \frac{\partial u_i}{\partial x_j} + \frac{\partial u_j}{\partial x_i} \right) - \frac{2}{3} \frac{\partial \bar{u}_k}{\partial x_k} \delta_{ij} \right] \text{-----(3)}$$

The Kronecker delta ( $\delta_{ij}=1$  if  $i=j$  and  $\delta_{ij}=0$  if  $i \neq j$ )

Energy Equation:

$$\frac{\partial}{\partial x_j} \left( \rho u_j \left( h + \frac{u_i^2}{2} \right) - p \right) = \frac{\partial}{\partial x_j} (u_i t_{ij}) - \frac{\partial}{\partial x_j} (q l_j) \text{-----(4)}$$

Where,  $h$  is the specific enthalpy.  $q l_j$  is the laminar heat flux vector, which is obtained from Fourier's law. This is:-

$$q l_j = -K \left( \frac{\partial T}{\partial x_j} \right) = - \left( \frac{\mu C_p}{Pr_l} \right) \frac{\partial T}{\partial x_j} \text{-----(5)}$$

$K$  is the thermal conductivity, and  $C_p$  is the specific heat capacity at constant pressure.  $Pr_l$ , is the molecular Prandtl number defined by:-

$$Pr_l = C_p \frac{\mu}{K} \text{-----(6)}$$

State Equation:

$$P = \rho RT \text{-----(7)}$$

## **Reynolds-Averaged Navier-Stokes Equations**

The turbulence model used in this study is based on averaging of the instantaneous equations. In order to time and mass average (Reynolds averaged) the conservation equations the various flow properties are decomposed as follows: -



$$\left. \begin{aligned} u_i &= \bar{u}_i + u_i' \\ u_j &= \bar{u}_j + u_j' \\ p &= \bar{p} + p' \\ \rho &= \bar{\rho} + \rho' \\ T &= \bar{T} + T' \end{aligned} \right\} \text{-----(8a)}$$

Neglect the fluctuating terms the turbulence structure remains unchanged, so Equation (8a) become (**Wang and Komori 1998**):

$$\left. \begin{aligned} u_i &= \bar{u}_i + u_i' \\ u_j &= \bar{u}_j + u_j' \\ p &= \bar{p} \\ \rho &= \bar{\rho} \\ T &= \bar{T} \end{aligned} \right\} \text{-----(8b)}$$

Substituting equations (8b) into equations (1), (2), (4) and (7).The time/ mass averaged mean equations of continuity, momentum, energy, and state can be written as (**Wang and Komori 1998**):-

#### Continuity Equation

$$\frac{\partial \bar{\rho}}{\partial t} + \frac{\partial}{\partial x_j} (\bar{\rho} u_j) = 0 \text{-----(9)}$$

#### Momentum Equations

$$\frac{\partial}{\partial t} (\bar{\rho} u_i) + \frac{\partial}{\partial x_j} (\bar{\rho} u_i u_j) = -\frac{\partial \bar{p}}{\partial x_i} + \frac{\partial}{\partial x_j} (\bar{\tau}_{ij} + \tau_{ij}) \text{-----(10)}$$

Where  $\bar{\tau}_{ij}$  is the averaged Reynolds stress tensor, defined as: -

$$\bar{\tau}_{ij} = -\overline{\rho u_i' u_j'} \text{-----(11)}$$

This will be determined from the Boussinesq Eddy Viscosity Model using the ( $k$ - $\varepsilon$ ) turbulence model [**Jones and Launder (1972)**]. The Reynolds stress tensor will be: -

$$\bar{\tau}_{ij} = \mu_t \left[ \left( \frac{\partial \bar{u}_i}{\partial x_j} + \frac{\partial \bar{u}_j}{\partial x_i} \right) - \frac{2}{3} \frac{\partial \bar{u}_k}{\partial x_k} \delta_{ij} \right] - \frac{2}{3} \bar{\rho} k \delta_{ij} \text{-----(12)}$$

Where  $\bar{k}$  is the averaged turbulent kinetic energy defined as: -



$$\bar{k} = \frac{1}{2} \overline{u_i' u_i'} \text{------(13)}$$

And  $\mu_t$  is the turbulent eddy viscosity expressed as: -

$$\mu_t = \frac{C_\mu \bar{\rho} \bar{k}^2}{\varepsilon} \text{------(14)}$$

Where  $C_\mu$  is constant ( $C_\mu = 0.09$ ) [Launder and Spalding (1974)].  $\bar{\varepsilon}$  is the averaged dissipation rate of turbulent kinetic energy, defined as:-

$$\bar{\varepsilon} = \nu \overline{\frac{\partial u_i'}{\partial x_j} \frac{\partial u_i'}{\partial x_j}} \text{------(15)}$$

### Energy Equation

$$\frac{\partial}{\partial x_j} (\bar{\rho} u_j' (H') - \bar{p}) = \frac{\partial}{\partial x_j} (u_i' (\bar{t}_{ij} + \tau_{ij})) + \frac{\partial}{\partial x_j} \left( -q l_j - q t_j + \left( \mu + \frac{\mu_t}{\sigma_k} \right) \bar{k} \right) \text{--- (16a)}$$

Where:

$$H' = C_p \bar{T} + \frac{1}{2} \overline{u_i' u_i'} + \bar{k} \text{------(16b)}$$

$q t$  is the turbulent heat flux vector defined as: -

$$q t = - \left( \frac{\mu_t C_p}{Pr_t} \right) \frac{\partial \bar{T}}{\partial x_j} \text{------(16c)}$$

$Pr_t$ , is the turbulent prandtl number that has different value for different flow. For gases, most common values suggested is 0.9 in the case of the boundary layer [Wang and Komori, (1998)].

### State Equation

$$\bar{p} = R \bar{\rho} \bar{T} \text{------(17)}$$

### **Turbulence Model (k-ε) Equations**

The transport equations of  $k$  and  $\varepsilon$  are formulated and modeled as in [Wang and Komori (1998)]:

#### Equation of Turbulent Kinetic Energy (k):

$$\frac{\partial}{\partial t} (\bar{\rho} \bar{k}) + \frac{\partial}{\partial x_j} (\bar{\rho} k u_j) = \frac{\partial}{\partial x_j} \left[ \left( \mu + \frac{\mu_t}{\sigma_k} \right) \frac{\partial \bar{k}}{\partial x_j} \right] + G_k - \bar{\rho} \bar{\varepsilon} \text{------(18)}$$

Where ( $\sigma_k$ ) is constant with value ( $\sigma_k = 1$ ),  $G_k$  is the production of turbulent kinetic energy (generation term) defined as: -

$$G_k = \tau_{ij} \frac{\partial \bar{u}_i}{\partial x_j} \text{-----} (19)$$

Substitution of  $(\tau_{ij})$  from equation (12) into equation (19) gives:

$$G_k = \mu_t \left[ \left( \frac{\partial \bar{u}_i}{\partial x_j} + \frac{\partial \bar{u}_j}{\partial x_i} \right) \right] \frac{\partial \bar{u}_i}{\partial x_j} - \frac{2}{3} \frac{\partial \bar{u}_i}{\partial x_j} \delta_{ij} \left[ \mu_t \frac{\partial \bar{u}_k}{\partial x_k} + \bar{\rho} k \right] \text{-----} (20)$$

Equation of Dissipation of Turbulent Kinetic Energy ( $\varepsilon$ ):

$$\frac{\partial}{\partial t} (\bar{\rho} \varepsilon) + \frac{\partial}{\partial x_j} \bar{\rho} u_j \varepsilon = C_{\varepsilon 1} \frac{\bar{\varepsilon}}{k} G_k + \frac{\partial}{\partial x_j} \left[ \left( \mu + \frac{\mu_t}{\sigma_\varepsilon} \right) \frac{\partial \bar{\varepsilon}}{\partial x_j} \right] - C_{\varepsilon 2} \bar{\rho} \frac{\bar{\varepsilon}^2}{k} \text{-----} (21)$$

Where  $(C_{\varepsilon 1})$ ,  $(C_{\varepsilon 2})$  and  $(\sigma_\varepsilon)$  are empirical constants and they having the following values, [Lauder and Spalding (1974)]: -

$$C_{\varepsilon 1} = 1.44, \quad C_{\varepsilon 2} = 1.92, \quad \sigma_\varepsilon = 1.3$$

Fourier equation for heat diffusion (solid vane)

$$q l_j = -K \left( \frac{\partial T}{\partial x_j} \right) \text{-----} (22)$$

## Boundary Conditions Equations

Boundary conditions specify the flow and thermal variables on the boundaries of the physical model. The boundary conditions types that used in the present work are shown in figure (1) and the equations of these boundary conditions are formulated and modeled as in (Veresteeg & Malalasekera, 1995) and (Lauder and Spalding, 1974).

## RESULTS AND DISCUSSIONS

The first view of geometry configuration and grid distributions are shown in Figs. (2) and (3). The computational domain has been discretized with 4362 nodes for fluid zone and 344 nodes for solid zone for gas turbine nozzle guide vane without cooling as shown in fig. (2), and 4362 nodes for fluid zone and 990 nodes for solid zone for gas turbine nozzle guide vane with internal convection cooling as shown in fig. (3), with unstructured grid generation, triangle elements by GAMBIT code from FLUENT.

The main stream operating condition was simulated for subsonic flow and the B.C set to give the same condition as in experimental work by (Hylton 1983), where, Hylton reported average Mach number at the vane trailing edge plane at the midspan, and that Mach number was converted to average static pressure by using isentropic flow relations. The operating condition and the B.C for the simulation of the flow through gas turbine nozzle guide vane is shown in Table (1). The vane material properties is shown in Table (2). The thermal boundary on each internal cooling channel is explicitly specified temperature values based on experimental data by (Hylton 1983). Table (3) lists the diameters and temperatures of each cooling hole. The hub and tip walls are moduled with no-slip and adiabatic conditions.

The velocity and Mach contour is shown in figure (4) and figure (5). In this figure (4), the flow speed sees high along the suction side near the leading edge. The maximum velocity in the vane passage is at the position about (25-30 %) from the suction side distance from the leading edge. In the pressure side, the velocity is low until (30-35 %) from the axial chord distance from the leading edge, and then the flow is accelerated toward the trailing edge. The contour of pressure is shown in figure (6). Figure (7) shows the temperature contour of the flow through gas turbine nozzle guide vane and inside the solid guide vane with cooling.

For the mainstream condition, the flow field is examined and then heat transfer. Fig. (8) and Fig. (9) shows the pressure distribution at wall of the vane midspan. On the suction side, the pressure falls rapidly from the stagnation line at the leading edge and then reaches to the minimum value at (25-30 %) from the axial chord length, and after that the pressure is increase to the trailing edge but in small range. On the pressure side the flow is still near to the total pressure ( $P^o$ ) from the leading edge until reached to (40-50 %) from the axial chord and then decrease toward the trailing edge. Fig. (10) and Fig. (11) shows the temperatures distribution at wall of the vane midspan (without and with cooling).

The results show a good agreement with experimental data by (**Hylton 1983**) as shown in figure (12) and figure (13).

The heat transfer is investigated with and without cooling van. The temperature dimensionless distribution ( $T_{wall}/T^o$ ) on the external surface at the midspan of the vane is plotted as shown in figure (12). This figure contains the comparison of the temperature distribution at the external surface of the vane with cooling that resulted by using (The Conjugate Methodology) with the experimental value by (**Hylton 1983**). The results show a good agreement with experimental data.

Figure (13) shows the comparison between the coupled and decoupled treatment of the static pressure on the suction and pressure side on the wall of gas turbine nozzle guide vane with cooling, with the experiment values by (**Hylton, 1983**). In this figure, the coupled treatment is more accurate than the decoupled treatment and that can be see clearly in suction side.

## CONCLUSIONS

- Using unstructured grid generation, triangle elements by GAMBIT code from FLUENT with Cartesian velocities as the dependent variables and collocated grid arrangement gave an easy solution to the problem.
- Introducing the concept of collocated grid arrangement by (**Rhie and Chow 1983**), with contravariant velocities implicitly in the discretized momentum equations simplifies the discretization of the flow equations.
- Conjugate numerical method is a good method and gives a good accuracy in prediction the temperature distribution over and inside gas turbine nozzle guide vane (NASA-C3X) without and with cooling where, the predicted mid-span temperature distribution on the vane external surface was in reasonable agreement with experimental data by (**Hylton 1983**).



- The cooling method of the gas turbine nozzle guide vane by the internal convection circular cooling passages in the present work gives more life to the vane materials by decreasing the thermal stresses and for the same design life it gives more efficiency for the gas turbine by increasing the temperature at the inlet of guide vane (TIT).
- The metal temperature everywhere was much closer to the temperature in the passage free stream than the coolant temperature. This was due to the fact that the thermal resistance due to internal convection was much greater than the resistance of the external convection or the conduction within the metal.
- The results were found to be in a reasonable agreement with experiment by (Hylton 1983).

## NOMENCLATURE

### Latin Symbols

Symbol	Description
$C_p$	specific heat capacity at constant pressure (J/kg K)
$C_\mu, C_{\varepsilon 1}, C_{\varepsilon 2}$	Constants in the k- $\varepsilon$ model
$G_k$	Production term of kinetic energy
$h$	Enthalpy (J)
$K$	thermal conductivity
$k$	Turbulent kinetic energy
$L_c$	Characteristic length of turbulence
$M$	Mass flow rate (kg/s)
$P$	Pressure (Pa)
$P^\circ$	Total Pressure (Pa)
$Pr_l$	Molecular Prandtl number
$Pr_t$	Turbulent prandtl number
$ql_j$	Laminar heat flux vector
$qt$	Turbulant heat flux vector
$R$	Gas constant (J/kg.K)
$Re$	Reynolds number
$S$	Pitch or vane spacing
$t_{ij}$	Viscous stress tensor
$T$	Temperature (K)
$T^\circ$	Total Temperature (K)
$T_{wall}$	Wall Temperature (K)
$T_u$	Turbulent intensity
$X$	Axial coordinate in the physical domain
$Y$	Pitchwise coordinate in the physical domain

## Greek Symbols

Symbol	Description
$\varepsilon$	Dissipation rate of turbulent kinetic energy
$\mu$	Laminar viscosity
$\mu_T$	Turbulent eddy viscosity
$\rho$	Density
$\sigma_k, \sigma_\varepsilon$	Effective Prandtl numbers
$\tau_{ij}$	Reynold's stress tensor

## Subscripts

Symbol	Description
$i, j$	Index counter in computational plane
$s$	Static
$x, y$	Partial derivative in the physical plane

## Superscripts

Symbol	Description
'	Fluctuating quantity in time- Mass averaging or correction quantity
—	Averaged quantity
◦	Total

## Abbreviations

Symbol	Description
AMGS	Algebraic Multi-Grid Solver
LE	Leading Edge
SIMPLE	Simi-Implicit Method For Pressure Linked Equations
TE	Tailing Edge
TIT	Turbine Inlet Temperature

## REFERENCES

- **Canelli, C., Sacchetti, M., and Traverso, S., 2003**, "Numerical 3-D conjugate flow and heat transfer investigation of a convection-cooled gas turbine vane", ATI-NASA , CFD Engineering S.r.l.Genova 16129, Italy [info@cf-engineering.it](mailto:info@cf-engineering.it), Ansaldo Energia S.p.A. Genova 16152, Italy [stefano.traverso@aen.ansaldo.it](mailto:stefano.traverso@aen.ansaldo.it) .
- **Hylton, Milhec, Turner, Nealy and York, (1983)**, “Analytical and Experimental Evaluation of the Heat Transfer Distribution Over the Surfaces of Turbine Vanes”, NASA CR 168015.
- **Jones W. P., and Launder B. E., (1972)**, “The prediction of the laminarization with a two-equation model of turbulence”, Int. J. heat transfer, Vol. 15, pp 301-314.
- **Launder, B. E. and Spalding, D. B., (1974)**, “The Numerical Computation of Turbulent Flows Comp”, Math. App. Mech. Eng., Vol. 3, pp 269-289.



- **Qingluan Xue, 2005**, "Development of conjugate heat transfer capability to an unstructured flow solver - U2NCLE", MSc. Thesis, Computational Engineering in the College of Engineering, Mississippi State University.
- **Rhie, C. M., and Chow, W. I., (1983)**, "Numerical study of the turbulent flow past an airfoil with trailing edge separation", AIAA J., Vol. 21, pp 1525-1532.
- **Versteeg, H. K., and Malalasekera, W., (1995)**, "An introduction to computational fluid dynamics-The finite volume method", Longman group Ltd.
- **Wang, Y., and Komori S., (1998)**, "Simulation of the subsonic flow in a high-speed centrifugal compressor impeller by the pressure-based method", Proc. Inst. Mech. Eng., part A, Vol. 212, pp 269-287.

## BIBLIOGRAPHY

- **Al-Deroubi, N. N., 2001**, "Analysis of two dimensional supersonic turbulent flow between impulse turbine blades using pressure-based method", MSc. Thesis, Mech. Engg. Dep. University of Baghdad.
  - **Ameri, Ali A., 1992**, "Navier-stokes turbine heat transfer prediction using two equation turbulence", (NASA Lewis Research Center, Cleveland, OH, United States); Arnone, Andrea (NASA Lewis Research Center, Cleveland, OH, United States). NASA Center for AeroSpace Information (CASI) NASA-TM-105817, 1992.
- **Cademartori, F., Facchini, B., Arcangeli, L., Carcasci, C., Abba, L., and Traverso, S., 2001** "Numerical prediction of metal temperature and heat transfer of gas turbine vane", ATI-NASA, CFD Engineering S.r.l. - Genova 16129, Italy [cademartori@cf-engineering.it](mailto:cademartori@cf-engineering.it) .
- **Carcasci, Zecchi, Oteri, (2002)**, "Comparison of Blade Cooling Performance Using Alternative Fluids." ASME paper GT-2002-30551, ASME Turbo Expo 2002, June 3-6, Amsterdam, NL.
- **David L. Rigby and Ronald S. Bunker, 2002**, "Heat Transfer in a Complex Trailing Edge Passage for a High Pressure Turbine Blade", Part 2: Simulation Results. NASA/CR—2002-211701.
- **Davidson, L., 2003**, "An Introduction to Turbulence Models", Chalmers University of Technology, Department of Thermo and Fluid Dynamics.
- **Ferziger, J. H., and Peric, M., 1996**, "Computational Methods for Fluid Dynamics", Springer-Verlag Berlin Heidelberg.
  - **Garcia Casado, R., Thierry, M., Fedrizzi, R., di Sante, A., and Arts, T., 2003**, "PIV investigation of internal cooling channels for gas turbines, with 45 degrees inclined ribs", von Karman Institute for Fluid Dynamics Turbomachinery and Propulsion Department, [www.vki.ac.be](http://www.vki.ac.be), [garcia@vki.ac.be](mailto:garcia@vki.ac.be).

- **Giulio Croce, 2001,**" A Conjugate Heat Transfer Procedure for Gas Turbine Blades", DIEM – Mechanical engineering department, university of Udine, 33100 Italy . © 2001 [New York Academy of Sciences](#).
- **Hah, C., 1984,** "A Navier-Stokes analysis of the three-dimensional turbulent flows inside turbine blade rows at design and off design conditions", J. Engineering of Gas Turbine and Power, Vol. 106, PP. 421-429.
  - **Hall, E.J., Topp, D.A., Heidegger, N.J., and Delaney, R.A., September 1994,** "Investigation of Advanced Counterrotation Blade Configuration Concepts for High Speed Turboprop Systems", Task 8–Cooling Flow/Heat Transfer Analysis-Final Report, NASA Contractor Report 195359.Prepared for Lewis Research Center Under Contract NAS3–25270.
- **Heidmann, J. D., Kassab, A. J., Divo, E. A., Rodriguez, F., and Steinthorsson, E., 2003,** "Conjugate Heat Transfer Effects on A Realistic Film-Cooled Turbine Vane," *ASME Paper 03-GT-38553*, June 2003.
- **Hoffmann, K. A., 1989,** "Computational Fluid Dynamics for Engineers", Engineering Education System, Austin, Tex.
- **Ivan Carlsson, February 2005,**" A reduced-order through-flow program for choked and cooled axial turbines" MSc. Thesis, Division of Thermal Power Engineering Department of Heat and Power Engineering Lund Institute of Technology, Box 118 S-221 00 LUND. ISRN LUTMDN/TMHP--05/5052—SE.
- **Jack D. Mattingly, 1996,** "Elements of Gas Turbine Propulsion". McGraw-Hill, Inc.
- **J.Alan Adams, David F.Rogrs, 1973,"**Computer Aided Heat Transfer Analysis", McGraw-Hill, Inc.
- **Jayatileke, C., 1969,** "The Influence of Prandtl Number and Surface Roughness on the Resistance of the Laminar Sublayer to Momentum and Heat Transfer".*Prog. Heat Mass Transfer*, 1:193-321.
  - **Karki, K., and Patankar, S., 1989,** "Pressure Based Calculation Procedure for Viscous Flows at All Speeds in Arbitrary Configurations", AIAA Journal, Vol.27, PP 1167-1174.
- **Karsten KUSTERER, Dieter BOHN, Takao SUGIMOTO, and Ryoza TANAKA, 2003,"**Conjugate Heat Transfer Analysis of a Test Configuration for a Film-cooled Blade". Institute of Steam and Gas Turbines, Aachen University, GERMANY. Kawasaki Heavy Industries, LTD., Akashi, JAPAN. IGTC2003Tokyo TS-083.
- **Kelkar, K. M., Choudhury, D., and Ambrosi, M., 1991,** "Numerical Method for the Computationof Conjugate Heat Transfer in Nonorthogonal Boundary-Fitted Coordinates," *Numerical heat Transfer, Part B*, vol. 20, 1991, pp. 25–40.
- **Khudor, D. S., 2003,** "Effective of cooling air passage shape on gas turbine blade temperature



- distribution" MSc. Thesis, Mech. Engg. Dep. Al-Mustansiria University.
- **Kristina Hermanson, Sacha Parneix, Jens von Wolfersdorf and Klaus Semmler, 2000** "prediction of pressure and heat transfer in internal blade cooling passages", ALSTOM POWER, CH-5405 Baden-Daettwil, Switzerland.
- **Luikov, A. V., 1974**, "Conjugate Convective Heat Transfer Problems", *International Journal of Heat Mass Transfer*, vol. 17, 1974, pp. 257–265.
  - **Masahiko Morinaga and Toshihiko Takahash (CRIEPI), 2004**, "Development of the Temperature Prediction Method for Hot Gas Path Parts of 1300 C° Class Gas Turbines" CRIEPI Report.
- **Patankar, S. V., 1980**, "Numerical Heat Transfer and Fluid Flow", Hemisphere, McGraw-Hill, New York.
- **Penelope Leyland, Peter OTT, and Roland RICHTER, 1994**, "Turbine cascade calculation with structured and unstructured meshes", Ecole Polytechnique Federale de Lausanne, CH-1015 Lausanne.
- **Rigby, D. L., and Lepicovsky, J., 2001**, "Conjugate Heat Transfer Analysis of Internally Cooled Configurations," *ASME Paper 01-GT-0405*, June 2001.
- **Robert A. Brewster and Sreenadh Jonnavithula, 2000** , "Analyses of heat transfer in stationary and rotating ribbed blade cooling passages using computational fluid dynamics", adapco, 60 Broadhollow Road, Melville, NY 11747 U.S.A.
- **Salih, E. A., 2004**, "super sonic flow over jet vane for a rocket engine", Ph.D. Thesis, Mech. Engg. Dep. University of Baghdad.
- **Sarkar, S., and Balakrishnan, L., 1990**, "Application of a Reynolds-Stress Turbulence Model to the Compressible Shear Layer". CASE Report 90-18, NASA CR 182002.
- **Sheet, Y. T. M., 2002**, "Numerical prediction of the compressible turbulent fluid flow inside a gas turbine stator passage", Ph.D. Thesis, Mech. Engg. Dep. University of Baghdad.
- **Thomas, P. D., and Middlecoff, J. F., 1980**, "Direct control of the grid point distribution in meshes generated by elliptic equations", *AIAA J*, Vol. 18, No. 6, PP. 652-656.
- **Thompson, J. F., Warsi, Z. U. A., and Mastin, C. W., 1985**, "Numerical Grid Generation", North-Holland, Amsterdam.
- **Weinberg, B. C., Yang, R.-J., McDonald, H., and Shamroth, S. J., 1986**, "Calculation of two and three-dimension transonic cascade flow fields using the Navier-Stokes equations", *Trans. of the ASME, J. of Eng. for Gas Turbine and Power*, Vol. 108, PP. 93-102.



- **William, W. B., 1996**, "Fundamental of Gas Turbine" Second edition, one Wiley& Sons.Inc.
- **Wolfgang H'ohn, Ralf Gombert and Astrid Kraus 2001**, "Unsteady aerodynamical blade row interaction in a new multistage research turbine, part 2: numerical investigation ", Proceedings of IGTT'01 ASME TURBO EXPO 2001 June 04-07, 2001, New Orleans, Louisiana, USA. 2001-GT-0307.

**Table (1) Operating and Boundary Conditions**

Case	Ma <sub>LE</sub>	Ma <sub>TE</sub>	M (kg/s)	Re	$T^\circ$ (K)	$P^\circ$ (bar)	$P_{s\ exit}$ (bar)	$T_u$ (%)	$L_c$ (m)	No. of Iteration to converge	Approx. Time to converge (minute)
1	0.17	0.88	1.15	$1.9 \times 10^6$	796	3.2	0.88	6.5	0.32	4320	45
2	0.15	0.76	1.15	$1.9 \times 10^6$	796	3.2	0.88	6.5	0.32	4000	40

Case 1: Turbulent compressible flow through turbine vane with internal convection cooling.  
Case 2: Turbulent compressible flow through turbine vane without cooling.

**Table (2) Property of the solid vane (ASTM type 310 stainless steel)**

Property of the solid vane	The values
density ( $\rho$ )	7900 kg/m <sup>3</sup>
specific heat ( $C_p$ )	586.15 J/ (kg. K)
thermal conductivity (K)	17.0 W/(m. K)

**Table (3) Cooling Channel, Diameter, and Temperatures (K)**

Holes No.	1	2	3	4	5	6	7	8	9	10
Diameter(cm)	0.63	0.63	0.63	0.63	0.63	0.63	0.63	0.31	0.31	0.198
Temperatures (K)	549.6	549.6	538.5	525.7	556.3	559.6	567.4	590.7	629.7	645.3

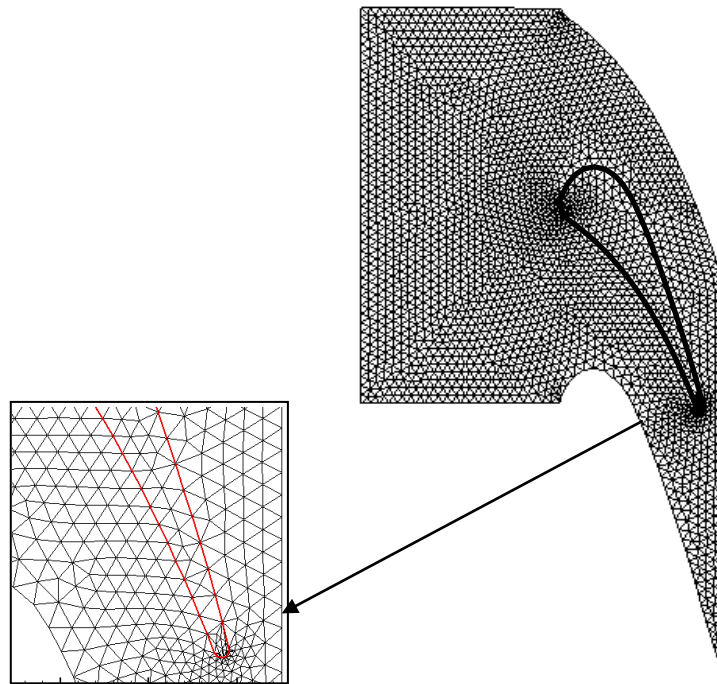


**Figure (2): Flow through gas turbine nozzle guide vane without cooling, triangle elements, and computational grid system =4362 grid for fluid zone and 344 grids for solid zone (GAMBIT code by FLUENT).**

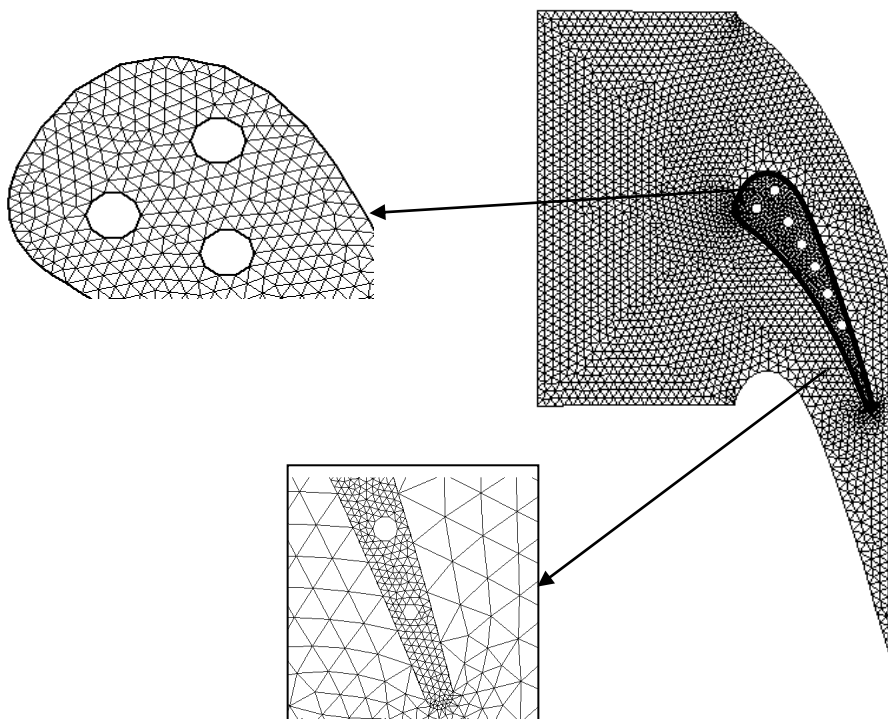


**Figure (3): Flow through gas turbine nozzle guide vane with cooling by ten circular holes, triangle elements, and computational grid system =4362 grid for fluid zone and 990 grids for solid zone (GAMBIT code by FLUENT).**

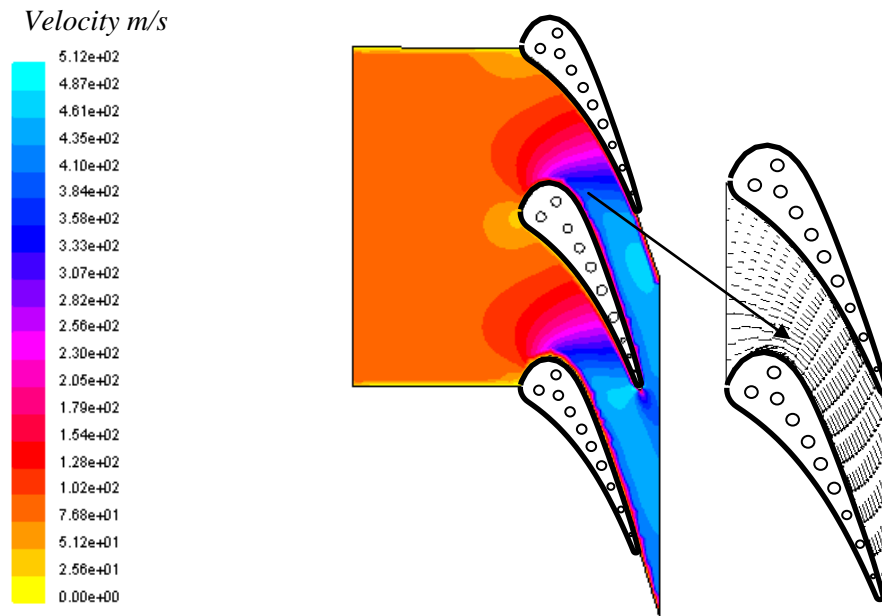


**Figure (4): Velocity contour and velocity vector for steady, 2-D, turbulent, and compressible flow through gas turbine nozzle guide vane at midspan (with cooling).**

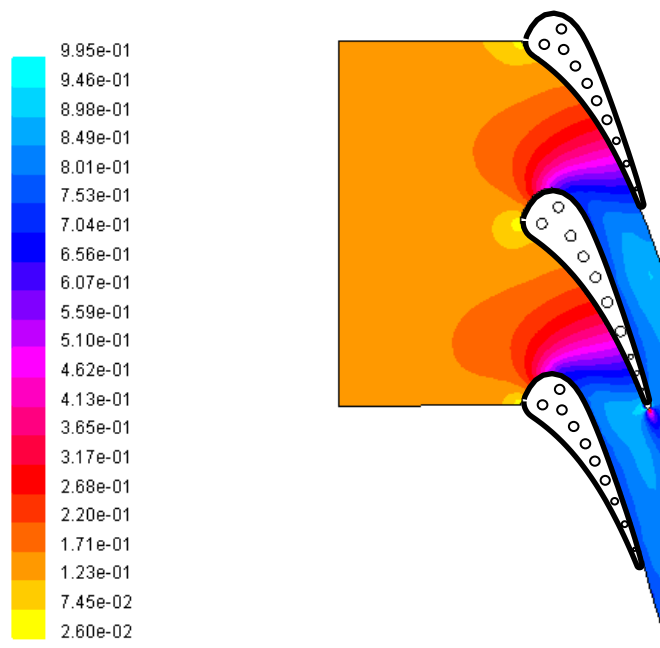


**Figure (5): Mach contour for steady, 2-D, turbulent, and compressible flow through gas turbine nozzle guide vane at midspan (with cooling).**

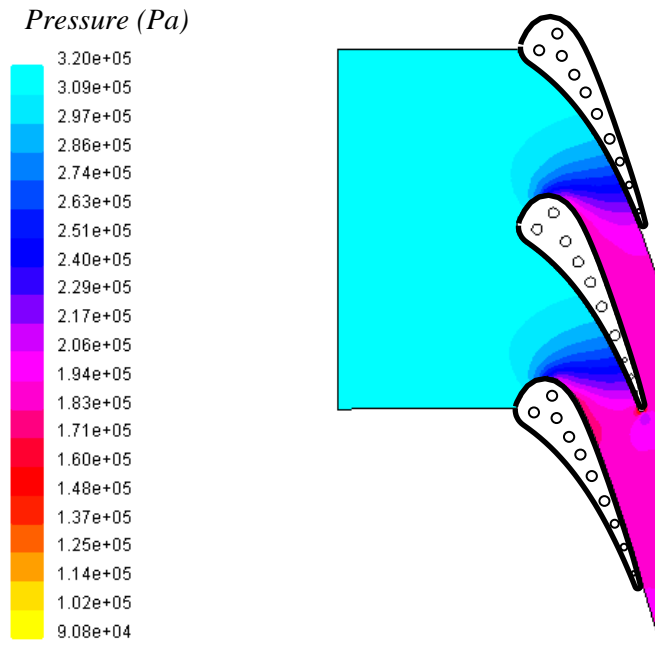


**Figure (6):** Pressure contour for steady, 2-D, turbulent, and compressible flow through gas turbine nozzle guide vane at midspan (with cooling).

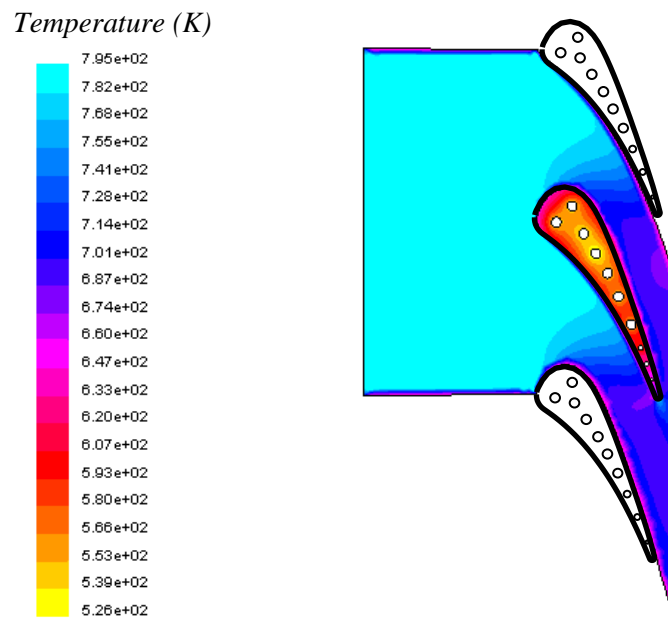


**Figure (7):** Temperature contour for steady, 2-D, turbulent, and compressible flow through gas turbine nozzle guide vane at midspan (with cooling).

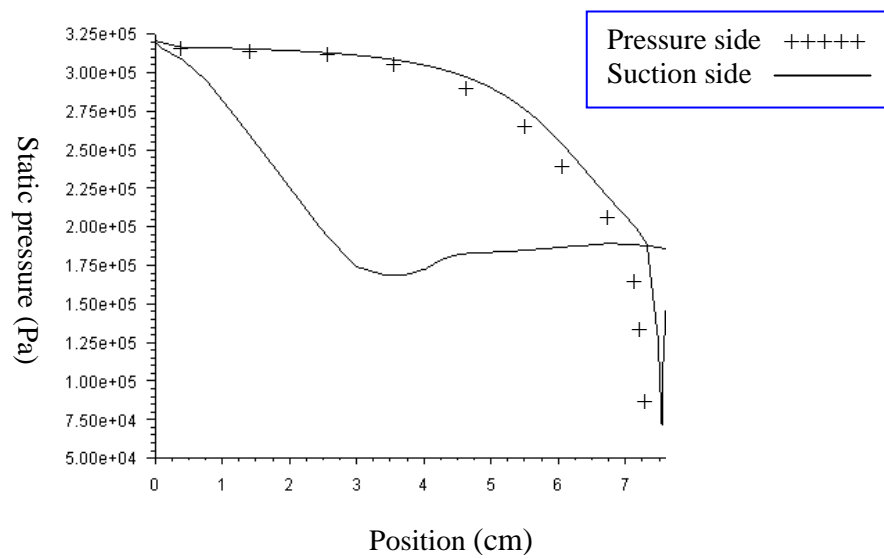


**Figure (8): Pressure distribution for steady, 2-D, turbulent, and compressible flow at gas turbine nozzle guide vane wall at the midspan (without cooling).**

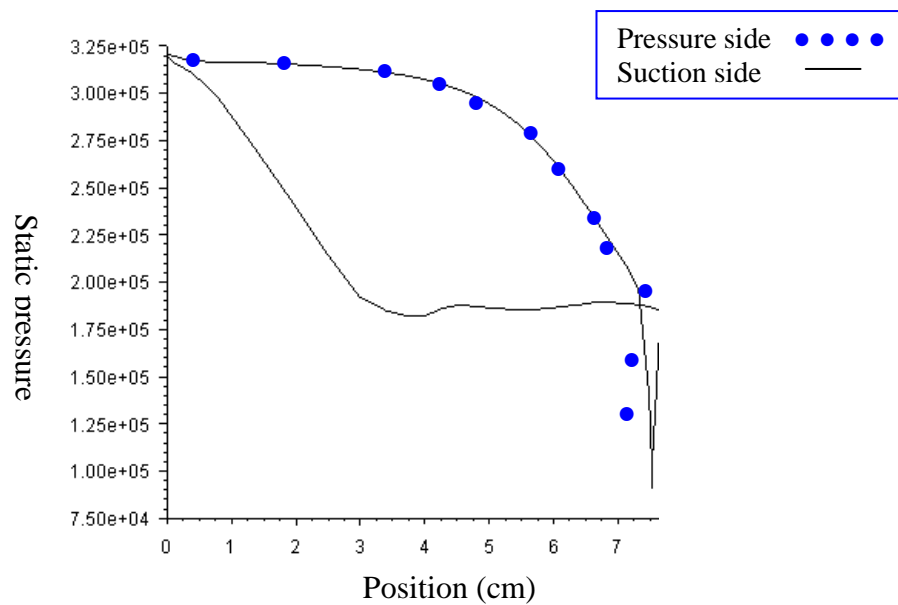


**Figure (9) Pressure distribution for steady, 2-D, turbulent, and compressible flow at gas turbine nozzle guide vane wall at the midspan (with cooling).**

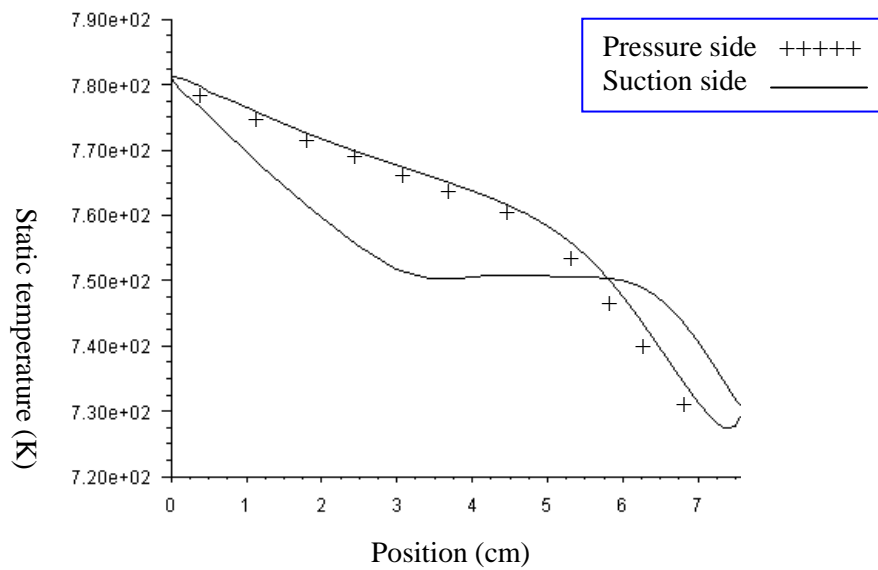


**Figure (10): Temperature distribution for steady, 2-D, turbulent, and compressible flow at gas turbine nozzle guide vane wall at the midspan (without cooling).**

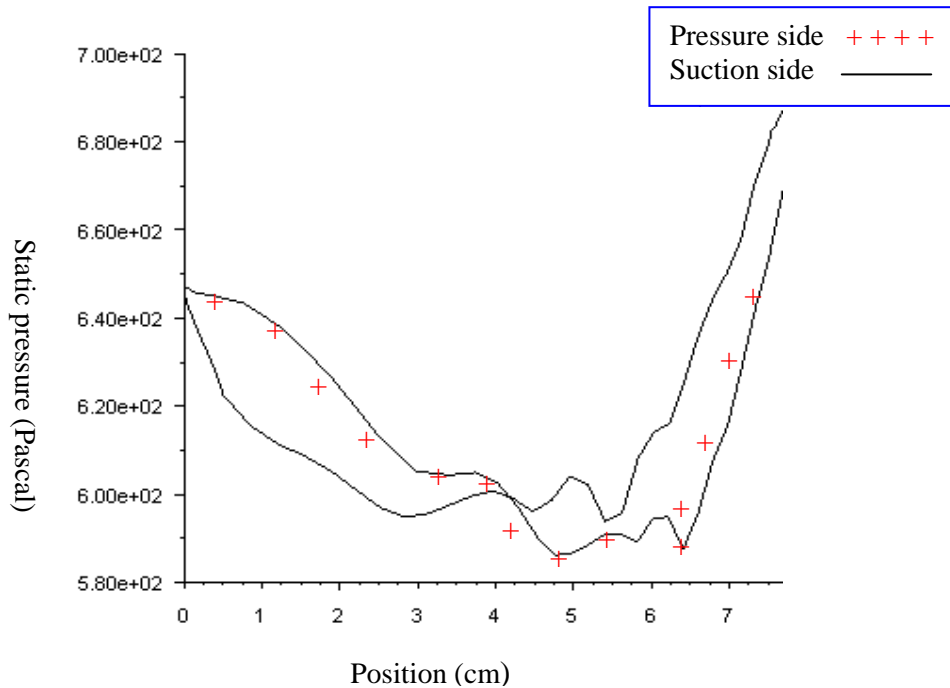


**Figure (11) Temperature distribution for steady, 2-D, turbulent, and compressible flow at gas turbine nozzle guide vane wall at the midspan (with cooling).**

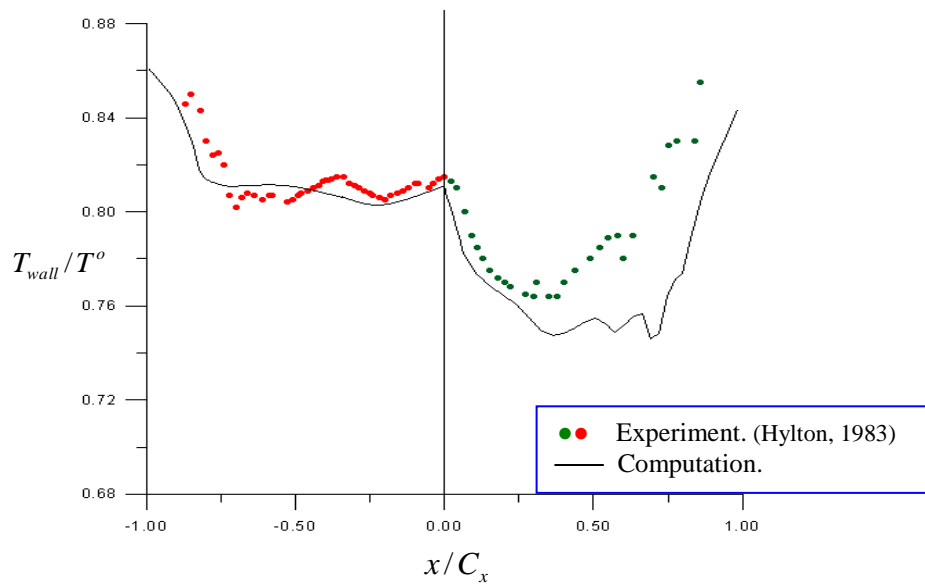


**Figure (12): Experimental and predicted temperature distribution ( $T_{wall}/T^o$ ) for steady, 2-D, turbulent, and compressible flow at gas turbine nozzle guide vane wall at midspan (with cooling).**

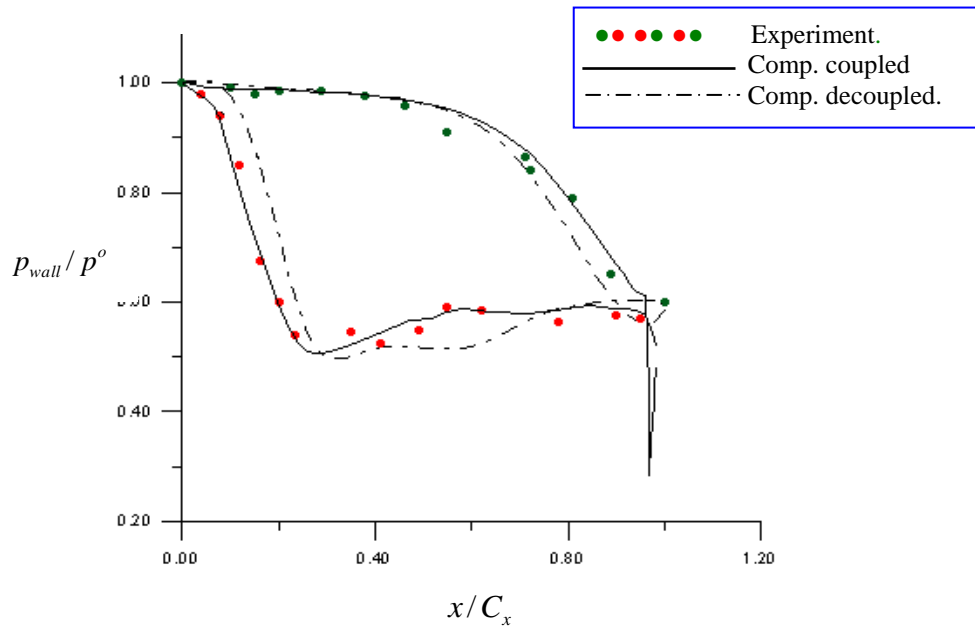


**Figure (13) Experimental and predicted pressure distribution ( $p_{wall}/p^o$ ) for steady, 2-D, turbulent, and compressible flow at gas turbine nozzle guide vane wall at midspan with coupled and decoupled treatment (with cooling).**

## COMPARATIVE ANALYSIS FOR LINK CROSS-SECTION OF MANIPULATOR ARMS

Dr. Ahmed Abdul Hussain Ali, Dler Obed Ramadhan  
Mech. Engr. Dept. /college of Engr. University of Baghdad

### ABSTRACT

The stresses and deflections in robot arm was analyzed using ANSYS software package. Industrial robot analyzed in this work consists of three arms that have 2-DOF. The analysis of each arm had been made separately.

The maximum stress and deflection have been analyzed for a static applied at one end of the arm while has the other end fixed. Links of various cross-sections having same masses, length, and material properties to make a choice of the shape that gives a high stiffness to weight ratio have been examined. After specifying the best section for the arms of the robot an optimization process began to determine the dimensions of the arms sections which give the least deformation this had been done by the aid of a program build up by using the MATHCAD software package. In the beginning the program finds the optimum section in which the stress in the members not exceeds the allowable stress and finds the total weight of the robot after that the program begins to change the dimensions to satisfy the condition of minimum deflection of the whole robot after that the program estimates the best choices of the dimension for each section that gives the minimum weight and deflection.

The dynamic behavior of the best chosen structure of industrial robot was studied to find the natural frequencies ( $w_n$ ) and mode shapes.

The result shows that the hollow circular section is the best section for the first link while a square section is the best section for the other two links.

### الخلاصة

تم استخدام طريقة العناصر المحددة في هذا البحث بالاستعانة ببرنامج (ANSYS) لتحليل الاجهادات والتشوهات في ذراع الروبوت, حيث تم تحليل ودراسة روبوت مكوّن من ثلاثة اذرع ذا درجتين من الحرية, وتم تحليل كل ذراع على الانفراد. تمت دراسة الاجهادات والتشوهات العظمى نتيجة القوى الساكنة المؤثرة على الطرف الحر للذراع, حيث تم اختيار مقاطع مختلفة لاذرع الروبوت والتي لها نفس الكتلة والطول والمعدن لاجل اختيار افضل مقطع والذي يعطي نسبة متانة الى وزن عالية. وبعد ان تم تحديد افضل مقطع لذراع الروبوت قمنا باجراء عملية الامثلية (OPTIMIZATION) لاجل تحديد ابعاد المقطع الذي يعطي اقل تشوه حيث تم الاستعانة ببرنامج مكتوب بواسطة ال (MATHCAD).

البرنامج في البداية حدد المقطع الامثل الذي يكون فيه الاجهاد اقل من الحد الاقصى المسموح به وبعدها تم ايجاد وزن هيكل الروبوت ومن ثم يقوم البرنامج بتغيير الابعاد لاجل تقليل التشوه الكلي عند نهاية ذراع الروبوت حيث تم تحديد ابعاد افضل مقطع يملك اقل وزن وتشوه.

كما وتم دراسة السلوك الديناميكي للهيكل الامثل وتحديد شكل الاطوار والترددات الرنينية. النتائج بينت بأن افضل مقطع للذراع الاول العمودي هو المقطع الدائري المجوف اما الذراع الثاني والثالث فالافضل هو المقطع المربع المجوف.



**KEYWORDS:** Manipulator design, Structural stiffness, Robotics, Robot design, Optimization, Comparative structural analysis, Finite-element analysis, Structural optimization

## INTRODUCTION

Industrial manipulators usually consist of a rigid kinematics chain built up of several rigid links which are connected by direct driven linear or rotational joints in order to move high payloads with high speed and high position accuracy. The slackness in the gears as well as the deformations in the links, which occurs under load, must be eliminated. This can only be reached using rigid joint actuators and rigid links resulting in heavy structure.

Rigid link manipulators require height stiff structures to achieve high accuracy and low inertias.

General handbooks to aid in the design of manipulator exist in literature (**Rivin 1988&Shimon1999**). Analysis of stiffness of manipulator links can be found in (**Rivin 1988**) and (**Leu et al. 1985**), optimization techniques and calibration techniques have been used to correct errors in accuracy.

Robot designers have attempted to systematically develop analytical criteria for the design of critical components. For example (**Fresonke et al. 1993**) has set analytical criteria for the deflection prediction of serial manipulators. (**Henessey et al. 2000**) has demonstrated the design of a light weight manipulator arm while (**Williams et al.1993**), has demonstrated the design of an isotropic six-axis manipulator arm. (**Rivin 1988**) has compared a variety of structural material used in manipulator arms and has studied critical design components. Fault-tolerant method for manipulator-joint development was introduced by (**Wu et al. 1993**), while the design of fault tolerant manipulators was addressed by (**Paredis 1996**).

Prismatic joints of manipulator arms based upon across sectional design of the links that provides a high stiffness to weight ratio compared with a hollow round cross-section has been addressed by (**Abdelmalek 1998**).

(**Alazard, 1992**) describe three different techniques to build up the dynamic model of SECAFLEX, a 2-DOF flexible in plane manipulator driven by geared Dc motors, they study the effect of angular configuration changes and physical parameters modifications and shows that the three techniques give similar result up to the first flexible modes of each link when concentrated masses and inertias are present.

(**Shiakolas et al. 2002**) discussed optimum robot design based on task specifications using evolutionary optimization approaches, these approaches were used for the optimum design of SCARA and articulated 3-DOF PUMA type manipulators.

The process of optimal design of robots having stochastic model parameters (e.g. material, geometry or load) had been viewed by (**Haubach 2002**) as a stochastic structural task, using flexible structures; the goal is the minimization of the total weight of the robot under certain constraints concerning the deviation between the actual and the prescribed path in workspace.

The work of (**Marcus et al. 2004**) presents an optimization procedure which shows how optimization can be used in the early phases of a development process in order to evaluate the potential of a concept. The objective in the optimization is to determine optimal gearboxes and arm lengths from an acceleration capability perspective. The arm lengths are treated as continuous variables where as the gearbox are selected from a list of available units. The object of their work is a 3-DOF robot modeled in the mathematics program and optimized using the complex optimization algorithm.

In this work a comparison had been made between five candidate sections (square, circular, two vertically tube, two horizontally tube and tri tube) to chose the best section for constructing a three arm robot manipulator that has 2-DOF. Analysis had been done by using ANSYS software package and its results are compared with those obtained by the traditional ways used in strength of materials and by the aid of MATHCAD software. An optimization problem for the dimensions of

the cross section had been analyzed to get the best construction that has the minimum weight and with stand the given payload and gives a minimum deflection.

### PROBLEM DEFINITION

When a robot is assigned to carry a payload, certain stress distribution develops along the arm. The characteristics of this stress depend on the material, the geometrical design of the robot arm and other external factors such as the interaction of the robot with the environment. It is necessary to know what the most critical configuration is in order to optimize the robot design. Although it depends on the overall kinematics' design of each robot in general this position corresponds to the configuration where the arm is fully extended so that the moment arm is maximized.

### DESIGN THEORY

The types of stresses subjected on the robot arm are bending (neither shear nor torsion). So a good criteria evaluator (for general and particular cases) that compiles them is the Von Misses theory. The Von Misses failure criterion is a theory based on the distortion energy in a given material; it is the energy associated with changes in the shape of the material. A given component is safe as long as the maximum value of the distortion energy per unit of volume in the assigned material remains smaller that the distortion energy per unit volume required causing yield in a tensile-test specimen of the same material. This theory later will be used to secure that no failure will occur in any of the arms (links).

Most manipulator link cross-sections are hollow. Hollow links provide convenient conduits for electric power and communication cables, hoses, power transmission members, etc.

In this research a different hollow cross-section is introduced, consisting of square, three tubes centered on the vertices of an equilateral triangle (this cross section is referred to as a tri-tube configuration), two horizontally tubes (this cross section is referred to as a 2H-tubes configuration), cylindrical link (will be referred to as a uni-tube configuration), and two vertically tubes (this cross section is referred to as a 2V-tubes configuration). As shown in **Fig. (1)**

Links with an open end manipulator are normally modeled as cantilevers .As shown in **Fig. (2)**.

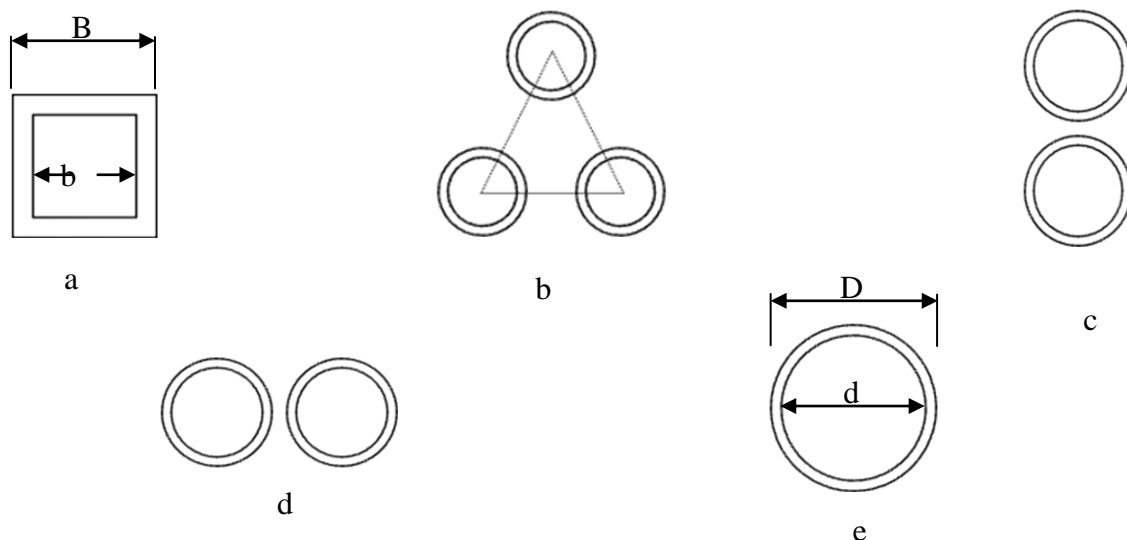
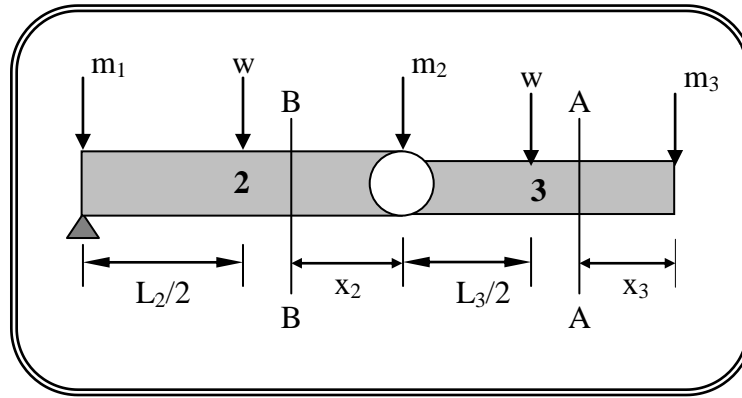


**Fig. (1) Type of sections studied**

**(a) Square Cross-Section, (b) Tri-Tube Cross-Section, (c) Two Vertically-Tube Cross-Section, (d) Two Horizontally-Tube Cross-Section, (e) Uni-Tube Cross-Section**



**Fig(2) Forces on Modeled Arm**

$$M_{A-A} = m_3 g x + q_3 \frac{x^2}{2} \quad (1)$$

Where:

$M_{A-A}$  = Bending moment at the third arm

$m_3$  = Payload = 10kg

$g$  = Specific gravity

$q_3$  = Weight per unit length of third arm

When  $x=L$  bending moment is maximum [8]

$$M_{A-A} \Big|_{\max} = m_3 g L_3 + q_3 \frac{L_3^2}{2} \quad (2)$$

$$\sigma_3 = \frac{M Y}{I} \quad (3)$$

Where:

$\sigma_3$  = Bending stress at the third arm

$I$  = Second moment of the cross-sectional area

$Y$  = Centroid-moment of the cross area

Substituting equation (2) into (3) gives the equation below:

$$\sigma_3 = \frac{\left( m_3 g L_3 + q_3 \frac{L_3^2}{2} \right) Y}{I} \quad (4)$$

$$\delta y_3 = \frac{W L^3}{3E I} + \frac{w L^4}{8E I} \quad (5)$$

$$= \left( \frac{m_3 g L_3^3}{2} + \frac{q_3 L_3^4}{8} \right) \frac{1}{E I} \quad (6)$$

$$q_3 = \gamma A = \rho g A \quad (7)$$

Where:

$\delta y_3$  = Deflection at the third arm.

$E$  = Modulus of elasticity.

$\rho$  = Density of material.



$$q_3 = 7850 * 9.81 * A \quad (8)$$

$$M_{B-B} = m_2 g x_2 + q_2 \frac{x_2^2}{2} + q_3 L_3 \left( \frac{L_3}{2} + x_2 \right) + m_3 g (L_3 + x_2) \quad (9)$$

Where [8]:

$M_{B-B}$  = Bending moment at the second arm

$m_2$  = Mass of the second arm

When  $x_2 = L_2$  bending moment is maximum

$$M_{B-B})_{\max} = m_2 g L_2 + q_2 \frac{L_2^2}{2} + q_3 L_3 \left( \frac{L_3}{2} + L_2 \right) + m_3 g (L_3 + L_2) \quad (10)$$

$$\sigma_2 = \frac{M Y}{I} \quad (11)$$

$$\sigma_2 = \frac{\left( m_2 g L_2 + q_2 \frac{L_2^2}{2} + q_3 L_3 \left( \frac{L_3}{2} + L_2 \right) + m_3 g (L_3 + L_2) \right) Y}{I} \quad (12)$$

Where:

$\sigma_2$  = Bending stress at the second arm

$$\delta y_2 = \frac{W L^3}{3E I} + \frac{w L^4}{8E I} + \frac{M L^2}{2E I} \quad (13)$$

$$= \frac{1}{E I} * \left( \frac{\left( (m_2 + m_3) g + q_3 L_3 \right) L_2^3}{3} + \frac{q_2 L_2^4}{8} + \frac{\left( \left( m_3 g L_3 + q_3 \frac{L_3^2}{2} \right) L_2^2 \right)}{2} \right) \quad (14)$$

$$W_{Total} = g (m_1 + m_2 + m_3) + q_3 L_3 + q_2 L_2 \quad (15)$$

$$M_{Total} = q_3 \left( L_3 L_2 + \frac{L_3^2}{2} \right) + q_2 \frac{L_2^2}{2} + m_3 g (L_3 + L_2) + m_2 g L_2 \quad (16)$$

$$\sigma_{bending} = \frac{M_{Total} * Y}{I} \quad (17)$$

$$P_{cr})_{strut} = \frac{\pi^2 E I}{4L^2} \quad (18)$$

Where:

$P_{cr}$  = Critical load.

$$\sigma_{strut} = \frac{P_{cr}}{A} \quad (19)$$

$$\sigma_1 = \sigma_{strut} + \sigma_{bending} \quad (20)$$

Where:

$\sigma_1$  = Combined stress at the first arm.

$\sigma_{strut}$  = Strut stress.

$$\frac{1}{\sigma_r A} = \frac{1}{\sigma_e A} + \frac{1}{\sigma_c A}$$

From this equation we see that:

$$\begin{aligned} \frac{1}{\sigma_r A} &= \frac{1}{\sigma_e A} + \frac{1}{\sigma_c A} \Rightarrow \frac{1}{\sigma_r} = \frac{1}{\sigma_e} + \frac{1}{\sigma_c} = \frac{\sigma_e + \sigma_c}{\sigma_e \sigma_c} \\ \sigma_r &= \frac{\sigma_c}{1 + \frac{\sigma_c}{\sigma_e}} \end{aligned} \quad (21)$$

Where:

$\sigma_r$  : Rankine stress

$\sigma_e$  : Euler stress

For a strut with one end fixed, the other free

$$\sigma_e = \frac{\pi^2 E I}{4 L^2 A} \quad (22)$$

$$I = A k^2 \Rightarrow k = \sqrt{\frac{I}{A}} = \sqrt{\frac{\frac{\pi}{64} (D_1^4 - d_1^4)}{\frac{\pi}{4} (D_1^2 - d_1^2)}} \quad (\text{For uni-tube section})$$

$$\Rightarrow k = \frac{1}{4} \sqrt{(D_1^2 + d_1^2)}$$

$$\sigma_e = \frac{\pi^2 E k^2}{4 L^2} = \frac{\pi^2 E}{4 \left( \frac{L}{k} \right)^2} \quad (23)$$

Substituting equation (23) into equation (21) yields (**Hearn 1977**):

$$\sigma_r = \frac{\sigma_c}{1 + \frac{\sigma_c}{\pi^2 E} 4 \left( \frac{L}{k} \right)^2} \quad (24)$$

For comparing between the sections the weight of the gears and gripper were neglected the parameter of each arm as bellow:

$L_1=0.3\text{m}$ ,  $L_2=0.2\text{m}$ ,  $L_3=0.15\text{m}$

$m_1=8.8781\text{kg}$ ,  $m_2=1.9691\text{kg}$ ,  $m_3=1.278\text{kg}$

Where:

$m_1, m_2, m_3$ = the mass of first, second and third arm, respectively

$E= 200 \times 10^9 \text{ N/m}^2$ ,  $\nu = 0.3$

$g= 9.81$

Payload= 100N

### **Deflections Due to Pure Bending**

The deflection  $\delta$  is evaluated using finite element analysis techniques when the manipulator is at its maximum reach (completely stretched out) since this will yield the maximum deflection. Any other configuration will yield a smaller deflection value considering that the same

payload is carried. The deflection evaluation is a function of the structural and material properties of the links and the payload.

- **Square Cross-Section**

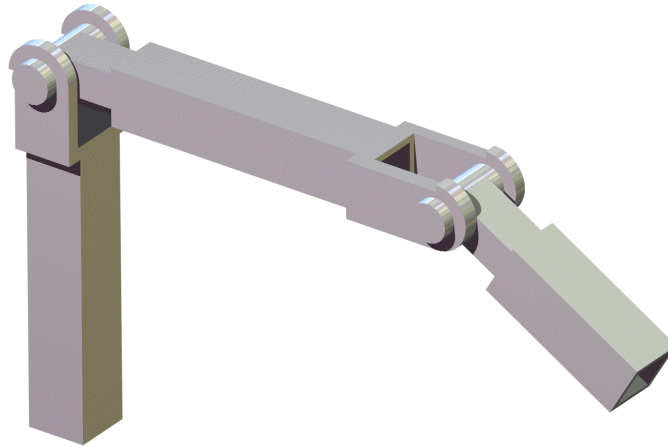


**Fig. (3) Robotic Arm of Square Cross-Section**

The cross-sectional parameters for each arm of the square section are given in **Table (1)**:

**Table (1a) Model Parameters for First Arm Square Cross-Section**

$B_1$ (m)	0.064	0.071	0.078	0.085	0.092
$b_1$ (m)	0.018	0.036	0.048	0.059	0.069

**Table (1b) Model Parameters for Second Arm Square Cross-Section**

$B_2$ (m)	0.04	0.047	0.054	0.061	0.068	0.075
$b_2$ (m)	0.0187	0.0309	0.0408	0.0497	0.0580	0.0661

**Table (1c) Model Parameters for Third Arm Square Cross-Section**

$B_3$ (m)	0.035	0.042	0.049	0.056	0.063	0.07
$b_3$ (m)	0.012	0.0261	0.0363	0.0453	0.0537	0.0618

- **Tri-Tube Cross-Section**

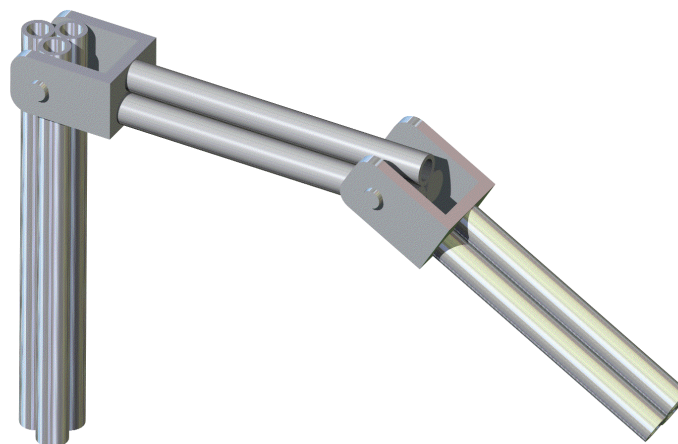


**Fig. (4) Robotic Arm of Tri-Tube Cross-Section**

The cross-sectional parameters for each arm are given in **Table (2)**:

**Table (2a) Model Parameters for First Arm Tri-Tube Cross-Section**

D <sub>1</sub> (m)	0.0425	0.0495	0.0565	0.0635	0.0705
d <sub>1</sub> (m)	0.0251	0.0357	0.0449	0.0534	0.0616

**Table (2b) Model Parameters for Second Arm Tri-Tube Cross-Section**

D <sub>2</sub> (m)	0.03	0.037	0.044	0.051	0.058
d <sub>2</sub> (m)	0.02465	0.03281	0.04054	0.04804	0.05542

**Table (2c) Model Parameters for Third Arm Tri-Tube Cross-Section**

D <sub>3</sub> (m)	0.0179	0.0249	0.0319	0.0389
d <sub>3</sub> (m)	0.00141	0.01736	0.02644	0.03456

- **Two Horizontally-Tube Cross-Section**

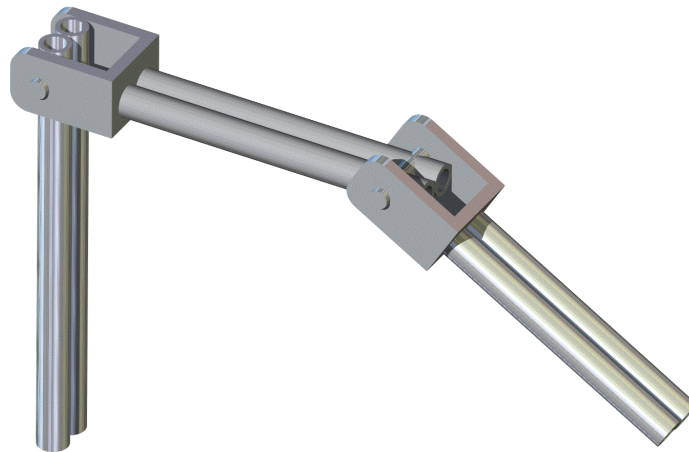


**Fig. (4) Robotic Arm of 2H-Tube Cross-Section**

The cross-sectional parameters for each arm are given in **Table (3)**:

**Table (3a) Model Parameters for First Arm 2H-Tube Cross-Section**

D <sub>1</sub> (m)	0.05	0.057	0.064	0.071	0.078
d <sub>1</sub> (m)	0.0279	0.0391	0.0487	0.0576	0.066

**Table (3b) Model Parameters for Second Arm 2H-Tube Cross-Section**

D <sub>2</sub> (m)	0.04	0.047	0.054	0.061	0.068
d <sub>2</sub> (m)	0.0362	0.04383	0.05127	0.05859	0.06585

**Table (3c) Model Parameters for Third Arm 2H-Tube Cross-Section**

D <sub>3</sub> (m)	0.02	0.027	0.034	0.041	0.048
d <sub>3</sub> (m)	0.0079	0.0197	0.0286	0.0366	0.04434

### Uni-Tube Cross-Section

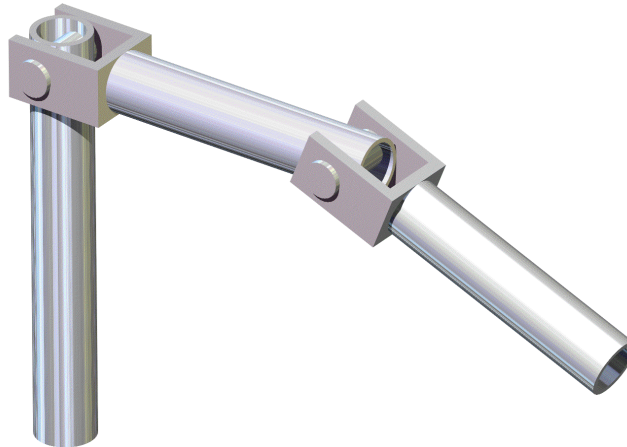


**Fig. (6) Robotic Arm of Uni-Tube Cross-Section**

The cross-sectional parameters for each arm are given in **Table (4)**:

**Table (4a) Model Parameters for First Arm Uni-Tube Cross-Section**

$D_1(m)$	0.07	0.077	0.084	0.091	0.098	0.105	0.112	0.119	0.126
$d_1(m)$	0.01	0.034	0.047	0.059	0.0693	0.079	0.088	0.097	0.105

**Table (4b) Model Parameters for Second Arm Uni-Tube Cross-Section**

$D_2(m)$	0.05	0.057	0.064	0.071	0.078	0.085
$d_2(m)$	0.03	0.0406	0.05	0.0586	0.067	0.075

**Table (4c) Model Parameters for Third Arm Uni-Tube Cross-Section**

$D_3(m)$	0.04	0.047	0.054	0.061	0.068	0.075
$d_3(m)$	0.015	0.0288	0.0392	0.0484	0.057	0.0651

- Two Vertically -Tube Cross-Section**

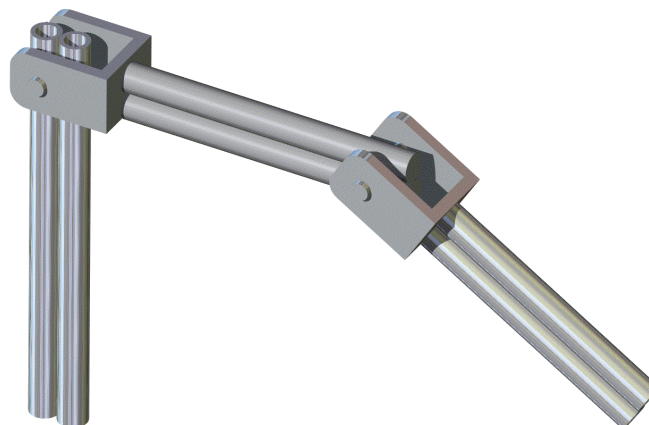


**Fig. (7) Robotic Arm of 2V-Tube Cross-Section**



The cross-sectional parameters for each arm are given in **Table (5)**:

**Table (5a) Model Parameters for First Arm 2V-Tube Cross-Section**

$D_1(m)$	0.05	0.057	0.064	0.071	0.078
$d_1(m)$	0.0279	0.0391	0.0487	0.0576	0.066

**Table (5b) Model Parameters for Second Arm 2V-Tube Cross-Section**

$D_2(m)$	0.04	0.047	0.054	0.061	0.068
$d_2(m)$	0.0362	0.04383	0.05127	0.05859	0.06585

**Table (5c) Model Parameters for Third Arm 2V-Tube Cross-Section**

$D_3(m)$	0.02	0.027	0.034	0.041	0.048
$d_3(m)$	0.0079	0.0197	0.0286	0.0366	0.04434

## OPTIMIZATION OF THE ROBOT STRUCTURE

Our overall goal is to design a robot arm that is stiff, lightweight, and exhibits minimum number of low natural frequencies for rigid-body structural dynamics (i.e., structural resonances). It is well known that, when a structure design is optimized to achieve high fundamental vibration frequencies, it also achieves the concomitant goal of low mass. Our initial design suggested that an arm design possessing high structural vibration frequencies while carrying a gripper payload, typically also satisfies the otherwise contradictory objectives of low mass, high stiffness, and high strength.

The objective function of these problems was to minimize the weight of the structures, subject to constraints on the stress in the robotic arm and displacement constraints at the end effectors. The design variables were the cross sectional shape of the robotic arm.

There are two cases of optimization in this research. The first case, which referred to as initial optimization, was to optimize the cross-sectional shape, and the second case, that referred to as final optimization, was to apply the optimization techniques to an actual structure.

### Initial Optimization:

### Optimization Invariants:

The following parameters shown in **Table (6)** are invariant over all five cross-sectional:

**Table (6) Invariant Parameters**

Structural Characteristics	First Arm	Second Arm	Third Arm
L	0.3m	0.2m	0.15m
Material	Steel	steel	steel
E	$200 \times 10^9 \text{ N/m}^2$	$200 \times 10^9 \text{ N/m}^2$	$200 \times 10^9 \text{ N/m}^2$
$\rho$	$7850 \text{ kg/m}^3$	$7850 \text{ kg/m}^3$	$7850 \text{ kg/m}^3$
$\nu$	0.3	0.3	0.3
A	$3.77 \times 10^{-3} \text{ m}^2$	$1.25 \times 10^{-3} \text{ m}^2$	$1.08 \times 10^{-3} \text{ m}^2$
Mass of arm	8.8781kg	1.9691kg	1.278kg

**Optimization Variables:**

The following variables were optimized for each link to achieve the highest stiffness and minimum deflection for the overall structure of the industrial robot:

- Shape of the arm cross-section.
- Moment of inertia for each arm.

**Final Optimization:****Optimization Invariants:**

The parameters shown in **Table (7)** are invariant over all five cross-sectional:

**Table (7) Invariant Parameters**

Structural Characteristics	First Arm	Second Arm	Third Arm
L	0.3m	0.2m	0.15m
Material	Steel	steel	steel
E	$200 \times 10^9 \text{ N/m}^2$	$200 \times 10^9 \text{ N/m}^2$	$200 \times 10^9 \text{ N/m}^2$
$\rho$	$7850 \text{ kg/m}^3$	$7850 \text{ kg/m}^3$	$7850 \text{ kg/m}^3$
$\nu$	0.3	0.3	0.3
T	0.002m	0.002m	0.002m
Mass of gears	15kg	15kg	30kg
Cross-section	Hollow circular	Hollow square	Hollow square

**Optimization Variables:**

The following variables were optimized for each link to achieve the highest stiffness, and minimum deflection for the overall structure of the industrial robot:

- Inner diameter for the first circular tube arm.
- The inner side dimension for the second and third square tube arm.
- Total mass of industrial robot.
- Natural frequencies ( $w_n$ ) and mode shapes.

Reducing the weight or changing the shape of a robot is not an easy task to accomplish; there are several factors involved in this, such as the type of external load that the manipulator is subjected to, material used (links of the robot) and the most complex variable to handle is its shape (geometry). The complexity introduced by these factors make it awkward to calculate the stress levels by hand. For this reason, an FEA package is needed; in this particular case ANSYS is used. This software will calculate how the von Misses stress is distributed along the links. Results are compared to the permissible or yield stresses, which make it possible to know if any arm is under failure mode.

$$\sigma (\text{Von Misses Stress}) \leq \sigma_y (\text{Yield Strength}).$$

To accomplish the goal of reducing the weight of the structure; therefore, improving its performance and the payload capacity, the weight distribution of the whole structure should be revised. Every link needs to be taken into account in order to avoid high inertial loads and an unstable robot design. A robotic design should follow the rule that the first link should be the most robust and the outermost as light as possible (The first link is going to hold the weight of the whole structure plus the payload).

## RESULTS AND DISCUSSION

In this work we chose five types of tube sections (square, circular, two vertical, two horizontal and three circular) to make a comparison between them and to choose the best section for constructing a three arm robot manipulator.

The procedure of analysis is based on assigning a certain mass and length for each of the first, second and third arm of the manipulator after that we calculate the cross sectional area for each arm and then we assume a certain dimension like the outer diameter of the circular tube and calculating the corresponding inner diameter after that we change the outer diameter by increasing it by a specific amount. The same procedure is used for all sections except for the 2V-tube, 2H-tube and tri-tube sections where the mass of the stiffeners must be subtracted from each arm before calculating the cross sectional area of each arm. After these initial calculations and after estimating the dimensions of each section we begin entering these data to the ANSYS software program to calculate the deformations and stress for each arm those results are shown in **Figures (8-13)** which demonstrates the regions where maximum stress and deformations occurs. The results for maximum deflections and those for maximum stresses for each arm and different cross sections are all collected from which we plot the figures and make the conclusions that for the first arm of the robot manipulator it is best to make its section as a circular tube this conclusion is clear from **Figure (14)** where for a given maximum stress the stiffness for the circular section is bigger as compared with the other sections this result is also clear in **Figure (15)** for a given maximum stress the uni-tube gives less deformation from other sections.

For the second arm we make a conclusion that the square section has a low stress for a given stiffness this is clear in **Figure (16)** and also in **Figure (17)** for a given deflection the stress will be minimum in the square section.

The same results is obvious in **Figure (18)** where for a given deflection the stress is minimum for the square section the same conclusion is clear in **Figure (19)** where for a given stiffness the stress is minimum in the square section, the same result may be achieved from **Figure (20)** where for a given moment of inertia the square section gives higher stiffness relative to the other sections.

To make a self checking for our results in ANSYS, a program had been built up using MATHCAD software. The results of calculation by MATHCAD are shown in **Figures (21-26)** where the same conclusion are drawn up from the curves that is the first arm of the robot manipulator is preferred to make its section as a circular tube while the other two arms it is preferred to make its section as a square tube to achieve higher stiffness to weight ratio. In this calculations the same dimensions of each section of each arm had been given as an input data for the program so as to make the comparison between the two ways of analysis essayer, the differences between the results is referred to the way of analysis in each software, where in ANSYS the analysis is based on finite element and in MATHCAD the analysis is based on the solution on the known equations of strength of materials for finding the maximum stress and deflections in beams and struts, due to those different ways of analysis a slight error is seen in those figures, such error don't play a big rule from the engineering point of view.

The next step in our work was to built another program to make an optimum design for a given robot having a given length of arms and payload and to find the best dimensions for its first, second and third arm.

The program had been written by MATHCAD software and it begins as assigning the length of the three arms and the mass of the first and second gear box actuator and the total mass of the payload, that the robot (manipulate), and its end effector actuator.

The sequence of calculations begins by finding the dimensions of the arm cross section that satisfies the condition of strength that is to let the stress in each arm be the maximum possible value it can reach, after that the program find the weight of the arms of the robot. The next step in this program is to change the dimension step by step to make the structure of the robot stiffer, the

iteration continuous until the program fined the dimension of each section that satisfies the limits of deflection on the end point of the robot arm that we want the robot to achieve in the same time the program makes checking on the weight of robot structure if it is higher than the limit that it is assigned to it. From all those iterations and results that the program reaches (which satisfy the conditions of weight and deflection) it chooses the best design parameter between all the result that has the less weight and deflection due to the given condition of loading.

The final dimension of the robot arms will be the next input for the ANSYS to calculate the dynamic characteristics of the structure of the robot to determine its natural frequency and mode shapes of vibration.

The iterations shows that if we increase the weight of the robot by about 25% of the initial weight calculated in our first analysis, in which ( $\sigma \leq \sigma_y$  in each arm), the iteration gives us 32 generation which satisfies our condition of deflection ( $0.005m < \delta_{max} < 0.002m$ ) those results for the dimensions of the inner diameter of the first arm and the inner side dimension of the second and third arm are show in **Figure (27)**.

A plot of the total deformation of the end effectors is shown in **Figure (28)** for each generation. **Figure (29)** shows the total weight of the robot structure for each generation.

The criteria for choosing the best dimensions for the robot structure from the 32 generation obtained is to multiply the weight of each generation by it's deflection the result of multiplication gives us an indication of the best generation which has the less value between them, and this criteria is referred to as the criteria of choice, which is shown in **Figure (30)** it is obvious that the 21 generation in the best between them the dimension of this generation entered to ANSYS to calculate the natural frequencies and mode shapes for the robot structure. The results of dynamic analysis show that the natural frequencies are (53.614, 59.171, and 138.70Hz). **Figure (31-33)** shows the mode shapes for each natural frequency calculated.

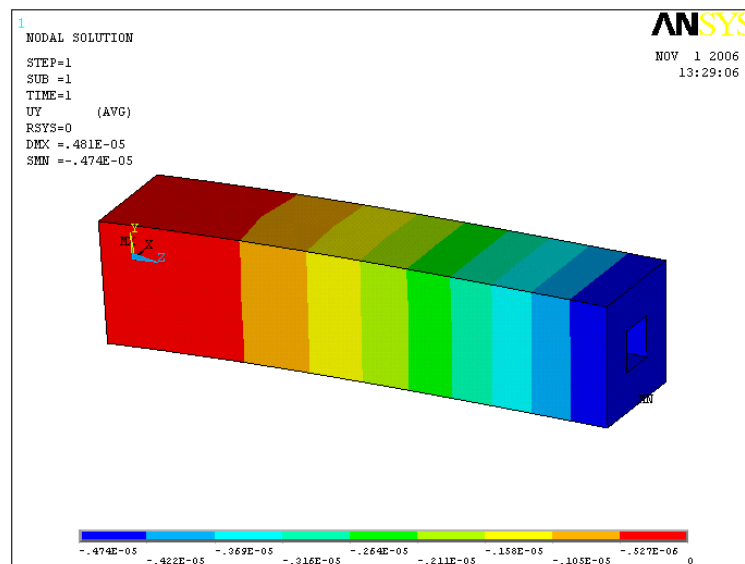


**Fig. (8) Deflection in the Third Arm of Square Cross-Section where B=0.035m, b=0.012m**

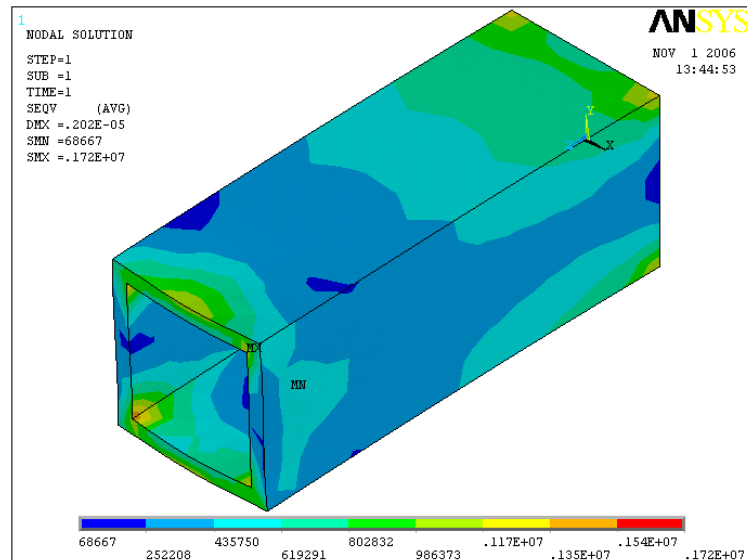


Fig. (9) Stress in the Third Arm of Square Cross-Section where  $B=0.056\text{m}$ ,  $b=0.0453\text{m}$

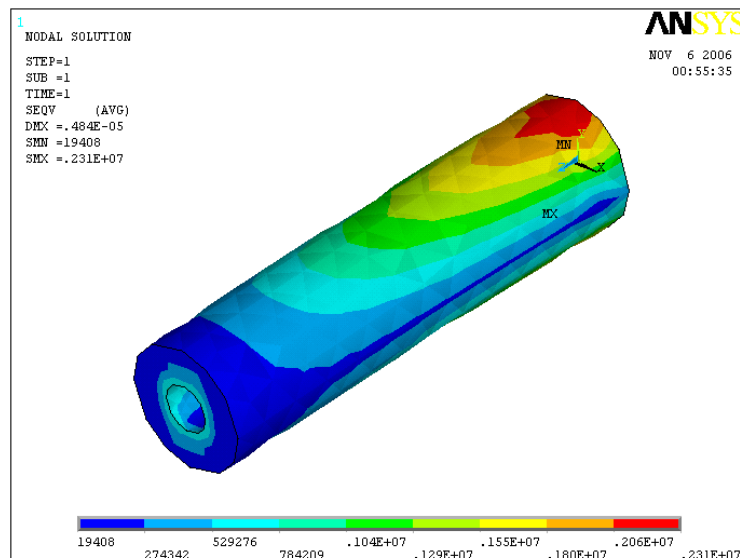


Fig. (10) Stress in the Third Arm of Uni-Tube Cross-Section where  $D=0.04\text{m}$ ,  $d=0.015\text{m}$

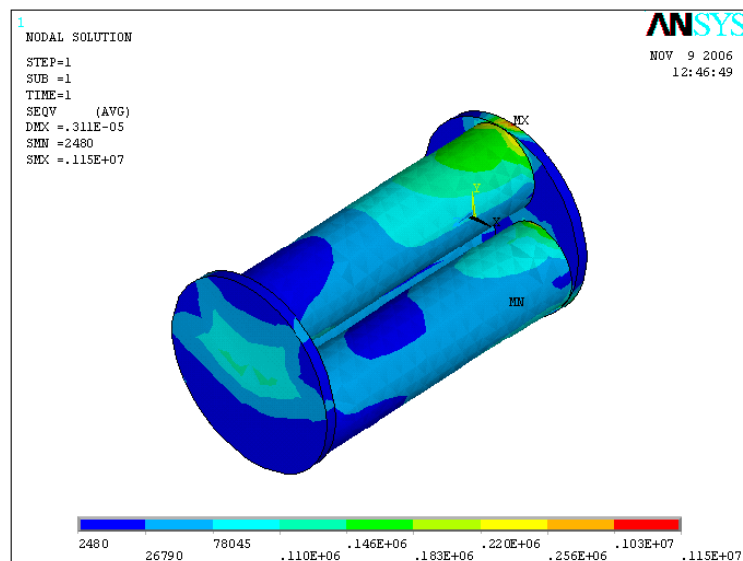


Fig. (11) Stress in the Third Arm of Tri-Tube Cross-Section where  $D=0.0389\text{m}$ ,  $d=0.03456\text{m}$

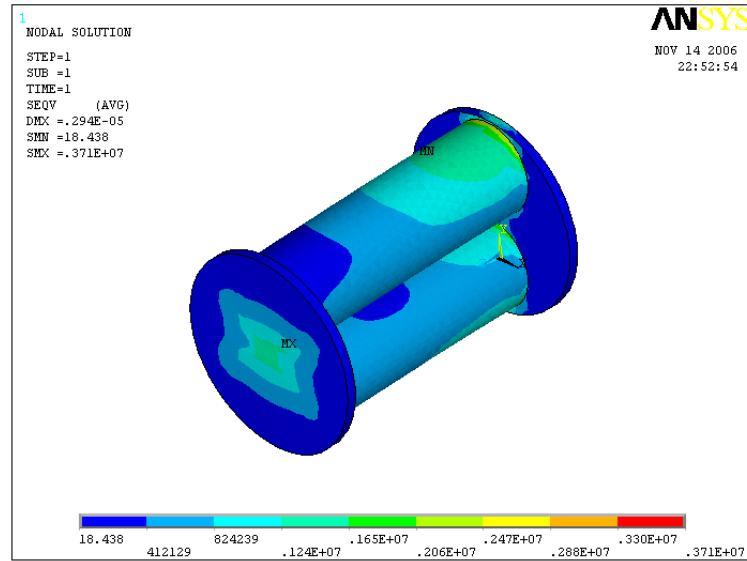


Fig. (12) Stress in the Third Arm of 2V-Tube Cross-Section where  $D=0.048\text{m}$ ,  $d=0.04434\text{m}$

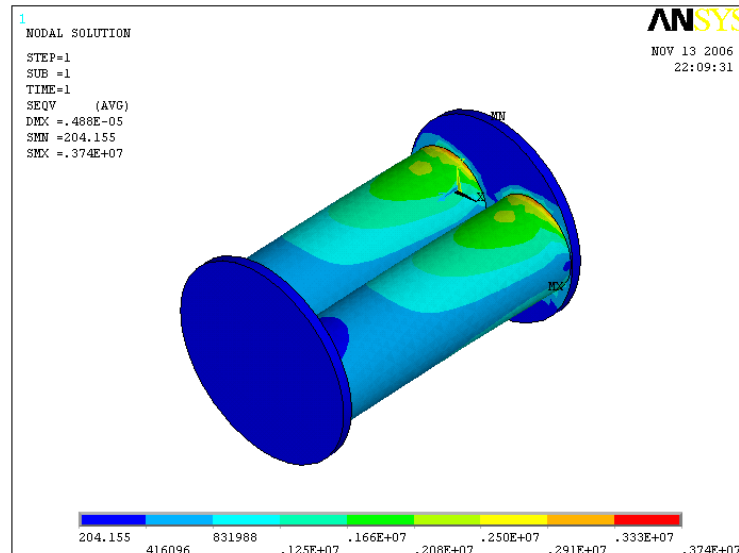


Fig. (13) Stress in the Third Arm of 2H-Tube Cross-Section where  $D=0.048\text{m}$ ,  $d=0.04434\text{m}$

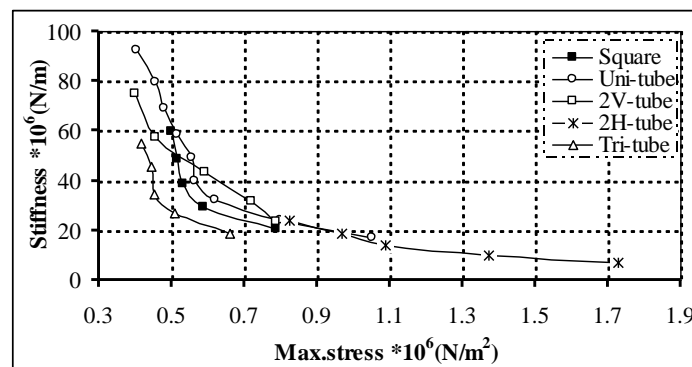
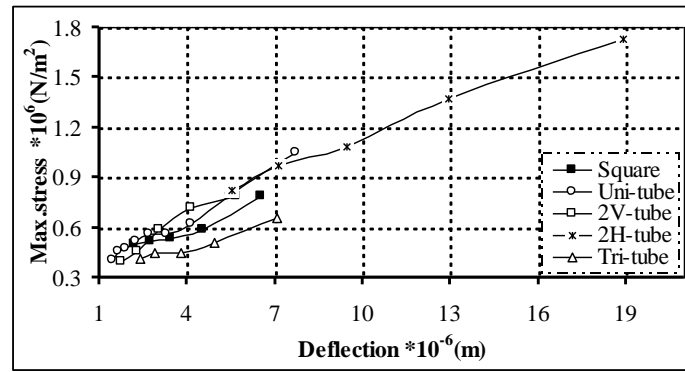
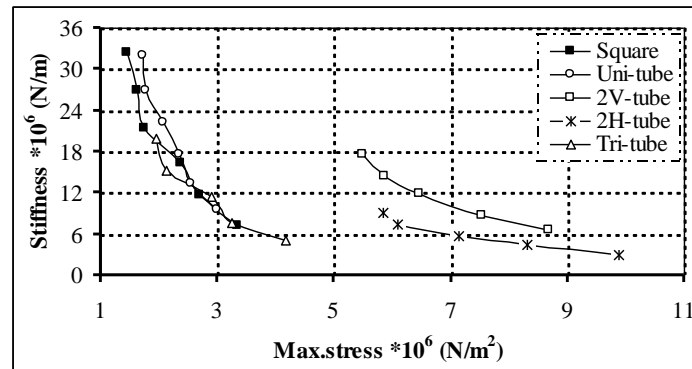


Fig. (14) Stiffness Versus Maximum Stress in the First Arm for Different Cross-Sections by ANSYS



**Fig. (15) Maximum Stress Versus Deflection in the First Arm for Different Cross-Sections by ANSYS**



**Fig. (16) Stiffness Versus Maximum Stress in the Second Arm for Different Cross-Sections by ANSYS**

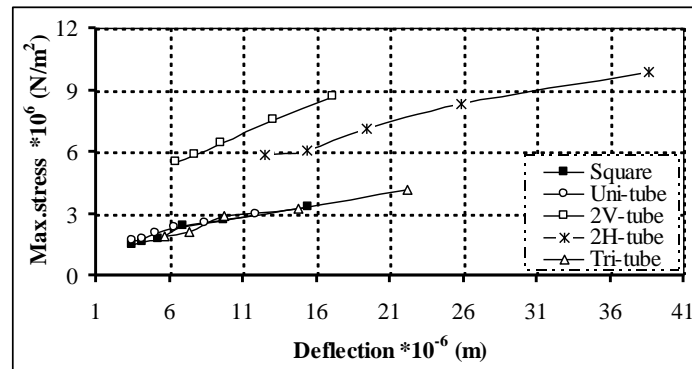


**Fig. (17) Maximum Stress Versus Deflection in the Second Arm for Different Cross-Sections by ANSYS**

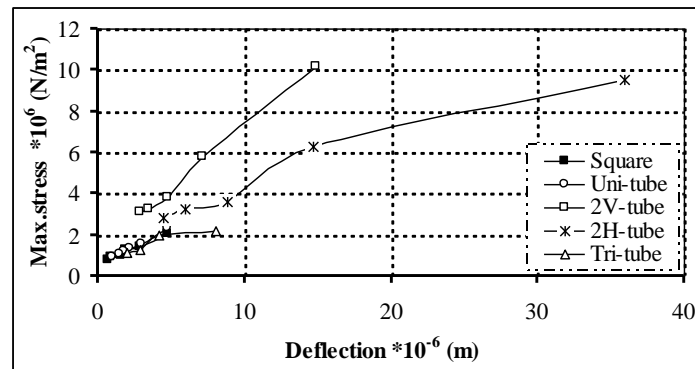


**Fig. (18) Maximum Stress Versus Deflection in the Third Arm for Different Cross- Sections by ANSYS**

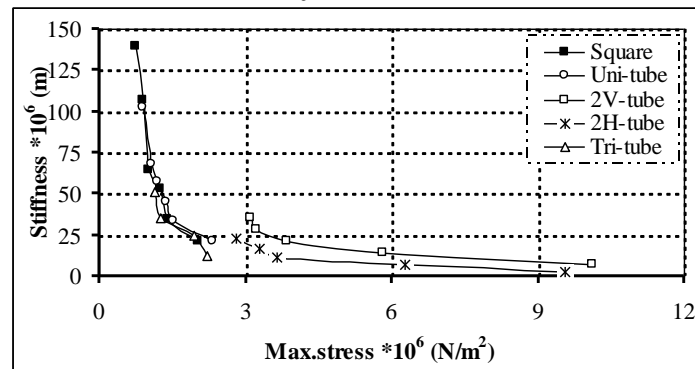


**Fig. (19) Stiffness Versus Maximum Stress in the Third Arm for Different Cross-Sections by ANSYS**

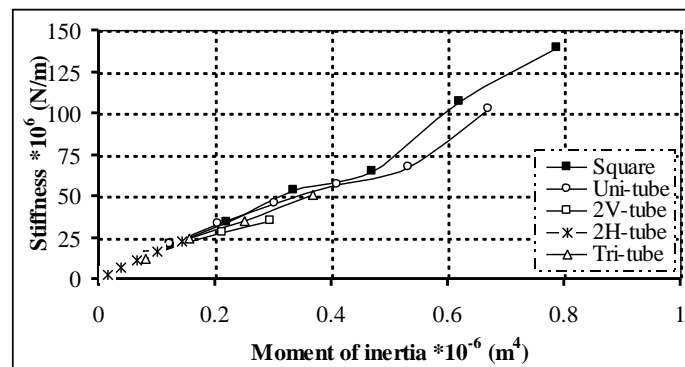


**Fig. (20) Stiffness Versus Moment of Inertia in the Third Arm for Different Cross-Sections by ANSYS**



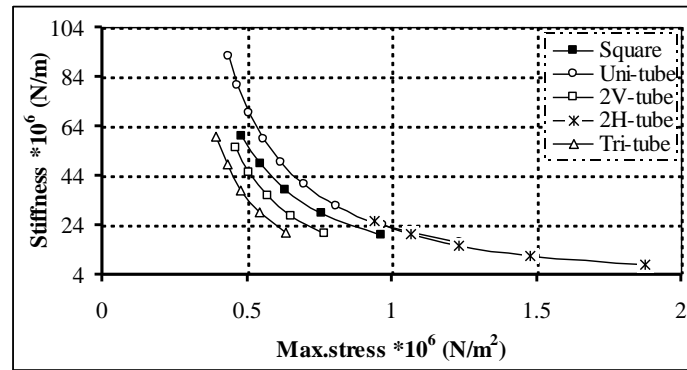


**Fig. (21) Stiffness Versus Maximum Stress in the First Arm for Different Cross-Sections by MATHCAD**

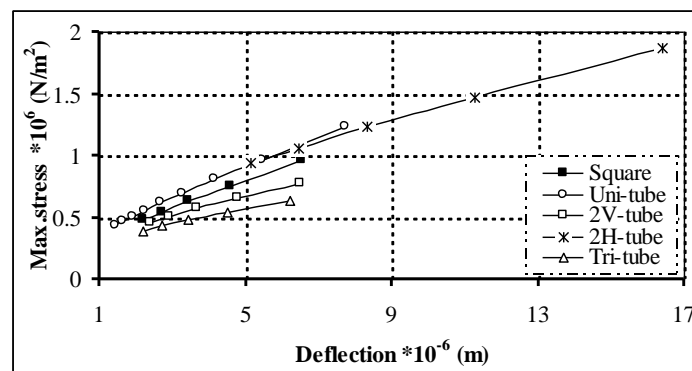


**Fig. (22) Maximum Stress Versus Deflection in the First Arm for Different Cross-Sections by MATHCAD**

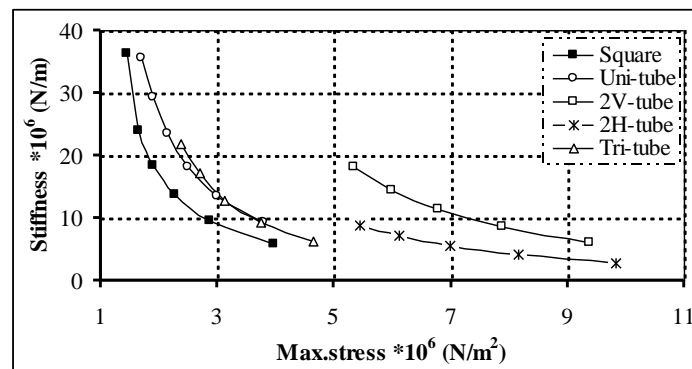


**Fig. (23) Stiffness Versus Maximum Stress in the Second Arm for Different Cross-Sections by MATHCAD**

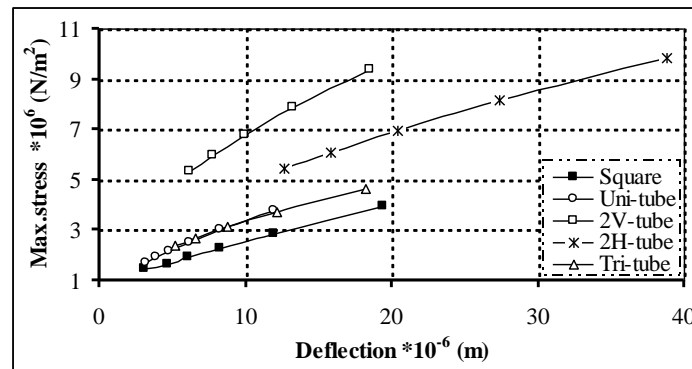


**Fig. (24) Maximum Stress Versus Deflection in the Second Arm for Different Cross-Sections by MATHCAD**

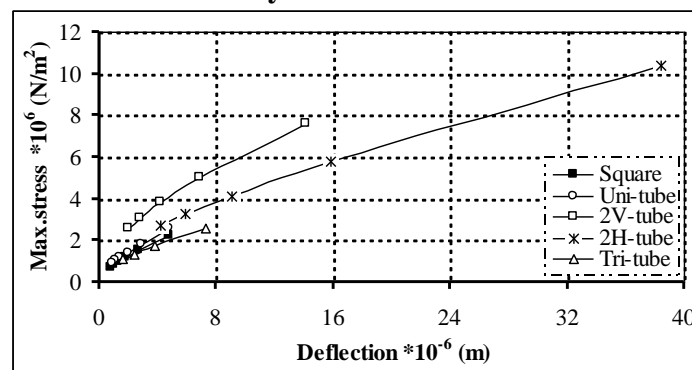


**Fig. (25) Maximum Stress Versus Deflection in the Third Arm for Different Cross-Sections by MATHCAD**

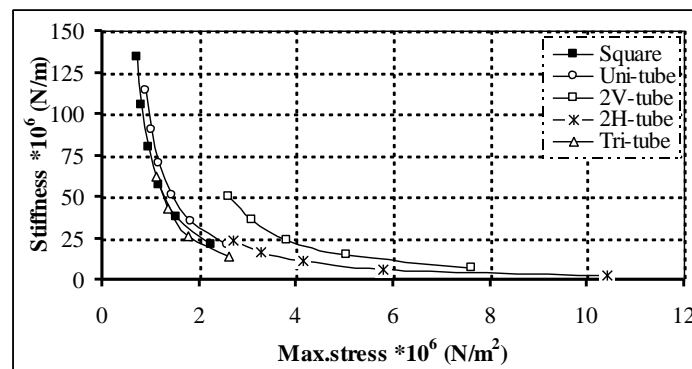


**Fig. (26) Stiffness Versus Maximum Stress in the Third Arm for Different Cross-Sections by MATHCAD**

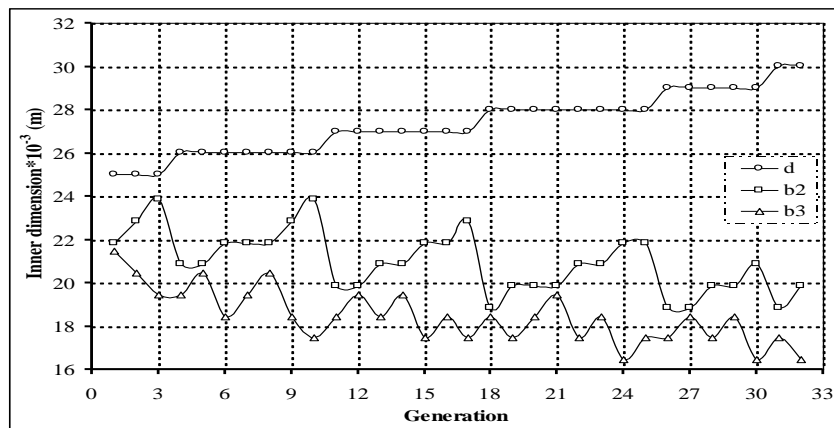


**Fig. (27) Relation Between Inner Dimensions and Generation**

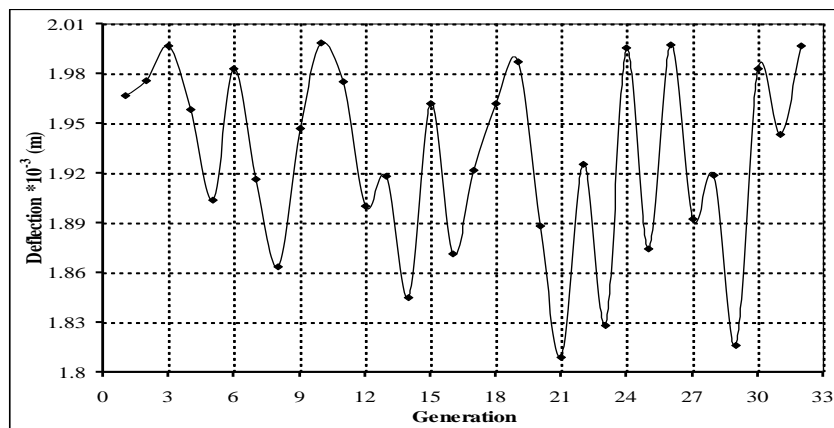


**Fig. (28) Relation Between Total Deflection and Generation**

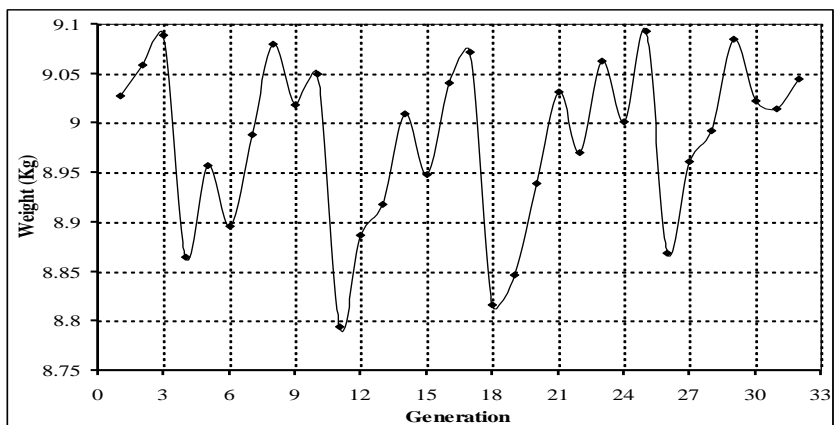


**Fig. (29) Relation Between Total Weight and Generation**

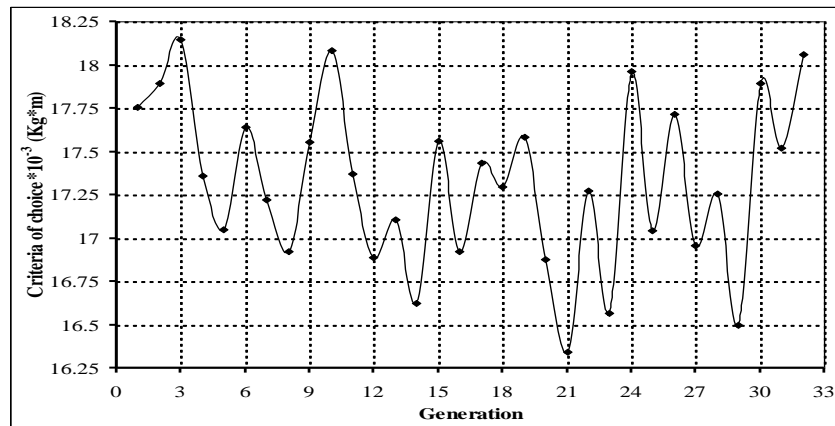


**Fig. (30) Relation Between the Criteria of Choice and Generation**

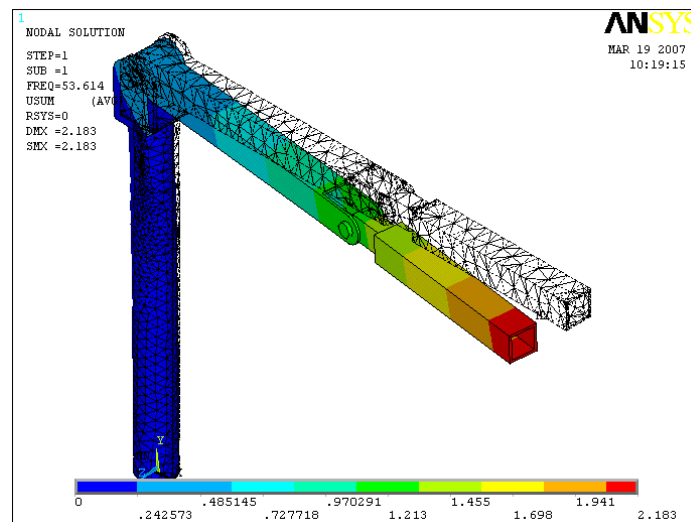


**Fig. (31) First Mode Shape of Arms at (53.614Hz)**

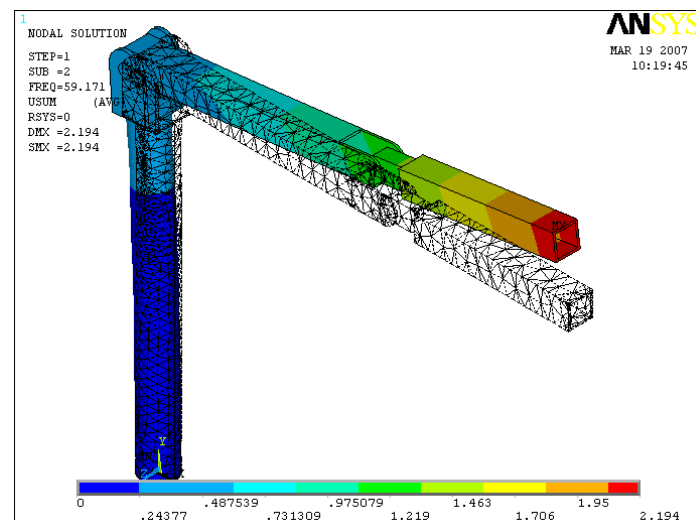


**Fig. (32) Second Mode shape of Arms at (59.171Hz)**

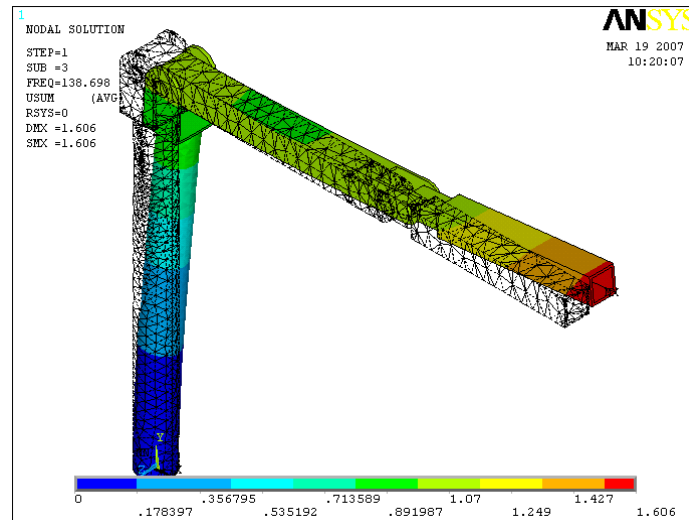


**Fig. (33) Third Mode Shape of Arms at (138.698Hz)**

## CONCLUSIONS

The main conclusions in our work (where we made a comparison between the five suggested sections for robot manipulator arms) is that to achieve best performance and high stiffness to weight ratio it is better to make the cross section of first arm as a circular tube and the other arms of the robot its better to make its section as a square tube.

Another perceptible notice is that the tri-tube section gives a results close to those of the uni-tube and square tube for the first, second and third arm respectively, the reason after this lag and retardation is that the stiffeners at the beginning and end of each arm takes parts of the metal or mass used in building or constructing the arms of the robot which make it weaker, this conclusion lead as to a results that the tri-tube section may gives a better results if an optimization had been made for it alone by varying the dimensions of the stiffness and the distance between the center's of the three tube and the diameter of each tube this may be as a suggestion for further work.

By the correct choice of cross section of each arm and by the appropriate choice of its dimensions based on the iteration and optimization process we may have a robot structure that has a weight, bigger by a little amount (about 25%) from the lightest weight which satisfies the condition of strength (i.e. the stress in each member reaches its maximum possible value) but satisfying the condition of stiffness which is the main feature of robot construction i.e. the error of the end effectors will be less than 2mm.

In case of increasing the weight or mass of the robot structure by an amount begin than 25% we can have a structure stiffer from the preceding and has deflection less than 0.002m but on the other hand we will sacrifices the benefit of low weight structure which minimizes the effect of inertia during the work of robot.

**REFERENCES**

- Abdel-Malek, K. and Paul, B. (1998). "Criteria for the Design of Manipulator Arms for a High Stiffness to Weight Ratio", SME Journal of Manufacturing Systems, Vol. 17, No. 3, P.P.209-220.
- Alazard, D.; Chretien, J. P. (1992). "The Impact of Local Masses and Inertias on the Dynamic Modeling of Flexible Manipulators".
- Ceccarelli, M.; Carobone, G. and Ottaviano, E. (2005). "Multi Criteria Optimum Design of Manipulators", Bulletin technical sciences Vol.53, No.1, P.P.9-18.
- Edward Mebarak. (2003). "On the Development of an Automated Design Procedure to Design Optimal Robots", Florida International University, Miami, Florida.
- Fresonke, D. A.; Hernandez, E. and Tesar, D. (1993). "Deflection Predictions for Serial Manipulators", in IEEE Conference on Robotics and Automation. Philadelphia, PA, pp482-487.
- Haubach, C. (2002) "Flexible Robots-an Example of Stochastic Structural Optimization". [www.stoch.net/daten/public1.htm#A](http://www.stoch.net/daten/public1.htm#A)
- Hearn, E. g. (1977). "Mechanics of Materials", Pergamon Press LTD.
- Hennessey, M. P.; Priebe, J. A.; Paul, C. H. and Grommes, R. J. (2000) "Design of a Lightweight Robotic Arm and Controller," IEEE Conference on Robotics and Automation, Raleigh, NC. P.P.779-785.
- Jaydeep Roy and Louis, L. Whitcomb. (1999). "Comparative Structural Analysis of 2-DOF Semi-Direct-Drive Linkages for Robot Arms", IEEE/ASME Transactions on Mechatronics, Vol.4, No.1, pp.82-86.
- Leu, M. C.; Dukovski, V. and wang, K. K. (1985). "An Analytical and Experimental Study of the Stiffness of Robot Manipulators with Parallel Mechanism", ASME Robotics and Manufacturing Automation, Vol.15, P.P.137-143.
- Marcus Pettersson; Petter Krus; Xiaolong Feng; Johan Andersson and Daniel Wappling. (2004). "Industrial Robot Design Optimization in the Conceptual Design Phase". [http://www.machine.ikp.lin.se/staff/johan/files/IEEE\\_mecanic\\_and\\_robot\\_2004.pdf](http://www.machine.ikp.lin.se/staff/johan/files/IEEE_mecanic_and_robot_2004.pdf)
- Paredis, C. J. and Khosla, P. K. (1996). "Designing Fault-Tolerant Manipulators: How Many Degrees of Freedom?", Int. J. Rob. Res., Vol. 15, No. 6, P.P. 611-628.
- Rivin, E. I. (1988). "Mechanical Design of Robots", McGraw-Hill, Inc, New York.
- Saeed Moaveni. (1999). "Finite Element Analysis Theory and Application with ANSYS", Prentice-Hall.
- Shiakolas, P. S.; Koladiya, D. and Kebrle, J. (2002). "Optimum Robot Design Based on Task Specifications Using Evolutionary Techniques and Kinematic, Dynamic, and Structural Constraints", International Journal of inverse problem in engineering. Vol.10, No.4, P.P.359-375.

- Shimon. Y. Nof. (1999). "Handbook of Industrial Robotics", John Wiley and Sons, Inc., Newyork.
- Williams, J. Angeles, and Bulca, F. (1993). "Design Philosophy of an Isotropic Six-Axis Serial Manipulator", Robotics and Computer-Integrated Manufacturing, Vol.10, No.4, P.P.257-322.
- Wu, E. C.; Hwang, J. C. and Chladek, J. T. (1993). "Fault-Tolerant Joint Development for the Space Shuttle Remote Manipulator System: Analysis and Experiment", IEEE Trans. Robot. Automat, Vol. 9, No. 5, P.P. 675-684.

## ANTISEIZURE CHARACTERISTICS OF LEADED ALUMINUM ALLOYS UNDER DRY SLIDING CONDITIONS

Dr. Akeel D. Subhi  
Department of Production Engineering and Metallurgy  
University of Technology  
Baghdad-Iraq

### ABSTRACT

Aluminum-Silicon alloys, with soft lubricant metal, are considered to be one of the important tribological alloys which resist seizure. The effect of different lead percentages (1-20%Pb) that added to the modified eutectic Al-12%Si alloy on the wear rate and resistance was studied by sliding these alloys under dry sliding conditions on a carbon steel disc at different sliding distances (2.24-40.37 km). The results showed that the wear rate was decreased and wear resistance increased with increasing lead percentage of Al-12%Si alloy. Furthermore, wear rate was increased linearly with increasing sliding distance.

خصائص مقاومة الالتصاق لسبائك الألمنيوم المحتوية على الرصاص تحت ظروف الانزلاق الجاف

### الخلاصة

تعد سبائك الألمنيوم-سليكون المحتوية على معدن مزيت من السبائك الترابيولوجية المهمة المقاومة للالتصاق. يهدف هذا البحث الى دراسة تأثير اضافة الرصاص بنسب مختلفة (1-20%Pb) على معدل ومقاومة البلى لسبيكة Al-12%Si الايوتكتيكية المحورة تحت تأثير الانزلاق الجاف على قرص من الفولاذ الكربوني عند مسافات انزلاقية مختلفة (2.24-40.37 km). اوضحت النتائج انخفاض معدل البلى وزيادة مقاومة البلى مع زيادة نسبة الرصاص لسبيكة Al-12%Si. علاوة على ذلك فان معدل البلى يزداد بصورة خطية مع زيادة مسافة الانزلاق.

### INTRODUCTION

Aluminum based alloys; especially eutectic aluminum-silicon alloys are regarded to be one of the most important tribological alloys due mainly to the presence of silicon [Lee 1998 and Yasmin 2004]. Silicon is the second most abundant impurity of aluminum. It imparts fluidity in casting, weldability and high mechanical properties [Mondolfo 1976]. These properties incited many researchers in order to approach the convenient application. Therefore, replacement of cast iron by aluminum based alloys in manufacturing automobile pistons is the start point in the early ninetieth century [Sarkar 1980]. Lead is technically and economically the best qualified metal for use as a soft phase alloying addition to aluminum based alloys. Leaded aluminum alloys are characterized



by low wear rate, antifriction and antiseizure characteristics suitable for a variety of bearing applications [Tiwari 1987]. Rudrakshi et al. (2004) found that the wear properties of spray formed Al-Si-Pb alloy were improved to be greater than that of Al-Si alloy as a result of microstructural features of spray formed alloy and the nature of the worn out surfaces. While Hao et al. [2005] showed that the main reason of decreasing wear in the hot extruded Al-4Si-20Pb alloy attributed to the constituents of lubricating film that created between the mating surfaces. They indicated that this film is composed of mixture of  $\text{Fe}_2\text{O}_3$ ,  $\text{Pb}_4\text{SiO}_6$  and a small amount of  $\text{Fe}_2\text{O}_3$  at room temperature, and  $\text{Pb}_4\text{Al}_{12}(\text{SiO}_3)_7$ ,  $\text{SiO}_2$ ,  $\text{Al}_2\text{O}_3$  and a small amount of  $\text{Fe}_2\text{O}_3$  at high temperature. The same result is concluded by An et al. [2006] when irradiated Al-Si-Pb alloys with high current pulsed electron beam in which the different constituents of lubricating film is the main reason of decreasing wear.

In this work, some light will be thrown to study the effect of lead addition on wear rate and resistance of modified eutectic Al-12%Si alloy.

## MATERIALS AND METHODS

Leaded aluminum alloys were prepared using commercial high purity aluminum, lead and Al-18%Si master alloy as starting materials. The master alloy of Al-18%Si was previously prepared by adding high purity silicon as chunks to the molten of commercial high purity aluminum using gas fired furnace under the pressure effect via graphite block in a graphite crucible to prevent any floatation of silicon on the molten surface of aluminum. The molten of Al-18%Si alloy was casted in a metallic mould to produce ingot of Al-18%Si master alloy. A specified amount of commercial high purity aluminum was added to the molten of Al-18%Si master alloy to obtain Al-12%Si alloy. Lead was added separately in different amounts, that corresponding to 1-20%Pb, to the diluted Al-18%Si master alloy with aluminum to produce different types of leaded Al-12%Si alloys. The addition of lead was carried out using vortex method as a result of no solubility and miscibility between lead and eutectic Al-12%Si alloy. In this method, lead was added as chips to the molten of diluted Al-18%Si master alloy with aluminum in a graphite crucible using graphite fan to prevent any reaction. The inclination angle of vortex mixing and speed of mixer rotation were  $30^\circ$  and 1256 rpm respectively. All leaded alloys were mixed at  $650^\circ\text{C}$  for 10 min individually to obtain homogenous distribution of lead inside the molten of Al-12%Si alloy. The pouring temperature for each alloy was fixed at the same temperature of vortex mixing in which each alloy was poured into a cooled carbon steel mould to obtain chilled ingots of Al-Si-Pb alloys. All casted ingots have the dimensions of 100 mm length and 15 mm diameter. Chemical composition of pure aluminum, master alloy and prepared Al-Si-Pb alloys is tabulated in table I. The ingots of Al-Si-Pb alloys were cut and turned to produce specimens suitable for microstructural and wear study. For microstructural study, each alloy specimen was cold mounted and then ground using different SiC emery papers. Primary polishing was carried out using slurry of alumina while final polishing was achieved using diamond paste. All microstructural study specimens were etched using 1% Vol. HF etching solution.

Pin on disc type wear testing apparatus with 450 Hv carbon steel disc was used in this work in order to determine antiseizure characteristics of Al-Si-Pb alloys. Wear test specimens that previously prepared have the dimensions of 10 mm length and 5 mm diameter. The sliding circle diameter and bearing pressure were fixed at 14 cm and 63.6 kPa respectively. A wide range of running periods was used ranging from 10 min to 3 hr in order to produce different sliding distances (2.24-40.37 km).

## RESULTS AND DISCUSSION

Figure 1 shows the microstructure of modified eutectic Al-Si alloys. It is clear from this figure that two phases are presented in the matrix of Al-Si-Pb alloys. These phases are eutectic and lead, while one phase presented in the matrix of Al-12%Si alloy which is eutectic. Figure 1 also shows the potent effect of chilling on producing modification of eutectic silicon in the matrix of leaded

alloys, in which fibrous eutectic silicon associated with aluminum dendrites can be recognized in the matrix for each alloy. This modification in eutectic silicon morphology from angular and flake as in ordinary conditions to the fibrous as in this work has a crucial role on increasing the mechanical and tribological properties of eutectic Al-Si alloys as mentioned elsewhere [Subramanian 1991, Fatahalla 1999 and Liao 2002]. It is explicit to know that lead decreasing the hardness of Al-Si alloys in a magnitude dependent on its percentage in the matrix. This decreasing in hardness value does not mean decreasing in wear properties of Al-Si alloys. This can be demonstrated by showing the relationship between sliding distance and wear rate as shown in figure 2. It is clear from this figure that the wear rate was increased linearly with increasing sliding distance for each alloy. In the other side, the wear rate was decreased with increasing lead percentage at any sliding distance. Plastic deformation always associated with wear in the subsurface region of the base matrix of Al-Si alloys. The deformation of aluminum phase results in fragmentation of silicon phase into fine particles distributed in the subsurface region [Pramila Bai 1984]. In this work, no fragmentation was occurred as a result of potent effect of modification that occurred in eutectic silicon morphology as explained above. The aluminum and silicon phases in the eutectic of Al-Si alloys behave independently on each other during dry sliding in which the silicon phase resists the applied bearing pressure while the aluminum phase accommodates the plastic deformation in the matrix. The presence of lead in the matrix of modified Al-12%Si alloy results in decreasing the wear rate as explained above. This is because the lead acts as a lubricant and reduces wear between mating surfaces as a result of its extrusion during dry sliding of leaded aluminum alloys on carbon steel disc and forming a trib-layer of low shear strength spreads over modified eutectic Al-12%Si alloy substrate. The smearing of lead prevents adhesion between the mating surfaces in areas dependent on lead location in the matrix of modified eutectic Al-12%Si alloy. Therefore, wear rate will be decreased and in the same time seizure resistance will be increased. This result can be demonstrated precisely from the relationship between lead percentage and wear resistance, as shown in figure 3, in which the wear resistance increases with increasing lead percentage. From curve fitting programme, the wear resistance ( $W_R$ ) changes with lead percentage ( $L_p$ ) according to the following formula:

$$W_R = -0.021L_p^2 + 1.267L_p + 35.83 \quad (1)$$

This illuminates the importance of lead addition; especially the adhesive compatibility of slid metals [Norton 1998] indicated clearly the low metallurgical compatibility between lead and iron where iron can be considered as a counterface material. This makes Al-Si-Pb alloys a suitable choice for bearing applications. The relationship between wear rate ( $W_r$ ) and hardness ( $H_v$ ) is shown in figure 4 in which the wear rate decreases with decreasing hardness, i.e. increasing lead percentage, according to the following formula obtained from curve fitting programme

$$W_r = 0.002H_v^2 - 0.2H_v + 6.250 \quad (2)$$

## CONCLUSION

Rapid cooling of leaded eutectic Al-12%Si alloys in a metallic mould could produce modification of eutectic silicon morphology in the matrix of these alloys. The presence of accompanied lead that added using vortex method with modified eutectic silicon led clearly to remarkable changes in the antiseizure characteristics of leaded alloys. These changes can be summarized by decreasing wear rate and increasing wear resistance with increasing lead percentage, i.e. decreasing hardness.

**REFERENCES**

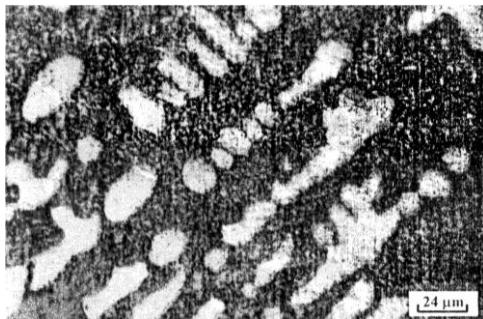
- An, J., Shen, X.X., Lu, Y., Liu, Y.B., Li, R.G., Chen, C.M. and Zhang, M.J., “Influence of High Current Pulsed Electron Beam Treatment on the Tribological Properties of Al-Si-Pb Alloy”, *Surface and Coatings Techno.*, 200 (2006) 5590.
- Fatahalla, N., Hafiz, M. and Abdulkhalek, M., “Effect of Microstructure on the Mechanical Properties and Fracture of Commercial Hypoeutectic Al-Si Alloy Modified with Na, Sb and Sr”, *J. Mater. Sci.*, 34 (1999) 3555.
- Hao, S.Z., An, J., Liu, Y.B. and Lu, Y., “Tribological and Structural Properties of Lubricating Films of Al-4Si-20Pb Alloy During Dry Sliding at Different Temperatures”, *Mater. & Design*, 26 (2005) 181.
- Lee, J.A., “High-Strength Aluminum Casting Alloy for High-Temperature Applications”, NASA, Marshall Space Flight Center, Dec., 1998.
- Liao, H., Sun, Y. and Sun, G., “Correlation Between Mechanical Properties and Amount of Dendritic  $\alpha$ -Al Phase in As-Cast Near Eutectic Al-11.6%Si Alloys Modified with Strontium”, *Mater. Sci. and Engg. A*, 335 (2002) 62.
- Mondolfo, L.F., “Aluminum Alloys: Structure and Properties”, Butterworths (London), 1976.
- Norton, R.L., “Machine Design-An Integrated Approach”, Prentice-Hall Inc. (New Jersey), 1998.
- Pramila Bai, B.N. and Biswas, S.K., “Subsurface Deformation in Dry Sliding of Hypo-Eutectic Al-Si Alloys”, *J. Mater. Sci.*, 19 (1984) 3588.
- Rudrakshi, G.B., Srivastava, V.C., Pathak, J.P. and Ojha, S.N., “Spray Forming of Al-Si-Pb alloys and Their Wear Characteristics”, *Mater. Sci. and Engg. A*, 383 (2004) 30.
- Sarkar, A.D., “Friction and Wear”, Academic Press (London), 1980.
- Subramanian, C., “Wear of Al-12.3Wt.%Si Alloy Slid Against Various Counterface Materials”, *Scripta Metall.*, 25 (1991) 1369.
- Tiwari, S.N., Pathak, J.P. and Malhotra, S.L., “Lead- A Potential Soft-Phase Alloying Addition to Aluminum Bearing Alloys”, *Aluminum*, 63 (1987) 411.
- Yasmin, T., Khalid, A.A. and Haque, M.M., “Tribological (Wear) Properties of Aluminum-Silicon Eutectic Base Alloy Under Dry Sliding Conditions”, *J. Mater. Proce. Techno.*, 153-154 (2004) 833.

Table

Elements	Si	Fe	Cu	Pb	Mn	Ti	Al
Al	0.11	0.11	0.008	0.001	0.007	0.005	Rem.
Al-18%Si	18.2	0.31	0.09	0.001	0.02	0.009	Rem.
Al-12%Si	12.4	0.24	0.03	0.001	0.01	0.007	Rem.
Al-12%Si-1%Pb	11.9	0.24	0.03	1	0.01	0.007	Rem.
Al-12%Si-6%Pb	12.7	0.24	0.03	6	0.01	0.007	Rem.
Al-12%Si-12%Pb	12.1	0.24	0.03	12	0.01	0.07	Rem.
Al-12%Si-20%Pb	12.4	0.24	0.03	20	0.01	0.07	Rem.

I

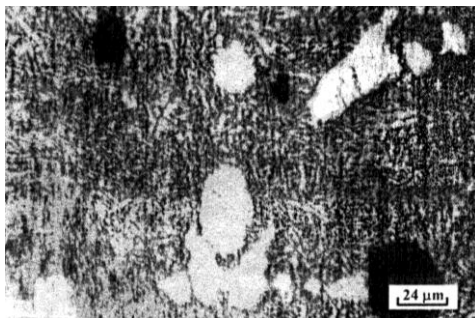
Chemical composition of pure aluminum, master alloy and prepared Al-Si-Pb alloys.



Al-12%Si



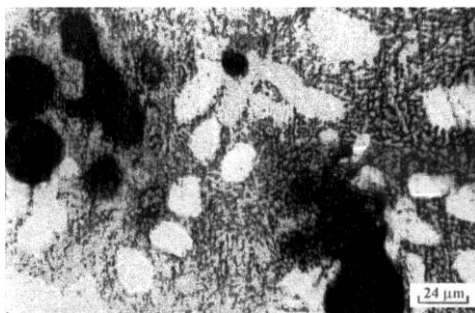
Al-12%Si-1%Pb



Al-12%Si-6%Pb



Al-12%Si-12%Pb



Al-12%Si-20%Pb

Figure 1 Microstructure of as-cast leaded modified eutectic aluminum-silicon alloys.

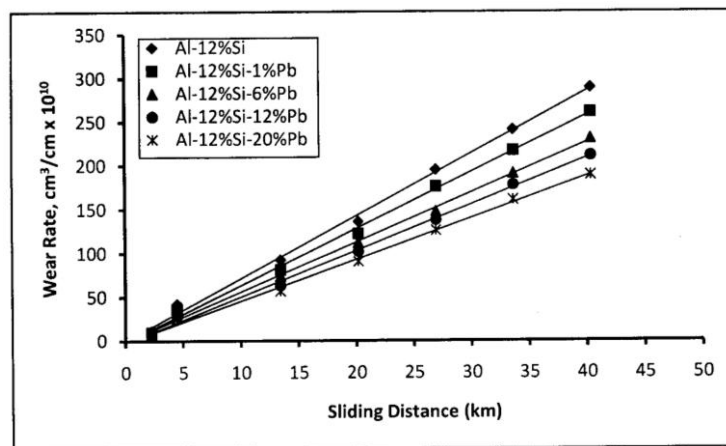


Figure 2 The relationship between sliding distance and wear rate of Al-Si-Pb alloys.

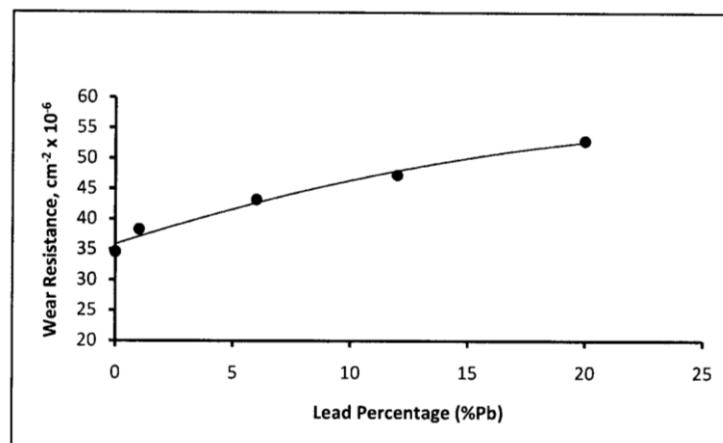


Figure 3 The relationship between lead percentage and wear resistance of Al-12%Si alloy. Sliding distance, 40.37 km.

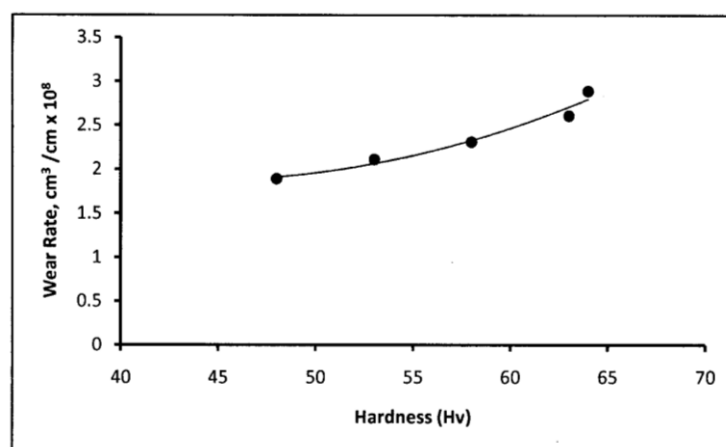


Figure 4 The relationship between hardness and wear rate of Al-Si-Pb alloys. Sliding distance, 40.37 km.

## DEPENDABLE DISCHARGES OF THE UPPER AND MIDDLE DIYALA BASINS

Haitham A. Hussein

Assist. Lecturer

Nahrain University \ College of engineering \ Dept. of Civil engineering

### ABSTRACT

The Diyala river is a major tributary of the Tigris river that runs through Iran and Iraq which drains an area of 32600 km<sup>2</sup>. The catchment area consist of four parts which are the area of the basin above Derbendi-Khan, Upper Diyala, Middle Diyala and lower Diyala. Through the last two decade the water coming to the upstream Derbendi-Khan reduced and this reduction reach to about 35%. This research focusing on the water dependable discharges reached to upper and middle Diyala river basin as compared with Russian study(water balance). The water balance mention that the discharge can be supplied the above basins with probability of 95% for the year (1947-1948). In this research consider the mean discharge down stream Derbendi-Khan dam for the period (1989-2007) in order to find the dependable probability for discharge which can be satisfied and equivalent to the water balance study .

In this research considered different probabilities (95%,80% and 50%) of each months (Oct-Sep) water year for the period (1989-2007) by using the empirical Wei Bull probability equation, and it was conclude that the probability of 50% can be considered the suitable probability for the water requirement to upper and middle basins.

### الخلاصة

يعتبر نهر دجلة واحد الروافد الرئيسية لنهر دجلة والذي ينبع من الأراضي الإيرانية والعراقية حيث تبلغ مساحة حوضه الكلي حوالي 32000 كلم<sup>2</sup>. ويمكن تقسيم الحوض إلى أربعة أجزاء , الحوض الواقع اعلى سد دربندخان والأخرى تباعا هي الحوض العالي والوسطي والسفلي. خلال فترة العقدين السابقين تظهر بان التصارييف القادمة قد قلت بحدود 35%. إن هذا البحث سوف يركز على التصارييف الواصلة إلى أعالي والوسطي لحوض نهر دجلة مقارنة مع دراسة الموازنة المائية (1982) المعدة من قبل الروس. إن دراسة الموازنة المائية اشارت بان التصارييف اللازمة للحوض أعلاه يمكن أن تكون باحتمالية 95% لسنة (1947-1948). في هذا البحث سوف يأخذ معدل التصارييف المطلقة بين سنة (1989-2007) وإمكانية إيجاد الاحتمالية المناسبة باستعمال معادلة وضعية من قبل Wei bull.

تم إيجاد احتمالية 95%,80% و 50% لمعدل التصارييف من سنة 1998-2007 ولكل شهر (تشرين الأول ولغاية شهر أيلول) حيث اتضح بان معدل التصارييف لاحتمالية 50% (1989-2007) هو الذي يمكن أن يعطي نتائج مقارنة لاحتمالية 95% (1947-1948) بموجب دراسة الموازنة المائية.

**KEY WORD:- Diyala River Basin****INTRODUCTION**

The Diyala river basin is a major tributary of the Tigris river and runs through Iran and Iraq drains an area of 32600 km<sup>2</sup>. The river basin are shown in figure (1). The character of the river basin verses widely from the semi-arid plans to the north of Baghdad at about 33 meter G.T.S where the average annual rainfall is only 140mm to the high mountainous of the west rain Iran where there are many peaks over 2500 meter rising the height 3370 meter G.T.S. in this region there are large area where the average annual precipitation exceed 1000 mm and the high peak are covered perennial snow . The area of these basin can be shown in table (1).

**Table 1.** Area of Diyala Basin (4)

	<b>Basin</b>	<b>Area km<sup>2</sup></b>
<b>1</b>	Above Derbendi-Khan dam	17900
<b>2</b>	Upper Diyala	3910
<b>3</b>	Middle Diyala	8850
<b>4</b>	Lower Diyala	1440
	<b>Total</b>	<b>32600</b>



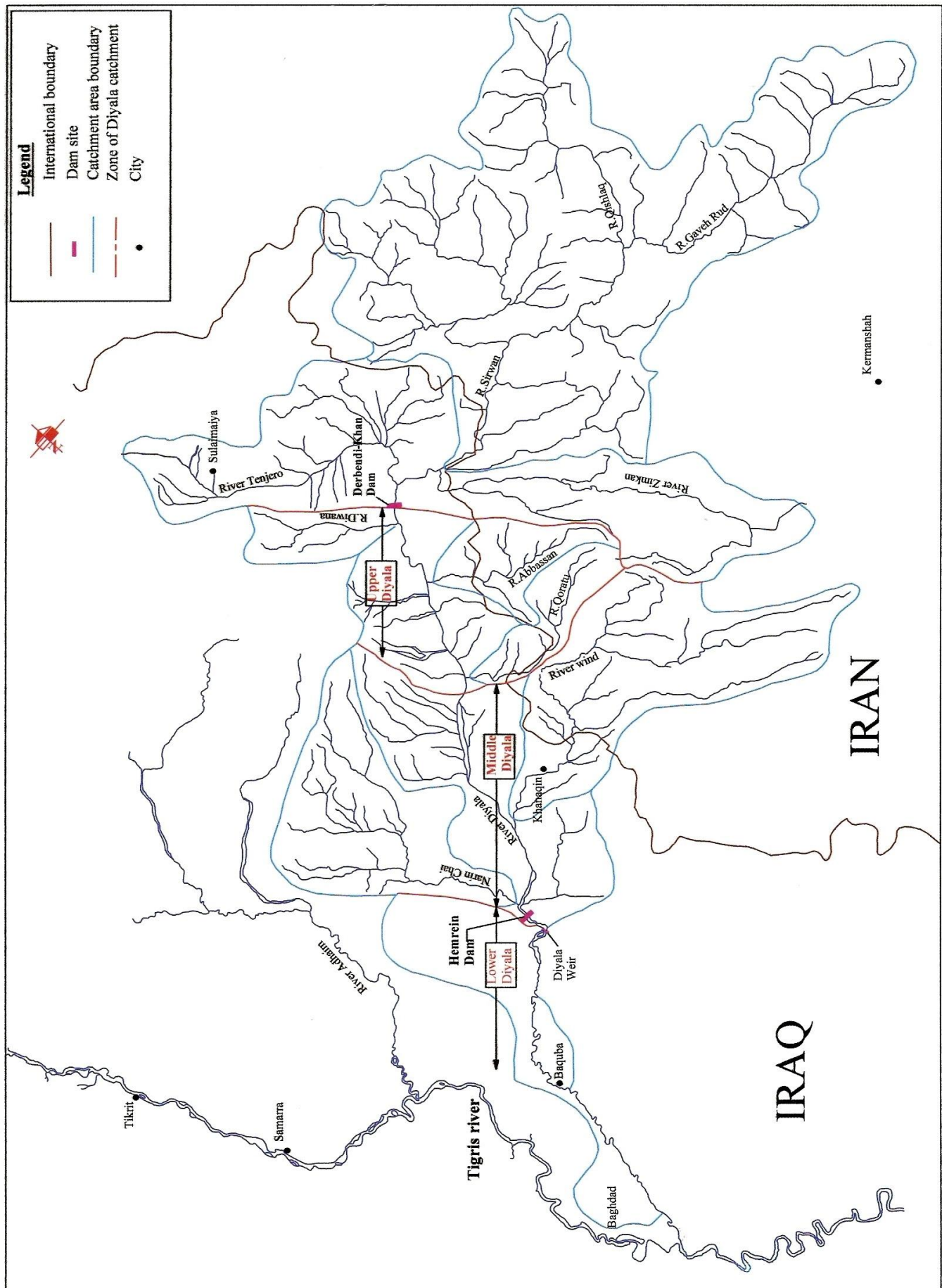


Fig. 1 Diyala River Basin (6)



The difference between two periods will be  $((6.4 - 4.14)/6.4) \times 100 = 35\%$ . Figure(2) and figure(3) shows the hydrograph of the two period. The water requirement for the year 2000 equal to  $3.87 \text{ km}^3$  as mentioned in the water balance (8) and this amount is less 6.8% than the average of the year (1989-2007) i.e. the water requirement for this region will need to increase 10% for each decade.

### **Discharge Down Stream Derbendi-Khan dam with 95% Probability**

This Research was worked by (8) experts for water resources and land development in Iraq (1982) which may called water balance and as referring to Diyala river basin they suggest three probabilities can be covered the requirement for upper and middle Diyala basin. Those probability are: 50% for the year (1935-1936), 80% for the year (1954-1955) and 95% for the year (1947-1948) and the mean discharge are  $103.67 \text{ m}^3/\text{sec}$ ,  $98.8 \text{ m}^3/\text{sec}$  and  $94.48 \text{ m}^3/\text{sec}$  respectively.

The study worked by (2) consider 95% probability for the upper and middle basin for the period (1947-1948) can be satisfied the requirement. Figure(4) shows the 95% for period (1947-1948).

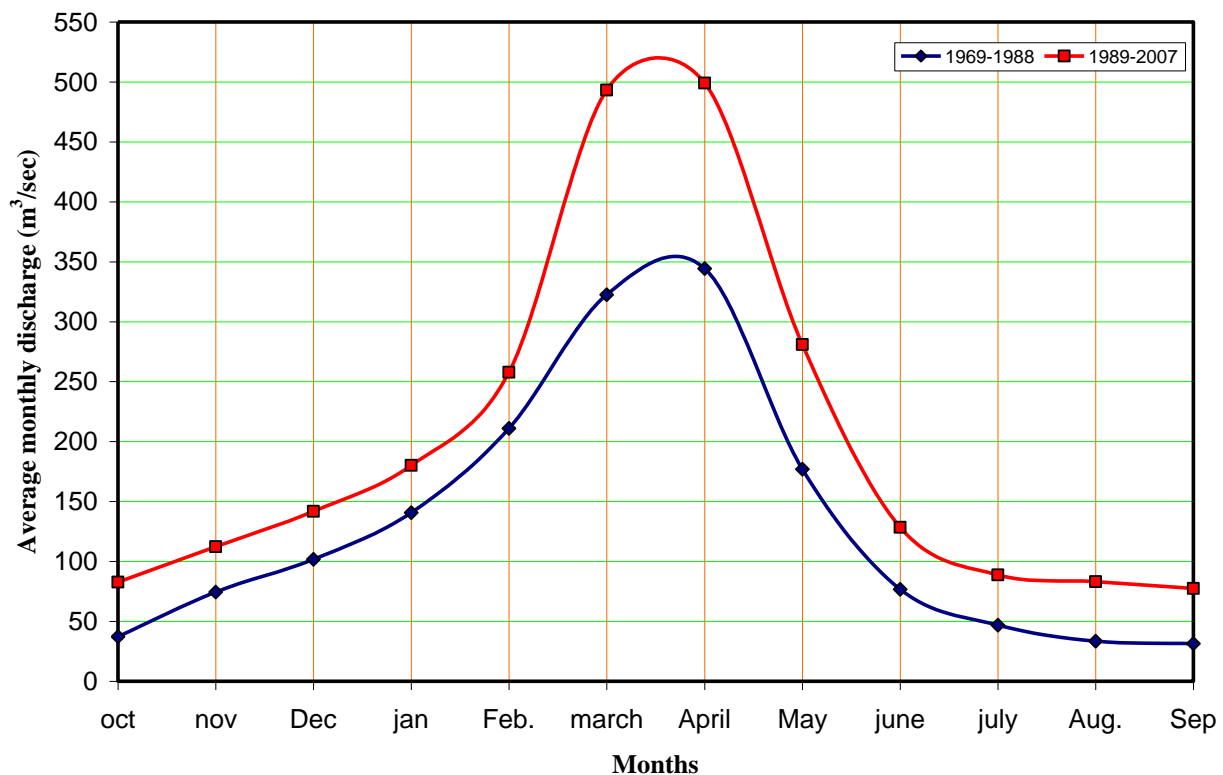


**Fig. 2** Monthly Average Discharge ( $\text{m}^3/\text{sec}$ ) for Upstream Derbendi-Khan Dam

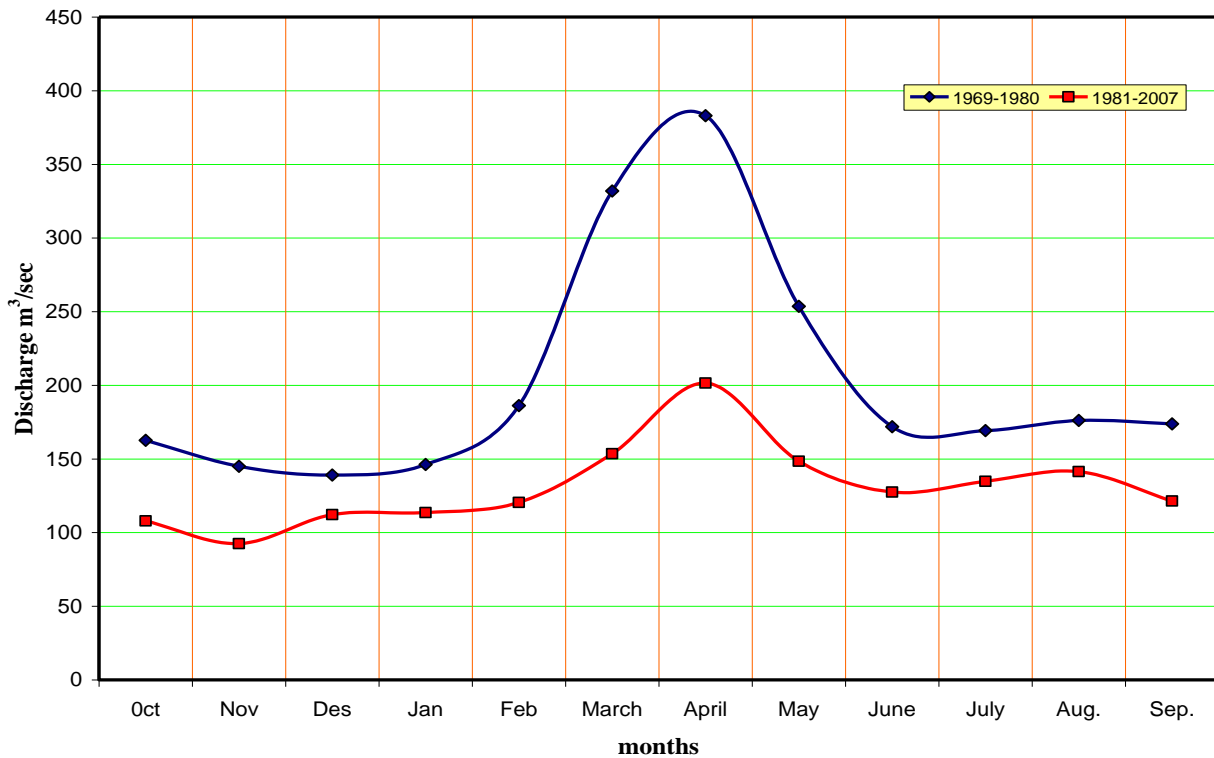


Fig. 3 Monthly Average Discharge ( $\text{m}^3/\text{sec}$ ) Down Stream Derbendi- Khan Dam flow.

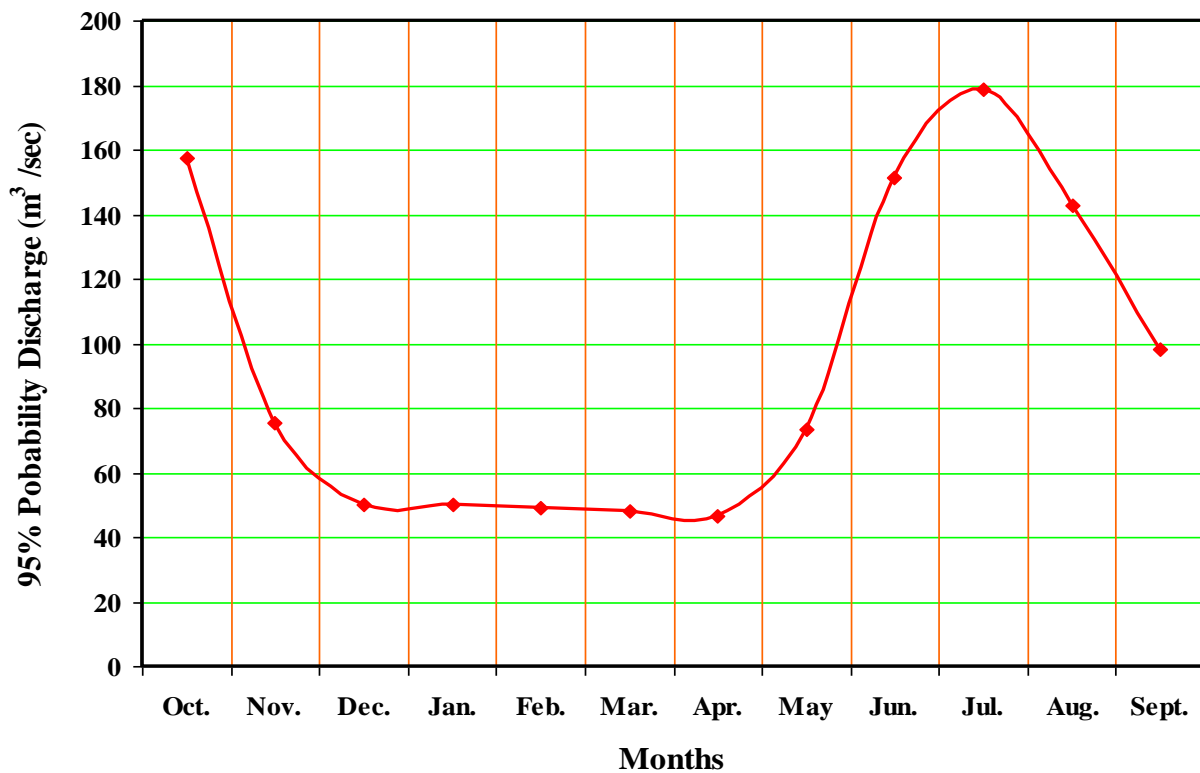


Fig. 4 95% Probability Discharge Downstream Derbendi-Khan for year 1947- 948(Water Balance).

### Probability for Discharge Downstream Derbendi-Khan dam for the period (1989-2007)

The analysis was consider the frequency percent for each month (water year) by using empirical Wei Bull probability equation (1) from October to September and find the probability of 95%,80% and 50% which can be shown in figure(5),(6) and (7). The average yearly flow for these probability are 38, 59.52 and 101 m<sup>3</sup>/sec respectively. Naturally the mean discharge of 101 m<sup>3</sup>/sec of probability 50% can be satisfied the requirement of upper and lower basin.

The 50% dependable discharge downstream Derbendi-Khan dam are shown in the following table (2) which the coefficient of variation  $C_v$  which can indicate large time variation and distribution.

$$P_m = \frac{m}{1+n} \quad (1)$$

Where:

$P_m$  : Frequency of recurrence of a certain term of the series

$m$  : Number carried by the term of the descending series.

$n$  : Number of the term in the series.

$p = \frac{1}{T}$  , T=Recurrence interval of return period.

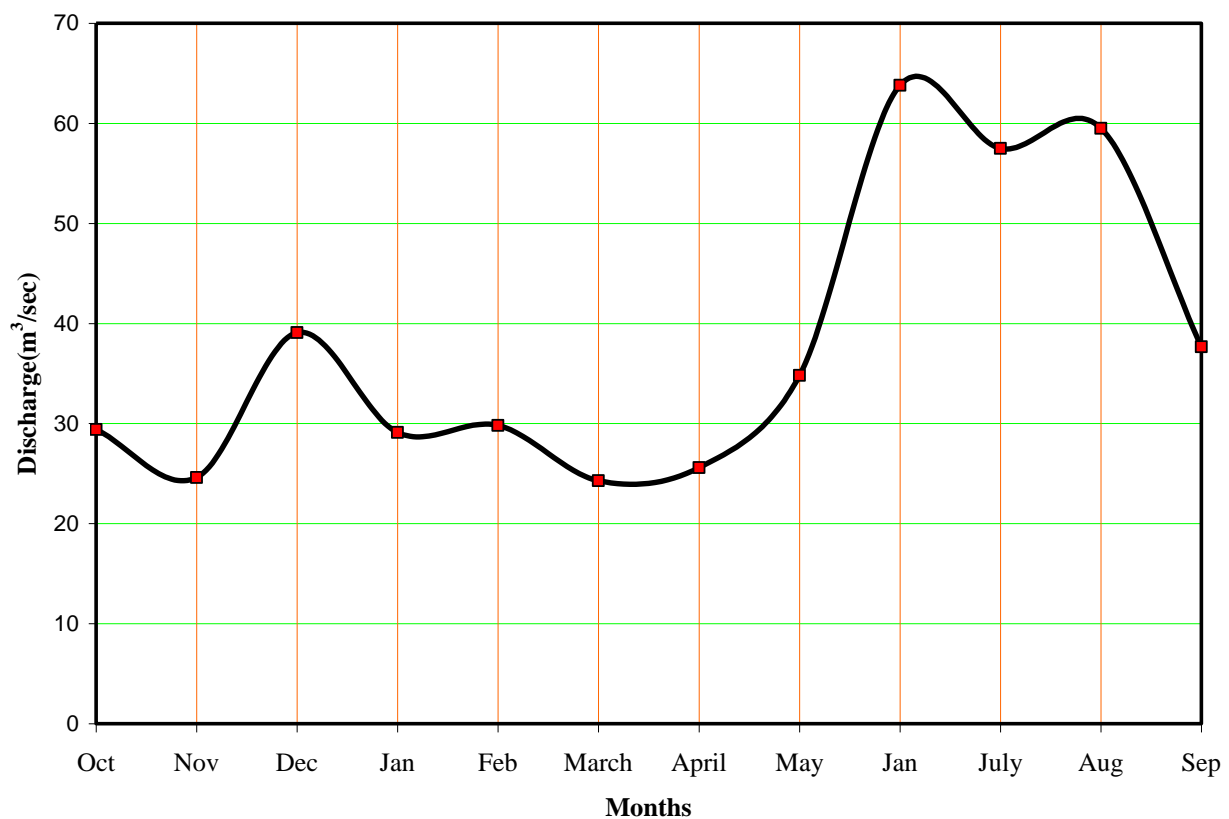


**Fig. 5** 95%Probability Average Discharge Derbendi-Khan (1989-2007).

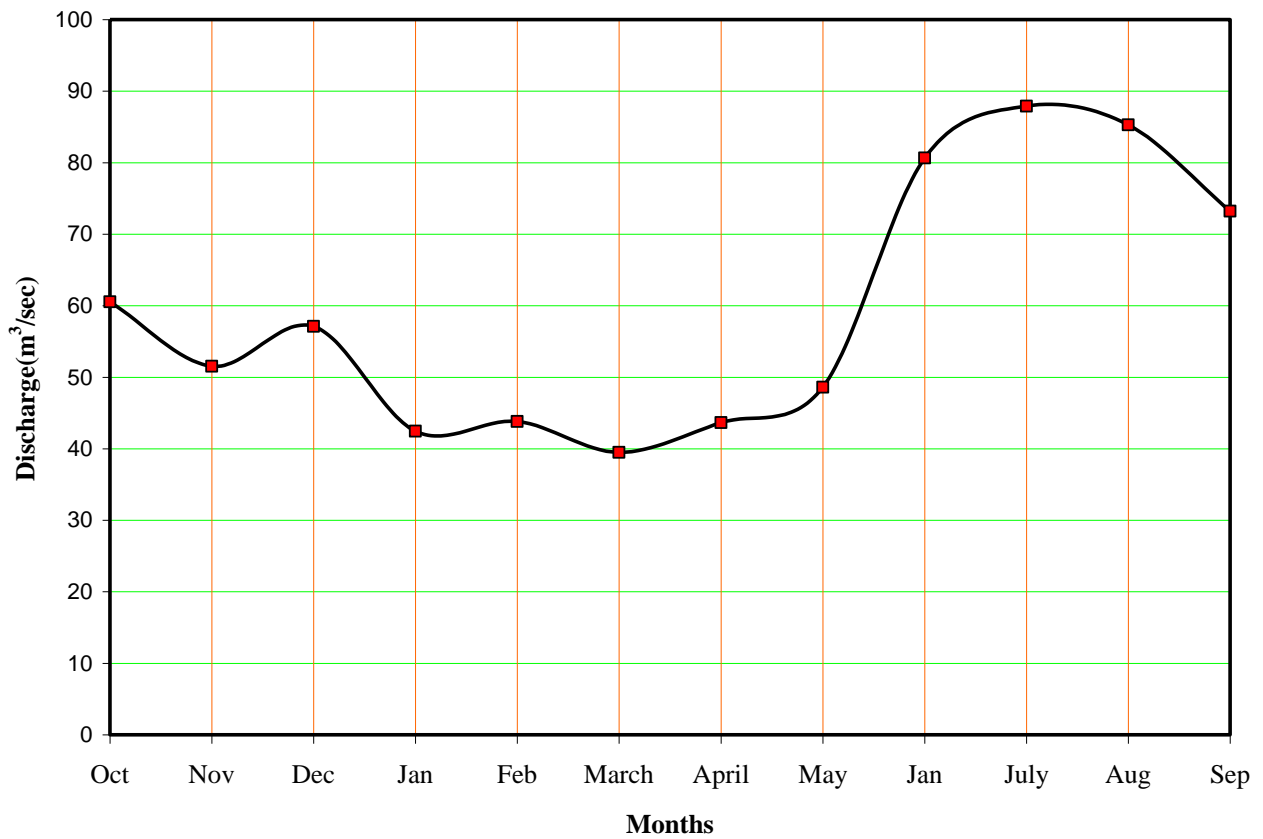


**Fig. 6** 80%Probability Average Discharge Derbendi-Khan (1989-2007).

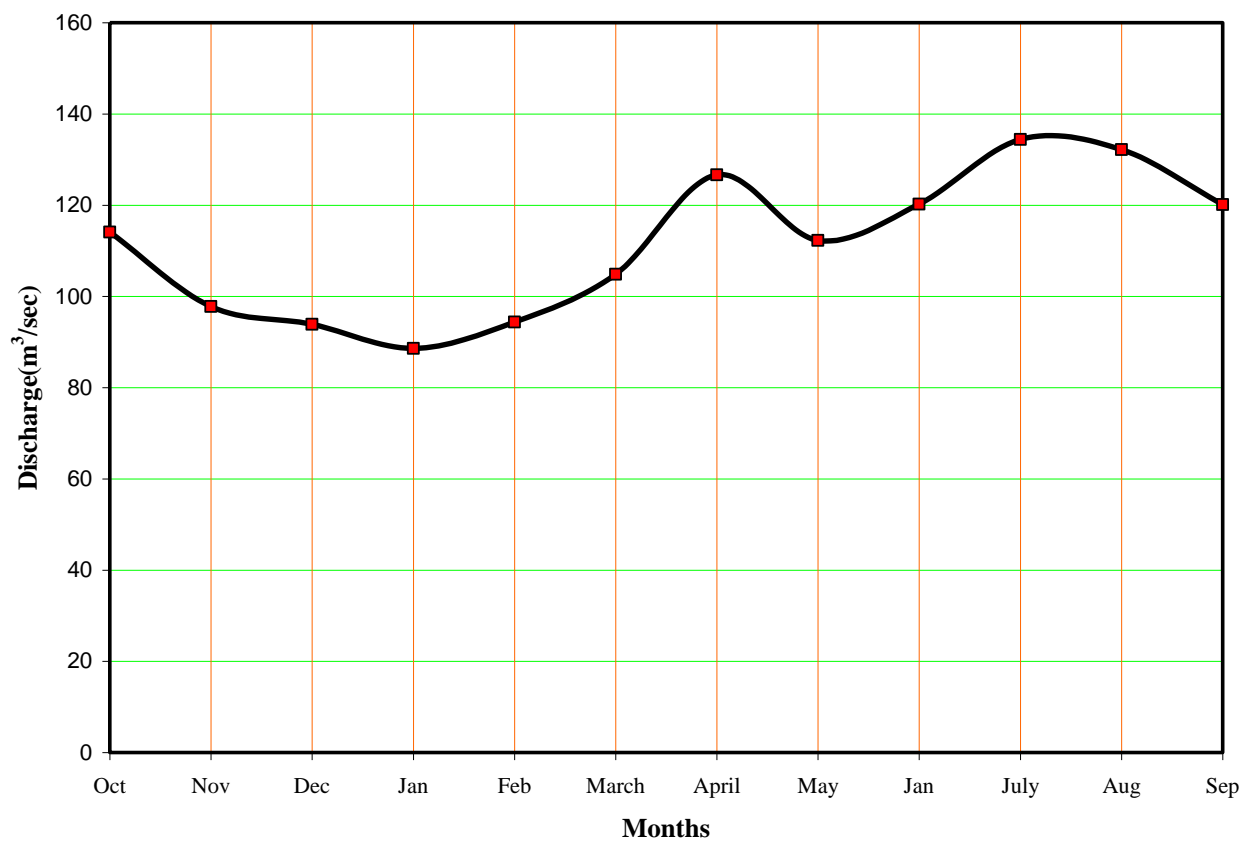


**Fig. 7** 50%Probability Average Discharge Derbendi-Khan (1989-2007).

**Table 2.** 50% Dependable Discharge Down Stream Derbedi-Khan dam

Month	Mean discharge m <sup>3</sup> /sec	Standard deviation ( $\sigma$ )	Coefficient of variation ( $C_v$ )	Skew coefficient ( $C_s$ )	Dependable discharge m <sup>3</sup> /sec 50% probability
Oct	107.95	43.63	0.404	-0.387	114.1
Nov	92.53	38.37	0.415	-0.418	97.8
Dec	111.84	55.89	0.499	0.756	93.9
Jan	111.79	79.58	0.711	1.447	88.6
Feb.	120.36	87.53	0.727	1.335	94.4
March	153.53	138.23	0.900	1.566	104.89
April	201.52	210.48	1.044	1.83	126.66
May	148.47	114.09	0.77	1.628	112.26
June	127.42	48.69	0.382	0.066	120.24
July	135.36	44.84	0.331	-0.116	134.38
Aug.	141.42	57.06	0.403	0.648	132.2
Sep.	120.73	47.02	0.389	0.213	120.10

### Water Requirement Down Stream Derbendi-Khan Dam

The water released downstream Derbendi-Khan dam will be shared different project located between down stream Derbendi-Khan dam and Hemrein dam. The main project are Shaik-Langer, Balajo Khanaqin, Qara Tappe, Jalawla and Al-Saadia.

The total water requirement for those project at maximum and minimum water requirement as mentioned in the water balance can be shown in the table (3) below. The maximum discharge in July and the minimum discharge are in January.

**Table 3.** Minimum Discharge required is in January and Maximum Discharge is in July

Name of project	Water requirement for January		Water requirement for July	
	Vol. Million m <sup>3</sup>	Discharge m <sup>3</sup> /sec	Vol. Million m <sup>3</sup>	Discharge m <sup>3</sup> /sec
Shaik-Langer	0	0	6.2	2.31
Balajo Khanaqin	0.26	0.1	16.16	6.03
Qara Tappah	0.59	0.22	24.7	9.22
Jalawla	0.09	0.034	3.90	1.46
Al-Saadia	0.11	0.041	10.78	4.03
<b>Total</b>	<b>1.05</b>	<b>0.395</b>	<b>61.74</b>	<b>23.05</b>

The maximum and minimum discharge for 50% probability of the period (1989-2007) can cover the water requirement of the project between Derbendi-Khan dam and upstream Hemrein dam. Figure (8),(9) show the water requirement for the above project during the year.

## CONCLUSIONS

The result of this research indicate the following conclusions

- There is reduction in discharge downstream Derbendi-Khan dam with 35% during about two decade.
- The existing discharge for the period (1981-2007) can be satisfy the discharge of Diyala river which 50%probability in order to be equivalent to the probability of 95%(1947-1948) worked by water balance.

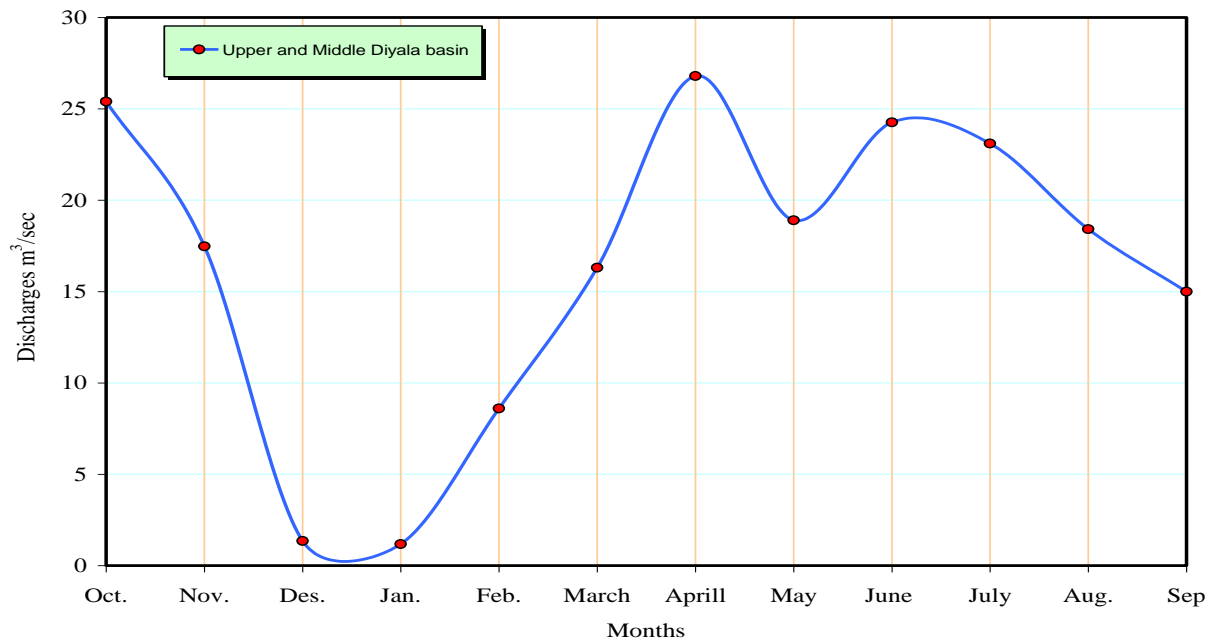


**Fig. 8** Mean Flow Discharge for D/S Derbindi-Khan and Hemreen Dam for the Period (1989-2007)

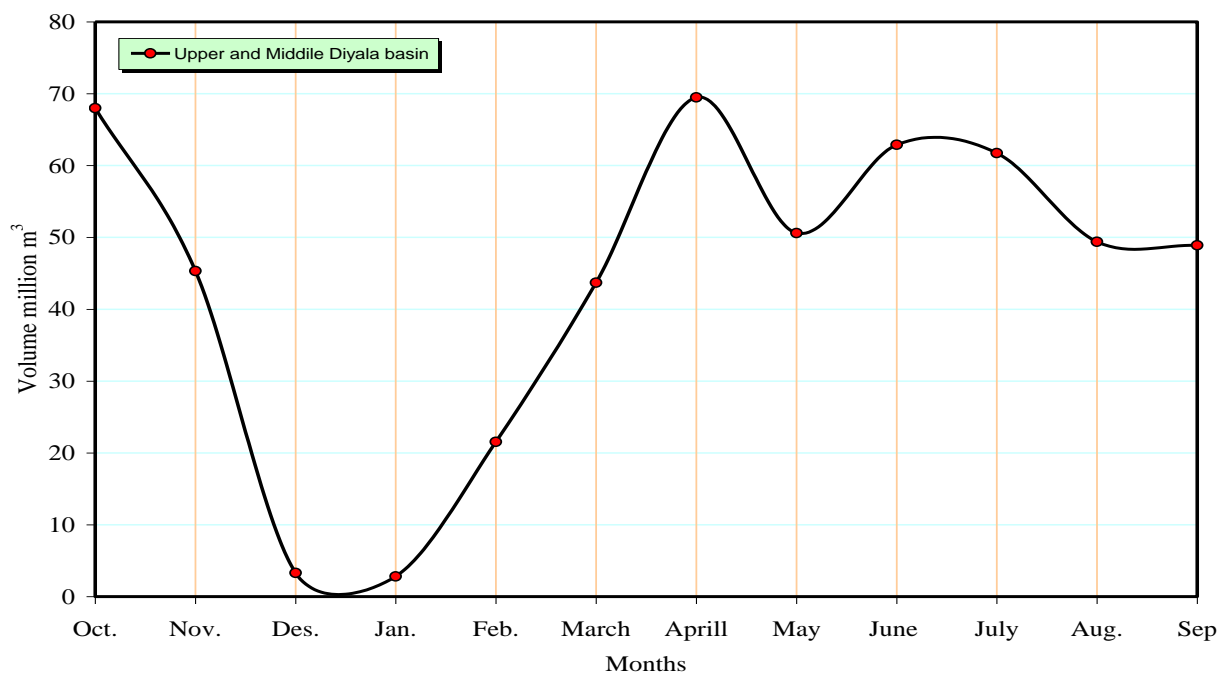


**Fig. 9** Water Requirement for Diyala Basin (Million  $m^3$ )

**REFERENCES**

- 1- Arora , K.R. Irrigation , Water Power and Water Resources Engineering , Standard Publishers Distributors ,Delhi . (2008)
- 2- Al-Furat Center for Studies and Design of Irrigation Project Part 1, Balajo Khanaqeen Irrigation Project (1989).
- 3- Dr.Alanssary Hydrological Studies and Sedimentation in Diyala River, Vol.3, University of Baghdad (Arabic Print)
- Harza Engineering Company Chicago and Binni, Deacon Amd Gourly, London Hydrological Survey of Iraq, (1963).
- Hydrological National Water Resource Center/ Water Control Dep. data for Discharge and Elevation to Derbendi-Khan dam.
- M.Macdonald Consulting Engineering, Diyala and Middle Tigris Project Report No.7 River Diyala Hydrology and Flood Control (1975).
- Richard A.Johnson, Gouri K.Bhattacharyya Statistics: Principle and Methods. Fifth Edithion.(2006).
- Selkhoz Pron Export U.S.S.R.General Scheme of Water Resource and Land Development in Iraq, (1982).
- Ven Te Chow Hand Book of Applied Hydrology (1973).

**SYMBOLS**

G.T.S: Greater Trigonometric Survey base for leveling in Iraq



## PARALLEL FUZZY LOGIC CONTROLLER IMPLEMENTATION USING MPICH2

By

Prof. Dr. Bakir A.R. AL-Hashemy  
Electrical Engineering Department  
Baghdad University

AboTalib H. Mahfoodh  
Electrical Engineering Department  
Baghdad University

### ABSTRACT

In this work FLC program is implemented using C++ codes. Two implementations are presented one with the rules stored inside the program, the other with rules in a rulebase file. The execution times of these two implementations, along with MATLAB FLC implementation, are compared using different simulated FLCs. Furthermore, to reduce the rulebase searching time, a parallel FLC is implemented using C++ and MPI (Message Passing Interface). The MPICH2 package is used to run the parallel FLC. A cluster of four computers is used as the parallel environment. The execution time of this FLC program is evaluated using servomotor, Anti Skid System, and other simulated applications. The speedup and efficiency are studied using different number of computers. The results show that decomposing the rulebase searching operation to more than a computer reduce the execution time significantly.

### الخلاصة

في هذا العمل برنامج FLC يكتب في سي ++. هناك طريقتين لتطبيق هذا البرنامج، واحد بالقواعد مخزونة داخل البرنامج، الآخر بالقواعد مخزونة في ملف. إنّ أوقات تنفيذ هذه التطبيقات، سوية مع تطبيق ال MATLAB، تقارن بإستعمال أنظمة FLC مختلفة. بالإضافة إلى ذلك، لتخفيض وقت البحث في ملف القواعد، ينفذ FLC متوازي بإستعمال سي ++ و MPI (وصلة مرور رسالة). رزمة MPICH2 تستعمل لتنفيذ ال FLC المتوازي. البيئة المتوازية عبارة عن عنقود من أربع حاسبات متصلة في شبكة واحدة. يقيم وقت التنفيذ بإستعمال نظام FLC لمحرك توازي، نظام ضد التزلج، وتطبيقات وهمية أخرى. إنّ التعجيل والكفاءة تدرس بإستعمال عدد مختلف من الحاسبات. النتائج تدل بأنه تجزئة عملية البحث في ملف القواعد إلى أكثر من حاسوب يخفّض وقت التنفيذ بشكل ملحوظ. \

**KEY WORDS:** Fuzzy Logic, Fuzzy Logic Controller, Parallel Computing, MPI.

### INTRODUCTION

Nowadays, the areas where Fuzzy Control has been applied comprise a wide variety of applications, with different complexities and performance. Fuzzy Controllers can be found in washing machines, automatic focusing for video cameras, automatic TV tuner, servo motor control, automotive anti-skid brake, and many other consumer appliances. The application of Fuzzy Logic exceeds the control domain since it is also employed for others knowledge-based decision making tasks. Among the latter, medical diagnosis, business forecasting, traffic control, network management, image processing, signal processing, computer vision, geology, and many more [1].

**Table 1** covers a range of research areas related to Fuzzy Logic as reported in the IEEE 2001 International Conference on Fuzzy Systems [1].



**Table 1** Main Research areas in Fuzzy Logic (FUZZ-IEEE 2001)

Research area	Main Topics
Fuzzy Mathematics	Foundations of fuzzy logic, approximate reasoning, evolutionary computation, identification and learning algorithms, rule base optimization.
Control systems	Fuzzy control theory and applications, process and environmental control, stability criterions issues, multilevel supervisory control.
Pattern recognition and image processing	Supervised and unsupervised learning, classifiers design and integration, signal/image processing and analysis, computer vision, multimedia applications.
Soft computing and hybrid system	Intelligent information systems, database systems, data mining, intelligent agents, reliability engineering, Nero-Fuzzy systems, internet computing, networks traffic modeling and control.
Electronic systems	Fuzzy hardware implementation and embedded applications.
Robotic and Automation	Fuzzy logic in robotics, industrial automation and other industrial applications.

There is rapid increasing in number of applications of FL (Fuzzy Logic), in the domain of Image Processing, Signal Processing and Power Electronics that have been reported in the last decade. Most of them need real-time processing, fast transient behavior, low-power consumption and/or autonomy. In such cases, an effective implementation is required. Implementing these applications on parallel computer can have direct effect on the system efficiency.

A parallel computer is a set of processors that are able to work cooperatively to solve a computational problem. This definition is broad enough to include parallel supercomputers that have hundreds or thousands of processors, networks of workstations, multiple-processor workstations, and embedded systems. The need for faster computers is driven by the demands of both data-intensive applications in commerce and computation-intensive applications in science and engineering [2].

In 1986 Gupta, Forgy, Newell, and Wedig [3] stated that Rule-based systems, appear to be capable of exploiting large amounts of parallelism. It is possible to match each rule to the data memory in parallel. In practice, however, they have showed that the speed-up from parallelism is quite limited, less than 10-fold. Howard, Taylor, and Allinson [4] presented Cellular automata (CA) mechanisms. York Fuzzy Automata Machine (FAMe) is a massively parallel fuzzy CA machine. They have described the structure of the Fuzzy Automata Machine and showed how large, complex fuzzy parallel systems may be constructed in consequence. Lees, Campbell, and Devlin [5] presented an application specific parallel rule inference architecture which is capable of performing an entire rule inference within one clock cycle. The design is targeted for high capacity Complex Programmable Logic Devices (CPLDs), whose ability to be reconfigured allows the application specific rule structure to be practical for real world systems.

In this work different type of FLC implementation were provided to reduce the execution time of an FLC program. An efficient FLC algorithm is designed, and implemented in C++. Complex FLC programs spend long time in searching the rulebase for fired rules. To decrease the program execution time, parallel FLC algorithm is designed and implemented in C++ using MPICH2 (Message Passing Interface Chameleon) package. MPICH2 is used to manage and

distribute the jobs over computers. The parallel FLC algorithm decreases the execution time by decomposing the rulebase searching operation into more than a task that can be done concurrently. Since minimum execution time is desired, number of computers in the parallel environment should be determined precisely to obtain the desired execution time.

## \* FUZZY LOGIC CONTROLLERS

The concept of FL was conceived by L. Zadeh [6] in 1965, and presented not as a control methodology, but as a way of processing data by allowing partial set membership rather than crisp set membership or non-membership. This approach to set theory was not applied to control systems until the 70's due to insufficient small-computer capability prior to that time.

### 2.1 Fuzzy Logic Controller Structure

The kind of a structure a fuzzy logic controller (FLC) will have, primarily depend on the controlled process and the demanded quality of control. Since the application area for fuzzy control is really wide, there are many possible controller structures, some differing significantly from each other by the number of inputs and outputs, or less significantly by the number of input and output fuzzy sets and their membership functions forms, or by the form of control rules, the type of inference engine, and the method of defuzzification. All that variety is at the designer's disposal, and it is up to the designer to decide which controller structure would be optimal for a particular control problem [7].

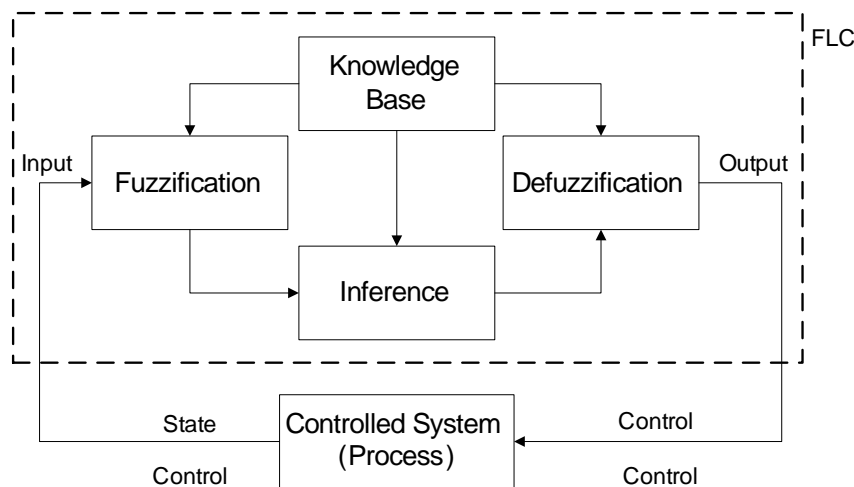


Fig. 1 The FLC structure.

The basic configuration of FLC is shown in **Fig. 1**. The configuration consists of four main components: fuzzification, knowledge base, Inference, and defuzzification [8].

- The fuzzification transforms input crisp values into fuzzy values and it involves the following functions.
  - a. Receives the input values,
  - b. Transforms the range of values of input variable into corresponding universe of discourse,
  - c. Converts input data into suitable linguistic values (fuzzy sets). This part is necessary when input data are fuzzy sets in the fuzzy inference.
- The knowledge base contains knowledge of the application domain and the control goals. It consists of the rulebase.
- The inference performs the following functions:

- simulates the human decision-making procedure based on fuzzy concepts,
- d. Infers fuzzy control actions employing fuzzy implication and rules.
- The defuzzification involves the following functions
- e. A scale mapping which converts the range of output values into corresponding universe of discourse
- f. Defuzzification which yields a non-fuzzy control action from an inferred fuzzy control action.

### **Design Procedure of Fuzzy Logic Controller**

- To design an FLC, bellow procedure can be followed [8]:
- Determination of state variables and control variables: In general, the control variable is determined depending on the property of process to be controlled. The state variables should be selected. In general, state, state error and error difference are often used. The state variables are input variables, and the control variables are output of the controller to be developed.
- Determination of inference method: one of the inference methods can be selected. The decision is dependent upon the properties of process to be studied.
- Determination of fuzzification method: It is necessary to study the property of measured data of state variables. If there is uncertainty in the data, the fuzzification is necessary, and the fuzzification method and membership functions of fuzzy sets should be selected. If there is no uncertainty, singleton state variables can be used.
- Discretization and normalization of state variable space: In general, it is useful to use discretized and normalized universe of discourse.
- Partition of variable space: The state variables are input variables of the controller and thus the partition is important for the structure of fuzzy rules. At this step, partition of control space (output space of the controller) is also necessary.
- Determination of the shapes of fuzzy sets: It is necessary to determine the shapes of fuzzy sets and their membership functions for the partitioned input spaces and output spaces.
- Construction of fuzzy rule base: Control rules can be built now. The variables and corresponding linguistic terms in antecedent part and consequent part of each rule are determined. The architecture of rules is dependent upon the inference method determined in step 2.
- Determination of defuzzification strategy: In general, the crisp control values are used and thus a defuzzification method should be determined.
- Test and tuning: It is almost impossible to obtain a satisfactory fuzzy controller without tuning. In general it is necessary to verify the controller and tune it until satisfactory results are achieved.

### **Complex Fuzzy Logic Controller**

The size of the fuzzy rulebase depends on the number of fuzzy rules, while the number of fuzzy rules depends on the number of inputs and on the number of linguistic values (fuzzy sets) associated with each of the variables [7].

In the case of having many input and output variables, it is efficient to parallelize and to inference many fuzzy rules simultaneously. For example for a system with five input variables, respectively the number of total rules are 16,807 ( $= 7^5$ ) assuming that the number of the linguistic variables for each fuzzy variable is 7 [9].



## \* PARALLEL COMPUTING

### Introduction

The past decade has seen tremendous advances in microprocessor technology. Clock rates of processors have increased from about 40 MHz (e.g., a MIPS R3000, circa 1988) to over 3.0 GHz (e.g., a Pentium 4, Intel 2006). At the same time, processors are now capable of executing multiple instructions in the same cycle. The average number of cycles per instruction (CPI) of high end processors has improved by roughly an order of magnitude over the past 10 years. All this translates to an increase in the peak floating point operation execution rate (floating point operations per second, or FLOPS) of several orders of magnitude. Even though it is expected that technology development will be continue to hold for the near future, there is a limit that will eventually be reached. The most easily understood physical limit is that imposed by the finite speed of signal propagation along a wire. This is sometimes referred to as the speed-of-light argument (or limit). The speed-of-light argument suggests that once the above limit has been reached, the only path to improve performance is the use of multiple processors [10].

The motivations for parallel processing can be summarized as follows:

1. Higher speed, or solving problems faster. This is important when applications have "hard" or "soft" deadlines. For example, there is at most a few hours of computation time to do 24 hour weather forecasting or to produce timely tornado warnings.
2. Higher throughput, or solving more instances of given problems. This is important when many similar tasks must be performed. For example, banks and airlines, among others, using transaction processing systems that handle large volumes of data.
3. Higher computational power, or solving larger problems. This would allow the use of very detailed, and thus more accurate, models or to carry out simulation runs for longer periods of time (e.g., 5-day, as opposed to 24-hour, weather forecasting).

The ultimate efficiency in parallel systems is to achieve a computation speedup factor of  $p$  with  $p$  processors. Although in many cases this ideal cannot be achieved, some speedup is generally possible. The actual gain in speed depends on the architecture used for the system and the algorithm executed on it [10].

### Parallelism Type Classification

Parallel computers can be divided into two main categories of control flow and data flow. In 1966, M. J. Flynn [10] proposed a four-way classification of computer systems based on the notions of instruction streams and data streams. Flynn's classification has become standard and is widely used. Flynn coined the abbreviations Single Instruction Single Data (SISD), Single Instruction Multiple Data (SIMD), Multiple Instruction Single Data (MISD), and Multiple Instruction Multiple Data (MIMD) for the four classes of computers shown in **Fig. 2**, based on the number of instruction streams (single or multiple) and data streams (single or multiple). The SISD class represents ordinary "uni-processor" machines [10].

Computers in the SIMD class, with several processors directed by instructions issued from a central control unit, are sometimes characterized as "array processors." Machines in the MISD category have not found widespread application, but one can view them as generalized pipelines in which each stage performs a relatively complex operation (as opposed to ordinary pipelines found in modern processors where each stage does a very simple instruction-level operation). The MIMD category includes a wide class of computers. For this reason, in 1988, E. E. Johnson [10] proposed a further classification of such machines based on their memory structure (global or distributed) and the mechanism used for communication/synchronization (shared variables or message passing). Again, one of the four categories (GMMP) is not widely used.

The GMSV class is what is loosely referred to as (shared-memory) multiprocessors. At the other extreme, the DMMP class is known as (distributed-memory). Finally, the DMSV class, combining the implementation ease of distributed memory with the programming ease of the shared-variable scheme, is sometimes called distributed shared memory. When all processors in a MIMD-type machine execute the same program, the result is sometimes referred to as single-program multiple data [10]. The parallel environment in this work falls into the DMMP section of the MIMD category.

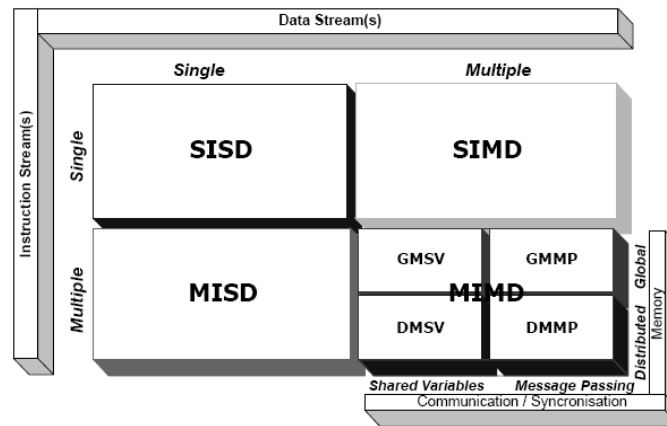


**Fig 2** The Flynn-Johnson classification of computer systems.

### Parallel algorithm design

Algorithm development is a critical component of problem solving using computers. A sequential algorithm is essentially a recipe or a sequence of basic steps for solving a given problem using a single computer. Similarly, a parallel algorithm is a recipe that tells how to solve a given problem using multiple computers or processors. However, specifying a parallel algorithm involves more than just specifying the steps. At the very least, a parallel algorithm has the added dimension of concurrency and the algorithm designer must specify sets of steps that can be executed simultaneously. This is essential for obtaining any performance benefit from the use of a parallel computer. In practice, specifying a nontrivial parallel algorithm may include some or all of the following [8]:

- Identifying portions of the work that can be performed concurrently.
- Mapping the concurrent pieces of work onto multiple processes running in parallel.
- Distributing the input, output, and intermediate data associated with the program.
- Managing accesses to data shared by multiple processors.
- Synchronizing the processors at various stages of the parallel program execution.
- Typically, there are several choices for each of the above steps, but usually, relatively few combinations of choices lead to a parallel algorithm that yields performance adequate with the computational and storage resources employed to solve the problem. Often, different choices yield the best performance on different parallel architectures or under different parallel programming paradigms [8].

The process of dividing a computation into smaller parts, some or all of which may potentially be executed in parallel, is called *decomposition*. *Tasks* are programmer-defined units of computation into which the main computation is subdivided by means of decomposition. Simultaneous execution of multiple tasks is the key to reducing the time required to solve the entire problem. Tasks can be of arbitrary size, but once defined, they are regarded as indivisible units of computation. The tasks into which a problem is decomposed may not all be of the same size [8].

The tasks, into which a problem is decomposed, run on physical processors. The term process is used to refer to a processing or computing agent that performs tasks. The term process does not adhere to the rigorous operating system definition of a process. Instead, it is an abstract

entity that uses the code and data corresponding to a task to produce the output of that task within a finite amount of time after the task is activated by the parallel program. During this time, in addition to performing computations, a process may synchronize or communicate with other processes, if needed. In order to obtain any speedup over a sequential implementation, a parallel program must have several processes active simultaneously, working on different tasks. The mechanism by which tasks are assigned to processes for execution is called *mapping*. A good mapping should seek to maximize the use of concurrency by mapping independent tasks onto different processes, it should seek to minimize the total completion time by ensuring that processes are available to execute the tasks on the critical path as soon as such tasks become executable, and it should seek to minimize interaction among processes by mapping tasks with a high degree of mutual interaction onto the same process. In most nontrivial parallel algorithms, these tend to be conflicting goals [8].

### **- Performance Indices of Parallel Computation**

To measure the performance of parallel computation some performance indices have been defined. Due to the level of complexity involved, no single measure of performance can give a truly accurate measure of a computer systems performance. Different indices are needed to measure different aspect. Some indices for global measurements are as follow [9]: (for more information about parallel algorithm performance indices refer to [10; 12]).

- Execution time: the execution time measures the time required to run the program, in this work it is the time it takes since the inputs are ready until the output is calculated.

- Speedup ( $S_p$ ): The speedup factor of a parallel computation using  $p$  processors is defined as the ratio:  $S_p = \frac{T_1}{T_p}$  Where  $T_1$  is the time taken to perform the computation on one processor and  $T_p$

is the time taken to perform the same computation on  $p$  processors. Normally the speedup factor is less than the number of processors because of the time lost to synchronization, communication time, and other overheads required by the parallel computation:  $1 \leq S_p \leq P$ .

However as mentioned before there are some cases where this does not apply.

- Efficiency ( $E_p$ ): The efficiency of a parallel computation is defined as the ratio between the speedup factor and the number of processors:  $E_p = \frac{S_p}{P} = \frac{T_1}{PT_p}$  Efficiency is a measure of the

cost-effectiveness of computations.

- Fired rules job: is the task of checking a rule to see if it is a fired rule or not, and if it is a fire rule, calculating its strength.
- Communication overhead or time: is the time it takes to transfer the required data between computers.

## **\* FUZZY LOGIC CONTROLLER IMPLEMENTATION**

### **Introduction**

There are different FLC implementation methods. Deciding which method is best appropriate for a plant depends on several parameters like plant circumstances, cost, execution time, performance, etc. Among FLC implementation classifications are stand alone hardware implementation and software implementation on a computer [13].

In this work C++ code is used to program a general FLC, with few changes, any type of FLC can be achieved. Visual Studio .NET 2003 [14] is used to compile the codes. FLC program have two types, one with the rules implemented inside the program and the other with rules stored in a rulebase file. These two types implementation are compared with FLC implementation using

MATLAB Fuzzy Toolbox. Finally to decrease the program execution time a parallel FLC algorithm is designed and implemented using MPICH2.

### **Serial FLC Algorithm**

The flowchart of the serial FLC algorithm is shown in **Fig. 3**.

Three FLC programs (MATLAB, C++ Type 1 (Rules stored inside the program), and C++ Type 2 (Rules stored in a file on Hard Disk)) are used to test the design. The execution time is the time difference between the time that output is ready and the time of applying inputs. 500 random inputs used to determine the average execution time.

To evaluate the serial FLC algorithm, a serial FLC for servomotor is implemented. The servomotor process shows nonlinear properties, and thus the fuzzy logic control is applied to the motor control. The task of the control is to rotate the shaft of the motor to a set point without overshoot. The set point and process output is measured in degree [8]. State variables (input variable of controller):

Error equals the set point minus the process output (e):  $e(k) = \theta_r(k) - \theta(k)$

While  $\theta$  is the shaft position,  $\theta_r$  is the shaft set point.

Change of error (ce) equals the error from the process output minus the error from the last process output:  $ce(k) = \frac{\theta(k) - \theta(k-1)}{\tau}$

Control variable (output variable of the controller): Control input (v) equals the voltage applied to the process.

FLC for servomotor has two inputs and 22 rules provided by the expert.

- If e is PB and ce is any, then v is PB.
- If e is PM and ce is NB, NM, or NS, then v is PS.
- If e is ZE and ce is ZE, PS, or PM, then v is ZE.
- If e is PS and ce is NS, ZE, or PS, then v is ZE.
- If e is NS and ce is NS, ZE, PS, or PM, then v is NS
- If e is NS or ZE and ce is PB, then v is PS.

The execution time of the serial FLC for servomotor on MATLAB and C++ are shown in Fig. 4.

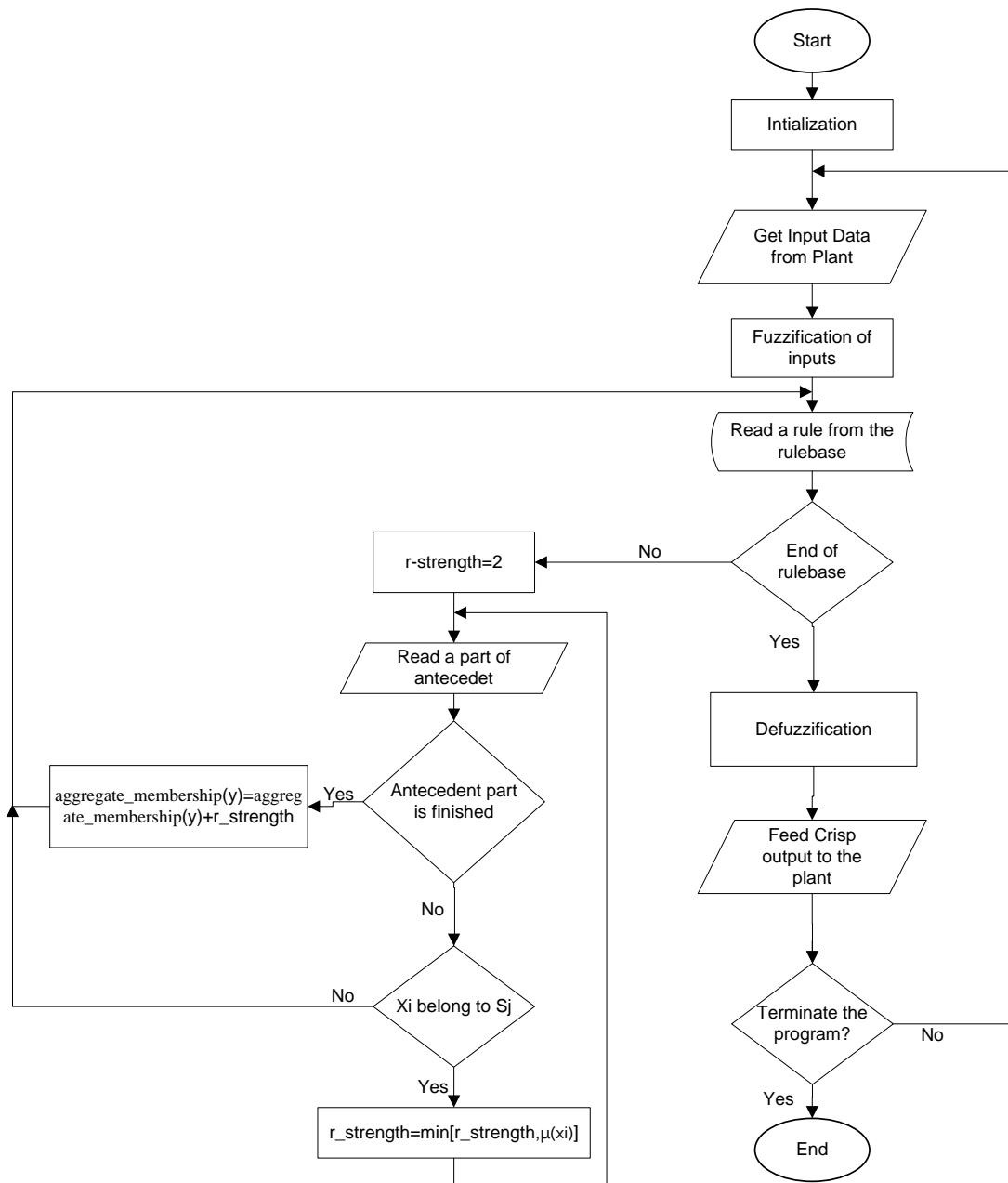


**Fig. 3** Flowchart of the serial Fuzzy Logic Controller algorithm.



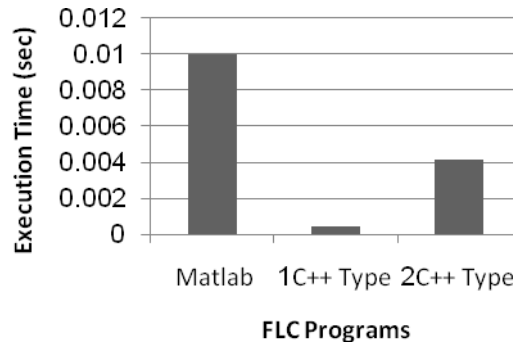


**Fig. 4** The execution time of servomotor FLC programs

**Fig. 5** shows the execution time of the three above mentioned serial implementations of various virtual FLC systems with different number of inputs and rules. As it is shown in **Fig. 5** execution time of all three programs grows rapidly with increasing number of rules.

The execution time of all FLC programs is combined in **Fig. 5.d**, while MATLAB has the highest execution time, the C++ type 1 shows the smallest execution time. Although C++ Type 1 program is show slow increase in execution time and even for 2401 rules it have very small execution time in comparison with other programs but this type of FLC cannot be used for complex problems because of memory problem.

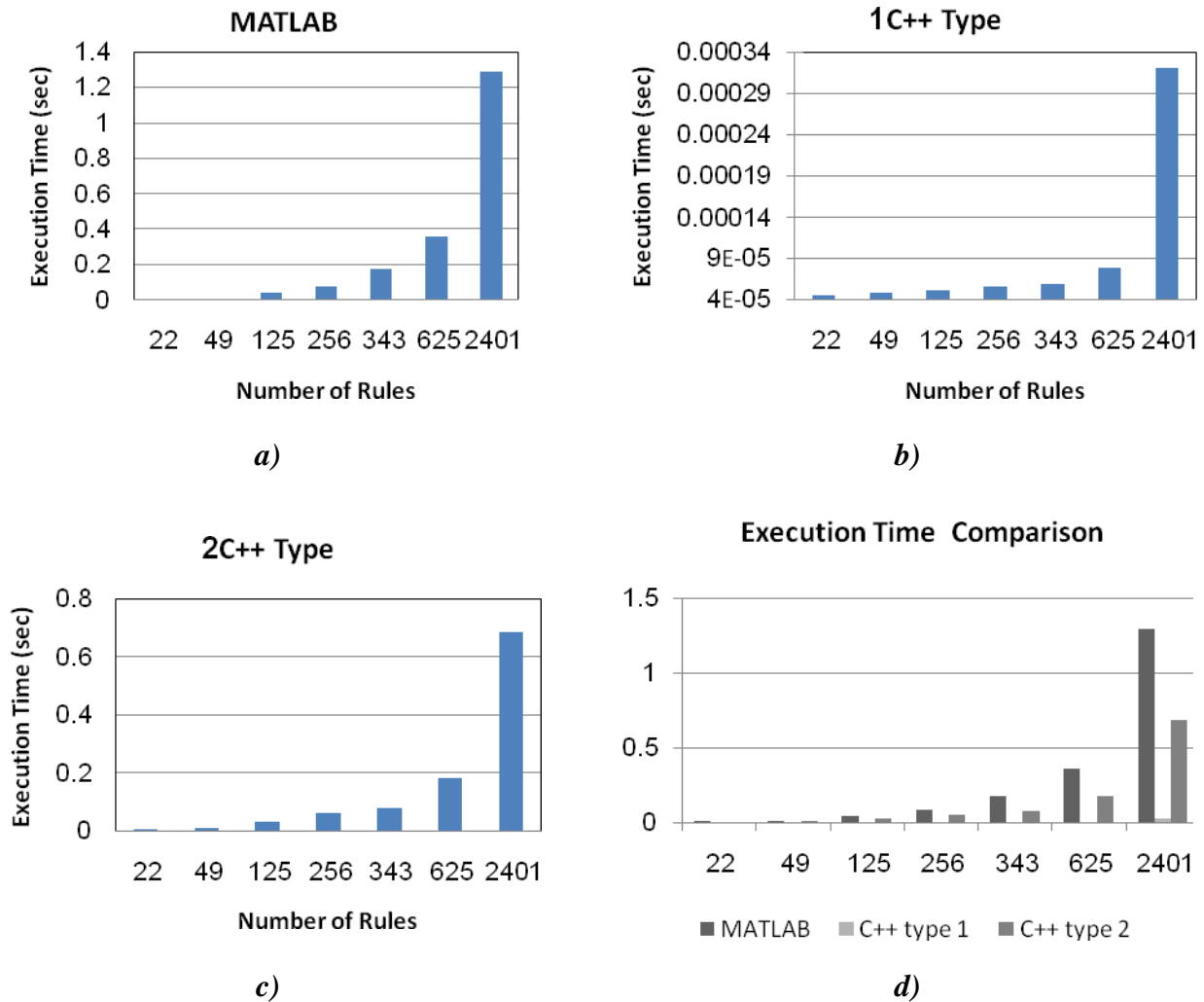


**Fig. 5** Execution Time of *a)* MATLAB FLCs, *b)* C++ type 1 FLCs, *c)* C++ type 2 FLCs, *d)* comparison of execution time of three FLC programs.

C++ type 2 FLC program can handle complex systems with any number of rules but as mentioned before, the execution time will grow exponentially with increasing number of rules. A solution for the high execution time problem is to use a parallel environment and to design a parallel algorithm for FLC program.

### **Parallel Programming Environment**

Computer systems are classified into four groups SISD, SIMD, MISD, and MIMD. Parallel FLC implemented in this work mimics a MIMD system. All processors execute the same program; the result referred to as single-program multiple data [10]. Parallel programming environment can be classified as multi-processors or multi-computers; each one has either bus or switch connection subdivision (**Fig. 6**) [12].

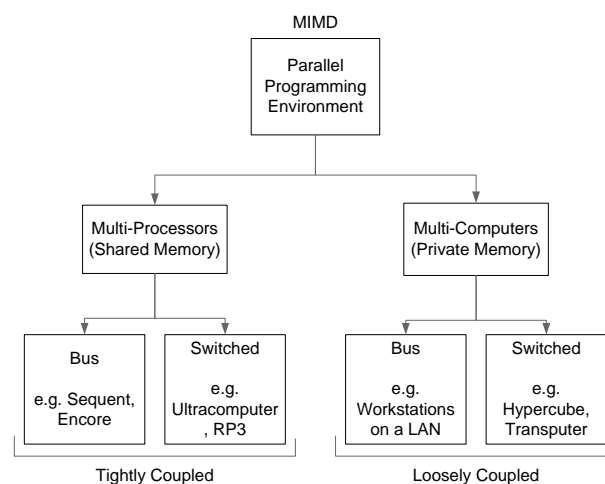


**Fig. 6** Classification of parallel and distributed computers.

In this work the parallel programming environment consists of four computers connected in a LAN through a switch. All computers belong to the same workgroup called "WORKGROUP". The computers IP addresses are from 192.168.0.1 to 192.168.0.4. All computers have the same characteristics. This parallel programming environment is called a cluster. **Fig. 7** shows the physical organization of a cluster of four computers.

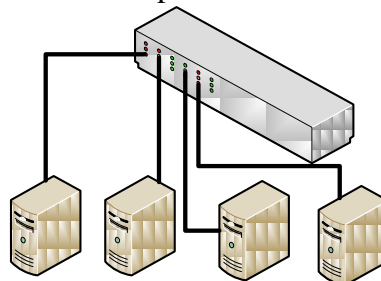


**Fig. 7** Physical organization of the cluster.

For this cluster, software is needed to distribute the jobs, synchronize processes, send and receive data, and manage the cluster. MPICH2 [15] is used to execute a parallel program. MPICH2 is one of the most perfect implementation of MPI-2 standard by Argonne National Laboratory.

### **Parallel FLC Algorithm**

To design the parallel FLC algorithm, the problem should be decomposed into more than one task that can be done concurrently on different computers. Most of computation time in a FLC program is due to the searching of rulebase for fired rules. Especially for a large rulebase file the time to open and search the file is large.

The reading and searching of the rulebase file operations can be decomposed, and more than one computer can handle these operations concurrently. To do so, the rulebase file should be divided into number of files equal to the number of computers in the parallel environment.

Each part of decomposed rulebase is stored in a computer and the operations of reading and searching this file are mapped to that computer. All computers in the cluster read their rulebases and search them for the fired rules concurrently during the execution of the program. They also aggregate the numerator and denominator of the output value based on the fired rules strength.

The input should be distributed to all computers in the cluster from the root computer. The root computer could be any computer in the cluster. It is the interface between the FLC and controlled plant, it also participate in problem solution. The inputs from the plant provided to the root computer then they will be distributed to all computers by the root computer. When all outputs in all computers are ready, they will be transferred to the root computer to calculate the final output. This final output will be fed to the plant by the root computer. The flowchart of the parallel FLC algorithm is shown in **Fig. 8**.

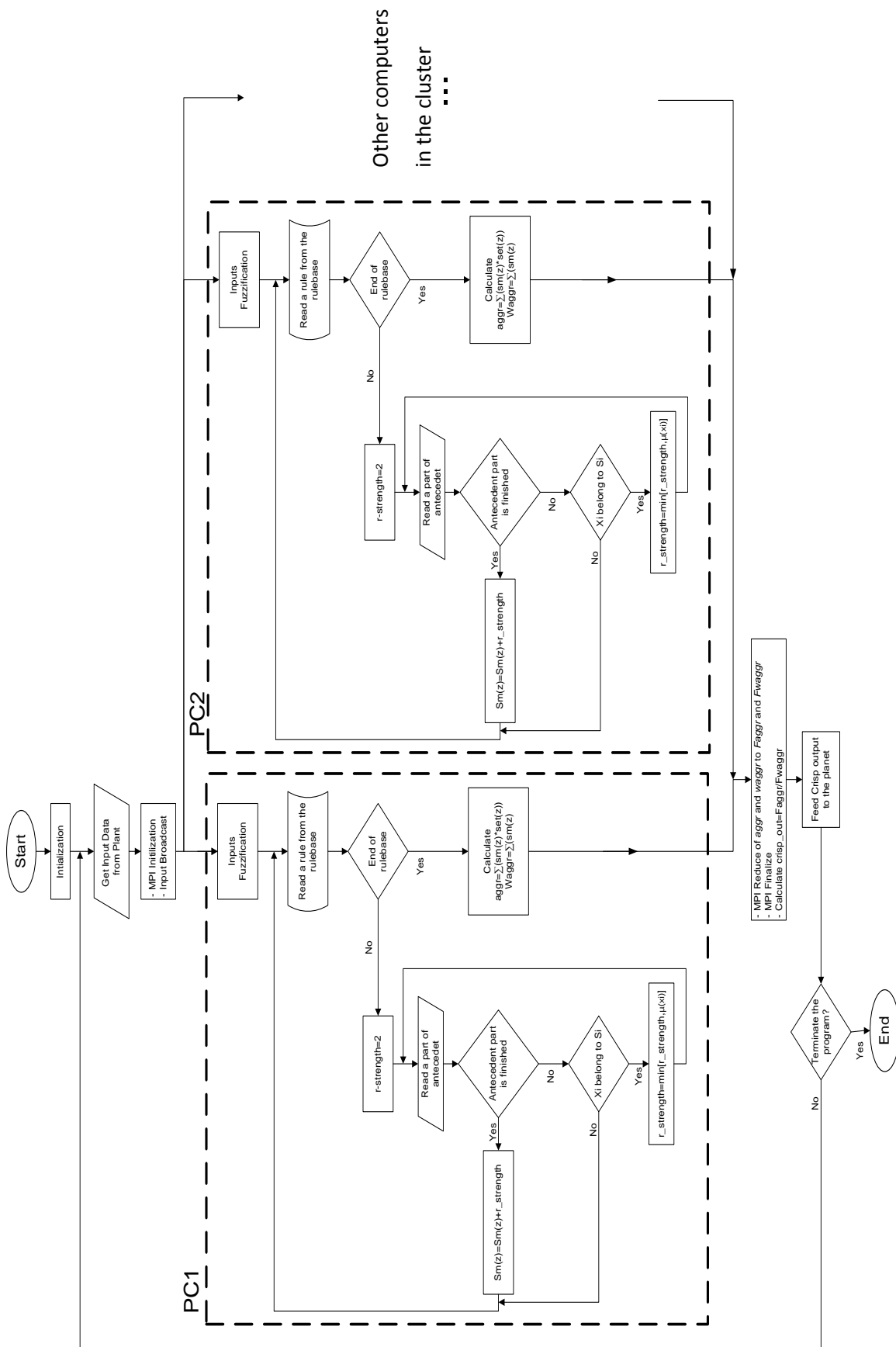
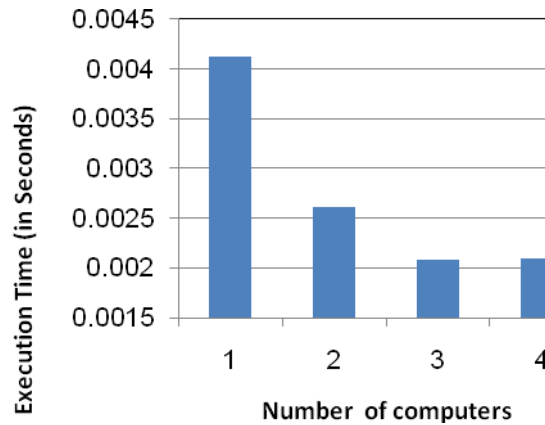


Fig. 8. Flowchart of the parallel FLC algorithm.

The FLC for servomotor is used here to evaluate the parallel FLC. The execution time of this FLC is shown in **Fig. 9**. It can be seen that using 4 computers increase the execution time in comparison with the employment of 3 computers. The servomotor FLC has 22 rules, executing of this controller on 4 computers will not reduce the execution time as much as the increase in communication time.



**Fig. 9.** Execution time of FLC for Servomotor.

The speed up factor and efficiency result of executing FLC for the servomotor using different number of computers in a cluster is shown in **Fig. 10**. It is obvious that maximum speedup for this simple FLC can be achieved by using three computers to solve the problem concurrently. Using more than 3 computers will increase the communication time without noticeable reduction in execution time.

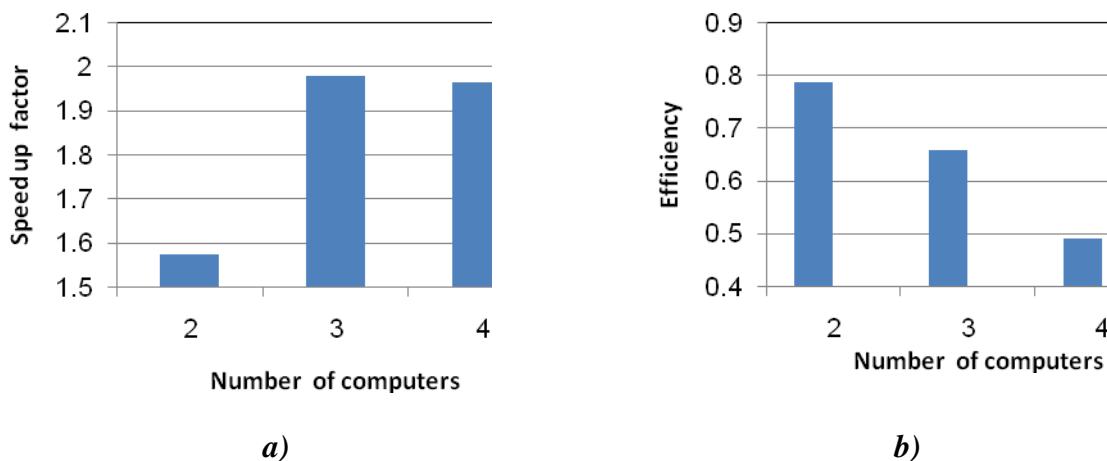


**Fig. 10.** Parallel servomotor FLC *a)* speed up, *b)* Efficiency.

The maximum efficiency of FLC for servomotor can be achieved using 2 computers in a cluster to execute the parallel servomotor FLC program.

Antiskid Steering System (ASS) is another FLC system used to evaluate the parallel FLC implementation. ASS is one of the most complex fuzzy-logic embedded systems ever developed. It reduces the steering angle applied by the driver through the steering wheel to the amount the road can take. It optimizes the steering action and avoids sliding since a sliding car is very difficult to re-stabilize, especially for drivers not accustomed to such situations [16].

The execution time of the ASS FLC with 600 rules using different number of computers is shown in **Fig. 11**.

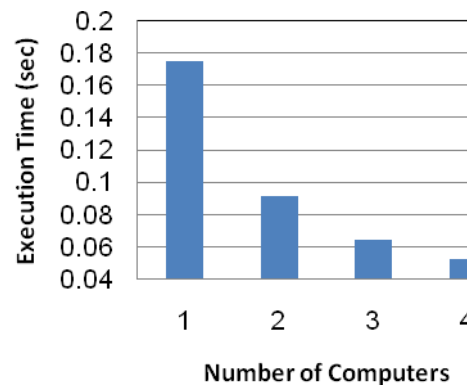


**Fig. 11.** Parallel ASS FLC execution time.

**Fig. 12.a** shows the speedup factor and **Fig. 12.b** shows the efficiency.

The result in **Fig. 12** shows that the maximum speedup is obtained when using 4 computers while the efficiency is minimum.

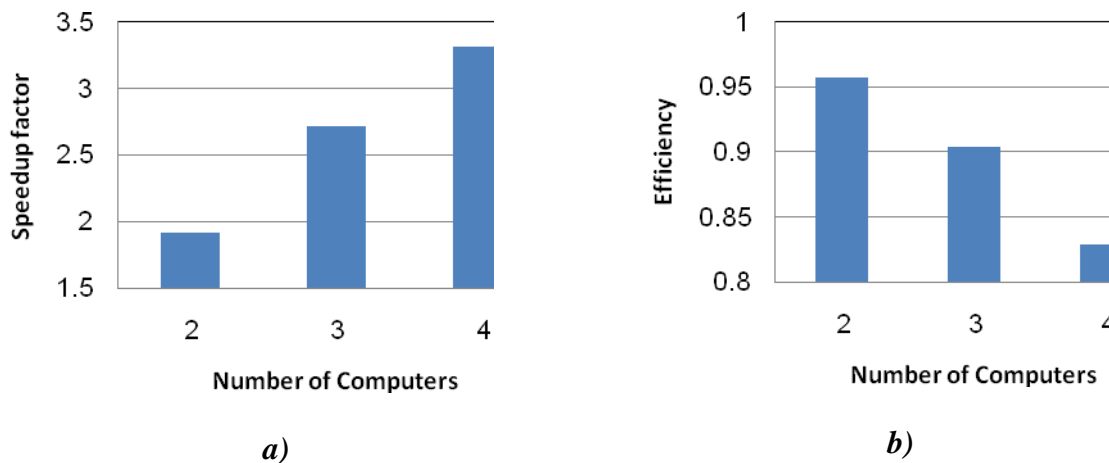


**Fig. 12.** Parallel ASS FLC *a)* Speedup, *b)* Efficiency.

Comparing servomotor FLC with ASS FLC it is obvious that the speedup factor and efficiency are higher in Parallel ASS FLC. **Fig. 13** shows the comparison between speedup and efficiency of servomotor and ASS FLCs.

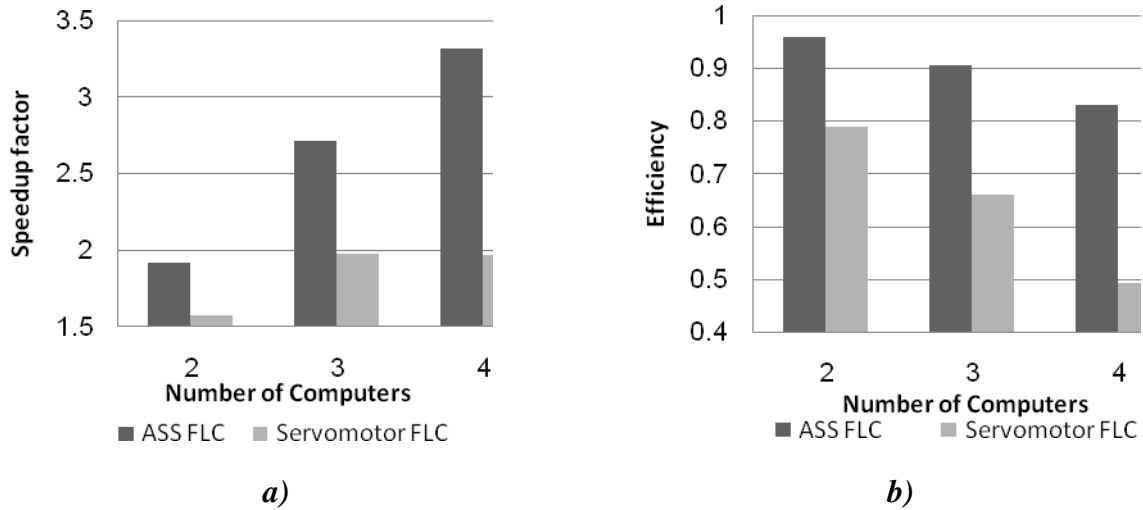


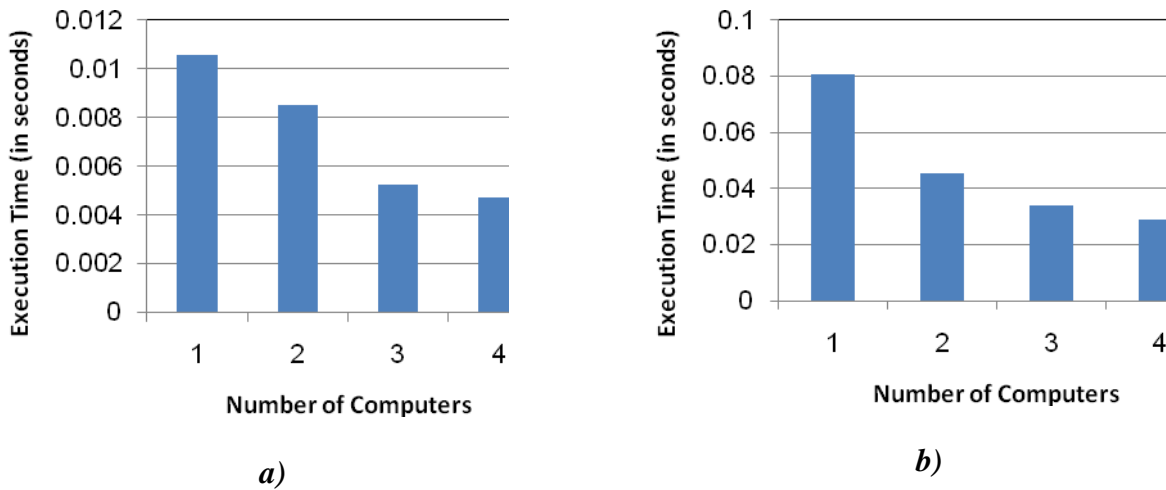
**Fig. 13.** *a)* Speedup, *b)* Efficiency; comparison between Servomotor and ASS FLCs.

Another four hypothetical FLC systems are used to evaluate the speedup and the efficiency of the parallel FLC program.

- 1- A FLC system with 2 inputs, 7 membership function, and 49 rules.
- 2- A FLC system with 3 inputs, 7 membership function, and 343 rules.
- 3- A FLC system with 4 inputs, 7 membership function, and 2401 rules.
- 4- A FLC system with 5 inputs, 7 membership function, and 16807 rules.

The above FLC systems will be used to calculate the execution time, speedup, and efficiency when executing on a cluster of 1, 2, 3, and 4 computers.

The execution time of these FLC systems are shown in **Fig. 14**.



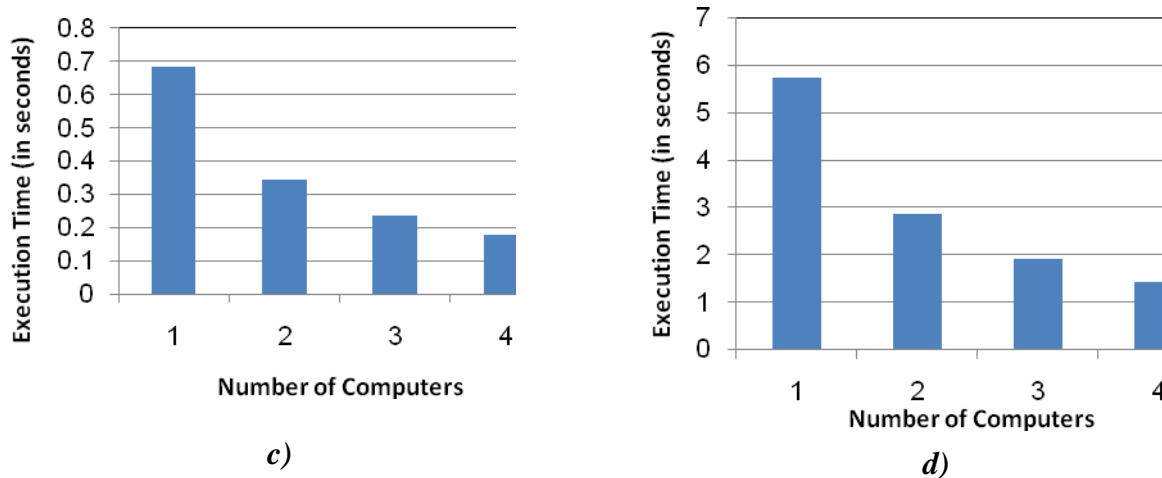


**Fig. 14.** Execution time of *a)* A FLC with 49 rules, *b)* A FLC with 343 rules, *c)* A FLC with 2401 rules, *d)* A FLC with 16807 rules.

To compare the effect of distributing these FLCs in a cluster the speed up factor must be calculated. The speedup factors are shown in **Fig. 15**. The efficiency values of the above FLCs are shown in **Fig. 16**.

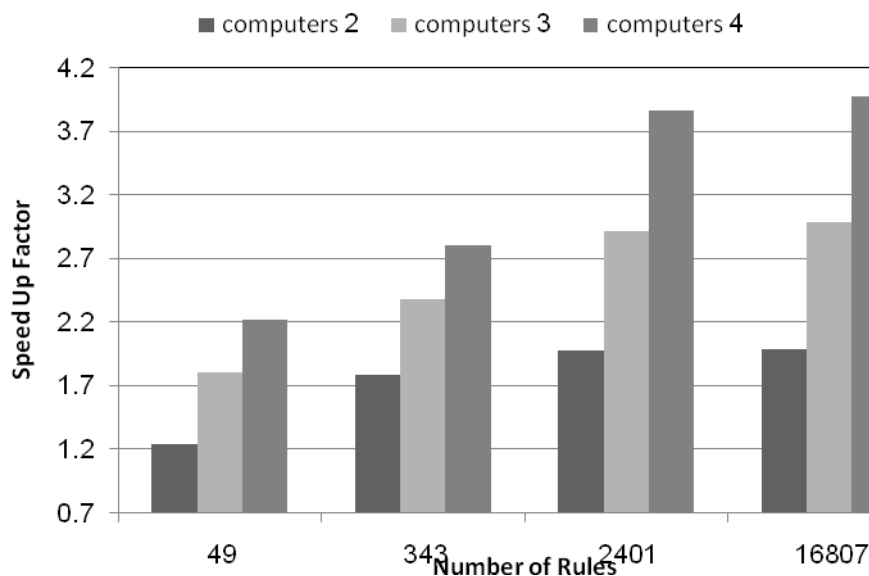


**Fig. 15.** The speedup Factors of various FLCs on clusters of different number of computers.

The results show that increasing in number of rules make the speedup factors becomes near to the number of computers. This means that for complex FLCs when speedup factor is close to its maximum amount, the communication time can be neglected. Also it is clear that for small FLCs increasing number of computers in the cluster will increase the communication time which will reduce the amount of speedup.

**Fig.16** shows that the maximum efficiency is achieved for the most complex FLC (the one with maximum number of rules). Although increasing number of computers in the cluster increase the speedup, but in other hand it reduces the efficiency factor.



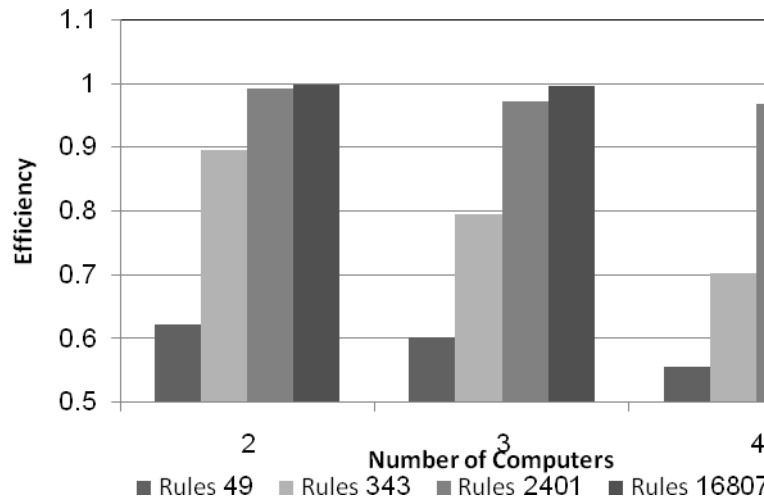


**Fig. 16.** Comparison of various FLC systems Efficiency.

The results show that choosing number of computers in the cluster that will participate in solution of the FLC problem has direct effect to speedup, efficiency, and communication time. So choosing the number of computers in the cluster is a tradeoff between speedup and efficiency.



## CONCLUSIONS

In this research three types of FLC implementations, were introduced. The first one implemented with the rules stored inside the program. Comparing this implementation with MATLAB fuzzy toolbox implementation, shows that the former one has less execution time.

The experimental results show that above two implementations are not appropriate for complex and large FLCs, since both have rulebase size limitation.

The second FLC implementation with rules stored in a file on hard disk solves the memory problem of the previous implementations on the account of execution time. Rulebase searching time is growth by increasing number of rules. Complex FLC spend much time in searching the rulebase file for fired rules. This operation can be decomposed and mapped to more than a computer. Running the FLC program, on a parallel environment, decrease the execution time especially for complex FLCs.

The third FLC implementation is based on decomposing the second FLC implementation to be executed on more than a computer. The experimental results shows that increasing number of computers, decreases the execution time until a point that because of the communication overhead, the execution time will not be decreased anymore. For simple FLCs this point is reached using few computers. But for complex FLCs with large number of rules, using more computers in the cluster can decrease the execution time.

Although adding more computers in the cluster increase the speedup factor but in the other hand, the efficiency will be decreased. Choosing number of computers in the cluster to solve a FLC program is a tradeoff between speedup and efficiency.

## REFERENCES

- [1] C. Dualibe, M. Verleysen, P.G.A. Jespers, Design of Analog Fuzzy Logic Controllers in CMOS Technologies Implementation, Test and Application, Kluwer Academic Publishers, 2003.
- [2] I. Foster, Argonne National Laboratory, Designing and Building Parallel Programs: Concepts and Tools for Parallel Software Engineering, Addison Wesley, 1995.
- [3] A. Gupta, C. Forgy, A. Newell, and R. Wedig, Parallel Algorithms and Architectures for Rule-Based Systems, Vol. 14 , Issue 2 , Proceedings of the 13th annual international symposium on Computer architecture (ISCA '86), P 28-37,ACM, 1986.
- [4] N. Howard, R. Taylor, N. Allinson, The Design and Implementation of a Massively-Parallel Fuzzy Architecture, Fuzzy Systems, IEEE International Conference, P552-554, IEEE Trans., 1992.
- [5] M.J. Lees, D. A. Campbell, J. C. Devlin, A Reconfigurable Parallel Inference Processor for High Speed Fuzzy Systems, Circuits and Systems, ISCAS '96., IEEE International Symposium, Vol. 3, P 539-542, 1996.
- [6] L.A. Zadeh, "Fuzzy Logic Systems, Origin, Concepts, and Trends", ALTANA Chair for Applied Computer Science, 2004.
- [7] Z. Kovačić, S. Bogdan, Fuzzy Controller Design Theory and Applications, Published in, CRC Press Taylor & Francis Group, 2006.
- [8] K. H. Lee, First Course on Fuzzy Theory and Applications, Springer, 2005

- [9] S.G. Lee, H.H. Lee, M. Miyazaki, K. Akizuki, Parallel Fuzzy Inference on Hypercube Computer, Fuzzy Systems Conference Proceedings, FUZZ-IEEE '99. IEEE International, Vol. 1, P 309-314, 1999.
- [10] B. Parhami, Introduction to Parallel Processing Algorithms and Architectures, Kluwer Academic Publishers, 2002.
- [11] A. Grama, A. Gupta, G. Karypis, V. Kumar, Introduction to Parallel Computing, Second Edition, Addison Wesley, 2003.
- [12] R.S. Morrison, Cluster Computing Architectures, Operating Systems, Parallel Processing & Programming Languages, 2003
- [13] B. Giacalone, M.L. Presti, F.D. Marco, Hardware Implementation Versus Software Emulation of Fuzzy Algorithms in Real Applications, Fuzzy Systems Proceedings, IEEE World Congress on Computational Intelligence., The 1998 IEEE International Conference, Vol. 1, P 7-12, 1998.
- [14] <http://support.microsoft.com/ph/3040>, Visual Studio .NET 2003 solution center, Microsoft, June 13, 2008.
- [15] <http://www.mpi-forum.org>, The official Standard documents for MPI-1 and MPI-2, Message Passing Interface Forum, April 22, 2008.
- [16] C.v. Altrock, Fuzzy Logic in Automotive Engineering, Issue 88, Circuit Cellar INK, 1997.

## LIST OF SYMBOLS AND ABBREVIATIONS

ASS	Antiskid Steering System
CPI	Cycles Per Instruction
DMMP	Distributed Memory Message Passing
DMSV	Distributed Memory Shared Variables
$E_p$	Efficiency Factor
FL	Fuzzy Logic
FLC	Fuzzy Logic Controller
FLOPS	Floating Point Operations Per Second
GMMP	Global Memory Message Passing
GMSV	Global Memory Shared Variables
MIMD	Multiple Instruction Multiple Data
MIPS	Million Instructions Per Second
MISD	Multiple Instruction Single Data
MPICH2	Message Passing Interface CHameleon version 2
SIMD	Single Instruction Multiple Data
SISD	Single Instruction Single Data
$S_p$	Speedup Factor

## BEARING CAPACITY OF SQUARE FOOTING ON GEOGRID-REINFORCED LOOSE SAND TO RESIST ECCENTRIC LOAD

Prof. Dr. Mosa J. Al-Mosawe

Civil Engineering Department, College of Engineering, University of Baghdad.

Dr.A'amal A. Al-Saidi

Civil Engineering Department, College of Engineering, University of Baghdad

Faris W.Jawad.

Civil Engineering Department, College of Engineering, University of Baghdad.

### ABSTRACT

This research presents and discuss the results of experimental investigation carried out on geogrids model to study the behavior of geogrid in the loose sandy soil. The effect of location eccentricity, depth of first layer of reinforcement, vertical spacing, number and type of reinforcement layers have been investigated. The results indicated that the percentage of bearing improvement about (22 %) at number of reinforced layers  $N=1$  and about (47.5%) at number of reinforced layers  $N=2$  for different Eccentricity values when depth ratio and vertical spacing between layers are (0.5B and 0.75B) respectively.

الخلاصة :-

نستعرض هنا النتائج لدراسة مختبرية لتقدير قابلية التحمل لتربة رملية مفككة بعد تسليحها بال ( geogrid ) وقد تمت دراسة تأثير بعض العوامل لغرض الحصول على التصرف العام للتربة المحسنة بال ( geogrid ) وتشمل هذه العوامل قيمة انحراف الحمل عن المركز عمق الطبقة الأولى من التسليح ، والمسافة العمودية بين طبقات التسليح ، عدد طبقات التسليح و نوع طبقة التسليح. وقد بينت النتائج أن نسبة التحسين قد وصلت إلى (22%) لطبقة تسليح واحدة و (47.5%) عند استخدام طبقتين من التسليح مع تغير موقع انحراف الحمل عن المركز عندما تكون عمق أول طبقه والمسافة العمودية بين الطبقات مثبتة لكل الفحوص ( 0.75B and 0.5B ) على التوالي.

### INTRODUCTION

The use of reinforced earth is a recent development in the design and construction of foundations and earth-retaining structures. Several authors studied strip foundations but reinforced with different materials such as steel bars (Milovic, 1977; Bassett and Last, 1978; Verma and Char, 1986), steel grids (Abdel-Baki et al. 1993), geotextiles (Das and Shin, 1994) and geogrids (Ismail and Raymond, 1995). All of these

researchers concluded that reinforcement increased the bearing capacity and reduced the corresponding settlement of the foundations compared to the unreinforced soil.

The present study was undertaken to investigate the bearing capacity of square footings on geogrid-reinforced sand. The parameters that are investigated include;

- Eccentricity value ( $e$ )
- Depth Ratio of first layer ( $u/B=0.75$ ), where  $u$  and  $B$  are depth of first reinforced layer and footing width respectively.
- Vertical spacing between layers ( $z/B=0.5$ ), where  $z$  and  $B$  are vertical distance between layers and footing width.

And  $B_r/B=3$  for tests where  $B_r$  and  $B$  reinforcement layers width and footing width.

The symbols of the geometric parameters used in the present paper are shown in Figure (1).

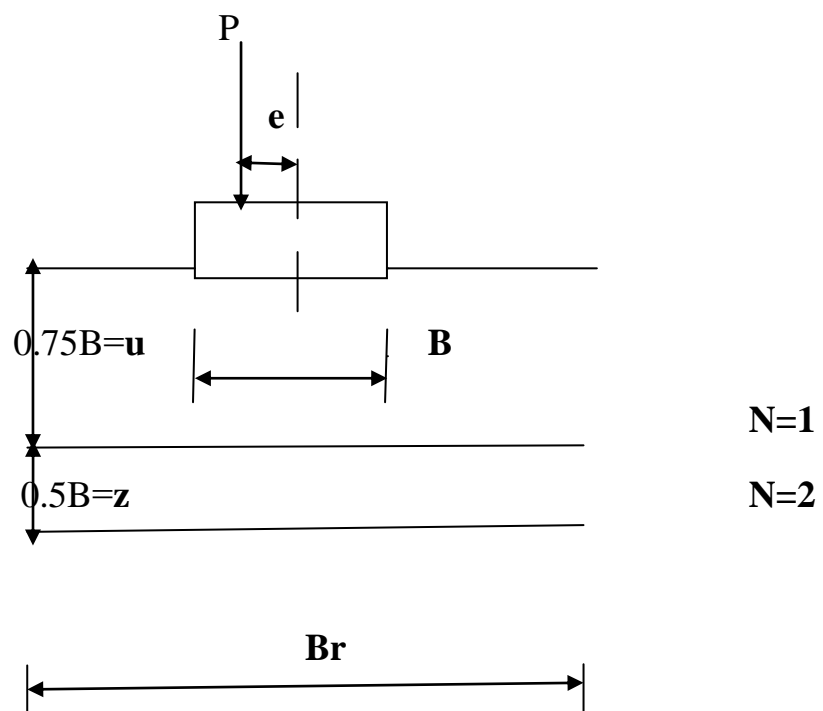


**Figure (1) Geometric Parameters of Reinforced Foundation.**

### EXPERIMENTAL TESTS:-

A series of model loading tests were conducted inside steel box of 600 X 600mm x 700mm in size the box was made of steel plate of 3mm thickness, stiffened with angle sections, as shown in Plate (1). The internal faces of the box were covered with polyethylene sheets in order to reduce the slight friction which might be developed between the box surface and soil. Static vertical loads were applied using electrical

hydraulic pump. Loads transferred from the pump to a hydraulic jack were carefully recorded by proving ring installed between the jack and the tested footing.

The footing was loaded at a constant loading rate to failure. The ultimate bearing capacity was defined as the state at which either the load reached a maximum value where settlement continue to without further increase in load or where there was an abrupt change in the load –settlement relationship. Settlement of the footing was measured using two dial gauges fixed in the middle and edge of footing.

The test footing was a square steel plate 60mm in plane and 5mm thick.



**Plate (1) General View of Testing Equipments**

### **SOIL PROPERTIES:-**

Clean, oven-dried, uniform quartz sand (Kerbela sand) was used in the tests. The sand was placed in the test box at unit weight of approximately  $15.2 \text{ kN/m}^3$  (relative density is 31%). Some properties of the sand are given in Table (1).

**Table (3.1) Sand Properties.**

Property	Values
Specific Gravity	$G_s = 2.63$
Void Ratio and Dry Unit Weight	$e_{\max} = 0.82, \gamma_{d\min} = 14.4 \text{ kN/m}^3$ $e_{\min} = 0.59, \gamma_{d\max} = 17.39 \text{ kN/m}^3$ $e_{\text{used}} = 0.75, \gamma_{d\text{used}} = 15.2 \text{ kN/m}^3$
Relative Density	$D_r = 31\%$
Angle of Internal Friction	$\phi = 29^\circ$

The value of ( $\phi$ ) was obtained from the direct shear test

### REINFORCEMENT PROPERTIES.

The reinforcement used in the research is polymer geomesh. The general view for three types used in tests described, Plate (2). The dimensions of the geogrid samples used in this study were listed in Table (2), the physical chemical properties for sample used were listed in Table (3) and the technical properties for sample used were listed in Table (4).

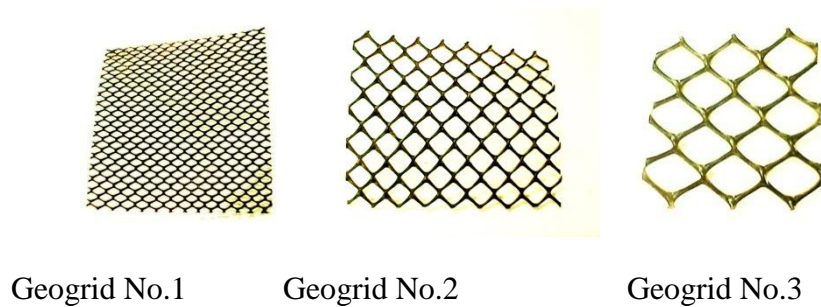


**Plate (2) The Reinforcement Used.**

**Table (2): Dimensional properties for geogrids used (Latifia Geogrid).**

Property	Unit	Data for geogrid No.1	Data for geogrid No.2	Data for geogrid No.3
Aperture Size	mm	6x10	26x26	39x39(±2)
Mass Per Unit Area	g/m <sup>2</sup>	700	520(±%)	770(±40)
Roll Width	m	2.0	1.0	2.5
Roll Length	m	20	20	30
Roll Diameter	m	0.40	0.43	0.50
Cross Roll Weight	kg	28.0	10.4	57.75

**Table (3): The physical, chemical and biological properties for geogrids used (Latifia Geogrid)..**

Property	Data for Geogrid No.1	Data for Geogrid No.2	Data for Geogrid No.3
Structure	Extruded Geogrid	Extruded Geogrid	Extruded Geogrid
Mesh Type	Diamond	Square	Diamond
Standard Color	Black	Black	Black
Polymer Type	HDPE	HDPE	HDPE
U.V Stabilized	Carbon Black	Carbon Black	Carbon Black
Chemical Resistance	Excellent	Excellent	Excellent
Biological Resistance	Excellent	Excellent	Excellent
Packaging	Rolls	Rolls	Rolls



**Table (4): The technical properties for geogrid used (Latifia Geogrid).**

Property	Unit	Data for Geogrid No.1	Data for Geogrid No.2	Data for Geogrid No.3
Tensile Strength at 2% Strain	kN/m	5.1	2.3	4.3
Tensile Strength at 5% Strain	kN/m	9.1	4.0	7.7
Peak Tensile Strength	kN/m	16.0	7.1	13.5
Yield Point Elongation	%	20.0	20.0	20.0

## STUDIED VARIABLE

### Effect of Eccentric Values:-

Figure (2) illustrates the load –settlement curve for a point at the footing edge while Figure (2) shows that curve for a point at the footing center for different eccentricity values. It can be seen that increase in the load carrying for reinforced sand with decrease the eccentricity values. But settlement edge dial decrease and settlement center dial gauge increase with decrease the eccentricity values.

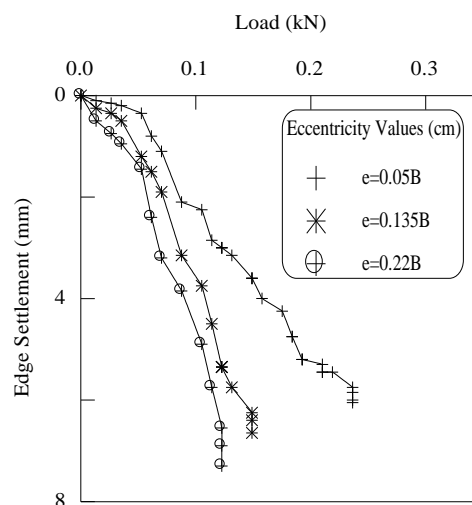


**Figure (2) Load – Edge Settlement Curves for Different Eccentricity Values,  $u/B=0.75$ ,  $Br/B=3$  and Number of Reinforced  $N=1$ .**

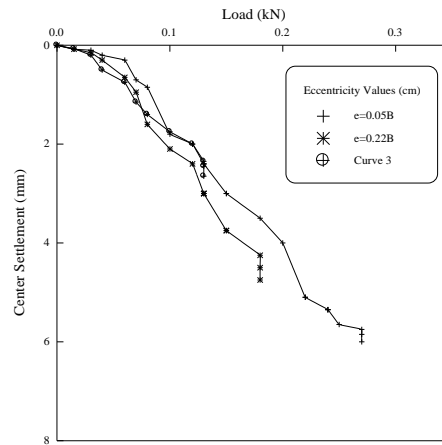


**Figure (3) Load – Center Settlement Curves for Different Eccentricity Values,  $u/B=0.75$ ,  $Br/B=3$  and Number of Reinforced  $N=1$ .**

The same conclusion can be drawn for figure (4 and 5) when number of reinforcement layers ( $N=2$ )

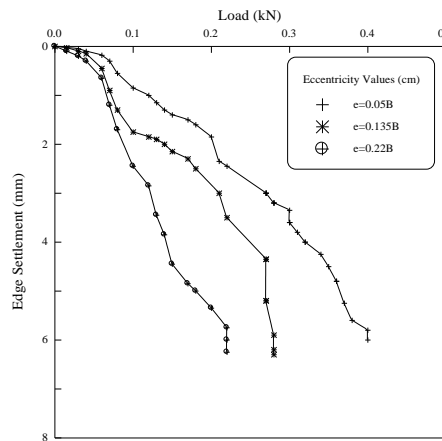


**Figure (4) Load – Edge Settlement Curves for Different Eccentricity Values,  $u/B=0.75$ ,  $z/B=0.5$ ,  $Br/B=3$  and Number of Reinforced  $N=2$ .**

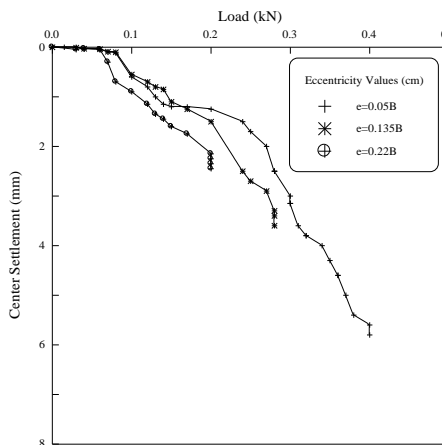


**Figure (5) Load – Center Settlement Curves for Different Eccentricity Values,  $u/B=0.75$ ,  $z/B=0.5$ ,  $Br/B=3$  and Number of Reinforced  $N=2$ .**

Figure (6) displays load variation with eccentricity values for different reinforced number. The load indicates an increase with increase reinforced number for each value of eccentricity. For each value of eccentricity, can be find the maximum load can sand bearing.

$$\ln(p) = -0.58 \ln(e) - 1.6 \quad e > 0$$

.....(1)

Where  $p$  = applied load (kN)

$e$  = eccentricity value (mm).

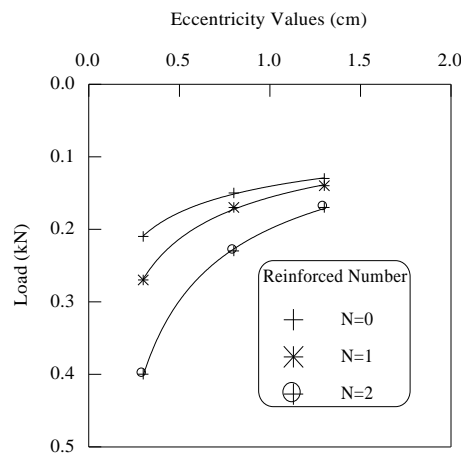


**Figure (6) Load Versus Eccentricity Values for Different Reinforced Number (N),  $u/B=0.75$ ,  $z/B=0.5$ ,  $Br/B=3$ .**

Figure (7) illustrates the variation of improvement percentage with reinforced number for different eccentricity values. The improvement percentage increases with increasing number of reinforcement layers and decreasing eccentricity values.

For each value of number of reinforced can be determined the improvement percentage.

$$I = 11.7(N) - 1.5$$

..... (2)

Where:  $I$  = improvement percentage (%)

$N$  = Number of Reinforced

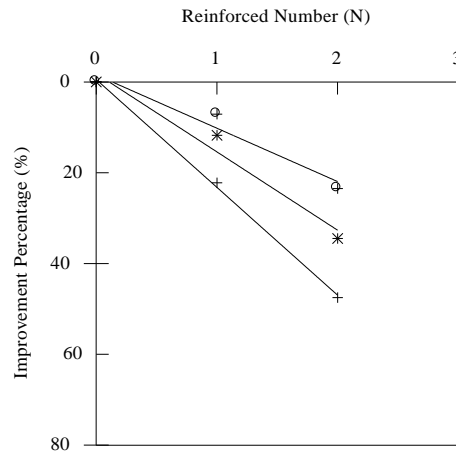


**Figure (7) Improvement Percentage Versus Reinforced Number for Different Eccentricity Values,  $u/B=0.75$ ,  $z/B=0.5$ ,  $Br/B=3$ .**

## CONCLUSIONS

- For single-layer reinforced sand when the depth ratio is  $0.75B$ , the improvement percentage increases about  $t(20\%)$  for different eccentricity values.
- For two layers reinforced sand when depth ratio is  $u/B=0.75$  and vertical spacing  $z/B=0.5$  improvement percentage increase to  $(47.5\%)$  for different eccentricity values.
- This equation can be used to calculate the maximum applied load on sand for  $N \leq 2$ .
- $\ln(p) = -0.58 \ln(e) - 1.6$   $e > 0$
- This equation can be used to calculate improvement percentage for  $N \leq 2$ .
  - $I = 11.7(N) - 1.5$

## REFERENCES

- Abdel-Baki, S., Raymond, G. P., and Johnson, P. (1993) "Improvement of The Bearing Capacity of Footing by Single Layer of Reinforcement." Proceedings, Vol. 2, Geosynthetics' 93 Conferences, Vancouver, Canada, pp. 407-416.
- Bassett, R. H., and Last, N. C. (1981). "Reinforcement Earth Below Footing and Embankments." *Symp. On Earth Reinforcement*, ASCE, New York, N.Y. 202-231.
- 22) Das, B. M., and Shin, E. C., (1994); "Strip Foundation on Geogrid-Reinforced Clay: Behavior under Cyclic Loading", *Geotextiles and Geomembranes*, 13, 657-67.
- Milovic, D. (1977); "Bearing Capacity Tests on Reinforced Sand ", Proc. Of the 9th Conf. on Soil Mech. and Fdn. Eng. Tokyo, Vol. 1, PP. 485-654.

- Verma, B.P., and Char, A.N.R. (1986) "Bearing Capacity Tests on Reinforced Sand Subgrades," Journal of Geotechnical Engineering, Vol. 112, No. 7, July, pp. 701-706.

## THEORETICAL SIMULATION OF STRESS-STRAIN RELATIONS FOR SOME IRAQI CLAYS USING THE ENDOCHRONIC MODEL

Dr. Mohammed Yousif Fattah  
Lecturer, University of Technology,  
Building and Construction  
Engineering Dept.

Maysm Th. Al-Hadidy  
Assistant Lecturer, University of  
Baghdad, College of Engineering,  
Civil Engineering Dept.

Akeel A.S. Al-Gharbawi  
Researcher, Ministry of  
Reconstruction and Housing.

### ABSTRACT

A constitutive law can be defined as a mathematical functional relation between physical quantities such as stress and strain and may take other factors like time ,temperature and additional material properties into account.

In this paper , the endochronic model is used to predict the stress-strain relations of two Iraqi clays. This model is a viscoplastic one but without introducing a yield surface. It encompasses material behaviour such that the current stress state is a function of strain history through a time scale called “intrinsic time” which is not the absolute time but a material property.

The simulation showed that the model overestimates the strains for all cases studied. This may be attributed to the material parameters which require a parametric study to determine their actual values for Iraqi clays.

**KEYWORDS:** Clay, Endochronic Model, Stress, Strain, Model Parameters

### التمثيل النظري لعلاقات الإجهاد – الانفعال لبعض الأطيان العراقية باستعمال نموذج الزمن الضمني

#### الخلاصة

يمكن تعريف قوانين العلاقات التكوينية بأنها دوال رياضية تربط بين كميات فيزيائية مثل الإجهاد و الانفعال و قد تأخذ عوامل عديدة أخرى مثل الزمن و الحرارة و خصائص أخرى للمادة بنظر الاعتبار .

أستعمل في هذا البحث نموذج الزمن الضمني للنتبؤ بعلاقات الإجهاد-الانفعال لترتين طينيتين عراقيتين. إن هذا النموذج هو من النوع اللدن – اللزج و لكنه لا يود خل سطح خضوع. و يعبر عن سلوك المادة بحيث أن حالة الإجهاد الحالية تكون دالة لتاريخ الانفعال من خلال مقياس زمني يدعى "الزمن الضمني" الذي يختلف عن الزمن المطلق من حيث أنه خاصية من خواص المادة. لقد بين التمثيل أن هذا النموذج يعطي قيمة عالية للانفعال لكل الحالات التي تمت دراستها. و يعزى هذا إلى معاملات المادة التي يتضمنها النموذج و التي تحتاج إلى دراسة معاملات لتحديد قيمها الحقيقية بالنسبة للترب الطينية العراقية.

### INTRODUCTION

Endochronic theory was first introduced by Valanis in 1971. He coined this Greek name “Endochronic” that consists of two roots, endos (meaning inner ) and chronos (meaning time). This

theory encompasses material behaviour such that the current stress state is a function of the strain history through a time scale called “intrinsic time” which is not the absolute time measured by a clock as in viscoplasticity but a material property. Hence, the endochronic theory is a “viscoplastic” one but without introducing a yield surface. Therefore, all the complexities and difficulties that develop in introducing a suitable yield criteria are avoided, (Valanis,1971).

Bazant in 1974 and later with his coworkers extended Valanis theory to predict the behaviour of different engineering materials such as concrete, and soils.

### GENERALIZED CONSTITUTIVE RELATIONS:

To generalize the uniaxial concept of the endochronic theory into three dimensions, first, the definition of the intrinsic time increment,  $dz$ , which is used in stead of real time increment,  $dt$ , is introduced. The intrinsic time for time-dependent behaviour is function of strain increments,  $d\epsilon_{ij}$  and time,  $dt$ . The dependence of  $dz$  upon  $d\epsilon_{ij}$  is assumed to be gradual to exclude ideal plastic reponse. The function of  $dz$  will be continuous, smooth, and monotonically increasing. Thus, function  $(dz)^s$  with an appropriate exponent “s”, can be expanded in a tensorial power series in  $d\epsilon_{ij}$  and  $dt$ , i.e., (Bazant and Bhat,1976):

$$(dz)^s = p + p_{ij} d\epsilon_{ij} + p_4 dt + p_{ijkl} d\epsilon_{ij} d\epsilon_{kl} + p_{ij4} d\epsilon_{ij} dt + p_4 dt^2 + p_{ijklmn} d\epsilon_{ij} d\epsilon_{kl} d\epsilon_{mn} + \dots \quad (1)$$

where:

$P$ = coefficient matrices, the subscripts refer to the components in the Cartesian coordinates  $x_i$ ,  $i = 1, 2, 3$ , and number (4) refers to the time axis.

Since,  $dz$  must vanish as  $d\epsilon_{ij} \rightarrow 0$  and  $dt \rightarrow 0$ , thus  $P=0$ . Setting  $s=1$ , and neglecting all quadratic terms, then  $dz = P_4 \cdot dt$  which is of no interest, thus  $P_4 = 0$ . Setting  $s=2$ , and satisfying the conditions of isotropy, the quadratic form of Equation (1) can be written in terms of the first two invariants of  $d\epsilon_{ij}$ , as follows, (Bazant and Bhat,1976):

$$(dz)^2 = P_0 J_2 + (P_1 I_1 + P_2 dt)^2 + P_3 (dt)^2 \quad (2)$$

where:

$P_0, P_1, P_2, P_3$  = non-negative coefficients.

$J_2$  = second deviatoric strain increment invariant, and

$I_1$  = first strain increment invariant.

Then,  $dz$  must vanish for both instantaneous time,  $dt = 0$ , and pure volumetric deformation,  $J_2 = 0$ , hence  $P_1 = 0$ . Thus, the remaining terms in Equation (2) can be rewritten in the following form:

$$(dz)^2 = \left(\frac{d\xi}{Z_1}\right)^2 + \left(\frac{dt}{\tau_1}\right)^2 \quad (3)$$

where:

$$d\xi = f_1(\sigma, \epsilon) \cdot d\zeta \quad (4.a)$$

$$d\zeta = \sqrt{J_2} = \sqrt{\frac{1}{2} d\epsilon_{ij} \cdot d\epsilon_{ij}} \quad (4.b)$$

$d\epsilon_{ij}$  = deviatoric strain increment tensor

$$= d\epsilon_{ij} - \frac{1}{3} \delta_{ij} \cdot d\epsilon$$

$\delta_{ij}$  = Kronecker delta.

$d\epsilon$  = Volumetric strain increment =  $d\epsilon_{kk}$

$z_I, \tau_I = \text{Constants.}$

$d\xi$  is scalar called “damage measure” that depends on strain increments and stresses to predict hardening and softening.  $d\zeta$  is called “deformation measure” that depends on strain increments only. From Equations (3) and (4),  $d\zeta$  and  $dz$  represent geometrically the length of path traced by material states in a six-dimensional strain space for  $d\zeta$ , or in a strain-time space for  $dz$ , (Ansal et al., 1979).

Secondly, generalizing of equations to three dimensions using  $dz$  instead of  $dt$ , and splitting the strain components into deviatoric and volumetric components to satisfy isotropy conditions, the following differential constitutive equations are deduced:

$$de_{ij} = \frac{dS_{ij}}{2G} + \frac{S_{ij}}{2G} \cdot dz \quad (5.a)$$

$$d\epsilon = \frac{d\sigma_m}{3k} + \frac{\sigma_m \cdot dt}{3k\tau_1} + d\lambda + d\epsilon^o \quad (5.b)$$

where:

$$de_{ij} = d\epsilon_{ij} - \frac{1}{3}\delta_{ij} \cdot d\epsilon$$

$$d\epsilon = d\epsilon_{11} + d\epsilon_{22} + d\epsilon_{33}$$

$$d\lambda = \text{inelastic dilatancy,}$$

$$S_{ij} = \text{deviatoric stress tensor,}$$

$$= \sigma_{ij} - \delta_{ij} \cdot \sigma_m$$

$$\sigma_m = \text{mean stress} = \frac{1}{3}\sigma_{kk}$$

$$G, K = \text{shear and bulk elastic moduli, and}$$

$$d\epsilon^o = \text{stress-independent inelastic strains (e.g. thermal strains).}$$

Both of the first terms of Equations (5.a) and (5.b) represent the elastic strain increments, while the remaining terms represent the inelastic strain increments. For instance, the term  $(\sigma_m \cdot dt / 3K\tau_1)$  represents the time-dependent inelastic volumetric strain, i. e. creep, while  $d\lambda$  represents the time-independent volumetric strain.

To develop a quasi-linear elastic incremental constitutive law for simplicity, the plastic stress increment tensor  $d\sigma_{ij}^p$  can be obtained from Equations (5) by multiplying Equation (5.a) by  $2G$ , and Equation (5.b) by  $3K$ , hence:

$$\begin{aligned} d\sigma_{ij}^p &= 2G \cdot de_{ij}^p + \delta_{ij} (3K \cdot d\epsilon^p) \\ &= S_{ij} dz + \delta_{ij} (\sigma_m dt / \tau_1 + 3K d\lambda + 3K d\epsilon^o) \end{aligned} \quad (6)$$

The stress increments  $d\sigma_{ij}$  are related to the elastic strain increments  $d\epsilon_{ij}^e$  by the following equations:

$$d\sigma_{ij} = 2G \cdot d\epsilon_{ij}^e + \delta_{ij} (3K \cdot d\epsilon^e) \quad (7)$$

Hence, the summation of Equations (7) and (8) yields:

$$d\sigma_{ij} + d\sigma_{ij}^p = D_{ijkl} \cdot d\epsilon_{kl} \quad (8)$$

where:

$$D_{ijkl} = \text{elastic coefficient matrix}$$



### **THE NUMERICAL PROCEDURE:**

The basic constitutive law, Equation (5), is of a differential form, and the variables that govern inelastic deformations are  $(dz)$  and  $(d\lambda)$ . Bazant and Bhat (1976) used the step-by-step integration or step-iterative algorithm in which for each loading step, a number of iterations are performed till satisfaction of equilibrium of stresses and strains occurs. This is assured when the change in values of  $(dz)$  and  $(d\lambda)$  for the same loading step becomes very small.

In this algorithm, the values of  $(dz)$  and  $(d\lambda)$  computed from the previous loading step provide an initial estimate for the next loading step.

### **Endochronic Hardening Functions and Parameters:**

The function  $f_1$  in Equation (4) that accounts for hardening or softening, should decrease as the inelastic strains accumulate, because  $d\xi$  is adopted as a measure of the accumulated inelastic strain, hence:

$$d\xi = \frac{d\eta}{f(\eta)} \quad ; \quad d\eta = F(\sigma, \epsilon) \cdot d\zeta \quad (9)$$

where:

$f(\eta)$  = Strain-hardening function.

$F(\sigma, \epsilon)$  = Strain-softening function.

Thus, the function  $f(\eta)$  has a significant effect on the non-linearity of the stress-strain relations, while the function  $F(\sigma, \epsilon)$  allows for a gradual decrease of these relations on approach to peak stress. Both functions depend mainly on material type.

### **Hardening Functions and Dilatancy for Normally Consolidated Clays:**

The function  $F$  in Equation (9) is determined semi-empirically from experimental data. The function  $F$  is governed by the effective confining stress  $I_1^\sigma$ , the volume change,  $I_1^\epsilon$ , and the second deviatoric strain invariant,  $J_2^\epsilon$ . Bazant et al. (1979) introduced the following formulation for function  $F$ :

$$F(\sigma, \epsilon) = a + \frac{|1 - a_1 I_1^\epsilon| / (1 + a_3 J_2^\epsilon)}{0.01 + a_2 (I_1^\sigma / Pa)} \quad (10)$$

where:  $a$ 's = material constants.

$Pa$  = atmospheric pressure = 101.3 kN/m<sup>2</sup>

The division of  $I_1^\sigma$  in Equation (10) by  $Pa$  is to make the relation dimensionless. Constant “ $a$ ” must be positive to ensure irreversible strain increment for the critical case of no hardening or softening, (Bazant et al., 1979).

The function  $f(\eta)$  represents the limiting critical case of no hardening or softening. Thus, for large values of  $\eta$ , this function,  $f(\eta)$ , must converge to one. The function  $f(\eta)$  takes the following form:

$$f(\eta) = 1 + \frac{\beta_1}{1 + \beta_2 \eta} \quad (11)$$

where:  $\beta_1$  and  $\beta_2$  = constants.

The dilatancy or densification function  $d\lambda$  of clays depends on shear and volumetric stresses and strains. Hence, the function  $d\lambda$  depends on  $J_2^\epsilon$ ,  $I_1^\sigma$  and  $I_1^\epsilon$ . Moreover,  $d\lambda$  depends on  $\lambda$  itself because the volumetric strain increment should decrease monotonically till zero as a limit in the case of failure. Hence  $d\lambda$  is equal to (Bazant et al., 1979):

$$d\lambda = \frac{C_o |1 + C_1 I_1| d\zeta}{(1 + C_2 I_1^\sigma / Pa)(1 + C_3 J_2^\epsilon)(1 + C_4 \lambda)} \quad (12)$$

where:  $c_o, c_1, c_2, c_3, c_4$  = material constants.

$d\lambda$  is determined empirically from tests and it depends on the clay type, stress path and stress history.

The tensile strengths of soils are very small and hence neglected.

The elastic moduli  $G$  and  $K$  of the soil element change during loading, and thus the accumulated densification-dilatancy measure  $\lambda$  and the effective normal stress also change. Thus, the effect of void ratio is:

$$\frac{de}{e_o} = \frac{\epsilon_v (1 + e_o)}{e_o} = \frac{3(1 + e_o) \lambda}{e_o n} = \frac{3\lambda}{n} \quad (13)$$

where:  $e_o$  = initial void ratio

$\epsilon_v$  = volumetric strain =  $\epsilon_{kk}$

$n$  = porosity.

while the effect of normal stress is the ratio  $(I_1^\sigma - I_1^{\sigma_o}) / I_1^{\sigma_o}$ , where  $I_1^{\sigma_o}$  is the initial first stress invariant. Hence, the elastic moduli will be equal to:

$$G = G_o \left( 1 + b_1 \frac{I_1^\sigma - I_1^{\sigma_o}}{I_1^{\sigma_o}} + b_2 \frac{3\lambda}{n} \right) \quad (14)$$

where:  $b_1$  and  $b_2$  = constants,

$$\text{and } K = \frac{2}{3} G(1 + \nu)/(1 - 2\nu) \quad (15)$$

### Model Parameters of Clays:

All material parameters in the previous equations are based on best fit of experimental results.

Constant “a” in Equation (10) affects the value of the peak stress. Constant  $a_3$  which is called “distortion coefficient” is determined by the following correlation proposed by Ansal et al. (1979). Based on general pattern of results:

$$a_3 = 153.8(e_o P_a / P_o) + 34.62 \quad (16)$$

where:

$P_o$  = consolidation pressure.

Similarly, the plasticity coefficient  $Z_1$  in Equation (3) that accounts for rigidity and deformability of clays, is determined from the following correlation:

$$Z_1 = 0.00294(e_o P_o / P_a)^2 - 0.0177(e_o P_o / P_a) + 0.0396 \quad (17)$$

Ansal et al. (1979) determined an approximate correlation for densification coefficient  $C_o$  in Equation (12), softening coefficient  $\beta_2$  in Equation (11), and the elastic modulus  $E$ , as shown in Figure (1). This correlation depends on the consolidation pressure  $P_o$ , and the liquidity index of the clay  $I_L$ , where (Mitchel, 1993):

$$I_L = \frac{w_{nat} - w_p}{I_p} \quad (18)$$

where:

$w_{ant}$  = natural water content.

$w_p$  = plastic limit

$I_p$  = plasticity index =  $w_L - w_p$

$w_L$  = liquid limit.

Choice of appropriate ratio of the liquidity index to the consolidation stress is tempered by judgement in the absence of test results.

All other constants are determined experimentally. The values of the parameters as proposed by Bazant et al. (1979) are shown in Table (1):

**Table (1)** – Material parameters of endochronic model for normally consolidated clays.

Parameter	Value
$a_0$	4
$a_1$	500
$a_2$	0.75
$\beta_1$	$5n$ (n = porosity)
$C_1$	2500
$C_2$	0.25
$C_3$	1000
$C_4$	9000
$b_1$	0.1
$b_2$	0.1

### **Computer Program:**

The computer program **Endoch**, coded in Fortran language, was written by the authors. The algorithm used in the endochronic model incorporates an iterative procedure. The program computes stresses, strains, all functions like  $F$ ,  $f(\eta)$ , and variables like  $\lambda$ ,  $\eta$ , at mid-step loading. Iterations are then performed till the tolerance of the values of  $dz$  and  $d\lambda$  becomes less than 0.05 %. The values of strain increments,  $d\varepsilon$ , intrinsic time,  $dz$ , and inelastic dilatancy,  $d\lambda$ , or the previous step are taken as an estimate for the current step.

### **APPLICATIONS:**

This model have been applied for simulating stress-strain relationships of two Iraqi soils:

#### **i) First application**

Al- Mufty (1990) carried out a series of tests on al-Fao soft clay. Block samples were obtained from an area close to the river Shatt-Al-Arab.

The top layer of Fao soil was found to be stiff to very stiff brownish gray silty clay with a desiccated crust. This layer is followed by a soft to very soft gray silty clay.

According to the unified classification system, the soil from both layers may be classified as CL-CH, inorganic clays of medium to high plasticity. According to, AASHTO M145-73, the soil is classified as A-7-6 (16).

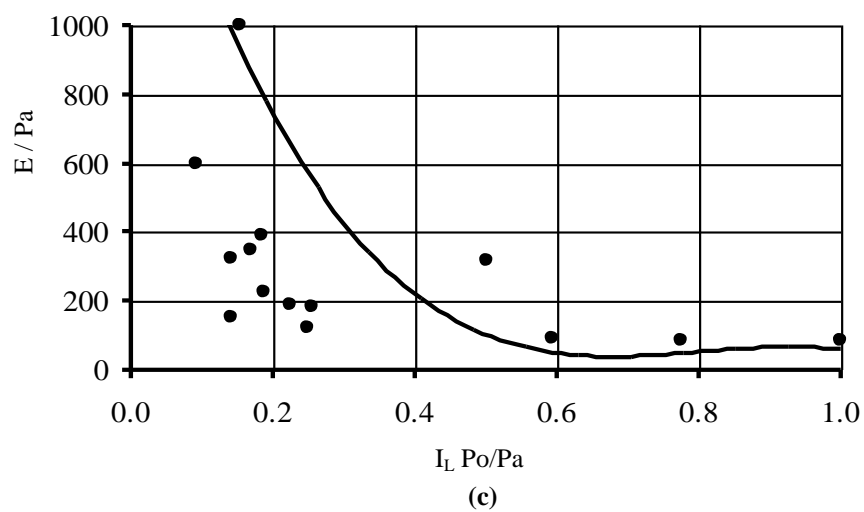
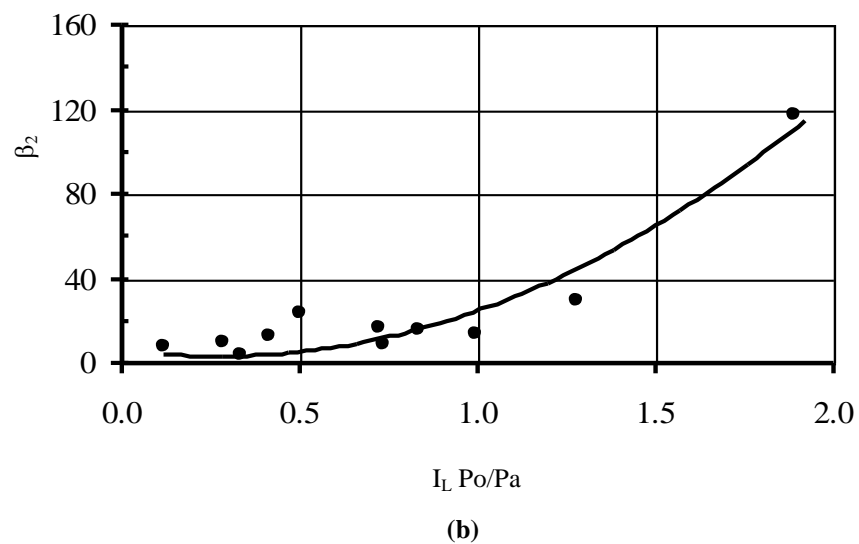
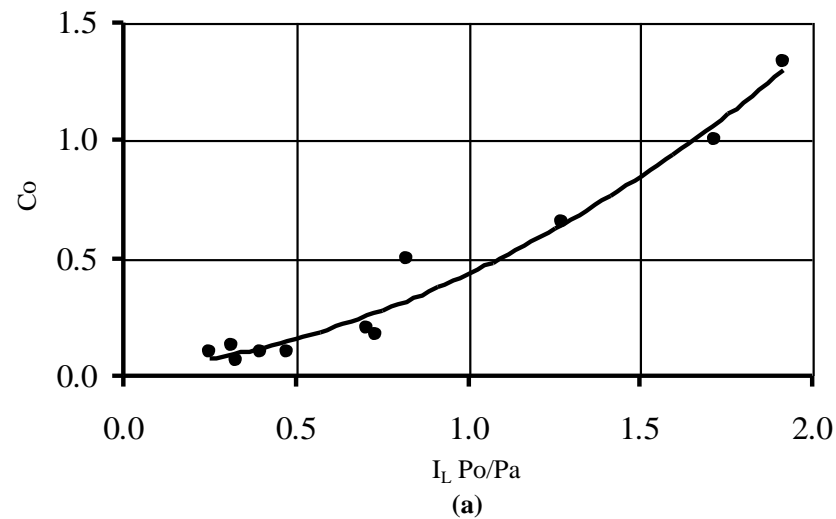


**Fig. (1)** – Approximate correlation for:  
a) Densification coefficient,  $C_o$ .  
b) Softening coefficient,  $\beta_2$ .  
c) Elastic modulus,  $E$ .

The average properties of the soil at sampling depths 1.25 m and 3 m respectively are listed in Table (2).

**Table (2)** - Average properties of the soft clay from Al-Fao, (from Al-Mufti, 1990).

Property	1.25 m depth	3 m depth
Total unit weight $\gamma_t$ , kN/m <sup>3</sup>	17.9	17.7
Water content w %	30	45
Liquid limit $w_L$ %	54	50
plasticity index $I_p$ %	27	24
Liquidity index $I_L$	0.11	0.79
Specific gravity G	2.7	2.72
Sand size fraction %	9	12
Silt size fraction %	58	60
Clay size fraction %	33	28
Activity A	0.82	0.86

Among the tests carried out by Al-Mufti (1990) unconsolidated undrained triaxial compression tests on samples compacted by the standard compaction test to the maximum dry density and optimum moisture content. These results are compared with those predicted by the endochronic model in Figures (2) to Figure (6).

Figures (2) and (3) represent the samples that are taken from the top layer, and the figures from (4) to (6) represent the samples that are taken from the layer below the top layer.

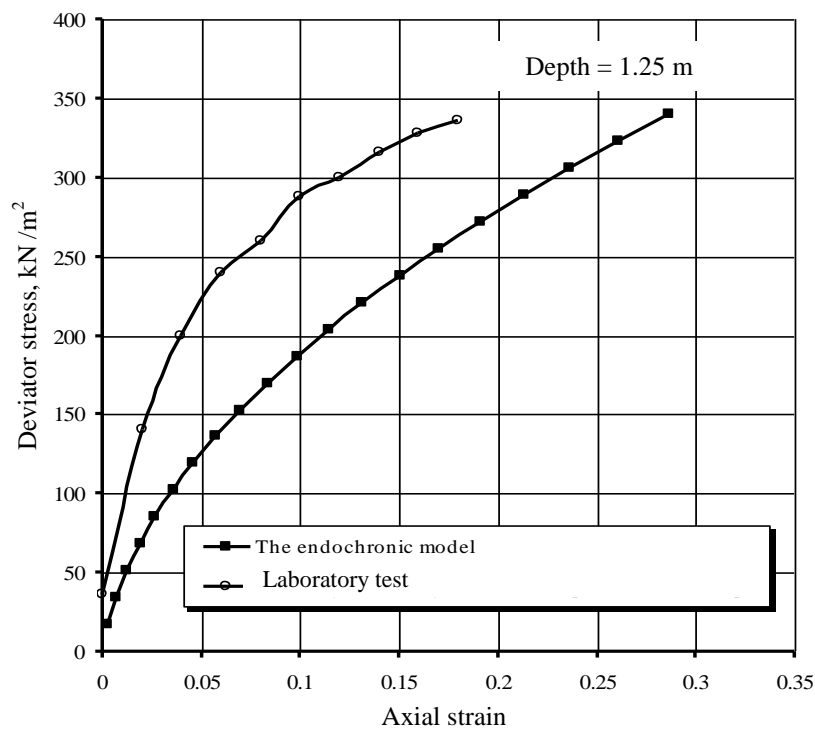


**Fig. (2)** - A comparison between the stress-strain relationships predicted by the endochronic model with laboratory tests of Al – Mufty (1990),  $\sigma_3 = 300$  kPa.

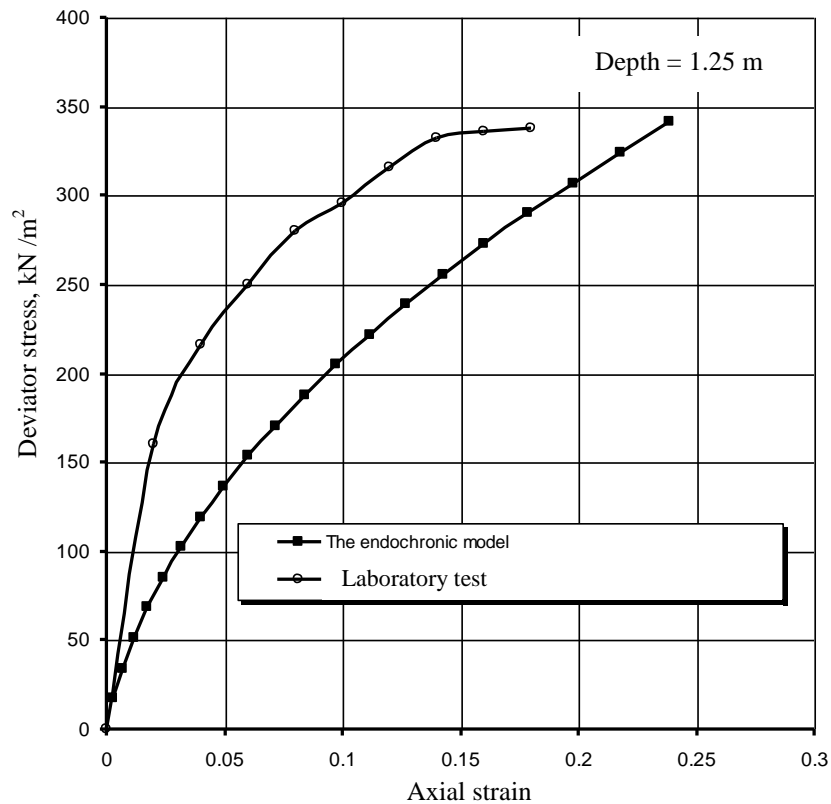


**Fig. (3)** - A comparison between the stress-strain relationships predicted by the endochronic model with laboratory tests of Al – Mufty (1990),  $\sigma_3 = 300$  kPa.

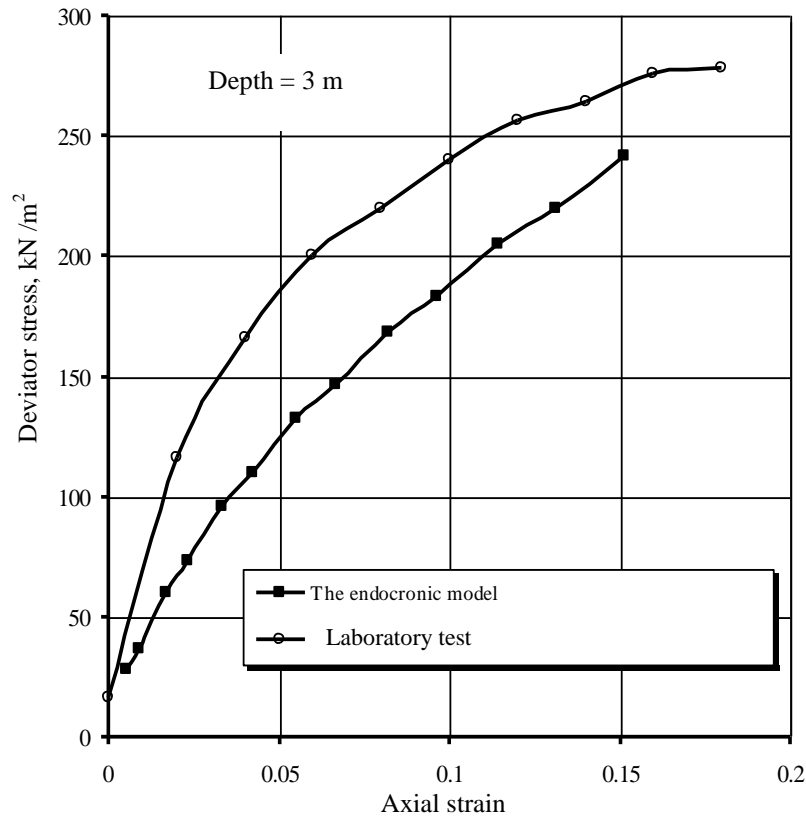


**Fig. (4)** - A comparison between the stress-strain relationships predicted by the endochronic model with laboratory tests of Al – Mufty (1990),  $\sigma_3 = 100$  kPa.

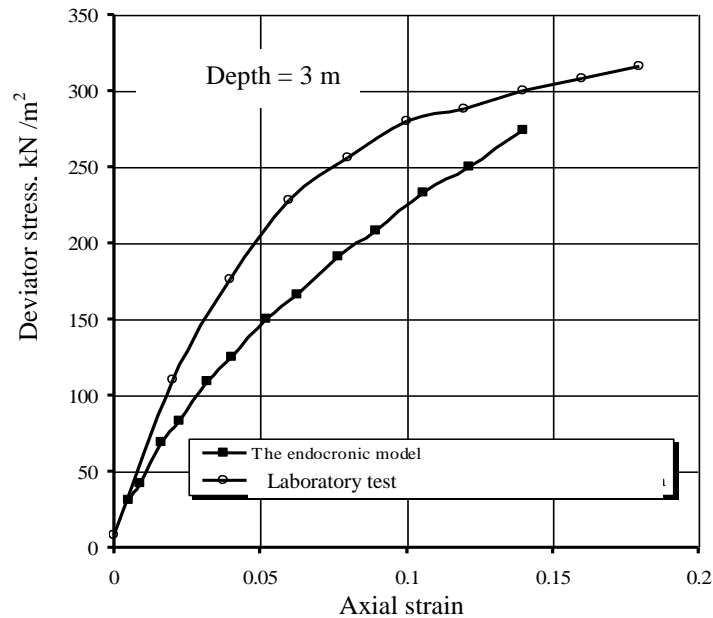


**Fig. (5)** - A comparison between the stress-strain relationships predicted by the endochronic model with laboratory tests of Al – Mufty (1990),  $\sigma_3 = 200$  kPa.

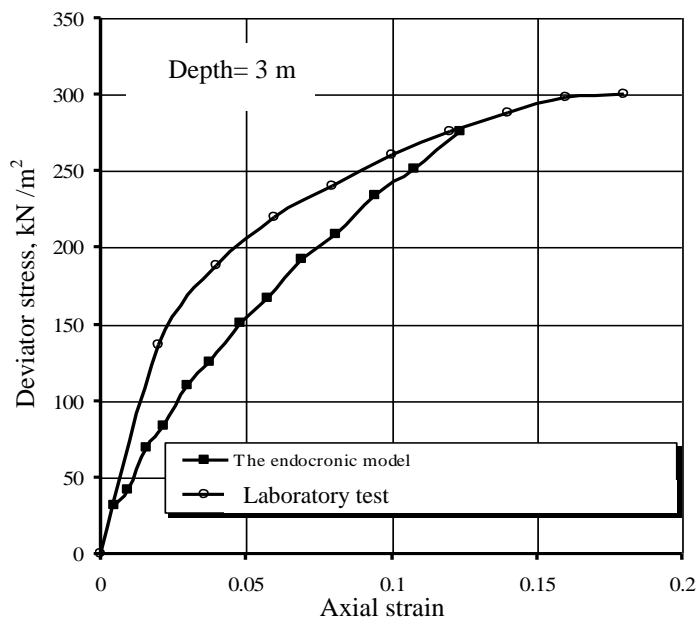


**Fig. (6)-** A comparison between the stress-strain relationships predicted by the endochronic model

with laboratory tests of Al – Mufty (1990),  $\sigma_3 = 300$  kPa.

It can be observed in these figures that the model overestimates the strains for all the cases studied under high stress increments.

In addition, there is no definite yield point can be obtained. Thus it is approximately suitable for normally consolidated clays where ductile behaviour of the stress-strain is expected.

## ii) Second application

Al- Saady (1989) carried out laboratory tests on an A-6 soil during construction of a road embankment. A representative area located at Al – Zafarania (south of Baghdad), was chosen for the research. The site covers an area of soil composed of silty clay with varying thickness. This stratum behaves as normally or slightly overconsolidated soil, have an upper desiccated crust 0.5-0.75 m thick.

The distribution of the particle sizes indicated:

Clay fraction = 45 %, silt fraction = 37 %, sand fraction = 18 %.

It is classed as “CL” in a Casagrande classification chart.

Among the tests carried out by Al- Saady (1989) consolidated undrained triaxial test which was designated as series D as shown in Table (3).

In addition, unconsolidated undrained triaxial test which was designated as series G as shown in Table (4).

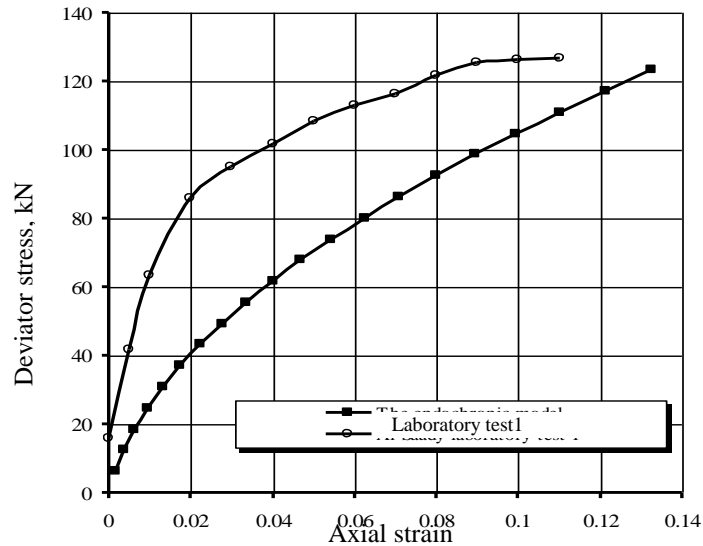
Consolidated undrained triaxial test results are compared with those predicted by the endochronic model in Figures (7) to (12) which show a comparison between the stress-strain relationships predicted by the endochronic model with laboratory tests of Al – Saady, (series, D).

Consolidated drained triaxial test results are compared with those predicted by the endochronic model in Figures (13) to (18). Figures (19) to (24) show a comparison between the volumetric strain–axial strain relationships predicted by the endochronic model with laboratory tests of Al-Saady, (series, G).

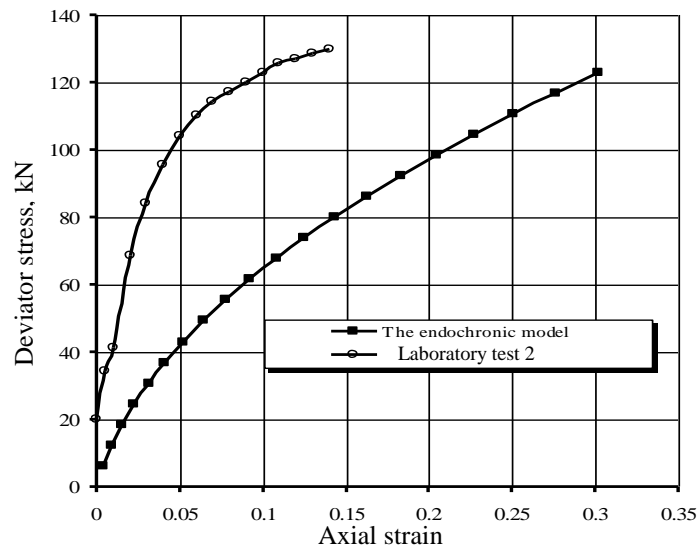


**Table(3)** - The results of series (D), (from Al-Saady, 1989).

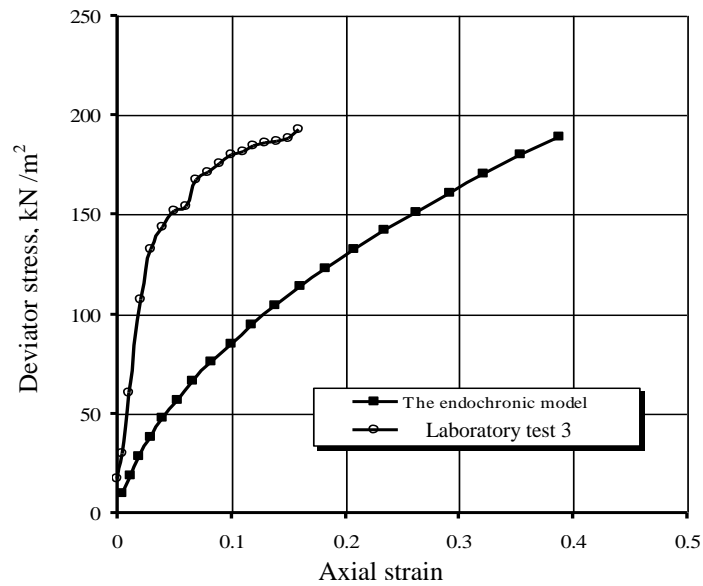
Test No.	$\sigma'_c$ kN/m <sup>2</sup>	$e_o$	$w_c$ %	$(\sigma_1 - \sigma_3)_f$ kN/m <sup>2</sup>	$(\sigma_1 / \sigma_3)_f$ kN/m <sup>2</sup>	$\Delta u_f$ kN/m <sup>2</sup>
1	79	0.76	26.0	123.24	3.50	30.81
2	100	0.70	24.3	123.00	3.55	52.22
3	150	0.74	25.6	189.21	3.30	72.45
4	200	0.69	24.6	219.60	3.25	104.45
5	300	0.75	25.4	279.00	3.25	176.68
6	376	0.73	26.0	348.01	3.30	224.07



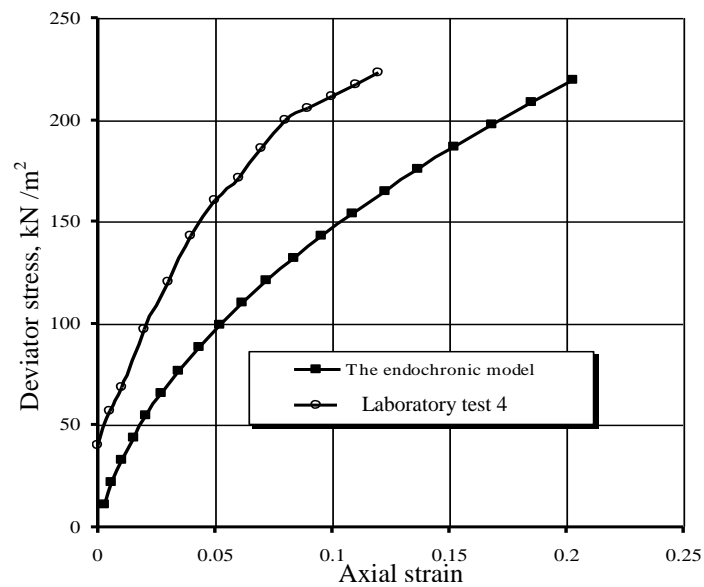
**Fig. (7)** - A comparison between the stress-strain relationship predicted by the endochronic model with laboratory tests of Al – Saady, Test 1, Series D.



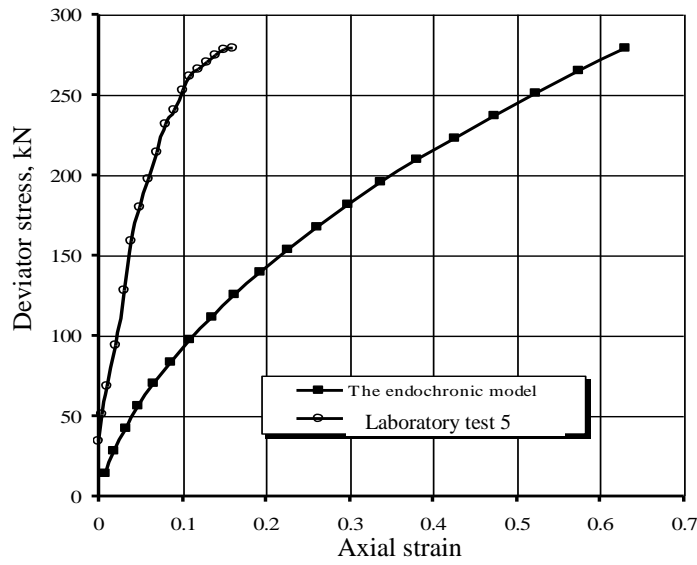
**Fig. (8)** - A comparison between the stress-strain relationship predicted by the endochronic model with laboratory tests of Al – Saady, Test 2, Series D.



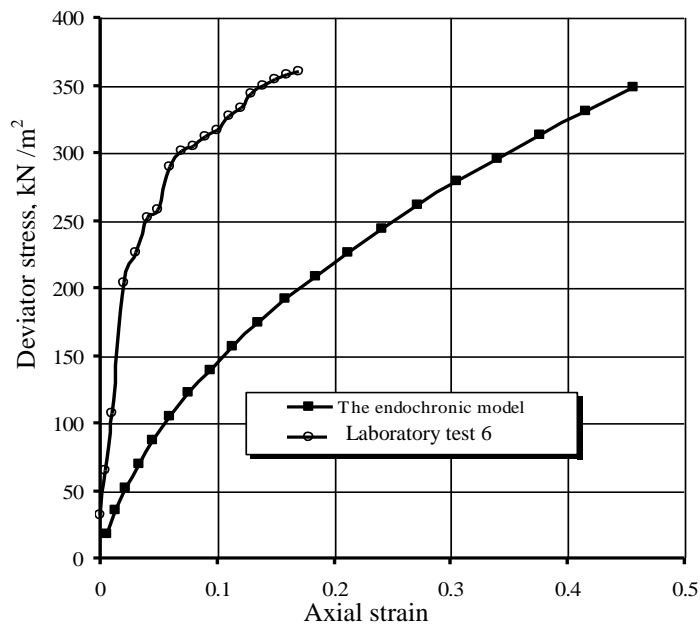
**Fig. (9)** - A comparison between the stress-strain relationship predicted by the endochronic model with laboratory tests of Al – Saady, Test 3, Series D.



**Fig. (10)** - A comparison between the stress-strain relationship predicted by the endochronic model with laboratory tests of Al – Saady, Test 4, Series D.



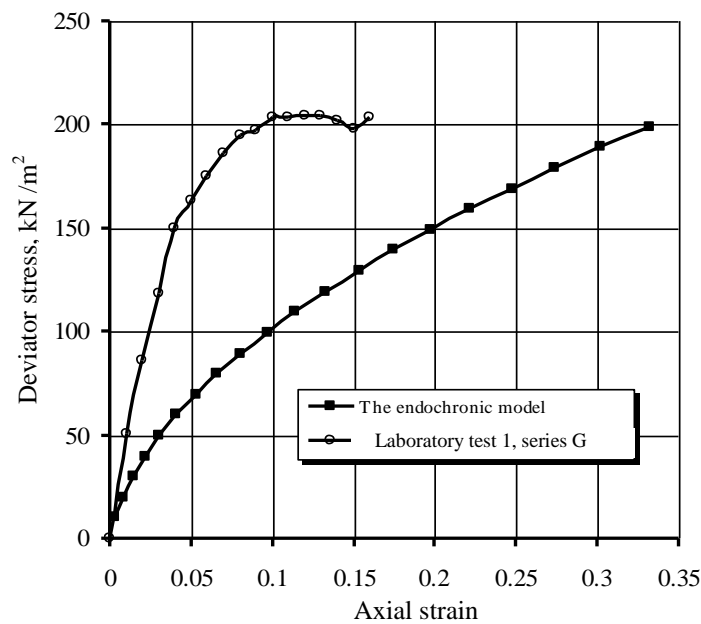
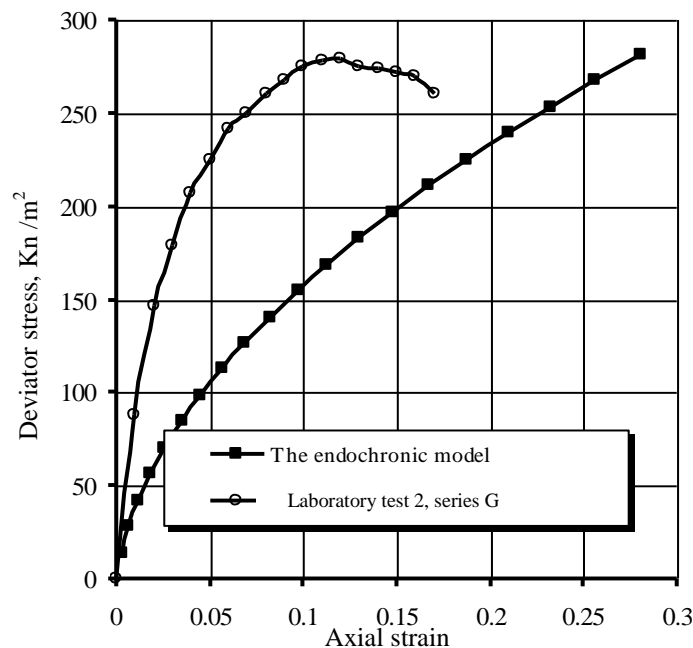
**Fig. (11)** - A comparison between the stress-strain relationship predicted by the endochronic model with laboratory tests of Al – Saady, Test 5, Series D.

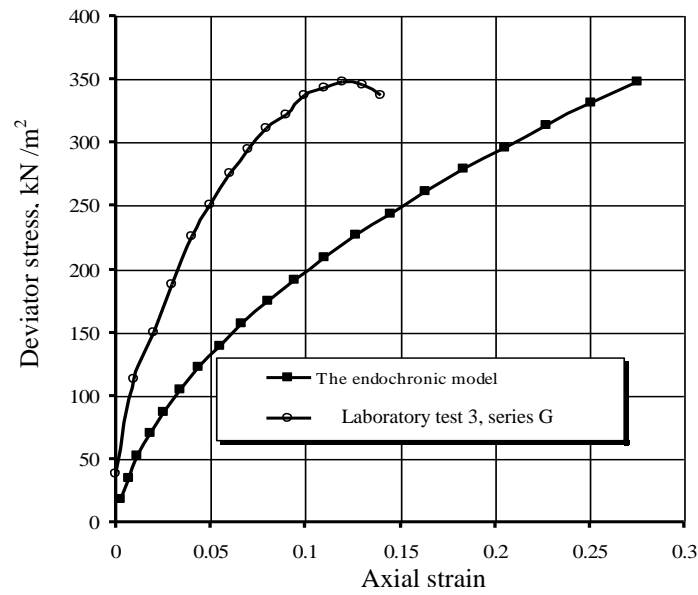


**Fig. (12)** - A comparison between the stress-strain relationship predicted by the endochronic model with laboratory tests of Al – Saady, Test 6, Series D.

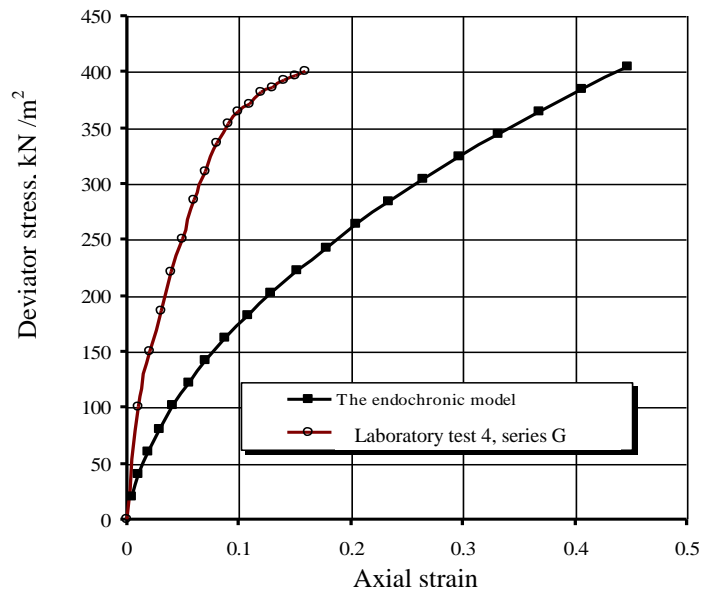
**Table (4)** - The results of series (G), (from Al-Saady, 1989).

Test No.	$\sigma'_c$ kN/m <sup>2</sup>	$e_o$	$w_c$ %	$(\sigma_1 - \sigma_3)_f$ kN/m <sup>2</sup>	$\left(\frac{\Delta V}{V_o}\right)_f$ kN/m <sup>2</sup>
1	79	0.66	23.5	198.87	2.300
2	100	0.69	24.7	281.18	2.283
3	150	0.75	26.0	348.03	3.026
4	200	0.75	27.0	405.03	3.016
5	300	0.69	25.2	752.55	3.590
6	376	0.72	25.0	913.52	3.710

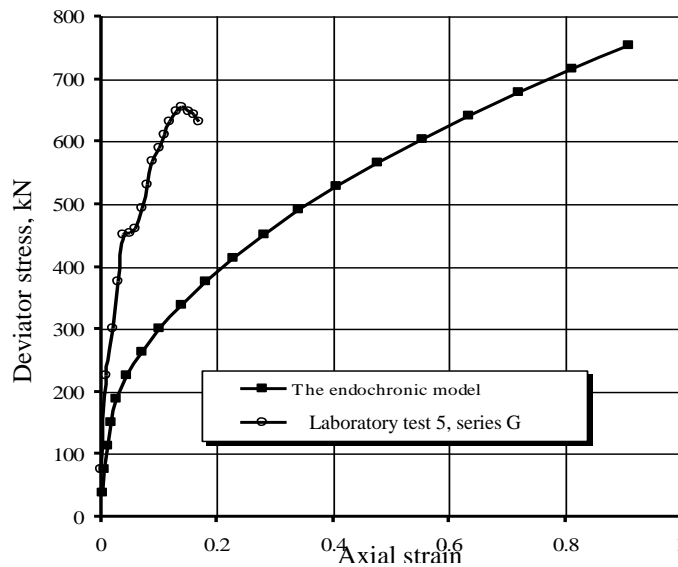

**Fig. (13)** - A comparison between the stress-strain relationship predicted by the endochronic model with laboratory tests of Al – Saady, Test1, series G.

**Fig. (14)** - A comparison between the stress-strain relationship predicted by the endochronic model with laboratory tests of Al – Saady, Test2, series G.



**Fig. (15)** - A comparison between the stress-strain relationship predicted by the endochronic model with laboratory tests of Al – Saady, Test3, series G.



**Fig. (16)** - A comparison between the stress-strain relationship predicted by the endochronic model with laboratory tests of Al – Saady, Test4, series G.



**Fig. (17)** - A comparison between the stress-strain relationship predicted by the endochronic model with laboratory tests of Al – Saady, Test5, series G.

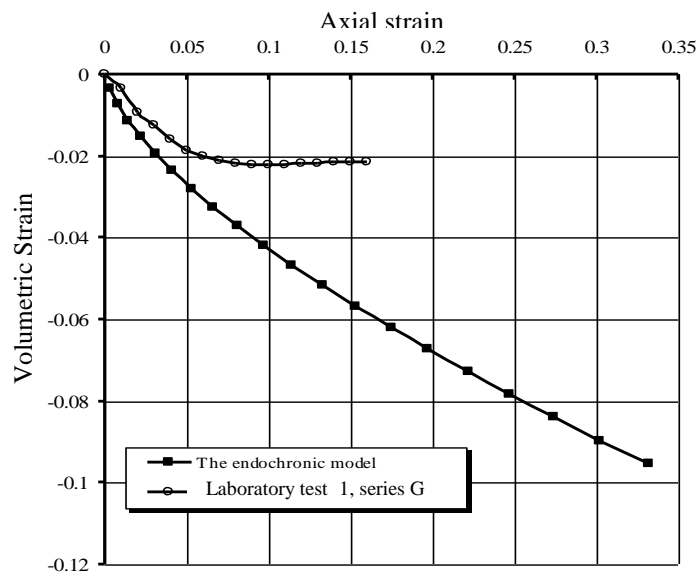


**Fig. (18)** - A comparison between the volumetric strain – axial strain relationship predicted by the endochronic model with laboratory tests of Al – Saady, Test1, series G.

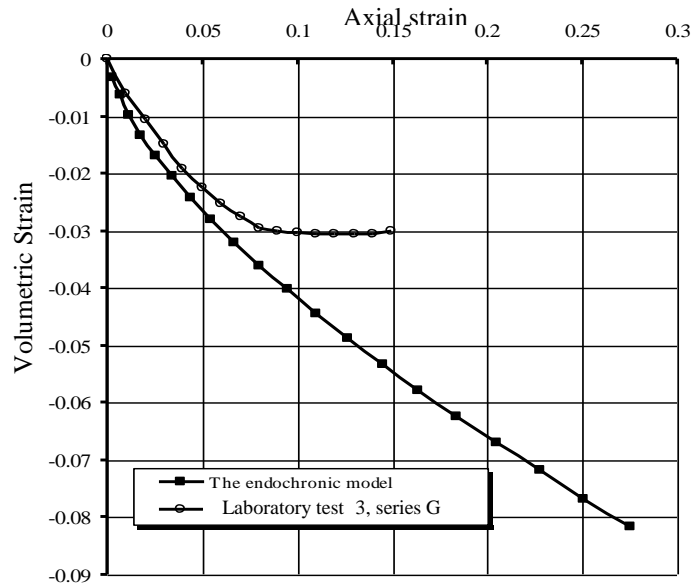


**Fig. (19)** - A comparison between the volumetric strain – axial strain relationship predicted by the endochronic model with laboratory tests of Al – Saady, Test2, series G.

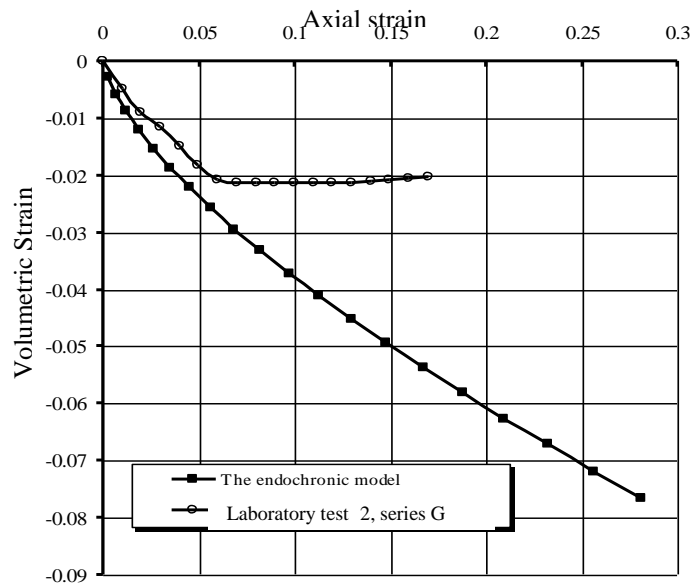


**Fig. (20)** - A comparison between the volumetric strain – axial strain relationship predicted by the endochronic model with laboratory tests of Al – Saady, Test3, series G.

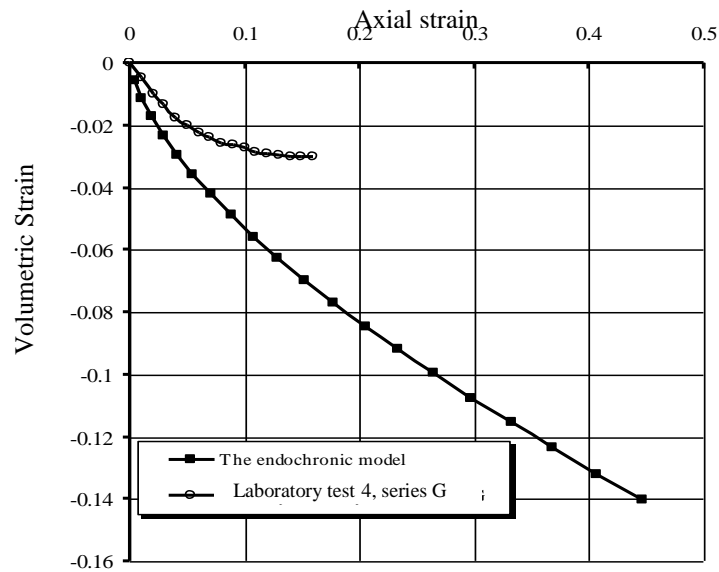


**Fig. (21)** - comparisons between the volumetric strain – axial strain relationship predicted by the endochronic model with laboratory tests of Al – Saady, Test 4, series G.

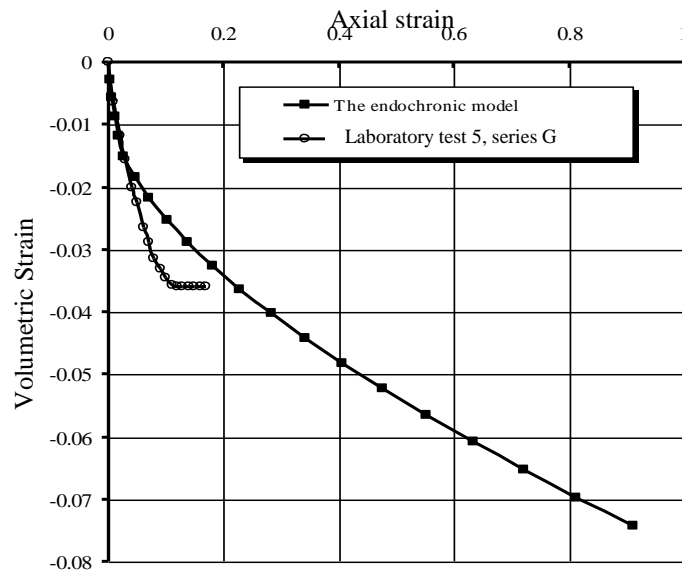


**Fig. (22)** - A comparison between the volumetric strain – axial strain relationship predicted by the endochronic model with laboratory tests of Al – Saady, Test 5, series G.

The same behaviour is noticed in this clay. The predicted volumetric strains are closer to measured strains under small stress increments. At large stresses, the predicted strains became larger.



## CONCLUSIONS:

- The endochronic model overestimates the strains for all the cases simulated under high stress increments.
- There is no definite yield point can be obtained when simulating the laboratory tests. This means that this model can be adopted for normally consolidated clays where ductile behaviour of the stress-strain is expected.
- The error in simulation may be attributed to the model parameters, which need to be evaluated by carrying out parametric study for Iraqi clays.

## REFERENCES:

- Al-Mufti, A. A. E., (1990). (Analysis of Stress Deformation Behaviour of Fao Soil), M.Sc. thesis, Civil Engineering Department, University of Baghdad.
- Al- Saady, N. H., (1989). (Analysis of an A-6 Soil During Construction of Road Embankment), M.Sc. thesis, Civil Engineering Department, University of Baghdad.
- Ansal, A. M., Bazant, Z. P. and Krizek, R. J., (1979). (Viscoplasticity of Normally Consolidated Clays), Journal of Geotechnical Engineering, ASCE, Vol. 105, No. GT4, p.p. 519 – 537.
- Bazant, Z. P. and Bhat, P. D. (1976). (Endochronic Theory of Inelasticity and Failure of Concrete), Journal of Engineering Mechanics, ASCE, Vol. 102, No. EM4, p.p. 701 – 722.
- Bazant, Z. P., Ansal, M. and Krizek, R. J., (1979). (Visco-Plasticity of Transversely-Isotropic Clays), Journal of Engineering Mechanics, ASCE, Vol. 105, No. EM5, p.p. 549 – 565.
- Mitchel, J. K. (1993). (Fundamentals of Soil Behaviour), Second Edition, John Wiley and Sons.
- Valanis, K. C., (1971). (A Theory of Viscoplasticity without a Yield Surface – Part I: General Theory, Part II: Application to Mechanical Behaviour of Metals), Archives of Mechanics, Vol. 23, No. 4, p.p. 517 – 551, Warszawa.

## NOTATION:

$d \in_{ij}$	Strain increments
$dt$	Time increments
$P$	Coefficient matrices
$J_2$	second deviatoric strain increment invariant
$I_1$	first strain increment invariant
$de_{ij}$	deviatoric strain increment tensor
$\delta_{ij}$	Kronecker delta
$d \in$	Volumetric strain increment
$z_1, \tau_1$	Constants
$d\xi$	damage measure
$d\zeta$	deformation measure
$d\lambda$	inelastic dilatancy
$S_{ij}$	deviatoric stress tensor
$\sigma_m$	mean stress
$G$	shear elastic moduli
$K$	bulk elastic moduli
$d \in^o$	stress-independent inelastic strains
$d\sigma_{ij}$	The stress increments
$D_{ijkl}$	elastic coefficient matrix



$d \in_{ij}^e$	elastic strain increments
$f(\eta)$	Strain-hardening function.
$F(\sigma, \epsilon)$	Strain-softening function.
$I_1^\sigma$	effective confining stress
$I_1^\epsilon$	the volume change
$J_2^\epsilon$	the second deviatoric strain invariant
a's	material constants
Pa	atmospheric pressure
$\beta_1$	constants
c's	material constants
$\beta_2$	softening coefficient
$e_o$	initial void ratio
$\epsilon_v$	volumetric strain
n	porosity
b's	constants
Po	consolidation pressure
C <sub>o</sub>	densification coefficient
E	elastic modulus
I <sub>L</sub>	the liquidity index of the clay
w <sub>ant</sub>	natural water content.
w <sub>p</sub>	plastic limit
I <sub>p</sub>	plasticity index
w <sub>L</sub>	liquid limit.



## **BUILDING OF AN EXPERT SYSTEM FOR WWTP OPERATION AND MANAGEMENT: RUSTIMIYAH SOUTH WWTP AS A CASE-STUDY**

Prof. Dr. Rafa H. Al-Suhaili

M.sc. Bashar J. Khalaf Al-Daami

Department of Environmental Engineering at University of Baghdad

### **ABSTRACT**

This paper presents the building of expert system to enable the inexperience plants operators to application of better of wastewater treatment plant. This methodology consists of three steps: (i) creation of a decision trees (algorithms) for the diagnosis operational problems; (ii) implementation into a real-based system; and (iii) verification. This system called expert system for Rustimiyah south wastewater treatment plant operation (ES-RS-WWTPO). The knowledge acquisitions to build this system were extracted from literature. Moreover local experience were also incorporated using the results of a well designed questionnaire. The results obtained in the application three operational states showed that the system was able to diagnosis (correctly) state of plant with reasonable accuracy. The programmer language for built this system id Visual Basic 6.0.

### **INTRODUCTION**

Wastewater is a combination of the waster-carried wastes produced from domestic, commercial and industrial sources. It has very complex composition, containing many different substances, both suspended, dissolved and a heterogeneous dispersion of organic and inorganic solids (11).

Wastewater treatment use complexity process and the success of wastewater treatment plants depended on their correct and safe operation. The treatment of the water and wastewater has become one of the most important environmental issues. Wastewater treatment id fundamental for keeping water natural resources (rivers, lakes, and seas) as high quality as possible (7). If wastewater id not effectively treated, several problems can occur: pollutants will be returned to the environment; decomposition of organic component evolves malodorous gases, disease may be spread by microorganisms present in the water or by poisoning due to toxic compounds, the organic nutrient in the wastewater may stimulate growth of aquatic plants (10).

### **Operational State of WWTP**

The operational state is described by a series of parameters (4). Also it is defined as a region that includes only influent parameters and process state variables, or it can also include adequate effluent quality variables (9). This may be a multidimensional region, where all the process state variables and parameters are located, thus if some of the state

variables or parameters drift a way from this region, the process is assumed to be in a different operational state, to determine this state, many measurement and observation are required (6).

### **Operational Problems**

A compilation of the different operational states that may occur in WWTPs were generated based on the explanation that found in literature as shown in table (1).

**Table (1)** typical operational problems that may occur in WWTPs

Rising sludge (Denitrification in the secondary clarifier).
Biological foams at the aeration tank (Foaming).
Industrial wastes.
Storms and Rainy water.
Toxic shock or poisoning.
Light filamentous bulking.
Primary sedimentation tank problems.
Strange wastes.
Many problems from mechanical or electrical origin.
Organic overloading.
Overflow.
High secondary clarifier sludge level.
Loading shock.
Solids shock.
Side streams.
Abnormal environmental temperature.
Other activated solids separation problems.

### **Artificial Intelligent**

Artificial intelligent is a branch of informatics that was widely adopted in industrial automation during the past fifteen years. AI programs are developed and used in computer science since the early days of digital computers (2).

Recently, application of AI techniques, such as decision support systems, expert systems for municipal sewage treatment in towns and cities of different sizes are increasingly attracting the interest of national and international private institutions and is gradually being considered as an attractive and proven alternative to conventional control (5).

### **EXPERT SYSTEMS (ES)**

There are popular AI techniques in industries. Where ES is a computer program that uses knowledge and inference procedures to solve problems that are ordinary solved through human expertise. The main components of an ES are: (i) Inference engine, (ii) Data base; and (iii) User-interface (12).

ES incorporated rule kind of programming. They are currently being used in many applications in the area of wastewater treatment plant, power systems and power electronics.

During the last decade, the research of wastewater treatment has been concentrated mainly on the operation rather than the design and construction of the treatment plants. This is due to the fact that the management and operation of the plants is the key step for the efficiency of water pollution control (8).

### **Advantages of Expert Systems**

According to Gonzales (3) an expert systems have a number of distinct advantages. The advantages are:

- Wide distribution of scares experts.
- Ease of modification.
- Consistency of answering.
- Preservation of experts.
- Perpetual accessibility.
- Solution of problem involving incomplete data.

### **Statement of problem**

In Iraq, by now suffer from sever lack of experience in wastewater treatment plant operation and management. This is due to the circumstances prevailed during the last two decades: wars; sanction; and low secure conditions led to the migration of so many expertises outside Iraq. Low and lack of maintenance and training capabilities forces the authorities to wastewater treatment plants. This is premise upon which the building of an efficient ES is necessary.

## **EXPERIMENTAL SYSTEM**

### **plant description**

An expert system to support the diagnosis and solution of the operational problems was built for Rustimiyah South wastewater treatment plant located in the Diyala river bank (Baghdad city, Iraq). According to Bechtel report (1) Rustimiyah south WWTP was designed to serve a total population equivalent of 1500000 capita and produce an average final effluent quality of 20mg/l BOD and 30mg/l TSS in order to meet the Iraqi national standards set by regulation No. 25 at 1967. It has three stages R0; R1; and R2.

This plant includes a primary treatment and a secondary treatment to remove organic matter and suspended solids from wastewater. Primary treatment is designed to physically remove solids material from the incoming wastewater. Coarse particles are removed by screens. Inorganic solids are removed in Detritor units and after that sewage flow passes to the pre-aeration tanks and many of the organic suspended solids are removed by sedimentation tanks. Table (2) shows the No. Detritors in plant and table (3) shows specifications of the pre-aeration tanks and table (4) shows No. of sedimentation tanks.

**Table (2)** the No. detritors in Rustimiyah south WWTP.

Plant: Process stream	Cross flow Detritos
R0	2
R1	1
R2 – stream A	2
R2 – stream B	2

**Table (3)** Specifications of the pre-aeration tanks in Rustimiyah south WWTP.

<b>Plant: process stream</b>	<b>No. of Pre-aeration tanks</b>	<b>Pre-aeration capacity (m3)</b>	<b>Aeration system</b>
R0	1	560	Diffused air-Blowers
R1	None	None	None
R2-stream A	1	445	Mechanical aerators
R2-stream B	1	445	=

**Table (4)** No. of sedimentation tanks in Rustimiyah south WWTP.

<b>Parameter</b>	<b>R0</b>	<b>R1</b>	<b>R2</b>
Maximum flow (l/s) (FTFT)	1852	2083	4166
Design surface over flow rate a DWF (m/hr) (SOR)	0.45	2.02	0.5
Design surface over flow rate max flow (m/hr) (SOR)	1.78	4.05	2.01
Surface area (m2)	3730	1850	7440
Total number of tanks	8	2	8
Diameter of each tank (m)	24.4	34.4	34.4

Secondary treatment consists of a biological conversion of dissolved and colloidal organic compounds into stabilized, low-energy compounds and new biomass cells, caused by a much diversified group of microorganisms, in the presence of oxygen. This mixture of microorganisms (living biomass) together with inorganic as well as organic particles contained in the suspended solids constitutes what is known as activated sludge. This mixture is kept in aeration tanks, where table (5) shows No. of aeration tanks in Rustimiyah south WWTP.

**Table (5)** No. of aeration tanks in Rustimiyah south WWTP.

<b>Plant: process stream</b>	<b>No. of Aeration tanks</b>	<b>Aeration capacity (m3)</b>	<b>Aeration systems</b>	<b>Total number of aerators</b>	<b>Aerator capacity for each unit (kw)</b>
<b>R0</b>	1	14000	Mechanical aerators	64	7.5
<b>R1</b>	1	18000	=	20	37.5
<b>R2</b>	1	25000	=	60	18.5

An aeration tank followed by a secondary sedimentation tanks (SSTs), Where table (6) shows No. of SSTs in Rustimiyah south WWTP.

**Table (6)** No. of SSTs in Rustimiyah south WWTP.

Parameter	R0	R1	R2
Number of installed tanks	4	4	8
Number of duty tanks	4	4	8
Diameter of each tank (m)	21.3	26	26
Original design MLSS (ml/g)	3500	4000	4000
Design SSVI <sub>3.5</sub> at average DWF (ml/g)	94	85	85
Recommended operating MLSS	2500	2500	2500
Design SSVI <sub>3.5</sub> at recommended MLSS and DWF (ml/g)	145	158	158
Average plant DWF (MLD)	40	45	90
FTFT (MLD)	80	90	180
RAS Flow(MLD)	68.6	63.6	68.7

### **ES-RS-WWTPO**

In this research an expert system is called expert system for Rustimiyah south wastewater treatment plant operation (ES-RS-WWTPO). This system was built in Visual Basic 6.0 language. The ES-RS-WWTPO takes into account the operational problems as mentioned in the literature review, questionnaire sheet, and these problems are occurred in Rustimiyah south WWTP as shown in table (7).

**Table (7)** types of problems these are applied in the ES-RS-WWTPO

Treatment types	Types of operational problems
Primary treatment	Old sludge, Septic sludge, Sludge removed systems break down, Clogged pumps or pipes, Low efficiency of grit removal, Primary high sludge density, Inadequate sludge purges, Hydraulic shock, High solids loading.
Secondary treatment	<b>(Biological origin)</b> Toxic shock Activated sludge solids separation problems: Filamentous bulking, Non-filamentous bulking, Biological foaming, Dispersed growth, Pin-point floc, Rising sludge.
	<b>(Non-Biological origin)</b> Clarifier problems Under loading Over loading

### **Establishing high; normal; and low values for most operational parameters**

At this point, the action range determined for every parameter high; normal; and low value for each operational parameters used in ES-RS-WWTPO as shown in table (8).

**Table (8)** High; normal; and low value for each operational parameter used in ES-RS-WWTPO.

Parameter	Low value	Normal value	High value
COD-I	<650	650-850	>850
COD-PE	<500	500-655	>655
COD-E	<98	98-128	>128
BOD-I	<300	300-400	>400
BOD-PE	<210	210-280	>280
BOD-E	<30	30-40	>40
SS-I	<230	230-330	>330
SS-PE	<70	70-100	>100
SS-E	<23	23-33	>33
DO	<1	1-2.5	>2.5
pH	<6.5	6.5-8.5	>8.5
SRT	<5	5-8	>8
V30	<50	50-200	>200
SVI	<50	50-100	>100
F/M	<0.25	0.25-0.35	>0.35
MLSS	<1000	1000-2000	>2000
COD (E)/P	<400	400-600	>600
COD (E)/N	<45	45-68	>68

### Description of ES-RS-WWTPO

The built system consists of many interaction windows, as explained in details:

**A- User name and password window:** as shown in figure (1)

**Figure (1)** The (input user name and password) window for ES-RS-WWTPO.



After the operator of plant was input the user name and password and click on cmd (ok), new window will appear; as shown in figure (2)



**Figure (2)** The starting window for ES-RS-WWTPO.

If the operator wants to run f ES-RS-WWTPO, he clicks on cmd (start).

**B- Start window:** as shown in figure (3)

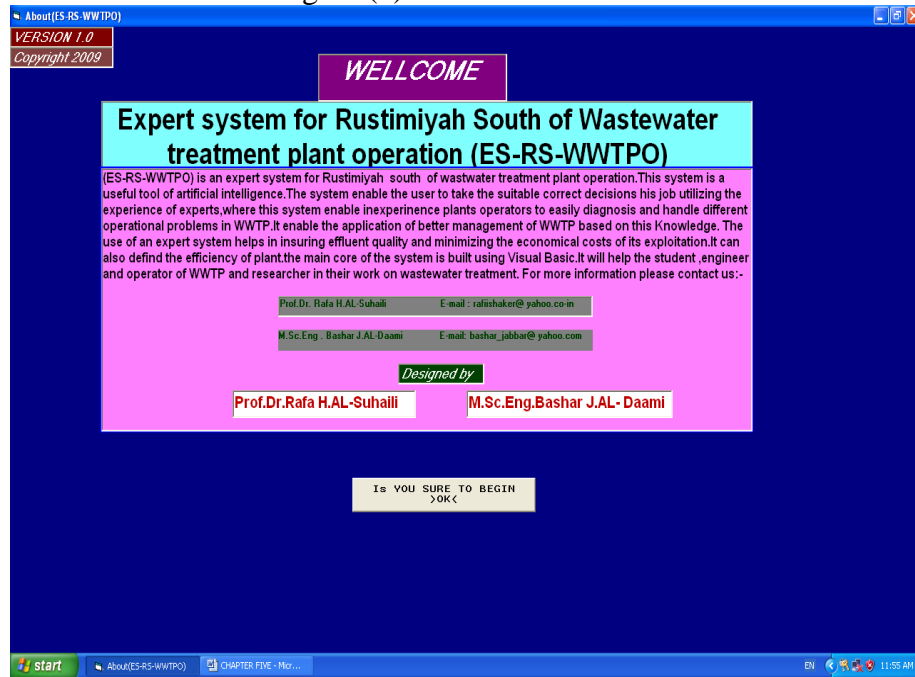


**Figure (3)** The (system name, version and copyright) window for ES-RS-WWTPO.

**C- Main window of ES-RS-WWTPO: as shown in figure (4)**

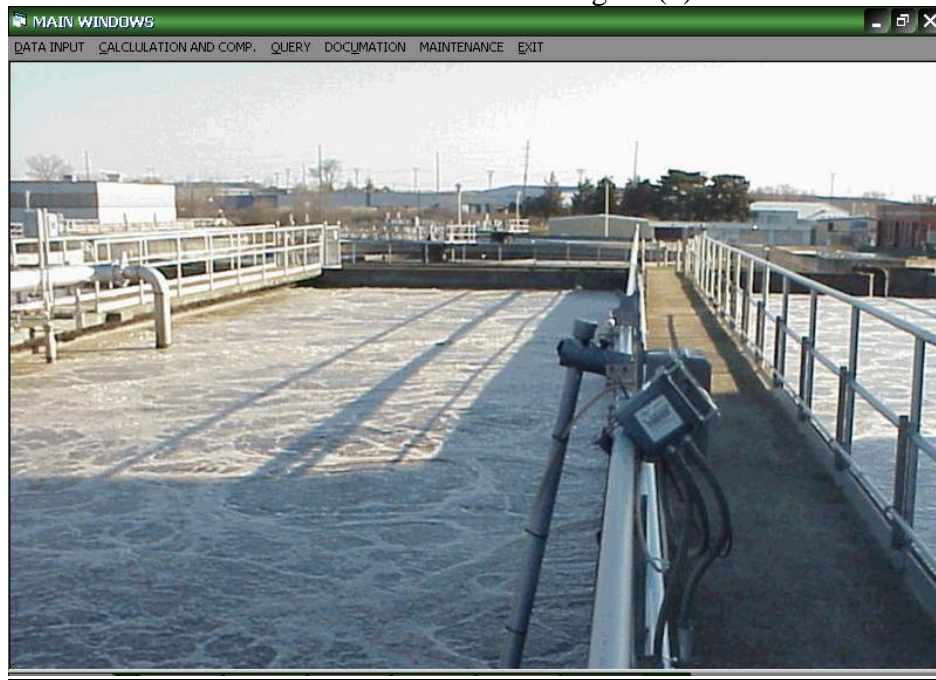


**Figure (4)** The main window for ES-RS-WWTPO.

**C1- Communication of ES-RS-WWTPO with the operator**

After the operator clicks on cms (DATA input window), window will appear as shown in figurer (5)

**Rustimiyah South WWTP / Plant Operation**  
**Data Registration**

**INPUT**

**Operator Name** BASHAR

**Date**  
hour 08:00  
Day Month Year 15/1 /2009

**Stage number** R2  
**Line number** A

**Off\_LINE DATA**  
**ON\_LINE DATA**  
**OTHER DATA**  
**BIOLOGICAL DATA**

**RETURN**

**Figure (5)** The data input window for ES-RS-WWTPO.



## C2- Role of the dynamic ES-RS-WWTPO

After the operator clicks on cmd (calculate and compared data), new window will appear as shown in figure (6)

Calculate the following data

SVI	137.5212	ml/g
F:M	0	Kg BOD / kg MLVSS.d
SRT	17.01582	day
HRT	0	hours
MCRT	17.28438	day
COD:N	157.1429	
COD:P	183.3333	
Total N	7	mg/l
SI %	81.66667	%
SS removal efficiency	93.6	%
COD removal efficiency	89.81818	%
BOD removal efficiency	94.3699	%

Check all Data if Low, Normal or High

COMPARED DATA WITH IRAQI LIMITS

SAVE RETURN

Figure (6) the calculation data window for ES-RS-WWTPO.

Where the operator clicks on cmd (calculate the following data), this system begins the calculate of the important parameters in the biological treatment. If the operator clicks on cmd (check all data), new window will appear as shown in figure (7)

Check all data

Parameter	I	PE	E
COD	1100	543	112
BOD	798	432	45
SS	1000	564	64
PH	8		8
Parameter	AT		
Temp C	44		
PH	7		

CHECK state of plant operation

Parameter	VALUE
MLSS recycle	3786
MLSS abs	4123
V30 abs	567
DO	2
Qwv	0
SVI	137.5212
F:M	0
SRT	17.01582
SS%	93.6
BOD%	94.3699
COD%	89.81818
COD/N	157.1429
COD/P	183.3333

RETURN

Figure (7) the level for each operational parameter window for ES-RS-WWTPO.

The above window will classify the input data and calculate data to high; normal; and low level for several pouts along treatment line.

Id the operator wants to check state of plant, he clicks on cmd (check state of plant operation), new window will appear as shown in figure (8)



**Figure (8)** The level for each operational parameter window for ES-RS-WWTPO.

When this system has concluded that the process is affected by (such as biological foaming problem), the operator can clicks on cmd (ok) that refers to the problem and new window will appear as shown in figure (9)

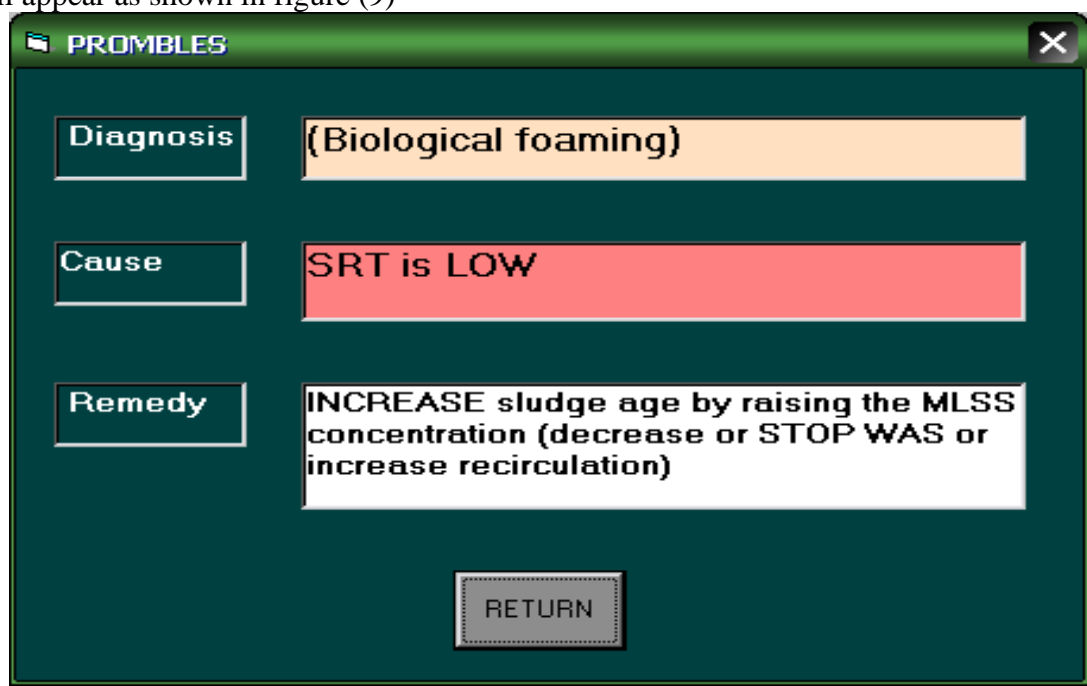


**Figure (9)** the results of diagnosis and remedies window for ES-RS-WWTPO.

The No. of interactive windows for all operational problems that included in ES-RS-WWTPO is 153 windows, as well as windows of results, documentation and maintenance methods for plant.

### C3- Query of ES-RS-WWTPO: as shown in figure (10).

ID	hour	data	stage	line	user_name	pcode	pcodepe	pcode	phodi	phodpe	phode	pssi	pspe	psse
2		10/22/2008	r1		all bbbb	500	750	600						
3						100	1000	1000	1000	1000	1000	10001	1000	1000
4						50	50	50	50	50	50	50	50	50
5						6000	6000	90	90	90	90	90	90	90

Data	Hour	Stage	Line	PHi	PHpe	PHe	Owastwater i	Owastwater pe	Owastwater
12/12/2009	12:00:00 PM	R1		6	7	6	85000	80000	80000
10/10/2008		R1		3	3	3	3	3	3
		R0		1	1	1	1	1	1

Data	Hour	Stage	Line	Low ss in sludge					
12/12/2009	8:00:00 AM	R2	A	0	0	0	0	-1	0
12/12/2009				0	-1	-1	0	0	0
12/12/2009				-1	0	0	0	0	0
12/12/2009				0	-1	0	0	0	0
12/12/2009				-1	0	0	0	0	0

Data	Hour	Stage	Line	Stdy settl.	Floc char.	foam pres.	Pred.micr.org	Protozoa P.	Zooplota P.
12/12/2009	8:21:22 AM	R0		type4	D	B	TYPE2	type1	M.farvecilia
13	9	R1		type1	A	G	2	0	Yes

Figure (10) (QUERY ALL DATA IN DATABASE) window for ES-RS-WWTPO.

## CONCLUSIONS

This paper presents an expert system to operation and management of Rustimiyah south WWTP. This system contribution id based on the methodology proposed and applied, which is based on build of decision trees (algorithms). An ES-RS-WWTPO was tests by application three real operational situation in WWTP. This application proved the capability of this system to diagnosis state of plant. This system can be exported as a protocol to any wastewater treatment plant with similar technology with minor changes. The ES-RS-WWTPO built and implemented in Rustimiyah south WWTP can be a useful tools to improve urban WWTP management.

## REFERENCES

- Bechtel international systems., (2004), "USAID Iraq Infrastructure Reconstruction Project", Project NO. 24910-609.
- C.C. Kontogiannis & A.N.Safacas, "AN EXPERT SYSTEM FOR POWER PLANTS", electromechanical energy conversion laboratory, Dept of electrical & computer engineering, university of patras.
- Gonza'lez, A., and Douglas, D.D., (1993), "The engineering of knowledge-based systems, theory and practice", prentice Hall Int. Editions, New Jersey.

- Joaquim, et al, *"Semi-automatic learning with quantitative and qualitative features"*, university of Gerona & politecnica.
- Joaquim, C., Matas., 2000, *"Development, Implementation and Evaluation of an Activated Sludge Supervisory System for the Granollers WWTP"*, PhD. Thesis, University of Girona.
- Martinez, M., 2005, *"Development and validation a KBDSS to support operators to handle solids separation problems of microbiological origin occurring in activated sludge systems "*, Ph.D. Thesis, College of Eng., University of Girona.
- M.Poch et al, 2000, *"Wastewater treatment improvement through an intelligent integrated supervisory system"*, contributions to science 1(4): 451-462, institute of studied Catalans, Barcelona.
- Nur. I. and Latifah, A., 2007, *"An Expert System for Troubleshooting in Wastewater Treatment Plant"*, Department of Environmental Sciences, University of Pura of Malaysia
- Rosen C. and Olsson G., (1998), *"Disturbance Detection in wastewater treatment plants"*, Wat. Sci. Techno., vol. 37, no. 12, pp. 197-205.
- Serra. P, M. Sanchez, j. Lafuente, V. Cortes and M. Poch., (1994), *"DEPUR: A knowledge-based tool for wastewater treatment plants, engineering application of artificial intelligent"*, 7, 23-30.
- T. Meenambal & R.UMA,. (2005), *" Principal of environmental science and engineering"*, first edition, S. Chand & Company LTD.
- Working Group of the line protection subcommittee, power system relying committee., (1994), *"Potential applications of expert systems to power system protection"*, IEEE Transactions on power Delivery, vol 9,
- No 2.



## “THE EFFECT OF VARIATION OF NONLINEAR LOAD ON POWER FACTOR OF THE AC SUPPLY NETWORK “

By

Mr. Mohammed Abdulla Abdulsada ,

Prof. Dr. Ali A. Al-killidar & Dr. Ziad Al-Azawi

Electrical Engineering Dept.

Electrical Engineering Dept.

Faculty of Engineering \ Tobruk

College of Engineering

Omar Al-Mukhtar University

University of Baghdad

### ABSTRACT

The aim of this paper is to evaluate the effect of the converter system on the power factor of the supply network .Therefore a 3-phase, 6-pulse , bridge converter is assembled and connected to a power supply through a 3-phase ac voltage regulator .The theoretical analysis is simulated using Fourier series analysis and Fast Fourier Transform ( FFT ) algorithm . The experimental measurements of distortion factor , displacement factor and total power factor are recorded . The experimental results are shown to be coincident with the theoretical results. The consideration of power factor improvement relative to distortion and displacement factors is discussed.

### الخلاصة

إن الهدف من هذا البحث هو تأثير مغير القدرة على معامل القدرة ( power factor ) للشبكة المجهزة. لذلك تم تجميع و ربط مجهر قدرة مستمر ثلاثي الطور ذو ست نبضات و باستعمال منظم فولتية في الطرف المتناوب . استخدمت طريقتان للتحليل النظري و هما : تحليل سلسلة فوريير ( Fourier series analysis ) و تحويل فوريير السريع ( Fast Fourier Transform ) . تم استنتاج النتائج العملية لمعامل الإزاحة ( displacement factor ) و معامل التشويه ( distortion factor ) و معامل القدرة و تم مقارنة النتائج النظرية مع النتائج العملية . تم مناقشة طرق تحسين معامل القدرة و ذلك عن طريق تحسين معامل الإزاحة و معامل التشويه .



**KEYWORDS:** power factor, displacement factor, distortion factor, harmonic currents, power factor correction, effect of dc inductance.

## INTRODUCTION

Power factor has increasingly become a topic of discussion when specifying loads and ac/dc power sources. When large nonlinear loads are connected to utility systems, significant harmonic currents are produced. The converter harmonics cause increased heating of the utility and other customer equipment and can lead to system resonance. Therefore, the harmonics need to be taken into account in various system evaluations[L. Cividino , 1992]. Harmonics can be defined as “ a sinusoidal component of a periodic wave or quantity having a frequency that is an integral multiple of the fundamental frequency”[ IEEE standard 519 – 1992, 1993] .The harmonics for a 6-pulse converter, 50 Hz fundamental frequency are the fifth (250 Hz), the seventh (350 Hz), the eleventh (550 Hz)...etc.

The most noticeable problem associated with electrical rectification was the inherently poor power factor of the power system. The power factor of a circuit is universally defined as “ the ratio of the active or average power, in watts, to the apparent power or product rms volt times rms amperes at the terminals". The above definition is based on the assumption that loads on the system have linear voltage-current characteristics and that harmonic distortion of the current and voltage is not significant. With these assumptions, the power factor is equal to the displacement factor. Harmonic distortion in the current and voltage caused by AC/DC converters in the system changes the way power factor must be defined[W. Shepherd and P. Zand , 1979]. In this case, the total power factor is defined as “the ratio of the total power input, in watt, to the total volt-amperes in the circuit” , the total power factor made up of two components; displacement and distortion factors. The displacement factor is “the ratio of the active power of the fundamental wave, in watt, to the apparent power , in volt-amperes”[P. Filipski S.,1991]. This is the power factor that is measured by metering. The distortion factor is that part associated with the presence of harmonic current and voltage [IEEE standard 519 – 1992, 1993].

The association of total power with displacement and distortion factors is important because it highlights the factors which determine the overall power factor of a system. A poor power factor can be the result of either a significant phase difference between the voltage and current at the load terminals, or it can be due to a high harmonic content or distorted/discontinuous current waveform. Poor load current phase angle is generally the result of an inductive load such as an induction motor, power transformer, lighting ballasts, welder or induction furnace. A distorted current waveform can be the result of a rectifier, variable speed drive, switched mode power supply, discharge lighting or other electronic load.

The power factor correction (PFC) can be made if the distortion factor and displacement factor are improved. The distortion factor is increased by reducing the harmonic currents from entering the main system by providing a shunt filter of low impedance to the harmonic frequencies. These shunt filters also supplies all or part of the reactive power consumed by the converter, the remainder being supplied by shunt capacitor banks Which used to improve the displacement factor. A large number of topologies and control strategies are implemented to achieve rectification in 3-phase supply with high power factor[H. Mao , etal , 1997 ; Y. Jang and M. Jovanovic , 1998].





The objective of this paper is to analyze the supply total power factor of the 3-phase, 6-pulse, ac\dc bridge converter with the use of 3-phase ac voltage regulator theoretically and experimentally.

### \* DISPLACEMENT FACTOR, DISTORTION FACTOR AND TOTAL POWER FACTOR

The angle between the fundamental supply voltage and the fundamental component of the supply line current is known as displacement angle ( $\phi$ ). The cosine of the input displacement angle is the displacement factor ( $\cos \phi$ ). The displacement factor can be also defined as the ratio of the active power to the fundamental apparent power.

The distortion factor is defined as the ratio of the rms amplitude of the fundamental component of the input supply line current, to its total rms amplitude, that is:

$$\cos \delta = \frac{I_1}{I_L} \quad (1)$$

The total power factor is defined as the ratio of the total active power input, in watt, to the total apparent power in the circuit, that is:

$$PF = \frac{\text{Total active power input (W)}}{\text{Total apparent power input (VA)}} \quad (2)$$

### \* POWER FACTOR UNDER LINEAR AND NONLINEAR LOADS

The linear load is that load that draws a sinusoidal current wave when supplied by a sinusoidal supply voltage. Only the fundamental component of the supply voltage and line current exist. The active input power could be described as:

$$P = \frac{1}{2\pi} \int_0^{2\pi} e(\omega t) \cdot i(\omega t) \cdot d\omega t = \frac{1}{2\pi} \int_0^{2\pi} \sqrt{2} E_n \sin(\omega t) \cdot \sqrt{2} I_1 \sin(\omega t + \phi_1) \cdot d\omega t \quad (3)$$

Which leads to:

$$P = E_n \cdot I_1 \cdot \cos \phi_1 \quad (4)$$

The apparent power will be given by :

$$S = S_1 = E_n \cdot I_1 \quad (5)$$

By definition the total power factor is given by:

$$PF = \frac{P}{S} = \frac{P}{S_1} = \cos \phi_1 \quad (6)$$

It can be deduced that in the linear loads the total power factor is equal to the displacement factor.

In the case of nonlinear load the current drawn from the main supply voltage is non-sinusoidal (distorted) and can be represented by Fourier summation of the fundamental and harmonics components:

$$I(\omega t) = \sqrt{2} I_1 \sin(\omega t + \phi_1) + \sum_{h=2}^{\infty} \sqrt{2} I_h \sin(h\omega t + \phi_h) \quad (7)$$

The active power drawn from the supply system due to each harmonic component of current is given by:

$$P_h = \frac{1}{2\pi} \int_0^{2\pi} \sqrt{2} E_n \sin(\omega t) \cdot \sqrt{2} I_h \sin(h\omega t + \phi_h) d\omega t = 0 \quad (8)$$

That means the active power transferred only by combination of voltage and current components of the same frequency

The total rms line current and total apparent power is given by:

$$I_L = \sqrt{I_1^2 + \sum_{h=2}^{\infty} I_h^2} = \sqrt{\sum_{h=1}^{\infty} I_h^2} \quad (9)$$

$$S = E_n \cdot I_L = E_n \cdot \sqrt{\sum_{h=1}^{\infty} I_h^2} \quad (10)$$

By the use of Eq. (1), the total power factor will be :

$$PF = \frac{I_1}{\sqrt{\sum_{h=1}^{\infty} I_h^2}} \cdot \cos \phi_1 = \frac{I_1}{I_L} \cdot \cos \phi_1 \quad (11)$$

Thus, the power factor of nonlinear load is made up of product of two components: displacement Factor (  $\cos \phi_1$  ) and the distortion factor (  $I_1 / I_L$  ) which associated with the harmonics present.

Since, by definition,  $I_L$  is greater than  $I_1$  due to the presence of harmonics current component, the distortion factor is less than unity and hence the power factor is less than unity even in those cases where  $\cos \phi_1$  has it is maximum value of unity.

The distortion power (  $D$  ) is created by the combination of voltage and current components of harmonic current . Only fundamental frequency powers (  $P$ ,  $Q$  and  $S_1$  ) can be represented by a triangle phasors as shown in **Fig.1.a** .The total apparent power and distortion power are only numerical values. The distortion power is perpendicular to the plane  $P$ ,  $Q$  and  $S_1$ , so that the total apparent power (  $S$  ) is conventional to represented geometrically by a three dimensional representation (space diagonal) as shown in **Fig.1.b**[Task Force , 1996].

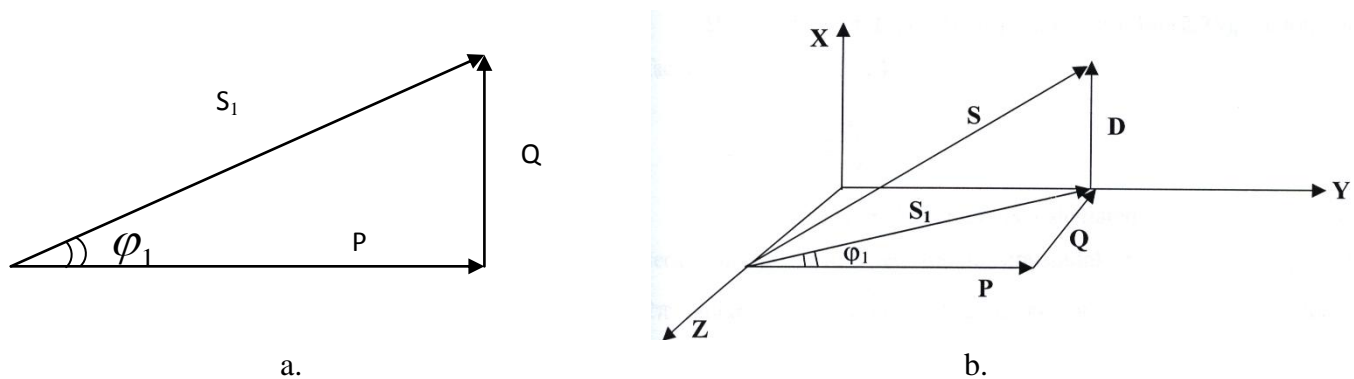


**Fig.1** Power phasor diagram ( a ) linear load ( b ) nonlinear load.

### \* POWER FACTOR IN TERMS OF FOURIER SERIES COEFFICIENTS

The total power factor can be calculated also by using the Fourier series analysis. For a periodic non-sinusoidal current  $I(\omega t)$  of a periodicity  $2\pi$  radians the Fourier coefficient  $a_1$  and  $b_1$  for the peak value of the fundamental line current are:

$$a_1 = \frac{1}{\pi} \int_0^{2\pi} i(\omega t) \cdot \cos \omega t \, d\omega t \quad (12)$$

$$b_1 = \frac{1}{\pi} \int_0^{2\pi} i(\omega t) \cdot \sin \omega t \, d\omega t \quad (13)$$

The rms value of fundamental line current ( $I_1$ ) is given by:

$$I_1 = \sqrt{(a_1^2 + b_1^2)/2} \quad (14)$$

The displacement factor can be shown to be:

$$\cos \phi_1 = \cos \left[ \tan^{-1} \frac{a_1}{b_1} \right] = \frac{b_1}{\sqrt{a_1^2 + b_1^2}} \quad (15)$$

The distortion factor is given by:

$$\cos \delta = \frac{\sqrt{a_1^2 + b_1^2}}{\sqrt{2} I_L} \quad (16)$$

The total power factor is found to be :

$$PF = \frac{b_1}{\sqrt{2} I_L} \quad (17)$$

### \* MODELING AND ANALYSIS OF AC\DC CONVERTER

At low ac level network ( i.e. 0.4 Kv ), 3-phase , 6-pulse , AC\DC bridge converters are recommended when dealing with power up to 150 Kw. In case of high dc current , it is preferable to control the supply ac voltage by means of 3-phase ac voltage regulator as shown in **Fig.2**. This allow the thyristors to control the lower primary current , which results in simpler more economical power circuit.

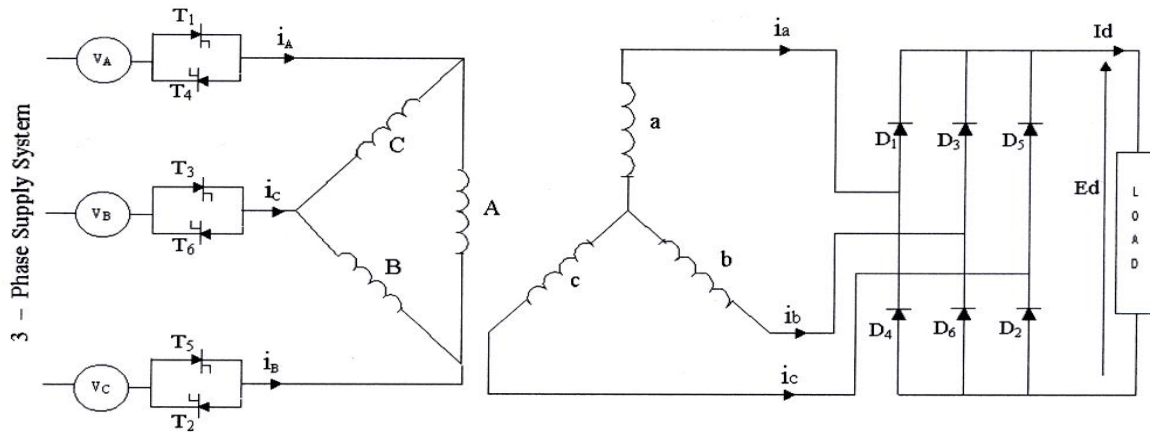


**Fig.2** Circuit configuration of ac voltage regulator with 3-phase bridge rectifier.

$$\left. \begin{aligned} V_A &= \sqrt{2} E_n \sin(\omega t) \\ V_B &= \sqrt{2} E_n \sin(\omega t - 2\frac{\pi}{3}) \\ V_C &= \sqrt{2} E_n \sin(\omega t - 4\frac{\pi}{3}) \end{aligned} \right\} \quad (18)$$

The corresponding line-to-line supply voltage be:

$$\left. \begin{aligned} V_{AB} &= \sqrt{6} E_n \sin(\omega t + \frac{\pi}{6}) \\ V_{BC} &= \sqrt{6} E_n \sin(\omega t - \frac{\pi}{2}) \\ V_{CA} &= \sqrt{6} E_n \sin(\omega t - \frac{7\pi}{6}) \end{aligned} \right\} \quad (19)$$

The operation of this model of AC\DC converter is depends on the firing angle values. On varying the firing angle  $\alpha$  from  $0^\circ$  to  $30^\circ$  as measured from zero transit of the phase voltage , there is no control on the thyristors conduction . The thyristors start to be controlled fully after  $\omega t = \pi \setminus 6$  of the transit of the phase voltage. During this period , the transformer is subjected to balance 3-phase supply voltages. At any instance of time, two diodes conduct one in the positive half and the other in the negative one.

For the range of  $\alpha$  ,  $30^\circ \leq \alpha \leq 60^\circ$  , there are certain periods when three thyristors conduct and another when two thyristors conduct simultaneously. This particular mode of operation is represented the notation mode 2\3. It may be noted that the period during which three-thyristors conduct simultaneously decrease as the firing angle is retarded and when the firing angle is  $60^\circ$  or more three-thyristors simultaneous conduction ceases. This operation of the circuit describe as mode 2\2 , extends over the firing angle rang from  $60^\circ$  to  $90^\circ$  . Last mode of operation is referred to as mode 0\2 describe the operation for firing angle rang from  $90^\circ$  to  $150^\circ$  which discontinuous condition is occur. **Fig.3** shows the waveforms of secondary and supply line currents for different modes of operation .

#### \* CALCULATION OF DISPLACEMENT FACTOR, DISTORTION FACTOR AND TOTAL POWER FACTOR

The displacement, distortion and total power factor at the supply side can be evaluated in terms of Fourier coefficients . The displacement factor can be found by using Eq.(15) and the Fourier coefficients and given by:

$$\cos \phi_1 = \left\{ \begin{array}{ll} 1 & \alpha \leq 30^\circ \\ \frac{(4\pi - 6\alpha \div 3\sin 2\alpha)}{\left[9(1 - \cos(2\alpha))^2 + \langle 4\pi - 6\alpha + 3\sin(2\alpha) \rangle^2\right]^{\frac{1}{2}}} & 30^\circ \leq \alpha \leq 60^\circ \\ \frac{2\pi + 3\sqrt{3} \cos 2(\alpha - 30^\circ)}{\left[27 + 4\pi^2 + 12\sqrt{3} \pi \cos 2(\alpha - 30^\circ)\right]^{\frac{1}{2}}} & 60^\circ \leq \alpha \leq 90^\circ \\ \frac{5\pi - 6\alpha - 3 \sin 2(\alpha - 60^\circ)}{\left[9(1 + \cos(2\alpha - 60^\circ))^2 + \langle 5\pi - 6\alpha - 3 \sin 2(\alpha - 60^\circ) \rangle^2\right]^{\frac{1}{2}}} & 90^\circ \leq \alpha \leq 150^\circ \end{array} \right\} \quad (20)$$

By Combination of Eq. (1) and the Fourier coefficients ,results in the following expression for distortion factor:

$$\cos \delta = \left\{ \begin{array}{ll} \left[ \frac{2\pi + 3\sqrt{3} \cos 2\alpha}{4\pi} \right]^{\frac{1}{2}} & \alpha \leq 30^\circ \\ \left[ \frac{9(1 - \cos(2\alpha))^2 + \langle 4\pi - 6\alpha + 3\sin(2\alpha) \rangle^2}{4\pi(4\pi - 5\pi \div 3\sin 2\alpha)} \right]^{\frac{1}{2}} & 30^\circ \leq \alpha \leq 60^\circ \\ \left[ \frac{(27 + 4\pi^2 + 12\sqrt{3} \pi \cos 2(\alpha - 30^\circ))}{4\pi(2\pi + 3\sqrt{3} \cos 2(\alpha - 30^\circ))} \right]^{\frac{1}{2}} & 60^\circ \leq \alpha \leq 90^\circ \\ \left[ \frac{9(1 + \cos(2\alpha - 60^\circ))^2 + \langle 5\pi - 6\alpha - 3 \sin 2(\alpha - 60^\circ) \rangle^2}{4\pi \langle 5\pi - 6\alpha - 3 \sin 2(\alpha - 60^\circ) \rangle} \right] & 90^\circ \leq \alpha \leq 150^\circ \end{array} \right\} \quad (21)$$

The supply total power factor is obtained by using Eq. (14), or can be expressed as the product of Eq. (20) and (21) and given by:

$$PF = \left\{ \begin{array}{ll} \left[ \frac{2\pi + 3\sqrt{3}}{4\pi} \right]^{\frac{1}{2}} & \alpha \leq 30^\circ \\ \left[ \frac{(4\pi - 6\alpha \div 3\sin 2\alpha)}{4\pi} \right]^{\frac{1}{2}} & 30^\circ \leq \alpha \leq 60^\circ \\ \left[ \frac{2\pi + 3\sqrt{3} \cos 2(\alpha - 30^\circ)}{4\pi} \right]^{\frac{1}{2}} & 60^\circ \leq \alpha \leq 90^\circ \\ \left[ \frac{5\pi - 6\alpha - 3 \sin 2(\alpha - 60^\circ)}{4\pi} \right]^{\frac{1}{2}} & 90^\circ \leq \alpha \leq 150^\circ \end{array} \right\} \quad (22)$$

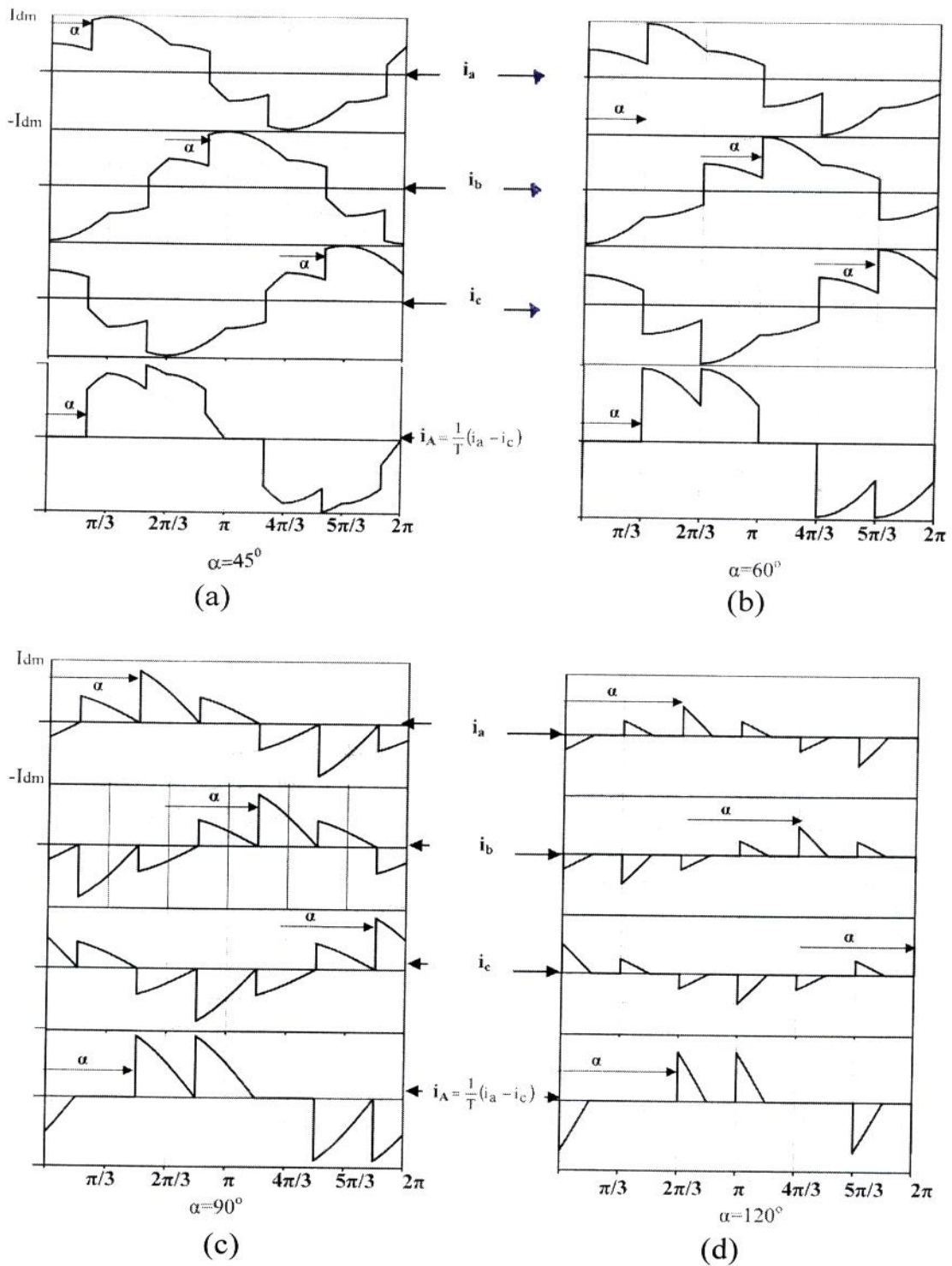


**Fig.3** Secondary and supply line currents for different firing angles.

## - Simulation and Experimental Results

The Harmonic current magnitudes are evaluated using two methods; Fourier series ( FS ) decomposition and Fast Fourier Transform ( FFT ).The FFT method described the current waveform in the time domain and can easily be performed via computer software to arrive at the constituent harmonics. The MatLap software is used to compute the FFT of the supply line current and the complete data vector input takes exactly one period to sample. The sampling rate is taken to be 180 sample per complete period ( i. e. 180 sample\ 20 msec. ).

A 3-phase , 6-pulse , 4.2 Kw is assembled and connected to 0.4 Kv power supply through 3-phase , ac voltage regulator (fig.(2)). The driver input signal to the firing circuit is in the range ( 0-6.3 ) which provides a firing angles from zero to  $150^\circ$  . A 5 KVA , delta\star transformer of 19 turns ratio ( step down ) is used and the load is a pure resistive of  $0.15 \Omega$  .

**Fig.3** shows the experimental waveform of the supply line current and the corresponding frequency spectrum. The displacement, distortion and total power factors computed by tow simulation methods and these results and the experimental results are shown in **Fig.4 – Fig.6**. Form **Fig.4** , it can be seen that the displacement factor has a maximum value of 0.94 at uncontrolled region (  $\alpha \leq 30^\circ$  ) . This is due to the supply current is approximately in phase with the supply phase voltage. With firing angle increases the displacement factor is rabidly decrease because the firing angle shifts the supply current waveform and this increase the displacement angle , hence , decrease the displacement factor.

The changes in the distortion factor values with the increase of the firing angles are small as shown in **Fig.5**. For firing angle greater than  $70^\circ$  , the harmonic currents begin to effect the values of distortion factor and this affect increases as the firing angle increases. The distortion factor is equals to 0.932 at  $\alpha = 70^\circ$  and decrease to 0.812 at firing angle equals to  $110^\circ$  . Also , the fundamental component of experimental results is found to be greater than the theoretical results , especially at higher firing angles, and this explain the reason of significant reduction in the distortion factor of the experimental results. From **Fig.6** , the maximum total power factor is 0.914 which is measured at no control angle and reaches zero at  $\alpha = 150^\circ$ .



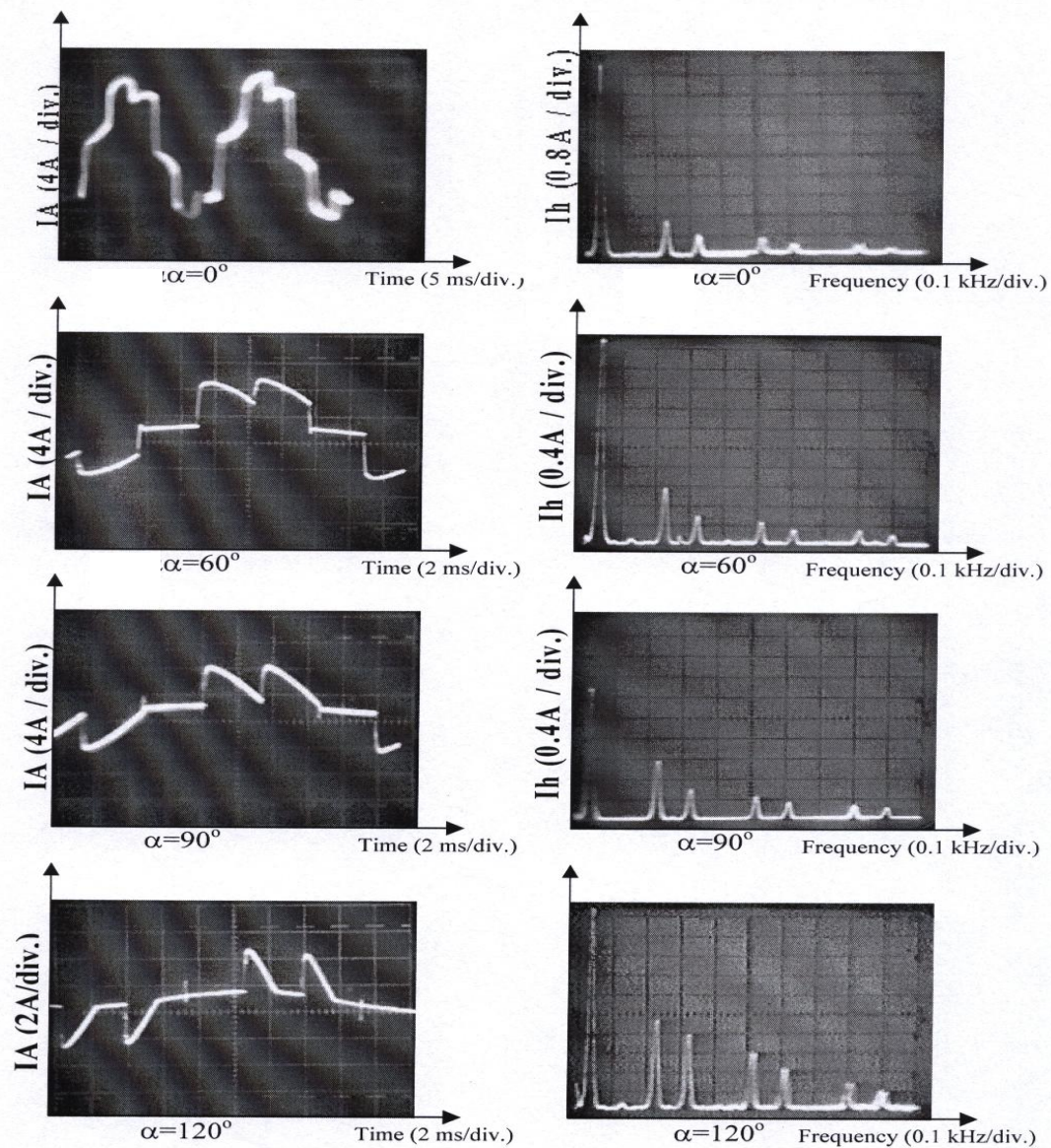


**Fig.3** Experimental waveforms of the supply line current and corresponding frequency spectrum.

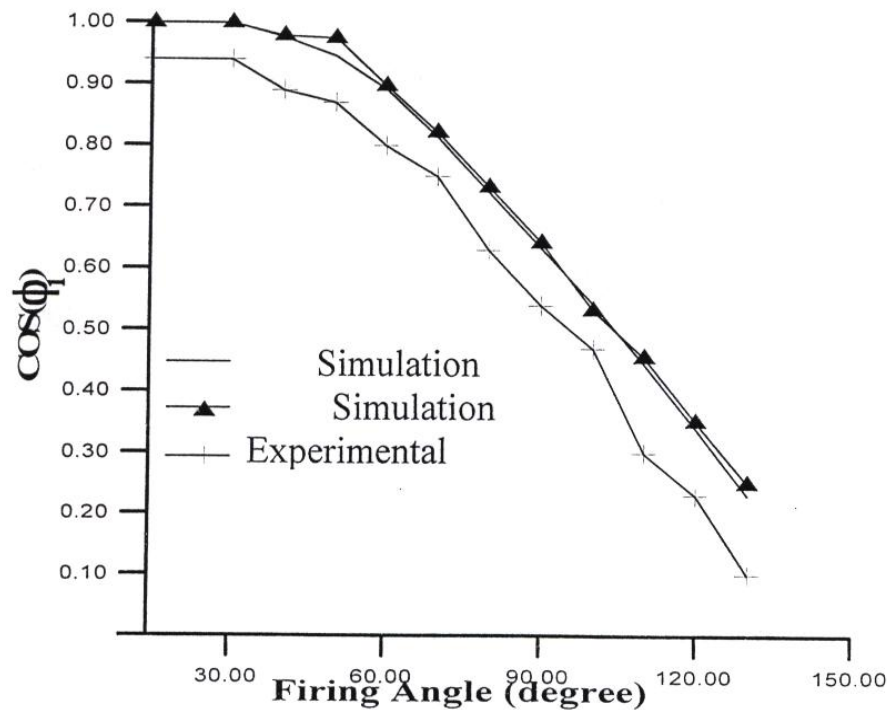


**Fig.4** Simulation and experimental results of displacement factor.

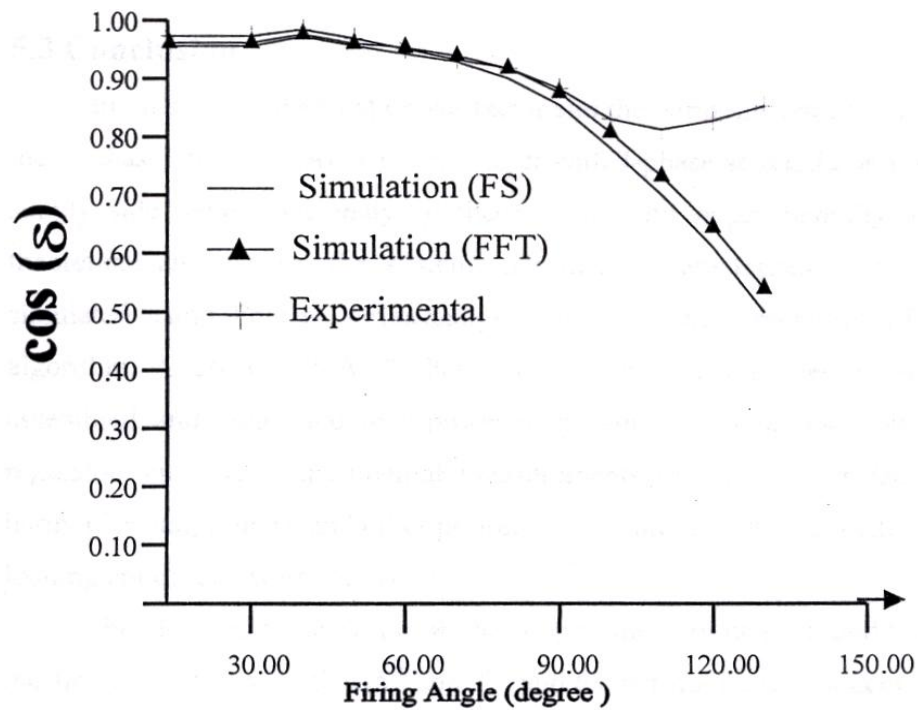


**Fig.(5)** Simulation and experimental results of distortion factor.

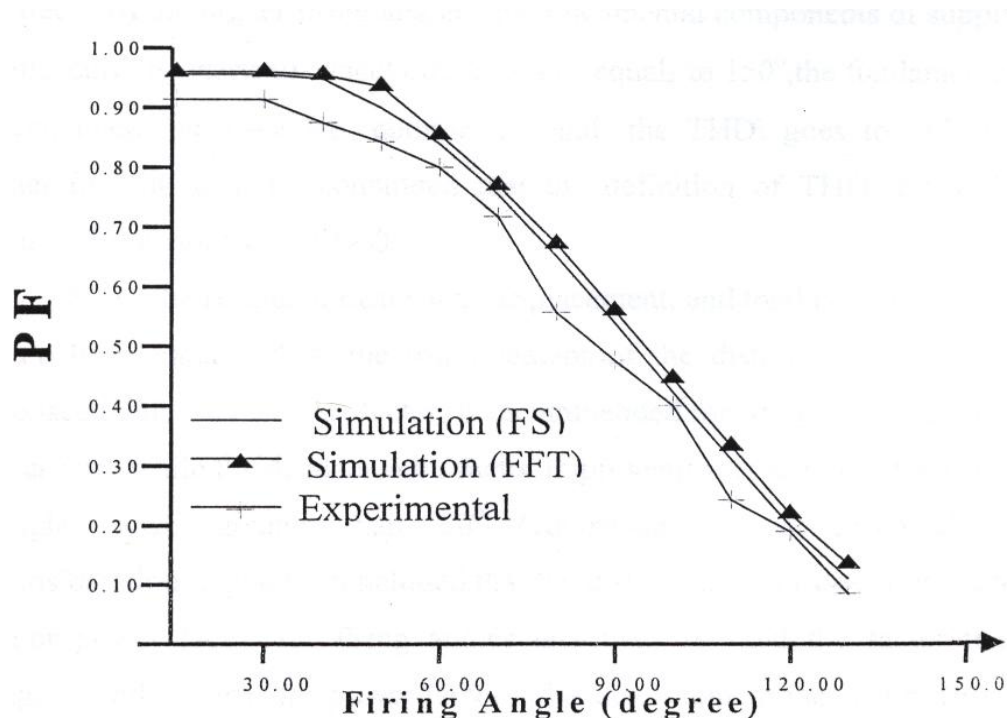


Fig.(6) Simulation and experimental results of power factor.

## CONCLUSION

In this paper , the total power factor of the 3-phase, 6-pulse , ac\dc converter with 3-phase ac voltage regulator at the supply side is analyzed theoretically and experimentally. The theoretical analysis for the harmonic current , and total power factor are simulated using Fourier series analysis and Fast Fourier Transform ( FFT ) algorithm . A 4.2 Kw ( 26 v \ 162 A ) , 3-phase, AC\DC converter is assembled and the experimental measurements of harmonics amplitudes, total power factor and other parameters were carried out. From the results of distortion factor , displacement factor and total power factor it can be deduce that the agreement between experimental and simulation results is fair but there are small differences between them . This is because of commutation effect , errors in measuring exactly the values of firing angle , and the instrument inaccuracies. The improvement of the distortion factor , and consequently the power factor , is recommended for firing angle greater than 70° , while the displacement factor improvement is required for firing angle greater than 30°. From above consideration , it can be concluded that the distortion factor does not cause poor power factor for firing angle less than 70° and the factor that significantly effects the power factor is the displacement factor. For firing angle greater than 70° , both the distortion and displacement factors are responsible of lower power factor.

The model of AC|DC converter ,which considered in this paper , is preferable to be used at low voltage level network to produce low dc voltage , high dc current . This allow the thyristors to control the lower primary current , which results in simpler more economical power circuit.

## REFERENCES

- H. Mao , etal , 1997,” Review of high performance three phase power factor correction circuits” , IEEE Trans. On Industry electronics , Vol.44 , No. 4 , Aug., PP 437-445.
- IEEE standard 519 – 1992 , 1993, “ IEEE recommended practices and requirements for harmonic control in electrical power systems” .
- J. Arrillaga , et al , 1997 “ Power system harmonic analysis “ , London: Wiley.
- L. Cividino , 1992 , " Power factor , harmonics distortion , causes , effects and considerations " 14'th international conference on telecommunication energy , Oct. , pp. 506 – 513.
- P. Filipski S.,1991 , " Polyphase apperent power and power factor under distorted waveorme condition " , IEEE Trans. On Power Delivery , Vol.6 , No. 3 , July, PP 1161-1165.
- R. D. Henderson and P. J. Rose , 1994, “ Harmonics: the effect on power quality and transformer “ , IEEE Trans. On Industry Applications , Vol.30 , No. 3 , May\June, PP 528-532.
- Task Force on Harmonics Modeling and Simulation , 1996 , “modeling and simulation of the propagation of harmonics in electric power networks “ , IEEE Trans. On Power delivery , Vol.11 , No. 1, Jan. ,PP 452-461.
- V. K. Mehta , 1998 ,“ Principle of power system “ , S. Chand and Company ltd. , India .
- W. Shepherd and P. Zand , 1979, “Energy flow and power factor in nonsinusoidal circuits “ , Cambridge university press .
- Y. Jang and M. Jovanovic, 1998 , “ A comparative study of single switch , three phase , high power factor rectifier “ , IEEE APEC'98 Conference record , part 2 , PP 1093-1099.

**LIST OF SYMBOLS**

$\alpha$  = Firing angle.

$\cos \varphi_1$  = displacement factor.

$\cos \delta$  = Distortion factor.

D = distortion power.

$E_d$  = Average direct voltage.

$E_n$  = ac supply line-to-neutral voltage (rms).

h = order of harmonic.

$i(\omega t)$  = Instantaneous supply current.

$I_d$  = Average value of dc load current.

$I_{dm}$  = crest value of dc load current.

$I_1$  = fundamental component of  $I_L$ .

$I_{10}$  = fundamental component of  $I_L$ , assuming zero phase control.

$I_L$  = supply line current (rms).

K = Integer no. , 1,2,3 , ...

P = Active input power.

PF = total power factor.

R = Resistance of dc load.

S = Total apparent power.

$S_1$  = fundamental component of apparent power.

T = Transformer turns ratio.

$V_A, V_B, V_C$  = Instantaneous line-to-neutral 3-phase supply voltages.

$V_{AB}, V_{BC}, V_{AC}$  = Instantaneous line-to-line 3-phase supply voltages.

## INFLUENCE OF LENS ON MIGRATION OF DENSE NON-AQUEOUS PHASE LIQUID IN SATURATED ZONE

Prof. Dr. Waleed M. S. Kassim

Dr. Ayad A. H. Al-Dulaimi

Tamara Kawther Hussein

Environmental Engineering Department, College of Engineering, University of Baghdad

### ABSTRACT

This study concerns the control of movement of Dense Non-Aqueous Phase Liquid (DNAPL) in saturated zone in the presence of relatively low permeability lens. A two-dimensional, finite-difference numerical model for the simultaneous movement of the DNAPL and water through the saturated zone of the soil is developed. The system is, actually, a three fluid phase system (water, DNAPL and air) but in the derivation of the model, air was treated as an immobile phase at constant atmospheric pressure. The flow equations for Dense Non-Aqueous Phase Liquid and water are cast in terms of the wetting and non-wetting fluid pressure heads respectively. The finite-difference equations are solved fully implicitly using Newton-Raphson iteration scheme with a Taylor series expansion to treat the nonlinearity. The present numerical results are compared with results of Kueper and Frind (1991b). The results of all tests showed that the presence of lens controls the vertical movement of Dense Non-Aqueous Phase Liquid (DNAPL) in heterogeneous porous medium.

### تأثير وجود حاجز على حركة السوائل العضوية الاثقل من الماء في الطبقة مشبعة من التربة

#### الخلاصة

تتعلق هذه الدراسة بالسيطرة على حركة السوائل العضوية الاثقل من الماء، المسماة (Dense Non-Aqueous Phase Liquids (DNAPL<sub>s</sub>)) في الطبقة المشبعة من التربة بواسطة استخدام حاجز قليل النفاذية نسبياً. تم تطوير نموذج عددي ذو بعدين واستخدام طريقة الفروق المحددة و اعداد خوارزمية لحساب حركة تلك السوائل العضوية، الماء خلال الطبقة المشبعة من التربة. في الواقع يتكون النظام من ثلاثة اطوار من السوائل (ماء، سوائل عضوية اقل من الماء (DNAPL) والهواء) لكن عند اشتقاق النموذج الرياضي تم معاملة الهواء كطور غير متحرك مع ثبوت ضغط الهواء عند الضغط الجوي. ان المعادلات التي تصف حركة الماء و السوائل العضوية وضعت بدلالة عمود الضغط لتلك السوائل. أن معادلات الفروقات المحددة حلت



(fully implicitly) وباستخدام طريقة (Newton-Raphson) مع (Taylor series) لمعالجة المعادلات اللاخطية. تمت عملية اختبار كفاءة النموذج الحالي من خلال مقارنة نتائجه مع نتائج النموذج المقدم من قبل Kueper and Frind (1991b) النتائج لجميع الاختبارات تشير إلى أن وجود حاجز (Len) يسيطر على الحركة العمودية (DNAPL<sub>s</sub>) خلال الوسط غير المتجانس .

## INTRODUCTION

Groundwater is one of the most widespread sources of water, and because of its extensive use, ground water contamination has become a major environmental concern. The great majority of groundwater contaminants are released either from leaking hazardous waste landfills and hazardous waste ponds, or from spills and leaks during the storage and transportation of Non-Aqueous Phase Liquids (NAPL<sub>s</sub>). The reason why NAPL<sub>s</sub> entering soil and ground water system consider serious because of the major environmental health and safety problems associated with hydrocarbon discharge to the subsurface environment (Hall and Quam, 1976). Hydrocarbon products are typically multi-component organic mixtures composed of chemicals with varying degree of water solubility. These components are carcinogenic and some at least have some diverse health effects (Haskell, 1997; Ali, 2002) (Saleem, 2005).

As the oil migrates, the quantity of mobile oil decreases due to the residual oil left behind. If the amount of oil spilled is small, all of the mobile oil will become exhausted and the oil will percolate no further. However, if the amount of oil spilled is large, mobile oil will reach the water table. When DNAPL such as Trichloroethylene (TCE) infiltrates into the soil in large amounts, gravity causes it to sink into the groundwater aquifer and remain at the bottom for extended periods of time (Kim and Corapcioglu, 2003).

Underground containment barriers are an important method of limiting and/or eliminating the movement of contaminants through the subsurface. Barriers are currently used for the containment of contaminated waste, as an interim step while final remediation alternatives are developed (or decided). The purpose and function of the containment system must be determined prior to design and construction of the barrier. Site characterization is an essential part of choosing an appropriate barrier (Rumer and Mitchell, 1996). The plume of NAPLs will migrate vertically downward under force of gravity until it reach low permeability layer. Then, it accumulates and migrates laterally. There are many subsurface barrier technologies commercially available and others in various stages of development such as: - (Slurry walls, Sheet pile walls, Frozen barriers ...etc) (Pearlman, 1999).

There is a significant progress in multi-phase flow modeling during the last two decades in groundwater. Multi-phase flow and transport model was presented by Abriola and Pinder (1985a). The one-dimensional, finite-difference model included an organic phase composed of one volatile and one nonvolatile organic component. Al-Dulaimi (2006) studied the infiltration and redistribution of Light Non-Aqueous Liquid for the state of three fluid phases (water, oil and air) in the unsaturated-saturated zone of the soil.

Migration of NAPL<sub>s</sub> can be controlled by barrier systems. Starting in the late 1950s, gelling liquids were used successfully in grouting by controlling the injection

operation. Particulate grouts generally cannot be injected into media finer than medium sand. In finer grain-size material, gelling liquids must be used (May et al. 1986). As noted by Karol (1990), gelling liquids have a greater radius of influence than particulate grouts due to their initial low viscosity before gelation. Rumer and Ryan (1995) reported that while several techniques have been demonstrated as the pilot scale and others are currently under development, horizontal barrier construction has not been developed to the extent of the vertical barriers. Newman (1995) barrier-material Zeolites treated with the Surfactant Hexa Decyl Tri Methyl Ammonium (HDTMA). HDTMA effectively traps many types of organic and inorganic contaminants in soil, while allowing water to pass through the barrier as cited by (Basri, 2001). Wipfler (2003) focused on the effect of an inclined soil layer with respect to the water table. There is a wide variety of possible barrier systems for sanitary landfills of Municipal Solid Waste (MSW) (Rowe, 2005).

The present study is aimed to develop a multi-phase, two-dimensional, finite-difference numerical simulator which tracks the percentage of oil saturation as well as the lateral and vertical position of the oil plume in the subsurface, resulting from oil spillage, in the presence of clay minerals lens as a barrier at the specified times with different types of boundary conditions.

## METHODS

The basis of the mathematical description of the multi-phase fluid flow in porous media is the mass conservation laws. In the present study, the pressure gradient in gas phase will be assumed negligible so that the gas pressure remains effectively constant at atmosphere (Faust et al., 1989). The mass balance equation for each of the fluid phase in Cartesian coordinates can be written as (Bear, 1972):-

$$-\frac{\partial}{\partial x_i}(\rho_f \cdot q_f) \mp Q_f = \frac{\partial}{\partial t}(\phi \cdot \rho_f \cdot S_f) \quad \dots\dots\dots(1)$$

Darcy's Law describes the relation between the flux and the individual phase pressure. The general multi-phase Darcy's Law is given by:-

$$q_f = -\frac{k \cdot K_{rf}}{\mu_f} \left( \frac{\partial P_f}{\partial x_i} + \rho_f \cdot g \cdot \frac{\partial z}{\partial x_i} \right) \quad \dots\dots\dots(2)$$

The relative permeability ( $K_r$ ) is a non-linear function of saturation. It ranges in value from 0 when the fluid is not present, to 1 when the fluid is present. Darcy's law can be written equivalently in the form of the pressure head as below:

$$q_f = -K_f \left( \frac{\partial h_f}{\partial x_i} + \frac{\rho_f}{\rho_w} \cdot \frac{\partial z}{\partial x_i} \right) \quad \dots\dots\dots(3)$$

By substituting Eq.(3) into Eq.(1), assume that the fluid and the porous medium are incompressible, and ignore the source-sink term, the resulting equation can be represented by:-

$$\frac{\partial}{\partial x_i} \left[ K_f \left( \frac{\partial h_f}{\partial x_i} + \frac{\rho_f}{\rho_w} \frac{\partial z}{\partial x_i} \right) \right] = \phi \frac{\partial S_f}{\partial t} \quad \dots\dots\dots(4)$$



## Two-Dimensional Numerical Solution

The previously derived mass balance equation (Eq.4) will be re-written as two equations in two-dimension, one for water phase and other for oil phase and expressed in terms of the phase pressure head as below:-

$$\frac{\partial}{\partial Z} \left[ K_w \left( \frac{\partial h_w}{\partial Z} + 1 \right) \right] + \frac{\partial}{\partial X} \left[ K_w \frac{\partial h_w}{\partial X} \right] = C_w \frac{\partial h_w}{\partial t} \quad \dots\dots\dots(5)$$

$$\frac{\partial}{\partial Z} \left[ K_o \left( \frac{\partial h_o}{\partial Z} + \rho_{ro} \right) \right] + \frac{\partial}{\partial X} \left[ K_o \frac{\partial h_o}{\partial X} \right] = C_o \frac{\partial h_o}{\partial t} \quad \dots\dots\dots(6)$$

where  $K_w = K_{ws} K_{rw}$  and  $K_o = K_{os} K_{ro} = \frac{K_{ws} K_{ro}}{\mu_{ro}}$ ; and  $C$  is the specific fluid capacity, It is defined by  $C_w = \phi \frac{\partial S_w}{\partial h_w}$  &  $C_o = \phi \frac{\partial S_o}{\partial h_o}$ .

The solution techniques used here consist of a finite-difference approximation (implicit method), the Newton-Raphson with a Taylor series expansion to treat the nonlinearities, and direct matrix solution (Gauss-Elimination method). These techniques result in the following equations:-

$$a_{fi,j}^k \delta_{fi-1,j}^{k+1} + b_{fi,j}^k \delta_{fi,j-1}^{k+1} + c_{fi,j}^k \delta_{fi,j}^{k+1} + d_{fi,j}^k \delta_{fi+1,j}^{k+1} + e_{fi,j}^k \delta_{fi,j+1}^{k+1} = -r_{fi,j}^k \quad \dots\dots\dots(7)$$

where

$$\begin{aligned} a_{fi,j}^k &= \left[ -R1 \left( K_{fi-1,j}^k + h_{fi-1,j}^k \frac{\partial K_{fi-1,j}^k}{\partial h_{fi-1,j}^k} \right) - R2 \frac{\partial K_{fi-1,j}^k}{\partial h_{fi-1,j}^k} \right] \\ b_{fi,j}^k &= \left[ -R3 \left( K_{fi,j-1}^k + h_{fi,j-1}^k \frac{\partial K_{fi,j-1}^k}{\partial h_{fi,j-1}^k} \right) \right] \\ c_{fi,j}^k &= \left[ C_{fi,j}^k + (h_{fi,j}^k - h_{fi,j}^n) \frac{\partial C_{fi,j}^k}{\partial h_{fi,j}^k} + R1 K_{fi-1,j}^k + R1 \left( K_{fi,j}^k + h_{fi,j}^k \frac{\partial K_{fi,j}^k}{\partial h_{fi,j}^k} \right) + R2 \frac{\partial K_{fi,j}^k}{\partial h_{fi,j}^k} \right. \\ &\quad \left. + R3 K_{fi,j-1}^k + R3 \left( K_{fi,j}^k + h_{fi,j}^k \frac{\partial K_{fi,j}^k}{\partial h_{fi,j}^k} \right) \right] \\ d_{fi,j}^k &= -R1 K_{fi,j}^k \\ e_{fi,j}^k &= -R3 K_{fi,j}^k \end{aligned}$$

$$\begin{aligned} C_{fi,j}^k (h_{fi,j}^k - h_{fi,j}^n) - R1 K_{fi-1,j}^k h_{fi-1,j}^k + R1 K_{fi-1,j}^k h_{fi,j}^k + R1 K_{fi,j}^k h_{fi,j}^k - R1 K_{fi,j}^k h_{fi+1,j}^k - R2 K_{fi-1,j}^k \\ + R2 K_{fi,j}^k - R3 K_{fi,j-1}^k h_{fi,j-1}^k + R3 K_{fi,j-1}^k h_{fi,j}^k + R3 K_{fi,j}^k h_{fi,j}^k - R3 K_{fi,j}^k h_{fi,j+1}^k = r_{fi,j}^k \end{aligned}$$

$$\begin{aligned} R1 &= \frac{\Delta t}{\Delta Z_i (Z_{i-1} - Z_i)} \quad , \quad R11 = \frac{\Delta t}{\Delta Z_i (Z_i - Z_{i+1})} \quad , \quad R2 = \frac{\Delta t}{\Delta Z_i} \quad , \quad R3 = \frac{\Delta t}{\Delta X_j (X_{j-1} - X_j)} \\ &\& \quad R33 = \frac{\Delta t}{\Delta X_j (X_j - X_{j+1})} \end{aligned}$$

**Fig.1** (a) shows soil cross section for unsaturated-saturated zone and Fig.1 (b) shows the discretized domain in X-Z plane with time.

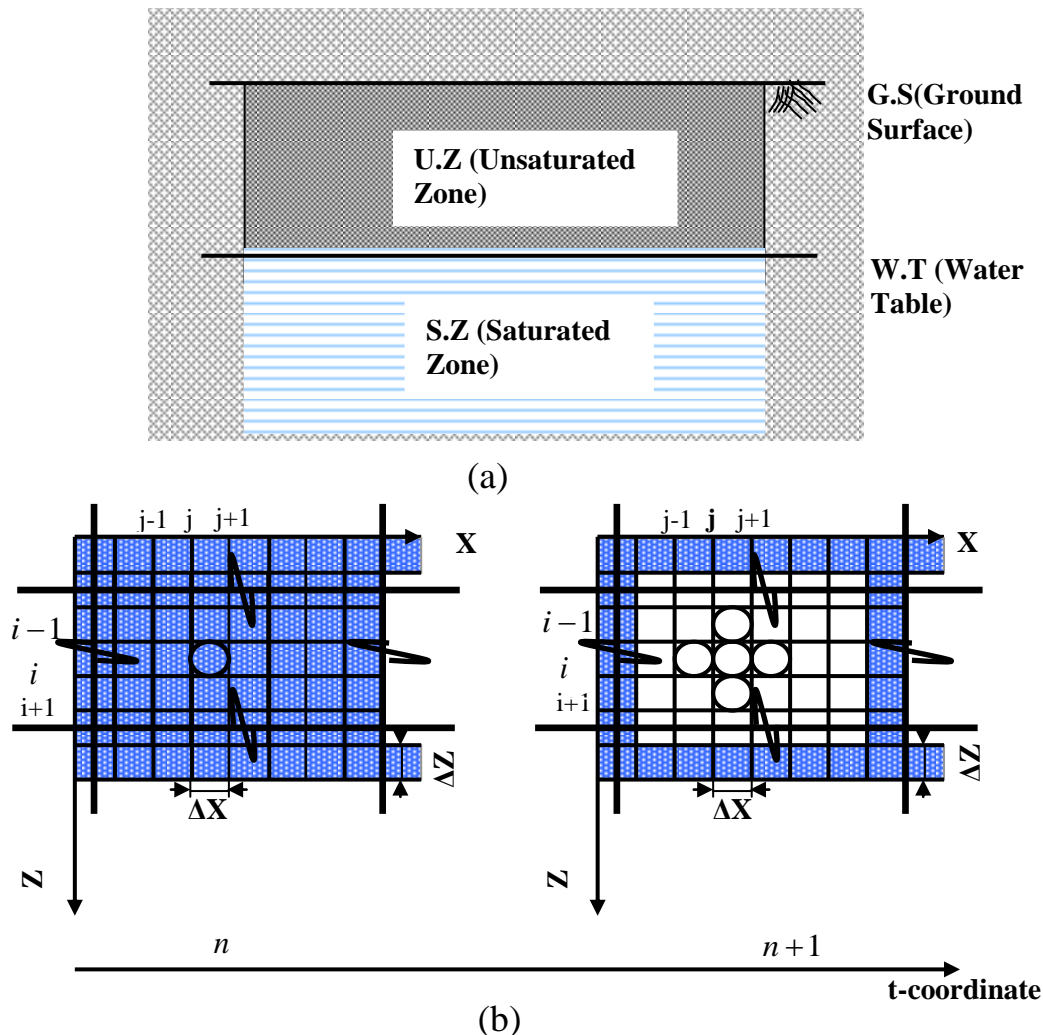


**Fig.1 :**(a) The common situation to the virtual solution cross section, (b) Image to the solution domain.

The coefficients in Eq.(7)  $a$ ,  $b$ ,  $c$ ,  $d$  and  $e$  are associated with  $\delta_{fi-1,j}^{k+1}$ ,  $\delta_{fi,j-1}^{k+1}$ ,  $\delta_{fi,j}^{k+1}$ ,  $\delta_{fi+1,j}^{k+1}$  &  $\delta_{fi,j+1}^{k+1}$  respectively, and in general it is formed as:-

$$A^k \delta^{k+1} = -r^k \quad \dots\dots\dots(8)$$

Where  $A = (a_{i',j'})$  is the coefficient matrix for the linearized system. The collection of equations for each solution node leads to have global diagonal coefficient matrix (its bandwidth equal to  $(2 * \text{noc} + 1)$ ). This matrix is solved for  $\delta$  and then the algorithm enters the next iteration with new values of  $h_f$  is evaluated as follows:-

$$h_{fi,j}^{k+1} = h_{fi,j}^k + \omega_f^{k+1} \delta_{fi,j}^{k+1} \quad \dots\dots\dots(9)$$

With highly nonlinear flow problems, the updating method introduced by Cooley (1983) which introduces an optimal relaxation scheme, which accounts for the

maximum convergence error for entire mesh, is used in the present study in conjunction with Newton–Raphson scheme. The convergence criterion used here for a given phase  $f$  ( $=o,w$ ) is as follows:-

$$\frac{\max |\delta_{fi}^{k+1}|}{\max |h_{fi}^k + \delta_{fi}^{k+1}|} \leq \varepsilon \quad \dots\dots\dots(10)$$

A typical convergence criterion for pressure head is 0.001 or less. A computer program written in MATLAB (version 6.5) was developed to implement the model described above. Inherent in any subsurface modeling algorithms are assumptions and limitations. The major assumptions include:-

- The pressure in the air phase is constant and equal to atmospheric pressure.
- Both water and NAPL viscosities and densities are pressure independent.
- Relative permeability of water is a function of water saturation.
- Relative permeability of NAPL is a function of air and water saturations.
- Capillary pressure is a function of water saturation.
- Air saturation is a function of NAPL pressure.
- Darcy's equation for multiphase flow is valid
- Intrinsic permeability is a function of space and there is no inter-phase mass transfer ( i.e ; the NAPL is truly immiscible in water).

The major limitations include:-

- Fractured systems are not treated; transport of dissolved NAPL is not treated
- The volatilization is not considered.

### **Constitutive Relationships**

Modeling of two-phase flow in porous media requires specification of functional relationships between capillary pressure-saturation ( $P_c - S$ ) and relative permeability-saturation ( $K_r - S$ ). The fluid saturation is a function of the difference between the pressures of the two fluids in the porous medium. This pressure difference is called the capillary pressure ( $P_{ow} = P_o - P_w$ ), or capillary pressure head ( $h_{ow} = h_o - h_w$ ). For two-phase system, the capillary pressure-saturation ( $P_c - S$ ) relations are typically determined experimentally and fitted with some empirical mathematical functions either a Brooks and Corey as cited by (Kueper and Frind, 1991b) or (Van Genuchten, 1980). The capillary pressure-saturation relationship ( $P_c - S$ ) developed by Brooks and Corey (1964) is adopted in the present study. These relations are:-

$$S_e = \left( \frac{h_{ow}}{h_d} \right)^{-\lambda} \quad h_{ow} \geq h_d \quad \dots\dots\dots(11)$$

$$\bar{S}_t = \left( \frac{h_{ao}}{h_d} \right)^{-\lambda} \quad \dots\dots\dots(12)$$

$$K_{rw} = S_e^{\left[ \frac{(2+3\lambda)}{\lambda} \right]} \quad \dots\dots\dots(13)$$

$$K_{rnw} = (1 - S_e)^2 \left( 1 - S_e^{\left[ \frac{(2+3\lambda)}{\lambda} \right]} \right) \quad \dots\dots\dots(14)$$

## EFFECT OF CAPILLARY PROPERTIES ON FLUID BEHAVIOR ABOVE A SINGLE LENS

A theoretical work presented by Kueper and Frind (1991b) was used as verification to the study of influence of porous media properties on the spreading of a non-wetting fluid above a single lens of low relative permeability. Numerical simulations were carried out within the solution domain illustrated in Fig.2. This system consists of a 200 cm-wide by 35 cm-high porous medium containing a single 5 cm-thick lens of low relative permeability material, the top of which is situated 15 cm below the upper boundary. The left- and right-hand side boundaries are subjected to a constant wetting phase pressure representative of hydrostatic conditions and are maintained fully saturated by water at all times. The top and bottom boundaries are set impermeable to each of the wetting and non-wetting phases, except for middle 4 cm of the top boundary which acts as the source area for the entry of non-wetting fluid under a small water equivalent TCE head of 29.9 cm to simulate an TCE spill. This source area is characterized by a constant wetting phase pressure and a constant distribution of fluid distribution.

The outlined solution domain with its prescribed boundary conditions is discretized into 800 finite-difference cells with constant nodal spacing of 5 cm in the vertical direction and 2 cm in horizontal direction. The initial condition in the cell is a hydrostatic distribution of wetting phase pressure, with the water table coinciding with the top of the solution domain and 100% saturation of the wetting phase throughout.

Variable time step sizes were used to solve this problem. Initially, when the infiltrating pressure front is steep and, consequently, the nonlinearities are strong, the small time step must be chosen. In this case, the initial time step size was 0.000001 hours. As time passes the infiltrating front smoothes and the nonlinearities weaken. This can be seen as the Newton-Raphson iteration scheme requires less iteration to converge as time passes. As the amount of iterations decreases, the time step size is increased. The final time step size was 0.1 hours for this simulation.

The simulations illustrate the effect of permeability of the 5 cm-thick lens on the spreading of a non-wetting phase infiltrating vertically downward from the source area. The non-wetting phase was assigned density of  $1400 \text{ kg/m}^3$  and a viscosity of  $0.57 \times 10^{-3} \text{ Pa.s}$ . The wetting phase was assigned a density of  $1000 \text{ kg/m}^3$  and viscosity of  $1.0 \times 10^{-3} \text{ Pa.s}$ . The source boundary condition was specified with a wetting phase pressure of 0.00 Pa and wetting phase saturation of 0.50. The fluid properties are characteristic of Tetrachlorethylene (TCE) a commonly used industrial solvent.

The host material of the solution was assigned permeability of  $K_f = 24.7 \text{ cm/hr}$  ( $k = 7.0 \times 10^{-12} \text{ m}^2$ ), while lens was assigned a range of permeabilities slightly lower than that of the host material. The parameters of porous media used in the present simulation are given in Table (1).

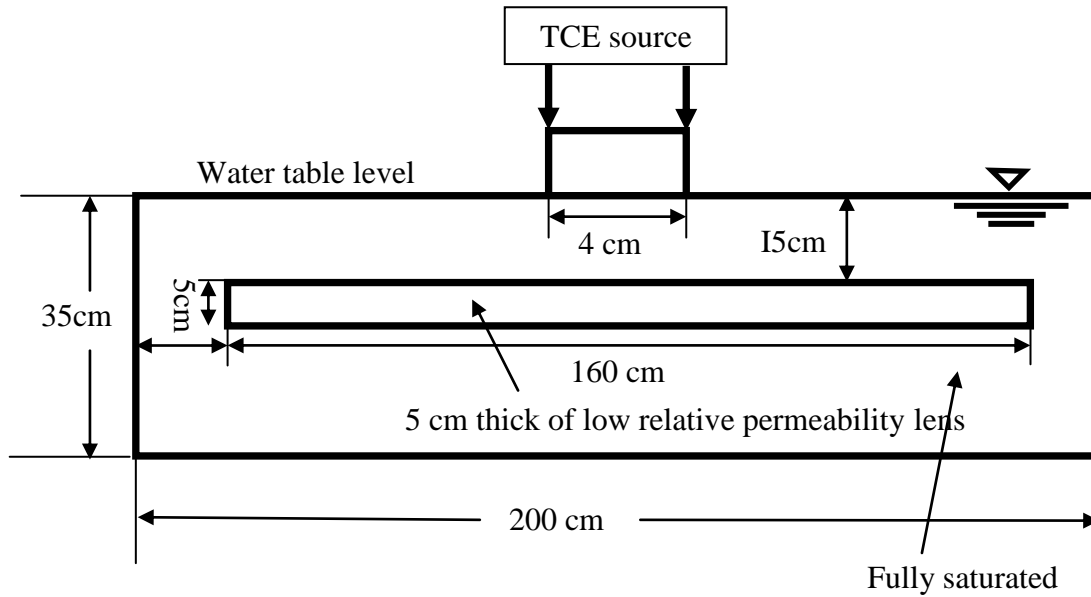


**Fig.2: Solution domain for single lens simulations (Kueper and Frind, 1991b).**

**Table1: Porous media properties used for simulation (Kueper and Frind, 1991b).**

parameters	values
Host permeability , cm/hr ( $K_{swh}$ )	24.7
Lens permeability, cm/hr ( $K_{swl}$ )	17.6
Host displacement pressure. cm ( $P_{dh}$ )	22.6
Lens displacement pressure .cm ( $P_{dl}$ )	28.6
Residual wetting phase % ( $S_r$ )	7.8
Pore size distribution index ( $\lambda$ )	2.48
Porosity ( $\phi$ )	0.34

## RESULTS AND DISCUSSION

The theoretical results of case study are compared with results of Kueper and Frind (1991b) as shown in Fig.3, Fig.4. There is a satisfactory agreement between the present results and those of Kueper and Frind (1991b). Fig.5 illustrates the distribution of non-wetting fluid in the solution domain for the case where the low relative permeability lens was assigned a permeability of  $K_f = 17.6$  cm/hr ( $k = 5.0 \times 10^{-12}$  m<sup>2</sup>) for times (0.57 hour, 1.13 hour, 1.99 hour and 4.59 hour) as calculated by the present model. In these figures, the darker shades indicate higher TCE content and the lighters shades lower TCE contents. According to these figures, non-wetting fluid encountered the lens; it would pool and spread laterally, allowing for a build up of saturation immediately above the lens. Once this saturation brings about a capillary pressure in excess of the displacement pressure of the lens,

penetration takes place. Lateral spreading continues beyond this point of penetration, since the lower permeability lens cannot transmit non-wetting fluid at a rate equal to the higher permeability host material.

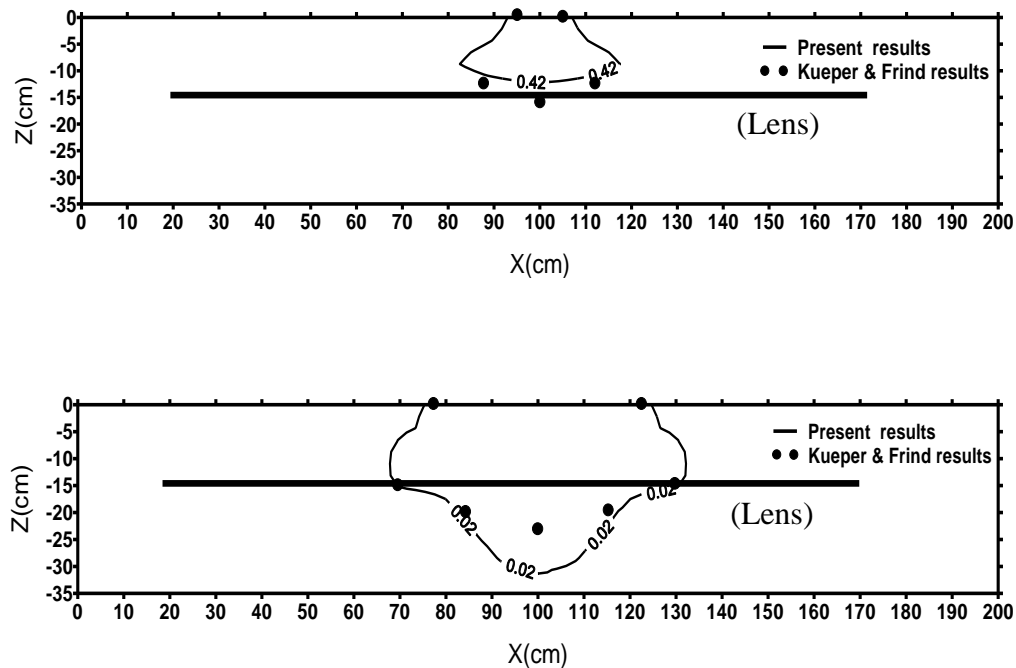


**Fig.3: DNAPL plume location during infiltration after 1.99 hour when (a) DNAPL Saturation=0.42 & (b) DNAPL saturation=0.02.**

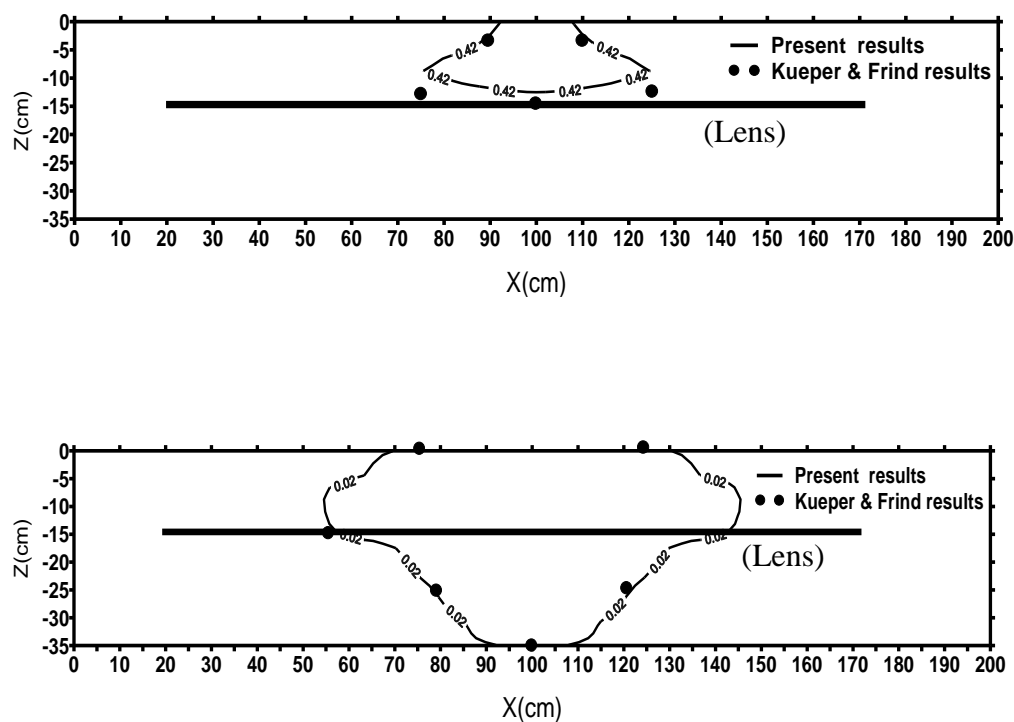


**Fig.4: DNAPL plume location during infiltration after 4.59 hour when (a) DNAPL Saturation=0.42 & (b) DNAPL saturation=0.02.**

(a) DNAPL Saturation=0.42 & (b) DNAPL saturation=0.02.

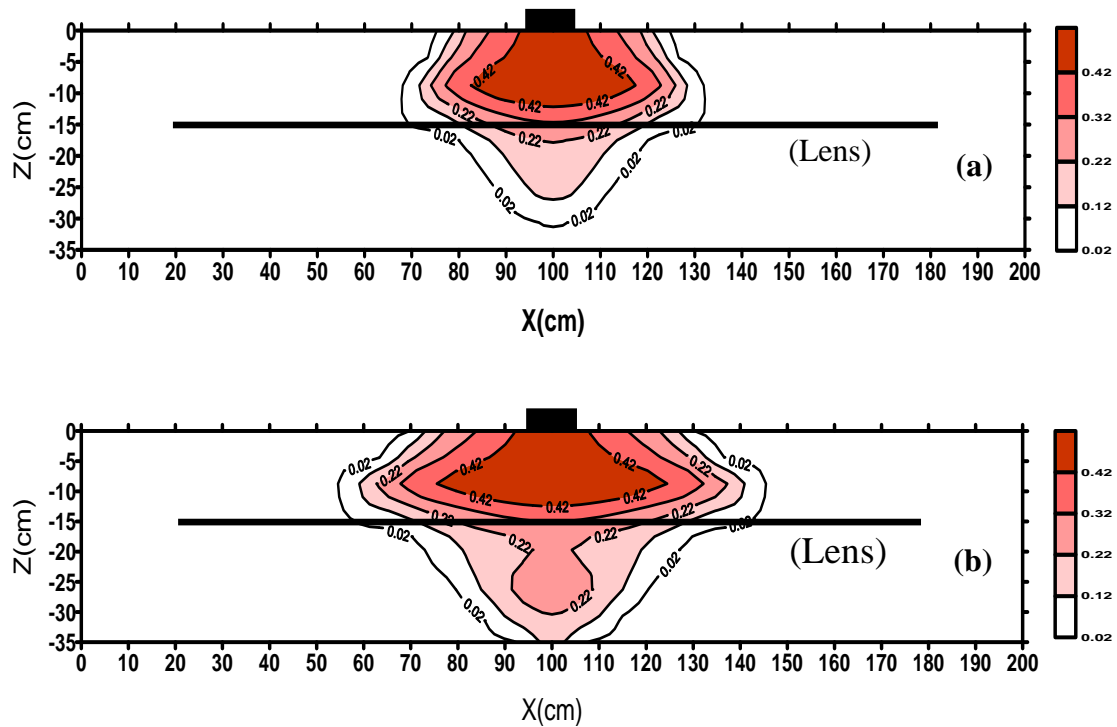


Fig.5: DNAPL saturation after (a) 1.99 hour and (b) 4.95 hour.

## CONCLUSIONS

The following conclusions can be deduced:-

- The numerical solution employed in this study based on the potential form of the governing equations with techniques consisted of Implicit Finite Difference, Newton-Raphson and Gauss-Elimination schemes showed to be an efficient procedure in solving problems of two-dimensional water and NAPL<sub>s</sub> flow through the unsaturated and/or saturated zone of three fluid phases system in the presence of low relative permeability lens.
- During infiltration of DNAPL, the maximum saturation occurred below the source and when it advanced the saturation will decrease.
- Observations of (DNAPL) plume migration through heterogeneous porous media, upon encounter with a low relative permeability lens, the non-wetting fluid must build up the required saturation to generate the necessary capillary pressure facilitating entry into the lens. This build up of saturation give rise to lateral pressure gradients, promoting lateral spreading of non-wetting fluid above the low relative permeability lens. Once the lens has been penetrated, lateral spreading continues because of inability of the lens to transmit fluid at rate equal to that of the higher-permeability material immediately above the lens.

**REFERENCES**

- Abriola, L. M., and G. F. Pinder, "A multi-phase approach to the modeling of porous media contamination by organic compounds: 1. Equation development". *Water Resources Research*, 21(1), 11-18, 1985a.
- Al-Dulaimi, A. A. H., "Numerical Modeling of Light Non-Aqueous Phase Liquid Spill Transport in an Unsaturated-Saturated Zone of the Soil". Ph.D. Thesis, Baghdad University, 2006.
- Basri, M. H., "Two New Methods for Optimal Design of Subsurface Barrier to Control Seawater Intrusion". Ph.D. Thesis, Manitoba University, 2001.
- Bear, J., "Dynamics of fluids in porous media". Elsevier, New York, 1972.
- Cooley, R. L., "Some new procedures for numerical solution of variably saturated flow problems". *Water Resources Research*, 19(5), 1271-1285, 1983.
- Durmusoglu, E., and M. Y. Corapcioglu, "Experimental study of horizontal barrier formation by Colloidal silica". *Journal of Environmental Engineering*, 126(9), 833-841, September, 2000.
- Faust, C. R., J. H. Guswa, and J. W. Mercer, "Simulation of three-dimensional flow of immiscible fluids within and below the unsaturated zone". *Water Resources Research*, 25(12), 2449-2464, 1989.
- Hall, P. L., and H. Quam, "Countermeasures to control oil spills in western Canada". *Groundwater*, 14, 1976.
- Karol, R. H., "Chemical grouting". 2nd Ed., Marcel Dekker, New York, 1990.
- Kim, J., and M. Y. Corapcioglu, "Modeling dissolution and volatilization of LNAPL sources migrating on the groundwater table". *J. of Contaminant Hydrology*, 65, 137-158, 2003.
- Kueper, B., and E. Frind, "Two-phase flow in heterogeneous porous media: 2. Model application". *Water Resources Research*, 27(6), 1059-1070, 1991b.
- May, J. H., R. J. Larson, P. G. Malone, J. A. Boa, and D. L. Bean, "Grouting techniques in bottom sealing of hazardous waste sites". Rep. EPA/600/S2-86/020, U.S. Environmental Protection Agency, Cincinnati, 1986.
- Newman, A., "Subsurface barrier trapped diverse contaminants, let water through". *Environmental / Science & Technology*, 29(8), 1995.
- Pearlman, L., "Subsurface containment and monitoring system: Barriers and beyond". [www.epa.gov/tio/download/remed/Pearlman.pdf](http://www.epa.gov/tio/download/remed/Pearlman.pdf), 1-61, 1999.
- Rowe, R. K., "Long-term performance of contaminant barrier system". [www.geoeng.ca/Directory/kerryPub/GeotechniqueRankine/Rowe.pdf](http://www.geoeng.ca/Directory/kerryPub/GeotechniqueRankine/Rowe.pdf), 55(9), 631-678, 2005.
- Rumer, R. R., and M. E. Ryan, "Barrier containment technologies for environmental remediation applications". Wiley, New York, 1995.



- Rumer, R. R., and J. K. Mitchell, "Assessment of barrier containment technologies a comprehensive treatment for environmental remedial application" Product of the
- International Containment Technology Workshop. National Technical Information Service, PB96-180583, 1996.
- Saleem, M., "Assessment of the Relation between the Spilled LNAPL Volume and its Thickness in Monitoring Well Considering the Water Table Fluctuation History". Ph.D. Thesis, King fahd University of Petroleum and Minerals, 2005.
- Van Genuchten, M., "A closed-form equation for predicting the hydraulic conductivity of unsaturated soils". Soil Sci. Soc. Am. J., 44, 892-898, 1980.
- Wipfler, E. L., "Effects of capillarity and heterogeneity on flow of organic liquid in soil". Ph.D Thesis, Wageningen University, Wageningen, library.wur.nl/wda/ dissertations/dis3384.pdf, 2003.

## SYMBOLS

$A$	Coefficient matrix	[—]
$C_w$	Specific water capacity	[—]
$C_o$	Specific oil capacity	[—]
$g$	Acceleration due to gravity	[m/s <sup>2</sup> ]
$h_f$	Fluid pressure head	[m]
$h_a$	Air pressure head	[m]
$h_{ao}$	Air-oil capillary pressure head	[m]
$h_o$	Oil pressure head	[m]
$h_{ow}$	Oil-water capillary pressure head	[m]
$h_w$	Water pressure head	[m]
$h_d$	Displacement pressure head	[m]
$i, j$	Grid identification in X,Z coordinates respectively.	[—]
$K_w$	Water Hydraulic conductivity	[m/s]
$K_o$	Oil Hydraulic conductivity	[m/s]
$K_f$	Hydraulic conductivity of phase $f$	[m/s]
$K_{fs}$	The conductivity when the medium is saturated with fluid $f$	[m/s]
$K_r$	Relative hydraulic conductivity	[—]
$K_{ro}$	Relative hydraulic conductivity of oil	[—]
$K_{rw}$	Relative hydraulic conductivity of water	[—]
$k$	The intrinsic permeability tensor of the medium in Eq. (2)	[—]
$k$	Iteration index	[—]
$K_{rf}$	Relative permeability of the phase $f$	[—]



$n$	Time step identification (if it is superscript)	[—]
$noc$	The number of columns	[—]
$non$	The $n^{\text{th}}$ grid identification	[—]
$nor$	The number of rows	[—]
$\lambda$	Pore size distribution index	[—]
$P_f$	Fluid pressure of phase $f$	[kg/m <sup>2</sup> s <sup>2</sup> ]
$P_c$	Capillary pressure of phase $f$	[kg/m <sup>2</sup> s <sup>2</sup> ]
$P_w$	Pressure of water phase	[kg/m <sup>2</sup> s <sup>2</sup> ]
$P_o$	Pressure of oil phase	[kg/m <sup>2</sup> s <sup>2</sup> ]
$Q_f$	Source or sink of phase $f$	[kg/m <sup>3</sup> s]
$q$	Volumetric flux (or Darcy's flux)	[m/s]
$r$	The residual due to approximation	[—]
$S$	Degree of saturation	%
$S_f$	Degree of fluid saturation	%
$S_a$	Degree of air saturation	%
$S_o$	Degree of oil saturation	%
$S_t$	Degree of total liquid saturation	%
$\bar{S}_t$	Degree of effective total liquid saturation	%
$S_e$	Degree of effective water saturation	%
$t$	Time coordinate	[s]
$X, Z$	Cartesian coordinates	[m]

### Greek symbols

$\delta$	The difference between the approximation and exact solution in fluid pressure head	[m]
$\varepsilon$	Convergence tolerance	[m]
$\mu_f$	Dynamic viscosity of fluid $f$	[kg/m s]
$\mu_{ro}$	Ratio of oil to water viscosity	[—]
$\rho_f$	Density of phase $f$	[kg/m <sup>3</sup> ]
$\rho_{ro}$	Ratio of oil to water density	[—]
$\rho_w$	Density of water at standard temperature and pressure	[kg/m <sup>3</sup> ]
$\phi$	Porosity of the medium	[m <sup>3</sup> /m <sup>3</sup> ]
$\omega$	Damping parameter	[—]
$\Delta t$	Time step size	[s]
$\Delta X$	Horizontal increment in X-direction	[m]
$\Delta Z$	Vertical increment in Z-direction	[m]

## DRAG FORCE OF TWO SPHERES IN POWER LAW FLUIDS

Prof. Dr. Abbas H. Sulaymon

Abeer Ibrahim Alwared

Environmental Engineering Department - Collage of Engineering-University of Baghdad

### ABSTRACT

The present research is concerned with studying of the drag force on two spheres moving side by side and in line in non-Newtonian liquid. Polyacryamide (PAA) solution with different concentrations (0.01, 0.03, 0.05 and 0.07)% by weight and water is used for comparison for obtaining the effect of fluid properties on the drag force.

Different types of spheres stainless steel, glass and plastic with different sizes and densities were used.

Within the considered range of power law index (0.6 - 1), and generated Reynolds number (1.1 - 75) in power law fluid and Reynolds number (100 - 1000) for water it was found the drag coefficient increases with increasing the power law index for constant generated Reynolds number and the drag force increases with fluid density increases but it decreases with the sphere density increases.

### الخلاصة

يهتم البحث بدراسة قوة الاحتكاك بين كرتين تتحركان جنباً إلى جنب أعلى طول الخطّ الواصل بين مركزيهما داخل اسطوانة مملوءة بمادة البولي اكراميد (PAA) وبتركيزات مختلفة (0.01, 0.03, 0.05 و 0.07%) وزناً كسائل غير نيوتيني ولغرض المقارنة مع السوائل النيوتينية تم استخدام الماء، وباستخدام انواع مختلفة من الكرات (حديدية مقاومة للصدأ، زجاجية وبلاستيكية) ذات اقطار وكثافات مختلفة. تبين من هذه التجارب ان ضمن مدى الـ power law index (مؤشر سلوك الجريان) المحدد بين (0.6 - 1) كان generated Reynolds number بين (1.1 - 75) في سائل البولي اكراميد (PAA) في حين كانت قيمة Reynolds number في الماء تتراوح ما بين (100 - 1000).

تبين من هذه التجارب ان معامل الاحتكاك يزداد بزيادة مؤشر سلوك الجريان عند ثبات قيمة الـ generated Reynolds number كما تم التوصل الى ان قوة الاحتكاك تزداد بزيادة كثافة السائل وتقل مع زيادة كثافة الكرة.

**KEY WORDS:** Two spheres, power law fluids, drag coefficient, interaction correlation, drag force,

### INTRODUCTION

The fluid dynamic drag on a sphere in an infinite fluid are important in numerous fields including chemical, mechanical and environmental engineering. As such, they have been subject to many experimental and theoretical investigations; despite such interest existing knowledge is less than perfect, and improvements in predictions could be useful in mathematical modeling of particle behaviour. In environmental engineering such predictions are used for modeling all particle process

in water (flocculation, sedimentation, boiling, flotation and filtration including back wash of filter media, liquid-liquid extraction) and particle capture and deposition in air (Brown and Lawler, 2003).

Considerable progress has been made towards the understanding of the accelerating motion of a sphere in Newtonian fluids, Clift et al., (1978) have presented a concise summary of the theoretical developments on this subject in their classic treatise. In contrast to this, the acceleration motion of a sphere in non-Newtonian fluids received less attention, some investigators have described the unsteady motion of a sphere in viscoelastic fluids that have constant viscosity (i.e. no shear thinning behavior) and exhibit quadratic normal stress differences.

However, most materials of practical interest (e.g. polymer solution, polymer melts, ... etc.) display what is called shear thinning characteristics, which its apparent viscosity decreases with increasing shear rate. This research concerned with the acceleration motion of two spheres in shear thinning type power law fluid.

The most common approach by previous investigators is by using the standard Newtonian relationships ( $C_D = f(Re)$ ) but using a modified (non-Newtonian or generalized) Reynolds number  $Re_{gn}$  (Kelessidis, 2003).

## DRAG COEFFICIENT CORRELATION DUE TO GENERATED REYNOLDS NUMBER

In Newtonian fluids there are many relationships for the standard drag  $C_D = f(Re)$  are available, the more widely used empirical form of drag correlation with the Reynolds number employed from 10 to  $10^3$  is Schiller and Naumann's correlation (1933).

$$C_D = \frac{24}{Re} \left( 1 + \frac{1}{6} Re^{\frac{2}{3}} \right) \quad (1)$$

Lali et al. (1989) used five different carboxymethylcellulose (CMC) solutions covering the range of power law fluid ( $n$ ) between (0.555 – 0.85), with different diameters of glass beads and steel balls, thus covering a range of  $Re_{gn}$  (0.1 – 200), the data correlated very well with the Newtonian curve defined by:

$$C_D = \frac{24}{Re} \left[ 1 + 0.15 Re^{0.687} \right] \quad 0.1 < Re < 1000 \quad (2)$$

Darby (1996) predicted the following expression which give an accurate representation for the drag in non-Newtonian fluids on condition that  $A$  and  $B$  are made depend on the power law index ( $n$ ).

$$C_D = \left( \frac{A}{\sqrt{Re}} + B \right)^2 \quad (3)$$

Where :

$$A = 4.8 \left( \frac{1.33 + 0.37n}{1 + 0.7n^{3.7}} \right)^{\frac{1}{2}} \quad (4)$$

and

$$B = \left[ \left( \frac{1.82}{n} \right)^8 + 34 \right]^{-1/8} \quad (5)$$

Equation (3) is based on the numerical results of Tripathi et al., (1994) and Tripathi and Chhabra (1995), it shows fair agreement with experimental results in the range  $0.4 \leq n \leq 1$  (as cited in Chhabra et al., 1998).

Kelessidis (2004) predicted the following drag coefficient correlation for power law fluid.

$$C_D = \frac{24}{\text{Re}_{gn}} \left[ 1 + 0.1466 \text{Re}_{gn}^{0.378} \right] + \frac{0.44}{1 + 0.2635 / \text{Re}_{gn}} \quad 0.1 < \text{Re}_{gn} < 1000 \quad (6)$$

A comparison of non-Newtonian data with Newtonian data on a  $C_D - \text{Re}$  plot reveals that the non-Newtonian data fall slightly below the underlying curve of the Newtonian data.

Dhole et al. (2006) correlated the following equation over the ranges of  $5 < \text{Re}_{gn} < 500$  and power law index values  $0.5 \leq n \leq 2$ .

$$C_D = \frac{24}{\text{Re}_{gn}} \left[ 1 + a \text{Re}_{gn}^{bn/(cn+d)} \right] \quad (7)$$

Where:  $a = 0.148$ ,  $b = 2.346$ ,  $c = 2.423$ , and  $d = 0.918$ .

They also concluded that the drag is seen to be enhanced above the Newtonian value in shear thickening fluids and reduces in shear thinning fluids at constant Reynolds number.

For the settling of sphere in shear thinning fluids ( $n < 1$ ), as noted by Graham and Jones (1994); Koziol and Glowacki (1988); Tripathi et al., (1995); Renaud et al., (2004); and Zhu et al., (2003) there exists a crossover Reynolds number of  $\text{Re}_{gn} \approx 4$ , up to which the total drag decreases with the power law index increases. From the above discussions, it is appeared that the majority of the investigators concluded that the use of Newtonian correlations for non-Newtonian fluids is justified by using the apparent viscosity. However, a single equation yielding accurate results is not available for non-Newtonian fluids (Kelessidis, 2003).

## DYNAMIC DRAG CORELATION IN NEWTONIAN FLUID

It is worthwhile to mention that, a large number of investigators worked theoretically and experimentally on the dynamic interaction coefficient of drag force of two spheres in Newtonian fluid. There are many correlations for particle interaction effects on drag coefficient  $\lambda = C_D/C_{D0}$  for two particles fall side by side with the same velocity and for two particles motion in line in Newtonian fluid. For two bubbles rising side by side Kok (1993) obtained for the drag coefficient the following correlation:

$$C_D = \frac{48}{\text{Re}} (1 + g(S)) + O\left(\text{Re}^{-3/2}\right) \quad (8)$$

With:

$$g(S) = S^{-3} + \frac{3}{4} S^{-6} + \frac{11}{3} S^{-8} + \dots \quad (9)$$

Where  $S = l/a$

The presence of the second bubble tend to increase the drag force due to the interaction results in a higher strain rate in the fluid located between the two bubbles. Legendre and Magnaudate (2003) found an improved expression for the drag force in Reynolds number range,  $0.02 \leq Re \leq 500$ .

$$C_D = \frac{48}{Re} (1 + g(S)) + (1 + S^{-3}) \frac{2.211}{Re^{1/2}} \quad (10)$$

They use a correlation factor for the drag force as:

$$\lambda = (1 + S^{-3}) = 1 + \frac{1}{8} \left( \frac{l}{d} \right)^{-3} \quad (11)$$

For two horizontally side by side bubbles at high Reynolds number ,Kendoush (2005) derived the following equation:

$$\lambda = \left[ 1 + \frac{1}{2} \left( \frac{a}{l} \right)^3 + \frac{1}{4} \left( \frac{a}{l} \right)^6 \right]^2 \quad (12)$$

For two spheres falling one above the other at very low Reynolds numbers Smoluchowski (1911) showed that:

$$\lambda = 1 - \frac{3}{4} \left( \frac{d}{l} \right) + \left( \frac{3d}{4l} \right)^2 \quad (13)$$

Equation (13) is an approximate expression and can only be applied for two equal-sized spheres falling with center-to-center distance greater than three diameters.

Oseen (1927) extended Smoluchawski's solution, equation (13) for the motion of two spheres so that it might be applied to higher Reynolds numbers. Oseen's equation for one sphere falling above another can be approximated when the spheres are not too far apart by the following equation: (Happel and Pfeffer, 1960)

$$\lambda = 1 - \frac{3}{4} \left( \frac{d}{l} \right) + \frac{3}{8} Re \quad (14)$$

The correlation proposed by Rowe and Henwood (1961) for two spheres in line was in a hyperbolic form. This is invalid for small interparticle distances since the drag ratio approaches either positive or negative infinity at contact (Zhu et al., 1994).

$$\lambda = 1 - \frac{0.85}{\delta} \quad (15)$$

Where  $\delta = x/d$

The above correlation is invalid for small inter-particle distance since the drag ratio approaches infinity at contact (Zhu et al., 1994).

Tsuji et al. (1982) measured the drag force on two spheres in the longitudinal direction with Reynolds number less than  $10^3$ .

$$\frac{C_D}{C_{Do}} = 1 - A \exp\left(-B \frac{l}{d}\right) \quad (16)$$

Where  $A=1.0083$  and  $B=0.4995$  with correlation coefficient  $R=0.9980$ .

Zhu et al. (1994) proposed an empirical equation for the drag force variation in the intermediate range of Reynolds number in a form similar to Tsuji et al. (1982) equation.

$$\frac{C_D}{C_{Do}} = 1 - (1 - A) \exp\left(-B \frac{l}{d}\right) \quad 20 \leq Re \leq 150 \quad (17)$$

The coefficients  $A$  and  $B$  are both function of  $Re$  and are empirically correlated as:

$$A = 1 - \exp\left(-0.483 + 3.45 \times 10^{-3} Re - 1.07 \times 10^{-5} \times Re^2\right) \quad (18)$$

$$B = -0.115 - 8.75 \times 10^{-4} Re + 5.61 \times 10^{-7} Re^2 \quad (19)$$

## DYNAMIC DRAG CORRELATIONS IN NON-NEWTONIAN FLUIDS

Analogous to Newtonian multiphase flows groups of multi-particles do not behave like those of an isolated particle unless the flow is extremely dilute, hence the study of the multi-particle group behavior and hydrodynamic interactions among particles is of great importance. Kawase and Ulbrecht (1981) used a free surface model and the boundary layer theory to estimate the motion of an assemblage of spheres moving in a power law non-Newtonian fluid at high Reynolds numbers and concluded that the drag coefficient for an assemblage of solid spheres decrease with the increase of the shear thinning anomaly at high and low Reynolds number. Staish and Zhu (1992) and Jaiswal et al., (1993) numerically investigated unbounded slow flows of a power law non-Newtonian fluid through an assemblage of spheres. Considering the effect of wall and the flow disturbance induced by upstream and downstream particle groups.

Subramaniam and Zuritz (1994) determined the drag force on multiple assemblies of spheres suspended in CMC solutions, from which an averaged drag force on each particle was deduced. However, this averaged drag force should not be used in the calculation of dynamic motions of particles with strong wake interactions. (Zhu et al., 2003).

Zhu et al. (2003) concluded experimentally and theoretically the drag coefficient ratio of an interacting spheres is independent from the power law index but strongly depends on the separation distance and the particle Reynolds number in a range of  $0.6 \leq n \leq 1$  and  $0.7 \leq Re_{gn} \leq 23$ .

Up to date, there is little published information about the interactions between two spheres in non-Newtonian fluids most of them are dealing with viscoelastic, viscoplastic and yield stress fluid.

It is worth mentioning that due to lack of any definitive dynamic correlation for two spheres (aligned side by side or in line) motion in power law fluid and due to the conclusion of Zhu et al. (2003) that the drag coefficient ratio of an interacting sphere is independent from the power law index but strongly depends on the separation distance and the particle Reynolds number at power

law index range between 0.6 to 1, the corresponding correlation for two spheres in Newtonian fluid will be used in this study as a first approximation.

## EXPERIMENTAL APPARATUS AND MEASUREMENT SYSTEM

The experimental apparatus is shown in figure 1. It consisted of a borosilicate glass cylindrical column of length 2.0 m and diameter of 0.3 m. Two types of liquid were used in this study polyacryamaide (PAA) solution as a non -Newtonian liquid with different concentrations of (0.01, 0.03 , 0.05 and 0.07 %) by weight and water as a Newtonian liquid .

The spheres used in the experiments were made of stainless steel, glass and plastic of different size and densities table (1). Each sphere pair was connected by a thin steel rod of approximately 1/50 of the sphere diameter. The effect of the connecting rod on the motion of the spheres is considered to be negligible. The distance between spheres was varied from 2 to 10 radii. A fishing string of 0.18 mm diameter, passed over an aluminum pulley to a drive weight that provided the driving force, suspended the spheres.

The external friction was reduced to a minimum with ball bearings on the pulley's shaft. The spheres were submerged in the liquid of the column at an initial position of approximately 0.5 m from the bottom. Upon release of the string the spheres rose under the action of falling weights. Measurements of the velocity of the pairs of spheres were carried out for different sphere diameters and sphere separation distances. On the top of the column there was a system of light source and a photo-cell. A small pieces of eight light blocks were fixed on the part of string that was un-submerged. As the spheres moved in the liquid, the light blocks also moved up through the collimator, which made the light intensity seen by the photo-cell varied and hence its resistance. This causes a variable voltage drop across the photo-cell. An electronic circuit was constructed to measure the time elapsed between two successive light blocks. The electronic circuit components consist of light source, photo-cell detector and an interface unit connected to a personal computer.

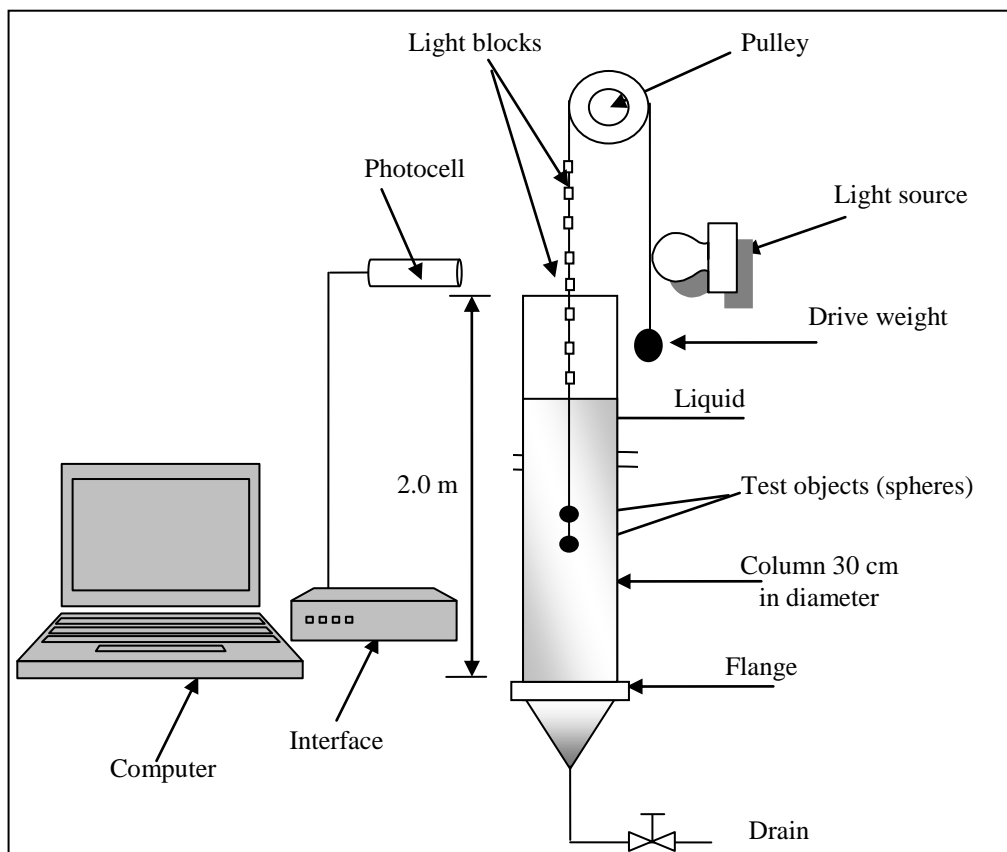


**Fig. 1** Schematic diagram of experimental apparatus



**Table1** Properties of spheres

<i>Type</i>	<i>Diameter(m)</i>	<i>Density (kg/m<sup>3</sup>)</i>
stainless steel	0.01	7660.22
	0.012	
	0.134	
	0.016	
glass	0.072	2520
	0.093	
	0.0204	
	0.0256	
Plastic	0.0114	1355
	0.0138	

## EXPERIMENTAL PROCEDURE

For calibrating the system, a single sphere submerged in the liquid column was accelerated under the action of a falling weight that was slightly heavier than the sphere. As the sphere moved up, the light blocks also moved up and passed between the light and the photo-cell. The interface unit fed the response to the computer until all light blocks were passed. The online computer displayed the velocity of the spheres versus time on the screen.

The experimental procedure for two spheres is similar to that with single sphere. The motion of two identical solid spheres rising along their line of centers and side by side was carried out for different sphere diameters and separation distances.

## RESULTS AND DISCUSSIONS

### • Modification of Stokes Drag Coefficient due to Reynolds Number

Consistent with previous studies (Clift et al, 1978; Bagchi and Chhabra, 1991; and Chhabra et al.1998), it is assumed here that the drag coefficient of the accelerated sphere is similar to that under constant velocity conditions. Equation (1) was used to evaluate the drag coefficient in water while equation (10) was used to evaluate the drag coefficient in the power law fluid to take into account the effect of generated Reynolds number  $1.1 \leq Re_{gn} \leq 76$  and power law index on the drag coefficient of the spheres.

The drag coefficient against  $Re_{gn}$  for non-Newtonian with different concentrations for two steel spheres side by side ( $d=10\text{mm}$ ,  $l/d=2$ ) is plotted in figure 2 .This figure shows good agreement with published data in the literature.

It can be seen that drag coefficient decreases for the generated Reynolds number increases at the same liquid , but when the shear thinning is increasing (power law index decrease) the generated Reynolds number will be decreased with increasing the drag coefficient

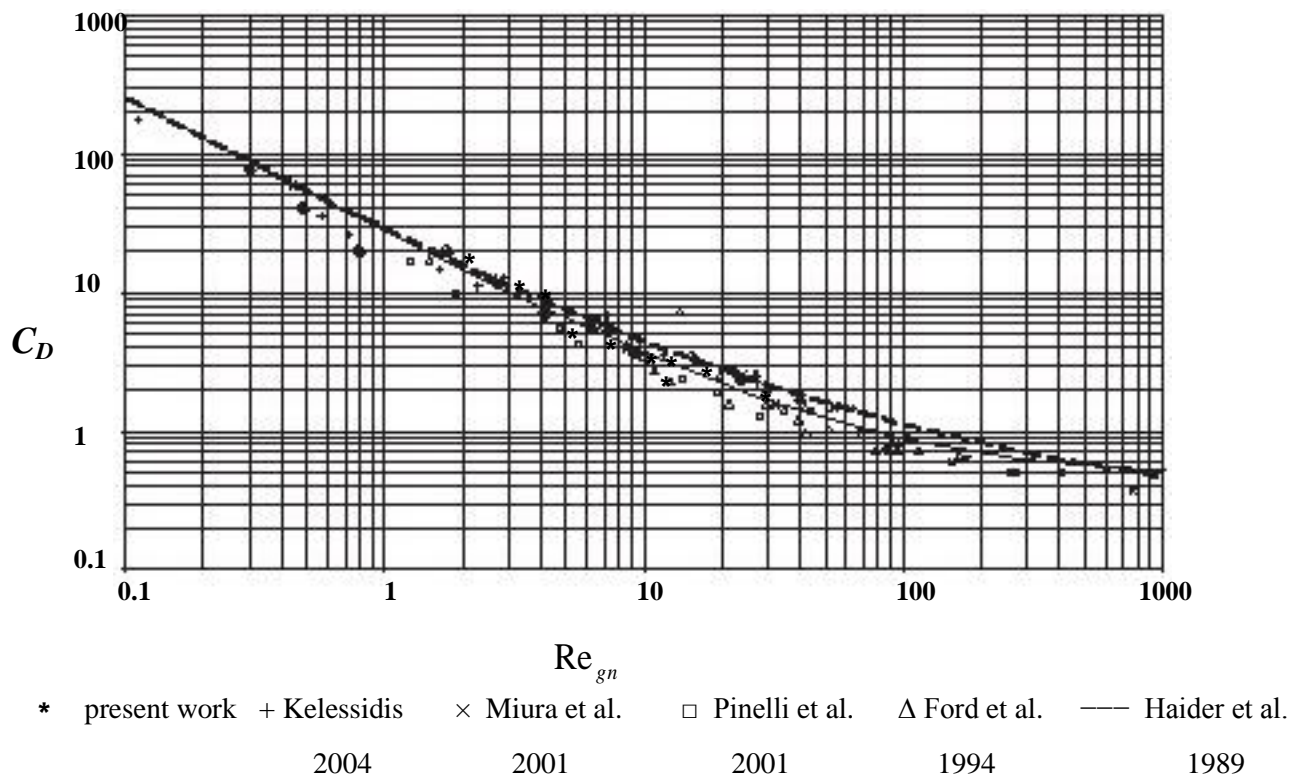


**Fig.2** Comparison of drag coefficients with generated Reynolds number for the present results and many other predicted results in non -Newtonian fluids

### • Drag Force Correction due to Interaction

For the motion of two spheres in power law fluids, no reliable correlations to describe this interaction were available and according to the result of Zhu et al. in 2003 , the ratio of drag coefficient in power law fluids is exponentially dependent on the separation distance and is strongly related to the particle Reynolds number but nearly independent of the power law index  $0.6 \leq n \leq 1$ . Therefore, Newtonian correlations are used in this study to predict an expression that relates the drag coefficient with the inter-particle distance in power law fluid.

### • Drag Force Correction for Two Spheres Moving Side by Side

The interaction parameter ( $\lambda = C_D/C_{D0}$ ) was calculated using equation (11) for two spheres moving side by side in polyacryamaide solution for  $0.02 \leq Re_{gn} \leq 500$ .

Figure 3 shows a comparison between the drag force calculated by equation (11) and Tsuji et al. (1982) result. This figure shows that when the spheres are close to each other, the drag increases, but the effect disappears at a distance larger than  $l/d = 2 \sim 3$ , and the drag ratio reaches that of a single sphere (i.e.  $C_D/C_{D0} = 1$ ). According to Kim et al., (1998), the drag increases when the two spheres get closer from each other probably due to the increase of the shear stress on the sphere surface and the change in the pressure distribution owing to the flow acceleration in the gap between them.

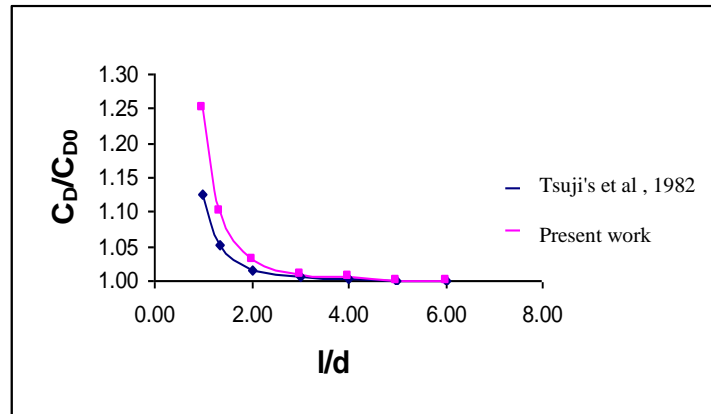


**Fig. 3** Drag ratio versus inter-particle distance for two steel spheres side by side

### • Drag Force Correction for Two Spheres Moving Along their Line of Centers

Within the considered range of Reynolds number,  $0.1 < Re_{gn} < 10^3$ , no dependable correlation available to describe the interaction parameter ( $\lambda = C_D/C_{D0}$ ) for two spheres moving in the direction parallel to their line of centers. So the interaction parameter was calculated from different correlations depending on the Reynolds number, Oseen's equation (14) was used for low generated Reynolds number (less than 20).

Zhu (1994) equation (17) was adopted for intermediate range of Reynolds number. This equation was examined at two limits of the separation distances between the two particles. As  $l \rightarrow \infty$ , the second term in equation (17) vanishes and the drag ratio becomes unity as expected. At contact, the drag ratio equals the coefficient A, which gives the minimum value of the drag ratio. Zhu (1994) found that the particle Reynolds number affects not only the magnitude of the drag force of an interacting particle but also its variation with the separation distance.

Zhu et al., (1994) results agree with the measurements of Rowe and Henwood (1961) and Tsuiji et al. (1982).

For Newtonian fluids, equation (13) was used. The coefficients of the fitted equation are determined as  $A=1.0083$  and  $B=0.4995$  with correlation coefficient  $R=0.9980$ , so equation (13) will be :

$$\frac{C_D}{C_{D0}} = 1 - \exp\left(-0.5 \frac{l}{d}\right) \quad (20)$$

The drag ratio is decreasing during the decreasing of distance between the spheres, but this effect disappears at a distance larger than  $l/d = 5 \sim 10$  and approaches the single sphere value.

The reason for this reduction according to Zhu et al., (1994) was the particle interaction renders the wake vortex of the leading particle longer than that of a single non-interacting particle. In addition, Liang et al. (1996) found that the reduction in the drag ratio results from the wake effect.

After that the interaction parameter ( $\lambda = C_D/C_{D0}$ ) was introduced into equation (6) in order to evaluate the effect of interaction on the drag coefficient. The drag force ( $F_D$ ) is then determined using:

$$F_D = \frac{1}{2} C_D \pi \rho_f a^2 u^2 \quad (21)$$

For the motion of spheres in water, the same method of evaluating the drag force will be used but instead of equation (6), equation (1) was used.

### • Effect of Fluid Rheology on the Drag Force

Figure (4) shows the relationship between the drag coefficient and power law index at constant generated Reynolds number for one steel sphere ( $d=10\text{mm}$ ). It can be seen from this figure that the drag coefficient increases with increases the power law index at constant generated Reynolds number and shows fair agreement with the result of Dohle et al., (2006).

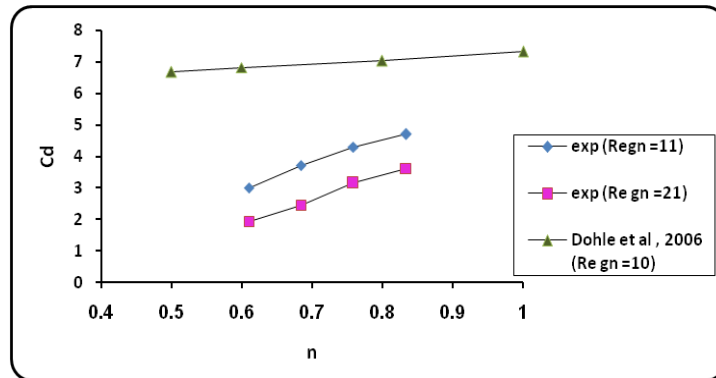


**Fig. 4** Relationship between drag coefficient and power law index at constant generated Reynolds number for one steel sphere,  $d=10\text{mm}$

### • Density Effect on the Drag Force

Examining the effect of fluid density on the drag force, the drag force was plotted as a function of velocity for different PAA concentration compared with water. Figure 5, shows the effect of fluid density on the drag force, i.e. the drag force increased as the fluid density increased.

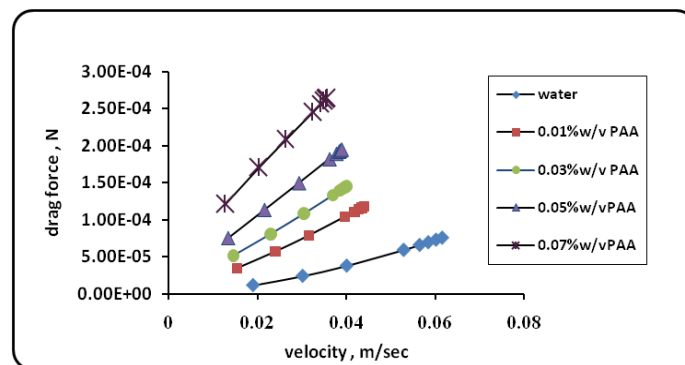


**Fig. 5** Change of drag force with velocity at different fluid densities, for two steel spheres side by side ( $d=10\text{mm}$ ,  $l/d=3$ )

To evaluate the effect of sphere density on the drag force, the drag forces are plotted as a function of sphere density at constant velocity. Figure 6, shows the effect of sphere density on the drag force for two spheres, side by side with 0.07% w/v PAA solution ( $l/d=1$ ), which indicates that the drag force decreases as the sphere density increases.

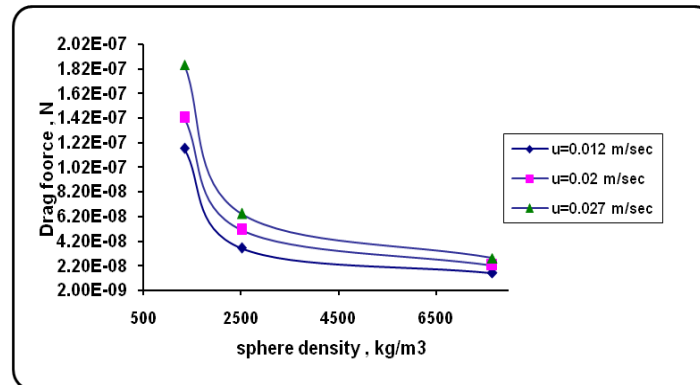


**Fig. 6** Effect of sphere density on the drag force, for two spheres, side by side ( $l/d=1$ ) in 0.07% w/v PAA solution

## CONCLUSIONS

- Newtonian correlations were used to predict an expression that relates the drag coefficient with the inter-particle distance in power law fluid in the range of generated Reynolds number between 1.1 and 76 and power law index is  $0.6 \leq n \leq 1$ , the following conclusion were obtained :
- For two spheres moving side by side, the drag increases when the spheres are close to each other, but the effect disappears at a distance larger than  $l/d$  about 3 and the drag ratio asymptotically reaches that of a single sphere similar to that in Newtonian fluid.
- For two spheres moving in line, according to this correlation, the drag decreases with decreasing distance between the spheres, but the effect of interaction disappears at a distance larger than  $l/d$  about 5 to 10 and asymptotically approaches the single sphere value.
- Drag coefficient increases with increases the power law index at constant generated Reynolds number.
- The drag force is related to the fluid and sphere density; it increases as the fluid density increased while it decreases as the sphere density increase, within the considered range of generated Reynolds number.

## RERERENCES

- Bagchi, A. and Chhabra, R.P. , (1991), " Acceleration motion of spherical particles in power law type non Newtonian liquids", J. of powder technology , 68, P. 85-90.
- Brown, Philip, P. and Desmond F. Lawler,(2003), "Sphere Drag and settling velocity Revisited", J. of Environmental Engineering, ASCE, 129 (3), P. 222-231.
- Chhabra, R. P. , Soares, A. and Ferreira, J. M. , (1998), " A Numerical Study of the Accelerating Motion of a Dense Rigid Sphere in non -Newtonian Power Law Fluids" , The Canadian Journal of chemical Engineering , 76, P.1051-1055.
- Clift, R., Grace, J. R. and Weber, M. E., (1978), "Bubbles, Drops and Particles", Academic Press, New York.
- Dhole, S. D., Chhabra, R. P. And Eswaran ,V. , (2006) , " Flow of Power-Law Fluids Past a Sphere at Intermediate Reynolds Numbers " , Ind. Eng. Chem. Res., 45(13) ,P.4773 -4781.
- Happel, J. and Pfeffer, R., (1960), "The Motion of Two Spheres Following each other in a Viscous Fluid", AIChE J., 6 (1), P.129-133.
- Kelessidie, V.,(2003), "Terminal Velocity of Solid Spheres Falling in Newtonian and non-Newtonian Liquids", Tech. Chron. Sci. J. TCG, V, No 1-2, P. 43-54.

- Kelessidie, V.,(2004)," Measurements and prediction of terminal velocity of solid spheres falling through stagnant pseudoplastic liquids", J. of Powder Technology ,147 , P.117– 125.
- Kendoush, A. A.,(2005), "The Virtual Mass of a Rotating Sphere in Fluids", J. Appl. Mech., 72, P. 801-802.
- Kim, I., Elghobashi, S. and Sirignano, W. A., (1998), "On the Equation for Spherical Particle Motion: Effect of Reynolds and Acceleration Numbers", J. Fluid Mech., 367, P. 221-253.
- Kok, J. B. W., (1993), "Collision Dynamics of Bubble Pairs Moving through a Perfect Liquid", Appl. Sci. Res., 50, P. 169-188.
- Lali, A. M., Khare, A. S., Joshi, J. B. and Migam, K. D. P., (1989), "Behavior of Solid Particles in Viscous non-Newtonian Solutions: Falling Velocity, Wall Effects and Bed Expansion in Solid - Liquid Fluidized Beds", J. of Powder Technol.,57, P.47-77.
- Legendre, D., Magnaudet, J. and Mougin, G.,(2003), "Hydrodynamic Interactions between Two Spherical Bubbles Rising Side by Side in a Viscous Liquid", J. of Fluid Mech., 497, P. 133-166.
- Liang, S.-C., Hong, T. and Fan, L.-S.,(1996), "Effects of Particle Arrangements on the Drag Force of a Particle in the Intermediate Flow Regime", Int. J. of Multiphase Flow, 22(2), P. 285-306.
- Rowe, P. N. and Henwood, G. A.,(1961), "Drag Forces in a Hydraulic Model of a Fluidized Bed-Part I", Trans. Instn. Chem. Engrs., 39, P. 43-54.
- Tsuji, Y., Morikawa, Y. and Terashima, K., (1982), "Fluid-dynamic Interaction between Two Spheres", Int. J. Multiphase Flow, 8, P. 71-82.
- Zhu, C., Lam, K., Tang, X. and Liu, G.,( 2003), "Drag forces of interacting spheres in power-law fluids", J. of mechanics research communications, 30, P.651-662.
- Zhu, C., Liang, S.-C. and Fan, L.-S., (1994), "Particle Wake Effect on the Drag Force of an Interactive Particle", Int. J. Multiphase Flow, 20, P. 117-129.

**Symbols**

$a$	<i>Sphere radius, m</i>
$n$	<i>power law index (flow behavior index), dimension less</i>
$C_D$	<i>Drag coefficient, -</i>
$C_{D0}$	<i>Drag coefficient of an isolated sphere, -</i>
$d$	<i>Sphere diameter, m</i>
$F_D$	<i>Drag force, N</i>
$k$	<i>consistency index, (Pa.s<sup>n</sup>)</i>
$l$	<i>Distance between the centers of spheres, m</i>
$u$	<i>Sphere velocity, m/s</i>
$Re$	<i>Reynolds number based on the sphere diameter (<math>\rho f \cdot u \cdot d / \mu</math>)</i>
$R_{egn}$	<i>Generated Reynolds number for power law fluid, <math>\rho V^{2-n} d^n / k</math></i>
$S$	<i>Dimensionless separation (<math>l/a</math>)</i>
$V$	<i>Fluid velocity, m/s</i>
$x$	<i>Distance between particle surfaces, m</i>
$\mu$	<i>Viscosity, kg/m.s</i>
$\delta$	<i>Dimensionless separation (<math>x/d</math>), -</i>
$\lambda$	<i>Drag interaction parameter (<math>C_D / C_{D0}</math>), -</i>
$\rho f$	<i>Density of fluid, kg/m<sup>3</sup></i>



## REMOVAL OF METHYL TERTIARY BUTYL ETHER FROM SYNTHETIC WASTEWATER

Suondos K. A. Barno

Chemical and Biological Monitoring Committee- University of Baghdad

### ABSTRACT

Methyl tertiary-butyl ether (MTBE) is the most fuel additive used through the world. Thus, it has been reported that MTBE is the second high concentration contamination found in ground water.

Study of the effect of reaction time and reaction temperature of 25 to 55° C on the kinetic of chemical oxidation has been done with 3000 ppm MTBE in water at pH range 3 to 7 and 1:1 hydrogen peroxide to Fenton's reagent ratio.

Also, Kinetic analysis was carried out to determine reaction order and activation energy for the reaction of MTBE disappearance during the reaction with Fenton's reagent.

### الخلاصة

مثيل رباعي بيثيل اثير هو من اشهر المضافات الى الوقود حول العالم. و سجل كثاني أعلى ملوث في المياه الجوفية. تم دراسة تأثير كل من زمن و درجة حرارة التفاعل من 25 الى 55° مئوية على حركية تفاعل الاكسدة لمحلل مصنع ذو تركيز 3000 جزء بالمليون من مثيل رباعي بيثيل اثير في الماء لمدى اس هيدروجيني بين 3 و 7 و بأستعمال نسبة بيروكسيد الهيدروجين الى معادل فينتون 1:1. حسبت من تحليل حركية التفاعل كل من درجة التفاعل و طاقة التنشيط.

**KEYWORDS:** Methyl tertiary butyl ether, wastewater, organic chemistry, oxidation, reaction rate, activation energy.

### INTRODUCTION

Methyl tertiary butyl ether (MTBE) is a synthetic chemical that was historically used as an octane booster additive to gasoline. Increasingly there have been concerns about its toxicity and potential carcinogenicity.

Because of its chemical characteristics, MTBE contaminated sites are difficult to remediate. MTBE readily dissolves and spreads in water. Additionally, MTBE resists biodegradation, does not sorb to soil, and has a low Henry's Law constant. As a result, the extent of MTBE contamination is usually much greater than that of the other common gasoline components. Because of these factors, remediation of MTBE-impacted groundwater can be very difficult and costly.

Methyl tertiary butyl ether (MTBE) is a synthetic chemical that was historically used as an octane booster additive to gasoline due to its many properties which including low production cost, ease of production, high octane rating [Shelly and Fouhy, 1994]. Increasingly there have been concerns about its toxicity and potential carcinogenicity [Carver and Brown, 2008]. The addition of MTBE to gasoline improves fuel combustion and reduces the resulting concentrations of carbon monoxide and un-burn



hydrocarbons. Accordingly, MTBE was added to about 30% of the gasoline nationwide at an average concentration of about 11% by volume [USEPA, 1994].

MTBE is a liquid with a molecular weight of 88 and a boiling point of 55°C under atmospheric pressure. It is soluble in all common solvents and is highly soluble in water (about 50 g/L). Therefore, MTBE is highly mobile, undergoing little or no retardation as it travels through a groundwater system. MTBE, through co-solvent effects, increases the solubility of other petroleum derivatives, such as benzene, toluene, ethyl benzene, and total xylenes [Schirmer and Barker, 1998]. It is resistant to biological degradation with a half-life of 10,000 days. Laboratory studies have shown that MTBE is recalcitrant to all forms of aerobic as well as anaerobic biodegradation, key components in the natural attenuation process [Vance, 1998].

National Water-Quality Assessment Program reported that MTBE was a second higher concentration component (after trichloromethane) out of 60 volatile components in different groundwater, rainwater of United State and eight other urban areas during 1993 to 1994 [Delzer, et al., 1996].

Chemical oxidation of organic component is the most practical and effective process to convert organic components (usually in aqueous solution) into carbon dioxide and water. Ray, et al. [2003] was summarized chemical oxidation techniques efficient for the reduction of organic components in water, these techniques including chemical oxidizing agent with and without catalyst and irradiation with and without chemical oxidizing agent.

Greater than 99% reduction of MTBE was achieved with initial concentrations of 170 and 196 ppm in pH region between 7.7 and 8.8 by using chemical oxidation with hydroxyl radical technique [Tornatore, et al., 2000].

Many metals have special oxygen transfer properties which improve the utility of hydrogen peroxide ( $H_2O_2$ ). The most common of these is iron which, when used in a prescribed manner, results in the generation of highly reactive OH ion. The reactivity of this system was first observed in 1894 by its inventor H.J.H Fenton. The procedure requires to adjusting pH of the wastewater (aqueous solution of MTBE in water) from 3 to 5, then addition the iron catalyst (as a solution of  $FeSO_4$ ) and finally addition of  $H_2O_2$  slowly to finish the reaction. Fenton's reagent is used to treat a variety of industrial wastes containing a range of toxic organic compounds (phenols, formaldehyde, BTEX, and complex wastes derived from dyestuffs, pesticides, wood preservatives, plastic additives, and rubber chemicals) [Ray, et al., 2003].

The reaction of aqueous MTBE with the hydroxyl radical generated by UV/ $H_2O_2$  was investigated by Carter, et al. [2000]. Results indicated that the rate of destruction of MTBE is influenced by the initial concentrations of both hydrogen peroxide and MTBE. The results also show that about 85 % reduction of initial MTBE concentration of about 87 ppm was noticed during 10 hours reaction time and the results reported that MTBE was disappear after 40 hours reaction time. In all cases, the decay of MTBE was found to follow first-order reaction kinetics with a pseudo first-order rate constant. The value of pseudo first-order rate constant increased with the decreasing concentrations of MTBE. Byproducts of the UV/ $H_2O_2$  degradation of MTBE were found to be tert-butyl formate (TBF), tert-butyl alcohol (TBA), methyl acetate, acetone, a per-oxy compound, formaldehyde, alkanes, and acetic and formic acids [Stefan, et al., 2000].

Ray, et al. [2003] studied the effect of hydrogen peroxide to Fenton's reagent ratio (0.1:1 to 100: 1), pH (3 to 7), 25° C temperature and time (up to 60 minutes) on the reduction of initially 1300 mg/l (ppm) MTBE concentration in groundwater and the probability of reduce this amount to regular accepted level of 20 mg/l (ppm) or less (as reported by USEPA [1997]). This goal was achieved at hydrogen peroxide to Fenton's reagent ratio of 1:1 and reaction pH of 5 and contact time about 10 minutes.

Carver and Brown [2008] compared four methods for producing TBA from MTBE which are: Fenton's reagent, permanganate, ozone and uncatalyzed persulfate. Fenton's reagent method done by using 500 mg/L  $H_2O_2$  and 100 mg/L  $Fe^{+2}$  at a pH of 2.8 to reduce MTBE to less than 10 % from its initial value (250 ppm) in 10 minutes.

The aim of this work is to study the effect of reaction time (up to 60 minutes) and reaction temperature (25 and 55° C) on the concentration of MTBE in treated solution and study the kinetic of chemical oxidation of 3000 ppm MTBE in water at pH range 3 to 7 and 55° C and 1:1 hydrogen peroxide to

Fenton's reagent ratio.

## EXPERIMENTAL WORK

### Materials

The following materials were used in this work:

**MTBE:** 99.5 wt. %, molecular weight of 88, boiling point 53.6° C and refractive index is 1.3692 (Aldrich).

**Hydrogen peroxide:** 35 wt. % solution in water (Annular).

**H<sub>2</sub>SO<sub>4</sub>:** 98 wt. % (Annular).

**FeSO<sub>4</sub>:** White crystal, molecular weight 151.9, melting point 400° C (decomp.) and the density is 2.841 g/cm<sup>3</sup> (Aldrich).

### Experimental Setup

MTBE was mixed with Fenton's reagent in 3-neck, 500 ml glass flask. The flask necks were fitted with thermo-meter (to measure temperature), condenser (to insure that no loss of solution due to heating occurs) and syringe to take samples (as shown in Figure 1). The flask was heated by magnetic-stirred type Hinotik-79-1 (rotation speed 0-2400 rpm, power of motor 40 W and heating power 300 W).

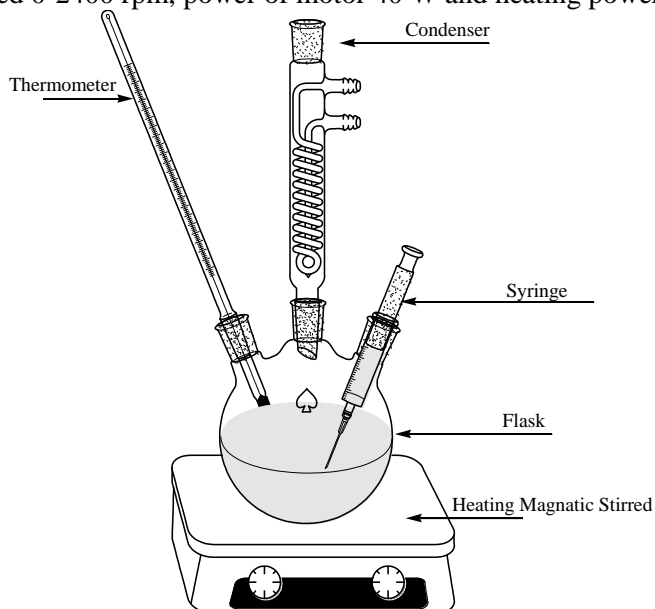


**Fig. 1 Experimental setup**

### Tests

**pH:** OAKION PH2100 Series pH-meter was used to measure solution and sample pH.

**MTBE concentration:** UVD-3500/UVD-3400 spectro-photometer was used to measure concentration of MTBE in sample.

## RESULTS AND DISCUSSION

### Effect of Temperature, pH and Time on MTBE Conversion

The effect of temperature, pH and time on MTBE conversion (disappearance) was studied in the range of temperature from 298 to 333 K, and pH range from 2 to 6 with a period of time up to 60 minutes, and this effect illustrated in Figures 2 to 4.

It is obvious from these figures, in the mentioned range of temperature, that MTBE conversion generally increasing with time and temperature and gives maximum value of 0.99 (about complete conversion of MTBE) at 333 K and 60 minutes in pH solution 5. This result is in good agreement with that reported by Carver and Brown [2008] who used Fenton's reagent method of 500 mg/L H<sub>2</sub>O<sub>2</sub> and 100 mg/L

$\text{Fe}^{+2}$  at pH of 2.8 and temperature of 298 K to reduce MTBE to less than 10 % from its initial value (250 ppm) in 60 minutes.

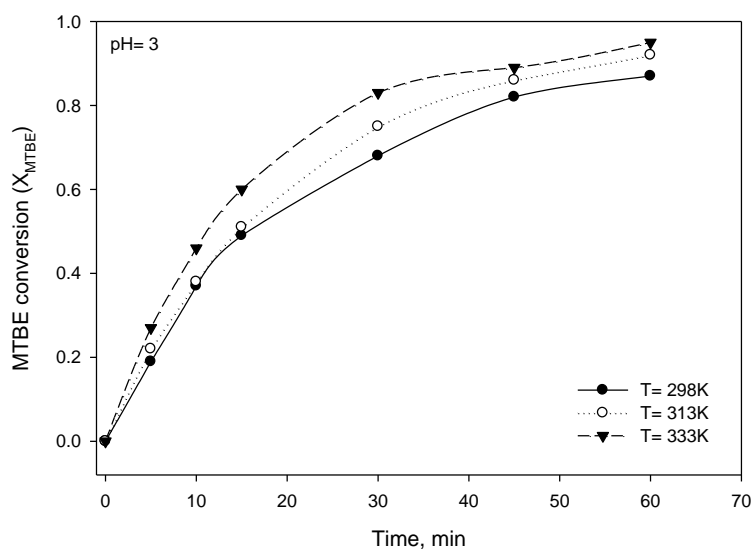


**Fig. 2 Effect of time and temperature on MTBE conversion at 3 pH solution**

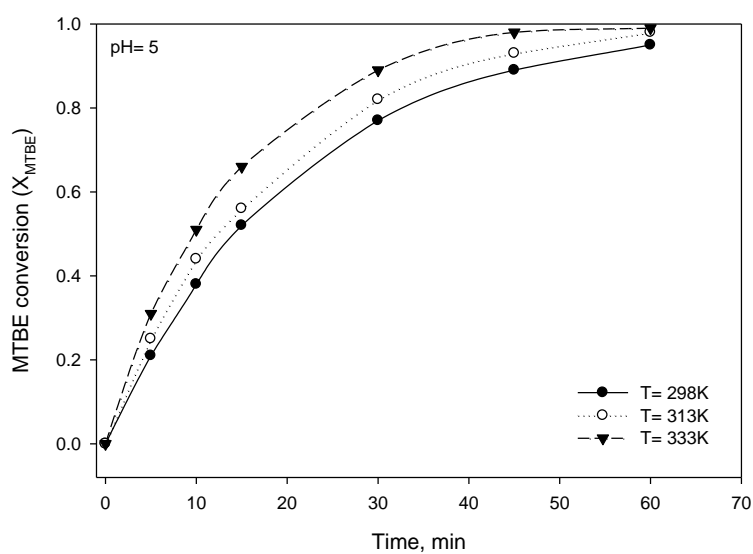


**Fig. 3 Effect of time and temperature on MTBE conversion at 5 pH solution**

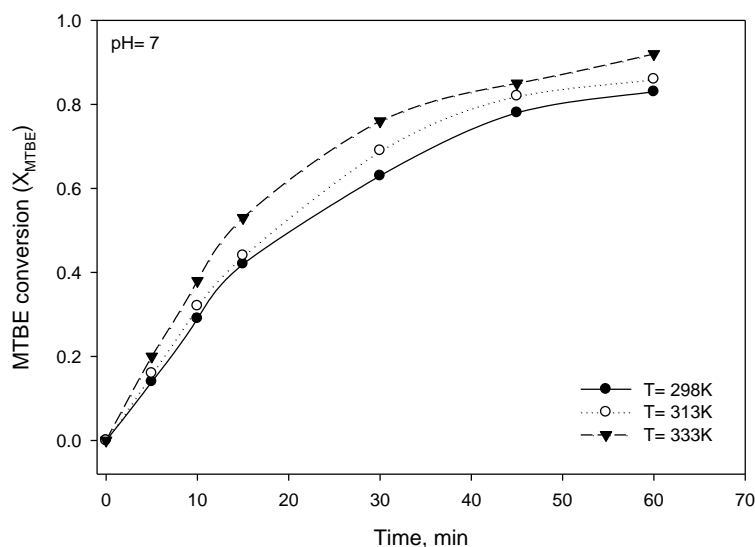


**Fig. 4 Effect of time and temperature on MTBE conversion at 7 pH solution**

The solution pH increases from 3 to 5 increases MTBE conversion, but more increasing in solution pH to neutral value (7) causes decrease in MTBE conversion, this effect shown in Figure 5.

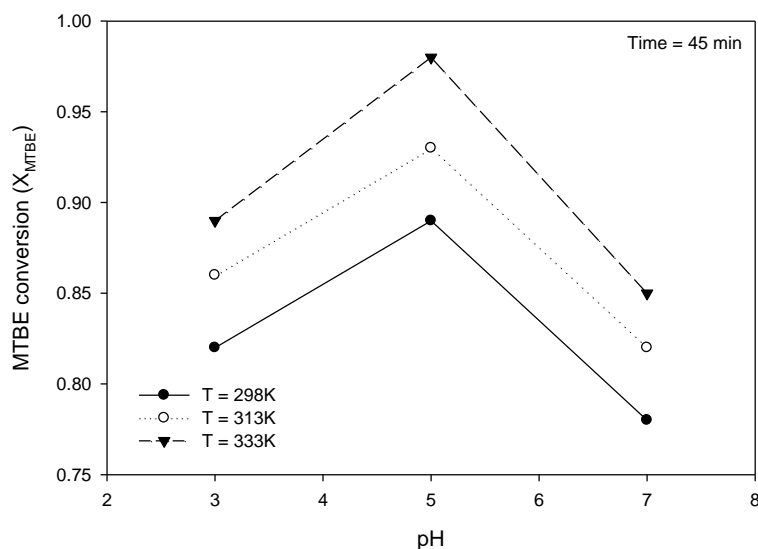


**Fig. 5 Effect of pH and temperature on MTBE conversion and 45 minutes time**

Hydrogen peroxide in the presence of ferrous iron ( $Fe^{2+}$ ) reacts to form hydroxyl radicals ( $OH^\bullet$ ), ferric iron ( $Fe^{3+}$ ), and hydroxyl ions ( $OH^-$ ). The hydroxyl ions are very powerful oxidizers, and react particularly with organic compounds. The generation of highly reactive ion ( $OH^\bullet$ ) affects the oxygenation of MTBE, this ion is generated according to the following equilibrium chemical equations [Ray, et al. 2003]:



When the pH decreasing (below 5), hydrogen ion  $H^+$  increasing, and the equilibrium reaction (Eq. 2) shifts backward and more amount of  $Fe^{+3}$  ion appears which cause also shifting backward in equilibrium reaction (Eq. 1) and the amount of reactive ion ( $OH^*$ ) available to react with MTBE decreases. The increasing in pH value of the reaction media more than 5, forced both equilibrium reactions (Eq. 1 and 2) forward and also the amount of reactive ion ( $OH^*$ ) available to react decreases.

This result is in good agreement with Ray, et al. [2003] who find that 20 ppm MTBE solution can be obtained from 1300 ppm solution at hydrogen peroxide to Fenton's reagent ratio of 1:1 and reaction pH of 5 but contact time about 10 minutes.

#### • KINETIC OF MTBE CONVERSION

Data obtained from the bench-scale for the MTBE conversion (disappearance) were analyzed by available kinetics models [Levenspiel, 1972].

First order reaction analyses show more accurate model to describe MTBE conversion variation with time.

$$-\ln(1 - x_{MTBE}) = \ln\left(\frac{C_{MTBE0}}{C_{MTBE}}\right) = kt \quad (3)$$

The reaction rate coefficients at each temperature can be easily evaluated from the straight lines slope of  $-\ln(1 - x_{MTBE})$  versus  $t$  as shown in Figures 6 to 8.

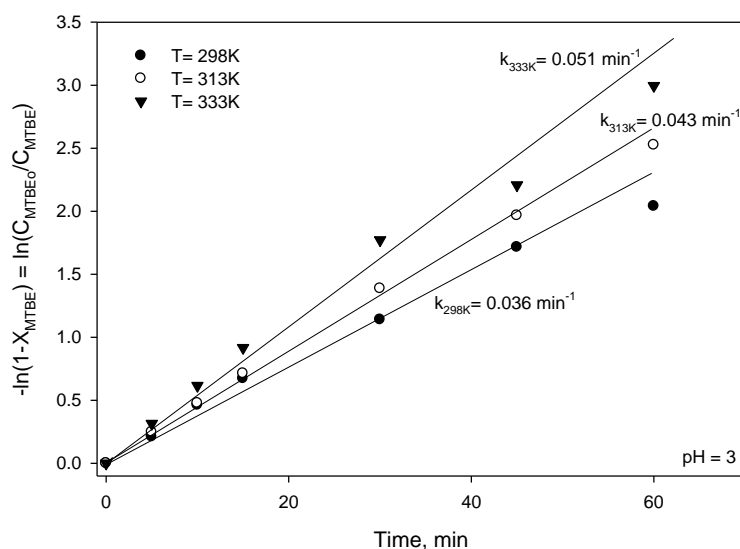


**Fig. 6 First order reaction model of MTBE conversion at different temperatures and 3 pH**

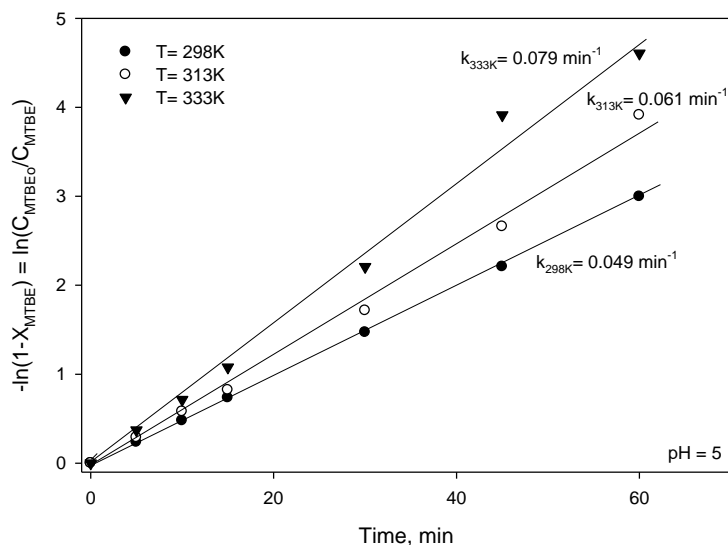


**Fig. 7 First order reaction model of MTBE conversion at different temperatures and 5 pH**

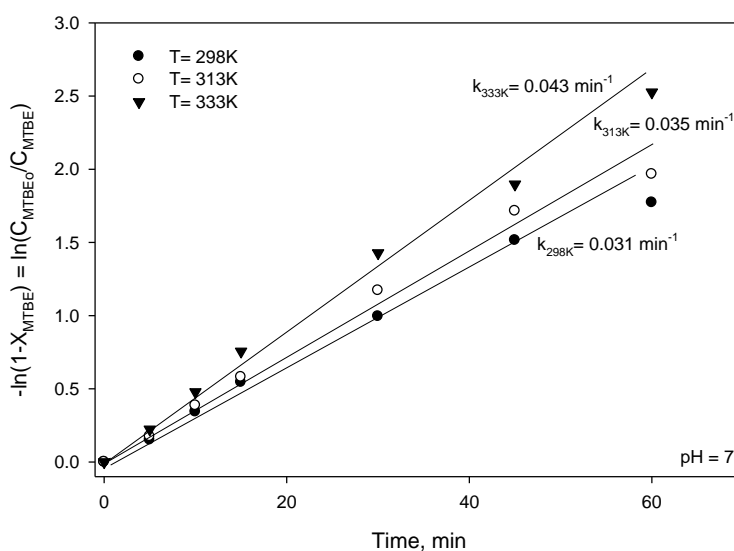


**Fig. 8 First order reaction model of MTBE conversion at different temperatures and 7 pH**

The values of the reaction rate coefficients for MTBE conversion appears to increase with temperature but increasing with pH in the range of 3 to 5 and then decreases when pH get neutral (pH=7), the reaction rate coefficient values are summarized in Table 1.

**Table 1 Reaction rate coefficient values at different reaction conditions**

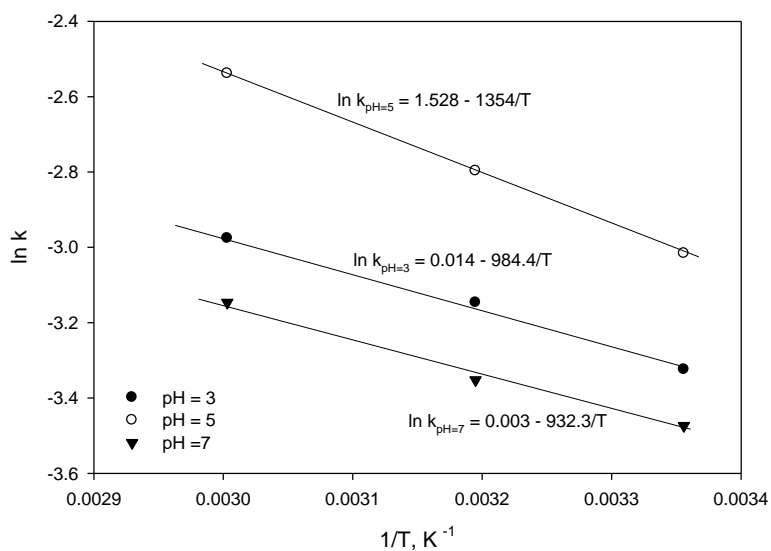
Temperature, K	Rate coefficient, min <sup>-1</sup> at 3 pH	Rate coefficient, min <sup>-1</sup> at 5 pH	Rate coefficient, min <sup>-1</sup> at 7 pH
298	0.036	0.049	0.031
313	0.043	0.061	0.035
333	0.051	0.079	0.043

Reaction rate coefficient is “pure” function to temperature, but the difference in reaction rate coefficient values with pH variation is due to variation of reactive ion (OH<sup>-</sup>) amount with pH as a result of reactions equilibrium shifting (Eq. 1 and 2).

The activation energy for MTBE conversion reaction was calculated by using Arrhenius equation, which satisfies the relation between reaction rate coefficient and the reaction temperature [Levenspiel, 1972].

$$k = A \exp \left( \frac{-E}{RT} \right) \quad (4)$$

A plot of  $\ln k$  versus  $\frac{1}{T}$  gives a straight line with a slope equal to  $\frac{-E}{R}$  from which the activation energy was calculated, as shown in Figure 9 and the extracted activation energy and frequency factor values are summarized in Table 2.

**Fig. 9 Arrhenius plot of first order reaction model of MTBE conversion at different pH**

**Table 2 Activation energy and frequency factor values at different pH**

Solution pH	E, kJ/mole	ln A	R <sup>2</sup>
3	8.18	0.014	0.9962
5	11.26	1.528	0.9992
7	7.75	0.0003	0.9908

Activation energy results show that reaction is more sensitive to temperature at pH 5 (high activation energy values reported) [Levenspiel, 1972]. No reported values of activation energy of MTBE conversion are found in literature survey.

### CONCLUSIONS

- MTBE conversion increases with time (up to 60 minutes) and temperature (between 298 and 333 K).
- The increasing in solution pH from 3 to 5 increases MTBE conversion, but more increasing in neutral solution pH causes decrease in MTBE conversion.
- MTBE conversion of 0.99 (about complete conversion of MTBE) was achieved at 333 K and 60 minutes in pH solution 5.
- The reaction of MTBE conversion (disappearance) was first order with activation energy of 11.26 kJ/mole and natural logarithm of frequency factor was 1.528 (frequency factor equal to  $4.61 \text{ min}^{-1}$ ) for the reaction at 5 pH solution.

### REFERENCES

- Carter, S. R., Stefan, M. I., Bolton, J.R. and Safarzadeh-Amiri, A., 2000, "*UV/H<sub>2</sub>O<sub>2</sub> Treatment of Methyl-tert-butyl Ether in Contaminated Waters*", Environmental Science and Technology, **Vol. 34**.
- Carver, M. and Brown, R. A., 2008, "*Chemical Oxidation of MTBE and TBA*", ERM, Inc., Ewing, New Jersey.
- Dezler, G. C., Zogorski, J. S., Lopes, T. J. and Bosshart, R. L., 1996, "*Occurrence of the Gasoline Oxygenate MTBE and BTEX Compounds in Urban Storm Water in the United States*".
- Levenspiel O., 1972, "*Chemical Reaction Engineering*", New York: John Wiley and Sons Inc..
- Ray, A. B., Selvakumar, A. and Anthony, N. T., 2003, "*Treatment of Methyl Tertiary-butyl Ether (MTBE) Contaminated Waters with Fenton's Reagent*", Urban watershed Management Branch, United State Environmental Protection Agency.
- Schrimmer, M. and Barker, J.F., 1998, "*A Study of Long-term MTBE attention in the Broden Aquifer*", Ground Water Monitoring and Remediation, **Vol. 8** (2), Ontario, Canada.
- Shelly, S. and Fouhy, K., 1994, "*The Drive for Cleaner Burning Fuel*", Chemical Engineering, **Vol. 101** (1).
- Stefan, M. I., Mack, J. and Bolton, J. R., 2000, "*Degradation Pathways during the Treatment of Methyl-tert-Butyl Ether by the UV/H<sub>2</sub>O<sub>2</sub> Process*", Environmental Science and Technology, **Vol. 34**.
- Tornatore, P. M., Powers, S. E., Cooper, W. J. and Isacoff, E. G., 2000, "*High Energy Electron Injection System Destroy MTBE in Drinking Water*", Water Online.
- USEPA, 1997, "*Drinking Water Advisory: Consumer Acceptability Advice and Health Effects Analysis on Methyl Tertiary-butyl Ether (MTBE)*", EPA 822-F-97-008, Office of



Research and Development, Washington D. C.

- USEPA. 1994, "*Health Risk Perspective on Fuel Oxygenates*", EPA/600/R-94/217, Office of Research and Development, Washington D. C.
- Vance, D. B., 1998, "*MTBE: Character in Question*", Environmental Technology, No. 1.

#### NOMENCLATURES

A	Frequency factor, $\text{min}^{-1}$
$C_{\text{MTBE}}$	Concentration of MTBE at any time(t), ppm
$C_{\text{MTBE}0}$	Initial concentration of MTBE, ppm (=3000 ppm)
E	Activation energy of reaction, J/mole
k	Reaction rate Coefficient, $\text{min}^{-1}$
R	Universal gas constant, (=8.314 J/mole. K)
T	Reaction temperature, K
t	Reaction time, min
$x_{\text{MTBE}}$	Conversion of MTBE, (dimensionless)

## SHEAR CAPACITY OF CONCRETE PRISMS WITH INTERFACE JOINTS

Assistant Professor Dr. Riyadh Jawad Aziz  
Civil Engineering Department, College of Engineering  
Nahrain University

### ABSTRACT:

Construction joints are frequently used in engineering structures for various reasons. When the size of the structure is relatively large stoppage of concrete casting at certain locations is necessary. Stoppage of casting may also occurs due to sudden failure of mixing machines, or when the concrete stock ingredients runs out of materials, or when weather conditions do not permit casting operations to continue. If stoppage of concreting occurs, a joint between old and new concrete forms, it is then necessary to evaluate the horizontal shear capacity at the interface between old and new concretes to prevent progressive slip from taking place and to insure satisfactory performance of the structure.

A total of 16 push-off tests were performed to quantify the shear strength capacity at the interface between old and new concretes and to recommend the necessary practice for such circumstances. Test parameters include different interface surfaces smooth and rough with and without shear keys. The variables also include presence of shear reinforcement across the interface surfaces.

Test results have indicated that leaving concrete surface at the end of casting rough with shear keys is essential to restore part of shear resistance between old and new concretes. Presence of shear reinforcement further improves the shear resistance at the interfaces. It was found that the average nominal shear capacity of concrete at the interface relative to the nominal shear capacity of control specimens cast monolithically is about 43% for rough surfaces having amplitude of 6mm and 55% for rough surfaces with shear keys. When 3- $\Phi$ 10 shear reinforcement is used along rough interface, shear resistance increased to 62% relative to the shear capacity of control specimens cast monolithically.

### مقاومة القص للمواشير الخرسانية التي تحوي على مفاصل إنشائية

#### الخلاصة:

تستخدم المفاصل الإنشائية في المنشآت لأسباب عديدة عندما يكون حجم المنشأ كبير نسبياً مما يتطلب توقف صب الخرسانة. إن توقف صب الخرسانة في المنشآت قد يحصل نتيجة العطل المفاجئ في أجهزة الخلط والصب أو عند نفاذ خزين المواد الإنشائية أو عندما تكون الظروف الجوية غير مناسبة لاستمرار عمليات صب الخرسانة. في مثل هذه الحالات يتولد مفصل إنشائي عند معاودة الصب. إن وجود مفصل إنشائي يتطلب احتساب قوى القص الأفقية التي تتولد على سطح الخرسانة المصبوبة قبل توقف الصب والخرسانة الجديدة لاتخاذ الإجراءات المناسبة لمنع الحركة الأفقية بين سطحي الخرسانة ولضمان أداء جيد للمنشآت. تم في هذا البحث فحص 16 موشور خرساني لتقييم مقاومة القص بين سطوح الخرسانة المصبوبة في أوقات مختلفة. وتضمن البرنامج العلمي الأخذ بنظر الاعتبار متغيرات نعومة وخشونة السطوح مع وجود جيوب القص. كما وتضمنت المتغيرات وجود حديد التسليح على هذه السطوح.

أظهرت النتائج بأنه عندما تكون السطوح الخرسانية المصبوبة خشنة مع وجود جيوب القص فإن جزء من مقدار مقاومة القص يمكن استرجاعها كما وإن استخدام حديد التسليح على سطحي الخرسانة يؤدي إلى تحسين مقاومة القص بين هذه السطوح. وقد وجد

بان استخدام أوجه خشنة مع جيوب القص يؤدي إلى الحصول على مقاومة قص تبلغ 57% من مقاومة القص للمواشير المصبوبة بدون مفاصل إنشائية وبإضافة حديد تسليح قطر 10 ملم وبعدد 3 فإن مقاومة القص تزداد إلى 65%.

**KEYWORDS:** shear, capacity, concrete, prism, interface joints, rough, smooth, surface

## INTRODUCTION:

The basic requirement at joints or at interface between new and old concretes is that all forces existing at the interface must be transmitted in the same manner. To accomplish such condition, it is essential to rely upon the surface condition at the interface and/or to place reinforcing bars across the interfaces (1, 3, and 4). In composite construction, failure may precipitate in the vicinity of the connection as a result of high shear stresses which may develop at the interface of pre-cast (old concrete) and cast-in-situ concrete (new concrete). If the interface surface is not well roughened or reinforcement is not provided failure may occur.

According to ACI code (1), shear transfer across a given plane such as an existing or potential crack; an interface between dissimilar materials or an interface between two concretes cast at different times; shear friction reinforcement is intended to transfer shear across an interface between concretes cast at different times.

Concrete is relatively strong in direct shear but it is possible that crack will form in unfavorable manner. Shear friction reinforcement is provided across the crack to resist relative slip between two surfaces of concrete cast at different times (1, 3, and 4). If the crack faces are rough and irregular, the slip is accompanied by separation of the crack faces. At ultimate, the separation is sufficient to stress the reinforcement crossing the crack to its yield point (3, 4). The reinforcement provides a clamping force across the crack faces. The applied shear is resisted by friction between the crack faces; by shearing off protrusions on the crack faces; and by dowel action of the reinforcement crossing the crack.

Fatmir Menkulasi (2) in his study on horizontal shear connectors for precast prestressed bridge deck panels indicated that in typical push-off tests, the specimens reach their maximum load immediately before the bond was broken. For specimens with no shear connectors, some small shear capacity is maintained, while specimens with shear connectors once the bond broken the load reduced and maintained for large slips at a value equal to the yield capacity of the connectors times some factor. The author also indicated that the equations available in ACI code are unconservative for precast panel system and give high shear stresses at the interface relative to the obtained test results.

Joseph A. Wallenfelsz (5) tested 29 push off tests to quantify peak and post-peak shear stresses at the interface at failure. The variables of study include surface treatment of the surface of the specimens, type and amount of shear connectors and presence of pocket shear keys. He indicated that when headed shear connectors is used an exposed aggregate surface treatment is not required. He also concluded that specimens with headed shear connectors behave in similar manner to stirrup shear connectors.

In this paper, an attempt have been made to quantify interface shear capacity of concrete prisms cast at different times with various combinations of smooth and rough surfaces with and without shear reinforcement along the interface.

## ACI CODE PROVISIONS FOR SHEAR FRICTION REINFORCEMENT:

ACI- 318M-08 (1) approach for shear transfer a cross a given plane is based on calculating the nominal shear strength using the following equation:

$$V_n = A_{vf} f_y \mu \quad (\text{kN}) \quad (2.1)$$

Where:

$V_n$  = nominal shear strength

$A_{vf}$  = area of shear friction reinforcement

$f_y$  = specified yield strength of shear friction reinforcement

$\mu$  = coefficient of friction

The coefficient of friction  $\mu$  shall assume a value which ranges between  $1.4\lambda$  for concrete placed monolithically to  $0.6\lambda$  for concrete placed against hardened concrete not intentionally roughened, where  $\lambda$  is a modification factor reflecting the reduced mechanical properties of lightweight concrete of the same compressive strength.  $\lambda = 1.0$  for normal strength concrete and equal to 0.75 for all lightweight concretes.

The ACI code also specify that for normal weight concrete placed monolithically or placed against hardened concrete with surface is intentionally roughened, the factored shear strength shall not exceeds the smallest of :

$$V_n = 0.2f'_c A_c \quad (2.2)$$

$$V_n = (3.3 + 0.08f'_c) A_c \quad (\text{kN}) \quad (2.3)$$

$$V_n = 11 A_c \quad (2.4)$$

Where  $A_c$  is the area of concrete section resisting shear transfer, and  $f'_c$  is the lower strength of the concretes used. The code also specifies that when concrete is placed against previously hardened concrete, the interface for shear transfer shall be clean and free from laitance. If in the calculation  $\mu$  is assumed equal to  $1.0\lambda$ , the interface shall be roughened to full amplitude of approximately 6mm.

### EXPERIMENTAL WORK:

To examine the horizontal shear transfer capacity at the interface surfaces, 16 push off tests were conducted. The variables include surface conditions (smooth or rough), presence of shear keys, and presence of shear reinforcement between the interfaces.

#### Push-off Tests:

Push off tests which were used to investigate shear resistance at the interface between new and old concrete is shown in Fig. 1. From this test an evaluation of the average nominal shear capacity at the interface of old and new concretes as well as the contribution of steel shear connectors to the interface shear strength can be made. Various combinations of surface treatment with and without steel reinforcement were employed for this purpose.

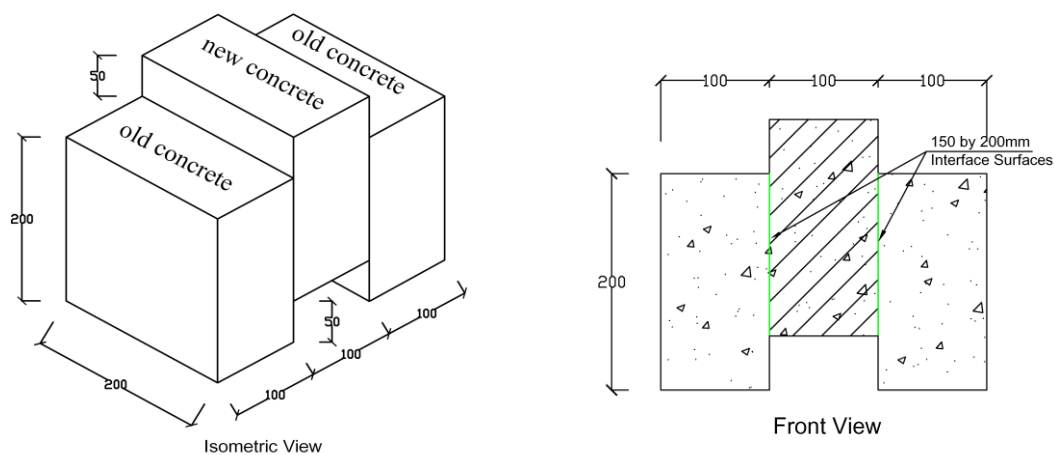


**Fig. 1: Isometric and Front Views of the Tested Specimens**

Plywood moulds were prefabricated to cast the specimens. It consists of three 100X100X200mm size prisms separated by thin plywood sheets. The edge prisms were cast first, while the middle prism was cast the next day. Surface treatments of the interface were done on the edge prisms, before casting the middle prism. Steel reinforcement across the interface was embedded in the edge prisms and was concreted the next day during casting the middle prism.

The concrete used were produced using mix proportions of 1:2:3 cement, sand, and aggregate by weight, and a w/c ratio of 0.5. The average strength of concrete calculated based on testing 150mm cubes at age of 28 days is 30 MPa (24 MPa cylinder strength).

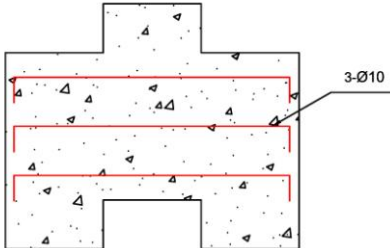
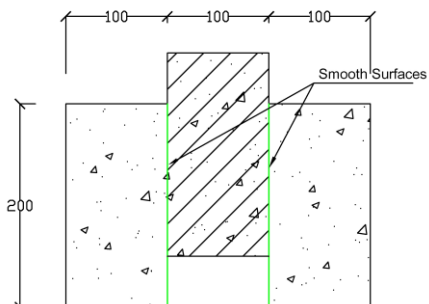
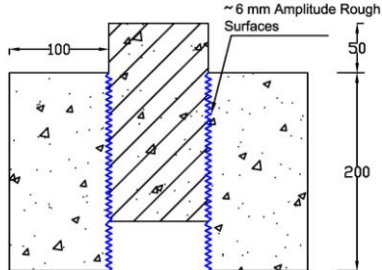
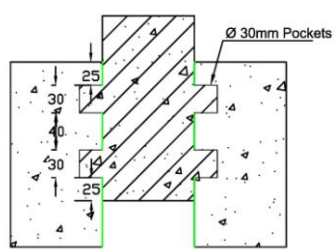
#### **Specimen Classification and Testing Procedure:**

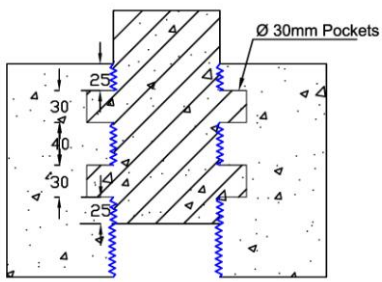
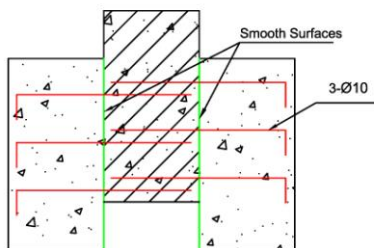
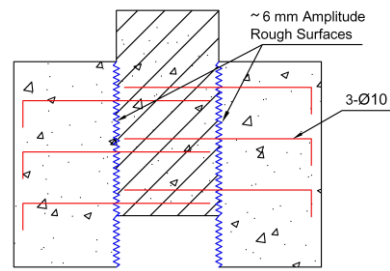
16 specimens were cast; four specimens of them were used as control specimens for no joint unreinforced specimens and no joint reinforced specimens across the interface. The rest of the specimens were divided into six groups, each group consists of two specimens for the variables investigated at the interface as shown in Table 1 below. 3- $\Phi$ 10 mm reinforcing bars were used at the interface between old and new concretes which provide a shear reinforcement ratio  $\rho_v = 0.785\%$ . The vertical spacing between these bars is 50 mm c/c. they were placed at the edge prisms extending to the end of the middle prism. The yield strength of the reinforcement used is 410 MPa.

**Table 1: Specimen Classifications and Details.**

Specimens Designation	No. of Specimens	Shape
Control specimen, no joints, no shear reinforcement	2	<p>Plain Concrete Specimen</p>



Specimens Designation	No. of Specimens	Shape
Control specimen, no joints, with 3-Ø10 shear reinforcement	2	 <p>Reinforced Concrete Specimen</p>
Smooth surfaces, no shear reinforcement	2	 <p>Specimen with Smooth Surfaces</p>
Intentionally roughened surfaces to 6mm amplitude, no shear reinforcement	2	 <p>Reinforced Specimen with Rough Surfaces</p>
Shear key specimens with smooth surfaces,	2	 <p>Shear Key Specimen with Smooth Surfaces</p>

Specimens Designation	No. of Specimens	Shape
Shear key specimens with intentionally roughened surfaces to 6mm amplitude	2	 <p style="text-align: center;">Shear Key Specimen with Rough Surfaces</p>
Smooth surfaces with shear reinforcement	2	 <p style="text-align: center;">Reinforced Specimen with Smooth Surfaces</p>
Intentionally roughened surfaces to 6mm amplitude, with shear reinforcement	2	 <p style="text-align: center;">Specimen with Rough Surfaces</p>

The specimens were tested using 2000 kN ELE compression testing machine. The tested specimen was placed concentrically within the platens of the test equipment and the load is applied continuously at a loading rate of 1 kN/sec until failure occurs. The time of test was about 4 to 8 minutes. Before testing, a dial gauge with sensitivity of 0.01mm was used to measure the displacement (slip) of the middle prism. An angle shaped plate, glued with epoxy resin to the front face of the middle prism, is used to support the dial gage movable lever. The top and bottom surfaces of the specimen were capped using thin layers of gypsum plaster. Test setup and instrumentation are shown in Figs. 2 and 3.





**Fig. 2: Specimen Inside the ELE 2000 kN Testing Machine.**



**Fig. 3: Dial Gauge Location to Measure Slip of the Middle Part of the Specimen.**

During tests, the tested specimens were visually inspected for cracks along the interfaces. It was observed that the specimens continue to carry load without distress until near failure where a crack along the interfaces appeared at which the specimen can not carry further load and the test is terminated. Figs. 4, 5 and 6, show typical failure pattern of reinforced specimens. Typical failure surfaces of specimens with and without shear keys are shown in Figs. 7 and 8.





**Fig. 4: Failure of Control Specimen with Shear Reinforcement.**



**Fig. 5: Failure of Reinforced Specimen with Smooth Interface Surfaces.**



**Fig. 6: Failure of Reinforced Specimen with Roughened Interface Surfaces to 6mm Amplitude.**



**Fig. 7: Failure Surfaces of Specimen with Two 30mm Shear Key Discs.**





**Fig. 8: Failure Surfaces of Specimen with Roughened Interface Surfaces to 6mm Amplitude.**

The average capacity of unreinforced control specimens without joints is 235 kN; while the strength of control reinforced specimens reinforced across the interface is 404 kN. One specimen with smooth joints failed during handling while the other failed at a very small load. Specimens with interface surfaces which were intentionally roughened to full amplitude of about 6mm shows an average strength before failure of about 101 kN. When shear key type shear connectors is used in the form of 30mm diameter disks the average shear capacity is increased by about 28% relative to the intentionally roughened surface specimens, regardless whether the interface surfaces are left smooth or intentionally roughened. Test results are presented in Table 2 below.

**Table 2: Interface Shear Transfer Capacity of the Tested Specimens**

Specimen Designation	$V_n$ (kN)	$V_n$ (kN) Average	$V_{\text{capacity}} / V_{\text{control}}$
Unreinforced 1 (control)	290	225	control
Unreinforced 2 (control)	160		
Smooth 1	40	20	0.085
Smooth 2	0		
Rough 1	85	101	0.43
Rough 2	117		
Shear key Smooth 1	110	123	0.52
Shear key Smooth 2	136		
Shear key Rough 1	114	129	0.55
Shear key Rough 2	144		
Rein. 1 (control)	464	404	control
Rein. 2 (control)	344		
Smooth Rein. 1	72	82	0.20
Smooth Rein. 2	92		
Rough Rein. 1	142	145	0.36
Rough Rein. 2	148		

The effect of surface type (smooth or rough) becomes apparent when the interface is crossed by shear reinforcement along the interface between old and new concretes. Test results indicate that the average shear capacity of reinforced specimens with smooth joint surfaces is 82 kN while the average shear capacity of reinforced specimens with roughened joints is 145kN.

The results also indicate that the shear capacity of reinforced specimens with rough interface surfaces is about 62% of the capacity of unreinforced control specimens. This mean that the shear capacity of the interface can better be restored if the interface surfaces are roughened to 6 mm amplitude supplemented with shear reinforcement.

#### - LOAD-SLIP RELATIONSHIP:

Typical load–slip plots for unreinforced and reinforced control specimens are shown in Fig.9. For unreinforced control specimen three stages of behavior can be recognized. In the first stage, the slope of the load- slip curve is small as compared to the slope of the second stage which shows stiffer response until near failure when the slope drops to zero indicating a crack has formed along the interface between the middle and the edge parts of the of the specimen.

The slope of the three stages of the reinforced specimen is higher than those of unreinforced specimen associated with smaller slip for the same load level. The presence of reinforcement increased the capacity of the specimen from 290 kN to 464 kN. The slip at failure is about 0.4mm for unreinforced specimen and about 0.58mm for reinforced specimen.

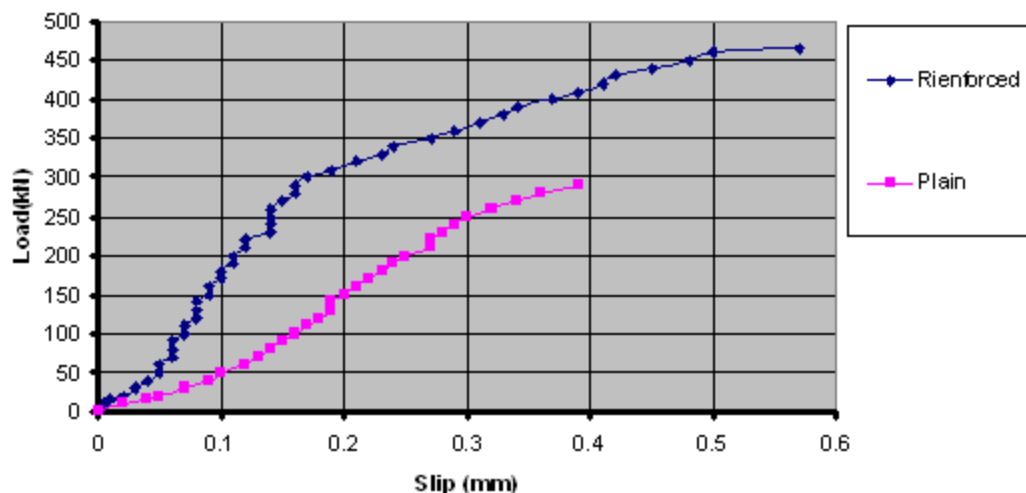


**Fig. 9 : Typical Load-Slip Relationship for Control Specimens.**

Typical load slip relationships for reinforced specimens with rough or smooth interface surfaces (joints) are shown in Fig.10. The curves show that the presence of joints has resulted in decrease in capacity relative to reinforced specimen. Specimen with smooth surfaces suffers more reduction in capacity than specimens with rough surfaces. The average capacity of smooth and rough surface specimens is 20% and 36% relative to the capacity of reinforced control specimen. The slip at failure is about 0.18mm for reinforced specimens with interfaces and about 0.58mm for reinforced control specimen without interfaces.

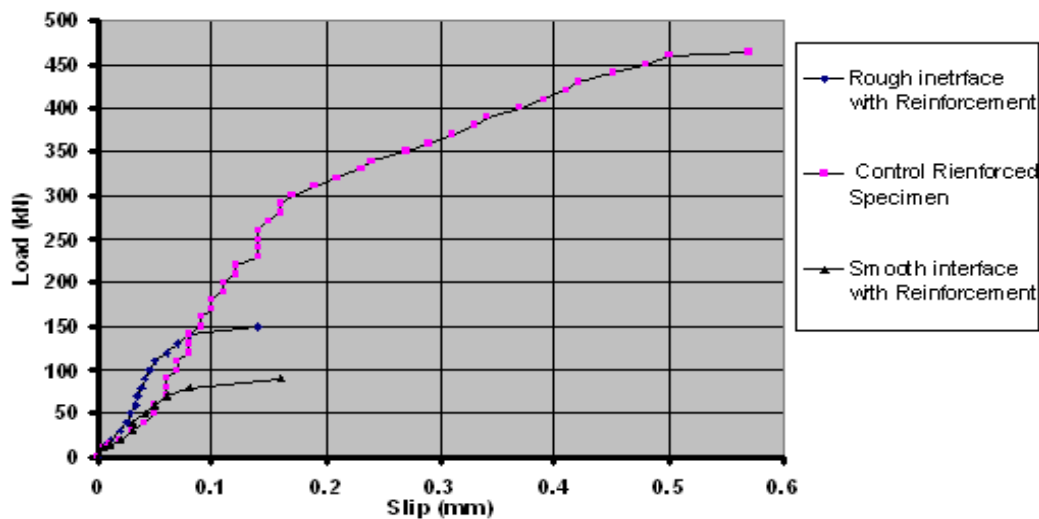


**Fig. 10 : Typical Load-Slip Relationship for Reinforced Specimens.**

#### - DISCUSSION OF RESULTS:

Control reinforced specimens with 3-Ø10 shear reinforcement (placed at the same locations of the reinforcement used to reinforce prisms with shear interfaces) and cast monolithically (without joints) shows an average capacity of 404 kN, while unreinforced control specimens shows an average capacity of 225 kN. If the shear resistance contribution of concrete at the location of the interfaces is assumed 225 kN, then the extra shear resistance of 179 kN can be thought of as the contribution of the reinforcement crossing the interfaces on both sides of the specimen. Based on the above, the stress in the reinforcement is about 380 MPa which means that at failure the reinforcement has not yielded.

According to ACI code limitations, the nominal shear contribution of concrete  $V_n$  should be the lesser of eqs. (2.2), (2.3) or (2.4) presented earlier, which according to specimen size and details are 288 kN. This is 63 kN greater than the nominal shear capacity of concrete obtained in this investigation. The ACI code equations seem to overestimate shear concrete contribution at the interfaces. Fatmir Menkulasi (2) also reported that the ACI equations are unconservative for precast panel systems and give high shear stress capacity relative to test results.

Reinforced specimens with shear interfaces were found to develop much less shear capacity as compared to reinforced control specimens without joints. The percentage reduction relative to reinforced control specimens is about 20% and 36% for smooth and rough surfaces respectively. This reduction in capacity may be discussed in terms of the shear resistance of concrete at the interface and the length of embedment of the reinforcement as follows:

The average shear capacity of roughened concrete surface specimens was found to be 101 kN, while the shear capacity of similar specimens with shear reinforcement is 145 kN as shown in Table 3. This means that the shear reinforcement contribution is only 44 kN (i.e. the reinforcement has not yielded). Comparison between capacity of control specimens and specimens with rough interface surfaces indicates that there is a decrease in concrete transfer capacity from 225 kN (for unreinforced no joint control specimens) to 101 kN (for specimens with rough interface surfaces), and a decrease in reinforcement contribution from 179 kN (for reinforced no joint control specimens) to 44 kN (for reinforced specimen with roughened interface joints) as shown in Table 3. If such an analysis is accepted, it means that when an interface is necessary, concrete can furnish about 45% of the shear strength of specimen without joints or interfaces (i.e. 101 kN), and the addition of shear reinforcement should compensate for the remaining 55 % of capacity (i.e.  $225\text{kN} - 101\text{kN} = 124\text{kN}$ ). It is believed that the contribution of reinforcement can be increased if the shear



reinforcement used is well anchored within the new concrete (middle prism of this investigation) using 90 degree hooks or the length of reinforcement embedment is increased so that the full yield strength of the reinforcement can be utilized. In addition the capacity can also be restored if the shear reinforcement ratio  $\rho_v$  is increased so that the shear capacity of specimens with interfaces approaches the shear capacity of control unreinforced specimens.

**Table 3: Contribution of Concrete and Reinforcement to Shear Transfer Capacity**

Specimen type	Shear capacity(kN)	Contribution of concrete (kN)	Contribution of reinforcement (kN)
control Unreinforced	235	235	-----
control reinforced	404	235	169
Rough no reinforcement	101	101	-----
Rough with reinforcement	145	101	44

### CONCLUSIONS:

Based on the experimental results presented, the following conclusions are drawn:

- \* At places where concrete casting is stopped, the surface of concrete should be left rough to at least 6mm amplitude to improve concrete shear strength contribution. It was found that rough concrete interfaces develop about 45% of the shear capacity of control specimens cast monolithically.
- \* Shear keys were found to improve concrete shear capacity at the interfaces between old and new concrete faces. It was found that specimens with rough interfaces and shear keys develop about 55% of the shear capacity of control specimens.
- \* Use of shear reinforcement across the interfaces enhances the shear resistance at the interface of old and new concretes. It was found that the shear capacity at the interfaces increased from 101 kN for specimens with rough surfaces to 145 kN for similar specimens with shear reinforcement ratio  $\rho_v = 0.785\%$ .
- \* When shear reinforcement is used, it is necessary to insure enough embedment length within the opposite interfaces of old and new concretes so that the yield strength of the reinforcement can be developed.
- \* It is necessary to validate the ACI code equations for shear capacity of concrete between the interfaces of old and new concretes. It was found that the shear resistance capacity of concrete specimens of this investigation at the interfaces calculated based on ACI code eqs. (2.2), (2.3) or (2.4) presented earlier is 288 kN while test results of control specimens of this investigation (without joints) develop an average concrete shear capacity along the interfaces of 225 kN.

### RECOMMENDATIONS:

The following recommendations were based on the results of this investigation:

- It is necessary to further investigate the interface shear capacity of concrete cast at different times to validate the ACI code equations.
- It is necessary to investigate the effect of using higher shear reinforcement ratios on shear capacity at the interfaces of old and new concretes.

- It is necessary to investigate the effect of presence of 90 degree hooks and embedment length of reinforcement on shear resistance capacity at the interfaces.

**REFERENCES:**

- ACI Committee 318;"Building Code Requirements for Structural Concrete (ACI 318M-08) and Commentary," American Concrete Institute, Farmington Hills, 2008, 473pp.
- Fatmir Menkulasi, "Horizontal Shear Connectors for Precast Prestressed Bridge Deck Panels," Thesis submitted to Faculty of Virginia Polytechnic institute, Blacksburg, Virginia, August 2002.
- MacGregor, J. G., Reinforced Concrete, Mechanic and Design, 3rd ed., Prentice Hall, Upper Saddle River, New Jersey, 1997.
- Nilson, A. H.; Darwin D.; and Dolan, C. W., Design of Concrete Structures, 13th ed. McGraw Hill, 2003.
- Wallenfelsz, J.A., "Horizontal shear transfer for Full-Depth Precast Bridge Deck Panels, " Thesis submitted to Faculty of Virginia Polytechnic institute, Blacksburg, Virginia, 25th February 2006.

## INVESTIGATION OF THE EFFECT OF THE WAKE GENERATED BY ROTOR BLADES ON THE FLOW THROUGH STATOR PASSAGE FOR LOW PRESSURE TURBINE

Prof. Dr. Ihsan Y. Hussain  
Mech.Engr.Dept.  
College of Engineering  
University of Baghdad  
Baghdad-Iraq

Dr.Ahmed W. Mustafa  
Mec.Eng.Dept.  
College of Engineering  
University of Tikrit

### ABSTRACT

The effects of incoming wakes of upstream rotor on the flow field in a low pressure turbine cascade are investigated. The flow field is studied numerically with and without inlet wake. The rotor effect is represented by moving bars that produce passing wakes at the entrance of the stator. The flow field is analyzed numerically by solving the steady and unsteady forms of the two-dimensional compressible Reynolds-averaged Navier-Stokes equations. Steady flow is performed without wake while the unsteady flow is performed with periodic inlet wake for Reynolds number of order  $10^5$ . A  $k-\epsilon$  turbulence model is used to obtain the eddy viscosity. The Cartesian velocity components and pressure on a collocated (non-staggered) grid are used as dependent variables in the momentum equations, which discretized by finite volume method, body fitted coordinates are used to represent the complex blade geometry accurately, and grid generation technique based on elliptic partial differential equations is employed. SIMPLE algorithm is used to adjust the velocity field to satisfy the conservation of mass. The results show that the wake passing produces unsteady pressure field in the direction of the rotor traverse. The comparison with the experimental data is acceptable and there is similar trend between the prediction and experimental data, except at the separation flow region due to the limitation of the turbulence model.

### الخلاصة

تأثيرات الاغقاب (wakes) القادمة من الدوار على حقل الجريان في سلسلة ريشات (cascade) توربين منخفض الضغط تم تحريها. حقل الجريان تم دراسة عدديا بوجود وبدون وجود اغقاب عند المدخل. تأثير الدوار تم تمثيله بواسطة اعمدة متحركة تنتج اغقاب عند مدخل الثابت. تم تحليل حقل الجريان عدديا بحل معادلات (Reynolds-averaged Navier Stokes) الثنائية الابعاد والانضغاطية للحالة المستقرة وغير المستقرة. الحالة المستقرة انجزت بدون وجود اغقاب بينما الحالة الغير مستقرة انجزت بوجود اغقاب دورية عند المدخل لرقم رينولد من رتبة  $10^5$ . نموذج اضطراب ( $k-\epsilon$ ) تم استخدامه للحصول على اللزوجة الدوامية. مركبات السرعة الديكارتية والضغط على شبكة متحدة الموقع تم استخدامها كمتغيرات معتمدة في معادلات الزخم التي تم تقطيعها بطريقة الحجم المحدد. احداثيات مطابقة الجسم تم استخدامها لتمثيل شكل الريشة المعقد بشكل دقيق. وتم استخدام طريقة توليد الشبكة على اساس معادلات تفاضلية جزئية بيضوية. خوارزمية SIMPLE



استخدمت لتعديل حقل السرعة لكي تحقق حفظ الكتلة. بينت النتائج ان الاعقاب المارة تنتج حقل ضغط غير مستقر باتجاه حركة الدوار. المقارنة مع البيانات العملية مقبولة وهناك تشابه في ميل او اتجاه البيانات العملية مع النتائج المحسوبة , ما عدا منطقة الانفصال بسبب تحديد نموذج الاضطراب.

**KEYWORDS: Wake, Low Pressure Turbine, Collocated Grid, Unsteady Flow**

## INTRODUCTION

Flow in an axial turbine blade rows is highly unsteady (with the exception of the first stator blade), because they periodically encounter flow distortions generated by upstream blade rows and combustors. This unsteadiness has important consequences for the turbine stage efficiency, blade loading, mechanical fatigue, heat transfer, thermal fatigue and noise generation. The induced unsteady flow depends upon the scale of the upstream disturbance like wakes. These unsteady flow-generating factors can be classified based on the physical mechanisms involved as: -

- Potential Interaction of Upstream and Downstream Rows.

Potential interactions arise because the entire blades have circulation and therefore a potential field propagates throughout the space. The magnitude of this effect depends on a number of factors. (**Parker and Watson, 1972**), gave series of relationships for unsteady pressure and velocity for two-dimensional cascade; the potential field associated with blade row propagates both upstream and downstream pressure and it varies approximately in proportion to the quantity  $(\exp(-2\pi\sqrt{1-M^2}\frac{x}{s}))$ , where “x”

is the axial distance from the blade row, “s” is the pitch of the blade row and “M” is the local Mach number. This equation means that in high Mach number flows, potential interactions will tend to be stronger than lower speed. If the Mach is high enough, then the potential field will propagate without decay. (**Parker and Watson, 1972**) confirmed that the effects of potential interactions would be insignificant for axial spacing greater than about 30% of the blade pitch. As the flow in the current study is subsonic with minimum blade row axial gap of about 25% in the present study, this potential interaction will be neglected.

- Wake-Blade Interaction.

One of the first studies of the interaction of wake with blade was conducted by (**Meyer, 1958**), who used thin airfoil theory and he presented a solution for the interaction of the upstream blade wake with moving downstream blade row. Each wake is initially represented as a perturbation of the uniform flow. The wakes are transported with the main flow and chopped into segments by the downstream blade row. Inside the blade passage, the wake continues to behave as a negative jet. The velocity induced by the negative jet causes a build up of the wake fluid on the suction surface and removal of the wake fluid from the pressure surface. (**Hodson, 1985**) developed a numerical solution to predict the unsteady wake-blade interaction phenomena observed in his experimental investigation. He used a two-dimensional inviscid formulation based on that of (**Denton, 1983**), who used time marching calculation. In the absence of any real viscous forces, artificial viscosity was used to model the viscous decay of the wake. He showed that the unsteadiness in the turbine passage determined by the convection phenomena associated with passing wakes through the passage. (**Giles, 1987**) also developed a numerical solution for calculating the two-dimensional inviscid flow of the wake-blade interaction. He solved the two-dimensional Euler equations using Lax-Wendroff method. His results were similar to those of (**Hodson, 1985**). (**Reda, 1989**) performed a numerical solution for predicting the flow between parallel plates subject to moving wake generated by moving

cylinders at the entrance of the channel. He solved the two-dimensional unsteady incompressible Navier Stokes Equations on a staggered grid and the eddy viscosity was obtained by using a k- $\epsilon$  model. The results showed that the upstream wakes produces a pressure field at the stator entrance that increases in the direction of the wake traverse and large oscillations in the mean velocities were introduced due to wake passing. **(Hodson and Dawes, 1998)** developed a numerical solution to predict the flow in turbine passage subject to passing wake at the inlet of the cascade. They solved the two-dimensional unsteady Reynolds Averaged Navier Stokes equations on unstructured mesh. They used low Reynolds number k- $\epsilon$  model to calculate the eddy viscosity. The results showed that the fluctuations in stagnation pressure and stagnation temperature downstream are greater than the defects that occur in the wake at the inlet of the blade row. **(Stieger, 2002)** has made measurements of the convection of turbulent wakes at the mid-span of a low-pressure linear cascade using 2D (Laser Doppler Anemometry LDA). The turbine blade in the cascade subject to incoming turbulent wakes; moving bars fitted between two belts generated these wakes. The wake generator is driven by a motor by means of mechanism of belts and pulleys and provides linear motion of the bars as shown in **Fig. (1)**. He used high response pressure transducers (Kulite) for pressure surface measurements. The measurements confirmed that the wake fluid convected through the blade passage.

## GOVERNING EQUATIONS

The present work considers the unsteady turbulent flow between stator turbine blade, the mass conservation and the Reynolds-averaged momentum equations are written in Cartesian tensor form as :-

$$\frac{\partial \bar{\rho}}{\partial t} + \frac{\partial}{\partial x_j} (\bar{\rho} u_j) = 0 \quad (1)$$

$$\frac{\partial}{\partial t} (\bar{\rho} u_i) + \frac{\partial}{\partial x_j} (\bar{\rho} u_i u_j) = - \frac{\partial \bar{p}}{\partial x_i} + \frac{\partial}{\partial x_j} \left[ (\mu + \mu_t) \left( \frac{\partial u_i}{\partial x_j} + \frac{\partial u_j}{\partial x_i} \right) - \frac{2}{3} \frac{\partial u_k}{\partial x_k} \delta_{ij} \right] - \frac{2}{3} \rho k \delta_{ij} \quad (2)$$

Where  $\rho$  is the mean density,  $u_j$  the mean velocity, and  $p$  the mean pressure. From the k- $\epsilon$  turbulence model, **(Launder and Spalding, 1974)**, the turbulence viscosity  $\mu_t$  is given by:-

$$\mu_t = C_\mu \frac{\rho k^2}{\epsilon} \quad (3)$$

Where  $k$  is the turbulence kinetic energy and  $\epsilon$  is the turbulence energy dissipation. The model is then composed of two equations; one for  $k$  and another for  $\epsilon$  presented as follows: -

$$\frac{\partial}{\partial t} (\bar{\rho} k) + \frac{\partial}{\partial x_j} (\bar{\rho} k u_j) = \frac{\partial}{\partial x_j} \left[ \left( \mu + \frac{\mu_t}{\sigma_k} \right) \frac{\partial k}{\partial x_j} \right] + P_k - \bar{\rho} \epsilon \quad (4)$$

$$\frac{\partial}{\partial t}(\overline{\rho \varepsilon}) + \frac{\partial}{\partial x_j} \overline{\rho u_j \varepsilon} = C_{\varepsilon 1} \frac{\overline{\varepsilon}}{k} P_k + \frac{\partial}{\partial x_j} \left[ \left( \mu + \frac{\mu_t}{\sigma_\varepsilon} \right) \frac{\partial \overline{\varepsilon}}{\partial x_j} \right] - C_{\varepsilon 2} \overline{\rho} \frac{\overline{\varepsilon}^2}{k} \quad (5)$$

Where  $P_k$  is the rate of production of turbulence kinetic energy, given by:-

$$P_k = \mu_t \left[ \left( \frac{\partial \overline{u_i}}{\partial x_j} + \frac{\partial \overline{u_j}}{\partial x_i} \right) \frac{\partial \overline{u_i}}{\partial x_j} - \frac{2}{3} \frac{\partial \overline{u_i}}{\partial x_j} \delta_{ij} \left[ \mu_t \frac{\partial \overline{u_k}}{\partial x_k} + \overline{\rho k} \right] \right] \quad (6)$$

This model contains five empirical constants which assume the following values:-

$$C_\mu = 0.09, C_{\varepsilon 1} = 1.45, C_{\varepsilon 2} = 1.9, \sigma_k = 1.0, \sigma_\varepsilon = 1.3$$

## BOUNDARY CONDITIONS

For the steady state there are four types of boundaries in the physical flow domain, inlet, outlet, solid surfaces and periodic boundary as shown in **Fig.(2)**. At the inlet of the cascade the velocity components and turbulent kinetic energy are specified, Pressure is assumed to be unchanging in the flow direction at the inlet, therefore the inlet should be located far enough upstream of the blade row to ensure that this assumption is valid. At the exit plane the values of the dependent variables are unknown. Therefore the outlet boundary should be placed far down from the region of interest, at a location where the flow properties are not varied. The outlet properties can be found by set the streamwise derivatives (gradients) of all unknown variables to zero. All the velocity components are set to zero on all solid boundaries (blade surfaces and end walls). Wall pressure is determined by setting the pressure gradient normal to the surface equal to zero. The turbulence scalar transport equations (4 and 5) are only valid for fully turbulent regions. An additional model must be introduced to treat the laminar sublayer region. The wall function method is used in the present study to eliminate the large number of grid points needed to resolve the laminar sublayer more detail about the wall function are available in (**Ahmed, 2005**). The cyclic or periodic boundary condition is a type of symmetry boundary condition. When applying this boundary condition, it is required to set the flux of all variables leaving the outlet cyclic boundary equal to the flux entering the inlet cyclic boundary on the opposite side.

## SIMULATION OF THE UNSTEADY FLOW

In an effort to remove some of geometrical and physical complexity associated with the unsteady flow in the turbine cascade (**Fig.3a**), (**Stieger, 2002**), investigated experimentally the wake blade interaction such that the wakes shed from the upstream rotor in a real machine are simulated by an array of cylindrical bars moving in the traverse direction in the stator inlet plane as shown in (**Fig.3b**), these wakes causes unsteadiness in the stator passage. **Schlichting (1968)** proposed a solution of turbulent wake behind a stationary bar, gave the solution of wake behind cylinder as: -

$$\frac{U(x, y)}{U_{\infty}} = 1 - \left[ \frac{\Delta U_{\max}}{U_{\infty}} \left( 1 - \left( \frac{y}{b} \right)^{\frac{3}{2}} \right)^2 \right] \quad (7)$$

Where

$$\left. \begin{aligned} \frac{\Delta U_{\max}}{U_{\infty}} &= 0.98 \sqrt{\frac{C_d d}{x}} \\ b &= 0.576 \sqrt{C_d x d} \end{aligned} \right\} \quad (8)$$

Where  $d$  is the diameter of the cylinder,  $C_d$  is the drag coefficient of the cylinder, and  $b$  is half-wake width.

In the present study, as the cylinders are moving at the inlet plane the decay laws are transformed to the coordinates of wake frame of reference, therefore equation (7) and (8) can be written as: -

$$\frac{U_r(x_r, y_r)}{U_{\infty}} = 1 - \left[ \frac{\Delta U_{\max}}{U_{\infty}} \left( 1 - \left( \frac{y_r}{b} \right)^{\frac{3}{2}} \right)^2 \right] \quad (9)$$

$$\left. \begin{aligned} \frac{\Delta U_{\max}}{U_{\infty}} &= 0.98 \sqrt{\frac{C_d d}{x_r}} \\ b &= 0.576 \sqrt{C_d x_r d} \end{aligned} \right\} \quad (10)$$

Where

$$\left. \begin{aligned} x_r &= x \cos \alpha_r + y \sin \alpha_r \\ y_r &= y \cos \alpha_r - x \sin \alpha_r \end{aligned} \right\} \quad (11)$$

And the velocity components in the wake are obtained as: -

$$\left. \begin{aligned} U_x(\text{wake}) &= U_r(x_r, y_r) \cos \alpha_r \\ U_y(\text{wake}) &= U_r(x_r, y_r) \sin \alpha_r - U_{bar} \end{aligned} \right\} \quad (12)$$

## TRANSFORMATION OF THE GOVERNING EQUATIONS

The set of conservation equation typically can be written in the Cartesian system of coordinates for a scalar transport as: -

$$\frac{\partial(\rho\phi)}{\partial t} + \frac{\partial(\rho u\phi)}{\partial x} + \frac{\partial(\rho v\phi)}{\partial y} = \frac{\partial}{\partial x} \left( \Gamma^\phi \frac{\partial\phi}{\partial x} \right) + \frac{\partial}{\partial y} \left( \Gamma^\phi \frac{\partial\phi}{\partial y} \right) + S_\phi \quad (13)$$

Where

$(\phi)$  is any dependent variable.

$(\Gamma^\phi)$  is the exchange coefficient of  $\phi$ .

$(S_\phi)$  is the source term of  $\phi$ .

Equation (14) can be transformed from physical domain to computational domain according to the following transformation:-

$$\left. \begin{aligned} \varsigma &= \varsigma(x, y) \\ \eta &= \eta(x, y) \\ \tau &= t \end{aligned} \right\} \quad (14)$$

The final form of the transformed equation can be written as, (Ahmed, 2005):-

$$\begin{aligned} \frac{\partial}{\partial \tau} \left( \frac{\rho\phi}{J} \right) + \frac{\partial}{\partial \varsigma} (\rho\phi G_1) + \frac{\partial}{\partial \eta} (\rho\phi G_2) &= \frac{\partial}{\partial \varsigma} \left( \Gamma^\phi J\alpha \frac{\partial\phi}{\partial \varsigma} \right) + \frac{\partial}{\partial \eta} \left( \Gamma^\phi J\gamma \frac{\partial\phi}{\partial \eta} \right) + S_{\varsigma,\eta} \\ &+ \frac{S_\phi}{J} \end{aligned} \quad (15)$$

Where

$$\left. \begin{aligned} \alpha &= \left( \frac{\partial x}{\partial \eta} \right)^2 + \left( \frac{\partial y}{\partial \eta} \right)^2, \beta = \left( \frac{\partial x}{\partial \varsigma} \frac{\partial x}{\partial \eta} \right) + \left( \frac{\partial y}{\partial \varsigma} \frac{\partial y}{\partial \eta} \right) \\ \gamma &= \left( \frac{\partial x}{\partial \varsigma} \right)^2 + \left( \frac{\partial y}{\partial \varsigma} \right)^2, G_1 = u \frac{\partial y}{\partial \eta} - v \frac{\partial x}{\partial \eta} \\ G_2 &= v \frac{\partial x}{\partial \varsigma} - u \frac{\partial y}{\partial \varsigma}, J = 1 / \left( \frac{\partial x}{\partial \varsigma} \frac{\partial y}{\partial \eta} - \frac{\partial y}{\partial \varsigma} \frac{\partial x}{\partial \eta} \right) \end{aligned} \right\} \quad (16)$$

And  $S_{\varsigma,\eta}$  is the source term due to the non-orthogonal and defined as: -

$$S_{\varsigma,\eta} = - \left( \frac{\partial}{\partial \eta} \left( \Gamma^\phi J\beta \frac{\partial\phi}{\partial \varsigma} \right) + \frac{\partial}{\partial \varsigma} \left( \Gamma^\phi J\beta \frac{\partial\phi}{\partial \eta} \right) \right) \quad (17)$$

## NONDIMENSIONALIZATION OF THE GENERAL EQUATION

To obtain the flow behavior around bodies of similar shape with minimum computational effort it is desirable to group all the parameters, such as the body length and freestream velocity, into nondimensional numbers. Two flows are dynamically similar if the nondimensional numbers that govern the flows have the same value,

even though the parameters contained in the nondimensional numbers have different values. The best way to identify the appropriate nondimensional groups is to nondimensionalize the governing equations. So that in the present study the general transformed equation (4.24) is nondimensionalized by using the following scales: -

Length scale	axial chord length ( $C_x$ )
Time scale	Wake passing time ( $t_w$ )
Velocity scale	freestream velocity ( $U_\infty$ )
Density scale	freestream density ( $\rho_\infty$ )
Pressure scale	$(\rho_\infty U_\infty^2)$
K.E. of turbulence	$(U_\infty^2)$
Dissipation of K.E.	$(U_\infty^3 / C_x)$

By using the above scales the nondimensional transport equation can be written as: -

$$\Omega \frac{\partial}{\partial \tau^*} \left( \frac{\rho^* \phi^*}{J^*} \right) + \frac{\partial}{\partial \zeta^*} (\rho^* \phi^* G_1^*) + \frac{\partial}{\partial \eta^*} (\rho^* \phi^* G_2^*) = \frac{\partial}{\partial \zeta^*} \left( \Gamma^{\phi^*} J^* \alpha^* \frac{\partial \phi^*}{\partial \zeta^*} \right) + \frac{\partial}{\partial \eta^*} \left( \Gamma^{\phi^*} J^* \gamma^* \frac{\partial \phi^*}{\partial \eta^*} \right) + S_{\zeta, \eta}^* + \frac{S_{\phi^*}^*}{J^*} \quad (18)$$

Where ( $\Omega$ ) is the reduced frequency and defined as ( $\Omega = C_x / U_\infty t_w$ ). **Table (1)** summarizes  $\phi^*$ ,  $\Gamma^{\phi^*}$  and  $S_{\phi^*}^*$  for each transport equation used in the present work.

## DISCRETIZATION OF THE GOVERNING EQUATIONS

The discretized governing equations are obtained by using a finite volume method on a non-staggered grid as discussed in the previous section. By integrating the general governing equation (19) over the control volume, we get: -

$$\begin{aligned}
 & \int_{\tau^* V^*} \int \Omega \frac{\partial}{\partial \tau^*} \left( \frac{\rho^* \phi^*}{J^*} \right) dV^* d\tau^* + \int_{\tau^* V^*} \left[ \frac{\partial}{\partial \zeta^*} (\rho^* \phi^* G_1^*) + \frac{\partial}{\partial \eta^*} (\rho^* \phi^* G_2^*) \right] dV^* d\tau^* \\
 &= \int_{\tau^* V^*} \left[ \frac{\partial}{\partial \zeta^*} \left( \Gamma^{\phi^*} J^* \alpha^* \frac{\partial \phi^*}{\partial \zeta^*} \right) + \frac{\partial}{\partial \eta^*} \left( \Gamma^{\phi^*} J^* \gamma^* \frac{\partial \phi^*}{\partial \eta^*} \right) \right] dV^* d\tau^* \\
 &+ \int_{\tau^* V^*} \left[ S_{\zeta, \eta}^* + \frac{S_{\phi^*}^*}{J^*} \right] dV^* d\tau^* \quad (19)
 \end{aligned}$$

Using the upwind scheme to interpolate the convection terms and Euler implicit for time term and central scheme for diffusion and source terms, (the details of discretization of equation (19) are found in **(Ahmed, 2005)**, the final discretized equation can be written as: -

$$\phi_P^* A_P = \phi_E^* A_E + \phi_W^* A_W + \phi_N^* A_N + \phi_S^* A_S + \Omega \frac{\left( \frac{\rho_P^* \phi_P^*}{J_P^*} \right)^{\tau^*}}{\Delta \tau^*} + S_{total} \quad (20)$$

Where

$$\left. \begin{aligned}
 A_E &= \max(-F_e^*, 0) + D_e^* \\
 A_W &= \max(F_w^*, 0) + D_w^* \\
 A_N &= \max(-F_n^*, 0) + D_n^* \\
 A_S &= \max(F_s^*, 0) + D_s^* \\
 A_P &= A_E + A_W + A_N + A_S + \frac{\Omega \left( \frac{\rho_P^*}{J_P^*} \right)^{\tau^*} \Delta V^*}{\Delta \tau^*} \\
 F_e^* &= (\rho^* G_1^* \Delta \eta^*)_e, F_w^* = (\rho^* G_1^* \Delta \eta^*)_w \\
 F_n^* &= (\rho^* G_2^* \Delta \zeta^*)_n, F_s^* = (\rho^* G_2^* \Delta \zeta^*)_s \\
 D_e^* &= \left( \frac{\Gamma^{\phi^*} J^* \alpha^* \Delta \eta^*}{\Delta \zeta^*} \right)_e, D_w^* = \left( \frac{\Gamma^{\phi^*} J^* \alpha^* \Delta \eta^*}{\Delta \zeta^*} \right)_w \\
 D_n^* &= \left( \frac{\Gamma^{\phi^*} J^* \gamma^* \Delta \zeta^*}{\Delta \eta^*} \right)_n, D_s^* = \left( \frac{\Gamma^{\phi^*} J^* \gamma^* \Delta \zeta^*}{\Delta \eta^*} \right)_s
 \end{aligned} \right\} \quad (21)$$

## PRESSURE CORRECTION EQUATION

When solving the momentum equations, the pressure field and density are unknown; therefore the velocity fields obtained after solving the momentum equations generally do not guarantee the conservation of mass unless the pressure field is

correct. This means that the velocity components such as  $(u^*, v^*, w^*, G_1^*, G_2^*)$ , pressure  $p^*$  and density  $\rho^*$  have to correct according to the continuity equation. The velocity components, pressure, and density can be corrected as: -

$$\left. \begin{aligned} u^* &= u^{**} + u'' \\ v^* &= v^{**} + v'' \\ G_1^* &= G_1^{**} + G_1'' \\ G_2^* &= G_2^{**} + G_2'' \\ p^* &= p^{**} + p'' \\ \rho^* &= \rho^{**} + \rho'' \end{aligned} \right\} \quad (22)$$

The details of the pressure correction equation are not mentioned here, and can be found in (Ahmed, 2005), the final form of the pressure correction equation can be written as:-

$$A_P^p p_P'' = A_E^p p_E'' + A_W^p p_W'' + A_N^p p_N'' + A_S^p p_S'' + S_m \quad (23)$$

Where coefficients A involve  $(\alpha, \beta, \gamma, \text{density, etc.})$  and given in (Ahmed, 2005),  $S_m$  represents the local imbalance of mass.

## SOLUTION PROCEDURE

The description of the entire solution procedure given in this section applies firstly to the steady-state solution. For an unsteady flow this description refers to one time step of the calculations. The steady state solution is started with arbitrary initial guesses for the  $(\phi^*)$  values while the unsteady solution begins with the converged steady values of  $(\phi^*)$  and the advancing to the next time step.

The overall SIMPLE solution procedure takes the following steps: -

- An intermediate velocity field is obtained by solving the momentum equations for u and v. the pressure field obtained from the initial guess.
- The local continuity constraint is enforced by solving equation (23).
- Correct velocities and mass flow rates from equations (22).
- For compressible flow, a constant stagnation enthalpy condition is employed with perfect gas relation to give density.
- Equation (20) is solved for remaining scalar variables, k and  $\epsilon$ .
- Iteration from steps 1-5 are repeated until satisfactory convergence is obtained.
- For unsteady flow, steps 1-6 are repeated for the next time step.

## RESULTS AND DISCUSSION

The unsteady velocity vector for  $(Re = 10^5, \Omega = 1)$  and for five instants of wake passing  $(\tau^* = 0.1, 0.25, 0.5, 0.75)$  are shown in **Figs. (4), (5), (6), and (7)** respectively. These figures reveal the development of the stator unsteady field caused by the rotor wake interaction, by referring to these figures and to **Fig.(8)** the incoming wakes create a slip velocity  $(V_{slip})$  directed against downstream blade suction side,



this causes a temporary transport of wake fluid towards the latter. The wake defect is initially uniform **Fig.(4)**, because of the uniform pressure near the pressure side, as the wake moves further in the traverse direction at the passage inlet the wake defect distorted as it approaches to the suction side (this distortion is clearly due to the pressure variations between the two sides) as shown in **Fig(5)** and **Fig(6)**. then the wake impinges the suction side blade, further downstream the wake defect after impinging the wake is chopped and transported downstream due to the large convection velocity near the suction side as shown in **Fig.(6)** and **Fig.(7)**.

The unsteady pressure fields ( $\Delta p^* = p^* - p_{steady}^*$ ), ( $Re = 10^5, \Omega = 1$ ) for five instants of wake passing ( $\tau^* = 0.1, 0.25, 0.5, 0.75$ ) are shown in **Fig (9), (10), (11), and (12)**. respectively. From these figure it can be noted that the main source of the unsteady pressure is the rotor wake, the wake generates a pressure oscillations on both the pressure and the suction surface. Although that the unsteady pressure magnitude (amplitude) on the pressure side is larger than on the suction side, the fluctuations on the suction side is stronger than the suction side, this can explained by the shorter interaction time on the pressure side. As the wake decay moves toward the suction side and impinges this side at nearly mid axial chord, this impinging generates a zone of high pressure as shown in **Fig.(11)** and **Fig.(12)**.

**Fig.(13)**, and **Fig.(14)** show the comparison of the numerical results with the experimental data at mid-span for steady inflow condition ( $\Omega = 0$ ) and for the time of the wake passing ( $\tau^* = 0.75$ ) respectively. In all the two cases the maximum relative deviation between the numerical results and experimental data is about (25%), the comparison for this complex flow for steady and unsteady is acceptable, in this comparison there is a similar trend between the numerical results and the experimental data, this trend is that in both the numerical results and the experimental data the static pressure on the suction surface decreases and reaches to a minimum value, passing through the minimum pressure and as the fluid particles begin to descend on the rear part of the suction surface, these particle within the boundary layer encounter a positive pressure gradient that causes a separation in that part. Although that there is similar trend between the numerical results and the experimental data, but the behavior of the numerical curve **Fig.(13)** dose not contain a constant pressure region as that shown in the experimental data, the separation zone in the experimental data is characterized by the presence of flat zone in the suction pressure distribution as shown in **Fig.(13)**, ( $SS \cong 0.62$  to  $SE \cong 0.81$ ) , the reason of this discrepancy is attributed to the deficiency of the standard ( $k - \varepsilon$ ) turbulence model in accurately predicting the flow separation that occurs due to the adverse pressure gradient. Beyond the location ( $x^* \cong 0.81$ ) the fluid reattached and the numerical results with the experimental data are approached.

## CONCLUSIONS

Wake passing produces unsteady pressure field in the direction of the rotor traverse. For two-dimensional flow the comparison of the numerical results at mid-span with the experimental data is acceptable and there is similar trend between the prediction and experimental data, except at the separation flow region due to the limitation of the turbulence model.

**REFERENCES**

- Ahmed, W. M., 2005, "Investigation of the Effect of the Wake Generated by Rotor Blades on the Flow in Stator Passage for Low Pressure Turbine", Ph.D. Thesis, University of Baghdad , Mechanical Engineering Department.
- Denton, D. J., 1983, "An Improved Time-Marching Method for Turbomachinery Flow Calculation", ASME Journal of Engineering for Power, Vol.105, PP 514-520.
- Giles, M. B., 1987, "Calculation of Unsteady Wake/Rotor Interactions", AIAA Paper No. 87-0006.
- Hodson, H. P., 1985, "An Inviscid Blade-to-Blade Prediction of A Wake Generated Unsteady Flow", ASME Journal for Gas Turbines and Power, Vol.107, PP 337-344.
- Hodson, H. P., and Dawes, W. N., 1998, "On the Interpretation of Measured Profile Losses in Unsteady Wake-Turbine Blade Interaction Studies", ASME Journal of Turbomachinery, Vol.120, April, 276-284.
- Launder, B. E., and Spalding, D.B., 1974," The Numerical Computational of Turbulent Flow", Computer Methods in Applied Mechanics and Engineering, Vol.3, PP 269-289.
- Meyer, R. X., 1958, "The Effects of Wakes on the Transient Pressure and Velocity Distributions in Turbomachines", ASME Journal of Basic Engineering, October, PP 1544-1552.
- Parker, R., and Watson, J. F., 1972, "Interaction Effects Between Blade Rows in Turbomachines", Proc. of I. Mech. E., 168, No.21.
- Reda R. M., 1989, "A Study of Unsteady Rotor-Stator Interactions" ASME Journal of Turbomachinery, Vol.111, October, PP 394-400.
- Stieger, R. D., 2002,"The Effects of Wakes on Separating Boundary Layers in Low Pressure Turbine", Ph.D. Thesis, Cambridge University Engineering Department.

## NOMENCLATURE

### LATIN SYMBOLS

$A$	Coefficient of the discretized equations
$b$	Wake width
$C_\mu$	Constant in turbulence model
$C_{\varepsilon 1}$	Constant in turbulence model
$C_{\varepsilon 2}$	Constant in turbulence model
$C_d$	Drag coefficient of the bars
$C_{Ptot}$	Total pressure coefficient
$C_x$	Axial chord of the blade
$d$	Bar diameter
$D$	Diffusion at the control volume faces
$F$	Mass flux at the control volume faces
$G_1$	Contravariant velocity in $\zeta$ direction
$G_2$	Contravariant velocity in $\eta$ direction
$J$	Jacobian transformation
$k$	Kinetic energy of turbulence
$p$	Pressure
$P_\varepsilon$	Production of dissipation of K.E. turbulence
$P_k$	Production of K.E. turbulence
$S_\phi$	Source term of $\phi$
$S_{\zeta\eta}$	Source term due to nonorthogonality
$S_{total}$	Total source terms
$t$	Time
$t_w$	Wake passing time
$u$	Velocity component in x direction
$U_{bar}$	Velocity of bar
$v$	Velocity component in y direction
$x$	Axial coordinate in the physical domain
$y$	Pitchwise coordinate in the physical domain

**GREEK SYMBOLS**

$\alpha, \beta, \gamma$	Coordinate transformation parameters
$\delta_{ij}$	Kronecker delta
$\Delta$	Grid spacing
$\Gamma$	Diffusion coefficient
$\varepsilon$	Turbulence energy dissipation
$\mu$	Laminar viscosity
$\mu_t$	Turbulent viscosity
$\zeta, \eta$	Curvilinear coordinates
$\rho$	Density
$\sigma_k, \sigma_\varepsilon$	Effective Prandtl numbers
$\tau$	Time
$\tau_{ij}$	Reynolds stress tensor
$\phi$	Dependent variable
$\Omega$	Reduced frequency

**SUBSCRIPTS**

$e, w, n, s$	Values associated with control volume faces
$E, W, N, S$	Values at neighbor nodes of point p
$P$	Values at center of the control volume
$\infty$	Value at freestream
$i, j$	Index Notations or coordinate direction identifiers
$oin$	Total pressure at inlet
$r$	Relative frame of reference
$slip$	Slip velocity
$steady$	Steady values

**SUPERSCRIPTS**

$'$	Fluctuating quantity
$*$	Dimensionless quantity
$''$	Corrected values
$\text{—}$	Time-averaged or linear interpolation values

**Table(1) Parameters in the General Transport Equation.**

Equation	$\phi^*$	$\Gamma^*$	$S_{\text{total}}$
Continuity	1	0	0
x*-Momentum	$\frac{u}{U_{\infty}}$	$\frac{1}{\text{Re}} + \mu_t^*$	$-\frac{1}{J^*} \left( \frac{\partial p^*}{\partial x^*} \right) + \frac{1}{J^*} \left[ \frac{1}{3} \frac{\partial}{\partial x^*} \left( \Gamma^* \frac{\partial u^*}{\partial x^*} \right) + \frac{\partial}{\partial y^*} \left( \Gamma^* \frac{\partial v^*}{\partial x^*} \right) \right]$ $-\frac{2}{3} \frac{1}{J^*} \left[ \frac{\partial}{\partial x^*} \left( \Gamma^* \frac{\partial v^*}{\partial y^*} \right) \right] - \frac{2}{3} \frac{1}{J^*} \frac{\partial}{\partial x^*} (\rho^* k^*) + S_{\zeta, \eta, u}^*$
y*-Momentum	$\frac{v}{U_{\infty}}$	$\frac{1}{\text{Re}} + \mu_t^*$	$-\frac{1}{J^*} \left( \frac{\partial p^*}{\partial y^*} \right) + \frac{1}{J^*} \left[ \frac{\partial}{\partial x^*} \left( \Gamma^* \frac{\partial u^*}{\partial y^*} \right) + \frac{1}{3} \frac{\partial}{\partial y^*} \left( \Gamma^* \frac{\partial v^*}{\partial y^*} \right) \right]$ $-\frac{2}{3} \frac{1}{J^*} \left[ \frac{\partial}{\partial y^*} \left( \Gamma^* \frac{\partial u^*}{\partial x^*} \right) \right] - \frac{2}{3} \frac{1}{J^*} \frac{\partial}{\partial y^*} (\rho^* k^*) + S_{\zeta, \eta, v}^*$
$k^*$	$\frac{k}{U_{\infty}^2}$	$\frac{1}{\text{Re}} + \frac{\mu_t^*}{\sigma_k}$	$\frac{1}{J^*} (P_k^* - \rho^* k^*) + S_{\zeta, \eta, k}^*$
$\varepsilon^*$	$\frac{\varepsilon}{U_{\infty}^3 / C_x}$	$\frac{1}{\text{Re}} + \frac{\mu_t^*}{\sigma_{\varepsilon}}$	$\frac{1}{J^*} \left( C_{\varepsilon 1} \frac{\varepsilon^*}{k^*} P_k^* - \rho^* C_{\varepsilon 1} \frac{\varepsilon^{*2}}{k^*} \right) + S_{\zeta, \eta, \varepsilon}^*$

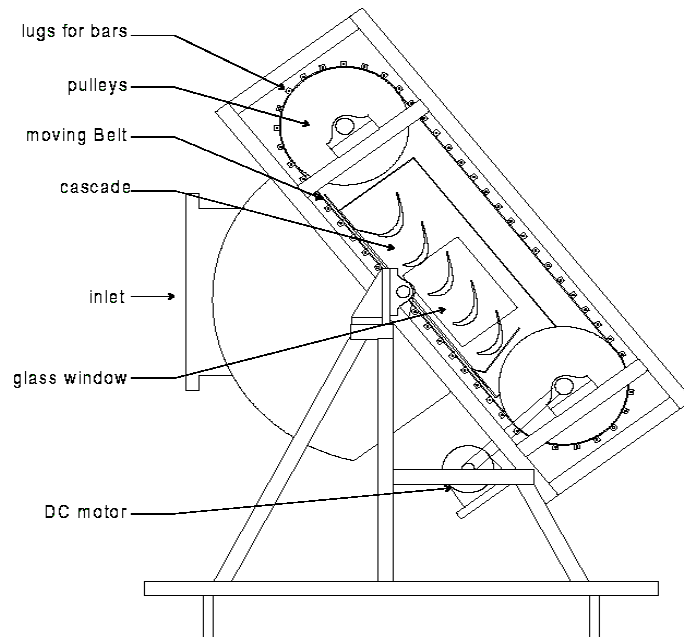


**Fig. (1) Bar Passing Cascade Facility Consisting of Wake Generator and Cascade, Stieger (2002).**

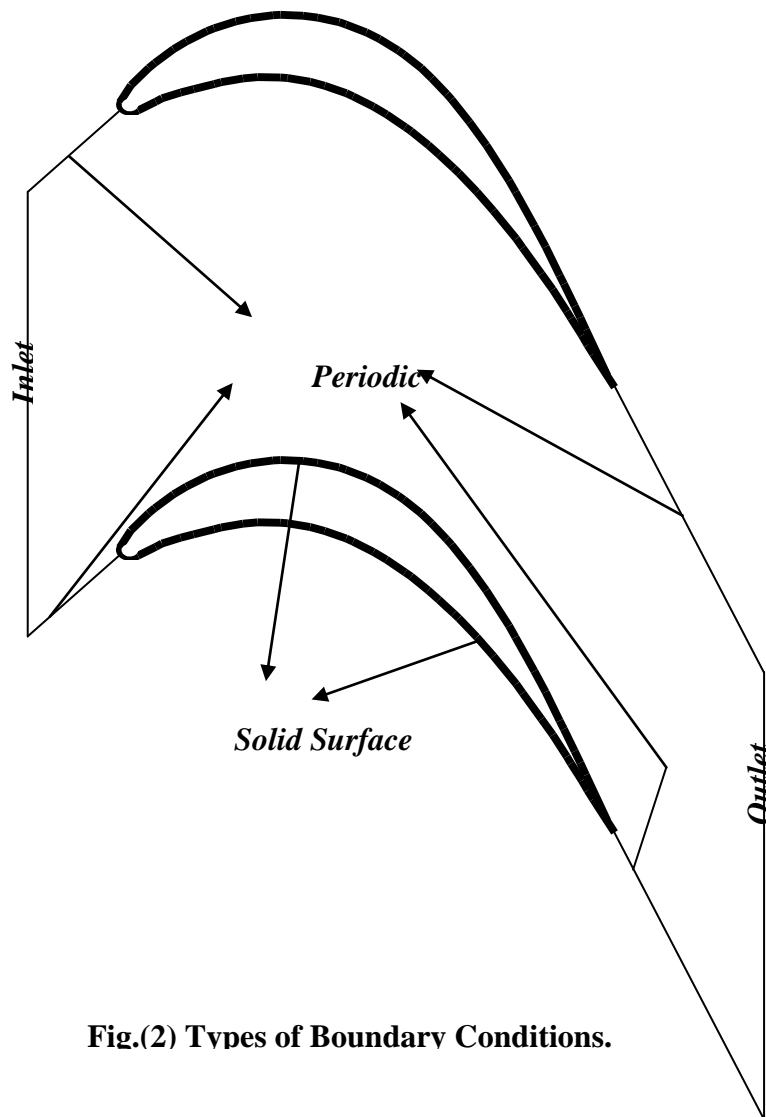


**Fig.(2) Types of Boundary Conditions.**

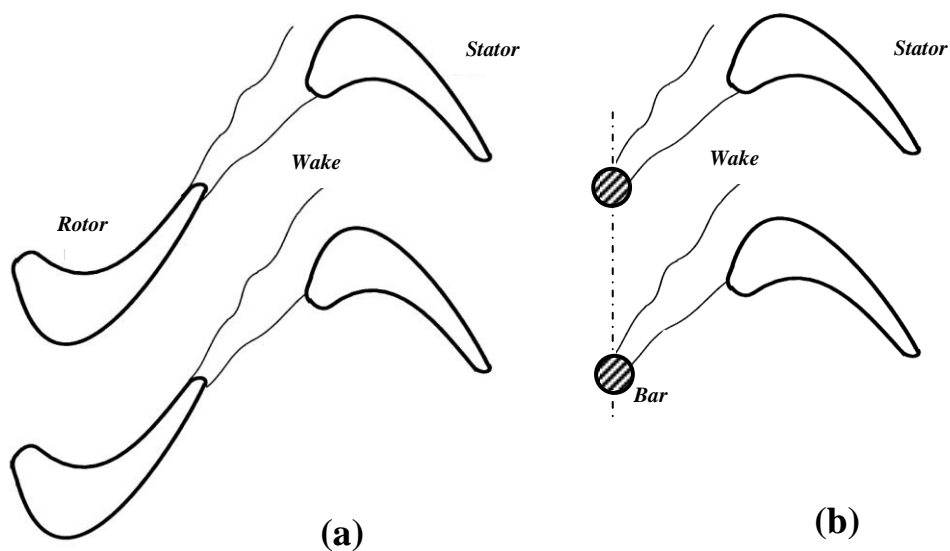


**Fig. (3) (a) Schematic of Rotor-Stator wakes Interaction.**  
**(b) Simulation of Rotor in Stieger, 2002, Experiment.**

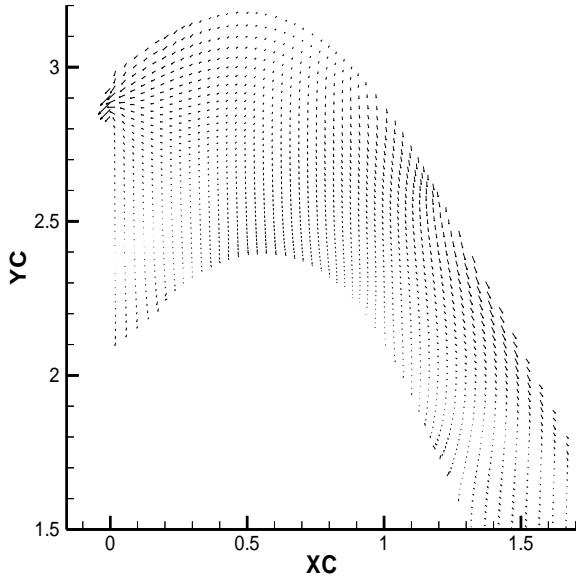


**Fig.(4) Unsteady Velocity Vector at  
Mid-Span at ( $\tau^* = 0.1$ )  
for  $Re = 10^5$  ( $\Omega = 1$ )**

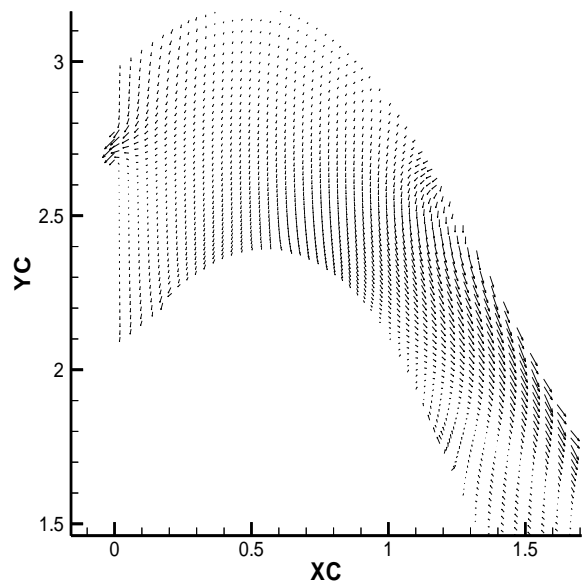


**Fig.(5) Unsteady Velocity Vector at  
Mid-Span at ( $\tau^* = 0.25$ )  
for  $Re = 10^5$  ( $\Omega = 1$ )**

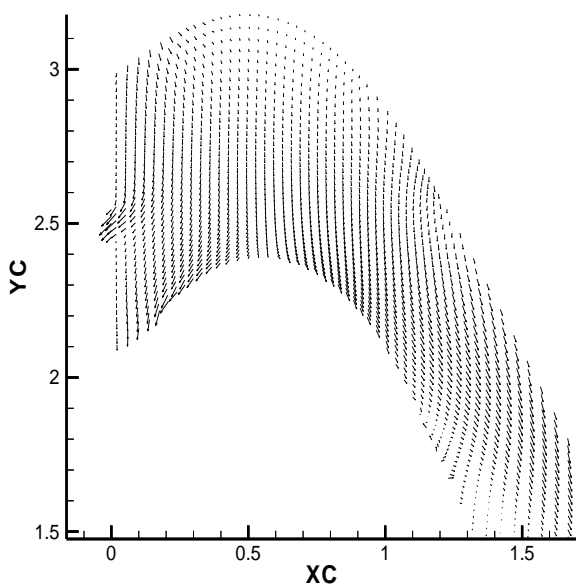


**Fig.(6) Unsteady Velocity Vector at  
Mid-Span at ( $\tau^* = 0.5$ )  
for  $Re = 10^5$  ( $\Omega = 1$ )**

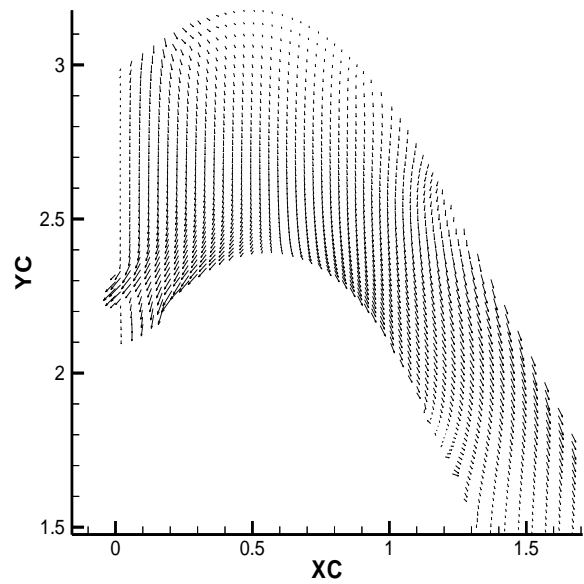


**Fig.(7) Unsteady Velocity Vector at  
Mid-Span at ( $\tau^* = 0.75$ )  
for  $Re = 10^5$  ( $\Omega = 1$ )**

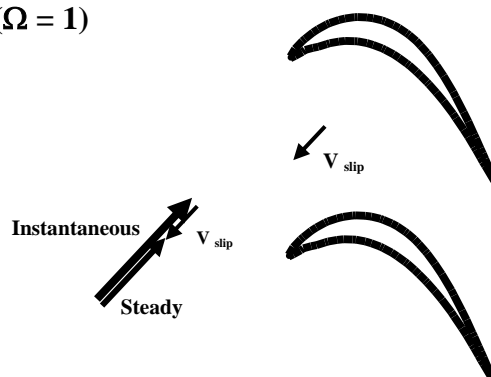


**Fig. (8) Instantaneous and Steady Velocities Resulting a Slip Velocity**

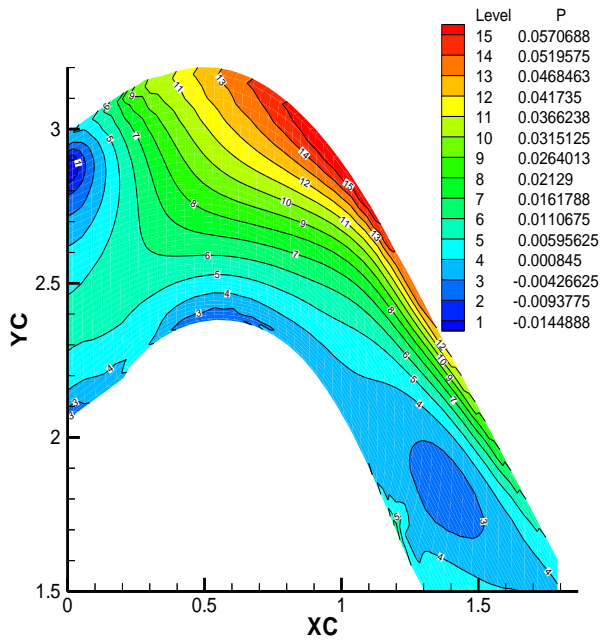


**Fig.(9) Unsteady Pressure at Mid-Span at ( $\tau^* = 0.1$ ) for  $Re = 10^5$  ( $\Omega = 1$ )**

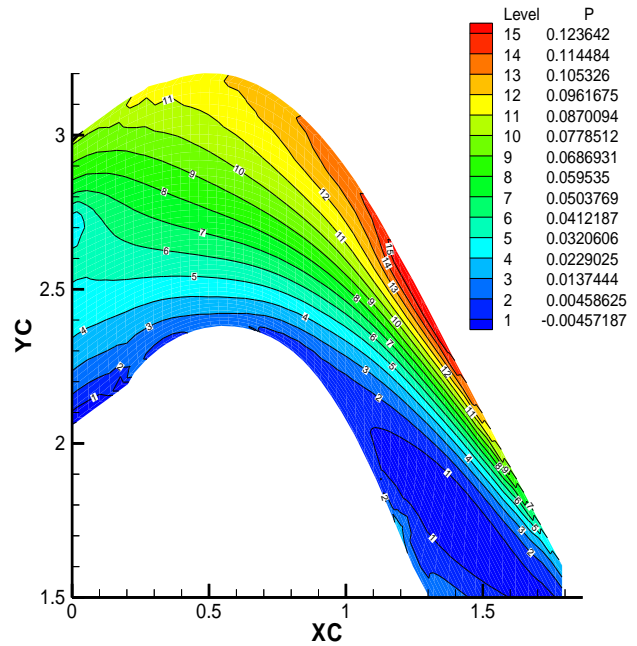


**Fig.(10) Unsteady Pressure at Mid-Span at ( $\tau^* = 0.25$ ) for  $Re = 10^5$  ( $\Omega = 1$ )**

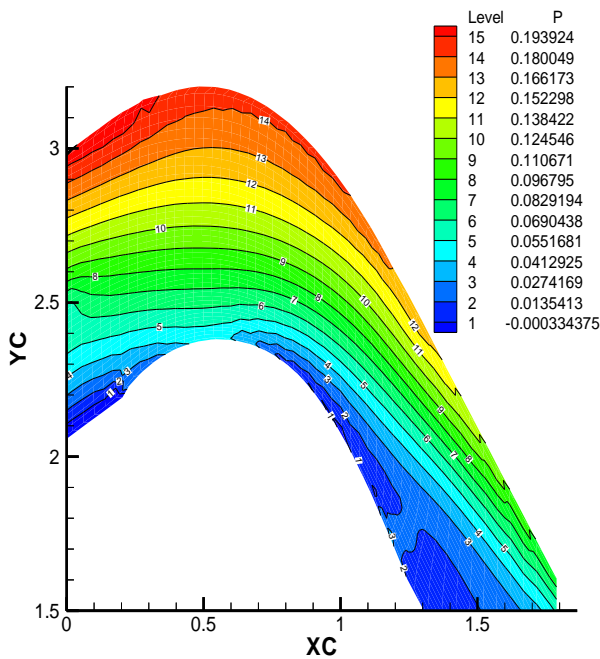


**Fig.(11) Unsteady Pressure at Mid-Span at ( $\tau^* = 0.5$ ) for  $Re = 10^5$  ( $\Omega = 1$ )**

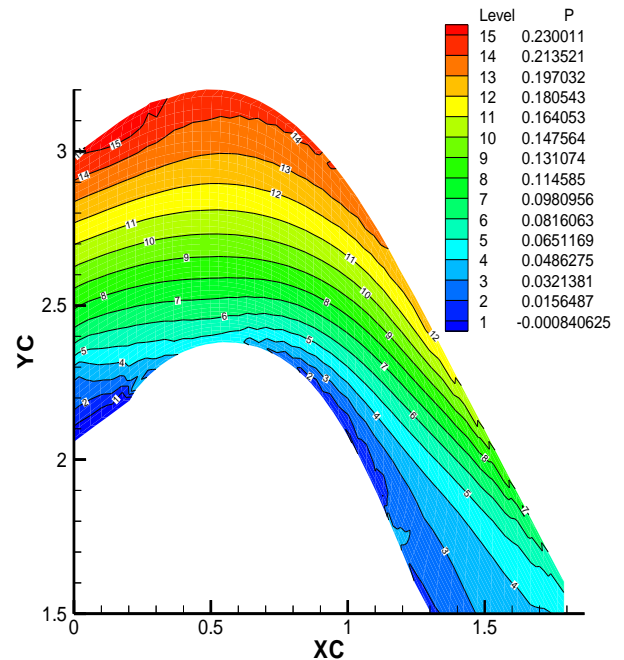


**Fig.(12) Unsteady Pressure at Mid-Span at ( $\tau^* = 0.75$ ) for  $Re = 10^5$  ( $\Omega = 1$ )**



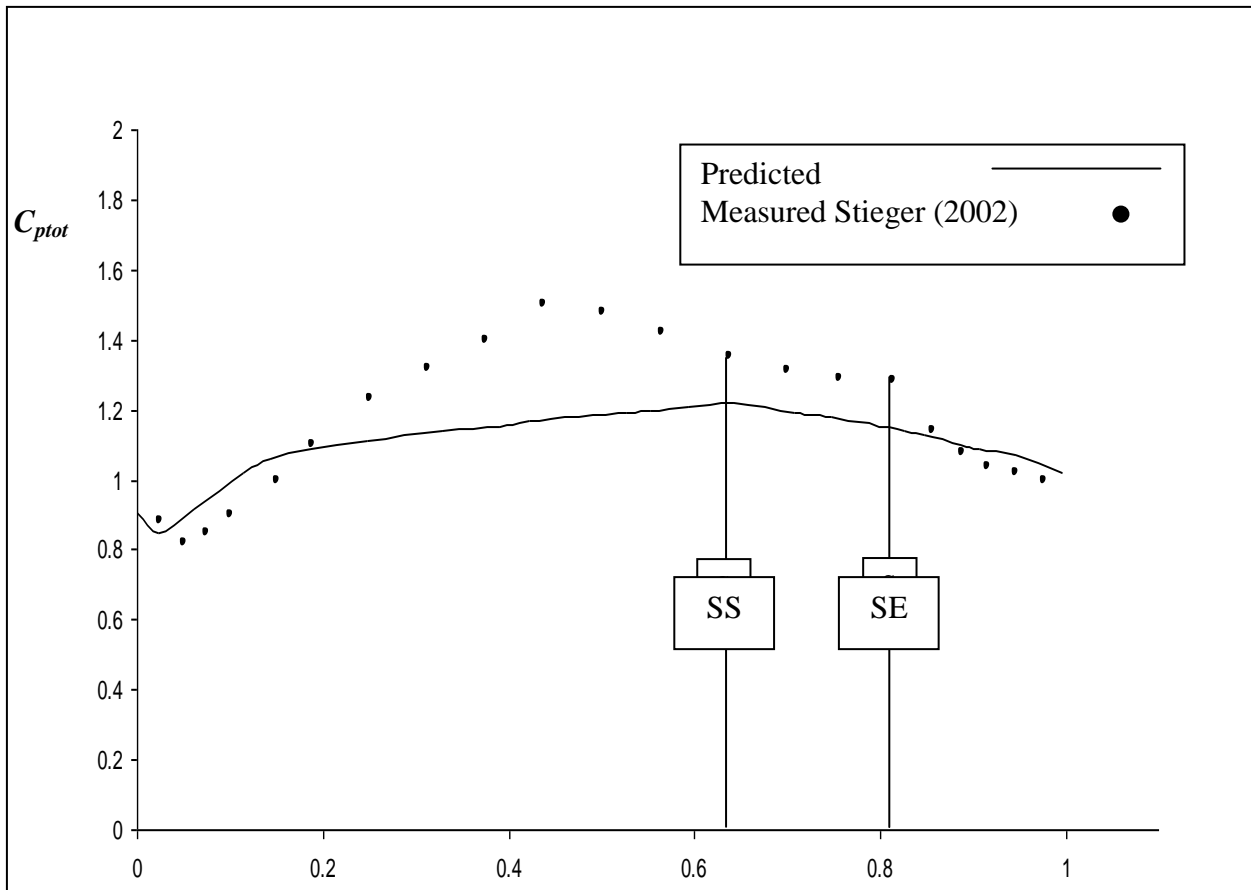


**Fig. (13) Comparison between the Numerical Results and Experimental Data for Steady Pressure Coefficient ( $Re_{2C} = 1.6 \times 10^5$ ,  $\Omega = 0$ ) (SS: Separation Start SE: Separation End)**

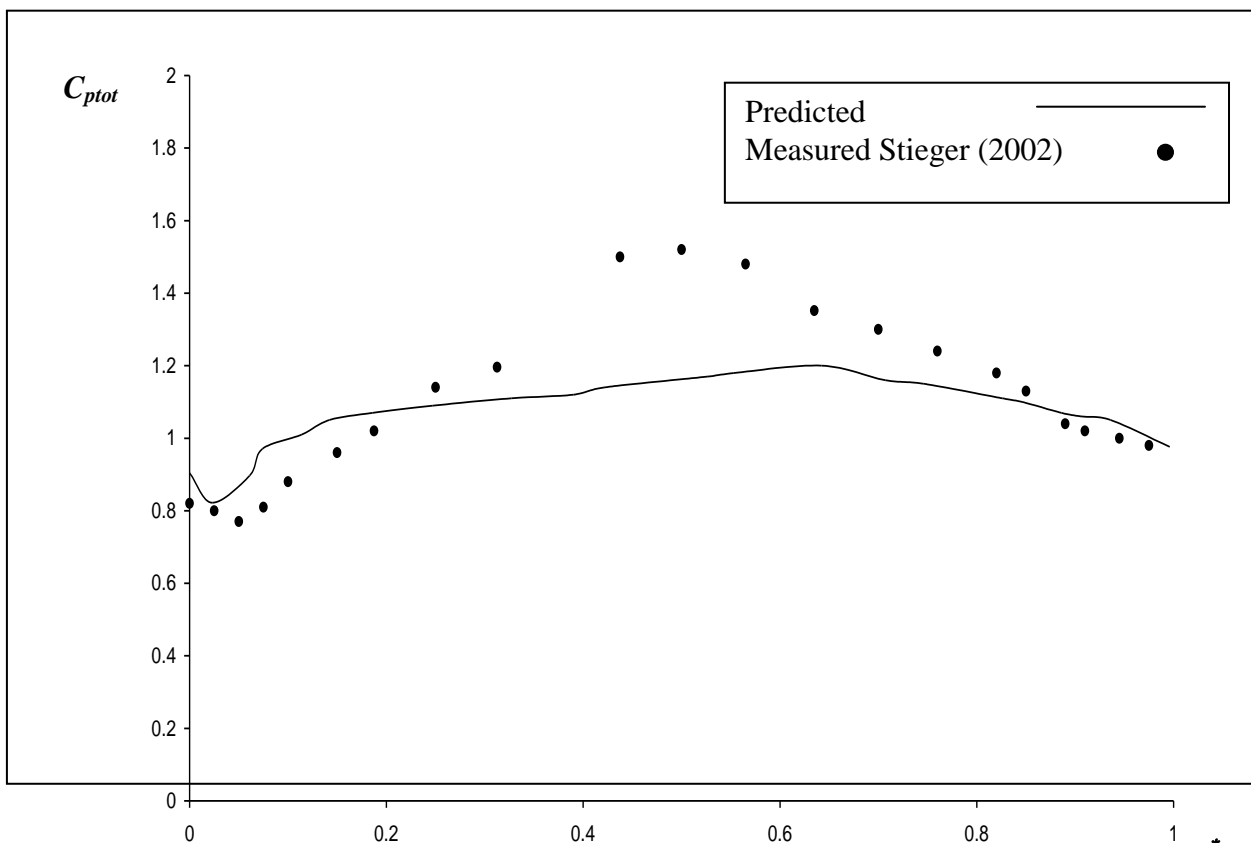


**Fig. (14) Comparison between the Numerical Results and Experimental Data for Ensemble Pressure Coefficient at time  $\tau^* = 0.75$  ( $Re_{2C} = 1.6 \times 10^5$ ,  $\Omega = 0.68$ )**

## CRACK DETECTION IN A ROTOR DYNAMIC SYSTEM BY VIBRATION MONITORING

Dr.Nabil H. H.  
Univ. of Baghdad  
College of Eng.

Jawad K.Z.  
Univ. of Baghdad  
College of Eng.

### ABSTRACT.

Vibration monitoring is one of the most important techniques which are used to detect the cracks or defects in rotating mechanical systems. To distinguish characteristics of the system response that may lead to the transverse crack in rotating shaft, local asymmetry crack model is used where crack simulated by increasing the flexibility of the shaft and transverse crack in the shaft is introduced.

The obtained results showed a decreasing in the resonance shaft speed with increasing the crack depth ratio. The feature is used for diagnostics the crack in the shaft by using the graphed results between the natural frequency and shaft speed. The method of detecting was applied for several crack depth ratios (uncracked, %10, %20 and %30) in a clamped-free rotor. Also for investigating the effect of position of crack and effect of mass location, a crack and mass with different locations are introduced in the shaft. Although, the presence of a transverse shaft crack has also been shown to induce an unstable response for some shaft speeds and the behavior of the 2x harmonic component of the system response is effective target observation for a monitoring system.

الخلاصه:

اكتشاف الشقوق او العيوب في الانظمة الديناميكية الدوار من خلال مراقبة الاهتزازات يعتبر ذو اهمية كبيره وقد استخدمت في عملية التحليل هذه نمودجين هما نمودج لشق شامل على طول العمود والاخر نمودج لشق موقعي اي في مكان محدد من العمود وذلك لغرض تحديد صفات استجابة النظام والتي تدلل على وجود شق عرضي في العمود وان هذا التحليل طبق على نوعين من الاعمده الدوار من حيث الشروط الحدوديه هما (Simply-Supported) و (Free) ولاعماق مختلفه ( 0%, 10%, 20%, 30% ) من قطر اتعمود حيث تم تمثيل الشق بزياده في مرونة العمود الدوار. كذلك بينت النتائج بوجود الشق يكون النظام غير مستقر عند سرع دوارانيه معينه.

**KEYWORDS:** Vibration, Rotor, Crack Detection, transverse crack, flexibility, resonance shaft speed.

## INTRODUCTION:

This research deals with detection of crack in clamped-free and simply-supported rotors by using of the resonance shaft speed. The magnitude of the crack depth will be determined by measuring the natural frequency of the rotor.

A uniform transverse crack, located on clamped-free and simply-support rotors of a circular cross-section which will be used as the physical model of the system. The crack on the shaft is assumed to be open during the transverse vibration of the rotor. This assumption will permit the effect of closing and opening of the crack in the analysis to be ignored.

An uncracked shaft has constant stiffness and has a constant displacement under a fixed load regardless of the angle of rotation. In cracked shaft, the cracked portion of the cross-section is not capable of supporting a tensile stress. Therefore, the displacement, as a function of the stiffness, is minimum when the crack is closed and maximum when the crack is open. This opening and closing behavior, which is referred to as "breathing", results in time dependent stiffness coefficients in the equation of motion of the system, which is difficult to work with. Obtaining solutions usually requires making broad simplifying assumption or some type of numerical approximation.

System in which the displacements and vibration amplitudes remain very small result in a crack that remains essentially open regardless, of the angle of rotation. This type of crack, which is essentially a local stiffness asymmetry, is referred to as a "gaping" crack. The analysis of systems containing a gaping crack is extremely useful since the response characteristics, on crack indicators, identified in the gaping crack analysis are also present in the analysis of systems containing a breathing crack. Furthermore, these indicators prove to be the most practical, in terms of implementation, in the detection of real cracks. Also, since the introduction of a crack into a rotating system, on the most basic level, results in a system with a stiffness asymmetry, the analysis of systems containing an asymmetry is fundamental to the study of the dynamics of cracked rotating systems.

The primary effect of the presence of a crack in a rotating shaft is clearly a local reduction in stiffness. This highly localized effect does not influence the stiffness of the regions of the rotor away from the cracked cross section. Regardless of the type of cracked model used for analysis, the effective overall stiffness of the rotor is no longer symmetric. The analysis of the response of a rotor with designed-in asymmetry is therefore part of the fundamental basis for the analysis of the dynamic of shaft containing a transverse crack. It is important to note that for rotating systems the terms "natural frequency" and "whirl-frequency" are synonymous. Also, the terms "critical speed" refers to a shaft speed for which one or more of the natural (whirl) frequencies of the system are equal to the shaft speed. Therefore, the maximum 2x harmonic response occurs at shaft speeds that are approximately one-half of a critical speed, i.e.  $1/2 n_{cr}$ .

In summery, the introduction of a gaping crack model into an existing system model has been shown to be a very effective method of obtaining reasonably accurate results from analysis, yet it avoids the inherent complexities of cracked shaft analysis due to breathing behavior. A discrete representation of the system allows the additional flexibility due to the crack to be placed arbitrarily along the axis of the shaft of the system. The 2x harmonic component of the system response is clearly the most practically implemented indicator for a monitoring and detection system.

## LOCAL MODEL OF CRACKED ROTATING SHAFT

The presence of transverse crack in a rotating shaft introduces highly localized flexibility. The additional flexibility that resulting from presence of crack must be determined and incorporated this flexibility into a discrete representation of the system. To achieve this localizing effect a transfer matrix method was used. The following are the general data table (1.1) for rotor in local model which was used for crack detection.

Table (1.1) rotor data, local model

Length	0.5m
Diameter	0.1m
Density	7850 kg/m <sup>3</sup>
Modules of elasticity (E)	200E9 N/m <sup>2</sup>
Crack depth (a)	Uncracked, 0.1D, 0.2D, 0.3D,
Poisson ratio ( $\nu$ )	0.3
Shaft speed (n)	125 Hz

**Figure 1.1** shows the three lumped stiffness elements;  $[F_1]$ ,  $[F_{\text{crack}}]$  and  $[F_2]$ , and the three lumped inertia elements;  $[m_{s1}]$ ,  $[m_{s2}]$  and  $[P]$  for a cracked system.

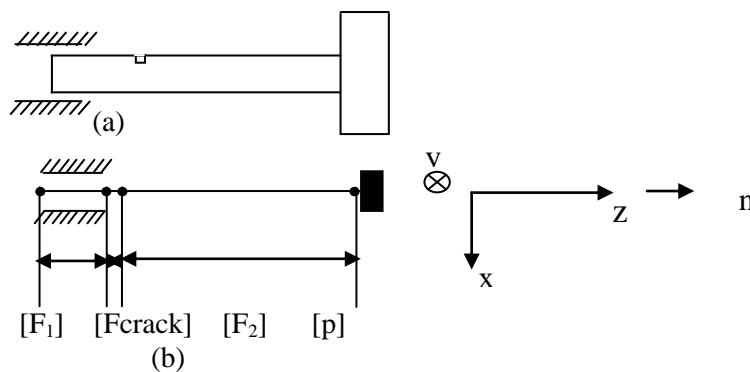
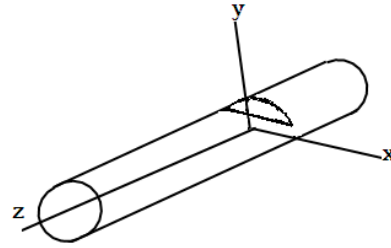


Figure (1.1) Local Model

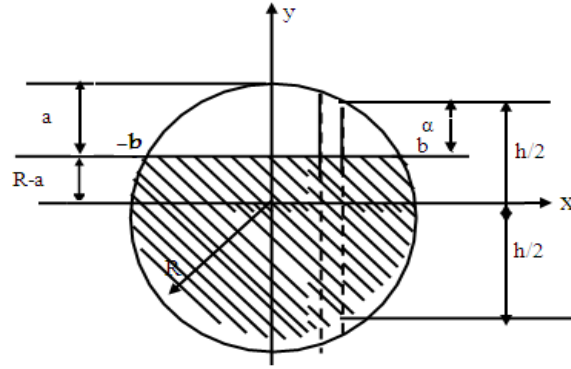
In this section we will use the Extended Transfer Matrix Method as by A.S. Lee and I. Green (1994) and by E.C. Pestel and F.A. Leckie. (1963) for free response analysis.

## Local Flexibility Matrix of Cracked Circular Cross- Section Shaft.

A crack on an elastic shaft introduces a local flexibility that affects the dynamic response of the system and its stability. To establish the local flexibility matrix of the cracked shaft under general loading, a shaft with a transverse crack is considered as shown in figure 1.2a. The crack has a uniform depth  $a$  along  $-y$ -axis and the shaft loaded with an axial forces  $P_1$ , transverse shear load  $P_2$  &  $P_3$ , bending moment  $P_4$  &  $p_5$  and torsion moment  $p_6$



(a) Shaft Containing Crack



(b) Cross-Section Crack

**Figure 1.2:** cross-section of the cracked shaft at the location of the crack.

The additional displacement  $u_i$  along the direction of loading  $p_i$  and  $U$  the strain energy due to the crack are related by Castigliano's theorem as follow

$$u_i = \frac{\partial U}{\partial P_i} \quad (1.7)$$

where  $U$  has the form:-

$$U = \int_0^{\alpha} J(\alpha) d\alpha \quad (1.8)$$

therefore

$$u_i = \frac{\partial}{\partial P_i} \int_0^{\alpha} J(\alpha) d\alpha \quad (1.9)$$

Where  $P_i$  is the generalized force associated with  $u_i$  and  $J(\alpha)$  is the strain energy density function according to Nikpour and Diamarogones (1988) given by :

$$J(\alpha) = E' \left[ \left( \sum_{i=1}^6 K I_i \right)^2 + \left( \sum_{i=1}^6 K I I_i \right)^2 + (1 + \nu) \left( \sum_{i=1}^6 K I I I_i \right)^2 \right] dy dx \quad (1.10)$$

where:-  $E' = \frac{1 - \nu^2}{E}$  for plane strain

E: Young's Modulus

$\nu$ : Poisson's ratio

$K_{ni}$ : crack stress intensity factor for mode n due to the type of applied load i.

In general the stress intensity factor (SIF)  $K_{ni}$  ( $n=1, II, III$ ) can not be taken as the same formats as the counterparts of isotropic material with the same geometry and loading. The SIFs,  $K_{ni}$  for a unit width strip of depth  $a$  is obtained as follow:-

$$K_{ni} = \sigma_i \sqrt{\pi a} F_n \left( \frac{a}{h} \right) \quad (1.11)$$

where:-

$\sigma_i$ : stress due to the load  $P_i$

$F_n \left( \frac{a}{h} \right)$  the correction function

h: total length for the strip

the local flexibility matrix  $[C_{ij}]$  per unit width has the components

$$C_{ij} = \frac{\partial^2}{\partial P_i \partial P_j} \int_0^a J(\alpha) d\alpha \quad (1.12)$$

after integration equation 4.12 along the crack edge length from b to (-b) becomes :-

$$C_{ij} = \frac{\partial^2}{\partial P_i \partial P_j} \iint J(\alpha) dy dx \quad (1.13)$$

Substitution of equation (4.10) into (4.12) yields:

$$C_{ij} = \frac{\partial^2}{\partial P_i \partial P_j} \iint_{-b}^b \frac{1-\nu^2}{E} \left[ \left( \sum_{i=1}^6 K_{Ii} \right)^2 + \left( \sum_{i=1}^6 K_{IIi} \right)^2 + (1+\nu) \left( \sum_{i=1}^6 K_{IIIi} \right)^2 \right] dy dx \quad (1.14)$$

Based on equations (4.11) the components of interest in the local flexibility matrix  $C_{ij}$  become:

$$c_{11} = 0, \quad c_{12} = 0, \quad c_{23} = c_{32} = 0$$

$$c_{22} = \frac{4(1-\nu^2)}{\pi E R} \int_0^{\frac{b}{R}} \int_0^{\frac{a}{R}} \frac{Y}{R} F_{111}^2 \left( \frac{Y}{h} \right) d \left( \frac{Y}{R} \right) d \left( \frac{X}{R} \right) \quad (1.15)$$

$$c_{33} = \frac{4(1-\nu^2)}{\pi E R} \int_0^{\frac{b}{R}} \int_0^{\frac{a}{R}} \frac{Y}{R} F_{111}^2 \left( \frac{Y}{h} \right) d \left( \frac{Y}{R} \right) d \left( \frac{X}{R} \right) \quad (1.16)$$

$$c_{44} = \frac{32(1-\nu^2)}{\pi ER^3} \int_0^{\frac{b}{R}} \int_0^{\frac{a}{R}} \left(\frac{X}{R}\right)^2 \left(\frac{Y}{R}\right) F_{1y}^2 \left(\frac{\frac{Y}{R}}{\frac{R}{h}}\right) d\left(\frac{Y}{R}\right) d\left(\frac{X}{R}\right) \quad (1.17)$$

$$c_{45} = c_{54} = \frac{64(1-\nu^2)}{\pi ER^3} \int_0^{\frac{b}{R}} \int_0^{\frac{a}{R}} \left(\frac{x}{R}\right) \left(\frac{Y}{R}\right) \sqrt{1-\left(\frac{\alpha}{R}\right)^2} F_{1x} \left(\frac{\frac{Y}{R}}{\frac{R}{h}}\right) F_{1y} \left(\frac{\frac{y}{R}}{\frac{R}{h}}\right) d\left(\frac{y}{R}\right) d\left(\frac{X}{R}\right)$$

$$c_{55} = \frac{64(1-\nu^2)}{\pi ER^3} \int_0^{\frac{b}{R}} \int_0^{\frac{a}{R}} \left\{1-\left(\frac{\alpha}{R}\right)^2\right\} \left(\frac{Y}{R}\right) F_{1x}^2 \left(\frac{\frac{Y}{R}}{\frac{R}{h}}\right) d\left(\frac{Y}{R}\right) d\left(\frac{X}{R}\right) \quad (1.18)$$

$$(1.19)$$

Where:  $F_{III}\left(\frac{\alpha}{h}\right) = \sqrt{\frac{\tan \lambda}{\lambda}}$

$$F_{II}\left(\frac{\alpha}{h}\right) = \left[1.122 - 0.561\left(\frac{\alpha}{h}\right) + 0.85\left(\frac{\alpha}{h}\right)^2 + 0.18\left(\frac{\alpha}{h}\right)^3\right] \sqrt{1-\frac{\alpha}{h}}$$

$$F_{1y}\left(\frac{\alpha}{h}\right) = \sqrt{\frac{\tan \lambda}{4P_1^2}} \left[0.752 + 2.02\left(\frac{\alpha}{h}\right) + 0.37(1-\sin \lambda)^3\right] / \cos \lambda$$

$$\sigma_1 = \frac{\pi d^2}{\pi d^2}$$

$$KI_4 = \sigma_4 \sqrt{\pi \alpha} F_6\left(\frac{\alpha}{h}\right)$$

$$\lambda = \left(\frac{\pi \alpha}{2h}\right)$$

$$\sigma_4 = \frac{32P}{\pi d^2}$$

In dimensionless form.

$$C_{22} = C_{22} \frac{\pi ER}{1-\nu^2}$$

$$C_{55} = c_{55} \frac{\pi ER^3}{1-\nu^2},$$

$$C_{44} = c_{44} \frac{\pi ER^3}{1-\nu^2}$$

$$C_{33} = c_{33} \frac{\pi ER}{1-\nu^2}$$

$$C_{45} = c_{45} \frac{\pi ER^3}{1-\nu^2}$$

$$\left. \begin{array}{l} C_{22} = c_{22} \frac{\pi ER}{1-\nu^2} \\ C_{55} = c_{55} \frac{\pi ER^3}{1-\nu^2} \\ C_{44} = c_{44} \frac{\pi ER^3}{1-\nu^2} \end{array} \right\} \quad (1.20)$$

For each crack depth ratio (0%-50%) of the shaft diameter the flexibilities are numerically evaluated, with a program coded in Maple version 7.

These integral expressions are a function of a/D and plotted in figure (1.3).

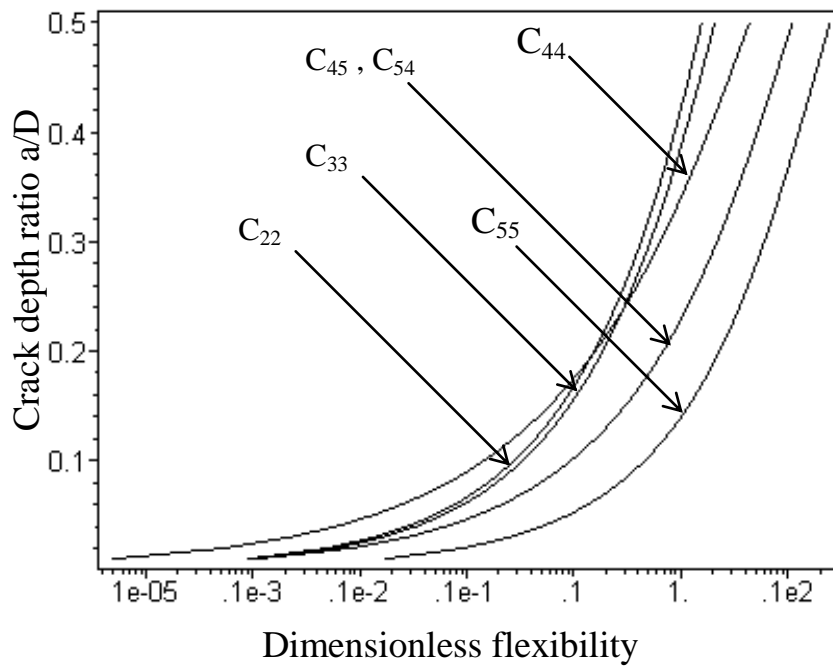


**Figure (1.3):** Dimensionless Crack Flexibility

Here, the torsion and axial loading is ignored to avoid the coupling therefore the final flexibility at the location of crack which is represented a field matrix may be written as:

$$[F_{crack}] = \begin{bmatrix} 1 & 0 & 0 & -c_{22} & 0 & 0 & 0 & 0 \\ 0 & 1 & c_{44} & 0 & 0 & 0 & c_{45} & 0 \\ 0 & 0 & 1 & 0 & 0 & 0 & 0 & 0 \\ 0 & 0 & 0 & 1 & 0 & 0 & 0 & 0 \\ 0 & 0 & 0 & 0 & 1 & 0 & 0 & -c_{33} \\ 0 & 0 & c_{54} & 0 & 0 & 1 & c_{55} & 0 \\ 0 & 0 & 0 & 0 & 0 & 0 & 1 & 0 \\ 0 & 0 & 0 & 0 & 0 & 0 & 0 & 1 \end{bmatrix} \quad (1.21)$$

## TRANSFER MATRIX

Transfer matrix (point matrix and field matrix) relate the state vectors at the ends of the shaft. The state vector at any station may be defined in xyz coordinate system as:

$$\{S\} = \{u_x \quad \theta_y \quad M_y \quad -V_x \quad -u_y \quad \theta_x \quad M_x \quad V_y\}^T \quad (1.22)$$

As mentioned before.

u: displacement (m)

$\theta$ : angle (rad)

V: shear force (N)

M: moment (N.m)

The field matrix  $F_i$  which has the form shown in equation (3.13) is related the state vector at the left  $\{S\}_i^L$  to the state vector at right  $\{S\}_{i+1}^R$  as following:



$$\{S\}_i^l = [F_i] \{S\}_{i-1}^R \quad (1.23)$$

while the state vector at the left of the station  $\{S\}_i^l$  is related to the state at the right lumped mass  $\{S\}_i^R$  by the point matrix  $[P_i]$

$$\{S\}_i^R = [P] \{S\}_i^l \quad (1.24)$$

## OVERALL TRANSFER MATRIX

The overall transfer matrix is found according to:

$$[U] = [P] [\text{shaft}_2] [F_{\text{crack}}] [\text{shaft}_1] \quad (1.25)$$

where:

[U]: Overall transfer matrix

[P]: Point matrix of the attached mass

$[F_{\text{crack}}]$ : Crack flexibility matrix

$[\text{shaft}_1] = [M_{S1}] [F_1]$

$[\text{shaft}_2] = [M_{S2}] [F_2]$

$M_{S1}, M_{S2}$ : Point matrix of part one and two of the shaft respectively [left and right of the crack]

$F_1, F_2$  = Field matrix of the two parts of the shaft.

The state vector at the left side  $\{S\}_i^l$  is related to the state vector at the right  $\{S\}_i^R$  by the following relation

$$\{S\}_i^R = [U] \{S\}_i^l \quad (1.26)$$

This equation can be solved for different boundary conditions at the left and right ends.

## UNDAMPED FREE RESPONSE

### clamped – free rotor

In this case the boundary conditions are no displacement or tilt at the support end and no shear or moment at the free end. Applying these conditions to the overall transfer matrix given in equation (4.26) leads to the following:

$$\begin{Bmatrix} u_x \\ \theta_y \\ 0 \\ 0 \\ -u_y \\ \theta_y \\ 0 \\ 0 \end{Bmatrix}^R = \begin{bmatrix} U_{11} & U_{12} & U_{13} & U_{14} & U_{15} & U_{16} & U_{17} & U_{18} \\ U_{21} & U_{22} & U_{23} & U_{24} & U_{25} & U_{26} & U_{27} & U_{28} \\ U_{31} & U_{32} & U_{33} & U_{34} & U_{35} & U_{36} & U_{37} & U_{38} \\ U_{41} & U_{42} & U_{43} & U_{44} & U_{45} & U_{46} & U_{47} & U_{48} \\ U_{51} & U_{52} & U_{53} & U_{54} & U_{55} & U_{56} & U_{57} & U_{58} \\ U_{61} & U_{62} & U_{63} & U_{64} & U_{65} & U_{66} & U_{67} & U_{68} \\ U_{71} & U_{72} & U_{73} & U_{74} & U_{75} & U_{76} & U_{77} & U_{78} \\ U_{81} & U_{82} & U_{83} & U_{84} & U_{85} & U_{86} & U_{87} & U_{88} \end{bmatrix} \begin{Bmatrix} 0 \\ 0 \\ M_y \\ -V_x \\ 0 \\ 0 \\ M_x \\ V_y \end{Bmatrix} \quad \text{damped}$$

$$\begin{Bmatrix} 0 \\ 0 \\ 0 \\ 0 \end{Bmatrix}_i^R = \begin{bmatrix} U33 & U34 & U37 & U38 \\ U43 & U44 & U47 & U48 \\ U73 & U74 & U77 & U78 \\ U83 & U84 & U87 & U88 \end{bmatrix} \begin{Bmatrix} M_y \\ -V_x \\ M_x \\ V_y \end{Bmatrix}$$

$$\begin{Bmatrix} 0 \\ 0 \\ 0 \\ 0 \end{Bmatrix}_i^R = [F3] \begin{Bmatrix} M_y \\ -V_x \\ M_x \\ V_y \end{Bmatrix} \quad (1.27)$$

Where:

$$[F3] = \begin{bmatrix} U33 & U34 & U37 & U38 \\ U43 & U44 & U47 & U48 \\ U73 & U74 & U77 & U78 \\ U83 & U84 & U87 & U88 \end{bmatrix}$$

$$\begin{Bmatrix} u_x \\ \theta_y \\ -u_y \\ \theta_y \end{Bmatrix}_i^R = \begin{bmatrix} U13 & U14 & U17 & U18 \\ U23 & U24 & U27 & U28 \\ U53 & U54 & U57 & U58 \\ U63 & U64 & U67 & U68 \end{bmatrix} \begin{Bmatrix} M_y \\ -V_x \\ M_x \\ V_y \end{Bmatrix}_{clamped}$$

$$\begin{Bmatrix} u_x \\ \theta_y \\ -u_y \\ \theta_y \end{Bmatrix}_i = [F4] \begin{Bmatrix} M_y \\ -V_x \\ M_x \\ V_y \end{Bmatrix} \quad (1.28)$$

Where:

$$[F4] = \begin{bmatrix} U13 & U14 & U17 & U18 \\ U23 & U24 & U27 & U28 \\ U53 & U54 & U57 & U58 \\ U63 & U64 & U67 & U68 \end{bmatrix}$$

## RESULTS:

By solving the eigenvalue problem of equation (1.27) four complex conjugate pairs of eigenvalues results and from which obtains the mode shape for a given eigenvalue which is the displacement and till portion of the state vector at the free end of the shaft.

From equation (1.28), the shear and moment portion of the state vector at the clamped is given by:

$$\begin{Bmatrix} M \\ -V_x \\ M_x \\ V_y \end{Bmatrix}_{clamped} = [F4]^{-1} \begin{Bmatrix} u_x \\ \theta_y \\ -u_y \\ \theta_x \end{Bmatrix}_i^R \quad (1.29)$$

Substitution this expression for  $\{M_y \quad -V_x \quad M_x \quad V_y\}_{\text{Clamped}}$  into equation (4.27) results in:

$$[F_3][F_4]^{-1} \begin{Bmatrix} u_x \\ \theta_y \\ -u_y \\ \theta_x \end{Bmatrix}_i^R = \begin{Bmatrix} 0 \\ 0 \\ 0 \\ 0 \end{Bmatrix} \quad (1.30)$$

Change of natural frequency versus depth of crack ratio also graphed for clamped-free rotor as shown in figure (1.4). This graph shows how crack may be predicated by frequency change.

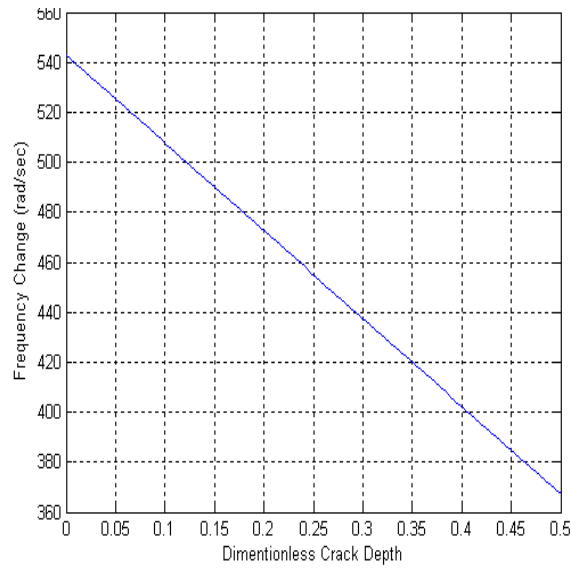


**Figure (1.4):** frequency change of clamped-free rotor for, local model with depth of crack

For each frequency magnitude, given by the four pairs of eigenvalue equation (4.30) forms a liner dependent system of equations. Solving this eigenvalue problem results in the corresponding mode shape or the vector  $\{u_x \quad \theta_y \quad u_y \quad \theta_x\}^T$ .

The eigenvalues and eigenvectors, or mode shapes, are determined whirl direction to each frequency, and the true natural frequency are plotted versus shaft speed.

Figure (1.4) shows the whirl frequency as a function of shaft speed for crack depths ranging from (0%-30%) of the shaft diameter. The “x” symbols along horizontal axis indicate shaft speeds for which one or more of the eigenvalues has a positive real part, i.e., shaft speeds for which the response is unstable. Two references lines indicating critical speeds and "2x resonance" shaft speed are also include in each figure.

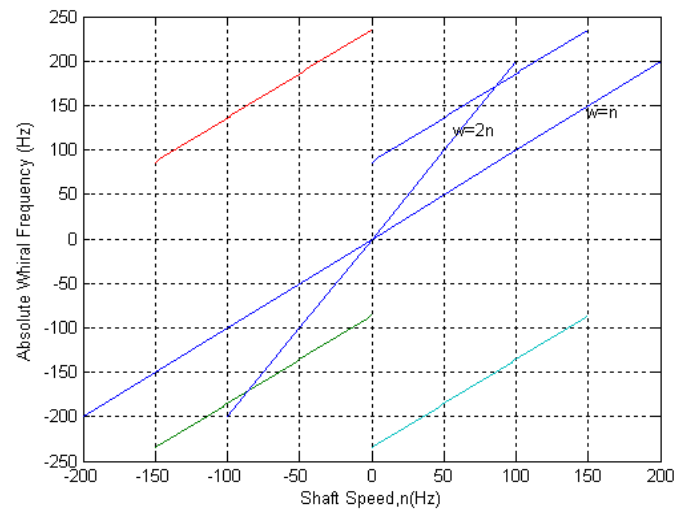


Figure: (1.4a), uncracked

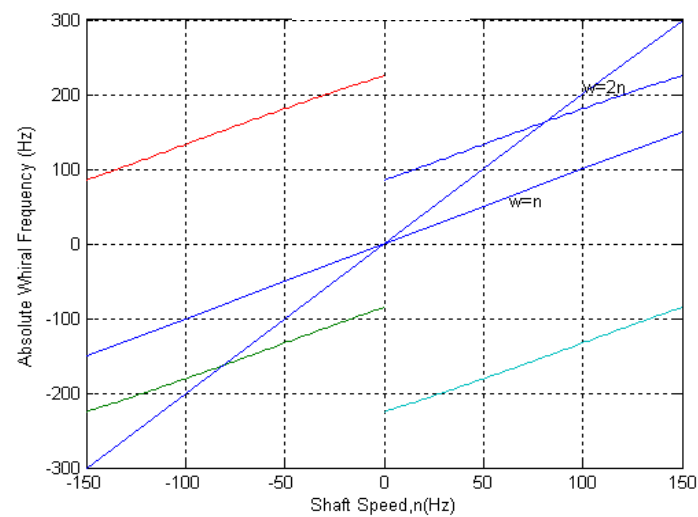


Figure: (1.4b), %10

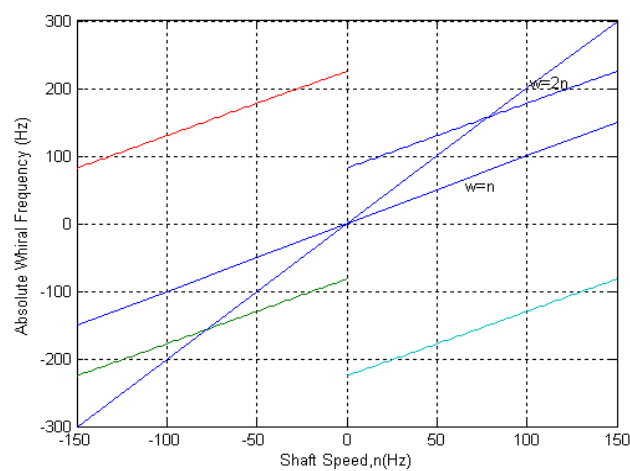
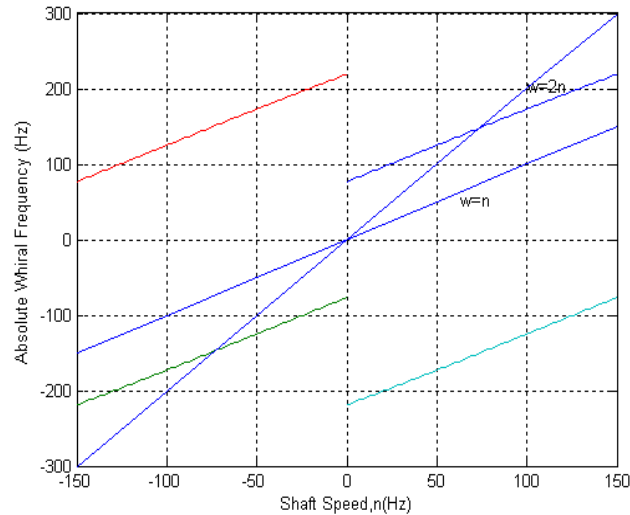


Figure: (1.4c), %20



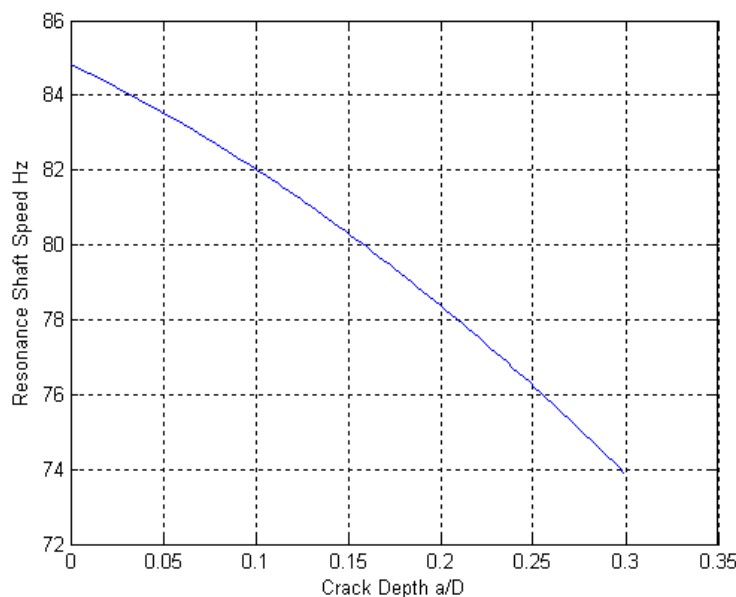
**Figure: (1.4d),**

Figure (4.10-a-b-c-d) Local Asymmetry Model Free Response at Various Crack Values for Clamped-Free

From this analysis, shaft speeds at which the 2x resonance is maximum can be predicated for various crack depths. Table (1.2) gives the predicated 2x resonance shaft speeds based on the local asymmetry crack model. The decrease in the 2x resonance shaft speeds indicates the decrease in the natural frequency of the system resulting from the flexibility increased by the presence of the crack. This free response analysis of the system containing the local asymmetry crack model indicates that a decrease in natural frequency, which may be observed in primary and secondary critical speeds, is a characteristic of the system response that can be directly attributed to the presence of a transverse crack. Also, these results plotted as can be shown in figure (1.5).

**Table (1.2): Resonance Shaft Speeds for Clamped-Free rotor, Local Asymmetry Crack Model**

% Crack depth	Resonance Shaft Speed Hz
uncracked	86
10	81.5
20	78.9
30	73.5



**Figure (1.5) Resonance Shaft Speed versus Crack Depth for Clamped-Free Rotor, Local Model**



The results obtained from current research for clamped-free rotor, local model compared with the results of the research presented by Sekhar, A. S., (2004) as shown in table below.

**Table (1.3) comparison of resonance shaft speed between current research and Sekhar research**

%Crack depth	Current research	Research of Sekhr, A. S (2004)	%error
uncracked	86	86	0
10	81.5	78.2	0.033
20	78.9	70	0.089
30	73.7	54.3	0.1189

This comparison shows adequate agreement between these results

## CONCLUSIONS

Crack monitoring was discussed for a clamped – free rotor and simply-supported rotor. It was observed that as crack introduced into the rotor, a drop in the natural frequencies occurred. Therefore, the major observation and conclusion can be summarized as follow:

- The behavior of the 2x harmonic component of the system response is effective target observation for a monitoring system where include an increase in magnitude for increasing crack depth as well as a decrease in the shaft speed at which the 2x harmonic component of the system response is maximum as in figures (1.4 and 1.7).
- The presence of a transverse shaft crack has also been shown to induce an unstable response for some shaft speeds as in figure
- The detection of the changes in the magnitude of the 2x harmonic component of the system response becomes much more difficult for shaft speed which is greater than 2x resonance speeds.
- The Transfer matrix method offered a successfully procedure to represented rotating system model and can be used to detect the crack which significantly reduces the flexibility of the rotor.
- It is possible to detect crack in rotor using measurements of change in the natural frequency without need for any analysis as in figures (1.4and 1.6).

## REFERENCES

- A.S. Lee and I. Green, 1994, "Rotor dynamics of a mechanical face seal riding on a flexible shaft", ASME Journal of Tribology, 116(2): 345-351.
- E. C. Pestel and F. A. Leckie., 1963, "Matrix Methods in Elastomechanics," McGraw-Hill Book Company, Inc.
  - Nikpour, K. and Dimarogononas, A., 1988, " Local Compliance of Composite Cracked bodies," Composite science and Technology, 32(3), 209-223.
  - Sekhar, A.S. , 2004, "Detection and Monitoring of cracks in a Cross-Down Rotor Supported on Fluid Bearings, "Tribology International", Vol. 37, No. 3, 279-287.



## USING PERSONAL COMPUTER FOR VIBRATION MEASUREMENTS AND ROTOR BALANCING

Roshen Tariq Ahmed  
Assistance Lecturer

Ayad Mahmoud Salman  
Assistance Lecturer

Waleed Khalid Ibrahim  
Assistance Lecturer

Energy and Fuel Research Center  
University Of Technology  
Iraq-Baghdad

### ABSTRACT

Most prime movers have vibrational problems due to the inherent unbalance in the engines. The unbalance may be due to faulty design or poor manufacture. Naturally, the structures designed to support heavy centrifugal machines, like motors, turbines and reciprocating pumps, are also subjected to vibration. In all these situations, the structure or machine component subject to vibration can fail because of material fatigue resulting from the cyclic variation of the induced stress. Furthermore, the vibration causes more rapid wear of machine parts such as bearings and gears and also creates excessive noise.

This research is an example in the field of reducing as much as possible the vibration. To accomplish this, a digital instrument, based on an industrial computer, designed to measure the vibration level and rotor speed. Thereafter, displaying the required amount of weight that must be added or removed from blade in order to reduce the unbalance, which cause vibration

**KEY WORD:** Vibration control, Helicopter Vibration, Vibration Measurement, Rotor Balance.

### الخلاصة

معظم الأجزاء المتحركة تعاني من مشاكل الاهتزازات بسبب عدم توازن أجزاء المحرك، أن عدم التوازن قد يكون بسبب أخطاء تصميمية أو أخطاء في الصناعة، فمثلاً عدم التوازن في محركات الديزل تؤدي إلى تولد اهتزازات في أرضية المحرك كافيه بدرجة تؤدي إلى حدوث أصوات في المنطقة المجاورة لها. أن محركات الطرد المركزي الثقيلة (ذوات الأجزاء الدوارة) كالمحركات والتوربينات كلها تعاني من الاهتزازات. وأن هذه الاهتزازات سوف تؤدي بالتالي إلى انخفاض كفاءة عمل المحركات و تقليل أعمارها. أن فكره البحث هو قياس فرق الطور بين موجتين أحدهما من متحسس السرعة و الآخر من متحسس الاهتزازات، يتم حساب فرق الطور هذا بواسطة برنامج داخل الحاسوب بعد أن يتم إدخال الإشارتين إلى الحاسبة بواسطة دائرة تعشيق خاصة، أن البحث هو مثال في مجال تقليل الاهتزازات إلى اقل حد ممكن للمكائن ذوات الأجزاء الدوارة.

## INTRODUCTION

One of the most important applications of vibration analysis is the solution of balancing problems. An unbalanced propeller, rotor or driveshaft will cause vibration and stress in the rotating part and in its supporting structure. Balancing of a rotating part is therefore highly advisable in order to accomplish one or more of the following (Prop and Rotor Balancing 2001):

- Increase quality of ride.
- Minimize vibration.
- Minimize audible signal noises.
- Minimize structural stresses.
- Minimize operator annoyance and fatigue.
- Increase bearing life.

Before attempting to balance the rotating parts of a unit, one may determine the possible sources of vibration and unbalance (Facilities Instructions Standards and Techniques 2002).

- Mechanical vibration sources.
- Electrical sources of vibration.
- The hydraulic passages of the unit should be checked for.

The aim of the work is to design and implement a computerized system to balance any rotating machine. The system must specify which blade on the rotor causes the unbalance condition and the amount of weight that must be added to the blades in order to balance the rotor.

It can be seen that if a rotating disc, see Fig. 1, is perfectly balanced, no vibration will be imparted to the supporting structure. If one adds a weight to the edge of the disc, the supports will be forced up and down once per revolution, as the disc rotates, generating a one-per-rev vibration. For simplicity, let us visualize that the supporting structure is in its farthest up position when the weight on the edge of the disc is up. If the weight on the edge of the disc is moved to a new location, it is clear that the support will still be up when the weight is up, as in the first instance. It follows that wherever the weight is fixed, the motion of the support will be “maximum up” when the heavy side of the disc is at the top of its rotation.

Now, starting with an unbalance disc, if one can determine the angular position of the disc when the support is “maximum up”, it should be able to balance the disc. Simply stop the disc, position it was observed, and a weight is added to the bottom (Clarence W. de Silva 1999).

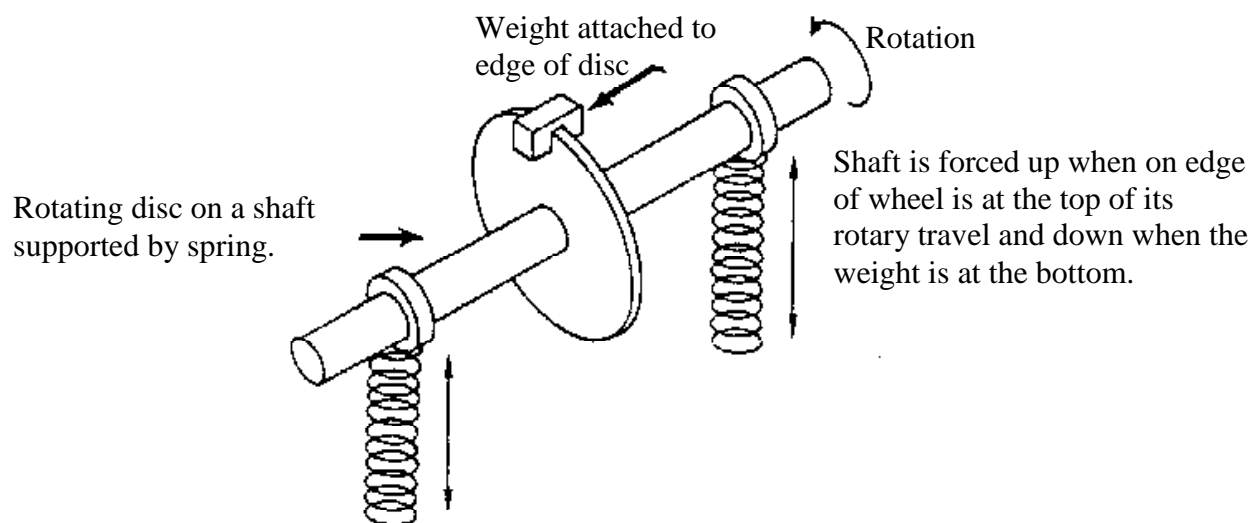


**Fig. 1** Rotating of unbalance disc.





## PRINCIPLE OF OPERATION

The basic principle of the suggested balancing system operation is depending on measuring phase difference between two signals. By using two sensors. One is the magnetic pickup, which gives the pulses per revolution, and these pulses will be the reference for all calculations and measurement. The second sensor is the accelerometer, which give signals corresponding to vibration level. The block diagram of the implemented system is shown below.

The magnetic pickup signal was converted to square waveform using appropriate circuit. This square wave will be sensed by a personal computer using an interface circuit.

Meanwhile accelerometer signals was filtered, smoothed and amplified by using an electronic circuit.

Magnetic pickup and the accelerometer signals are in an analog form converted to digital form by the interface card. The two digital signals then fed to the computer for later signal processing. Inside the computer, the Revolution Per Minute (RPM) will be measured from the magnetic pickup, and from the RPM the frequency can be measured which is used as the center frequency for the BandPass Filter (BPF). The accelerometer signal is representative of all the mechanical motion (vibration) of the point to which it is attached. To derive a useful signal, all of the signals except that from the one per revolution of the rotor being worked must be rejected. The bandpass filter passes only the signal at the working RPM, which is the center frequency of the BPF.

The output signal from the BPF is then converted to square wave in order to measure the phase difference between these signals. This phase indicates an angle between ( $0^{\circ}$ - $360^{\circ}$ ). The amount of vibration (amplitude) is measured from the output signal of the accelerometer.

After that the additive weights which assigned from the pervious measurements must be added in order to reduce the vibration depend on charts supplied by the manufacturer of the machine. Fig. 2 shows the complete block diagram of the system.

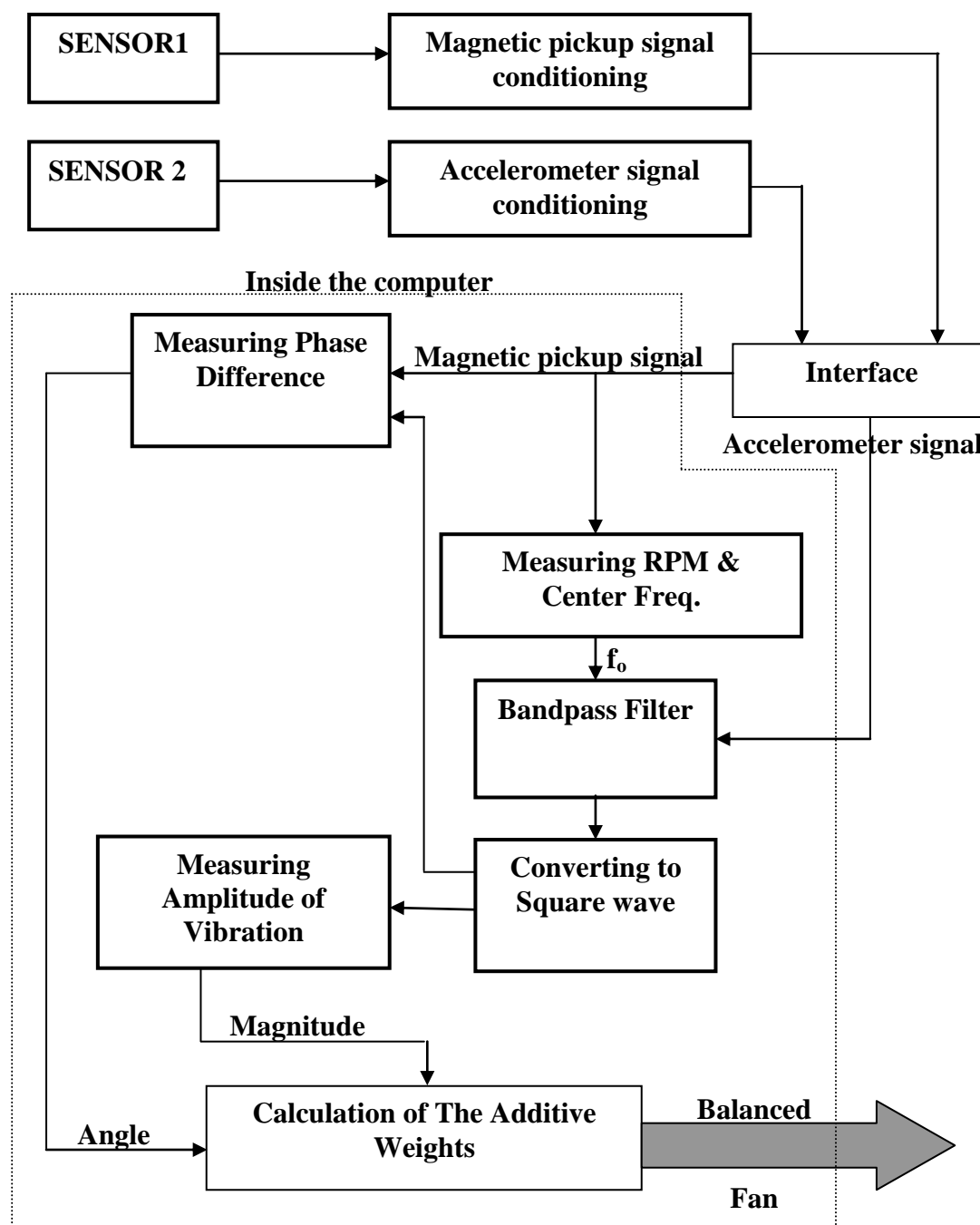


**Fig. 2** Block diagram of the complete system.

### TRANSDUCER USED IN THIS WORK

The two transducers used in this project are magnetic pickup for speed measurements and accelerometer for vibration measurements.

## THE MAGNETIC PICKUP

The first transducer is the magnetic pickup, which is used to measure the speed of rotation (RPM). The principle of operation is very simple and depends on (Faradays law), it consist of a permanent magnet and coil, when a piece of metal moves in its magnetic field it cuts the magnetic flux and generate a pulse just like the principle of generators. The magnetic pickup is fixed on the fixed plate (unrotating part) while a piece of metal (target) is fixed on the rotating part of the rotor. The target must be small and light as possible. When the rotor began to rotate, the target cut the magnetic field and generates a signal on the output of the magnetic pickup. The distance or air gap between the target and the magnetic pickup is between (0.5 – 2) mm and it depends on the type of magnetic pickup used.

Amplitude of the output signal depend on speed of rotation (speed at which the target cut the magnetic flux), air gap, size and the shape of target itself (Chadwick-Helmuth 1981). The magnetic pickup used has the specification that its operating temperature ranges (-10 to +120 °C), mass 380 gram, inductance 115 mH, DC resistance (220 to 260)  $\Omega$  at 25 °C (Magnetic Pickup & In-Line Preamplifier) . The detected frequency in Hz is obtained from the relation:

$$f = \frac{RE}{60} \quad (1)$$

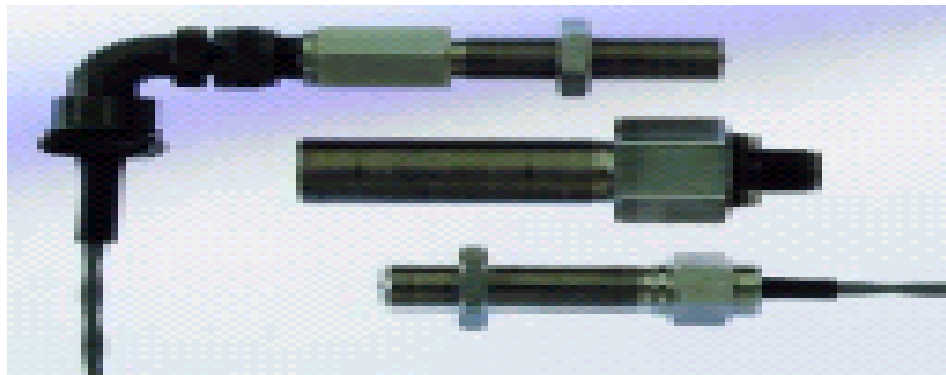
Where f = Detected frequency in Hz.

R = Number of revolution (RPM).

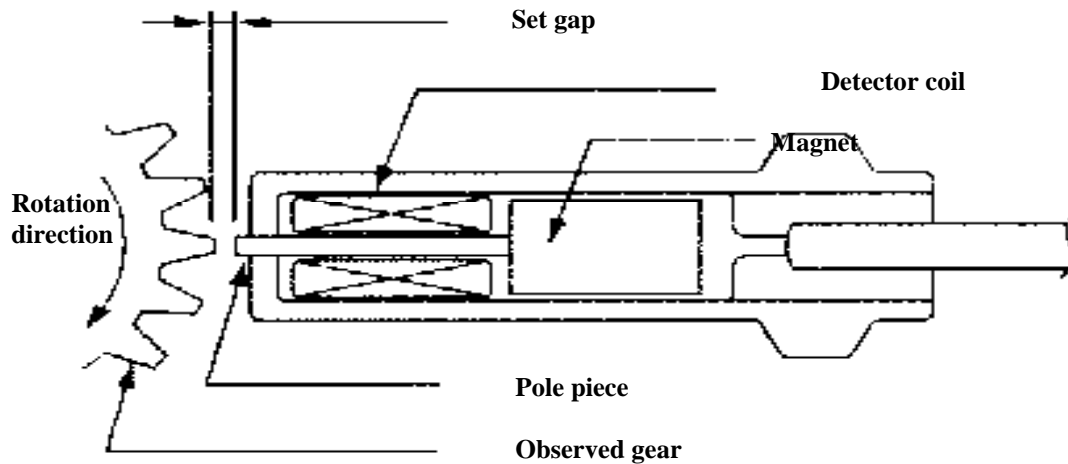
E = Number of targets.

Fig. 14 is a result of a test with RPM=160 and sampling time equal to 1 milliseconds with target one is closer than target two to the sensor.

And finally the fig. 3A and fig. 3B below shows the magnetic pickup external and internal construction (Maurice L. Adams 2000).



**Fig. 3(A) External construction of the magnetic pickup.**



**Fig. 3(B) External construction of the magnetic pickup.**

## MAGNETIC PICKUP SIGNAL CONDITIONING CIRCUIT

The magnetic pickup signal must be converted to square waveform using appropriate electronic circuit. This square wave will be sensed by a personal computer using a suitable interface circuit.

A suitable circuit will convert the signal from the magnetic pickup to a square wave. Fig. 4(A) and fig. 4(B) shows the circuit diagram and a simplified block diagram for the circuit used. The first block is a low pass filter, which pass the required signal frequency from magnetic pickup.

The second block is a comparator, in order to convert the sine wave to square wave, and the output signal of the second part is shown in Fig. 15. In order to get a pure square wave with 50% duty cycle the third block is added, which is a J-K flip flop. Because of using JK flip-flop output signal frequency of the overall circuit will be half frequency of the system-input signal as shown in Fig. 16. This problem will be solved in the program (software). Magnetic pickup signal is in an analog form converted to digital form by the interface card. The signal then fed to the computer for later signal processing. Inside the computer, the Revolution Per Minute (RPM) will be measured from the magnetic pickup (Chadwick-Helmuth 1981).

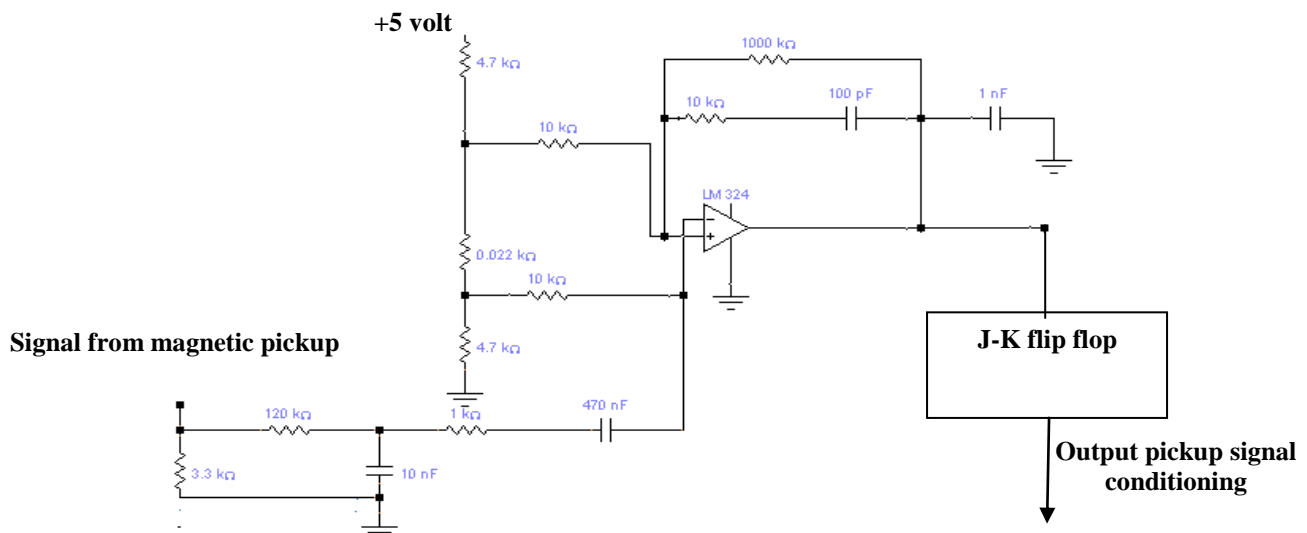


**Fig. 4(A) Circuit diagram for magnetic pickup signal conditioning.**



**Fig. 4(B) Magnetic pickup signal conditioning block diagram.**

The above electronic circuit is very easy, simple, components are available in markets and over all its operation is very efficiency with low maintenance.

### THE ACCELEROMETER

The second transducer is the accelerometer, which provides the balancer with an electrical representation of the physical motion of the point to which it is attached.

Fig. 17 shows the accelerometer output signal. Notice that the output signal is a combination of various signals with different frequencies. This is because the accelerometer is very high sensitive device and there are many other vibration sources acts on the point to which the accelerometer is attached such as shafts, gears, and other rotating parts (S. Q. Reza Moheimani and Andrew J. Fleming 2006) and (Maged Mostafa Alaa El Din Sayed 2006).

### ACCELEROMETER SIGNAL CONDITIONING CIRCUIT

In Fig. 5 shows the circuit diagram related to the accelerometer (Chadwick-Helmuth 1981). Fig. 6 shows a simplified block diagram of Fig. 5.

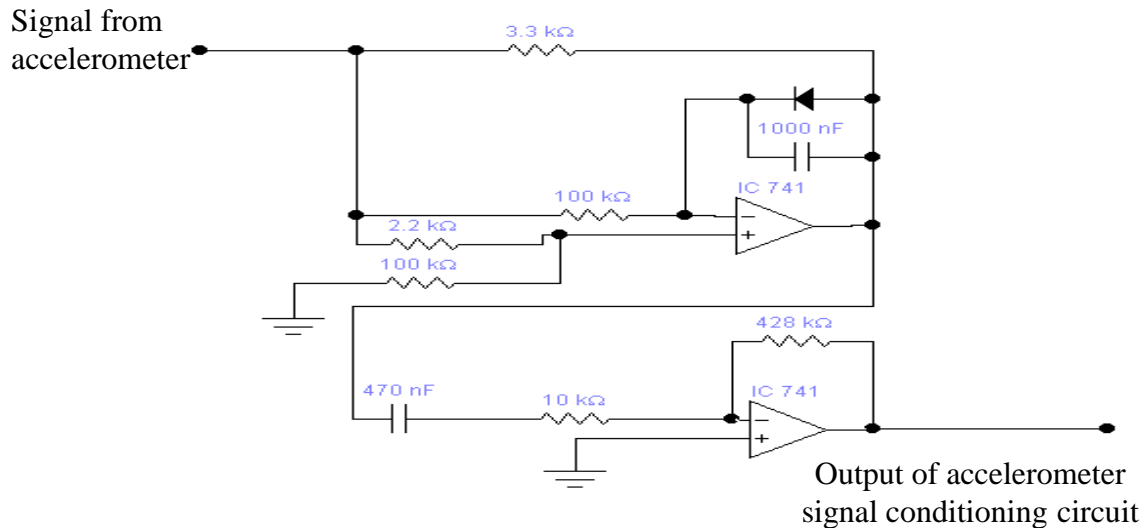


**Fig. 5 Accelerometer signal conditioning circuit diagram.**

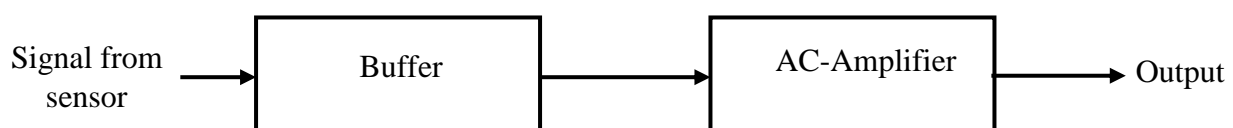


**Fig. 6 Accelerometer signal conditioning circuit block diagram.**

The accelerometer signal is very small (millivolts) with dc components, therefore an AC-amplifier is used to amplify the signal. In order to do this the second part of the circuit is used which removes all dc components, and amplifies the input signal. Because of using inverting amplifier this part will change the polarity of signal to its original polarity. Fig. 18 shows the output signal of the second part. Fig. 19 shows difference between accelerometer signal before and after amplification.

### THE INTERFACE CARD

The output signal from the magnetic pickup and the accelerometer are in analog form. In order to feed these signals to a digital computer, a suitable interface card designed. The interface card contain analog to digital converter (ADC), ADC are widely used for data acquisition.

Digital computers use discrete values, but in the physical world everything is continues (analog) such as temperature, pressure and velocity etc.

The 0804 IC is an ADC it works with (+5 volt) and has a resolution of 8 bits. The sampling rate can be controlled by these 8 bits with clock frequency 1.16 microseconds and connected to the parallel port. The language of programming is written in visual basic. The complete flow chart of the interface card is shown in fig. 7 (Sood 1990) and (User's Manual 1995).

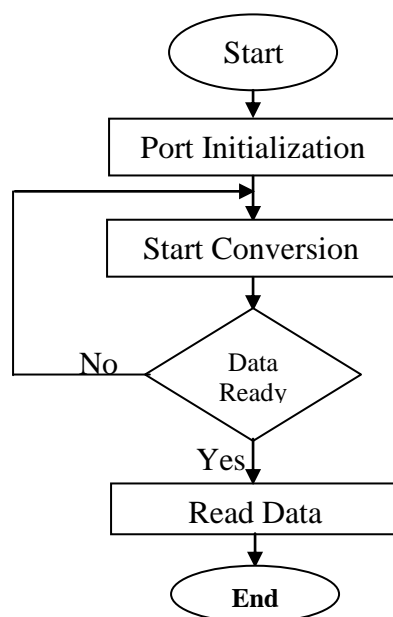


**Fig. 7 Complete flow chart of the interface card.**

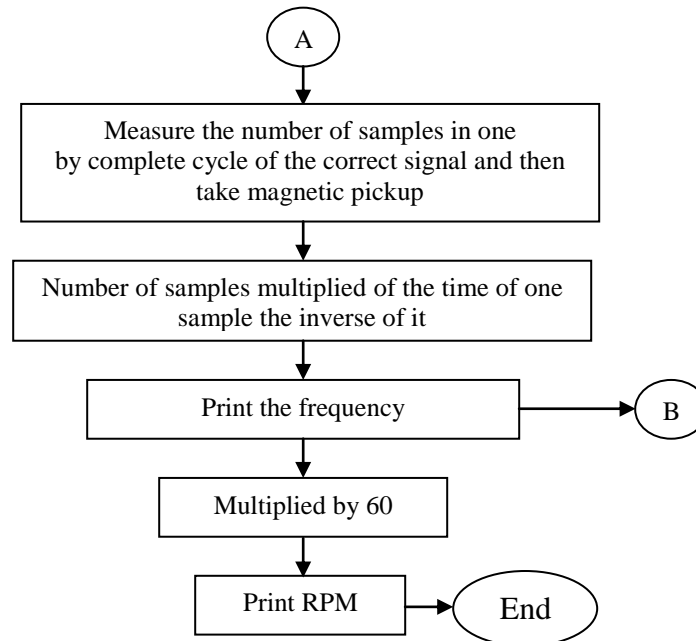
### THE SOFTWARE

Till now the hardware feeds the computer with magnetic pickup signal (square wave) and the amplified accelerometer signal. Principle of operation is to measure the phase difference between these two signals and to measure the amplitude of vibration.

In order to measure the phase difference between these two signals they must be of the same form (square wave) and same frequency. Therefore the accelerometer signal must be converted to square wave. Before doing this, the signal must be filtered, because the accelerometer signal is a combination of many signals with different frequencies as was shown in Fig. 18, so the accelerometer signal must be filtered

from all these undesirable signals except the signal with rotation frequency (Michael R. hatch 2000) and (Nian-Zhao Jiang et. al. 2007)

Step one: Frequency and speed measurement, Figure below shows the flow chart of this part of the software



### Step two : Filtering the accelerometer signal

The heart of the Balancer is its tunable electronic band pass filter. The accelerometer generates an electrical signal which is representative of all the mechanical motion (vibration) of the point to which it is attached other than one-per-revolution of concern, such as shafts, gears, engines, bearings, all will contribute their own vibrations. The accelerometer is “a high fi” device and reads all the vibration presents at the point to which it is attached to derive a useful signal, all of the signal except that from the one-per-revolution of the rotor being worked, must be rejected (Moschytz and Horn 1981).

Filters, often called wave filters, are frequency-selective networks designed to ‘pass’ or transmit sinusoidal waves in one or more continues frequency bands and to ‘stop’ or reject sinusoidal waves in the complementary bands. Filters with single pass band are typically classified as low pass, high pass, and band pass, depending on the band of frequency, which are passed. For example, the pass band of the band pass filter illustrated in Fig. 8(A) extends from the frequency  $\omega_1$  to  $\omega_2$ .

A band pass filter is a circuit that permits the passage of frequency components of a signal over a frequency band and rejects all other frequency components of the signal. A filter can be built by using, for example, resistors, inductors, and capacitors. Fig. 8(B) illustrates the response characteristics of a Band pass filter whose lower and upper cutoff frequencies are  $f_L$  and  $f_H$ , respectively. A practical filter will have a response characteristic deviation from the ideal rectangle as shown by the solid line in Fig. 8(B). For a good band pass filter, the ripples within the band will be minimum and the slopes of the filter skirts will be steep to maintain the actual band pass close to the ideal value the bandwidth is  $BW = f_H - f_L$ . For a practical filter, the frequencies  $f_L$  and  $f_H$  at which the response is 3 db below its mean band pass response are called the cutoff frequency (Bogner and Constantinides 1980).

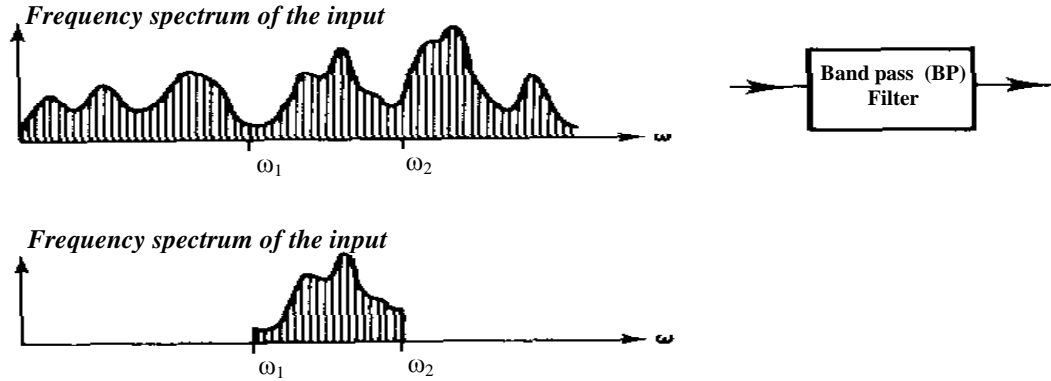


Fig. 8(A) Typical input and output frequency spectrum of band pass filter.

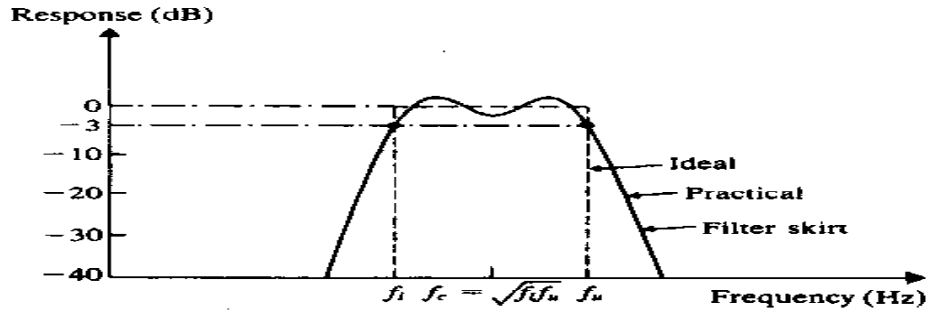


Fig. 8(B) Response of a Band pass filter.

The frequency obtained in the previous part is used as the center frequency of the bandpass filter. The bandpass filter is a Butterworth digital bandpass filter and used to pass only the frequency corresponds to the one-per-revolution (Bogner and Constantinides 1980).

Since the software do the work of the filter so it is digital filter used. The digital filter transfer function is derived by Z-transforming the transfer function of a known analogue filter  $G(s)$ , that is  $G(z)=Z[G(s)]$

In general

$$G(z) = \frac{a_0 + a_1 Z^{-1} + a_2 Z^{-2} + \dots + a_p Z^{-p}}{1 + b_1 Z^{-1} + b_2 Z^{-2} + \dots + b_q Z^{-q}} = \frac{Y(z)}{X(z)}$$

Where  $a_i$  ( $0 \leq i \leq p$ ) and  $b_j$  ( $1 \leq j \leq q$ ) are the digital filter coefficients. It follows that:

$$X(z)[a_0 + a_1 Z^{-1} + a_2 Z^{-2} + \dots + a_p Z^{-p}] = Y(z)[1 + b_1 Z^{-1} + b_2 Z^{-2} + \dots + b_q Z^{-q}]$$

$$\begin{aligned} \text{i.e. } a_0 X(z) + a_1 X(z)Z^{-1} + a_2 X(z)Z^{-2} + \dots + a_p X(z)Z^{-p} \\ = Y(z) + b_1 Y(z)Z^{-1} + b_2 Y(z)Z^{-2} + \dots + b_q Y(z)Z^{-q} \end{aligned} \quad (2)$$

But  $Z^{-k}$  corresponds to a delay equal to  $k$  sampling periods, consequently eq. (2) may be written in a linear difference equation form:

$$\begin{aligned} a_0 x_k + a_1 x_{k-1} + a_2 x_{k-2} + \dots + a_p x_{k-p} &= y_k + b_1 y_{k-1} + b_2 y_{k-2} + \dots + b_q y_{k-q} \\ \therefore y_k &= a_0 x_k + a_1 x_{k-1} + a_2 x_{k-2} + \dots + a_p x_{k-p} - b_1 y_{k-1} - b_2 y_{k-2} - \dots - b_q y_{k-q} \end{aligned} \quad (3)$$

Eq. (3) is recursive, whereby the present output sample value  $y_k$  is computed using a scaled version of the present input sample  $x_k$  and scaled versions of previous input and output samples. This form corresponds to an Infinite Impulse Response (IIR) digital filter. Sometimes it is useful to represent the linear difference equation in a block diagram form, as shown in Fig. 9 (Bogner and Constantinides 1980).



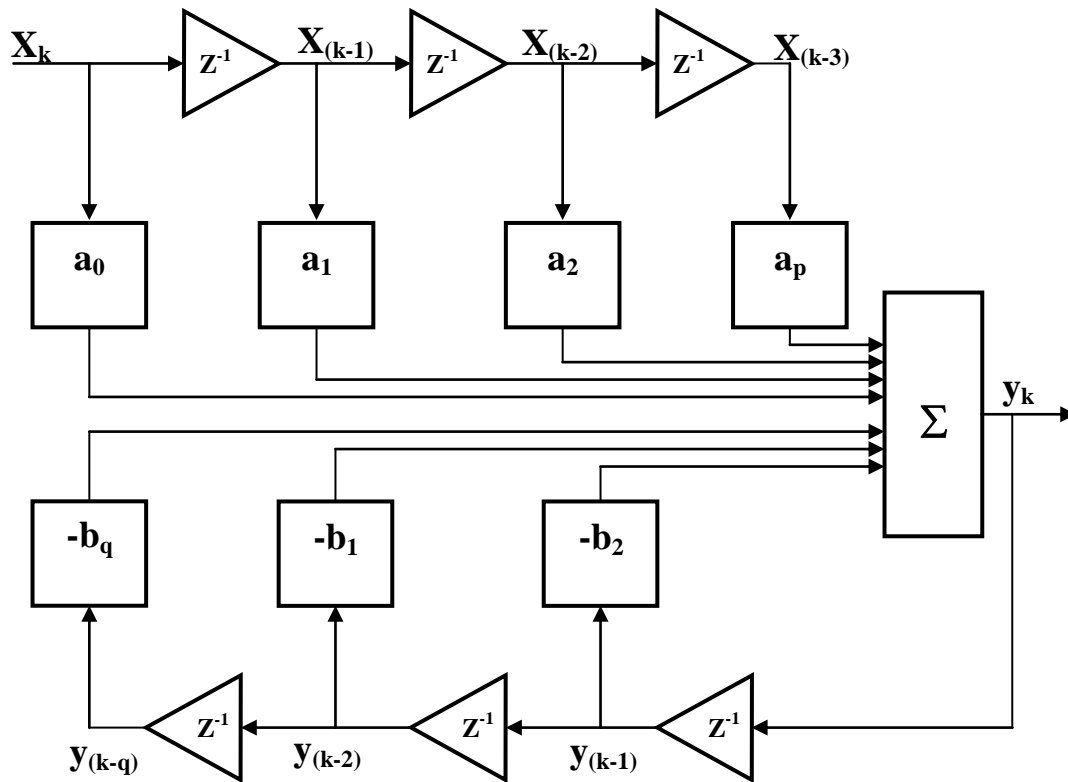


**Fig. 9 Block diagram of IIR digital filter.**

Butterworth is used because of its good properties such as fast response with fewer ripples. Fig. 10 shows the Butterworth bandpass filter output when it is applied to the accelerometer signal.

Because of different speeds (RPM) of different machines, the center frequency is varied. The bandpass filter used is designed to be general one (i.e. for different speeds). Therefore it is suitable for different frequencies and this is done by obtaining the parameters of the bandpass for each speed (center frequency) (E. F. Berkman and E. K. Bender 1997).

The software measures the RPM and according to that, it will select the appropriate parameter, from a look up table parameter order to get the correct filter. This table is obtained by using Matlab programming (Bogner and Constantinides 1980). The aim of this filtering is to get accelerometer signal frequency equivalent to magnetic pickup signal frequency in order to measure the phase shift.

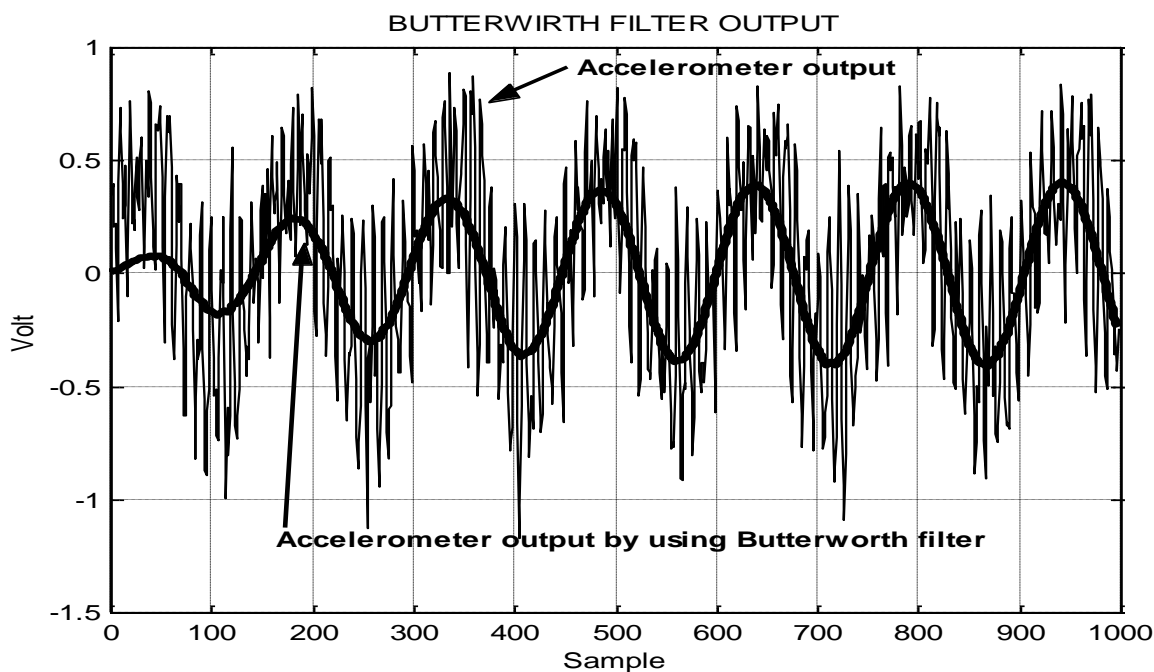
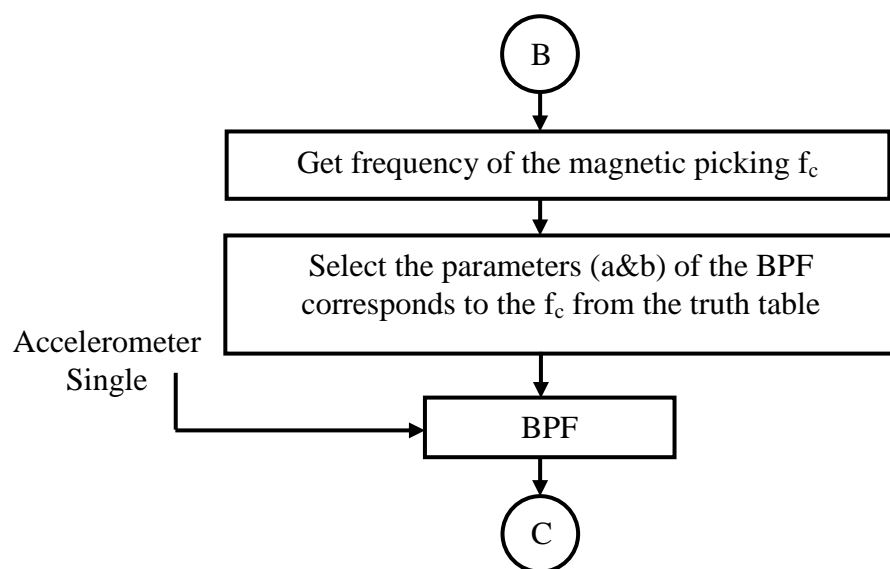
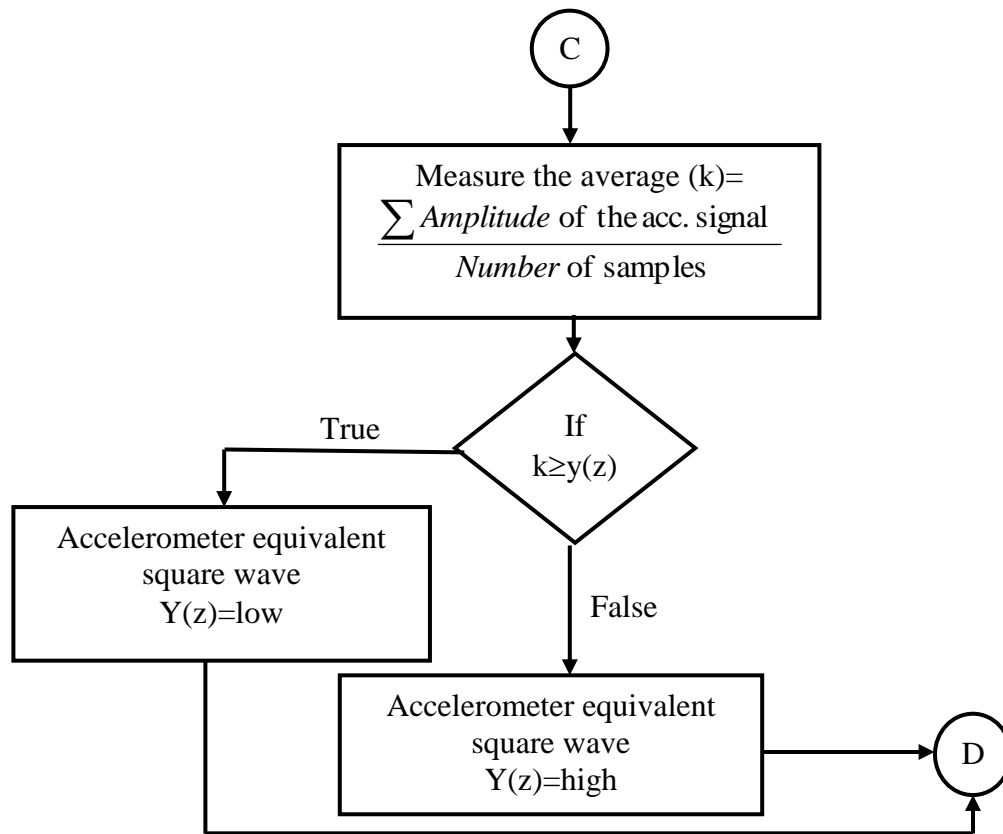


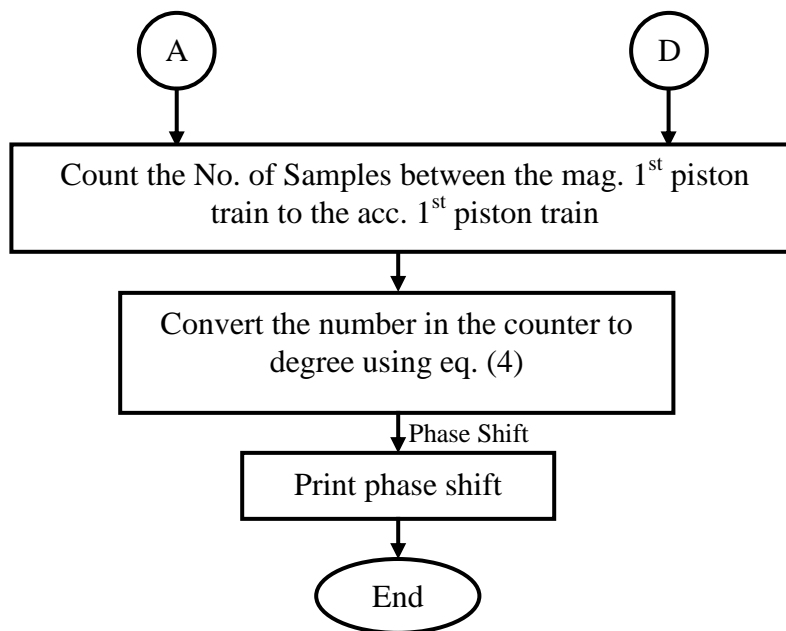
**Fig. 10 Butterworth bandpass filter output for the accelerometer signal.**



Step three : Accelerometer equivalent square wave

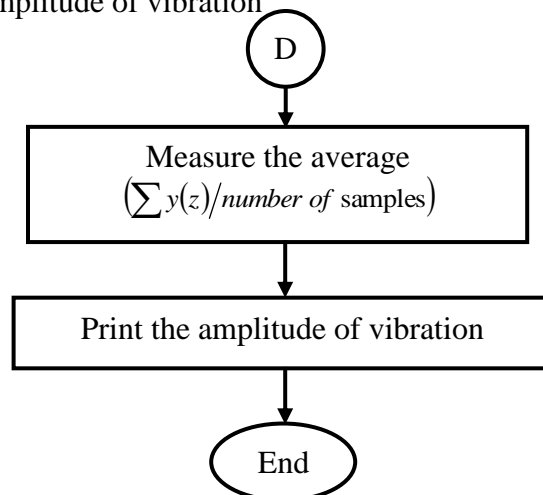


Step four : Phase shift measurement



$$\text{Phaseshift (deg ree)} = \frac{\text{Measured phase shift (in samples)} \times 360}{\text{Number of samples for one complete cycle}} \quad (4)$$

Step five : Measuring the amplitude of vibration



Step six : Calculation of the additive weights

Until now the phase shift (degree or Clock angle) and amplitude (Volt) of vibration is obtained. The final part of the software is to calculate the additive weights for balancing. The manufacturer of each machines provides a certain chart for evaluating the amount of these weights.

The balance charts receives the measurement of vibration (amplitude and location of additive weight) and calculate the weights required for balance the rotor, These charts came from the calculations of the designer of the rotor machines (Peter Konstanzer et. al. 2008).

A balance chart consist of:

- A clock face ( 12 radial lines ) representing "clock angle".
- A set of 10 concentric circles representing "Volt" , drawn over the clock face, with zero at the center and 1.0 at the outside.
- A graph over the clock face and "Volt" circles, whose axes are geometrically related to the available weight attachment points (as provided by the manufacturer). If the weight attachment points are 90° apart (as on 4-blade rotor) the axes of the "graph" are at 90° to each other. If for a 3-blade rotor, the axes are 120° apart, etc.

The intersection of "Volt" circle and "clock angle" lines define a point on the chart. From this point, lines to the axes of the graph show amount and location of the weight to be added or subtracted required to accomplish balance.

Fig. 11 shows one sample of the charts used in main rotor of helicopters with 3-blade type (Gazelle).

example (1):

Vibration amplitude 0.65 volt and clock angle 1.33 there fore the additive weight for balance is 8 grams to the Target blade and 8 grams to the A blade.

example (2):

Vibration amplitude 0.85 volt and clock angle 5.5 there fore the additive weight for balance is 12 grams to the B blade blade and 10.5 grams to the target blade.

example (3):

Vibration amplitude 0.8 volt and clock angle 7.75 there fore the additive weight for balance is 4 grams to the A blade and 12 grams to the B blade.

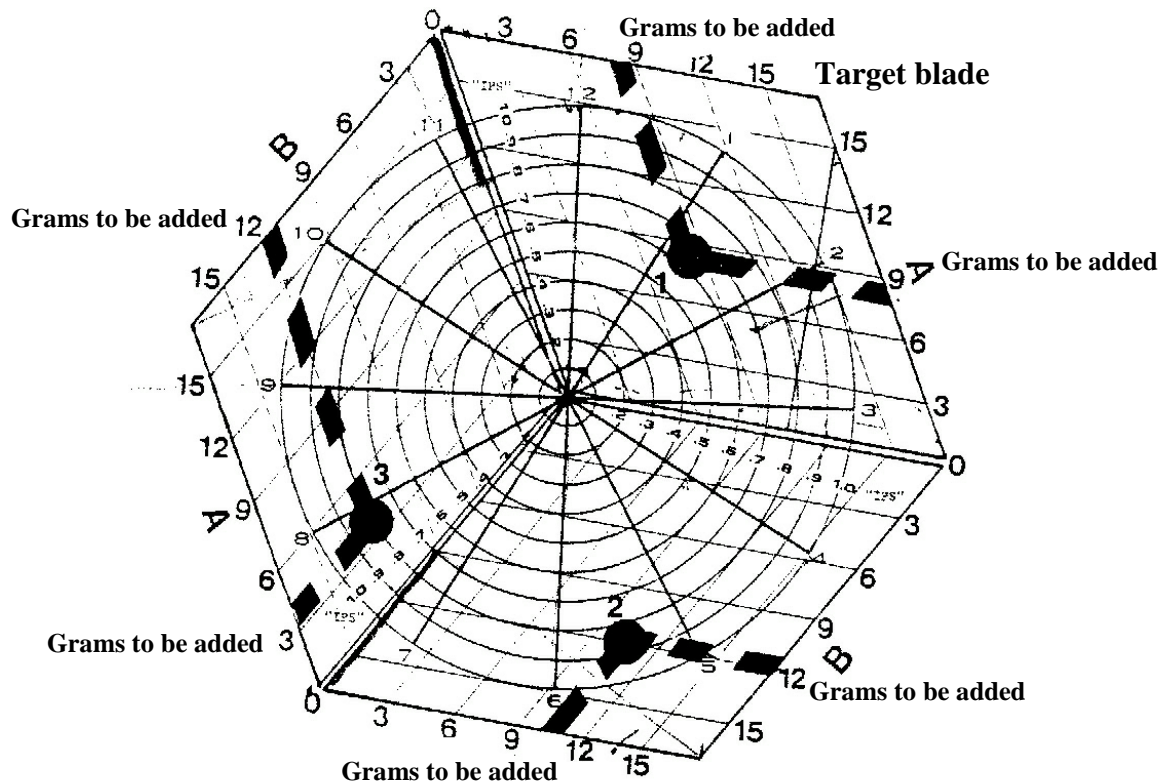


**Fig. 11 Chart for three-blade rotor.**

## SIMULATOR

In order to test the designed balance system, i.e. the hardware and software, a simulator is needed. . The simulator consists of a DC motor operates from 12 volt with full load current about 8 Ampere. The speed of rotation can be varied from the DC power supply, which is designed specially for the simulator.

The motor maximum speed is 900 RPM (full load) and can be varied through a potentiometer on the output of the power supply. The motor is positioned vertically and fixed on metal plate, which can be used to hold the magnetic pickup and the accelerometer. This small metal plate is connected to the base of the simulator through three legs with springs to allow free movement of the motor when it is unbalance. There is a vertical shaft used to fix the motor so that it prevents the motor from any movement. This situation is useful for some measurements and tests when considering the motor to be completely balanced.

The motor has two shafts, the first one is upward and connected to a three-blades fan. Different weights can be fixed to the blades to control vibration. The second shaft is downward and with a small metal plate (Target) used to operate with the magnetic pickup.

The simulator is a general purpose one, so one can change the fan to another fan with different number of blades. Also one can change the number of targets to give more pulses per revolution (pinion) such application like turbine, the simulator is shown in fig. 12.

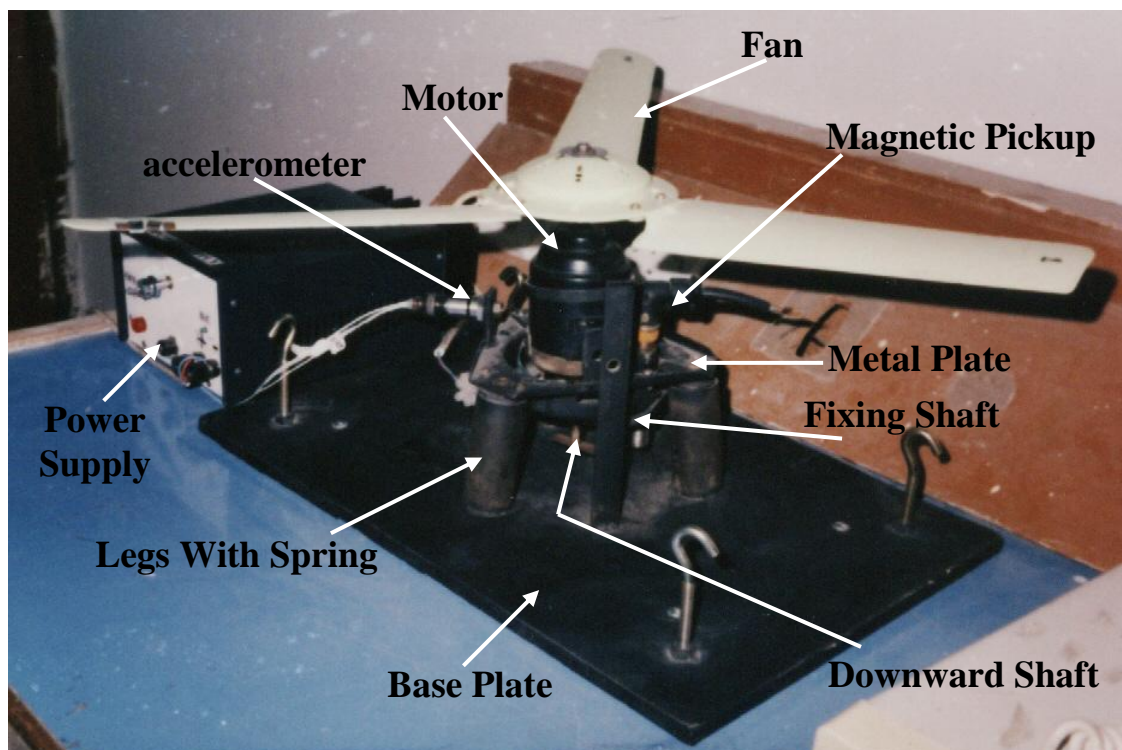


**Fig. 12 The simulator.**

### **PRACTICAL EXPERIMENTS BY USING THE SIMULATOR**

The system is tested using the simulators. During the test carried on the simulator, different cases were considered such as:

Different weights on different blades.

Different positions of the sensors.

Longitudinal axis of the accelerometer.

Different number of targets.

Different speeds (RPM).

The configuration relating the blades with target is shown in Fig. 13 This configuration is used during all tests. The term “heaviest” means that a weight is added to the correspond blade. The output of the experiment is phase shift (degree or Clock angle) and amplitude (Volt) of vibration. The final part of the experiment is to calculate the additive weights for balancing that can be calculated from the charts as explained previously.

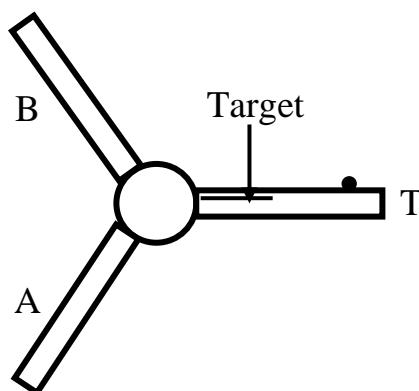


Fig. 13 The configuration relating the blades with target.

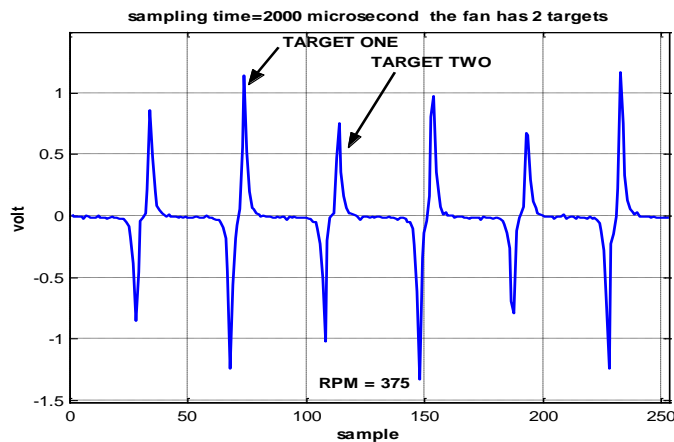
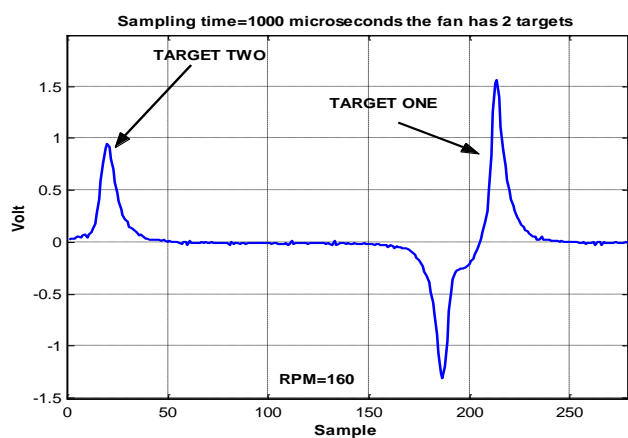


Fig. 14 Magnetic pickup output signal.

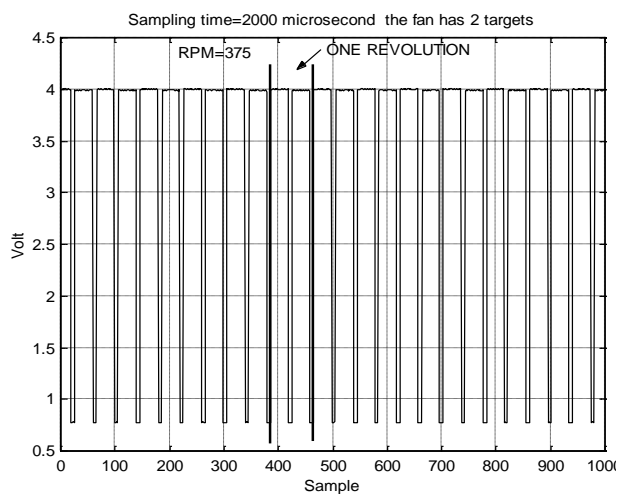


Fig. 15 Output of the second part (comparator) of the magnetic pickup signal conditioning.

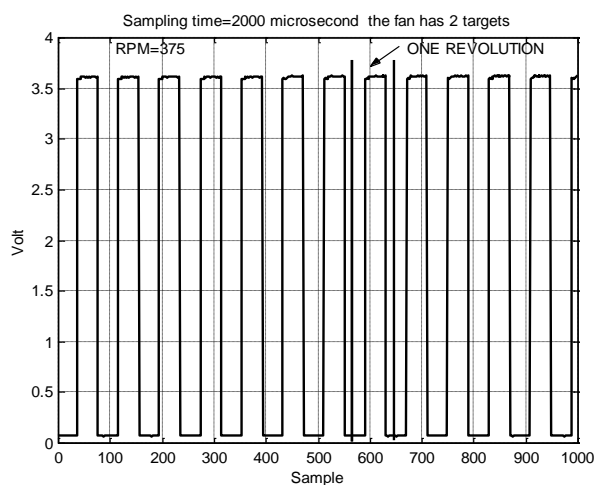
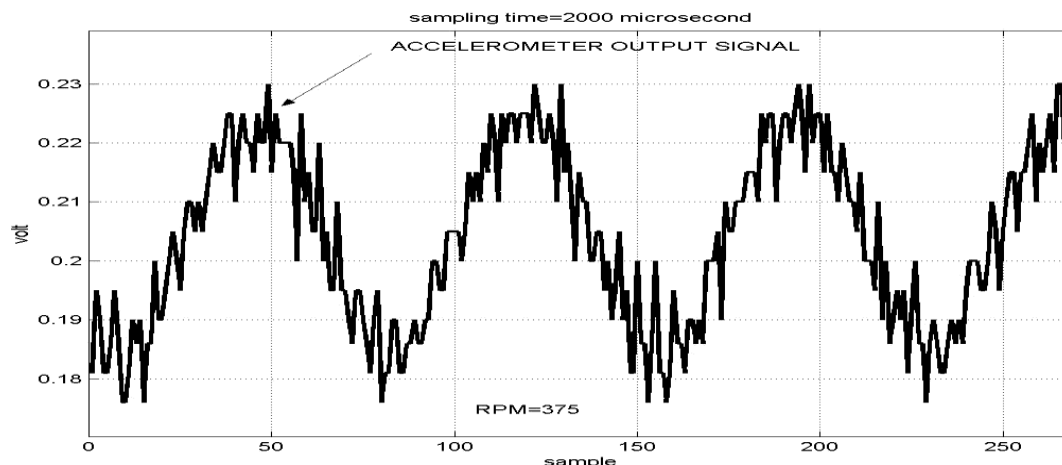
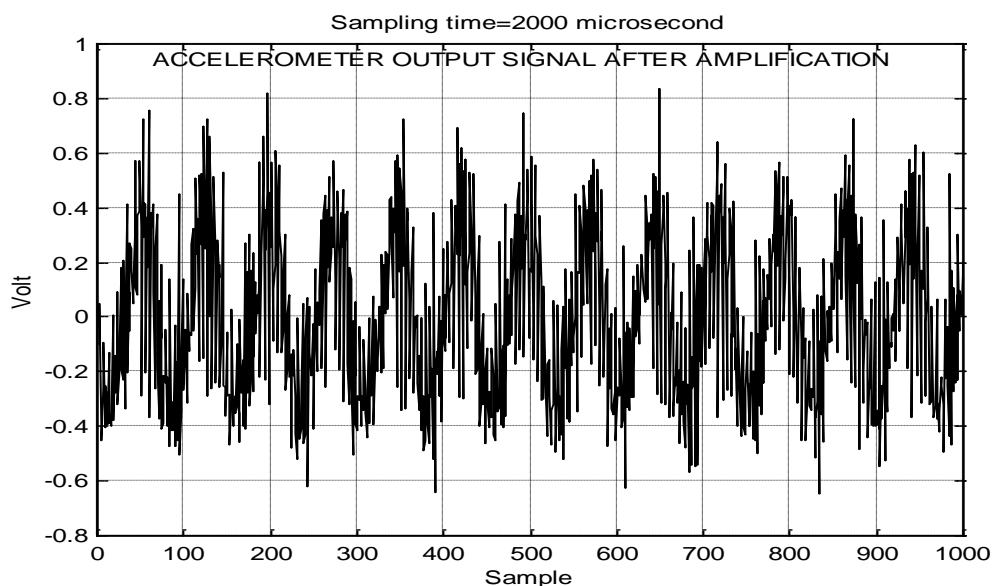


Fig. 16 Magnetic pickup signal conditioning output.



**Fig. 17 Accelerometer output signal.**



**Fig. 18 Accelerometer signal conditioning circuit output.**

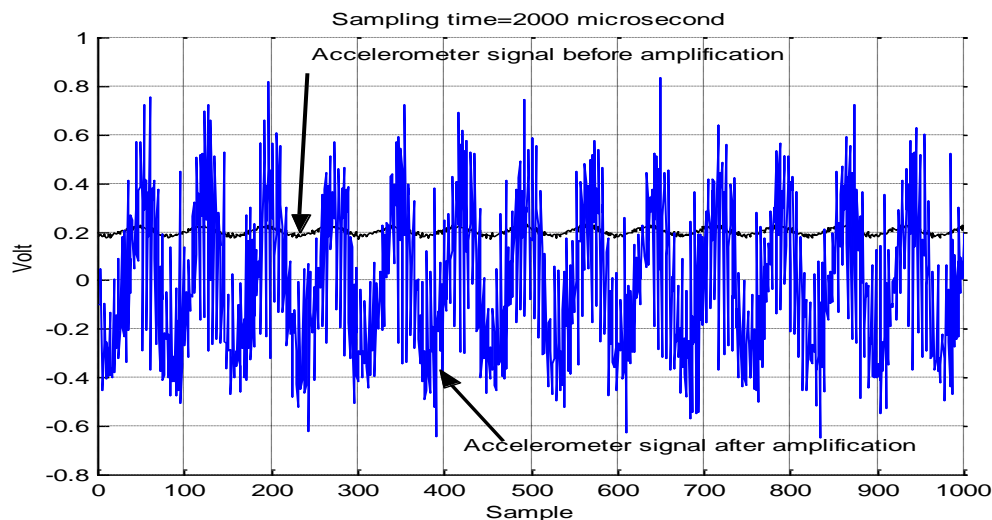


**Fig. 19 Accelerometer signal before and after amplification.**



Case (1):

The heaviest blade is T.

The fan has one target.

Angle between two sensors = 180 degr

Magnetic pickup frequency = 5.95 Hz.

Accelerometer frequency = 5.95 Hz.

Accelerometer average value = 0.6 vol

Accelerometer RMS value = 0.75 volt.

RPM = 357

Phase shift = 356 degree

Clock angle = 12

Case one is shown in Fig. 20

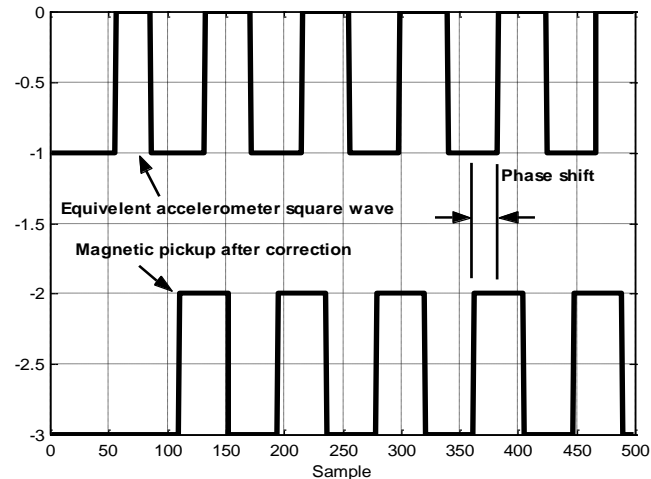


**Fig. 20 Magnetic pickup and accelerometer waveform for case one.**

Case (2):

The heaviest blade is B.

The fan has one target.

Angle between two sensors = 180 degr

Magnetic pickup frequency = 5.95 Hz.

Accelerometer frequency = 6.25 Hz.

Accelerometer average value = 0.55 vc

Accelerometer RMS value = 0.70 volt.

RPM = 360

Phase shift = 240 degree

Clock angle = 8

Case two is shown in Fig. 21

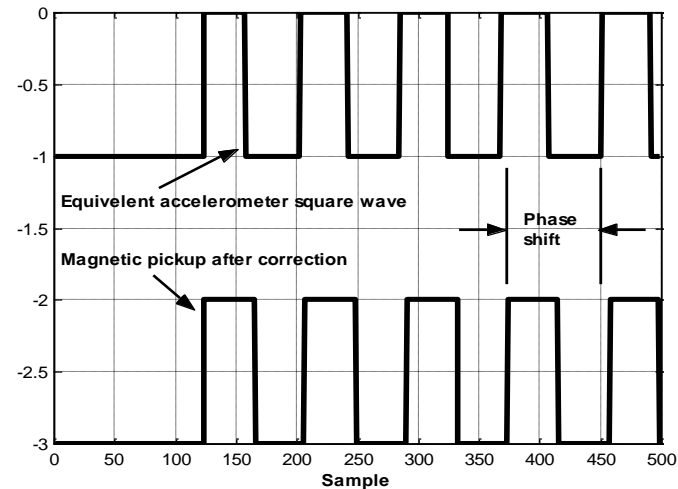


**Fig. 21 Magnetic pickup and accelerometer waveform for case two.**

Case (3):

The heaviest blade is A.

The fan has one target.

Angle between two sensors = 180 de

Magnetic pickup frequency = 5.95 H

Accelerometer frequency = 5.81 Hz

Accelerometer average value = 0.57

Accelerometer RMS value = 0.66 vo

RPM = 357

Phase shift = 110 degree

Clock angle = 4

Case three is shown in Fig. 22

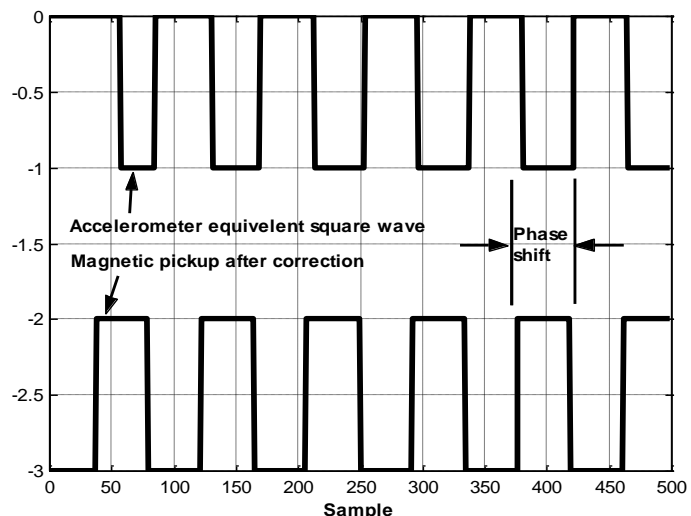


**Fig. 22 Magnetic pickup and accelerometer waveform for case three.**

## CONCLUSION

- Vibration measurement and analysis is an important tool for creating a smooth operation of the machines. The relationship between unbalance of a rotating body and the vibration produced is highly dependent upon rotor speed and other operating conditions. When making vibration measurements for the purpose of determining and correcting unbalance, the operator must operate the machine in a consistent and repeatable manner to insure that repeatable measurements can be made.
- To measure the vibration due to rotor unbalance, a vibration transducer (sensor) is attached to the vibrating body when measuring imbalance. The vibration sensor converts this mechanical motion into an electrical signal that corresponds to the body's motion in space. The vibration analyzer is then used to sample this electrical signal and make various calculations based on the electrical signal's properties.
- In addition to the vibration measurement, a tachometer signal is collected. A tachometer sensor (magnetic pickup) is used to detect the position of the rotating body with respect to time. As in the case of the vibration transducer, the tachometer sensor converts this information into an electrical signal, which can then be sampled by the vibration analyzer and used in various calculations.
- The analyzer will collect a series of narrowband vibration readings called peak phase measurements since each reading is composed of a peak value and a phase reading. The peak reading (amplitude) is proportional to the amount of mass unbalance in the rotating machine.
- The phase reading (phase angle) provides information about the location of the mass unbalance. The analyzer based on the amplitude and phase angle of the vibration reading computes a balance solution (corrective weight) depending on charts that supplied by manufacturer. The corrective weight is then applied to the machine and the measurement process is repeated. The balancing job is finished when the vibration is reduced below an acceptable level (Prop and Rotor Balancing 2001).

## REFERENCES

- Chadwick-Helmuth, 1981, "VIBRATING BALANCING", Helicopter electronics and mechanics, Vol .1, No.1, pp.10-22.
- Clarence W. de Silva, 1999, "VIBRATION FUNDAMENTAL and PRACTICE", CRC.
- E. F. Berkman and E. K. Bender, 1997, "PERSPECIVE on ACTIVE NOISE and VIBRATION CONTROL", Sound and Vibration Magazine.
- FACILITES INSTRUCTIONS, STANDARDS AND TECHNIQUES, from Internet, FIELD BALANCING LARGE ROTATING MACHINERY.htm. Volume 2-2, 2002.
- G. S. Moschytz and Peter Horn, 1981, "ACTIVE FILTER DESIGN HANDBOOK", John Wiley & Sons Ltd, institute of fernmeldetechnik/Zurich.
- J. B. Catlin, 1976, "USE of TIME WAVEFORM CHARACTERISTICS and PHASE MEASUREMENTS for VIBRATION SIGNAL ANALYSIS", The Journal of the Acoustical Society of America, November Vol. 60, No. 11, pp. S29-S30.



- Maged Mostafa Alaa El Din Sayed, 2006, "Vibration Attenuation of Rotating Beams Using Periodically Distributed Piezoelectric Controller" M. Sc. Thesis, Cairo University.
- MAGNETIC PICKUP & IN-LINE PREAMPLIFIER, from Internet, red lion, [www.redlion-controls.com](http://www.redlion-controls.com)
- Maurice L. Adams, 2000, "ROTATING MACHINERY VIBRATION: From ANALYSIS to TROUBLESHOOTING", CRC.
- Michael R. hatch, 2000, "VIBRATION SIMULATION USING MATLAB and ANSYS", Chapman & Hall/CRC.
- Nian-Zhao Jiang, Xiang-Lin Ma and Zhi-Qing Zhang, 2008, "THE DYNAMIC CHARACTERISTICS ANALYSIS OF ROTOR BLADE BASED ON ANSYS", Nanjing,210016, PR China.
- P. K. Sood,1990, "ANALOG-TO-DIGITAL CONVERSION", McGraw Hill, London.
- PROP AND ROTOR BALANCING, 2001, from Internet, [www.rotordynamicsamericas.com/Rotor\\_dynamics\\_Americas\\_vibration.htm](http://www.rotordynamicsamericas.com/Rotor_dynamics_Americas_vibration.htm).
- Peter Konstanzer, Bernhard Enenki, Pierre-Antoine Aubourg and Paul Cranga, 2008, "RECENT ADVANCES IN EUROCOPTER'S PASSIVE and ACTIVE VIBRATION CONTROL", American Helicopter Society International, Inc.
- R. E. Bogner and A. G. Constantinides,1980, "INTRODUCTION TO DIGITAL FILTERING", John Wiley & Sons Ltd, (Bogner) Department of Electrical Engineering / University of Adelaide, Australia & (Constantinides) Department of Electrical Engineering / Imperial College of Science and Technology, London.
- S. Q. Reza Moheimani and Andrew J. Fleming, 2006,"PIEZOELECTRIC TRANSDUCERS for VIBRATION CONTROL and DAMPING", Springer.
- T. J. Terrell,1988, "INTRODUCTION TO DIGITAL FILTERS", Macmillan Education Ltd, second edition, London.
- User's MANUAL, 1995, "PC-LabCard", Advantech Co., 4th Edition.
- Zhaochun Yang and Qing-Ming wang, 2006, "TRANIDENT RESPONSE OF PIEZOELECTRIC THIN FILM VIBRATION SENSOR UNDER PULSE EXCITATION", Journal of applied physics, Vol.99, No. 1.

## DESIGN AND IMPLEMENTATION OF INFORMATION SYSTEM FOR GENERAL DIAGNOSTIC AND REMEDY OF CASTING DEFECTS

Dr.Qasim M. Daws

University of Baghdad / College of Engineering  
Mechanical Dept.

Ban Bakir Jawad

University of Baghdad / College of engineering  
.Mechanical. Dept..

### ABSTRACT:

Casting defects are ones of the important problems occurring in the casting process .The large number of the defects make the diagnosis of them difficult and depend on the inspector experience and his information of the defects property. This diagnostic perhaps being wrong and not accurate. Therefore in this research an inclusive program through information system was designed to diagnose the defects and its causes then put the suggested remedy, this program contains four methods to recognize the defects in castings .The methods are 1.Use selection of the listed property of the defects 2.Benefit from the pictures of defects to diagnose the defect. 3. The questions and answers method .4.Combo box that contains all the defects name .The last method was designed only for the workers having a great experience in this field. It is found after verification that the method of picture is the simplest and rapidly one because the user needs to see the picture that is given to him and compare them with the castings defect. The program was designed by the use of Visual Basic language, which allows making dealing with the methods easy. The arrangement of this number of defects was done by use general classification that classify them to seven groups and these were divided to subdivision groups .The verification was done to check the effectiveness of the program and it gave good results .

### الخلاصة

من اهم المشاكل التي تواجه عملية السباكة هي العيوب التي تظهر في المسبوكات .ان عدد هذه العيوب كبير بحيث يجعل تشخيصها صعب ويعتمد على خبرة الفاحص ومعلوماته عن عيوب السباكة .وهذا التشخيص ربما يكون خاطى احيانا او غير دقيق لذلك تم تصميم هذا البرنامج الشامل من خلال نظام معلومات يعمل على تشخيص العيوب ويحدد اسبابها ومن ثم وضع العلاجات المناسبة لها بحيث يحتوي على اربعة طرق من خلالها يتم معرفة العيوب في المسبوكات وهذه الطرق هي 1- استخدام الاختيار لخواص العيوب ضمن قائمة معينة 2- استخدام الصور والاستفادة منها لتشخيص العيوب 3- عن طريق الاسئلة والاجوبة في تحديد نوع العيب 4- عن طريق اسماء العيوب الموجودة جميعها ضمن قوائم مدرجة .ان الطريقة الاخيرة مصممة فقط للعاملين في هذا المجال ولهم الخبرة فيه وقد وجد بعد التطبيق ان طريقة التعرف على العيب عن طريق الصور هي اسهل واسرع الطرق لان المستخدم يحتاج فقط لمقارنة شكل العيوب الموجودة لديه في المسبوكة مع الصور المعطاة له في البرنامج

وتحديد نوع العيب .وقد تم تصميم البرنامج عن طريق لغة Visual basic والتي يكون التعامل من خلالها مرناً ومفيداً جداً مع أنظمة المعلومات .لقد تم تصنيف العيوب إلى سبعة مجاميع رئيسية وهذه المجاميع قسمت إلى مجاميع فرعية ثم أدرجت ضمن الطرق الأربعة .وقد تم إجراء تحقيق للتأكد من فعالية البرنامج ووجد أنه يعطي نتائج لها نسبة جيدة من الدقة.

## KEY WORDS

Defects, remedy, diagnostic, casting , information

## INTRODUCTION

There are many defects that appear in castings products due to some reasons such as the existence of gases in molten metal, the inclusions in metals and mould, the moisture in sand mould and improper pouring temperature (British standard, 1956) . Most of these defects appear in sand casting and less in other types of casting. Some defects can be accepted with them because their effects are negligible others are refused that led to losses in time and money for the manufacturer .The methods that available to recognize these defects are slow and randomly and depend only on worker experience. Some literatures survey approach from this subject such as: (Mery, 2002) who make review of methods for automated reduction of casting defects , (Naro, 2002) deals with porosity defects in iron casting from mold metal interface reactions .(Mark, 2005) study the analysis and reduction of casting defects . The present work is a practical method for diagnostic because it depends on computer technique to design and implementation information system for general diagnostic and remedy of casting defect. The user can choose one of the methods that designed in the program to get the final result of the search, and this is done by following the steps of every method until reaching the final result which contains the properties of the defect, its causes and the suggested remedy.

## DESIGN OF PROGRAM

The experimental work includes:

**1** Design the program contains all casting defects through suitable classification which divides the defects into seven groups according to their properties (Technical council, 1950)

Group A (Metallic Projections)

Group B (Cavities )

Group C (Discontinuities)

Group D (Defective surface).

Group E (Incomplete casting).

Group F (Incorrect Dimensions and Shape).

Group G (Inclusions or Structural Anomalies).

These groups were divided to subdivision groups (Groover, 1996)

2 In the program there are four methods **Fig. (1)** designed to diagnose the defect by choosing one of them:



**Fig (1)** The main window of the program.

### **METHOD OF SELECT**

The user can choose this method by click on point (1) in the main window then **Fig. (2)** appear. Now it should select if the defect seem to be external or internal and if it is unknown select (not known), also select if it general (alloy) or (steel), because the program is separately searching these two alloys. In this window the user should choose one of the seven groups because they are all actives, the chosen was done by the user decision when compare its castings defect with them. Now when select one of the groups a window appear that contains all the properties of the external or internal defect according to the previous choice **Fig. (3)**. All the properties are actives, but before click on any one and in order to make sure of the choice there is a command (show picture) when click on it, the picture of the selected properties is appear **Fig. (4)**, then it can select the right property. It will take to the next window, which includes the mean defect for that property through the general classification of its group. In this classification, the exact defect is only active and appears with the color different from the others defects in the groups which they are non-actives in that time **Fig (5)**. When click on the block of this defect the final result will appear which contains the properties of the defect, its causes and the suggested remedy for it, also a small picture for the defect **Fig (6)**.

MAIN FORM OF SELECTION

Determine by correct choice if your defect external or internal or you don't know:

is the defect  or  or

Determine whether you used alloys or steel casting

is it  or

**Casting Defects**

- Metallic projections — Group A
- Cavities — Group B
- Discontinuous — Group C
- Defective surface — Group D
- Incomplete casting — Group E
- Incorrect dimensions of shape — Group F
- Inclusions or structural anomalies — Group G

select from the combo box the kind of defect you have

Fig. (2) The selection of the groups with the type of the defect

Form3

choose the form of defect you have:

- ☒ irregular crack, like projections on the surface of castings, it can only be removed by chipping or grinding
- ☐ Excessive fin, Excessive flash along parting line
- ☐ Network of projections on the surface of die casting
- ☐ A rough irregular projection on the surface of a casting, some times containing embedded Sand
- ☐ Thin metallic projection, located at a re-entrant angle, it dividing the angle in two parts
- ☐ Thick fin, attached to the casting at the parting line
- ☐ Partial lift of top part or displacement of the sand in the mould by metal pressure, causing the mould surface to crack with the consequent formation of fins or flash on the casting
- ☐ Formation of fins in planes related to the direction of mold assembly
- ☐ displacement of sand, at mould joints or core prints, irregular shaped cavities, projections on the castings

Fig.(3) The Selection of the property



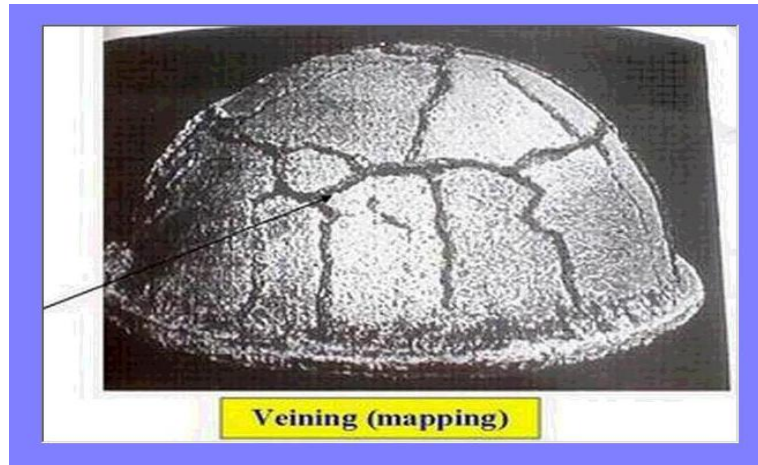


Fig. (4) The picture of the defect of the selected property

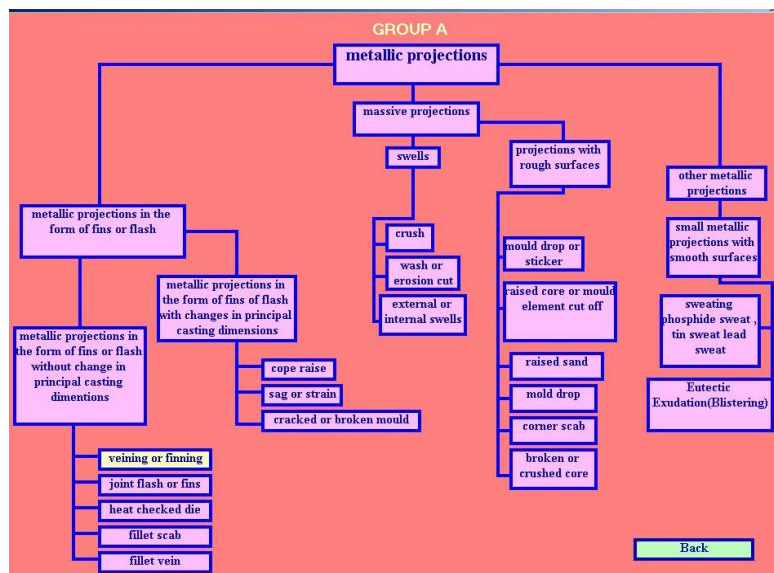


Fig. (5)The general classification of the mean defect

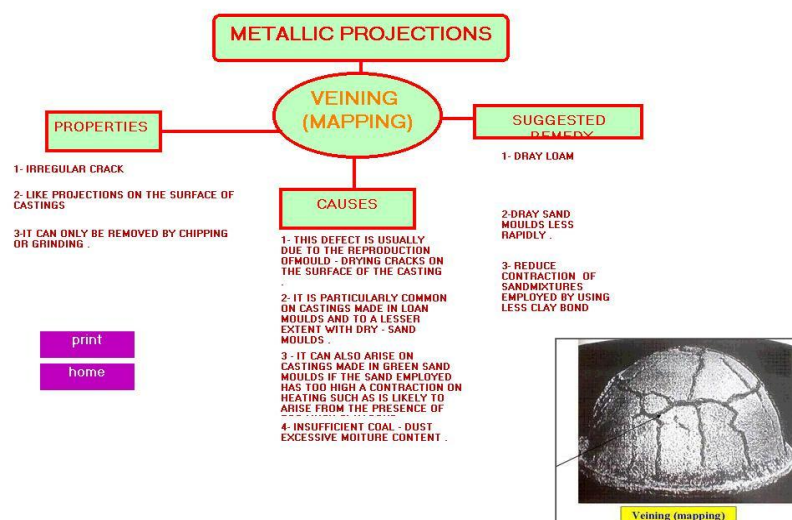


Fig. (6) The final result



## THE METHOD OF PICTURES

The second method is the use of pictures **Fig. (7) (a)** and **(b)** to recognize the defect by comparing the picture of the defect in defective casting with the pictures of all defects listed after choosing the type of defect and the kind of the alloy. Also it should choose one of the seven groups, **Fig. (8)**. Then the pictures appear until find the same picture of defect same as of the defect in defective casting. **Fig. (9)**. This picture is active in that time, when click on it the general classification of that defect appear **Fig. (10)**. The defect in this classification is the only one active and appears with different color while other defects in the classification are not active **Fig. (11)**.



**Fig. (7) (a) The choose of the second method**



**Fig. (7) (b) The start of the second method**

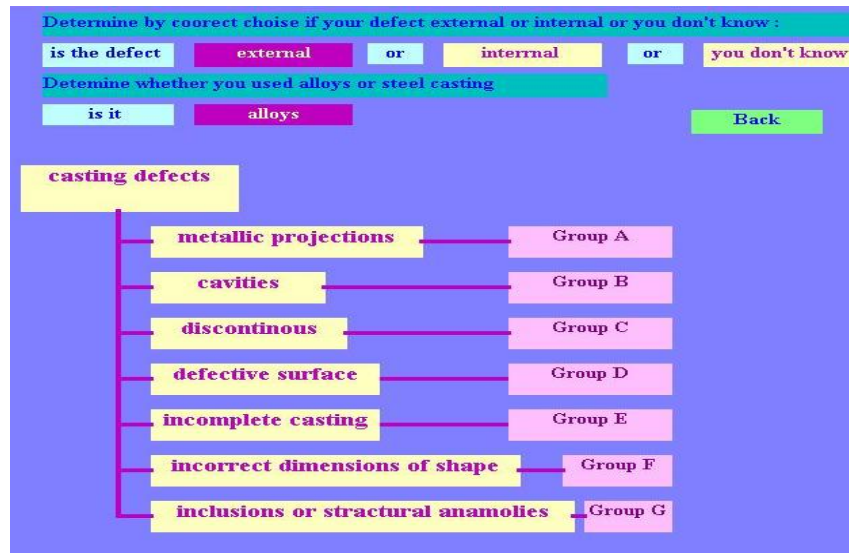


Fig. (8) The choice of types of the defect, the kinds of alloy and the group of defect.



Fig. (9) One of the listed pictures

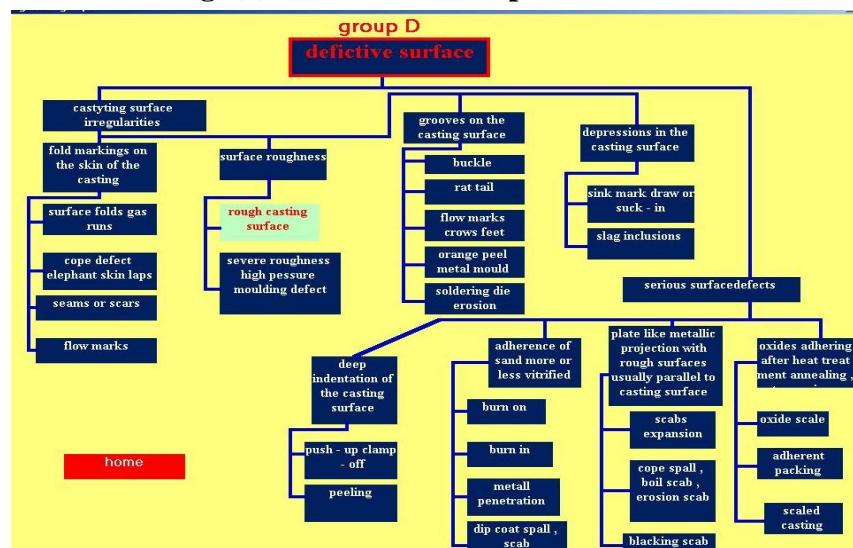


Fig. (10) The general classification of the mean defect



Fig (11) The final result.

## METHOD OF QUESTIONS AND ANSWERS

There is method of diagnose the defect in the defective casting by using the questions and choose answers that give the exact result. First it should take point three in main window **Fig. (12)** then the next window appear to choose the types of the defect and the kinds of casings **Fig. (13)** After that the starting window of the method appears **Fig. (14)** .In that time many questions related to the properties of the choosing types appears **Fig. (15)**, the questions can changed by clicking (No) for the question that not give the right property until reach to the question give the property similar to the defect in the castings. When click (Yes) to that property, the general classification of the mean defect appear with the different color between the other defects in this classification **Fig. (16)**.Clicking on the mean defect give final result **Fig. (17)**.

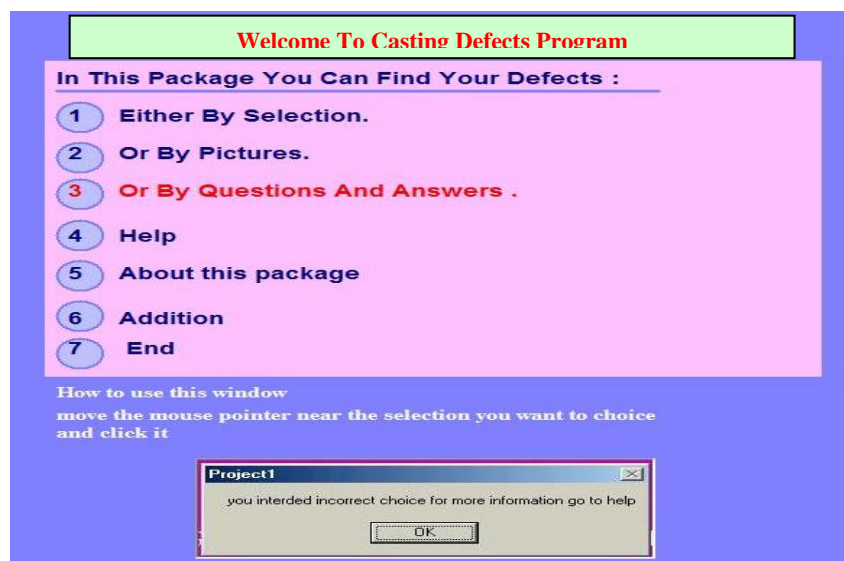


Fig (12) Selection of third method

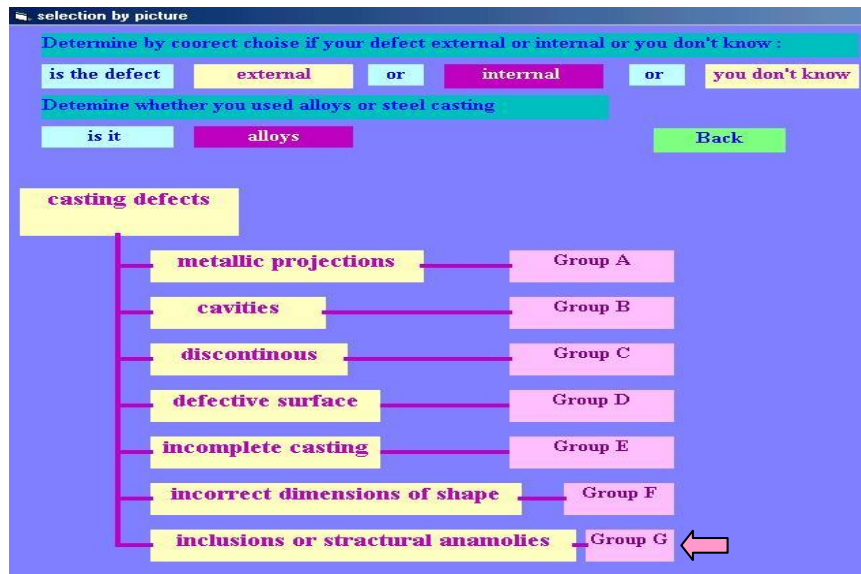


Fig (13) Choose the types of defect and the kind of casting

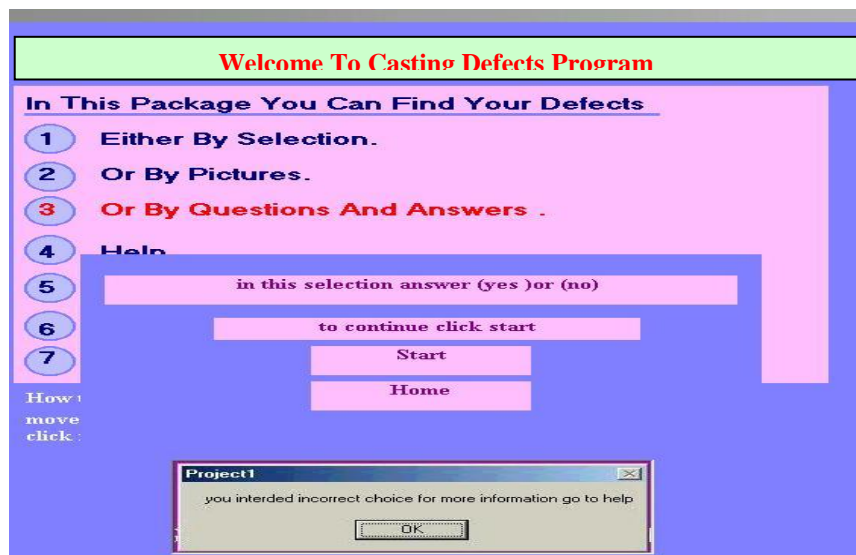


Fig (14) The starting of third method



Fig (15) The questions of properties of defects



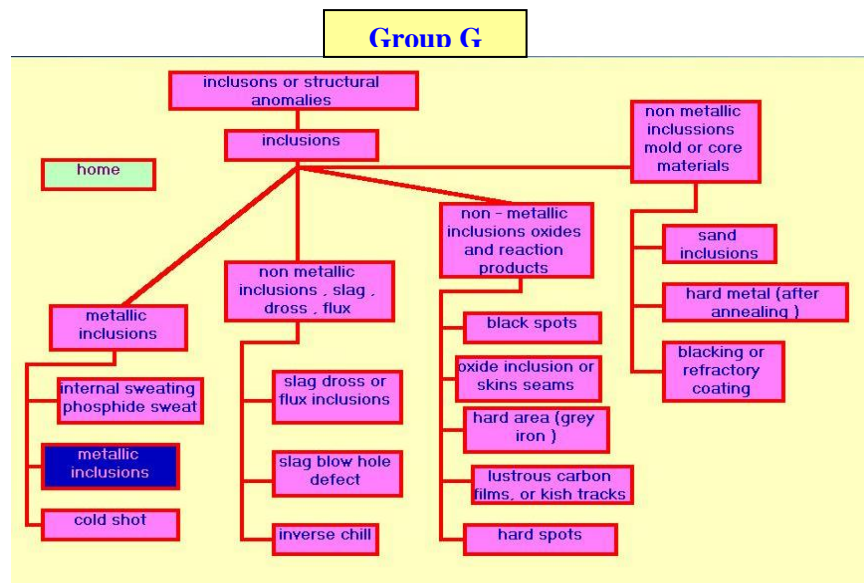


Fig. (16) The classification of the defect

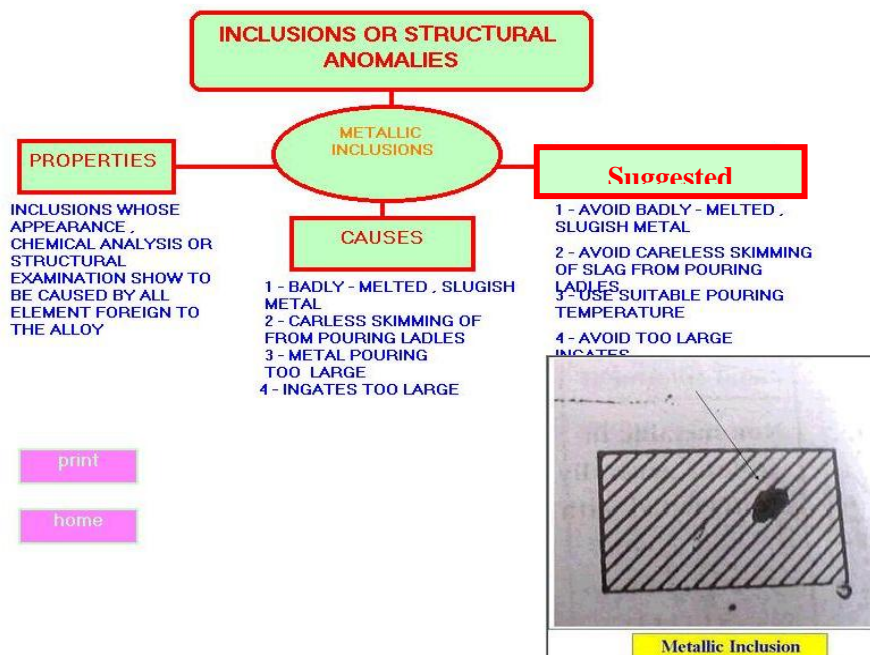


Fig. (17) The final result

## RESULTS AND VERIFICATION

In order to check the results of the program and its accuracy, verification was done by casting three castings with planning to create many particular defects that appointed premature. Therefore three samples were taken, the first one include a (Flash) defect. It is aluminum alloy cast with sand casting method, the second achieved with existence of (Shift) defect by intending no corresponding between the upper part of the mould with the lower part, while the third defect which is (blow holes) create by preventing the gases in the molten metal to exit through the mould, and make the molten metal exposed to the atmospheric gases. Then the diagnoses for these defects

were done by applying the program step by step to check its effectiveness in work with properly form to recognize the defect.

### Application Of First Method To Find (Flash) Defect

The defective parts appear in **Fig.(18)** ,they are used to make verification to the first method of information program was done .By using selection of properties of the defects to find the defect it is seen that this sample has defects seems to be additional metals from the side of the part. At the first it have to distinguish the general properties of this defect, it is external defect with aluminum alloy and it is suitable with first group of defects (Metallic projections).when following the steps of the method with **Fig.(19)**,**Fig.(20)** , **Fig.(21)** ,**Fig.(22)** the final results will appear in **Fig.(23)**, **Fig.(24)** Which explain that this defect is (Metallic projections ) in the form of fins called(flash) with all his causes and suggested remedy.



**Fig (18) The first samples for first defect**



**Fig .(19) Choice of the first method**

Fig .(20) Choice of the types of the

Fig .(21) Choice the right property



Fig (22) The Picture of the selected property

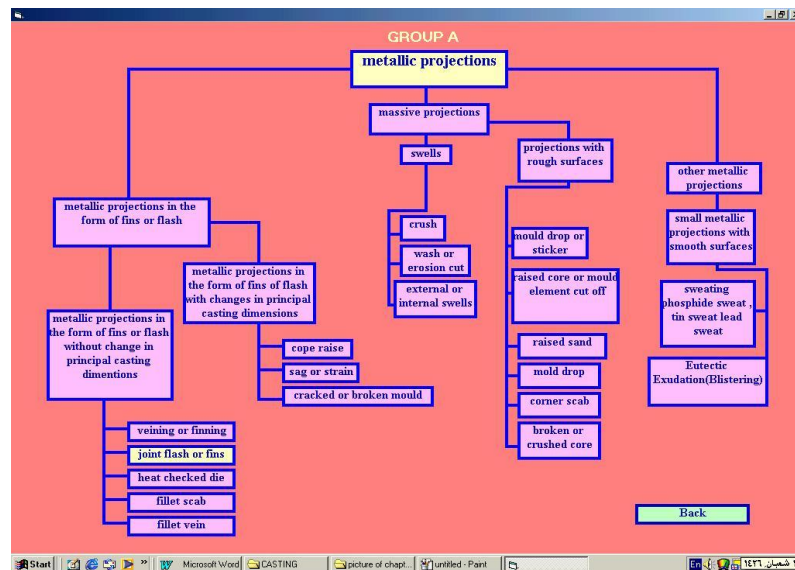


Fig (23) The general classification of the mean defect

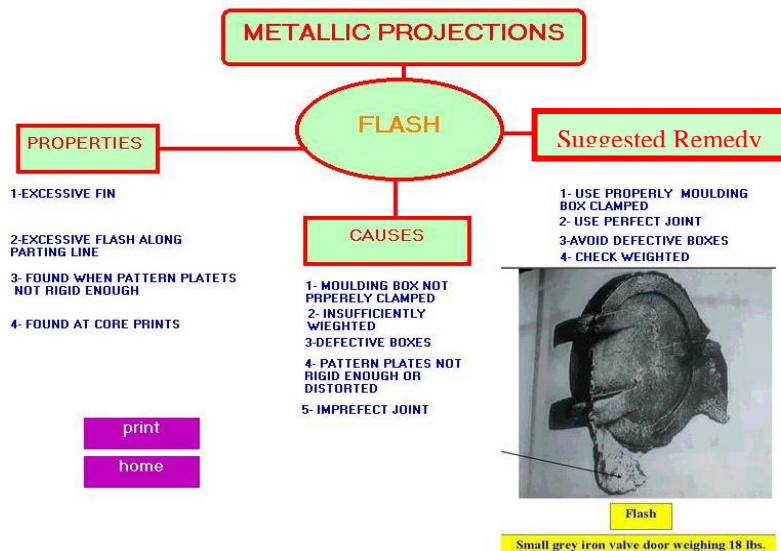


Fig (24) The final result of the mean defect



### **Application Of The Second Method To Find (Shift ) Defect :**

The second defective sample **Fig.(25)** is used to make the verification on the second method of the program which is used pictures to recognize the type of the defect choosing all the conditions of this defect and following the steps of the second method **Fig.(26)** ,**Fig.(27)**, **Fig.(28)** it is seen that this defect is classify to (group f)**Fig.(29)** which is called incorrect dimensions of shape with sub division(casting shape incorrect overall or in certain locations)and his name is (shift)or (mismatch) or (cross joint).Final results appear in **Fig.(30)** .the defect ,its properties,causes,and Remedy.



**Fig. (25) The samples of the second defect**

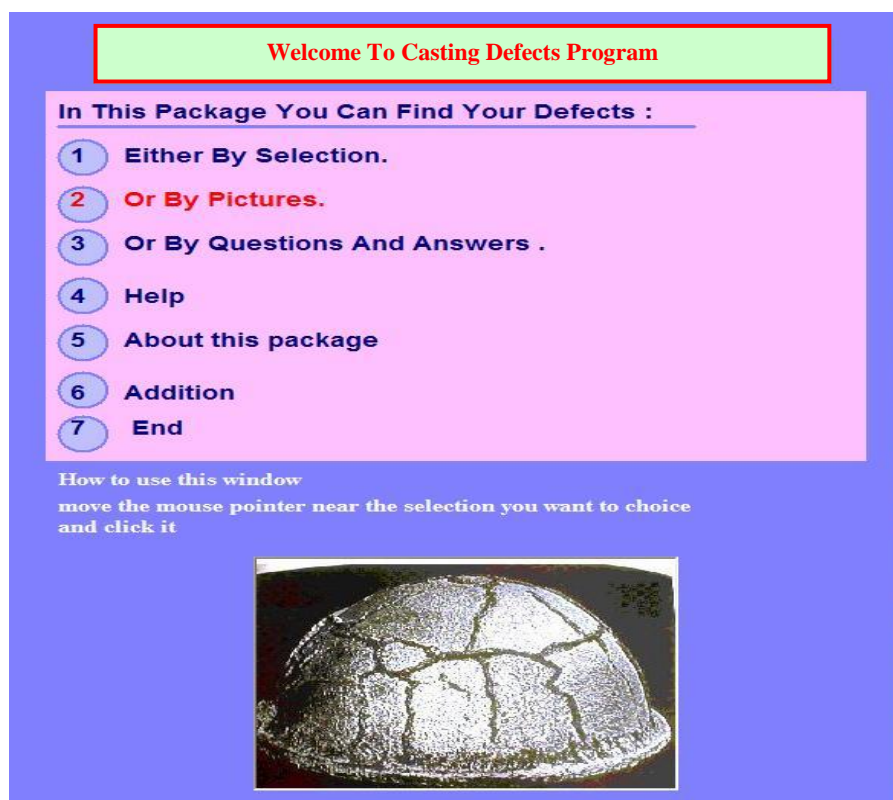


**Fig. (26) The samples of the second defect**

selection by picture

Determine by correct choice if your defect external or internal or you don't know :

is the defect  or  or

Determine whether you used alloys or steel casting

is it

**casting defects**

<input type="button" value="metallic projections"/>	<input type="button" value="Group A"/>
<input type="button" value="cavities"/>	<input type="button" value="Group B"/>
<input type="button" value="discontinous"/>	<input type="button" value="Group C"/>
<input type="button" value="defective surface"/>	<input type="button" value="Group D"/>
<input type="button" value="incomplete casting"/>	<input type="button" value="Group E"/>
<input type="button" value="incorrect dimensions of shape"/>	<input type="button" value="Group F"/>
<input type="button" value="inclusions or stractural anamolies"/>	<input type="button" value="Group G"/>

Fig. (27) The choice of the type of defect and castings

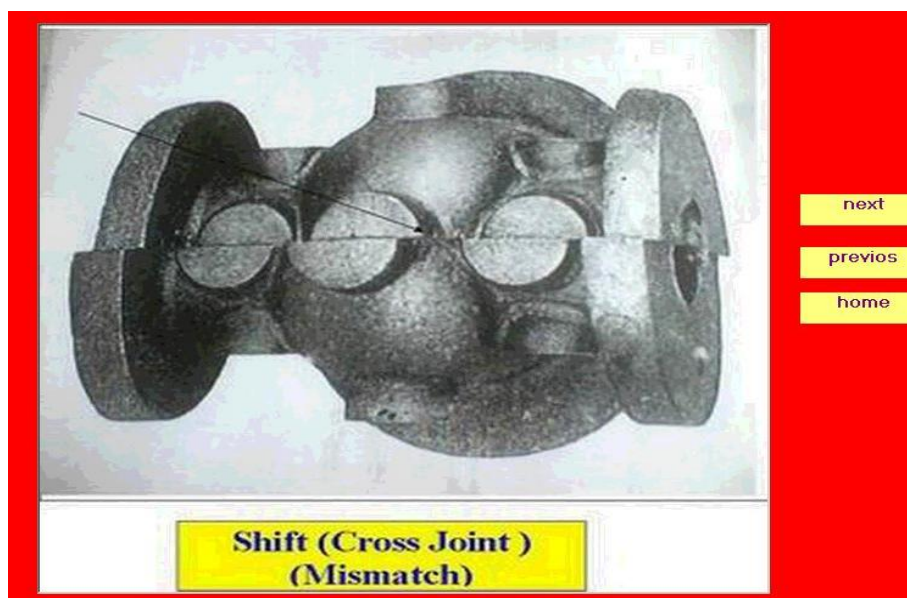


Fig. (28) The picture of the same defect

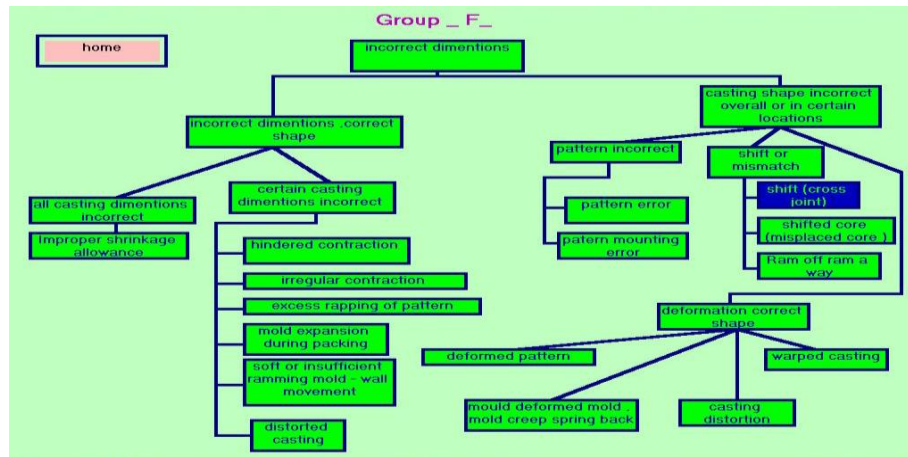


Fig. (29) The general classification of the mean defect

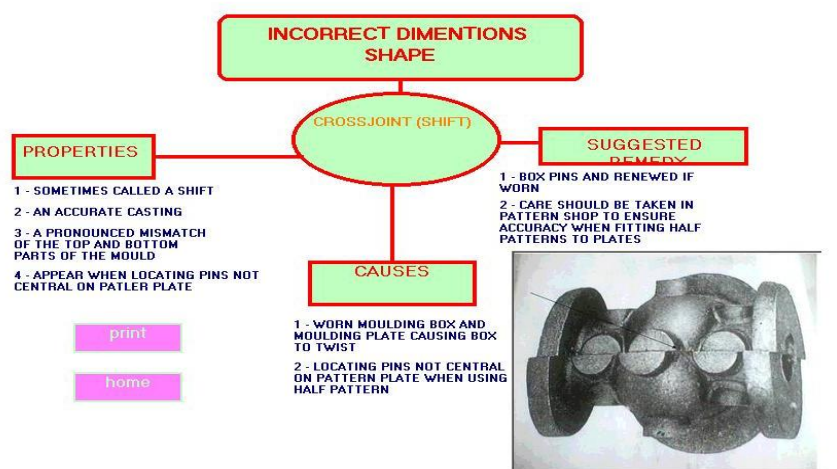


Fig. (30) The final result of the mean defect

### Application Of The Third Method To Find (gas holes) Defect

The third method is used to find the defect in third sample **Fig.(31)**. This method depend on questions and answers **Fig.(32)** ,according to the steps of program and by choosing the group of defect between the seven groups listed **Fig.(33)**.It is seen that the group is (B) called cavities ,when following the questions related with the properties of defects **Fig.(34),Fig.(35)** ,the results appear in **Fig.(36)** with the classification of this defect .It is cavity with generally rounded smooth wall internal and called (Blow holes pin holes) ,finally **Fig.(37)** give the properties, causes and suggested remedy.

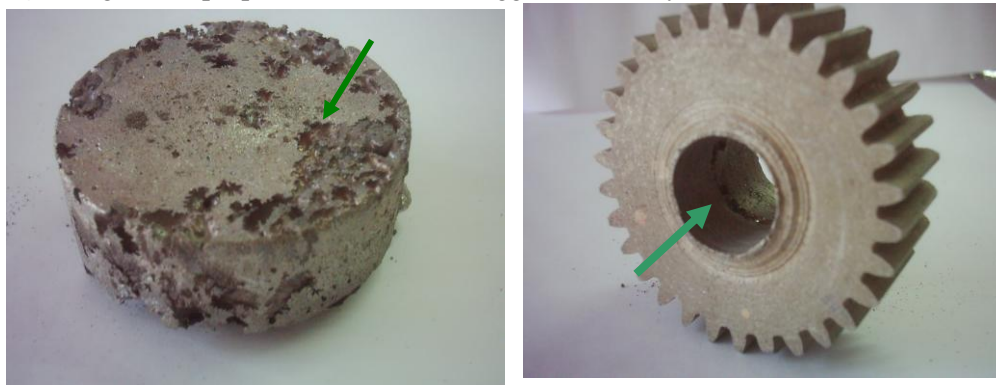


Fig. (31) The samples of the third defect



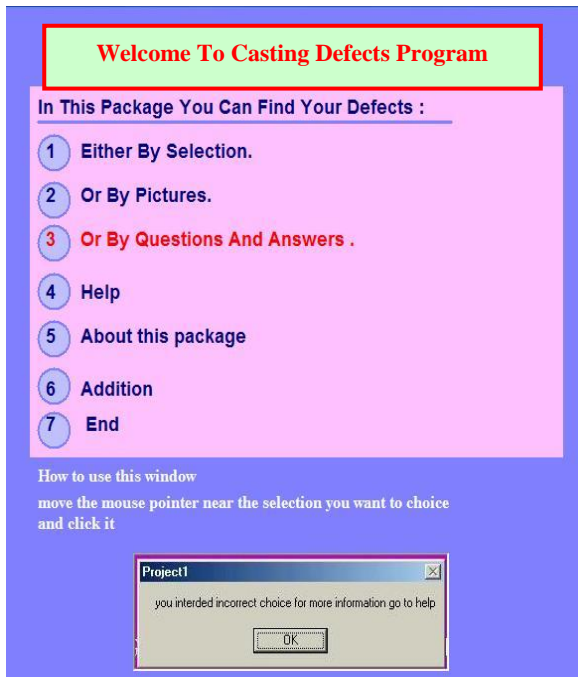


Fig. (32) The choice of third method

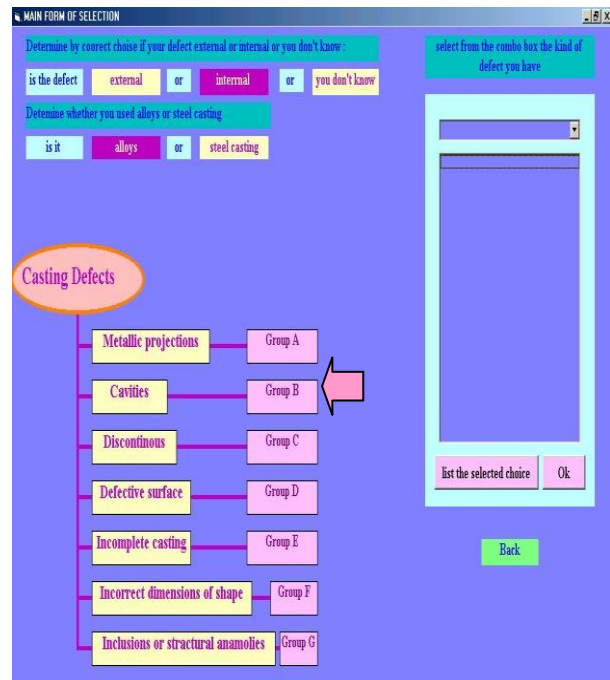


Fig. (33) The choice of the types of the defect and castings and the groups

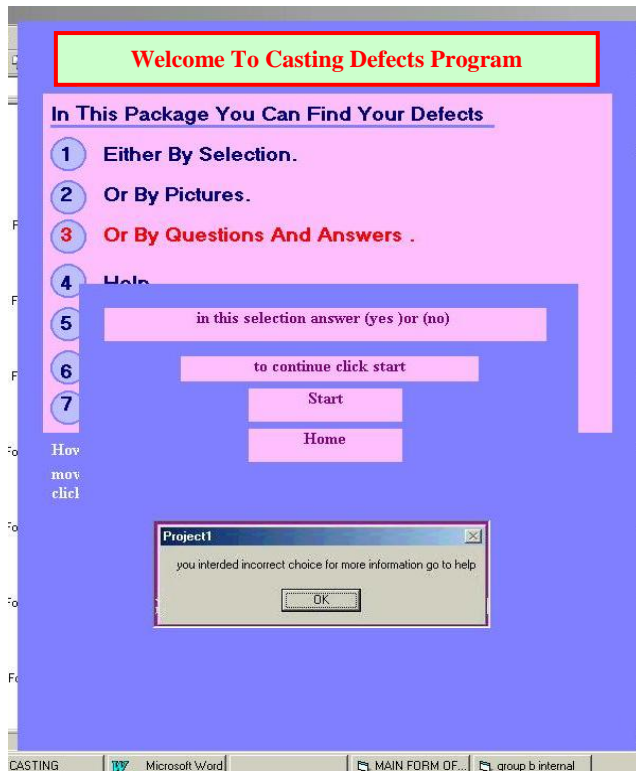


Fig. (34) The starting of third method

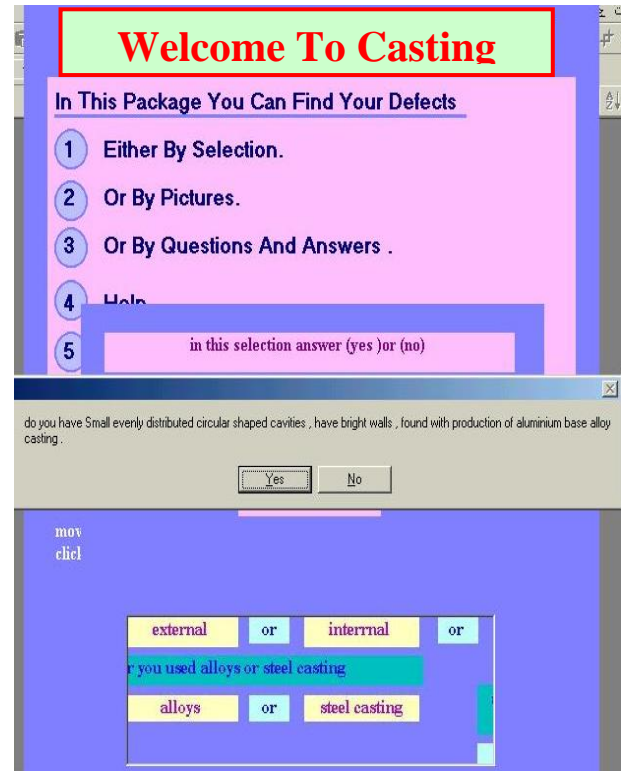


Fig. (35) The questions of third method

## DISCUSSION

It is seen after this verification to the program that it is useful in diagnostic the defects. It is save time for the user and manufacturer by reduce the time of searching because it give the limitations of properties of the defects in different castings with simple search when following the steps in every method. Although the program contains large number of defects but the classification that put and the methods of diagnose make the program useful and practically . The program helps to give right results for large number of defective castings in order to help the user to reach to properly process of casting and then for less-defective castings. It is clear from the previous applications that the diagnostic of the defect by this information system among this number of defects is with good accuracy and speed.

## CONCULUSIONS

- There are a great need to make useful program to deal with the large number of casting therefore in this research an information system is design by use visual basic language in order to put these defects in suitable classification to make a methods for diagnostic.
- The program is with high speed for diagnostic of casting defects when compared with diagnostic from the experts that require long time and perhaps being wrong.
- The program information is a result of long experiences with hard work on casting defects, from many companies, in this program the information are assembled from large references then put them in information system.
- The program use general classification of defects then it is divided to sub division. The user can choose one of the four methods established to give him the path that he led to the final result.
- It is seen that the method of picture is the simplest one because it need only looking and make comparison.
- The methods of diagnostic in this program are simple to give the user final results of searching about the defects properties, causes and remedy without need a great experience to deal with it.

## REFERENCES

- British Standard terminology. « **Internal Defects In Castings** » as revealed by radiography B.S 1956 2737. (1956).
- Groover P.Mikell « **Fundamentals Of Modern Manufacturing** ». Prentice Hall, Vpper Saddle River, New Jersey 07458, A simon and Schuster Company. (1996)
- Jean – christophe Gebelin, Aleksander M. Cendrowicz Mark R. Jolly.
- « **Modelling Of The Wax Injection Process For The Investment Casting Process, Prediction Of Defects** » IRC in Materials processing, The university of Birmingham edgbaston, Birmingham B<sub>15</sub> 2TT, UK, International conference on CFD in the Minerals and process Industries (2003).



- Mark Nagel, Ian kay. « **Analysis And Reduction Of Casting Defects** » Cast Metals Institute (CMI) INC, AFS Headquarters Schaumburg, Illinois, 1695 N. Penny Lane. (2005)
- Mery Domingo, Thomas Jaeger, Dieter Filbert « **Review Of Methods For Automated Recognition Of Casting Defects** » (2002).
- Naro R.L ASI International « **Porosity Defects In Iron Casting From Mold-Metal Interface Reactions** » Inc. Cleveland, Ohio. Silver Anniversary paper, Div.5. (2002)
- Sirvio Matti, Sami Vapalahti, Jukka Vainola «**Complete Simulation Of High Pressure Die Casting Process In Order To Reduce Castings Defects** » VTT Industrial Systems, Control Team, P.O, Box 1702, Fin -020441 Finland (2000).
- Technical Council, Sub – Committee « **ATLAS Of Defects** » T. S. G of the Revised and Enlarged edition. ( 1950)



## A STUDY OF FREE VIBRATION AND FATIGUE FOR CROSS-PLY CLOSED CYLINDRICAL SHELLS USING GENERAL THIRD SHELL THEORY (GTT)

Dr. Muhsen J. Jweeg  
Nahrain University  
Mech. Eng. Dep.

Dr. Wedad I. Alazzawy  
Baghdad University  
Mech. Eng. Dep.

### ABSTRACT:

Free vibration solution will be developed for laminated simply supported closed cylindrical shells. This solution is obtained using General Third Shell Theory (G.T.T.). Also the critical in-plane fatigue load is studied and the required equilibrium equations are developed, the effects of tension or compression in-plane load on the natural frequencies are discussed also. The natural frequencies and in-plane fatigue load results are very close to those obtained by other researchers.

### الخلاصة:

الاهتزاز الحر لقشريات طباقية مسندة بصورة بسيطة تم تطوير حل له باستخدام نظرية القشريات العامة الرتبة الثالثة. كذلك تم دراسة حمل الكلال الحرج في المستوي كما تم تطوير معادلات التوازن الضرورية، كذلك تم مناقشة تأثير حمل الانضغاط أو التمدد في المستوي على التردد الطبيعي. نتائج التردد الطبيعي وحمل الكلال في المستوي قريبة جدا لتلك المحصل عليها من قبل باحثين اخرين.

### KEYWORDS:

**Free vibration, fatigue, cross-ply, cylindrical shells, general third shell theory.**

### INTRODUCTION:

The last decay is marked by a transition in use of composites has expanded from aerospace and defense applications into a wider commercial arena. Today composites are used in the power generation industry, the automotive industry, biomedical engineering and various consumer goods. In service similarly to other materials, advanced composites age, suffer physical or chemical degradation and accumulate micro mechanical damage. As cured laminated composites cool to room temperature, stresses develop at the laminae and fiber-matrix interfaces due to the different consistent expansion characteristics. Hence, initially stable composites could become unstable in an actual space application. In all above applications, it is important to achieve low weight, high strength, stiffness and safety which can be achieved by good fatigue performance. Most of structural theories used till now to characterize the behavior of composite laminates fall into the category of equivalent single

layer (ESL) theories. In these theories the material properties of constituent layers are “smeared” to form a hypothetical single layer whose properties are equivalent to through-the-thickness integrated sum of its constituents. This category of theories have been found to be adequate in predicting global response characteristics of laminates, like maximum deflection, maximum stresses, fundamental frequencies, forced response, or critical buckling load. Continuum based theories give an analytical (3-D) elasticity solutions for beam, plate and shells but it cumbersome. High order shell theories are those in which the transverse strains are accounted. The (in-plane) fatigue loading (presented as buckling load in present work) of shell of revolution such as cylinder or conical has been studied by many researchers.

(**Altan Kayran & Vinson 1990**) presented an analysis for the free vibration characteristics of isotropic and laminated composite truncated circular shells including transverse shear deformation. All components of translatory and rotatory inertia are included. The applicability of linear shell theory due to Reissner is assumed, and governing equations are solved for the natural frequencies and mode shapes by using a combination of modal iteration and transfer matrix approach for different boundary conditions.

(**Narita et al 1992**) developed a theoretical method for solving the free vibration angle-ply laminated cylindrical shells. The angle-ply laminated shell is macroscopically modeled as a thin shell of General anisotropy by using the classical lamination theory. Shell theory is minimized by following the Ritz procedure, and arbitrary combinations of boundary conditions at both ends are accommodated by introducing newly developed admissible functions.

(**Liyong Tong 1993**) used a particularly convenient coordinate system, a simple and exact solution is obtained directly for the Donnell-type governing equations of the free vibration of composite laminated conical shells, with orthotropic stretching-bending coupling. The solution is in the form of a power series, and its convergence condition is investigated.

(**Tong 1996**) obtained an analytical solution in the form of a power series for the three governing equations of free vibrations of axially loaded orthotropic conical shells. Numerical results are presented for the frequency parameters and associated circumferential wave numbers of axially loaded shells with different geometric and material parameters and under two types of boundary conditions.

(**Korjakin et al (1998)**) investigated the damping of free vibrations of laminated composite conical shells. Finite element analysis of conical shells is performed by using first-order shear deformation theory (FOSDT). Based on proposals of other researchers a damping model is developed in connection with energy method (EM) and applied in order to calculate the modal loss factors of laminated composite conical shells.

(**Xi et al 1999**) investigated the effects of shear non-linearity on free vibration of laminated composite shell of revolution using a semi-analytical method based on Reissner-Mindlin shell theory. The coupling between symmetric and anti-symmetric vibration modes of the shell is considered in the shear deformable shell element.

(**Pinto Correia et al 2001**) presented a numerical method for the structural analysis of laminated conical shell panels using a quadrilateral isoperimetric finite element based on the higher order shear deformation theory.

(**Werner Hufenbach et al 2002**) developed analytical solution for lightweight design using dynamically loaded fiber-reinforced composite shells. The analytic results were fully corroborated by accompanying FE calculations for special lay-ups.

(**Lee et al 2002**) used the finite element method based on Hellinger-Reissner principle with independent strain to analyze the vibration problem of cantilevered twisted plates, cylindrical and conical laminated shells.



(**Kabir et al 2003**) presented a hitherto unavailable analytical solution to the boundary value problem of the free vibration response of shear flexible antisymmetric cross-ply laminated cylindrical shell, using (FSDT) theory.

(**Young-Shin Lee et al 2003**) investigated the free vibration analysis of a laminated composite cylindrical shell with an interior rectangular plate by analytical and experimental methods. The frequency equations of vibration of the shell including the plate are formulated by using the reacceptance method.

(**Darvizeh et al 2005**) presented a calculation of overall dynamic response of thin orthotropic cylindrical shells. Due to the obvious importance of the effects of transverse shear deformation and rotary inertia, these terms are included in the analysis. The exact method is modified to predict the dynamic behavior of an orthotropic circular cylindrical shell.

The (in-plane) fatigue loading of shell of revolution such as cylinder or conical has been studied by many researchers. (**George J. Simites & John S. Anastasiadis 1992**) developed a higher order theory, which includes initial geometric imperfections and transverse shear effects for a laminated cylindrical configuration under the actions of lateral pressure, axial compression, and eccentrically applied torsion.

(**Seishi Yamada & Croll 1993**) used nonlinear Ritz analysis to investigate the elastic (in-plane) loading behavior of pressure loaded cylinders. Careful analysis of the energy changes during the loading process allows definition of a reduced stiffness theoretical model.

(**NG et al 1998**) studied the dynamic stability of then, laminated cylindrical shells under combined static and periodic axial forces using Love's classical theory of thin shells. A normal-mode expansion of the equations of motion yields a system of Mathieu-Hill equations. Bolton's method is then employed to obtain the dynamic instability regions. The present study examines the dynamic stability of antisymmetric cross-ply circular, cylindrical shells of different lamination schemes. The effect of the magnitude of the axial load on the instability regions is also examined.

(**NG et al 1998**) investigated the parametric resonance of rotating cylindrical shells periodic axial loading. The formulation is based on the dynamic version of Connell's equations for thin rotating cylindrical shells. A modified assumed-mode method is used to reduce the partial differential equation of motion to a system of coupled second order differential equations with periodic collisions of the Mathieu Hill type. The instability regions are determined based on the principle of Bolton's method. Or special interests here are the effects of the centrifugal and Carioles forces on the instability regions which were examined in detail.

(**Romil Tanov et al 1999**) presented the results obtained while investigating the behavior of cylindrical laminated shells under suddenly applied lateral pressure. The investigations were based on a finite-element approach using an explicit time integration scheme. The Budianski- Roth and phase- plane criteria were used to assess (in-plane) loading.

(**Meyers & Hyer 1999**) used results from semi analytical predictions and experiments to study the response of composite cylinders with elliptical cross sections loaded axially to a significant percentage of their (in-plane) loading load. The semi analytical approach is based on the methods of Marguerre, Rayleigh-Ritz, and Kantorovich.

(**Youngjin Chung (2001)** aimed in this study, is to improve the strength of conical shells and reduce the weight of the structure. Buckling of composite conical shells subjected to combine axial loading, external pressure, and bending is investigated using energy and finite element methods.

(**Andrea Spagnoli 2001**) studied the local shell and stringer buckling modes and global buckling mode in conical shells under axial compression through a linear eigenvalue finite element analysis. In order to examine buckling modes in isolation as well as competing

modes together, use is made of different finite element model, including discrete and smeared models.

(**Geier et al 2002**) studied the (in-plane) loading load of laminated cylinders which strongly depend on the position of the differently oriented layers, his work deals with two different laminated orthotropic cylinders with opposite stacking sequence of the laminate layers. Analytical and semi analytical method have been used to predict the (in-plane) loading loads, the results are compared with those tested.

(**Hunt et al 2003**) presented a hypothesis for prediction of the circumferential wave number of (in-plane) loading of thin axially-compressed cylindrical shell, based on the addition of a length effect to classical (Koiter circle) critical load result.

(**Sofiyev 2005**) provided an analytical solution for stability behavior of cylindrical shell made of compositionally graded ceramic-metal materials under axial compressive loads varying as a power function of time. The material properties of compositionally graded shells are assumed to vary continuously through the thickness of the shell according to arbitrary distribution of the volume fraction of the constituents. The fundamental equations for thin shells of compositionally graded ceramic-metal material are obtained Loves shell theory.

(**Azam Tafreshi 2005**) carried out a series of finite element analyses on the delaminated composite cylindrical shell subjected to combined axial compression and pressure by which the delamination thickness and length, material properties and stacking sequence are varied. The characteristics of (in-plane) loading and post (in-plane) loading behavior of delaminated composite cylindrical shell are investigated.

In present work, a unified third order theory (G.T.T.) to evaluate the performance of some displacement based (ESL) theories in natural frequencies and fatigue characteristics in laminated composite cylindrical shell.

## EQUATIONS OF MOTION:

In present study high-order theory displacement field is:

$$\begin{aligned} u(x, \theta, z, t) &= u_0(x, \theta, t) + z \times \phi_1(x, \theta, t) + z^2 \times \psi_1(x, \theta, t) + z^3 \times \theta_1(x, \theta, t) \\ v(x, \theta, z, t) &= v_0(x, \theta, t) + z \times \phi_2(x, \theta, t) + z^2 \times \psi_2(x, \theta, t) + z^3 \times \theta_2(x, \theta, t) \\ w(x, \theta, z, t) &= w_0(x, \theta, t) + z \times \psi_3(x, \theta, t) + z^2 \times \theta_3(x, \theta, t) \end{aligned} \quad \dots\dots\dots(1)$$

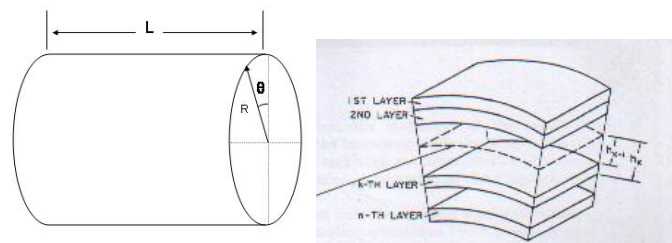


**Figure (1): Coordinate system and structure of laminated cylinder.**



$$\begin{aligned}
\varepsilon_1 &= \frac{\partial u}{\partial x} \\
\varepsilon_2 &= \frac{1}{R} \times \left( \frac{\partial v}{\partial \theta} \right) + \frac{w}{R} \\
\varepsilon_3 &= \frac{\partial w}{\partial z} \\
\varepsilon_6 &= \frac{1}{R} \times \left( \frac{\partial u}{\partial \theta} \right) + \frac{\partial v}{\partial x} \\
\varepsilon_5 &= \frac{\partial u}{\partial z} + \frac{\partial w}{\partial x} \\
\varepsilon_4 &= \frac{\partial v}{\partial z} - \frac{v}{R} + \frac{1}{R} \times \left( \frac{\partial w}{\partial \theta} \right)
\end{aligned} \quad \dots \dots \dots (2)$$

Assuming vanishing transverse shear stress at top and bottom of laminated composite layers, and hence transverse strain also vanishes, so:

$$\begin{aligned}
\varepsilon_3(x, \theta, \pm h/2, t) &= \frac{\partial u}{\partial z} + \frac{\partial w}{\partial x} = 0 \\
\varepsilon_4(x, \theta, \pm h/2, t) &= \frac{\partial v}{\partial z} - \frac{v}{R} + \frac{1}{R} \times \left( \frac{\partial w}{\partial \theta} \right) = 0
\end{aligned} \quad \dots \dots \dots (3)$$

According to Hamilton's Principles:

$$\int_{t_2}^{t_1} (\delta U - \delta K) \delta t = 0 \quad \dots \dots \dots (4)$$

Where:

$$\begin{aligned}
\delta U &= \iint_{A_z} (\sigma_1 \delta \varepsilon_1 + \sigma_2 \delta \varepsilon_2 + \sigma_3 \delta \varepsilon_3 + \sigma_6 \delta \varepsilon_6 + \sigma_5 \delta \varepsilon_5 + \sigma_4 \delta \varepsilon_4) \times R d\theta dz dx \\
\iint_{A_z} \sigma_1 \delta \varepsilon_1 &= R \times \left\{ \iint_{x \theta} -\frac{\partial N_1}{\partial x} \delta u_0 - \frac{\partial M_1}{\partial x} \delta \phi_1 - \frac{1}{2} \times \frac{\partial^2 P_1}{\partial x^2} \delta \psi_3 + \left( \frac{4}{3h^2} \right) \times \frac{\partial S_1}{\partial x} \delta \phi_1 - \left( \frac{4}{3h^2} \right) \times \frac{\partial^2 S_1}{\partial x^2} \delta w_0 \right. \\
&\quad \left. - \left( \frac{1}{3} \right) \times \frac{\partial^2 S_1}{\partial x^2} \delta \theta_3 \right\} d\theta dx \\
\iint_{A_z} \sigma_2 \delta \varepsilon_2 &= R \times \left\{ \iint_{x \theta} -\frac{\partial N_2}{\partial \theta} \delta v_0 + N_2 \delta w_0 - \frac{\partial M_2}{\partial \theta} \delta \phi_2 + M_2 \delta \psi_3 - \frac{1}{2R} \times \frac{\partial^2 P_1}{\partial \theta^2} \delta \psi_3 + P_2 \delta \theta_3 + \left( \frac{4}{3h^2} \right) \times \frac{\partial S_2}{\partial \theta} \delta \phi_2 - \right. \\
&\quad \left. \left( \frac{4}{3h^2 R} \right) \times \frac{\partial S_2}{\partial \theta} \delta v_0 - \left( \frac{4}{3h^2 R} \right) \times \frac{\partial^2 S_2}{\partial \theta^2} \delta w_0 - \left( \frac{1}{3R} \right) \times \frac{\partial^2 S_2}{\partial \theta^2} \delta \theta_3 \right\} d\theta dx \\
\iint_{A_z} \sigma_3 \delta \varepsilon_3 &= R \times \left\{ \iint_{x \theta} N_3 \delta \psi_3 + 2M_3 \delta \theta_3 \right\} d\theta dx \\
\iint_{A_z} \sigma_6 \delta \varepsilon_6 &= R \times \left\{ \iint_{x \theta} -\left( \frac{1}{R} \right) \frac{\partial N_6}{\partial \theta} \delta u_0 - \frac{\partial N_6}{\partial x} \delta v_0 - \left( \frac{1}{R} \right) \frac{\partial M_6}{\partial \theta} \delta \phi_1 - \frac{\partial M_6}{\partial x} \delta \phi_2 - \frac{1}{R} \times \frac{\partial^2 P_6}{\partial \theta \partial x} \delta \psi_3 + \left( \frac{4}{3h^2} \right) \times \right. \\
&\quad \left. \left[ \frac{\partial S_6}{\partial x} \delta \phi_2 - \left( \frac{2}{R} \right) \times \frac{\partial^2 S_6}{\partial x \partial \theta} \delta w_0 - \left( \frac{h^2}{2R} \right) \times \frac{\partial^2 S_6}{\partial x \partial \theta} \delta \theta_3 - \left( \frac{1}{R} \right) \frac{\partial S_6}{\partial x} \delta v_0 + \left( \frac{1}{R} \right) \frac{\partial S_6}{\partial \theta} \delta \phi_1 \right] \right\} d\theta dx \\
\iint_{A_z} \sigma_5 \delta \varepsilon_5 &= R \times \left\{ \iint_{x \theta} Q_5 \delta \phi_1 - \frac{\partial Q_5}{\partial x} \delta w_0 - \left( \frac{4}{h^2} \right) K_5 \delta \phi_1 + \left( \frac{4}{h^2} \right) \frac{\partial K_5}{\partial x} \delta w_0 \right\} d\theta dx \\
\iint_{A_z} \sigma_4 \delta \varepsilon_4 &= R \times \left\{ \iint_{x \theta} Q_4 \delta \phi_2 - \frac{Q_4}{R} \delta v_0 - \left( \frac{1}{R} \right) \frac{\partial Q_4}{\partial \theta} \delta w_0 - \left( \frac{4}{h^2} \right) K_4 \delta \phi_2 + \left( \frac{4}{h^2} \right) K_4 \delta v_0 + \left( \frac{4}{h^2 R} \right) \frac{\partial K_4}{\partial \theta} \delta w_0 \right\} d\theta dx
\end{aligned}$$

Where:

$$(Ni, Mi, Pi, Si) = \int \sigma_i(1, z, z^2, z^3) \times dz \longrightarrow i = 1, 2, 3, 6 \quad \dots \dots \dots (5)$$

$$(Qi, Ki) = \int \sigma_i(1, z^2) \times dz \longrightarrow i = 4, 5$$

$$\delta K = - \int \int \int_V R \rho \left( \ddot{u} \delta u + \ddot{v} \delta v + \ddot{w} \delta w \right) dz dx d\theta dt$$

$$\frac{\partial N_1}{\partial x} + \left( \frac{1}{R} \right) \frac{\partial N_6}{\partial \theta} = I_1 \ddot{u} + I_2 \ddot{\phi}_2 - \left( \frac{I_3}{2} \right) \frac{\partial \ddot{\psi}_3}{\partial x} - \left( \frac{4I_4}{3H^2} \right) \left( \ddot{\phi}_1 + \frac{\partial \ddot{w}}{\partial x} \right) - \left( \frac{I_4}{3} \right) \frac{\partial \ddot{\theta}_3}{\partial x} \quad \dots \dots \dots (6)$$

$$\frac{\partial N_2}{\partial \theta} + R \frac{\partial N_6}{\partial x} + Q_4 - \left( \frac{4}{H^2} \right) K_4 + \left( \frac{4}{3H^2} \right) \left( \left( \frac{1}{R} \right) \frac{\partial S_2}{\partial \theta} + \frac{\partial S_6}{\partial x} \right) = \left( R I_2 - \left( \frac{4R I_4}{3H^2} \right) - \left( \frac{16I_7}{9H^4 R} \right) + \left( \frac{4I_5}{3H^2} \right) \right) \ddot{\phi}_2 \quad \dots \dots \dots (7)$$

$$+ \left( R I_1 + \left( \frac{8I_4}{3H^2} \right) + \left( \frac{16I_7}{9H^4 R} \right) \right) \ddot{v} - \left( \left( \frac{I_3}{2} \right) + \left( \frac{4I_6}{6RH^2} \right) \right) \frac{\partial \ddot{\psi}_3}{\partial \theta} + \left( \left( \frac{4I_4}{3H^2} \right) - \left( \frac{16I_7}{9H^4 R} \right) \right) \frac{\partial \ddot{w}}{\partial \theta} - \left( \frac{I_4}{3} + \left( \frac{4I_7}{9H^2 R} \right) \right) \frac{\partial \ddot{\theta}_3}{\partial x}$$

$$\left( \frac{4}{3H^2} \right) \left( \frac{1}{R} \frac{\partial^2 S_2}{\partial \theta^2} + R \frac{\partial^2 S_1}{\partial x^2} + 2 \frac{\partial^2 S_6}{\partial x \partial \theta} \right) - N_2 - \left( \frac{4}{H^2} \right) \left( \frac{\partial K_4}{\partial \theta} + R \frac{\partial K_5}{\partial x} \right) + \left( \frac{\partial Q_4}{\partial \theta} + R \frac{\partial Q_5}{\partial x} \right) + N_5 \frac{\partial^2 w}{\partial x^2} = \left( \left( \frac{4I_4}{3H^2} \right) + \left( \frac{16I_7}{9H^4 R} \right) \right) \frac{\partial \ddot{v}}{\partial \theta} \quad \dots \dots \dots (8)$$

$$+ \left( \frac{4I_4}{3H^2} \right) \frac{\partial \ddot{u}}{\partial x} + \left( - \left( \frac{16I_7}{9H^4 R} \right) + \left( \frac{4I_5}{3H^2} \right) \right) \frac{\partial \ddot{\phi}_2}{\partial \theta} + R I_2 \ddot{\psi}_3 - \left( \frac{4I_6}{6RH^2} \right) \frac{\partial^2 \ddot{\psi}_3}{\partial \theta^2} + \left( \frac{4I_4}{3H^2} \right) - \left( \frac{16I_7}{9H^4} \right) \left( \left( \frac{1}{R} \right) \frac{\partial^2 \ddot{w}}{\partial \theta^2} + R \frac{\partial^2 \ddot{w}}{\partial x^2} \right)$$

$$- \left( \frac{4I_7}{9H^2 R} \right) \left( R \frac{\partial^2 \ddot{\theta}_3}{\partial x^2} + \frac{1}{R} \frac{\partial^2 \ddot{\theta}_3}{\partial x^2} \right) + R \left( - \left( \frac{16I_7}{9H^4 R} \right) + \left( \frac{4I_5}{3H^2} \right) \right) \frac{\partial \ddot{\phi}_1}{\partial x} + R I_1 \ddot{w} + R I_3 \ddot{\theta}_3$$

$$R \frac{\partial M_1}{\partial x} - \left( \frac{4R}{3H^2} \right) \frac{\partial S_1}{\partial x} + \frac{\partial M_6}{\partial \theta} - \left( \frac{4R}{3H^2} \right) \frac{\partial S_6}{\partial \theta} - R Q_5 + \left( \frac{4R}{H^2} \right) K_5 = \left( R I_2 - \frac{4R I_4}{3H^2} \right) \ddot{u} + \left( R I_3 - \frac{8R I_5}{3H^2} + \frac{16R I_7}{9H^4} \right) \ddot{\phi}_1 + \quad \dots \dots \dots (9)$$

$$\left( \frac{4R I_6}{6H^2} - \frac{R I_4}{2} \right) \frac{\partial \ddot{\psi}_3}{\partial x} + \left( - \frac{8R I_5}{3H^2} + \frac{16R I_7}{9H^4} \right) \frac{\partial \ddot{w}}{\partial x} + \left( - \frac{R I_5}{3} + \frac{4R I_7}{9H^2} \right) \frac{\partial \ddot{\theta}_3}{\partial x}$$

$$\frac{\partial M_2}{\partial \theta} - \left( \frac{4R}{3H^2} \right) \frac{\partial S_2}{\partial \theta} + R \frac{\partial M_6}{\partial x} - \left( \frac{4R}{3H^2} \right) \frac{\partial S_6}{\partial x} - R Q_4 + \left( \frac{4R}{H^2} \right) K_4 = \left( R I_2 - \frac{16R I_7}{9H^4} \right) \ddot{v} + \left( R I_3 - \frac{8R I_5}{3H^2} + \frac{16R I_7}{9H^4} \right) \ddot{\phi}_2 + \quad \dots \dots \dots (10)$$

$$\left( \frac{4I_6}{6H^2} - \frac{I_4}{2} \right) \frac{\partial \ddot{\psi}_3}{\partial \theta} + \left( - \frac{4I_5}{3H^2} + \frac{16I_7}{9H^4} \right) \frac{\partial \ddot{w}}{\partial \theta} + \left( - \frac{I_5}{3} + \frac{4I_7}{9H^2} \right) \frac{\partial \ddot{\theta}_3}{\partial \theta}$$

$$\left( \frac{R}{2} \right) \frac{\partial^2 P_1}{\partial x^2} + \left( \frac{1}{2R} \right) \frac{\partial^2 P_2}{\partial \theta^2} + \frac{\partial^2 P_6}{\partial x \partial \theta} - R N_3 - M_2 = \left( \frac{R I_3}{2} \right) \frac{\partial \ddot{u}}{\partial x} + \left( \frac{R I_4}{2} - \frac{4R I_6}{6H^2} \right) \frac{\partial \ddot{\phi}_1}{\partial x} + \left( \frac{I_3}{2} + \frac{4I_6}{6RH^2} \right) \frac{\partial \ddot{v}}{\partial \theta} \quad \dots \dots \dots (11)$$

$$- \left( \frac{R I_5}{4} \right) \frac{\partial^2 \ddot{\psi}_3}{\partial x^2} - \left( \frac{I_5}{4R} \right) \frac{\partial^2 \ddot{\psi}_3}{\partial \theta^2} + R I_3 \ddot{\psi}_3 + \left( - \frac{2R I_6}{3H^2} \right) \frac{\partial^2 \ddot{w}}{\partial x^2} + \left( - \frac{4I_6}{6RH^2} \right) \frac{\partial^2 \ddot{w}}{\partial \theta^2} + R I_2 \ddot{w} + \left( - \frac{R I_6}{6} \right) \frac{\partial^2 \ddot{\theta}_3}{\partial x^2} - \left( \frac{I_6}{6R} \right) \frac{\partial^2 \ddot{\theta}_3}{\partial \theta^2}$$

$$+ R I_4 \ddot{\theta}_3 + \left( \frac{I_4}{2} - \frac{4I_6}{6H^2} \right) \frac{\partial \ddot{\phi}_2}{\partial \theta}$$

$$\left( \frac{R}{3} \right) \frac{\partial^2 S_1}{\partial x^2} + \left( \frac{1}{3R} \right) \frac{\partial^2 S_2}{\partial \theta^2} + \left( \frac{2}{3} \right) \frac{\partial^2 S_6}{\partial x \partial \theta} - 2R M_3 - P_2 = \left( \frac{R I_4}{3} \right) \frac{\partial \ddot{u}}{\partial x} + \left( \frac{R I_5}{3} - \frac{4R I_7}{9H^2} \right) \frac{\partial \ddot{\phi}_1}{\partial x} + \left( \frac{I_4}{3} + \frac{4I_7}{9RH^2} \right) \frac{\partial \ddot{v}}{\partial \theta} \quad \dots \dots \dots (12)$$

$$- \left( \frac{R I_6}{6} \right) \frac{\partial^2 \ddot{\psi}_3}{\partial x^2} - \left( \frac{I_6}{6R} \right) \frac{\partial^2 \ddot{\psi}_3}{\partial \theta^2} + R I_4 \ddot{\psi}_3 + \left( - \frac{4R I_7}{9H^2} \right) \frac{\partial^2 \ddot{w}}{\partial x^2} + \left( - \frac{4I_7}{9RH^2} \right) \frac{\partial^2 \ddot{w}}{\partial \theta^2} + R I_3 \ddot{w} + \left( - \frac{R I_7}{9} \right) \frac{\partial^2 \ddot{\theta}_3}{\partial x^2} - \left( \frac{I_7}{9R} \right) \frac{\partial^2 \ddot{\theta}_3}{\partial \theta^2}$$

$$+ R I_5 \ddot{\theta}_3 + \left( \frac{I_5}{3} - \frac{4I_7}{9H^2} \right) \frac{\partial \ddot{\phi}_2}{\partial \theta}$$

The resultants forces-displacement components relations are:

$$N_1 = \int \sigma_1 dz = \int (Q_{11} \varepsilon_1 + Q_{12} \varepsilon_2 + Q_{13} \varepsilon_3 + Q_{16} \varepsilon_6) dz \quad \dots \dots \dots (13)$$

From the constitutive relations of the kth lamina:

$$\begin{Bmatrix} \sigma_1 \\ \sigma_2 \\ \sigma_3 \\ \sigma_6 \end{Bmatrix} = \begin{bmatrix} Q_{11} & Q_{12} & Q_{13} & Q_{16} \\ Q_{21} & Q_{22} & Q_{23} & Q_{26} \\ Q_{31} & Q_{32} & Q_{33} & Q_{36} \\ Q_{61} & Q_{62} & Q_{63} & Q_{66} \end{bmatrix} \times \begin{Bmatrix} \varepsilon_1 \\ \varepsilon_2 \\ \varepsilon_3 \\ \varepsilon_6 \end{Bmatrix} \quad \dots \dots \dots (14)$$

And:

$$\begin{Bmatrix} \sigma_4 \\ \sigma_5 \end{Bmatrix} = \begin{bmatrix} Q_{44} & Q_{45} \\ Q_{54} & Q_{55} \end{bmatrix} \times \begin{Bmatrix} \varepsilon_4 \\ \varepsilon_5 \end{Bmatrix} \dots\dots\dots(15)$$

Substituting the resultants forces in motion-equations and then the assumed displacement components according to Navier's Solution (**Reddy J.N 2004**) (for simply supported boundary conditions).

$$\begin{aligned} u_0(x, \theta, z, t) &= \sum_{m=1}^{\infty} \sum_{n=1}^{\infty} A_{mn} \cos \alpha x \sin \beta \theta e^{i \omega t} \\ v_0(x, \theta, z, t) &= \sum_{m=1}^{\infty} \sum_{n=1}^{\infty} B_{mn} \sin \alpha x \cos \beta \theta e^{i \omega t} \\ w_0(x, \theta, z, t) &= \sum_{m=1}^{\infty} \sum_{n=1}^{\infty} C_{mn} \sin \alpha x \sin \beta \theta e^{i \omega t} \\ \phi_1(x, \theta, z, t) &= \sum_{m=1}^{\infty} \sum_{n=1}^{\infty} D_{mn} \cos \alpha x \sin \beta \theta e^{i \omega t} \\ \phi_2(x, \theta, z, t) &= \sum_{m=1}^{\infty} \sum_{n=1}^{\infty} E_{mn} \sin \alpha x \cos \beta \theta e^{i \omega t} \\ \psi_3(x, \theta, z, t) &= \sum_{m=1}^{\infty} \sum_{n=1}^{\infty} F_{mn} \sin \alpha x \sin \beta \theta e^{i \omega t} \\ \theta_3(x, \theta, z, t) &= \sum_{m=1}^{\infty} \sum_{n=1}^{\infty} J_{mn} \sin \alpha x \sin \beta \theta e^{i \omega t} \dots\dots\dots(16) \end{aligned}$$

$$\text{Where } \alpha = \left( \frac{m\pi}{L} \right), \beta = n$$

Developing mass matrix and stiffness matrix from solution of homogeneous equations, eignvalue equation is derived and the natural frequencies of vibration for simply supported cylindrical shell are obtained when solving the later equation:

$$[C] - \omega^2 [M] \{A\} = 0 \dots\dots\dots(17)$$

The failure of laminates cylindrical shell under in-plane fatigue load is studied in this work using G.T.T. theory to calculate the critical (in-plane) fatigue load which cause the failure of fiber or matrix of laminate or both of them, and study the effect of this load on the natural frequencies of the shell. Using the same Navier's solution (putting right side =0) for equations ((6)-(12)) and rearranging the obtained matrices we get:

$$\begin{bmatrix} C_{33} - \alpha^2 N_x & C_{34} & C_{35} & C_{36} & C_{37} & C_{32} & C_{31} \\ C_{43} & C_{44} & C_{45} & C_{46} & C_{47} & C_{42} & C_{41} \\ C_{53} & C_{54} & C_{55} & C_{56} & C_{57} & C_{52} & C_{51} \\ C_{63} & C_{64} & C_{65} & C_{66} & C_{67} & C_{62} & C_{61} \\ C_{73} & C_{74} & C_{75} & C_{76} & C_{77} & C_{72} & C_{71} \\ C_{23} & C_{24} & C_{25} & C_{26} & C_{27} & C_{22} & C_{21} \\ C_{13} & C_{14} & C_{15} & C_{16} & C_{17} & C_{12} & C_{11} \end{bmatrix} \begin{Bmatrix} W \\ \phi \\ \phi \\ \phi \\ \psi \\ \theta \\ V \\ U \end{Bmatrix} = 0 \dots\dots\dots(18)$$

Following the condensation of variables procedure to eliminate the displacement components (U,V, $\phi^1, \phi^2, \psi^3, \theta^3$ ), the critical value of ( $N_x$ ) is obtained.

## **VALIDITY OF THE DEVELOPED EQUATIONS:**

General Third Order Theory (G.T.T.) is employed to investigate its capability level for dynamic analysis of the symmetric and non-symmetric cross-ply laminated cylindrical shells, and compared with other theories used by other researchers such as HSDT, FSDT, CST.

The fundamental natural frequency of laminated closed cylindrical shell are listed for each (L/mR) ratio (for thin shell R/H=100) in **Table (1)** and compared with those obtained by using CST (but without neglecting (z/R)) in (Mohammad S. Qatu 2004), the results obtained by present work give excellent agreement with them, where maximum percentage error is (.127%) (error percentage is taken with relative to the reference results).

**Table (2)** lists the natural frequencies for [0-90] graphite/epoxy closed cylindrical shell with two different thickness ratio (R/H=20 & R/H=500). As can be seen from this table, thicker shells have lower frequency parameter than thinner shells for shorter shells (L/mR=1 and 2). It is interesting to note that the thickness ratio has minimal effects on natural frequencies when n=0 and 1. For n>1, the thickness ratio has a much greater effect. It is also observed that the fundamental frequency occurs at lower value for higher thickness ratios. In all calculation the material properties are as follows:

$$E_1=20E6 \quad E_2=E_3=1.3E6 \quad G_{12}=G_{13}=1.03E6 \quad G_{23}=.9e6 \quad \nu_{12} = \nu_{13} = .3 \quad \nu_{23} = .49 ,$$

$$\text{Frequency parameter} = \Omega = \left( \frac{\omega L^2}{100H} \right) \sqrt{\frac{\rho}{E_2}} .$$

While in **Table (3)**, minimum frequency parameter of laminated cylindrical shell for different lamination type are obtained and compared with other shell theories published in (Reddy and Liu 1985), a good agreement between results of theory GTT and HSDT, maximum relative percentage error is (3.7%), while with FSDT and CST are (3.7%, 17.2%) respectively, as presented in the table, also the frequency parameter is increased when number of layers is increased. For this results material properties are as follows:  $E_1=40 \text{ Gpa}$   $E_2=E_3=1 \text{ Gpa}$   $G_{12}=G_{13}=.6 \text{ Gpa}$   $G_{23}=.5 \text{ Gpa}$   $\nu_{12} = \nu_{13} = .3$   $\nu_{23} = .49$  (L/R)=2 (R/H)

$$=5, \quad \text{frequency parameter} = \Omega = \left( \frac{\omega L^2}{100H} \right) \sqrt{\frac{\rho}{E_2}} , \quad \text{percentage (\%)} \quad \text{in all tables}$$

$$= \left| \frac{\text{presentworkresults} - \text{refrenceresult}}{\text{refrenceresults}} \right| * 100 .$$

It is interesting to note that for thin shells the relative percentage error between GTT and FSDT or CST, is smaller then that for moderately thick shells, as shown in **Table (1)** (for thin shell) and **Table (3)** (for moderately thick shell), but fortunately GTT made fair with most accurate one of HSDT for both thin and moderately thick cylindrical shells. Also, each pairs of (m x n) values relates with seven successive bending frequencies by using GTT, and the increasing orders of these frequencies, for different combinations of (m, n) values, show no systematic trend, as being the case in rectangular plates where the fundamental frequency is always associated with the mode indices (1, 1) as being noted in **Table (3)** where minimum frequency parameter is found at indices (m=1, n=2).

In-plane load results are compared with that published in (Reddy J. N. and Liu C. F. 1985) as shown in **Table(4)**, also GTT agree well with HSDT. Also the effect of ( $N_x$ ) on the natural frequencies of cylinder, when it is compressive load it decreases natural frequency for cylindrical shell but when it tension load it increases it as shown in **Table (5)**.

**Table (1): Frequency parameters for [0-90] graphite/epoxy closed cylindrical shells, (R/H) =100.**

(L/mR)	Reference	Frequency parameter= $\Omega = \left( \frac{\omega L^2}{100H} \right) \sqrt{\frac{\rho}{E_2}}$					
		n					
		0	1	2	3	4	5
2	Present	.35629	.239718	.145541	.09647	.070251	.059134
	(Mohammad S. Qatu 2004)	.35629	.23975	.14556	.09650	.07025	.05915
	Discrepancy (%)	0	.013	.013	.031	.001	.027
1	Present	.71258	.442059	.291537	.208603	.159365	.129270
	(Mohammad S. Qatu 2004)	.71259	.44205	.29163	.20869	.15935	.12928
	Discrepancy (%)	.001	.002	.031	.041	.009	.007
.5	Present	.7347119	.637573	.49575	.389404	.316127	.265658
	(Mohammad S. Qatu 2004)	.73565	.63822	.49616	.38973	.31622	.26575
	Discrepancy (%)	.127	.101	.082	.083	.029	.034

**Table (2): Frequency parameters for [0-90] graphite/epoxy closed cylindrical shells.**

(L/mR)	Frequency parameter= $\Omega = \left( \frac{\omega L^2}{100H} \right) \sqrt{\frac{\rho}{E_2}}$						
	n						
	Reference	0	1	2	3	4	5
(R/H)=20							
2	Present	.35647	.23789	.14591	.09626	.06763	.04991
	(Mohammad S. Qatu 2004)	.35629	.24015	.14590	.09623	.06761	.04991
	Discrepancy (%)	.05	.94	.0068	.03	.02	0
1	Present	.71294	.44170	.29620	.20845	.14758	.12397
	(Mohammad S. Qatu 2004)	.71258	.44245	.29191	.20838	.15753	.12393
	Discrepancy (%)	.05	.16	1.4	.03	6.3	.03
.5	Present	.73177	.63517	.49319	.38572	.31010	.25606
	(Mohammad S. Qatu 2004)	.73190	.63517	.49310	.38561	.31000	.25597
	Discrepancy (%)	.01	0	.01	.02	.03	.03
(R/H)=500							
2	Present	.35647	.24025	.14595	.11073	.12298	.16966
	(Mohammad S. Qatu 2004)	.35633	.23799	.14609	.11114	.12399	.17190
	Discrepancy (%)	.03	.94	.09	.36	.81	1.3
1	Present	.71294	.44258	.29202	.22644	.20670	.22753
	(Mohammad S. Qatu 2004)	.71266	.44283	.29705	.22751	.20855	.23095
	Discrepancy (%)	.03	.05	1.6	.47	.88	1.4
.5	Present	.77913	.68365	.55557	.47426	.43687	.43493
	(Mohammad S. Qatu 2004)	.78908	.69140	.56195	.48080	.44477	.44535
	Discrepancy (%)	1.2	1.1	1.1	1.3	1.7	2.3



**Table (3): The effect of lamination type on minimum frequency parameters (m=1, n=2) of (graphite/epoxy) closed cylindrical shells.**

Lamination	Theory	Frequency parameter= $\Omega = \left( \frac{\omega L^2}{100H} \right) \sqrt{\frac{\rho}{E_2}}$	Discrepancy (%)
(0/90)	Present theory(G.T.T.)	.156047	-
	HSDT (Reddy J. N. and Liu C. F. 1985)	.1566	.35
	FSDT (Reddy J. N. and Liu C. F. 1985)	.1552	.54
	CST (Reddy J. N. and Liu C. F. 1985)	.1630	4.2
(0/90/0)	Present theory(G.T.T.)	.171515	-
	HSDT (Reddy J. N. and Liu C. F. 1985)	.1777	3.4
	FSDT (Reddy J. N. and Liu C. F. 1985)	.1779	3.5
	CST (Reddy J. N. and Liu C. F. 1985)	.2073	17.2

**Table (4): The dimensionless critical buckling loads of cross-ply circular cylindrical shell as predicted by various theories. (m=1, n=3, L/R=1, R/H=10, N=NL<sup>2</sup>/100H<sup>3</sup>E<sub>2</sub>)**

Lamination	Theory	SS	Discrepancy (%)
[0-90]	HSDT (Reddy J. N. and Liu C. F. 1985)	.1687	3.9
	Present work GTT	.162065	
	FSDT (Reddy J. N. and Liu C. F. 1985)	.1670	2.9
	CST. (Reddy J. N. and Liu C. F. 1985)	.1817	10.8
[0-90-0]	HSDT (Reddy J. N. and Liu C. F. 1985)	.2794	1.7
	Present work GTT	.274399	
	FSDT (Reddy J. N. and Liu C. F. 1985)	.2813	2.4
	CST (Reddy J. N. and Liu C. F. 1985)	.4186	34.4

**Table (5): The effect of the in-plane load ( $N=NL^2/100H^3E_2=.25$ ) on the dimensionless minimum frequencies of cross-ply closed circular**

**cylindrical shells.**  $\bar{\omega} = \left( \frac{\omega L^2}{100H} \right) \sqrt{\frac{\rho}{E_2}}$

Lamination	Theory	Compressive in-plane load	Discrepancy (%)	Tension in-plane load
[0-90]	Present work (GTT)	.071682	-	.194108
	HSDT (Reddy J. N. and Liu C. F. 1985)	.0786	8.8	-
	FSDT (Reddy J. N. and Liu C. F. 1985)	.0761	5.8	-
	CST(Reddy J. N. and Liu C. F. 1985)	.0932	23.08	-
[0-90-0]	Present work (GTT)	.109846	-	.221492
	HSDT (Reddy J. N. and Liu C. F. 1985)	.1089	.86	-
	FSDT(Reddy J. N. and Liu C. F. 1985)	.1095	.315	-
	CST(Reddy J. N. and Liu C. F. 1985)	.1533	28.3	-
[0-90-0-90.....] 10 layers	Present work (GTT)	.14733	-	.228323
	HSDT (Reddy J. N. and Liu C. F. 1985)	.1533	3.8	-
	FSDT (Reddy J. N. and Liu C. F. 1985)	.1531	3.7	-
	CST(Reddy J. N. and Liu C. F. 1985)	.1607	8.3	-

**CONCLUSIONS:**

In this work General Third order shell Theory (GTT) is developed to derive the governing equations for free vibration and obtaining in-plane critical load of simply supported cylindrical shells, for first time, and these equations are solved using Navier's solution. Good agreement between results obtained using GTT in present work with those obtained by other researchers using HSDT, FST for analyzing dynamic behavior of laminated cylindrical shells (maximum discrepancy with HSDT is 3.7%), however high order theory does not require the use of correction factor. Also the effect of the type of this in-plane load on the natural frequencies is studied, compressive axial load decrease natural frequencies, while tension in-plane load increase them, as proved by many other papers.

**REFERENCES:**

- Altan Kayran & Jack R. Vinson, 'Free vibration analysis of laminated composite truncated circular conical shells', AIAAJ, vol. 28, no.7, 1990.
- Azam Tafreshi, 'Delamination buckling and post buckling in composite cylindrical shells under combined axial compression and external pressure', Composite Structures, Article in press, 2005.
- Andrea Spagnoli, 'Different buckling modes in axially stiffened conical shells', Engineering Structures, vol.23, 2001.
- Darvizeh M., Haftchenari H., Darvizeh A., Ansari R., Sharma C.B., 'The effect of boundary conditions on the dynamic stability of orthotropic cylinders using a modified exact analysis', Composite Structures, article in press, 2005.
- George J. Simitses & John S. Anastasiadis, 'Shear deformable theories for cylindrical laminates-equilibrium and buckling with applications', AIAA J., vol.30, no.3, 1992.
- Geier B., Meyer-Piening H.-R., Zimmermann R., 'On the influence of laminate stacking on buckling of composite cylindrical shells subjected to axial compression', Composite Structures, vol.55, 2002.
- Hunt G.W., Lord G.J., Peletier M.A., 'Cylindrical shell buckling: a characterization of localization and periodicity', Discrete and continuous dynamical systems-series B, vol.3, no.4, 2003.
- Lee J. J., Yeom C.H., Lee I., 'Vibration analysis of twisted cantilevered conical composite shells', J. of Sound and vibration, vol. 255, no.5, 2002.
- Liyong Tong, 'Free vibration of composite laminated conical shells', Int. j. Mech. Sci., vol.35, no.1, 1993.
- Kabir H.R.H., Al-Khaleefi A.M., Chaudhuri R.A., 'Frequency response of a moderately thick antisymmetric cross-ply cylindrical panel using mixed type of Fourier solution functions', J. of Sound and vibration, vol.259, no.4, 2003.

- Korjakin A., Rikards R., Chate A., 'Analysis of free damped vibrations of laminated composite conical shells', *Compo.Stru.* vol.41, 1998.
- Meyers C.A. & Hyer M.W., 'Response of elliptical composite cylinders to axial compression loading', *Mechanics of Composite Materials and Structures*, vol.6, 1999.
- Mohammad S. Qatu, 'Vibration of laminated shells and plates', Elsevier Academic Press, 2004.
- Narita Y., Ohta Y., Yamda G., Kobayashi Y., 'Analytical method for vibration of angle ply cylindrical shells having arbitrary edges', *AIAA*, vol.30, no.3, 1992.
- NG T.Y., Lam K.Y., Reddy J.N., 'Dynamic stability of cross-ply laminated composite cylindrical shells', *Int. J. Mech. Sci.*, vol.40, no.8, 1998.
- NG T.Y., Lam K.Y., Reddy J.N., 'Parametric resonance of a rotating cylindrical shell subjected to periodic axial loads', *J. of Sound and vibration*, vol.214, no.3, 1998.
- Pinto I.F. Correia, Motasoaes C.M., Herskovits J., 'Analysis of laminated conical shell structures using higher order models', C. M. Mota Soares, 2001.
- Seishi Yamada & Croll G.J.A., 'Buckling and post-buckling characteristics of pressure-loaded cylinders', *J. of Applied Mechanics*, vol.60, 1993.
- Sofiyev A.H., 'the stability of compositionally graded ceramic-metal cylindrical shells under a periodic axial impulsive loading', *Composite Structures*, vol.69, 2005.
- Soedel W., 'Vibration of shells and plates', 2000.
- Romil Tanov, Ala Tabiei, George J. Simitses, 'Effect of static preloading on the dynamic buckling of laminated cylinders under sudden pressure', *Mechanics of Composite Materials and Structures*, vol.6, 1999.
- Reddy J.N., 'Mechanics of laminated composite plates and shells', CRC Press 2004.
- Reddy J.N. and Liu C.F., 'A higher-order shears deformation theory of laminated elastic shells' *I.J.Eng.Sci.*, vol.23, no.3, 1985.
- Tong T., 'Effect of axial load on free vibration of orthotropic truncated conical shells', *ASME, J. of vib. & acous.* vol.118, 1996.
- Werner Hufenbach, Carsten Holste, Lothar Kroll, 'Vibration and damping behavior of multi-layered composite cylindrical shells', *Comp.Stru.* vol.58, 2002.
- Xi Z.C., Yam L.H. & Leung T.P., 'Free vibration of composite laminated shell of revolution: Effects of shear non-linearity', *Int. J. Mech. Sci.*, vol.41, 1999.



- Young-Shin Lee, Myung-Hwan Choi, Jae Hoon Kim, 'Free vibrations of laminated composite cylindrical shells with an interior plate', J. of Sound and vibration, vol.265, 2003.
- Youngjin Chung, 'Buckling of composite conical shells under combined axial compression, external pressure and bending', Ph. D. thesis submitted to New Jersey Institute of Technology, 2001.

### **NOMENCLATURE:**

a, b	Dimensions of shell.
$A_{mn}, B_{mn}, C_{mn}, D_{mn}, E_{mn}, F_{mn}, J_{mn}$	Arbitrary constants
{A}	Displacement vector
$C_{ij}$	stiffness matrix elements
$E_1, E_2, E_3$	Elastic Modulus components (Gpa)
$G_{12}, G_{13}, G_{23}$	Shear modulus components (Gpa)
H	Thickness (mm)
K	Kinetic energy
L	Cylinder length (mm)
[M]	Inertia matrix
m, n	indices
$N_i, M_i, P_i, S_i, Q_i, K_i$ (i=1,2,3,4,5,6)	Resultant reactions (N/mm),(N.mm)
$N_x$	Buckling load (N/mm)
$Q_{ij}$	Elastic stiffness coefficients
R	Cylinder radius (mm)
U	Potential energy (N.m)
u, v, w, $\phi_1, \phi_2, \psi_1, \psi_2, \psi_3, \theta_1, \theta_2, \theta_3$	Displacement components (mm)
z	Distance from neutral axis (mm)
$\varepsilon_{1,2,3,4,5,6}$	Strain components in principle axes direction.
$\nu_{12}, \nu_{13}, \nu_{23}$	Poisons ratio components
$\rho$	Density ( $\text{Kg/m}^3$ )
$\omega$	Frequency (rad/s)
$\Omega$	Frequency parameter for cylindrical shell.
$\sigma_{1,2,3,4,5,6}$	Stress components (Mpa), in principle axes direction.

### **ABBREVATIONS:**

CST	Classical shell theory
CLPT	Classical plate theory
ESL	Equivalent single layer
FSDT	First order shear deformation theory
HSDT	High shear deformation theory
GTT	General third order theory

## EXPERIMENTAL STUDY OF FATIGUE CHARACTERISTICS OF LAMINATED COMPOSITE PLATES

Prof. Dr. Muhsin J. Jweeg, Dr. Ali Hussain Al-Hilli, Hussain Mohan Suker  
Nahrain University/ College of Engineering

### ABSTRACT

The fatigue damage is a dangerous and could be considered as the most unwanted failure in the materials that are used to construct the engineering components. As composites take an advanced position in the industry of aircraft, marine and many other high performance components, because of their high ability and their light weight and for their strength, this forces us to find the deformation and data to give a good expectation for the composite behavior under fatigue and other types of damage.

In this study the material used is the glass fiber with a polyester resin; the experiment used a device to force the composite to be under a bending fatigue through specified deflection and then the force is measured. The results for different values of imposed deflection and different thicknesses are presented, as S-N curves and in a logarithmic way.

Fractography has been used to characterize the fatigue damage in the composite, it is shown that the fatigue damage in the composite is a complex, interactive damage process and combines between several damage mechanisms such as delamination, fiber breakage, matrix cracking and fiber matrix debonding.

### دراسة عملية لخواص الكلال للصفائح المركبة الطباقية

#### الخلاصة:

إن ضرر الكلال هو اخطر أنواع الإضرار الميكانيكية التي قد تحصل في داخل المواد ويعتبر الأقل رغبة. بينما تأخذ المواد المركبة موقعا متقدما في صناعة الطائرات، السفن والعديد من المكونات العالية الأداء الأخرى، بسبب قدرتها العالية ووزنهم الخفيف ومتانتها العالية، هذا يجبرنا لإيجاد المعلومات والبيانات إعطاء توقع جيد لسلوك المواد المركبة تحت الإعياء والأنواع الأخرى من الضرر.

في هذه الدراسة، المادة المستعملة هي الليف الزجاجي والمادة المستخدمة كمصفوفة هي راتنج البولستر؛ استعملت التجربة أداة لإجبار المواد المركبة لكي تكون تحت انحناء الإعياء من خلال امالة محددة لفرض قوة محددة.

إن النتائج للقيم المختلفة من النتائج العملية لعدد من العينات ذات الأسماك المختلفة وتحت أحمال إجهاد مختلفة كانت موضوعة على شكل منحني بياني لكل من القوة مع الإجهاد المسلط لكل حالة من الحالات وتم وضع شكل بياني يمثل الإجهاد مع عدد الدورات على محاور لوغاريتمية.

من خلال كل هذا تم التوصل إلى إن ضرر الإعياء في المواد المركبة عملية تفاعلية معقدة بين عدة و فقدان قابلية التفصيح (Delamination) آليات ضرر مثل تكسر الألياف، تصدع المصفوفات و بين الألياف والمصفوفة.

**KEY WORDS:** Fatigue, Composite, Delamination, Matrix debonding, S-N curve.

## INTRODUCTION

In general fatigue of fiber-reinforced composite materials is a quite complex phenomenon, and a large research effort is being spent on it today. Fiber-reinforced composites have a rather good rating as regards life time in fatigue. The same does not apply to the number of cycles to initial damage nor to the evolution of damage. Composite materials are inhomogeneous and anisotropic, and their behavior style is more complicated than that of homogeneous and isotropic materials such as metals. The main reasons for this are the different types of damage that can occur (e.g. fiber fracture, matrix cracking, matrix crazing, fiber buckling, fiber-matrix interface failure, delaminations,...etc), their interactions and their different growth rates.

The fatigue models can be classified in three major categories:

1. Fatigue life models , which do not take into account the actual degradation mechanisms but use S-N curves (influence of stress amplitude on occurrence of final failure )or Goodman –type 22 diagram (influence of mean stress level) and introduce some sort of fatigue failure criterion.
2. Residual strength models, which describe the degradation in the initial static strength, equally without taking into account stiffness reduction.
3. The last category uses one or more damage variables related to measurable manifestation of damage (number of transverse matrix cracks, delamination size) or to the residual stiffness.

Phenomenological residual stiffness model which predicts the stiffness degradation as well as final failure of the composite component was presented by [Paepegem 2001], the reserve to failure has been evaluated by means of modified use of Tsai-Wu static failure criterion. The fatigue damage model has been applied to displacement-controlled bending fatigue experiment of plain woven glass/epoxy specimens, the damage and stress redistribution, as well as the force- cycle history have been simulated and compared to experimental result.

[Liu 2004] proposed a damage cumulative model for fatigue life predication of composite laminates, it is constructed on the ply level and uses a multiaxial damage index to quantify the damage caused by different stress components .[Daneila 2007] developed a model for damage progress to fatigue failure in cyclic loaded woven composite materials with polymer, the relative stiffness is changed per cyclic loading at given stress or strain level.

The correlation between the stiffness degradation rate and the loading parameter is described as power function dependence; this model divides the S-N curve of the fiber reinforced polymer composite into three regions, the first region approaches a nearly horizontal line where the number of cycles to failure depends more on statistical strength distribution than the stress level, the second region is more classical fatigue behavior where the S-N correlation can be describe as a power low function and the third region suggest a fatigue limit where an infinite lifetime is found below a given stress or strain level –the fatigue strength.

[Diawekar 2002] produced an analytical model supported by numerical simulation which describes the behavior of the energy release of composite materials subjected to the fatigue, this model established that accumulation of damage due to intermittent surge in applied load reduces the energy release rate ((G)) of the material . The effect of constant amplitude, regularly applied overloads to the energy release rate of [0/90]<sub>n</sub> graphite/epoxy composite appears diminished as the structural integrity reduces over time suggesting the effect of the overloads is more severe during the initiation of delamination growth, their investigation shed light on the nature and extent of damage accumulation during spectral fatigue.

They established that the energy release rate reduces as the delamination length increases, indicating that during growth a delamination requires smaller amounts of energy in order to progress.

[Mohamed 1997] built a model for predication the behavior of laminates composite under fatigue loading this model uses a technique called progressive fatigue damage modeling which is capable of predicating the residual strength ,residual stiffness, and fatigue life of composite laminate.



The stress analysis, failure analysis and material property are the three major components of the model for the stress analysis. There is a finite element technique proposed, it is based on the state of stress of different failure modes detected by a set of fatigue failure criteria. This technique restricts the application of failure criteria to limited states of stresses.

The model determines the state of damage at any load level and number of cycles from failure initiation and propagation to catastrophic failure. The model is able to predict the residual strength residual life, final failure mechanisms and final fatigue life of composite laminate under general fatigue loading condition.

[Miyano 1997] proposed a prediction method of fatigue strength of polymer composites for an arbitrary frequency, stress ratio and temperature. This method is based upon the four hypotheses (i) same failure mechanism for static, creep and fatigue failure, (ii) same time-temperature superposition principle for all failure strengths, (iii) linear cumulative damage law for monotone loading and (iv) linear dependence of fatigue strength upon stress ratio. J Lee W et. al [Lee 1989] proposed a model for predicting fatigue life of cross-ply laminates which develop transverse cracking up to the characteristic damage state (CDS) level before fatigue failure. The fatigue life consists of two portions: the portion necessary to reach the CDS and the residual life after attainment of the CDS. The CDS life is described based on the relationship between residual stiffness and crack density and the stress-life curve of the 900 lamina. The residual life after CDS was obtained by calculating the stress carried by the 0 plies and assuming that these plies within the damaged laminate behave like a 900 lamina under cyclic loading.

Fatigue life predictions were in good agreement with experimental results for three graphite/epoxy cross-ply laminates.

[Hwang 1985] and [Han 1985] built damage models using fatigue modulus and resultant strain, and prediction of fatigue life of composite materials using degradation and damage models, this approach can predict accurately the multi-stress level fatigue life as well as single-stress level fatigue life of composite materials.

Fatigue life is predicted by the following procedures:

- (1) Establish the fatigue modulus degradation model [Mahmood 2007].
- (2) Find fatigue life equation as a function of fatigue modulus.
- (3) calculate the fatigue life using strain failure criterion, degradation models for composite damage are generalized; the three-parameter degradation model is found most suitable for predicting fatigue life of composites.

Theoretical equation for predicting fatigue life is formulated using the fatigue modulus and its degradation rate, this relation is simplified by strain failure criterion for the practical application, it is proved that the final formula predicts the fatigue life of a glass fiber epoxy composite material better than S-N curve. "Fatigue modulus concept" is defined as a slope of applied stress and resultant strain at a specific cycle.

Fatigue modulus degradation is studied using an assumption that the fatigue modulus degradation rate follows a power function of fatigue cycle.

[Mahmood 2007] presented a simulation process by which the cyclic stresses and fatigue loadings on its constituents could be predicted for an under fatigue loading lamina model introduces a new coupled stiffness/strength technique by relating lamina stiffness to the stress field in its constituents. Therefore, the stress field and strength considerations in its constituents could be studied when the lamina stiffness is determined by a non-destructive process. For representing a complete description of the constituents' properties and their interactions, the effect of fiber/matrix interface debonding is introduced into the model.

## PREPERATION OF MAKING THE SPACIEMEN

The specimens which fabricated consisted of plain E-glass woven fiber piles in a thermosetting polyester matrix They were manufactured by hand lay-up technique, the thickness of the glass



fabrics was approximately (4.6, 3.75 and 2.5 mm) with a 400g/m<sup>2</sup> density and a warp number 3 per 10 mm.

The resin matrix employed was a low viscosity thermosetting polyester resin commonly used for hand lay-up at room temperature. This resin is cured at 70°C and is designed to wet easily the reinforcement fabrics employed in hand lay-up construction.

Fabrication of laminates was conducted by first cutting four 15cmx15 cm sections, and each section was ply oriented in the same direction as the previous ply . The fabrics were placed in a mold consisting of 30 cm x 30 cm ceramic plates with two X-ray photo sheets to avoid abrasive and insure flattening of specimen surfaces. As shown Fig. 1.

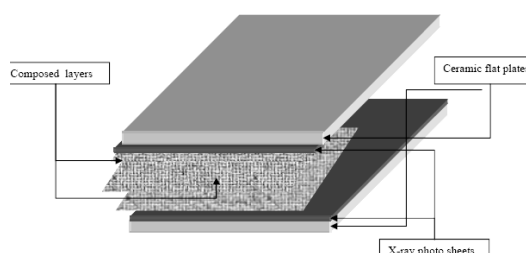


**Figure.(1) Schematic of mold of test specimen**

The X-ray photo sheet, which was first placed on the bottom ceramic plate, was wet with the catalyzed polyester resin before the first ply was placed on it. More catalyzed resin was applied to this first ply with brush until it was thoroughly wet. Following this, the remaining plies were placed in the mold following the same sequence. Once all the plies were placed on top of the stack, the assembly was heated to 70°C in an oven with sufficient pressure to get rid of the excess resin and the entrapped air bubbles. The cure time was 3 hours to ensure complete cross-linking. The volume fraction was determined to be 0.56 for the glass fiber composites (based on weighing of the fabric before impregnation, and the laminate after curing and using the weight density of the fibers and the resin)[ Ali Al-Hilli 2006].

The samples were cut into a 20 mm wide and a 150 mm long in rectangular shape using a steel saw and then finished by abrasive grinding of the edges.

## EXPERIMENTAL ARRANGEMENT AND PROCEDURE FOR THE FATIGUETEST

The experiments were carried out using a HSM20 alternating bending machine{Fig. 2} which was developed specially for flexural fatigue test on cantilever beam specimens and {Fig. 3}.

The device was modified by adding a new clamping device which consists of a metal shoulder which has two holes for a 8 mm bolt which connects the shoulder to the bridge of the machine so it is firmly connected to the bridge, a metal plate with 6 hexagonal bolts of 8 mm diameter is connected to the shoulder and produces the clamping device in which the rotating faceplate carries an adjustable eccentric bearing driving a connecting rod attached to the cantilever, shown in Fig. 4.

The bridge to which this test piece is clamped can be adjusted vertically so that the imposed displacement can be varied, shown in Fig. 5. A counter with a 50:1 reduction gear is driven by the electric motor, offering a 1:100 or 1:25 count depending on the frequency of the reciprocation.

This mechanism imposes an alternating displacement on the hinge (point C ) Fig.6 ,that connects the linkage with the lower clamp of the composite specimen ,at the other end the specimen is clamped ,hence the sample is loaded as a composite cantilever beam, the amplitude of the imposed displacement is a controllable parameter and the adjustable crank allows to choose between single-side and fully-reversed bending ,i.e. the deflection can vary from zero to the maximum deflection in one direction or in two directions respectively.



Figure (2) HSM20 alternating bending fatigue machine

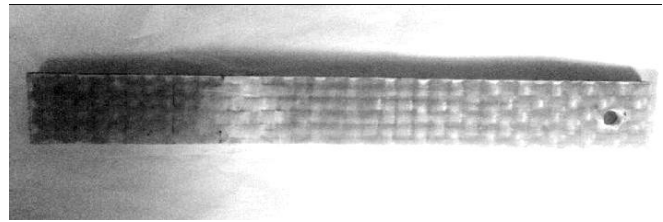


Figure (3) Composite specimen, 20mm wide and 150mm long dimension

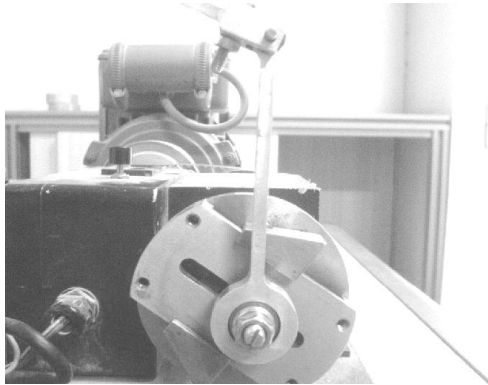


Figure (4) Rotating faceplate carries an adjustable eccentric bearing driving a connecting rod attached to the cantilever

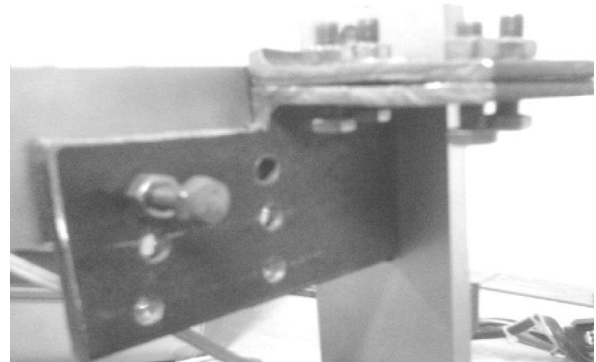


Figure (5) The shoulder connected to the bridge

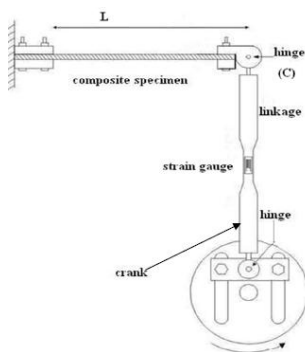


Figure (6) Schematic drawing of the crank-linkage mechanism.



Figure (7) Strain meter

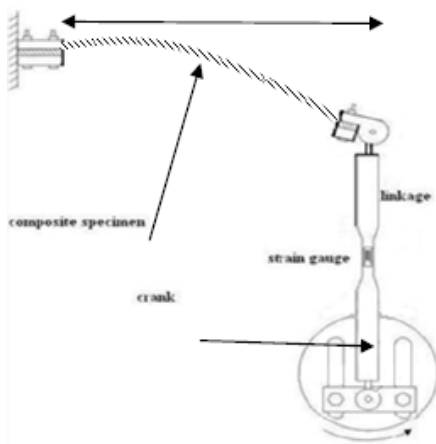


Figure (8) Schematic drawing of the crank-linkage mechanism howing

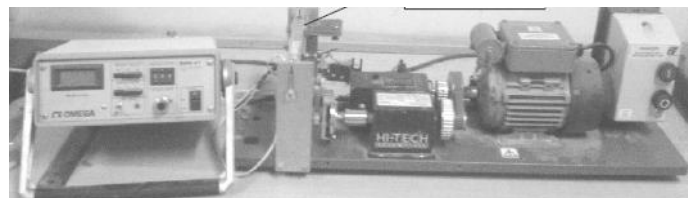


Figure (9). The complete device consisting of the strain meter and the fatigue machine

The connecting rod was molded from aluminum, the connecting rod contains a narrow region in which a strain gauge is connected, The strain gauge is used to measure any strain that affects the connecting rod this, strain is a result of the force which has effect on the specimen. The relation of the force and the strain gauge is calculated from a previous calibration, this calibration was made by putting the connecting rod under a known force and the strain of the force was measured using the strain meter shown in Fig. 7 from which a calibration curve was made, the calibration was remade at every beginning of the experiments.

When the experiment started the force which has effect on the specimens is taken to be the first point at which the number of cycles is zero the strain reading was taken when the connecting rod reached the lower point in which the maximum displacement is implied and it is the maximum force effecting the specimens, as number of cycles increased many reading were taken each reading present the maximum force affect the specimens. Fig. 6 a schematic drawing of the crank-linkage mechanism and it shows the machine before any movement and the displacement imposed is zero in this position while in Fig. 8 the machine is at lower point and the imposed deflection is maximum, the other Figures show the machine parts and the strain meter and the clamp, the machine at lower point and the imposed deflection is maximum.

The complete system of the experiments is shown in Fig. 9.

## RESULTS

It was well established that the composite materials are significantly different from their metal counterpart in manner in which fatigue fracture initiates and develops during the load cycling, It must be deal with a number of considerations which are unique to composite materials where only one or two fatigue damage characterization technique may be sufficient to completely characterize the damage in metals.

The unique phenomena by which the damage occurs in composite necessitate the use of several damage characterization techniques to understand the damage mechanism in the composite material.

The specific elements that need to be carefully examined are:

1. The typical failure modes.
2. The interplay of various failure modes.
3. Initiation and producing mechanism during various stages of fatigue life.

The following presentation of results of the present study and ensuing discussion is an effort to add on the existing knowledge of the fiber reinforced composites

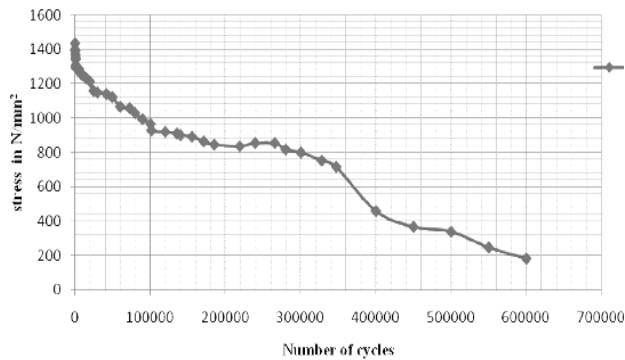
The S-N curves are the most important method for the presentation of the fatigue effect on any kind of material whether is metal or it is made from the composite materials, in the Figures below the relation between the stress and the number of cycles is presented, these Figures are for different values of stress for a different thicknesses of composite specimens.

Fig. 10 gives the relation between the stress and number of cycles for the 10 layer composite with thickness 4.6 mm under a deflection of 15 mm, the initial stress is equal to (1435.2) N/mm<sup>2</sup> and it final failure is at (600123) cycle in which the stress indicated is to be equal to (184) N/mm<sup>2</sup>, there is another way for presentation of the stress versus number of relation in fatigue, this method uses a logarithmic relation in which both the stress and number of cycles are transferred into the logarithms with the passes 10, in Fig. 11, the relation between stress and number of cycles for the 10 layer composite with thickness of 4.6 mm under a deflection of 15 mm is presented in the logarithmic way.

The stress decreases during the test in different percentages as it decreases rapidly during the first two thousand cycles and this is first region in which the fatigue life initiates the first damages, most of these damages are a transverse crack that takes place in the composite structure, as cycles increase the decrease in the stress takes new pattern and the decrease is less sharp than the first two

thousand, and starts to take a linear decreasing and could be seen as a slope between two points these two points start around the 80 thousand cycles to the 300 thousand cycles.

After that the decrease returns to be a rapid drop in the value, to the final failure at the end of the 600000 cycles, this behavior can be explained as that the damage in the first few thousand cycles was because of the transverse crack and then it starts to grow in the composite and starts to produce the fiber matrix debonding, and then a delamination area which is noticeable and after that a final failure or breakage of fiber happens.



**Figure(10).** The relation between stress and number of cycles for the 10 layer 4.6 mm thick composite specimens under a deflection of 15mm.

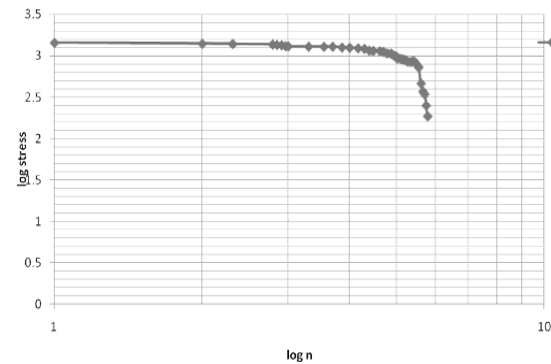


**Figure (11)** The relation between stress and number of cycles for the 10 layer composite with thickness 4.6 mm under a deflection of 15 mm is presented in the logarithmic way.

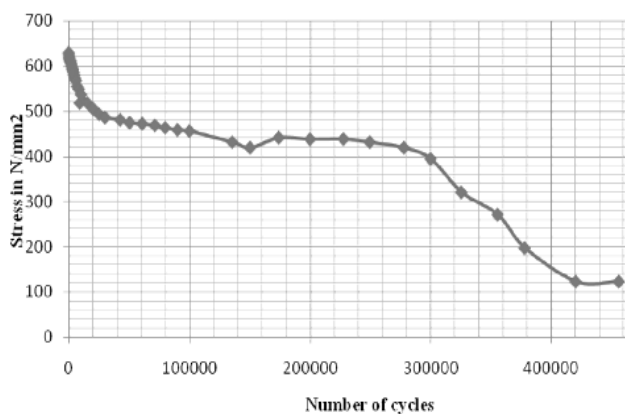


**Figure (12).**The relation between stress and number of cycles for the 10 layer 4.6 mm thick composite specimens under a deflection of 10mm.

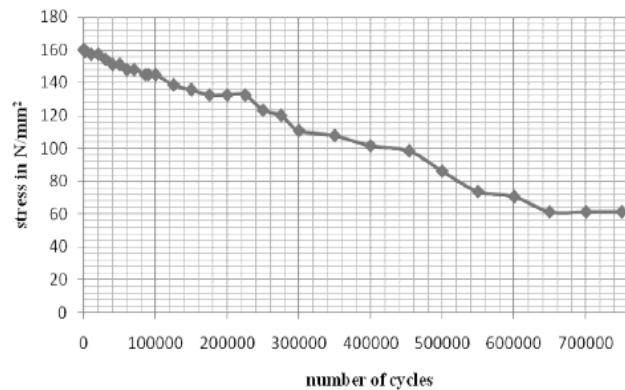


**Figure (13).**The relation between stress and number of cycles for th 10 layer 4.6 mm thick composite specimens under a deflection of 5mm.

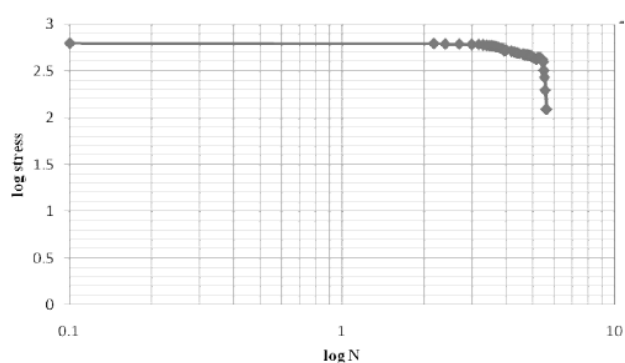


**Figure (14).** The relation between stress and number of cycles for the 10 layer composite with thickness 4.6 mm under a deflection of 10 mm is presented in the logarithmic way.

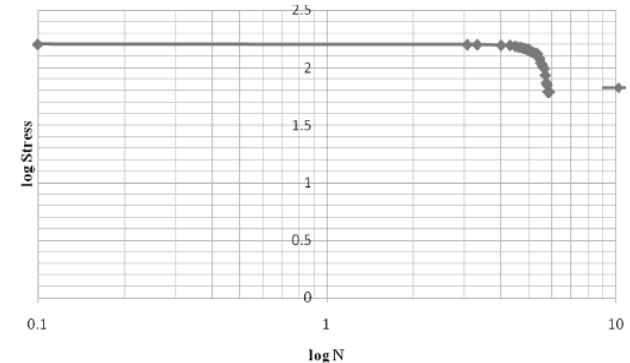


**Figure (15).** The relation between stress and number of cycles for the 10 layer composite with thickness 4.6 mm under a deflection of 5 mm is presented in the logarithmic way.

The modulus of elasticity is affected by the damage inside the composite material and this is because the modulus depends on the microstructure of the composite and as damage takes place in composite it affects the property of the composite, in the start the modulus which calculated from the material during the fatigue experiments was equal to 21.36 which had a 0.6 percentage of error for the value calculated from tensile tests, this number drops to the half after 340000 cycle and it ends at 2.7 in the final failure of the specimen.

Fig. 12 and Fig. 13 gives the relation of stress and number of cycles for the 10 layer with 4.6mm thickness composite materials under 10mm and 5mm deflection respectively ,also the relation in logarithmic way is also presented in the Fig. 14 and Fig. 15 respectively.

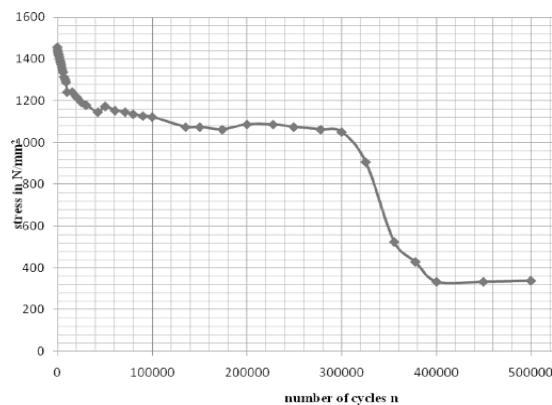


Figure (16).The relation between stress and number of cycles for the 8 layer 3.75 mm thick composite specimens under a deflection of 15mm.

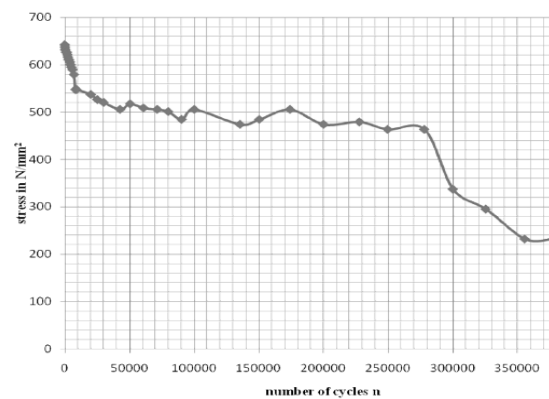


Figure (17).The relation between stress and number of cycles for the 8 layer 3.75 mm thick composite specimens under a deflection of 10mm.

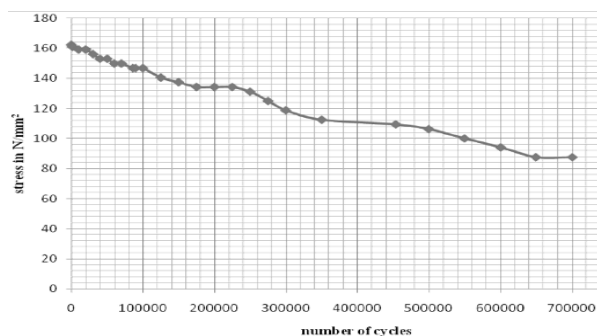


Figure (18).The relation between stress and number of cycles for 8 layer 3.75 mm thickness under 5 mm deflection.

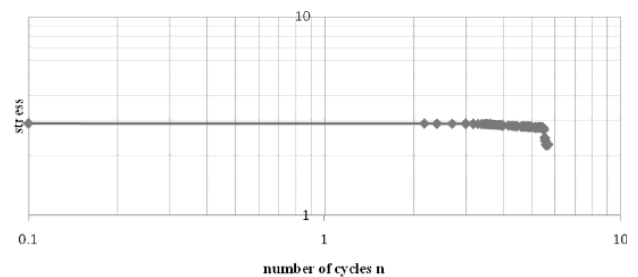


Figure (19).The relation between stress and number of cycles for the 8 layer composite with thickness 3.75 mm under a deflection of 15 mm is presented in the logarithmic way.

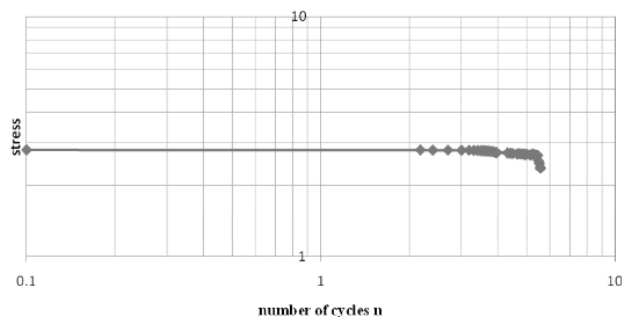


Figure (20).The relation between stress and number of cycles for the 8 layer composite with thickness 3.75 mm under a deflection of 10 mm is presented in the logarithmic way.

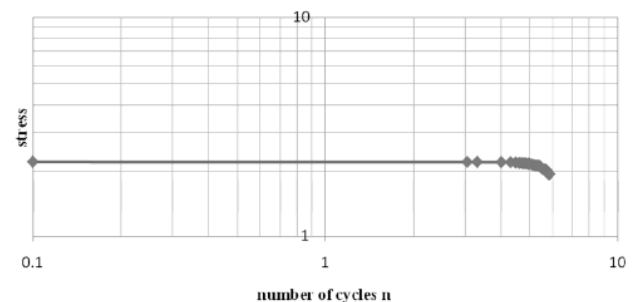


Figure (21).The relation between stress and number of cycles for the 8 layer composite with thickness 3.75 mm under a deflection of 5 mm is presented in the logarithmic way.

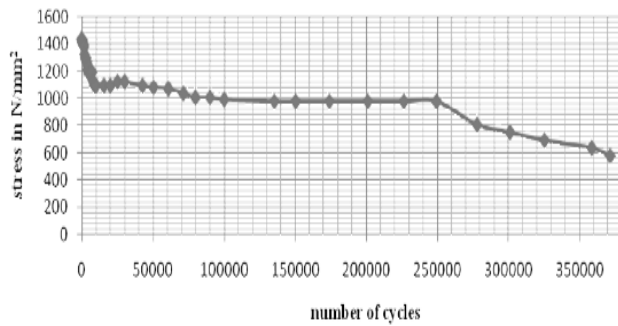


Figure (22) The relation between stress and number of cycles for 6 layer 2.5 mm thickness under 15 mm deflection.

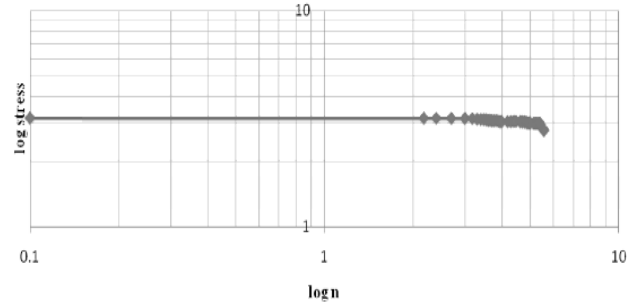


Figure (23) The relation between stress and number of cycles for the 6 layer composite with thickness 2.5 mm under a deflection of 15 mm is presented in the logarithmic way.

The relation between stress and number of cycles is shown here for the composite material of 8 layer and 3.75 mm thickness in the first one {Fig. 16}, the deflection is equal to 15 mm and in the second {Fig.17} it is 10mm while the third it is 5 mm {Fig.18} .Also the relation between stress and number of cycles is presented in logarithmic method in Fig. 19, Fig. 20, and Fig. 21, for 8 layer with 3.75mm thickness composite specimen for deflection of 15mm,10mm , and 5 mm respectively. For the specimens of 6 layer with a 2.5mm thickness under deflection 15 mm, stress relation with number of cycles is shown in Fig. 22 and in Fig.23 but in logarithmic relation.

Equations were found for each of the Figures that show the relation between the stress and the number of cycles for the different thicknesses and different deflections as a polynomial equation with the 3rd degree, this is useful to fit all the data granted during experiments, the equation expression form is :

$$\sigma = a + b n + c n^2 + d n^3 \quad (1)$$

Table 1 shows these coefficients for conditions used in the present work, in which higher order coefficients (c and d) have negligible values hence linear behavior is dominant.

**Table (1). Polynomial coefficients for equation (1)**

Thickness (mm)	Deflection (mm)	<i>a</i>	<i>b</i> (10 <sup>-3</sup> )	<i>c</i> (10 <sup>-9</sup> )	<i>d</i> (10 <sup>-15</sup> )
4.6	15	1233.53	-2.72876	5.34	-6.54
4.6	10	553.76	-1.51825	6.85	-12.92
4.6	5	136.24	0.140561	-0.87	0.73
3.75	15	1285.43	-1.20413	1.01	-6.21
3.75	10	573.92	-1.48141	9.09	-20.85
3.75	5	138.51	0.119892	-0.73	0.67
2.5	15	1217.27	-3.73584	20.09	-40.21

Fig. 24 shows the load versus the number of cycles. The initial load for the 4.6mm thickness specimen starts with 156 N and it decreases to reach 20 N at the end, the first 10000 cycles show a rapid decrease in the load needed to produce deflection and reaches to about 136 N, this decrease is about 13% of the initial loading, and as it reach the first 100000 cycles the load equal to 105 N and it equal to 32% from initial load, and as the cycles continue and the time go on the load reaches a 50% of the initial load at 3.4\*10<sup>5</sup> cycles, but before that we notice that the decrease below the 10<sup>5</sup> cycles is very limited and it is a small percentage of decrease , in comparison to the first 10<sup>4</sup> cycle, after the 4\*10<sup>4</sup> cycles the load decreases and reaches the failure position at around 600000.

While the decrease in the 8 layer 3.75 mm thickness specimens starts from 84.5 N and reach the 72.8 N which is equal to a 14% of the initial load and reaches to 75% of the initial load at 135000

cycles and reaches 50% at about  $3 \times 10^5$  cycle when it reaches the  $3 \times 10^5$  cycle a rapid decrease was shown and a final failure occurs .

The third thickness is equal to 2.5 mm which comes from 6 layer of fiber glass yarns as in previous curves it decrease at a fast rate and reaches to a position in which the decrease to the final failure in a study range that starts from the  $1.6 \times 10^4$  cycle to the end and the final failure.

The relations between the load and number of cycles and the stress versus number of cycles for the 10 layer 4.6 mm thickness composite subjected to 15mm,10mm, and 5mm deflection are shown in Fig.25 and Fig.26 respectively.

The relations between the load and number of cycles and the stress versus number of cycles for the 8 layer 3.75 mm thickness composite subjected to 15mm,10mm, and 5mm deflection are shown in Fig. 27 and Fig. 28 respectively.

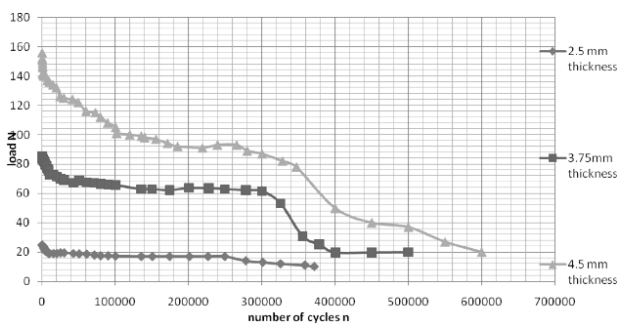


Figure (24) The relation between 3 different thicknesses of composite they are, 4,6mm ,3.75mm, and 2.5 mm under 15 mm deflection.

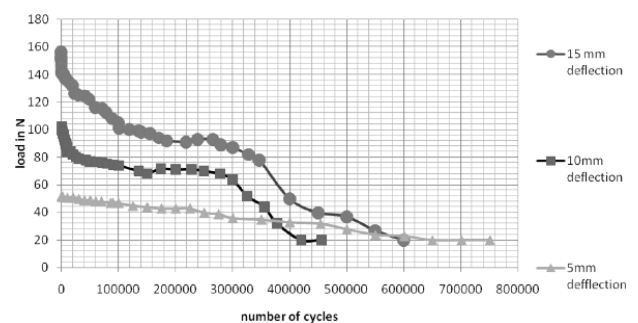
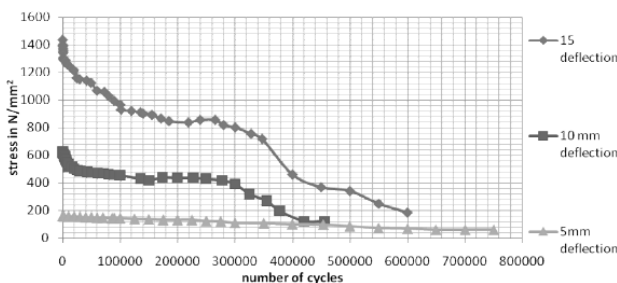
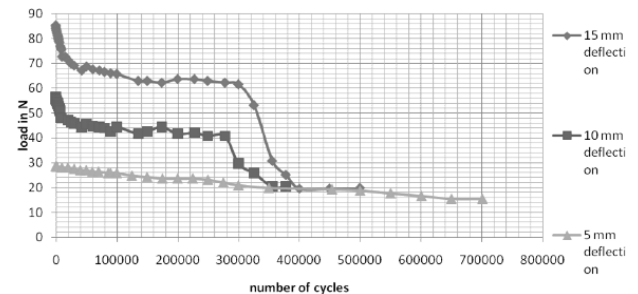


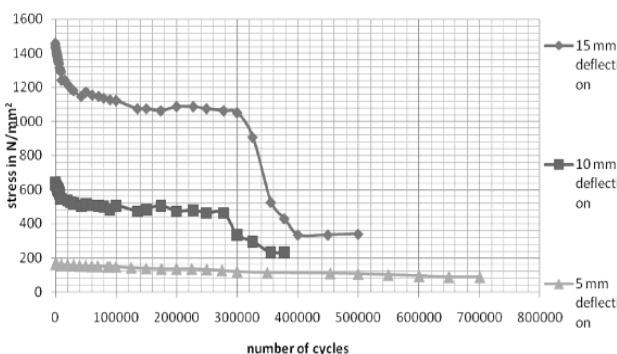
Figure (25).The relation between load and number of cycles for the 10 layer 4.6 mm thickness composite subjected to 15 mm,10mm, and 5mm deflection.



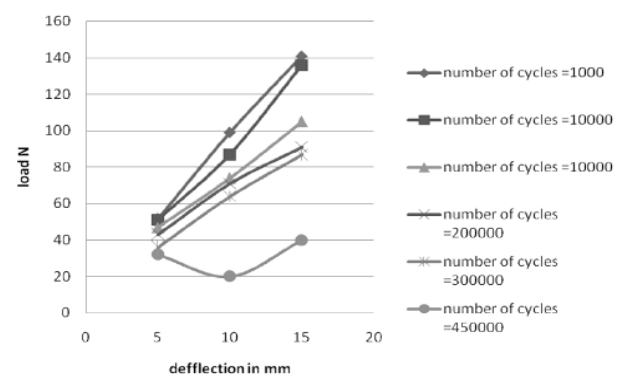
Figure(26).The relation between the stress and number of cycles for the 10 layer 4.6 mm thickness composite subjected to 15 mm,10mm, and 5mm deflections.



Figure(27).The relation between the stress and number of cycles for the 8 layer 3.75 mm thickness composite subjected to 15 mm,10mm, and 5mm deflections.

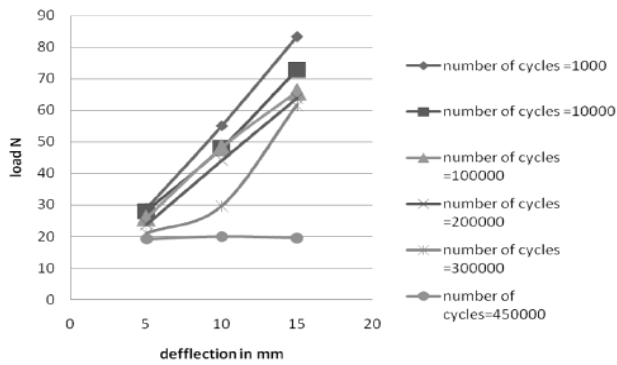


Figure(28).The relation between the stress and number of cycles for the 8 layer 3.75 mm thickness composite subjected to 15 mm,10mm, and 5mm deflections.

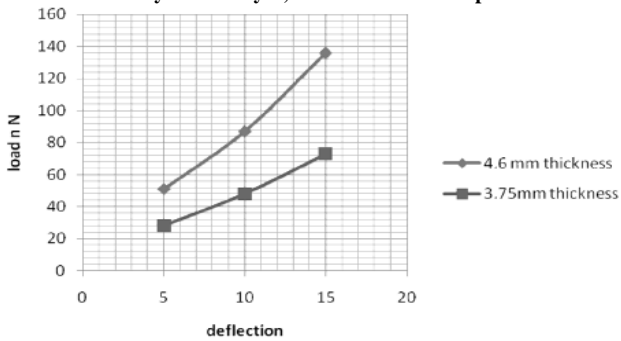


Figure(29).The relation between the deflection and load at various number of cycles of 10layer 4.6 mm thickness specimens.

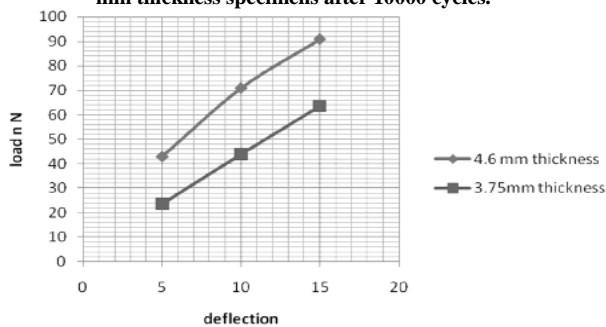




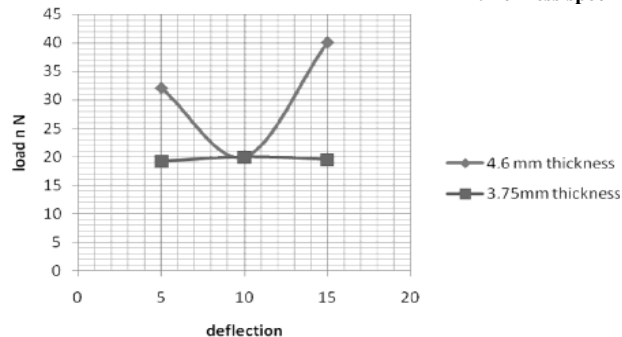
Figure(30).The relation between the deflection and load at various number of cycles of 8layer, 3.75 mm thickness specimens.



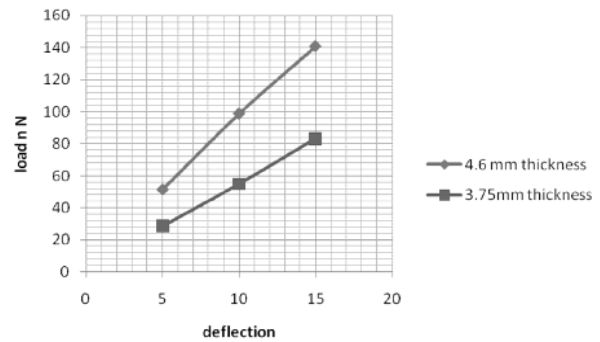
Figure(32).The relation between the deflection and load at various number of cycles for 10 layer, 4.6mmthickness and the 8layer, 3.75 mm thickness specimens after 10000 cycles.



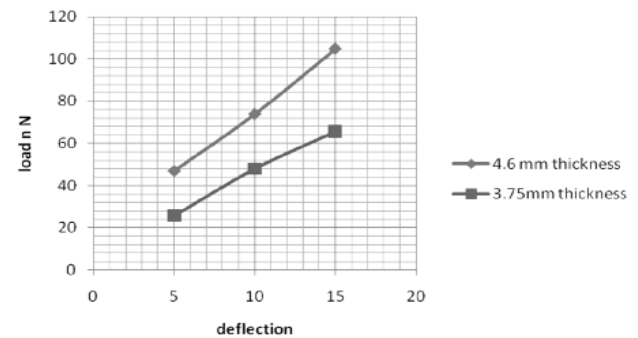
Figure(34).The relation between the deflection and load at various number of cycles for 10 layer, 4.6mmthickness and the 8layer, 3.75 mm thickness specimens after 200000 cycles.



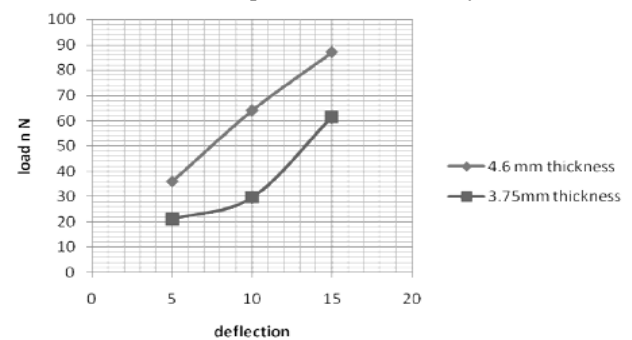
Figure(36).The relation between the deflection and load at various number of cycles for 10 layer, 4.6mmthickness and the 8layer, 3.75 mm thickness specimens after 450000 cycles.



Figure(31).The relation between the deflection and load at various number of cycles for 10 layer, 4.6mmthickness and the 8layer, 3.75 mm thickness specimens after 1000 cycles.



Figure(33).The relation between the deflection and load at various number of cycles for 10 layer, 4.6mmthickness and the 8layer, 3.75 mm thickness specimens after 100000 cycles.



Figure(35).The relation between the deflection and load at various number of cycles for 10 layer, 4.6mmthickness and the 8layer, 3.75 mm thickness specimens after 300000 cycles.



In Fig. 29 and Fig. 30 the load against the deflection as the x-axis shows the difference between different values and curves for different numbers of cycles which show how number of cycles affect the load and its values during the tests, the first Fig. is to 10 layer 4.6 mm thickness composite under different deflections at various selected numbers of cycles and the second is for the 8 layer 3.75 mm thickness specimens under the same conditions.

As it seen from the Fig. 29 and Fig. 30, the initial values are in a linear increase to reach top value at the maximum deflection and from there as the test progress and the cycles increase the load for the lest deflection decreases at a study rate to reach failure point but for maximum deflection the decrease is concentrated in the first hundred thousand of fatigue and then it slows to decreasing rate and at the end the rate increase to reach it failure value.

In Fig. 31, Fig. 32, Fig. 33, Fig. 34, Fig. 35, and Fig.36 represent the relation between the load and deflection for two different thicknesses under three different deflections for different points of the number of cycles.

As it is seen from the Fig. 32 to Fig. 36 the difference between the two curves increases as the load required deflection increases and as the experiment moves on the difference for the small deflection stays the same, but this thing doesn't apply to the other two points where the difference decreases as the cycles increase.

### **Damage Characterization through Optical Microscopy**

The specimens were polished and viewed under the light microscope at different magnification ranges.

It can be clearly seen that the composite have a very complex structure because of the use of the fabric instead of the use of fiber in the composite fatigue.

The inter woven nature of the fabric provides some extra components of stress because of the presence of the extra weft fiber in the transverse direction .The micrographics shown provides a summary of events taking place in a variety of computations, the revels matrix cracking, delamination ,splitting of fiber and matrix, and breaking of fiber bundle. In Fig. 37 a micrographics of the composite specimen shows the nature of the composite and its fiber arrangement in the site of the composite.

The transverse cracks that take place in the fiber matrix interface are shown in Fig. 38 where also it shows the matrix cracks which result from the tensile stress at the top of the specimen.

In Fig. 39 the fiber matrix debonding is seen along the edge of the fiber, this is because of the complex nature of the normal stresses then cracks move in almost a perpendicular way to the 0o fiber on the other side in a 90° to the fiber direction, leading to break the interface inside the composite and inside the layer.

Fig.40 shows the fiber is being pulled out from the matrix, complete failure of the specimen is shown in Fig. 41 where the delamination and total splitting are present, for a more clear view of the delamination and fiber fracture and the fiber matrix debonding, see Fig. (42), which is for the scanning electron fractography [Zham 2002].



Figure (37). Micrographics for composite material shows it fiber arrangement.

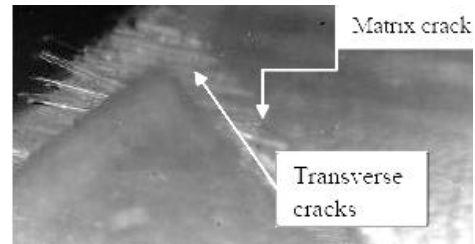


Figure (38) The transverse cracks in the composite specimen

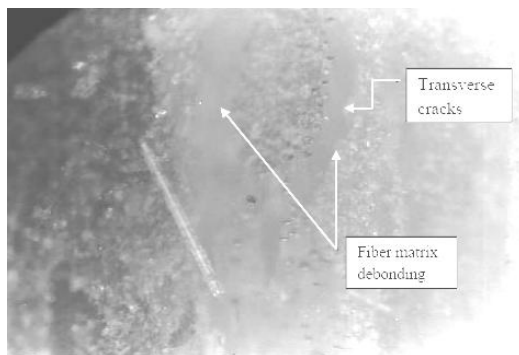


Figure (39) The fiber matrix debonding.

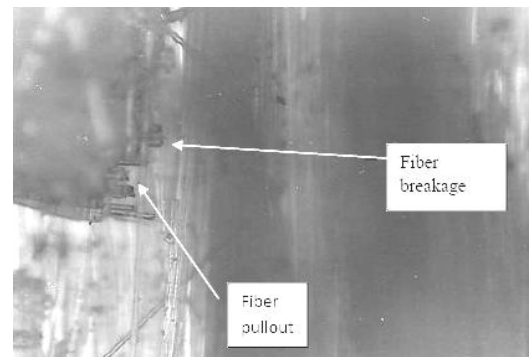
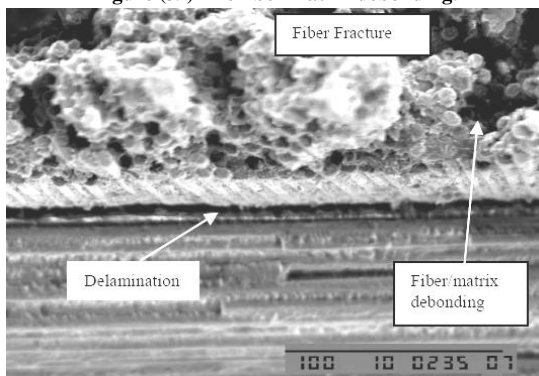


Figure (40) Fiber is being pulled out from the matrix.



Figure(41) Scanning electron fractograph showing damage events in the composite[Zham 2002].

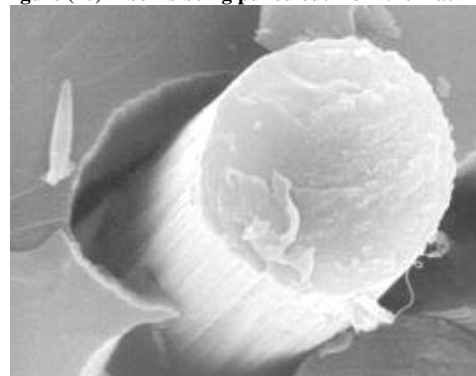


Figure (42) The fiber matrix debonding [Zham 2002].

## CONCLUSIONS

The main conclusions drawn from this work are listed below:

- The delamination was found to be the major damage mode in the glass fiber reinforced composite while the matrix cracking plays a secondary role as it is the key for the delamination.
- The fatigue damage mostly starts with transverse crack and it leads to the other type of damage such as fiber fracture, fiber matrix debonding and delamination.
- The fatigue life is effected by both the thickness of the specimens and the load value, and it has a significant behavior that could be divided to three major regions the first is with a very fast drop in the strength and this drop depends on the load factor and the thicknesses, and a second region

that could be considered is the face where the crack propagation takes place till it reaches the limit in which the composite drops rapidly and goes to the final failure.

## REFERENCES

- Ali Hussain Mohammed Al-Hilli,” Analytical and Experimental Analysis of High Velocity Impact on Composite Material Targets”, Ph.D., Nahrain University, 2006
- Daneila Popescu,” A Model for damage predication in polymer matrix composite subjected to bending fatigue loading “, Proceedings of the Romanian academy, Series A, Volume 8, Number2, (2007).
- Diawekar Keddlaya and Assimina A. Pelegri ,” Failure redicationof graphite/epoxy laminates with induced intermittent load during fatigue “, Acta materialia , Volume 50, Pages 4813-4821,(2002).
- Hwang W, Han K. S.,” Fatigue of Composite Material Damage Model and Life Predication “, ASTM special technical publication (1985).
- Hwang W, Han K. S.,” Fatigue of Composite-Fatigue modulus Concept and Life Predication “,Journal of Composite Materials, Volume 20, Pages 154-165,(1986).
- Lee J-W, Daniel IM, Yaniv G.,” Fatigue Life Prediction of Cross- Ply Composite Laminates “, ASTM International,(1989).
- Liu Y.M. and S.Mahadeven,” Fatigue Damage Modeling of Composite Laminates “, 9th ASCE Conference on Probabilistic Mechanics and Structural Reliability, (2004).
- Mahmood Zabihpoor and Saeed Adibnazari,” A Micromechanics Approach for Fatigue of Unidirectional Fibrous Composites “,Iranian Polymer Journal, Volume 16, Pages 219-232, (2007).
- Miyano Y. Nakada M.”Predication of Flexural fatigue strength of CFRP Composite Under Arbitrary Frequency Stress Ratio and Temperature “ Journal of Composite Material ,Volume 31 ,(1997).
- Mohamed Shorieh and Larry B. Lessard,” progressive fatigue modeling of laminated composite pinned/bolted connections “, proceeding of ICCM, volume 2,fatigue,fractureand ceramic matrix composites, Pages II-156-II166,(1997).
- Paepegem W. Van and J.Degerick.” Fatigue degradation modeling of palin woven glass/epoxy composite “. Composite Materials, Composite Material part a, 32(10), Pages 1433-1441, (2001).
- Zham, R. Khan, F. Al-Sulaiman, N. Merah,” Fatigue Damage in Woven Carbon Fabric/Epoxy Laminate at Non-Ambient Temperature “, The 6th Saudi Engineering Conference, KFUPM, Dhahran, Volume 5,Pages 313-326,(2002).



## PARAMETRIC STUDY OF LAMINAR FREE CONVECTION IN HORIZONTAL ANNULUS WITH AND WITHOUT FINS ON THE INNER CYLINDER

Asst. Prof. Dr. Saad M. Saleh  
Mechanical Engineering Department  
University of Baghdad

Jasim Mohammed Mehdi  
Mechanical Engineering Department  
University of Baghdad

### ABSTRACT

An experimental and numerical study has been carried out to investigate the heat transfer by natural convection in air-filled annulus between two horizontal isothermal concentric cylinders with and without annular fins under steady state conditions; the inner cylinder surface is maintained at a higher temperature and the outer cylinder surface at a lower one.

In the experimental study, the annulus inner surface is maintained at high temperature by applying uniform heat flux to the inner cylinder while the annulus outer surface is subjected to ambient temperature and maintained at low temperature. The experiments were carried out at a range of Rayleigh number ( $1.81 \times 10^3 - 4.03 \times 10^4$ ) for case without fins and ( $1.08 \times 10^3 - 2.94 \times 10^4$ ) for case with fins, at different diameter ratios ( $\eta = 2.0, 2.6$  and  $3.0$ ). The results showed that: (1) increasing the diameter ratio ( $\eta$ ) strongly increases the heat transfer rate, (2) increasing Rayleigh number increases the heat transfer rate for any  $\eta$  and (3) attaching annular fins to the inner cylinder surface of (No. of fins/cm) of 1.25 and (fin height/gap width) of 0.143, 0.186 and 0.286 reduced the mean Nusselt number ( $Nu$ ) within (16.3 - 29.7) percent of that for the case without fins at the same Rayleigh number. In the numerical study, only the case without fins was investigated. The buoyancy driven fluid flow resulting from the temperature difference between the cylinders, is assumed to be steady, laminar, two dimensional and symmetric about the vertical center-line. Only half of the domain needs to be modeled from symmetry considerations. Navier-Stokes and energy equations are expressed in vorticity-stream function form and discretized via finite difference method. The Rayleigh number (based on gap width) varied from  $10^2$  to  $10^5$  with the influence of diameter ratio obtained near a Rayleigh number of  $10^4$ . Results for the local and mean Nusselt number, the contour maps of the streamlines and isotherms are presented, to show some of the flow and heat transfer characteristics. The results numerically obtained showed a good agreement with the present experimental data.

### الخلاصة

أجريت دراسة عملية ونظرية لاستقصاء انتقال الحرارة بالحمل الطبيعي خلال فجوة حلقيّة مملوءة هواء تقع بين اسطوانتين أفقيّتين متحدتي المركز بثبوت درجة حرارة السطحين الداخلي و الخارجي للفجوة و بوجود و عدم وجود زعانف حلقيّة، تحت شروط حالة الاستقرار، وأن تكون الاسطوانة الداخلية ذات درجة حرارة أعلى من الخارجية.

في الدراسة العملية تم حفظ السطح الداخلي للفجوة بدرجة حرارة أعلى عن طريق تسليط فيض حراري منتظم على السطح الداخلي للأسطوانة الداخلية فيما حفظ السطح الخارجي للفجوة بدرجة حرارة أقل بتعريض الاسطوانة الخارجية الى درجة حرارة الجو. أجريت التجارب ضمن مدى لعدد رالي تراوح بين  $(1.81 \times 10^3 - 4.03 \times 10^4)$  للحالة بدون زعانف، و  $(2.94 \times 10^4 - 1.08 \times 10^3)$  للحالة بوجود زعانف، و عند نسبة أقطار (2.0, 2.6, 3.0). أظهرت النتائج بان زيادة نسبة الاقطار تزيد من معدل انتقال الحرارة بين الاسطوانتين، كذلك إن الزيادة في عدد رالي تؤدي الى زيادة معدل انتقال الحرارة لاي نسبة أقطار، و إن اضافة زعانف حلقيّة الى الاسطوانة الداخلية بشكل تكميلي بمعدل 1.25 زعنفة لكل سنتيمتر واحد و بنسبة (ارتفاع الزعنفة/ سمك الفجوة) 0.143, 0.186, 0.286 يقلل من رقم نسلت المعدل بحوالي (29.7% - 16.3%) مقارنة بالحالة بدون زعانف و لرقم رالي نفسه. تناولت الدراسة النظرية حل مسألة انتقال الحرارة بالحمل الحر خلال فجوة حلقيّة أفقيّة و للحالة بدون زعانف فقط، إذ تم افتراض جريان المائع الناشيء عن قوى الطفو و نتيجة للفارق في درجة حرارة الاسطوانتين، هو جريان مستقر، طباقى، ثنائي البعد و متناظر حول الخط المستقيم الشاقولي المار بالمركز. و نتيجة لاعتبارات التناظر فقط نصف واحد من نصفي الفجوة أخضع للدراسة. تم تمثيل معدلات نافير-ستوكس بالاضافة الى معادلة الطاقة بصيغة الدوامية- دالة الجريان و من ثم فُكّت باستخدام طريقة الفروقات المحددة. و قد تم الحصول على نتائج مُثلت بمخططات دالة الجريان وخطوط تساوي درجة الحرارة، وتوزيع عدد نسلت الموضعي و المعدل خلال الفجوة ولأعداد رالي تتراوح بين  $10^2$  الى  $10^5$  و نسب قطر خارجي الى قطر داخلي (2.0, 2.6, 3.0). بينت النتائج التأثير المهم للمتغيرات (رقم رالي و نسبة الاقطار) على عملية انتقال الحرارة خلال الفجوة و قد أظهرت النتائج المستحصلة عددياً توافقاً جيداً مع النتائج العملية.

**KEYWORDS:** Free Convection, Fins, Laminar, Horizontal Annulus.

### INTRODUCTION

Natural convection in the annulus between two horizontal concentric cylinders has been investigated widely in the past owing to a number of practical applications associated with this geometry such as heat transfer and fluid flow in parabolic cylindrical solar collector, under-ground electrical transmission lines and pressurized water reactors. **Kuhen and Goldstein [1]** carried out an experimental and numerical investigation of natural convection heat transfer for air and water in concentric horizontal annuli for values of Rayleigh number up to  $10^7$ . Their work was carried out for a diameter ratio equal to 2.6. In their experimental study, it was reported that the transition from laminar to turbulent flow occurs at Rayleigh number equal to  $10^6$ . Later, **Hessami et al. [2]** studied experimentally the free convection in a horizontal annulus with a large diameter ratio of (11.4). The test fluids were air, glycerin and mercury. This study was unique as they claimed because there are no experimental details in the literature for  $\eta > 8.1$ . In addition, no experimental data exist for mercury. Recently **Nada [3]** conducted an experimental study of natural convection in horizontal and inclined annuli at Rayleigh number of ( $5 \times 10^4 \leq Ra_{Di} \leq 5 \times 10^5$ ) for different diameter ratios ( $\eta = 1.85, 2.5$  and  $3.85$ ) and different inclination angle of the annulus ( $\phi = 0^\circ, 30^\circ$  and  $60^\circ$ ). The results showed that increasing the annulus gap width strongly increases the heat transfer rate and the heat transfer rate slightly decreases with increasing the inclination of the annulus from the horizontal. Also, several numerical investigations of laminar natural convection in a concentric horizontal annulus have been conducted [4–6]. In these previous works, maximum transition time to attain steady state in underground electrical transmission lines, the

effects of variable properties on the laminar natural convection of gases in horizontal isothermal annulus and the effect of application constant heat flux on the inner cylinder as compared to an isothermal inner cylinder were studied.

An essential restriction in natural convection in annulus is the heat transfer limitation due to the fixed area of the inner and outer cylinders. One approach affecting heat transfer rate in annulus is to equip the surface of the inner cylinder with some annular fins. From a practical point of view, the existence of such fins is of interest due to the possibility of heat transfer augmentation in such geometry; but also heat transfer reduction is expected since existence of fins will resist the natural circulation inside the annulus. **Patankar and Chai [7]** studied the flow and heat transfer for an annulus with six radial fins attached to inner cylinder at ( $Ra \leq 10^6$ ); for two different orientations; the first is when two fins of the six are vertical and the second is when two fins are horizontal. They observed that the orientation of the fins has no significant effect on mean Nusselt number prediction, while the blockage due to the presence of fins has a significant effect on the flow and temperature fields and therefore on heat transfer. Their results indicate that the mean Nusselt number decreases with increasing fin height. **Rahinam and Farhadi [8]** investigated the effect of radial fins on heat transfer by turbulent natural convection for an annulus with a number of radial fins ranged from 2 to 12 attached to inner cylinder. They examined two different orientations used by Patankar and Chai [7] to reveal the effect of fin height and fin orientation. The Rayleigh number considered in this study ranges from  $10^6$  to  $10^9$ . Their results show that the higher fin height has a blocking effect on flow causing lower heat transfer rate. they concludes that there is a reduction of heat transfer rate in all of the orientations considered in this study as compared to the case of no fin at the same Rayleigh number.

The main aim of the present experimental investigation is to determine the effect of the annular fins, diameter ratio and Rayleigh number on mean Nusselt number prediction across the annulus. The numerical study objectives are to develop a mathematical model capable of predicting fluid flow and heat transfer in horizontal concentric annuli without fins using finite difference method for a range of Rayleigh numbers and diameter ratios.

## NUMERICAL STUDY

### Mathematical modeling

The governing equations for the natural convection in the annulus between horizontal concentric cylinders under steady-state conditions can be written as: [1]

$$\frac{1}{r} \frac{\partial}{\partial r} (ru) + \frac{1}{r} \frac{\partial v}{\partial \phi} = 0 \quad \dots\dots\dots (1)$$

$$\rho_o \left[ u \frac{\partial u}{\partial r} + \frac{v}{r} \frac{\partial u}{\partial \phi} - \frac{v^2}{r} \right] = - \frac{\partial p}{\partial r} + \mu \left[ \frac{\partial}{\partial r} \left( \frac{1}{r} \frac{\partial}{\partial r} (ru) \right) + \right. \\ \left. \frac{1}{r^2} \frac{\partial^2 u}{\partial \phi^2} - \frac{2}{r^2} \frac{\partial v}{\partial \phi} \right] - g \rho_o [1 - \beta(T - T_o)] \cos \phi \quad \dots\dots\dots (2)$$

$$\rho_o \left[ ru \frac{\partial v}{\partial r} + v \frac{\partial v}{\partial \phi} + uv \right] = - \frac{\partial p}{\partial \phi} + \mu \left[ r \frac{\partial}{\partial r} \left( \frac{1}{r} \frac{\partial}{\partial r} (rv) \right) + \right.$$

$$\left[ \frac{1}{r} \frac{\partial^2 v}{\partial \phi^2} + \frac{2}{r} \frac{\partial u}{\partial \phi} \right] + g \rho_o r [1 - \beta(T - T_o)] \sin \phi \quad \dots\dots\dots (3)$$

$$u \frac{\partial T}{\partial r} + \frac{v}{r} \frac{\partial T}{\partial \phi} = \alpha \left[ \frac{1}{r} \frac{\partial}{\partial r} \left( \frac{\partial T}{\partial r} \right) + \frac{1}{r^2} \frac{\partial^2 T}{\partial \phi^2} \right] \quad \dots\dots\dots (4)$$

where the co-ordinate  $r$  is measured from the center of the system, and  $\phi$  is measured clockwise from the upward vertical line; as shown in Fig.(1). The use of vorticity–streamfunction formulation can simplify the solution procedure. With the streamfunction, the velocity components  $u$  and  $v$  can be expressed as

$$u = \frac{1}{r} \frac{\partial \psi}{\partial \phi}, \quad v = -\frac{\partial \psi}{\partial r}$$

Furthermore, by setting

$$R = \frac{r}{\delta} \quad \Psi = \frac{\psi}{\alpha} \quad \Omega = \frac{\delta^2}{\alpha} \omega \quad \theta = \frac{T - T_o}{T_i - T_o}$$

where  $\alpha = k/\rho c$  is the thermal diffusivity,  $\delta$  is the gap between the cylinders and  $\omega$  is the vorticity, Equations (1)–(4) can be simplified as

$$\nabla^2 \Omega = \frac{1}{Pr} \left[ U \frac{\partial \Omega}{\partial R} + \frac{V}{R} \frac{\partial \Omega}{\partial \phi} \right] + Ra \left[ \frac{\cos \phi}{R} \frac{\partial \theta}{\partial \phi} + \sin \phi \frac{\partial \theta}{\partial R} \right] \quad \dots\dots\dots (5)$$

$$\nabla^2 \Psi = -\Omega \quad \dots\dots\dots (6)$$

$$U = \frac{1}{R} \frac{\partial \Psi}{\partial \phi}, \quad V = -\frac{\partial \Psi}{\partial R} \quad \dots\dots\dots (7)$$

$$\nabla^2 \theta = U \frac{\partial \theta}{\partial R} + \frac{V}{R} \frac{\partial \theta}{\partial \phi} \quad \dots\dots\dots (8)$$

$\nabla$  is Laplacian in polar coordinates and defined as;  $\nabla^2 = \frac{\partial^2}{\partial R^2} + \frac{1}{R} \frac{\partial}{\partial R} + \frac{1}{R^2} \frac{\partial^2}{\partial \phi^2}$

The dimensionless parameters appearing in the Equations (5)–(8) are the Prandtl number  $Pr = \nu/\alpha$  and the Rayleigh number  $Ra = g\beta(T_i - T_o)\delta^3/\alpha\nu$ .

For the natural convection in an annulus between two concentric cylinders, the flow is symmetric with respect to the vertical centerline. Thus, half of the annulus can be taken as the computational domain, i.e. attention is restricted to  $(0 < \phi < \pi)$ .

The boundary conditions on two impermeable isothermal walls are given by

$$\Psi = U = V = 0 \quad \Omega = -\frac{\partial^2 \Psi}{\partial R^2} \quad \theta = 1$$

on the inner cylinder and

$$\Psi = U = V = 0 \quad \Omega = -\frac{\partial^2 \Psi}{\partial R^2} \quad \theta = 0$$

on the outer cylinder. When half of the annulus is taken as the computational domain, the following symmetric condition is applied along two vertical lines of symmetry at  $\phi = 0$  and  $\phi = \pi$ :

$$\Psi = U = V = 0 \quad \Omega = 0 \quad \frac{\partial \theta}{\partial \phi} = 0$$

The local and mean Nusselt number on inner cylinder surface is respectively expressed by the equations below: [4]

$$Nu = -\frac{\partial \theta}{\partial R} \Big|_{R=R_i} \dots\dots\dots (9)$$

$$\overline{Nu} = \frac{1}{\pi} \int_0^\pi Nu.d\phi \dots\dots\dots (10)$$

Simpson rule has been used to compute mean Nusselt number.

### **Numerical solution**

A finite difference method (FDM) is used to discretize system of the partial differential equations (5 through 8) into algebraic equations system. The new algebra equations system will be solved using iterative under relaxation method, to give approximate values of the dependent variables at a number of discrete points called (grid points or nodes) in the computational domain. A grid was established by subdividing the computational domain in the  $R$  and  $\phi$  directions with indexes  $i$  and  $j$  that are integers describing the number of radial grid lines from the inner cylinder and the number of angular grid lines from the top symmetry line respectively, as shown in Fig.(4.2). The spacing of the grid lines in the  $R$ -direction is uniform and given by  $\Delta R$  and that of the grid lines in the  $\phi$ -direction is also uniform and given by  $\Delta \phi$ . The number of the grid points will be  $[m \times n]$  where  $(m)$  represents the number of gridlines in the  $R$ -direction and equals  $[(1/\Delta R)+1]$  while  $(n)$  represents the number of gridlines in the  $\phi$ -direction and equals  $[(\pi/\Delta \phi)+1]$ .

The partial differential equations (5)-(8) were finite-differenced using central difference schemes for all of the derivatives. In particular, let  $\xi$  represents  $\Psi, \Omega$ , or  $\theta$ , then

$$\frac{\partial \xi}{\partial R} = \frac{\xi_{i+1,j} - \xi_{i-1,j}}{2\Delta R}, \quad \frac{\partial \xi}{\partial \phi} = \frac{\xi_{i,j+1} - \xi_{i,j-1}}{2\Delta \phi}, \quad \frac{\partial^2 \xi}{\partial R^2} = \frac{\xi_{i+1,j} - 2\xi_{i,j} + \xi_{i-1,j}}{2\Delta R} \quad \text{and} \quad \frac{\partial^2 \xi}{\partial \phi^2} = \frac{\xi_{i,j+1} - 2\xi_{i,j} + \xi_{i,j-1}}{2\Delta \phi}$$

Equations (5)-(8) were put in the form convenient for iterations with under relaxation method as;

$$\Psi^{\zeta+1}_{i,j} = \Psi^{\zeta}_{i,j} + \gamma_{\Psi} \left[ h_1 \Psi_{i+1,j} + h_2 \Psi_{i-1,j} + h_3 (\Psi_{i,j+1} + \Psi_{i,j-1}) + \frac{(\Delta R)^2}{h} \Omega_{i,j} - \Psi_{i,j} \right] \dots\dots (11)$$



$$\Omega^{\zeta+1}_{i,j} = \Omega^{\zeta}_{i,j} + \gamma_{\Omega} \left[ h_4 \Omega_{i+1,j} + h_5 \Omega_{i-1,j} + h_6 \Omega_{i,j+1} + h_7 \Omega_{i,j-1} - \Omega_{i,j} + \right. \\ \left. h_8 (\theta_{i+1,j} - \theta_{i-1,j}) + h_9 (\theta_{i,j+1} + \theta_{i,j-1}) \right] \dots\dots\dots (12)$$

$$\theta^{\zeta+1}_{i,j} = \theta^{\zeta}_{i,j} + \gamma_{\theta} \left[ h_{10} \theta_{i+1,j} + h_{11} \theta_{i-1,j} + h_{12} \theta_{i,j+1} + h_{13} \theta_{i,j-1} - \theta_{i,j} \right] \dots\dots\dots (13)$$

Where  $h_1, h_{13}$  are parameters from the discretization;

$$h = 2 \left[ 1 + \frac{1}{R^2} \left( \frac{\Delta R}{\Delta \phi} \right) \right] \quad h_1 = \left( 1 + \frac{\Delta R}{2R_i} \right) / h \quad h_2 = \left( 1 + \frac{\Delta R}{2R_i} \right) / h \quad h_3 = \frac{1}{R_i^2} \left( \frac{\Delta R}{\Delta \phi} \right)^2 / h$$

$$h_4 = \left( 1 + \frac{\Delta R}{2R_i} - \frac{\Delta R}{2Pr} U_{i,j} \right) / h \quad h_5 = \left( 1 - \frac{\Delta R}{2R_i} + \frac{\Delta R}{2Pr} U_{i,j} \right) / h \quad h_6 = \left( \frac{1}{R_i^2} \left( \frac{\Delta R}{\Delta \phi} \right)^2 - \frac{(\Delta R)^2}{2Pr R_i \Delta \phi} V_{i,j} \right) / h$$

$$h_7 = \left( \frac{1}{R_i^2} \left( \frac{\Delta R}{\Delta \phi} \right)^2 + \frac{(\Delta R)^2}{2Pr R_i \Delta \phi} V_{i,j} \right) / h \quad h_8 = -Ra \frac{\Delta R}{2} \sin \phi_j / h \quad h_9 = -Ra \frac{(\Delta R)^2}{2R_i \Delta \phi} \cos \phi_j / h$$

$$h_{10} = \left( 1 + \frac{\Delta R}{2R_i} - \frac{\Delta R}{2} U_{i,j} \right) / h \quad h_{11} = \left( 1 - \frac{\Delta R}{2R_i} + \frac{\Delta R}{2} U_{i,j} \right) / h \quad h_{12} = \left( \frac{1}{R_i^2} \left( \frac{\Delta R}{\Delta \phi} \right)^2 - \frac{(\Delta R)^2}{2R_i \Delta \phi} V_{i,j} \right) / h$$

$$h_{13} = \left( \frac{1}{R_i^2} \left( \frac{\Delta R}{\Delta \phi} \right)^2 + \frac{(\Delta R)^2}{2R_i \Delta \phi} V_{i,j} \right) / h$$

and  $\gamma_{\Psi}, \gamma_{\Omega}$  and  $\gamma_{\theta}$  are relaxation factors chosen from numerical experiments as:

$$\gamma_{\Psi} = 0.8, \gamma_{\Omega} = 0.07 \text{ \& } \gamma_{\theta} = 0.7.$$

These values of relaxation factors have been found to stabilize the computation procedure for Rayleigh number ranges ( $10^2 - 10^5$ ) and increase considerably the rate of convergence. Number of iterations ranges (1000 - 1500) was enough to attain the required convergence. For the cases when Ra was increased to a critical value which was beyond the experimentally known laminar flow regime ( $Ra > 10^5$ ) the solution diverged and the method becomes unstable.

During the computation, because of the slow rate of convergence for the stream function and vorticity compared with that of temperature, iteration was performed in weighted cyclic pattern as  $(\Psi - \Omega - \Psi - \Omega - \theta)$ . The convergence criteria needed for termination of the computation were preassigned as:

$$(\Psi^{\zeta} - \Psi^{\zeta-1}) / \Psi^{\zeta} \leq 10^{-5}, (\theta^{\zeta} - \theta^{\zeta-1}) / \theta^{\zeta} \leq 10^{-5} \text{ and } (\Omega^{\zeta} - \Omega^{\zeta-1}) / \Omega^{\zeta} \leq 10^{-5}$$

The calculations were performed on P4-computer using MATLAB-7 software.

## EXPERIMENTAL STUDY

### Experimental apparatus

The apparatus was designed and constructed specially for investigating the effect of Rayleigh number, diameter ratio and existing of annular fins on the natural convection heat transfer between two horizontal concentric cylinders of constant wall temperature under steady state conditions. The experimental apparatus is diagrammatically shown in Fig.(2). The test-section consists of a fixed (27mm) outside diameter, (5 mm) thick and (200 mm) long aluminium inner cylinder to which one of three different aluminium outer cylinders (200 mm) long, (4 mm) thick with 55,70 and 82 mm outside diameter were assembled to yield diameter ratios of 2, 2.6 and 3, respectively. The inner cylinder was made in two configurations, one in which the inner cylinder is being unfinned and another in which it being finned. Finned inner cylinder, shown in plate (1), is fixed to one of three different outer cylinders mentioned above, to give (fin height/gap width) of 0.286, 0.186 and 0.143. The test section is mounted on a wooden supporting-frame and stored horizontally with aid of a spirit level. The inner cylinder was heated by passing an alternative current through a 0.2-mm-dia, 5-m-length, 95-ohm nichrome wire wounded as spiral inside glass tube, (8 mm) in diameter and (190 mm) long. The heater, i.e. the glass tube and the nichrome wire, was mounted concentrically in the inner cylinder by two fictile pieces. The space between the glass tube and the inside surface of inner cylinder, also the space inside glass tube was filled by very fine sand to avoid generation of heat convection in it and to smooth any irregularities in the heat flux generated from the heater. The heater was connected in series to the power supply to ensure that incoming mains voltage is constant (220 V), and in parallel with the variac to adjust the heater input voltage as required. The voltage and current supplied to the heater were measured by digital voltmeter and ammeter of accuracy  $\pm 0.05$  volt and  $\pm 5 \times 10^{-4}$  ampere. Temperatures on the inner and the outer cylinder surfaces were measured by thermocouples type T; several holes of (1.5 mm) in diameter were cut over along the surface of the cylinders to accommodate thermocouples. These holes are distributed as follows:

1. Six holes of (5 mm) deep on the surface of unfinned inner cylinder; two located at a distance of (30 mm) from the ends and four at the mid-plane  $90^\circ$  apart between them.
2. Six holes on the surface of finned inner cylinder, two of (5 mm) deep, located at a distance of (30 mm) from the ends and four of (9 mm) deep at the mid-plane  $90^\circ$  apart between them.
3. Four of (2 mm) deep on the outer cylinder surface; two located at a distance of (30 mm) from the ends and two at the mid-plane  $180^\circ$  apart between them.

The ends of the test-section were plugged with Teflon (an insulating material) pieces in order to minimize the axial end losses and to mount the inner cylinder concentrically inside the outer cylinder. The Teflon piece is a disc (85 mm) in diameter and (20 mm) thick, cut out radially in a (10 mm) thick to get a diameter equal to the inside diameter of the outer cylinder, and drilled axially in a distance of (10 mm) and diameter of (27 mm) to get a diameter equal to the outside diameter of the inner cylinder. A hole of (5 mm) in diameter was drilled axially in each Teflon piece to draw the heater terminals and the thermocouples lead outside the test-section. Two thermocouples (type T) were fixed on the inside and outside surface of each teflon piece to estimate conduction heat losses from the test section ends. The distance between these thermocouples was 14 mm. knowing the thermal conductivity of the teflon; the ends conduction losses could thus be calculated.

### **Experimental Procedure**

Components of experimental rig were assembled in a windowless large room, free of air currents, to avoid occurrence of fluctuations in the room temperature.

The following Procedure steps have been followed in each test run:

- Mount the inner cylinder to appropriate outer cylinder to obtain a certain diameter ratio.
- Adjust the input power to the heater to obtain a certain Rayleigh number.
- Allow the test to run for a period until steady state condition was achieved. The steady state condition was considered to be achieved when the differences in the measured temperatures were not more than 0.2 °C over 30 min. In all the experiments, the steady state condition period was within 3–4 hours.
- After steady state condition has been established, the readings of all thermocouples, the input power and the ambient temperature were recorded.
- Repeat steps 2–4 for nine different Rayleigh numbers.
- Repeat steps 2–5 twice, once for case without fins and another for case with fins.
- Repeat steps 1–6 three times for different diameter ratio; 2.0, 2.6 and 3.0 .

## **RESULTS AND DISCUSSION**

### **Experimental Results**

Fig.(3) shows the variation of mean Nusselt number ( $\overline{Nu}$ ) with Ra for different diameter ratios. This figure shows that for any diameter ratio, ( $\overline{Nu}$ ) generally increases with increasing Rayleigh number.

Fig.(4) shows that ( $Nu$ ) increases with increasing diameter ratio, and also shows that the curves of the different diameter ratios converge to each others as Ra decreases. This means that the effect of the diameter ratio on the heat transfer rate decreases with decreasing Ra.

Figs.(5) show the influence of attaching fins on inner cylinder surface on mean Nusselt number prediction . This figure indicates that there is a reduction in mean Nusselt number in the presence of fins as compared with case without fins. For the same value of Rayleigh number, reduction in Nusselt number may be ranged between (16.3% - 29.7%). The reason for this reduction is although the annular fins increase the surface area; they also resist the airflow. This resistance has been caused a decrease in heat transfer coefficient more than the increase in the surface area; as a consequence lower heat transfer rate was resulted.

Fig.(6) presents the effect of the ratio (fin height/gap width) on mean Nusselt number. At a lower value of fin height (14.3 percent of gap width) the mean Nusselt number seems to be relatively larger. One can conclude as the (fin height/gap width) increase the heat transfer coefficient decreases, this probably because of a larger (fin height/gap width) mean more obstruction for the fluid motion inside the cavity; consequently less convective heat transferred from inner cylinder.

## **Numerical Results**

### **Effect of Rayleigh number**

Left sides of Figs. (7) - (11) present streamlines at  $\eta=3.0$  for different values of Rayleigh number ( $10^2$ - $10^5$ ). Fig.(7) depicts the streamlines at Rayleigh number of  $10^2$  which form a single cell rotates clockwise. This cell does not occupy uniformly the whole gap width. At this value of Rayleigh number the buoyancy force is very small to influence the temperature field and develop a fluid motion inside the annulus. A transition region exists for Rayleigh number between  $10^3$  and  $10^4$ , Figs.(8-9). In this region, the flow remains in essentially the same pattern but become strong enough to influence the temperature field. As the Rayleigh number increases to  $10^4$  -  $10^5$ , Figs.( 9-10), A steady laminar boundary layer exists and the flow tends to occupy more uniformly the whole cavity and the center of circulation which defined as the point of the extremum of the stream function, begins to move higher up toward the upper symmetry line. The lower portion of the gap looks to be streamlines-free because this region is filled with a cold fluid and becomes stagnant. It is stagnant because the viscosity forces overcome the buoyancy forces and inhibit the fluid motion through it.

Right sides of Figs. (7) - (11) show the isotherms for diameter ratio of 3.0 with different values of Rayleigh numbers ( $10^2$ - $10^5$ ). For smaller Rayleigh number ( $10^2$ ), the velocity is too small to affect the temperature distribution which remains essentially as in pure conduction. This makes the convection term in Eq.(8) vanish, therefore Eq.(8) can be approximated by ( $\nabla^2\theta=0$ ), so the isotherms are almost uniformly concentric as shown in Fig.(7). For Rayleigh number of  $Ra=10^3$ , the isotherms indicates that the conduction stills the dominant heat transfer mechanism in the cavity. In other words, buoyancy forces are not strong enough to trigger significant convection. As the Rayleigh numbers increase to  $10^4$ , convection becomes dominant mode of heat transfer, and stronger recirculation for the fluid will be occurred making the outer fluid layer warmer than the inner one causing at the core so called temperature reversal phenomenon. This phenomenon is depicted by isotherms of Figs.(9),(10) and (11). It is noticed in Figs.(10) and (11) that the isotherms are spaced more closely against the bottom of the inner cylinder and top of the outer cylinder, where the inner and outer cylinder thermal boundary layers are, respectively, thinnest. This mean maximum heat transfer from inner cylinder is from its lower portion while maximum heat transfer to outer cylinder is from upper portion; therefore heat is being essentially convected from lower portion of the inner cylinder to the top of the outer cylinder. In comparison of isotherms in Figs.(10) and (11) one can conclude as Rayleigh number increases isotherms at the lower portion of the inner cylinder and at the upper portion of the outer cylinder are further compressed.

Fig.(12) illustrates the distribution of local Nusselt number along the circumference of the inner cylinder for the cases of Rayleigh number of  $10^3$ ,  $10^4$ ,  $5 \times 10^4$  &  $10^5$ . The local Nusselt number has an increasing trend from the top ( $0^\circ$ -position) to the bottom ( $180^\circ$ -position), where the highest values are reached. There are three regions can be distinguished in Fig.(12):

First region ( $140^\circ < \phi < 180^\circ$ ), in this region local Nusselt number is relatively constant since the inner boundary layer is of relative uniform thickness (see isotherms), and gives a little variation in local Nusselt distribution.

Second region ( $10^\circ < \phi < 140^\circ$ ), in this region local Nusselt number loses the uniformity and a large gradient in its distribution can be observed, this because the

inner boundary layer get thicker in this region since heat removal by fluid decreases as the fluid scends up

Third region ( $0^\circ < \phi < 10^\circ$ ), here values of local Nusselt number approach to its minimum values, this due to formation of plume in this region. formation of the plume occurs where the two convective currents coming from the two annulus halves, impinging with each other and moving together upward without mixing, leaving a relatively stagnant region under impinging point. This behavior is roughly similar for most of Rayleigh numbers.

Fig.(13) illustrate the relation between mean Nusselt number and Rayleigh number at  $\eta = 3.0$ .  $\overline{Nu}$  is nearly constant at ( $10^2 < Ra < 10^3$ ) because of the predominance of conduction mode on heat transfer process. Beyond  $Ra$  of  $5 \times 10^3$  convection become predominant mechanism and  $\overline{Nu}$  begins to largely increase.

### **Effect of diameter ratio**

The left side of Fig.(14) illustrates the flow patterns moving inside the gap. Although the flow pattern does not change significantly, the center of rotation moves towards the top with increasing diameter ratio. That mean as the diameter ratio increases the flow become stronger.

Fig.(15) illustrates the effect of increasing  $\eta$  on local Nusselt number distribution around the inner cylinder circumference. It can be seen from this figure that for all the cases decreasing the diameter ratio decreases the local Nusselt number since the resistance to the circulation motion of the convection cells increases as  $\eta$  decreases and this leads to slower replacement of the hot air adjacent to the inner annulus surface by the cold air adjacent to the annulus outer surface and this results in a decrease of the heat transfer rate.

### **Comparison of present numerical and experimental results**

		$\overline{Nu}$		
		Exp.	Num.	% Dev.
$\eta = 2.0$	$Ra = 1.81 \times 10^3$	1.823	1.653	9.3
$\eta = 2.0$	$Ra = 5.76 \times 10^3$	2.656	2.406	10.4
$\eta = 2.6$	$Ra = 5.40 \times 10^3$	2.933	2.766	5.6
$\eta = 2.6$	$Ra = 1.76 \times 10^4$	4.086	3.813	6.6
$\eta = 3.0$	$Ra = 1.14 \times 10^4$	3.662	3.796	3.6
$\eta = 3.0$	$Ra = 4.03 \times 10^4$	4.880	5.184	6.2

$$\%Dev. = ((exp. value - num. value) / exp. value) \times 100\%$$

### **CONCLUSIONS**

Natural convection heat transfer between two horizontal concentric cylinders with and without annular fins attached to the inner cylinder was investigated numerically (for case without fins only) and experimentally (for both cases) under steady-state conditions. The experimental results showed that annular fins of (No. of fins/cm) of 1.25 and (fin height/gap width) of 0.143, 0.186 and 0.286 have negative effect on heat

transfer results and cause a reduction in mean Nusselt number within (16.3 – 29.7) percent of that for the case without fins at the same Rayleigh number, and higher (fin height/gap width) has some blocking effect on fluid motion inside the cavity, therefore If there is a tendency toward reducing heat transfer rate between the horizontal concentric cylinders, it is better to use high (fin height/gap width). The numerical results showed that the heat is essentially transferred from the bottom of the inner cylinder to the top of the outer cylinder owing to the strong convective motion due to the buoyancy at these positions and decreasing of the diameter ratio increase the resistances to the circulation motion which leads to slower replacement of the hot air adjacent to the inner cylinder by the cold air adjacent to the outer cylinder and this results in a decrease of the heat transfer rate.

## REFERENCES

- **Kuehn, T. H. and Goldstein, R. J.**, “An Experimental and Theoretical Study of Natural Convection in the Annulus between Horizontal Concentric Cylinders”, J. Fluid Mech., Vol. 74, Part 4, Pp. 695-719, 1976.
- **Hessami, M. A., Pollard, A. and Rowe, R.W.**, “A Study of Free Convective Heat Transfer in A Horizontal Annulus with A Large Radii Ratio”, ASME, J. Heat Transfer, Vol. 107, Pp. 603-610, 1985
- **Nada, S. A.**, “Experimental Investigation of Natural Convection Heat Transfer In Horizontal and Inclined Annular Fluid Layers”, Int. J. Heat Mass Transfer, Vol. 50, 2007.
- **Tsui, Y. T. and Tremblay, B.**, “Transient Natural Convection Heat Transfer in the Annulus between Concentric Horizontal Cylinder with Isothermal Surfaces”, Int. J. Heat Mass Transfer, Vol. 27, No. 1, Pp. 103-111, 1984.
- **Mahony, D.N., Kumar, R., and Bishop, E. H.**, “Numerical Investigation of Variable Property Effects on Laminar Natural Convection of Gases between Two Horizontal Concentric Cylinders”, ASME, J. Heat Transfer, Vol. 108, Pp. 783-789, November 1986.
- **Kumar, R.**, “Study of Natural Convection in Horizontal Annuli”, Int. J. Heat Mass Transfer, Vol. 31, No.6, Pp. 1137-1148, 1988.
- **Patankar, S.V. and Chai, J.C.**, “Laminar Natural Convection in Internally Finned Horizontal Annulus”, Numerical Heat Transfer, Vol. 24, Pp. 67–87, 1993.
- **Rahnam, M. and Farhadi, M.**, “Effect of Radial Fins on Two-Dimensional Turbulent Natural Convection in A Horizontal Annulus”, Int. J. Thermal Sciences, Vol. 43, Pp. 255-264, 2004.

- **Padilla, E. L. M., Campregher, R. And Silveira-Neto, A.,** “Numerical Analysis of Natural Convection in Horizontal Annuli at Low and Moderate Rayleigh Numbers”, Thermal Engineering, Vol. 5, No.4, Pp. 58-65, 2006.
- **Teertstra, P. And Yovanovich, M. M.,** “Comprehensive Review of Natural Convection in Horizontal Circular Annuli”, University Of Waterloo, 1998.
- **Roach. , P.J.** “Computational Fluid Dynamics”, Hermosa, Albuquerque, New Mexico, 1985.
- الشمري، منار صالح، ” دراسة نظرية و عملية لانتقال الحرارة بالحمل الحر خلال فجوة حلقيّة مائلة ، أطروحة ماجستير، جامعة تكريت 2005.

## NOMENCLATURE

D	diameter	$\Delta$	laplacian in polar coordinates
g	acceleration	$\eta$	diameter ratio
m	number of gridlines in R-direction	$\nu$	kinematic viscosity
n	number of gridlines in $\phi$ -direction	$\omega$	vorticity
Nu	local Nusselt number	$\Omega$	dimensionless vorticity
$\overline{Nu}$	mean Nusselt number	$\psi$	stream-function
p	pressure	$\Psi$	dimensionless stream-function
Pr	Prandtl number	$\rho$	density
Ra	Rayleigh number base on gap width	$\theta$	dimensionless temperature
Ra <sub>Di</sub>	Rayleigh number based on annulus inner diameter	Subscripts	
r	radial coordinate	i	radial mesh point
R	dimensionless radial coordinate	j	angular mesh point
T	temperature	i	inner cylinder
u,v	velocity components in R-, $\phi$ -directions	°	degree
U,V	dimensionless velocity components in R-, $\phi$ -directions	o	outer cylinder
Greek symbols		Superscripts	
$\alpha$	thermal diffusivity	$\zeta$	current iteration number
$\beta$	thermal expansion coefficient	$\zeta + 1$	next iteration number
$\delta$	gap width	—	mean

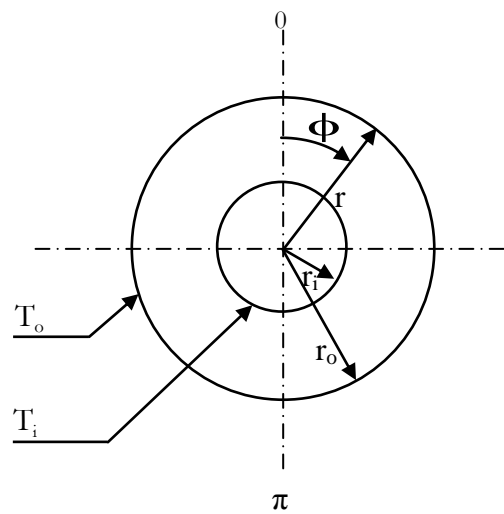


**Fig.(1) Physical and Coordinate system**

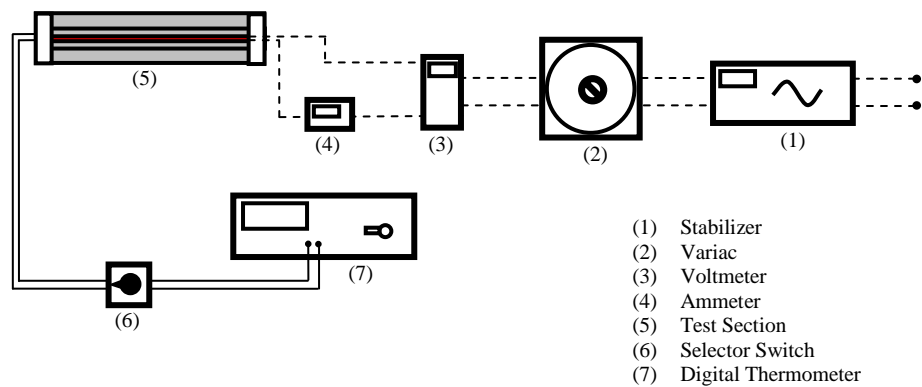


**Fig. (2) Schematic diagram of experimental apparatus**

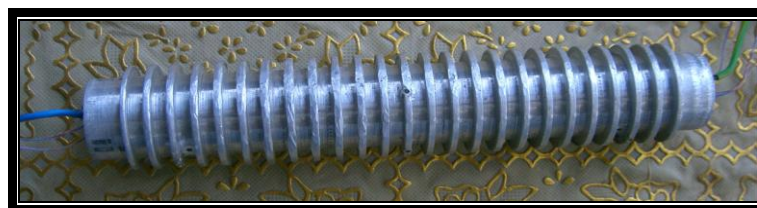


**Plate (1) Inner finned cylinder**



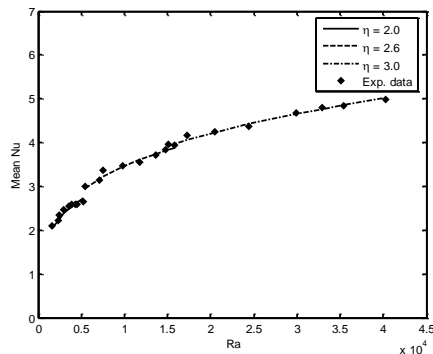


Fig (3) Mean Nusselt number as a function of Rayleigh number

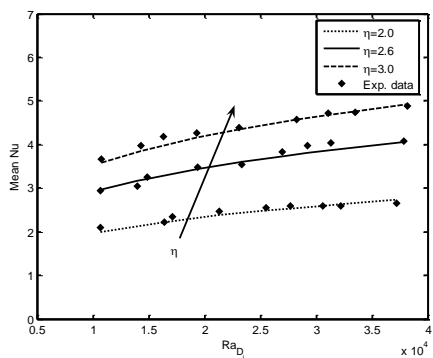


Fig (4) Effect of diameter ratio on mean Nusselt number predictions

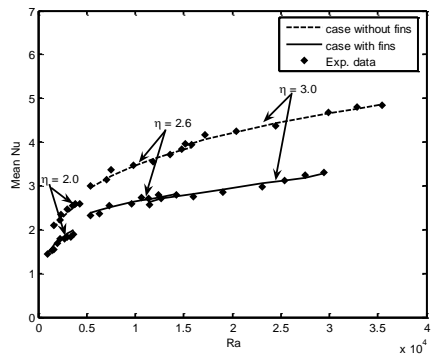


Fig (5) Effect of annular fins on mean Nusselt number predictions

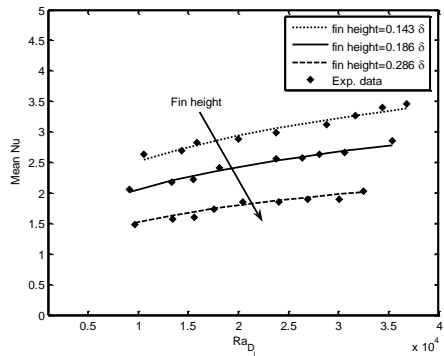


Fig (6) Effect of (fin height/gap width) on mean Nusselt number predictions

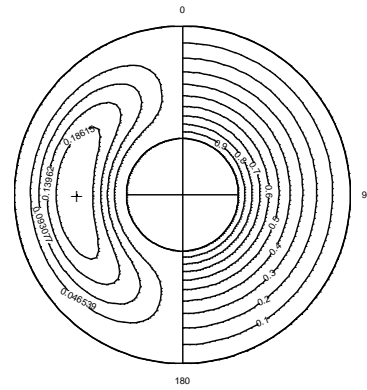


Fig (7) Isotherms and streamlines at  $\eta=3.0$ ,  $Ra=10^2$

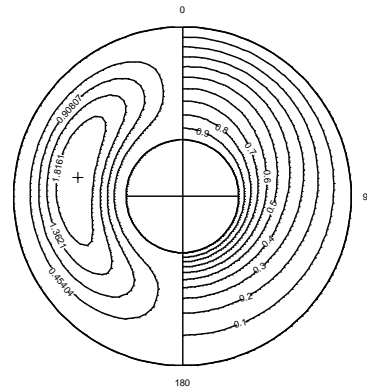


Fig (8) Isotherms and streamlines at  $\eta=3.0$ ,  $Ra=10^3$

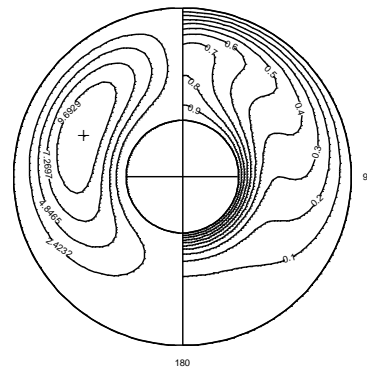


Fig (9) Isotherms and streamlines at  $\eta=3.0$ ,  $Ra=10^4$

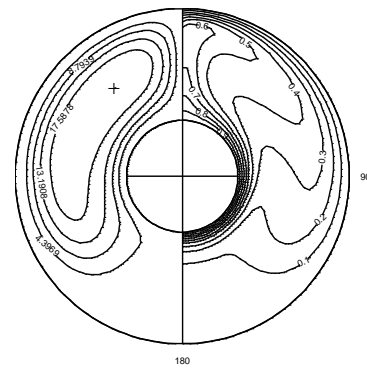


Fig (10) Isotherms and streamlines at  $\eta=3.0$ ,  $Ra=5 \times 10^5$

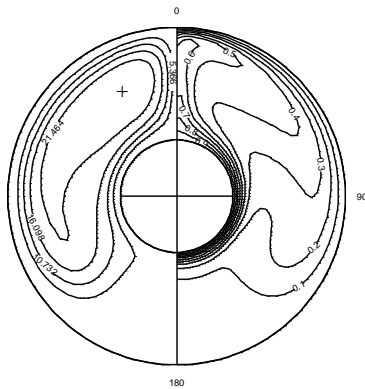


Fig (11) Isotherms and streamlines at  $\eta=3.0$ ,  $Ra=10^5$

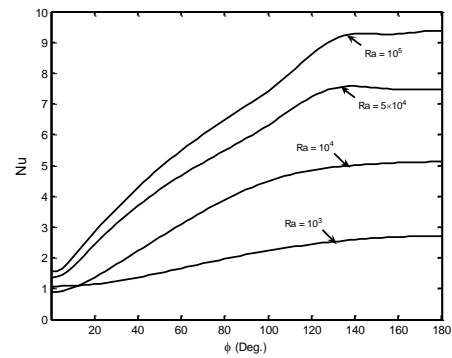


Fig (12) local Nusselt number distribution around the circumference of the inner cylinder at  $\eta=3.0$  and different Rayleigh numbers

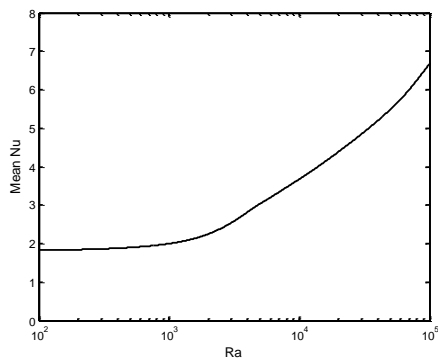


Fig (5.27) Mean Nusselt number versus Rayleigh number at  $\eta=3.0$

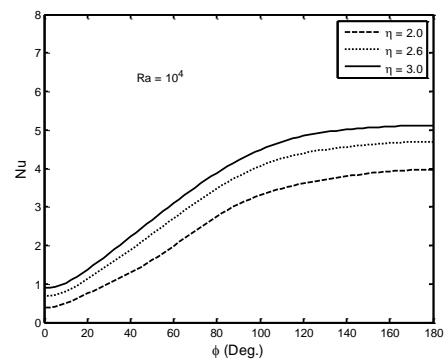


Fig (14) local Nusselt number at  $\eta=2.0, 2.6, 3.0$  and  $Ra=10^4$

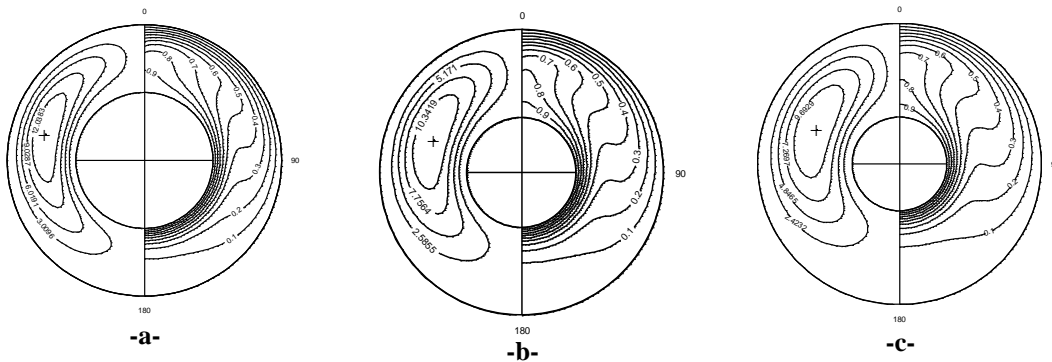


Fig (15) Streamlines and isotherms for  $Ra=10^4$  at: a-  $\eta=2.0$ , b-  $\eta=2.6$  and c-  $\eta=3.0$

## FAULT TREE ANALYSIS AS A MODERN TECHNIQUE FOR INVESTIGATING CAUSES OF SOME CONSTRUCTION PROJECT PROBLEMS

Assistant Lecturer Abbas M. Burhan,  
Baghdad University, College of Engineering

### ABSTRACT:

Construction projects contain many problems that can occur during the execution. Each problem results from many causes. Fault tree analysis (FTA) technique is a graphical model for analyzing causes of a problem (or undesired event) using logic gates to describe combinations of individual faults that can create an undesired event. Each level of the tree lists the lower level events that are necessary to cause the event shown in the level above it. The assessment process of a problem with FTA technique can be divided into two types: qualitative and quantitative assessment. As a case study to apply FTA technique in construction field, the researcher studied a building in Baghdad that had *punching shear* problem to analyze the causes lead to this problem.

This research aims to introduce the main principles of FTA technique and how to use in identifying and analyzing the causes of problems that can occur in the construction projects. Also, it aims to compute the probability of occurrence of any problem or undesired event.

### الخلاصة:

أن المشاريع الإنشائية تحتوي على الكثير من المشاكل أثناء التنفيذ وكل مشكلة تنتج من عدة أسباب. تقنية تحليل شجرة العيب (FTA) هي نموذج تصويري لتحليل أسباب مشكلة معينة (أو حدث غير مرغوب) باستخدام رموز منطقية (Logic Gates) لوصف مجموعة من العيوب أو الأسباب التي تولد الحدث الغير مرغوب فيه. كل مستوى من شجرة العيب يضم الأحداث الأقل مستوى التي حدوثها يكون ضروري لتسبب الحدث الذي في أعلى المستوى من الشجرة.

أن عملية تقييم أي مشكلة ضمن تقنية تحليل شجرة العيب يمكن تقسيمها الى نوعين: تقييم نوعي وتقييم كمي. كدراسة حالة لتطبيق تقنية (FTA) في حقل الأنشاء، أخذ الباحث بناية في بغداد تعاني مشكلة قص الانتقاب لتحليل الأسباب التي أدت الى هذه المشكلة.

يهدف هذا البحث الى تقديم المبادئ الأساسية لتقنية FTA وكيفية استخدامها في تحليل أسباب المشاكل التي قد تحصل في المشاريع الإنشائية وكيفية احتساب احتمالية حدوث أي مشكلة.

**KEYWORDS:****Fault Tree Analysis, FTA, Project Problems, punching shear****MAIN PRINCIPLE:**

A fault tree analysis technique can be simply described as an analytical technique, whereby an undesired state of the project is specified. Fault tree itself is a graphical model of the various combinations of faults that will result in the occurrence of predefined undesired event. The faults can be events that are associated with errors and omissions or any risks which can lead to the undesired event. A fault tree thus depicts the logical interrelationships of basic events that lead to the undesired event which is the top event of the fault tree.

**HISTORY OF FTA TECHNIQUE:**

FTA was first used by Bell Telephone Laboratories in connection with safety analysis of the minuteman missile launch control system in USA in 1962, and improved by Boeing Company. FTA is now widely used in the electronics, nuclear, and aerospace industries (Burke and Weiss 1980)(Haasl 1965). Because the construction industry is one of most important industries, the researcher developed this technique to be used in the construction industry to analysis causes of any problem can be occurred.

**WHAT IS FTA:**

FTA technique evaluates hypothesized undesired event in a project to expose their causes. FTA is a top-down approach to failure analysis, starting with a potential undesired event (problem) called a top event, and then determining all the ways it can happen. The analysis proceeds by determining the causes of occurrence the top event which will be connected through logic gates(Rausand 2004). In this research, two types of gates are used(Clemens 1993):

\* AND Gate:



An event is connected to its causal events through AND gate if all the causal events must happen in order for the resulting event to take place as shown in Fig.1.

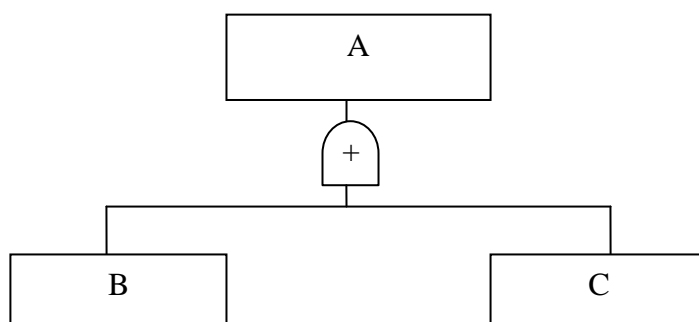


**Fig.1, Three Events Connected through AND Gate**

\* OR Gate:



An event is connected to its causal events through OR gate if the resulting event can be produced by any of the causal events as shown in Fig.2.

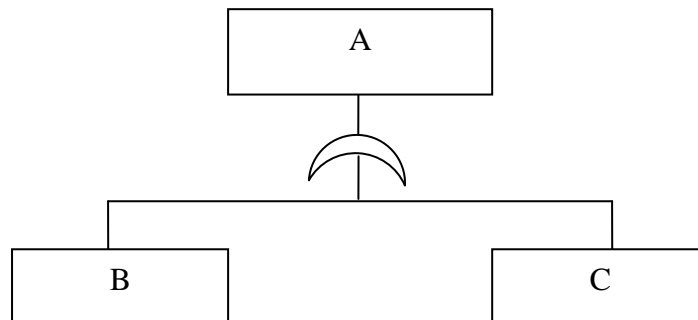
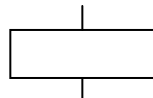


**Fig.2, Three Events Connected through OR Gate**

### **BUILDING BLOCK OF FAULT TREE:**

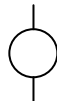
A typical fault tree is composed of a number of symbols which are described in detail below(Ericson2000)( Andrews 1998):

\* Rectangle:



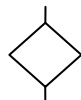
This symbol is used to represent events are considered to be the results of other events within the project.

\* Circle:



This symbol is used for a basic event, which is independent of all other events; hence no further investigation is necessary.

\* Rhombus:



This symbol is for events that are not basic but are considered to be so for the purpose of the FTA. The rhombus may be used for some lower-level events for the expediency of not exploring events of little consequence, or for events that are analyzed on a separate fault tree.

\* Triangle:



This symbol is used for transferring a branch of the FTA onto another page. It is consist of a triangle containing the page number of continuation.

\* Ellipse:



This ellipse is used to record any conditions or restrictions that apply to any logic gate.

### **STEPS OF BUILDING FAULT TREE:**

There are many steps that be adopted when building fault tree as follows:

- Define the problem (or undesired event) for analysis.
- Draw a box at the top of the tree diagram and list the topic of problem inside it.
- Identify all faults related to the problem.
- Identify causes for each fault. List all applicable causes for faults in ovals below the fault. Connect the ovals to the appropriate fault box.

- Work towards a root cause. Continue identifying causes for each fault until you reach a root or controllable cause.
- Give probability of occurrence for roots of fault tree depending on historical collected data or the experience.

### THE CONCEPT OF UNDESIRED EVENT:

Fault tree analysis is a deductive failure analysis which focuses on one particular undesired event and which provides a method for determining causes of this event. The undesired event constitutes the top event in a fault tree diagram constructed. Careful selection of the top event is important to the success of the analysis. If it is too general, the analysis become unmanageable; if it is too specific, the analysis does not provide a sufficient broad view of the problem. Fault tree analysis can be an expensive and time consuming exercise and its cost must be measured against the cost associated with the occurrence of the relevant undesired event. Some examples of top events that might be suitable for beginning a fault tree analysis such as:

- a. Time delay problem which occur in most of construction projects. Since many causes may lead to this problem such as drawing and design delay, poor planning, poor incorporating between subcontractors, labour accidents, etc.
- b. Catastrophic failures which occur in the structures of a building because of causes related to design or execution phases.
- c. Contractor's failure to complete the project within the budget because of poor planning, errors in calculations of estimation, etc. Since, according to UK Department of Trade and Industry Key Performance Indicator (DTI 2002):
  - 50% of all construction projects finish over budget.
  - 54% of all construction projects finish behind budget.
  - 24% of construction projects are completed unsatisfactory, 48% of those having a significant negative impact on business operations.
- d. Labours accident problem related to the manners of safety adopted in the site.

### THE ASSESSMENT OF PROBLEM:

In this research, the assessment process is divided into two types: qualitative assessment and quantitative assessment; as detailed below.

#### Qualitative Assessment:

It is the type of assessment that deals with a problem that has already taken place in a project, in order to diagnose the causes behind this problem.

#### **Case Study:**

In this study, the researcher has investigated a problem of *punching shear* which occurred during the construction of a certain building in Baghdad, as an example to illustrate the process of qualitative assessment. The punching shear was encountered in the flat plate slab of this building, as some of the columns had gone through (punched) the concrete slab as shown in Fig.3.

The investigation started with a field study including visiting and inspecting the site, taking photos to the case features, and collecting data through interviewing some of the specialists in the fields of design and implementation. This field study procedure aims at diagnosing the possible reasons and factors that had led to this punching shear occurrence; then a fault tree is to be drawn to analyze the situation more accurately. There are two points must be considered before drawing fault tree:

1. Defining the top event (the problem) in clear and unambiguous way, e.g.:
  - What is the problem: "punching shear"
  - Where: "building in Baghdad"

- When: “after the execution”

2. Determining the necessary events and conditions causing the top event.

Here, FTA can be prepared to explain and show the causes that led to the main problem (punching shear) as shown in Fig.4.



(a)



(b)



(c)



(d)

**Fig.3, Punching Shear was Encountered in the Flat Plate Slab of a Building in Baghdad.**

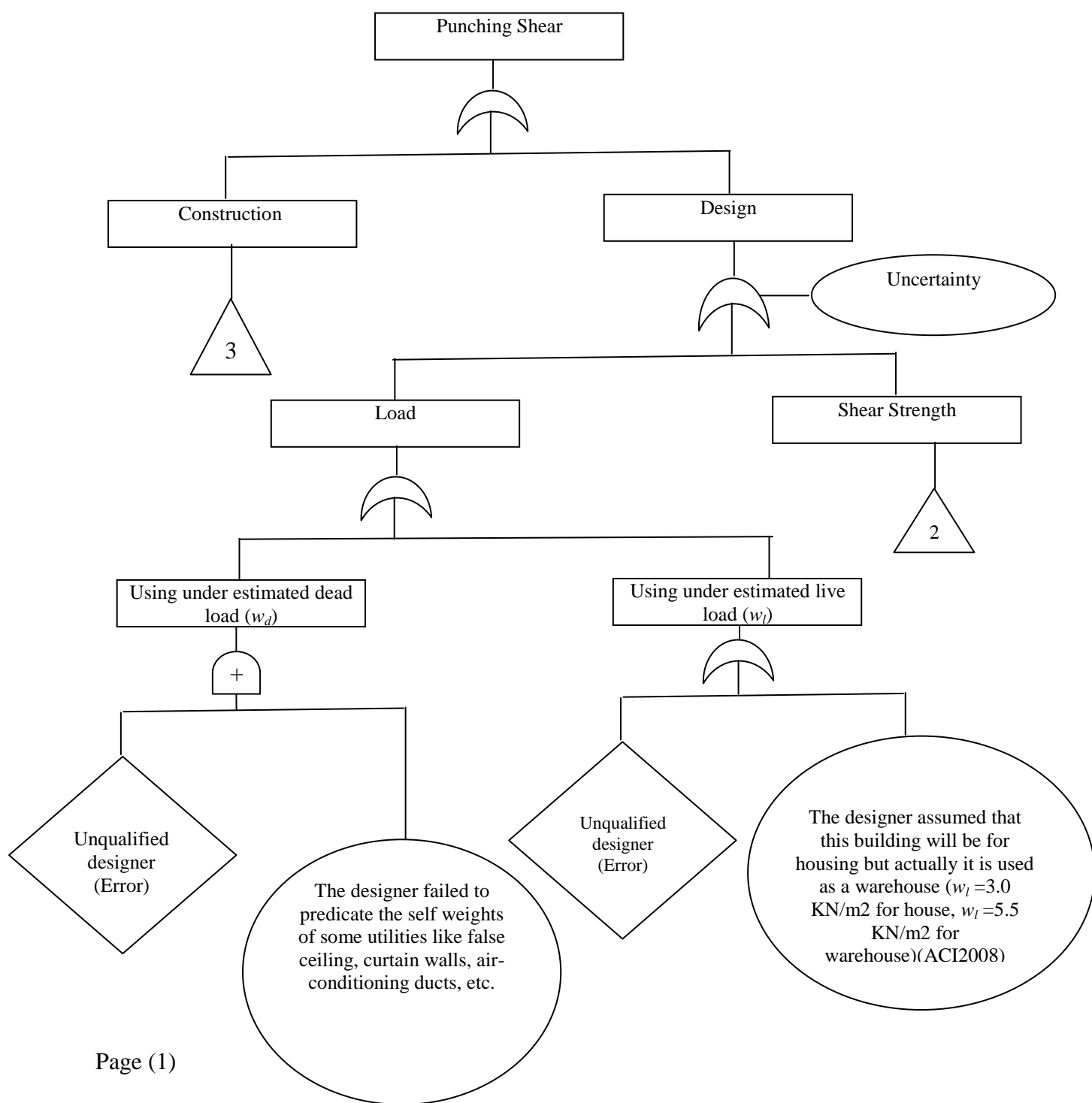
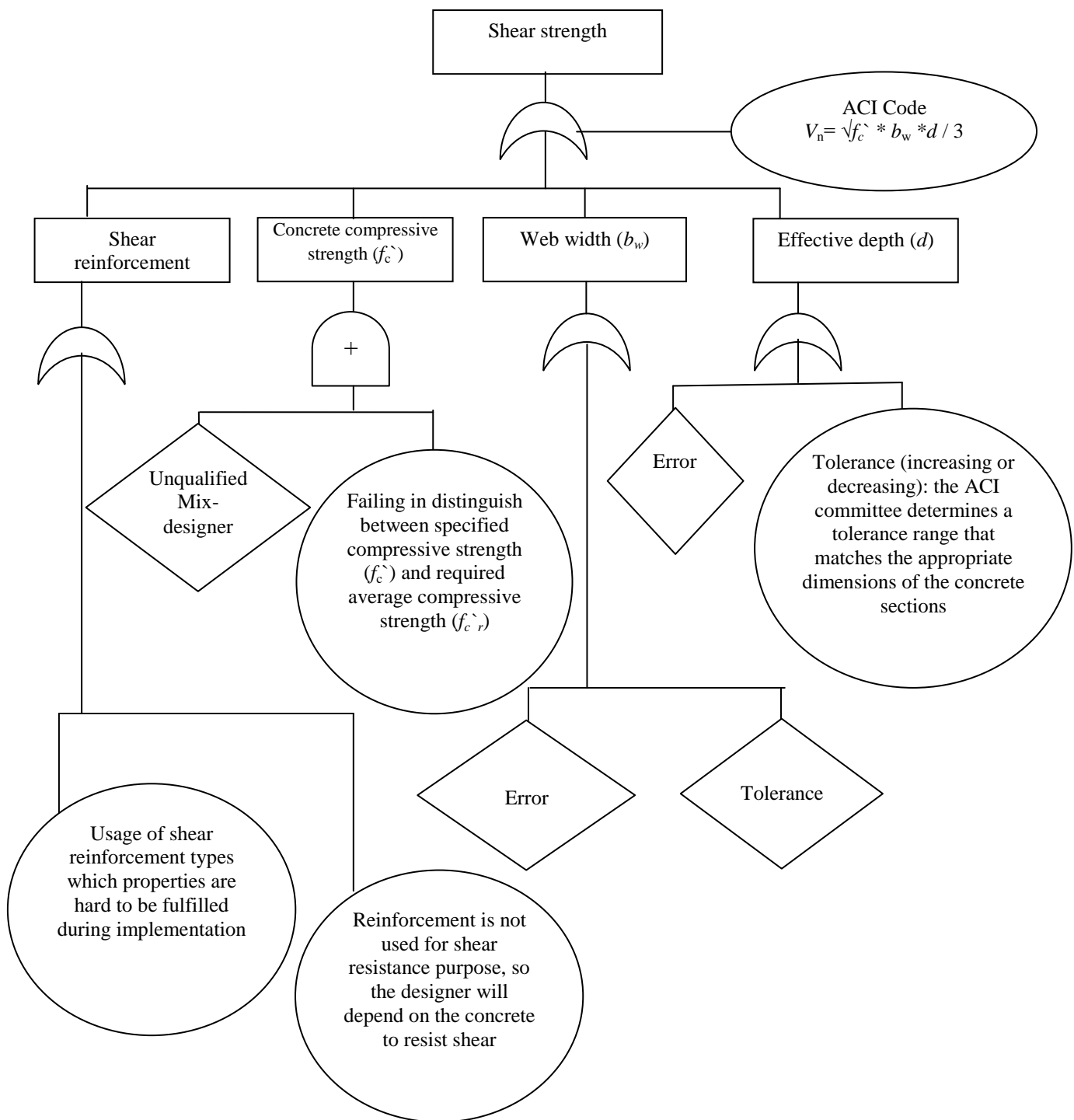


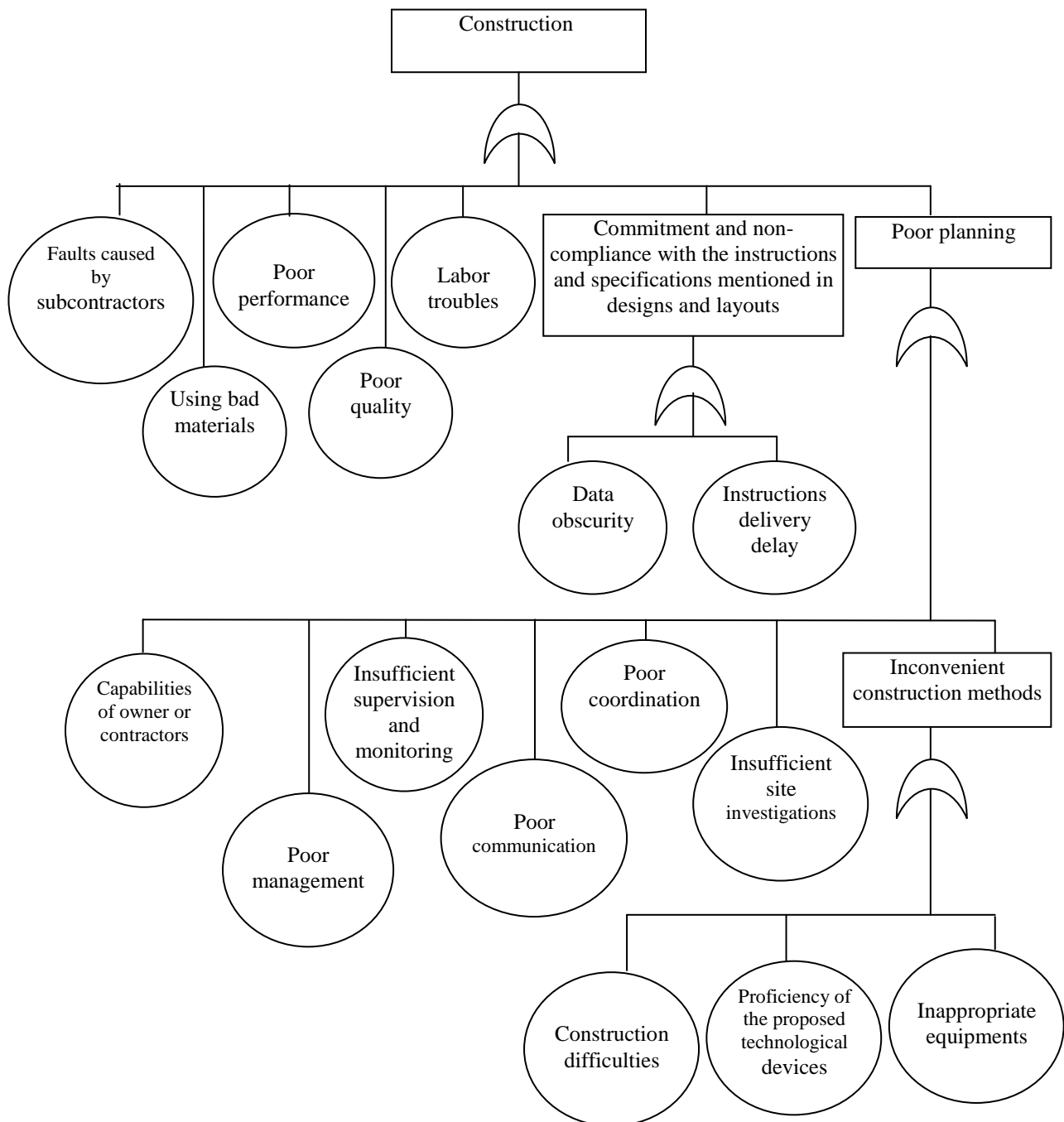
**Fig.4, Fault Tree Diagram for Punching Shear Failure**





Page (2)

**Fig.4-continued, Fault Tree Diagram for Punching Shear Failure**

**Fig.4-continued, Fault Tree Diagram for Punching Shear Failure**

**QUANTITATIVE ASSESSMENT:**

This type can be used for the sort of assessment that deals with a proposed problem (hasn't occurred yet); but it is predicted so that this assessment process can diagnose the causes and factors that had led to the main problem. The analysis provides failure probabilities at the system level that are needed for assessing the problems involved in a construction project; e.g. safety, subcontractors ability to deliver on time, equipment productivity, and costs and schedules associated with construction activities.

In the quantitative assessment, it is possible to assess the probability of a top event from estimates of probabilities of the basic events in the fault tree. When events are connected to a higher order event through OR-gate, we add the probabilities. When events are connected to a higher order event through AND-gate, we multiply their probabilities (Kales 1998). The estimation of probabilities of occurrence any basic event depend on the experience and records or information about previous projects. For example, if all the probabilities of basic events and events assumed to be basic in the fault tree of Fig.5 are estimated to be the follow:

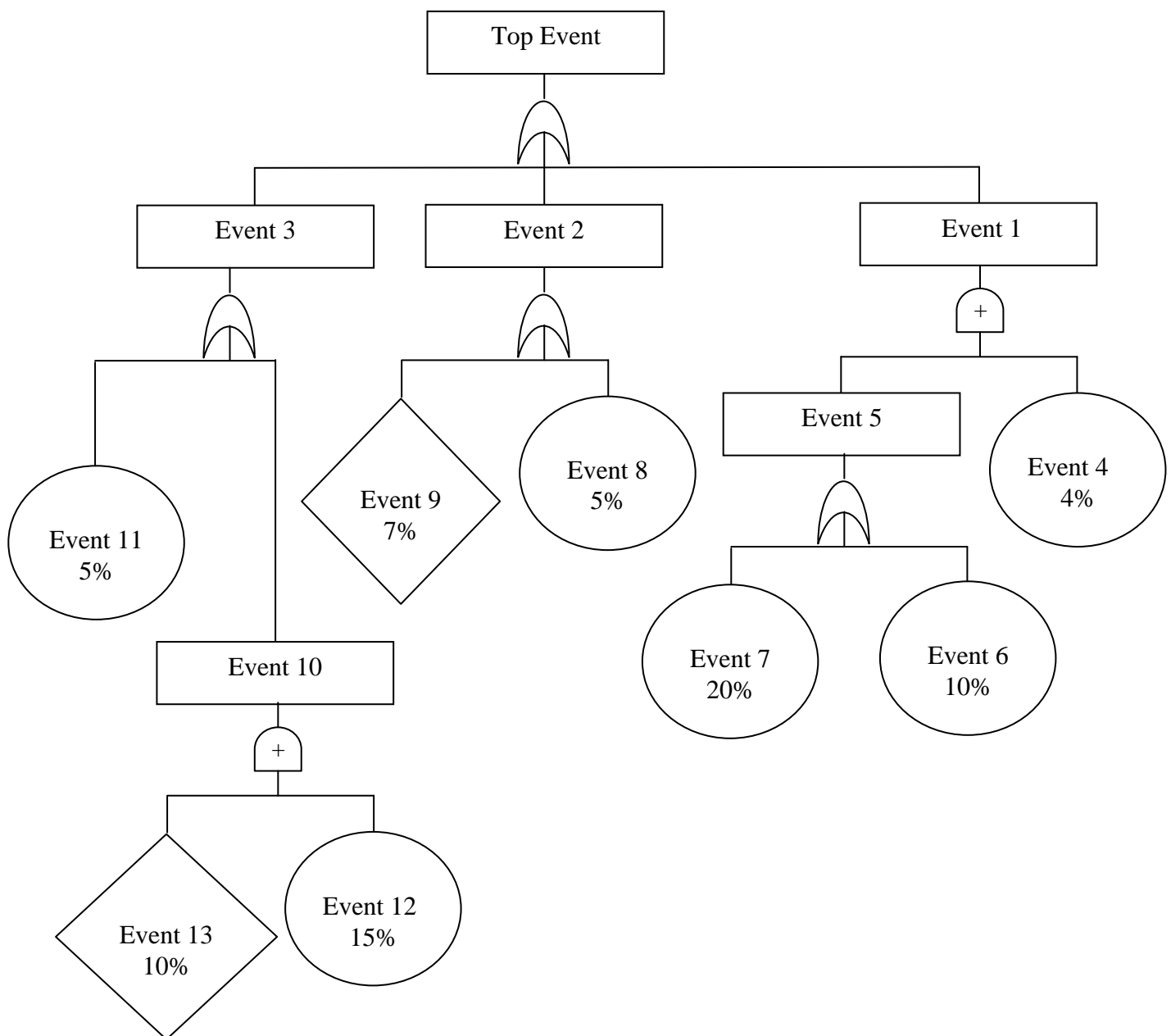


**Fig.5, Fault Tree Diagram which Example**

$P(\text{Event 4}) = 4\%$   
 $P(\text{Event 6}) = 10\%$   
 $P(\text{Event 7}) = 20\%$   
 $P(\text{Event 8}) = 5\%$

$P(\text{Event 9}) = 7\%$   
 $P(\text{Event 11}) = 5\%$   
 $P(\text{Event 12}) = 15\%$   
 $P(\text{Event 13}) = 10\%$

Then the probability of the top event can be determined as shown:

$P(\text{Event 5}) = P(\text{Event 6}) + P(\text{Event 7}) = 0.10 + 0.20 = 0.30$   
 $P(\text{Event 1}) = P(\text{Event 4}) * P(\text{Event 5}) = 0.04 * 0.30 = 0.012$   
 $P(\text{Event 2}) = P(\text{Event 8}) + P(\text{Event 9}) = 0.05 + 0.07 = 0.12$   
 $P(\text{Event 10}) = P(\text{Event 12}) * P(\text{Event 13}) = 0.15 * 0.10 = 0.015$   
 $P(\text{Event 3}) = P(\text{Event 10}) + P(\text{Event 11}) = 0.015 + 0.05 = 0.065$

So,  $P(\text{Top Event}) = P(\text{Event 1}) + P(\text{Event 2}) + P(\text{Event 3})$   
 $= 0.012 + 0.12 + 0.065 = 0.197 = 19.7\%$

This value (19.7%) represents the probability of occurrence the problem (Top Event). Based on this value, the management can decide the level of problem and put good plan to avoid this problem or decrease its effects on the project or parties.

## CONCLUSION:

- Fault tree analysis technique is used in all industries, but it can be used effectively for investigating the problems which occur in the construction projects. It is effective tool to show the events or causes which lead to the main problem or top event (undesired event).
- Fault tree analysis (FTA) technique is a graphical model of the pathways within a system that lead to a foreseeable undesired event. The pathways interconnect contributory events and conditions using standard logic symbols called AND-gate and OR-gate. Numerical probabilities of event occurrence can be entered and propagated through the model.
- The user of FTA technique must carefully select the top event (undesired event) in order to success the analysis of problem.
- The assessment process of any problem can be divided into two types: qualitative and quantitative assessment. The first type deals with problems which have already been taken place in a project, while the second type deals with a proposed problem (hasn't occurred yet; but it is predicted).
- In quantitative assessment, the user of FTA technique depends on his experience and records or information about previous projects to estimate the probabilities of occurrence any basic event.

**REFERENCES:**

- ACI Code, (2008) “Building Code Requirement for structural concrete” ACI 318RM.
- Clifton A. Ericson, (2000) “fault tree analysis” [www.fault-tree.net/papers/ericson-fta-tutorial.pdf](http://www.fault-tree.net/papers/ericson-fta-tutorial.pdf).
- Department of Trade and Industry UK (2002) *Construction Industry KPI's Industry Progress Report 2002*.
- David F. Haasl, (1965) “advanced concepts in fault tree analysis” presented at system safety symposium sponsored by University of Washington and the Boeing Company, [www.fault-tree.net/papers/haasl-advanced-concept.pdf](http://www.fault-tree.net/papers/haasl-advanced-concept.pdf).
- John J. Burke, and Volker Weiss, (1980) “Risk and failure analysis for improved performance and reliability” P 34.
- John Andrews, (1998) “fault tree analysis” proceedings of the 16<sup>th</sup> International System Safety Conference, [www.fault-tree.net/papers/andrews-fta-tutr.pdf](http://www.fault-tree.net/papers/andrews-fta-tutr.pdf).
- Marvin Rausand, (2004) “system reliability theory” Wiley 2<sup>nd</sup> ed., P36, [www.ntnu.no/ross/str/slides/fta/.pdf](http://www.ntnu.no/ross/str/slides/fta/.pdf).
- Paul Kales, (1998) “reliability for technology, engineering and management), Printice-Hall, Inc., U.S., 1<sup>st</sup> Ed., P(288-303).

## OPTIMIZATION OF DEM INTERPOLATION

Dr. Hussain Zaydan Ali  
Expert / Image processing

Ministry of Science and Technology / Remote Sensing Center

Ahmed Kasim Hameed AL- Akaby  
Master in surveying engineering

### ABSTRACT

Digital Elevation Models (DEMs) are simply regular grids of elevation measurements over the land surface. DEMs are mainly extracted by applying the technique of stereo measurements on images available from photogrammetry and remote sensing. DEMs play a vital role in many scientific, environmental, engineering as well as military applications which need accurate and dense DEMs. However, generating a dense and accurate DEM comes with the price of spending both time and money on the field measurements. Fortunately, advanced space technology has provided much single (if not stereo) high resolution satellite imageries almost worldwide with the available global or local DEMs. This study included evaluating both DEM produced from topographic map and raster DEM after resolution enhancement by using single satellite image. According to the results of these experiments, a strategy was proposed for using the reflectance data to enhance the accuracy of DEM interpolation. The proposed the reflectance data models were implemented in a software package and successfully tested.

[Keywords: Densification of DEM, Spatial Enhancement of DEM, Shape from Shading, Optimization Algorithms]

### الخلاصة

نماذج الارتفاع الرقمية (DEMs) هي ببساطة شبكات منتظمة من الارتفاعات مقاسة على سطح الأرض. نماذج الارتفاعات الرقمية (DEMs) تستنبط بشكل رئيسي بتطبيق النماذج المجسمة (زوج من الصور) المتوفرة من المسح التصويري وبيانات التحسس النائي. على أية حال، هنالك الكثير من التطبيقات الهندسية والتطبيقات العسكرية تحتاج الى نماذج الارتفاع الرقمية (DEMs) ذات قابلية تحليل عالية (High Resolution) ومتوفرة محلياً وعالمياً. لحسن الحظ، التقدم الحاصل في تكنولوجيا الفضاء وفرت لنا صورة فضائية منفردة (ليست مجسمة) ذات قابلية تحليل عالية (تقريباً لكل العالم) يمكن أن تستخدم لزيادة كثافة النقاط لنموذج الارتفاع الرقمي (بمعنى آخر، زيادة قابلية تحليل النموذج). تماشياً مع هذا التوجه فإن البحث تتناول إنتاج النموذج الارتفاع الرقمي من خارطة طوبوغرافية مقرأية ضوئياً ومن ثم تحسين قابلية تحليل نموذج الارتفاع الرقمي باستخدام صورة فضائية منفردة.

## INTRODUCTION

DEMs are used for the analysis of topographical features in GIS and numerous engineering computations as well as scientific applications. Digital Elevation Models (DEMs) are simply regular grids of elevation measurements over the land surface. DEMs are mainly extracted by applying the technique of stereo measurements on images available from photogrammetry and remote sensing [Allam, 1978].

A GIS is a technology which can be used for scientific investigations, resource management, and development planning. Broadly speaking, a GIS consists of four different components: - 1) data collection, 2) data storage, 3) data analysis and processing, and last but not least 4) information retrieval. Among many types of data, Digital Elevation Models (DEMs) as well as remote sensing play a key part in the development of GIS [Khalaf, 2004].

Today, with the need for the better management of the limited natural resources, there are numerous geosciences and engineering applications which require denser DEM data than available. Unfortunately stereo satellite imagery is not available everywhere. Obviously, time and cost are two important factors that often prevent us from field measurements. While interpolation techniques are fast and cheap, they have their own inherent difficulties and problems, especially in terms of accuracy of interpolation in rough terrain [Rajabi, 2006].

On the other hand, the availability of single satellite imagery for nearly all of the Earth is taken for granted nowadays. This research paper was an attempt to explore the feasibility of enhancing the DEM interpolation accuracy using the reflectance data with single (as opposed to stereo) satellite imageries. The motivation for this investigation is the availability of relatively inexpensive but up to date, multiresolution, multispectral single satellite imageries for almost the whole world [Rajabi, 2006]. In this paper we will discuss generation of digital elevation models from scanned topographic map and spatial (resolution) enhancement by using single satellite imagery which is used as a main tool in this research.

Digital elevation model (DEM) is an important and interesting field for many engineering applications, as attested by the large volume of published literature. The relevant work may be summarized as follows:-

[Patrice Arrighi and Pierre Soille, 2007] presented a general methodology for the generation of digital elevation models (DEMs) starting from scanned topographic maps. they concentrate on the extraction and filtering of the contour lines from the input maps. This is a difficult problem due to the presence of complex textured backgrounds and information layers overlaid on the elevation lines (e.g., grid lines, toponymy, etc.). Results are presented on a wide variety of samples extracted from a (1:50000) plate scanned at 300 DPI.

[Makki A. 2007] presented a study to evaluate the most suitable and accurate interpolation method in producing digital elevation model for the data gathered from existed topographic maps which are also compared with data gathered from field survey. Different map scales (1:100000, 1:50000, 1:25000) with different contour intervals (50m, 10m, 5m) were chosen in the tests. The accuracy tests based on the National Mapping Accuracy Standards (NMAS) by comparing the result of Root Mean Square Error (RMSE) in elevations with the typical standard deviation ( $\sigma_z$ ) proposed by (NMAS) which depends on the scale of maps and contour intervals. From testing four interpolation techniques ((Kriging, Triangulated Irregular Network (TIN), Inverse Distance Weighting (IDW)

and Polynomial)) it was found that kriging is the best method followed by TIN method while IDW method failed in some tests, and the polynomial model failed in all tests.

[A. Rajabi, 2003] discusses the application of shape from shading (SFS) techniques to improve the quality of the interpolated DTM grid data with single satellite imagery of better resolution than the DTM data. The idea is highly motivated by the wide availability of satellite remotely sensed imagery such as Landsat TM and SPOT HRV imagery.

## EXPREIMENTAL WORK

### Study Area Site Description

The study area is a part of Chamchamal region in the northeast of Iraq, exactly in the northeast part of Chamchamal region. The study area is located on both sides of Tigris River. Chamchamal region bounded by the coordinate, it extends between latitudes (from  $35^{\circ} 55' 00''$  to  $36^{\circ} 00' 00''$ ) and longitudes (from  $44^{\circ} 55' 00''$  to  $45^{\circ} 00' 00''$ ) in zone 38N according to UTM cartographic coordinate system. Figure (1) shows the location of this region.

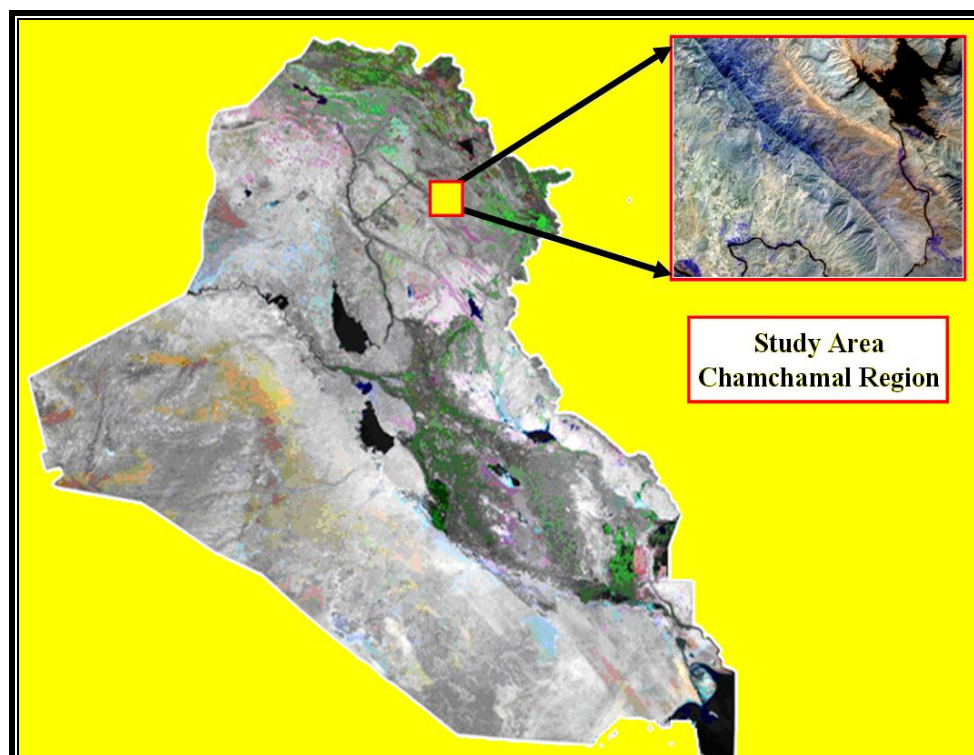


**Fig. (1): Study Area (Chamchamal region).**

### Topographic Map Features

Topographic map with the following specification are used scale of (1:100,000) with contour interval of (50) meter, which was produced in general surveying directorate. The main features in the topographic map for study area are, Valleys and mountains is the most active features of land cover in the Chamchamal region due to high slopes of this region, also the Small Zap River passes through this region. This region is composed of many layers that covered the features in the topographic map. The terrain is generally not flat. Figure (2) shows the study area map.





**Fig. (2): Study Area (Chamchamal Map).**

### **Characteristics of Satellite Image**

Satellite image is Landsat 7 ETM+, which was acquired in September 2002. Satellite image with eight bands provided as eight image files with GeoTIFF extension, six represents multispectral band with spatial resolution of (30) meters, one represents panchromatic band with spatial resolution of (15) meters and one represents thermal band with spatial resolution of (60) meters. The satellite image is geometrically corrected with the following map properties, UTM projection, Clarke, spheroid (1880), and zone (38N) and unites in meters. Figure (3) shows satellite image of study area.

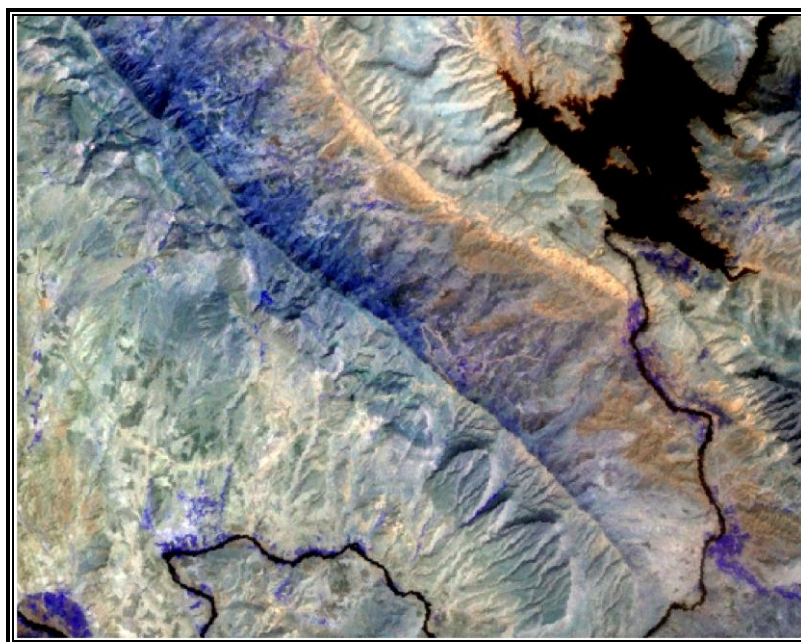


**Fig. (3): Study Area (Chamchamal Satellite Image).**

## PRODUCTION OF DIGITAL ELEVATION MODEL FROM TOPOGRAPHIC MAP.

### Extraction of Contour Lines

A contour is an imaginary line of constant elevation on the ground surface. It may be thought of as the trace formed by the intersection of a level surface with the ground surface, for example, the shoreline of a still body of water [Anderson and Mikhail, 1998]. The semi-automatic digitization of the contour lines of the topographic map was done by using ArcMap package in ArcGIS version (9.1) by creating shapefile\* (A vector data storage format for storing the location, shape, and attributes of geographic features. A shapefile is stored in a set of related files and contains one feature class [ESRI, 2002]) used for this purpose, with indicating for the value of each line. Understanding this step, with more details can be made from the illustration contour line layer which will be given in figures (4) of the study area.

Errors may result, when the contour lines are drawn. These errors are dependent on the regions (study areas) nature. When some of the regions like (Chamchamal) includes high slopes (i.e. very high contour line density), the probability of obtaining errors is increased. These errors result from the cutting in the lines or the removing of the extra lines.

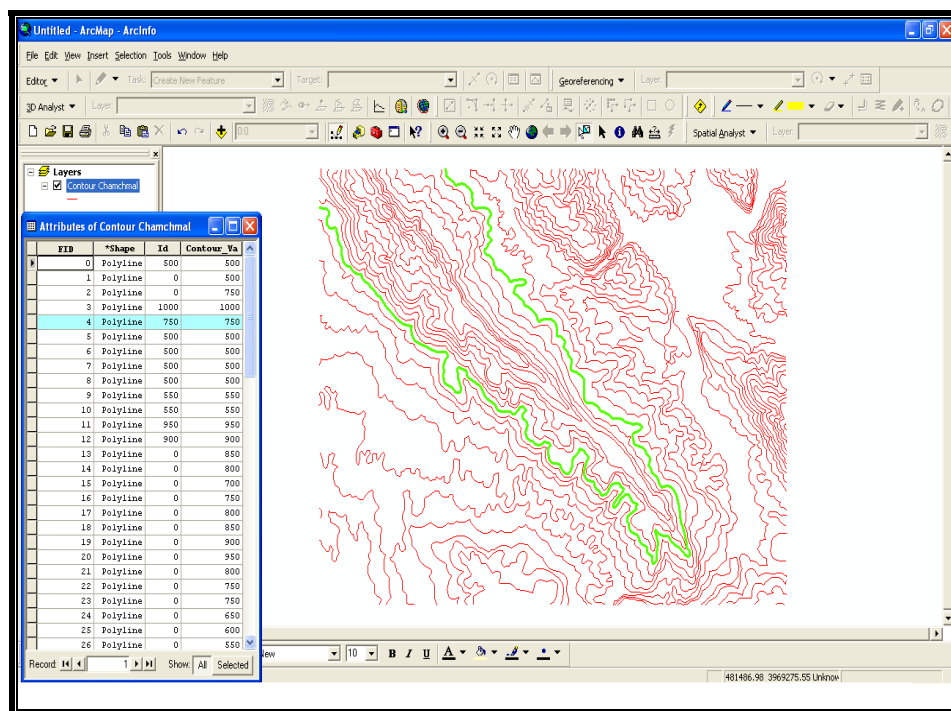


**Fig. (4): Contour map of Chamchamal area with labeled contours.**

### **Building of Digital Elevation Model**

The production of raster DEM from contour lines includes two steps: The first step is by creating the points as (X, Y and Z) coordinate from shapefile format by using ERDAS IMAGINE package. The ERDAS IMAGINE system incorporates the functions of both image processing and GIS. These functions include importing, viewing, altering and analyzing raster data and vector data sets [ERDAS, 1999]; these points are then exported as text file with (.txt) extension. The second

step is creating surface (DEM) from these points, It is then so easy to open the text file format (with .txt extension) in text editor and save it as ASCII data file format (with .dat extension) in ERDAS IMAGINE Package. The ASCII data file is used to create a surface represented as Digital Elevation Model (DEM). The raster image format (DEM) with (.IMG) extension. This process is called surfacing in ERDAS IMAGINE package. This surface was decided to consist of (1092) points as (X, Y and Z), the output cell size (resolution) (100\*100) m<sup>2</sup>. After that the digital elevation model is displayed as a perspective view as shown figure (5).

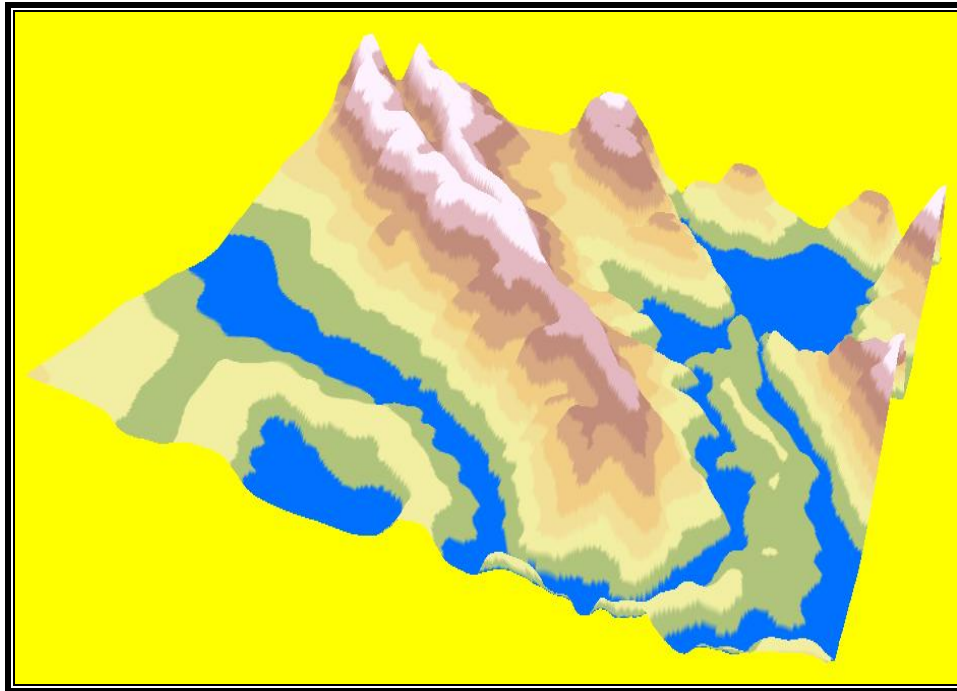


**Fig. (5): 3D view of the produced DEM.**

## **RESOLUTION ENHANCEMENT OF DIGITAL ELEVATION MODEL**

After the production of the digital elevation model (DEM) from topographic map, the elevation values (Z coordinates) were computed in a regular grid (100 meter grid spaces). The main goal of this study is to improve the accuracy (resolution) of DEM grid data by using single satellite imagery (i.e. the elevation values (Z coordinates) will be computed in a regular grid (30 meter grid spaces).

### **Satellite Image Classification**

The purpose of classification is to extract information from image. Information will be transferred to separate raster layers, each layer represent a type of land cover and/or land use. The results of digital image classification include unsupervised classification results that represent the two approaches used to classify the raw data. In this study we choose unsupervised method to classify the satellite image, because no extensive prior knowledge of the region is required, the opportunity for human error is minimized and unique classes are recognized as distinct units [Gonzalez, 1992].



## Unsupervised Classification

The purpose of classification is to extract information from image. Information will be transferred to separate raster layers, each layer represent a type of land cover and/or land use. The results of digital image classification include unsupervised classification results that represent the two approaches used to classify the raw data.

One of the most unsupervised classification methods is the ISODATA, whose algorithms calculate class means evenly distributed in the data space and then iteratively cluster the remaining pixels using minimum distance technique (The minimum distance decision rule also called spectral distance) calculates the spectral distance between the measurement vector for the candidate pixel and the mean vector for each signature [ERDAS, 1999].

The unsupervised classification operation was performed. In this study we classified the satellite image with six spectral classes. From six classes we choose three classes for propose this study. Figures (6) show the results of these operations with a summarized explanation for each class based on ground truth information. The figures show that for trial, the unsupervised classification technique gives good representation of some classes and merges among others, and this method may categorizes some classes into more than one spectral class (such as streets and soil, streets and vegetation, and soil and vegetation). This may be attributed to many reasons such as the difference in the type density and its non homogeneity, sensor resolution, sensor angle of view, and the sun's altitude angle.

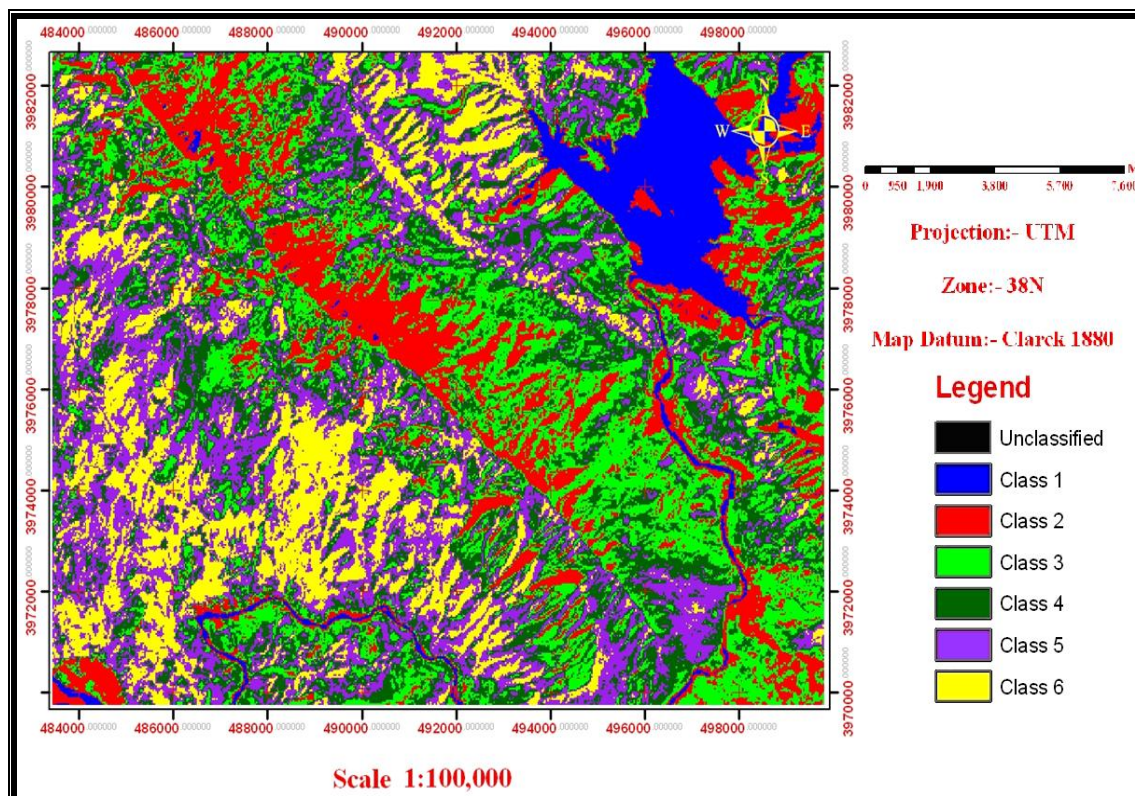


Fig. (6): Classification of Satellite image.

## CONVERTING THE DIGITAL NUMBER TO REFLECTANCE

Obviously, any band from satellite image consist of number of cells is called pixels, each pixel also has a numerical value, called a digital number (DN) that records the intensity of electromagnetic energy measured for the ground resolution cell represented by that pixel [Gonzalez, 1992]. For satellite (Landsat) data, there is often need to calculate radiances from the digital values and calculate reflectance from radiances provided as image data, usually because specific analyses require radiances or because it is necessary to compare data from one scene to another illustrated in figure (7). The DN images are converted first to at satellite radiance and then to at satellite reflectance using the following equations [USGS, 2001].

$$L\lambda = (\text{Gain}\lambda * \text{DN}\lambda) + \text{Bias}\lambda \quad \dots\dots\dots (2.1)$$

$$\rho\lambda = (\pi * L\lambda * d^2) / (\text{ESUN}\lambda * \sin(\theta)) \quad \dots\dots\dots (2.2)$$

Where:-

$\lambda$  = ETM+/TM band number.

$L$  = At-satellite radiance.

Gain = Band specific, provided in the header file.

Bias = Band specific, provided in the header file.

$\rho$  = At-satellite reflectance, unit less.

$d$  = Earth-Sun distance in astronomical unit. The Earth-Sun distance can be derived from table (2.3).

ESUN = Solar exoatmospheric spectral irradiance from table (2.2).

$\theta$  = Sun elevation angle

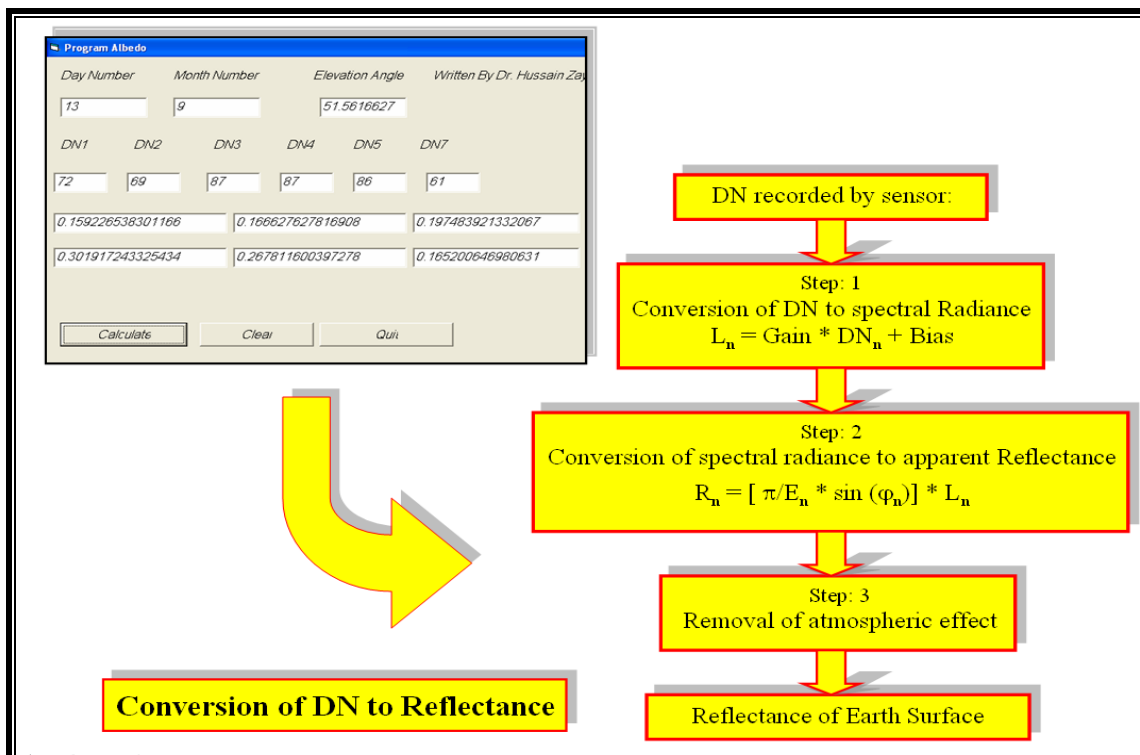


Figure (7): Reflectance Values Calculation.

**Table (2.2): ESUN Solar Spectral Irradiances [USGS, 2001].**

Band	L7 ETM+	L5 TM
1	1969.000	1957.000
2	1840.000	1826.000
3	1551.000	1554.000
4	1044.000	1036.000
5	255.700	215.000
6	82.070	80.670
7	1368.000	

**Table (2.3): Earth-Sun Distance in Unit [USGS, 2001].**

Julian Day	Distance	Julian Day	Distance	Julian Day	Distance
1	0.9832	121	1.0076	242	1.0092
15	0.9836	135	1.0109	258	1.0057
32	0.9853	152	1.0140	274	1.0011
46	0.9878	166	1.0158	288	0.9972
60	0.9909	182	1.0167	305	0.9925
74	0.9945	196	1.0165	319	0.9892
91	0.9993	213	1.0149	335	0.9860
106	1.0033	227	1.0128	349	0.9843
				365	0.9833

In this study we convert the digital number to reflectance value. However, we used code (program) in Visual Basic language to extract reflectance value. This program uses data obtained from Landsat 7 ETM+ raw image with six bands (1, 2, 3, 4, 5 and 6) such as sun elevation, sun azimuth, exposure dated, earth sun distance and constants values for detectors found in Landsat 7 ETM+.

#### **Densification of DEM Grid Data**

After converting the digital number values for each band from classes to the reflectance values. Now we have classes consist from these bands, bands are in matrix form which holds the reflectance values. To densify the DEM grid data, it should be converting the reflectance values to elevations. The following steps are involved in the densification of DEM grid data.

The first step: subscribed points taken between a part from DEM (low resolution) and classes by using ERDAS IMAGE package. This is process is called Geolink.

The second step: computing the best fitting (relationship) between the elevations (H) and spectral reflectance values (R) (i.e. high correlation coefficients and low residual error). The above processing was done by using statistical program called (Curve Expert (ver. 1.3)). This program it sifts through every possible curve fit. Ranks the fits from best to worst, and presents you with the best equation (high coefficients and low residual error) from (30) equations and the best fit is then displayed in the graphing window. The sinusoidal fitting ( $y=a+b*\cos(c*x+d)$ ) were the best fitting in this tests. But found simple difference by correlation coefficient, residual error and coefficients from fitting to fitting another. Table (1) shows the parameter of fitting for each class, figure (8) shows the best equations chosen for classes by using Curve Expert (ver. 1.3) package.

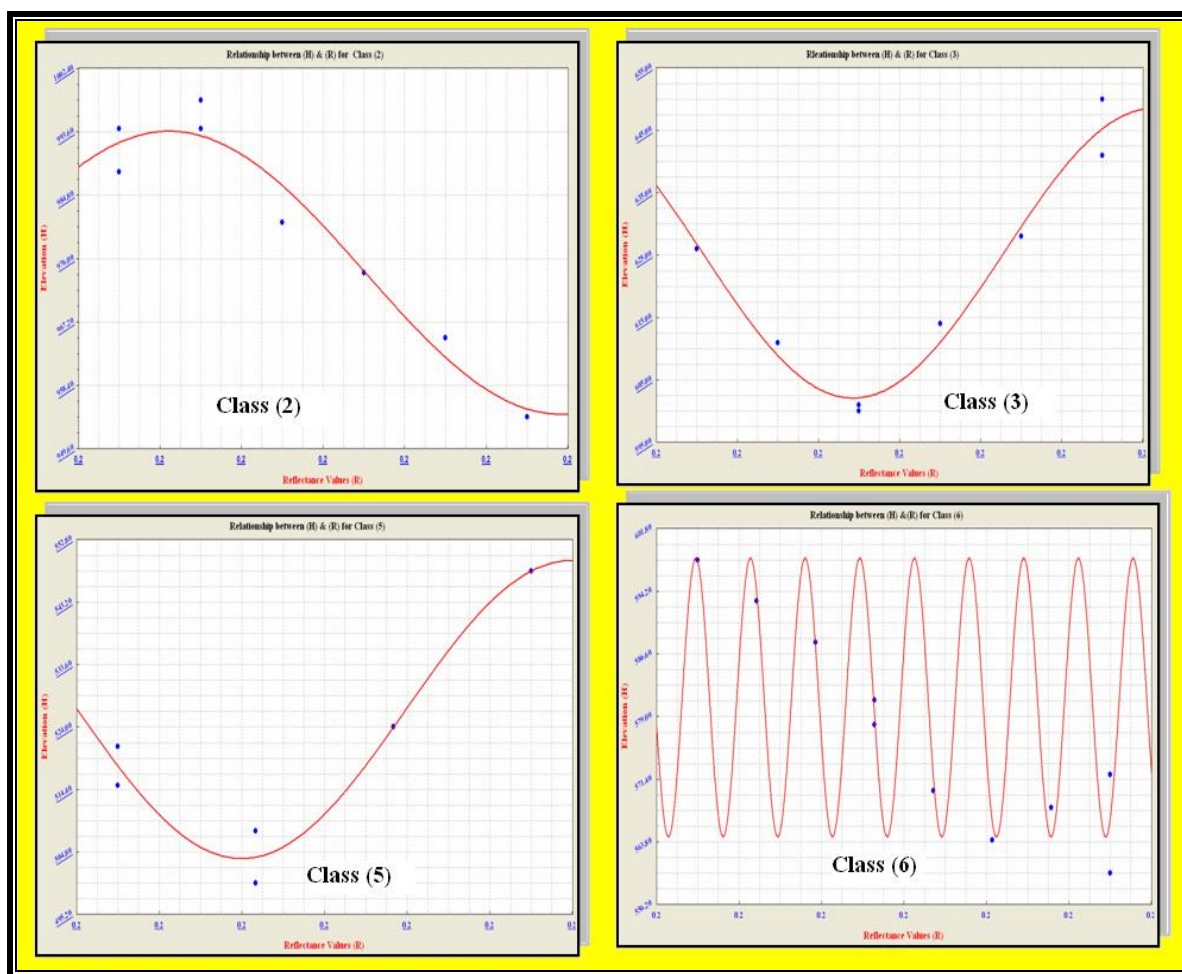


**Fig. (8): Relationship between Elevation and Reflectance Values for the Classes (2,3,5 and 6).**

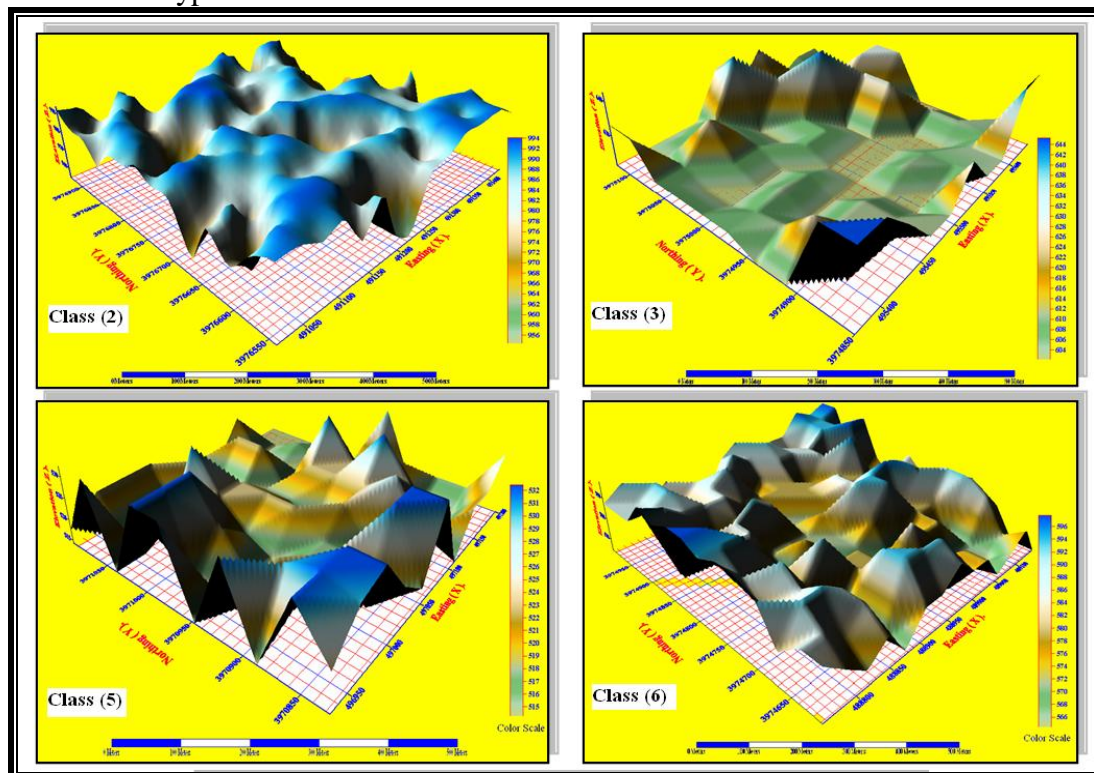


**Table (1): Parameter of the Sinusoidal Fitting for each Class.**

NO. of Classes	Coefficients				Correlation Coefficient	Residual Error
	a	b	c	d		
2	974.013	19.638	272.371	-22.959	0.9759728	4.505158
3	625.306	23.226	353.602	-16.740	0.9862825	3.961472
5	523.538	9.7274	505.751	4.66391	0.9448530	3.904637
6	581.322	16.933	2827.56	33.7233	0.9652660	4.058228

The third step: After computing the best fitting (relationship) between the digital elevation model (low resolution) and classes. We converted each reflectance values (R) to elevation (H) and then we give (X, Y) coordinates for each elevation. The above processing was done by using MATLAB.

The fourth step: It is then so easy to open the text file format (with .txt extension) in text editor and save it as ASCII data file format (with .dat extension) in ERDAS IMAGINE Package. The ASCII data file is used to create a surface represented as Digital Elevation Model (DEM) [ERDAS, 1999]. The resulted DEM is geometrically corrected. This surface is consist of Enormous points (as X, Y & Z), the output cell size (resolution) (30\*30) m<sup>2</sup>. In figure (9) the results of DEM spatial (resolution) enhancement by using single satellite image data were satisfactory, as revealed by the RMSE obtained. These results suggest, first, that single satellite image gives a high resolution better than from the digital elevation model (DEM) which is obtained from scanned topographic map, second, that single satellite image is multispectral, third, that of the method used in this study are appropriate for this type of data and this area.


**Fig. (9): Raster DEM after Resolution Enhancement for Classes.**



## THE EVALUTION OF ACCURACY FOR DIGITAL ELEVATION MODEL

After producing the digital elevation model from the scanned topographic map and after resolution enhancement of digital elevation model by using single satellite image, the models are transferred to (Raster Digital Elevation Model). Thirty well distributed the find DEM points were chosen on the transferred model and its coordinates were recorded (E, N AND Elev.) then projecting them the topographic map which are related to the same model, using the value of elevation by traditional methods and taking in consideration the distance between the two lines, the point lies between them and the contour interval value, then computing the value of (RMSE) in elevations with the typical standard deviation proposed by National Mapping Accuracy Standard (NMAS) depending on the used map scale and contour interval (See Table (2)). The resulting accuracy of digital elevation models (high resolution) was found to be the best from accuracy for digital elevation model produced previous from scanned topographic map.

**Table (2): The Computed Standard Deviation of DEM for the Study Area.**

NO.	Type of Error	Results	
		Raster DEM Before Resolution Enhancement	Raster DEM after Resolution Enhancement
1	Computed Standard Deviation	<b>3.161 m</b>	<b>2.814 m</b>

## CONCLUSIONS

- The digital elevation model (DEM) produced from scanned topographic map by using simple automatic method were compared on the basis of computing the root mean square error (RMSE). It was found that the proposed method gives improved results. Generally, the scale of map and the contour interval affect the accuracy of the produced digital elevation model (DEM).
- Although the densification process for grid data gives a good results in digital elevation model (DEM) in this study, but cannot be adopted for large areas, because it is limited. Other conditions and constrains must be taken to over come this limitation. It is obvious there is no fixed relationship between the elevations and spectral reflectance values.
- The use of large scale topographic map (1:10000, 1:5000, 1:1000 ...) with small contour interval (10, 5) for production of digital elevation model (DEM).
- The use of modern software which automatically converts contour maps from its raster format into vector format like (ArcScan) software in a process called vectorization.
- Using raw satellite images of high resolution (from one meter to five meter) such as those from SPOT or IKONOS satellites, and use multispectral image with high spectral resolution to extract more information from satellite image.
- It is preferred to use the field survey is very essential and important to notice the variance among the soil classes, to obtain and fix the ground truth throughout the laboratory tests and to determine earth covers classes.



- 5- It is preferred in future work to use supervised classification method, because supervised classification method gives good presentation of the classes with overall accuracy (for training regions) equal to (96%).
- Use the shape from shading (SFS) to densification of digital elevation model (DEM) grid data.

## REFERENCES

- Allam M. M., 1978, "DTM Application in Topographic Mapping", PE and RS Journal Vol.44, No.12, pp (1513-1520).
  - Anderson J. M. and Mikhail E. M., 1998, "Surveying Theory and Practice", Seventh Edition, University of California Berkeley, pp (792-793).
  - ESRI, 2002, "Help of ArcGIS", Computer Program.
  - ERDAS Felid Guide, 1999, Fifth Edition, Revised and Expanded, ERDAS, Inc. Atlanta, Georgia.
- Gonzalez, R. C., 1977, "Digital Image Processing", Department of Electrical Engineering, University of Tennessee, Addison-Wesley Publishing Company, Advanced Book Program Reading, Massachusetts.
- Khalaf, S., 2004, "Digital Elevation Model Using GPS and GIS System", M.Sc. Thesis, College of Engineering, Department of Surveying, Baghdad University.
  - Mohammed Rajabi, 2003, "Densification of DTM Gird Data Using Single Satellite Imagery", M.Sc. Thesis, Department of Geometrics Engineering, University of Calgary, and Retrieved December 2007 from:  
• <http://www.geomatics.ucalgary.ca/links/GradTheses.html>
  - USGS Science for a Changing World, 2001, "Image Processing Procedure", Retrieved March 2008 from: <http://edc.usgs.gov/glis/hyper/guide/nlapssys3.html>.

## **LIST OF ABBREVIATIONS**

DEM: Digital Elevation Model.  
DEMs: Digital Elevation Models.  
DN: Digital Number.  
ERDAS: Earth Resources Data Analysis System.  
ETM+: Enhanced Thematic Mapper +.  
GIS: Geographic Information System.  
GeoTIFF: Geographic Tagged Image File Format.  
ISODATA: Iterative Self Organizing Data Analysis.  
Landsat: Land Satellite.  
NMAS: National Mapping Accuracy Standard.  
RMSR: Root Mean Square Error.  
UTM: Universal Transverse Mercator Projection.  
VMAS: Vertical Map Accuracy Standard.

## IMAGE SEGMENTATION USING MULTIWAVELET TRANSFORM

Manal Fadel Younis  
Computer Engineering Department  
Baghdad University

### ABSTRACT

This paper presents region growing image segmentation method which unifies region and boundary information. Several studies shown that segmentation based on image features can improve the accuracy of the interpretation. The goal of segmentation is to simplify and/or change the representation of an image into something that is more meaningful and easier to analyze. Image segmentation is typically used to locate objects and boundaries (lines, curves, etc.) in images. More precisely, image segmentation is the process of assigning a label to every pixel in an image such that pixels with the same label share certain visual characteristics.

A problem that frequently arises when an image is segmented is that the number of feature variables or dimensionality is often quite large. It becomes necessary to decrease the number of the variables to manageable size. The other main difficulty of traditional image segmentation is the lack of adequate tools to characterize different scales of image effective. In this paper it proposed three dimension multiwavelet algorithm to overcome this difficulty and then the region growing method is applied to segment this image.

### الخلاصة

في هذا البحث تم تقديم طريقة لتقسيم صورة معتمدة على نمو المناطق التي توحد مناطق وحدود المعلومات. حيث هناك دراسات عديدة بينت انه التقسيم الذي يعتمد على خصائص الصورة يستطيع ان يحسن في دقة التفسير. الهدف من التقسيم هو تبسيط و تغيير تمثيل الصورة بشكل اكثر مفيد واسهل بالتحليل. تقسيم الصورة نموذجيا يستخدم في تحديد الاشياء والحدود (الخطوط، المنحنيات،... الخ) في الصور. ويتوضح أدق، تقسيم الصورة هو عملية تحديد الصفة لكل نقطة في الصورة لذلك النقاط بنفس الصفات تشترك بخصائص محددة و مرئية.

المشكلة التي تظهر دائما عند تقسيم الصورة هي عدد متغيرات الخصائص او الابعاد عادة تكون كبيرة جدا. فمن الضروري تقليل عدد المتغيرات الى حجم معقول. ومشكلة صعبة اخرى هي التقسيم العادي للصورة يحتاج الى ادوات وافية للحاجة لتخصيص مقاييس مختلفة ذات تاثير على الصورة.

في هذا البحث تم اقتراح طريقة متعدد الموجات ذات ثلاثية البعد (3D-Multiwavelet) لتجاوز هذه المشاكل و تم تطبيق طريقة نمو المناطق لتقسيم الصورة.

**KEYWORDS:** Image Segmentation, 3-D Multiwavelet, Symmetry, Orthogonality, Region growing methods, and Seed point.

### INTRODUCTION

Image segmentation is important research area in computer vision. Several segmentation methods are based on two basic properties of the pixels in relation to their local neighborhood: discontinuity and similarity. Method based on pixel discontinuity is called boundary-based methods whereas methods based on pixel similarity are called region-based methods [Pajdla 2004].

Several image segmentation algorithms have been proposed in the last 30 years. In this research related work are listed below:

#### **"Testing of Image Segmentation Methods"**

In this paper, an approach is developed which allows quantitative and qualitative estimation of segmentation programs. It consists in modeling both difficult and typical situations in image segmentation tasks using special sets of artificial test images. The description of test images and testing procedures are given [GRIBKOV 2008].

#### **"Multi-class image segmentation using Conditional Random Fields and Global Classification"**

A key aspect of semantic image segmentation is to integrate local and global features for the prediction of local segment labels. An approach is presented to multi-class segmentation which combines two methods for this integration: a Conditional Random Field (CRF) which couples to local image features and an image classification method which considers global features [Plath 2009].

#### **"VARIATIONAL APPROACH TO IMAGE SEGMENTATION"**

This paper focuses on a second order functional depending on free discontinuity and free gradient-discontinuity, whose minimizers provide a variational solution to contour detection problem in image segmentation [Carriero 2009].

#### **"Optimization-Based Image Segmentation by Genetic Algorithms"**

Many works in the literature focus on the definition of evaluation metrics and criteria that enable to quantify the performance of an image processing algorithm. These evaluation criteria can be used to define new image processing algorithms by optimizing them. In this paper, general scheme it proposed to segment images by a genetic algorithm. The developed method uses an evaluation criterion which quantifies the quality of an image segmentation result. The proposed segmentation method can integrate a local ground truth when it is available in order to set the desired level of precision of the final result [Chabrier 2008].

#### **"Image Segmentation by Branch-and-Mincut"**

The main contribution of this paper is a new global optimization framework for a wide class of such energies. The framework is built upon two powerful techniques: graph cut and branch-and-bound. These techniques are unified through the derivation of lower bounds on the energies. Being computable via graph cut, these bounds are used to prune branches within a branch-and-bound search [Victor 2008].

#### **"Image Segmentation Method Using Thresholds Automatically Determined from Picture Contents"**

This work develops an image segmentation method based on the modified edge-following scheme where different thresholds are automatically determined according to areas with varied contents in a picture, thus yielding suitable segmentation results in different areas [Yuan 2009].

#### **"Non-Parametric Probabilistic Image Segmentation"**

The proposed model is principled, provides both hard and probabilistic cluster assignments, as well as the ability to naturally incorporate prior knowledge. While previous probabilistic approaches are restricted to parametric models of clusters (e.g., Gaussians) it eliminates this limitation. The suggested approach does not make heavy assumptions on the shape of the clusters and can thus handle complex structures. Our experiments show that the suggested approach outperforms previous work on a variety of image segmentation tasks [Andreetto 2007].

**"Semi-automatic Handwritten Word Segmentation Based on Character Width Approximation via Maximum Likelihood Method and Regression Model"**

This paper presents a method of word image segmentation into images of individual characters. The method is semi-automatic; because it requires that the character sequence constituting the word on the image is known. It is assumed that widths of the characters in the alphabet are random variables and that the parameters of probability distribution are specific for each character [Springer 2008].

**"Unsupervised Segmentation of Natural Images via Lossy Data Compression"**

We cast natural-image segmentation as a problem of clustering texture features as multivariate mixed data. We model the distribution of the texture features using a mixture of Gaussian distributions. Unlike most existing clustering methods, we allow the mixture components to be degenerate or nearly-degenerate. We contend that this assumption is particularly important for mid-level image segmentation, where degeneracy is typically introduced by using a common feature representation for different textures in an image. We show that such a mixture distribution can be effectively segmented by a simple agglomerative clustering algorithm derived from a lossy data compression approach. Using either 2D texture filter banks or simple fixed-size windows as texture features, the algorithm effectively segments an image by minimizing the overall coding length of the feature vectors. We conduct comprehensive experiments to measure the performance of the algorithm in terms of visual evaluation and a variety of quantitative indices for image segmentation. The algorithm compares favorably against other well-known image segmentation methods on the Berkeley image database [Hong 2007].

**"A Variational Level Set Approach to Segmentation and Bias Correction of Images with Intensity Inhomogeneity"**

This paper presents a variational level set approach to joint segmentation and bias correction of images with intensity inhomogeneity. Our method is based on an observation that intensities in a relatively small local region are separable, despite of the inseparability of the intensities in the whole image caused by the intensity inhomogeneity [Chunming 2008].

**THE PROPOSED METHOD OF SEGMENTATION:**

Image segmentation is a set of segments that collectively cover the entire image, or a set of contours extracted from the image. Each of the pixels in a region is similar with respect to some characteristic or computed property, such as color, intensity, or texture. Adjacent regions are significantly different with respect to the same characteristic(s) [Linda 2001].

Applications some of the practical applications of image segmentation are [Wikipedia 2009]:

- Medical Imaging
  - Locate tumors and other pathologies
  - Measure tissue volumes
  - Computer-guided surgery
  - Diagnosis
  - Treatment planning
  - Study of anatomical structure
- Locate objects in satellite images (roads, forests, etc.)
- Face recognition
- Fingerprint recognition
- Traffic control systems
- Brake light detection
- Machine vision

The proposed image segmentation is shown below in fig. (1):

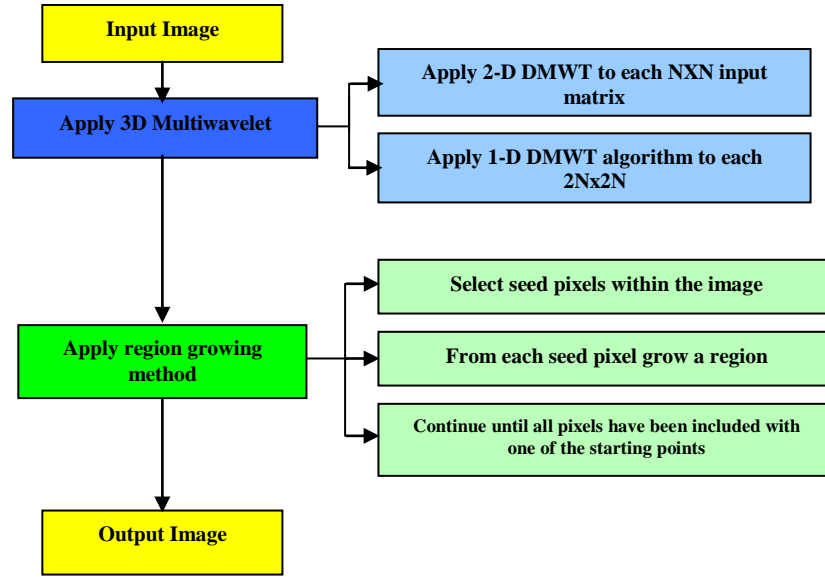


Fig. (1): The diagram of the proposed method

### 3-D Multiwavelet Transform:

In this paper, the proposed an approach is 3-D multiwavelet transformation as an image extraction tool for segmenting images.

The general form for the procedure of 3-D FDMWT [Hadeel 2005]:-

The algorithm is initially run in x-direction, row by row for all slices. The algorithm splits the volume into two halves, the left half representing the low-frequency coefficients while the right half represents the detail coefficients. In the second stage of the algorithm, the entire volume is then again transformed in y-direction splitting the volume into four quadrants. For the final run, the volume is transformed in z-direction splitting the volume into eight octants. The upper left front octant contains the low-frequency coefficients that are initially transmitted over the network.

### 3 Dimensional Multiwavelet Computations

1- Let

$$X = \begin{bmatrix} 16 & 2 & 3 & 13 \\ 5 & 11 & 10 & 8 \\ 9 & 7 & 6 & 12 \\ 4 & 14 & 15 & 1 \end{bmatrix} \begin{bmatrix} 1 & 2 & 0 & 1 \\ 1 & 1 & 2 & 0 \\ 3 & 0 & 1 & 1 \\ 2 & 1 & 1 & 0 \end{bmatrix} \begin{bmatrix} 1 & 1 & 0 & 1 \\ 2 & 1 & 1 & 0 \\ 0 & 2 & 1 & 1 \\ 3 & 0 & 1 & 2 \end{bmatrix} \begin{bmatrix} 3 & 2 & 1 & 5 \\ 2 & 1 & 4 & 1 \\ 1 & 0 & 1 & 1 \\ 3 & 1 & 0 & 1 \end{bmatrix}$$

2- Apply 2-D DMWT to each NXN input matrix, which result in a 2NX2NXM matrix.

$$Y = \begin{bmatrix} a_{0,0} & a_{0,1} & a_{0,2} & a_{0,3} & a_{0,4} & a_{0,5} & a_{0,6} & a_{0,7} \\ a_{1,0} & a_{1,1} & a_{1,2} & a_{1,3} & a_{1,4} & a_{1,5} & a_{1,6} & a_{1,7} \\ a_{2,0} & a_{2,1} & a_{2,2} & a_{2,3} & a_{2,4} & a_{2,5} & a_{2,6} & a_{2,7} \\ a_{3,0} & a_{3,1} & a_{3,2} & a_{3,3} & a_{3,4} & a_{3,5} & a_{3,6} & a_{3,7} \\ a_{4,0} & a_{4,1} & a_{4,2} & a_{4,3} & a_{4,4} & a_{4,5} & a_{4,6} & a_{4,7} \\ a_{5,0} & a_{5,1} & a_{5,2} & a_{5,3} & a_{5,4} & a_{5,5} & a_{5,6} & a_{5,7} \\ a_{6,0} & a_{6,1} & a_{6,2} & a_{6,3} & a_{6,4} & a_{6,5} & a_{6,6} & a_{6,7} \\ a_{7,0} & a_{7,1} & a_{7,2} & a_{7,3} & a_{7,4} & a_{7,5} & a_{7,6} & a_{7,7} \end{bmatrix} \begin{bmatrix} b_{0,0} & b_{0,1} & b_{0,2} & b_{0,3} & b_{0,4} & b_{0,5} & b_{0,6} & b_{0,7} \\ b_{1,0} & b_{1,1} & b_{1,2} & b_{1,3} & b_{1,4} & b_{1,5} & b_{1,6} & b_{1,7} \\ b_{2,0} & b_{2,1} & b_{2,2} & b_{2,3} & b_{2,4} & b_{2,5} & b_{2,6} & b_{2,7} \\ b_{3,0} & b_{3,1} & b_{3,2} & b_{3,3} & b_{3,4} & b_{3,5} & b_{3,6} & b_{3,7} \\ b_{4,0} & b_{4,1} & b_{4,2} & b_{4,3} & b_{4,4} & b_{4,5} & b_{4,6} & b_{4,7} \\ b_{5,0} & b_{5,1} & b_{5,2} & b_{5,3} & b_{5,4} & b_{5,5} & b_{5,6} & b_{5,7} \\ b_{6,0} & b_{6,1} & b_{6,2} & b_{6,3} & b_{6,4} & b_{6,5} & b_{6,6} & b_{6,7} \\ b_{7,0} & b_{7,1} & b_{7,2} & b_{7,3} & b_{7,4} & b_{7,5} & b_{7,6} & b_{7,7} \end{bmatrix} \begin{bmatrix} c_{0,0} & c_{0,1} & c_{0,2} & c_{0,3} & c_{0,4} & c_{0,5} & c_{0,6} & c_{0,7} \\ c_{1,0} & c_{1,1} & c_{1,2} & c_{1,3} & c_{1,4} & c_{1,5} & c_{1,6} & c_{1,7} \\ c_{2,0} & c_{2,1} & c_{2,2} & c_{2,3} & c_{2,4} & c_{2,5} & c_{2,6} & c_{2,7} \\ c_{3,0} & c_{3,1} & c_{3,2} & c_{3,3} & c_{3,4} & c_{3,5} & c_{3,6} & c_{3,7} \\ c_{4,0} & c_{4,1} & c_{4,2} & c_{4,3} & c_{4,4} & c_{4,5} & c_{4,6} & c_{4,7} \\ c_{5,0} & c_{5,1} & c_{5,2} & c_{5,3} & c_{5,4} & c_{5,5} & c_{5,6} & c_{5,7} \\ c_{6,0} & c_{6,1} & c_{6,2} & c_{6,3} & c_{6,4} & c_{6,5} & c_{6,6} & c_{6,7} \\ c_{7,0} & c_{7,1} & c_{7,2} & c_{7,3} & c_{7,4} & c_{7,5} & c_{7,6} & c_{7,7} \end{bmatrix} \begin{bmatrix} d_{0,0} & d_{0,1} & d_{0,2} & d_{0,3} & d_{0,4} & d_{0,5} & d_{0,6} & d_{0,7} \\ d_{1,0} & d_{1,1} & d_{1,2} & d_{1,3} & d_{1,4} & d_{1,5} & d_{1,6} & d_{1,7} \\ d_{2,0} & d_{2,1} & d_{2,2} & d_{2,3} & d_{2,4} & d_{2,5} & d_{2,6} & d_{2,7} \\ d_{3,0} & d_{3,1} & d_{3,2} & d_{3,3} & d_{3,4} & d_{3,5} & d_{3,6} & d_{3,7} \\ d_{4,0} & d_{4,1} & d_{4,2} & d_{4,3} & d_{4,4} & d_{4,5} & d_{4,6} & d_{4,7} \\ d_{5,0} & d_{5,1} & d_{5,2} & d_{5,3} & d_{5,4} & d_{5,5} & d_{5,6} & d_{5,7} \\ d_{6,0} & d_{6,1} & d_{6,2} & d_{6,3} & d_{6,4} & d_{6,5} & d_{6,6} & d_{6,7} \\ d_{7,0} & d_{7,1} & d_{7,2} & d_{7,3} & d_{7,4} & d_{7,5} & d_{7,6} & d_{7,7} \end{bmatrix}$$

3- Apply 1-D DMWT algorithm to each  $2N \times 2N$  (64 element) in all  $M$  matrices in  $z$ -direction. This can be done as follows:

- For each  $i, j$  construct the  $M \times 1$  input vector  $Y(i, j) = [a_{i,j} \ b_{i,j} \ c_{i,j} \ d_{i,j}]_{1 \times M}^T$  where  $i, j = 0, 1, 2, \dots, N$
- Preprocessing the input vector by repeating the input stream.
- Constructing a  $2M \times 2M$  transformation matrix using GHM low and high pass filters.
- Apply matrix multiplication to the  $2M \times 2M$  constructed transformation matrix by the  $2M \times 1$  preprocessing input vector.
- Permute the resulting  $2M \times 1$  matrix

4- Repeat step 3 for all  $i, j$ .

5- Finally, a  $2N \times 2N \times 2M$  DMW matrix results from the  $N \times N \times M$  original matrix using repeated row preprocessing.

### **Advantages of Multiwavelet:**

Some reasons for choosing multiwavelets can be shown as follows [Hadeel 2005]:

- 3-D FDMWT decreases the number of variables to manageable size, at the same time, retaining as much discriminatory information as possible.
- Multiwavelets can be used to reduce restrictions on the filter properties. But a scalar wavelet cannot simultaneously have both orthogonality and a symmetric impulse response that has length greater than 2. Symmetric filters are necessary for symmetric signal extension, while orthogonality makes the transform easier to design and implement.
- The length and the number of vanishing moments are directly linked to the filter length for scalar wavelets.
- Multiwavelets are able to possess the best of all these properties simultaneously. For example, the GHM multiwavelet is orthogonal, has second order of approximation, has symmetric scaling and wavelet functions (and thus symmetric filters), and has short support for both of its scaling functions. But scalar wavelet impossible support for these properties.
- Multiwavelets better than scalar wavelet because they can give performance comparable to scalar wavelets with shorter filters of the length of half. Thus for the same quality of decomposed levels multiwavelets require about half the number of operations.

### **Region Growing Method**

The first region growing method was the seeded region growing method. This method takes a set of seeds as input along with the image. The seeds mark each of the objects to be segmented. The regions are iteratively grown by comparing all unallocated neighboring pixels to the regions. The difference between a pixel's intensity value and the region's mean,  $\delta$ , is used as a measure of similarity. The pixel with the smallest difference measured this way is allocated to the respective region. This process continues until all pixels are allocated to a region [Dzung 2000].

Seeded region growing requires seeds as additional input. The segmentation results are dependent on the choice of seeds. Noise in the image can cause the seeds to be poorly placed. Unseeded region growing is a modified algorithm that doesn't require explicit seeds. It starts off with a single region  $A_1$  – the pixel chosen here does not significantly influence final segmentation. At each iteration it considers the neighboring pixels in the same way as seeded region growing. It differs from seeded region growing in that if the minimum  $\delta$  is less than a predefined threshold  $T$  then it is added to the respective region  $A_j$ . If not, then the pixel is considered significantly different from all current regions  $A_i$  and a new region  $A_{n+1}$  is created with this pixel [Dzung 2000].



### **Basic Concept of Seed Point**

First of all, it chooses a set of seed points. And the initial region now is the exact location of these seeds [Wikipedia 2009].

Then the regions are grown from these seed points to adjacent points depending on a threshold or criteria we make. The threshold could be made by user. It could be intensity, gray level texture, or color [Wikipedia 2009].

There are several important issues about region growing [Wikipedia 2009]:

- b. The suitable selection of seed points is important: The selection of seed points is depending on the users. For example, in a gray-level lightning image, it segments the lightning from the background.
- c. More information of the image is better: The connectivity or pixel adjacent information is helpful for us to determine the threshold and seed points.
- d. The value, “minimum area threshold”: No region in region growing method result will be smaller than this threshold in the segmented image.
- e. The value, “Similarity threshold value”: If the difference of pixel-value or the difference value of average gray level of a set of pixels less than “Similarity threshold value”, the regions will be considered as a same region. The criteria of similarities or so called homogeneity that it chooses are also important. It usually depends on the original image and the segmentation result it want.

### **Region Growing Algorithm:**

1. Select seed pixels within the image.
2. From each seed pixel grow a region.
  - 2.1. Set the region prototype to be the seed pixel.
  - 2.2. Calculate the similarity between the region prototype and the candidate pixel;
  - 2.3. Calculate the similarity between the candidate and its nearest neighbour in the region;
  - 2.4. Include the candidate pixel if both similarity measures are higher than experimentally-set thresholds;
  - 2.5. Update the region prototype by calculating the new principal component;
  - 2.6. Go to the next pixel to be examined.

Examples of region growing shown in fig. (2) and fig. (3):

⇒ Starts with a set of seeds (starting pixels)

- Predefined seeds
- All pixels as seeds
- Randomly chosen seeds

⇒ Region growing steps (bottom-up method)

- Find starting points
- Include neighboring pixels with similar features (grey-level, texture, color), a similarity measure must be selected.
- Continue until all pixels have been included with one of the starting points.

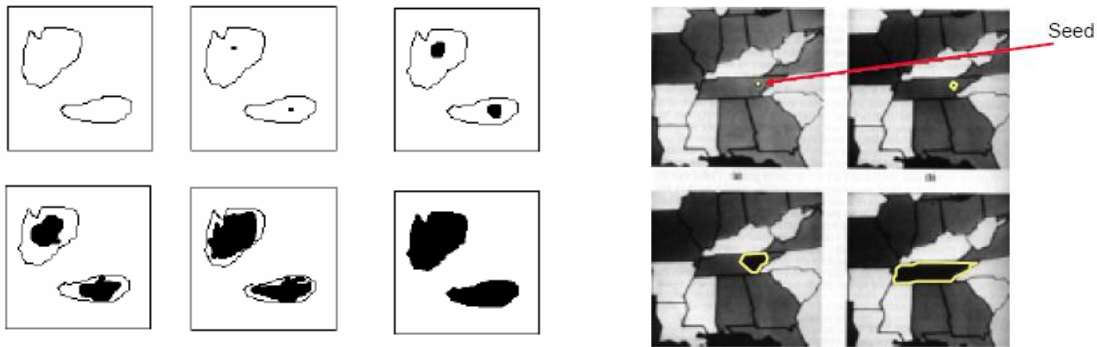


**Fig. (2) and Fig. (3):** Region growing examples

## RESULTS AND DISCUSSIONS

In this paper an image of size (512 X 512) pixels divided into four parts of size (256 X 256) pixels, and then applied 3D-multiwavelete for each part in Matlab V.2008a, as shown below in fig. (5).



**Fig. (4):** Original image

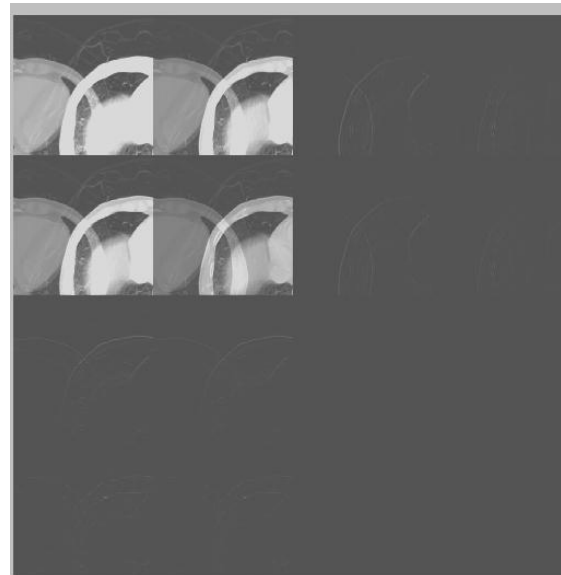


**Fig. (5):** After apply 3D Multiwavelete of the second part

After that Sobel filter used to detect the edge of the LH band for the second part. The gradient of the Sobel filter is high at the borders of objects and low inside the objects. As shown in fig. (7):

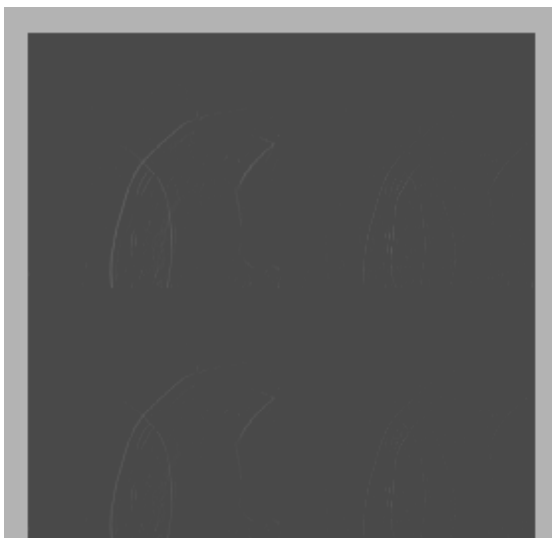


**Fig. (6):** The LH band of the second part

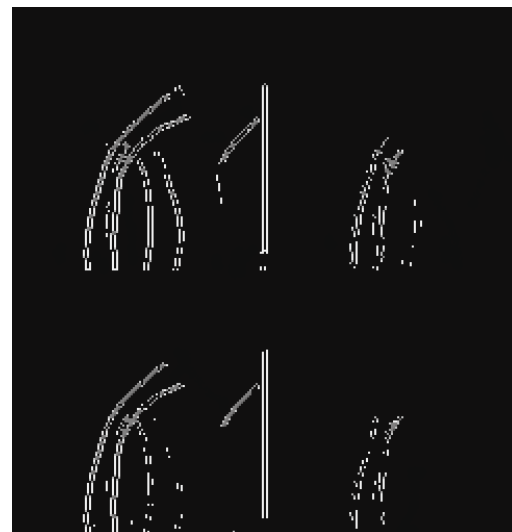


**Fig. (7):** After apply Sobel Filter to the LH band

The resulting image of Sobel filter show the intensity gradients for each pixel in the LH band, then the final step of this work is implement the region growing method to this result by taking seed point and for each seed pixel grow a region by adding neighboring pixels that have properties similar intensity to seed. The region grows based on similarity criteria and stops growth when no more neighboring pixels satisfy this criterion, for this algorithm a threshold of 0.2 value can be used for stopping, when the intensity difference for all neighboring pixels is above this threshold, growth the region stops. The value of threshold is taken from several experiments of this algorithm. Thus the result is As shown in fig. (8).

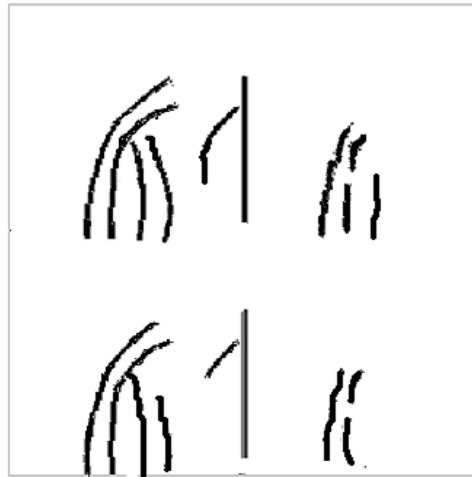


**Fig. (8):** After apply region growing method of the result of Sobel filter

This application differs from other related work in applying 3D multiwavelet before image segmented for many reasons are referred to in this paper.

## CONCLUSION

In this paper a discrete multiwavelet technique is used for the image features extraction. Multiwavelet offers the advantages of combining symmetry, orthogonality which can not be achieved by scalar two-channel wavelet systems of the same time. Then, this output is segmented in region-growing method.

Because this method presents several advantages over other color image segmentation algorithms. First, it is based on the concept of color vector angle; the vector angle is a shading-invariant color similarity measure, implying that intensity variations will be discounted in the region growing process, which is clearly not the case when using the Euclidean distance. Secondly, since spatial information is taken into account, regions having a slightly different color, but still spatially distinct, should appear as separate regions due to the region growing process.



## REFERENCES

- Carriero M., Leaci A. , Tomarelli. F., "VARIATIONAL APPROACH TO IMAGE SEGMENTATION", 2009.
- Chunming Li<sup>1</sup>, RuiHuang<sup>2</sup>, Zhaohua Ding, Chris Gatenby<sup>1</sup>, Dimitris Metaxas, and John Gore<sup>1</sup>, "A Variational Level Set Approach to Segmentation and Bias Correction of Images with Intensity Inhomogeneity, 2008.
- Dzung L. Pham, Chenyang Xu, and Jerry L. ,“Current Methods in Medical Image Segmentation”, 2000.
- [http://www.en.wikipedia.org/.../Segmentation\\_\(image\\_processing\)](http://www.en.wikipedia.org/.../Segmentation_(image_processing)), 2009.
- Hadeel Nasrat Al-Taai, "Optical Flow Estimation Using DSP Techniques", 2005.
- I.V.GRIBKOV, P.P.KOLTISOV, N.V.KOTOVICH, A.A. KRAVCHENKO, A.S.KOUTSAEV, A.S. OSIPOV, A.V. ZAKHAROV, "Testing of Image Segmentation Methods", Scientific Research Institute for System Studies, Russian Academy of Sciences (NIISI RAN), Nakhimovskii pr. 36-1, Moscow, 117218 RUSSIAN FEDERATION, vokbirg@yauza.ru, koltsov@niisi.msk.ru, Issue 8, Volume 4, August 2008.
- Linda G. Shapiro and George C. Stockman, "Computer Vision", pp 279-325, New Jersey, Prentice-Hall, ISBN 0-13-030796-3, 2001.
- [8] M. Andreetto, L. Zelnik-Manor, and P. Perona, "Non-Parametric Probabilistic Image Segmentation", ICCV 2007.
- Plath, Nils and Toussaint, Marc and Nakajima, Shinichi, "Multi-class image segmentation using Conditional Random Fields and Global Classification ", 2009.
- S. Chabrier, C. Rosenberger, B. Emile, and H. Laurent, "Optimization-Based Image Segmentation by Genetic Algorithms", 8 February 2008
- Springer Berlin, "Semi-automatic Handwritten Word Segmentation Based on Character Width Approximation Via Maximum Likelihood Method and Regression Model", 2008.
- T. Pajdla and J. Matas, pp. 250-261, C\_Springer\_Verlag Berlin Heidelberg 2004.
- Yuan Been Chen and Oscar T.-C. Chen, "Image Segmentation Method Using Thresholds Automatically Determined from Picture Contents", Accepted 28 January 2009.
- Victor Lempitsky, Andrew Blake and Carsten Rother, "Image Segmentation by Branch-and-Mincut", 2008.
- Wei Hong, John Wright, and Allen Y. Yang, "Unsupervised Segmentation of Natural Images via Lossy Data Compression" (c) Copyright. University of California, Berkeley. 2007, [yang@eecs.berkeley.edu](mailto:yang@eecs.berkeley.edu).

## REMOVAL OF DYES FROM TEXTILE EFFLUENT BY ADSORPTION ONTO OVEN DRIED ALUM SLUDGE

Rasha H. Salman

Chemical Engineering Department, College of Engineering, University of Baghdad

### ABSTRACT

The present study deals with the removal of dyes from the effluent of the state company for cotton textile industries located at Al-Khadmya by using oven dried alum sludge (ODS) as adsorbent. Two different dyes; Direct black and solar brown are studied. Alum sludge was collected from Al-Qadisiya water treatment plant; it was heated in an oven at 105°C for 24 hours, then cooled at room temperature and crushed to produce particle sizes of 1.18-2.36 and 4-4.75 mm. Batch and fixed bed mode were used. In batch experiments the effect of oven dried alum sludge weight on adsorption process and equilibrium isotherm were studied by using 15-125 g/l of oven dried alum sludge for direct black and 15-175 g/l for solar brown, with constant initial dyes concentration of 10 mg/l and constant particle size of 4-4.75 mm. Batch kinetics experiments showed that equilibrium time was about 12-14 days. The three models Freundlich, Langmuir and Freundlich-Langmuir gave good fitting for the adsorption capacity. In the fixed bed isothermal adsorption column, the effect of initial dye concentration ( $C_0$ ), particle size, influent flow rate ( $Q$ ) and bed depth ( $H$ ) were studied. The results showed that the oven dried alum sludge was effective in adsorbing dyes with removal efficiency ranged between 90% to 92%.

### الخلاصة:

تم في هذا البحث دراسة قابلية أطيان الشب المعالجة حرارياً على امتزاز وتقليل اللون من المياه الملوثة من الشركة العامة للصناعات القطنية في مدينة الكاظمية. الأصباغ التي تم استخدامها في الدراسة هي direct black و solar brown. أطيان الشب التي تم استخدامها قد جمعت من مشروع القادسية لمعالجة المياه في بغداد. تم معالجة أطيان الشب حرارياً في فرن بدرجة حرارة 105 م° ولمدة 24 ساعة وترك ليبرد إلى درجة حرارة الغرفة ثم تكسيره إلى أحجام 1.18-2.36 و 4-4.75 ملم. تم استخدام نمطين من التشغيل في هذا البحث وهي تجارب النمط الدفعي وتجارب النمط المستمر. في تجارب النمط الدفعي تم دراسة تأثير كمية أطيان الشب المعالجة حرارياً على عملية الامتزاز باستخدام 15-125 غم/لتر من المادة الممتزة لصبغة direct black و 15-175 غم/لتر لصبغة solar brown بثبوت تركيز الصبغة الابتدائي 10 ملغم/لتر وحجم ثابت لجزيئات المادة الممتزة 4-4.75 ملم، أظهرت النتائج أن نسبة إزالة الأصباغ تزداد بزيادة كمية أطيان الشب المعالجة حرارياً. كذلك أظهرت النتائج أن الوصول إلى حالة التعادل تستغرق تقريباً 12 إلى 14 يوم، تم تحليل النتائج باستخدام موديلات (Langmuir, Freundlich and Freundlich-Langmuir) وأظهرت النتائج أن جميع الموديلات ذات تقارب جيد. في تجارب النمط المستمر تم دراسة تأثير تركيز الأصباغ الابتدائي وحجم جزيئات المادة الممتزة ومعدل الجريان وارتفاع عمود الامتزاز على عملية الامتزاز. لقد أظهرت النتائج أن أطيان الشب المعالج حرارياً فعال في امتزاز الأصباغ من مياه الصرف وكانت نسبة إزالة الأصباغ تتراوح بين 90% إلى 92%.

**KEYWORDS:** Wastewater treatment, Adsorption, Alum sludge, dyes removal.

## INTRODUCTION

Textile industries use large amount of water and chemicals for the finishing and dying processes. The chemical structures of dyes vary enormously and some have complicated aromatic structures that resist degradation in conventional wastewater treatment processes because of their stability to sunlight, oxidizing agents, and microorganisms. Dye wastewater usually consists many of contaminants, including acids, bases, dissolved solids, toxic compounds and color. Color is the most noticeable contaminant even at low concentrations, and it needs to be removed or decolorized before the discharging the wastewater (Chu, 2001). Wastewater from textile and tannery effluents attracts attention of environmental protection agencies all over the world. Many methods have been used to treat wastewaters from effluents. Physical and chemical methods are considered very expensive in terms of energy and reagents consumption. Another account that limits their use is the excessive sludge they generate (Yakubu et al., 2008). Adsorption has been found to be superior to other techniques for water re-use in terms of initial cost, simplicity of design, ease of operation and insensitivity to toxic substances. At the present time, there is a growing interest in using low-cost, commercially available materials for the adsorption of dyes (Yavuz and Aydin, 2006). Alum sludge is a waste material generated during the coagulation / sedimentation process in drinking water treatment plant. This sludge contains precipitated alum hydroxides and the some contaminants related to the raw water chemistry (Galarneau and Gehr, 1997). The adsorbents are usually used in the fixed bed process because of the ease of operation. To design and operate a fixed bed adsorption process successfully, the column dynamics must be understood, that is the breakthrough curves under specific operating conditions must be predictable (Markovska and Meshko, 2001).

Abbas H. (2005) investigated the capability of activated alumina from bauxite compared with activated carbon adsorption capability to reduce the color from wastewater of textile company (Al- Hilla- Babel). The results showed that the adsorption process which using activated carbon insuring a good degree of reduction of color (99.7%) and is better than activated bauxite which reach (95%) removal percentage. Also, the capacity of adsorption increased with increase of bed depth and decrease in flow rate.

Ibtehal K. (2002) reported the treatment and recycling of industrial wastewater from cotton textile industry in Iraq which contains three different dyes namely, direct blue, sulphur black and vat yellow. Two dyes removal methods were used, chemical coagulation and adsorption onto activated carbon. The results showed that the best chemical coagulant for complete dye removal was found to be aluminum sulphate. Also adsorption onto granular activated carbon was found to be very effective for dyes removal.

Sarmad A. (2009) investigated the removal of phosphorous from wastewater by using oven dried alum sludge. The results showed that the oven dried alum sludge were effective for adsorbing phosphorous and the removal percentage was up to 85%.

The present study deals with the removal of dyes from the effluent of textile company (Al-Khadmya- Baghdad) using oven dried alum sludge (ODS) as adsorbent. Two dyes, direct black and solar brown which are mainly used in this industry will be tested to study the different variables affecting the adsorption behavior.

## EXPERIMENTAL WORK

### Materials:

- **Adsorbent:** In this research alum sludge was collected from Al-Qadisiya treatment plant, Baghdad, Iraq. The alum sludge was tested in Ibn Sina State Company to determine the inorganic contents. Table 1 represents the combination of this sludge.

**Table 1: Inorganic materials in alum sludge**

Constituent	Weight percent, %	Constituent	Weight percent, %
Aluminum	3.38	Zinc	0.0098
Iron	0.819	Lead	0.0001
Manganese	0.16	Barium	0.0001
Chromium	0.013	Arsenic	0.0002
Vanadium	0.002	-	-

Alum sludge was heated in an oven at 105° C for 24 hours, and then dried sludge was cooled to room temperature, crushed to produce particle sizes of 1.18-2.36 and 4-4.75 mm. The physical properties of these particles are listed in Table 2.

**Table 2: Physical properties of oven dried alum sludge**

Property	Oven dried alum sludge
Bulk density (kg/m <sup>3</sup> )	786.7
Particle porosity	0.7
Bed porosity	0.65
BET surface area (m <sup>2</sup> /g)	191

### **Tests for Characterizing Oven Dried Alum Sludge**

**(A) IR Spectroscopy:** The samples for infrared spectra (Bruker Vector FT-IR spectrometers) were prepared with methylene chloride (CH<sub>2</sub>Cl<sub>2</sub>) mulls on CsI plates. Vibrational spectra were reported in wavelengths (cm<sup>-1</sup>) against ranked infrared absorption, values of wavelengths at peak correspond to the characteristics of active groups present on the surface of the sludge. This test was done in University of Baghdad/ College of science / Chemistry dept. and the results are shown in Fig. 1.



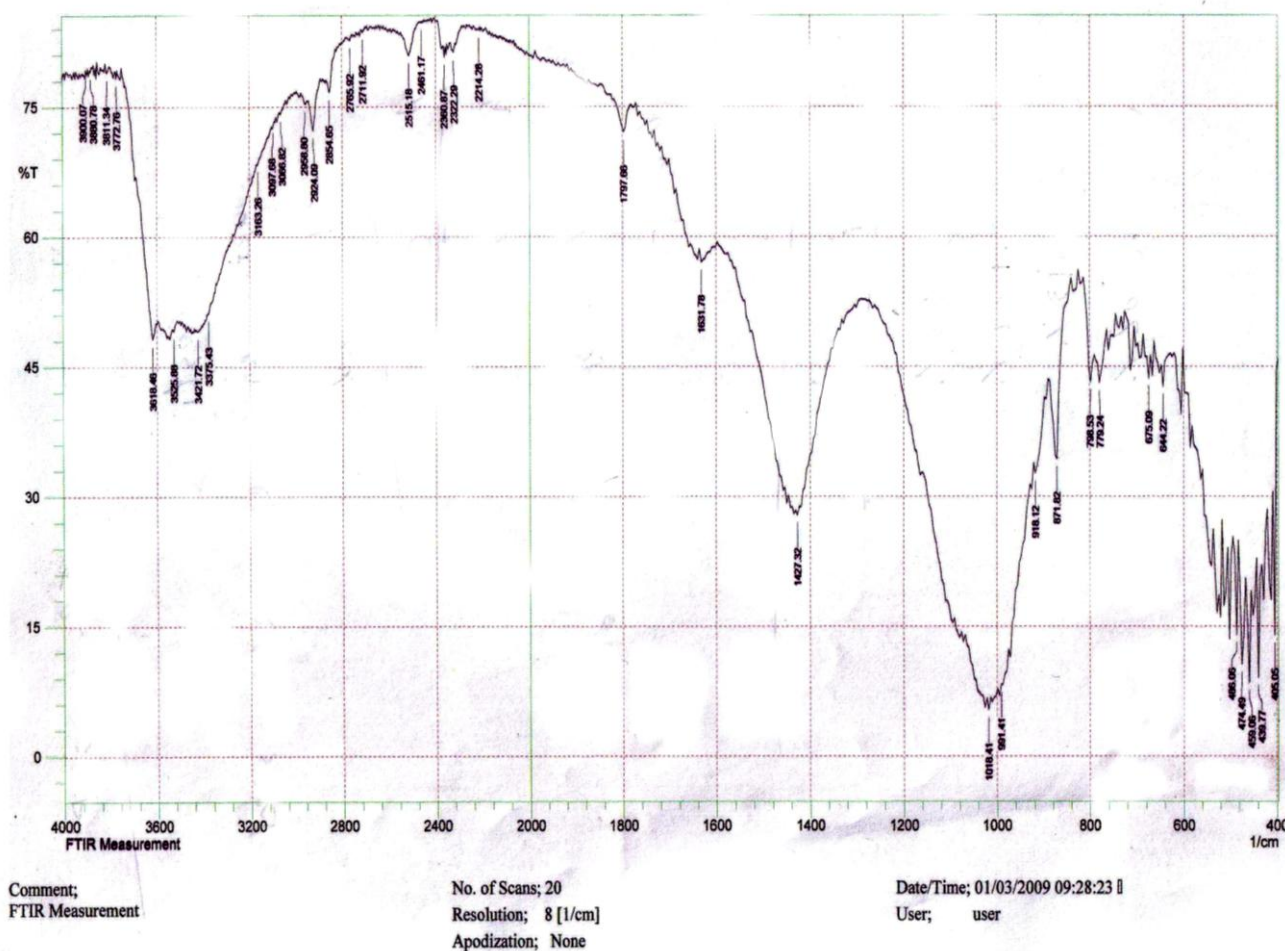


**Fig. 1: IR Spectroscopy of ODS**

**(B) X-Ray Diffraction:** X-Ray powder diffraction patterns of oven dried alum sludge (ODS) were obtained from gently pressed specimens of random powder particles that are less than 0.45  $\mu\text{m}$ . Powder X-ray diffraction data were collected from 10 to 60°  $2\theta$  with a Nicolet X-ray powder diffract meter (graphite monoachromatized Cu KR radiation, 0.05°  $2\theta$  step size, and 2-s count time per steps), this test was performed also in University of Baghdad/ College of science / Chemistry dept. and the results obtained are shown in Fig. 2.



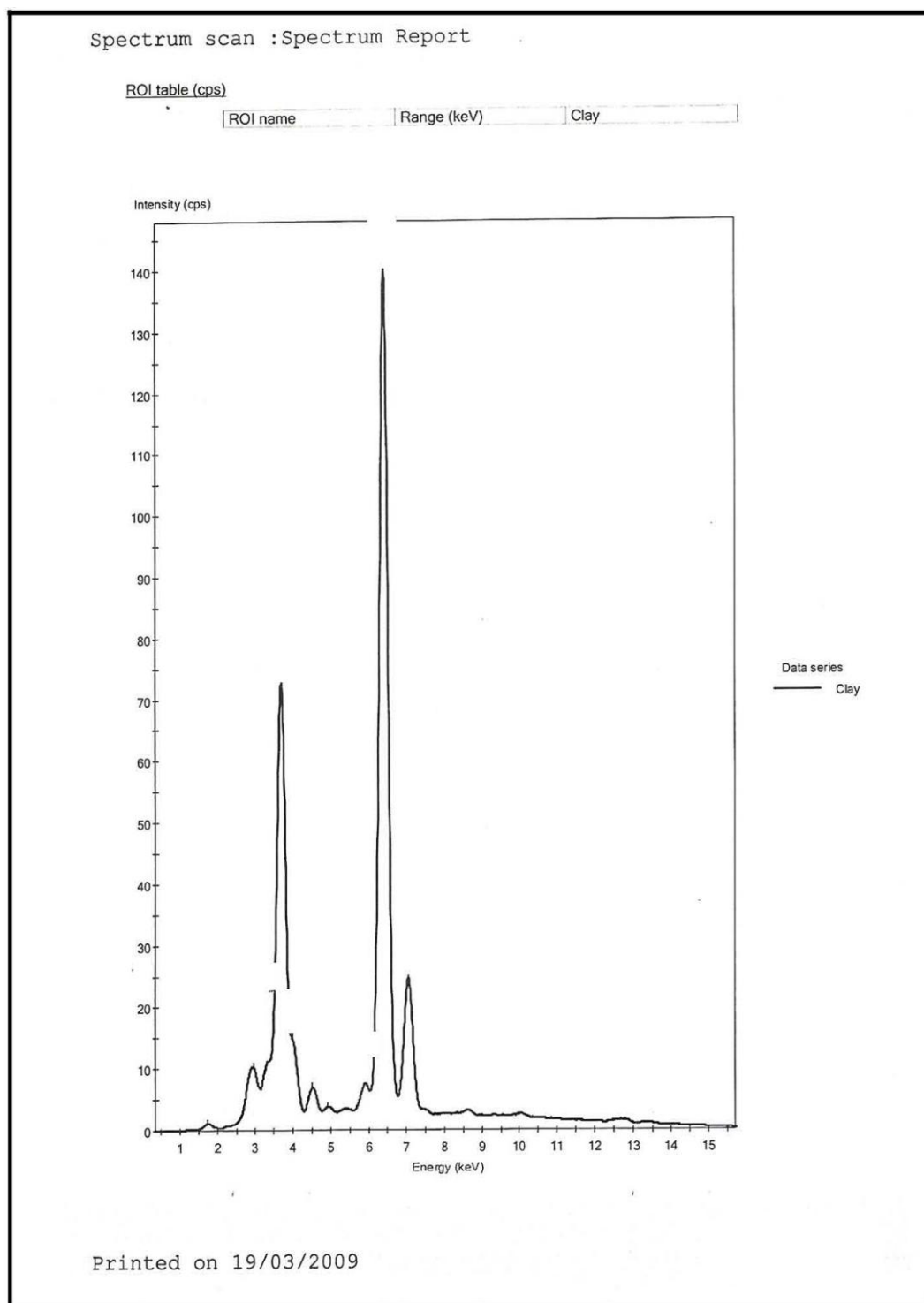


**Fig. 2: X-ray diffraction of ODS**

**(C) Specific Surface Area:** In practice, the method used for determining the specific surface area is the BET (Brunauer, Emmett and Teller) method based on the physical adsorption of an inert gas at constant temperature of liquid nitrogen. This test was done in the Research of oil and development center.

**(2.1.3) Adsorbate:** Two direct dyes were used as adsorbate; direct black and solar brown. The concentrations of the two dyes were measured with Shimadzu UV Spectrophotometer at wave length corresponding to the maximum absorbance for each dye, 566 nm for direct black and 419 nm for solar brown. According to the Lambert-Beer law, the absorbance was found to vary linearly with concentration.

## **Experimental Modes**

### **- Batch Experiments**

Batch experiments were used to obtain the equilibrium isotherm curves and then the equilibrium data. In batch mode the following experiments were carried out:

- Effect of oven dried alum sludge (ODS) weight on the adsorption process.
- Equilibrium isotherm experiments.

All experiments were carried out at  $25^{\circ}\text{C} \pm 1$ . Six 1 L flasks were used for each dye. For experiments conducted with an initial dye concentration of 10 mg/L, alum sludge was used in concentration of 15, 35, 55, 75, 95 and 125 g/l for the direct black and 15, 55, 95, 125, 150 and 175 g/l for the solar brown. Samples were taken from the flasks and tested. Dye that was lost from the solution was assumed to be adsorbed onto the adsorbents. Data obtained from batch tests were conducted on deionized water fitted to Freundlich, Langmuir and Freundlich-Langmuir adsorption isotherm equations.

### **- Fixed Bed Column Experiments**

Column experiments were carried out for various initial dye concentrations ( $C_0$ ), particle size (dp), flow rate (Q) and bed depth (H) to measure the breakthrough curves for the systems.

The fixed bed adsorber studies were carried out in Q.V.F. glass column of 2 in. (50.8 mm) I.D. and 700 mm in height. The oven dried alum sludge (ODS) was confined in the column by fine stainless steel screen at the bottom and a glass cylindrical packing at the top of the bed to ensure a uniform distribution of influent through the adsorbent. The influent solution was introduced to the column through a perforated plate, fixed at the top of the column.

The experimental procedure was as follow:

- The oven dried alum sludge was placed in the adsorption column for the desired bed depth and particle size.
- The wastewater with the desired concentration of dye was prepared in the feed container, using distilled water.
- The wastewater was pumped to the adsorption column through the calibrated rota meter at the desired flow rate.
- Samples were taken periodically and the concentration of dye in these samples was measured using an UV spectrophotometer.
- The breakthrough curves were determined by plotting effluent concentrations ( $C/C_0$ ) against time (t). The schematic diagram of the experimental set-up is shown in Fig. 3.

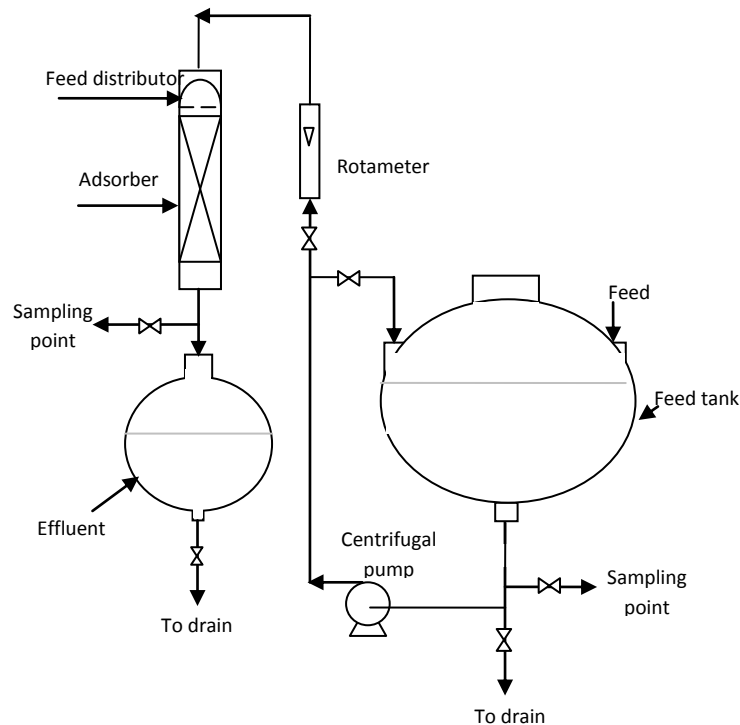


**Fig. 3: Schematic diagram of experimental set-up**

## RESULTS AND DISCUSSION

### Batch experiments

(i) **Adsorption isotherms:** Adsorption isotherm studies were performed to obtain equilibrium isotherm curves and data required for the design and operation of the fixed bed adsorber. The adsorption isotherm curves were obtained by plotting the weight of the solute adsorbed per unit weight of the adsorbent ( $q_e$ ) against the equilibrium concentration of the solute ( $C_e$ ). **Figs. 4 and 5** show the adsorption isotherm curves for adsorption of direct black and solar brown dyes onto oven dried alum sludge at 25° C respectively.

The obtained data of both dyes were fitted with Langmuir, Freundlich and Langmuir-Freundlich models. The Langmuir model describing adsorption can be described as (Weber and Walter, 1972):

$$\frac{x}{m} = \frac{a b C_e}{1 + a C_e} \quad (1)$$

The Freundlich adsorption model is of the form (Weber and Walter, 1972):

$$\frac{x}{m} = K C_e^{1/n} \quad (2)$$

Combination of Langmuir-Freundlich Isotherm Model, i.e. the Sips model for single component adsorption (Sips, 1984) is:

$$q_e = \frac{b q_m C_e^{1/n}}{1 + b C_e^{1/n}} \quad (3)$$

The parameters for each model were obtained from a non-linear statistical fit of the experimental data. All parameters with their correlation coefficients are summarized in Table 3.

**Table 3: Isotherm parameters for dyes adsorption onto ODS.**

Direct black			Solar brown		
Model	Parameters	Values	Model	Parameters	Values
Langmuir (1)	a	0.002305	Langmuir (1)	a	0.000716
	b	33546.28		b	68852.21
	Correlation coefficient (R)	0.9921		Correlation coefficient (R)	0.9869
Freundlich (2)	K	146.3275	Freundlich (2)	K	230.243
	n	0.899925		n	0.782
	Correlation coefficient (R)	0.9941		Correlation coefficient (R)	0.9948
Combination of Langmuir- Freundlich (3)	$q_m$	16817.88	Combination of Langmuir- Freundlich (3)	$q_m$	12605.77
	b	0.008702		b	0.018267
	n	0.899915		n	0.7819
	Correlation coefficient (R)	0.9942		Correlation coefficient (R)	0.9973

From the statistical analysis, high values of the correlation coefficients were found. Indicating that adsorption of dyes by oven dried alum sludge could be well described by the three isotherm models. The correlation coefficients were in the range 99.21-99.42% for direct black and 98.69-99.73% for solar brown at 10 mg/l initial dye concentration. The three models Freundlich, Langmuir and Freundlich-Langmuir gave good fitting for the adsorption capacity.

**(ii) Effect of Mass of Oven Dried Alum Sludge on the Adsorption Process:** The effect of mass of oven dried alum sludge on adsorption of dyes at constant adsorbate concentration was studied. The results of the dependence of dyes on the mass of oven dried alum sludge of size 4-4.75 mm at 25°C are shown in Figs. 6 to 9. These figures show that the removal percentage of each dye increased with increasing the weight of the oven dried alum sludge. The increase in the removal percentage of each dye is due to the greater availability of adsorption sites or surface area of adsorbent. An identical trend was observed by other investigations (Kim et al., 2003a and Maruf et al., 2006).

To reach 90% removal of direct black dye a mass of 125 g/l of ODS should be used, as for solar brown, 175 g/l is required.

### **Fixed bed experiments:**

**(i) Effect of initial dye concentration:** The initial dye concentration of the influent is important since a given mass of adsorbent can only adsorb a fixed amount of the dye. Therefore, the more concentrated the influent is, the smaller is the volume of effluent that a fixed mass of adsorbent can purify. So experiments were undertaken to study the effect of varying the initial dye concentration on the rate of dye adsorption and are shown in Figs. 10 and 11. The initial dye concentration in the inlet flow is one of the limitation factors and a main process parameter. Increasing the inlet dye concentration increases the slope of the breakthrough curve and makes it much steeper, reducing the volume of the effluent treated and reducing the throughput until breakthrough. This may be caused by saturation of adsorbent more quickly with high dye

concentrations; there by decreasing the breakthrough time, the rate of diffusion is controlled by the concentration gradient, so a longer contact time is required to reach saturation for the case of low values of initial solute concentration. Wastewater treatment is limited by the breakthrough point or the dynamics of reaching that point. These systems have a small time delay with higher concentrations in the inlet, so the dye solutions have to be diluted before separation for better removal. The same conclusions were obtained by (Markovska and Meshko, 2001 and Maruf et al., 2006).

**(ii) Effect of volumetric flow rate:** In the design of a fixed bed adsorption column, the contact time is the most significant variable. Therefore, the bed depth and the dye flow rate are the major design parameters (Markovska and Meshko, 2001). The effect of volumetric flow rate was investigated for both dyes and the breakthrough curves are presented in Figs. 12 and 13. Increasing the flow rate from 1 to 3 l/h caused a reduction in the breakthrough time to about the half. It decreased from 800 to 400 min for the direct black and 1200 to 600 min for solar brown. It is obvious that increasing the flow rate decreases the treated volume reaching the breakthrough point and therefore the service time of the bed. This is due to the decreased contact time between the dye and the adsorbent at higher flow rate. Increasing the flow rates may be expected to make reduction of the surface film. Therefore, this will decrease the resistance to mass transfer and increase the mass transfer rate, resulting of easy passage of the adsorbate molecules through the particles and entering easily to the pores. These results agree with that obtained by (Kim et al., 2003a; Maruf et al., 2006, Sarmad, 2009).

**(iii) Effect of bed height:** The effect of bed depths were investigated for dyes adsorption onto the oven dried alum sludge; the experimental breakthrough curves are presented in Figs. 14 and 15 for both dyes. The breakthrough curves were obtained for different bed depths 15 30 40 and 50 cm at a constant flow rate 1 l/h and constant dye concentration of 10 mg/l. It is clear that increasing the bed depth increases the breakthrough time and the residence time of the solute in the column, providing greater surface area for adsorption (Malkoc and Nugoglu, 2006).

Increasing the depth from 15 to 40 cm for direct black and 15 to 50 cm for solar brown as shown in Figs. 14 and 15 increased the breakthrough time from 400 to 800 min for the two dyes.

A comparison in Figs. 16 and 17 for the two dyes, where bed depths are different but the residence time was kept constant by changing the flow rate. These results show that increasing the fluid velocity had no significant effect. Thus, the residence time in the column is more effective in improving the removal efficiency.

**(iii) Effect of particle size:** Using adsorbent particles of smaller sizes will eliminate interparticle mass transfer resistance, so that the rate determining step is diffusion through the film around each particle. The effect of varying the particle size was investigated and the experimental breakthrough curves are presented in Figs. 18 and 19 for both dyes. The breakthrough curves were obtained for different particle sizes 1.18-2.36, 4-4.75 mm at a constant initial concentration of the dyes 10 mg/l, bed depth and constant flow rate 1 l/h. The experimental results showed that fine particle sizes 1.18-2.36 mm showed a higher dye removal than the coarse particle sizes 4-4.75 mm. This was due to the large surface area available for adsorption when using fine particles.

## CONCLUSIONS:

The present study has led to the following conclusions:

- Oven dried alum sludge was effective in adsorbing dyes from deionized water.
- In batch experiment the removal percentage of dyes increases 90-92 % with increasing in the oven dried alum sludge dose 125-175 gm/l.

- Batch kinetics experiments showed that equilibrium time was about 12-14 days without mechanical mixing at an initial concentration 10 mg/l and adsorbent weight 125 g/l for direct black and 175g/l for solar brown.
- The isotherm models, Langmiur, Freundlich and Langmiur- Freundlich gave good fitting for the adsorption of oven dried alum sludge versus equilibrium concentration of dyes. The correlation coefficients (R) obtained from “Satistica Program” for these models were in the range of 99.21-99.42% for direct black and 98.69-99.73% for solar brown.
- In fixed bed experiment, the removal percentage of dyes increased with increasing contact time, adsorbent surface area, bed height and decreasing flow rate.

### NOMENCLATURE:

a	Langmiur constant (l/mg)
b	Langmiur constant (mg/g)
B	The Brunauer, Emmett and Teller
C	Concentration of solute in solution at any time (mg/l)
$C_e$	Concentration of solute in solution at equilibrium (mg/l)
$C_0$	Initial concentration of adsorbate (mg/l)
dp	Adsorbent particle size
K	Freundlich equilibrium constant indicative of adsorption capacity
m	Mass of solute adsorbent (g)
n	Freundlich constant indicative of adsorption intensity
ODS	Oven dried alum sludge
H	Bed depth (cm)
Q	Flow rate (l/h)
$q_e$	Amount of metal ion adsorbed at equilibrium (mg/g)
$q_m$	The maximum adsorption density in Langmiur equation
QVF	Quality vessels fabrication
R	Correlation coefficient
t	Time (min)
UV	Ultra violet
x	Mass of solute adsorbed (mg)

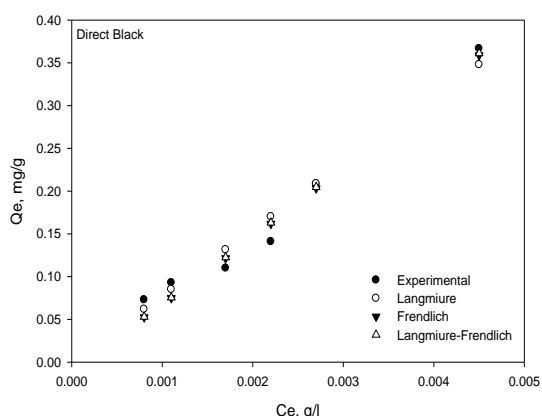


**Fig. 4: Adsorption isotherm for direct black onto oven dried alum sludge ( $C_0=10$  ppm, Temp. =25° C)**

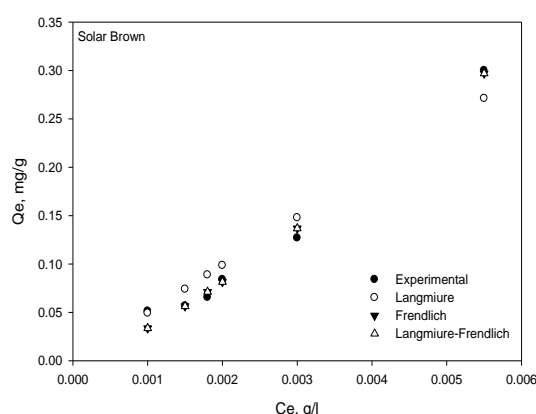


**Fig. 5: Adsorption isotherm for solar brown onto oven dried alum sludge ( $C_0=10$  ppm, Temp. =25° C)**

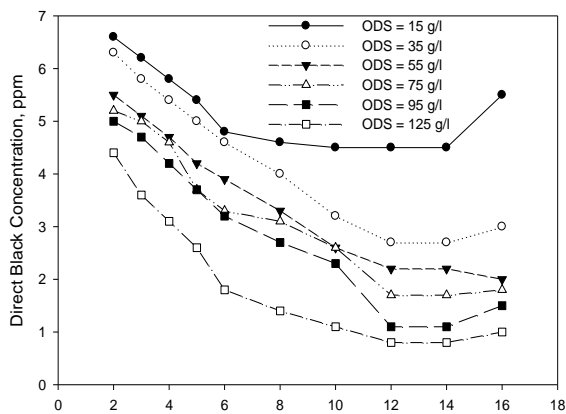


**Fig. 6: Variation of direct black concentrations with time of batch tests ( $C_0=10$  ppm, Temp.  $=25^\circ$  C, particle size=4 mm)**

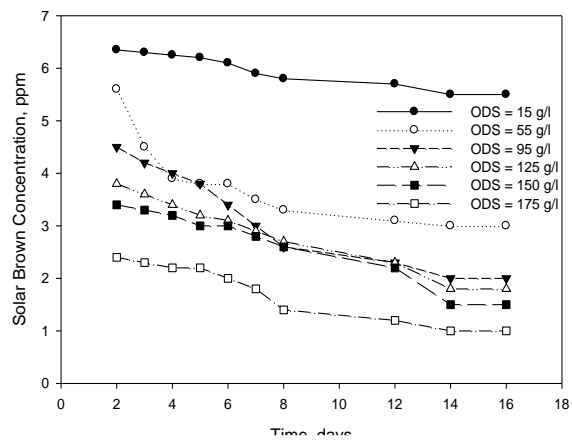


**Fig. 7: Variation of solar brown concentrations with time of batch tests ( $C_0=10$  ppm, Temp.  $=25^\circ$  C, particle size=4 mm)**

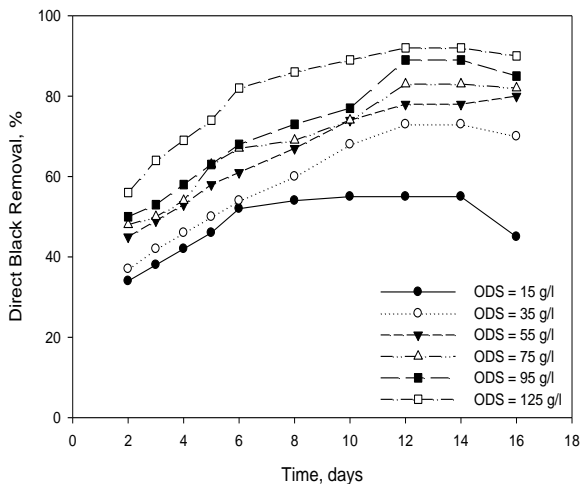


**Fig. 8: the effect of ODS on direct black removal ( $C_0=10$  ppm, Temp.  $=25^\circ$  C, particle size=4 mm)**

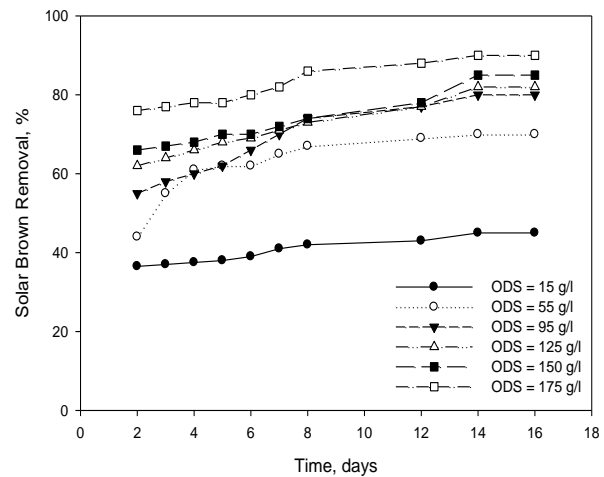


**Fig. 9: the effect of ODS on solar brown removal ( $C_0=10$  ppm, Temp.  $=25^\circ$  C, particle size=4 mm)**

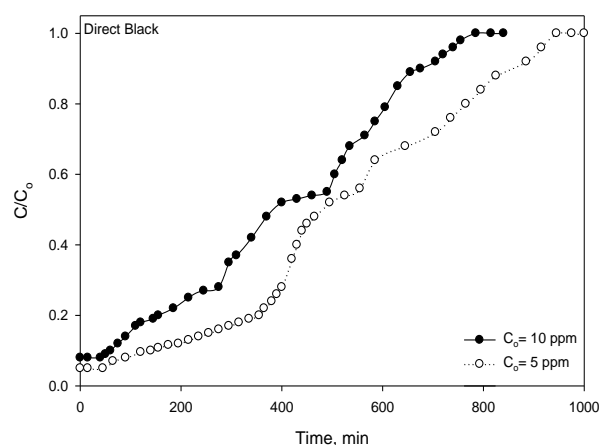


**Fig. 10: Experimental breakthrough curves for adsorption of direct black onto ODS at different initial concentration**

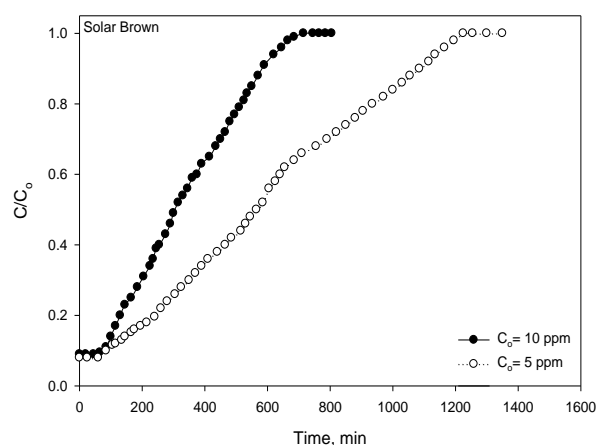


**Fig. 11: Experimental breakthrough curves for adsorption of solar brown onto ODS at different initial concentration**

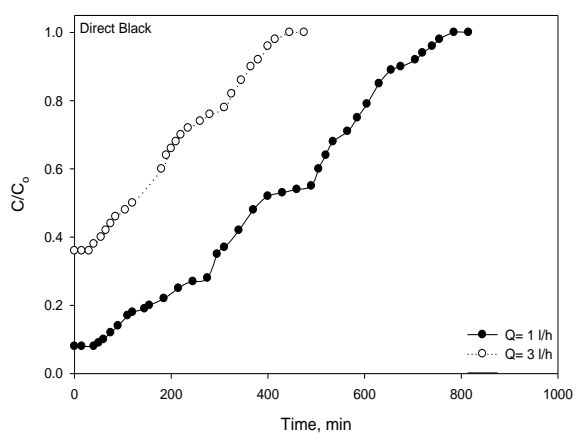


**Fig. 12: Experimental breakthrough curves for adsorption of direct black onto ODS at different flow rates**

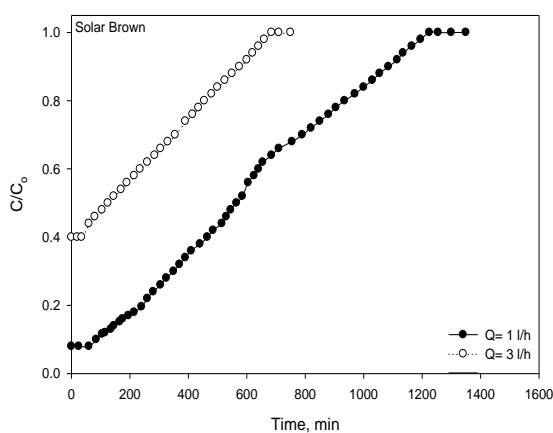


**Fig 13: Experimental breakthrough curves for adsorption of solar brown onto ODS at different flow rates**



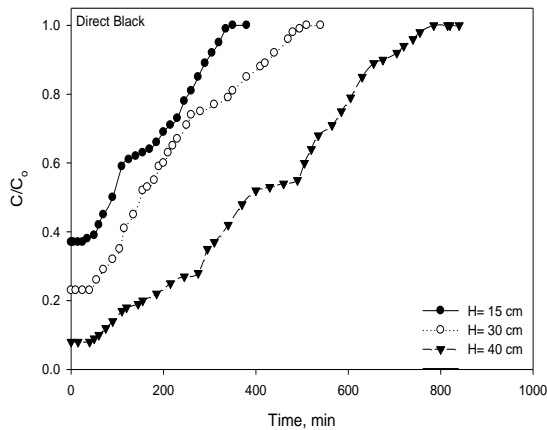


**Fig. 14: Experimental breakthrough curves for adsorption of direct black onto ODS at different bed depth**

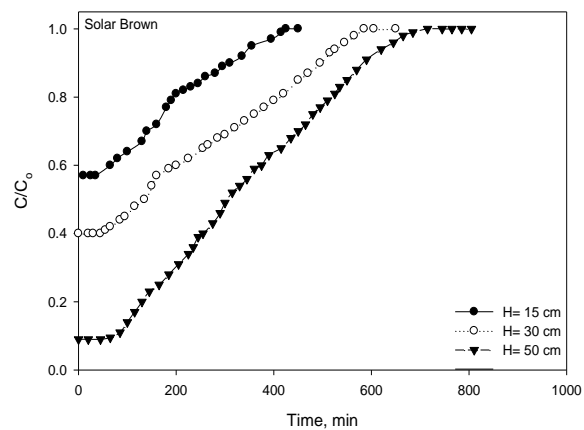


**Fig. 15: Experimental breakthrough curves for adsorption of solar brown onto ODS at different bed depth**

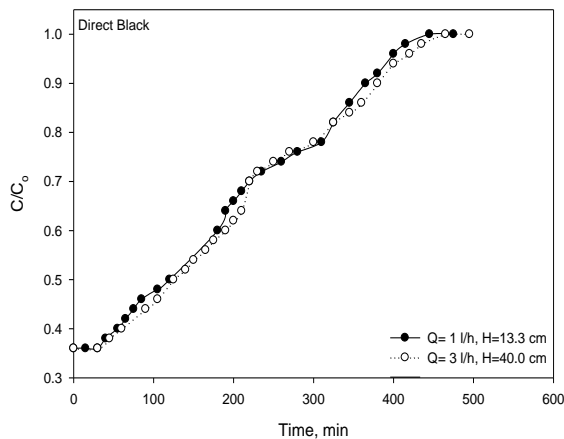


**Fig. 16: Experimental breakthrough curves for adsorption of direct black onto ODS at constant residence time**

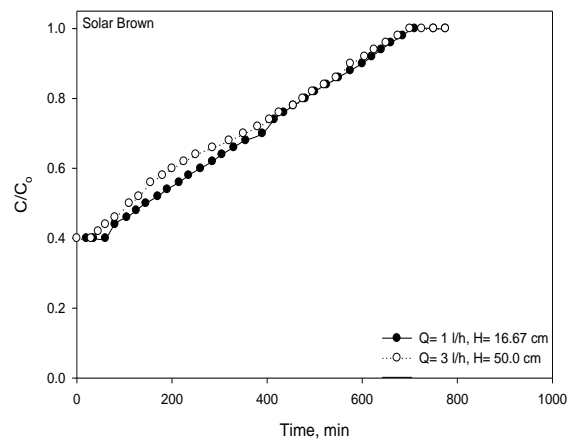


**Fig. 17: Experimental breakthrough curves for adsorption of solar brown onto ODS at constant residence time**

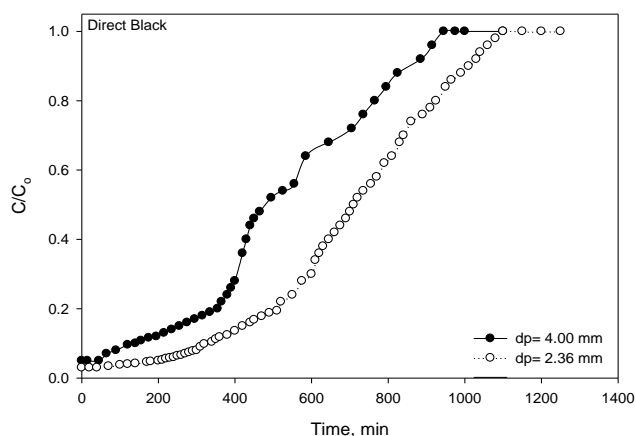


**Fig. 18: Experimental breakthrough curves for adsorption of direct black onto ODS at different particle size**

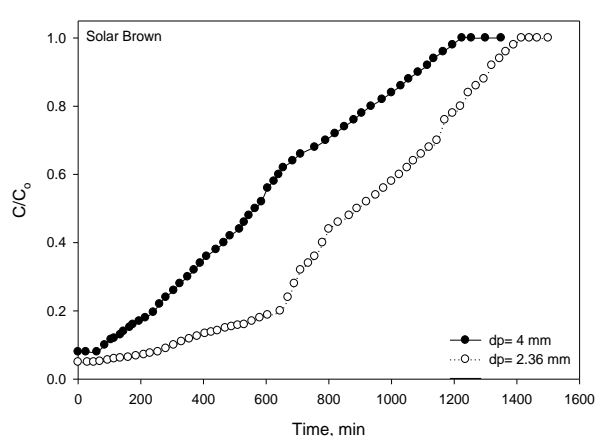


**Fig. 19: Experimental breakthrough curves for adsorption of solar brown onto ODS at different particle size**

**REFERENCES**

- Abbas H.B., 2005, "Removal of Dyes from Wastewater of Textile Industries Using Activated Carbon and Activated Alumina", M.Sc. Thesis, Chem. Eng. Dept., Collage of Eng., University of Baghdad.
- Chu, W., 2001, "Dye Removal from Textile Dye Wastewater Using Recycled Alum Sludge", Water Researches, 35(13), pp. 3147-3152.
- Galarneau, E. and Gehr, R., 1997, "Phosphorus Removal from Wastewaters: Experimental and Theoretical Support for Alternative Mechanisms", Water Research, 31 (2), pp 328-338.
- Ibtehal K.SH., 2002, "Study of Industrial Wastewater Treatment and Recycling Process For Cotton- Textile Industry", Ph.D. Thesis, Chem. Eng. Dept., Collage of Eng., University of Baghdad.
- Kim, J.G., Kim, J.H., Moon, H.S., Chon, C.M. and Ahn, J.S., 2003a, "Removal Capacity of Water Plant Alum Sludge for Phosphorus in Aqueous Solutions", Chemical Speciation and Bioavailability, 14, pp 67-73.
- Malkoc, E. and Nuhoglu, Y., 2006, "Fixed Bed Studies for the Sorption of Chromium (VI) onto Tea Factory Waste", Chemical Engineering Science, V.61, pp 4363-4372.
- Markovska, L. and Meshko, V., 2001, "Solid Diffusion Control of The Adsorption of Basic Dyes onto Granular Activated Carbon and Natural Zeolite in Fixed Bed Column", J. Serb. Chem. Soc., 66 (7), pp 463-475.
- Maruf Mortula, Meaghan Gibbons and Graham, A. Gagnon, 2006, "Phosphorus Adsorption by Naturally-Occurring Materials and Industrial by-Products", J. Environ. Eng. Sci., 6, pp 157-164.
- Sarmad A. R., 2009, "Phosphorous Removal from Wastewater using Alum", M.Sc. Thesis, Chem. Eng. Dept., Collage of Eng., University of Baghdad.
- Sips, R., 1984, Journal Of Chemical Physics, 16, pp 490-495.
- Weber, J. R. and Walter, J., 1972, "Physicochemical Processes for Water Quality Control", Wiley-Interscience, New York.
- Yakubu, M.K., Gumel M.S. and abdullahi A.M., 2008, "Use of activated carbon from date seeds to treat textile and tannery effluents", African Journal of science and technology (AJST), Science and Eng. Series, 9(1), pp.39-49.
- Yavuz, O. and Aydin, A.H., 2006, "Removal of Direct Dyes from Aqueous Solution using Various Adsorbents", Polish Journal of environmental studies, 15(1), pp.155-161.



## COUPLED VERTICAL – TORSIONAL AND LATERAL FREE VIBRATION OF THIN-WALLED CURVED BEAM

By

Shatha Dhia Al Khazraji  
College of Engineering  
University of Baghdad  
Baghdad-Iraq

### ABSTRACT

This study is concerned with the derivation of differential equation of motion for the free coupled vertical – torsional and lateral vibration of opened thin-walled curved beams. The curved beam to be considered in this study is of isotropic opened thin – walled (I) section with equal top and bottom flanges.

The derivation depends on Hamilton's principle which required finding the potential and kinetic energy of the curved beam section due to internal stresses and all types of movements (Vertical, Torsional and Lateral). The effect of restrained warping displacement is also considered in this study.

Three differential equations are derived for vertical, torsional and lateral movement. and approximate solutions are developed by using the method of multiple scale via a perturbation technique. The resulting natural frequencies and modes for vertical, torsional and lateral movements are compared with those calculated by using finite element approach ( STAAD Pro. 2007 ) and with the results other studies.

### الخلاصة :

تعنى هذه الدراسة باشتقاق المعادلة التفاضلية للاهتزازات الحرة بالاتجاه العمودي والالتوائي والأفقي ( Vertical, Torsional and Lateral ) للجسور المقوسة، وتختص هذه الدراسة بالجسور المقوسة التي تتكون من صفائح رقيقة تشكل مع بعضها بواسطة اللحام لتكون مقاطع مفتوحة بشكل الحرف (I).

اعتمد مبدأ هاملتون (Hamilton's principle) في اشتقاق المعادلات التفاضلية بصورة رئيسة وقد تطلب هذا احتساب الطاقة الكامنة والحركية المتولدة في مقطع الجسر المقوس نتيجة الاجهادات المتولدة فيه ونتيجة لجميع أنواع الحركة الناتجة عن الاهتزاز الحر، وقد أخذ بالاعتبار تأثير تقييد الحركة الالتوائية للمقطع (Warping Displacement) في هذه الدراسة.

توصل البحث الى اشتقاق ثلاث معادلات لاهتزازات الحرة بالاتجاه العمودي والالتوائي والأفقي وتم حل كل منها باستعمال طريقة ( Perturbation Technique ) و قورنت النتائج التي تم التوصل إليها (الترددات الطبيعية والأطوار) بمثيلاتها في دراسات أخرى.

**KEYWORD****Thin-walled curved beams, Free vibration, Differential Equation of Motion****INTRODUCTION**

Thin-walled beam represents an efficient case for most metal and some concrete structures. Wide development in modern structures, especially the needing for long span elements ( with reduced self weight) increases the applications of thin-walled beams in the design due to it's substantial flexural rigidity more over this type of structure should be carefully analyzed because it has low resistance for torsional deformation.

History of thin-walled beams started in 1961 when Vlasov <sup>(15)</sup>, derived the linear theory of thin-walled beam by a set of four ordinary differential equations, and was later employed by Timoshington, S.P., and Gere. S. M <sup>(14)</sup> to develop the theory of torsional and torsional-flexural instability.

Culver 1967<sup>(4)</sup>, studied the vibration of horizontally curved beams in a direction normal to the plane of curvature including the effecting of warping. The natural frequencies of prismatic and thin – walled opened sections were determined in this study. Rutenberg 1979<sup>(13)</sup>, evaluated the natural frequencies of curved thin – walled beams with opened cross sections using two simple hand calculation methods. In this study the effecting of shear deformation and flexural rotary inertia were neglected and only the vibrations which is normal to a plane of curvature were considered..

Yoo and Fehrenbach 1981<sup>(19)</sup>, determined the natural frequencies of thin – walled curved beams by using the means of variation procedure to formulate the stiffness relationship taking into consideration the effecting of warping contribution. Another study was represented by Yoo 1987<sup>(20)</sup>, in which mass matrix of order (12x12) was obtained for curved beam element. Warping contribution to torsional behavior has been assessed (in this study) according to the magnitude of a cross – sectional parameter ( $L^2 G J / E I_w$ ).

Simple closed form solution had been obtained by Roberts, T.M. 1987<sup>(12)</sup> for the lowest natural frequency of flexural, torsional and flexural-torsional vibration of strait thin-walled beams of opened cross sections. The beam in this study was under the effect of axial force and moment. The derivation depends on an assumption that the sum of potential and kinetic energy (V and KE, respectively) is constant.

Wekezer J.W. 1987<sup>(16)</sup>, used the finite element method to analyze thin-walled beams of variable opened cross sections. The finite element which is considered in this study is a special case of membrane shell with internal constants (Vlasov's and Wagner's assumptions).

In 1989, Wekezer J.W <sup>(17)</sup>, developed a general constant mass matrix for thin-walled curved beams of constant cross section for the case of small amplitude vibration. Finite elements process was used by more than one study (2,8,9) to determine the natural frequencies of curved beams. Ann N. A. 2002<sup>(1)</sup>, developed two and three dimensional curved beam elements with six and seven degree of freedom per node (the seventh degree of freedom was accomplished for the explicit inclusion of warping). Lumped and consistent process were used in this study to developed the mass matrix of order (12x12) and (14x14) (for both six and seven degree of freedom, respectively) .

Genshu Tong, Qiang Xu. 2002<sup>(7)</sup>, provided a detailed derivation of an exact theory for biaxial ending and torsion of thin-walled circularly curved beams with any open profile. The derivation is based on two well-accepted assumptions in the theory of thin-walled members. Exact expressions for longitudinal displacement, longitudinal normal stress and shear stress and their resultants are presented. Simplified theories are also given for practical applications.



Kim N. and Kim M. 2005<sup>(10)</sup>, presented a curved beam theory based on centroid-shear center formulation for the spatially coupled free vibration and elastic analysis. For this, the displacement field is expressed by introducing displacement parameters defined at the centroid and shear center axes. The elastic strain and kinetic energies considering the thickness-curvature effect and the rotary inertia of curved beam were rigorously derived by degenerating the energies of the elastic continuum to those of curved beam and then the equilibrium equations and the boundary conditions are consistently derived for curved beams having non-symmetric thin-walled cross section.

## BASIC ASSUMPTIONS

- The formulation of the curved beam elements is depend on basic assumptions which are <sup>(19)</sup> :
- The element is prismatic.
- The cross-section maintains its original shape.
- The deformations are small with respect to the dimensions of the cross-section (linearized problem).
- The material is homogeneous, isotropic and obeys Hooke's law.
- The cross-section dimensions are small in relation to the radius of the curvature.
- Shear deformation in the middle surface vanishes for solid and considered linear across the thickness for tubular sections (for curved beam element without warping ), and the position of the center may be considered solely as a geometric property.

## FORMULATION OF THE DIFFERENTIAL EQUATION OF FREE VIBRATION

In order to derive the differential equation of free vibration, Hamilton's principle <sup>(3)</sup> given in eq (1) will be used;

$$\int_{t_1}^{t_2} \delta(T - V)dt + \int_{t_1}^{t_2} \delta W_{nc} dt = 0 \quad (1)$$

For the case of free vibration, there is no directly applied dynamic load and the curved beam is assumed to have elastic damping ( $C=2\xi\omega m$ )<sup>(3)</sup>, thus there is no non- conservative force to be considered. Consequently, Hamilton's principle will take the form ( eq (2)):

$$\int_{t_1}^{t_2} \delta(T - V)dt = 0 \quad (2)$$

An element of ( dL) length will be considered to calculate the kinetic and potential energy that stored in the carved beam ( see **Fig 1** ) and method of integration over the whole length of the curved beam will be used to find the total energy ( Kinetic or Potential ) . The limits of integration were changed to be in term of ( $\theta$ ) in stead of (L) using the following equation:

$$dL = R d\phi \quad (3)$$

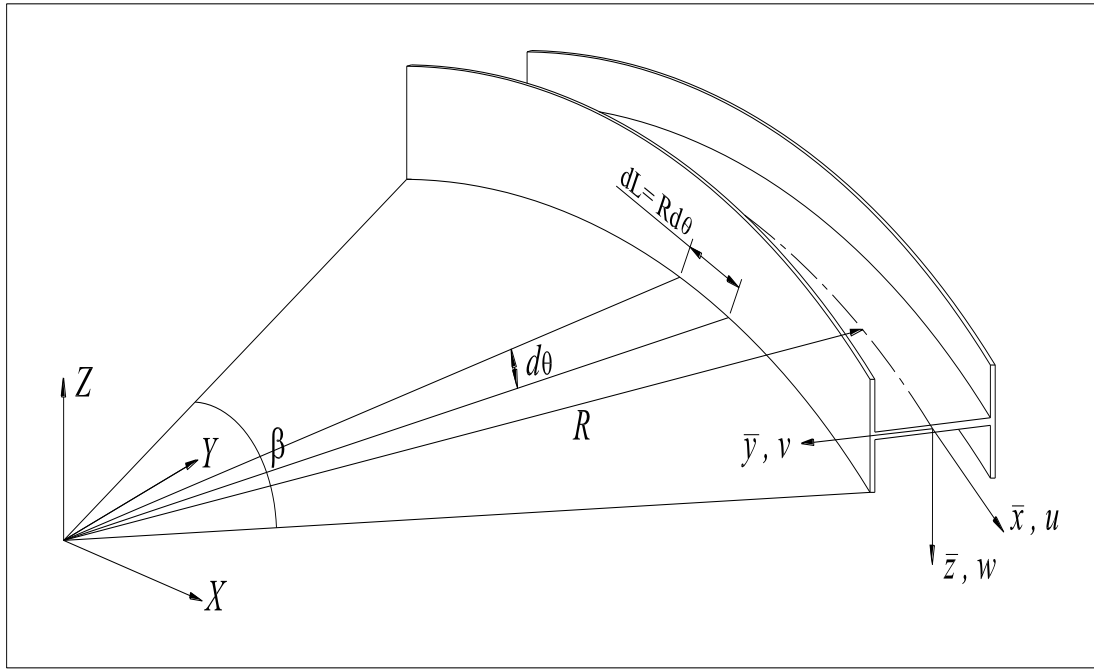


**Figure 1: Thin-walled curved Beam layout and Coordinates**

### Kinetic Energy Of Thin-Walled Curved Beam

The kinetic energy of any system is given by <sup>(3)</sup>;

$$\Pi = \frac{1}{2} \text{mass}(\text{velocity})^2 \quad (4)$$

where :

$\Pi = \text{Kinetic Energy}$

Using equation (4), kinetic energy (stored in thin-walled curved beam) produced in free vibration will be calculated and it will include:

a- Kinetic energy produced due to vertical movement.

$$T_1(t) = \frac{R}{2} \int_0^\beta m \left( \frac{\partial w}{\partial t} \right)^2 d\theta \quad (5)$$

b- Kinetic energy developed due to Lateral movement.

$$T_2(t) = \frac{R}{2} \int_0^\beta m \left( \frac{\partial v}{\partial t} \right)^2 d\theta \quad (6)$$

c- Kinetic energy produced due to rotation of the beam section.



$$T_3(t) = \frac{R}{2} \int_0^\beta I_p \left( \frac{\partial \phi}{\partial t} \right)^2 d\theta \quad (7)$$

Total Kinetic energy will be:

$$T = T_1 + T_2 + T_3 \quad (8a)$$

$$= \frac{R}{2} \int_0^\beta \left( m \left( \frac{\partial w}{\partial t} \right)^2 + m \left( \frac{\partial v}{\partial t} \right)^2 + I_p \left( \frac{\partial \phi}{\partial t} \right)^2 \right) d\theta \quad (8b)$$

### Potential Energy of Thin-Walled Curved Beam.

It's well known that the potential energy is calculating by multiplying the applied force by the corresponding displacement. This concept will be applied to calculate the potential energy that produced in the thin-walled curved beam.

The strain energy produced in the thin-walled curved beam of an ( I section ) can be divided to :

a- Strain energy stored in the right and left flange due to both normal and flexural stresses ( $\sigma_t, \sigma_f$ ) respectively (see **Fig 2a&c**)

$$V_1 = \frac{R}{2} \int_0^\beta \left( \frac{A_f}{E} (\sigma_t + \sigma_f)^2 + \frac{A_f}{E} (\sigma_t - \sigma_f)^2 \right) d\theta \quad (9a)$$

Or in terms of strain;

$$V_1 = \frac{1}{R} \int_0^\beta \left( A_f E \left( \frac{\partial u}{\partial \theta} \right)^2 + I_{fz} E \left( \frac{\partial w}{\partial \theta} \right)^2 \right) d\theta \quad (9b)$$

b- Strain energy stored in the web due to longitudinal direct stress ( $\sigma_t$ ) (see **Fig 2a**)

$$V_2 = \frac{R}{2} \int_0^\beta \frac{A_w}{E} \sigma_t^2 d\theta \quad (10a)$$

Or in terms of strain;

$$V_2 = \frac{1}{2R} \int_0^\beta E A_w \left( \frac{\partial u}{\partial \theta} \right)^2 d\theta \quad (10b)$$

c- Strain energy stored in the web and flanges due to shear stress ( $\tau_w, \tau_f$ ). ( see **Fig 2d**)

$$V_3 = \frac{R}{2} \int_0^\beta \left( \frac{A_w}{G} \tau_w^2 + \frac{2A_f}{G} \tau_f^2 \right) d\theta \quad (11a)$$

Or in terms of strain;

$$V_3 = \frac{RG}{2} \int_0^\beta \left( A_w \gamma_w^2 + 2A_f \gamma_f^2 \right) d\theta \quad (11b)$$

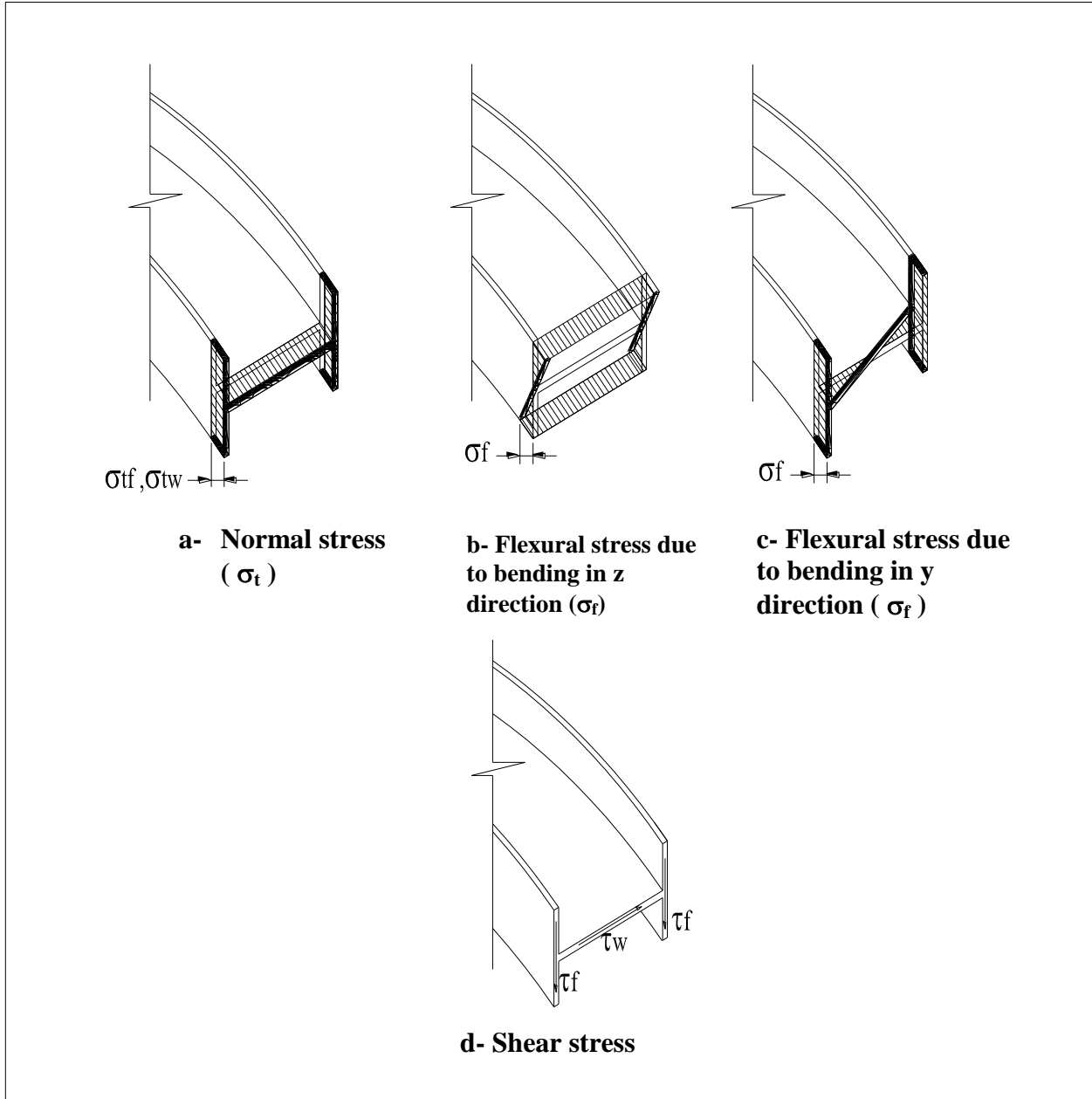


**Figure 2 : Types of stress produced in curved thin-walled beam**

Examining the estimated movements (vertical, longitudinal, lateral and torsional) for the section of thin-walled curved beam (Fig 3), shear strain for the flange and web can be written as;



$$\gamma_f = \frac{1}{R} \frac{\partial w}{\partial \theta} + \frac{b_f}{2R} \frac{\partial \phi}{\partial \theta} - \frac{2u}{b_f} \quad (12a)$$

$$\gamma_w = \frac{1}{R} \frac{\partial v}{\partial \theta} + \frac{d_w}{2R} \frac{\partial \phi}{\partial \theta} \quad (12b)$$

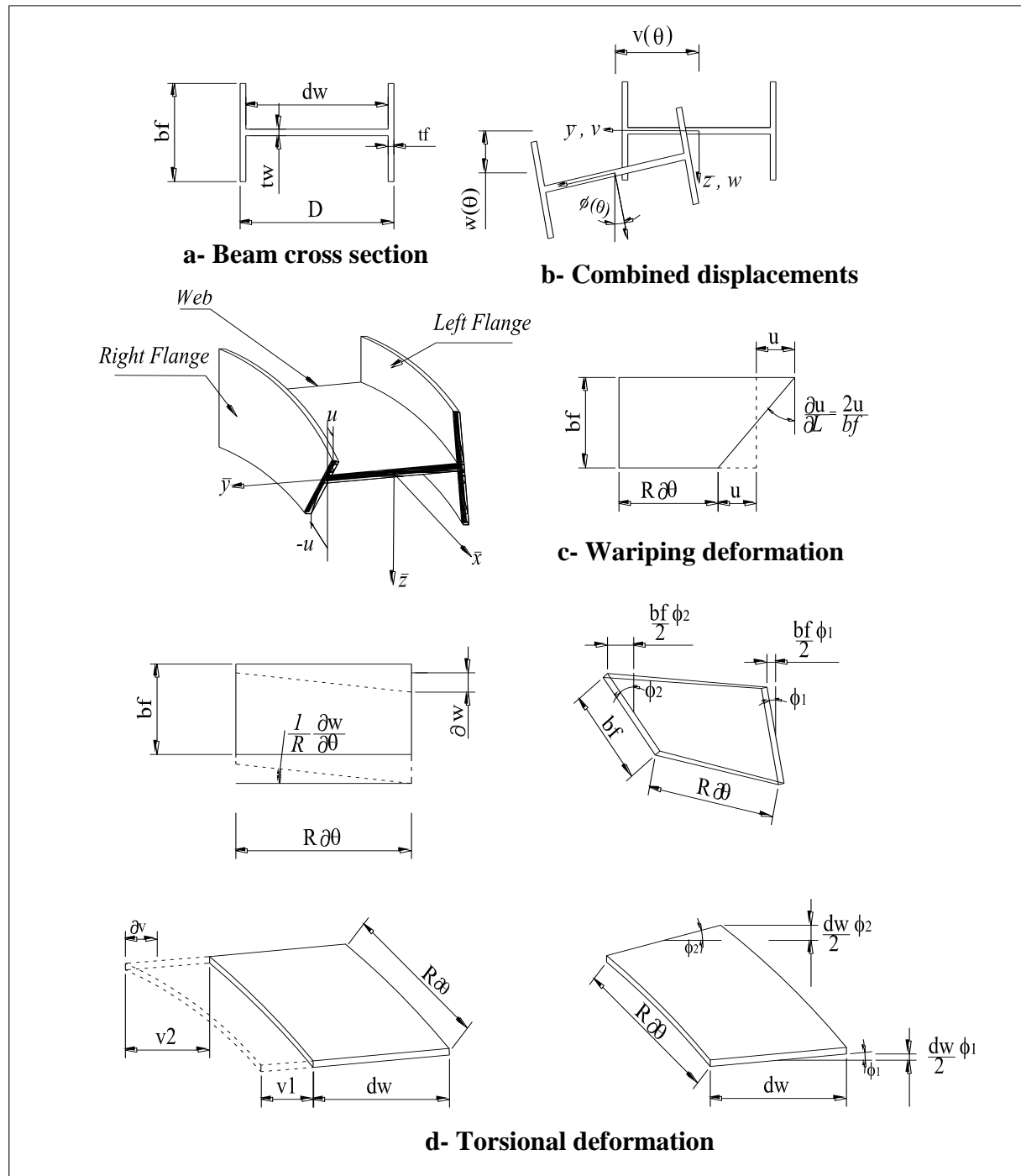


Figure 3 : Types of deformation in thin-walled curved beam

Substituted ( Eq. 12 ) into ( Eq. 11) and making the suitable simplification , (V<sub>3</sub>) can be written as;

$$V_3 = \frac{RG}{2} \int_0^\beta \left( \frac{A_w}{R^2} \left[ \left( \frac{\partial v}{\partial \theta} \right)^2 + d_w \left( \frac{\partial \phi}{\partial \theta} \right)^2 + \frac{d_w}{2} \left( \frac{\partial v}{\partial \theta} \right) \left( \frac{\partial \phi}{\partial \theta} \right) \right] + \frac{2A_f}{R^2} \left[ \left( \frac{\partial w}{\partial \theta} \right)^2 + \frac{b_f^2}{4} \left( \frac{\partial \phi}{\partial \theta} \right)^2 + \frac{4u^2}{b_f^2} + b_f \left( \frac{\partial w}{\partial \theta} \right) \left( \frac{\partial \phi}{\partial \theta} \right) + \frac{4Ru}{b_f} \left( \frac{\partial w}{\partial \theta} \right) + 2Ru \left( \frac{\partial \phi}{\partial \theta} \right) \right] \right) d\theta \quad (13)$$

In order to replace all terms of (u) by an equivalent expression (in term of v,w and φ ), the following relationships will be depends:

Using Hooke's law <sup>(6)</sup>, the shear strain for the web (γ<sub>w</sub>, γ<sub>f</sub>) can be defined as;

$$\gamma_w = \frac{\tau_w}{G} = \frac{F_y}{GA_w} \quad (14a)$$

and

$$\gamma_f = \frac{\tau_f}{G} = \frac{F_z}{2GA_f} \quad (14b)$$

References (5,17,19) mentioned the relationship between internal force and the displacements at a point on the middle surface of the member ( see **Fig 4**);

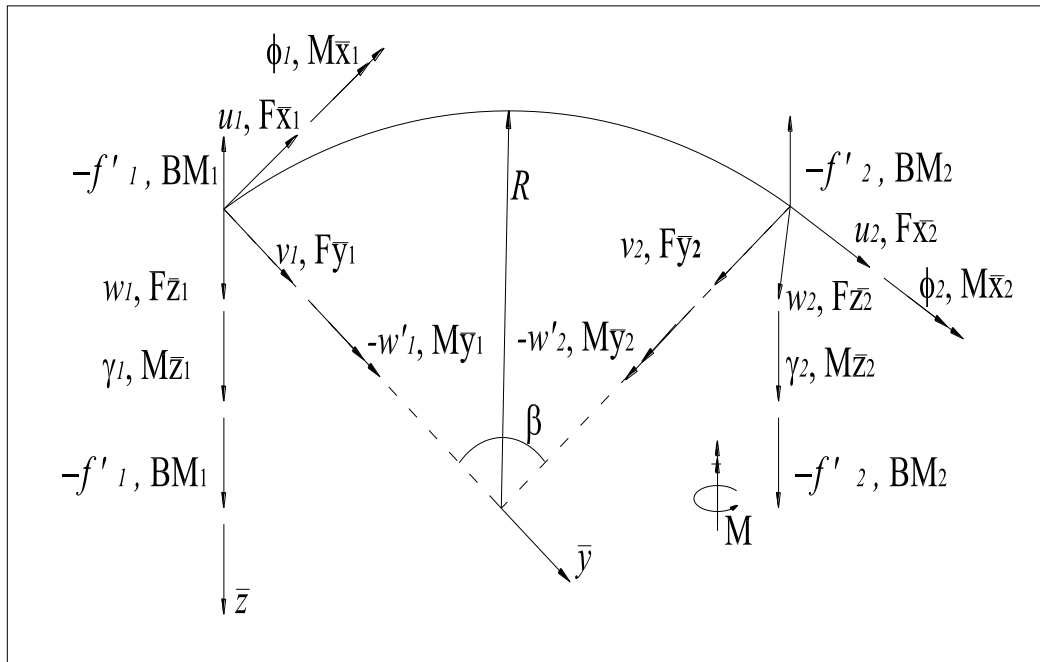


**Figure 4 : Generalized forces and displacements for curved beams with warping<sup>(1)</sup>**



$$F_z = -M_y' + \frac{M_x'}{R} \quad (15a)$$

and

$$F_y = -M_z' \quad (15b)$$

where

$$M_y = EI_y \left( \frac{\partial^2 w}{\partial \theta^2} + \frac{\phi}{R^2} \right) \quad (16a)$$

$$M_z = EI_z \left( \frac{\partial^2 v}{\partial \theta^2} + \frac{v}{R^2} \right) \quad (16b)$$

$$M_x = GJ \left( \frac{\partial \phi}{\partial \theta} + \frac{1}{R} \frac{\partial w}{\partial \theta} \right) \quad (16c)$$

Substituted ( Eq. 15 ) into ( Eq. 14 ) and making the suitable simplification , (  $\gamma_w, \gamma_f$  ) can be written as;

$$\gamma_f = \frac{\partial \phi}{\partial \theta} \left( \frac{J}{2RA_f} - \frac{EI_y}{2GRA_f} \right) + \frac{J}{2R^2 A_f} \frac{\partial w}{\partial \theta} - \frac{EI_y}{2GA_f} \frac{\partial^3 w}{\partial \theta^3} \quad (17a)$$

and

$$\gamma_w = \frac{EI_z}{2GA_f} \left( \frac{\partial^3 v}{\partial \theta^3} + \frac{1}{R^2} \frac{\partial v}{\partial \theta} \right) \quad (17b)$$

Substituted value of ( Eq. 18a ) into ( Eq. 13a ) , the value of the warping displacement can get as;

$$u = b_f \left[ \frac{\partial \phi}{\partial \theta} \left( \frac{J}{4RA_f} - \frac{EI_y}{4GRA_f} - \frac{b_w}{4R} \right) + \frac{\partial w}{\partial \theta} \left( \frac{J}{4R^2 A_f} - \frac{1}{R} \right) - \frac{EI_y}{4GA_f} \frac{\partial^3 w}{\partial \theta^3} \right] \quad (18a)$$

$$= b_f \left[ K_1 \frac{\partial \phi}{\partial \theta} + K_2 \frac{\partial w}{\partial \theta} - K_3 \frac{\partial^3 w}{\partial \theta^3} \right] \quad (18b)$$

where

$$K_1 = \left( \frac{J}{4RA_f} - \frac{EI_y}{4GRA_f} - \frac{b_w}{4R} \right) \quad (19a)$$

$$K_2 = \left( \frac{J}{4R^2 A_f} - \frac{1}{R} \right) \quad (19b)$$

$$K_3 = \frac{EI_y}{4GA_f} \quad (19c)$$

and

$$\frac{\partial u}{\partial \theta} = b_f \left[ K_1 \frac{\partial^2 \phi}{\partial \theta^2} + K_2 \frac{\partial^2 w}{\partial \theta^2} - K_3 \frac{\partial^4 w}{\partial \theta^4} \right] \quad (20)$$

Using the expression of warping displacement (Eq.18), the strain energy (  $V_1, V_2, V_3$  and  $V_4$  ) can be simplified to be in terms of (  $w, v$  and  $\phi$  ) as shown below .

$$V_1 = \frac{1}{R} \int_0^\beta [EA_f b_f^2 (K_1^2 (\frac{\partial^2 \phi}{\partial \theta^2})^2 + K_2^2 (\frac{\partial^2 w}{\partial \theta^2})^2 + K_3^2 (\frac{\partial^4 w}{\partial \theta^4})^2 + 2K_1 K_2 (\frac{\partial^2 \phi}{\partial \theta^2} \frac{\partial^2 w}{\partial \theta^2}) - 2K_1 K_3 (\frac{\partial^2 \phi}{\partial \theta^2} \frac{\partial^4 w}{\partial \theta^4} - 2K_3 K_2 (\frac{\partial^2 w}{\partial \theta^2} \frac{\partial^4 w}{\partial \theta^4})) + (EA_f b_f^2 K_2^2 + I_f E) (\frac{\partial w}{\partial \theta})^2] d\theta \quad (21)$$

$$V_2 = \frac{EA_w b_f^2}{2R} \int_0^\beta \left[ K_1^2 (\frac{\partial^2 \phi}{\partial \theta^2})^2 + K_2^2 (\frac{\partial^2 w}{\partial \theta^2})^2 + K_3^2 (\frac{\partial^4 w}{\partial \theta^4})^2 + 2K_1 K_2 (\frac{\partial^2 \phi}{\partial \theta^2} \frac{\partial^2 w}{\partial \theta^2}) - 2K_1 K_3 (\frac{\partial^2 \phi}{\partial \theta^2} \frac{\partial^4 w}{\partial \theta^4} - 2K_3 K_2 (\frac{\partial^2 w}{\partial \theta^2} \frac{\partial^4 w}{\partial \theta^4})) \right] d\theta \quad (22)$$

$$V_3 = \frac{GA_w}{2R} \int_0^\beta \left[ \left( \frac{\partial v}{\partial \theta} \right)^2 + d_w \left( \frac{\partial \phi}{\partial \theta} \right)^2 + \frac{d_w}{2} \left( \frac{\partial v}{\partial \theta} \right) \left( \frac{\partial \phi}{\partial \theta} \right) \right] d\theta \quad (23)$$

$$V_4 = \frac{A_f G}{R} \int_0^\beta \left[ \left( \frac{\partial w}{\partial \theta} \right)^2 + \frac{b_f^2}{4} \left( \frac{\partial \phi}{\partial \theta} \right)^2 + 4 \left[ K_1^2 \left( \frac{\partial \phi}{\partial \theta} \right)^2 + K_2^2 \left( \frac{\partial w}{\partial \theta} \right)^2 + K_3^2 \left( \frac{\partial^3 w}{\partial \theta^3} \right)^2 + 2K_1 K_2 \left( \frac{\partial \phi}{\partial \theta} \frac{\partial w}{\partial \theta} \right) - 2K_1 K_3 \left( \frac{\partial \phi}{\partial \theta} \frac{\partial^3 w}{\partial \theta^3} \right) - 2K_2 K_3 \left( \frac{\partial w}{\partial \theta} \frac{\partial^3 w}{\partial \theta^3} \right) + b_f \left( \frac{\partial w}{\partial \theta} \right) \left( \frac{\partial \phi}{\partial \theta} \right) + b_f \left( \frac{4R}{b_f} \frac{\partial w}{\partial \theta} + 2R \frac{\partial \phi}{\partial \theta} \right) \left( K_1 \frac{\partial \phi}{\partial \theta} + K_2 \frac{\partial w}{\partial \theta} - K_3 \frac{\partial^3 w}{\partial \theta^3} \right) \right] d\theta \quad (24)$$

The total Potential energy will be:

$$V = V_1 + V_2 + V_3 + V_4 \quad (25)$$

Applying Hamilton's principle and use it's role (The value of  $\delta v$ ,  $\delta w$  and  $\delta \phi$  are vanish at the limit of integration  $t_1$  and  $t_2$  ), the three equations of motion will be ( method of integration by parts are used to simplified the equations and all terms of higher derivatives than four were neglected in the final result ):

### Vertical Vibration:

$$-\frac{\partial^4 w}{\partial \theta^4} \left[ (Eb_f^2 K_2^2) \left( A_f + \frac{A_w}{2} \right) - 4GA_f K_3 (4K_2 + R) \right] + \frac{\partial^2 w}{\partial \theta^2} \left( EA_f b_f^2 K_2^2 + EI_f + GA_f + 4K_2^2 GA_f + \frac{4RGA_f K_2}{b_f} \right) - \frac{\partial^4 \phi}{\partial \theta^4} (Eb_f^2 K_1 K_2 A) + \frac{\partial^2 \phi}{\partial \theta^2} (8K_1 K_2 GA_f + GA_f b_f + 4RK_1 GA_f + 2RK_2 b_f GA_f) - m \frac{\partial^2 w}{\partial t^2} = 0 \quad (26a)$$

### Lateral Vibration:

$$\frac{\partial^2 v}{\partial \theta^2} \left( \frac{GA_w}{2} \right) + \frac{\partial^2 \phi}{\partial \theta^2} \left( \frac{GA_w d_w}{4} \right) - m \frac{\partial^2 v}{\partial t^2} = 0 \quad (26b)$$

### Torsional Vibration:

$$-\frac{\partial^4 \phi}{\partial \theta^4} (Eb_f^2 K_1^2) \left( A_f + \frac{A_w}{2} \right) + \frac{\partial^2 \phi}{\partial \theta^2} \left( \frac{GA_w d_w}{2} + \frac{GA_f b_f^2}{4} + 4GA_f K_1^2 + 2GA_f RK_1 \right) - \frac{\partial^4 w}{\partial \theta^4} (Eb_f^2 K_1 K_2 A + 8K_1 K_3 GA_f + 2RK_3 b_f A_f G) + \frac{\partial^2 w}{\partial \theta^2} (8K_1 K_2 GA_f + GA_f b_f + 4RK_1 GA_f + 2RK_2 b_f GA_f) + \frac{\partial^2 v}{\partial \theta^2} \left( \frac{GA_w d_w}{4} \right) - I_p \frac{\partial^2 \phi}{\partial t^2} = 0 \quad (26c)$$

## PERTURBATION TECHNIQUE

The three derived differential equation of motion ( Eqs. 26 ) are solved analytically by expansion the solution to be in term of the normal modes of the linearized problem and using the perturbation technique ( multiple scale method )<sup>(11)</sup> according to the following steps:

- 1- Assume the expression of the vertical, lateral and torsional displacement ( w,v and  $\phi$  ) to be:

$$\begin{aligned} w(x,t) &= \sum_{m=1}^{\infty} \Phi_{wm}(x) Z_{wm}(t) \\ v(x,t) &= \sum_{m=1}^{\infty} \Phi_{vm}(x) Z_{vm}(t) \\ \phi(x,t) &= \sum_{m=1}^{\infty} \Phi_{\phi m}(x) Z_{\phi m}(t) \end{aligned} \quad (27)$$

Where  $\Phi_{wm}(x)$ ,  $\Phi_{vm}(x)$  and  $\Phi_{\phi m}(x)$  are the linear undamped natural vertical, lateral and torsional mth modes, respectively.

- 2- Substituting the assumed expressing of the three displacement into ( Eqs. 26 ) , multiplying by (  $w_n, v_m$  and  $\phi_o$  ) and using the orthogonality properties of the linear mode, three coupled

system of N-coupled second order ordinary differential equation for  $Z_{vn}$ ,  $Z_{wm}$  and  $Z_{\theta o}$  will be obtained.

3- Mode by mode analysis will be used to solve the differential equation.

### CASE STUDY :

The three derived differential equation of motion ( Eqs. 26 ) are solved using perturbation technique ,the results ( natural frequencies and modes ) of the present study was compared with those calculated by Ann N. A. 2002<sup>(1)</sup>, the geometry and material property of the case study will be the same of one used in problem 3 of Ref (1) ( see **Fig 5** and **Table 1 & 2** ) .

**Table 1 : Geometric properties of the study case**

Sectional Property	
$b_f = 1.00 \text{ m}$	$A_w = 0.05 \text{ m}^2$
$d_w = 1.45 \text{ m}$	$J = 1.4583333\text{E-}4 \text{ m}^4$
$t_w = t_f = 0.05 \text{ m}$	$I_y = 8.3489583\text{E-}3 \text{ m}^4$
$A = 0.175 \text{ m}^2$	$I_z = 7.033333\text{E-}2 \text{ m}^4$
$A_f = 0.0725 \text{ m}^2$	$R = 25.00 \text{ m}$

**Table 2 : Material properties of the study case**

Material Property
$E = 200000 \text{ Mpa}$
$G = 200 \text{ Mpa}$
$m = 7834.6 \text{ kg/m}^2$



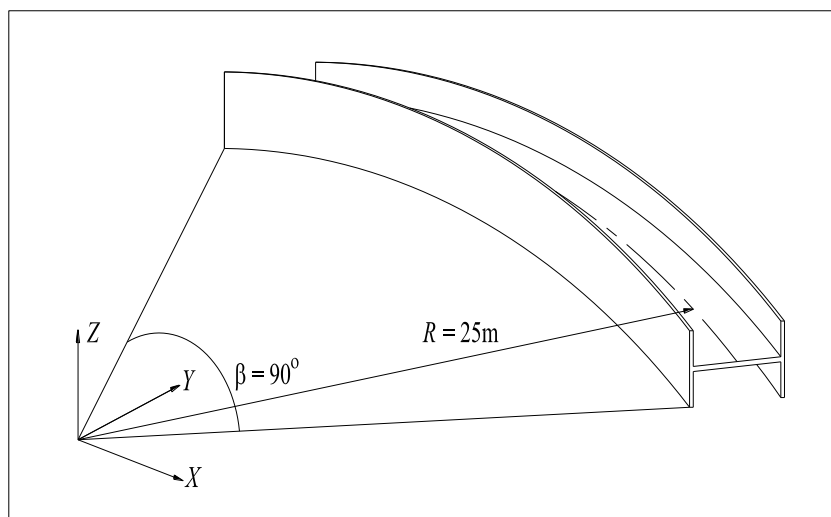
Table 3 : Natural frequency of the study case

Mode		Cyclie Frequency ( Hz )			
Type	No.	STAAD Pro. F.E.	Study present in Ref (1)		Present study
			Lumped mass	Consistent mass	
FY	1	1.984	2.015906	1.998710	1.8851
FY & T	2	5.107	5.543756	5.273648	5.082
FY & T	3	9.558	11.850720	10.820084	9.483
FY & T	4	10.574	--	11.583677	10.324
FY & T	5	13.129	--	14.379131	13.100
FZ	1	17.055	18.215634	18.302639	17.104
FZ	2	24.368	25.096167	25.275968	24.233

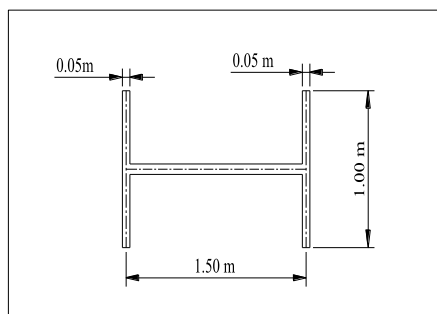
FY: Flexural mode in Y- direction .  
 T : Torsional mode .  
 FZ : Flexural mode in Z- direction .

Table 4 : Percentage of difference between the presented study and other theories

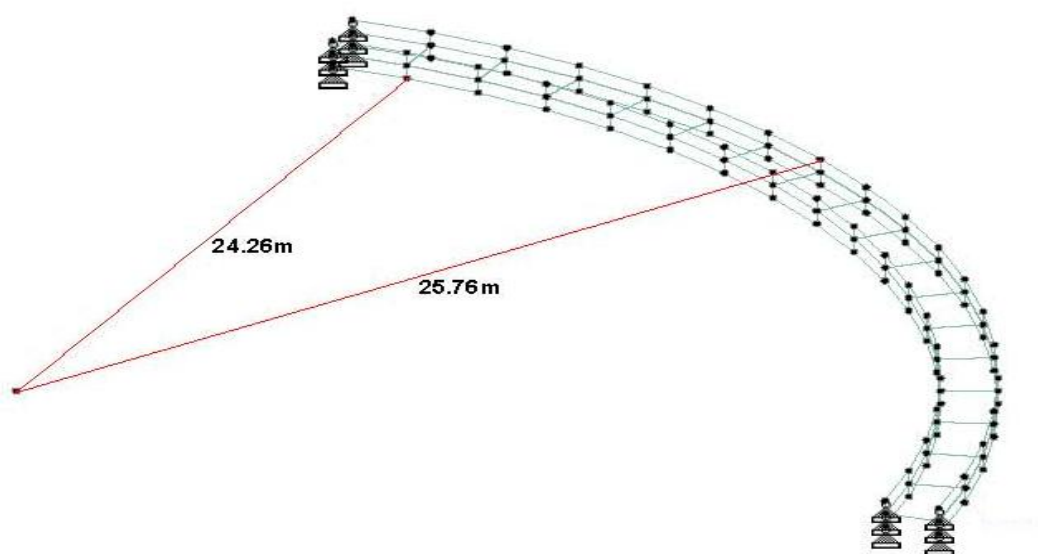
Mode		Percentage of difference		
Type	No.	STAAD Pro. F.E.	Study present in Ref (1)	
			Lumped mass	Consistent mass
FY	1	5.25	6.49	5.68
FY & T	2	0.49	8.33	3.63
FY & T	3	0.79	19.98	12.36
FY & T	4	2.42	---	10.87
FY & T	5	0.22	---	8.90
FZ	1	0.29	6.10	6.55
FZ	2	0.56	3.44	4.13



a- Layout of curved beam



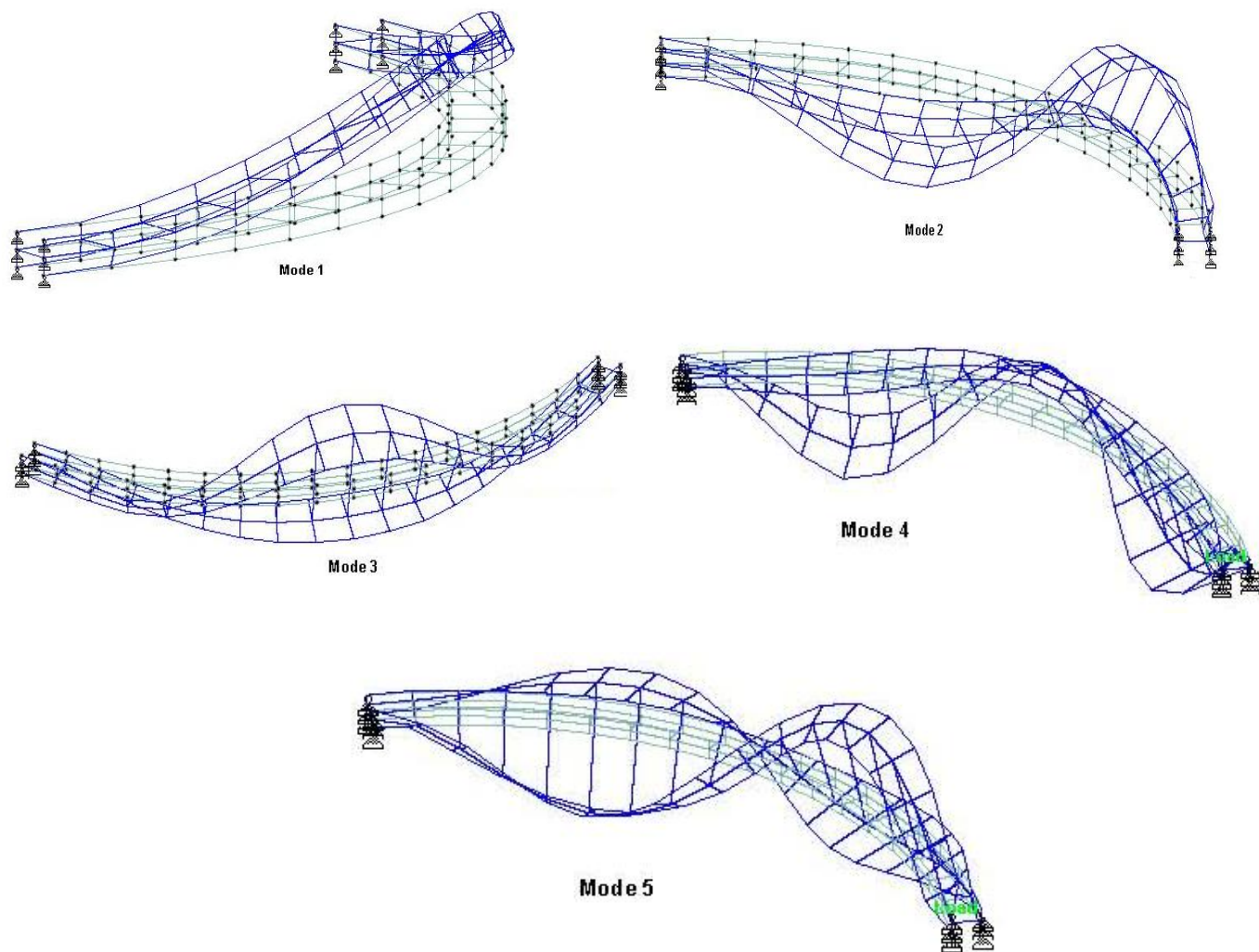
b- Cross section dimensions



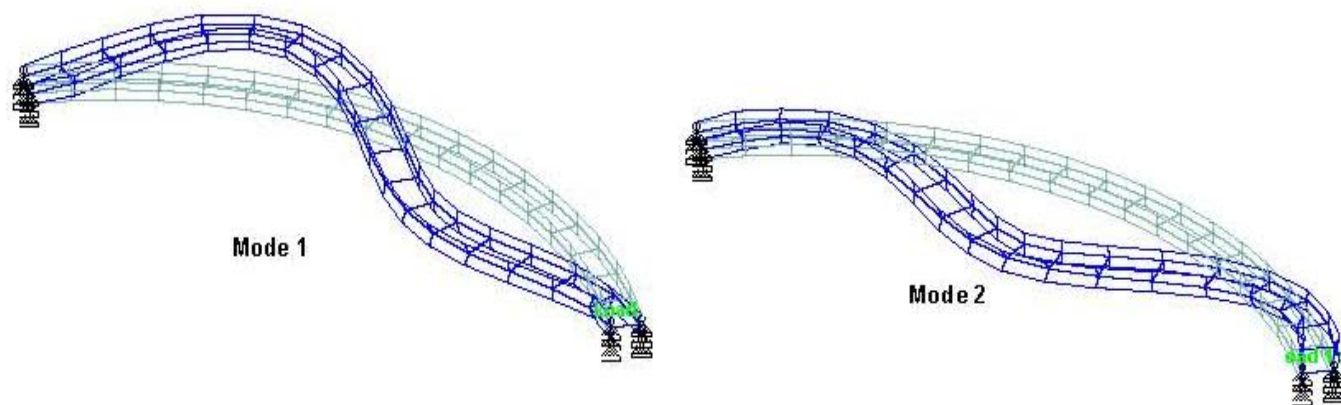
c – Finite element mesh

**Figure 5: Case study No.1 of curved thin walled beam**





**a- Flexural and Torsional modes of out- of- plane action**



**b- Flexural modes of in- plane action**

**Figure 6 : Mode shapes of the study case**

## CONCLOSIONS

In the present study, the differential equations of motion (D.E.O.M) for combined vertical, torsional and lateral vibration of thin-walled curved beam are derived and solved. The calculated natural frequencies are compared with those calculated by the finite element approach (STAAD Pro. 2007) and with the results of the estimating element developed by Ann N. A. 2002<sup>(1)</sup>.

Based on the result obtained from different case study that considered to study the effecting of different parameters on the natural frequencies, this study arrives with the following objectives and conclusion:

### - Effecting of shear deformation:

The values of natural frequencies which obtained from the present study ( Table 3) are differ from those obtained by an estimating element developed by Ann N. A. 2002<sup>(1)</sup> due to the effecting of shear deformation which is included in the present study while its ignored in the estimating element<sup>(1)</sup>. It's also clear that the effect of shear deformation can be neglected in deep thin – walled beam element

### - Effecting of flange's width on the natural frequency :

The width of the flange has a direct and inverse effect on the value of the natural frequency for both vertical and lateral vibration respectively (see Fig 7 and 8) .Figure (7) shows the effect of the flange width on the frequency of vertical vibration and its seem that the relation is a direct relation, while figure (8) shows the effecting of the same parameter on the frequency of the lateral vibration. The previous conclusion is due to the influence of the flange width on the inertia of the curved beam in both vertical and lateral direction.

### - Effecting of the web's width on the natural frequency :

This study detects an effecting for the web width on the vertical frequency differs from the one produced by the flange width (see Fig 9). The relationship between the web width and the vertical frequency can be divided into two parts, the first part (value of  $b_w/b_f$  approximately less than 60% ) shows that  $b_w$  effects on the value of the vertical frequency directly , while the effecting will be inversely for the other value of  $b_w/b_f$  .  $b_w$  has also a direct action on the frequency of the lateral vibration ( see Fig 10).

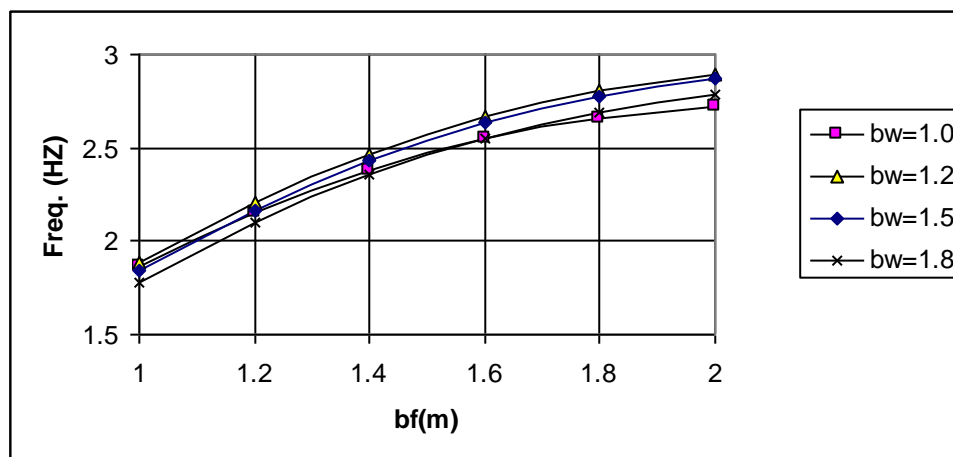


Figure 7 : Effects of  $b_f$  on the natural frequency of vertical vibration

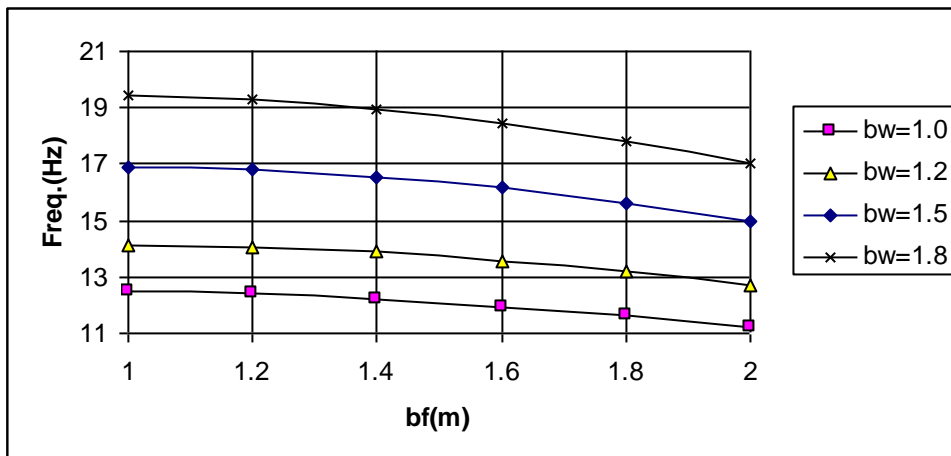


Figure 8 : Effects of  $b_f$  on the natural frequency of lateral vibration

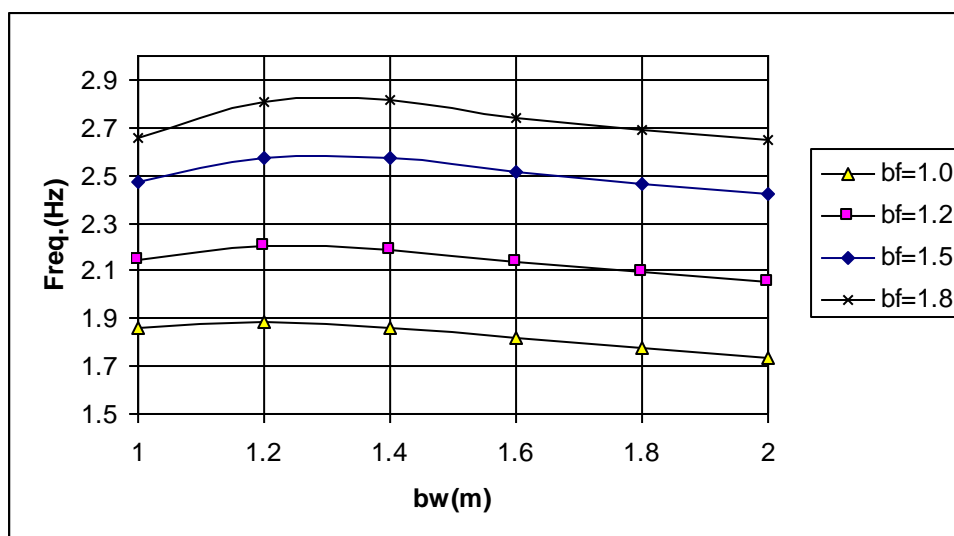


Figure 9 : Effects of  $b_w$  on the natural frequency of vertical vibration

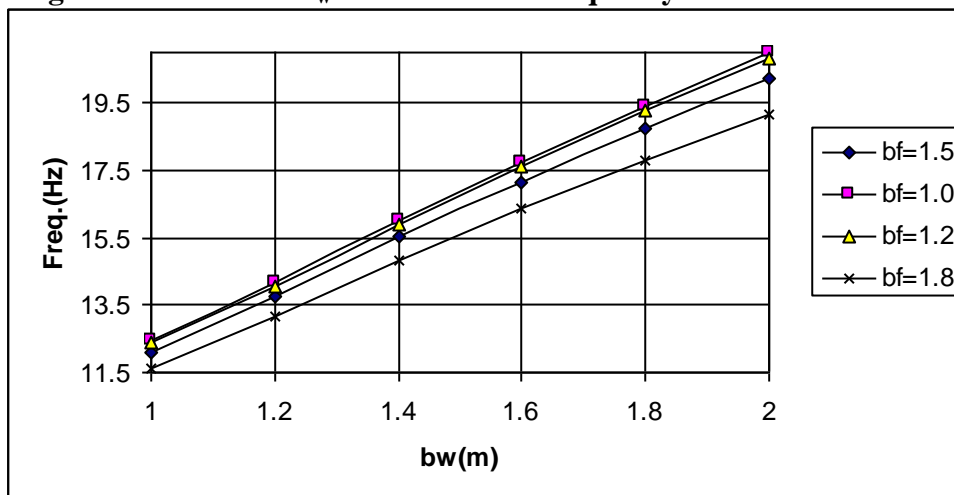


Figure 10 : Effects of  $b_w$  on the natural frequency of lateral vibration

**REFERENCES**

- Ann, N. A., " Earthquake Response Analysis of Large Diameter Circular Steel Ribbed Dome " M. Sc. Thesis, Department of Civil Engineering, University of Baghdad, Iraq, 2002.
- Archer, R.R. , " Small Vibration of Thin Incomplete Cellular Rings " , International Journal of Mechanical Science , Vol .1, pp. 45-56, 1960.
- Clough, R.W., and Penzin, J., " Dynamic of Structures " , McGraw-Hill, Lnc. , 1975.
- Culver, C. G., "Natural Frequencies of Horizontally Curved Beams", Journal of Structural Division, ASCE, Vol. 93, No. ST2, pp. 189-203, 1967.
- Dabrowski, R., "Curved Thin-Walled Girders", Cement and Concrete Association, London, England Translation No. 144, 1968.
- Ferdinand L. Singer & Andrew Pytel, " Strength of Materials " ,Third Addition 1983
- Genshu Tong, Qiang Xu, " An Exact Theory for Curved Beams with Any Thin-walled Open Sections",Advances in Structural Engineering, Vol. 5, No. 4 , pp 195-209, 2002.
- Haitham, H. M. , " Liner and Non- Linear Static and Free Vvibration Analysis of Thin-Walled Cellular and Ribbed Spherical Domes by Spherical Grillage Analysis " , P. HD. Thesis, Department of Civil Engineering, University of Baghdad, Iraq, 2000.
- Husain, H.M., Alrajihi, A.A., and Aldami, H.H. ."Natural Frequencies of multi span bridge with thin-walled curve bridge " , The Scientific Journal of Tkrit University, Engineering Science section ,Vol.7, No. 1, April, pp. 31-44,2000.
- Kim Nam and Kim Moon-Young , Journal of Mechanical Science and Technology Vol. 19, No 2 , February, pp 589-604, 2005
- Nayfeh, A.H. and Mook, D. T., " Nonlinear Oscillation " , Johan Wiley and Sons Inc., New York, N. Y. , 1979.
- Roberts, T.M. "Free vibration of thin walled bar",Jornal of .Engineering Mechanics., ASCE,Vol..113,No.110, pp 1584-1593, 1987.
- Rutenberg, A., "Vibration Properties Of Curved Thin – Walled Beams " Journal of Structural Division, ASCE, Vol. 105, No. ST7, pp.1445 – 1455,1979.
- Timoshington, S.P., and Gere. S. M., " Theory of Elastic Stability" , 2<sup>nd</sup> ed., Mc Graw-Hill, Book Co., New York, N.Y., 1961.
- Vlasov,V.Z., "Thin- Walled Elastic Beam" , National Science Foundatiom, 1961.



- Wekezer J. W., "Free vibration of thin walled bar", Journal of Engineering Mechanics., ASCE, Vol. 113, No. 110, pp 1441-1453, 1987.
- Wekezer J. W., "Vibrational Analysis of Thin-walled bar with open cross section", Journal of Engineering Mechanics., ASCE, Vol. 113, No. 110, pp 1441-1453, 1989.
- Yoo, C.H., "Matrix Formulation of Curved Girder", Journal of Structural Division. ASCE, Vol. 105, No. EM6, pp 971-988, 1979.
- Yoo, C.H., and Fehrenbach, J.P., "Natural Frequencies of Curved Girders", Journal of Engineering Mechanics Division, ASCE, Vol. 107, No. EM2, PP. 339-354, 1981.
- Yoo, C.H., "A Consistent Discrete Elements Technique For Curved Members", Computer & Structure, Vol. 25, No. 1, pp. 137-146, 1987

## LIST OF SAMBOLS

$A_f$	Cross sectional area of the right or left flange.
$A_w$	Cross sectional area of the web.
$b_f$	Width of the flange.
$D$	Total depth of the thin-walled curved beam.
$d_w$	Total depth of the web
$E$	Modulus of elasticity.
$G$	Shear Modulus of elasticity.
$I_{f\bar{z}}$	Second moment of inertia of the right or left flange about $\bar{z}$ axes.
$I_p$	Mass polar moment of inertia.
$I_{\bar{y}}$	Second moment of inertia about $\bar{y}$ axes.
$I_{\bar{z}}$	Second moment of inertia about $\bar{z}$ axes.
$J$	St. Venant's torsional constant.
$m$	Mass per unit length.
$R$	Radius of curvature .
$t_f$	Thickness of the of the right or left flange.
$t_w$	Thickness of the web.
$T$	Total kinetic energy.
$u, w, v$	Displacements in direction of $\bar{x}, \bar{z}$ and $\bar{y}$ axes, respectively.
$\bar{x}, \bar{z}, \bar{y}$	Local curvilinear coordinate.
$X, Y, Z$	Global coordinate.
$V$	Potential energy.
$W_{nc}$	Non-Conservative work.
$\beta$	Angle of curvature for the thin-walled curved beam.
$\phi$	Angle of twist.
$\sigma_t$	Direct longitudinal stress.

$\sigma_f$	Flexural stress.
$\tau_f$	Shear stress produced in the left or right flange.
$\tau_w$	Shear stress produced in the web.
$\gamma_w$	Shear strain of the web.
$\gamma_f$	Shear strain of the left or right flange.
$\delta$	Variation operator taken during the indicated time interval

## استخدام التطبيقات البرمجية في حل صعوبة إرساء العطاءات في المقاولات (الإنشائية, التجهيز)

صدى عبد الخالق حسن

جامعة القادسية- كلية الهندسة

### خلاصة البحث

يهدف البحث إلى استعمال الحاسوب وإمكانياته لتحديد واختيار أمثل العروض المقدمة من قبل شركات المقاولات حيث كان للزيادات الغير متوقعة في أجور العمال وأسعار المواد البنائية وتباينها الأثر الكبير في عدم قدرة الكثير من شركات المقاولات من أكمال التنفيذ بالوقت المعين أو الكلفة المحسوبة وهذا خلق الكثير من المشاكل التنفيذية والتي أثرت على سرعة ونوعية الأعمال المنجزة لذا فالإدارة الجيدة لأي مناقصة و التخطيط الجيد خلال التنفيذ يعكس واقع وإمكانيات كل شركة من شركات المقاولات المتقدمة لأي مناقصة لذا فمعرفة إمكانيات كل شركة ومقارنتها مع الأخرى وفقاً للآلية المرادة في التنفيذ معتمدة على طبيعة كل المشروع إذا كانت ( كلفة أو مدة أو نوعية ) تمكنا من الاختيار الأمثل للعروض المقدمة من قبل الشركات وبالتالي قيادة المشروع بما يراد من كلفة وجودة وبالوقت المطلوب.

تعامل البحث مفردات وعوامل نجاح عملية المفاضلة بين الشركات لإختيار أفضل العروض بالاعتماد على العوامل المؤثرة على الاختيار , وتحديد نسب مئوية لها وفقاً للكثير من الزيارات الميدانية ومن المقابلات الشخصية مع الكثير من ذوي الاختصاص بعملية فتح وتحليل العطاءات وإعداد برنامج حاسوبي يضع بين يدي المستخدم الطريقة المثلى للمفاضلة بين الشركات المتقدمة على أساس [ الكلفة أو المدة أو النوعية وكفاءة الشركة والمحسوبة وفقاً للعوامل المحصاة أو من خلال الموازنة بينهم وفق نسبة مئوية تخصص لكل مفردة من مفردات ( الكلفة , المدة , النوعية ) وحسب سياسة الدائرة التي طرحت المناقصة ونوع المشروع ] . بالإضافة إلى تحديد نوع المناقصة هل هي مناقصة تجهيز أم إنشاء ؟

**كلمات رئيسية:** عقود المقاولات, أمثل العروض, مستندات المقاولات, العوامل المؤثرة, مقاولات الإنشاء

## USING PROGRAMMING APPLICATION TO SOLUTION THE DIFFICULT AWARD OF CONTRACTS (SUPPLIED- CONSTRUCTION)

### ABSTRACT

The research aims to use the computer and it's potential to identify and choose the best offers submitted by companies contracting with the third-expected increases in the wages of labor and prices of building materials and the large variability in the impact of the inability of many of the construction to complete the implementation of the specific time or the estimated cost and thus create a lot of problems executive, which affected the speed and quality of works. A good management and good planning through implementation to reflect the realities and possibilities of each of the contracting companies to tender for any contract so a knowledge of possibilities of each company and compare it with the other , according to the mechanism in the desired implementation , depending on the nature of each project if we were able to optimize( cost , duration , quality ) the selection of the presentations developed by the companies and thus the achievement of the project , including and appraiser of the cost , quality and needed time . The research has dealt with the items and factors of success of the trade-off between the companies to choose the best offer depending on the factors instrumental to the selection and identification of a percentage and in accordance with the increases Field of personal interviews with many of the professionals and the process of opening and analysis of tenders and the number of software made in the hands of the user the best way to differentiate between companies on the basis of cost or duration , or the quality and efficiency of the company , calculated in accordance with the factors previously or by including the budget allocated according to percentage of each individual of items ( cost , duration , quality ) and by political department raised the auction and the type of project , as well as to identify the type of auction is it a construction or the establishment .

### هدف البحث :

يهدف البحث إلى معرفة واقع حال نظام تحليل وإرساء العقود ( تجهيز أو تشييد ) في دوائر الدولة و إدخال التقنيات والعلوم الحديثة على عملية المفاضلة بين الشركات المتقدمة للمنافسة والمساعدة في اختيار أفضل العروض وبالتالي تجاوز مشاكل إرساء العطاءات والمشاكل التي تحدث عند التنفيذ نتيجة تضخم أسعار الفقرات الأولى في العقد من قبل بعض الشركات لأغراض المنفعة الاقتصادية المتأنية من التسليف على الأعمال المنجزة.

### مقدمة:

من خلال معرفة مستندات المقاول الواجب جلبها مع كل عطاء ومعرفة العوامل والفقرات المهمة والمؤثرة والتأكد من كونها متوفرة في العطاء وإهمال العطاءات الغير متوفرة فيها المستندات المهمة (غير مستوفية للشروط) يتم تحديد العروض المثلى للشركات وفقاً لمدة أو كلفة التنفيذ وكفاءة الشركة .

### مستندات العقد الهندسي ( عقد المقاوله ) :

وتشمل ما يلي [ 2 ], [6], [5], [ 8 ]:

- الشروط العامة ( الحقوقية والمالية ) أو ما قد يسمى تعليمات إلى مقدمي العطاءات

وهي مجموعة من الشروط والالتزامات التي تتحقق له , وهذه كلها لها انعكاسات معينة

على حساب الكلفة وأساليب العمل .



- الشروط الفنية العامة والخاصة بالعرض , وهي الشروط والمواصفات التي يجب أن تتم الأعمال المطلوب تنفيذها والالتزام بها بدقة , ما لم يوافق صاحب العمل أو من يفوضه على تعديلها كلياً أو جزئياً , فتصبح الشروط المعدلة هي الشروط الواجب مراعاتها عند التنفيذ, وقد تشمل نوعية الأعمال وأسلوب العمل والمعدات اللازمة لتنفيذها.

- الخرائط والمخططات والنماذج ترفق لتوضح المكونات الأساسية للمشروع وقد تتضمن بعض المعلومات عن المواد وطريقة التنفيذ .

- المستندات المطلوبة مع العطاء وتشمل :

أ- مستندات العرض .

ب- إشعار بالتأمينات الأولية.

ج- مستندات أصولية تتعلق بتسجيل المقاول وشهادات التصنيف .

د- برنامج العمل وأسلوب التنفيذ.

- الملاحظ: أي مرفقات مهمة يرى ضرورتها.

### العوامل المؤثرة و المعتمدة في تحديد ثم اختيار امثل العروض:

من خلال الزيارات الميدانية والمقابلات الشخصية مع المهندسين وذوي العلاقة بقسم العقود في محافظة القادسية تم الحصول على أهمية كل عامل من العوامل المعتمدة في اختيار امثل العروض وذلك بنسب مئوية خصصت لكل عامل وهذه النسب تتراوح بين قيمتين (حد أعلى و أدنى) وذلك حسب عدد الأعمال التي تخص كل شركة وفقاً لفقرات العقد المبينة تفصيلها سابقاً , حيث تم الحصول على استمارة لدرج العوامل المؤثرة في تحديد واختيار امثل العروض ثم المصادقة والتعديل على فقرات كل عامل منها من قبل قسم العقود التابع لمحافظة القادسية وقد وجد إن هناك تباين في تحديد النسبة المئوية لكل عامل ويرجع ذلك لتباين عدد الأعمال التي قامت بها كل شركة من شركات المقاولات المتقدمة لنيل العطاء لصالحها إذ إن الشركة ذات الأعمال الكثيرة والتي هي لصالح المقاوله الحالية تمنح النسبة الأعلى حيث يرجع ذلك إلى تاريخ الشركة وممارستها الجيدة والقديمة في هذا المجال أو تلك الفقرة وهذا يعتبر من الإيجابيات حيث لا يتم المساواة بين شركات ممارسة لأكثر من عمل وبين شركات مارست القليل من الأعمال والجدول الموضح أدناه يبين تفاصيل العوامل والفقرات مع حدود النسب المئوية لها والتي تم وضعها من قبل قسم العقود في المحافظة بعد دخول كوادرهم احد دورات التعليم المستمر الخاصة بإدارة وتحليل العقود التي اقيمت في كلية الهندسة , [1], [4], [9] .

جدول رقم (1) حدود النسب المئوية للعوامل المؤثرة في اختيار افضل عطاء

العامل	حدود النسبة المئوية
<b>1- الأعمال المماثلة التي قام بها المقاول مع ذكر الجهة التي قام بالعمل لحسابها:</b>	<b>23%</b>
أ- توجد أعمال مماثلة منجزة لمصلحة الدائرة المستفيدة أو المحافظة في الوقت المحدد	23% - 16%
ب- توجد أعمال مماثلة منجزة لغير الدائرة المستفيدة وفي الوقت المحدد وبشكل جيد .	15% - 11%
ج - توجد أعمال مماثلة منجزة بشكل جيد مع تأخر في الإنجاز .	10% - 6%
د- توجد أعمال مماثلة غير منجزة لحد تأريخ المناقصة .	5% - 1%
<b>2- الأعمال قريبة من التخصص والمنجزة وقد تم تخصيص نسبة لها :</b>	<b>12%</b>
أ- توجد أعمال قريبة من التخصص ومنجزة حسب عدد الأعمال .	12% - 8%
ب- توجد أعمال غير مماثلة منجزة في الوقت المحدد و بشكل جيد .	7% - 5%
ج- توجد أعمال غير مماثلة منجزة بشكل جيد مع تأخر في الإنجاز .	4% - 1%
<b>3- الأعمال التي يقوم المقاول بتنفيذها وقت تقديم العطاء وتكون بإحدى الحالات التالية :</b>	<b>7%</b>
أ- لا توجد أعمال .	7%
ب- توجد أعمال في مراحلها الأخيرة .	6% - 5%
ج- توجد أعمال يقوم بها المقاول .	4% - 0%
<b>4- وجود شهادات تثبت حسن تنفيذ من الجهات التي قام المقاول بالعمل لحسابها</b>	<b>8%</b>
أ- توجد شهادات من الجهة المستفيدة أو المحافظة نفسها .	8% - 4%
ب- توجد شهادات من الوزارات أو المحافظات الأخرى .	3% - 1%
<b>5- حجم الأعمال المنفذة سابقاً :</b>	<b>10%</b>
أ- توجد أعمال منفذة لأكثر من 5 مليار دينار عراقي .	10% - 7%
ب- توجد أعمال منفذة لأكثر من 1 مليار .	6% - 4%
ج- توجد أعمال لأقل من 1 مليار .	3% - 2%
د- لا توجد أعمال .	0%
<b>6- الوضع المالي للشركة أو المقاول :</b>	<b>20%</b>
أ- مستقر .	20% - 10%
ب- متوسط .	9% - 6%



ج- ضعيف وغير مستقر .	%5 - %1
7- مدى امتلاك الشركة معدات وآلات مستخدمة في تنفيذ المشاريع :	% 10
* امتلاك آليات تخصصية في تنفيذ المشاريع حددت النسب على عدد الآليات وأنواعه	%10 - %7
* امتلاك الآلات أخرى .	%6 - %1
* عدم امتلاك آلات .	% 0
8- امتلاك الشركة أو المقاول لكوادر فنية متخصصة بالعمل :	% 5
* يمتلك كادر ماهر .	% 5 - % 1
* لا يمتلك كادر .	% 0
9- مدى توفر جدولة زمنية بفعاليات المشروع ومدة التنفيذ الكلية .	% 5 - % 0

هذا بالنسبة لمقاولات التشييد أما بالنسبة لمقاولات التجهيز فالعوامل المؤثرة كما مبينة في الجدول رقم (2) حيث وضع كل عامل مع حدود نسبته المئوية.

جدول رقم (2) حدود النسب المئوية للعوامل المؤثرة في اختيار أفضل عطاء (التجهيز)

العامل	حدود النسبة المئوية
1- الأعمال المماثلة " حدد الإجابة حسب العدد " أو الدائرة المستفيدة :	% 30
أ- هل توجد أعمال مماثلة منجزة في المحافظة أو الدائرة المستفيدة من قبل الشركة وفي الوقت المحدد وبشكل جيد .	% 30 - %21
ب- هل توجد أعمال مماثلة منجزة في المحافظات الأخرى أو الدوائر الأخرى التابعة لغير المحافظة .	% 20 - % 1
2- الوضع المالي للشركة أو المقاول :	% 30
أ- الوضع المالي مستقر .	% 30 - %21
ب- الوضع المالي متوسط .	% 20 - % 1
ج- الوضع المالي ضعيف أو غير مستقر .	% 0
3- وضع الشركة وعلاقتها بالشركات المصنعة الأصلية .	% 20
* وكيل حصري .	% 20 - %16
* وكيل معتمد .	% 15 - % 1
4- قيمة المواد المجهزة سابقاً في مقاولات أخرى .	% 20
* القيمة المالية أكثر من 5 مليار دينار .	% 20 - % 11
* القيمة المالية أكثر من 1 مليار .	% 10 - % 11

تحليل العوامل المؤثرة :

سوف يتم اعتماد القوانين التالية لحساب كفاءة الشركة الفنية أو كفاءة السعر أو المدة وبالتالي النسبة الكلية للترجيح حيث :

80 % من المبلغ التخميني

نسبة كفاءة السعر =  $\frac{\text{مبلغ العطاء}}{\text{النسبة المئوية المستخدمة (المدخلة)}} \times$

حيث سياسة قسم العقود تنص على ان الحد الادنى المقدر للكلفة يقل ب 20% من الكلفة التخمينية وان العطاء يعتبر مقبول عندما يكون ضمن الحد الاعلى والادنى المقدرين للكلفة وغير مقبول في بقية الحدود لذلك يعتبر العطاء كفوء عند تحقيقه 80 % من المبلغ التخميني.

مدة التنفيذ في العطاء

كفاءة المدة =  $\frac{\text{النسبة المئوية المستخدمة (المدخلة)}}{\text{المدة التخمينية}}$

الكفاءة الفنية النوعية = كفاءة الشركة ( المحسوبة من البرنامج ) %  $\times$  النسبة المئوية المستخدمة (المدخلة)

المدة التخمينية

نسبة كفاءة المدة =  $\frac{\text{النسبة المئوية المستخدمة (المدخلة)}}{\text{مدة العطاء}} \times$

النسبة الكلية للترجيح = كفاءة السعر + الكفاءة الفنية للشركة + كفاءة المدة

### إعداد برنامج حاسبي لاختيار أمثل العروض

يجب الاستفادة من إمكانيات الحاسب في عملية تحليل العروض والاختيار الأمثل لها بحيث يتم توظيفه من اجل زيادة قدرة وقابلية وكفاءة الاختيار الأمثل لمشاريع التشييد في العراق بالإضافة إلى مقاولات التجهيز وذلك لتحقيق السرعة والدقة في التوصل إلى الاختيار المناسب عن طريق تصميم وبناء برنامج حاسبي متفاعل يضع أمام المستخدم عدة خيارات وما عليه إلا اختيار الفقرات المتوفرة في كل عطاء وفي ضوء تلك الاختيارات يقوم البرنامج بتحديد المسار الذي يتخذه للوصول إلى القرار المناسب .

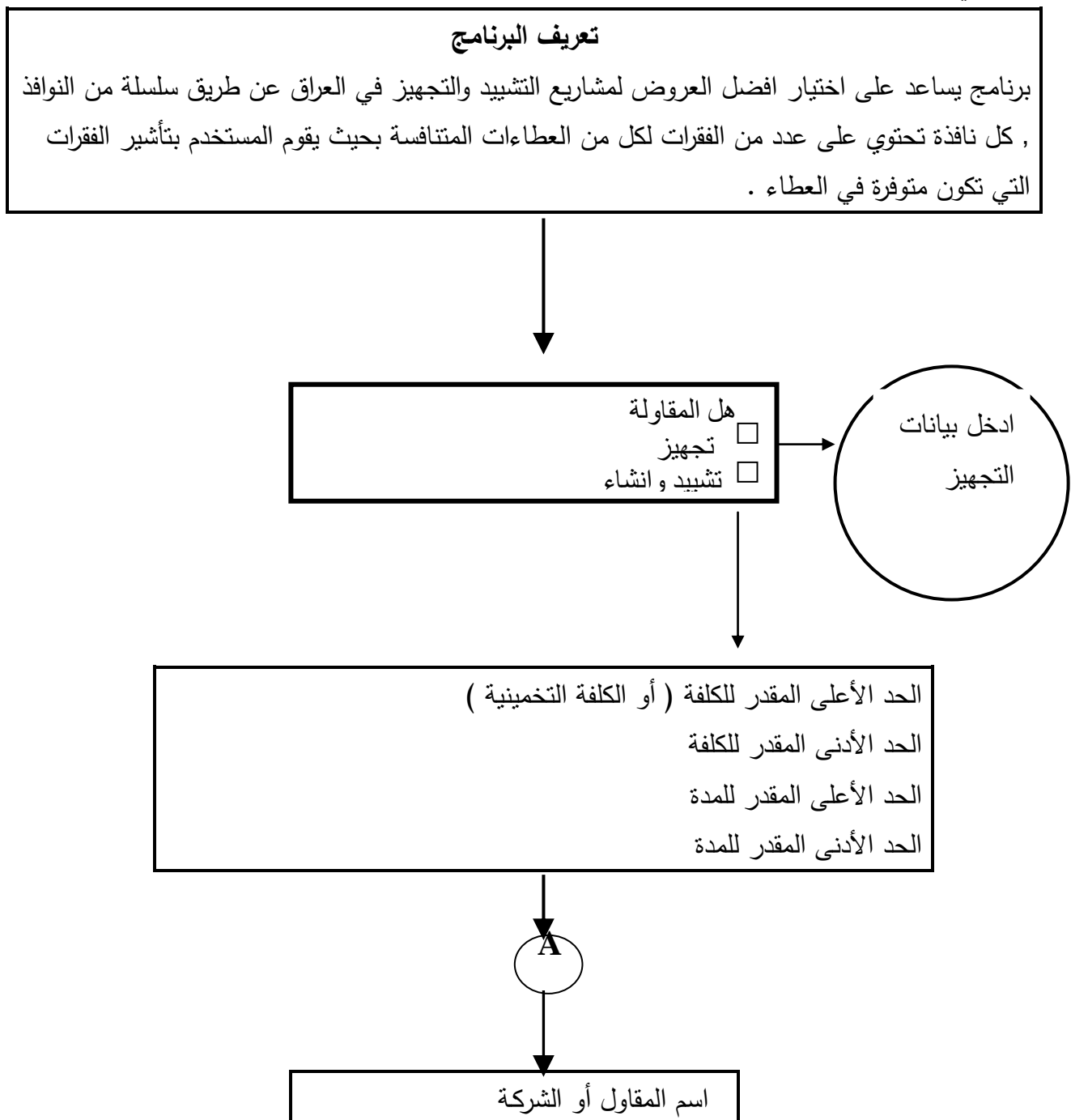
### لغة البرنامج :

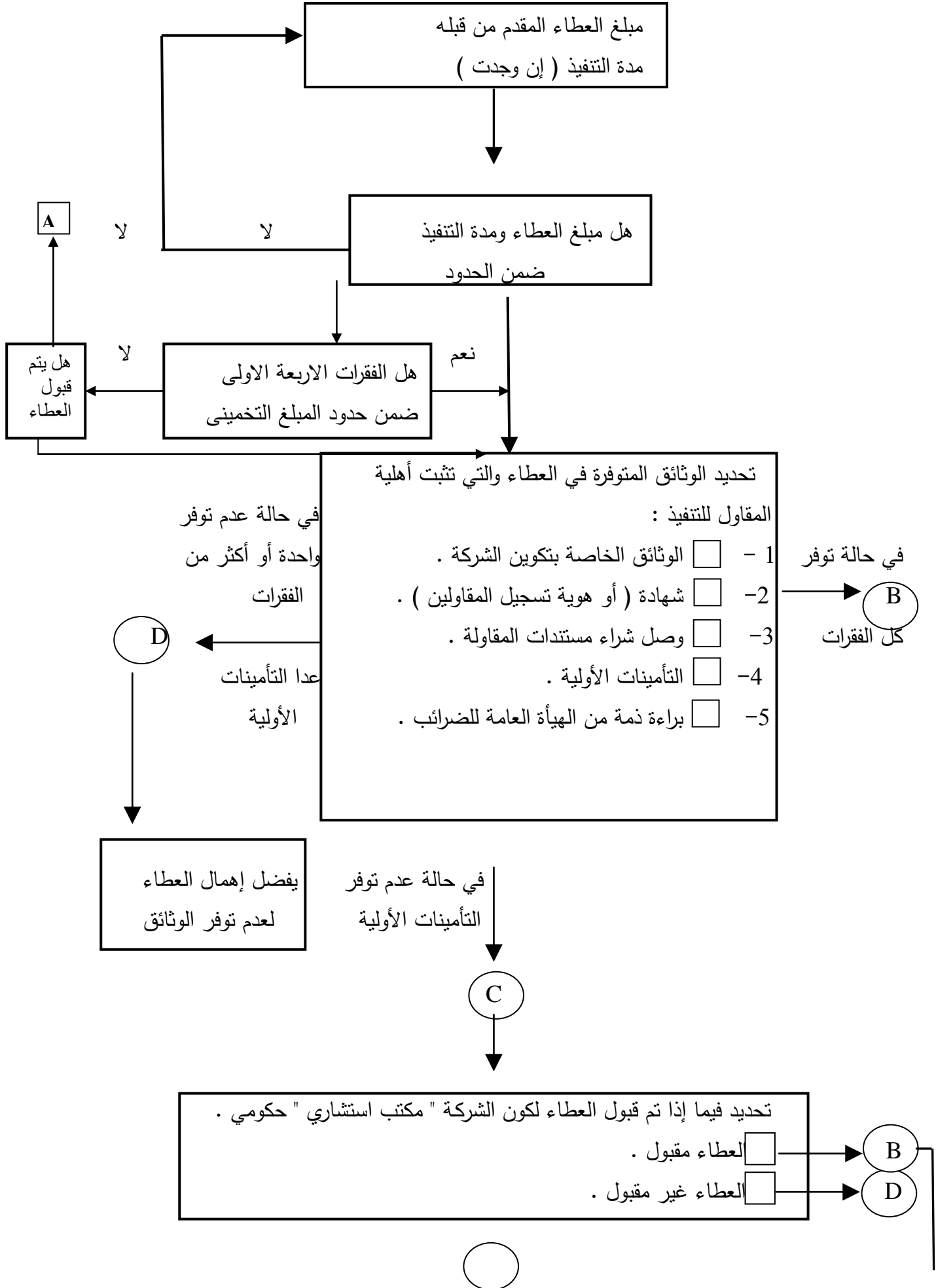
أطلقت شركة مايكروسوفت الإصدار العاشر من لغة البرمجة الشهيرة بفجوال بيسك Visual Basic باسم Visual Basic.NET 2008 حيث مرت بمراحل تطور مختلفة , حتى وصلت إلينا في شكلها الحالي , لنذهلنا بقدراتها المدهشة , التي تجمع بين البساطة وسهولة التعلم , وصياغتها التي تجعلها قريبة من اللغة الإنجليزية المبسطة العادية , وقوة وكفاءة البرامج المكتوبة بها , مع ثروة من الأدوات والدوال الجاهزة التي تتوفر فئات إطار العمل Framework Classes في بيئة دوت نت NET . , والتي تريح من عناء البدء من الصفر , والتي تملو بذلك عن تركيب الجهاز بل ونظام التشغيل Operating System

بحيث يستطيع البرنامج أن يعمل على أي نظام دون أن تخشى من مشاكل عدم التوافق ncompatibility u بينهما [3] .

### هيكلية البرنامج :

تم إعداد برنامج حاسوبي بلغة فيجوال بيسك (Visual Basic .NET2008 [ 7 ] ) لإيجاد اسم ثلاث شركات للمقاولات قد حصلت على أعلى النسب وذلك لإحالة المقولة للأولى وحسب هيكلية البرنامج وكالتالي :





B ←



لتحديد المعلومات والوثائق التي تعتبر مقياس لكفاءة المقاول أو الشركة  
( اجب عن أحد الفقرات ) :

### 1- مدى وجود الأعمال المماثلة التي قام بها المقاول مع ذكر الجهة التي قام بالعمل لحسابها

أ- \* توجد أعمال مماثلة منجزة لمصلحة الدائرة المستفيدة " أو المحافظة " في الوقت المحدد وبشكل جيد "  
حدد النسبة المئوية الملائمة " حسب عدد الأعمال :

%16 ☐ %17 ☐ %18 ☐ %19 ☐ %20 ☐ %21 ☐ %22 ☐ %23 ☐

ب- \* توجد أعمال مماثلة منجزة لغير الدائرة المستفيدة وفي الوقت المحدد وبشكل جيد  
( حدد النسبة الملائمة وحسب عدد الأعمال ) :

%11 ☐ %12 ☐ %13 ☐ %14 ☐ %15 ☐

ج- \* توجد أعمال مماثلة منجزة بشكل جيد مع تأخر في الإنجاز :

%6 ☐ %7 ☐ %8 ☐ %9 ☐ %10 ☐

د- \* توجد أعمال مماثلة غير منجزة لحد تاريخ المناقصة :

%1 ☐ %2 ☐ %3 ☐ %4 ☐ %5 ☐

2- الأعمال قريبة التخصص ومنجزة وقد تم تخصيص نسبة 12% لها  
" حدد النسبة حسب عدد الأعمال " :

أ- \* توجد أعمال قريبة من التخصص ومنجزة :

%8 ☐ %9 ☐ %10 ☐ %11 ☐ %12 ☐

ب- \* توجد أعمال مماثلة منجزة في الوقت المحدد وبشكل جيد :

%5 ☐ %6 ☐ %7 ☐

ج- \* توجد أعمال غير مماثلة منجزة بشكل جيد مع تأخر في الإنجاز :

%1 ☐ %2 ☐ %3 ☐ %4 ☐

- الأعمال التي يقوم المقاول بتنفيذها وقت تقديم العطاء وتكون بإحدى

الحالات التالية وقد تم تخصيص نسبة 7% لها :

أ- \* لا توجد أعمال " 7% " .

ب- \* توجد أعمال في مراحلها الأخيرة :

☐ توجد أعمال كثيرة ( 5% ) . ☐ أعمال قليلة ( 6% ) .

ج- \* توجد أعمال يقوم بها المقاول :

عدد كثير جداً ( 0% ) كثير ( 1% ) متوسط ( 2% ) قليل ( 3% ) قليل جداً ( 4% )  
☐ ☐ ☐ ☐ ☐

4- وجود شهادات تثبت حسن التنفيذ من الجهات التي قام المقاول بالعمل لحسابها

وقد تم تخصيص نسبة 8% لها :

أ- \* توجد شهادات من الجهة المستفيدة أو المحافظة نفسها

" حدد النسبة حسب عدد الشهادات "

☐ 4% ☐ 5% ☐ 6% ☐ 7% ☐ 8%

ب- \* توجد شهادات من الوزارات أو المحافظات الأخرى " حدد النسبة حسب العدد "

☐ 1% ☐ 2% ☐ 3%

5- حجم الأعمال المنفذة سابقاً وتم تخصيص نسبة 10% لها " حدد النسبة حسب عدد الأعمال " :

أ- \* توجد أعمال منفذة لأكثر من 5 مليار دينار عراقي :

☐ 7% ☐ 8% ☐ 9% ☐ 10%

ب- توجد أعمال منفذة لأكثر من 1 مليار دينار عراقي :

☐ 4% ☐ 5% ☐ 6%

ج- \* توجد أعمال لأقل من 1 مليار دينار عراقي :

☐ 2% ☐ 3%

د- \* لا توجد أعمال : ( 0% ) ☐

6- الوضع المالي للشركة أو المقاول :

أ- \* مستقر :

☐ 10% ☐ 11% ☐ 12% ☐ 13% ☐ 14% ☐ 15%  
☐ 16% ☐ 17% ☐ 18% ☐ 19% ☐ 20%

ب- \* متوسط :

☐ 6% ☐ 7% ☐ 8% ☐ 9%

ج- \* ضعيف وغير مستقر :

☐ ☐ ☐ ☐ ☐





%1      %2      %3      %4      %5

7- مدى امتلاك الشركة معدات و آلات مستخدمة في تنفيذ المشاريع وقد تم تخصيص نسبة 10% لها " حدد النسبة حسب عدد الآلات وأنواعها "

أ- \* امتلاك آلات تخصصية في تنفيذ المشاريع :

%7 ☐ %8 ☐ %9 ☐ %10 ☐

ب- \* امتلاك آلات أخرى :

%1 ☐ %2 ☐ %3 ☐ %4 ☐ %5 ☐ %6 ☐

ج- \* عدم امتلاك آلات : ☐

( 0 % )

8- امتلاك الشركة أو المقاول لكوادر فنية متخصصة بالعمل وقد تم تخصيص نسبة 5% لها :

أ- \* يمتلك كادر ماهر :

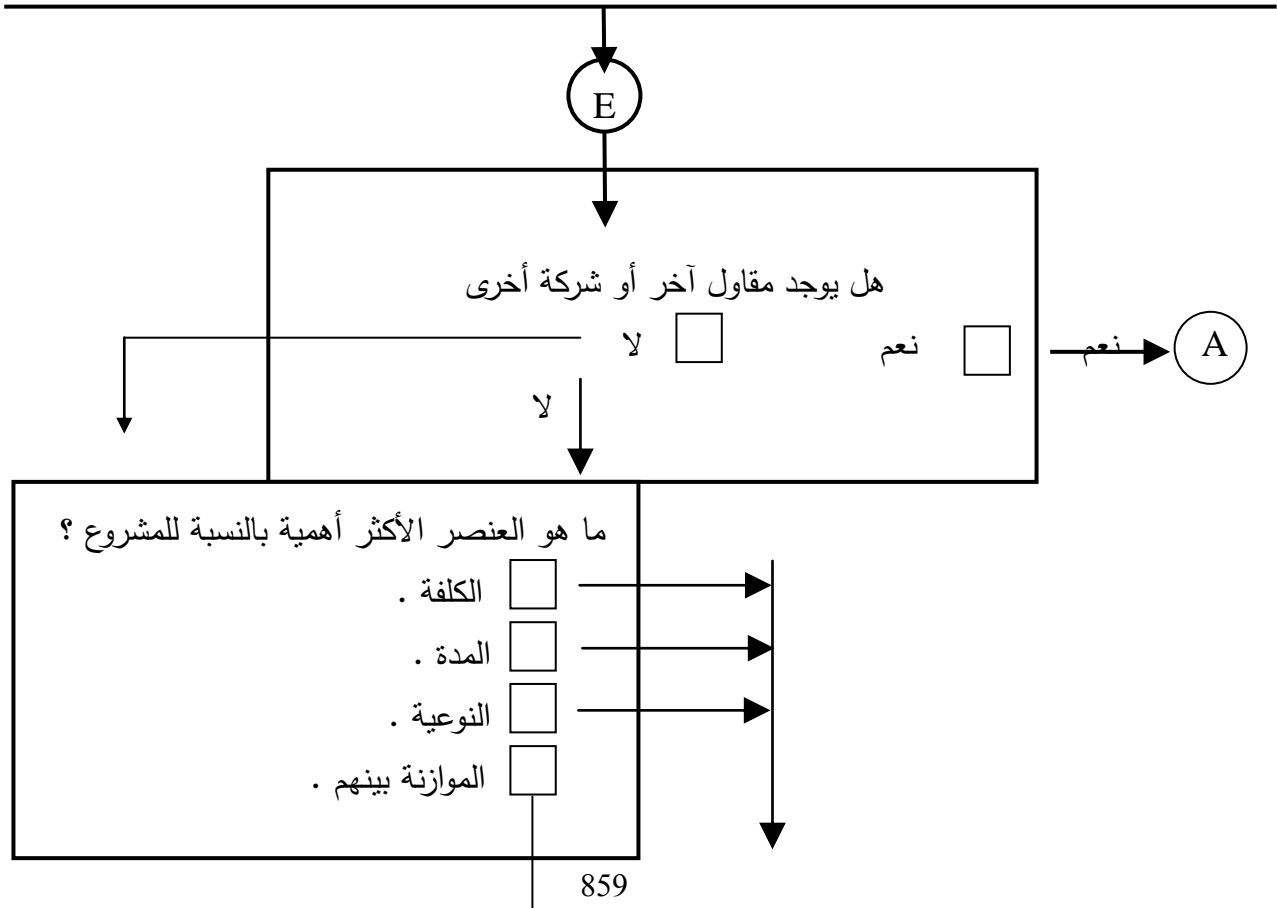
%1 ☐ %2 ☐ %3 ☐ %4 ☐ %5 ☐

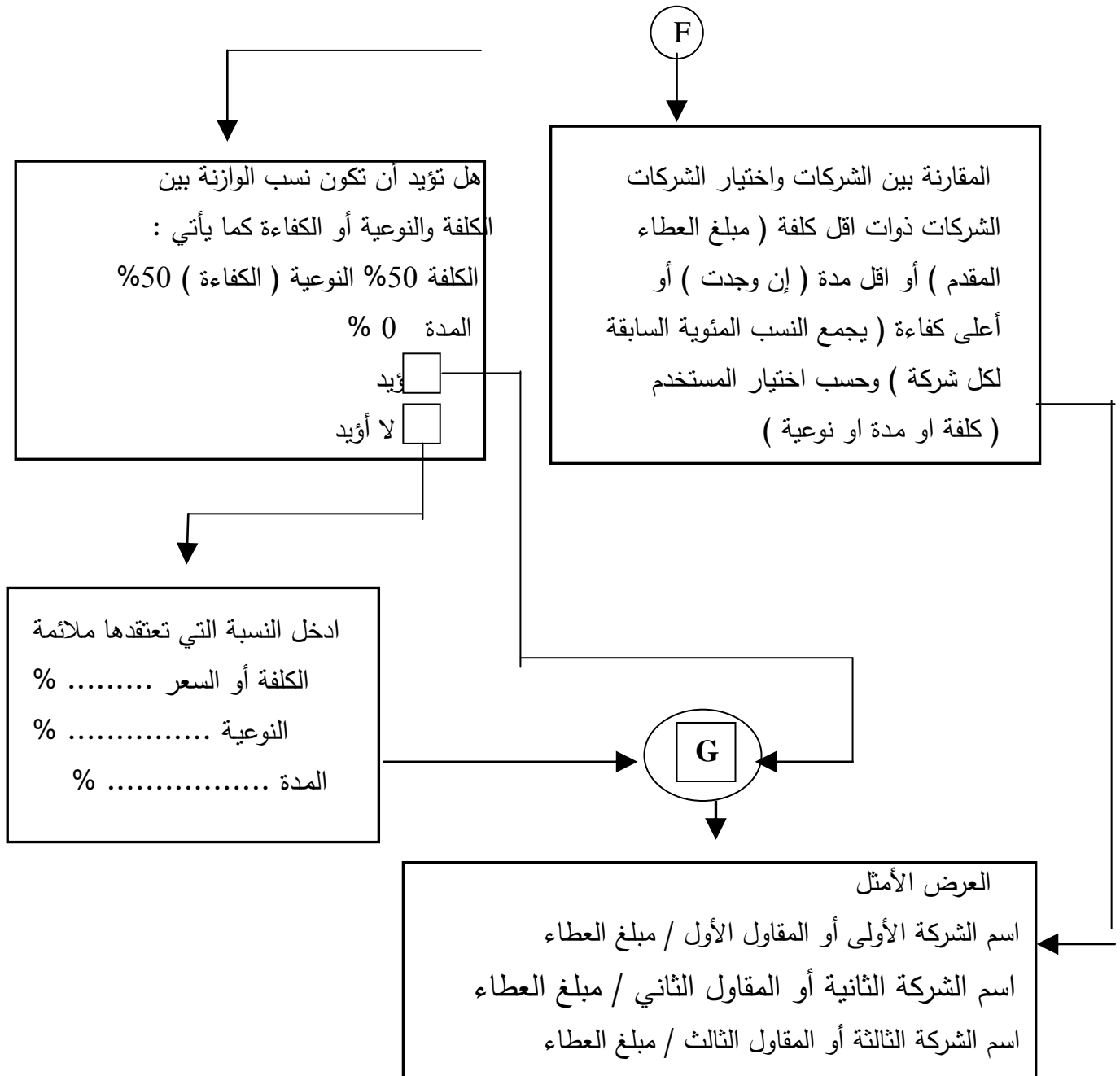
ب- \* لا يمتلك كادر : ☐ ( 0 % )

9- مدى توفر جدولة زمنية بفعاليات المشروع وحدة التنفيذ الكلية وقد تم تخصيص

نسبة 5% لها :

%0 ☐ %1 ☐ %2 ☐ %3 ☐ %4 ☐ %5 ☐





أما في حال كون المقاوله هي مقاوله تجهيز فتعاد نفس الفقرات السابقة باستثناء الفقرة B والتي تكون بالشكل التالي :



B

تحديد المعلومات التي تعتبر مقياس لكفاءة المقاول أو الشركة

( يكون التأشير لأربع فقرات ولكل فقرة جواب واحد ) :

1- الأعمال المماثلة ( حدد الإجابة حسب العدد ) :

\* هل توجد أعمال مماثلة منجزة في المحافظة أو الدائرة المستفيدة من قبل الشركة وفي الوقت المحدد:

%25	<input type="checkbox"/>	%24	<input type="checkbox"/>	%23	<input type="checkbox"/>	%22	<input type="checkbox"/>	%21	<input type="checkbox"/>
%30	<input type="checkbox"/>	%29	<input type="checkbox"/>	%28	<input type="checkbox"/>	%27	<input type="checkbox"/>	%26	<input type="checkbox"/>

\* هل توجد أعمال مماثلة منجزة في المحافظات الأخرى أو الدوائر الأخرى تابعة لغير المحافظة

%7	<input type="checkbox"/>	%6	<input type="checkbox"/>	%5	<input type="checkbox"/>	%4	<input type="checkbox"/>	%3	<input type="checkbox"/>	%2	<input type="checkbox"/>	%1	<input type="checkbox"/>
%14	<input type="checkbox"/>	%13	<input type="checkbox"/>	%12	<input type="checkbox"/>	%11	<input type="checkbox"/>	%10	<input type="checkbox"/>	%9	<input type="checkbox"/>	%8	<input type="checkbox"/>
%20	<input type="checkbox"/>	%19	<input type="checkbox"/>	%18	<input type="checkbox"/>	7	<input type="checkbox"/>	6	<input type="checkbox"/>	15	<input type="checkbox"/>		<input type="checkbox"/>

2- الوضع المالي للشركة أو المقاول :

\* الوضع المالي مستقر :

%25	<input type="checkbox"/>	%24	<input type="checkbox"/>	%23	<input type="checkbox"/>	%22	<input type="checkbox"/>	%21	<input type="checkbox"/>
%30	<input type="checkbox"/>	%29	<input type="checkbox"/>	%28	<input type="checkbox"/>	%27	<input type="checkbox"/>	%26	<input type="checkbox"/>

\* الوضع المالي متوسط :

%7	<input type="checkbox"/>	%6	<input type="checkbox"/>	%5	<input type="checkbox"/>	%4	<input type="checkbox"/>	%3	<input type="checkbox"/>	%2	<input type="checkbox"/>	%1	<input type="checkbox"/>
%14	<input type="checkbox"/>	%13	<input type="checkbox"/>	%12	<input type="checkbox"/>	%11	<input type="checkbox"/>	%10	<input type="checkbox"/>	%9	<input type="checkbox"/>	%8	<input type="checkbox"/>
%20	<input type="checkbox"/>	%19	<input type="checkbox"/>	%18	<input type="checkbox"/>	%17	<input type="checkbox"/>	%16	<input type="checkbox"/>	%15	<input type="checkbox"/>		<input type="checkbox"/>

3- وضع الشركة وعلاقتها بالشركات المصنعة الأصلية :

\* وكيل حصري :

%20	<input type="checkbox"/>	%19	<input type="checkbox"/>	%18	<input type="checkbox"/>	%17	<input type="checkbox"/>	%16	<input type="checkbox"/>
-----	--------------------------	-----	--------------------------	-----	--------------------------	-----	--------------------------	-----	--------------------------

\* وكيل معتمد :

%8	<input type="checkbox"/>	%7	<input type="checkbox"/>	%6	<input type="checkbox"/>	%5	<input type="checkbox"/>	%4	<input type="checkbox"/>	%3	<input type="checkbox"/>	%2	<input type="checkbox"/>	%1	<input type="checkbox"/>
%15	<input type="checkbox"/>	%14	<input type="checkbox"/>	%13	<input type="checkbox"/>	%12	<input type="checkbox"/>	%11	<input type="checkbox"/>	%10	<input type="checkbox"/>	%9	<input type="checkbox"/>		<input type="checkbox"/>

4- قيمة المواد المجهزة سابقاً في مقاولات أخرى :

• القيمة المالية أكثر من 5 مليار دينار :

%15	<input type="checkbox"/>	%14	<input type="checkbox"/>	%13	<input type="checkbox"/>	%12	<input type="checkbox"/>	%11	<input type="checkbox"/>
%20	<input type="checkbox"/>	%19	<input type="checkbox"/>	%18	<input type="checkbox"/>	%17	<input type="checkbox"/>	%16	<input type="checkbox"/>

\* القيمة المالية أكثر من 1 مليار دينار :

%5	<input type="checkbox"/>	%4	<input type="checkbox"/>	%3	<input type="checkbox"/>	%2	<input type="checkbox"/>	%1	<input type="checkbox"/>
%10	<input type="checkbox"/>	%9	<input type="checkbox"/>	%8	<input type="checkbox"/>	%7	<input type="checkbox"/>	%6	<input type="checkbox"/>

شكل رقم (1) هيكلية البرنامج

### كيفية عمل البرنامج وإدخال البيانات :

- يتم تشغيل البرنامج بعد الضغط على ( setup ) الموجودة في البرنامج .
- تظهر شاشة على شكل مجموعة من البيانات والحقول الخاصة بالمناقصة وهل هي
- ( تجهيز ) أم ( تشييد ) .
- يتم إملأ الحقول السابقة بالبيانات .
- يتم إدخال جميع بيانات الشركات واحدة تلو الأخرى وهذا بعد أن تظهر شاشة يتم
- فيها سؤال الشخص فيما إذا كانت هناك شركة أخرى داخلة في المنافسة أم لا .
- تظهر واجهة لتحديد النسب المعتمدة في تحليل ومنافسة العطاءات وفقاً للسياسة المتبعة
- من قبل الدائرة المستفيدة (السعر، النوعية، المدة) وحسب نوع المشروع المحال للمناقصة
- يتم تنفيذ البرنامج بالنقر على المربع ( النتائج ) الموجود أسفل واجهة إدخال البيانات للحصول على النتائج .

- 7- عندما نريد التغيير في أي من المدخلات فإننا نرجع إلى واجهات إدخال البيانات بالنقر

على المربع ( الشاشة الرئيسية ) الموجود في مربع أسفل الشاشة .

تطبيق البرنامج الحاسبي على مشروع أعمال تأهيل الممر الثاني من شارع مديرية الزراعة و فلكه الساعة  
لمحافظة الديوانية (حالة دراسية) :

### إدخال البيانات:

من خلال المسح والدراسة الميدانية والمقابلات الشخصية التي قامت بها الباحثة لقسم العقود التابع  
للمحافظة، تم اختيار أحد المشاريع التي تم تنفيذها وتسليمها تماماً خلال العام 2008 ( سنة البحث ) ، حيث  
تم وبالتنسيق والتعاون مع هذا القسم الحصول على جميع المعلومات التي تخص الشركات المتقدمة للمنافسة  
والاشكال (2,3,4) يوضح كيفية إدخال البيانات إلى البرنامج باستخدام نوافذ البرنامج .

### بيانات الشركات :

يبين الجدول رقم ( 3 ) البيانات المطلوب إدخالها والخاصة بمناقصة تأهيل الممر الثاني من شارع مديرية الزراعة والأرصفة المجاورة مع استدارة الساعة والتابعة للمحافظة ضمن مشاريع تنمية الأقاليم / مديرية البلدية , حيث كان المبلغ التخميني للمشروع ( 1,153,474,000 ) دينار ومدة التنفيذ التخمينية ( 240 ) يوم , أما عدد الشركات المتقدمة للمنافسة فكان عددها أربعة شركات .

علما ان تحديد النسب المئوية يتم من قبل لجنة فتح العطاءات بالاعتماد على اعطاء حدود النسبة العليا لأكثر الشركات المطبقة للعامل وتطبيق مبدأ (نسبة وتناسب) على بقية الشركات مقارنة بالشركة الاعلى نسبة وفي حالة كون النتيجة اقل من الحد الأدنى المحدد في البرنامج ,تعطى الشركة النسبة الأدنى وتقريب النتيجة بالنسبة لبقية النتائج لما ماهو محدد في البرنامج فمثلا بالنسبة للعامل الاول :

النسبة المئوية للعامل الاول لاحدى الشركات = عدد الاعمال المماثلة للشركة x الحدود العليا للعامل (%)

أكبر عدد للاعمال المماثلة التى قامت بها احدى الشركات

جدول رقم ( 3 ) ملخص بيانات الشركات الداخلة في المنافسة .

اسم الشركة	المبلغ للعطاء	مدة العمل	مستندات المقاوله	الأعمال المماثلة	حسن الأداء	حجم الأعمال	الوضع المالي	امتلاك معدات	امتلاكات (6)
(1)	(2)	(3)	(4)	(5)	(6)	(7)	(8)	(9)	(10)
A	1662310000	240	كاملة كلها	صفر	10	1	11	5	5
B	1214440000	150	كاملة كلها	صفر	1	1	15	صفر	4
C	1125254000	180	كاملة كلها	15	10	5	15	15	7
D	1092920000	180	كاملة كلها	15	10	5	20	5	5

### النتائج النهائية والمناقشة :

من خلال ملاحظة الشكل رقم ( 5 ) والذي يبين نتائج الحاسبة الخاصة باختيار امثل العروض نجد

إن الشركة D قد أخذت المرتبة الأولى بقيمة عرض ( 1,092,920,000 ) دينار عراقي تليها الشركة C

بقيمة عرض ( 1,125,254,000 ) دينار عراقي ولا توجد شركة ثالثة في الترتيب مع العلم إن هناك

شركتين أخر مشتركه في تقديم العطاءات الخاصة بها , وهذا يرجع إلى استبعاد الحاسب لهذه الشركات عند

إدخال بياناتها أصلاً منذ البداية وعدم إشراكها في عملية المنافسة وهذا يرجع إلى عدم استيفاء هذه الشركات

لشروط المنافسة المحددة داخل البرنامج .

كما نلاحظ إن أسلوب المنافسة قد تم على أساس النسبة الكلية للترجيح التي أعطت كفاءة السعر نسبة

60% وكفاءة الشركة 40% , حيث على الرغم من كون الشركة C لها كفاءة نوعية أعلى من الشركة D

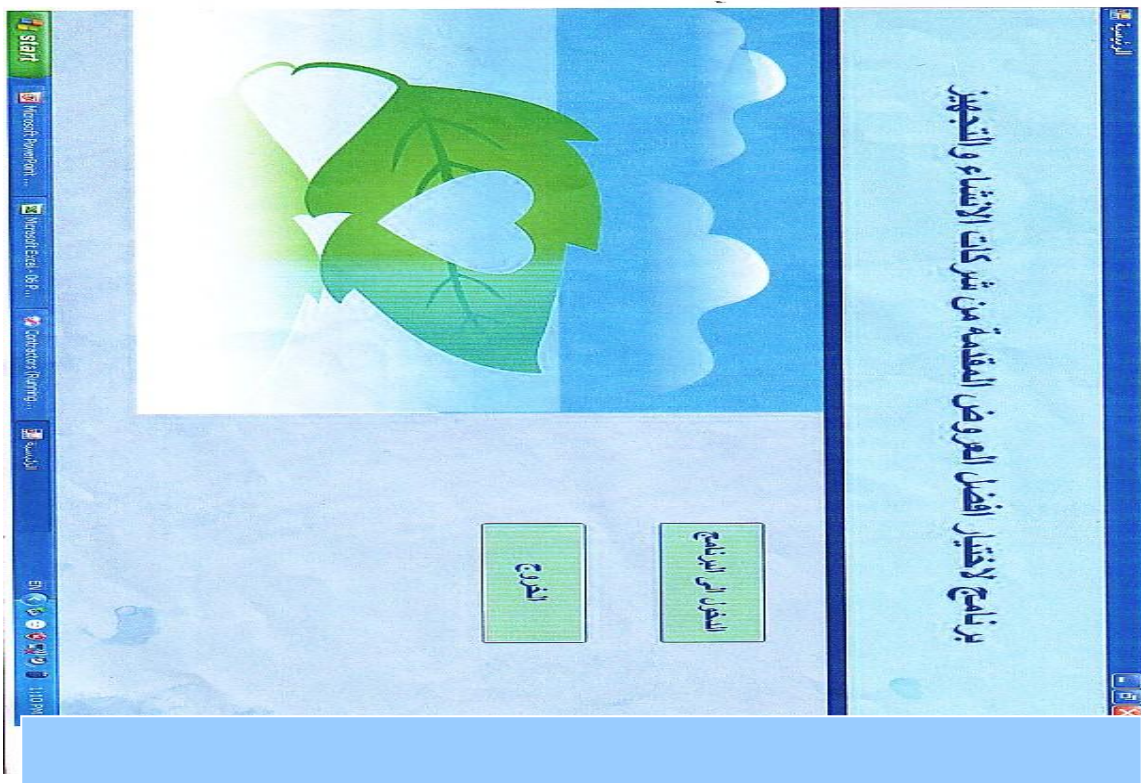
إلا إن كفاءة السعر للأخيرة أعلى , مما أدى إلى حصول هذه الشركة على المرتبة الأولى .لقد تم إهمال

كفاءة مدة التنفيذ في عملية المنافسة لهذا المشروع حسب سياسة المحافظة لهذا المشروع وأخذت كفاءة السعر

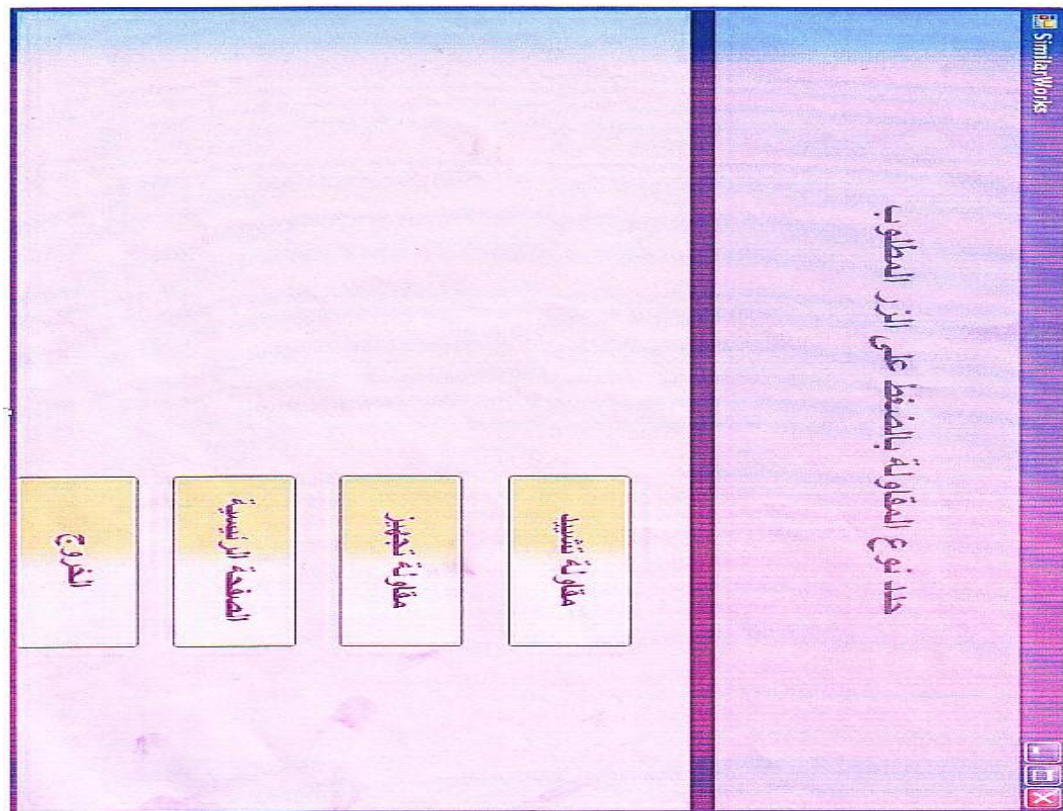
وكفاءة الشركة المحسوبة فقط كنسبة ترجيح كلية وهذا يرجع إلى كون جميع الشركات المتقدمة للمنافسة لها مدة إنجاز عمل مقبولة , لذا فإن التركيز على نوعية العمل وكلفته يرجح من الأولويات لإنجازه .

إن فائدة هذا البرنامج تكمن عندما تكون هناك عدد كبير من الشركات المتقدمة للعطاء , بحيث يصعب معها إجراء كل الحسابات الخاصة بتقييمها وإجراء عملية المنافسة بينها وبالتالي اختيار الأمثل منها فلتوفير الوقت والجهد ودقة الاختيار نرجع إلى استخدام الحاسب وتوظيف إمكانياته لحل مثل هذه الصعوبات .

بالإضافة إلى ذلك فإن تصميم استمارة خاصة ببيانات كل شركة كما موضح في الملحق يعطي ملخص بيانات عطاء كل شركة وبالتالي سهولة إدخالها البرنامج. إن المرونة المتوفرة في لبرنامج والتي تعطي خيارات نسب الترجيح, تعطي أهمية للبرنامج في تغطية مختلف أنواع العقود ولمختلف الظروف والمشاريع ذلك لإدخاله عامل الزمن أو ( وقت التنفيذ ) في عملية الترجيح وذلك لكون بعض المشاريع الحكومية تكون مدة التنفيذ لها ذات أولوية كبيرة لحاجة الدولة لها بغض النظر أو بإعطاء نسبة كفاءة قليلة لعامل الكلفة ( مبلغ العطاء ) وهذا من الأمور الواجب الانتباه لها في سياسة فتح وتحليل ثم إرساء العطاءات هذا بالإضافة إلى كون بعض الشركات تعمل على تضخيم مبالغ الفقرات الأولى في العقد ضمن مبلغ المفاوضة بغية الاستفادة من ذلك بعد الإحالة وعند التسليف على الأعمال وبالتالي عدم الالتزام والتقصير بإكمال الفقرات الأخرى كون مبالغها قليلة وبالتالي الدخول بمشاكل قانونية مع أمثال هذه الشركات وهذه من المشاكل التي عانت منها المحافضة لذا جاء البرنامج لاستبعاد مثل هذه الشركات أو تنبيه المستخدم عنها وتخيره بقبولها أو رفضها



شكل رقم (2) واجهة البرنامج عند التشغيل



شكل رقم (3) واجهة اختيار نوع المقابلة









شكل رقم ( 5 ) واجهة تنفيذ البرنامج

## الاستنتاجات والتوصيات :

1- من الممكن أن تكون هناك عدة خيارات للعرض الأنسب وفق البرنامج الحاسبي وحسب رغبة صاحب العمل وهي:

- أ- الاختيار على أساس أوطأ الأسعار : بسبب توفر الحد الأدنى من الكفاءة المطلوبة .
  - ب- الاختيار على أساس أفضل الكفاءات : يتم ذلك بعد أن يتم استبعاد العطاءات التي تكون أسعارها ومدة تنفيذها خارج الحدود المسموح بها .
  - ج- الاختيار على أساس الموازنة بين أوطأ الأسعار التي تقابل أعلى النسب
- 2- ممكن قبول أو رفض الشركات التي تعمل على تضخيم الفقرات الأولى من العقد وحسب سمعة الشركة
- 3- يقترح أن يتم استدعاء المقاولين كلاً على حدة وبالتسلسل حسب أعلى النسب المئوية التي تبين كفاءة الشركة في التنفيذ للتفاوض معهم على تقليل الأسعار التي حددوها في عطاءهم ومن ثم اختيار أوطأ الأسعار بعد التفاوض .

4- يقترح تعديل النسب المئوية المعتمدة حالياً في المحافظة بالنسبة لكفاءة الشركة (50%) وكفاءة السعر ( 50 % ) وإدخال كفاءة مدة التنفيذ وذلك لكون المشاريع تختلف من واحد لآخر فثبوت هذه النسب وإهمال

نسبة كفاءة مدة التنفيذ يعتبر من السلبات لكون بعض المشاريع تحتاج إلى الإنجاز بسرعة للضرورة أو للحاجة الماسة لها بغض النظر عن كلفة الإنجاز لذا جاء البرنامج لتغطية مختلف المشاريع بمختلف الظروف .

## المراجع

- Demmers , Lenda,Carole,"Furniture and shelving :specification and Bidding" London2006
- Hardice GM "construction contracts and specification "John Wiley and Sons , 1981 .
- -Steven Roman ,Roman ,Ron petrusha,"VB0NET Language in Nutshell"20043
- 4-البنك الدولي "طلب العروض القياسي -اختيار الاستشاريين" واشنطن العاصمة 2004
- 5-جعلوك , د . محمد علي " أعمال المقاولات " دار – الراتب الجامعية – بيروت 1999 .
- 6-حلمي , د . محمد عبد الحميد " عقود ومواصفات الأعمال في الهندسة المدنية " دار – الراتب الجامعية بيروت 1991 .
- 7-غانم م/محمد حمدي محمد,"احتراف فيجوال بيسك دوت نت" 2008
- Msbnet @ hotmail.com
- 8-كريم , عزيز نوري " مبادئ في عقود المقاولات الإنشائية " جامع بغداد 1984 .
- 9-وزارة التخطيط والتعاون الانمائي"وثائق العطاءات النموذجية "تنفيذ الاشغال-توريد السلع" جمهورية العراق 2008



بسم الله الرحمن الرحيم

استمارة تحليل العطاءات

(المناقصات) (الانشائية)

رقم المناقصة:

اسم المشروع:

الجهة المستفيدة:

اسم الشركة او المقاول:

تاريخ تحليل العطاء:

**اولا - مستندات المقابولة**

- ا- وصل شراء مستندات المقابولة . ☐
- ب- شهادة ( أو هوية تسجيل المقاولين ) ☐
- ج- التأمينات الأولية . ☐
- د- الوثائق الخاصة بتكوين الشركة ☐
- هـ- براءة ذمة من الهيئة العامة للضرائب ☐

**ثانيا - كفاءة الشركة**

- 1) ا- الأعمال المماثلة منجزة لمصلحة الدائرة المستفيدة في الوقت المحدد وبشكل جيد- ☐ 23-16 % 23 %  
 ب- الأعمال المماثلة المنجزة لغير الدائرة المستفيدة في الوقت المحدد وبشكل جيد ----- ☐ 15-11 % 15 %  
 ج- الأعمال المماثلة المنجزة مع تأخر في الإنجاز----- ☐ 10-6 % 10 %  
 د- الأعمال المماثلة غير المنجزة لحد الآن----- ☐ 5-1 % 5 %
- 2) ا- الأعمال قريبة من التخصص المنجزة----- ☐ 12-8 % 12 %  
 ب- الأعمال غير المماثلة المنجزة في الوقت المحدد وبشكل جيد----- ☐ 7-5 % 7 %  
 ج- الأعمال غير المماثلة المنجزة بشكل جيد مع تأخر في الإنجاز----- ☐ 4-1 % 4 %
- 3) الأعمال الجارية للمقاول وقت تقديم العطاء  
 أ - لا توجد أعمال او أعمال في مراحلها الأخيرة----- ☐ 7-5 % 7 %  
 ب - توجد أعمال----- ☐ 4-0 % 4 %
- 4) شهادات او شكر وتقدير للأعمال المنجزة----- ☐ 8 %  
 ا- من الدائرة المستفيدة في المحافظة----- ☐ 8-4 % 8 %  
 ب- من محافظات أخرى----- ☐ 3-1 % 3 %
- 5) حجم الأعمال المنفذة سابقا  
 ا- لاكثر من 5 مليار دينار عراقي----- ☐ 7-1 0 % 7 %  
 ب- لاكثر من 1 مليار دينار عراقي----- ☐ 4-6 % 4 %  
 ج - اقل من 1 مليار دينار عراقي----- ☐ 0-3 % 0 %
- 6- الوضع المالي----- ☐ 20-1 0 % 20 %  
 ا- مستقر----- ☐ 6 % 6 %  
 ب- متوسط----- ☐ 5-1 % 5 %  
 ج - غير مستقر او ضعيف----- ☐ 1 0 % 1 %
- 7) امتلاك الالات والمعدات----- ☐ 10-7 % 10 %  
 ا- امتلاك الالات تخصصية في التنفيذ----- ☐ 6-1 % 6 %  
 ب- امتلاك الالات اخرى----- ☐ 0 % 0 %  
 ج- لا يمتلك الالات----- ☐

1-5% ☐  
0% ☐  
0-5% ☐

8) ا- امتلاك المقاول او الشركة كوادر فنية متخصصة بالعمل-----  
ب- لا يمتلك كادر-----  
9) مدة التنفيذ-----

## تأثير استخدام خبث الحديد على خواص مزيج رمال السباكة

د.خضير جاسم محمد / الجامعة التكنولوجية

### الخلاصة :-

يتناول هذا البحث موضوع الخبث الناتج من عمليات صهر الحديد ( حديد الصب - cast iron والفولاذ - steel) باعتباره من المخلفات الصناعية الصلبة الملوثة للبيئة بصورة عامة إذ تنتج كميات كبيرة منه في المسابك ومجمعات الحديد والصلب حيث تتراوح بين (10-30) % من كمية سبائك الحديد المنتجة فيها . ولغرض الاستفادة منه موقعياً - في المسابك المنتجة له نفسها - فقد تم في هذا البحث تجربة استخدامه في مزيج رمال السباكة , حيث استعملت نسب (10%, 20%, 30%, 40%) من مسحوق الخبث المطحون إلى حجوم مقارنة لحجوم رمال السباكة بديلاً عن رمال السباكة - وتحضير نماذج قياسية من المزيج وفحص نفاذية الغاز ومقاومة الانضغاط لها .

أظهرت نتائج الفحوصات تحسن واضح في مقدار مقاومة الانضغاط وكذلك في نفاذية الغاز في الحالة الرطبة بزيادة نسبة الخبث .

أما في الحالة الجافة فلم يكن بالإمكان كسر العينات في جهاز الفحص عند إضافة الخبث بنسبة تزيد عن 10% لان مقدارها تجاوز الحد الأعلى لقراءة جهاز الفحص (6.5 كغم /سم<sup>2</sup>) وبذلك أصبح بالإمكان الاستفادة من الخبث المذكور في تحسين خواص مزيج رمال السباكة والتخلص من تأثيره الملوث للبيئة وتقليل كلفة النقل .  
تدوير النفايات أفضل طريقة لحماية البيئة -

## EFFECT OF USING IRON SLAG ON FOUNDRY- MOLDING MIXTURE PROPERTIES

### ABSTRACT:

This work deals with slags produced from melting processes of cast iron and steel .as an industrial solid by product with investigate effect environment in general .Huge quantities of slag are produced from foundries and steel work complexes , as (10-30)% of iron alloys produced .In order to use those quantities at the same foundries , this work investigates the using of slag in sand moulding mixtures 10,20,30 and 40 % of milled slag to the same size of silica sand , instead of silica , and prepared standard specimens to test green compression strength and gas permeability in green and dry cases.Results showed improvement in comp.strength in green tests, by using slag. While in dry tests, however, that comp. strength increased by using slag.But we couldn't break dry specimens to have given results over 10% slag because their values were over the rang of tester ( $6.5\text{kg/cm}^2$ ) . Accordingly we can state that slag can be used in moulding mixture at the same foundries to improve properties and to get rid from its pollution effect and transport costs.

**-Rejects recycling is the best way to save environment -**

### هدف البحث – Aim of work –

يهدف البحث إلى تخليص البيئة العامة من ملايين الأطنان من خبث الحديد الناتج من عمليات صهر وصب الفولاذ وحديد الصب (الاهين) سنوياً على مستوى العالم , وذلك باستخدامها في مجالات نافعة في مواقع قريبة من أماكن إنتاجها لتتلافى تكاليف عمليات النقل العالية التي تصرف عادة لنقلها إلى مواقع بعيدة لطمرها وبذلك يمكن تحقيق هدف بيئي مهم وهو التخلص من أحد الملوثات الصناعية الصلبة التي يؤدي تراكمها إلى تلوث البيئة إن لم تستغل بصورة نافعة , إضافة إلى تحسين مواصفات المزيج الرملي المستخدم في صنع القوالب الرملية واللباب وفي نفس مواقع المسابك بحيث لا تحتاج إلى عمليات نقل بعيدة وفي ذلك جدوى بيئية وفنية واقتصادية .

### الجانب النظري

### المقدمة – INTRODUCTION :-

ينتج الخبث عرضياً من عمليات صهر المعادن والسبائك وخاصة الحديدية منها . حيث ينتج حوالي (0.25-0.35) طن خبث من كل طن من الحديد المصهور في الفرن العالي النفاخ ( Blast furnace) وحوالي (0.10-0.15) طن خبث من كل طن فولاذ منتج من أفران الصهر الخاصة به . وهذه كميات كبيرة من المخلفات الصناعية العرضية الصلبة , إذ بلغت كمياتها عالمياً عام (2003) حوالي (180) مليون طن متري من خبث حديد الصب (Cast iron) وأكثر من (100) مليون طن متري من خبث الفولاذ. [ Portland cement A. 2004,Hendrik G. 2003] . ويتكون خبث الحديد عادة من الشوائب وبعض مركبات المواد المضافة أثناء عمليات الصهر وأهم تلك المركبات أكاسيد السيليكون والمغنيسيوم والحديد والألمنيوم والكالسيوم وقليل غيرها. ويزال من فوق سطح المعدن المصهور عادة لمنع دخوله إلى قالب الصب ويبرد بالماء وهو المفضل أو بالهواء . وتعتمد كثافته على تركيز مكوناته . ويطفو الخبث فوق سطح

المعدن المصهور بسبب قلة كثافته مقارنة بكثافة الحديد , إذ تبلغ كثافته الظاهرية (Bulk density) حوالي (1.0 1.4) غم/سم<sup>3</sup> ووزنه النوعي يتراوح بين (3.02.4) .

[ Clarkson U.-CE 453- 2005, Klarkson U. 2005 ] .

أما التركيب الكيميائي للخبث فيختلف باختلاف الشوائب الموجودة في مواد الصهر والإضافات المستخدمة فيه فضلاً عن طريقة الصهر .

فهو يحتوي بصورة عامة على السيليكا ( $\text{SiO}_2$ ) والالومينا ( $\text{Al}_2\text{O}_3$ ) والنورة حيث تشكل بمجموعها حوالي (90%) من تركيب الخبث في حين يتكون الباقي من أكاسيد الحديد والصدويوم والكبريت والبوتاسيوم بنسب مختلفة [ FHW Home 1990, Australian steel mill services PTY 2006 ] .

لقد استخدم الخبث بمجالات مختلفة منها في صناعة الاسمنت أو بإضافته إلى المواد المستعملة في صهر سبائك الحديد [ National R.C.Canada 2005, Australian steel mill services PTY 2006 ]

[Iron and steel 1996

كما تم استخدامه في المجالات الإنشائية الخرسانية وفي تعبيد الطرق .

[ Clarkson U.-CE 453- 2005, Hendrik G. 2003 ] وقام معهد شنغهاي للتعبدين بدراسة شاملة

للخبث الحبيبي المبرد بالهواء وخبث الفرن العالي النفاخ الناعم جداً لاستخدامها في مجالات صهر الفولاذ وكما مادة مقاومة للبلى (Unti-wear) في الرصف (pavement) أو كمادة للرش لتنعيم سطوح السفن أو كعامل مساعد في تصفية المياه [Cen.y. 1994, د.حسن حميد 2004].

كذلك استعمل ركام الخبث الخشن في الخرسانة بدلاً من الركام ( الحصى ) الطبيعي

[ Kamal I.et. 2002, Brantz .H. 1990, د.حسن حميد 2004 ] وكذلك في الإسفلت . وتمت دراسة

استخدام خبث الفولاذ للتعويض عن الحصى الطبيعي في الخرسانة الكونكريتية وبحجوم (5-19) ملم وأعطى نتائج جيدة في تحسين مقاومة الانضغاط وزيادة الكثافة وتقليل امتصاص الماء فيها . [د.خضير جاسم محمد

2008] . كما تم استخدامه من قبل آخرين [Marizane.Y. 1999] بحجوم (10 - 40) ملم في أعمال

الهندسة المدنية . وعند سحق الخبث إلى درجة نعومة مناسبة فإن تركيبه الكيميائي وتركيبته الزجاجية

(Glassy-Nature) خاصة عند خلطه مع الماء يكون مركبات إسمنتية - ذات ميوعه ( Cementation

hydration) تعتمد كمياتها على التركيب الكيميائي وخاصة هيدروكسيد الكالسيوم والمحتويات الزجاجية ودرجة نعومة الخبث .

من جهة أخرى فإن نسبة فقدان رمال السبابة جراء الاستعمال تصل إلى 10% منها 5% غبار مما يتطلب

إضافة كميات من الرمال باستمرار لسد حاجة المسابك منها [Foseco Handbook 2000] ومن هنا فإن

استخدام مسحوق الخبث بالحجوم المناسبة في مزيج رمال السبابة له الكثير من المزايا الاقتصادية والفنية خاصة عند استعماله في مواقع المسابك المنتجة له .

## المتطلبات الأساسية للرمال المستخدمة في السباكة :-

تستخدم في عمليات صنع القوالب الرملية في السباكة مواد عديدة أهمها رمال السيليكا ( $\text{SiO}_2$ ) التي تمتاز بمقاومتها الحرارية وقابليتها على التشكيل عند المقابلة إضافة إلى الماء والمواد الرابطة .  
واهم ميزات رمال السباكة ما يلي :-

- الاستقرار في الأبعاد في درجات الحرارة المعتدلة واستقرارها الحراري .
- ذات حبيبات مناسبة من حيث الحجم والشكل .
- لا تتفاعل كيميائياً مع المعدن المصبوب في القوالب الرملية ولا تتداخل معه .
- خالية من الشوائب والمواد الطيارة التي تكون غازات عند التسخين .
- قابليتها على التشكيل بوجود الرطوبة والمواد الرابطة .
- توفرها وقلة ثمنها نسبياً .

واهم المواد الرابطة المستعملة مع رمال السباكة هي الطين ( البنتونايت ) وتستعمل أحياناً مواد رابطة أخرى إضافة إلى الماء .

إن التركيب الكيميائي والبنوي لرمال السيليكا وشكل البلورات والتوزيع الحبيبي لها تمتاز بأهمية كبيرة في عملية المقابلة وصنع اللباب الرملية .

كما أن تطبيق نظام (آيزو-ISO) على هذه الرمال لا يتطلب استخدام رقم نعومة الرمل (AFS) وإنما يستخدم معدل حجم حبيباتها ( ميكرون ) ولتحديد حجم وتوزيع حبيبات الرمل لا بد من تصور شكل الحبيبات كونها ذات صلة بمساحة سطح الرمل وإن توزيعها يتحكم بنفاذية الغاز من القالب الرملي . وكلما زادت مساحة سطح الرمل زادت الحاجة لاستخدام المادة الرابطة في المزيج الرملي . ويفضل استخدام حبيبات الرمل المدورة أو شبه الدائرية عادة في صنع القوالب واللباب الرملية لقلة المساحة السطحية للرمل وبذلك تقل الحاجة لاستخدام مواد رابطة .  
ويعبر عن درجة نعومة الرمل (AFS) بعدد الفتحات في كل انج مربع من الغربيل الذي تمر منه حبيبات الرمل . ويمكن حساب (AFS) بأخذ (100) غم من الرمل الجاف ووضعها في مجموعة غرابيل قياسية . وتحديد وزن الرمل في كل غربيل وضرب ذلك الوزن × رقم الغربيل الذي يكون فوقه . وجمع حاصل الضرب في كل حالة وقسمة الناتج على (100) يمكن معرفة درجة النعومة كما في الجدول رقم (3) .

إن رقم النعومة (AFS) لرمال السيليكا تتراوح بين (50-60) عادة وإن أفضل توزيع لحجم الحبيبات هو حين تتوزع على (3-5) غرابيل في كل منها (10%) فأكثر من الوزن الكلي .

[Foseco Handbook 2000]



### مواصفات خبث الحديد :-

يعرف الخبث بأنه الناتج العرضي في عمليات صهر المعادن والسبائك وتنقيتها . حيث يتجمع عادة فوق سطح المعدن المصهور لقلته كثافته مقارنة بكثافة المعدن . ويزال عادة قبل صب المعدن لمنع دخوله القوالب مع المعدن . ويبرد أما بالماء وهو المفضل أو بالهواء ويجمع عادة لينقل مع النفايات للتخلص منها . وتعتمد الخواص الفيزيائية للخبث على تركيبه ودرجة الحرارة . وتعتمد كثافة الخبث بشكل كبير على تركيز الأكاسيد الثقيلة فيه . حيث يتكون الخبث من أكاسيد السيليكون ( $\text{SiO}_2$ ) كثافته (2.26 غم/سم<sup>3</sup>) و ( $\text{MgO}$ ) كثافته (3.65 غم/سم<sup>3</sup>) و ( $\text{FeO}$ ) وكثافته (5.7 غم/سم<sup>3</sup>) و... الخ.

إن الكثافة الاعتيادية للخبث تتراوح بين (2.4-3.0) غم/سم<sup>3</sup> أما لزوجة الخبث السائل فتتغير حسب تركيبه ودرجات الحرارة حيث تقل لزوجة الخبث بشكل مباشر مع زيادة درجة حرارة الخبث وحالته وعند إزالة الخبث من سطح الحديد المنصهر يفضل تبريده بالماء ليكون فعالاً لان تبريده بالهواء يضعف خواصه السمنتية [Clarkson U.-CE 453- 2005] .

### القسم العملي

#### التحضير للعمل :-

تم في سياق هذا البحث مجموعة من الأعمال التحضيرية أهمها :-

- استلام خبث الحديد موضوع البحث وتحضيره للاستعمال وذلك بطحنه للحصول على النعومة المطلوبة وحسب تدرج الحبيبات وكما مبين في الجدول رقم (2) حيث كان الخبث على شكل قطع تصل أبعادها حوالي (20-70) ملم وتم تكسيروها وطحنها .

- غريلة مسحوق الخبث الناتج من الطحن لمعرفة أحجام الحبيبات وكما مبين في الجدول رقم (2) .

- وزن كل حجم من حبيبات الخبث لتحديد نسبة كل منها في المسحوق في ميزان حساس .

- خلط مكونات مسحوق الخبث بعد وزنها جيداً لغرض استخدامها في مزيج رمل اللباب . وكان مجموع أوزانها (500غم) .

- غريلة الرمل - رمل ارضمه - وتحديد تدرج حبيباتها وكما في جدول رقم (3) باستخدام مجموعة من الغرابيل وميزان حساس .

- فحص الأجهزة المستخدمة في العمل والتأكد من صلاحيتها للاستعمال وهي خلاطة الرمل ، جهاز فحص النفاذية ، جهاز فحص مقاومة الانضغاط .

- البدء بتحضير الخلطات وعينات الفحص وبالنسب المحددة وكما مبين في الجدول رقم (4) .

- إجراء الفحوصات المطلوبة ، وهي فحوصات النفاذية ومقاومة الانضغاط في الحالة الرطبة والجافة

## المواد والأجهزة المستخدمة :-

إن المواد المستعملة في البحث هي رمال السيليكا وخبث الحديد والطين ( البنتونايت ) والماء والمبينة خواصها في الجداول المرقمة (2و3) .

أما أهم الأجهزة المستخدمة فهي :-

- جهاز تحضير وطحن الخبث الخام .
- الغرابيل الميكانيكية الهزازة .
- ميزان حساس .
- جهاز الخلاط.
- جهاز دك العينات .
- جهاز قياس نفاذية العينات .
- جهاز فحص مقاومة الانضغاط .
- فرن التجفيف الكهربائي.

وشملت إجراءات البحث طحن الخبث الخام وتحضيره بالمواصفات المطلوبة المبينة في الجدول رقم (2) وتصنف حجوم حبيباته وحبيبات رمل السباكة المستعمل باستعمال مجموعة الغرابيل القياسية المبينة في الشكل رقم (1) بموجب المواصفات البريطانية (BS-410/1976) والميزان الحساس نوع (Mettler pn /2 / 0) .

ولغرض تحضير المزيج الرملي المطلوب لأغراض البحث استخدم جهاز الخلاط المختبري الذي تضاف فيه المواد الصلبة أولاً وتخلط لوحدها مدة (3-5) دقيقة يضاف بعدها الماء ويستمر الخلط بعد ذلك للحصول على المزيج المطلوب .

تصنع نماذج الفحص القياسية بأبعاد (Ø50 × 50) ملم من المزيج الناتج باستعمال قالب معدني خاص . ويتم فحص نفاذية الغاز أولاً ثم فحص مقاومة الانضغاط ( في الحالتين الرطبة والجافة ) بعد ذلك .

إن المعادلة العامة لقياس النفاذية يمكن التعبير عنها كما مبين :-

$$P = (v \times h) / (p \times a \times t)$$

حيث أن :-

P = رقم النفاذية .

v = حجم الهواء المار خلال النموذج ( مليلتر ) أو (سم<sup>3</sup>) - 2000 سم<sup>3</sup>.

h = ارتفاع النموذج المفحوص ( سم ) - 5 سم .

p = ضغط الهواء أثناء مروره بالعينة ( غم / سم<sup>2</sup> ) .

$a =$  مساحة مقطع النموذج (سم<sup>2</sup>) - 19.52 (سم<sup>2</sup>) .

$t =$  الزمن اللازم لمرور الهواء خلال العينة (دقيقة) .

أما مقاومة الانضغاط فيتم فحصها بجهاز الفحص الذي يحتوي مقياسين أحدهما لمقاومة الضغط الرطب وأعلى حد قراءة له (1.3) كغم / سم<sup>2</sup>. والآخر للحالة الجافة ولحد قراءة (6.5) كغم / سم<sup>2</sup>.

### خطوات العمل :-

بعد أن تم تحضير المواد المستعملة في البحث والمذكورة في بداية الفقرة 2-2 والواردة مواصفاتها في الجداول (1-2-3) قمنا بتحضير المزيج الرملي في كل حالة ثم تحضير نماذج الفحص منها ابتداءً من نماذج بدون إضافة الخبث ثم بإضافة النسب المبينة في الجدول رقم (4) تباعاً وكانت أوزان كل خلطة ثابتة (400) غم كما في الجدول رقم (4) كما أن نسبة البنتونايت والماء المضاف كانت ثابتة أيضاً ، 24 غم لكل منها في كل خلطة .

ثم بدأت إضافة نسب من الخبث (10,20,30,40) % على التوالي حيث مثلت المجال الخاص بالبحث وصنعت من كل منها عينات قياسية لفحص النفاذية ومقاومة الانضغاط الرطب . ويحتوي الجدول رقم (5) على نتائج تلك الفحوصات .

أما في الحالة الجافة فقد تم تجفيف النماذج المصنعة في فرن خاص لمدة (75) دقيقة في درجة حرارة (150م°) وبعد ترك العينات المجففة لتبرد تم فحص النفاذية ومقاومة الانضغاط في الجهاز المذكور وهو الوحيد المتوفر في المختبر وكانت النتائج كما في الجدول رقم (6) حيث أمكن تحديد مقاومة الانضغاط الجاف بدون استخدام الخبث وكذلك عند إضافة (10)% خبث . ولم يمكن تحديدها في النسب الأعلى بسبب محدودية قراءة الجهاز . علماً أن نتيجة فحص النفاذية في الحالة الأخيرة كانت ثابتة ولم تتجاوز (49) وحدة .

### نتائج البحث - Results

لقد كانت نتائج فحص مقاومة الانضغاط ونفاذية الغاز للمزيج الرملي كما مبين في الحالتين الرطبة والجافة جيدة وكما في الجدول رقم (5) وذلك عند استعمال النسب المبينة في الجدول رقم (4) من الخبث وبقية مكونات مزيج الرمل حيث :

- تحسنت مقاومة الانضغاط في الحالة الرطبة من 0.24 كغم/سم<sup>2</sup> بدون استخدام الخبث إلى 0.445 كغم/سم<sup>2</sup> عند نسبة خبث 40% - أي بزيادة إلى الضعف تقريباً.
- كما تحسنت نفاذية الغاز في الحالة الرطبة من 46 وحدة بدون الخبث إلى 77 وحدة باستخدام 40% خبث كما في الجدول رقم (5) .

- وتحسنت مقاومة الانضغاط في الحالة الجافة من 5.6 كغم/سم<sup>2</sup> بدون الخبث إلى (6.5) كغم/سم<sup>2</sup> عند بداية إضافة الخبث (10) % علماً انه لم يمكن الحصول على نتائج محددة لمقاومة الانضغاط في الحالة الجافة لأكثر من نسبة (10) % خبث لان أعلى قراءة لجهاز الفحص هي (6.5) كغم/سم<sup>2</sup>.
- ولعل من النتائج المهمة لهذا البحث هو تحقيق إمكانية استخدام خبث الحديد في تحسين مواصفات مزيج الرمال في الوقت الذي يشكل استخدامه فائدة كبيرة للبيئة .

## مناقشة النتائج - Discussion Of Results :-

لمناقشة نتائج البحث يجب النظر إليها من وجهات نظر فنية أو تكنولوجية واقتصادية وبيئية . فمن الناحية الفنية أدى استخدام مسحوق خبث الحديد بالحجوم المناسبة لحجوم حبيبات رمال السيليكا المستعملة إلى تحسين خواص المزيج الرملي كما مبين في الجدول رقم (5) في الحالة الرطبة باستعمال الخبث وزيادة قيم مقاومة الانضغاط ونفاذية الغاز كلما زادت نسب الخبث المستعملة , ويعود السبب في ذلك إلى أن الخبث بخواصه الإسمنتية - الزجاجية يلعب دوراً مهماً كمادة رابطة إضافية في المزيج الرملي . كما تحسنت الخواص الجافة أيضاً وبذلك تحققت الفائدة الفنية جراء استخدام مسحوق الخبث في المزيج الرملي . وهذا أدى إلى مضاعفة مقاومة الانضغاط تقريباً عند بلوغ نسبة الخبث في المزيج 40% من وزن رمل السيليكا المستعمل في الحالة الرطبة في حين ازدادت في الحالة الجافة عند إضافة (10)% و (20) % خبث ولم يمكن تأشير زيادتها بالتحديد لأكثر من هذه النسب كما يتضح في الجدول رقم (6) .

ومن الناحية الاقتصادية , فان المصادر العلمية تشير إلى استعمال (0.850-1.200) كغم من رمل السيليكا لكل طن من المصبوبات الحديدية وان كلفة رمل السيليكا المستعمل تعادل (50) دولار أمريكي / لكل طن مسبوكات حسب المصادر البريطانية وهو ما يقارب (50) دولار أمريكي / لكل طن من رمل السيليكا وعند التعويض عن رمل السيليكا بخبث الحديد فان ذلك يعني أن طن مسحوق الخبث الذي استعويض به عن الرمل هو نفس المبلغ - أي (50) دولار أمريكي للطن الواحد من الخبث . وإذا علمنا أن النقص في كميات الرمال أمر حتمي أثناء استعماله في إنتاج المسبوكات سواء كغبار أو نفايات رملية وغيرها , فانه يجب التعويض عنه برمال جديدة . وفي حالة استخدام الخبث بدلاً من 40% من الرمال فان ذلك يحقق مردوداً اقتصادياً واضحاً يزيد عن 20 دولار أمريكي لكل طن مسبوكات . علماً أن كلفة تحضير الخبث عالمياً تتراوح بين (3-7) دولار أمريكي / لكل طن خبث - حسب مصادر أمريكية متعددة . وهذا يعني أن قيمة الخبث ازدادت أكثر من ثلاثة أضعاف كلفتها عند استخدامها في مزيج الرمل . أما من الناحية البيئية فان تكون الخبث أمر لا مفر منه عند صهر المعادن , ولكون الخبث ملوث بيئي فان توجيه استخدامه في مجالات نافعة تحقق سلامة البيئة من تأثيراته الضارة فضلاً عن تكاليف نقله للتخلص منه . ومن هنا يمكن القول أن إنشاء وحدة تحضير الخبث في المسابك - خاصة ذات الإنتاج الواسع - يعود على تلك المسابك بالفائدة حيث يمكن استخدام الحجوم الناعمة منه في مزيج رمل السباكة والحجوم الكبيرة في استعمالات أخرى مثل الإنشائية وغيرها.

**الاستنتاجات - CONCLUSIONS :-**

من خلال نتائج هذا البحث يمكن التخلص من العوامل الملوثة للبيئة التي يسببها خبث الحديد الناتج من المسابك بالاستفادة منه في تحسين خواص مزيج رمال السباكة بدلا من طرحه في البيئة حيث أمكن زيادة النفاذية في الحالة الرطبة للمزيج الرملي بنسبة حوالي (70) % عما كانت عليه بدون إضافة الخبث كما إن مقاومة الانضغاط الرطب ازدادت إلى ضعفها عند بلوغ نسبة خبث (40) % كما لاتخفى زيادة مقاومة الانضغاط الجافة في حالتي نسبة خبث (10,20) % كما يتضح من الجداول (5,6) وعلى ضوء ذلك يصبح من المناسب إنشاء وحدة تكسير الخبث مناسبة في كل مسبك أو مجمع تعديني لغرض تكسير وطحن الخبث والاستفادة منه في أغراض عدة منها الناعمة في المزيج الرملي والأكبر حجما (5-19) ملم في الاستخدامات الإنشائية في نفس مواقع تكون الخبث دون الحاجة إلى تكاليف نقله إلى أماكن خارج المسبك .

**جدول رقم (1) تصنيف رمال السباكة حسب حجم حبيباتها**

الرقم	حجم الفتحات (ملم)	الفصيلة	تسمية فصيلة الرمل	حجم الحبيبات (ملم)
1	(0.4,0.63,1)	063	كبير الحجم	1.0-0.4
2	(0.315,0.4,0.63)	04	خشن جدا	0.63-0.315
3	(0.4,0.315,0.25)	0315	خشن	0.4-0.25
4	(0.315,0.25,0.16)	025	متوسط	0.315-0.16
5	(0.1,0.16,0.25)	016	ناعم	0.25-0.10
6	(0.063,0.1,0.16)	01	ناعم جدا	0.16-0.063
7	(0.063,0.05,0.01)	0063	اكثر نعومة	0.10-0.05
8	(0.0063,0.005, غبار ناعم)	005	دقيق النعومة	<0.05 (اقل من)

**المصدر :- Prof.N.P.Dubinina Steel Casting Handbook Moscow 1961.**

**\*\* Gost 2138-56 المواصفة الروسية**

**جدول رقم (2) نتائج غربلة الخبث المطحون المستعمل في البحث**

التسلسل	رقم الشبكة	فتحة المنخل / ملم	الكمية المتبقية فوق كل منخل / غم	نسبة التجمع
1	3	2.0	0.143	
2	5	1.7	0.048	0.144
3	10	1.0	4.231	21.155
4	20	710	7.342	73.42
5	30	500	12.216	244.33
6	40	350	20.012	600.36
7	50	250	26.212	1048.48
8	70	150	16.673	833.65

9	100	106	5.759	403.13
10	220	75	2.533	253.3
11	300	53	1.022	224.84
12	330	الوعاء الأخير	2.171	651.3
			المجموع 99.371	المجموع 4354.089

درجة نعومة الخبث =  $4354.089 = 43.816$

99.371

جدول رقم (3) نتائج غربلة الرمل ارضمة المستعمل في البحث

نسبة التجمع	الكمية المتبقية فوق كل منخل (غم)	فتحة المنخل (مم)	رقم الشبكة (الغربيل)	التسلسل
	0.166	2.0	3	1
0.156	0.052	1.7	5	2
24.045	4.809	1.0	10	3
71.720	7.172	710	20	4
251.620	12.581	500	30	5
590.430	19.681	350	40	6
1095.840	27.396	250	50	7
898.450	17.969	150	70	8
335.160	4.788	106	100	9
237.100	2.371	75	220	10
25.080	0.114	53	300	11
835.500	2.785	الوعاء الأخير	330	12
المجموع 4365.10	المجموع 99.884			

درجة نعومة الرمل =  $4365.10 = 43.712$

99.861

جدول رقم (4) مكونات مزيج الرمل المستعمل مع الخبث

وزن الماء (مللتر (غم))	وزن البنتونايت (غم)	وزن الخبث (غم) ونسبته	وزن الرمل (غم)	وزن الخلطة (غم) ما عدا الماء	رقم الخلطة
24	24	0	376	400	1
24	24	37 - (10%)	339	400	2
24	24	74 - (20%)	302	400	3
24	24	111 - (30%)	265	400	4
24	24	150 - (40%)	226	400	5



جدول رقم (5) نتائج فحص مقاومة الانضغاط الرطب ونفاذية الغاز

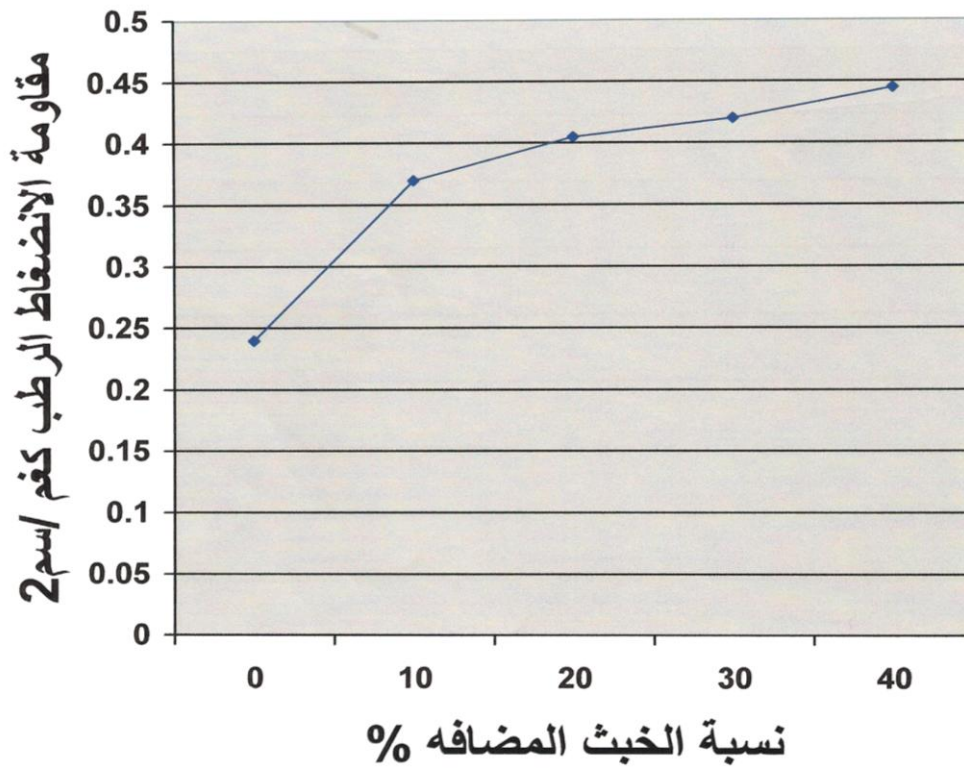
رقم الخلطة	نسبة الخبث المضاف %	النفاذية الرطبة		مقاومة الانضغاط (كغم/سم <sup>2</sup> )	
		القراءات	المعدل	القراءات	المعدل
1	%0	47 45	46	0.20 0.28	0.24
2	%10	64 73	68	0.36 0.38	0.37
3	%20	78 70	74	0.40 0.41	0.405
4	%30	73 77	75	0.40 0.44	0.42
5	%40	74 79	77	0.43 0.46	0.445

جدول رقم (6) نتائج فحص مقاومة الانضغاط الجاف ونفاذية الغاز

رقم الخلطة	نسبة الخبث المضاف %	النفاذية الجافة	مقاومة الانضغاط الجاف (كغم/سم <sup>2</sup> )
1	%0	49 49	5.6
2	%10	49 49	6.5
3	%20	49 49	أكثر من 6.5
4	%30	49 49	أكثر من 6.5
5	%40	49 49	أكثر من 6.5

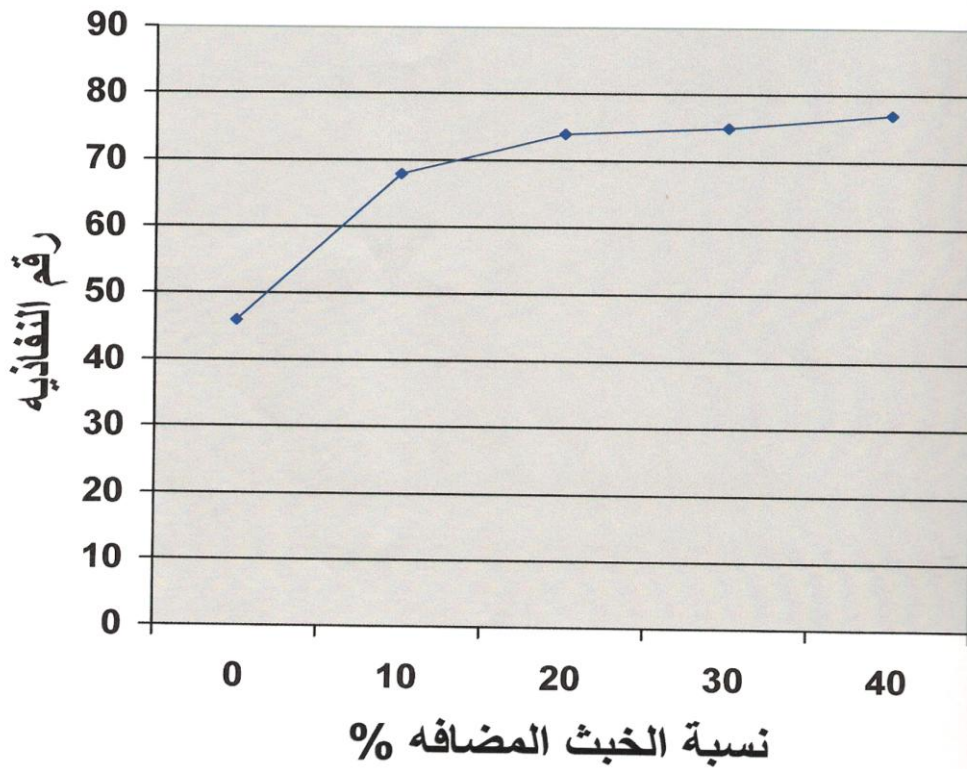


شكل رقم (1) مجموعة الغرايل الميكانيكية المستخدمة في الفحص حسب المواصفة البريطانية (BS 410/1976)



شكل رقم (2) العلاقة بين نسبة الخبث ومقاومة الانضغاط الرطب





شكل رقم (3) العلاقة بين نسبة الخبث ورقم النفاذيه في الحالة الرطبة

#### REFERENCE:-

- -Australian steel mill services PTY.product data sheet- Tech. services- Rev.4,ABF 259 and Rev.0,ABF 225- 2006.
- -Brantz .H. Cement Limited . Australian Slag Association.Australia Sep 1990.
- -Cen.y.development of disposal and application of iron and steel slag-Iron and Steel Vol.29 No.5- 1994.
- Cherry solomol slag- iron and steel- USA 1996.
- Clarkson university-CE 453-553 Properties and performance of concrete materials-properties of slag Neithalath,Fall , 2005.
- FHW Home- Material Group –Blast furnace slag – USA 1990.
- Foseco Ferrous Foundryman's Handbook-Oxford- 2000.
- Hendrik G.Van OSS-.US geological survey minerals, year book - slag iron and steel – 2003 .
- Iron and steel slag specialist (703) 648 mineral commodity sunnaries-Jan. 1996.

- Kamal I.et.al -6th International Conference on concrete tech.For aggregate for developing countries.Amman- 2002.
- Klarkson University Neithalath fall Properties of slag – 2005.
- Marizane.Y.Ozturk,Bmetals - Slag's and Glasses.High temp.properties.Vol.30 B 1999.
- National research council Canada-blast furnace slag – 2005.
- Portland cement association – slag. Iron and Steel Monitor vol.14 No.5 may 2004.

• استخدام خبث الحديد في تحسين خواص الخرسانة الكونكريتية -

• - مركز بحوث البيئة - د.خضير جاسم محمد وآخرين - 2008

• سلوك الخرسانة المصنوعة من مخلفات معمل الحديد والصلب - البصرة-

• د.حسن حميد- مجلة الهندسة والتكنولوجيا العدد/5/ 2004.

## المسكن المستدام بين محددات البيئة واعتبارات التصميم

د. عمر حازم خروقة

مدرس - قسم الهندسة المعمارية

كلية الهندسة . جامعة الموصل

### الملخص

يمثل هدف الاستدامة واحداً من أهم الأهداف التي يسعى المعمارون اليوم إلى تحقيقها، ويبرز العامل الاقتصادي ليحتل الصدارة ضمن مجموعة العوامل الموصلة إلى هذا الهدف، إذ يظهر تأثير هذا العامل بوضوح أكثر في مشاريع الإسكان مقارنة بالأنواع الأخرى من الأبنية، ومن خلال ذلك، فقد اعتمدت عدة محاولات وتجارب في مجال الإسكان الاقتصادي منخفض الكلفة في أماكن مختلفة من العالم، وارتبطت هذه المحاولات بجوانب عديدة ذات صلة بموضوع تحقيق الاقتصادية الممكنة للمسكن على كافة المستويات، وعلى الرغم من المحاولات العديدة التي تم اعتمادها على المستوى المحلي لوضع خطوط عامة لتوجهات الإسكان الاقتصادي فإن النتائج لم تكن بالمستوى المطلوب خاصة إذا ما نظرنا إلى الموضوع ضمن محددات البيئة المحلية واعتباراتها المناخية القاسية.

يتناول هذا البحث شروط المسكن المستدام ضمن محورين، الأول بيئي يراعي شروط البيئة المحلية والثاني منشئي يرتبط بتحديد أنماط ووسائل ومواد الإنشاء، ويمثل المحور الثاني الاعتبارات الخاصة بالتصميم من حيث طرق ووسائل التشييد، كما ويعطي المحورين مجتمعين من خلال تفرعاتهما مداخل مهمة لتحقيق هدف الاستدامة للمسكن.

اعتمد البحث الأسلوب الوصفي التحليلي لعدة نماذج سكنية اقتصادية منفذة في أماكن مختلفة من العالم وأعطى تقييماً لإمكانية الاستفادة منها محلياً.

## SUSTAINABLE HOUSE BETWEEN ENVIRONMENT DETERMINERS AND DESIGN CONSIDERATIONS

### ABSTRACT

The aim of sustainability represents one of the most important aims that most architects sought for achieving it. Thus, the economical factor appears to have the priority within the set of factors leading to this aim, where the effect of this factor appears much clearly in housing projects in comparison to other types of buildings. Therefore, many attempts and experiments were adopted in the field of economical low cost housing in different places of world. These attempts were associated with many aspects concerning the subject of achieving the possible economy of house of all levels.

In spite of the numerous attempts that were adopted on the local level for putting general lines for the economical housing directions; the results were not in the desired level especially if we look at the subject within the determiners of local environment and their hard climatic considerations.

This research deals with the conditions of sustainable house within two pivots; the first is environmental that looks after the conditions of local environment and the second is constructive where it is related to determine the modes, devices and constructional material. The second pivot represents the considerations concerning the design regarding the methods and devices of construction. Thus, the two pivots together throughout their subdividing give important stages for achieving the aim of sustainability of house.

The research depends on the analytical descriptive technique for several economical executive housing samples in different places of world and gives and evaluation of the possibility of getting benefit of them locally.

### مقدمة:

لقد تزامنت حاجة الإنسان المستمرة إلى المسكن مع حاجته لتأمين الجانب الاقتصادي ومواجهة الظروف الصعبة، فكان أن جاءت المساكن الأولى بسيطة للغاية ثم ما لبثت أن تعقدت شيئاً فشيئاً مع تطور الزمن وازدياد الحاجات الإنسانية، ولكن المصممين تمكنوا من التكيف مع هذا الجانب لتأتي المساكن متوازنة بين تحقيق ناحية وظيفية ملائمة وكلفة معقولة يراعى فيها الجانب الاقتصادي، فضلاً عن اعتماد طرق ووسائل مناسبة للتشييد مع ضرورة التكيف مع البيئة واعتباراتها المختلفة، ومن خلال مجمل الجوانب السابقة تظهر إمكانية تحقيق التواصل

والديمومة للمسكن ضمن إطار مفهوم الاستدامة بتوجهاته المختلفة، ومن هنا فقد مثل موضوع المسكن المستدام **المشكلة العامة للبحث**.

وخلال النصف الثاني من القرن العشرين ظهر انطباع بوجود علاقة مؤثرة بين توجهات معمارية معينة وبين مشاريع الإسكان في دول العالم الثالث، وبرزت مشكلة عدم قدرة الدول على تأمين العدد الكافي من المساكن اللازمة لإيواء الأعداد المتزايدة من السكان وخاصة في المدن المكتظة والكبيرة، ولقد ظهرت جملة مفاهيم مرتبطة بالإسكان منخفض الكلفة، وكانت تلك المفاهيم تحمل سمة مشتركة في كل المناطق التي ظهرت فيها تمثلت بالسعي نحو تحقيق هدف التواصل للمسكن ضمن جوانب عديدة منها الجانبين البيئي و المنشئي، فظهرت المشكلة الخاصة للبحث وتمثلت بـ : **النقص المعرفي فيما يتعلق بتقييم إمكانية تطبيق تجارب عالمية ناجحة لمساكن مستدامة ضمن البيئة المحلية باعتباراتها المناخية والمنشئية**.

لقد ركّز البحث على حقيقة مفادها، أنه في الدول النامية، وفي تلك الدول التي تعاني من عجز في الرصيد السكاني و في إنتاج الوحدات السكنية، يمكن ملاحظة تكيف في إنشاء هذه الوحدات بما بلّغ الظروف الاقتصادية التي تمر بها تلك الدول، وجاء هذا التكيف بصيغ عديدة منها ما هو بيئي ومنها ما هو منشئي ومنها ما هو وظيفي، وسنكتفي في هذا البحث بتحليل الجوانب البيئية والمنشئية نظرا لتشعب الموضوع.

### أهداف البحث:

- لقد حدد البحث هدفين واضحين حاول تحقيقهما وتمثلا بما يلي:
- الكشف عن التجارب العالمية المعتمدة في مجال الإسكان الاقتصادي (المستدام) فيما يتعلق بتحليل الجوانب البيئية والمنشئية.
- محاولة التوصل إلى سياق واضح لإمكانية تطبيق تلك التجارب على المستوى المحلي باعتباراته البيئية والمنشئية.

### فرضيات البحث:

لغرض التوصل إلى تحقيق الهدفين السابقين فقد تناول البحث الفرضيتين التاليتين:

-إن الوصول إلى تحليل الجوانب البيئية للمنظومة السكنية فيزيائيا يقودنا إلى التعامل مع ثلاثة جوانب أساسية تتمثل بـ: (طبيعة البيئة التي نفذ فيها المشروع، مدى توافقها مع البيئة المحلية، وإمكانية التحويل في المشروع لكي يتلاءم مع طابع العمارة المحلية).

2-يمكن اعتبار التكنولوجيا المطروحة من خلال تحليل المشاريع ملائمة لتحديد سياق محلي ناجح منشئيا في مجال عمارة المساكن المستدامة إذا كانت هذه التكنولوجيا ايجابية في علاقتها مع ثلاثة عوامل هي: (توفر التقنية على المستوى المحلي، توفر المواد، والجانب التعبيري من

حيث الانسجام مع طابع العمارة المحلية لتحقيق بعض المفاهيم الاجتماعية كالعزل والخصوصية والتوافق مع المجاورات ضمن بيئة حضرية معينة).

### المسكن المستدام مطلب للجميع:

إن الغاية المباشرة للسكن منخفض الكلفة هي تحسين المأوى وإحياء الحالة المعيشية للفقراء والمحرومين في أماكن متعددة من العالم وخاصة في البلدان النامية، حيث توجد أعداد كبيرة من الذين لا يستطيعون توفير مأوى مناسب وتفتقد معيشتهم للخدمات الضرورية المرتبطة بالسكن، كما أن هذه الفئة لا تملك إلا الخيار في أن تعيش في ظل ظروف غير مقبولة من حيث الاكتظاظ السكاني وانعدام الأمن والنظافة والبيئة الصحية السليمة ( المدينة العربية ، 1987 ).

ومن خلال ذلك فإن السعي إلى تحقيق هدف المسكن المستدام يعالج مشكلة أن الكثير من محدودي الدخل غير قادرين على تحسين ظروف معيشتهم بسبب افتقارهم للدعم الحكومي مع ثبوت دخولهم التي هي أصلاً غير كافية، مما يتطلب إستراتيجيات فعالة تضعها الحكومات وتكون ذات مرونة عالية لأنها تتعامل مع طبقة من الناس تمثل اليد العاملة التي يظهر تأثيرها الواضح على السياسة الاقتصادية ( Suyono & Juliman , 1999 , P.20 ). كذلك فإن مشروع الإسكان بشكل عام يتطلب توفير الأرض الملائمة، ثم إعداد التصاميم المطلوبة على مستوى الوحدة السكنية المفردة ثم على مستوى المشروع السكني ككل، مع مراعاة استيعاب المشروع لأكبر عدد من السكان ضمن ظروف معيشية ملائمة ( Aranya , 2001 , P.21 ).

إن الناحية العلمية والتكنولوجية تعتبر مؤثرة في حقل الإسكان بشكل عام، وهي مؤثرة في الجزئيات المرتبطة بالإسكان الاقتصادي (المستدام) كونه يمثل إحدى السياسات المتبعة لإسكان أعداد كبيرة من البشر خاصة في الدول النامية والفقيرة، وإن تلك الدول التي أصبحت اليوم مكتظة إلى حد كبير باتت تعاني من عجز هائل في إمكانية توفير المساكن لهذه الأعداد المتزايدة من السكان، ولقد رفعت الأمم المتحدة شعار تحقيق المأوى للجميع وتبنت إستراتيجية فعالة خلال العقد الأخير ممن القرن العشرين من أجل تحقيق هذا الشعار، إذ أن توفير المأوى لكافة المجاميع البشرية هو مطلب إنساني ينبغي تحقيقه ( Mathur , 1992 , P.1,12 ).

ويؤكد (Parry-2000) بأن تحقيق المسكن المستدام يمثل طموح الكثيرين في أغلب مناطق العالم، خاصة في تلك الدول التي تفتقر إلى مقومات تؤها لها لأن توفر السكن الملائم لمواطنيها تحت ظروف طبيعية، وإن من أهم العقبات التي تقف أمام توفير هذا النوع من المساكن الاقتصادية رخيصة التكاليف هي توفير المواد البنائية المناسبة بأسعار زهيدة، ولا يمكن تحقيق هذا الأمر إلا من خلال سياسات منظمة للعمل والإنتاج أو للاستيراد خاصة في الدول التي لا

تمكنها موادها الأولية المتوفرة محليا" من تحقيق السكن العصري المتطور ضمن البيئة الحضرية الحديثة مما يتطلب البحث عن منافذ إضافية من الخارج ( Parry , 2000 , P.3 ).

### الدراسات السابقة حول موضوع الإسكان الاقتصادي (المستدام):

لقد ظهرت الكثير من الدراسات السابقة التي أشارت إلى موضوع الإسكان الاقتصادي (المستدام)، وكانت هذه الدراسات في أماكن مختلفة من العالم وبشكل خاص في دول العالم الثالث، وركزت على جوانب مختلفة ذات صلة بتحقيق الجانب الاقتصادي في المسكن سواء من حيث التعامل مع الكثافات السكانية العالية ومشاكل خدمات البنية التحتية، أو من حيث توفير قطع الأراضي الخاصة وغير ذلك من الجوانب الأخرى، ولكن المهم هو تناول بعض الدراسات المرتبطة بالجانب البيئي و المنشئي سعيا وراء تحقيق هدف الاستدامة للمسكن بما يخدم توجه البحث.

ففي دراسته : ( Low Cost Housing In The USSR ) يتناول (Morton-1976) مشكلة السكن في الإتحاد السوفيتي السابق، إذ أدخل الإحصاءات الرقمية الخاصة بأعداد القطع السكنية والمشاريع المنفذة ثم المساحات المخصصة للسكن للفترة من 1950 - 1973 في محاولة للحصول على العجز الحقيقي في السكن ثم تحديد الاحتياجات المستقبلية في ضوء النمو السكاني المتزايد على امتداد الرقعة الواسعة لذلك البلد، وقد تطرق Morton إلى طرق الإنشاء التقليدية وضرورة الاستفادة منها وتطويرها لتلائم التقنيات الحديثة وتنسجم مع تطور التكنولوجيا وظهور الأساليب البنائية الحديثة مع تقييم إمكانية الديمومة والتواصل للمساكن .

إن عملية تخطيط البناء واستخدام الوحدات القياسية في التصميم والإنشاء والتصنيع إنما تمثل إحدى الطرق الرائدة في السيطرة على الكلفة خاصة في المشاريع السكنية التي تتشابه فيها الوظائف ( Morton , 1976 , PP.110 - 111 ). ومن خلال تناوله لنماذج من دور سكنية ضمن مشاريع إسكان منفذة في الإتحاد السوفيتي السابق، فقد عرض (Morton) تحليلا لتلك النماذج تطرق فيه إلى المقترحات والحلول الخاصة بضرورة جعل المسكن اقتصادي إلى أقصى حد ممكن خاصة عندما يرتبط الأمر بإسكان ذوي الدخل المنخفض الذين أصبحوا اليوم يشكلون عبئا كبيرا في مساكنهم القديمة والمتهترئة ضمن المناطق القديمة للمدن، وإن عملية جعل المسكن اقتصادي لا تعني التقليل من كفاءة ذلك المسكن بل هي توفير لظروف العيش ضمن حدود دنيا مقبولة، وقد تطلع (Morton) إلى ضرورة تأمين السكن الملائم للأعداد الكبيرة من طالبيه من خلال تخفيض كلفة البناء وبالتالي تحديد أسعار المساكن داخل المدن.

وفي دراسة (Davis-1976) ( Low- Cost Self – Help Housing In Rural Philippines ) تمت الإشارة إلى تقليل كلف البناء باستخدام ما يتوفر من مواد طبيعية تلائم

الحالة المناخية السائدة وظروف الموقع، ومن خلال تقييمه لأحد المشاريع السكنية المنفذة في الريف الفلبيني قام ( Davis ) بتحليل بنية تلك المساكن ذات الكلف الواطئة واستنتج أن الحل الأمثل هو استخدام المواد المحلية المتوفرة واقتراح نموذجاً "مثالياً" مستداماً لطريقة الإنشاء وطبيعة المواد المستخدمة حسب المتطلبات البيئية للمنطقة، وحتى تلك الوظيفية المنسجمة مع طبيعة المجتمع الريفي الذي يفتقر في وضعه الحالي إلى أبسط الخدمات الأساسية الخاصة بمتطلبات السكن العصري من خدمات البنية التحتية فضلاً عن باقي النواحي التقنية البسيطة بما يؤمن الحد الأدنى من ظروف العيش الصحي الآمن (Davis,1976,p.69).

أما ( Haygreen-1976 ) فقد تناول موضوع استخدام مادة الخشب على شكل ألواح لبناء المساكن في بعض الدول النامية، حيث ذكر في دراسته:

( Wood – Base Panel Materials For Housing In Less Developing Countries ) بأن المواد البنائية المحلية الرخيصة تعد أهم مقومات الإنشاء الاقتصادي في الدول النامية في حالة توفرها، وقد ناقش (Haygreen) تقنيات إنشاء المساكن الريفية باستخدام مادة الخشب إذ غالباً ما يتم استخدام الطين كمادة أساسية للبناء الريفي، والمشكلة برأيه ترتبط بتقييم مدى كفاءة استخدام الخشب في البناء كمادة أساسية من خلال التطرق إلى التقنيات البنائية المستخدمة لهذه المادة فضلاً عن تأثير الظروف والعوامل المختلفة عليها من كافة النواحي بما لا يؤثر على مقاومتها وديمومتها، وإن من أهم المشاكل الرئيسة المرتبطة بموضوع الإسكان الاقتصادي (المستدام) هي مشكلة مواد البناء وتوفرها فضلاً عن أسعارها ثم ديمومتها وقابليتها على العزل والتحمل أو بمعنى آخر مدى كفاءتها العملية، إذ تعد الكثير من المواد البنائية غير كفوءة نظراً لما يظهر عليها من عيوب بعد مرور فترة زمنية قصيرة نسبياً على الاستعمال مما يزيد من معدل السليبيات المطروحة حول موضوع السكن الاقتصادي ( Haygreen , P.1050 , 1976 ).

وفي دراسته:

(Sand Encroachment On Lower – Cost Housing Development In Arid Areas)

أشار ( Akili-1976 ) إلى موضوع استخدام أنواع خاصة من الرمل كمادة أساسية في تطوير بناء المساكن الاقتصادية (المستدامة) في شبه الجزيرة العربية ومنطقة الخليج، حيث أكد على أن تزايد أعداد الأسر محدودة الدخل من الوافدين على هذه المنطقة سعياً وراء فرص للعمل يتطلب من الحكومات وضع سياسات فعالة لاحتواء أزمة السكن الناتجة عن ذلك، ومن خلال استعراضه لمشاريع سكنية قليلة الكلفة منفذة في فترات زمنية سابقة، أظهر



( Akili ) بعض النقاط السلبية التي بالإمكان تجاوزها خلال وضع الخطط الحالية والمستقبلية لتحقيق النجاح المطلوب، إذ أن طبيعة البيئة الصحراوية الجافة في هذه المنطقة توفر أنواعاً مختلفة من الرمال النقية التي تعد مواد أولية مهمة في بناء المساكن خاصة تلك التي تحمل الطابع التقليدي والشعبي، أو بمعنى آخر تلك المساكن الاقتصادية التي اعتبرت ناجحة في التجمعات السكنية المحدودة قرب المشاريع الصناعية وفي أطراف المدن والتي أصبحت اليوم تؤوي مئات الأسر من الوافدين على هذه المنطقة، وإن مادة الرمل النقي ذات المواصفات الجيدة فيما لو أحسن استغلالها لتصنيع مواد بناءية مميزة فأنها بالتأكيد ستمثل بديلاً ناجحاً لتلك المواد الدخيلة ( Akili , 1976 , pp.1304 – 1305 ).

كذلك هناك دراسة ( Wilson-1976 ):

( Modern Technology Provides Housing Economy And Safety )

التي تطرق فيها إلى استخدام التكنولوجيا الحديثة في مجال الإسكان من حيث تحقيق الناحية الاقتصادية وتوفير الاستمرارية والأمان، فلقد أصبحت أغلب المنشآت مكلفة مع تزايد الطلب على مواد البناء وتوسيع رقعة المدن وازدياد الأبنية والمرافق الخدمية والعامة، ولعل مشاريع الإسكان هي من أهم أنواع المشاريع ذات العلاقة المباشرة بدخل الأفراد، إذ بدأ السعي مع ظهور تقنيات ومواد بناءية حديثة نحو تقليل كلف المنشآت السكنية بما يجعل تلك المشاريع اقتصادية بالنسبة للجهات الممولة والمنفذة لها ثم للشاغلين فيما بعد، ومع ازدياد الطلب على المساكن ظهر توجه نحو استغلال تقنيات بناءية رخيصة بعدما وفرت التكنولوجيا المتطورة في مجال البناء والإنشاء إمكانات كبيرة وحلولاً ومواد جديدة أقل كلفة من المواد التقليدية السابقة المستخدمة في الأبنية بشكل عام وفي المساكن خاصة ( Wilson , 1976 , P.442 ).

أما ( Seaton & Vogel-1976 ) فقد تطرقا إلى نوعية خاصة من المساكن (المستدامة) منخفضة الكلفة من خلال إمكانية استخدامها كبديل ناجح للمساكن الاعتيادية في بعض الدول، وذلك في دراستهما التي حملت عنوان:

( The Mobile Home As A Source Of Lower Cost Housing ) إذ أن بعض

المشاريع الخدمية التي تقام في مناطق نائية ومعزولة تحتاج إلى نوعية خاصة من المساكن لخدمة العاملين فيها، وإن تلك المساكن الخاصة يجب أن تحمل المرونة اللازمة لنقلها من مكان لآخر فضلاً عن كونها قليلة الكلفة ولا تؤثر سلباً على ميزانية المشروع، ولهذه الأسباب تم استخدام المنازل المتحركة التي يسهل تحريكها حسب الحاجة والتي من الممكن استخدامها ضمن ظروف خاصة في موقع معين حتى في داخل المدينة، وإن هذه النوعية الخاصة من المساكن

المتحركة بالإمكان أن تساهم إلى حد ما في حل مشاكل السكن على الرغم من كونها تمثل حلاً مؤقتاً ولكنها على العموم قليلة الكلفة واقتصادية بشكل جيد (Seaton & Vogel, 1976, p.575). وناقش ( Bourne-1976 ) في دراسته:

#### ( Speed Wall: A Low Cost Insulated Concrete Wall System )

نوعية خاصة من التقنيات المنشئية المستخدمة في المساكن ذات الكلف الواطئة، إذ أن السياسات المتبعة في بعض المشاريع السكنية تضع مجموعة من القيود على العمل لأسباب متعددة، ومن ضمن تلك القيود تحديد المدة الزمنية لإنشاء المشروع مما يتطلب الإسراع في عملية التنفيذ بما لا يؤثر على نوعية المساكن المنتجة منشئياً بالدرجة الأولى، ومن هنا ظهرت أهمية استخدام أنواع خاصة سريعة التركيب من الجدران الكونكريتية العازلة ذات المواصفات التقنية الناجحة والتي تعتبر قليلة الكلفة مقارنة بالأنواع الأخرى المتوفرة، وأن هذه الجدران هي ألواح مسبقة الصب تنقل إلى موقع العمل بعد تصنيعها، وأن هذا الاستخدام لتقنية البناء الجاهز في الأبنية السكنية قد أثبت نجاحاً كبيراً في الدول الصناعية وفتح المجال لانتشارها واستخدامها في الكثير من الدول ( Bourne , 1976 , P.915 ).

#### اعتبارات البيئة المحلية:

سيتناول البحث نوعين من الاعتبارات الخاصة بالبيئة المحلية بما يخدم توجهه وكما يلي:

#### -الاعتبارات الخاصة بالبيئة المحلية مناخياً:

تمثل الاعتبارات القاسية للمناخ المحلي المتطرف في القطر العراقي جانباً مهماً ينبغي التعامل معه من قبل المصممين باهتمام بالغ، ومن الملاحظ أن أساس فكرة المعالجات المناخية واحد بالنسبة لمختلف المناطق الجغرافية من حيث محاولة إيجاد الجو الملائم للراحة الإنسانية والاختلاف هو في الشكل والتطبيق وأساليب المعالجات المعالجات المحلية الخاصة بعبادات وتقاليد العمارة في كل منطقة، وفي هذا الصدد يشير (الجوادي و النعيمي - 2001) إلى أن تقارب البيوت في العمارة التراثية المحلية يمثل أحد المسببات الرئيسة في جعل الأحياء السكنية ذات مناخ معتدل مختلف عن المناخ العام المحيط بالمنطقة، وأن ابتعاد المساكن عن بعضها البعض في المدينة المعاصرة - بسبب كبر مساحات الأراضي المخصصة لكل مسكن ودخول السيارة ووسائل النقل - ساهم في تغيير أبعاد المدينة ومسالكها (الجوادي و النعيمي، 2001، ص1).

كذلك فقد ذكر (هولي و جماعته - 1979) أن حواس الإنسان تساهم في إيجاد الشعور بالراحة ضمن بيئة معينة، وأن البيئة التي ينشأ فيها الإنسان هي الأكثر ملاءمة له للعيش حتى وإن ابتعدت (دونما تطرف) عن حدود الراحة المقبولة إنسانياً، وهنا يظهر مفهوم التكيف وكيف أن مشاعر الارتياح تجاه المناخ هي التي تنشئ الشعور بالراحة، ويجب من خلال ذلك أن تتوفر

في البيئة المعنية علاقات فيزيائية متناسبة بين الإنسان والبيئة التي يعمل ويتحرك ضمنها، كما أن التمييز بين الجانبين العاطفي (الشعوري) والعقلاني (التأملي) في حياة الإنسان يعد أمراً مهماً لتحقيق التوازن ضمن البيئة (هولي و آخرون، 1979، ص28).

### -الاعتبارات الخاصة بالبيئة المحلية منشئاً:

لما كانت العمارة المحلية نابعة من أسس وتقاليد البيئة المحلية وما يتوفر فيها من إمكانات فقد جاءت هذه العمارة متوافقة مع ما هو موجود ضمن هذه البيئة من مواد ووسائل تشييد تتوافق وتتسجم مع تلك المواد، وعلى هذا الأساس يتناول (التميمي - 1982) موضوع استخدام المواد المحلية في البناء من خلال إشارته إلى أن المناطق التي تمتاز بتوفر مواد طبيعية يمكن استخدامها في البناء والإنشاء تعتبر مناطق مكتفية ذاتياً في هذا الجانب، وضمن بيئتنا المحلية تستخدم الأحجار في المناطق الجبلية والأخشاب في المناطق التي تتوفر فيها، فضلاً عن استخدام أنواع من أخرى من مساكن القصب والبردي في الأهوار والمستنقعات، هذا مع أن توفر مادة الطين في جميع أنحاء العالم جعل منها واحدة من أكثر المواد الإنشائية استخداماً، إذ يستعمل الطين بطرق مختلفة ذات اقتصادية عالية في الإنشاء قياساً بالطرق الحديثة، وبانتشار العلم والمعرفة اتضحت لنا وحددت الخواص المتوخاة من هذه المواد ومدى نجاحها على كافة المستويات (التميمي، 1982، ص25).

كذلك فأن العامل المنشئي بالتوافق مع تحقيق الجوانب الاقتصادية كان له الدور المؤثر والفعال في هذا المجال، بمعنى أن حل المشكلة إنما يكمن في مساكن اقتصادية تراعي البيئة ومشيدة ضمن مواصفات منشئية مناسبة وتحقق الغاية الأساسية التي شيد المسكن لأجلها ألا وهي تلبية الاحتياجات الإنسانية المتزايدة لأطول فترة ممكنة بكفاءة عالية أديمومة المسكن ضمن العمر الافتراضي له.

### أسلوب التحليل:

لغرض التحليل سيتم التعامل مع نماذج منتخبة للدراسة وهي تمثل مشاريع عالمية مقيمة بنجاح ضمن البيئات التي شيدت فيها، وبالنسبة لطريقة التعامل مع هذه المشاريع ومناقشتها سيتم اعتماد الصيغ الوصفية من خلال تحليل كل مشروع ضمن كلا الجانبين البيئي والمنشئي سعياً وراء إعطاء تقييم لمدى توافقه مع البيئة المحلية في القطر العراقي، ومن خلال ذلك سيتم اعتماد استمارة خاصة لغرض التحليل الوصفي بما يخدم توجه البحث.\*

### مناقشة الأمثلة المطروحة للتحليل:

\* أنظر ملحق البحث.

## -المثال الأول: ما طرحه (Sangu-1976) حول استخدام تقنية القطع المكافئ المخروطي القشري:

الفكرة الأساسية لهذا النوع من المساكن مأخوذة من الأشكال الدائرية للمساكن البدائية التي استوطنتها الإنسان وكانت تمثل مجرد مأوى بسيط لتوفير الحماية ضد عوامل الطبيعة\* (شكل رقم 1)، والطرح الجديد الذي تناوله (Sangu) هو استخدامه لتقنية القطع المكافئ المخروطي القشري لتسقيف المخطط الدائري للمسكن، إذ استخدمت هذه التقنية لإنشاء أعداد من المساكن في الولايات المتحدة، وقد أوضح (Sangu) أنه بالإمكان استخدام عدة وحدات مرتبطة مع نفسها ضمن نفس التقنية لزيادة مساحة المخطط الأفقي للدار، ومن خلال تناوله للموضوع فقد طرح (Sangu) مسألة أن الشكل المقرب لهذه المساكن له مردودات ايجابية كثيرة فيما يتعلق بالجانب البيئي المناخي من حيث التعامل مع الظلال والعزل فضلا عن تقليل الضوضاء (Sangu, 1976, P. 1197) (شكل رقم 3).

## -المثال الثاني: ما تم طرحه من قبل كل من (Hurd-1997) و (South-2001) حول المساكن القشرية المنفوخة على شكل قباب:

جاء هذا الطرح ضمن نفس التوجه السابق ولكن باستخدام تقنية أكثر تطوراً، وفي هذا الصدد فقد أشارت (Hurd) إلى أن نوعية خاصة من المساكن المقامة كحلول سريعة في الولايات المتحدة الأمريكية يمكن الحصول عليها بأسعار اقتصادية جداً، وإن هذا المسكن في أسوأ حالاته يوفر مأوى مناسب للعيش لعائلة صغيرة، وتوفر هذه التقنية إمكانية الحصول على مسكن بمساحة أوسع وبنفس المواصفات كلما زاد حجم العائلة (Hurd, 1997, P.99) (شكل رقم 4)، وقد جاء طرح (South) للموضوع بعد عدة سنوات كمحاولة إضافة وتعديل على النموذج السابق بإدخال التكنولوجيا بشكل أوسع للتعامل مع عوامل أخرى كالعزل الحراري والصوتي وتحسين المظهر الخارجي للمسكن باستخدام مواد مناسبة لذلك (شكل رقم 5) وتتضح طريقة الإنشاء والتنفيذ لهذا النوع من المساكن بتهيئة الأرض كقاعدة مدورة ثم يتم استخدام طريقة النفخ لنوع خاص من البالونات التي تعمل على إيقاف الهيكل، ومن ثم يستند حديد التسليح الخفيف عليها، وتنتهي العملية برش كونكريت خفيف على الهيكل، ويكون هذا الكونكريت سريع التصلب، وبعد ذلك يفرغ البالون من الهواء وينقل للاستخدام في وحدة أخرى (South, 2001, P.8) (شكل رقم 6).

## -المثال الثالث: استخدام تقنية البناء الجاهز لمساكن من عدة طوابق:

\* يلاحظ ضمن نفس التوجه وجود قرية طينية قرب مدينة حلب في سورية استخدمت فيها المساكن المدورة ضمن المخطط الأفقي (شكل رقم 2).

في عام (1981م) ظهرت طروحات عديدة تدعو إلى إيجاد حلول منشئية وتصميمية ذات اقتصادية عالية مع تقدم التكنولوجيا واتساع مجالات الفهم والإدراك الإنساني وشمولية المشكلة على المستوى العالمي، وضمن هذا التوجه فقد ناقشت (Hurd-1981) تقنية متطورة لتسقيف المنشآت - ومنها الأبنية السكنية - من خلال استغلال التكنولوجيا المتطورة أثناء مرحلة الإنشاء بما يؤمن سرعة الإنجاز فضلا عن الاقتصاد في الكلفة مع مراعاة الجانب البيئي عند التعامل مع المخططات الأفقية والواجهات، وقد استخدمت هذه الطريقة الاقتصادية السريعة بنجاح كبير في مشاريع سكنية في الولايات المتحدة والمكسيك وفنزويلا وأندونيسيا، وتتألف هذه الطريقة من خمس مراحل إذ تقضي المرحلة الأولى باستخدام ألواح السقف والجدران على شكل مجاميع عند مستوى الطابق الأرضي مع توفير إمكانية رفعها في المراحل التالية، وبنفس طريقة عمل الرافعة الهيدروليكية يتم في المرحلة الثانية دفع ألواح الجدران بتحريكها من الوسط عن طريق رافعة خاصة مما يؤدي إلى ارتفاع ألواح السقف إلى مستوى الطابق الأعلى، وتستخدم في هذه العملية معدات ميكانيكية معقدة، وفي المرحلة الثالثة تتكامل عملية الدفع إلى أعلى إذ تنتصب ألواح الجدران للطابق السفلي وتستند عليها ألواح السقف والتي هي في نفس الوقت تمثل أرضية الطابق العلوي، ثم تأتي المرحلة الرابعة التي يكون استناد السقف العلوي فيها مؤقتا إلى أن تتكامل باقي المراحل لأن المعدات المستخدمة في هذه التقنية تبقى متحركة عند مستوى كل طابق، وفي المرحلة الخامسة والأخيرة تتكرر العملية بالنسبة للطابق الذي يلي وبنفس الطريقة السابقة إلى أن نصل عند مستوى الطابق الأخير إذ ترفع المعدات التي استخدمت كمساند ويرتكز المبنى باستقرار كامل

(Hurd, 1981, P.719) (شكل رقم 7).

#### -المثال الرابع: استخدام السقوف القشرية المنحنية:

جاء طرح (Castro et al.-1976) موضحا استخدام هذه الطريقة الاقتصادية في المكسيك على نطاق واسع، إذ وجد أن هذه السقوف ذات كفاءة عالية من حيث التعامل مع الشمس وتوفير الظلال وتصريف مياه الأمطار فضلا عن كفاءتها المنشئية، وقد تطرق (Castro) وجماعته بشكل تفصيلي إلى موضوع استخدام هذه الأنواع الخفيفة من السقوف على أساس أن طريقة التسقيف للمسكن تمثل خطوة مهمة من مراحل التحليل المنشئي للمبنى فضلا عن كونها تخضع لعدة عوامل تلعب دورا رئيسيا في تحديد المواصفات النهائية للمسكن (Castro et al. 1976, p.1276) (شكل رقم 8).

#### -المثال الخامس: استخدام التسليح بالخيزران:

في هذا المثال تطرق (Pakotiprapha et al.-1976) إلى موضوع كون الدول النامية تزداد فيها الحاجة إلى تطوير واستخدام مواد جديدة ذات كلف قليلة في البناء، إذ تستخدم المواد المحلية في تلك الدول كبديل ناجح عن المواد المستوردة من الخارج، ومن خلال ذلك فقد تم استخدام ألواح الخيزران في هذا المثال في بعض دول جنوب شرق آسيا ذات المناخ الاستوائي كمادة أساسية تلعب دوراً مهماً ضمن الجانب المنشئي للمبنى فضلاً عن ملاءمتها البيئية من حيث كونها مادة محلية مأخوذة من الطبيعة وليس لها تداعيات بيئية سلبية كالتلوث وغير ذلك أي أنها صديقة للبيئة، بيد أن استخدام هذه المادة بصيغها التقليدية لازال يفتقر إلى الأساليب العلمية والتقنية التي تتطلب إدخال التكنولوجيا الحديثة لتوسيع ذلك الاستخدام، كما وان تطوير استخدام هذه المادة الجديدة يتطلب إجراء الدراسات اللازمة لتحقيق أفضل استغلال ممكن لخصائصها والتي من بينها الميزات الاقتصادية العالية التي تتمتع بها (Pakotiprapha et al. , 1976 , p.1100 ( شكل رقم 9 ).

#### –المثال السادس: المساكن الريفية في الهند:

تناول كل من (Arockiasamy & Vijayaraghavan-1976) في هذا المثال نوعاً مميزاً من المساكن ذات الكلف الواطئة في الهند، وجاء هذا الطرح ضمن تحليل تمت مناقشته في (المؤتمر الدولي لمشاكل السكن - 1976)، وقد ذكر التحليل أن الجانب المنشئي لهذه المساكن تضمن استخدام الطابوق من خلال نظام الجدران الحاملة للثقل مع تسقيف جملوني مائل بكلا الاتجاهين وتغطية بالقرميد، وان ضرورة استخدام هذا الميلان بكلا الاتجاهين ترجع لكون المنطقة استوائية غزيرة الأمطار مما توجب مراعاة التصريف، والتقنية بسيطة للغاية وتوفر إنشاء وحدتين سكنيتين ضمن كل منشأ كما هو موضح في المخططات التوضيحية (Arockiasamy & Vijayaraghavan, 1976, p.184 ( شكل رقم 10 ).

#### –المثال السابع: مساكن مدورة بمواد تقليدية:

في هذا المثال ناقش (Mink-1976) استخدام نوع من الطابوق المحلي في بعض مناطق شمال ألمانيا لإنشاء مساكن صغيرة ذات مواصفات اقتصادية جداً، والفكرة مأخوذة من بيوت الاسكيمو في المناطق القطبية الباردة التي يستخدم فيها قطع من الجليد لتوفير الحماية والدفع ( Mink , 1976 . P.1087 )، ويلاحظ بأن الشكل الهندسي النهائي لهذا النوع من المساكن مشابه لما طرحه (Sangu-1976) في المثال الأول حول القطع المكافئ المخروطي القشري، إذ أن البناء بهذا الشكل يوفر قابلية عالية على تحمل التشوه تحت تأثير القوى المسلطة على المنشأ من الأعلى، وتتوضح طريقة التشييد من خلال الشكل رقم ( 11 ).

#### –المثال الثامن: استخدام المنشآت الخفيفة:

هذا المثال يوضح استخدام نوع من المنشآت الخفيفة ذات المواصفات الجيدة لإنشاء مساكن اقتصادية في كندا، وعلى الرغم من كون هذه المساكن ذات سعة محدودة لأنها صغيرة نوعاً ما إلا أنها تمثل حلاً مثلى خاصة في الكثير من الدول ذات الكثافات السكانية العالية والتي هي بأمر الحاجة وهكذا نوع من المساكن خاصة إذا ما كانت مراعية لظروف وتقلبات المناخ من حيث العزل مع الإشارة إلى ضرورة كونها مقاومة للحريق، وتقنية التشييد هي استخدام رقائق مصنعة جاهزة تتركب مع بعضها ضمن مقاييس محددة لتكوين المنشأ الخفيف (Majzub , 1976 , p.1114 ( شكل رقم 12 ).

### -المثال التاسع: الاستفادة من طبيعة الموقع:

يمثل هذا المثال محاولة جادة للاستفادة من طبيعة الموقع في كندا، ففي بعض المواقع لا تسمح طبيعة الأرض بإنشاء المساكن الاعتيادية الأمر الذي يتطلب تعاملًا خاصًا يؤدي إلى تحقيق الاستغلال الأمثل لهذه المواقع خاصة عندما يتزايد الطلب على المساكن وتقل إمكانية توفيرها، عندئذ وفي هذه الحالة يلجأ المخططون أولاً إلى تحديد الأماكن الملائمة لاستغلالها كمواقع سكنية، ثم يأتي دور المماريين في إيجاد التصاميم الناجحة لهذه المواقع المميزة خاصة في المناطق الجبلية أو تلك التي تظهر فيها فروقات طبوغرافية تسمح بإيجاد مساكن دون مستوى سطح الأرض وهنا يظهر الدور المميز للتفاعل مع الطبيعة من حيث توفير المناظر الجميلة فضلاً عن تحقيق جوانب العزل الحراري والصوتي ( Aughenbaugh & Rockaway , 1976 , P.1230 ( شكل رقم 13 ).

### -المثال العاشر: حسن فتحي وعمارته الطينية:

في هذا المثال تظهر طروحات (حسن فتحي-1981) حول العمارة الطينية لتشكل خطوة جادة حول عمارة شعبية مميزة في الدول الفقيرة، إذ يركز فتحي على طرق الإنشاء التقليدية باستخدام المواد المحلية ويعتبرها عاملاً مؤثراً له أهمية كبيرة نحو تحقيق الاقتصادية للوحدة السكنية (فتحي ، 1981، ص 1)، وهو هنا يتناول الموضوع من وجهة نظر تحترم التراث وتضعه في مقدمة الحلول الناجحة لتحقيق الاقتصادية على كافة المستويات والتي من أهمها الجوانب البيئية والمنشئية، وقد ركّز في طروحاته على وجوب التعامل مع البيت الإسلامي التقليدي باعتباره أساساً ناجحاً للتصاميم السكنية، وفي تقنيته المطروحة اعتمد على الطين كمادة أساسية في البناء مع إدخال القباب والأقبية في التسقيف كحل مناسب لهذه المادة ( شكل رقم 14 ).

### -المثال الحادي عشر: مساكن الفقراء في مدينة الخرطوم-السودان:

في هذا المثال ناقش (Kramel-1996) موضوع إسكان الفقراء في العاصمة السودانية-الخرطوم، وقد طرح الموضوع في دراسة متكاملة جاءت تحت عنوان:

( Shelter For The Poor In Khartoum , Sudan , 1996 ) وعالج في هذه الدراسة أربعة أنواع من المشاكل هي: (الاقتصادية، الاجتماعية، البيئية، والأمنية) ، وعلى الرغم من أهميتها جميعاً إلا أن ما يهمنا هنا هو ما يرتبط بالعامل الاقتصادي المؤثر بصورة فعالة في اختيار طرق وتقنيات التشييد، وفي النموذج الذي طرحه أشار (Kramel) إلى أن مراعاة الطابع المحلي التقليدي هو أمر ضروري ولكن لا مانع من إدخال مواد جديدة بالإمكان تسخيرها ضمن نفس التوجه ( Kramel ,1996 , P.46 )، ومن حيث التعامل مع البيئة هناك النحت في كتلة المبنى على المستويين الأفقي والعمودي بوجود الأفنية الوسطية ضمن المخططات الأفقية مع فتحات قليلة في الواجهات تكون موجهة باتجاه الريح، وقد أستخدم (Kramel) في نمودجه مادة الطابوق مع الأسمنت ضمن نظام الجدران الحاملة للنقل، مع إدخال بعض الطرق التقليدية في التسقيف كالعقادة، فضلاً عن استخدام السقوف المستوية من الكونكريت ( شكل رقم 15 ).

### تحديد العوامل الخاصة بالتحليل:

تطرق البحث إلى جملة عوامل أساسية اعتبرها مفردات خاصة لغرض التحليل والتطبيق على الأمثلة المنتخبة للدراسة، منها ما ارتبط بالتحلي البيئي ومنها ما ارتبط بالتحليل المنشئي، وقد تمثلت هذه العوامل بما يلي:

#### -مفردات التحليل البيئي:

-طبيعة البيئة التي نفذ فيها المشروع: وهذه الطبيعة تكون ضمن ثلاثة جوانب (طبيعة مناخية، طبيعة اجتماعية، وطبيعة اقتصادية) وسيكون التركيز على (الطبيعة المناخية) بتفاصيلها حسب توجه البحث، مع الإشارة إلى كل من (الطبيعة الاجتماعية و الطبيعة الاقتصادية) كونهما على صلة مباشرة بالمعالجات التي تتطلبها (الطبيعة المناخية).

-مدى التوافق مع البيئة المحلية: وهذا التوافق قد يكون ( توافق تام، توافق جزئي، أو لا يوجد توافق).

-إمكانية التحويل في المشروع كي يتلاءم مع طابع العمارة المحلية بشكل عام: وهنا فأن المشروع يكون (له قابلية جيدة للتحويل، له قابلية جزئية للتحويل، أو أنه لا يقبل التحويل)\*.

#### -مفردات التحليل المنشئي:

-نوع التقنية المستخدمة في التشييد: وهذه التقنية تكون (تقنية حديثة، تقنية مركبة، أو تقنية تقليدية).

\* يكون التحويل هنا خدمة أهداف بيئية.



-توفر التقنية على المستوى المحلي: التقنية قد تكون (متوفرة، يمكن توفيرها مستقبلاً، أو أنها غير موجودة ولا يمكن توفيرها مستقبلاً).

-توفر المواد المستخدمة على المستوى المحلي: المواد قد تكون (متوفرة، يمكن توفيرها مستقبلاً، أو أنها غير موجودة ولا يمكن توفيرها مستقبلاً).

-الانسجام معمارياً وسياقياً مع طابع العمارة المحلية (الجانب التعبيري)\*: وهنا قد يكون المبنى (منسجم تماماً، منسجم جزئياً، أو لا يوجد انسجام).

وقد تضمنت استمارة التحليل على مجمل هذه المفردات.

### النتائج:

يبرز الجدول رقم (1) في ملحق البحث والخاص بمعلومات التحليل البيئي نتائج تحليل المفردات الثلاث المرتبطة بهذا التحليل وهي: (طبيعة البيئة التي نفذ فيها المشروع، مدى التوافق مع البيئة المحلية، وإمكانية التحوير في المشروع)، ففيما يتعلق بالمفردة الرئيسة الأولى (طبيعة البيئة) هناك ثلاثة جوانب تمثل جزئياتها وتتمثل بـ (طبيعة مناخية، طبيعة اجتماعية، وطبيعة اقتصادية)، فيما يخص مفردة (الطبيعة المناخية) ظهرت نسبة 27% من الأمثلة ضمن المناخ الحار الجاف ونسبة 27% أيضاً ضمن المناخ البارد مع نسبة 46% ضمن المناخ الحار الرطب، وهذا الأمر يعطي إمكانية الاستفادة من هذه الأمثلة للتطبيق على المستوى المحلي فيما يخص هذه المفردة الجزئية نظراً لكون المناخ المحلي في القطر العراقي متطرف ومتنوع بين الشمال والوسط والجنوب.

أما فيما يخص المفردة الجزئية الثانية (الطبيعة الاجتماعية) فقد ظهرت نسبة 46% من العينات بمجتمع فقير يندرج ضمن قائمة البلدان النامية، مع نسبة 18% لكل من السكن الريفي المنفرد والسكن المتنقل غير المستقر ونسبة 9% لكل من السكن السياحي والسكن التقليدي المراعي لقيم وتقاليد المجتمع العربي الإسلامي، وهذا التنوع فيما يخص هذه المفردة إنما يؤشر إمكانية الاستفادة من الأمثلة المطروحة فيما يخص هذا الجانب.

وبخصوص المفردة الجزئية الثالثة (الطبيعة الاقتصادية) فقد ظهرت من خلال النتائج نسبة 82% ضمن السكن الاقتصادي ونسبة 18% ضمن المساكن متوسطة المستوى الاقتصادي وهذا الأمر يعطي الأفضلية للإسكان الاقتصادي وهو مناسب للشريحة الأوسع ضمن المجتمع العراقي فيما يخص مستوى دخل الفرد وما هو مطلوب ضمن هذه المرحلة.

\* يكون الانسجام هنا ضمن حدود المنشأ.

فيما يتعلق بالمفردة الرئيسية الثانية (مدى التوافق مع البيئة المحلية) جاءت النتائج لتعطي نسبة 46% للتوافق الجزئي و 36% لا يوجد توافق مع 18% للتوافق التام، وإن ظهور التوافق - وإن كان بشكل جزئي - يفتح الباب أمام إمكانية الاستفادة من الأمثلة المطروحة ضمن حدود هذه المفردة بشكل يتكامل مع باقي المفردات الأخرى.

أما فيما يتعلق بالمفردة الرئيسية الثالثة من مفردات التحليل البيئي والمتمثلة بـ (إمكانية التحوير في المشروع) فقد جاءت النتائج بنسبة 73% لتعطي قابلية جزئية على التحوير مع نسبة 18% بقابلية جيدة ونسبة 9% لا يقبل التحوير، والكلام على هذه المفردة ينطبق على المفردة التي سبقتها.

من جانب آخر، يبرز الجدول رقم (2) في ملحق البحث والخاص بمعلومات التحليل المنشئي نتائج تحليل المفردات الأربع المرتبطة بهذا التحليل وهي: (نوع التقنية المستخدمة في التشييد، توفر التقنية على المستوى المحلي، توفر المواد المستخدمة، والانسجام معماريا وسياقيا مع العمارة المحلية)، ففيما يتعلق بالمفردة الأولى (نوع التقنية المستخدمة في التشييد) ظهرت النتائج بنسبة 55% تقنية مركبة مع نسبة 27% تقنية تقليدية ونسبة 18% تقنية حديثة، وهذا الأمر يؤشر إمكانية التوفيق بين ما هو تقليدي وما هو حديث ضمن حدود هذه المفردة.

أما بخصوص المفردة الثانية (توفر التقنية على المستوى المحلي) فقد جاءت النتائج لتعطي نسبة 55% يمكن توفيرها مستقبلا ونسبة 27% نعم متوفرة مع نسبة 18% غير موجودة ولا يمكن توفيرها مما يؤشر إمكانية الاستفادة محليا من جانب كبير مما هو مطروح ضمن الأمثلة فيما يتعلق بهذه المفردة.

وبالنسبة للمفردة الثالثة من مفردات التحليل المنشئي وهي (توفر المواد المستخدمة) فقد أظهرت النتائج نسبة 55% يمكن توفيرها مستقبلا مع نسبة 36% نعم متوفرة ونسبة 9% غير موجودة ولا يمكن توفيرها مستقبلا لينطبق هنا نفس الكلام الخاص بالمفردة التي سبقتها.

وأخيرا جاءت نتائج تحليل مفردة (الانسجام معماريا وسياقيا مع العمارة المحلية) لتعطي نسبة 46% منسجم جزئيا و 36% لا يوجد انسجام مع نسبة 18% منسجم تماما مما يقيد بعض الأمثلة للتطبيق على المستوى المحلي ضمن حدود هذه المفردة على الرغم من وجود أفضلية لأمثلة أخرى في إمكانية التطبيق من حيث كونها منسجمة جزئيا أو كليا.

### الاستنتاجات:

- خلاص البحث إلى مجموعة من الاستنتاجات يمكن تلخيصها إجمالاً بما يلي:
  - إن المسكن (المستدام) من خلال مفهوم الإسكان منخفض الكلفة لا يعني أبداً الحصول على نوعية رديئة من المساكن بل هو توجه معتمد في الكثير من الدول للحد من مشاكل السكن.
  - يمكن اعتماد الكثير من المحاولات الجادة المطبقة في أنحاء مختلفة من العالم على المستوى المحلي للحد من العجز الحاصل في قطاع السكن.
  - لا بد للمساكن الاقتصادية (المستدامة) من أن تراعي الإنسان بمعنى أنها لا تكون اقتصادية على حساب النوعية، ومن خلال ذلك يظهر تأثير البيئة المناخية لما لها من علاقة مباشرة بحياة الناس دونما تقليل لدور البيئة الاجتماعية التي لا بد من مراعاتها ضمن الجوانب الوظيفية للمسكن.
  - إن تطبيق الأفكار والتقنيات الحديثة المستوردة لا يعني بالضرورة التطبيق الحرفي لها والانقلاب على الماضي بكل تراكماته بل يمكن التعامل معها لبناء قاعدة أولية تفتح المجال نحو تقدم تقني منشود على المستوى المحلي.
  - من جانب آخر يمكن الاستفادة من الطابع التقليدي للعمارة المحلية في بناء صيغ كفيلة بتحقيق توجه وسياق متفرد لعمارة محلية معاصرة (مستدامة) على مستوى المشاريع السكنية.
  - إن من غير الممكن التوصل إلى تحقيق تكامل اقتصادي على المستوى المحلي ما لم يتم حل مشكلة السكن التي كانت ولا زالت تثقل كاهل المواطن.
  - ومن خلال البحث فإن بالإمكان تلمس صيغ أولية تمثل أساس نظري لسياق محلي مميز وناجح بيئياً و منشئاً في مجال الإسكان، وهذا السياق إنما يتوضح من خلال التركيز على إعادة تأهيل الإمكانيات الذاتية المتوفرة في هذا القطاع من خلال الاحتكاك بتجارب ذات مواصفات من الممكن اعتمادها محلياً ضمن هذا التوجه.

### المصادر باللغة العربية:

- التميمي، سعدي، في الخصائص المشتركة لعمارة دول العالم الثالث، بحث منشور في مجلة فنون عربية، 1982 - العدد 6 - المجلد 2، ص 16 - 55.
- الجوادي، مقداد حيدر و سعد فوري النعيمي، أثر الارتدادات الجانبية والخلفية في كمية الطاقة المسلطة على المبنى في النسيج الحضري في المشاريع السكنية، المؤتمر القطري السنوي الأول للهندسة المعمارية - بغداد - كانون الثاني - 2001، ص 135 - 145.
- أمدينة العربية، 1987. تطور الإسكان وتوفير المأوى في المدن العراقية وبخاصة بغداد، دراسة منشورة في مجلة المدينة العربية. العدد 28.

- حمودي، وديع حماد، 1985 . دراسة مستلزمات الخصوصية للمجمعات السكنية المتعددة الأسر في مدينة بغداد، رسالة ماجستير غير منشورة، كلية الهندسة-جامعة بغداد.
- فتحي، حسن، 1981- **حسن فتحي وقصة المشربية**، حوار صحفي أجراه أرداش كاكافيان منشور في مجلة فنون عربية . العدد 3.
- هولي، ميلوش و هي ريجيها و جي سلاك، **الانسان والبيئة**، ترجمة: عصام عبد اللطيف، الموسوعة الصغيرة – 39 – منشورات وزارة الثقافة والفنون، بغداد، 1978.
- يوسف، شريف، 1982 . **تأريخ فن العمارة العراقية في مختلف العصور**، دار الرشيد للنشر، بغداد.

## REFERENCES :

- **AKILI W. ; 1976 - Sand Encroachment On Lower-Cost Housing Developing In Arid Areas** , International Symposium On Housing Problems , V.1 , Clemson University , South Carolina .
- **AOUGHENBAUGH N. B. & Rokaway J. ; 1976 - Go Underground For Low-Cost Housing** , International Symposium On Housing Problems , V.2 , Clemson University , South Carolina .
- **ARANYA ; 2001 - Low-Cost Housing At Indore** , The Indian Concrete Journal , V.13 , New Delhi .
- **AROCKIASAMY M. & Vijayaraghavan K. ; 1976 - Low-Cost Housing Slum Clearance Project In Madras City-Case Studies** , International Symposium On Housing Problems , V.2 , Clemson University , South Carolina .
- **BOURNE R.; 1976 – A Low Cost Insulated Concrete Wall System** International symposium On Housing Problems , V.2 , Clemson University , South Carolina .
- **CASTRO J. , Pina , Irigoyen , Vilasante & Rojas ; 1976 - Ferro Cement Roofs As A Solution To Low Cost Housing** , International Symposium On Housing Problems , V.2 , Clemson University , South Carolina .
- **DAVIS M. ; 1976 - Low - Cost Self – Help Housing In Rural Philippines** , International Symposium On Housing Problems , V . 1 , Clemson University , South Carolina .
- **HAYGREEN J. ; 1976 - Wood – Base Panel Materials For Housing In Less Developing Countries** , International Symposium On Housing Problems , V.2 , Clemson University , South Carolina .
- **HURD M. ; 1997 - Low – Cost Concrete Storage Building** , Concrete Construction – Dec. , USA .
- **HURD M. ; 1981 - International Development With Second Generation Lift Slab** , Concrete Construction – Sept. , USA .
- **KRAMEL H. ; 1996 - Amal I : Shelter For The Poor In Khartoum – Sudan** , The Ministry Of Engineering Affairs – State Of Khartoum-In Collaboration With The Habitat Group At The Swiss Federal Institute Of Technology , Zurich .
- **MAJZUB I. ; 1976 - Low Cost Shelter Of Low- Cost Waste Materials** , International Symposium On Housing Problems , V.2 , Clemson University , South Carolina .

- **MATHUR G.** ; 1992 - **Low – Cost Housing In Developing Countries** , Center For Science & Technology Of The Non – Aligned And Other Developing Countries , New Delhi .
- **MINK G.** ; 1976 - **Potential Use Of waste And Surplus Material For Self – Help Low Cost Housing** , International Symposium On Housing Problems , V.2 , Clemson university , South Carolina .
- **MORTON H.** ; 1976 - **Low Cost Housing In The USSR** , Inter National Symposium On Housing Problems , V.2 , Clemson University , South Carolina .
- **PAKOTIPRAPHA B. & Pama & Lee** ; 1976 – **Development Of Bamboo Pulp Boards For Low Cost Housing** , International Symposium On Housing Problems , V. 2 , Clemson university , South Carolina .
- **PARRY J.** ; 2000 – **Parry News** , An Occasional News Letter From Gradly Helth , Jpm Parry & Associated Ltd. , Isse No. 28 , Des. UK .
- **SANGU S.** ; 1976 – **A Simple And Quick Method Of Construction Paraboloid Shells And Paraboloid Frame Structures For Use In Low Cost Housing** , International Symposium On Housing Problems , V.2 , Clemson University , South Carolina .
- **SEATON F. & Vogel R.** ; 1976 – **The Mobil Home As A Source Of Lower Cost Housing** , International Symposium On Housing Problems , V.1 , Clemson University , South Carolina .
- **SOUTH R.** ; 2001 – **Tomorrow’s Building Available Today** , Monolithic Dome Institute , Free Information , Feb. Italy .
- **SUYONO M. & Juliman D.** ; 1999 – **Community – Based Low – Cost Housing Movement In Indonesia** , Habitat II Conference , V.13 , Jakarta .
- **WILSON A.** ; 1976 – **Modern Technology Provides Housing Economy And Safty** , International Symposium On Housing Problems , V.1 , Clemson University , South Carolina .

## الملحق: نموذج استمارة التحليل

معلومات التحليل المنشئي	معلومات التحليل البيئي	معلومات عامة
-نوع التقنية المستخدمة في التشييد (تقنية حديثة، تقنية مركبة، تقنية تقليدية)	-طبيعة البيئة التي نفذ فيها المشروع (طبيعة مناخية: ،طبيعة اجتماعية: ،طبيعة اقتصادية: )	-اسم المشروع:
-توفر التقنية على المستوى المحلي (نعم متوفرة، يمكن توفيرها مستقبلا، غير موجودة ولا يمكن توفيرها)	-مدى التوافق مع البيئة المحلية (توافق تام، توافق جزئي، لا يوجد توافق)	-المصمم:
-توفر المواد على المستوى المحلي (نعم متوفرة، يمكن توفيرها مستقبلا، غير موجودة ولا يمكن توفيرها)	-إمكانية التحوير في المشروع كي يتلاءم مع طابع العمارة المحلية بشكل عام (قابلية جيدة للتحوير ، قابلية جزئية، لا يقبل التحوير)	-الموقع:
-الانسجام معماريا وسياقيا مع طابع العمارة المحلية ( منسجم تماما ، جزئيا، لا يوجد انسجام		-سنة الإنجاز:

## دور التدريسي في تفعيل تقنية التعليم الرقمي في المدرسة المعمارية العراقية

الباحثة ليلى غانم  
الجامعة التكنولوجية / قسم المعماري

دكتورة وحدة شكر  
الجامعة التكنولوجية / قسم المعماري

### مستخلص البحث

أشارت العديد من الدراسات إلى أهمية النهوض بالحركة التعليمية للهندسة المعمارية في التصميم المعماري لمواكبة ظاهرة التعليم الرقمي ، ومن الملاحظ أن تلك الدراسات قد أسهبت في اهتمامها بمفردات المناهج المعمارية وطرق التدريس إضافة إلى إشارتها إلى دور التدريسي ليعطي تلك التغييرات الحاصلة. إلا أن معظم تلك الدراسات لم تؤكد على طرح آليات تفعيل التعليم الرقمي في المدارس المعمارية العراقية ، ولم يتم التركيز على دور التدريسي في ذلك التفعيل ، من خلال قيادته للتعليم الرقمي وفق منهج وخطة دراسة جديدة في ضوء التقنية الرقمية ومن هنا ظهرت مشكلة البحث في :

عدم وجود دراسات تؤكد على دور التدريسي في تفعيل تقنية التعليم الرقمي في المدرسة المعمارية العراقية ، ضمن مفردات (المعرفة الرقمية – الرغبة والحماسة للاستزادة من المعرفة الرقمية – استعداده لتوظيف التقنية الرقمية – موقف التدريسي بين التأييد والمعارضة) ومن هنا جاء هدف البحث في محاولة تشخيص دور التدريسي في تفعيل تقنية التعليم الرقمي في المدرسة المعمارية العراقية لاستكشاف مدى استعداده الفعلي لتوظيف معرفته ورغبته باستخدام التقنية الرقمية في تطوير العملية التعليمية المعمارية عموماً وتطبيق مفاهيمها في الأقسام المعمارية على وجه الخصوص وبناء الآلية المناسبة التي يمكن من خلالها تفعيل ممارسة هذه التقنية في المدارس المعمارية العراقية .

لغرض تحقيق هدف البحث تم استطلاع المناهج التعليمية المعمارية وخاصة درجة استحضارها لمفردات التعليم الرقمي وما هي أهم الأساليب المتبعة في توظيف تلك المفردات و استطلاع الدراسات حول واقع التعليم الرقمي في المدارس المعمارية العالمية والعربية ، وتم توظيف هذا المستخلص في تصميم قائمة استبيان وزعت على المدارس المعمارية العراقية حيث تم تحليل نتائج الاستبيان ومقارنتها بين المدارس المعمارية بغية استخلاص أهم الاستنتاجات والتوصيات التي تساهم في تفعيل تقنية التعليم الرقمي في المدرسة المعمارية العراقية.

### The effect of architecture staff in activate the technology of digital education in the Iraqi school of architecture

#### ABSTRACT:

Many researches assigned the importants of enhance the architectural education movement. It is obvious that these studies have elaborated in their interest in architectural curriculum and teaching methodm in addition to the important of qualifying the staff to cover these changes. Most of these studies couldn't define a specific solutions to improve teachers method to lead the digital education

According to this the research problem was defined as:

"There is no comprehensive study clear the real attitude of the architectural teachers in Iraqi schools of architecture from the digital teaching...within the vocabulary of (digital knowledge– desire for more information about digital knowledge - the attitude of digitalizing architectural curriculum between accepting and denying – employing this technolgly on selected sample)".

Thus the research goal is defined as:

**"Give a clear vision about architectural teacher attitude in Iraqi schools of architecture in relating to** to discover his real preparation to employ his knowledge using the digital technology in developing the architectural education in general, and applying their concepts in department of architecture in particular. In order to **"built the propitiate mechanism in which may be used to activate this technique in Iraqi schools of architecture".**

Reviewing architectural teaching curriculum and the degree which it may send for the digital education vocabulary, and define the most important ways to employ them , reviewing the studies about the reality of digital learning in Iraqi schools of architectural and analyzing the results and compare them between the architectural schools attitude the conclusions and recommendations

in order to qualify them in activating the digital education technique in these schools .

## مقدمة

لعبت الثورة الرقمية مع نهاية الألفية الثانية وبداية الألفية الثالثة دوراً فاعلاً في التطور العلمي والتقني في شتى المجالات، كما كان لها مردود واضح على الفنون والعمارة حيث ظهرت الأشكال والعمارة الرقمية، كما انعكس ذلك على تشكيل وتكوين النسيج الحضري للمدينة وتصميم الفضاءات الخارجية. الأمر الذي دفع مجموعة من الاتجاهات الفكرية الحديثة إلى اعتماد فلسفة إعطاء دور فاعل للرقميات في التصميم المعماري والحضري ليس كوسيلة للرسم والتنفيذ فقط بل في عمليات الإبداع والتصميم المعماري.

ولما كانت فلسفة المدارس المعمارية العراقية تهئية كادر من الخريجين الذين يمتلكون القدرة على تطبيق المعرفة النظرية في حقل العمل واستيعاب التغيرات الفكرية والتقنية والتعامل معها<sup>1</sup> كان لابد للقائمين على العملية التعليمية في مجال العمارة والتصميم الحضري مواكبة هذا التطور التقني بهدف تأهيل الخريجين لمواجهة تحديات المستقبل بكل ما يشمله من توجهات ونظريات معمارية متلاحقة تحت مظلة الرقميات كأساس ومرتكز مستقبلي رئيس.

أشارت الأدبيات المختلفة إلى ضرورة تطوير وتحديث العملية التعليمية فهي أساس تكوين شباب المستقبل ليكون مؤهل للانطلاق إلى آفاق جديدة من الإبداع والابتكار لإضافة الجديد لمواكبة الثورة الرقمية وما ينتج عنها. وبمراجعة الجدول المثار حول آثار التقنيات المتقدمة الناتجة عن الثورة الرقمية، وتسببها فيما سوف يحدث من ضياع المهارات الأساسية مثل القراءة والكتابة و الرسم والعمل اليدوي، وجد أن واقع الأمر يعكس غير ذلك في أن تلك المهارات ستصبح أكثر أهمية في عصر الثورة الرقمية وسوف تزداد الحاجة إلى أشخاص يتمتعون بأساس قوي من المهارات الأساسية، فعلى سبيل المثال ليست أجهزة الحاسب بديلاً للأساتذة والعملية التعليمية وإنما هي أدوات تساعد وتدفع التعليم وتطور من فاعلية المدرس، كما أنها لن تحل أبداً محل الروح الإنسانية والمهارات والمثابرة التي تميز الجنس البشري .

وبناء على ما تقدم ظهرت أشكالاً واتجاهات معاصرة مرتكزة على التكنولوجيا الرقمية، الذي أنتج فكراً متطوراً ومتجدداً يعتمد الرقميات في شتى المجالات ، ولمواكبة هذا التطور الفكري لابد من تطور التعليم المعماري، بهدف تأهيل جيل جديد من الخريجين يواكب متطلبات العصر .

– المحور الاول : دور التدريسي في التعليم الرقمي المعماري

## مبادئ التعليم المعماري الرقمي

**تعريف التعليم الرقمي :** يطلق على هذا النوع من التعليم أيضاً بالتعليم الالكتروني .. وقد عرفت الدراسات المختلفة التعليم الرقمي حسب تخصص كل دراسة، حيث عرف (الموسى) التعليم الالكتروني باعتقاده التقنية الالكترونية (الرقمية) لتقديم المحتوى التعليمي للمتعلم بطريقة جيدة وفعالة ، مختصراً الوقت والجهد والتكلفة في العملية التعليمية (الموسى ، 2005، ص1 من 8).

مفردات الخطة الدراسية لقسم الهندسة المعمارية/ الجامعة التكنولوجية للأعوام 2003-2007 ص 3<sup>1</sup>



وتعطي الدراسات أيضا مفهوماً للتعليم الالكتروني بـ "طريقة للتعليم باستخدام آليات الاتصال الحديثة من حاسب وشبكاته ووسائطه المتعددة من صوت وصورة ورسومات ، وآليات بحث ، ومكتبات الكترونية ، وكذلك بوابات الانترنت سواء كان عن بعد أو في الفصل الدراسي" ، ويقصد استخدام التقنية بجميع أنواعها في إيصال المعلومة للمتعلم بأقصر وقت ممكن وأقل جهد وأكبر فائدة (الموسى ، 2005، ص2 من8). إضافة إلى إمكانية الحاسوب في تحسين المستوى العام للتحصيل الدراسي ، ومساعدة المعلم والطالب في توفير بيئة تعليمية جذابة ، لا تعتمد على المكان أو الزمان.

وقد يتخذ التعليم الرقمي أشكالاً متعددة وهي (الموسى ، 2005، ص7 من8) :

- استخدام الحاسوب في التعليم .
- استخدام الانترنت في التعليم (التعلم عن بعد) .
- التعليم الرقمي الذي يعتمد على التقنية الالكترونية (الرقمية) .

**مما ذكر أعلاه يمكن تعريف التعليم الرقمي بأنه : التعليم الذي يعتمد التقنية الرقمية لتقديم المحتوى التعليمي للمتعلم بطريقة جيدة وفعالة ، مختصراً الوقت والجهد والتكلفة في العملية التعليمية ، ويتخذ اشكالاً عدة وهي استخدام الحاسوب في التعليم واستخدام الانترنت في التعليم (التعلم عن بعد) والاعتماد على التقنية الالكترونية (الرقمية) .**

وعليه فان التعليم الرقمي لا يمكن ان يطبق بدون وجود محتوى علمي وتقديم فالمحتوى العلمي يقصد به المعرفة الرقمية ، اما التقديم فيشمل الكادر التدريسي.

ان استخدام مثل هذه البرامج والاجهزة لا تعطل دور المدرس في العملية التعليمية ولا تكون بديلاً عنه، وانما تعمل على خلق حالة من الامتزاج بين ما هو مستجد في الدروس العملية وبذلك يمنح الطالب فرصة اضافية لتعلم المهارات وتدفعه الى التدريب والتكرار من خلال خلق الرغبة لديه كونها شيئاً جديداً يطبق في المحاضرات العملية ويختلف عن الاسلوب التقليدي السائد. (علي ، 2005)

#### \* التعليم المعماري

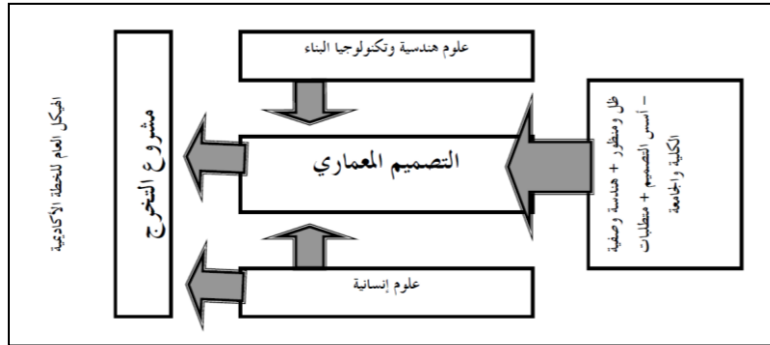
#### مفهوم منهجية وبرامج التعليم المعماري

هناك شبه إجماع على أن المنهجية بمفهومها العام تتكون من الأركان الأربعة التالية : (الأهداف المرجوة، المحتوى العلمي، طرق التدريس، التقويم المستمر) (الطبيبي ، 2005، ص5-25))

ففيما يخص موضوع البحث الحالي هو ركن طرق التدريس حيث ، من المعروف أن هناك ترابطاً كبيراً بين المحتوى العلمي والطريقة التي يدرس بها ، ويصعب أحياناً الفصل بينهما .ويمكن اعتبار طرق التدريس هي ترجمة للأهداف التربوية المرجوة وتحولها إلى واقع فعلي .وعلى الرغم من عدم إجماع التربويين على تحديد أساليب التدريس الجيدة ، إلا أن البعض يصنف خصائص التدريب الجيد إلى ثلاث أقسام هي: (الطبيبي ، 2005، ص5-26))

- المؤهلات العلمية الجيدة لعضو هيئة التدريس.
- الخبرات التربوية و المهنية لعضو هيئة التدريس.
- السمات الشخصية لعضو هيئة التدريس من حيث استقامته و حماسه للتدريس ، وموضوعيته و قدرته على التجديد و الإبداع .

ان أهمية مادة التصميم المعماري غير قابلة للجدل ضمن منهجية التعليم المعماري ، ومن بين أهم الدراسات التي اكدت ذلك هي دراسة الطيبي ، حيث اشار في الشكل ادناه الى تركز مادة التصميم المعماري ضمن منهجية التعليم المعماري ويوضح علاقته باعتباره مادة أساسية بالمواد التكميلية . حيث أدى الظهور القوي و التطور السريع للحاسوب و دخوله في جميع مجالات الحياة إلى إعادة التفكير في كثير من الأمور التي كانت مأخوذة كبديهيات أو كمسلمات . و من أهم هذه المسلمات في مجال العمارة هو التصميم المعماري و ما يحتويه من أسس و طرق و نظريات و خبرات و تدريسي و أبداع و خلافة، حيث يعتبر التصميم المعماري هو الركيزة الأولى و الأساس في كل ما يتعلق بمهنة العمارة و الهندسة المعمارية .فالتصميم هو أكثر المواد الدراسية أهمية في التعليم المعماري و يحتل اكبر مساحة من الجداول الدراسية و يتم تخصيص أكبر قدر من التقييم الدراسي للتصميم المعماري.(الطيبي ، 2005، ص(31-5))



شكل رقم (1) يوضح كيفية تحقق منهجية التعليم المعماري كما يوضح علاقة التصميم المعماري كمادة أساسية بالمواد التكميلية المصدر (الطيبي ، 2005، ص(26-5))

وعليه لغرض البحث في جانب التعليم المعماري الرقمي .. لا بد من الولوج أولاً في مبادئ تعليم التصميم المعماري .. ومن ثم الانتقال تدريجياً للتعرف على خصائص التعليم المعماري الرقمي .

### \* تعليم التصميم المعماري

#### أولاً :- التصميم المعماري التقليدي

تتضمن عملية التصميم المعماري عدة مراحل كما اقترحها لاسو (Laseau) \* مثل مرحلة تطوير البرنامج، التصميم الأولي، التصميم الابتدائي، تطوير التصميم، مستندات التنفيذ، رسومات التنفيذ، التنفيذ. و في حين يبدو هذا التحديد مناسباً في فهم مراحل التصميم و لكن تطوير طرق جديدة للتصميم يحتاج إلى تقسيم التصميم إلى أنواع مختلفة. و من المناسب أن نحدد ثلاث أنواع على الأقل (كما أقترحهم جبرو و ماهر و زانج (Gero , Maher and Zhang) <sup>٥</sup>): التصميم التقليدي، التصميم الابتكاري، و التصميم الإبداعي، ومن خلال تقابل الأنواع المختلفة بالمرحلات المختلفة للتصميم يمكن أن نحدد مستويات التصميم، ويمكن تفهم مدى تعقيد عملية التصميم من خلال تحديد تلك المستويات وتحديد نقاط البحث التي لم يتم معالجتها في هذا المجال.

\* Laseau :

أستاذ هندسة معمارية ، لديه أكثر من 25 سنة من الخبرة في تعليم الرسم اليدوي (الحر) sketching freehand والرسم التصميمي design drawing . هو مؤلف الكتب التالية :

"Graphic Thinking for Architects and Designers," "Graphic Problem Solving for Architects and Designers," "Inkline Drawing," "Architectural Drawing: Options for Design" , "Handbook of Architectural Representation" and "Visual Notes" with Norman Crowe.

<sup>٥</sup> John S. Gero, Mary Lou Maher and Rabee M. Reffat

Key Centre of Design Computing and Cognition

University of Sydney, Australia

Email {john,mary,rabee@arch.usyd.edu.au}

فالبرامج المساعدة للتصميم المتوفرة تجارياً تساعد فقط أنواع التصميم التقليدية، ويمكن الخطأ الاعتقاد بأن أي برنامج بذاته أو وحده يمكن أن يوفر كل متطلبات عملية التصميم، إذ تتطلب كل مرحلة من مراحل التصميم أنواع مختلفة من البرامج المساعدة. (محبوب- a - 2006، page 6 of 26).

#### أ - مبادئ التصميم المعماري التقليدي

يتضمن وصف التصميم الكثير من العناصر غير الملموسة مثل التخيل والإحساس والإبداع، ولما كان من الصعب وصف هذه العمليات، كان التصميم المعماري يشبه بالصندوق الأسود، (The Black Box) الذي لا يظهر محتوياته ولا تفاصيله. وبدأ الاحتياج لتغيير هذا التشبيه لفهم ماهيته ونشاطاته، لذلك تم تشبيه التصميم بالصندوق الزجاجي (The Glass Box)، الذي تظهر محتوياته ومكوناته (النجدي، 1992، ص 11).

يبدأ التصميم الفعلي لمشروع ما بفرد أو مجموعة أفراد يقومون باستحداث أفكار لتغيير البيئة المادية و تقديمها في شكل يناسب التنفيذ. ويقصد التصميم المعماري امران اساسيان على الاقل، يشير الاول الى جملة الاجراءات والافعال التي يقوم بها المهندس المعماري منذ استلامه امرالمباشرة بالعمل لحين تقديم الرسوم والمواصفات المطلوبة لغرض التنفيذ (النجدي، 1992، ص 9). ينتهي التصميم عادة عندما يتم البناء. ويقسم المصممون التصميم إلى المراحل التالية: إعداد البرنامج الوظيفي - تصميم ابتدائي - تصميم نهائي - رسومات تنفيذية - إشراف على التنفيذ.

إن الطريقة التقليدية التي اعتمدها المعمارون لتطوير ووصف تصميماتهم خلال الـ (400) سنة الماضية كانت الرسومات الخطية. حيث يبدأ التصميم عادة بوضع الفكرة التصميمية في التسلسل من العام الى الخاص، او من الكل الى الجزء. إذ تتخذ أهم القرارات التصميمية في البداية وتسمى عادة الفكرة (concept)، وتتعاقب القرارات بعدها، وتزداد الرسوم وضوحاً مع استمرارية معالم الفكرة الأولية في كل الرسومات التي توضح المراحل المختلفة لعملية التصميم (النجدي، 1992، ص 14).

تتخلل العملية التصميمية أساليب استكشافية وأخرى بنائية الأولى تتمثل بـ (الفكرة الابتدائية Sketch) و تعديلات متعاقبة من خلال الورق الشفاف) اما الاساليب البنائية فهي تأتي من خلال لظهور إمكانيات في التصميم لم تكن معروفة للمصمم من قبل (محبوب- a - 2006، page 5 of 26).

#### ب - تعليم التصميم المعماري التقليدي

قدم دنيس ثورنلي Dennis Thornley بحثاً عنوانه "طرق التصميم في التعليم المعماري" كنتيجة لدراسات قام بها منذ عام 1958 عندما عاد للتدريس بعد ممارسة المهنة في جامعة مانشستر حيث لاحظ أن "التصميم الذي يتم تدريسه في مدارس العمارة له علاقة ضئيلة لما يحدث في الممارسة و تدهور مستوى تعليم التصميم. حيث أن شكل المبنى و شكل الرسومات هو أهم شيء دون النظر للتحليلات الوظيفية او التفاصيل. و لم يكن هناك أي أساس منطقي للتحكيم حيث كان التحكيم يتم بناء على أهواء المعلمين والمهم هو تطابق المسلمات بين المعلم والطالب.

حاول ثورنلي إرساء قواعد لتعليم التصميم بالتفكير فيما يفعله المعماري عندما يقوم بالتصميم. و الطريقة تتكون من أربعة مراحل :

- جمع المعلومات Accumulation of data
- تحديد الفكرة العامة أو الشكل Isolation of a General Concept or Form
- تطوير الشكل للتصور النهائي Development of Form into Final Scheme
- تقديم التصور النهائي Presentation of Final Scheme

وقد كانت طريقة ثورنلي أساساً أداة تعليم التي يتمكن من خلالها المعلم من متابعة عمل الطالب. فكل مرحلة يتم تقييمها في حين كانت الدرجة الكاملة في الماضي تعطى للمشروع النهائي.

أما القزاز (2005) فقد أشارت إلى مفهوم النمطية واعتبرت ان له دور في التعليم المعماري ، واتخذت من قسم الهندسة المعمارية – جامعة الموصل حالة دراسية ، حيث أوجزت فعاليات تدريس مادة التصميم المعماري في هذا القسم للمرحلتين الثالثة والرابعة (موضع البحث) بما يلي (القزاز ، 2005، ص105):

- البدء بدراسة المشروع لفترة 3 أسابيع تقريباً متمثلة بدراسة الموقع ، ودراسة وظيفة المشروع متمثلة بدراسة كلا الأبعاد القياسية الوظيفية (Standards) والعلاقات الوظيفية لمكونات المشروع ، ودراسة الأمثلة المعمارية المشابهة لوظيفة المشروع .
- تقديم الفكرة الأولية في نهاية الأسبوع الثالث تقريباً ، ثم تطويرها خلال الأسابيع التالية وصولاً إلى التقديم النهائي للمشروع .

وأهم المستويات التي اعتمدتها دراسة القزاز (المستتبطة من دراسة أبو جادو 1998) لتتوصل الى هدفها هي (القزاز، 2005، ص98) :

- مستوى المعرفة (التذكر) Knowledge - مستوى الاستيعاب Comprehension - مستوى التطبيق Application - مستوى التحليل Analysis - مستوى التركيب Synthesis - مستوى التقييم Evaluation .

يلاحظ مما تقدم ان تعليم التصميم التقليدي احتوته مدارس مختلفة وبصيغ واشكال مختلفة ، وكما مبين فهي تضع تسلسلاً لأحداث التصميم والتقييم ، وبالتالي فان مراحلها تتطلب مناورات واضحة بين التصميم والتقييم وما يترتب عليه من تواصل بين التدريسي والطالب ، وان عملية استيعاب الطالب لا بد ان تقتزن بعملية النقد .

## ثانياً:- التصميم المعماري الرقمي

### أ - مبادئ التصميم المعماري الرقمي

#### ○ وصف التصميم المعماري بمساعدة الحاسوب

بالرغم من صعوبة وصف التصميم المعماري لتضمنه الكثير من العناصر غير الملموسة مثل التخيل و الإحساس و الإبداع، إلا أن الكثيرين حاولوا تعريف التصميم في ضوء وجود الحاسوب. بانه حساب المعلومات الموجودة في الأشكال اللازمة للقيام بالتصنيع أو الإنشاء. إذ تحدد هذه المعلومات عادة أشكال الأشياء (الأقطاب و الأركان و المسطحات و الحجم) و أبعادها و زواياها الخ، و قد يوجد كذلك رموز مصاحبة للأشكال لتحديد أنواع المواد والخواص الأخرى الأشكال. تأخذ العملية التصميمية أشكالاً مختلفة حسب الظروف المحيطة و لكن عادة ما تكون عمليات حسابات كتغيير أو إضافة الأشكال في الرسومات ذات البعدين أو المجسمات ذات الثلاث أبعاد، (محجوب-a- 2006، page 5 of 26).

قد يبدو هذا التعريف مبسطاً و مجرداً حيث لا يدع مجالاً للعملية الإبداعية في التصميم. و لكن هل يمكن توضيح أين تتدخل العملية الإبداعية في التصميم من خلال اتخاذ رؤية حسابية للتصميم؟.

#### ○ استخدام الحاسوب في التوجهات المعمارية الحديثة

حدث دخول الحاسوب التصميم المعماري تحولاً كبيراً تطلب مشاركة الجميع من الطالب إلى التدريسي في هذا التحول وإعادة النظر في ماهية عملية التصميم والأنشطة التي يتضمنها وتكوين رؤية جديدة للتصميم المعماري في ضوء وجود الحاسوب . (الطويل ، 2005، ص) وعليه فالحاسوب أداة جديدة في الرسم والتصميم ومعالجة المعلومات.

والرسم بطبيعة الحال مختلف عن التصميم. فالرسم هو وسيلة التعبير عن التصميم وهو نسق عملي مقنن يتبع أسس و أساليب محددة للتعبير يتطلب دقة عالية. أما التصميم فهو نسق فكري لتصور و تسجيل المشروع يتضمن الرسم بطبيعة

الحال. كما يتضمن التصميم العديد من الأنشطة الأخرى التي لا يتم التعبير عنها بالرسم. و التعبير الدارج (CAD) يرمز عند اغلب الناس إلى الرسم بمساعدة الحاسوب و لكن بالنسبة للعمارة فهو يعنى التصميم بمساعدة الحاسوب. و إذا كان الرسم هو الأداة المعمارية الأولى للتعبير عن التصميم فان التصميم يظهر في صورة رسومات و لكن الرسومات ليست هي الهدف بل هي الوسيلة للتعبير عن التصميم.

وهناك أيضا فرق بين التصميم بمساعدة أو باستخدام الحاسوب فعندما نقول التصميم باستخدام الحاسوب نعني أن التصميم يتم بالطرق التقليدية مع استخدام الحاسوب في التعبير عنها. أما التصميم بمساعدة الحاسوب فيعني أن للحاسوب دور أساسي في العملية التصميمية و أن نسق التصميم يسير بطريقة مختلفة عن الطريقة التقليدية.

أن هناك أدوات جديدة دخلت مجال مهنة العمارة وجميعها تعتمد على الحاسوب وتقنيات المعلومات، ليس فقط كأداة جديدة تضاف إلى الأدوات التقليدية التي كانت تستخدم، فالحاسوب سوف يغير كيف كنا نرسم وكيف نصمم وكيف نرى المعلومات، ولكن ما هو أهم أنها تغير الطريقة التي نصمم بها، ولم يطرأ على مهنة التصميم مثل هذا التغيير السريع من قبل وهي خطوة كبيرة أن يبدأ استخدام أداة جديدة في التصميم المعماري.

يدخل استخدام الحاسوب في المهارات الفكرية وطريقة التفكير فكلما تم اعتماد المهارات الفكرية المتداولة إضافة إلى المهارات التقنية التي يضيفها الحاسوب يزداد التقدم في النتاج من حيث السرعة والدقة، إذ انه يوفر وقت الدقة ويعالج أخطاء الرسم إضافة إلى السرعة.

يثير استخدام الحاسوب في العمارة الكثير من الجدل حول تأثيره على التصميم المعماري و على مهنة العمارة ككل. و يتحفظ الكثيرون على استخدام الحاسوب في التصميم المعماري باعتباره يؤثر على العملية الإبداعية و قدرات المهندس المعماري على الابتكار، بل إن البعض يتخوف من أن يحل الحاسوب محل المهندس المعماري و إن يتم الاستغناء عن المهندس المعماري تماما.

#### ○ كيف يساعد الحاسوب في التصميم المعماري

من الممكن استخدام الحاسوب لإنتاج الرسومات دون الاستفادة من إمكانياته في التصميم. وحتى العديد مستعملي الحاسوب المتمرسين قاموا بتحويل مهاراتهم اليدوية في الرسم التقليدي إلى الرسم بالحاسوب في حين تقدم برامج التصميم بمساعدة الحاسوب العديد من المميزات بطرق مختلفة عن مهارات الرسم التقليدي. و من المهم تعلم كيفية الاستفادة الكاملة من تلك المميزات. ومن أهم المبادئ الأساسية التي تمكنا من التصميم بمساعدة الحاسوب بكفاءة منها: ( محجوب-a - 2006، 1-16 of page):

التصميم بالعناصر (Design with Objects)، الإنتاج بالجملة (Mass Production)، الطبقات و المجموعات (Layers and Other Collections)، مستويات التصميم (Cycles of Design)، استخدام المقياس الحقيقي (Real-World Scale)، السرعة و المراجعة (Speed and Feedback)، التخطيط قبل الرسم (Planning Before Drawing)، الرسومات الذكية (Intelligent Drawings)، التفاعل مع العميل (Interaction with Client)، رسومات و نماذج البعد الثالث (3Dimensional Drawings and Models)

#### ب - تعليم التصميم المعماري الرقمي

يقوم الحاسوب بتغيير كيفية تدريس الهندسة المعمارية. وليس هناك اتفاق عما إذا كان هذا التغيير أساسيا في العملية التعليمية أم في تقنيات التعليم فقط. و لكن الواضح ان هناك تأثير متزايد على مستوى مساقات تقنية متقدمة أو مراسم التصميم على كل المستويات. والرغبة في التغيير تأتي أساسا من الطلبة و المشتغلين بالمهنة. و لم تتخذ العديد من مدارس العمارة دور قيادي في هذا المجال بالرغم من ان قوة التنافس تزداد بين المدارس و حتى داخل المدارس في مجال دور الحاسوب في التعليم المعماري. هناك عدد من الاتجاهات يمكن التفكير فيها لتعليم التصميم المعماري بمساعدة الحاسوب فالتصميم الرقمي يعني التفكير ضمن مراحل التصميم وليس فقط النتاج (بصورة رقمية). (محجوب-c - 2006، 1page)

- تأهيل الطالب بالأفكار و المهارات اللازمة لاستخدام نظم التصميم المعماري بمساعدة الحاسوب بعد تخرجهم.
- تأهيل الطالب للتحكم في تطور نظم التصميم المعماري بمساعدة الحاسوب و تطوير و استحداث تلك النظم بأنفسهم.
- توفير التجهيزات المناسبة تجارياً و فنياً لطلبة العمارة لاستكشاف النواحي التصميمية أثناء عمل مشروعاتهم
- توفير المعامل لتجربة تصميماتهم من خلال بيئة تصميمية جديدة

### ثالثاً :-مقارنة بين التصميم المعماري التقليدي والتصميم المعماري الرقمي

من خلال تعريف التصميم بواسطة الحاسوب يمكن أن نستوضح أين تتدخل العملية الإبداعية في التصميم ، وبالأخص ما هو دور الغموض و عدم الاستمرارية في تفسير الأشكال و عدم الاستقرار على قواعد حساب الإشكال و عدم اتفاق أساليب المنطق الناقد في تحديد ما إذا كان التصميم قد اكتمل أو أصبح مناسباً.

و للغموض و عدم الثبات في تفسير الأشكال دور هام ، فعدم الثبات على قواعد محددة لتفسير الأشكال يؤدي إلى رؤية وتاويل جديدين لها، إذ يرى المصمم الأشكال المرسومة مختلفة حسب الظروف المحيطة بها و في الأحوال المختلفة.

فالتصميم ليس وصف شيء ما ولكنه استكشاف ما يمكن أن يكون، فالرسومات تكون مفيدة عندما نراها غنية بالاحتمالات و المعاني التي يمكن أن نراها بطرق مختلفة. تحديد معنى واحد فقط لما نراه في الرسم يضعف العملية الإبداعية، ومن هنا يأتي دور القابلية التعبيرية للمصمم في أغناء الفكرة التصميمية، ويمكن ملاحظة الفرق بين التصميم التقليدي والتصميم بمساعدة الحاسوب في الجدول (1).

جدول رقم (1) مقارنة بين التصميم المعماري التقليدي وبمساعدة الحاسوب/ اعداد الباحث

مجال المقارنة	الطريقة التقليدية	بمساعدة الحاسوب
مستويات التعبير عن التصميم	مقيد بمستويات التعبير المتدرجة و المتزايدة في الدقة مع تطور التصميم	غير مقيد بمستويات تعبير في المراحل المختلفة من التصميم
طرق التعبير عن التصميم	الرسومات التقليدية و المجسمات	طرق متعددة تعتمد على الامكانيات
اتخاذ القرارات التصميمية	قرارات محددة في رسومات محددة	قرارات مستمرة في اى وقت
العملية التصميمية	التوجه من أعلى إلى أسفل تبدأ بالعموميات و تنتهي بالتفاصيل	ليس لها توجه يمكن أن تبدأ من أسفل إلى أعلى أو من أعلى إلى أسفل
المعلومات الأساسية	يتم إعداد النظم و التفاصيل و حساب الكميات بالطرق التقليدية	النظم و التفاصيل و الكميات متاحة بطريقة اليكترونية دائمة التحديث
التحليلات البيئية و الإنشائية	بطيئة و غير دقيقة	سريعة و دقيقة
عمل المرادفات	بطيئة	سريعة
تقييم المرادفات	أسلوب شخصي	أسلوب علمي

ويمكن اعطاء وجه اخر للمقارنة بين هذين النوعين من التعليم المعماري باعتماد المستويات التي طرحتها دراسة القزاز .. وكما مبين في الجدول ادناه .

### رابعاً: مقارنة بين تعليم التصميم المعماري التقليدي وتعليم التصميم المعماري الرقمي

يمكن ملاحظتها من الجدول رقم 2

جدول رقم (2) مقارنة بين تعليم التصميم المعماري التقليدي وتعليم التصميم بمساعدة الحاسوب/ اعداد الباحث

المقارنة	الطريقة التقليدية	بمساعدة الحاسوب
تعليم التصميم المعماري	الطرق التقليدية في تعليم التصميم من خلال انتقال الخبرة الشخصية	الاهتمام بان تكون العملية التصميمية أكثر وضوحا و تقنية
الأهداف التعليمية	اكتساب الخبرات التقليدية اللازمة لممارسة المهنة	اكتساب الخبرات التقليدية و الجديدة اللازمة لممارسة المهنة
أسلوب التدريس	الطرق التقليدية في التعليم من خلال المراسم و المحاضرات	توفير التجهيزات والمراسم الاليكترونية و شبكات الاتصال بالمكتبات توجيه الطالب للتعلم الذاتي
التفاعل بين الطالب و الأستاذ	تفاعل مستمر داخل المراسم بهدف نقل الخبرات	تفاعل متبادل بهدف النقد و توجيه و توفير التجهيزات
الطالب	يعتمد على الأستاذ في فهم العملية التصميمية	الاعتماد على النفس في تكوين فهم للعملية التصميمية و الدقة التقنية
الأستاذ	العملية التصميمية و الأهداف التعليمية و تطور الطالب	العملية التصميمية و الأهداف التعليمية و تطور الطالب و التمكن من التكنولوجيا و تطوير الوسائل التعليمية

مما تقدم يتضح أن التعليم الرقمي يستند أساساً إلى العملية التصميمية والتعليم الرقمي الذي يؤكد أهمية التفاعل بين التدريسي والطالب ، من حيث التوجيه والتقييم وعليه يتناول هذا البحث دور التدريسي في تفعيل تقنية التعليم الرقمي في المدارس المعمارية .

**\* موقف التدريسي من تقنية التعليم الرقمي واستخدامها في التعليم المعماري عموماً وفي مادة التصميم المعماري بشكل خاص .**

يعتمد صميم الدراسة المعمارية في مجال العمارة بشكل أساسي على مادة التصميم المعماري والمواد الساندة، وهذه المواد تتطلب تواصل مستمر ومباشر بين الطلبة والتدريسي المعماري لتوجيه النقد المباشر سواء عن طريق الوسائل المتاحة أثناء تواجدهم في المراسم أو عن طريق التواصل عبر الانترنت. وقد أشارت العديد من الدراسات إلى أهمية توظيف تقنية التعليم الرقمي في ما يخص مادة التصميم المعماري ولكنها تباينت مع التقنيات والامكانيات المتاحة في كل دراسة وحسب الظروف المتاحة للتدريسي.

تخصص البحث باستطلاع الدراسة في مجال تعليم التصميم المعماري الرقمي كما سبق ذكره في فقرات المحور الأول ، وعليه ولغرض الوصول الى استخلاص مفردات دور التدريسي في التعليم الرقمي المعماري ، كان لا بد من استطلاعه من خلال تأثيره في تعليم التصميم المعماري الرقمي ، وللوصول الى ذلك سوف يتم استكشاف تجارب مجموعة من المدارس المعماري على المستوى العالمي والعربي والعراقي .. وكالاتي:

دور التدريسي في تعليم التصميم المعماري الرقمي في المدارس المعمارية العالمية .

سيتم استعراض واقع التعليم الرقمي في المدارس المعمارية العالمية من خلال الدراسات التالية .. التي طرحت بشكل مباشر أو غير مباشر هذا الواقع .. ومن هذه الدراسات : دراسة (Gero&Maher&Reffat,2001)، دراسة الطيبي(2005)، دراسة محجوب (1996)، دراسة الطويل (2005) .

اولا: دراسة (Gero&Maher&Reffat,2001) – (مثال جامعة استراليا)

تتناول الدراسة مثال التعليم الرقمي في جامعة استراليا، حيث تهتم الجامعة بدراسة التصميم المعماري بالحاسوب وتضم 300 طالب دراسات أولية في القسم المعماري منهم 90 طالب تخرجوا من نموذج صف دراسي لدراسة التصميم بالحاسوب وجاءت خبراتهم من 30 سنة في المجال الأكاديمي والبحثي لطرق التدريس والتصميم باستعمال الحاسوب . (Gero&Maher&Reffat,2001,P.11 of 13)

وقد اعطيت شهادة التصميم بالحاسوب في الكلية المعمارية لجامعة سدني (Faculty of Architecture , University of Sydney) حيث يحقق الطالب ثلاث أساسيات هي :

### جدول رقم (3) : مسميات المواد المعتمدة في دراسة الطيبي

المادة	المرحلة	جامعة واشنطن - أمريكا	جامعة كاليفورنيا - أمريكا	جامعة تورنتو - كندا	جامعة شيفلد - انكلترا	جامعة ماربورج - ألمانيا
مواد الرسم والتصميم الرقمي	1. الرسم والتصميم بالحاسوب	•			•	
	2. الرسم والتصميم المعماري الرقمي	•			•	
مواد الاظهار والنماذج الثلاثية الابعاد	3. الاظهار والنماذج الثلاثية الابعاد	•			•	
	4. النماذج الثلاثية الابعاد		•			•
مواد الاستكشافات (الرسم اليدوي)	5. الاستكشاف الرقمي					•
	6. الاستكشاف في الرسم الرقمي			•		
مواد التصميم الاقتراضي	7. تصميم البيانات الافتراضية		•			
	8. التصميم المعماري الافتراضي			•	•	•
مواد التصميم المعماري بالحاسوب	9. التصميم بالحاسوب			•		•
	10. التصميم المعماري بالحاسوب		•			
	11. برمجة الرسم بالحاسوب للتصميم		•			
	12. التصميم المعماري الرقمي		•	•	•	•

• تطوير البيئة التعليمية للتصميم الرقمي (تطور المفردات والمفاهيم)

• التصميم الرقمي (التفاعل مع برامجيات التصميم الرقمي)

• التفاعل مع المشاريع المصممة رقمياً .



ولكون ان البيئة التعليمية ترتبط ارتباط مباشر بالكادر التدريسي ، فعليه ان أي تطور يحدث في تلك البيئة يستلزم تهيئة كادر تدريسي قادر على تحقيق هذه المتطلبات .

ثانيا : دراسة الطيبي 2005 (مثال جامعات : واشنطن ، كاليفورنيا ، تورنتو ، شيفلد ، ماربورج)

يلاحظ من الجدول رقم (3): ان تسمية المادة الاكثر اعتماداً في الجامعات المذكورة هي مادة التصميم المعماري الرقمي ، بنسبة 66,7 % ثم مادة التصميم المعماري الافتراضي بنسبة 50 % ، أما المواد (الرسم والتصميم بالحاسوب ، الرسم والتصميم المعماري الرقمي ، الاظهار والنماذج الثلاثية الأبعاد ، النماذج الثلاثية الأبعاد ، التصميم بالحاسوب) فقد شكلت الجامعات التي تستخدمها نسبة 33,3 % من الجامعات المذكورة ، وما تبقى من المواد اقل استخداماً لفظياً ، ونسبة 16,7 % .

ثالثا: دراسة محجوب 1996 (مثال جامعات : مدرسة هارفارد للتصميم ، كورنيل،أوهايو، ميتشيجان ، ماساشوستس ، أريزونا ، مونتانا ، هيوستون ، ويسكونسون-ميلواكي ، جامعة بنجوب كاليفورنيا بلوس انجلوس ، اوريجون)

تضمنت الدراسة بيان موقف الهيئات التدريسية للجامعات المذكورة من تقنية التعليم الرقمي، وكان موقف التدريسيين بين المؤيد والمعارض مع مراعاة الفرق بين موقف الهيئة الادارية والهيئة التدريسية وعدم ثبات الموقف مع تطور تقنية التعليم الرقمي في المدارس المذكورة

ثالثا: دراسة الطويل 2005 (مثال جامعة جورجيا ، مانيتوبا ، فيلادلفيا)

طرح (الطويل) في دراسته الموسومة ( الثورة الرقمية وأثرها على تطوير التعليم الرقمي) استبيان لمجموعة كبيرة من الجامعات وكليات العمارة على مستوى العالم، منها كلية التصميم البيئي بجامعة (جورجيا) التي أعتمد نظام تدريس الحاسوب فيها على أربعة مواد تحوي اثنتان منها التعامل والإظهار بالحاسوب ، أما الاثنان الآخران فيعتمدان بصورة أكثر تدقيقاً ومستوى حيث يجمعان دراسة متطورة للبرامج مع استخدامهما في مشروعات التصميم البيئي والتخطيط، أما كلية العمارة بجامعة (مانيتوبا) اعتمدت على التجاوب بين اليد الحرة والحاسوب في المنهج الأول إما الثاني فيشمل معلومات مفصلة ودراسة أكثر وضوحاً باستخدام الكمبيوتر، كلية العمارة بجامعة (فيلادلفيا) ، والتي تتألف من أربعة أقسام هي (العمارة والتصميم الداخلي - التصميم الرقمي - تصميم الكرافيك والاتصالات - التصميم الصناعي - تصميم الفضاءات الخارجية) والتي تعتمد دراستها الأساسية بقسم الكرافيك أكثر منه في باقي الأقسام، قسم العمارة والتصميم الداخلي يشمل الدراسة فيه على خمسة مناهج تعتمد الحاسوب أداة رئيسية للتدريس بها.

أشرت دراسة الطويل تبايناً في توجه الجامعات والتدريسين باعتماد التعليم الرقمي في التصميم والاطهار المعماري اذ اظهر تدريسي بعض الجامعات الحماس للتعليم الرقمي والرغبة في مواكبة الحركة العالمية مقابل تمسك ادارة الجامعة بالطرق التقليدية في التعليم وان اعتماد التعليم الرقمي يعتمد اساسا تايبد الادارة وامكانية التدريسين في مواكبة التطور . (الطويل ، 2005، ص 72)



شكل (2) تجربة جامعة بيروت في التعليم المعماري المتمزج  
Faculty of Architecture  
Engineering P.49 (2004-2005) مجلة

\* دور التدريسي في تعليم التصميم المعماري الرقمي في المدارس المعمارية العربية

بينت دراسة الطويل تحليل تجربة جامعة بيروت العربية (BEIRUT ARAB UNIVERSITY). اعتمدت ورقة بحث الطويل الخاصة بماهية المناهج التدريسية للحاسوب بالجامعات المختلفة، ومحتواها في دعم مادة التصميم المعماري ودور الحاسوب الفاعل في عملية التصميم المعماري، كل حسب النسب أو إذا ما كان هناك إجابات أخرى بهدف تفعيل المرونة في الورقة، كذلك نسبة ساعات وتقييم

تدريس مواد ومناهج الحاسوب مقارنة بالعدد الإجمالي لمرحلة البكالوريوس. حيث يبين الجدول رقم (2) تقارب معظم الجامعات العربية في تدريس مواد الحاسوب بما يساهم في عمليات الرسم والإسقاط بالحاسوب ضمن مشروعات التصميم المعماري ، كما استنتجت دراسة الطويل عدم تدخل الحاسوب في العملية التصميمية بأي شكل من الأشكال ولا يتعدى دوره في الرسم والإظهار إلى حد بعيد (الطويل، 2005).

كما اوضحت دراسة النجار صورة التعليم الرقمي الحالي في الوطن العربي واشترت معوقات تطورها في جانبين مهمين هما (النجار ، 2003 ، ص 7 / 20):

- التطبيق الجزئي لبعض تقنيات المعلومات والاتصالات.
- التأخير في الاستفادة من التقدم الكبير في تقنيات المعلومات والاتصالات في التعليم والتدريب.

حيث اوضحت معوقات التطور في عدم التوافق بين رغبة الطالب في مواكبة التقدم العالمي التي تتيح له فرص عمل جيدة بعد التخرج وامكانية المدارس المعمارية من حيث التقنيات المطلوبة وامكانيات التدريسيين في مواكبة وسائل التعليم الرقمي هذا اضافة الى مدى استجابة الهيئات الاداري وامكانية تطوير مناهج التعليم المعماري لتحقيق ذلك.

طرحت دراسة الطويل تجربة جامعة بيروت كتجربة رائدة في الوطن العربي نحو تطبيق التعليم الرقمي في التصميم المعماري باشراف مجموعة من التدريسين ذوي الخبرة والكفاءة في استخدام الحاسوب في التصميم المعماري واستخدام برامج التصميم بالحاسوب مثل : برنامج (AutoCAD) وبرنامج (3D studio MAX)، وبرنامج (PhotoShop) وبرنامج (3D home)، وبرنامج (Archi cad)، وبرنامج (3D VIZ)، وبرنامج (Maya) ... الخ ، في اعتماد التعليم الرقمي في المرحلتين الرابعة والخامسة واعتماد ورش عمل خاصة ساهمت في تطوير امكانية الطالب وابداعه في العمل ، شكل (2). اذ تم اعتماد مفردات مناهج خاصة تعتمد التصميم الرقمي ابتداء بمراحل التصميم الاولى وانتهاء بمراحل الاظهار المعماري واعداد الرسوم النهائية للمشروع، الا ان التجربة اقتصرت على المرحلتين المنتهية فقط وباشراف عدد محدد من التدريسين.

كما افرزت الدراسة امكانية اعتماد منهج قسم العمارة والتصميم الداخلي كلية العمارة - جامعة فيلادلفيا ، منهجاً مثالياً



شكل (3) أعمال طلبة العمارة للمرحلة الرابعة في الجامعة التكنولوجية

التقديم النهائي لمشروع التصميم الحضري (2006) .

لتفعيل دور الرقميات بكليات العمارة لما له من تنوع في البرامج والمحتويات العلمية المساهمة بشكل فاعل في تأهيل الطلاب لمواجهة المستقبل الرقمي ، خاصة ما يتعلق بالدراسات البصرية والواقع الافتراضي بمادة البصريات . (الطويل، 2005، ص 72)

\* دور التدريسي في تعليم التصميم المعماري الرقمي في المدارس المعمارية العراقية .

تدرس الحاسبات في الأقسام المعمارية في الجامعات العراقية بصيغة منفصلة وكمواد مستقلة عن مادة التصميم المعماري، إضافة إلى أن طبيعة المحاضرات لا زالت عامة خلال الأعوام الماضية أي بمعنى آخر لا زالت تستخدم كوسيلة في الإظهار وليس مؤثر مهم في العملية التصميمية إلا ما ندر من الحالات

إذ هناك بعض التوجيهات الضمنية التي تحفز عمليات الخلق

والإبداع لدى الطلبة سيما وان الكثير منهم قد وصل إلى مرحلة لا بأس بها من التصميم بالحاسوب، إلا أنها في اغلب الأوقات ترتكز على التقادير النهائية، فقلما ينطلق الطالب من التفكير الرقمي منذ بدء التصميم، وهذا ما يمكن ملاحظته كمثال في أعمال

طلبة العمارة للمرحلة الرابعة في الجامعة التكنولوجية، وبالتالي من الصعب تحديد ما اذا كان الطالب يعتمد الحاسوب في التصميم ام كاداة للرسم والاطهار فقط، ولكن مما لا شك فيه، انها توفر رؤيا واضحة للبعد الثالث في التصميم وتعطي صورة شمولية اكثر للطالب والاستاذ، وكما يظهر في نماذج من مشاريع الطلبة، (شكل رقم 3).

### خلاصة دور التدريسي في تفعيل تقنية التعليم الرقمي في المدرسة المعمارية

اشرت الدراسات اهمية التعليم الرقمي سواء في حقول العمارة أو من خارج العمارة وبينت الفرق بين التصميم المعماري التقليدي والتقني، حيث تبين الامكانيات التي توفرها برامجيات التصميم بواسطة الحاسبة في زيادة الدقة والسرعة، اضافة الى امكانية توفير الرسم في البعد الثالث وإنتاج رسومات لها علاقات مباشرة بين المسقط الأفقي و الواجهات و القطاعات و المنظور الامر الذي يتيح رؤيا شاملة للتصميم بالبعد الثالث ، الامر الذي يتطلب مهارات وامكانيات لدى الطالب والتدريسي على حد سواء في مواكبة التعليم الرقمي في المدارس المعمارية.

كما بينت الدراسات تداخل وتشعب الجوانب المتعلقة باعتماد تقنية التعليم الرقمي في التصميم المعماري، اذ تشمل جميع الاطراف المشتركة من الطالب الى الهيئة التدريسية من تدريسي وإدارة، اضافة الى الامكانيات المادية والتكنولوجية.

تمت الاشارة في دراسة الطيبي في فقرة (1-2-1) الى خصائص التدريب الجيد ، وممكن اعتمادها لكي تكون منطلق لخصائص التدريب الجيد في التعليم الرقمي .. حيث ان المؤهلات العلمية الجيدة لعضو هيئة التدريس والخبرات التربوية و المهنية له تتمثل هنا (بالمعرفة الرقمية الجيدة لعضو هيئة التدريس) ، أما السمات الشخصية لعضو هيئة التدريس من حيث استقامته وحماسه للتدريس يمكن ان تنعكس رقمياً (بالرغبة والحماسة للاستزادة من المعرفة الرقمية من جانب ) و ( استعداداه لتوظيف معرفته ورغبته باستخدام التقنية الرقمية في تطوير العملية التعليمية المعمارية عموماً وتطبيق مفاهيمها في الأقسام المعمارية على وجه الخصوص من جانب آخر) .. كما ورد في الفقرة نفسها أن هناك ترابطاً كبيراً بين المحتوى العلمي والطريقة التي يدرس بها، ويصعب أحياناً الفصل بينهما وبالتالي فان ذلك سيتمثل ب (موقف التدريسي أي تحديد المؤيد والمعارض لاستخدام المحتوى العلمي الرقمي) .

وعليه يمكن تلخيص أهم المفردات التي يعتمد عليها دور التدريسي في تفعيل التقنية الرقمية بما يأتي:

- المعرفة الرقمية الجيدة لعضو هيئة التدريس.
  - الرغبة والحماسة للاستزادة من المعرفة الرقمية .
  - استعداده لتوظيف التقنية الرقمية .
  - موقف التدريسي بين التأيد والمعارضة لاستخدام المحتوى العلمي الرقمي.
- وبعد أن تم استخلاص هذه المفردات سيتم توظيفها ضمن الدراسة العملية الموضحة لاحقاً .

### **\* المحور الثاني (الدراسة العملية)**

اعتمد البحث اسلوب الاستبيان المباشر وعبر الانترنت للحصول على الصورة الواضحة التي تبين موقف التدريسيين من التعليم الرقمي وفق مفردات الاطار النظري.

### - تصميم قائمة الاستبيان

هدفت الأسئلة الاستبائية الموجهة إلى العينة المستبينة إلى التوصل إلى حصيلة معرفية عن مدى معرفة التدريسي في المدارس المعمارية العراقية بتقنية التعليم الرقمي (البرمجيات والأدوات الساندة والأساليب) ، واستكشاف مدى رغبته الفعلية في الاستزادة من المعرفة الرقمية ، والتعرف على موقفه المؤيد أو المخالف من استخدام التقنية الرقمية في التعليم المعماري ومدى قدرته على توظيفها في المنهج المعماري عموماً ومادة التصميم المعماري على وجه الخصوص.

تم تصميم قائمة الاستبيان ملحق (1) ، وتوزيعها على تدريسي المدارس المعمارية العراقية في بغداد وباقي محافظات العراق عن طريق التسليم المباشر او عبر الانترنت، شمل الاستبيان : جامعة بغداد-قسم الهندسة المعمارية ، الجامعة التكنولوجية - قسم الهندسة المعمارية ، جامعة السليمانية - قسم الهندسة المعمارية ، جامعة أربيل - قسم الهندسة المعمارية، جامعة دهوك - قسم الهندسة المعمارية، جامعة كوة - قسم الهندسة المعمارية، اعتمد البحث نتائج استبيان تدريسي الأقسام المعمارية في جامعة بغداد والجامعة التكنولوجية وجامعة أربيل وذلك للأسباب الآتية:

- اعتبارها من اقدم المدارس المعمارية في العراق.
- عدد التدريسيين المعماريين مقارنة بالمدارس المعمارية الاخرى.

- الاجابة على عدد من استمارات الاستبيان يمكن

اعتمادها في تحقيق هدف البحث.

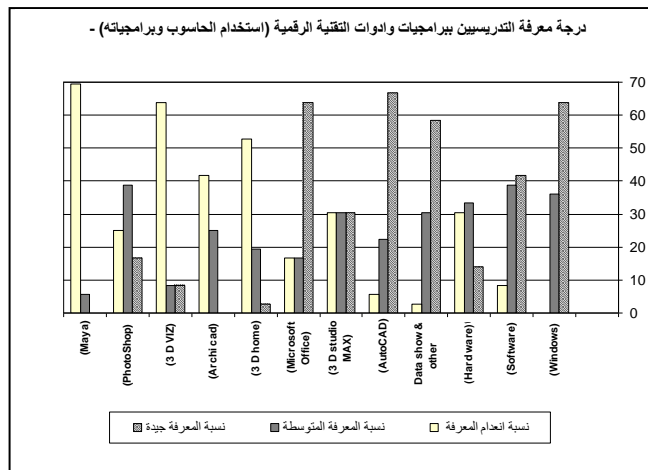
### - النتائج والاستنتاجات والتوصيات

#### - نتائج الاستبيان

اظهر تحليل قوائم الاستبيان المتضمنة جوانب (المعرفة الرقمية - الرغبة بالاستزادة من المعرفة الرقمية - الموقف من رقمنة المناهج المعمارية - تطبيق التقنية الرقمية على عينة منتخبة) الآتي:

أولاً :- النتائج المتعلقة بدرجة معرفة التدريسي ببرامجيات التقنية الرقمية:

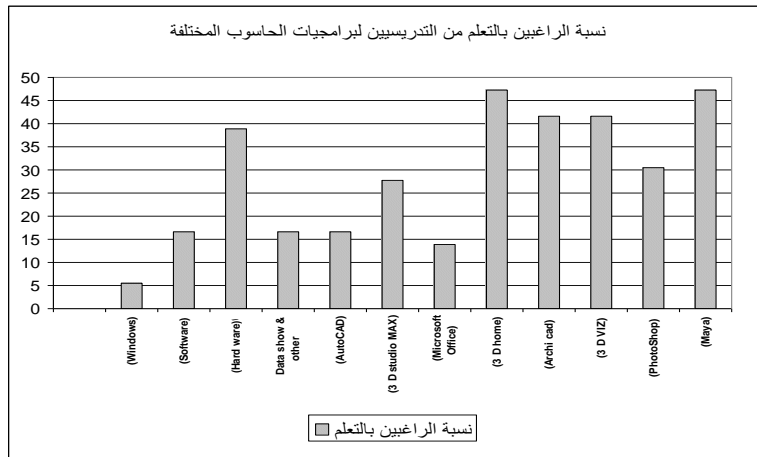
اظهرت نتائج الاستبيان في الجانب المتعلق بدرجة معرفة التدريسيين ببرامجيات وأدوات التقنية الرقمية (استخدام



شكل رقم (4) يوضح درجة معرفة التدريسيين ببرامجيات وأدوات التقنية الرقمية (استخدام الحاسوب وبرامجياته)

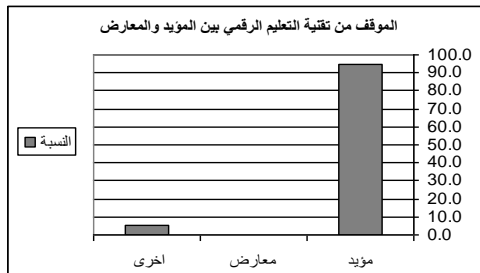
الحاسوب وبرامجياته) وكما موضح في الشكل رقم (4). اعلی نسبة للمعرفة الجيدة في بتشغيل برنامج أوتوكاد (AutoCAD) بنسبة (66.7%) مما يعكس ناحية ايجابية في إمكانية توظيف هذا البرنامج في الخطة المنهجية المعدلة لإمكانية توفير الكادر الملائم لذلك في هذه الجامعة ، يليها معرفة جيدة في التعامل من أنظمة تشغيل الحاسبة (Windows) وتشغيل برنامج (Microsoft Office) بنسبة (63.9%).. أما البرامجيات المتعلقة بالرسم بالبعد الثالث فقد اظهرت نتائج الاستبيان نسبة معرفة قليلة بها فقد كانت نسبة المعرفة بتشغيل برنامج (3D studio MAX) (30.6%)، وهذه النسبة ضئيلة بالنظر إلى ما يمتلكه هذا البرنامج من أهمية كبيرة ، مما يتطلب أخذه بنظر الاعتبار بشكل أساسي عند وضع الخطة التدريبية للتدريسيين.

ثانياً:- النتائج المتعلقة بدرجة رغبة التدريسي بتعلم برامجيات التقنية الرقمية:



شكل رقم (5) يوضح نسبة الراغبين من التدريسيين بتعلم برامجيات الحاسوب المختلفة

عام (Software) بنسبة (16.7%) ومن ثم رغبة تعلم تشغيل برنامج (3D studio MAX) بنسبة (27.8%)، وتشغيل برنامج (PhotoShop) بنسبة (30.6%)، أما التعامل مع الـ (Hard ware) فنسبة الرغبة بتعلمه بلغت (38.9%) ثم تشغيل برنامج (Archi cad) وتشغيل برنامج (3D VIZ) وصلت الرغبة



شكل رقم (6) يوضح موقف التدريسيين من التعليم الرقمي بين المؤيد والمعارض

بتعلمها إلى نسبة (41.7%)، وأخيراً تشغيل البرنامج الأخرى وبنسبة أعلى بلغت (47.2%). نلاحظ من النسب أعلاه للبرامجيات (Windows)، (Microsoft Office)، (AutoCAD) و (Software) رغبة ضئيلة بالتعلم من قبل التدريسيين وهذا يؤكد بدوره النسب المرتفعة التي ظهرت سابقاً في درجة معرفة التدريسيين لهذه البرامجيات مما يتطلب بناء الآليات المناسبة في اعداد المناهج وفق هذا المنظور.

ثالثاً:- النتائج المتعلقة بموقف التدريسي من استخدام تقنيات التعليم الرقمي

أ. موقف التدريسي من استخدام تقنية التعليم الرقمي عموماً وفي إمكانية تطبيقها على التصميم المعماري والمواد المختلفة. يلاحظ من الشكل (6) أن موقف التدريسيين المؤيد لتقنية التعليم الرقمي واضح جداً حيث تصل نسبته إلى (94.4%)، وكذلك تطبيقها على المواد التي يقومون بتدريسها في أقسامهم بنسبة (83.3%) (شكل (7)، أما ما يتعلق بوجهة نظر التدريسي في إمكانية توظيف الحاسوب في تدريس مادة التصميم المعماري فكانت النسبة ايجابية أيضاً بلغت (83.3%) (شكل (8).

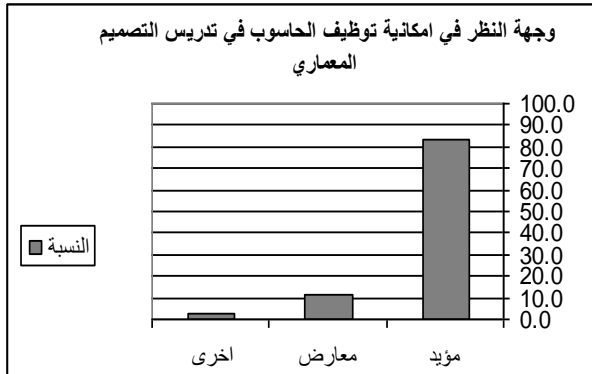
ب. موقف التدريسيين من جدوى التقنية الرقمية في التعليم المعماري .

هذا الأمر يتضح من خلال الجوانب الآتية لاحظ شكل رقم (9) :

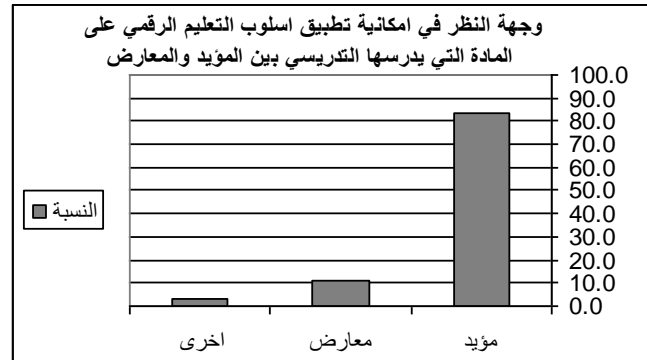
+اعتقاد بأنه يجب أن نبدأ من وجهة نظر العمارة وننظر إلى ما يناسبنا في الحاسوب:

لاقى هذا الأمر تأييداً تاماً من قبل التدريسيين .. وبنسبة (94.4%) وهذه النسبة كانت مماثلة لتفضيل أن يكون التغير في مناهج التعليم المعماري عند استخدام تقنيات التعليم الرقمي بشكل تدريجي متضمناً بعض المواد الأساسية .. ومن ثم يتم توظيف باقي المواد الدراسية تدريجياً ضمن الخطة المنهجية المعدلة .

+الاعتقاد بان الحاسوب يستخدم في توليد الأفكار ويعد كأداة للعصف الذهني (أي يدخل في صميم التفكير الذهني المعماري .



شكل رقم (8) يوضح وجهة نظر التدريسي في إمكانية توظيف الحاسوب في تدريس مادة التصميم المعماري



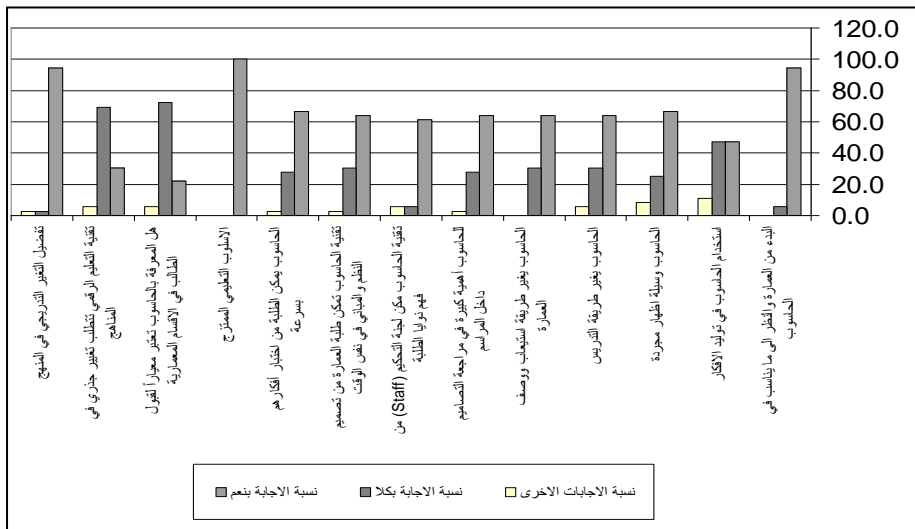
شكل رقم (7) يوضح امكانية تطبيق اسلوب التعليم الرقمي على المادة التي يؤيدها التدريسي (بين المؤيد والمعارض)

لاقى هذا الأمر اجابات غير مؤيدة، اذ لم يؤيد تدريسيي الجامعات المنتخبة استخدام الحاسوب في توليد الأفكار فكانوا بين المعارضين أو لديهم وجهات نظر أخرى وعليهم فان نسبة تأييدهم للأمر كانت منخفضة.

+الاعتقاد بان الحاسوب يعتبر كوسيلة مجردة تستخدم للإظهار المعماري من خلال استخدام برامجيات الرسم والاطهار المختلفة. شأنها شأن باقي أدوات الإظهار المعماري وبأنه يحدث تغيير أساسي في طريقة تدريس العمارة وله أهمية كبيرة في مراجعة التصاميم داخل المراسم بالإضافة إلى تمكينه لجنة التحكيم (Staff) من فهم نوايا الطلبة لأنهم يستطيعون رؤية المبنى وبذلك

يتخذ التقييم مسار مماثل

للمهنة والاعتقاد بان الحاسوب سوف يمكن طلبة العمارة من تصميم النظم والمباني في نفس الوقت وتصميم المباني من رؤية شاملة بالإضافة إلى أنه سوف يمكن الطلبة من اختبار أفكارهم بسرعة وان جودة تصاميمهم سترتفع إلى عدة اضعاف واقعها تحت ظل المنهج التقليدي... كل هذه الجوانب المتعلقة بجدوى



شكل رقم (9) يوضح موقف تدريسيي الجامعات المستبينة من جدوى التقنية الرقمية

التقنية الرقمية في التعليم المعماري لاقت قبولاً متوسطاً تراوحت نسبته بين (61.1%-66.7%) .

أما أكثر الجوانب تأييداً من قبل كافة التدريسيين الذين تم استبيانهم فقد كان تفضيلهم لأن يكون الأسلوب التعليمي ممتزج (أي يستخدم وسائط ممتزجة) من رسوم حرة ، وسكيتشات ، رسوم حاسوب ... الخ حيث كانت نسبته (100%) ، وعلى العكس من ذلك فان أقل نسبة تأييد كانت (22%) بخصوص اعتبار دراية الطالب الفائقة في مجال تقنيات الحاسوب عاملاً أساسياً في قبوله في الأقسام المعمارية في يومنا

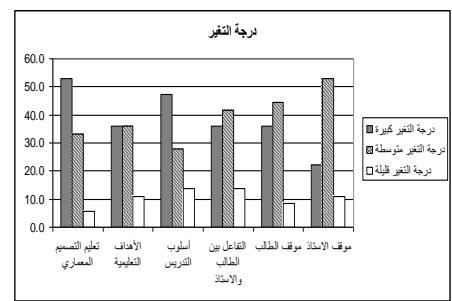
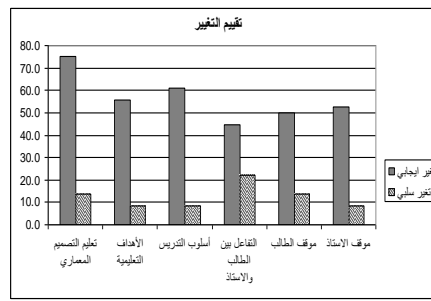
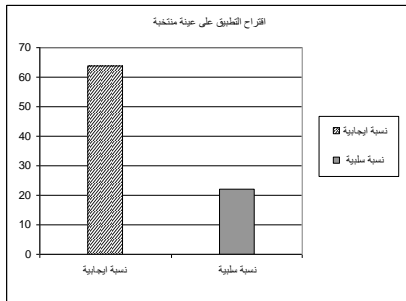


هذا ، وكذلك فيما اذا يتطلب العمل بتقنية التعليم الرقمي تغييراً جذرياً في مناهج التعليم المعماري لاقى تأييداً ضعيفاً بنسبة (30.6%) .

### ج. موقف التدريسيين من درجة التغيير وتقييمه بين مفردات التعليم التقليدي والتعليم الرقمي .

حيث أعتبرت مفردة تعليم التصميم المعماري من وجهة نظر التدريسيين هي الأكثر تغييراً بتغيير أسلوب التعليم من التقليدي إلى الرقمي وبنسبة (52.8%) يليها تغيير أسلوب التدريس بنسبة (47.2%) تلتها نسبة (36.1%) لكل من مفردات تغيير الأهداف التعليمية ومفردة التفاعل بين الطالب والأساتذ ومفردة موقف الطالب ، أما موقف الاساتذ فهو الأقل تغييراً وبنسبة (22.2%) شكل (10) أما ما يتعلق بتقييم التغيير فيلاحظ ان التغيير في مفردة تعليم التصميم قد لاقى تأييداً ملحوظاً وبنسبة (75%) وعلى العكس فان مفردة تغيير التفاعل بين الطالب والاساتذ اعتبر تغييراً سلبياً شكل (11) .

### رابعاً:- النتائج المتعلقة باستعداد التدريسي لتوظيف معرفته ورغبته باستخدام التقنية الرقمية في تطوير العملية التعليمية



شكل رقم (12) يوضح استعداد التدريسي لتوظيف معرفته ورغبته باستخدام التقنية الرقمية في تطوير العملية التعليمية المعمارية

شكل رقم (11) يوضح موقف التدريسي في تقييم التقرير

شكل رقم (10) يوضح موقف التدريسي من درجة التغيير

### المعمارية عموماً وتطبيق مفاهيمها في الأقسام المعمارية على وجه الخصوص :

أظهرت النتائج و كما مبين في الشكل(12) تأييد التدريسيين بشكل ملحوظ لتجربة تطبيق التعليم الرقمي في التصميم المعماري وبنسبة (63.9%) على أن يكون بتدرج في عدد الطلاب وابتداء من المرحلة الثالثة لضمان امتلاك الطالب المهارات اليدوية في الكرافيك والتصميم التي يتناولها في المرحلتين الاولى والثانية.

### \* الاستنتاجات .

- يشهد العالم اليوم ثورة تكنولوجية ورقمية تمتد لتشمل جميع ميادين الحياة ، ولما كانت العمارة احد الواجه المعبرة عن التحولات الحضرية في العالم كان لابد لها من مواكبة الثورة الرقمية والاشكال الافتراضية على مستوى الواقع او على المستوى الاكاديمي باعتبارها احد التيار الفكرية التي يشهدها العالم اليوم.
- تعتمد العملية التصميمية على تقييم واسترجاع المعلومات ولما كان ذهن الإنسان محدود في تخزين واسترجاع المعلومات كان لابد من الاستعانة بوسائل التخزين الخارجية ومساعدته في التصميم فكانت الإشارات الأولى لأهمية الحاسوب في العملية التصميمية. أن الوسيلة الجديدة في التصميم باستخدام الحاسوب ليست إضافة للوسائل القديمة ولا يمكن التعامل معها دون تغيير في نمط التفكير والمفردات والمناهج الدراسية.
- يدخل استخدام الحاسوب في المهارات الفكرية وطريقة التفكير اضافة الى امكانياته في سرعة ودقة الاظهار المعماري، ويظهر الطلاب اهتمام كبير في استخدام تقنيات الحاسوب في التصميم والاطهار لامكانياته التعبيرية على مستوى التصميم بالبعد الثالث، والذي يظهر في نتاجات الطلاب وخاصة في المراحل الدراسية المتقدمة، الامر الذي يتطلب اشراف وادارة اكااديمية

لحصول الطالب على الصورة الصحيحة لاستخدام الحاسوب في التصميم المعماري، الأمر الذي يتطلب شمول تقنيات التعليم الرقمي ضمن مناهج التصميم المعماري.

- يعتمد الإبداع المعماري على غنى الاحتمالات ، ليس في وصف العمل وإنما في تأويل العمل المعماري ، فكلما كانت الرسومات غنية بالاحتمالات والمعاني ازداد عمل المعماري إبداعاً، وأن المعنى الواحد يعدد العملية الإبداعية من هنا جاء دور الحاسوب في التصميم في زيادة غنى العمل مقارنة بالرسم اليدوي وإمكانية استعمال التصميم الطباق .
- يفضل أن يكون الأسلوب التعليمي ممتزج (أي يستخدم وسائط ممتزجة) من رسوم حرة ، وسكينشات ، رسوم حاسوب ... الخ، فالرسم اليدوي مكون أساسي لممارسة التصميم المعماري ، من المهم أن يساعد المصمم في العملية التصميمية بالتوازي مع الرسم بالحاسوب، فالتثنية أكفاء معا في التصميم المعماري.
- يظهر الاتفاق واضحاً حول التأثير المتزايد للتكنولوجية المتطورة في التصميم المعماري على كل المستويات وأهمية مواكبة التطور التكنولوجي الذي يشهده العالم اليوم.
- أن موقف التدريسيين بشكل عام كان إيجابياً جداً مما يفتح المجال أمام الأقسام المعمارية للمباشرة بوضع الخطط التطويرية سواء على مستوى المنهج التطويري المعماري أو على مستوى الخطة التدريبية للتدريسيين.
- أن نسبة كبيرة من التدريسيين في مختلف الجامعات تمتلك معرفة جيدة ببرامج تشغيل الحاسبة والأجهزة التابعة الذي يعكس مواكبة التدريسي المعماري للتطور التكنولوجي في التعليم، وعليه يمكن استخدام هذه المعرفة في تصميم الخطة التعليمية الجديدة للأقسام المعمارية .
- التدريسي المعماري هو مصمم معماري أولاً، ولابد أن يواكب التطور التكنولوجي وهذا ما يؤكد ضرورة أن تتم العملية ضمن إطار وتوجيه أكاديمي ليحظى الطالب بفرص التعليم الرقمي أكاديمياً.
- لم تتخذ العديد من المدارس المعمارية الدور القيادي في مجال التصميم بالحاسب وعليه لا بد من المباشرة بمحاولة النهوض بالواقع التعليمي في المدارس المعمارية العراقية .. وقد أجمعت نسبة كبيرة من التدريسيين على ضرورة أن يكون التعليم ممتزج أي لا يكون رقمياً صرفاً خاصة في المرحلة الانتقالية .. كما بينوا ضرورة المباشرة بالمرحلة الأولى .

### \* التوصيات

- تطوير المناهج والمفردات لتتوافق مع متطلبات فكر التصميم بالحاسوب بالتوازي مع المفردات التقليدية التي تساهم في رفع أداء الطالب حيث يجب أن تدرس برامجيات الحاسوب بأسلوب لا يبتعد عن روح الإبداع، وأن تقيم أعمال ومشاريع الطلبة وفق معايير التقييم المعماري.
- تفصيل أن يكون التغيير في مناهج التعليم المعماري عند استخدام تقنيات التعليم الرقمي بشكل تدريجي متضمناً بعض المواد الأساسية .. ومن ثم يتم توظيف باقي المواد الدراسية تدريجياً ضمن الخطة المنهجية المعدلة ،أي بمعنى آخر يستوجب أن يكون هنا التعليم ممتزج وانطلاقاً من تطوير المواد الأساسية التي تدرس الحاسوب في القسم مع تحديد برامجيات أخرى خاصة من شأنها أن تمكن الطلبة من تنفيذ تصاميمهم بسهولة وطلاقة .. وتساعدهم على الخلق والإبداع.
- الاهتمام بتزويد مكتبات الكليات بالدوريات والكتب المتخصصة التي تبرز الفلسفات المعمارية المتطورة في التعليم الرقمي بالإضافة إلى ردها المستمر بأحدث البرامجيات ليتواصل الطالب مع التطور التكنولوجي الذي يحدث في المادة المعينة.
- تطوير مفردات مادة نظرية العمارة لتشمل طروحات الإشكال الرقمية والعمارة الرقمية، وتوجهاتها الفكرية.
- تطوير وسائل التعليم المعماري إذ يجب أن تصمم المراسم المعمارية بصيغة صف رقمي يحتوي بالإضافة إلى لوحات الرسم (البوردا) على جهاز حاسوب لكل طالب يستخدم داخل المرسوم، أما الأجهزة الساندة فيكفي أن تتوفر قطعة واحدة منها في كل مرسوم لكي يتم استخدامها من قبل الجميع.



- يجب أن لا يقتصر التعليم الرقمي على المراسم المعمارية، إذ يجب أن يتعداه ليشمل التعليم عن بعد.
- كما هو واقع الحال في بعض الجامعات العالمية فيمكن أن تتفرع الدراسة المعمارية إلى عدة أقسام، من بينها التصميم والكرافيك المعماري بالحاسوب، أو قسم التعليم الرقمي.. الخ من المسميات التي هي بالأساس تخصيص مهم في مجال التعليم المعماري.
- التأكيد على مواكبة أساتذة المدارس المعمارية للتطورات التقنية والتكنولوجية في مجال التصميم والتنفيذ المعماري .

### - لمصادر:

أولاً : المصادر العربية

- الطويل، حاتم عبد المنعم (2005): "الثورة الرقمية وأثرها على تطوير التعليم المعماري" مقالة في مجلة Architectural @ planning journal vol.16، April- 2005 ، ( pp67-82 )
- الطيبي ، د. أحمد مسعد ، 2005 ، "اتجاهات التعليم المعماري والتقنيات المستقبلية للثورة الرقمية" دراسة مقدمة في المؤتمر المعماري الدولي السادس الموسوم "الثورة الرقمية وتأثيرها على العمارة والعمران" ، قسم العمارة - كلية الهندسة - جامعة أسيوط، ١٧ مارس ٢٠٠٥ م- ١٥ ، قسم العمارة ، كلية الفنون الجميلة ، جامعة الإسكندرية .
- القزاز ، ضحى عبد الغني عبد العزيز ، 2005 "تفعيل دور النمطية في التعليم الجامعي لمادة التصميم المعماري" ، دراسة في قسم الهندسة المعمارية - جامعة الموصل ، بحث منشور في المجلة العراقية للهندسة المعمارية ، السنة الثانية - العدد الثامن ، آذار 2005 .
- الموسى (2005) : ورقة عمل مقدمة إلى ندوة مدرسة المستقبل - جامعة الملك سعود) تاريخ الحصول على المقالة 2006-2-21
- محجوب ، د. ياسر كتاب (Design Book) ، الموقع الالكتروني التالي : <http://www.fortunecity.com/victorian/paintbrush/1127/dsgnbk/DSGNBK0.html>
- محجوب، د.ياسر (1996-a- Design Book - التصميم المعماري و الحاسوب .
- محجوب ، د.ياسر (1996-b- Design Book - ردود الأفعال تجاه استخدام الحاسوب في العمارة
- محجوب، د.ياسر (1996-c- Design Book - تعليم التصميم المعماري باستخدام الحاسوب .
- محجوب، د.ياسر (1996-d- Design Book أمثلة طرق تدريس التصميم بالحاسوب .
- التعليم الالكتروني في الدول النامية ، 2005 ، <http://www.ituarabic.org/E-Education/Doc24-SuezCanalUniv.doc>
- النجدي، د.حازم راشد، (1992) منهجية التصميم المعماري دراسة مقدمة إلى قسم الهندسة المعمارية .
- الدهوي، سهى حسن عبد الله ، (1994) ، تقييم المشاريع المعمارية في المؤسسات الأكاديمية العراقية ، رسالة ماجستير غير منشورة، مقدمة إلى قسم الهندسة المعمارية في الجامعة التكنولوجية، بغداد.
- على ، د.عادل فاضل ، 2005 ، الحاسب الالكتروني استخداماته في التعلم والتعلم الحركي ، <http://www.ituarabic.org/E-Education/Doc24-SuezCanalUniv.doc>
- النجار ، أ.د. فريد ، 2003 ورقة عمل حول إستراتيجيات التعليم الرقمي : الموقف العربي .
- مفردات الخطة الدراسية لقسم الهندسة المعمارية الجامعة التكنولوجية (2007-2003)
- مفردات الخطة الدراسية لقسم الهندسة المعمارية جامعة السليمانية . (2007-2003)
- مفردات الخطة الدراسية للكلية التقنية - السليمانية . (2007-2003)
- مفردات الخطة الدراسية لقسم الهندسة المعمارية جامعة أربيل . (2007-2003)

- هيكل ، د.نمير اسماعيل و فادان، د.يوسف بن محمد ، 1998 ، "سبل تطوير برامج التعليم المعماري" د.نمير اسماعيل هيكل : أستاذ مشارك/قسم العمارة وعلوم البناء/كلية العمارة والتخطيط/جامعة الملك سعود د.يوسف بن محمد فادان :أستاذ مساعد/قسم العمارة وعلوم البناء/كلية العمارة والتخطيط/جامعة الملك سعود .
- 1962 دنيس ثورنلي Dennis Thornley و تعليم التصميم المعماري - سبتمبر 1962 المؤتمر الأول لطرق التصميم - الكلية الملكية - لندن

## ثانياً: المصادر الأجنبية

- Graduate Courses ، in Landscape Architecture، School of Environmental Design ، University of Georgia ، (2004) .
- Graduate Courses ، Faculty of Architecture \_ University of Manitoba.(2000)
- The School of Architecture and Design Undergraduate Courses ، Philadelphia University ، (2004) .
- Faculty of Architecture Engineering ،BAU (Beirut Arabic University) year (2004-2005) .

## ملحق رقم (1) قائمة الاستبيان

## قائمة استبيان

اعزانا التدريسيين

لغرض الارتقاء بالمستوى التعليمي في قسم الهندسة المعمارية .. والانتقال به من الأسلوب التقليدي في التعليم إلى المستوى الرقمي الحديث (أي باستخدام الكمبيوتر) .. فقد قمنا بأجراء دراستنا هذه ونحن الآن في صدد اعداد الدراسات الاستكشافية التطبيقية لها .. وعليه فقد صممت هذه القائمة الاستبائية .. لتستكشف مدى قابليتكم في مجال التعليم الرقمي .. وماهو استعدادكم الفعلي للاستزادة من المعرفة الرقمية للمساهمة في هذه العملية التطويرية .. ومدى مصداقية ودقة اجاباتكم .. سنتعكس على نجاح ومصادقية بحثنا هذا .. الذي يهدف بالدرجة الاساس الى تطوير العملية التعليمية المعمارية بشكل عام وتطبيق مفاهيمها في قسمنا بشكل خاص .. ولكم جزيل الشكر سلفاً

اولاً:- معلومات عامة عن المستبين

اسم التدريسي:				
الجامعة:				
اللقب العلمي				
عنوان البريد الالكتروني :				
الدرجة	عنوان المشروع او الأطروحة			
بكالوريوس <input type="checkbox"/>	التحصيل الدراسي			
ماجستير <input type="checkbox"/>				
دكتوراه <input type="checkbox"/>				
AutoCAD	3 D studio MAX	Maya	Archi cad	الدورات الحاسوبية التي اجتزتها
Photoshop	3 D home	Windows	Microsoft Office	
برامج اخرى تذكر:				

ثانياً:- ماهي المواد التي تدرسها في القسم ولأي مرحلة

المادة	المرحلة	عدد سنوات التدريس
1-		
2-		
3-		

ثالثاً:- حدد درجة المعرفة التي تمتلكها في التطبيقات البرمجية التالية مؤشراً ازاء الدرجة التي ترتئيتها :

المادة	معرفة جيدة	معرفة متوسطة	انعدام المعرفة	إذا كنت لا تمتلك اي معرفة بهذه المادة هل لديك رغبة في تعلمها
				نعم كلا
1				
2				
3				
4				
5				
6				
7				
8				
9				
10				
11				
12				
13				

رابعا:- الاسئلة الاستبائية : (إذا وجدت اي اشكال أو غموض في بعض الفقرات ممكن ان تتجاهل اجابتها)  
س1: ماهو موقفك من تقنية التعليم الرقمي بشكل عام , ومن استخدامها في التعليم المعماري على وجه الخصوص ؟

مؤيد ☐ معارض ☐



أخرى تذكر .....  
 س2 : ماهي وجهة نظرك في إمكانية تطبيق أسلوب التعليم الرقمي على المادة التي تقوم بتدريسها في القسم وماهي أكثر البرمجيات علاقة بهذا المجال .. إذا كان لديك مقترح في ذلك يرجى ان ترفقه طياً مع هذه القائمة الاستبائية .. مشكوراً  
☐ مؤيد ☐ معارض

أخرى تذكر .....  
 س3 : ما هي وجهة نظرك في إمكانية توظيف الحاسوب في تدريس مادة التصميم المعماري ؟ وما هو مقترحك في تأثير الحاسبة على العملية التقييمية .  
☐ مؤيد ☐ معارض

أخرى تذكر .....  
 س4 : أي الجوانب تعتقدها الأكثر تديلاً بتغيير نظام التعليم من التقليدي الى الرقمي وأي الفقرات تعتقدها ايجابية او سلبية .. حدد ذلك من خلال الجدول التالي .

	مفردات المقارنة بين التعليم التقليدي والرقمي	درجة التغيير			تقييم التغيير	
		كبيرة	متوسطة	قليلة	ايجابي	سلبي
1	تعليم التصميم المعماري					
2	الأهداف التعليمية					
3	أسلوب التدريس					
4	التفاعل بين الطالب والاستاذ					
5	موقف الطالب					
6	موقف الاستاذ					

س5 : هل تعتقد بأنه يجب أن نبدأ من وجهة نظر العمارة وننظر إلى ما يناسبنا في الحاسوب ؟	نعم <input type="checkbox"/>	كلا <input type="checkbox"/>	أخرى تذكر <input type="checkbox"/>
س6 : هل تعتقد ان الحاسوب يستخدم في توليد الافكار ويعد كاداة للعصف الذهني (أي يدخل في صميم التفكير الذهني المعماري) ؟	نعم <input type="checkbox"/>	كلا <input type="checkbox"/>	أخرى تذكر <input type="checkbox"/>
س7: هل تعتقد ان الحاسوب يعتبر كوسيلة مجردة تستخدم للأظهار المعماري من خلال استخدام برمجيات الرسم مثل الـ (AutoCAD) والـ (3 d studio max) والـ (Photo Shop) وغيرها .. شأنها شأن باقي ادوات الاظهار المعماري ؟	نعم <input type="checkbox"/>	كلا <input type="checkbox"/>	أخرى تذكر <input type="checkbox"/>
س8 : هل تعتقد ان الحاسوب يحدث تغيير أساسي في طريقة تدريس العمارة أم انه يتوقع أن يغير الحاسوب طريقة استيعاب ووصف العمارة ؟	نعم <input type="checkbox"/>	كلا <input type="checkbox"/>	أخرى تذكر <input type="checkbox"/>
س9 : هل تعتقد ان للحاسوب أهمية كبيرة في مراجعة التصاميم داخل المراسم .	نعم <input type="checkbox"/>	كلا <input type="checkbox"/>	أخرى تذكر <input type="checkbox"/>
س10: اذا كانت اجابتك على السؤال السابق (نعم) فهل تعتقد ان السبب هو لان هذه التقنية تمكن لجنة التحكيم (Staff) من فهم نوايا الطلبة لأنهم يستطيعون رؤية المبنى وبذلك يتخذ التقييم مسار مماثل للمهنة .	نعم <input type="checkbox"/>	كلا <input type="checkbox"/>	أخرى تذكر <input type="checkbox"/>
س11: هل تعتقد ان الحاسوب سوف يمكن طلبة العمارة من تصميم النظم والمباني في نفس الوقت وتصميم المباني من رؤية شاملة ؟	نعم <input type="checkbox"/>	كلا <input type="checkbox"/>	أخرى تذكر <input type="checkbox"/>
س12: هل تعتقد ان الحاسوب يمكن الطلبة من اختبار أفكارهم بسرعة وأن جودة تصاميمهم سترتفع إلى عدة اضعاف واقعا تحت ظل المنهج التقليدي .	نعم <input type="checkbox"/>	كلا <input type="checkbox"/>	أخرى تذكر <input type="checkbox"/>
س13 : هل تفضل ان يكون الاسلوب التعليمي ممتزج (أي يستخدم وسائط ممتزجة) من رسوم حرة , وسكيتشات , رسوم كومبيوتر ... الخ .	نعم <input type="checkbox"/>	كلا <input type="checkbox"/>	أخرى تذكر <input type="checkbox"/>
س14 : هل تعتبر دراية الطالب الفانقة في مجال تقنيات الحاسوب عاملاً أساسياً في قبوله في الاقسام المعمارية في يومنا هذا ؟	نعم <input type="checkbox"/>	كلا <input type="checkbox"/>	أخرى تذكر <input type="checkbox"/>
س15 : هل يتطلب العمل بتقنية التعليم الرقمي تغييراً جذرياً في مناهج التعليم المعماري ؟	نعم <input type="checkbox"/>	كلا <input type="checkbox"/>	أخرى تذكر <input type="checkbox"/>
س16 : هل يفضل ان يكون التغيير في مناهج التعليم المعماري عند استخدام تقنيات التعليم الرقمي بشكل تدريجي متضمناً بعض المواد الأساسية .. ومن ثم يتم توظيف باقي المواد الدراسية تدريجياً ضمن الخطة المنهجية المعدلة ؟	نعم <input type="checkbox"/>	كلا <input type="checkbox"/>	أخرى تذكر <input type="checkbox"/>
س17 : لو تم اقتراح تطبيق هذا النظام الرقمي على عينة منتخبة من خريجي المرحلة الثانية بعد اجراء اختبار لهم ليتم تشكيل صف خاص يدرس كافة المواد باستخدام الحاسوب (بعد تخصيص منهج خاص بهذا النوع من التعليم يتماشى مع المفردات الخاصة بالقسم) بعد توفير كافة التقنيات اللازمة لذلك وان لا يتجاوز عدد الطلبة المنتخبين عن (10) طلاب فهل تعتقد انها تجربة ايجابية أم سلبية ؟	ايجابية <input type="checkbox"/>	سلبية <input type="checkbox"/>	أخرى تذكر <input type="checkbox"/>